GSI

GSI Report 2010-1
June 2010

SCIENTIFIC REPORT 2009

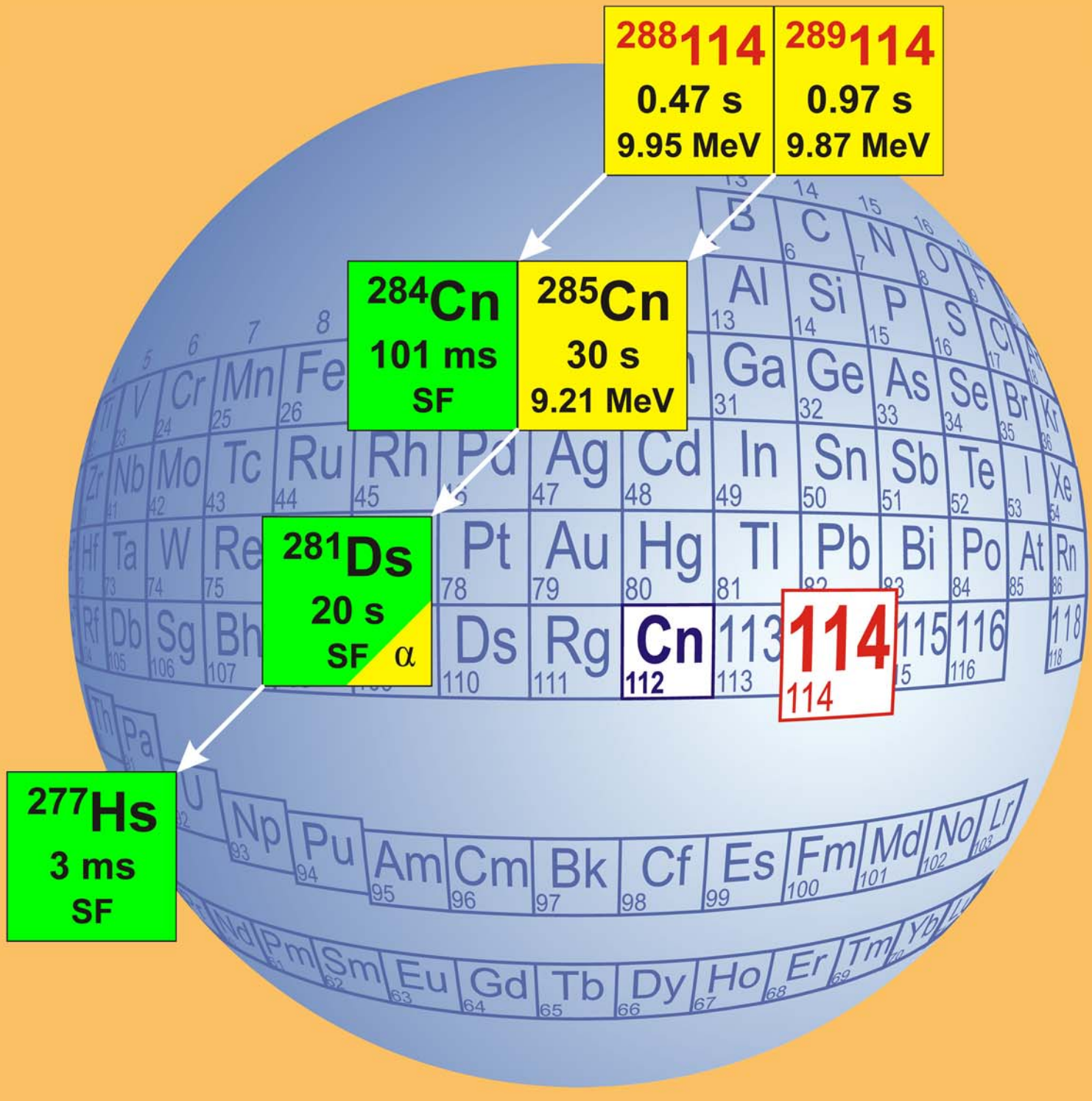

GSI Helmholtzzentrum für Schwerionenforschung GmbH

Cover Illustration:

The front cover shows in summary the nuclear decay chains measured in the first element 114 experiment at the GSI Helmholtzzentrum für Schwerionenforschung. This is the heaviest element ever observed at the GSI. A ^{48}Ca beam from the UNILAC impinging on ^{244}Pu targets was used for its synthesis. The isotopes ^{288}114 and ^{289}114 were separated with the highly efficient gas-filled recoil separator TASCA (TransActinide Separator and Chemistry Apparatus), and statistically highly significant data were obtained. A newly developed focal plane detector allowed for the safe identification of the nuclear decays of the element 114 isotopes and their daughter nuclides. A so far unknown α-decay branch in ^{281}Ds as well as the new isotope ^{277}Hs, which exhibits an interestingly short spontaneous fission half-life, were discovered in the course of this experiment, which was performed in the summer of 2009. Relatively high cross sections were measured for the element 114 isotopes, which pave the way for further experiments with this element.
The background displays in an artist's view the periodic table. It does not only reflect chemist's main "road map" but it also emphasizes the position of element 114 and alludes to the first element 114 chemistry experiment performed at GSI in the fall of 2009. Element 112, which was discovered several years ago by the SHIP group at GSI, is also highlighted. Most recently, the International Union of Pure and Applied Chemistry accepted the name Copernicium and the chemical symbol Cn for element 112, as proposed by the discovery team.

GSI Scientific Report 2009

GSI Report 2010-1
<http://www.gsi.de/library/GSI-Report-2010-1/>

ISSN: 0174-0814
and GSI Report 2010-1

Publisher: GSI Helmholtzzentrum für Schwerionenforschung GmbH,
Planckstr. 1, 64291 Darmstadt, Germany, <http://www.gsi.de>
GSI is a member of the Helmholtz association of national research centres <http://www.helmholtz.de>.
E-only-edition: <http://www.gsi.de/library/GSI-Report-2010-1/>

Editor: Katrin Große,
Contact: gsilibrary@gsi.de, phone: +496159 712610, fax: +496159 713049.
Cover: Brigitta Schausten.
Publication Date: June 2010
Technical Team at GSI: I. Giese, K. Große, U. Meyer, V. Schaa and K. Schiebel.

For the production of this report templates and scripts of the JACoW collaboration (Joint Accelerator Conferences on Web <http://www.jacow.org>) were used.

Contents

The FAIR Project Status*

FAIR Joint Core Team
GSI, Darmstadt, Germany

In 2009 the future management of FAIR has been selected. Boris Sharkov became the designated FAIR Scientific Director and Simone Richter became the designated FAIR Administrative Director. The planning for FAIR reached a milestone at which the future of the project had to be decided. German law requires that a project has to be fully funded at the start of construction. It became clear that the raised funds at that time were not sufficient to start the project as described in the Baseline Technical Report. The decision to be taken was: raise more funds until the entire facility is covered and delay the start of the entire construction or devise a startversion that allows the earliest start of construction.

The International Steering Committee (ISC) decided to go for the latter option. The FAIR Joint Core Team was ordered to generate together with the international science community a startversion of the FAIR project that fulfils the boundary conditions: does not exceed the funding, gives competitive and excellent research opportunities for all scientific pillars of FAIR, allows future upgrades that will ultimately cover the entire project as it is described in the Baseline Technical Report. This resulted in the so called *Modularized Startversion (MSV)*. It was described in the so called Green Paper, which reflects the consensus that was reached after intensive discussions with the scientific community. The MSV was only made possible by the generous offer of the State of Hesse and the German Federal Government to cover the site related costs of 110 Meuro. After intensive scientific and financial review the MSV was approved by the ISC in November 2009.

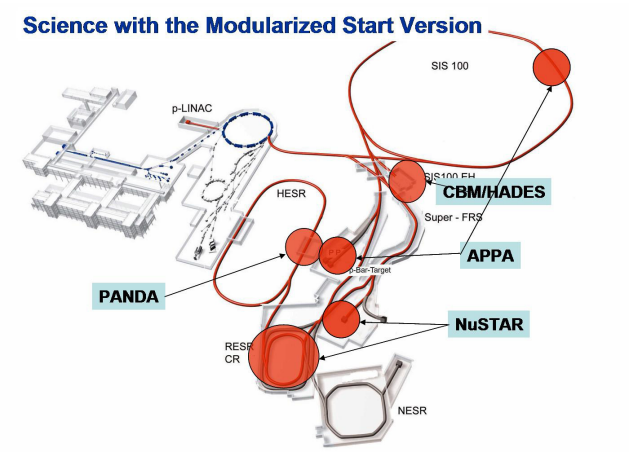

At this point the formal finalization of the various international documents that are a prerequisite for the creation of the FAIR company (and the respective funding) could be tackled. It is intended to formally sign the FAIR convention, which is an international treaty, in summer 2010. The creation of the FAIR GmbH will follow immediately after that event.

In autumn 2009 Saudi Arabia signed a declaration to become FAIR member state.

The GSI management decided to implement the structures of the FAIR GmbH within GSI as a separate department. This allows the build-up of FAIR staffing and a subsequent smooth transition from FAIR department to FAIR GmbH. The FAIR department consists of the following groups: administration, research, accelerators, site and building and the project office.

In parallel the FAIR experiment collaborations were successfully working towards the construction of the respective experiments, which is reflected in the 75 contributions to this annual scientific report. PANDA and CBM presented physics reports outlining their research opportunities. Several Technical Design reports by various collaborations have been submitted, resulting in some cases in early funding of components. Many collaborations tested prototypes of subcomponents. Great effort was made to optimize algorithms for reconstruction of data, which in some case led to a reduction of needed CPUs by orders of magnitude.

* Work supported by EU, FP7-211382

An improved alkali MOTRIMS target for experiments at HITRAP

S. Götz[1], T. Mullins[1], T. Amthor[1], R. Wester[3], A. Sokolov[2], W. Quint[2], and M. Weidemüller[1]
[1]Universität Heidelberg, Germany; [2]GSI, Darmstadt, Germany; [3]Universität Freiburg, Germany

We plan to investigate coherence effects in multiple charge transfer between neutral atoms and highly charged ions provided by the HITRAP facility. Neutral atoms trapped and cooled in a magneto-optical trap (MOT) will serve as a high-precision target. First experiments will focus on multiple-electron transfer reactions in collisions of many-electron atoms with highly charged ions such as $Rb+U^{92+}$. Before the start of these experiments, test measurements will be performed with Ar^{12+} and Ar^{16+} at the EBIT. So far, multiple electron transfer has been investigated in supersonic jet targets, where the targets were restricted to noble gases. This is why only multiple charge transfer for electrons from the same shell could be observed [1]. In addition, the initial momentum of the jet target limits the resolution on the recoil ion momentum.

Laser cooling can be realized with alkali atoms, whose shell structure allows for the observation of correlation effects between electrons from different shells [2]. Due to the very low temperature, the MOT provides a stationary target and the differential cross-sections in multiple charge transfer can be measured with very high accuracy [3]. Furthermore, full control over the internal state of the target can be obtained by optical pumping.

The ultracold target for HITRAP consists of an ultracold gas of rubidium atoms confined in a MOT in dark-SPOT configuration, reaching densities of $10^{11}\mathrm{cm}^{-3}$ in a volume of 0.8mm diameter. The temperature of the captured gas is around 100 μK which corresponds to momentum uncertainties of the individual target atoms of 0.01 a.u. The trap captures atoms of the isotope ^{85}Rb with nearly 100% isotope selectivity, and can, if desired, be reconfigured to store ^{87}Rb. Furthermore, the dark-SPOT configuration allows one to prepare the target atoms in a single hyperfine state of the electronic ground state with an efficiency of 99%.

The trap has been combined with a recoil ion momentum spectrometer. The whole setup is fully transportable and can be implemented into various setups at the GSI [4]. In preparation for the experiments at the EBIT and HITRAP at GSI trapped rubidium atoms have been ionized with ultrashort laser pulses via two-photon ionization. These tests revealed deviations from the behaviour expected from numerical simulations of the spectrometer [5], which are attributed to residual stray electric fields. For this reason, a new spectrometer will be implemented in the chamber, following the design described in [6]. More sophisticated and reliable simulations have been performed to determine the optimal resolution in both the time and position, and the new spectrometer is now in the process of being constructed (see Fig. 1).

With the recent move of the group to Heidelberg, two additional major improvements of the experimental setup are being implemented: First, the homebuilt diode lasers are currently being replaced with a commercial tapered amplifier system from Toptica [7], which provides more power while being more stable and more compact. Second, the loading concept of the magneto-optical trap has been redesigned. Instead of capturing atoms from the background gas, the MOT will be loaded from a slow atom beam provided by a 2D-MOT [8] which is currently under construction (Fig. 2). The 2D-MOT pre-cools the atoms in two dimensions down to a few tenths of m/s, while providing a high flux of up to 10^{10} atoms/s. This results in a faster loading of the 3D-MOT and in a significant increase of the measurement repetition rate, thus allowing for the detection of multiple electron capture in ion-atom collisions where the cross-sections are expected to be on the order of $10^{-15}\,\mathrm{cm}^2$.

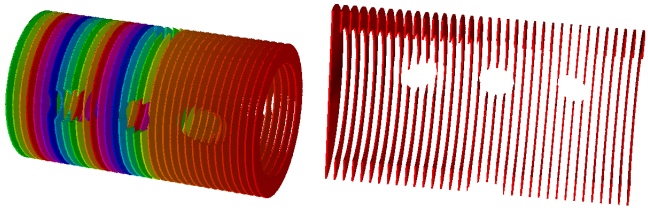

Figure 1: New recoil ion momentum spectrometer to be implemented in the setup: full 3d-arrangement of electrodes (left) and vertical cut (right). The holes provide access for laser beams and projectile ions.

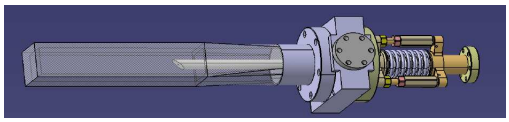

Figure 2: 2D-MOT setup with glass cell and mechanical parts for atom beam alignment.

References

[1] J. Ulrich et al., Rep. Prog. Phys. 66, 1463-1545 (2003)
[2] S. Knoop et al. Europhys. Lett. 74 (6), pp. 992 -998 (2006)
[3] B. DePaola et al., Adv. At. Mol. Opt. Phys. 55, 139 (2008)
[4] W. Salzmann, Dissertation, Universität Freiburg (2007)
[5] I. Blank, Diplomarbeit, Universität Freiburg (2008)
[6] H. Nguyen et al., Rev. Sci. Inst. 75, 2683 (2004)
[7] http://www.toptica.com
[8] K. Dieckmann et al., Phys. Rev. A 58, 3891 (1998)

Micro-fabrication of MMC arrays for high resolution x-ray spectroscopy

A. Fleischmann[1], L. Gastaldo[1], S. Kempf[1], A. Kirsch[1], A. Pabinger[1], C. Pies[1], J.P. Porst[1], P. Ranitzsch[1], S. Schäfer[1], F.v. Seggern[1], T. Wolf[1], and C. Enss[1]

[1]Kirchhoff-Institut für Physik, Universität Heidelberg, INF 227, 69120 Heidelberg, Germany

Metallic magnetic calorimeters (MMC) are calorimetric particle detectors operated at temperatures below $100\,\mathrm{mK}$, that make use of a paramagnetic temperature sensor to transform the temperature rise upon the absorption of a particle in the detector into a measurable magnetic flux change in a dc-SQUID. They combine high energy resolution, high quantum efficiency and large dynamic range [1], turning them into promising tools for numerous precision experiments in atomic and nuclear physics at GSI/FAIR. An attractive count-rate should be achievable even in experiments with a rather small photon flux by using arrays of MMCs to increase the covered solid angle.

We recently started to develop the thin film deposition and structuring techniques for the micro-fabrication of two types of MMC arrays, one for photon energies up to 10 keV with an energy resolution below 2 eV (FWHM), the other for energies up to 200 keV with $\Delta E_{\mathrm{FWHM}} \leq 50\,\mathrm{eV}$.

All of our presently developed MMCs consist of a x-ray absorber made of electro-deposited Au and a paramagnetic temperature sensor made of sputtered Au:Er. A superconducting meander-shaped pickup coil made of a sputter-deposited niobium is used to generate the magnetic field in the sensor volume and to pickup the change of magnetization upon the absorption of a photon. The meander is connected to the input coil of a SQUID, forming a completely superconducting circuit. An on-chip persistent current switch is used to inject the field generating current into the superconducting circuit.

The performance of micro-fabricated MMCs depends strongly on the thermodynamical properties of the deposited thin film materials. Of particular importance are the critical current of the niobium structures, the paramagnetic behavior of the Au:Er temperature sensor as well as the specific heat and the thermal conductivity of the x-ray absorbers. The involved deposition techniques, i.e. sputtering and electro-plating, have been continuously improved during the last years and most of the thermodynamical properties are reaching values close to the ones of bulk material [1], allowing for a detector performance close to optimum.

The SEM pictures in fig. 1a-d show some details of the presently developed detectors for soft x-rays [1]. In most of these devices the niobium lines of the meander-shaped pickup are $2.5\,\mu\mathrm{m}$ wide as shown in fig. 1a. The critical current density is about a factor of two larger than required for optimal operation. The persistent current switch, labelled 'SW' in fig. 1b, is formed by a U-shaped extension of the meander-circuit that can be heated above T_c by a AuPd heater. The Au:Er sensors on top of the meanders are co-sputtered form a pure gold target and Au:$\mathrm{Er}_{750\mathrm{ppm}}$ target to adjust the Er concentration. They are connected

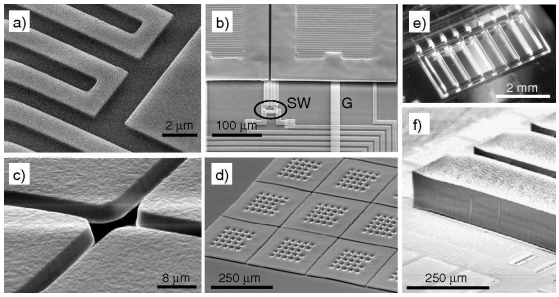

Figure 1: SEM and microscope pictures of MMCs.

to the thermal bath via metallic thermal links made of gold ('G' in fig. 1b) to tune the thermalization time to $1\,\mathrm{ms}$. The $5\,\mu\mathrm{m}$ thick, overhanging x-ray absorbers (fig. 1c, d) are produced by electroplating Au into a two-layer photo-resist mold. In recent devices the absorber is connected to the sensor only through 10 to 20 stems with $10\,\mu\mathrm{m}$ diameter, to reduce the loss of athermal phonons to the solid substrate, which otherwise would cause low energy tails of lines in x-ray spectra. The imprint of the stems in the absorber surface can be seen fig. 1d.

Pickup coil and Au:Er sensor of MMCs for photon energies up to 200 keV are fabricated similarly, but cover a larger area of $0.5 \times 2\,\mathrm{mm}^2$. The electro-deposition of the $200\,\mu\mathrm{m}$ thick Au absorbers had been a challenge for a while, which was recently solved using molds of tall SU-8 photo-resist walls as shown in fig. 1e and described in [2]. Fig. 1f shows three Au absorbers of the first 1×8 array.

One of the MMCs for soft x-rays described above was tested with x-rays from an ^{55}Fe source. Fig. 2a shows the measured K_α line of ^{55}Mn and, superimposed, the natural line shape convoluted with a 2.8 eV (FWHM) wide gaussian instrumental line shape. The detector response to 3 single x-rays is shown in 2b. The fast signal rise is well described by the expected Korringa relaxation time of $\tau \simeq 90\,\mathrm{ns}$ of Er in Au as discussed in [1].

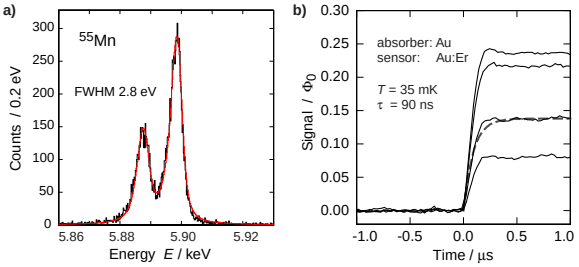

Figure 2: a) K_α line of ^{55}Mn. b) Signal rise of MMCs.

References

[1] A. Fleischmann et al., *Metallic magnetic calorimeters*, AIP Conf. Proc. **1185**, 571 (2009)

[2] C. Pies et al., *MMCs for high precision QED tests at GSI/FAIR*, AIP Conf. Proc. **1185**, 603 (2009)

Recovery and Damage of PWO-II Crystals of the PANDA-EMC*

R. W. Novotny[1], D. Bremer[1], W. Döring[1], V. Dormenev[1], P. Drexler[1], T. Eissner[1], M. Moritz[1], R. Schubert[1], and for the PANDA collaboration
[1]2nd Physics Institute, JLU, Giessen, Germany

For the realization of the electromagnetic calorimeter (EMC) of the target spectrometer of PANDA [1] several major steps have been achieved.

The delivery and the quality control of the ~7.500 PWO-II crystals were completed end of 2009. The available crystals serve completely both end-caps as well as a small part of the barrel section. The quality control, performed partly in collaboration with CMS-ECAL at CERN, covers the geometrical dimensions, optical and scintillation quality as well as the radiation hardness using a high integral dose imposed by a set of strong ^{60}Co sources. The excellent performance was confirmed by a low rejection rate of approximately 10% primarily due to the very selective limit on radiation hardness.

The final operation of the calorimeter at low temperatures of T=-25°C requires extremely high radiation resistivity. The overall loss of the effective light yield at the emission wavelength near 420nm depends on the concentration of defects in the crystal. In order to quantify the radiation hardness, the longitudinal optical transmission of the full size PWO-II crystal is measured before and immediately after irradiation with γ-rays (30Gy) in the region of wavelengths between 300nm and 900nm, respectively, in order to determine the induced absorption coefficient dk. The two top curves in Fig. 1 show the spectral distribution of the induced absorption 1 and 31 minutes, respectively, after irradiation to illustrate thermally induced recovery.

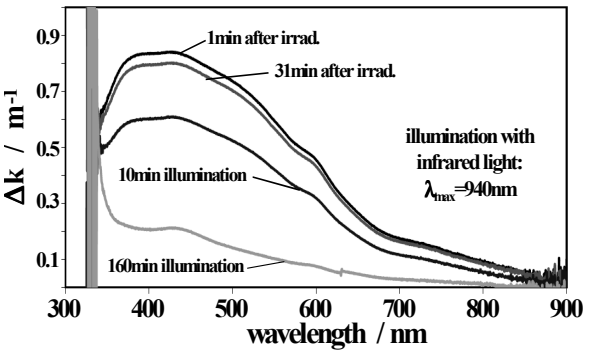

Figure 1: Change of the spectral distribution of the induced absorption coefficient dk after irradiation with γ-rays (30Gy) due to thermal and stimulated recovery with infrared light of 940nm wavelength. The measurement was performed at room temperature.

During detailed investigations an unexpected new effect, described as stimulated recovery [2], was observed. It turned out that exposing the crystal to external light could significantly enhance the relaxation processes. Light emitting diodes (LED) of different colours with relatively narrow emission bands have been used. Even infrared light with a wavelength well above 1000nm can recover the optical transparency within a short period as illustrated in Fig. 1 for a wavelength of 940nm measured at room temperature. In contrast to the well known bleaching technique with high-energetic light leading to an ionization of the excited colour centres, stimulated recovery relies only on a moderate excitation.

The mechanism has been observed as well at low temperatures. Fig. 2 illustrates the recovery of the signal amplitude of a cooled detector due to illumination with blue light (λ_{max}=464nm, photon flux $6 \cdot 10^{16}$photons/s). Similar results were obtained as well applying infrared light.

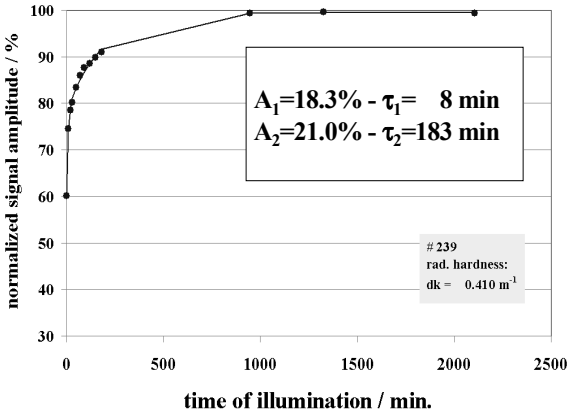

Figure 2: Recovery of a PWO-II detector after irradiation with 30Gy using blue light for stimulation. The device was cooled down to a temperature of T=-25°C.

The reported experimental results propose the unexpected opportunity to cure the radiation damage by illumination with external light with minimal energy in the infrared region, which the photo sensors used to convert the scintillation light into an electrical signal might even not recognize. Therefore, a concept of an on-line recovery during PANDA operation is under investigation.

The application concepts for recovery of PWO crystals on- or off-line with respect to the detector operation in an ionizing radiation environment and the basic layout are part of the submission of a national patent in Germany (TM 382_DE).

References

[1] "Technical Design Report for: PANDA Electromagnetic Calorimeter (EMC)", arXiv:0810.1216v1, October 2008.

[2] R. W. Novotny et al., Conference Record, IEEE NSS 2009, Orlando, FL, 25-31 October, ISBN: 978-1-4244-3962-1, N32-2.

The backward endcap of the $\overline{\text{P}}$ANDA electromagnetic calorimeter

D. Khaneft[1,2], Y. Ma[1,2], F.E. Maas*[1,2], M.C. Mora Espí[1,2], D. Rodriguez Pineiro[1,2], and M. Zambrana[1,2]

[1]GSI, Darmstadt, Germany; [2]KPH, Mainz University, Germany

The backward endcap EMC[1, 2] is a part of electromagnetic calorimeter of the $\overline{\text{P}}$ANDA experiment as shown in Fig.1. It is designed for detection of low energy particles produced at target region. The angular range covered by the backward endcap is $\theta = 145.7^\circ - 167.1^\circ$ and energy range is $0.01 - 0.7$ GeV.

For calculation of a energy resolution and efficiency of the endcap a series of simulations have been performed. Following simulation parameters were used:

- Energy: $0.03, 0.1, 0.25, 0.5, 0.7$ GeV
- $\phi : 1^\circ, 22.5^\circ, 45^\circ$
- $\theta : 145^\circ, 150^\circ, 155^\circ, 160^\circ, 165^\circ$

These energies have been chosen in order to cover energy range of particles which are expected in a backward direction. Angular sets of parameters corresponds to possible trajectories of particles. For each set of parameters 50000 event have been generated. All detectors has been implemented except for materials representing cabling, cooling, readout electronics or support structure.

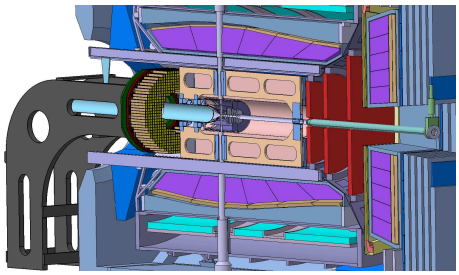

Figure 1: $\overline{\text{P}}$ANDA target spectrometer. EMC backward endcap crystals are shown with a yellow color

For event selection a special cut was used in order to select one bump with the highest energy per event before applying a Novosibirsk function[3] for data analysis (see Eq.1).

$$f(E) = A \cdot exp\{-\frac{1}{2}[\frac{ln^2(1+\Lambda\tau(E-E_0))}{\tau^2} + \tau^2]\}, \quad (1)$$

where $\Lambda = \sinh(\tau\sqrt{ln4})/(\sigma\tau\sqrt{ln4})$, the peak position E_0, the width is σ and τ is a parameter for tail part.

For calculation of the energy resolution and efficiency of the backward endcap EMC Eq. 2 and Eq. 3 were used. Energy resolution was calculated as a half width at half maximum of a fit of an energy spectra(see Fig. 2).

$$E_{res} = 2\sigma\sqrt{ln4}/E \quad (2)$$

$$Eff = \frac{1}{50000}\int_{\mu-3\sigma}^{\mu+2\sigma} f(E)dE \quad (3)$$

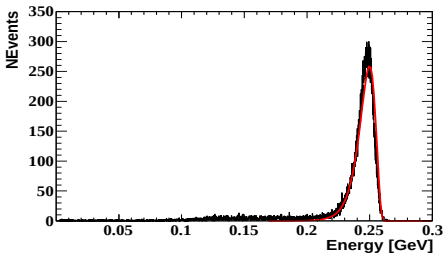

Figure 2: Energy spectra (black line) and fit by the Novosibirsk function (red line) with following parameters of the generated photons: $E_{photon} = 0.25$ GeV, $\phi = 45^\circ, \theta = 155^\circ$

Results of the analsysis for one energy are shown in table 1. During the analysis all data simulated with $\theta = 145^\circ$ and $\theta = 165^\circ$ was rejected because at these angles photons pass through edges of the backward endcap only. The results show that the backward endcap EMC has a very good energy resolution and efficiency but more simulations are needed in order to take into account not only influence of detectors but also the dead materials between target and the endcap.

	$E = 0.25$ GeV		
	$\theta = 150^\circ$	$\theta = 155^\circ$	$\theta = 160^\circ$
$\phi = 1^\circ$	$Eff = 0.86$	$Eff = 0.84$	$Eff = 0.94$
	$E_{res} = 0.24$	$E_{res} = 0.06$	$E_{res} = 0.06$
$\phi = 22.5^\circ$	$Eff = 0.83$	$Eff = 0.85$	$Eff = 0.94$
	$E_{res} = 0.19$	$E_{res} = 0.06$	$E_{res} = 0.06$
$\phi = 45^\circ$	$Eff = 0.85$	$Eff = 0.85$	$Eff = 0.94$
	$E_{res} = 0.18$	$E_{res} = 0.06$	$E_{res} = 0.07$

Table 1: Results of simulations for photons with energy $E = 0.25$ GeV

References

[1] $\overline{\text{P}}$ANDA collaboration, Physics performance report for $\overline{\text{P}}$ANDA.

[2] $\overline{\text{P}}$ANDA collaboration, Technical design report for $\overline{\text{P}}$ANDA Electromagnetic Calorimeter.

[3] R. Sobie, Nucl. Phys. Proc. Suppl. 169 (2007)

* f.maas@gsi.de

Low kaon identification using a TOF system at PANDA*

A. Sanchez Lorente†[1] and J. Pochodzalla[1]
[1]U Mainz, Germany

Mandatory for the performance of hypernuclei physics at the $\overline{\mathrm{P}}$anda experiment, is the production of low momentum Ξ^- via the $\overline{p} + p \rightarrow \Xi^-\overline{\Xi}^+$ reaction(See ref. [1, 3]). Because the value of this cross section is likely 4 order of magnitude lower than the one corresponding to the $\overline{p} + p$ annihilation process, the background suppression plays an important role in the unique identification of hypernuclei. Moreover, the mayor part of the associated $\overline{\Xi}^+$ annihilates inside the residual target nucleus releasing in most cases two positive kaons. Theses kaons are emitted particularly into the forward region, providing with its identification a possibility to tag the production of Ξ^- hyperons. In the present work, we introduce a strategy to identify low momentum kaons via a TOF(Time of flight system) in combination with the tracking performance of the TPC detector at $\overline{\mathrm{P}}$ANDA. The TOF system consist of a scintillating fibers array and a cylindrical scintillator detector, which provide the start and stop time measurement respectively.

The TOF scintillator barrel at $\overline{\mathrm{P}}$anda consist of 16 slabs ($3\times0.5\times180$ cm) and it is place between the TPC and the DIRC detectors. The scintillating fibers array is placed upstream around the hypernuclear target. It consist of 1200 scintillating fibers(1. meter length) arranged into two rings parallel to the beam axis.

Kaons emitted from the annihilation of $\overline{\Xi}^+$ process, have typically a momentum of 500 MeV/c. The identification procedure consist in measuring the time of flight of particles track candidates crosssing the fibers array, the TPC and the scintillator barrel detector. With a magnetic field of 2 T only particles(kaons) above 300 MeV/c will fulfil this condition. Reducing the magnetic field to 1 T, the number of low momentum particles fulfilling the above condition is then larger. The mass of the particle is then reconstructed, making use of time of flight measurent, the track length and the momentum provided by the tracking algorithm.

The efficiency of the discussed low momentum kaon trigger has been tested by using a montecarlo simulation of the above mentioned detector setup(Fig. 1). The simulation revealed that for low momentum kaon identification the stop detector must provide a time resolution of < 100 ps, whereas the fiber detector has to provide the start time with a minimum resolution of about 400 ps.

Of course, the choice of start detector with a time resolution comparable to the one of the stop detector improves enormously the identification efficiency(See Fig. 2).

For instance, in the simulation of the hypernuclei signal(ref. [4], from 50000 produced Ξ^- + $\overline{\Xi}^+$ pairs, only 15000 Ξ^- leads to the hypernuclei formation. Taking into account the low kaon trigger under the conditions of 1 T magnetic field and a start time resolution of about 80 ps, one obtain an efficiency of the 25% which means a value of 3000 produced hypernuclei.

One can concludes that a background suppression strategy based on the identification of low momentum kaons is not enough as stand-alone method but it can be combined with other techniques discussed in previous reports(See [2]) providing better results.

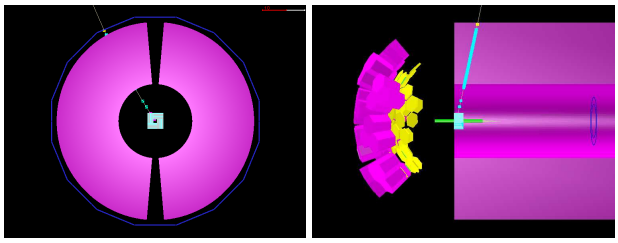

Figure 1: Left and right panel show respectively the X-Y and Y-Z view of the TOF system layout. In both cases a kaon track is denoted by its hits on the fibers array, TPC and TOF barrel.

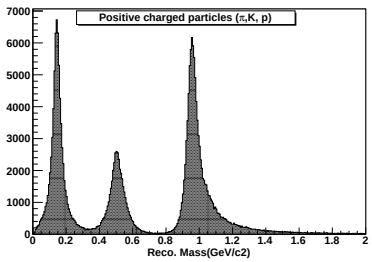

Figure 2: Mass reconstruction for positive charged pion, proton and kaons. The time resolution of TOF start and stop detector is 80 ps, the resolution of the reconstructed momentum and length is 1% and 3% respectively. The magnetic field value was reduced to 1 T to increase the detector acceptance.

References

[1] Technical Progress Report for PANDA
[2] A. Sanchez Lorente et al., Spectroscopic studies of ΛΛ–Hypernuclei at PANDA, in GSI Sci. Rep. 2008
[3] Physics Book Report for PANDA
[4] A. Sanchez Lorente. PhD thesis, U Mainz.

*This research is part of the EU integrated infrastructure initiative Hadronphysics project under contract number RII3-CT-2004-506078 and by the BMBF under contract number 06MZ225I.
† lorente@kph.uni-mainz.de

Lifetime Measurements of Microchannel Plate PMTs*

A. Lehmann†[1], A. Britting[1], W. Eyrich[1], S. Reinicke[1], F. Uhlig[1], and PANDA Cherenkov group

[1]Physikalisches Institut IV, Universität Erlangen-Nürnberg, Erwin-Rommel-Str. 1, D-91058 Erlangen

Introduction

Microchannel plate (MCP) PMTs are promising candidates for the photon sensors of the DIRC Cherenkov detectors at the PANDA experiment. They allow the detection of single photons with an outstanding time resolution of ≈ 50 ps even inside a high magnetic field. The main drawback of these devices is, however, their limited lifetime, usually given as the accumulated anode charge per area. Since the flux of charged particles in PANDA will be quite high, a photon rate of up to several MHz/cm^2 is expected at the sensor surface. Assuming a gain of 10^6/photon this flux can add up to an integrated anode charge of several C/cm^2/year, dependent on the size of the focal planes of the DIRC.

Setup

Usually the manufacturers do not provide information about the lifetime of their MCP-PMTs. For this reason our group has built a test bench that allows a long-term illumination of MCPs with pulsed LED light (480 nm, $<$2 MHz rate). While the light attenuated to the few photon level shines onto the MCP-PMT its signal is continuously monitored and recorded with a CAMAC DAQ system. From the pulse height distribution the gain and the number of photo electrons can be deduced. In irregular time intervals the quantum efficiency (QE) of the MCP's photo cathode is determined with an in-house setup.

The setup for the QE measurements consists of a halogen lamp, a grid-based monochromator with a resolution of $\sigma_\lambda \approx 1$ nm, and a calibrated reference diode (Hamamatsu S6337-01). After a certain warm-up period the lamp is stable enough that the following consecutive steps can be performed: first the current of the illuminated reference diode is measured between 200-800 nm; afterwards the current of the MCP-PMT (with cathode, MCPs and anode shorted) is determined over the same spectral band. Together with the calibration curve of the reference diode the QE of the MCP's photo cathode can then be calculated from these two measurements. The whole procedure is automated and takes only about 30 minutes.

The first lifetime measurement was performed with a single anode MCP-PMT (#82) with 6 μm pores from BINP in Novosibirsk, Russia. This device is equipped with a 5-10 nm aluminium-oxide layer at the entrance of the first MCP stage to stop feed-back ions. The data taking was started with a gain of $\approx 7 \cdot 10^5$, an LED rate of 200 kHz (later 500 kHz) and $\approx$3 photo electrons per light pulse. The stability of the LED was monitored with a photo diode.

* Work supported by BMBF and GSI

† lehmann@physik.uni-erlangen.de

Results

The results of the first lifetime measurements are shown in Fig. 1. From the plot it is obvious that the long-term behaviour of the QE depends on the wavelength: at an anode charge of 80 mC/cm^2 the QE is reduced by $\approx$50% at 400 nm and by a factor 10 at 700 nm.

During the whole illumination period the gain remained almost constant. The dark current of the MCP-PMT did also not change. This indicates that the QE is the most important parameter to characterize the MCP-PMT's lifetime.

Fig. 2 shows anode charge versus illumination time. At 200 kHz LED rate the slope of the curve gets shallower which reflects the diminishing QE. The kink at $4.6 \cdot 10^6$ s is caused by an increase of the LED rate to 500 kHz.

The next lifetime measurements are planned with an 8x8 pixel multi-anode MCP-PMT of Photonis-Burle with 25 μm pore diameter and with the new Hamamatsu R10754-00-L4 1x4 pixel linear array MCP-PMT with 10 μm pores.

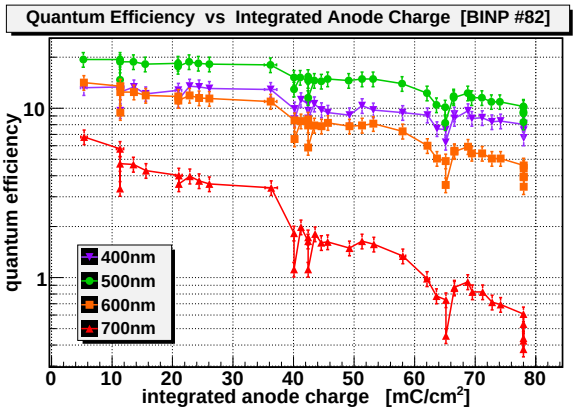

Figure 1: Quantum efficiency of the BINP MCP-PMT as a function of the integrated anode charge.

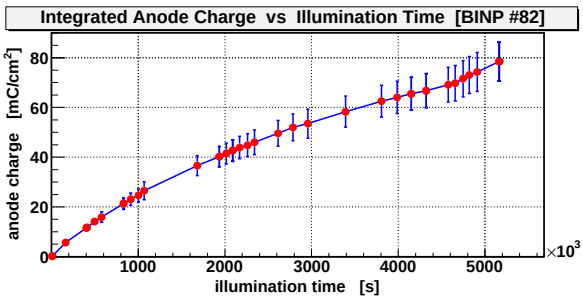

Figure 2: Integrated anode charge as a function of the illumination time. The covered period corresponds to roughly 2 months of permanent illumination.

Progress in the simulation of PANDA barrel DIRC *

D. Dutta[†1], B. J. Roy[‡1], K. Goetzen[1], R. Hohler[1,2], D. Lehmann[1], K. Peters[1,2], G. Schepers[1], C. Schwarz[1], J. Schwiening[1], and C. Sfienti[1,3]

[1]GSI, Darmstadt, Germany; [2]Goethe Universität Frankfurt, Germany; [3]Università degli Studi di Catania, Italy

An excellent particle identification (PID) of hadrons and leptons over a large range of solid angle and momenta is an essential requirement for the precision measurement aims in PANDA experiment at FAIR, GSI [1]. For charged hadron identification in the barrel region of the PANDA detector, a compact imaging Cherenkov detector following the DIRC (Detection of Internally Reflected Cherenkov light) principle is foreseen [2]. The simulation, realistic digitization and reliable reconstruction of the Cherenkov angle is mandatory for the performance study of the full PANDA detector system. In this contribution, we will discuss the progress in the simulation of the barrel DIRC in the PandaRoot framework.

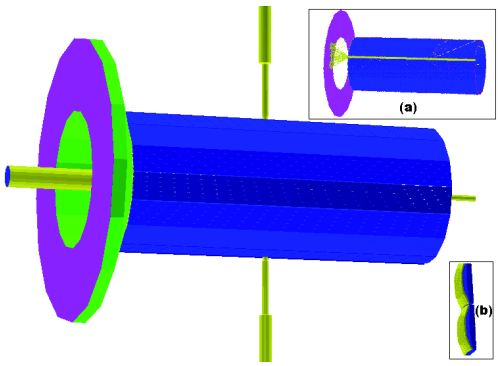

Figure 1: Picture of barrel DIRC of PANDA detector in the PandaRoot framework.

The barrel DIRC of PANDA covers the angular region from $\theta = 22^\circ$ to 140°. Fig 1. shows the barrel DIRC as implemented in the PandaRoot. It consists of 1.7 cm thick quartz radiators in a 16 fold geometry (blue colour) surrounding the beam line at a radial distance of 48 cm. The beam comes from the left. The target beam pipe crosses the barrel vertically through a split in the barrel. In the forward direction the ends of the radiators are covered with mirrors reflecting the Cherenkov light back towards the photon detector. In the backward direction, each radiator bar is coupled to two convex lenses at the end. Behind the lens, after a separation of thin air gap, the entrance window of the photon detector vessel (green colour) follows. The Cherenkov photons will be focussed by the lens on the photon detector plane (magenta colour) at a distance of 25 cm from the entrance window. The propagation of Cherenkov photons through the bar to the photon detection plane is shown in the insert (a) of Fig. 1 and the detailed lens structure is shown in the insert (b) of Fig. 1.

Simulation is a crucial requirement for detector optimization and a realistic digitization is necessary to get an output which is close to the expected experimental measurement. A C^{++} class has been implemented in PandaRoot which includes the following realistic detector information motivated by the expected choice of photon detector (e.g. MCP PMT):

- Pixelisation of the photon detector (6.5 mm grid),
- Convolution with detection efficiency of photocathode,
- Gaussian smearing of time (σ = 50 ps).

Fig. 2 shows the wavelength spectrum of the detected photons after convolution of the Cherenkov photon spectrum with the detection efficiency of bi-alkali photocathodes. The x-y distribution of the hits in the photon detector plane for an incident kaon of momentum 2 GeV/c, after efficiency correction and pixelisation of the detector plane, is shown in Fig. 3. This shows the expected ring like structure in the photon detector plane. Based on this hit information a reconstruction algorithm will be developed providing the Cherenkov angle as input for a global PID estimation.

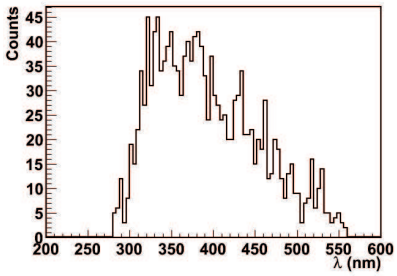

Figure 2: The wavelength spectrum of the detected photons.

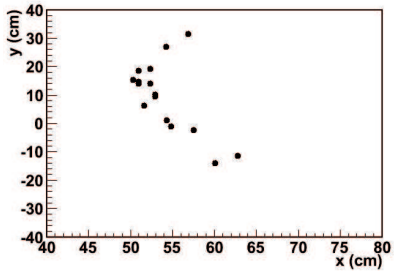

Figure 3: The expected ring structure in the photon detector plane for an incident kaon with momentum 2 GeV/c.

References

[1] Physics Performance Report, PANDA Collaboration (W. Erni et al.), arXiv:0903.3905v1.

[2] C. Schwarz et al., NIM A 595 (2008) 112, "The barrel DIRC of the PANDA experiment".

* Work supported by HIC for FAIR

† Also at Nuclear Physics Division, BARC, Mumbai, India

‡ Also at Nuclear Physics Division, BARC, Mumbai, India

Studying Disc DIRC Prototype Detectors for PANDA*

M. Düren[†1], I. Brodski[1], K. Föhl[1], A. Hayrapetyan[1], P. Koch[1], K. Kreutzfeldt[1], B. Kröck[1], O. Merle[1], M. Sporleder [1], H. Stenzel[1], and M. Zühlsdorf[1]

[1]II. Phys. Inst., Justus-Liebig-Universität, Heinrich-Buff-Ring 16, 35392 Giessen, Germany

Disc DIRC Designs for PANDA

The upcoming PANDA antiproton experiment at FAIR will focus on hadron spectroscopy in the charmonium region, and a particular interest is the identification and study of candidates for exotic states such as glueballs and hybrids. This requires excellent particle identification (PID) capabilities in the whole detector acceptance. In the forward endcap region a PID detector based on the DIRC principle [1] is proposed, as it allows a very compact and cost saving design of the PANDA target spectrometer.

In the proposed DIRC detector Cherenkov light is generated in a transparent radiator disc where it propagates by internal total reflection to the photon detectors at the rim of the disc. There are two basic approaches to access the Cherenkov angle from the registered photons. Using focussing light-guides the PID information can be accessed by converting angular to position information on a pixelized photon detector [4]. Without focussing light-guides the angular information can be accessed by measuring the time-of-propagation (TOP) of the Cherenkov photons inside the radiator disc [2, 3].

In a novel hybrid design the two concepts are combined by using small light-guides at the rim of the disc that allow a TOP and an angular measurement at the same time.

Testing DIRC detectors at GSI

A TOP disc DIRC prototype, which had been installed at a DESY test beamline in 2008 using 4 GeV electrons has been further investigated in Giessen using cosmic radiation. Fast multi-channel-plate PMTs (MCP-PMTs) from BINP Novosibirsk Institute were used to detect the Cherenkov photons.

A first prototype of a simple hybrid detector has been build from acrylic glass and tested in 2009 at the GSI beam facilities using $T = 2$ GeV protons. It has a small focussing light-guide (see Figure 1) that is attached to a small radiator bar. The prototype was mounted on a rotatable table so that the focussing properties of the detector could be tested.

The Cherenkov photons were detected by four $1\times1\,\mathrm{mm}^2$ MEPhI-PULSAR Geiger mode APDs. The G-APDs have excellent resolution as shown in Figure 2 [5]. The analysis of the test data that were taken at several radiator angles is still continuing, and we prepare to measure again with this setup in early 2010.

* Work supported by GSI and BMBF

† Michael.Dueren@uni-giessen.de

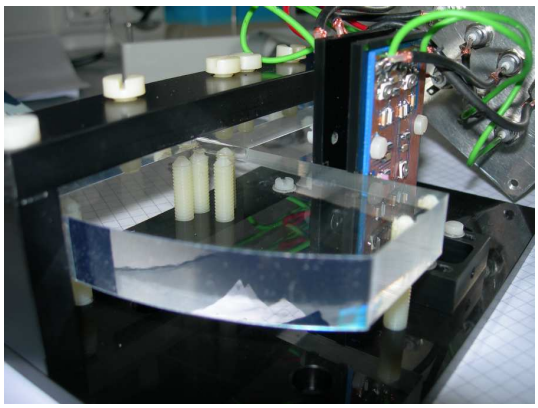

Figure 1: A first hybrid DIRC detector made from an acrylic glass radiator bar and a focussing element that is instrumented with 4 Geiger mode APDs.

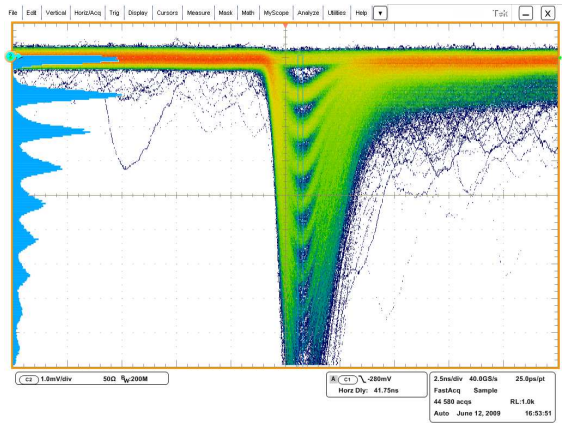

Figure 2: Accumulated G-APD pulse shapes. The vertical blue amplitude histogram at the left side resolves photo electron multiplicities.

References

[1] The BaBar-DIRC Collaboration, I. Adam *et al.*, The DIRC Particle Identification System for the BABAR Experiment, Nucl. Instr. and Meth. A **538** (2005) 281

[2] M. Düren *et al.*, The Panda time-of-propagation Disc DIRC, 2009 JINST 4 P12013

[3] O. Merle *et al.*, Reconstruction methods for the $\bar{\mathrm{P}}$ANDA Time of Propagation Disc DIRC, 2009 JINST 4 P09008

[4] K. Föhl *et al.*, The focussing light guide disc DIRC design, 2009 JINST 4 P11026

[5] B. Kröck, diploma thesis, Univ. Giessen 2009

Beam test of a DIRC-barrel-segment for the PANDA Experiment *

R. Hohler[1,2], D. Dutta[†1], D. Lehmann[1], K. Peters[1,2], B. Roy[‡1], G. Schepers[1], C. Schwarz[1], J. Schwiening[1], C. Sfienti[§1], and A. Vañó Viñuales[3]

[1]GSI, Darmstadt, Germany; [2]Goethe Universität Frankfurt, Germany; [3]Universitat de les Illes Balears, Spain

Particle identification (PID) for hadrons and leptons over a large range of solid angles and momenta is an essential requirement for meeting the physics objectives at the PANDA detector. The charged PID in the barrel section of the target spectrometer [1] has to work in a strong magnetic field of $B = 2$ T. Additionally, it cannot take too much radial space, since it is surrounded by an electromagnetic calorimeter which should be kept small in volume. The detection of momenta up to 3.5 GeV/c can be performed by the Detection of Internally Reflected Cherenkov (DIRC) [1] light as realized in the BaBar detector [2, 3]. Particles in the angular range of $22^\circ - 140^\circ$ are relatively slow, so that one can use materials with high refraction indices favoring the internal reflection of photons. The lower momentum threshold of kaons producing Cherenkov light is as low as $p = 460$ MeV/c for an refractive index of $n = 1.47$.

A prototype of a segment of this counter was tested in a 2 GeV test beam with protons in September 2009. The setup is a radiator coupled to an expansion box with photon detection on its back. The readout electronics operate in close distance to the photon detector and send the data by network to the backend computers.

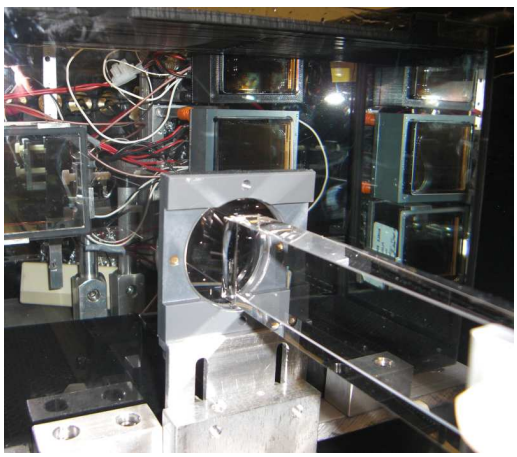

Figure 1: Prototype setup for measurements in proton beams. The radiator coming from the bottom right is hit by a relativistic proton beam and the Cherenkov photons propagate towards the photon detectors seen as square objects at the back of the expansion volume.

The proton beam hit the quartz bar with different adjustable angles. A scintillator paddle is used as coincident trigger. Four 8x8 pixel MCP-PMTs from Burle are attached at the rear side of a expansion box filled with Marcol-81 oil (Fig. 1. The synthetical fused quartz radiators are coupled to this expansion box with a focussing lens. The oil with a refractive index similar to that of the radiator minimizes image distortions of the Cherenkov rings. The NINO-discriminators of each amplified (x10) MCP-PMT channel are set to thresholds of 44 mV. Finally, for the readout 2 HADES-TRB (TRBv2) are used [4].

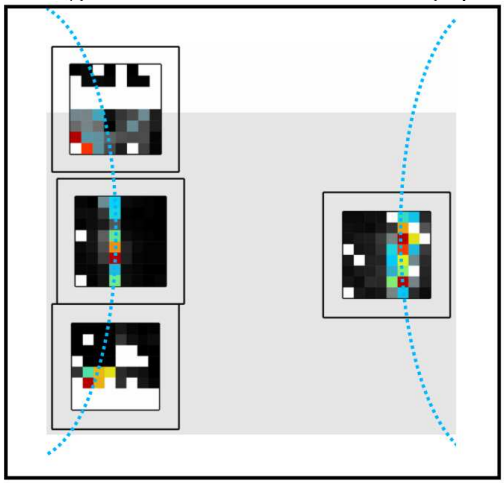

Figure 2: The observed Cherenkov ring pattern with the expected position (dotted lines). The shaded area is explained in the text

The measured pixel pattern of the four MCP-PMTs is shown in Fig. 2. The left top detector covers only partially the acceptance of the expansion volume indicated by the gray shaded area. The left bottom detector suffers from broken electronic channels. The expected ring structures as indicated by the dotted lines are cleary seen. They also move in the right way, when the inclination angle of the beam with the radiator is changed.

References

[1] C. Schwarz, J. Inst. 4 (2009) P12016,

[2] I. Adam et al. , Nucl. Inst. Meth. **A538**, 281 (2005).

[3] J. Schwiening, J. Inst. 4 (2009) P10004

[4] M. Traxler et al., Scientific Report 2006

* Work supported by EU, HadronPhysics2 contract No. 227431, DESIGN STUDY contract No. 515873

† Nuclear Physics Division, BARC, Mumbai, India

‡ Nuclear Physics Division, BARC, Mumbai, India

§ Università degli Studi di Catania, Italy

[1]pronunciation: [d ərk]

A Pattern Recognition for the Straw Tube subdetector in PANDA *

G. Boca[1]

[11]Fair Joint Core Team and GSI, Darmstadt, Germany and Dipartimento di Fisica Nucleare e Teorica dell'Universitá, via Bassi 6, 27100 Pavia, Italy

In the experiment PANDA, at FAIR, GSI, the central detector and the inner silicon pixel and strip detector[1] will play an essential role in tracking charge particles, produced in the target. An antiproton beam of maximum 15 GeV/c momentum will impinge on a pointlike pellet target. The silicon tracker is positioned just around the interaction region, at few mm from the beam axis up to about 16 cm of distance from it. The central detector will cover the region from about 16 cm up to about 42 cm of distance from the beam axis (which runs in the Z direction) and it will be approxiamtely 1 meter long along Z. While the silicon detector provides the most precise measurement of the track parameters, the central tracker helps disentangling the confusion and assigning all the hits found to the right track candidates. At the moment in PANDA there are two options for the central tracker, the first is a set of Straws Tubes (ST), the second is a Time Projection Chamber. This report will concentrate on the performance of the Pattern Recognition code written for the ST option. The ST system consists in approximately 4500 straws, 1 cm diameter, 1 m long. The majority of the straws axex are parallel to the Z direction. About 1100 of the straws have a tilt angle of $\pm 3^0$ with respect to it (skew straws). The magnetic field in the central region is also directed along Z. Therefore the charged particle trajectories are helices with axis parallel to the Z direction and passing through the interaction point. Consequently their projection on the transverse plane (the XY plane) is a circle passing through the interaction vertex. Without going into all the details, the pattern recognition for the ST is divided into two steps. First the radius and center of the circle in XY projection are found by using only the hits of the straws parallel to Z (this makes it possible to determine 3 out of 5 parameters of the helix). The second step consists in associating hits from the skew straws to each XY projection. When successful, this enables the determination of the remaining 2 parameters. Table 1 show the results from a montecarlo simulation. The first column shows the total momentum of the number (shown in column 2) of tracks generated. Their number is shown in column 2. The efficiency in finding the correct track is 100% in all cases, while the ghost tracks are in general a negligible fraction. The efficiency in finding the hits of the parallel straws ranges between 97 and 100 %. The efficiency in associating the skew hits is 93 % in the very worst case, ranging between 95 and 100% in general. The spurious hits associated to a true track are a negligible fraction for the parallel straws and remains below 17% (worst case).

Table 1: Performance of pattern recognition for Straw Tubes.

track momentum (GeV/c)	generated tracks per event	% reconstructed tracks	% ghost tracks	% found hits in parallel straws	% spurious hits in parallel straws	% found hits in skew straws	% spurious in skew straws
0.3	1	100	0	100	0.3	100	0
0.3	6	100	0	99	1.8	97	8
0.3	10	100	0	100	3.8	93	17
1	1	100	0	100	0	98	0
1	6	100	0	100	2.2	97	11
1	10	100	1.8	100	2	96	12
2	1	100	0	100	0	100	0
2	6	100	3.7	100	0.5	95	11
2	10	100	1.8	100	1.9	95	11
5	1	100	0	97	0	100	0
5	6	100	2.3	99	2.2	99	13
10	1	100	0	100	0	99	1

References

[1] Physics Performance Report, PANDA Collaboration, W: Erni *et al.*; arXiv:0903.3905v1

* Work supported by EU, FP7 contract No. 211382.

Standalone track finding for the GEM-Tracker of the PANDA experiment

R. Karabowicz, B. Voss, and J. Kunkel
GSI, Darmstadt, Germany

Detector description

A set of planar Gaseous Electron Multipliers (GEM) stations will be used as a first forward detector after the central tracker of the PANDA experiment, placed about 1.5 m after the target along the beam axis in a solenoid 2 T magnetic field. The exact number of planes and their positions are yet to be determined based on the simulation studies performed using the PandaRoot package. Current implementations include 3 or 4 GEM stations depending on the length of the central tracker [1]. The stations cover polar angles from 3° to 20° and are placed at (81), 117, 153 and 189 cm from the target.

The geometry of the stations in the PandaRoot software follows closely the design of the GEM-Discs presented in [2]. Thanks to the double-sided read-out planes located in the center of each station, the position of the particles passing through the detector will be recorded in four projections per station. This allows unambiguous determination of the hit position with a resolution of better than 100 μm.

Track finder

The particle tracking in the PANDA experiment is based on a global conformal mapping, but each tracking subsystem is expected to develop a standalone track finding code. This will identify the possible track candidates thus reducing the number of combinatorial hits. The goal of the algorithm presented in this paper is to find primary particle tracks.

In the first step of the track finding algorithm hits from any two GEM stations are combined into "track segments" depending on their position. Taking the target position as the third point it is possible to calculate the track segment momentum at collision vertex. Consequently these track segments are matched into track candidates if they share hits and the calculated momenta are comparable. In the last stage the set of track candidates is cleaned according to the following criteria:

- number of hits belonging to other track candidates,
- differences in the momenta calculated for the segments belonging to the track candidate,
- number of track segments in the track candidate.

Such simple algorithm provides surprisingly good results in the low track density environment of the PANDA experiment. However, the obtained track finding efficiency depends strongly on the number of particles passing through the GEM detector. For the geometry with 4 stations the efficiency varies from 99.7% through 99.2% to 93.4% for events with 1, 7 or 20 particles, respectively. In the case of 3 stations the code does not perform as well, and the corresponding percentages are 99.3%, 97.2% and 88.4%. The above efficiencies are for fast primary tracks, emitted from the target with momenta larger than 1 GeV/c. The overall efficiency dependence on momentum is presented in Figure 1. The comparison between the true and the reconstructed momenta allows to determine the momentum resolution, which varies from 2% to 3% for tracks with momenta of 1 GeV/c and 4 GeV/c, respectively (see Figure 2). It should be mentioned that obviously the algorithm is unsuitable for reconstructing secondary particles, and even for fast secondaries with a large number of hits the efficiency is about 50%.

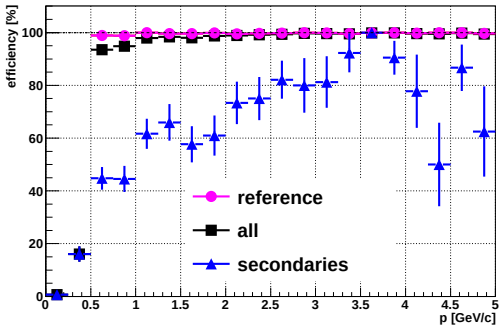

Figure 1: Track efficiency versus momentum.

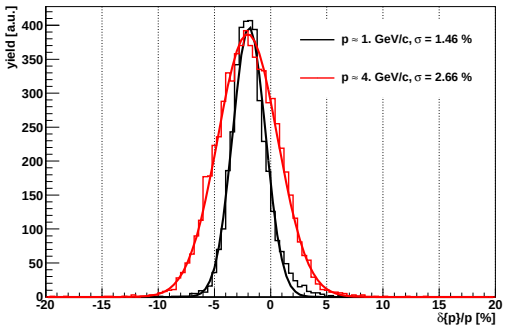

Figure 2: Track momentum resolution.

The simplicity of the presented algorithm results in a good time performance, with a mean time per reconstructed track varying from 0.1 to 1 millisecond depending on the track density.

References

[1] B. Voss *et al*, "GEM-Trackers for the PANDA Target-Spectrometer - Design studies", GSI Scientific Report 2008, page 242.

[2] B. Voss *et al*, "The GEM-Discs for the PANDA experiment", this report.

Status of the NuSTAR experiment at FAIR

R. Krücken[1] and C. Scheidenberger[2] for the NuSTAR collaboration

[1]TU München, Germany, [2]GSI Darmstadt, Germany

The NuSTAR facility at FAIR aims at the investigation of **Nu**clear **ST**ructure, nuclear **A**strophysics and **R**eactions. The goal is the understanding of structure and dynamics of nuclei far away from stability in order to make major contributions towards answering fundamental questions such as:

- What are the limits of existence of nuclei?
- What is the isospin dependence of the effective nucleon-nucleon interaction and of the equation of state of nuclear matter?
- How is the shell structure modified in exotic nuclei and how do new collective modes appear far away from stability?
- How are the heavy elements produced in the universe?

To investigate these questions, the NuSTAR collaboration will produce exotic nuclei and investigate them with dedicated complementary setups, each of them specialized for particular observables. The central instrument is the Super-FRS, a three-stage fragment separator for in-flight separation of exotic nuclei produced in fragmentation or fission reactions in the production target at its entrance. The Super-FRS will have a much larger phase-space acceptance and thus approximately ten-fold higher transmission compared to the current FRS. The secondary beams of the Super-FRS will be available at its three experimental areas at the low-energy branch, at the high-energy branch, and at the storage-ring branch. At the start-up of FAIR, the Super-FRS is planned to receive primary beams from the SIS-18, which are up to ten times higher than present intensities. Later on, it will be coupled to the SIS-100, which will provide accumulated primary beams with up to 10^{12} ions per second. Thus an overall increase of secondary-beam intensities up to three to four orders of magnitude is expected. Therefore, radiation hardness and safety issues are demanding for all Super-FRS components, especially around the production target and its handling installations. An extensive design and R&D effort is underway for the development of critical components of the Super-FRS such as the radiation-hard super-conducting magnets, high-power targets, the beam dumps and the surrounding shielding as well as tracking detectors for particle identification at high rates, see contribution by M. Winkler et al. in this report. The Super-FRS is schematically shown in Figure 1.

The year 2009 has seen major modifications of the overall layout of the Super-FRS at FAIR, and also the civil construction is affected. However, with module 2 of the FAIR modularized start version, the NuSTAR experimental programme can enter new territory and will largely benefit from increased secondary beam intensities.

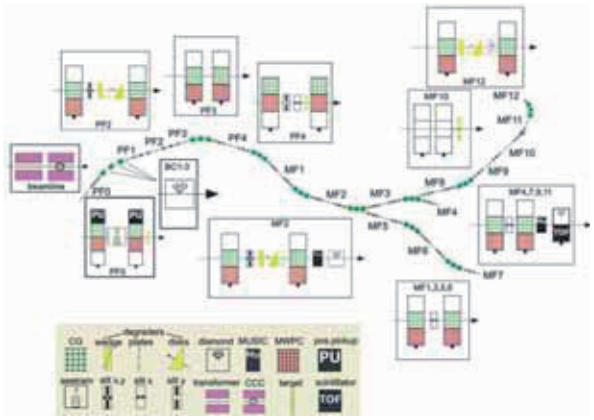

Figure 1: The Super-FRS up to its final achromatic focal planes. The equipment at all focal-planes is indicated.

The R3B setup at the high-energy branch is an evolution of the ALADIN-LAND setup at the present Cave C, which is being upgraded and extended in the coming years. It aims at the study of a broad spectrum of reactions at relativistic energies in complete kinematics to investigate single-particle and collective excitations in nuclei near the driplines as well as nuclear matter properties and reaction rates for nuclear astrophysics. The central element of the R3B is the large acceptance dipole magnet GLAD (GSI Large-Aperture Dipole magnet), that is currently under constructions. Intensive R&D efforts are underway for the various detector systems of the R3B setup, such as diamond heavy ion tracking detectors, the CALIFA electromagnetic and charged particle calorimeter, the silicon target recoil tracking detector and the NEU-LAND neutron detector. These detector systems will be constructed and implemented step by step as they become available at the current R3B program in Cave C at the FRS.

The low-energy branch comprises various detector systems for precision measurements. The novel multi-purpose device for particle identification, precision momentum spectroscopy and longitudinal phase-space compression is the energy buncher-spectrometer. Its ion-optical and technical design is almost completed. Together with a cryogenic stopping cell, which has undergone first off-line tests, the buncher-spectrometer will

provide re-accelerated beams for trapping and laser spectroscopy experiments.

HISPEC experiments for in-beam spectroscopy of exotic nuclei will make use of the AGATA gamma-ray spectrometer for gamma spectroscopy in conjunction with particle identification of reaction products with the LYCCA detector, for which a TDR has been approved and other ancillary detectors. A first version of LYCCA will be used together with the RISING spectrometer and later on with the AGATA Demonstrator at the FRS. The DESPEC decay spectroscopy experiment for the study of isomeric states and beta-, proton-, and alpha-radioactivity will use the AIDA implantation detector, for which a TDR has been submitted, surrounded by a high efficiency gamma-ray spectrometer and a neutron detector array, for which R&D efforts are under way. The PRESPEC campaign in the coming years at the FRS will follow on the very successful RISNG fast-beam and stopped beam campaigns, gradually leading to HISPEC/DESPEC at the Super-FRS.

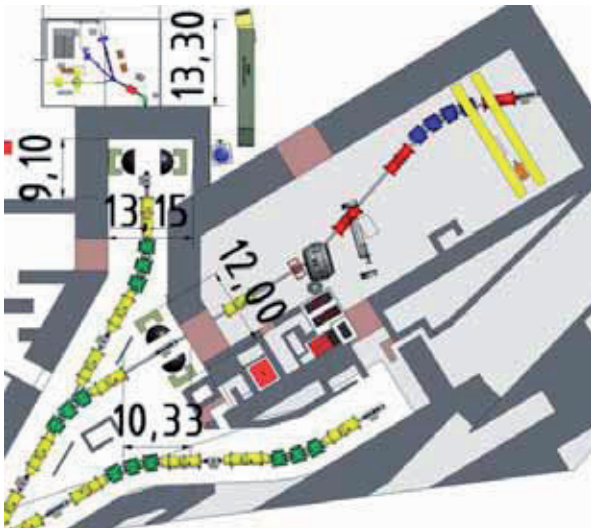

Figure 2: Layout of the caves at the low-energy and high-energy branch of the Super-FRS according to the modifications for the modularized start version. The third branch leads to the CR collector ring.

MATS and LASPEC, which have just submitted their TDR, aim at measuring ground state properties such as masses, spins, and electromagnetic moments of short-lived nuclei using Penning trap and laser spectroscopy set-ups. For both experiments first prototype set-ups will be constructed and used at the Mainz TRIGA reactor before they will be moved to the low energy branch of the Super-FRS. At a later stage the exo+pbar experiment shall take advantage of the unique opportunities at FAIR, where exotic nuclei and low-energy anti-protons (from FLAIR) are available at the same area: it will produce anti-protonic exotic nuclei for the study of nuclear peripheries in neutron-rich or neutron-deficient nuclei, an approach which is complementary to the AIC experiment (see below).

The storage-ring branch contains several challenges, which are common for all NuSTAR storage-ring experiments: the efficient injection of secondary beams, which are characterized by a large longitudinal and transversal phase-space volume, the fast manipulation and phase-space reduction on the time scale of 100 ms, and the development of experimental instruments which are compatible with the prevailing UHV conditions. Intense R&D is ongoing.

Based on the substantial experience concerning measurements of half-lives and masses of exotic nuclei in the ESR storage ring the ILIMA experiment will develop more sensitive Schottky pick-ups and in-ring detectors in order to prepare for experiments with more reach into the terra incognita of the nuclear chart. It should be mentioned that in 2010 a new Helmholtz young investigator group was approved, one of its scientific goals being half-life studies of nuclei along the r-process path using the ESR at GSI and later on the NESR at FAIR.

The EXL experiment for low-momentum transfer experiments at the internal gas-jet target of the FAIR NESR is carrying out a substantial R&D effort for the complex system for the detection of charged particles, photons, and neutrons. Methodological developments and first reaction experiments on exotic nuclei will be carried out at the ESR where also first demonstrator set-ups of the full EXL detectors systems will be implemented. For the ESR a new ion-optical mode to use dipole sections after the internal target as a high resolution spectrometer for momentum measurements of the heavy reaction products has been developed.

The ELISe electron-ion collider experiment plans to use the electron storage ring ER coupled to the NESR heavy ion storage ring to perform electron scattering experiments in short lived nuclei. This will enable the study of charge density distributions and collective modes via ealstic and inelastic scattering, respectively. The AIC experiment plans to use the ER to store antiprotons and measure matter radii of exotic nuclei via high energy antiproton annihilation.

With NuSTAR at FAIR the field of exotic nuclei will enter a new era. Many new isotopes, not known to date, will be produced and studied with a variety of detector systems covering a large range of particles, energies and multiplicities. New applications will arise. R-process nuclei can be studied in the laboratory. Complementary methods will yield the complete picture and a comprehensive view of the strong force at extreme isospin. Thus, NuSTAR has a huge and unique discovery potential. The collaboration will smoothly move from the ongoing program at FRS, ESR and ALADIN-LAND to NuSTAR at FAIR.

Super-FRS Design Status Report*

M. Winkler[1,#], K.-H. Behr[1], E. Berdermann[1], A. Brünle[1], H. Geissel[1,2], M. Gleim[1], C. Karagiannis[1], A. Kelic[1], B. Kindler[1], E. Kozlova[1], A. Kratz[1], M. Krause[1], H. Leibrock[1], Yu.A. Litvinov[1], B. Lommel[1], J.A. Maruhn[3], G. Moritz[1], C. Mühle[1], G. Münzenberg[1], I. Mukha[4,1], C. Nociforo[1], W.R. Plaß[2], A. Prochazka[1], C. Scheidenberger[1,2], H. Simon[1], K. Sümmerer[1], N. Tahir[1], An. Tauschwitz[3], M. Tomut[1,5], H. Weick[1], J.S. Winfield[1], and M. Yavor[6]

[1]GSI, Darmstadt, Germany; [2]JLU Giessen, Germany; [3]JWGU Frankfurt, Germany; [4]CSIC, University of Valencia, Spain; [5]NIMP, Bucharest, Romania; [6]IAI RAS, St. Petersburg, Russia;

System and building design

The system design of the Super-FRS has been further detailed. The resulting requirements have been incorporated into the preliminary building design which, however, will need some further adaptation to conform to the now approved FAIR modularized version.

Particular effort has been spent into the design of the target building which includes the heavily shielded target and beam catcher area, several supply and infrastructure facilities, as well as a hot-cell allowing the maintenance of components exposed to high-dose rates. It is proposed to build a 'sandwich-type' shielding consisting of about 8.000 ton iron (note: this is approximately the weight of the Eiffel Tower!) and 12.000 ton concrete. The iron shielding could be realized using rather simple main castings with only a few different types in size (see Figure 1). They could in principle also be produced from cheap but slightly activated iron coming from dismantling of inoperative nuclear power plants.

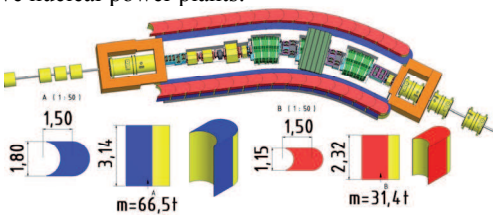

Figure 1: Target area shielding of the Super-FRS. The iron shielding is achieved by using simple castings.

A hot-cell design study was initiated in collaboration with Siempelkamp, a German nuclear technology company. The planning of the hot-cell includes radiologic and regulation aspects, the material flow and handling concept, the interfaces to the adjacent facilities as well as the definition of the hot cell components itself.

High-Power Target

Long-term off-line tests of the rotating graphite-wheel prototype target [1] have been started. Subject of the investigations are the bearings and other crucial parts which must guarantee a sufficient long life time under high temperature conditions and in a high-radiation environment. Concerning the target material, investigation of graphite exposed to high ion doses at temperatures relevant for target operation show significant annealing of the radiation damage [2]. A 20 kW induction generator was installed last year which is used as an external heating source for the target. Experimental studies on He implanted graphite were conducted to asses additional contributions to swelling and damage induced by He accumulation during target and beam catchers operation [3].

Magnets

The production of the radiation resistant dipole magnet was continued at BINP Novosibirsk. The coils were wound from a mineral insulated cable. 8 coil units consisting of 2 double pan cakes and a radiator each were potted in solder. The magnet was completely assembled (see Figure 2) including the remote alignment system. It is possible to align the 100t magnet remotely by hand. The first power tests started at the end of 2009.

Figure 2: Prototype of the radiation resistant dipole magnet at BINP Novosibirsk.

The development of the superferric prototype dipole magnet in collaboration with the FAIR China Group was pursued, too [4]. The magnet was assembled completely at IMP Lanzhou and first cold measurements have been performed. The maximum required magnetic flux density was reached for a current of 233 A which agrees well with the computed design value. Also the measured field homogeneity stays within the required limits of $\pm 3 \cdot 10^{-4}$ for a large aperture of ±200 mm. No unexpected quench occurred during the tests. The heat load at 4.4 K was about 5 W. The maximum stored field energy is more than 400 kJ.

[1] M. Winkler *et al.*, GSI Report (2009-1) 87.
[2] M.Tomut *et al.*,, this report.
[3] M. Krause *et al.*, ths report
[4] H. Leibrock *et al.*, IEEE Trans. on Appl. Supercond., accepted for pblication

* Work supported by the European Community under the FP6 DESIGN STUDY (contract 515873 - DIRACsecondary-Beams).
#m.winkler@gsi.de

Radiation Damage in High-Temperature Ion-Irradiated Graphite for Super-FRS Target and Beam Catchers

M. Tomut[1,2,#], M. Krause[1,3], K.H. Behr[1], M. Bender[1], W. Ensinger[3], H. Geissel[1], A. Keliç[1], B. Kindler[1], B. Lommel[1], D. Severin[1], C. Scheidenberger[1], C. Trautmann[1], H. Weick[1], M. Winkler[1]
[1]GSI, Darmstadt, Germany, [2]NIMP, Bucharest, Romania, [3], TU Darmstadt, Germany

The lifetime of Super-FRS target and beam catchers is ultimately determined by the amount of radiation damage accumulated during operation. For intense irradiation conditions, beam-induced heating could have a positive contribution to damage annealing and lifetime extension. ANSYS calculations give a maximum temperature of 750°C for the graphite wheel due to energy deposition by primary ^{238}U beam in slow extraction regime. We performed high temperature swift heavy ion irradiation experiments to study annealing of defects within ions tracks for further estimation of components lifetime extension.

Fine-grained isotropic graphite (grade R6650, SGL Carbon) proposed as material for beam catchers and rotating target at the Super-FRS, FAIR has been investigated. Samples were irradiated with focused beams of different ion species (Cr, Ru, Xe, Au, Pb, U), with initial energies of 11.4 MeV/u and 4.8 MeV/u at the linear accelerator UNILAC at GSI. Irradiation has been performed at temperatures between 300 ºC and 800 ºC, up to fluences of 2x10^{13} ions/cm^2. A programmable heating stage set-up that could be installed either at X0 or M3 beamlines at UNILAC has been used. The temperatures of the stage and of the samples were measured using thermocouples. Pristine and ion-irradiated graphite samples were analyzed by Micro Raman spectrometry.

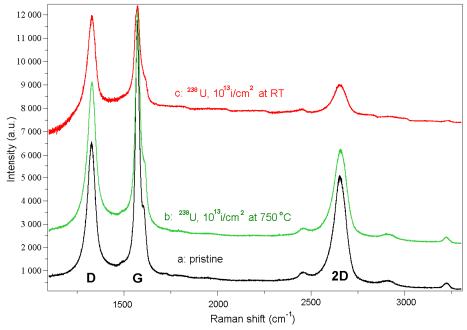

Figure 2: First and second order Raman spectra of isotropic graphite sample: (a) pristine, (b) irradiated with 1×10^{13} U ions/cm^2 at 750 ºC and (c) irradiated with 1×10^{13} U ions/cm^2 at room temperature.

Damage has been quantified using graphitic indices derived from first and second order Raman spectra of irradiated graphite samples (Figure 2). The first-order Raman spectrum is commonly used for the characterization of disordered carbon. It exhibits a graphite (G) peak at 1580 cm−1 and a disorder-related (D) peak at 1336 cm−1. We also analysed the second-order indices (2D-peak at about 2700 cm^{-1}) of the Raman spectrum of irradiated graphite to get additional information on ion-induced bending of graphene layers within the crystallites [1].

Parameters shown in Table 1 allow a straightforward comparison of damage in irradiated samples at room temperature (RT) and at 750 ºC. We have chosen here a benchmark case for the Super-FRS target, consisting of a isotropic graphite sample irradiated with a fluence of 1×10^{13} U ions/cm^2 (for which a steep increase in damage due to the overlapping of tracks has been observed [2]) at a temperature corresponding to ANSYS calculation for ^{238}U primary beam on the target.

Sample	A_D/A_G	$FWHM_G$ (cm^{-1})	A_{2D}/A_D	L_{eq}/L_a
Pristine	0.74	28	1.27	1.88
750 ºC, 10^{13} i/cm^2	0.94	34	0.97	1.88
RT, 10^{13} i/cm^2	1.27	40	0.44	1.12

Table 1: First and second order Raman graphitic indices for spectra shown in Figure 1.

Parameters in columns 2-4 are related to: ratio of area of defect peak to graphitic peaks (AD/AG), second order defect peak to first order defect peak (A2D/AD) and broadening of graphitic peak due to disordering. Their evolution show annealing of defects for high-temperature irradiation compared to room temperature irradiation. The ratio L_{eq}/L_a describes the bending of the graphene plane. The pristine and high-temperature irradiated sample have the same value of the L_{eq}/L_a. indicating a bent grapheme plane but with a good interconnection and graphitic quality at the curvature. This means that properties related to propagation of phonons and electrons are less affected when the irradiation takes place at high temperature. Therefore, operating the Super-FRS graphite target at elevated temperatures is less detrimental to the thermal conductivity of the material. The maximum operating temperature should not exceed 1600 ºC due to the high sublimation rate of graphite (about 10 mg/g/year).

[1] N. Larouche et al, Carbon 48 (2010) 620.
[2] M. Tomut *et al*., GSI Report (2007) 69.

m.tomut@gsi.de

Simulations of the Beam Stripper for the Super–FRS Production Target in a Fast Extraction Mode*

N.A. Tahir[1], V. Sultanov[2], V. Kim[2], A. Matveichev[2], A. Shutov[2], A. Ostrik[2], I.V. Lomonosov[2], H. Geissel[1], A.R. Piriz[3], and D.H.H. Hoffmann[4]

[1]GSI, Darmstadt, Germany; [2]IPCP, Chernogolovka, Russia; [3]UCLM, Ciudad Real, Spain; [4]TU Darmstadt, Germany

Previously, we reported 3D hydrodynamic simulations of interaction of a wheel shaped solid graphite Super–FRS production target with the SIS100, 1.5 GeV/u uranium beam [1]. These simulations have shown that the target will survive (retain its elastic properties) for a beam intensity of up to $3x10^{11}$ ions per 50 ns long bunch if one uses a focal spot size that is characterized with σ = 4 mm. However, it is very important that the thin metallic stripper behind the production target also remains intact after the impact of the secondary beam. For this purpose, we report in the present contribution, 3D numerical simulations of the beam–stripper interaction. The stripper thickness is assumed to be 225 mg/cm^2 and we consider three different materials, namely, Al, Cu and Nb.

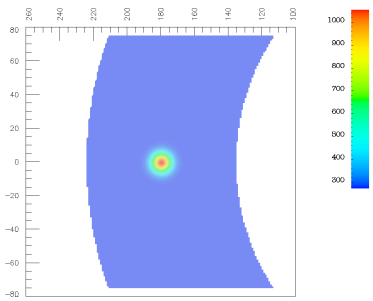

Figure 1: Temperature distribution in Al.

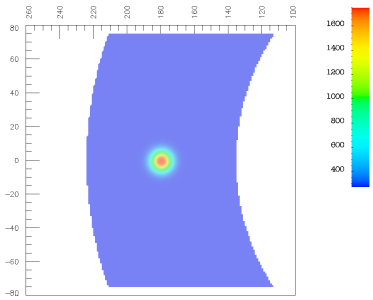

Figure 2: Temperature distribution in Cu.

In Fig. 1 we present the temperature distribution at t = 50 ns (end of the bunch) in case of an Al target. It is seen that the maximum temperature at the center of the focal spot is of the order of 1100 K whereas the melting temperature of Al is 930 K. Therefore with this beam intensity, an aluminum stripper will be severely damaged in a single experiment.

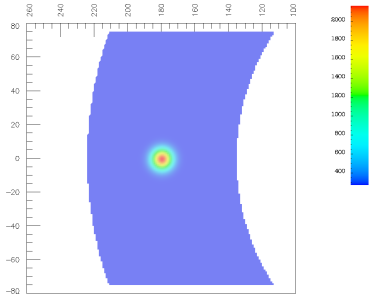

Figure 3: Temperature distribution in Nb.

Fig. 2 shows the target temperature in case of a copper target at t = 50 ns. It is seen that a maximum temperature of the order of 1800 K is achieved which is again higher than the melting temperature (1360 K) of copper. Hence a stripper made of copper will also be destroyed in a single experiment.

Fig. 3 shows the temperature in case of a Nb target at t = 50 ns. It is seen that the maximum temperature is about 2100 K whereas the melting temperature for Nb is 2670 K and the target will therefore survive. However, the beam heated region will be plastified as is seen from Fig. 4 where we present the von Mises Parameter, M, at t = 1 μs and it is seen that M achieves the critical value of 1. However, this may not affect the stripper performance.

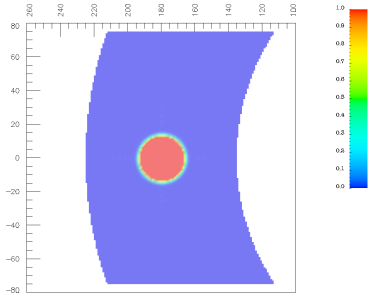

Figure 4: von Mises parameter in Nb at 1 μs.

* Work supported by the BMBF grant 06 DA90331 and RFBR grant 08-02-92882-NNIO-a

References

[1] N.A. Tahir et al., LPB 27 (2009) 9.

Progress in the design & construction of the R^{3}B-GLAD superconducting magnet*

B. Gastineau[1], B. Baudouy[1], C. Berriaud[1], P. Charon[1], P. Contrepois[1], G. Disset[1], A. Donati[1], J.-É. Ducret[1], D. Eppellé[1], P. Fazilleau[1], P. Graffin[1], J.-L. Jannin[1], D. Loiseau[1], J.-P. Lottin[1], M. Massinger[1], C. Mayri[1], H. Neyrial[1], C. Pes[1], Y. Queinec[1] and Z. Sun[1]

[1]IRFU, CEA-Sacla , Gif sur Yvette, France

The R^{3}B–GLAD superconducting Magnet will provide the field required for a large acceptance spectrometer, dedicated the physics program of the R^{3}B collaboration (Reactions studies with Relativistic Radioactive ions Beams). It is presently being designed & built at the CEA-Saclay.

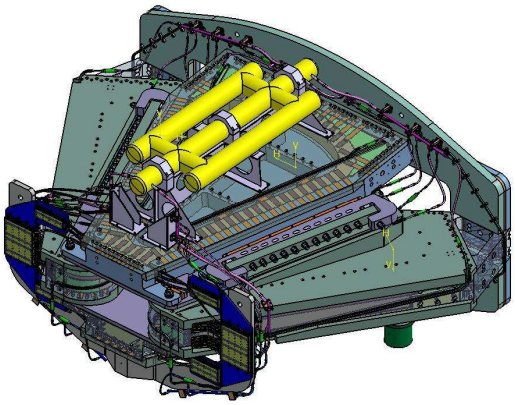

Figure 1: cold mass of R^{3}B-GLAD.

R^{3}B-GLAD project activity [1] was focused during the last two years on the following items: the production of the superconducting cable, the experimental tests of the basic concept of the magnet, and the study of a new simplified design. Following the internal peer-review in July 2008, the manufacturing of the cold mass began in early 2009. The studies towards a final design of the cryostat are in progress, as well as the preparation of the cold-mass test, which should occur in Saclay in 2010.

In order to cope with the experimental requirements (large angular aperture, high field integral & low fringe fields in the target region, angular & momentum achievable resolution) the design of the R^{3}B-GLAD magnet is based on the magnetic active shielding. Consisting of six superconducting coils, it minimises the magnetic volume & the energy stored in the coils, while keeping the fringe field low. But our mechanical study [2] on the first graded-coil design concluded to the existence of too large stresses, especially shear stresses, which appeared impossible to keep in acceptable levels mainly because of the orthotropic behaviour of the coils, together with differential shrinkage and high level of magnetic forces. Hence a new design for R^{3}B-GLAD without grading was done in 2009, which allowed to: Decrease the stresses; Wind the conductor to respect more precise mechanical tolerances; Decrease the peak-field on the superconducting cable, hence increasing the temperature margin that will ensure a better stability to the superconducting coils.

Figure 2: winding of the prototype coil (*ASG Super. S.p.A., Genova, Italy*).

The cold mass (Fig. 1) production started in 2009. A prototype (Fig. 2) will test the procedure for winding and impregnation. The new design study of the magnet cryostat is an elliptical cylinder with fewer stiffeners, and a side satellite, to minimize its cost. The total magnet weight should be about 50 tons.

* Work supported by EU, CNI contract No. 515876.

References

[1] B. Gastineau *et al.*, Magnet Technologies conference MT 21, Hefei, China (2009)

[2] Sun Z, *et al. IEEE Trans. Appl. Supercond.* **18-2**, 375-378

MRPC prototypes for the NeuLAND neutron time-of-flight detector at R^{3}B*

T. Aumann[1], D. Bemmerer[2], K. Boretzky[1], C. Caesar[1], M. Ciobanu[1], Z. Elekes[2], M. Elvers[3], J. Hehner[1], M. Heil[1], M. Kempe[2], J.V. Kratz[4], V. Maroussov[3], O. Nusair[1,5], R. Reifarth[1,6], D. Rossi[4], H. Simon[1], D. Stach[2], A. Wagner[2], D. Yakorev[2], A. Zilges[3], K. Zuber[7], and the R3B collaboration

[1]GSI, Darmstadt; [2]Forschungszentrum Dresden-Rossendorf (FZD); [3]Universität zu Köln; [4]Universität Mainz; [5]Al Balqa' Applied University, Salt, Jordan; [6]Universität Frankfurt; [7]TU Dresden

A detector for momentum measurements of high-energy neutrons in the energy range 200-1000 MeV is being developed for the R^{3}B experiment at FAIR. It builds on the experience with the existing LAND detector [1]. Prototypes are developed that should detect those neutrons based on a sequence of converter material, to produce secondary charged particles, and Multigap Resistive Plate Chambers (MRPC's) to detect the secondary particles.

A total depth of the NeuLAND detector of ≈100 cm, 50% of which are high-Z converter (nuclear interaction length ≈17 cm) should ensure a detection efficiency close to 100% for energetic neutrons. This presupposes that the secondary charged particles are detected with close to 100% efficiency. The aimed for time resolution is $\sigma <$ 100 ps. The MRPC-based working principle depends instead on the high-Z converter material placed in close proximity to the gas gaps which detect charged particles, so the best is to include the converter material in the MRPC structure itself.

Prototypes with a 4 mm thick central anode have been developed and built at FZD and at GSI, using standard-issue float glass with 0.3 mm thick gas gaps. One question under study was how the unusally thick anode influences the performance of the MRPC. Another question was how to implement a differential read-out when metallic converter material must be in close proximity to the MRPC structure. This requires impedance matching to the preamplifier electronics.

Tests with muons, electrons, and neutrons

In addition to the usual MRPC tests with cosmic-ray muons, regular benchmarking tests are performed at the ELBE superconducting electron linac at FZD. The accelerator provides a time reference of just a few ps resolution [2]. Owing to a new, one-electron-per-bunch, mode of operation, coincident trigger rates up to the kHz range can be used with rather low background. This allows rapid testing of prototypes regarding efficiency and time resolution, and such MRPC benchmarking experiments are now conducted every other month at ELBE.

The two-dimensional spectrum exhibits the usual banana structure (fig. 1), with a time resolution equivalent to about 6 channels (150 ps). Applying a time-walk correction and averaging both ends of one strip (thereby removing the ≈2 cm position resolution of the electron beam), in this case a resolution of 3.7 channels (σ = 93 ps) is obtained, still before subtracting the ≈35 ps electronics resolution.

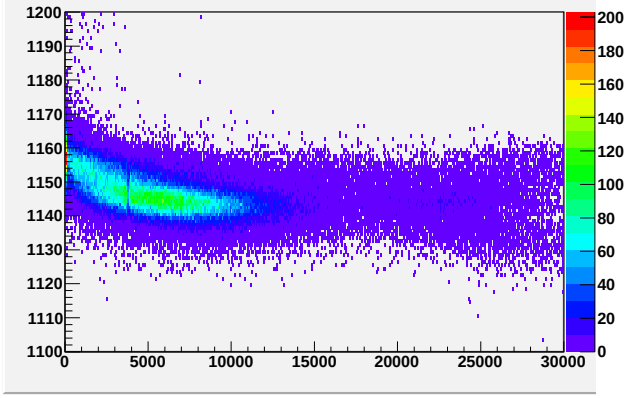

Figure 1: Time (in units of 25 ps) versus charge (single-ended readout, units of 25 fC) for one side of one strip of a NeuLAND prototype. The spectrum has been taken with the one-electron-per-bunch mode of the ELBE linac. The time is measured relative to the accelerator RF signal.

In order to study the response of the NeuLAND prototypes to neutrons, an experiment has been performed at the TSL Uppsala neutron facility [3]. The beam was a quasi-monochromatic neutron beam of 175 MeV energy and average intensity in the 10^4 cm^{-2} s^{-1} range. The data are still under analysis.

Conclusions and outlook

The prototypes show satisfactory performance as to time resolution and efficiency in the electron beam experiments, for single-ended readout. For differential readout, problems with matching the preamplifier limited the performance in the tests conducted so far. An effort to describe all existing NeuLAND prototypes in the R$_3$BRoot simulation framework is underway. The construction of a full-size (2 m) prototype will start soon, in preparation for an experiment with deuteron breakup in 2011.

References

[1] T. Blaich *et al.*, Nucl. Inst. Meth. A **314**, 136 (1992).

[2] R. Kotte *et al.*, Nucl. Inst. Meth. A **564**, 155 (2006).

[3] A. Prokofiev *et al.*, Radiat. Prot. Dosimetry **126**, 18 (2007).

*Supported by BMBF (06DR134I, 06DR9058I, 06MZ222I, 06DA129I, 06KY9136I), GSI F&E (DR-GROS), and the European Union (FP6-EFNUDAT TA 036434).

A High Resolution Spectrometer for R3B

J.S. Winfield[1], T. Aumann[1], H. Geissel[1,2], C. Nociforo[1], H. Weick[1] and M. Winkler[1]
for the R3B collaboration
[1]GSI, Darmstadt, Germany; [2]Justus-Liebig Univ., Gießen, Germany.

It is proposed to extend the Phase A R3B facility with a High Resolution Spectrometer (HRS). The spectrometer would go after the GLAD dipole, the dispersive power of which is used as part of the spectrometer. The scientific motivations for the HRS include: Elastic proton scattering, Total absorption measurements, Knockout reactions, Quasifree scattering such as (p,2p) and (p,pn), Charge exchange reactions, Projectile fragmentation and fission, and Heavy-ion induced electromagnetic excitation.

The required momentum resolution may be estimated from the example of a knockout reaction, where the momentum of the recoiling nucleus after one-nucleon removal provides information on the wave-function of the removed nucleon. The shapes and widths of the momentum distribution depend on the separation energy E_{sep} and the orbital angular momentum l. If E_{sep} = 5 MeV then for l = 0, 1, 2, 3 the momentum widths would be about 75, 100, 140, 200 MeV/c, respectively. Given that a mass 200 particle with a magnetic rigidity Bρ of 15 Tm has a momentum of about 340 GeV/c, a resolution of about 10^{-4} is needed to resolve different l-values. The other main design goals are a relative momentum acceptance of ±2.5 % and a maximum Bρ equal to that of R3B, namely 15 Tm.

High-resolution tracking detectors would be used (i) at the Super-FRS mid-plane (FMF2) to measure the $B\rho$ of the secondary beam, (ii) before and after the R3B target, and (iii) at the focal plane of the HRS.

Calculations have shown that the design momentum resolution can be achieved provided that the tracking detectors have an intrinsic resolution of at least 0.1 mm and that the incident energy of heavy ion beams is greater than 400 MeV/u.

Ion Optics

Ion optical calculations have been performed with a spectrometer lattice of **Q3DQ3-Q3D4Q3**, where the first dipole (**D**) is GLAD with standard Super-FRS quadrupole triplets (**Q3**) either side. The four succeeding dipoles and adjacent triplets, are large-aperture magnets, somewhat similar to those proposed for the Energy Buncher in the LEB cave.

The optics calculations start at the final focal plane of the High Energy Branch of the Super-FRS. At this point the beam emittances in the horizontal (x) and vertical (y) directions are both 150 π mm mrad. We assume a beam spot size of Δx = ±10 mm and Δy = ±15 mm and a momentum acceptance of ±2.5%. The optimised ion optics is shown in Fig. 1. The first triplet focuses the beam onto the R3B target. The second triplet after the GLAD dipole gives an intermediate focus which enables the subsequent large acceptance triplet to make use of the full resolving power of the main dipoles.

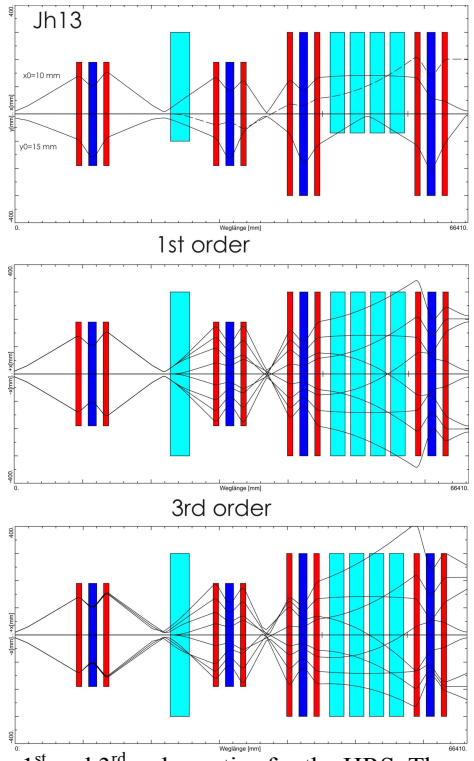

Fig. 1. 1st and 3rd order optics for the HRS. The upper panel shows the trajectories in the x and y direction for δ = 0 together with the dispersion line. The lower two panels compare the x-trajectories for three different δ at 1st and 3rd order.

The first order resolving momentum power obtained is 36400 with a dispersion of 7.82 cm/% relative momentum. The lower panel in Fig. 1 shows that the focal plane is very inclined. This could be corrected by adding hexapole magnets to the lattice, with the penalty of increasing the length of the spectrometer. Tracking alone may not be sufficient.

Summary

A High Resolution Spectrometer for R3B is described which greatly enhances the R3B phase A by the capability of high momentum resolution measurements of relativistic heavy ions. In addition it provides a clean separation of medium-heavy and heavy nuclei by magnetic rigidity.

CALIFA: a Photon and High Energy Charged Particle Calorimeter for R^{3}B

D. Cortina-Gil[1]
[1]on behalf of the CALIFA Working Group and the R^{3}B/FAIR collaboration

CALIFA [1] is the detector of the R^{3}B/FAIR experiment that acts as total absorption γ calorimeter and spectrometer as well as identifier of charged particles from target residues when operating in coincidence with the Target Recoil (tracking) Detector (TRD). This versatility is its most challenging requirement, demanding a huge dynamic range, covering from low energy γ to 300 MeV protons.
A typical R^{3}B experiment will investigate inverse kinematics reactions induced by projectiles with energies up to 1 A GeV (nominal value 700 A MeV). In the present design version CALIFA subtends the angular polar region 7^o - 130^o and provides $>$ 75% total absorption efficiency and an energy resolution of 5 % for 1 MeV γ and $<$ 1% for charged particles. Relativistic kinematics introduces non-negligible Lorentz boost and Doppler shift broadening of the emitted γ rays, which are strongly dependent of the polar angle emission [2]. Thus, it is suitable to search for optimal detector material and geometry in a small-angle, 7^o - 40^o, "Forward EndCap" and a large-angle "Barrel", 40^o - 130^o, separately.
The detector will be highly segmented ($\sim$ 5000 individual crystals) with different shape and angular aperture for different polar angle regions. The high granularity and total absorption efficiency determine the shape of the crystals.
The choice of Barrel material, CsI(Tl), is based on its good intrinsic resolution, high probability for γ interactions, simpleness to handle and relatively low price. Two versions of the Forward EndCap are still under consideration. The first one, based on phoswich detectors ($LaBr_3$(Ce) + $LaCl_3$(Ce)) provides very good energy resolution [3] and allow to identify high energy charged particles with a modest crystal thickness. The main drawback is associated with the hygroscopy of the La crystals that requires a specific development to optimize the encapsulation. The second version would include long ($\geq$ 200 mm) CsI(Tl) detectors which are cheaper but will have somewhat worse γ energy resolution and a large efficiency loss for charged particles due to inelastic and elastic reactions [4].
The wide dynamic range makes delicate the choice of readout device. PMTs, even though providing the necessary dynamic range, good energy resolution and low threshold for γ, need strong protection against the magnetic field from the superconducting dipole and a dedicated wavelength matching for CsI(Tl). They seem particularly well suited to readout $LaBr_3$(Ce) + $LaCl_3$(Ce) phoswich [3], allowing the simultaneous detection of low energy γ and energetic protons. On the other hand, APDs provide very good energy resolution and low threshold for low energy γ [5], and they need much less electrical power. The possibility of increasing the light collection area with a double APD (S8644-1010) system, developed with Hamamatsu, connected to a single CsI(Tl) crystal is investigated.
The detailed response of the CALIFA to high energy protons and γ has been tested with prototypes [3, 4, 6] and is also been investigated by means of simulation codes [2, 4].
One specific development for the readout electronics is the pre-amplifier stage. This analogue solution based on existing MPR16 Mesytec modules implements a full gain compensation by temperature and bias control. For the further electronics chain analogue and a fully digital solutions are currently carefully evaluated and first prototype tests have already shown the different advantages of both systems.
The mechanical support for CALIFA is based on epoxy-carbon fibre boxes in alveolar structure. Such a structure will minimize the geometrical loss, is self-standing, very rigid and allows modularization.

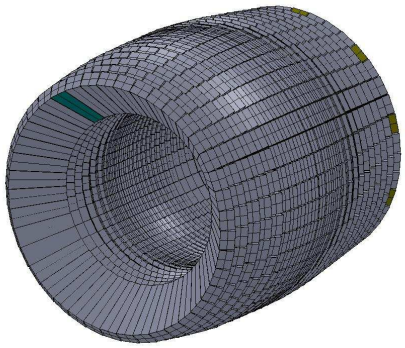

Figure 1: Barrel mechanical design based on epoxy-carbon fibre alveolar structures

References

[1] Technical Proposal for design, construction, commissioning and operation of R3B.

[2] H. Alvarez et al., nucl. Ins.Meth B 266(2008) 4616

[3] A High Resolution Phoswich detector for the CALIFA front cap, O.Tengblad et al, in this Annual report

[4] D.D. DiJulio et al., Nucl. Instr. Meth A 612 (2009) 127, and Response of a CALIFA CsI(Tl) prototype to protons V. Avdeichikov et al, in this Annual report

[5] M. Gascón et al, IEEE Trans. Nuc. Sci (2010) in press, and Overview of the CALIFA CsI(Tl) crystals and LAAPDs characterization, H. Alvarez-Pol et al, in this Annual report

[6] Characterisation of a CALIFA Barrel Prototype at the Tagging Photon facility NEPTUN, Darmstadt,L.Schnorrenberget et al, in this Annual report

Characterisation of a CALIFA Barrel Prototype at the Photon Tagging Facility NEPTUN, Darmstadt*

L. Schnorrenberger[1], I. Duran[2], J. Glorius[1], B. Löher[1], N. Pietralla[1], D. Savran[1], K. Sonnabend[1], H. Alvarez-Pol[2], J. Benlliure[2], D. Cortina-Gil[2], M. Gascon[2], D. Gonzalez[2], and N. Montes[2]

[1]Institut für Kernphysik, TU Darmstadt, Germany; [2]Universidade de Santiago de Compostela, Spain

At the future R^{3}B setup at FAIR experiments in complete kinematics are to be performed. A calorimeter (CALIFA [1]) has been proposed to surround the target position for photon detection. Understanding its response function is necessary for reliable measurements of the reaction cross sections of interest. Due to the Lorentz boost photon energies up to 10 MeV are relevant. The detector response is usually simulated using Monte-Carlo codes like GEANT4 [2]. It is mandatory to experimentally check the reliability of such simulations. We have started measurements on the response function of CALIFA barrel prototype detectors at the Darmstadt photon tagging facility NEPTUN.

Photon Tagger NEPTUN

NEPTUN is a setup at the superconducting electron accelerator S-DALINAC. It provides a quasi-monoenergetic photon beam well-suited to characterise photon detectors. A monoenergetic electron beam of about $E_0 = 30$ MeV

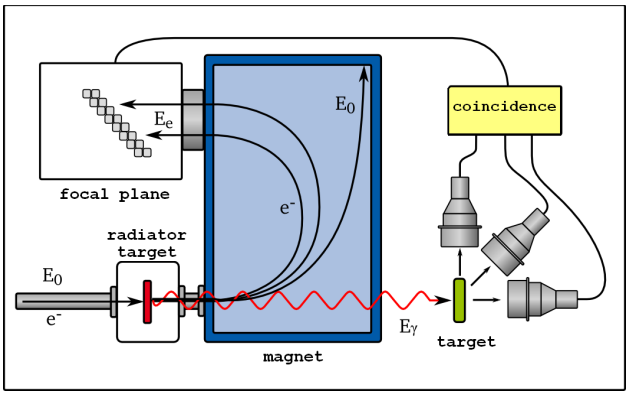

Figure 1: NEPTUN Tagging Facility, Darmstadt

hits a gold foil producing bremsstrahlung photons. The foil is thin enough (10 μm) to guarantee each electron produces at most one photon. The scattered electrons are analysed in the field of a dipole magnet. A position sensitive detector array in its focal plane determines the electrons' energy E_e, from which one obtains the photon energy $E_\gamma = E_0 - E_e$. The energy of the tagged photons can be chosen with a resolution of 20 keV. A window of 1.4 MeV width can be measured with a single setting of the magnetic field of the tagging magnet. [3]

*Work supported by DFG (SFB 634), BMBF (06 DA 9040 I) and LOEWE (HIC for FAIR)

Characterisation of a CALIFA barrel prototype

At NEPTUN we investigated the detector response of a CALIFA barrel prototype (ProtoZero, Santiago de Compostela) from 2.9 to 4.3 MeV and 6.4 to 7.8 MeV. ProtoZero is an array of 16 CsI crystals of 90°-shape connected to APDs. The beamspot was located in the center crystal. Figure 2 shows typical spectra taken with a coincidence condition on a focal plane position. No addback has been applied yet. At 3 MeV the full energy as well as single and double escape peaks can be seen. At 7 MeV the full energy peak disappears. Further evaluations und comparisons to simulations are in progress.

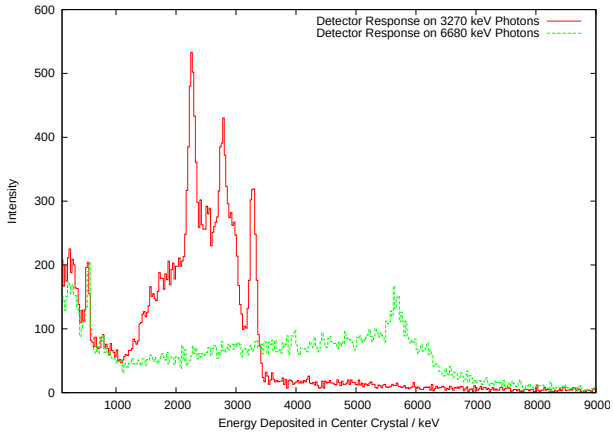

Figure 2: Detector Response on a 3.27 MeV and 6.68 MeV photon beam. At low energies the photo peak as well as the single- and double-escape lines can be seen. At higher energies the double-escape peak dominates the spectrum. Absolute efficiencies should not be compared due to arbitrary scales.

References

[1] H. Alvarez-Pol, J. Benlliure, E. Casarejos, D. Cortina, I. Duran, M. Gascon for the R^{3}B Collaboration, Nucl. Instr. and Meth. B **266** (2008) 4616.

[2] S. Agostinelli *et al*, Nucl. Instr. and Meth. A **506** (2003) 250.

[3] D. Savran, K. Lindenberg, J. Glorius, B. Löher, S. Müller, N. Pietralla, L. Schnorrenberger, V. Simon, K. Sonnabend, C. Wälzlein, M. Elvers, J. Endres, J. Hasper, A. Zilges, Nucl. Instr. and Meth. A (in press).

A High Resolution Phoswich detector for the CALIFA front cap

O. Tengblad[1], J.A. Briz, M. Carmona[1], J. Bergström[2], E. Blomberg[2], E. Gallneby[2], J. Hagdahl[2], H.T. Johansson[2] T. Nilsson[2], M. Nordström[2] and H. Wittler[3]

[1]IEM-CSIC, Madrid, Spain; [2]Chalmers University of Technology/[3]Gothenburg University, Gothenburg, Sweden

The calorimeter CALIFA that will surround the target position of the R^{3}B experiment should, in addition to gamma detection, detect high-energy protons emitted in the reactions. Several different avenues are being studied, here is presented a possible innovative solution how to cope with the very big dynamic range when both detecting gammas of 1-10 MeV and protons of up to 300 MeV. This is based on using two stacked scintillator crystals in a so-called Phoswich configuration with only one common readout.

Simulations show that gamma photons deposit most of the energy in the first interactions and this with high probability happens already in a few cm of material. By combining two materials, first a relatively short but high-resolution material followed by a longer piece of a less expensive material, one could distinguish at what depth the interaction happens. The second layer is used to fully absorb the gamma energy or in the case of first hit in the second layer to veto that specific event.

For protons, a two-layered detector is also capable to determine the initial energy through the traditional ΔE-E method. Instead of using one very long crystal (25-30 cm) it is possible to determine the initial energy from ΔE-ΔE in two shorter crystals e.g. 3cm $LaBr_3$(Ce) + 5 cm $LaCl_3$(Ce), which also reduces the probability for nuclear reactions that can lead to incomplete energy detection.

The $LaBr_3$(Ce) and LaCl3(Ce) crystals have very good energy resolution in the order of 2-3% for 662 keV gammas. In addition, these materials exhibit a very good light yield (63 ph/keV respectively 32 ph/keV). Simulations show that detectors formed by 30 mm $LaBr_3$(:Ce) and 150 mm LaCl3(:Ce) can detect protons up to 280 MeV energy with a resolution better than 2%. This combination has good enough E_γ, as well as Ep, resolution even if one takes a shorter LaCl crystal.

Results

The following results has been obtained with a phoswich detector made from $LaBr_3$(:Ce) (30 mm) stacked with $LaCl_3$(:Ce) (50 mm) together with a Hamamatsu R5380 PMT. The aim is to distinguish the energy deposited in each individual crystal-part the $LaBr_3$ and the $LaCl_3$. To achieve this one have to separate the temporal signal of each crystal. Experimental results showed below indicate that such separation of the energy signals of the phoswich is possible, this although the materials present very similar time response (τ_{LaBr3} = 16 ns; τ_{LaCl3} = 28 ns).

First test of the crystals comparing the energy resolution in the case of the phoswich with two separate crystals shows that the phoswich combination does not deteriorate the resolution.

The prototype was as well irradiated with up to 180 MeV protons at TSL, Uppsala. The protons penetrated the LaBr-part and were stopped in the LaCl, in a normal ΔE-E geometry. Since photons from the both parts were overlapping in time, the pulses read out from the common PM-tube had to be sampled and subsequently pulse shape analysed (PSA). Figure 1 shows a simple, yet efficient method to disentangle the two components by plotting the pulse integral versus height. The two intense spots correspond to fully absorbed protons of 180+155 MeV, whereas the other structures stem from protons escaping or reacting in the detector, with the two delimiting lines corresponding to signals from only the LaBr or the LaCl, respectively.

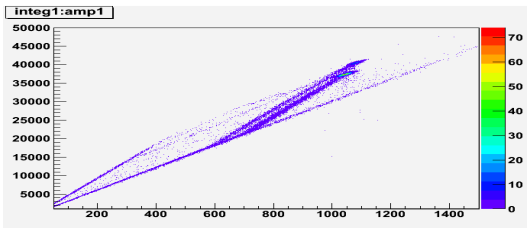

Figure 1 PSA plot for 180+155 MeV protons

Overview of the CALIFA CsI(Tl) crystals and LAAPDs characterization*

H. Alvarez-Pol[1], J. Benlliure[1], E. Casarejos[1], D. Cortina-Gil[1], I. Durán[1], M. Gascón[1], D. González[1], and N. Montes[1]

[1]GENP, Dpto. Física de Partículas, Universidade de Santiago de Compostela, 15782 Santiago de Compostela.

CALIFA is the calorimeter proposed for the detection of gamma-rays and light charged particles originated in nuclear reactions from relativistic exotic beams [1]. It would surround the target of the R^3B experiment [2], a versatile reaction setup with high efficiency, acceptance, and resolution for obtaining kinematically complete measurements of reactions induced by high-energy radioactive beams.

The present report summarizes the characterization of CsI(Tl) crystals and LAAPDs, done in the framework of the CALIFA calorimeter R&D, looking for the best performances on their properties (such as energy resolution, low energy detection threshold, non-uniformity, ...)

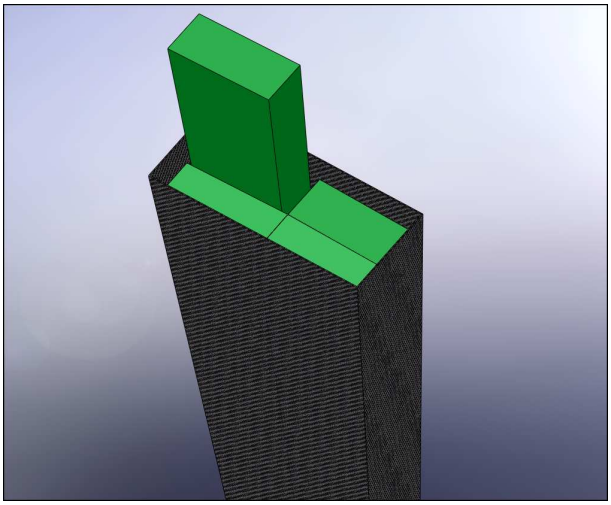

Figure 1: Artistic view of a set of four CALIFA crystals in a carbon fiber alveolus.

Test with Frustrum-like CsI(Tl) crystals

Crystals from different providers with the shape selected for the CALIFA Barrel region have been tested [4]. The crystal shape has been determined based on the optimization of several design criteria, namely the energy resolution in the projectile frame, the use of a reduced set of different crystal shapes and the minimization of the space and material (wrapping and support structures) within the active volume [5] (see Figure 1). The results obtained in simulation confirm the calorimeter design capabilities to reconstruct the gamma energies within the required resolution, being the geometrical contribution below 4%. The use of long crystals is supported by the measured small dependence of the resolution with the crystal length [3]. We have optimized both the crystal wrapping and acquisition time and the procedure for the bias voltage selection.

We observe important differences between light-collection non-uniformities and energy resolution values for each crystal, even for two samples coming from the same provider [4]. Moreover, the best energy resolution is not necessarily obtained for the best light-collection non-uniformities. The best resolution achieved is around 5% at 1 MeV, similar to the CALIFA calorimeter requirements.

We have developed a technical procedure to measure the relative light output of CsI(Tl) crystals and to characterize separately the LAAPDs [6]. Those crystals with largest exit face have the largest light output, increasing a 50% when moving from 1 to 2 cm^2.

LAAPD characterization

Different LAAPDs has been characterized using a tunable LED source [6]. The number of equivalent electron-hole pairs created in each APD sample is obtained from the 5.9 keV X-rays produced by a ^{55}Fe source. The position of the LED pulse centroid and the corresponding multichannel channel for the X-ray pulse results in the number of equivalent electron-hole pairs for the LED pulse. It shows to have a linear correlation with the LED light yield. The contribution of the APD to the energy resolution has an asymtotic limit lower than 0.5%, associated with the noise contribution of the electronic chain. Comparison between different APDs is possible through the light-pulse resolution achieved at the nominal bias voltage

As a concluding remark, the results obtained in the cited publications are close or better that 5% energy resolution for 1 MeV gammas, indicating that they are a suitable solution for the CALIFA Barrel.

References

[1] http://www-land-gsi.de/r3b/docu/R3B-TP-Dec05.pdf

[2] T. Aumann et al. R3B Technical proposal. FAIR-PAC/NUSTAR/R3B (Jan 2005). http://www-land.gsi.de/r3b/

[3] M. Gascón et al., IEEE Trans. Nuc. Sci 55 (2008)1259-1262.

[4] M. Gascón et al., IEEE Trans. Nuc. Sci 56 (2008) 962-967.

[5] H. Álvarez-Pol et al., Nucl. Inst. and Meth. B 266 (2008) 4616-4620.

[6] M. Gascón et al., accepted for publication in IEEE Trans. Nuc. Sci.

* Work partially supported by Spanish Ministerio de Ciencia e Innovacion (FP2005-00732) and Xunta de Galicia (PGIDIT07PXIB206124PR)

Proton in-beam test of a R^{3}B CsI(Tl) prototype

V. Avdeichikov[1,2], D.D. DiJulio[1], J. Cederkall[1], P. Golubev[1], B. Jakobsson[1]
[1]Department of Physics, Lund University SE 221 00 Lund, Sweden; [2]Joint Inst. for Nucl. Res., 141980 Dubna, Russia
for the CALIFA Working Group [1]

The R^{3}B calorimeter/spectrometer CALIFA[1] consists of 4000 CsI(Tl) crystals of 7 different shapes in a densely packed geometry. The prototype, produced at Lund University, belongs to the polar angular region 40°- 80°. It has 3x5 crystals, each with 10x30 mm^2 front area, 15x42 mm^2 back area, 10x10 mm^2 readout area and a total length of 130 mm. The extension of the detector part (100-130 mm) was used as light guide. 44-51% of the primary light was collected on the readout area in this geometry.

The crystals were supplied by Amcrys-H Ltd. (Ukraine). On delivery, all surfaces were highly polished which results in a smooth exponential drop of the light output along the main axis from front area to back area. By applying a special technique of polishing/lapping the side areas, the uniformity, $(LO_{max} - LO_{min})/LO_{average}$, was adjusted to be better than 0.7%.

Two types of photosensors have been used – standard photodiodes (PD) which were used in the proton tests while avalanche photodiodes (APD) of Hamamatsu S8664-1010 type were used for gamma tests. Bench tests of the crystals using radioactive sources were carried out with the APDs operating at T = 22°C. The result is that the energy resolution in the range 0.569 - 2.50 MeV, can be approximated by the relation,

$$R(\%) = 5.15/\sqrt{E} \qquad (1)$$

with E in MeV.

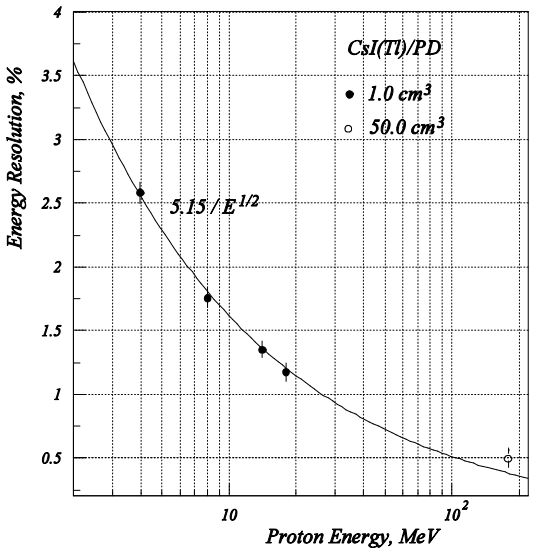

Figure 1: CsI(Tl) energy resolution of protons obtained in elements with crystal volumes 1 cm^3 [3] and 50 cm^3 [4].

The prototype was also exposed to a 178.2 MeV proton beam at TSL (Uppsala, Sweden) [2]. Two single-sided strip detectors, with an active area 60x60 mm2 and a pitch size of 1.86 mm, were placed in front of the prototype to get the position of the incoming proton and the shape of the proton beam. Calibration of individual detectors was accomplished with a 25 mm Cu collimator with a central hole of 8 mm diameter. The results on the detector energy resolution is presented in Fig. 1 which also contains a compilation of other data at lower energies. The solid curve represents Eq. (1), i.e. the result is similar to that obtained for gammas.

A charged particle passing through a crystal undergoes inelastic interactions and multiple elastic scattering. Due to the second process, the primary energy is deposited in a number of elements. Gain corrected summing must be applied to get the total energy of the primary proton entering the active area of the central crystal. For the crystals of the mentioned geometry, multiplicity up to M = 3 must be taken into account. The summing results in an asymmetry of the proton full energy peak. This effect arises due to the 65 μm thick ESR reflector foil used as wrapping substance.

The percentage of events that are lost due to inelastic interactions is shown in Fig. 2 (lower curve).

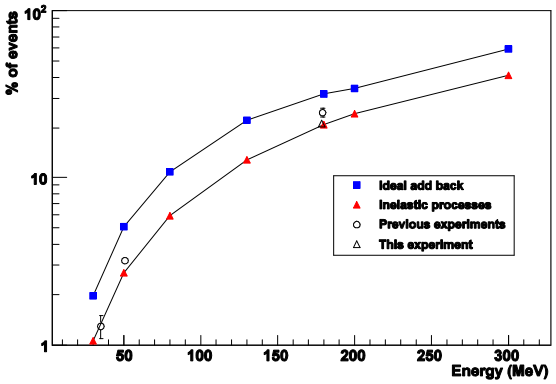

Figure 2: The percentage of the events which can be recovered by the gain corrected summing and those lost due to inelastic ineractions [4].

References

[1] CALIFA web page, http://www.usc.es/genp
[2] V. Avdeichikov et al., GSI Sci. Report 2007.
[3] V.Avdeichikov et al.,Nucl. Instr. and Meth. A349(1994)216.
[4] D.D.DiJulio et al.,Nucl. Instr. and Meth. A 612 (2009) 127.

S357: Beam tests for the conceptual design of a TPC for the FAIR/R^{3}B set-up

J.-É. Ducret[1], T. Aumann[2], A. Boudard[1], M.-P. Combet[1], B. Czech[3], R. Durand[1], T. Gorbinet[1], P. Le Bourlout[1], P. Legou[1], S. Leray[1], J. Lukasik[3], V. Matousek[4], P. Pawlowski[3], M.-D. Salsac[1], and O. Yordanov[5]

[1]IRFU, CEA-Saclay, Gif sur Yvette, France; [2]GSI/KR, Darmstadt, Germany; [3]Institute of Nuclear Physics, Polish Academy of Sciences, Krakow, Poland; [4]Institute of Physics, Slovak Academy of Sciences, Bratislava, Slovakia; [5]Institute of Nuclear Research & Nuclear Energy, Bulgarian Academy of Sciences, Sofia, Bulgaria

Within FAIR/R^{3}B the S357 collaboration is working on the conceptual design of a time projection chamber (TPC) to be installed behind the future large aperture superconducting magnet R^{3}B/GLAD presently under construction in Saclay. This detector will provide charge identification & tracking information for each individual fragment produced in multi-particle final state experiments such as spallation or fission (in inverse kinematics). This TPC is hence being designed to track & identify from hydrogen isotopes to heavy nuclei up to uranium ($Z = 92$) for energies around 1000 MeV per nucleon (i.e. on a 10^4 primary-signal dynamical range). This tracking will permit the reconstruction of the characteristics of the excited projectile needed for a detailed understanding of the reaction mechanisms.

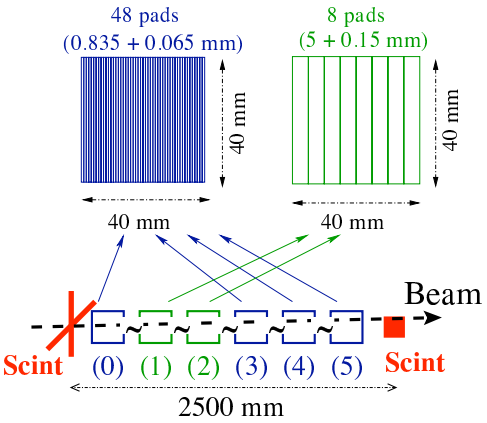

Figure 1: Six-tracker set-up used in our experiment of 2009. Blue trackers have 835 μm wide pads, (0), (3) & (5) have "conventional MicroMegas amplification while (4) have "resistive" MicroMegas (see text). Green trackers have 5 mm wide pads with only "resistive" MicroMegas. The upstream & downstream scintillators whose coincidence provides the DACQ trigger are in red. The total length of the set-up is 2.5 m. $40 \times 40\ mm^2$ is the dimension of the active area of each tracker.

This design is the subject of simulation studies (full detector & fragment transport), detailed engineering design as well as beam tests. In this paper, we present the tests we performed with prototypes based on MicroMegas [1].

After beam tests in 2008 with ^{12}C & ^{58}Ni beams we have performed an experiment in 2009 with six trackers such as displayed in Fig. 1 with a ^{197}Au beam at 250 MeV per nucleon on the test line of Cave C. Such a measurement was aiming at comparing the position resolution achievable for different pad widths (either 835 μm with dead zones of 65 μm in between pads or 5 mm with dead zones of 150 μm) & different MicroMegas amplification techniques: conventional [1] or resistive [2]. The resistive technique allows for a larger spreading of the amplified signal over a few pads, which should be, in principle, more favourable for position reconstruction.

The data analysis has given preliminary results, part of which being shown in Fig. 2 for a 5 mm tracker. During this run, we could measure position resolution around 100 μm (RMS) for the 835 μm trackers, in agreement with our previous experiment at higher energies & with lighter ions, i.e. with smaller signals. It seems that the needed resolution of 200 - 300 μm (RMS) can be obtained with 5 mm trackers. However, as can be seen on Fig. 2, the resolution is not constant over the whole area of the trackers, which is still to be understood: electrostatic edge effects, misalignment, inhomogeneities in the MicroMegas... The data analysis & the simulation of the experiment will be finalised soon. Our first results will be presented in February 2010 at the Vienna Conference on Instrumentation.

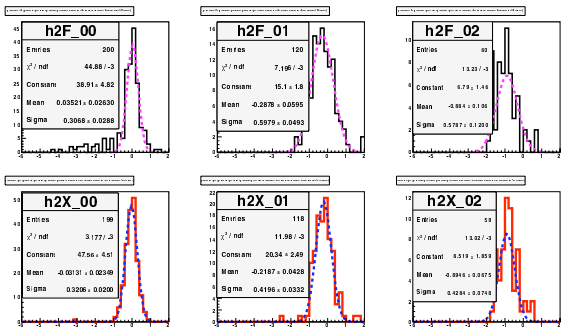

Figure 2: Position reconstruction in the tracker (2) for different positions within this tracker, obtained with two different formula (upper & lower plots). Full line: data; dotted line: fits. The resolution is proportional to "Sigma".

References

[1] G. Charpak, J. Derré, Y. Giomataris & P. Rebourgeard, Nucl. Instrum. Methods **A478**, 26 (2002)

[2] M.S. Dixit, J. Dubeau, J.-P. Martin & K. Sachs, Nucl. Instrum. Methods **A518**, 721 (2004)

Development of a Cryogenic Stopping Cell for the Low-Energy Branch of the Super-FRS at FAIR

S. Purushothaman[1], P. Dendooven[2], H. Geissel[1,3], I. Moore[4], W. R. Plaß[1,3], H. Penttilä[4], M. Ranjan[2], D. Schäfer[3], C. Scheidenberger[1,3], P. Thirolf[5], and H. Weick[1]

[1]GSI, Darmstadt; [2]KVI, University of Groningen, Netherlands; [3]Justus-Liebig-Universität Gießen; [4]University of Jyväskylä, Finland; [5]Ludwig-Maximilians-Universität, München

Precision studies of exotic nuclei far from stability, such as high-resolution particle decay spectroscopy or ion studies in particle traps require transformation of energetic nuclear reaction products with high emittance and large energy spread into a low energy radioactive nuclear beam. This conversion is an essential part of the future low-energy branch of the Super-FRS at FAIR. The traditional approach is the so-called "gas catcher method", based on the Ion Guide Isotope Separator On-Line method developed three decades ago in Jyväskylä. Traditional gas catchers use room temperature noble gas as the stopping medium and employ DC fields or a combination of DC and RF fields to guide the ions towards the exit hole.

It is well known that the presence of impurities in the stopping gas is one of the factors limiting the performance of gas catchers. The construction of large ultra-pure gas catchers, although possible, is far from trivial. A high ionisation rate of the stopping gas has a negative effect on the gas catcher efficiency, it determines the maximum beam intensity a system can handle. The large stopping volume of gas catchers, dictated by the high energies of the ions, requires a high DC electric field for fast and efficient extraction.

A new approach that will be used for the stopping cell at the Super-FRS, is to use cryogenic noble gases as stopping media. The high purity of the helium gas will be ensured by operation at low temperature. The choice for cryogenic operation (down to about 60 K) is based on earlier work on ion survival and transport in a closed cell [1, 2]. Efficient stopping of Super-FRS beams requires, after range bunching, from about 2 to 20 mg cm^{-2} helium, depending on reaction type and primary beam energy. An area 10 cm high and 25 cm wide should be covered to accommodate the cross-sectional area of the beam. Following these requirements a cryogenic gas catcher with a stopping volume of length 1 m and diameter 30 cm has been designed and is currently under construction.

To ensure fast and efficient extraction of the ions stopped throughout the volume of the cell a DC field throughout the length of the cell is needed. An RF carpet superimposed with a DC field is employed at the exit side to guide the ions towards the exit-hole without hitting the wall. The whole system is designed to operate at high density (up to 0.2 mg cm^{-3}) and high DC fields in order to handle ionization densities much higher than what has so far been demonstrated with similar systems. The RF carpet uses an electrode spacing of 0.25 mm (see Figure 1) and an RF frequency of 5 MHz. A detailed simulation on ion transport and extraction, by including the electric fields and gas flow through the nozzle, is underway.

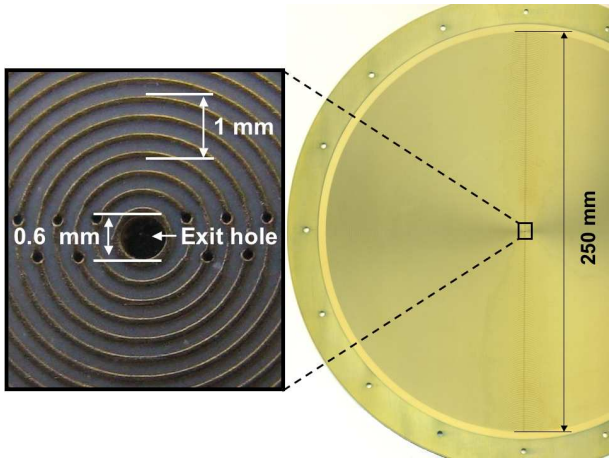

Figure 1: Photo of the RF carpet. The electrode structure has 500 concentric ring electrodes. (***Inset***) Enlarged view of the central part of the carpet.

The electrode structure is mounted inside the cryogenic inner cylinder which is located inside an outer, room temperature cylinder. The cryogenic inner cylinder can be cooled down to 60 K. Helium gas used as the stopping medium is also pre-cooled to the same temperature. All the components used inside the cryogenic inner cylinder are cryogenic rated and bakable up to 420 K.

The mechanical structure is under construction and will be delivered by February 2010. Off-line tests will be be performed at KVI using a ^{223}Ra recoil ion source. The fully functional cryogenic gas catcher will be ready for experiments at the FRS Ion-Catcher [3] at GSI by the end of 2010.

References

[1] P. Dendooven, S. Purushothaman, and K. Gloos, Nucl. Instrum. Meth. A, 558 (2006) 580.

[2] S. Purushothaman, P. Dendooven, I. Moore, H. Penttilä, J. Ronkainen, A. Saastamoinen, J. Äystö,K. Peräjärvi, N. Takahashi, and K. Gloos, Nucl. Instrum. Meth. B 266 (2008) 4488.

[3] M. Petrick, W.R. Plaß et al., Nucl. Instrum. Meth. B 266 (2008) 4493.

Performance of a Prototype MR-TOF-MS for the LEB of the Super-FRS*

T. Dickel[1], W. R. Plaß[1,2], A. Becker[1], B. Sun[1], U. Czok[1], H. Geissel[1,2], E. Haettner[1,2], C. Jesch[1], W. Kinsel[1,2], F. Lautenschläger[1], M. Petrick[1], C. Scheidenberger[1,2], and M. I. Yavor[3]

[1]Justus-Liebig-Universität, Gießen, Germany; [2]GSI, Darmstadt, Germany; [3]Institute for Analytical Instrumentation of the Russian Academy of Sciences, St. Petersburg, Russia

A multiple-reflection time-of-flight mass spectrometer (MR-TOF-MS) [1] will be an important part of the MATS/LaSpec beam-line at the Low-Energy-Branch (LEB) of the Super-FRS at FAIR. The MR-TOF-MS is a fast (∼ms), multi-purpose, non-scanning mass spectrometer with single-ion sensitivity and will be used as a broad-band mass spectrometer, as isobar separator or for direct mass measurements of very short-lived nuclei [2].

A prototype MR-TOF-MS has been built and characterized. In the spring of 2009 it was tested at the tandem accelerator of the Maier-Leibnitz-Laboratory Garching (Germany). All important performance characteristics have been studied and are discussed in the following:

Mass Resolving Power. The resolving power and the transmission efficiency have been investigated with stable Cs ions. A time-of-flight of 5 ms is sufficient for a resolving power (FWHM) of 100,000, 12 ms lead to a resolving power 200,000 and the limit in resolving power amounts to 320,000. Thus a flight time of 12 ms (corresponding to 256 turns) is a good compromise between resolution and measurement time. For this setting the resolving power at different peak heights has been measured and Gaussian-like peak shapes down to the 1% level have been found. At 0.1% the resolving power still amounts to 20,000.

Transmission Efficiency. The transmission efficiency through the whole device for pass-through (zero turns) is 70% and decreases exponentially with the number of turns due to collisions with the residual gas. The decay constant is 670 turns, which results in a transmission efficiency of ∼ 50 % for 256 turns.

Mass Measurement Accuracy. The mass measurement accuracy has been investigated for an isobaric triplet at mass 78 u ($C_3H_5{}^{37}Cl$, C_5NH_5 and C_6H_6) for 256 turns. Space charge has been found to be the main source of systematic errors. The impact of space charge effects on the mass measurement accuracy increases linearly with the number of detected ions [3]. Thus mass measurements can be extrapolated to zero space charge. Then, the residual systematic error is less than 1×10^{-7}. The major contribution of this residual error is known and could be parameterized for further improvement in accuracy.

Isobar Separation. Mass separation has been demonstrated for the isobar doublet of $^{13}C^{12}C_5H_5$ and $^{12}C_6H_6$ (figure 1). The mass difference of the doublet is only 4.164 MeV and the intensity ratio in this experiment was ∼170. The ability to separate such close-lying masses with strongly different abundances will enable experiments with nuclei that are currently not accessible, e.g. mass measurements and nuclear decay spectroscopy of heavy N=Z nuclei at SHIPTRAP.

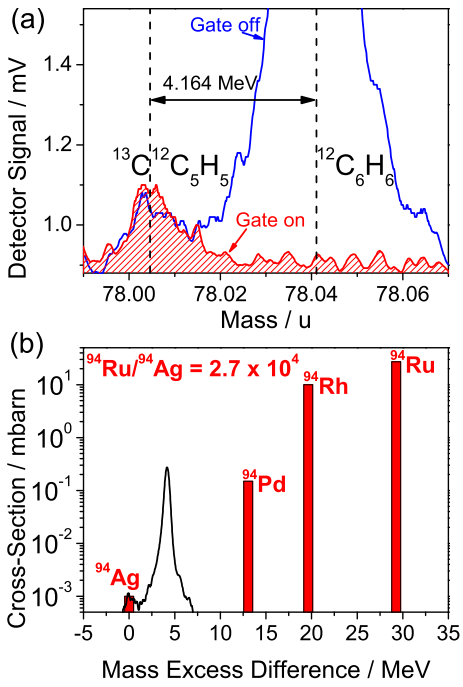

Figure 1: (a) Part of the mass spectrum of benzene measured after 256 turns with an time-of-flight detector behind the ion gate. The $^{12}C_6H_6$ is 170 times more intense than $^{13}C^{12}C_5H_5$. If the gate is off, both ion species pass through and impinge on the detector. If the ion gate is turned on with the correct timing, $^{12}C_6H_6$ is deflected and only $^{13}C^{12}C_5H_5$ impinges on the detector. (b) Fusion-evaporation production cross-sections calculated with PACE4 for ^{94}Ag and the spectrum from figure (a) (gate off) normalized to the ^{94}Ag cross section.

Ion Capacity. The System can handle more then 10,000 ions per cycle without deterioration of the transmission efficiency. Repetion frequencies of up to 100 Hz have been realized so far. Thus the ion capacity amounts to at least 10^6 ions per second.

References

[1] W. R. Plaß et al., Nucl. Instrum. Methods B, 266 (2008) 4560.

[2] T. Dickel et al., GSI Scientific Report 2008, p. 63.

[3] B. N. Kozlov et al., Proceedings of the 54th ASMS Conference on Mass Spectrometry and Allied Topics (2006)

*Work supported by the BMBF under contract 06GI185I and 06GI9114I and by GSI under contract GIMET2

PRESPEC: Driving on the FAIR road of HISPEC/DESPEC

A. Algora[1], A.M. Bruce[2], J. Gerl[3], M. Górska[3], M. Pfützner[4], N. Pietralla[5], D. Rudolph*[6], H.J. Wollersheim[3], and on behalf of the PRESPEC, HISPEC, and DESPEC collaborations[1]

[1]IFIC Valencia, Spain; [2]University of Brighton, United Kingdom; [3]GSI Helmholtzzentrum, Darmstadt, Germany; [4]University of Warsaw, Poland; [5]Technische Universität Darmstadt, Germany; [6]Lund University, Sweden

Fingerprinting excited nuclear states by γ-ray spectroscopy has been a viable tool to benchmark nuclear models for decades. Since contemporay nuclear structure investigations aim at the study and understanding of very exotic nuclei at the limits of stability and their decay properties, large and thus highly efficient γ-ray spectroscopy instruments are the basis for continued discoveries into the terra incognita of the nuclidic chart, while the key for future breakthroughs in high-resolution in-beam spectroscopy at relativistic energies lies in the implementation of highly segmented Ge-detector arrays such as AGATA, which are going to phase out the present-day limitations of Doppler broadened γ-ray lines.

The HISPEC/DESPEC collaboration within NUSTAR has its roots in the major pan-European programme 'Rare Isotope Spectroscopic INvestigations at GSI' (RISING), which started in the year 2003. RISING combined the concept of efficient and high-resolution γ-ray spectroscopy based upon 105 Ge-detector crystals confined in fifteen former EUROBALL Cluster-detectors with well-defined relativistic radioactive ion beams. The latter are at present produced in-beam by fragmentation or relativistic fission of primary beams from the heavy-ion synchrotron (SIS) at GSI, and subsequently the reaction products are separated, identified on an ion-by-ion basis, and finally focussed towards the RISING spectrometer by means of the FRagment Separator (FRS).

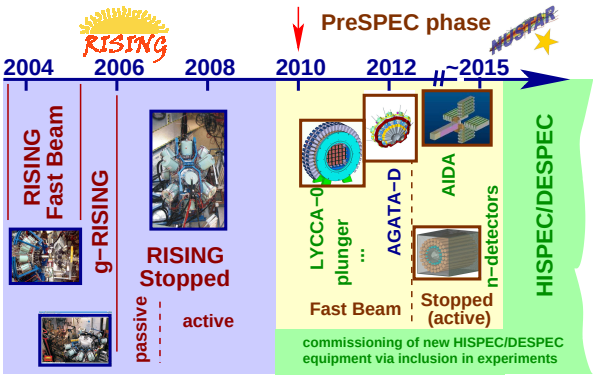

Figure 1: Sketch of the roadmap of HISPEC/DESPEC towards FAIR.

The roadmap for Ge-based nuclear structure investigations at presently GSI Darmstadt and later-on FAIR Darmstadt is depicted in Fig. 1: Following upon the successful RISING campaigns, the PRESPEC phase bridges towards FAIR by foreseeing physics-driven implementation and commissioning of FAIR instrumentation for high-resolution in-flight spectroscopy (HISPEC) and decay spectroscopy (DESPEC) within the NUSTAR frame. Upon applicability, HISPEC/DESPEC equipment will be made available for Super-FRS commissioning.

In 2009, the success of RISING was celebrated in Darmstadt [1-12] and the handover to PRESPEC took place, with more countries than ever actively participating.

In 2010, the collaboration plans to run a series of G-PAC approved in-flight experiments using the former RISING Fast-Beam set-up but coupled to LYCCA-0, the new identification device for tertinary reaction products. With LYCCA being the first TDR-approved NUSTAR device, it is one of several examples for FAIR instrumentation being implemented for NUSTAR-GSI experiments within the HISPEC/DESPEC community to allow continued frontline research until FAIR and in particular the Super-FRS become operational. The anticipated in-beam PRESPEC campaign will be highlighted in about 2012 by using highly-segmented AGATA detectors in conjunction with also several other HISPEC equipment such as a plunger device or cryogenic targets and/or new methodological approaches, which are in the TDR process and/or have already parasitic beam time approved.

The latter holds also true for AIDA, which marks the new high-granularity implantation device for DESPEC. TDRs are also being prepared for DESPEC neutron-detector devices aiming at decay studies of neutron-rich nuclear matter of potential relevance for astrophysical processes. Both the respective TDRs and the real FAIR detectors are envisaged to be ready by the time PRESPEC moves into the phase for decay experiments.

* D.Rudolph@nuclear.lu.se

References

[1] A. Bürger *et al.*, Phys. Lett. B **622**, 29 (2005).
[2] A. Banu *et al.*, Phys. Rev. C **72**, 061305(R) (2005).
[3] A. Jungclaus *et al.*, Phys. Rev. Lett. **99**, 132501 (2007).
[4] P. Doornenbal *et al.*, Phys. Lett. B **647**, 237 (2007).
[5] A.B. Garnsworthy *et al.*, Phys. Lett. B **660**, 326 (2008).
[6] T.R. Saito *et al.*, Phys. Lett. B **669**, 19 (2008).
[7] D. Rudolph *et al.*, Phys. Rev. C **78**, 021301(R) (2008).
[8] S.J. Steer *et al.*, Phys. Rev. C **78**, 061302(R) (2008).
[9] O. Wieland *et al.*, Phys. Rev. Lett. **102**, 092502 (2009).
[10] M. Górska *et al.*, Phys. Lett. B **672**, 313 (2009).
[11] L. Cáceres *et al.*, Phys. Rev. C **79**, 011301(R) (2009).
[12] Zs. Podolyák *et al.*, Phys. Rev. C **79**, 031305(R) (2009).

Beam Profile Monitor, ToF and Tracking Detector Set-up for HISPEC/DESPEC

M. Pfeiffer*[1], G. Pascovici[1], N. Warr[1], F. Naqvi[1], and J. Jolie[1]
[1]Institut für Kernphysik, Universität zu Köln, Germany

In the context of the HISPEC/DESPEC part of NUSTAR at FAIR-GSI we are investigating the development of new tracking detectors to reconstruct the kinematics of the ions after they are decelerated to energies of about $5\mathrm{MeV/u}$. The main issue encountered with slowing down relativistic beams are the energy straggling and the spread in space and direction of these beams. Thereby, new generations of beam-characterization detectors are requested, to allow not only the precise determination of the position of an incoming ion and its energy loss but also the arrival time (for time of flight purposes-TOF) and if possible also to reconstruct the ion track (Beam Tracking Detector).

The solutions we are investigating basically uses the secondary electrons generated by charged ions passing a thin sheet of material $(80 - 120\mu\mathrm{g/cm^2})$. Using a triangular electrostatic configuration (i.e. accelerating grids and mirror [1]) the secondary electrons are confined away from the primary ion beam path and further injected and multiplied in a pair of large MCPs in chevron configuration. The 2D coordinate system, namely the position-sensitive read-out sub-assembly consists of two pairs of mutually perpendicular delay lines [2] with an active area slightly larger as the MCPs effective area.

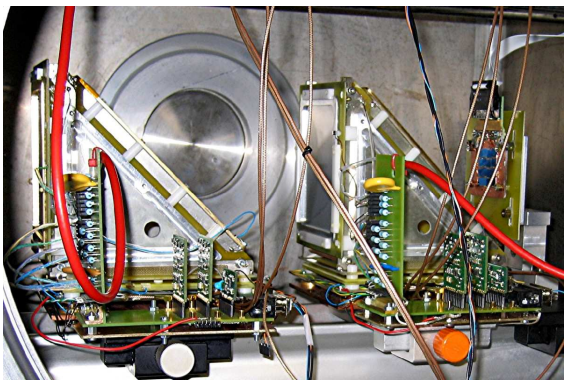

Figure 1: Layout of the BPM test-bed, the configuration with two BPMs and one matrix of 16 solar cells as beam stopper.

The most remarkable feature of this ion beam tracking detector is its modular structure. The basic unit has a large sensitive area of $\sim 80 \times 100\mathrm{mm}$ and its outputs are the 2D beam profile and a fast timing signal. Similar outputs are provided by an identical unit placed downstream on the beam axis and thus one gets the tracking of the ions. The aim of the further designs is to increase the sensitive area by factors of 2 to 4 with minimum dead area between the basic units.

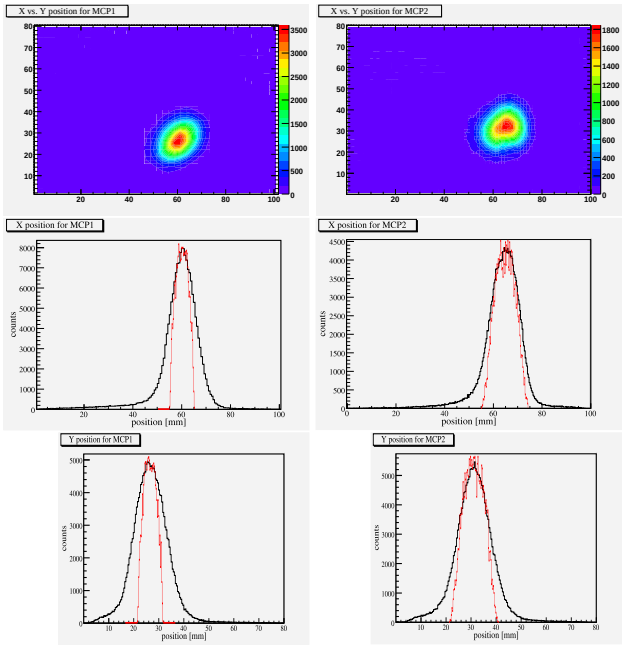

Figure 2: Measured profile of a collimated ^{241}Am source, in the BPM1 (left column) and BPM2 (right column) in different representations. The red histograms represent the simulated profiles at the input foil positions of each BPM.

The detector transparency for the primary ion beam, the space angular resolution and the sub-nanosecond timing resolution are the most relevant parameters. With transparencies of each component of $\sim 85 - 90\%$ we get an overall transparency of $\sim 65 - 70\%$ for one unit and we attain an angular resolution of about $2.5 \cdot 10^{-2}\mathrm{sr}$. The S/N ratio per current pulse is larger then 10/1, but we are facing a very high pulse shot noise at the MCP outputs, causing a broadening of the measured profiles (as one can see in Fig. 2, especially for the Y positions of MCP1). The source of this pulse shot noise is under investigation. Work supported by F & E project KJOLIE.

References

[1] E.M. Kozulin et al, Instr. and Exp. Tech. (2008), Vol. 56, No. 1, p. 44

[2] S.E. Sobottka and M.B. Williams, "Delay line readout of MCP", IEEE Trans. NS, 1988, Vol. 35, No. 1, p. 348

* pfeiffer@ikp.uni-koeln.de

Fast timing with DSSSD detectors.

P. Boutachkov[1], F. Naqvi[1], W. Koenig[1], E. Gregor[1], W. Prokopowicz[1], M. Górska[1], H. J. Wollersheim[1], H. Schaffner[1], Z. Abou-Haidar[2], and M.A.G. Alvarez[2]

[1]GSI, Darmstadt, Germany; [2]Seville University, Seville, Spain

Introduction

The NuSTAR HISPEC slowed down beams project at GSI/FAIR aims to produce rare isotopes with energies of 10 MeV/u and less. The setup requires tracking and Time of Flight(ToF) information [1]. An energy loss measurement is desirable in order to determine Z of the slowed down fragments. The detector should have a time resolution of ΔT$\sim$100 ps, position resolution of the order of a mm and energy resolution of ΔE/E$\sim$1%. A combination of commercially available Double Sided Silicon Strip Detector(DSSSD) and a 16ch fast pre-amplifier developed at GSI was investigated for this purpose.

DSSSD Readout

A 5x5 cm^2, 40 μm DSSSD model W(DS)-40 9G produced by Micron was used. The DSSSD has 16 X and Y strips. The detectors were mounted on a 16ch low power pre-amplifier [2] based on GALI-S66 RF amplifier by Mini Circuits (see Fig. 1). The pre-amplifier suitable for mounting in vacuum were developed and built at GSI by W. Koenig. The final shaping is done by external amplifiers followed by level discriminator, mounted in air on a 5x10 cm board. For timing measurements the fast pre-amplifiers were connected to one of the DSSSD sides, while the other side was read out with MESYTEC MPR-32 charge sensitive pre-amplifier to determine the deposited energy.

Results

Coulomb scattering of ^{48}Ca beam on Au target at UNILAC was used to test the detector readout. The setup utilized two transmission MCP detectors [3] followed by two 40 μm DSSSDs. The energy of 5.9 MeV/u was sufficient for the ^{48}Ca beam to punch through the first DSSSD. Typical rise times (10% - 90%) of 2 ns were measured in this detector. A CAEN 1290A TDC with 25ps LSB was used to measure the ToF between the MCP detectors and the DSSSDs. An example spectrum gated on a pixel of the Si detector is shown in Fig. 2. A FWHM$\sim$100 ps was obtained for a set of pixels after subtracting the contribution from the MCP. Due to the noise jitter this resolution was not obtained for all pixels. The measured DSSSD energy resolution was ΔE/E$\sim$5%. The events in the smaller intensity peak in Fig. 2 are related to a feedback in the discriminators which will be addressed in future revisions.

Outlook

Improvements in the stability and performance of the fast pre-amplifiers and compact discriminator board should lead to a detector system suitable for the slowed down beams project at GSI/FAIR.

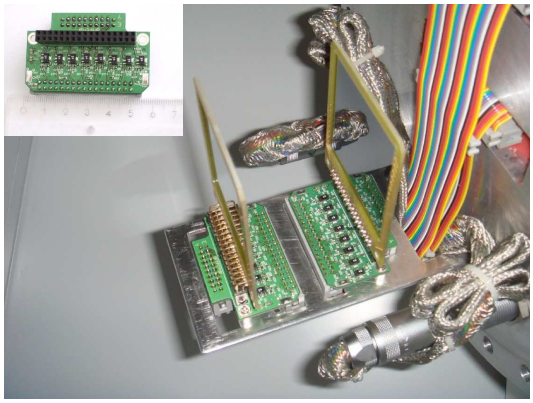

Figure 1: An assembly of the 40 μm DSSSD and the 16ch pre-amplifiers. The inset shows a magnified picture of the fast pre-amplifiers.

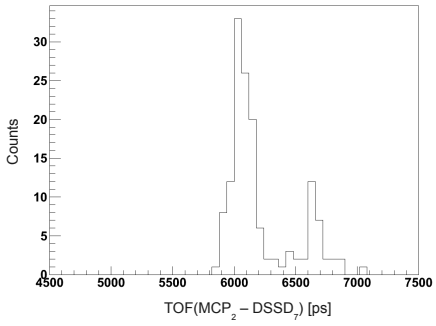

Figure 2: A representative ToF between the first MCP detector and a pixel from the DSSSD.

References

[1] P. Boutachkov *et al.*, GSI Scientific Rep. (2007) 215.

[2] W. Koenig and J. Pietraszko, GSI Scientific Rep. (2008) 218.

[3] P. Boutachkov *et al.*, GSI Scientific Rep. (2008) 236.

Status of the MATS facility: completion of the Technical Design Report*

D. Rodríguez[†1], K. Blaum[2], J. R. Crespo López-Urrutia[2], F. Herfurth[3], A. Jokinen[4,5], and the MATS collaboration[1]

[1]Universidad de Granada, Spain; [2]Max-Planck-Institute for Nuclear Physics, Heidelberg, Germany; [3]GSI Helmholtz Centre for Heavy Ion Research, Darmstadt, Germany; [4]University of Jyväskylä, Finland; [5]Helsinki Institute of Physics, Helsinki, Finland

The Penning-trap based setup MATS (precise Measurements on very short-lived nuclei using an Advanced Trapping System) is one of the NUSTAR experiments (NUclear STructure Astrophysics and Reactions) at the future FAIR facility, which will allow to extend the knowledge of a fundamental property such as the mass for nuclei further into the region far from stability. Masses with high accuracy serve for tests of mass models and formulae, nuclear structure studies, astrophysics and tests of fundamental symmetries covering a wide range of physics topics [1]. MATS will also allow to apply several techniques to very short-lived nuclei like in-trap conversion electron and alpha spectroscopy, and trap-assisted spectroscopy and neutron time-of-flight spectrometry. In the field of atomic physics, spectroscopy on Highly Charged Ions (HCI) in or from the Electron Beam Ion Trap (EBIT) will also be feasible.

MATS at FAIR is part of the Low Energy Beamline (LEB) of the Superconducting Fragment Separator (Super-FRS). The layout is shown in Fig. 1.

MATS will use advanced trapping techniques developed during the last five-year period. MATS will also for the first time combine cryogenic trapping systems and the use of high charge states for radioactive species with high production yields. Therefore, the performance is expected to be better compared to the existing facilities in terms of precision and number of exotic radionuclides accessible. For short-lived nuclei ($T_{1/2} \approx 10$ ms) with productions of 10^6 ions/s, we can easliy reach 10^{-8} mass accuracy. For long lived species with 1 s half-life but production rates of only 1 ion/s, still 10^{-8} mass accuracy can be reached [2]. The technique in use for these cases is the so-called time-of-flight resonance.

Non-destructive narrow-band Fourier-Transform Ion-Cyclotron-Resonance (FT-ICR) detection technique on single stored ions, which is under development at TRIGA-TRAP [3], is foreseen at MATS. This technique in the precision Penning trap will provide true single ion sensitivity, essential to access isotopes that are produced with minimum rates ($\ll$ 1 ion/s) and are very often the most interesting ones. In addition to mass measurements, novel spectroscopic tools, like for instance a trap structure made of detector units will be applied aiming $e.g.$ at measuring quadrupole moments and E0 strengths. The use of the detector trap will be combined with non-destructive broad-band FT-ICR detection in the preparation Penning trap allowing for quick identification of all radioactive species. This will also benefit trap-assisted spctroscopy experiments. Recent results using a broad-band detection system for fundamental applications are presented in Ref. [4].

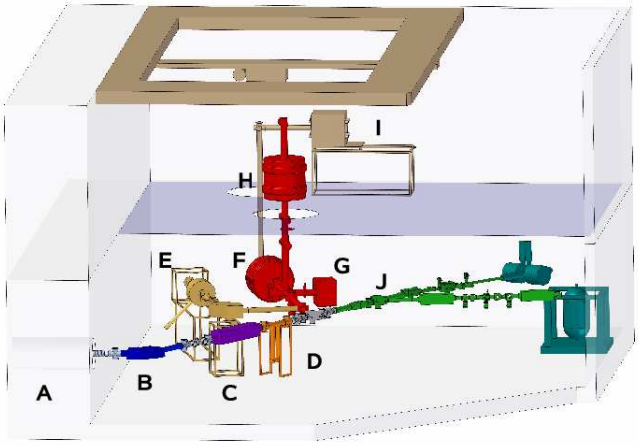

Figure 1: Layout of the MATS facility at the end of the LEB of the Super-FRS of FAIR. A) Gas-filled stopping chamber, B) RFQ buncher, C) MR-TOF, D)Switchyard, E) EBIT, F) Penning trap with broad-band FT-ICR, G) Off-line ion source, H) Precision Penning trap with TOF and narrow-band FT-ICR techniques, I) Setup for spectroscopy and J) LaSpec beam line including beta-NMR setup.

All these techniques and developments for ion detection are described in detail in the Technical Design Report of the MATS and LaSpec facilities recently submitted [5].

References

[1] K. Blaum, Phys. Rep. 425 (2006) 1-78.

[2] M. Block *et al.*, Nature, in print.

[3] J. Ketelaer *et al.*, Nucl. Instrum. Methods Phys. Res. A 594 (2008) 162-177.

[4] M. Ubieto-Díaz *et al.*, Int. J. Mass Spectrom. 288 (2009) 1-5.

[5] MATS & LaSpec TDR: A Technical Design Report for High-Precision Experiments at FAIR. http://www.mpi-hd.mpg.de/blaum/penningtrap-facilities/mats/documents.en.html

* Picture: Dr. Christopher Geppert

† danielrodriguez@ugr.es

Commissioning of *TRIGA-LASER* - tests and developments of the LaSpec beamline*

J. Krämer[1], K. Blaum[2], K. Eberhardt[1], Ch. Geppert[1,3], M. Hammen[1], A. Krieger[1], R. Neugart[1], W. Nörtershäuser[1,3], R. Sánchez[1,3], B. Sieber[1], and the TRIGA-SPEC collaboration

[1]Universität Mainz, Institut für Kernchemie, Germany; [2]Max-Planck-Institut für Kernphysik, Heidelberg, Germany; [3]GSI Helmholtzzentrum für Schwerionenforschung, Darmstadt, Germany

Introduction

The major parts of the TRIGA-LASER experiment for collinear laser spectroscopy on exotic fission products from the TRIGA research reactor [1] are now installed and are currently being commissioned. Besides the exploration of unknown ground in the nuclear chart with respect to spins, moments and charge radii, the experiment is the prototype of the the LaSpec experiment [2] at FAIR, GSI and will serve as a development platform until the final installation at FAIR.

Experimental

For commissioning, laser spectroscopy experiments were carried out with stable Rb ions from an offline ion source. The charge exchange cell (CEC) and the optical detection system were installed at the beamline and tested. Charge exchange of the rubidium ions was accomplished with potassium vapor produced in the cell at temperatures of $100-200^\circ$ C. A charge exchange efficiency of 99% can be reached. However, laser spectroscopy experiments will be performed with efficiencies of $20-40\%$ at about 140° C to avoid artificial broadening of the resonance lines. To change the velocity of the neutralized beam for Doppler tuning, the CEC can be floated to a potential of up to 10 kV. Voltage scans can either be performed with a Heinzinger PNChp10000 high-precision high-voltage power supply programmed via GPIB or with a Kepco HV amplifier controlled by the voltage of a 16 Bit DAC. The fluorescence detector after the CEC is a combination of a light collecting elliptical mirror with a light guide and a photomultiplier. The Hamamatsu R1017 multiplier exhibits 5% quantum efficiency at the Rb transition wavelength of 780 nm.

Results

The first laser spectroscopy experiments were performed with Rb atoms after charge exchange with an acceleration voltage of 10 kV and a maximum Doppler tuning voltage of ± 1 kV. This range is equivalent to approximately 9.5 GHz and sufficient to record the full Rb hyperfine structure of both naturally abundant isotopes ^{85}Rb and ^{87}Rb simultaneously. This is shown in Fig. 1, which shows the complete hyperfine structure as a function of the scanning voltage. The inset shows the strongest peak and demonstrates the resolution. The linewidth of 25 MHz is close to the natural linewidth of 6 MHz. The detection efficiency was optimized and a value of $\epsilon \approx 1$ photon / 360 atoms was achieved. The background caused by scattered laser light is about 150 kHz and therefore still too high. However, a signal-to-noise ratio of ≈ 2 in a 6 h integration time, assuming a resonance scan with 20 points, can be achieved with an atom beam intensity of 1×10^4 atoms/s.

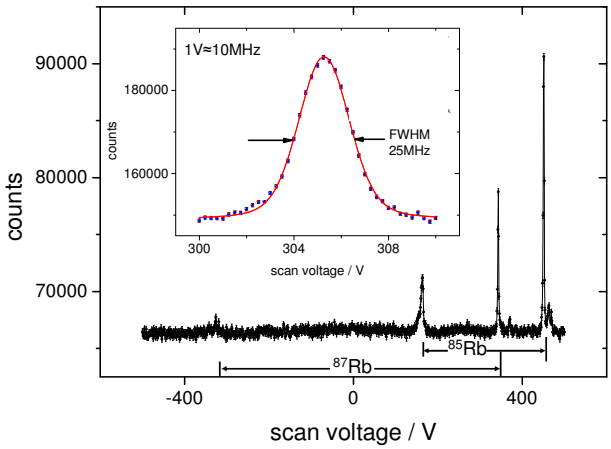

Figure 1: Full hyperfine spectrum of ^{85}Rb and ^{87}Rb and enlarged scan of the strongest peak. Spectra are the sum of 10 and 50 scans for the overall spectrum and the single peak, respectively ($P_{\text{Laser}} = 0.54$ mW, $I = 3 \times 10^7$ atoms/s).

Currently, a particle detection system for low count rates is being tested which will allow to perform particle-photon coincidence measurements to increase the sensitivity [3]. Lower stray-light background and higher detection efficiency of fluorescence light are the objectives of a new light collection module which is currently being designed and simulated. Coupling to the reactor and first online experiments are expected for the end of 2010.

References

[1] J. Ketelaer, J. Krämer, et al., Nucl. Instrum. Methods Phys. Res., Sect. **A 594** (2008) 162-177.

[2] W. Nörtershäuser, P. Campbell, and the LaSpec collaboration, Hyp. Int. **171** (2006) 149.

[3] D.A. Eastham, Jour. Phys. **G12** (1986) L205

*Work supported by HGF under contract VH-NG-148 and 'Stiftung Rheinland-Pfalz für Innovation' under contract 961-386261/854.

Isomeric beams, Lifetimes and Masses: ILIMA Project at FAIR

Yu.A. Litvinov[1,2], P.M. Walker[3], H. Weick[1], and ILIMA@NuSTAR Collaboration[0]
[1]GSI, Darmstadt; [2]MPI-K, Heidelberg; [3]Uni. Surrey

The foreseen modularized realization of FAIR has dramatic implications on the future storage ring experiments including the ILIMA project [1]. Nevertheless, a significant part of the ILIMA will be realized when the Collector Ring (CR) coupled to the Super-FRS becomes operational. The CR will be used in the isochronous mode, and will give access to the shortest lived, i.e. most exotic, nuclides (down to half-lives of less than 0.1 ms). The proven ability to detect and measure the properties of single ions gives unparalleled sensitivity in comparison with other techniques worldwide [3]. This will provide exceptional discovery potential, for example:

- masses and lifetimes of r-process nuclides and possible shell-gap quenching at N=82 and 126
- neutron-unbound high-spin isomers close to the neutron drip-line

The ILIMA collaboration will use the present FRS-ESR facility for the development and commissioning of the experimental equipment. Improved isochronous operational mode of the ESR along with the adjusted ion-optical setting of the FRS is being prepared [2]. One of the key developments for the future experiments is the new generation Time-of-Flight (TOF) detector. Some specific points are described in Ref. [4]. The isochronous conditions are fulfilled only for a limited range of the broad-band spectrum of stored exotic nuclei [5]. Two such detectors will be installed in one of straight sections of the CR to enable the in-ring measurement of velocities of each stored ion. This velocity measurement will allow us to correct for the "non-isochronicity" thus achieving the high resolving power over the entire spectrum. The first tests of the proposed procedure will be done at at IMP in Lanzhou, where it is planned to install two TOF detectors in the CSRe ring. In the present FRS-ESR experiments we use a so-called $B\rho$-tagging method in which we–at the cost of the strongly reduced transmission–inject only ions with well-defined magnetic rigidities, $B\rho$ [5].

A new generation Schottky pick-up detector is being developed for the Schottky Mass Spectrometry experiments at the ESR. This new detector is based on the resonator-cavity principle. The detector will be assembled and tested with beam during 2010. If successful, it is expected to achieve a significantly better signal-to-noise characteristics as with the present pick-up.

The new developments will allow us to make mass and lifetime measurements of extremely exotic nuclei. Storage ring data require external calibration. New mass data in the relevant regions on the chart of nuclides will be very scarse or fully absent. Therefore, the question of the mass calibration in future experiments is of utmost importance. One suggestion is to inject stable nuclides in an atomic charge state selected such, that their mass-over-charge ratio fall into the measured spectrum. Another suggestion is connect the newly measured mass values to the well-known masses via a global network of measured mass relations. The storage ring data contain correlations between masses of *all* nuclides measured in a given experiment (see Figure 1). In the future we will combine together the correlations from different data sets of IMS and SMS experiments [7] and incorporate them into the Atomic Mass Evaluation (AME) for the consistent calibration. Thus a global network of correlations between all nuclides ever measured will be established. A single new mass value measured, e.g., with a Penning trap will constrain the entire mass surface via these correlations.

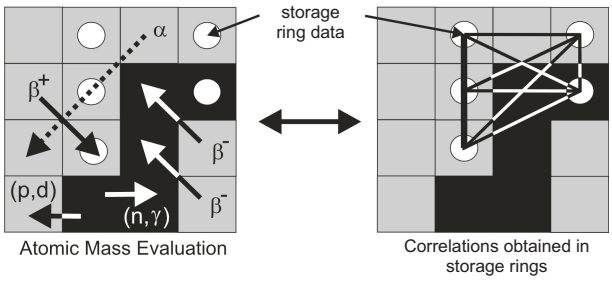

Figure 1: Schematic view of the AME principle [6] (left) and the correlated data measured with storage ring mass spectrometry (right). In the AME, Q-values from α- and β- decays, reactions (e.g., (n,γ), (p,d) etc.) are collected. Every mass value obtained directly (e.g. with Penning traps or storage rings) is related to a reference isotope (e.g. ^{12}C) and is added as a single relation. The storage ring data provide correlations between all masses measured in a given experiment, and the correlations from different experiments can be combined together [7]. In the future the measured correlations will be incorporated into the AME.

References

[1] R. Krücken, C. Scheidenberger, GSI Annual Report 2009, *this issue*.
[2] S.A. Litvinov et al., GSI Annual Report 2009, *this issue*.
[3] M. Reed et al., GSI Annual Report 2009, *this issue*.
[4] N. Kuzminchuk et al., GSI Annual Report 2009, *this issue*.
[5] H. Geissel *et al.*, *Hyperf. Interactions* **173** (2006) 49.
[6] A. Wapstra et al., *Nucl. Phys.* **A729** (2003) 129.
[7] Yu.A. Litvinov *et al.*, *Hyperf. Interactions* **173** (2006) 55.

[0]http://www.gsi.de/fair/experiments/NUSTAR/ilima.html

Rate Acceptance and Timing Performance of a Time-of-Flight Detector for Isochronous Mass Measurements in the CR*

N. Kuzminchuk[1,2], S. Ayet[1], M. Diwisch[2], H. Geissel[1,2], C. Kozhuharov[1], R. Knöbel[1,2], Y. Litvinov[1,3], W. R. Plaß[1,2], C. Scheidenberger[1,2], B. Sun[1,2], H. Weick[1]

[1]GSI, Darmstadt, Germany; [2]Justus-Liebig Universität, Giessen, Germany; [3]MPI-K, Heidelberg, Germany.

Isochronous Mass Spectrometry (IMS) in the ESR has successfully applied recently [1]. At FAIR, IMS will be performed in the Collector Ring (CR) in combination with the Super-FRS and thus substantially extend the reach of mass measurements to more exotic ions.

In IMS the masses of the nuclei are directly determined from the revolution frequencies measured by a micro-channel plate (MCP) time-of-flight detector. In the detector, ions passing a thin carbon foil release secondary electrons (SE), which are transported to microchannel plates by electric and magnetic fields [2]. The detector for the CR is currently under development; it is based on the IMS detector in the ESR.

Rate Acceptance

Because of the high revolution frequency in the CR, the rate acceptance of the detector is an important performance parameter. It was determined and increased [3]. The rate capability of MCPs is influenced by their channel diameter. One of the parameter, which can be used to characterise the rate acceptance of MCPs, is the change of the pulse-height distribution (PHD). At higher rates the PHD shifts to smaller amplitude values and changes from peaked to an exponential shape (Fig. 1).

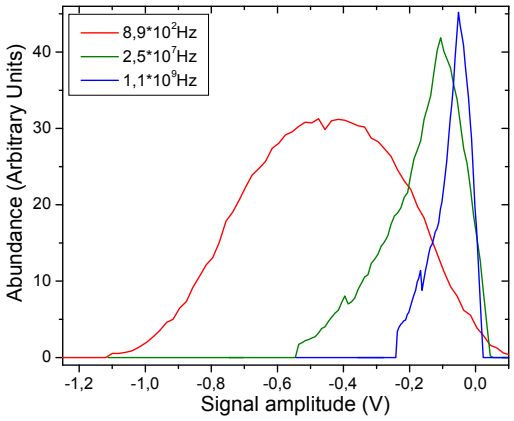

Figure 1: PHD for different rates of incident electrons. MCPs with a channel diameter of 5 µm with an acceleration voltage of 200 V between the plates were used. For a rate of $8.9 \cdot 10^2$ Hz the PHD is peaked and at $1.1 \cdot 10^9$ Hz it changes completely to an exponential shape.

MCPs with the same active diameter but with a pore sizes of 5 µm and 10 µm were tested with an electron source with variable electron beam current. Measurements showed that indeed 5 µm microchannel plates are about 4 times more resistant to higher rates than plates with 10 µm channel diameter (Fig. 2).

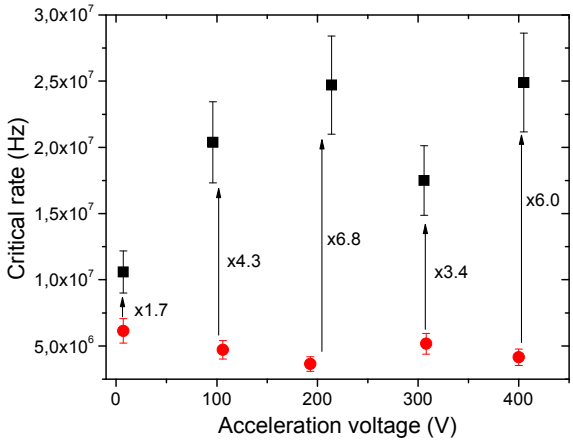

Figure 2: Comparison of the critical rate (onset of shift of PHD) of MCPs with 5 µm (black squares) and 10 µm (red circles) pore sizes at different acceleration voltages between the MCPs.

Timing Characteristics

The timing accuracy of the TOF detector currently amounts to about 50 ps and can be further improved by changes to the MCP detector design. The differences in the time-of-flight of the secondary electrons are due to (i) the electron transport from the foil to the MCPs and (ii) the electron transit in the MCP channels.

The electron transport from the foil to the MCPs was simulated. Simulations show that by increasing the kinetic energy of the SE, the error in the time-of-flight due to field imperfections and different initial velocities can be decreased.

The spread as well as the event jitter in the electron transit times through the MCP scales inversely proportionally with the channel diameter. In addition the width of the signal depends on the number of initial SE emitted from the foil [4]. Therefore the use of 5 µm MCPs will improve timing characteristics.

A new design of an anode was made to optimise the MCP signal quality. First tests show that by decreasing the capacitance between the anode and the MCPs the peak width can be reduced by a factor of up to two.

References

[1] B. Sun, Nucl. Phys. A 812 (2008), 1.
[2] B. Fabian, PhD thesis, Universität Gießen, 2008.
[3] M. Diwisch, Bachelorthesis, Universität Gießen, 2009.
[4] J. Va'vra et al., Nucl. Instrum. Methods A 595 (2008) 270-273.

* Work supported by the BMBF under contract No. 06GI9115I

In-beam EXL demonstrator tests

P.J. Börger[1], T. Davinson[2], P. Egelhof[3], S. Ilieva[3], N. Kalantar-Nayestanaki[1], X.C. Le[3], M. Mutterer[3], A. Najafi[1], C. Rigollet[1], B. Streicher[3], M. von Schmid[3], P.J. Woods[2]

1 KVI, University of Groningen, the Netherlands; 2 University of Edinburgh, United Kingdom; [3]GSI, Darmstadt, Germany

Introduction

The EXL [1] demonstrator represents a key element of the EXL Silicon recoil detector array. In a first instance, we performed an in-beam test at KVI, where the demonstrator comprised a stack of two DSSDs (Double Sided Silicon-Strip Detector) [2] followed by two Si(Li)s [3]. The goals of this experiment were to investigate the operation of the four detectors together, as well as to evaluate the capability of the system for tracking and energy reconstruction of the incident particle. An additional aim was to study the DSSD response on punching through particles.

Experimental setup

All four detectors were placed in a stainless-steel chamber with an entrance window made of a thin foil of mylar and closed by a flange holding the detectors, DSSDs preamplifiers and cooling system (see Figure 1). This flange is equipped with many feedthroughs for the connection of the preamplifiers to the rest of the electronic chain and the cooling outside of the chamber. During the experiment the preamplifiers and Si(Li)s were cooled down to -10° C. The vacuum chamber was placed at about 60 cm from the exit of the beam-line. The incident protons lose 1.1 ± 0.25 MeV in air and entrance window before reaching the first DSSD.

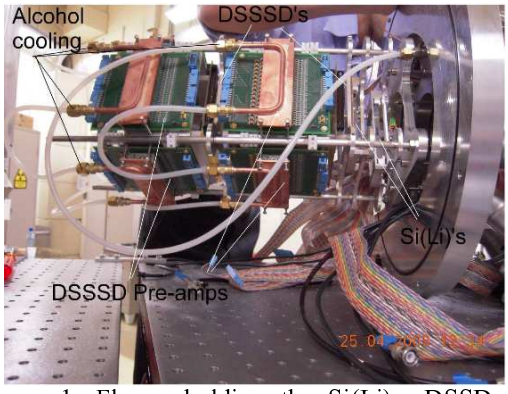

Figure 1: Flange holding the Si(Li)s, DSSDs, their preamplifiers and the cooling system.

The DSSDs are 300 μm thick with an active area of 21 by 21 mm^2. The first one placed in the beam has 64 by 64 strips, whereas the following DSSD has 64 by 16 strips. The two DSSDs are separated by 10 cm in the chamber and the second DSSD is closely followed (1 cm) by the two Si(Li)s. The latter have dimensions of 50 by 80 mm^2, with a thickness of 6.5 mm and each is divided into eight pads. The size of the beam spot was chosen to be about 20 mm in order to irradiate an essential part of the active area of the first DSSD.

Results

The result of the energy reconstruction (event by event) is shown in Figure 2, and was obtained after a careful calibration, with conditions imposed on the full energy deposited in the detectors. The centroid of the peak is at 48.57 MeV and the FWHM is 300 ± 3 keV. The value for the reconstructed energy doesn't include the 1.1 MeV energy loss suffered in air and entrance window by the incident protons. Finally we obtain a value of 49.67 ± 0.25 MeV for the incident energy.

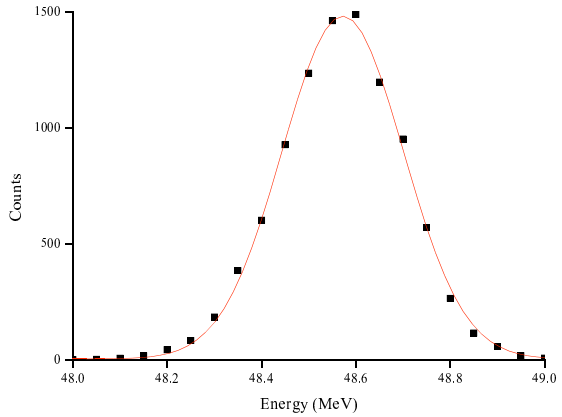

Figure 2: Energy reconstruction of the incident proton with an energy of 50 MeV.

The tracking of particles showed that the beam spot increased in both x and y directions by 17% between the two DSSDs.
These are very encouraging results for the feasibility study of EXL and its expansion to the Silicon full array.

Further tests and outlook

The full EXL recoil detector also comprises a calorimeter around the Silicon array. To test the full demonstrator, we recently performed a second experiment at GSI, using a similar setup as the previous one and adding two CsI detectors to investigate the calorimeter part of the full array. This time, proton beams with energies of 100 and 150 MeV were used to ascertain that the particles go through all the detection elements and stop in the CsI. The data analysis is currently in progress.

References

[1] www.rug.nl/kvi/exl
[2] GSI Scientific Report 2008, p55
[3] GSI Scientific Report 2006, p.33

Pulse-Shape Discrimination with DSSD prototypes for the EXL project*

M. von Schmid[1,2], P. Egelhof[2], V. Eremin[3], R. Gernhäuser[4], T. Kröll[1], M. Mutterer[2,1], N. Pietralla[1], B. Streicher[2], and M. Weber[4]

[1]IKP, TU Darmstadt; [2]GSI, Darmstadt; [3]PTI, St. Petersburg, Russia; [4]Physik-Department E12, TU München

Motivation

Pulse-shape discrimination (PSD) with silicon detectors has been evolved into a powerful method for the discrimination of charged particles with some advantages over classical methods like ΔE-E measurements. For more information about PSD see for example [1-5] and references therein. Nevertheless highly segmented detectors have not been used for PSD yet.

In a first approach ([6], [7]) we have used double-sided silicon strip detectors (DSSD) available as prototypes for the planed EXL experiment [8], a part of NuSTAR at the future FAIR facility. The used DSSDs are segmented into 16 strips per side with a pitch of 300 μm, are 300 μm thick and have outer dimensions of 7.1×7.1 mm^2 (see also [9]). PSD can be a useful tool for the first layer of EXL's Silicon Particle Array (ESPA), where light particles have to be distinguished.

Technical Procedure

Our method of deriving particle information from the detector signal is based on the measurement of the pulse width of the current signal, induced on the contacts of the silicon detector. Together with the measured energy, particles can be separated by their nuclear charge and partly even by their mass (for more details see [4]). The current signal is measured with a modified version of the CSTA2 preamplifier (developed and manufactured at the electronics lab of the IKP at TU Darmstadt), which is a wide band hybrid preamplifier with a slow output for energy measurements and a fast timing output. With the applied modification, the fast timing signal represents a good approximation of the actually induced current signal. This signal is amplified and shaped with a TFA2000-6 timing filter amplifier, which is also a development of the IKP at TU Darmstadt. All other electronics including the energy measurement on both sides of the detector was standard electronics.

Besides several preparative tests with α-sources, carried out at GSI, we have performed a test experiment at the tandem accelerator of the Maier-Leibnitz-Laboratorium (MLL) in Garching. A ^{12}C beam of 70 MeV impinged on a 2 μm thick mylar target. With an absorber foil in front of the detector, mainly light particles up to helium plus the elastically scattered protons were registered. The detector was placed at an angle of $17.8^\circ \pm 0.5^\circ$ with regard to the beam axis using rear-side injection. An additional silicon detector diode behind the DSSD was used as a veto detector for particles punching through the DSSD.

* Work supported by BMBF (06DA9040I), MLL and HIC for FAIR

Results

Figure 1 (top) shows a 2D spectrum of the measured energy versus the pulse width (plus an electronic offset), for strip #16 as an example. By selecting only strip-strip events, which means that each event is seen only by one strip at each side, the spectrum is cleaned (see figure 1 (bottom)) and α-particles and protons can clearly be distinguished down to an energy of about 3-4 MeV. The drawback of this procedure is, that roughly 50 % of all events are rejected. Under these conditions, the performance of the DSSD turned out to be comparable to unsegmented silicon detectors. Motivated by these encouraging results, further research on this topic will be done.

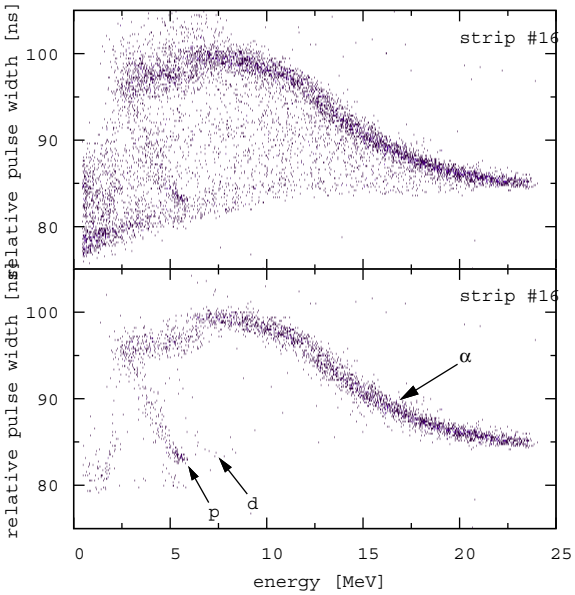

Figure 1: Energy versus relative pulse width (including an electronic offset) of DSSD strip #16 (p-side); *top:* all events stopped in the DSSD; *bottom:* with condition on strip-strip events

References

[1] C. Ammerlaan et al., Nucl. Instr. and Meth. A 22 (1963) 189.

[2] G. Pausch et al., Nucl. Instr. and Meth. A 337 (1994) 573.

[3] G. Pausch et al., Nucl. Instr. and Meth. A 349 (1994) 281.

[4] M. Mutterer et al., IEEE Trans. Nucl. Sci. NS-47 (2000) 756.

[5] M. Mutterer et al., Nucl. Instr. and Meth. A 608 (2009) 275.

[6] M. von Schmid, Master Thesis, IKP TU Darmstadt, 2009.

[7] M. von Schmid et al., publication in preparation.

[8] EXL website: `http://www.rug.nl/kvi/EXL`

[9] B. Streicher et al., GSI Scientific Report 2008, FAIR-Experiments-53.

Upgraded electron ring design for the electron-nucleus collider (ELISe)*

D.Shwartz[1], P. Shatunov[1], I.Koop[1]
[1]BINP, Novosibirsk, Russia

This report is dedicated to an upgrade of the design of the Electron ring (EAR) adopted to the ELISe experiments needs. The arrangement of magnetic elements, lattice functions, dynamic aperture simulations in the EAR are described.

The conceptual design of the Electron-Ion Collider (EAR) is described in [1]. In order to fulfil the demanding requirements, especially for fission experiments at ELISe, the interaction zone (IZ) at the intersection of the EAR with the bypass section of the NESR has to be optimized. Nevertheless the already defined base parameters should remain unchanged: the working point $\nu_x = 4.2$, $\nu_y = 3.2$; the beta-functions at the IZ; $\beta_x^* = 100$ cm, $\beta_y^* = 15$ cm; and the emittances $\varepsilon_{x,z} = 4 \cdot 10^{-6}$ cm·rad. A variety of other lattice options is in principle available, due to the flexible arcs optics. The maximum for the β-functions is increased up to 45 m, in order to restore problems with nonlinear dynamics and dynamic aperture (DA).

A chromaticity correction of the betatron tunes and other investigations addressing chromatic aspects, together with a simple DA estimation were discussed previously [2]. This work concentrates on working out a routine procedure for chromaticity compensation with simultaneous DA optimization.

The idea of the DA enlargement, chromaticity compensation through sextupole lenses is the following [3], [4]: (i) the initial vector of natural chromaticity (ξ_x, ξ_y) is divided into small portions. (ii) Each portion is compensated with a single pair out of the sextupole families (SX_i, SY_j) that gives the largest DA for this step. (iii) Finally the chromaticity is compensated with a DA being optimized simultaneously. Let's call this procedure "best pairs method".

The DA was estimated through track calculations using the SAD code [5]. With 10 "independent" chromatic sextupoles available, one can find 45 different combinations. For each pair at each step of the chromaticity compensation the DA is calculated. The number of chromaticity compensation steps should be at least close to the number of possible combinations [3]. As far as the DA is affected not only by sextupole fields but also by the fringe fields of the quads, the latter were switched on during DA optimization. That helps, for example, to suppress the tune-amplitude dependence, generated by fringes.

* This work was supported by the EC via the Intas programme contract number 05-1000008-8272.

Another improvement to the "best pairs" method is the introduction of DA estimations with finite momentum deviations during the procedure.

This helps avoiding that the DA optimized for a particular momentum shrinks dramatically for the other ones. Finally, the DA of the EAR lattice with optimized chromaticity correction is presented at Figure. 1.

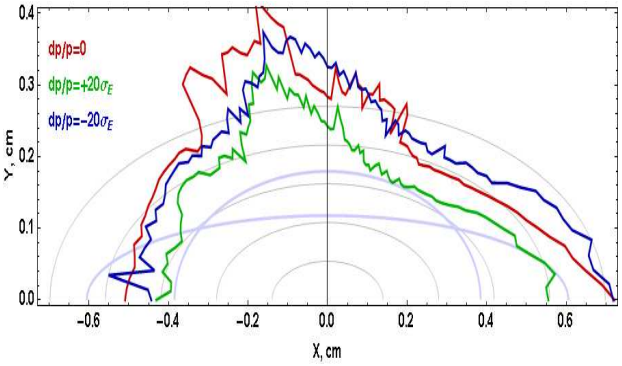

Figure 1: Optimized DA for the base lattice of the EAR as seen in the centre of the interaction zone. The light-blue ellipsis corresponds to the mechanic apertures restriction (∅40 mm vacuum chamber). The grey ellipses show beam size multiplied by 10, 20, 30, 40, 50, respectively.

The Electron ring (EAR) was successfully adopted to the needs given by ELISe's physics program. A tunes chromaticity compensation procedure, including dynamic aperture optimization ("best pairs" method) was implemented. It shows good results and should be used as routine technique for further lattice modifications. Chromatic aspects (lattice functions chromaticity, second-order dispersion function etc.) have been studied, and no serious problems are revealed. The dynamic aperture of the current optics seems to be sufficient, being slightly larger than the mechanical limitations and as large as 25σ in all three directions.

References

[1] I. Koop et al., "Conceptual Design of the Electron-Nucleus and Antiproton-Nucleus Scattering Facility for FAIR project.", BINP, Novosibirsk, 2006.
[2] I. Koop, Yu. Shatunov, P. Shatunov, D. Shwartz, BINP report, 07/2008.
[3] E. Levichev, P. Piminov, "Algorithms for Chromatic Sextupole Optimization and Dynamic Aperture Increase.", EPAC'2006, Edinburg, p.2116.
[4] D.Einfeld, et al., "ALBA Dynamic Aperture Optimization.", EPAC'2008, Genoa, Italy, p.3140.
[5] SAD code homepage, http://acc-physics.kek.jp/SAD/sad.html.

A novel spectrometer concept for exotic nuclear structure research at the electron/ion collider ELISe at FAIR*

T. Adachi[1], G.P.A. Berg[2], N. Kalantar-Nayestanaki[1], H. Simon[3], M.N. Harakeh[1], H.J. Wörtche[1], I.A. Koop[4], M. Couder[2], and M. Fujiwara[5]

[1]KVI, Groningen, The Netherlands; [2]JINA, Notre Dame, U.S.A.; [3]GSI, Darmstadt, Germany; [4]BINP, Novosibirsk, Russia; [5]RCNP, Osaka, Japan

Electron scattering on stable target nuclei has been the most reliable tool to study nuclear structure. This tool will be available for the investigation of exotic nuclei at the electron-ion collider ELISe at FAIR.

The ELISe facility is based on the colliding storage rings EAR and NESR for electrons and ions, respectively. The main instrument of ELISe will be an electron spectrometer that accepts a large fraction of scattering angles. The spectrometer consists of a Pre-Deflector (PD), a Quadrupole (Q), a Hexapole (H) and a vertically bending Dipole (D) magnets [1,2]. This spectrometer allows to measure scattering angles as small as 10˚ all the way to backward angles of approximately 60˚.

The conceptual design study with a vertically opening gap but constant field PD [1] was completed. The next task is the optimization of the final lay-out for the ELISe spectrometer. In order to verify the conceptual design and to establish design parameters, ion-optical calculations have been performed with the code COSY INFINITY.

An example of the ion optical calculation is shown in Fig. 1. The incident electron energy is at 517.6 MeV and the electron scattering angle is at 22.7˚. The radii of the bore of Q and H are 17.0 cm and the (horizontal) gap of D is 15.5 cm. The polar and azimuthal angle acceptances of the spectrometer at 22.7˚ are $\theta = \pm 30$ mrad and $\varphi = \pm 72$ mrad, respectively, for an energy acceptance of $\delta E/E \approx \pm 5\%$.

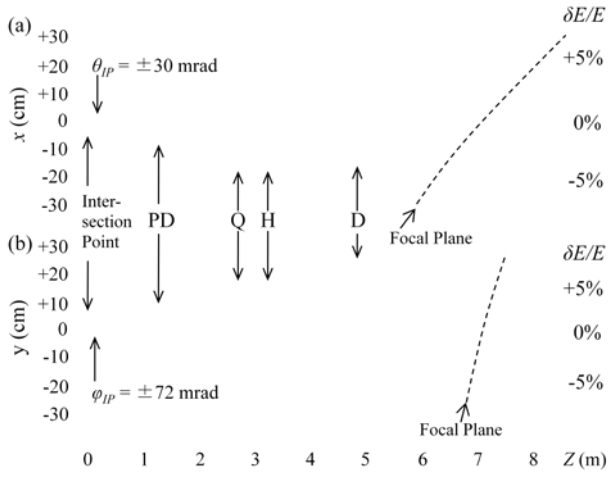

Figure 1: Selected rays through the ELISe spectrometer. (a) Rays for different polar scattering angles (θ). (b) Rays for different azimuthal scattering angles (φ).

In order to verify the angle acceptances at different spectrometer angles, ion-optics calculations were performed from 11.4˚ to 62.8˚. Fig. 2 shows the angle acceptances as a function of electron scattering angle. The polar angle acceptance increases as the electron scattering angle increases. The azimuthal angle acceptance is the largest at 19.0˚ (±140 mrad) and decrease as the electron scattering angle increases. At forward angles smaller than 19.0˚, the azimuthal angle acceptances are smaller due to the strong vertical focusing at the front-edge of the PD.

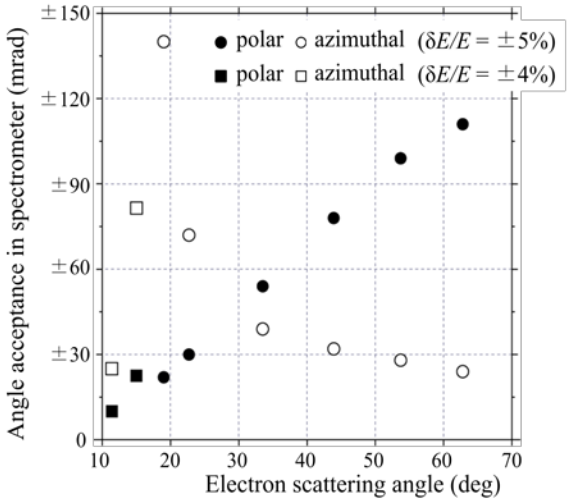

Figure 2: Angle acceptances in spectrometer as the function of electron scattering angles. At 11.4˚ and 15.0˚, the angle acceptances are estimated for $\delta E/E = \pm 4\%$. At scattering angles larger than 19.0˚, the angle acceptances are estimated for $\delta E/E = \pm 5\%$.

*This work was supported by the EC via the Intas programme contract number 05-1000008-8272.

References

[1] H. Simon et. al., GSI scientific report (2009) p. 61.
[2] G.P.A. Berg et. al., Nucl. Inst. Meth. B, in preparation.

New option of the interaction region of the electron-nucleus collider adopted for the fission experiment.*

P. Shatunov[1], I. Koop[1], D. Shwartz[1], J. Taieb[2], L. Chulkov[3], H. Simon[3]
[1]BINP, Novosibirsk, Russia; [2]CEA-DAM, Bruyères-le-Châtel, France; [3]GSI, Darmstadt, Germany

During year 2009, the ion optical development work on the ELISe experiment was mainly dedicated to accommodating the demands for the rings and the interaction zone (IZ), to the, in terms of resolution and acceptance, most demanding fission experiments.

The main experimental requirements are: (i) small beam sizes in the IP and (ii) large enough beam currents to achieve high luminosity; (iii) a long enough interaction region to place the electron spectrometer with sufficient energy resolution; (iv) an energy acceptance of the ion ring which should be at least ±1.5% for detection of the residual ions altered magnetic rigidity depending on their A/Z ratio.

In these experiments the fissioning ions decay into two fragments with rather large relative angles and kinetic energies. Furthermore their A/Z ratio may deviate substantially from the one of the initially stored secondary beam ion. Thus, such particles cannot be accumulated into the acceptance of the ring. They will be subsequently detected outside the ring acceptance e.g. using a time of flight system which demand free space of about 7 meters length in order to achieve mass resolution with a recently demonstrated FWHM for the time resolution of 35ps.

Simulations calculations within the range of possible angles were carried out for different nuclei. These simulations show that for detecting all fission products of a free cone with opening angle of ±40mrad would have to be provided. It is obvious taking into account the length of the involved magnetic elements and drift regions in the IZ, the necessary apertures would be prohibitively large.

After a variety of lattice simulations and optimizations a technically feasible compromise was found that allows for emerging fission fragments covering angles of ±20mrad. The newly found layout (see Figure 1) preserves the good properties achieved in a previous approach to the interaction region's optics layout and provides a good enough solid angle for the foreseen fission experiments.

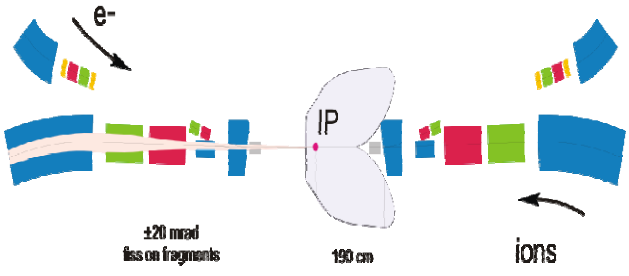

Figure 1: New Option of the interaction region.

Electrons and ions collide inside the IZ. The orbits of ions and electrons divorce inside the separation dipole guiding electrons into the electron ring arc while ions continue passing through NESR's bypass section, which is exclusively used in collider operation. This area accommodates several dipoles and final focusing quadrupole magnets in order to allow for ion optically matching the IZ with the rest of the NESR ring.

Due to the newly developed shape for the predeflection dipole (as shown elsewhere in this report) of the electron spectrometer, the separating dipole can be shifted closer to the IZ and is now situated at 190cm distance. Here electrons are bent to an angle of 16.5º. The angle for the ion orbit depends on the ratio of energies. The reference orbit is defined by ions and electrons at energies of 740MeV/u and 325MeV, respectively.

Following a short straight section a steering dipole is situated. This dipole is used to compensate ion orbit deviations from the reference orbit.

The length of final focusing quads has been increased to 100 cm now. This is necessary to preserve the integral of magnetic field gradient with a much larger aperture.

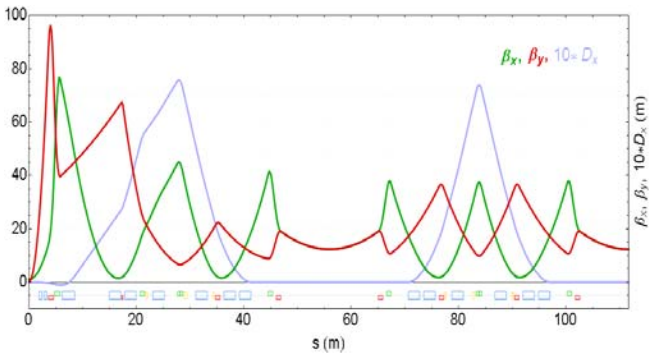

Figure 2: Structure functions for the collider.

The adjacent compensating dipole bends the ion orbit for ≈15º and guides it into the NESR arc. The guiding magnetic field in this dipole is equal to the guiding fields in the main NESR magnets but the length of the dipole is longer to compensate the angle gained in the separation dipole. In the IZ (see Figure 2) the beta-functions are now β_x=15cm and β_z=100cm, the betatron tunes are ν_x=3.55, ν_z=2.55, while the beta-functions in the final focusing quads have reached a value of 100m. This could dramatically decrease the dynamic aperture of the ring.

For ions with reference energy the dynamic aperture is 50σ (50 beam sizes), while for particles with energy deviating by ±1.5% the value of the dynamic aperture decreases to only 10σ. This should be sufficient, but additional simulation calculations should be carried out in order to increase these values.

* This work was supported by the EC via the Intas programme contract number 05-1000008-8272.

Status of the CBM Experiment at FAIR*

P. Senger[1] and the CBM Collaboration
[1]GSI, Darmstadt, Germany

Exploring the QCD phase diagram

The goal of present and future heavy-ion collision experiments at high beam energies is the precise scanning of the QCD phase diagram. The measurements at RHIC and LHC concentrate on the region at very high temperatures and almost zero baryon-chemical potential. The complementary approach is to explore the QCD phase diagram in the region of high net-baryon densities. Such experiments allow to address fundamental physics questions: What are the properties of very dense nuclear matter? Is there a first order phase transition between hadronic and partonic matter? Is there a critical or a triple point, and, if yes, where are these points located? Is there a chiral phase transition, and, if yes, does it coincide with the deconfinement phase transition? Are there new QCD phases such as "quarkyonic" matter? Figure 1 illustrates possible phases of strongly interaction matter (taken from [1]).

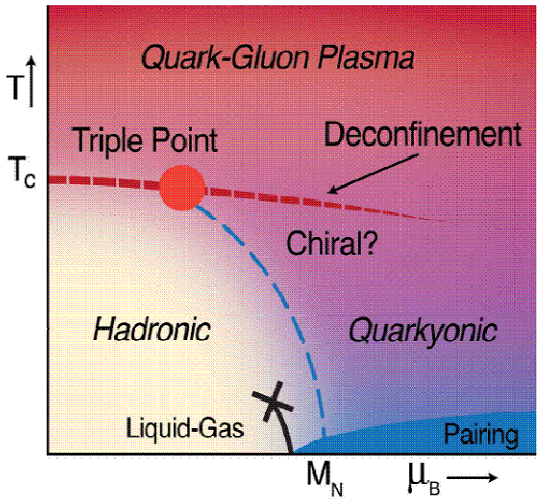

Fig.1: Sketch of a possible QCD phase diagram [1]

The discovery potential of nuclear matter experiments at intermediate beam energies triggered new experimental activities at the major heavy-ion laboratories: the beam energy scan program at RHIC, the fixed-target NA61/SHINE experiment at CERN-SPS, the NICA collider project at JINR in Dubna, and the fixed-target Compressed Baryonic Matter (CBM) experiment at FAIR. The collider experiments at RHIC and NICA have the advantage of a constant acceptance as function of beam energy. On the other hand, when running at low beam energies, collider experiments are restricted to the measurement of abundantly produced particles due to limitations in luminosity. The same is true for the experiment NA61/shine at the SPS which is limited by the detector rate capability. In contrast, the experiments at FAIR are designed for extremely high luminosities, enabling the systematic measurement of multi-differential cross sections with unprecedented statistics even for rare diagnostic probes like multi-strange hyperons, lepton pairs, charmonium and open charm.

* Work supported by EU, Hadronphysics2

CBM /HADES within the modular FAIR start version

The full realization of the CBM research program requires beams from SIS300 (up to energies of 45 A GeV), but the experiments can already be started at SIS100 using the upgraded HADES detector and an initial implementation of CBM. The upgrade of HADES with timing RPC detectors is already in progress. The SIS-100 accelerator at FAIR will deliver heavy-ion beams with energies up to 14 A GeV. This energy range is ideally suited to produce and to investigate net-baryon densities as they exist in the core of a neutron star. For the first time, penetrating probes like dileptons and multi-strange particles such as Ω-hyperons will be used to systematically study the properties of baryonic matter in this beam energy range. The 29 GeV proton beams from SIS-100 will permit to perform pioneering measurements on (open) charm production at threshold energies, and detailed studies of charm propagation in cold nuclear matter. Figure 2 depicts the HADES detector together with a start version of the CBM detector system.

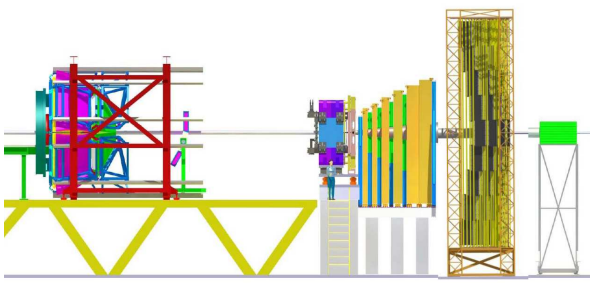

Fig.2 Experimental setups for measurements at SIS 100 consisting of the HADES detector (left) and an initial version of the CBM detector (right, "muon option").

R&D activities for CBM

The experimental task of the CBM detector system is to identify hadrons and leptons in collisions with up to 700 charged primary particles per event in the acceptance of the setup. Event rates of up to 10 MHz are needed for high statistics measurements of rare probes such as charmonium. These experimental conditions require fast and radiation hard detectors, free-streaming read-out electron-

ics, an ultra-fast online event-selection based on future CPU/GPU architectures, and a high-speed data acquisition (DAQ) system. The full version of the CBM detector system designed for measurements at SIS300 is sketched in figure 3. The CBM setup will be equipped both with electron and muon detectors.

The silicon tracking and vertexing system

The core of the CBM experimental setup is the Silicon Tracking System (STS) based on double-sided micro-strip sensors. The arrangement under study comprises 8 planes distributed within a distance of 1 m, and located in a magnetic dipole field. The challenge is to built a radiation hard (up to 10^{15} n_{eq}/cm^2) and low-mass (well below 8% radiation length) detector system which enables the reconstruction of primary and secondary tracks with an efficiency of 90% or above. The simulation model of the STS has been improved by implementing a detailed layout of the sensor arrangement within the stations, and taking into account a realistic detector response. The track reconstruction routines have been modified to cope with the new detector geometry and with charge sharing between neighbouring strips. Several prototype Silicon microstrip detector stations coupled to a free streaming data read-out and a common data acquisition system have been successfully tested at GSI with a proton beam.

The Micro-Vertex Detector (MVD) will provide high-precision vertexing for open charm measurements. The R&D on the MVD concentrates on the development of radiation hard and fast Monolithic Active Pixel Sensors (MAPS). A radiation hardness of better than $3 \cdot 10^{13}$ n_{eq}/cm^2 has been achieved by partially depleting the sensors of MAPS. Moreover, a large prototype MAPS featuring the massive parallel readout and all discrimination and data sparsification circuits required for open charm measurements has been successfully tested at CERN.

Electron measurements

Detailed feasibility studies of electron-pair measurements have been performed based on a compact size Ring-Imaging Cherenkov (RICH) detector. Although the compact RICH detector is substantially reduced both in volume and number of readout channels with respect to the initial design, its performance is not significantly deteriorated. These studies also took into account a segmented layout of the TRD detector including frames and support structures. The detector R&D resulted in a real-size prototype TRD with a double-sided pad-plane which was tested successfully with radioactive sources. A demonstrator of a RICH photon counter consisting of a MAPMT with 64 channels read-out via a self-triggered n-XYter chip was successfully tested with the GSI proton beam.

Muon measurements

The layout of the muon detection system within the GEANTsimulations was improved by taking into account a realistic detector module arrangement and their mechanical support structure. The track reconstruction algorithms have been adapted to the new geometry. Simulations based on the improved layout of the STS and the muon system demonstrate the feasibility of vector meson measurements via the dimuon decay channel in central Au+Au collisions at FAIR energies. A muon detector start version has been developed for charmonium measurements in proton-nucleus collisions at SIS100. The detector R&D concentrates on the construction and test of prototype gaseous detectors based on GEM technology. Two prototype GEM detectors read out by a free streaming FEE and DAQ system have been successfully tested with the GSI proton beam.

Hadron identification

Hadrons will be identified in CBM by measuring the particle momentum with the STS in the magnetic field, and its time-of-flight using a wall of timing Resistive Plate Chambers (RPC). The R&D on prototype timing RPCs concentrates on high rate capability, low resistivity material, long term stability and the realization of large arrays with overall excellent timing performance. Various prototype RPC time-of-flight detectors have been successfully tested in 2009 with a proton beam at GSI in Cave B.

Projectile spectator detector

The task of the Projectile Spectator Detector (PSD) is to determine the centrality of the collision and the orientation of the reaction plane. Simulations were performed in order to calculate the response of the PSD to projectile protons, neutrons and fragments, and to optimize the reaction plane resolution

First level event selection

All main reconstruction packages (STS, MuCh, TRD, RICH and Vertexing) were significantly optimized and parallelized resulting in a speed-up of the event reconstruction by 2- 3 orders of magnitude. Therefore, the First Level Event Selection (FLES) can be based on the information delivered by several or even all subdetectors.

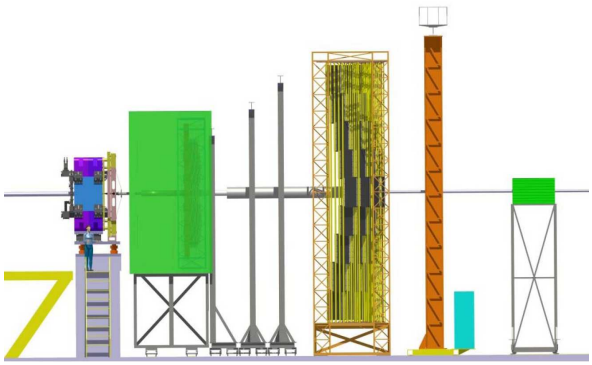

Fig.3: CBM setup for measurements at SIS 300 ("electron version"). From left to right: Dipol magnet with MVD and STS, RICH, 3 TRD stations, ToF-RPC, ECAL, PSD.

References

[1] A. Andronic et al., arXiv:0911.4806

Hadron identification with CBM at SIS 100*

D. Kresan[1], V. Friese[1], C. Höhne[1], and P. Senger[1]
[1]GSI, Darmstadt, Germany

The Compressed Baryonic Matter (CBM) detector will be the future heavy-ion fixed target experiment at the Facility for Antiproton and Ion Research (FAIR). It will investigate matter at high baryon density and moderate temperature by measuring hadrons, leptons, photons and rare probes together with HADES in A + A collisions at $2A$ - $45A$ GeV beam energy. For a detailed description of the scientific research program and detector components of the CBM experiment see [1].
The investigation of p+A up to 30 GeV and A+A from $4A$ to $11A$ GeV beam energies is considered as part of the research program and will be performed in the first phase of FAIR with a start version of the CBM detector at the SIS100 accelerator. This start version consists of two detector systems: the Silicon Tracking System (STS) placed in a magnetic field for the measurement of momenta and vertices; and a Time-Of-Flight (TOF) wall placed 10 m downstream of the target for hadron identification. For the study presented here, the standard CBM magnetic field was assumed. The time resolution of the TOF detector was assumed to be 80 ps.

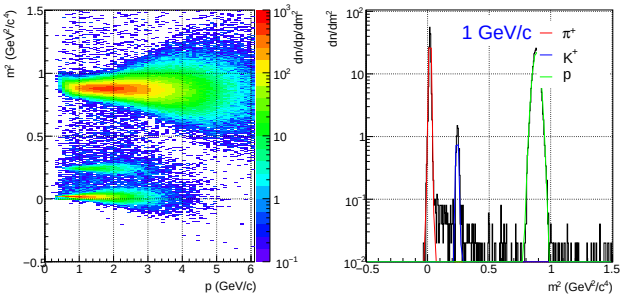

Figure 1: Squared mass versus momentum distribution for reconstructed primary particles from central (b=0 fm) Au + Au collisions at $4A$ GeV beam energy (left picture). Projection of the squared mass distribution for momentum of 1 GeV/c (right picture).

Central (b=0 fm) Au + Au collisions at $4A$ GeV, as one of the lowest energies considered for CBM, were generated with the UrQMD model [4] and simulated in the CBM setup with the CBMROOT software package. No intermediate tracking system is used; tracks from the STS are directly extrapolated over 9 m to the TOF wall and merged with TOF hits. For details of the event reconstruction algorithm implemented in the current framework see [2]. The method used for hadron identification in CBM with the TOF wall at a beam energy of $25A$ GeV can be found in [3] and was also applied in this study.

* Supported by BMBF and HQM.

The distribution of the squared mass versus momentum of reconstructed primary particles is shown in figure 1. Pions, kaons and protons are well separated, thus a clean particle identification is possible by selecting tracks within a momentum-dependent window in m^2 around the expectation value for each particle type. The distribution of the transverse momentum at midrapidity of reconstructed and identified primary K^+ from central (b=0 fm) Au + Au collisions at $4A$ GeV beam energy is shown in figure 2. The dotted line shows the distribution in full acceptance, the solid red line kaons within the CBM acceptance and the filled region reconstructed and identified kaons.

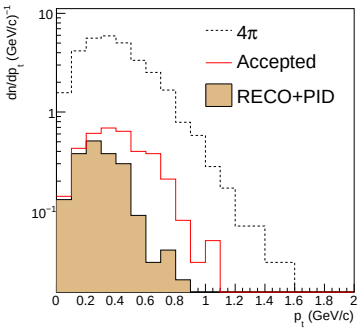

Figure 2: Transverse momentum distribution at midrapidity ($1.0 < y_{LAB} < 1.1$) for primary K^+ from central (b=0 fm) Au + Au collisions at $4A$ GeV beam energy (simulated with UrQMD).

The acceptance losses are due to the decay in flight of the kaons and The inefficiencies at high transverse momentum are mainly due to the overlap of the pion and kaon contributions in the squared mass distribution at high momentum.
We conclude an overall good performance of the primary hadron measurements with a start version of the CBM detector at SIS100 at FAIR.

For this study, both the STS and TOF were assumed to be unmodified with respect to the full CBM setup. In the future, the setup will be optimised to lower beam energies, such as placing the TOF wall closer to the target in order to decrease kaon decay in flight, or lowering the magnetic field to improve on the geometrical acceptance. A systematic study of the effect of the time resolution of the stop detector on the kaon/pion separation is also planned.

References

[1] CBM Collaboration, Technical Status Report (2005), https://www.gsi.de/documents/DOC-2005-Feb-447-1.pdf
[2] I.Kisel *et al.*, this report.
[3] D.Kresan *et al.*, GSI Scientific Report 2008, p.44.
[4] S. A. Bass *et al.*, "Microscopic models for ultrarelativistic heavy ion collisions," Prog. Part. Nucl. Phys. **41** (1998) 255.

Study of electron reconstruction in CBM at SIS100*

E. Belolaptikova[1], T. Galatyuk[1], C. Höhne[2], and J. Stroth[1]
[1]Goethe-Universität, Frankfurt, Germany; [2]GSI, Darmstadt, Germany

The CBM experiment is being designed to measure hadronic, leptonic and photonic observables. The core of the experiment will be a silicon tracking and vertex detection system installed in a large acceptance dipole magnet. Electron identification in CBM is provided by the RICH and TRD detectors. In addition, the Time-of-Flight (TOF) detector can also be used for the electron identification at low momenta ($p < 1$ GeV/c). Moreover, mismatches of proton and kaon tracks to electron rings can be fully eliminated using TOF information. Three TRD stations have to provide sufficient identification capability for high energy electrons and positrons and additional pion suppression for momenta large than 1.5 GeV/c. However, at 8 GeV/u kinetic beam energy, the momentum distribution of signal and background (leptonic and hadronic) sources change towards smaller values. Therefore, for electron identification one may rely to a large extend on the RICH and ToF information only.

Simulations were performed for central (b = 0 fm) Au+Au collisions at a beam energy of 8 GeV/u. The final state phase space distributions of hadrons were generated using the relativistic transport code UrQMD. Five electrons and five positrons are generated uniformly distributed in p, θ and ϕ and embedded into each UrQMD event. An important requirement for efficient background rejection is high efficiency and high purity of the identified electrons. After electron identification, each of the identified tracks is associated to its Monte Carlo information for studying the quality assessment of the electron identification. Important quantities are:

$$\text{Electron efficiency} = \frac{\text{truly identified electrons}}{\text{electrons in RICH acceptance}}, \quad (1)$$

and

$$\text{Pion suppression} = \frac{\text{pions identified as electrons}}{\text{pions in RICH acceptance}}. \quad (2)$$

Two different methods were used to optimize these quantities: 2-dimensional cuts and an Artificial Neural Network (ANN). The trained neural network gives continuous output values between -1 and 1, -1 resembles wrong, $+1$ true electron candidates. A cut value of -0.5 was selected. The final electron identification efficiency as a function of track momentum is shown in Fig. 1. After the full identification procedure, close to 60% of electron efficiency is achieved for $p > 2$ GeV/c. The efficiency drops towards low momentum, e.g. for $p < 1$ GeV/c the electron reconstruction efficiency is 30% only, and increases to 40% when electrons would be identified in RICH and TOF only. The pion suppression using RICH and TOF information only is more than 1000 and can be further increased after cut optimization.

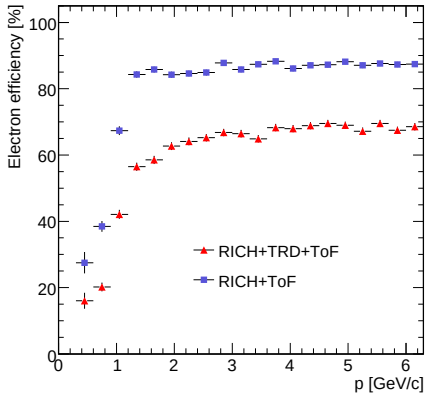

Figure 1: Electron identification efficiency: red triangles - using RICH, TRD and ToF, blue squares: combination of RICH and TOF information only. The ANN cut value is -0.5.

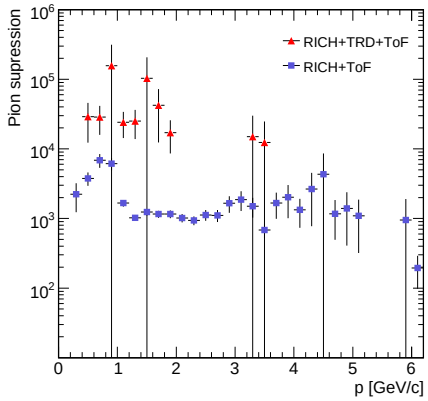

Figure 2: Pion suppression factor: red triangles - using RICH, TRD and ToF, blue squares: combination of RICH and TOF information only. The ANN cut value is -0.5.

* Work supported by BMBF, HQM, HGS-Hire.

Di-electron reconstruction with CBM

T. Galatyuk*[1], C. Höhne[2], and J. Stroth[1] for the CBM Collaboration

[1]Goethe - Universität Frankfurt am Main; [2]GSI Helmholtzzentrum für Schwerionenforschung GmbH, Darmstadt;

A strong excess of dilepton pairs over the yield expected from neutral meson decays was observed by hitherto existing high energy heavy-ion dilepton experiments (CERES, NA60, PHENIX). It is expected that electromagnetic radiation from the dense phase of the collision appears at low transverse momentum: pion-pion fusion, being the dominant process for populating ρ-like states in a hot pion gas, will favor ρ mesons located at low invariant mass and low transverse momentum. Special care should thus be taken by the CBM experiment to cover this range experimentally.

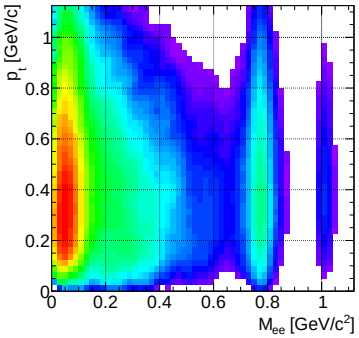

Figure 1: Distribution of accepted signal e^+e^- pairs in the transverse momentum and invariant mass plane after all cuts excluding any p_t cut. The data shown correspond to $2 \cdot 10^5$ simulated central Au+Au collisions at 25 GeV/u. Event reconstruction was performed using the compact RICH geometry [1].

The NA60 and CERES experiments have difficulties to access low pair p_t and low masses at the same time. The NA60 experiment measures low-mass vector mesons via their electromagnetic decay to muons using the muon absorber technique. This technique works perfectly well for high momentum muons; the major difficulty for NA60 lies in the identification of low-momentum muons. The acceptance of muons with $p_t < 0.2$ GeV/c drops by almost 2 orders of magnitude if compared to muons with $p_t > 0.5$ GeV/c [2]. A measurement of dilepton pairs with muons is naturally restricted to the invariant mass region above the 2-muon threshold of 2 times 210 MeV/c^2. The CERES experiment, on the other hand, has to apply a transverse momentum cut of 0.2 GeV/c on single electron tracks in order to suppress a huge combinatorial background from Dalitz decays of neutral pions.

In Fig. 1, the p_t-mass distribution within the CBM detector acceptance excluding any transverse momentum cut is presented. The acceptance is extended up to very low transverse momenta and very low masses. This shows that in CBM it will be possible to access the lowest invariant masses in a wide range of transverse momentum. Of course, the S/B ratio in particular in the enhancement region would increase if including a transverse momentum cut. Figure 2 shows the resulting e^+e^- invariant-mass distribution without transverse momentum cut is shown for pairs with $0.2 < p_t/(\mathrm{G}e\mathrm{V}/c) < 0.4$. The S/B ratio in the omega mass region is unchanged compared to the pt-integrated spectrum (S/B = 0.4) with single-electron p_t cut > 0.2 GeV/c. In the region where an enhanced dielectron yield is expected, i.e. from 0.2 to 0.6 GeV/c^2, the S/B ratio drops from $1/27$ to $1/50$ for the same comparison.

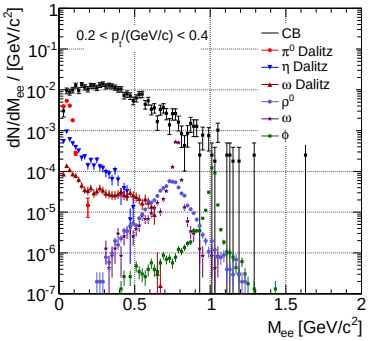

Figure 2: Invariant mass distribution for transverse momentum of the pairs = $0.2 < p_t/(\mathrm{G}e\mathrm{V}/c) < 0.4$ after all cuts excluding any p_t cut. The data shown correspond to $1 \cdot 10^6$ simulated central Au+Au collisions at 25 GeV/u.

In this contribution we have shown with simulations including realistic detector descriptions to our current knowledge that CBM will be able to measure low-mass electron pairs in central Au+Au collisions at 25 GeV/u beam energy. The expected performance in terms of S/B ratio is well comparable to existing dilepton experiments [3]. A strong benefit of the CBM experiment will be that because of large availability of beam time and high reaction rates large statistics will be collected. This will allow for a multi-differential and systematic analysis of different observables, in particular of low-mass vector mesons.

References

[1] S. Lebedev *et al.*, GSI Scientific Report (2008) 15.

[2] S. Damjanovic *et al.*, Nucl. Phys. A 783 (2007) 327.

[3] T. Galatyuk *et al.*, GSI Scientific Report (2008) 41.

* Work supported by Helmholtz Alliance HA216/EMMI

Reconstruction of J/ψ meson p_T spectra via di-muons in CBM*

A. Kiseleva[†1], C. Höhne[1], E. Kryshen[2], A. Lebedev[1,3], M. Ryzhinskiy[2], and P. Senger[1]
[1]GSI, Darmstadt, Germany; [2]PNPI, Gatchina, Russia; [3]JINR-LIT, Dubna,Russia

The reconstruction of J/ψ mesons via di-muon decays in CBM involves several detector systems: the silicon tracking stations for momentum and vertex reconstruction, the muon detection system for hadron absorption, and the Time-of-Flight system (ToF) for further background rejection of protons and kaons passing the absorber.

The muon detection system (MuCh) and the muon simulations are described in [1]. For the J/ψ measurements we use the first Transition Radiation Detector (TRD) station as a muon tracker station behind the last absorber (see fig. 1).

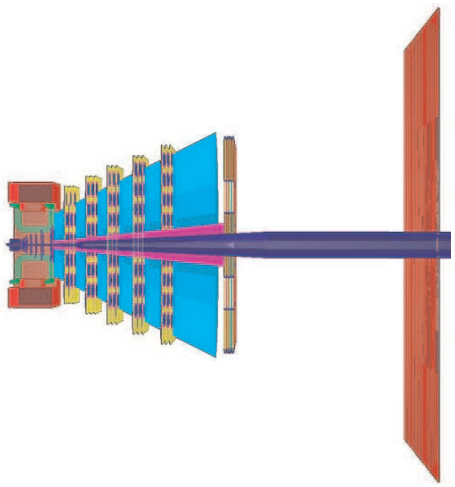

Figure 1: The CBM detector system for muon measurements. Left to right: Silicon Tracking Stations (STS), muon system (MuCh) with the first station of the Transition Radiation Detector (TRD) behind the last absorber, Time-of-Flight system (ToF).

The LIT global tracking package [2] is used for full track reconstruction. The resulting signal-to-background ratio for central Au+Au collisions at 25 AGeV is S/B = 3, and the detection efficiency for J/ψ mesons is ϵ = 14%.

Invariant mass spectra of the reconstructed muon pairs are shown in fig.2 for different p_T intervals. The background was determined using the invariant mass spectrum of like-sign pairs, and a Gauss-function was fitted to the signal peak. This background description works well for $p_T < 1.8 GeV/c$. For higher p_T bins more careful background description methods have to be developed. The p_T distribution of the reconstructed J/ψ mesons (red) is shown in fig.3 together with the distribution generated by PLUTO (black). The red histogram corresponds to 2.7×10^4 reconstructed J/ψ mesons which can be recorded within 19 hours assuming a reaction rate of 10^7 events/second.

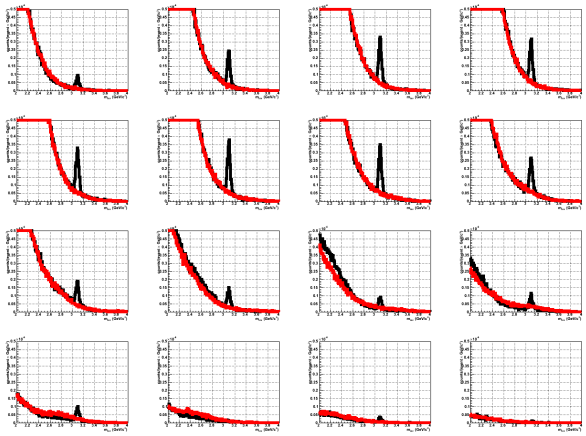

Figure 2: Invariant mass spectra of reconstructed muon pairs from central Au+Au collisions at 25 AGeV for different p_T intervals: from [0, 200] MeV/c (top left) up to [3.0, 3.2] GeV/c (bottom right). Black line – invariant mass spectra of the unlike-sign pairs, red line – like-sign pairs.

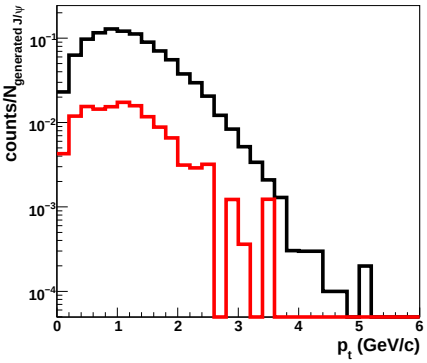

Figure 3: p_T distributions of J/ψ mesons generated by PLUTO (black line), and of reconstructed J/ψ mesons (red line), simulated for central Au+Au collisions at 25 AGeV.

References

[1] A. Kiseleva, et al., Muon simulations based on a realistic layout of the CBM muon detector system, GSI Scientific Report 2009.

[2] A. Lebedev et al., Status of the global track reconstruction algorithms for the CBM experiment at FAIR, GSI Scientific Report 2009.

* Work supported by EU/FP6 HADRONPHYSICS
† a.kiseleva@gsi.de

The di-muon trigger at CBM*

A. Kiseleva†[1], C. Höhne[1], E. Kryshen[2], A. Lebedev[1,3], M. Ryzhinskiy[2], and P. Senger[1]
[1]GSI, Darmstadt, Germany; [2]PNPI, Gatchina, Russia; [3]JINR-LIT, Dubna,Russia

The investigation of vector meson production in heavy ion collisions is one of the main goals of the CBM experiment. The experimental challenge is to perform high-statistics measurements of vector mesons via their dileptonic decays, because the branching ratios and/or the production crosssection is small. For example, according to the HSD transport code [1], in central $Au + Au$ collisions at 25 AGeV the dilepton yield per event is 1.05×10^{-3} for ρ, 3.42×10^{-3} for ω, and 1.15×10^{-6} for J/ψ mesons. Therefore, fast and efficient online event selection based on dilepton signatures is mandatory to reduce the data volume to the recordable rate.

The CBM muon detection system and the muon simulations are described in [2]. The strategy for an online selection of muon pairs from J/ψ decays has been presented in [3]. In this report, we outline a method to generate a trigger on muon pairs from the decay of low-mass vector mesons (LMVM) in the environment of a heavy-ion collision. Many of the muons from LMVM decays are too soft to pass the whole hadron absorber which has a total thickness of 225 cm of iron. Therefore, we use as muon trigger stations the two detector triplets located in front of the second last and the last absorber layer (see figure 1). Moreover, we place a time-of-flight (TOF) detector in the gap between the third last and the second last absorber layer (see figure 1) providing a time resolution of 80 ps.

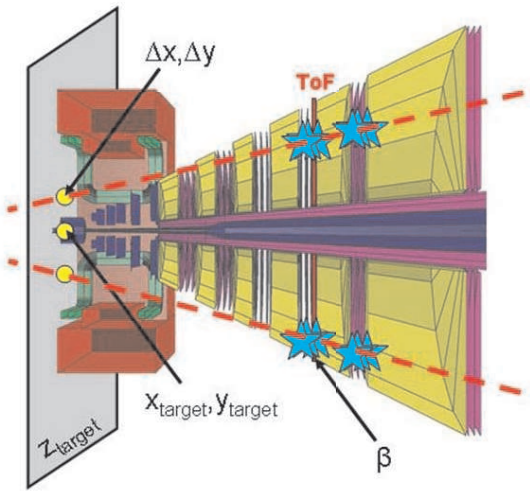

Figure 1: The CBM muon detection system. The stars correspond to hits required for the trigger. The dashed lines represent linear extrapolations of the tracks towards the target.

In order to be selected as a dimuon candidate, the event has to meet the following conditions:

1. a minimum of 2 tracks should be reconstructable by the hit triplets in each station;
2. the tracks obtained by a linear fit to the hits in both detector triplets should point towards the target;
3. the velocity of the two particles should be close to the velocity of light (see figure 2).

If all these requirements are fulfilled the event is recorded. It turns out that only 1 event out of 35 $Au + Au$ minimum bias collisions at 25 AGeV passes the trigger conditions. The trigger efficiency for omega mesons is 50%.

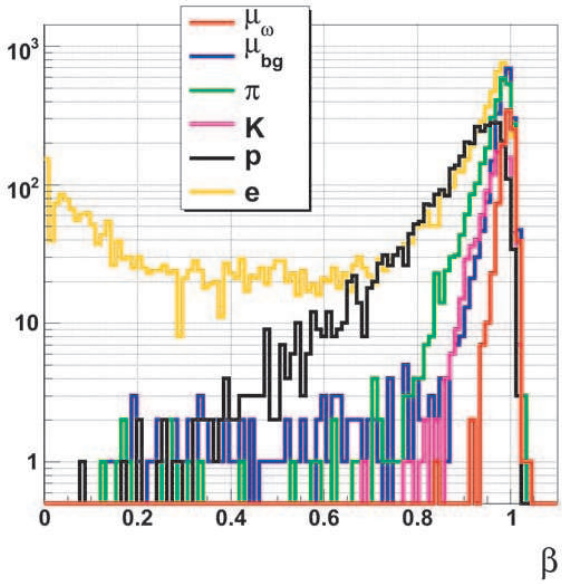

Figure 2: The velocity of the particles measured by Time-of-Flight system inside the muon system (see fig.1).

References

[1] O. Linnyk et al., Nucl. Phys. A 786 (2007) 183

[2] A. Kiseleva, et al., Muon simulations based on a realistic layout of the CBM muon detector system, GSI Scientific Report 2009.

[3] A. Kiseleva, et al., Muon trigger in CBM, GSI Scientific Report 2008.

* Work supported by EU/FP6 HADRONPHYSICS
† a.kiseleva@gsi.de

Ξ^- on-line reconstruction at Au+Au at 25AGeV in the CBM experiment

I. Vassiliev[1,2], I. Kisel[2], M. Zyzak[2,3], and the CBM Collaboration

[1]Goethe-Universität, Institut für Kernphysik, Frankfurt am Main, Germany; [2]GSI, Darmstadt, Germany; [3]Taras Shevchenko National University of Kyiv, Ukraine

The main goal of the CBM experiment is to study the behaviour of nuclear matter in the conditions of high baryonic density in which the transition to a deconfined quark gluon plasma phase is expected. One of the signatures of this new state is the enhanced production of strange particles, therefore hyperon reconstruction is essential for the understanding of the heavy ion collision dynamics. Hyperons will be measured in CBM by their decay into charged hadrons, which are detected in the Silicon Tracking System (STS).

To study the feasibility of hyperons on-line reconstruction in the CBM experiment a set of 10^4 central Au+Au UrQMD events at 25 AGeV were simulated. At 25 AGeV central Au+Au UrQMD event contains in average 0.98 Ξ^-. The Ξ^- decays to $\Lambda + \pi^-$ with branching ratio 99.9% and $c\tau$ = 4.91 cm. Λ decays most offten happen in the STS detector. The STS geometry with 2 MAPS at 5 cm and 10 cm (thickness 500 μm) and 8 double-sided segmented strip detectors were used for tracking. No kaon or pion identification with Time-of-Flight detector (TOF) is applied, however, it is important to use the TOF measurements in order to select proton tracks from the sample and reconstruct the $\Lambda \rightarrow p\pi^-$ decay.

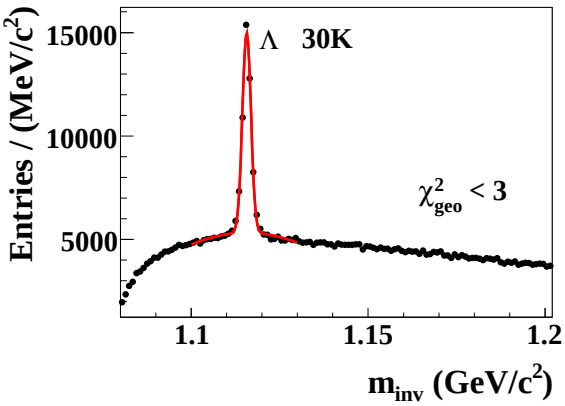

Figure 1: The proton π^- invariant mass spectrum. About 3 Λs per event were found

The Ξ^- event on-line reconstruction includes several steps: fast tracks finding and fitting [1, 2], where all tracks (isec =2) are found; tracks with $(\chi^2_{primary} > 3\sigma)$ are selected for a Λ search, where protons, identified by the TOF detector, are combined with the π^- tracks to Λ-KFParticle [3]; good quality geometrical vertex $(\chi^2_{geo} < 3\sigma)$ were used to suppress combinatorial background. The obtained invariant mass spectrum is shown in Fig. 1.

The invariant mass of the reconstructed pair is compared with the PDG's Λ mass value, only pairs inside $\pm 3\sigma = 10MeV$ window were accepted; primary Λ rejection, where only Λ with $(\chi^2_{primary} > 5\sigma)$ and z-vertex greater than 4 cm are chosen; and, finally, detached (more then 3 cm downstream the target) Ξ^- reconstruction step. Selected Λs were combined with the secondary π^- $(\chi^2_{primary} > 3\sigma)$ tracks and Ξ^--KFParticle were created. The Ξ^--KFParticle were accepted if it has good quality geometrical and topological detached vertex: $(\chi^2_{geo} < 6\sigma,\ \chi^2_{topo} < 5\sigma)$ and z-vetrex greater than 3 cm.

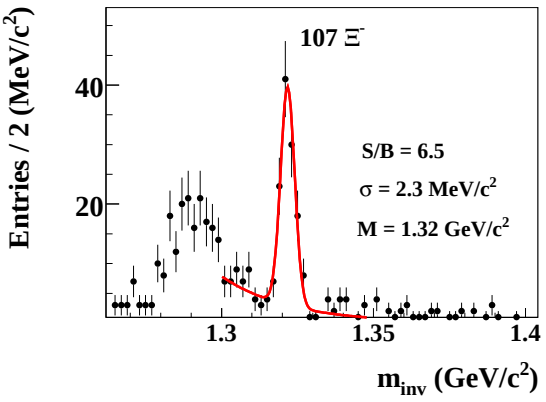

Figure 2: Reconstructed invariant mass distribution of $\Lambda\pi^-$ candidates. 107 Ξ^- were reconstructed, S/B ratio is 6.5, reconstructed mass value is 1.321 GeV/c^2

The invariant mass spectrum is shown in Fig. 2. The signal reconstruction efficiency is about 1.07%. The reconstructed mass value 1.321 ± 0.003 GeV/c^2 is in a good agreement with the simulated one: 1.321 GeV/c^2. Invariant mass resolution value is 2.3 (MeV/c^2).

References

[1] I. Kisel, Event reconstruction in the CBM experiment, Nucl. Instr. and Meth. A566 (2006) 85-88.

[2] S. Gorbunov, U. Kebschull, I. Kisel, V. Lindenstruth and W.F.J. Müller, Fast SIMDized Kalman filter based track fit, Comp. Phys. Comm. 178 (2008) 374-383.

[3] M.Zyzak, I.Kisel, Vertexing status, 14. CBM Collaboration Meeting, October 6-9, 2009, Split, Croatia

D^+ decay feasibility study in the CBM experiment

I. Vassiliev[1,2], I. Kisel[2], and the CBM Collaboration
[1]Goethe-Universität, Institut für Kernphysik, Frankfurt am Main, Germany; [2]GSI, Darmstadt, Germany

A measurement of the different charmed mesons, and the Λ_c is important for getting a solid estimate on the total charm production cross section at the threshold. $D^{\pm}$-mesons have lifetime of 312 μm, therefore, the most important step in their identification is a precise detection of the secondary decay point. For this purpose the high resolution MVD detector (two MAPS detectors of 300 μm at 5cm and of 500 μm at 10 cm downstream the target) is used in order to suppress the background from kaons and pions emitted at the primary vertex. No kaon or pion identification with TOF is applied, however, it is important to use the time-of-flight measurements in order to reject proton tracks from the sample. A novel fast track finder [1] has been developed for $D^{\pm}$-meson daughter particles selection. Only tracks with momentum above 1 GeV/c from the target region have been selected. In order to reconstruct

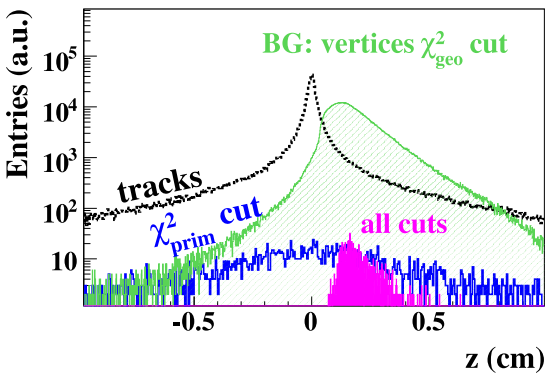

Figure 1: Distribution of single tracks and secondary vertices along the beam line for $D^+ \rightarrow K^-\pi^+\pi^+$ reconstruction. All primary tracks (black line) and those selected by χ^2_{prim} cuts as single track candidates for D^+ daughters (blue), 3-particle secondary vertices after first geometrical cuts (light green), and finally selected D^+ candidates including more stringent topological cuts (magenta).

the $D^{\pm}$-mesons with a reasonable signal-to-background ratio, a set of mainly topological cuts applied to single tracks as well as to reconstructed vertices. As example, Figure 1 presents the resulting background suppression of such cuts for the 3-particle decay of the D^+ meson. Single track χ^2_{prim} cuts mainly rely on the back-extrapolation of the tracks to the primary vertex requiring them to miss it. For the reconstructed charmed mesons, the back-extrapolation is required to stem from the primary vertex which allows to reduce strongly the geometrically reconstructed 3-particle vertices.

The reconstructed invariant mass spectra of the $D^{\pm}$-mesons in central Au+Au collisions at 25 AGeV beam energy are shown in Figure 2. Numbers for efficiency and acceptance are presented in Table 1. Multiplicities have been taken from the HSD model.

	D^+ and D^-
decay channel	$K^-\pi^+\pi^+$ ($K^+\pi^-\pi^-$)
multiplicity HSD	$4.2 \cdot 10^{-5}$ and $8.9 \cdot 10^{-5}$
multiplicity SM	$8.4 \cdot 10^{-5}$ and $2.9 \cdot 10^{-4}$
branching ratio	9.5%
geometrical acceptance	39.6%
single track rec. eff.	97.5%
z-resolution	47 μm
total efficiency	2.6%
$\sigma_m[MeV/c^2]$	10.0
$S/B_{2\sigma}$ ratio	1.1 (2.4)
yield (10^{12}central)	103K D^+ and 195K D^-

Table 1: Acceptance and efficiencies, mass resolution, and signal to background ratio (S/B) in a $2\sigma_m$ region around the peak for open charm reconstruction in central Au+Au collisions at 25 AGeV beam energy. The total efficiency is calculated from the product of geometrical acceptance, reconstruction and cut efficiencies.

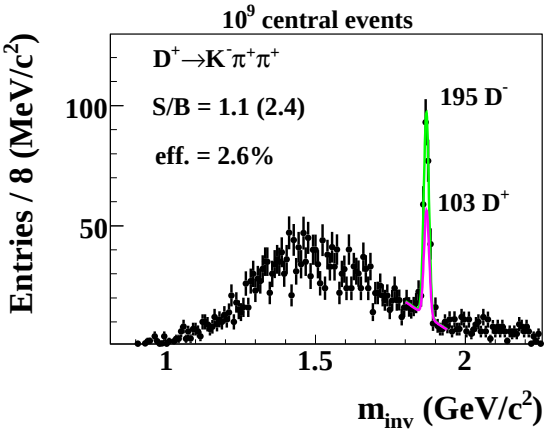

Figure 2: Reconstructed $D^{\pm}$-mesons in 10^9 central Au+Au collision at 25 AGeV. Magenta - D^+ signal, green line is D^-.

References

[1] I. Kisel, Event reconstruction in the CBM experiment, Nucl. Instr. and Meth. A566 (2006) 85-88.

$(\Xi^0\Lambda)_b$-dibaryon detectability study in the CBM experiment

I. Vassiliev[2,1], I. Kisel[2], D. Malakhov[3], and the CBM Collaboration

[1]Goethe-Universität, Institut für Kernphysik, Frankfurt am Main, Germany; [2]GSI, Darmstadt, Germany; [3]Taras Shevchenko National University of Kyiv, Ukraine

The recent experimental evidence [1] for the existence of H-dibaryon ($uuddss, I = J = 0$) provides the motivation to continue experimental search for it. The CBM setup gives an opportunity to detect H-dibaryons decay via the $\Lambda\Lambda$ channel using the predicted decay length of $c\tau \approx$ 1-5 cm [2]. Λ decay length is 7.89 cm and this allows to reconstruct the event topology and efficiently distinguish the signal from the background.

To study the feasibility of H-dibaryon detection in the CBM experiment a set of 10^4 central Au+Au UrQMD events at 25 AGeV were simulated. The $(\Xi^0\Lambda)_b$ decay ($c\tau$ = 3 cm) to $\Lambda\Lambda$ were forced and added to each event in order to simulate the signal in the environment of background hadrons.

The main part of the background is created by the 32 primary Λ particles produced per central UrQMD event. In the STS detector acceptance about 8 Λ particles are reconstructed on average. The realistic STS geometry with 2 MAPS at 5 cm and 10 cm (thickness 500 μm) and 8 double-sided segmented strip detectors were used for tracking. No kaon or pion identification with TOF is applied, however, it is important to use the time-of-flight measurements in order to select proton tracks from the sample and reconstruct the $\Lambda \rightarrow p\pi^-$ decay. A typical signal event $H \rightarrow \Lambda\Lambda \rightarrow p\pi^- p\pi^-$ is shown in Fig. 1.

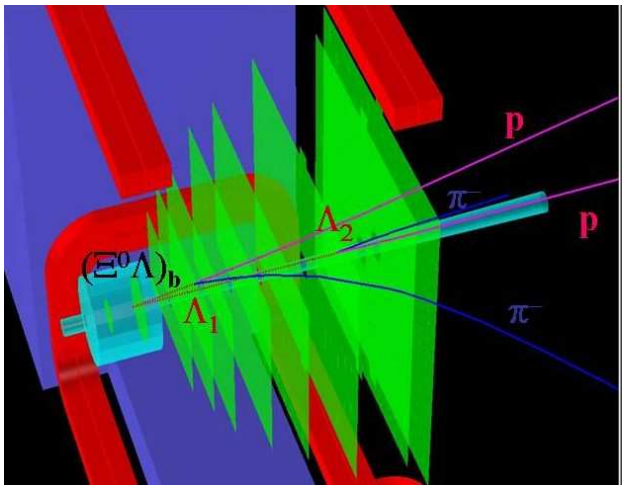

Figure 1: Event display with a H-dibaryon decay into $\Lambda\Lambda$

The H-dibaryon decay point is typically located about 5-15 cm downstream of the target. Λ decays most offten happen in the STS detector. The event topology reconstruction includes several steps: tracks reconstruction, where all tracks are found but only tracks with $\chi^2_{primary} > 3\sigma$ are selected; Λ search, where protons, identified by the TOF detector, are combined with the π^- tracks and the invariant mass of the reconstructed particle is compared with the PDG's Λ mass value; primary Λ rejection, where only Λ with $\chi^2_{primary} > 3\sigma$ are chosen; and, finally, detached (more then 3 cm downstream the target) H-dibaryon reconstruction step. At the last step good quality geometrical ($\chi^2_{geo} < 3\sigma$) and topological ($\chi^2_{topo} < 3\sigma$) vertices for the reconstructed H-dibaryon are required. The shape of the background invariant mass was obtained using the event mixing technique. The main part of the background is $\Lambda\Lambda$ correlated background, while the combinatorial part is one oder of magnitude lower.

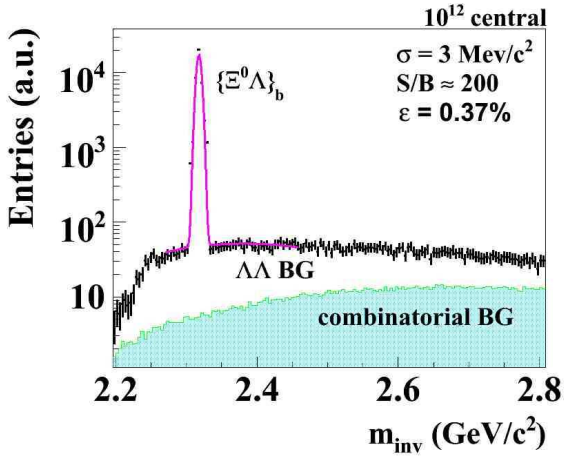

Figure 2: Reconstructed invariant mass distribution of $\Lambda\Lambda$ candidates

The signal and background invariant mass (IM) spectra are shown in Fig. 2. The signal reconstruction efficiency is about 0.37%, H-dibaryon multiplicity $7 \cdot 10^{-3}$ is assumed, the branching ratio is 2%. The reconstructed mass value $2.32 \pm 0.03\ GeV/c^2$ is in a good agreement with the simulated one: $2.318\ GeV/c^2$. Invariant mass resolution value is 3 (MeV/c^2).

References

[1] C.J. Yoon et al., Search for the H-dibaryon resonance in $C(K^-, K^+\Lambda\Lambda\ X)$. Phys. Rev C 75, 022201(R) (2007).

[2] J. Schaffner-Bielich, R. Mattielo and H. Sorge, Dibaryons with strangeness: their weak nonleptonic decay using SU(3) symmetry and how to find them in relativistic heavy-ion collisions. arXiv:nucl-th/9908043v2, March 2000.

Study of the capabilities of the CBM detector for open charm elliptic flow measurements

S. Seddiki[1,2] and F. Rami[2]
[1]IKF, Frankfurt, Germany; [2]IPHC, Strasbourg, France

Open charm will be one of the key observables of the future CBM experiment, as it is a penetrating probe of the early dense phase of the collision. In particular, its elliptic flow should be sensitive to the degrees of freedom of the medium at the early stage. In a purely hadronic scenario, open charm has a moderate interaction rate and should develop a low elliptic flow compared to lighter hadrons. The observation of a strong elliptic flow for open charm at FAIR would indicate the creation of a partonic medium [1]. The elliptic flow of open charm particles is also of particular importance for the issue of thermalization.

The present study aimed at investigating the capabilities of the CBM detector in measuring the elliptic flow of open charm. The latter will be measured using a Micro-Vertex Detector (MVD) based on MAPS-pixels. Previous studies [2] demonstrated that the experiment will allow to reconstruct a few 10^4 D-mesons per year. The measurement of their elliptic flow will require the determination of the collision reaction plane. This will be done in CBM using a forward hadron calorimeter, the Projectile Spectator Detector (PSD) [2].

In a first step, we have evaluated the perfomance of the PSD detector for the reaction plane reconstruction. This has been done for Au+Au collisions at 25 AGeV using the UrQMD event generator and the CBM simulation framework (based on GEANT). Simulated events have been transported through a set-up including the MVD, the Silicon Tracking System (STS), dumped in a magnetic dipole field of 1 Tesla, and the PSD. Using the energy deposited in the PSD by spectator particles, the reaction plane of each event has been reconstructed using standard methods [3]. The results show that a very good proton/neutron separation is mandatory, since the protons are deflected by the magnetic field and spoil the azimuthal correlation of the particles with the reaction plane. The expected resolution on the reaction plane (σ_{Φ_R}), assuming an ideal proton/neutron discrimination, is plotted in Figure 1 as a function of the collision centrality. As one can see, a quite good accuracy can be achieved, in particular for mid-central collisions ($3fm \leq b \leq 9fm$).

The elliptic flow signal has been simulated for D^+ mesons, using a thermal model in which the particle azimuthal anisotropy with respect to the reaction plane has been introduced. For each event, the reaction plane resolution was accounted for by smearing the azimutal angle of the particles according to a gaussian distribution with σ = 40 degrees (Figure 1). The v_2 parameter has been reconstructed using the Fourier analysis of the simulated azimutal distributions ([3]). After applying a correction factor to

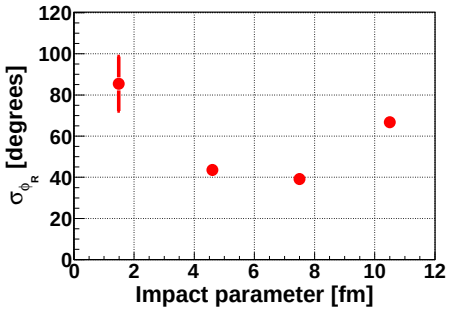

Figure 1: Reaction plane resolution as a function of the collision impact parameter. See text for details.

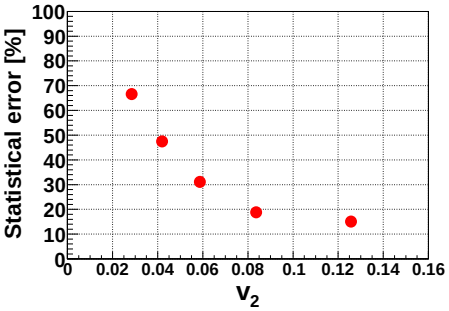

Figure 2: Statistical error on v_2 versus the magnitude of v_2 for a statistics of D^+ particles corresponding to roughly 1-year data taking with CBM.

account for the reaction plane resolution, the reconstructed v_2 was found to be very close to the input value within statistical errors. Figure 2 shows the expected statistical error on the integrated v_2 as a function of its magnitude using a statistics of D^+ particles corresponding to one year data taking with CBM. The results indicate that, within 1-year operation, small D^+ azimuthal anisotropies could be measured but only with large statistical uncertainties, while for larger v_2 values the experiment will be able to achieve good statistical accuracy (less than 15% for $v_2 \geq 0.1$). Further studies will take into account the effect of the combinatorial background contamination (not considered in the present work). The feasibility of p_t-differential elliptic flow measurements of D-mesons will be also investigated.

References

[1] O. Linnyk et al., Int.J.Mod.Phys.E17:1367-1439,2008
[2] CBM Progress Report 2007
[3] P. Danielewicz and G. Odyniec, Phys. Lett. B 157 B (1985)

Systematic investigations of RICH and TRD detector parameters on electron identification in the CBM experiment *

S. Lebedev[1,2], C. Höhne[1], G. Ososkov[2], and F. Uhlig[2]
[1]GSI, Darmstadt, Germany; [2]JINR, Dubna, Russia

RICH detector

Several new features were implemented in the RICH detector simulation to improve the realistic detector response: mirror surface inhomogeneities, photodetector coverage with wavelength shifter (WLS) films, collection efficiency of the photodetector. These features mostly influence the ring finder, which was tested in order to obtain limitations for the detector parameters. For this study central UrQMD Au+Au collisions at 25 $AGeV$ beam energy with 10 embedded primary e^+ and e^- were simulated.

The effect of light scattering due to mirror surface inhomogeneities was implemented as additional error with gaussian distribution to the hit measurement. As a reference point $\sigma_{gauss} = 0.6\ mm$ was taken, which is expected for new CBM-RICH mirror prototypes (corresponding D_0=2.4 mm). Different values of σ_{gauss} were tested, results are presented in Tab. 1.

Table 1: Ring finding efficiency vs. σ_{gauss}.

σ_{gauss}, mm	0.4	0.6	1	2	4	6
Eff., %	91	90.4	91.4	90	87.5	84.7
Fakes/ev.	3.8	3.7	3.9	4.3	5.8	7.6

The quantum efficiency (QE) of photomultipliers is typically limited by the window material and extends down to (250-300)nm. In order to enhance QE in the near UV region the coverage of PMTs with WLS films as e.g. p-terphenul (PT) was studied [1]. Also one might consider a reduced photoelectron collection efficiency (CE) of about 70% due to the construction of the photodetector Hamamatsu H8500. The ring finding efficiency in dependence on different photodetector effects is presented in Tab. 2

Table 2: Ring finding efficiency in dependence on different photodetector effects.

	No WLS		WLS (PT)	
CE, %	100	70	100	70
Efficiency, %	90.4	85.5	91.5	88.2
Fakes/event	3.6	2.6	5.5	3.9

TRD detector

In TRD simulations the dependence of the pion suppression factor on different radiator parameters was studied. In the cbmroot framework energy losses for TRD are calculated the following way: ionization losses are taken from GEANT, and transition radiation (TR) is calculated by an implemented model [2]. Three parameters for the radiator are used as input for the model: number of foils, thickness of foil, distance between two foils. The radiator parameters which were used in our study are presented in Tab. 3. The first set overestimates preliminary experimental results, the second set underestimate these results. The third set was tuned to describe the experimental results [3].

Table 3: Three sets of parameters for TR simulation.

	set1	set2	set3
Number of foils	130	60	70
Foil thickness, cm	0.0013	0.0015	0.0014
Distance between foils, cm	0.02	0.05	0.04

To calculate the pion suppression factor $1 \cdot 10^6$ electrons and $1 \cdot 10^6$ pions were simulated with parameters $\theta = (2.5°, 25°)$, $\phi = (0°, 360°)$ for certain momenta (1, 1.5, 2, 3, 4, 5, 7, 9, 11, 13 GeV/c). The BDT method was used for this study [4]. Results are presented in Tab. 4.

Table 4: Pion suppression for different radiator parameters.

P, GeV/c	1.5	3	5	9	13
set1	2892	2621	2149	1591	1189
set2	400	593	529	421	314
set3	660	845	690	525	395

The robustness of the pion rejection factor to experimental factors such as the calibration of the energy loss measurements, pile up of signals etc. was studied by implementing an additional error with gaussian distribution to the energy loss for each hit: $E_{loss} = E_{loss} + Gauss(0, \sigma_{error})$. Note that the most probable value of E_{loss} for pions with 1.5 GeV/c momentum is around 1.1 keV. Pion suppression results assuming 90% electron efficiency for different σ_{error} are presented in Tab. 5 (P=1.5 GeV/c, radiator parameters-set3). The study showed that the tested method for electron identification is very robust.

Table 5: Pion suppression in dependence on σ_{error}.

σ_{error}, keV	0.01	0.025	0.05	0.1	0.25	0.5
pion supp.	659	636	626	637	585	466

References

[1] P. Koczon et al., GSI Scientific Report 2008, p. 17.
[2] M. Castellano et al. Comp. Phys. Comm. **61** 1990.
[3] A. Andronic et al., GSI Scientific Report 2006, p. 233.
[4] G. Ososkov et al. "e^-/π separation with TRD", https://www.gsi.de/documents/DOC-2009-Oct-232-1.pdf

* Work supported by BMBF.

Status of the global track reconstruction algorithm for the CBM experiment

A. Lebedev[1,2], C. Höhne[1], I. Kisel[1], and G. Ososkov[2]
[1]GSI, Darmstadt, Germany; [2]JINR, Dubna, Russia

In this report the status of the LIT global track reconstruction package for the CBM experiment is presented. The package is organized to be flexible with respect to feasibility studies of different physics channels and to the optimization of the detector geometry. Global track reconstruction in the electron and muon setup of the CBM detector, i.e. with either TRD or MUCH system, is based on track following using reconstructed tracks in the STS as seeds. In the STS track reconstruction is based on the cellular automaton method [1] and provides initial track parameters as starting point for the following track prolongation. This track following is based on the standard Kalman filter technique and is used for the estimation of track parameters and trajectory recognition in TRD and MUCH. Tracks are prolongated subsequently from one detector station to the next adding additional hits in each detector. The global tracking algorithm uses a precise track propagation algorithm [2].

The detailed layout of the detectors is still under discussion. In the high track density region of the TRD and MUCH stations, a pad layout is foreseen based on MWPC or GEM technology. For the upstream detector stations in MUCH, where track densities are low, straw tube chambers are under discussion. Moreover, the first TRD station can be used as tracking station after the last MUCH absorber.

The track reconstruction algorithm was tested for the standard TRD setup with segmented detector chambers and for four different MUCH geometries: 1) `MUCH1` is the standard MUCH with 6×3 detectors with pad readout, 2) `MUCH2` with 3×3 detectors with pad readout and straw tube detectors in the last 3×3 stations, 3) `MUCH3` is the same as `MUCH1` but with TRD after the last absorber, 4) `MUCH4` is the same as `MUCH2` but with the TRD after the last absorber (see Fig. 1).

The algorithm was tested with central Au+Au collisons at $25A$ GeV beam energy from UrQMD. In addition, for the reconstruction in TRD, 5 primary e^+ and 5 primary e^- with momenta 1 GeV/c $\leq$ p $\leq$ 10 GeV/c were embedded in each event. The performance in the MUCH system was evaluated by embedding 5 primary μ^+ and 5 primary μ^- per event with momenta 2.5 GeV/c $\leq$ p $\leq$ 25 GeV/c.

The mean TRD track finding efficiency for reference tracks (primary tracks with $p > 1$ GeV/c) is 93% at a ghost rate of 3%. The reconstruction efficiency for electrons is 89%. The MUCH track finding efficiency for the four discussed geometries is presented in Table 1. Fig. 2 depicts the global tracking efficiency in dependenceon momentum for the standard `MUCH1`.

In summary, the LIT track reconstruction package provides good tracking efficiency for both, the electron and muon setup of CBM. It is suitable for layout studies of different MUCH setups. The reconstruction efficiency is only slightly different for the different MUCH layout options.

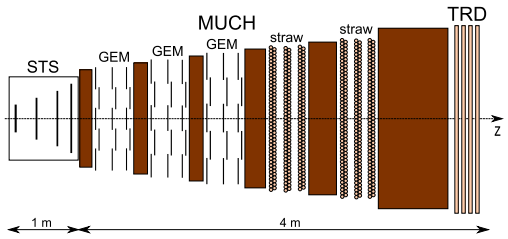

Figure 1: Sketch of the silicon tracking system (STS) and the muon detector (MUCH) with 3×3 GEM stations, 2×3 straw tube stations and the TRD after the last absorber.

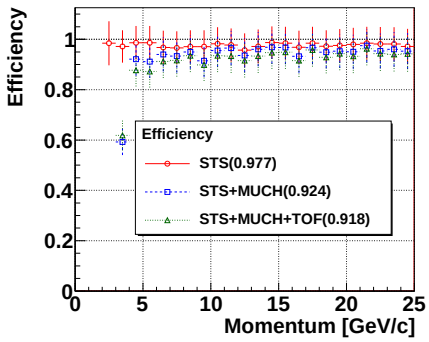

Figure 2: Global track finding efficiency for muon tracks in dependence on momentum for the `MUCH3` geometry.

Geometry	`MUCH1`	`MUCH2`	`MUCH3`	`MUCH4`
Efficiency [%]	95.2	94.1	94.7	94.0

Table 1: Track finding efficiency for muon tracks for four different MUCH geometries: `MUCH1` the standard MUCH with 6×3 GEM stations, `MUCH2` with 3×3 GEM stations and 3×3 straw tube stations, `MUCH3` the same as standard MUCH but with the TRD after the last absorber and `MUCH4` same as `MUCH2` but with the TRD after the last absorber.

References

[1] I. Kisel, Event reconstruction in the CBM experiment, Nucl. Instrum. Meth. **A566** (2006) 85–88

[2] A. Lebedev, G. Ososkov, LIT Track Propagation for CBM, CBM note (2008) `http://www.gsi.de/documents/DOC-2008-Dec-182-1.pdf`

Primary Vertex Finding in Multivertex Events

I. Kisel[1] and M. Zyzak[2,3]

[1]GSI, Darmstadt, Germany; [2]Uni-Frankfurt, Germany; [3]Uni-Kiev, Ukraine

In the CBM experiment [1] the Kalman filter based algorithm of primary vertex reconstruction is implemented [2]. The algorithm is developed for the case of single primary vertex events: all found tracks are used for the primary vertex reconstruction. The multivertex events availability is assumed by the physics program of the CBM experiment. In case of the multivertex event the situation is more complicated: the number of interaction points is unknown and there is no information about the belonging of the certain track to the certain vertex.

Another problem is related to events with low track multiplicity. In this case the currently implemented algorithm will be very sensitive to each measurement, where measurements are tracks included to the primary tracks clusters. If the tracks, which are created by the secondary particles, are included into this primary tracks clusters the errors of the reconstructed primary vertex position could be increased dramatically and the position could be determined incorrect.

Therefore the goal of this investigation is to develop the algorithm, which should determine the number of primary vertices and find the clusters of primary tracks, which form each vertex. The developed cluster finder algorithm is based on two assumptions: there is only one target and all primary vertices are positioned on the target. The algorithm consists of the following steps:

1. Extrapolate all tracks to the target plane.
2. Determine the weight of each track (by default, equal to zero). Find the track with the maximal weight.
3. Form the cluster around this track. All tracks with distance less than 3.5·sigma are included into the cluster; they are rejected from the array of considered tracks for the next step as well.
4. The procedure is continued until there are remaining tracks, which could form clusters.
5. Then, all found tracks clusters are given to the Kalman filter reconstruction routine [2].

	Residuals, μm	Pulls
x	18.9 / 21.2	1.14 / 1.28
y	18.6 / 20.6	1.13 / 1.28
z	100.6 /116.8	1.18 / 1.36

Table 1: Residuals and pulls with/without the cluster finder routine for single vertex events

The algorithm was tested with the proton-carbon UrQMD events at 30 AGeV. The residuals and pulls for single vertex events were obtained by the algorithm [2] with and without cluster finder and are presented in the Table 1 and on the Fig. 1 with all coordinates having similar shape distributions. The results with the cluster finder are more accurate. It is due to the fact, that we reject secondary tracks from the cluster of tracks, which are used for primary vertex reconstruction in this case.

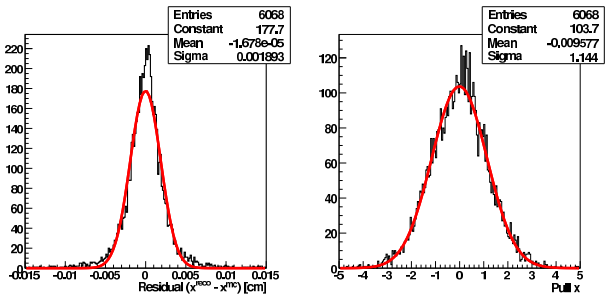

Figure 1: Residuals and pulls of x coordinate for single vertex events with the cluster finder algorithm

The quality of primary vertices reconstruction in case of two and more vertices is the same as in one vertex case. The algorithm reliably distinguishes vertices with the distance between them larger than 100 μm. With shorter distances the reconstructed vertices have tendency of merging.

Concluding, the developed algorithm allows reconstructing of more than one vertex in one event. The claster finder routine usage gives better residuals and pulls also for the case of one primary vertex rejecting secondary tracks from the primary tracks clusters, that is particularly important in case of small track multiplicity. The algorithm is built in such a way that it can be easily extended to the case of the targets with different z-positions.

References

[1] CBM Progress Report 2008, GSI Report 2009-03.

[2] S. Gorbunov and I. Kisel, Reconstruction of decayed particles based on the Kalman filter, CBM-SOFT-note-2007-003, 7 May 2007.

SIMDized Particle Reconstruction in the CBM Experiment

I. Kisel[1] and M. Zyzak[2,3]

[1]GSI, Darmstadt, Germany; [2]Uni-Frankfurt, Germany; [3]Uni-Kiev, Ukraine

Particle reconstruction is an inherent stage in high-energy physics experiments. At first, primary vertex reconstruction is needed for physics analysis. At second, mother particles reconstruction from daughter particles is one of the main steps of the physics analysis. Since reconstruction function can be called many times during the analysis, the parallelization of this function is needed with respect to time consumptions.

Single instruction, multiple data streams (SIMD) allows to parallelize the operations. The basic data unit of SIMD is a vector — a row of individual numbers or scalars. Using a 4-element, one can do four-way single-precision floating-point calculations in parallel. SIMD instructions implementation can increase the program execution speed up to 4 times [1]. Since all modern processors have the SIMD instructions support, the code SIMDization is a suitable way of the program parallelization.

SIMD instructions were implemented into the scalar version of the particles reconstruction algorithm [2]. The algorithm was tested with the proton-carbon UrQMD events at 30 AGeV for the primary vertex reconstruction case and with the central Au+Au UrQMD events at 25 AGeV using the Λ reconstraction procedure for the secondary particle case. For the tests Pentium Dual E2180 at 2 GHz processor with 1 MB L2 cache was used. The coordinates estimation difference of the scalar and SIMDized versions is at the level of 0.01 μm for primary vertices and 10 μm for Λ-particles, while residuals and pulls are almost the same in case of SIMDized and scalar versions of the particles reconstruction class (Tables 1 and 2). The reconstruction function speedup factor after SIMDization is at the level of 1.5.

	Residuals	Pulls
x	18.9 / 19.0 / 19.0, μm	1.14 / 1.15 / 1.21
y	18.6 / 18.5 / 18.7, μm	1.13 / 1.13 / 1.14
z	100.6 / 101.2 / 101.4, μm	1.18 / 1.20 / 1.23

Table 1: Residuals and pulls for scalar / SIMD / SIMD with field approximation code versions in the case of the primary vertex reconstruction

In the scalar version of the code the full magnetic field map is used, which complicates the implementation of SIMD instructions. Because of this the maximal speed up of 4 times was not reached. The approximation of the magnetic field was done in order to SIMDize the algorithm in a more efficient way. All three components of the magnetic field were approximated with parabolas along the particle trajectory (three closest to the target hits were used for the approximation). Parabola's coefficients were stored as the parameters of the particle. This step allows to reduce the number of the magnetic field map accesses and simplifies SIMDization of the code. Currently the magnetic field map is still accessed at the field approximation step.

The magnetic field approximation was implemented in the SIMDized version of the code. The residuals and pulls of the coordinates are similar to that of the code version with the full map usage (Tables 1 and 2). The speedup factor as compared to the scalar version is about 3.

	Residuals	Pulls
x	0.011 / 0.013 / 0.011, cm	1.50 / 1.51 / 1.64
y	0.015 / 0.015 / 0.015, cm	1.42 / 1.50 / 1.48
z	0.18 / 0.18 / 0.20, cm	1.63 / 1.69 / 1.74
M	1.2 / 1.2 / 1.5, MeV/c^2	1.54 / 1.54 / 1.67

Table 2: Residuals and pulls for scalar / SIMD / SIMD with field approximation code versions in the case of the secondary particles reconstruction

Concluding, SIMDization of the particle reconstruction code was done, the speedup factor of about 3 was reached. Further speed increasing can be achieved by the full magnetic field approximation, also on the detectors stations.

References

[1] S. Gorbunov, U. Kebschull, I. Kisel, V. Lindenstruth and W.F.J. Müller, Fast SIMDized Kalman filter based track fit, Comp. Phys. Comm. 178 (2008) 374-383.

[2] S. Gorbunov and I. Kisel, Reconstruction of decayed particles based on the Kalman filter, CBM-SOFT-note-2007-003, 7 May 2007.

Scalability of the SIMD Kalman Filter Track Fit Based on the Vector Classes

I. Kisel[1], M. Kretz[2], and I. Kulakov[3,4]

[1]GSI, Darmstadt, Germany; [2]Uni-Heidelberg, Germany; [3]Uni-Frankfurt, Germany; [4]Uni-Kyiv, Ukraine

The core of the data reconstruction in the CBM experiment [1] is the Kalman filter (KF). Therefore, the speed of KF based algorithms is of crucial importance in on-line data processing.

One of processors features, which can speed up the algorithm, is a SIMD instruction set [2], which allows to pack several data items in one register and to operate on all of them in one go, thus achieving more operations per clock cycle.

A standalone benchmark have been written for development of Kalman Filter based algorithms [3]. It uses the interface header for SIMD instructions.

A useful interface for SIMD instructions has been recently created. This is the vector classes (Vc) library [4]. It supports all types of CPU's instructions, and also the GPU's LRBni instructions set. Thus, Vc usage expands development possibilities for benchmark.

In order to implement vector classes into the SIMD KF fit benchmark some types and constants have been redefined to use correspondent Vc types. Also the procedure for input data packing into the SIMD vectors has been added.

	header		Vc	
	w/o TBB	TBB	w/o TBB	TBB
Time [μs]	0.448	0.053	0.422	0.052

Table 1: Fitting time per track of different SIMD KF track fit versions executed with and without TBB

The final version of SIMD KF track fit was tested on the 8-cores computer lxir039 with two Xeon X5550 processors at 2.7 GHz and 8 MB L3 cache. A gcc 4.4.2 compiler has been used for tests. The Intel Threading Building Blocks (TBB) software package has been used for execution parallelization between cores.

Fitting quality tests show good results with residuals equal to 49 μm and 44 μm for x and y track parameters and relative momentum resolution of 0.7%.

In order to compare with the initial version the fitting time per track has been estimated by both versions (see Table 1). In addition each version was run both on one core and on all 8 cores by usage of TBB.

As can be seen from Table 1, the version based on Vc shows slightly better results in comparison with the initial version. It is expected because SIMDized operations in the benchmark are simple enough, thus are less sensitive to implementation.

Scalability of the benchmark on lxir039 also has been investigated. For this purpose two possibilities have been added into the benchmark: to run SIMD KF fit on any set of cores and to specify different distributions of tasks between cores.

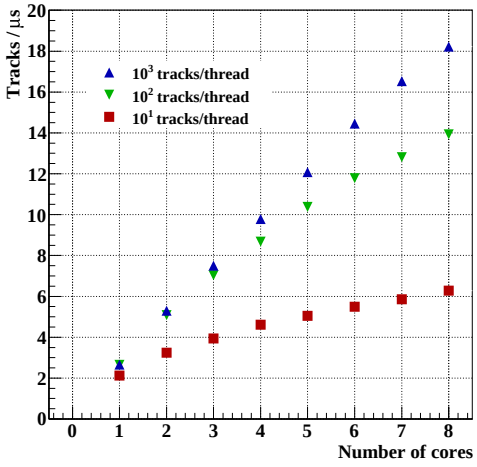

Figure 1: Scalability of SIMD KF track fit

Each physical core on lxir039 has two logical cores because of the hyper-threading technology. In order to investigate scalability of the benchmark, track fitting has been run on various numbers of cores. In Figure 1 the scalability on the physical cores is shown. Here track fitting has been parallelized by execution of one thread per one logical core. Fitting of 10, 100 and 1000 tracks have been consistently executed per each thread.

As one can see, for small number of tracks per thread the speed up is not as high as possible, and dependence is not linear too. It can be explained by the large overhead with respect to the execution time. The maximum speed up of factor 8 has been reached for the case of 1000 tracks per thread. It is in a good agrement with what is expected for the 8-cores computer. The dependence of the speed versus the number of cores is linear. It proves, that the tasks are performed independently on each core.

References

[1] I. Kisel, Event reconstruction in the CBM experiment. Nucl. Instr. and Meth. A566 (2006) 85-88.

[2] IA-32 Intel Architecture Optimization Reference Manual. Intel, June 2005.

[3] S. Gorbunov, U. Kebschull, I. Kisel, V. Lindenstruth and W.F.J. Müller, Fast SIMDized Kalman filter based track fit, Comp. Phys. Comm. 178 (2008) 374-383.

[4] Vector Classes, `http://gitorious.org/vc` .

Speed Optimization of the CA Based Track Finder in the CBM Experiment

I. Kisel[1] and I. Kulakov[2,3]

[1]GSI, Darmstadt, Germany; [2]Uni-Frankfurt, Germany; [3]Uni-Kyiv, Ukraine

The cellular automaton (CA) based track finder (CAT) will be used both for off-line and for on-line track reconstruction in the CBM experiment [1]. Thus very fast and flexible realisation of the CAT algorithm is required. Therefore, the standalone CAT has been modified for time optimization and execution parallelization.

First, the number of considered combinations of hits to find track segments has been significantly decreased. Also one branching operator in loop has been deleted. The speed up obtained at this stage was of factor 1.5.

Second, in order to avoid the repetition of calculations in loops, the needed values were prepared in advance. In addition, some loops have been merged. All this modifications have led to the additional speed up of factor 1.25.

Algorithm parallelization was done by reorganisation in such a manner that commands of separate iterations of loops could be executed concurrently on several cores. For this purpose iterations of main loops have been reorganised, so that for each iteration the execution result of any other iteration would not be required. Also, data needed for each iteration have been separated in memory, such that they become independent, and search of track segments, which takes 98% of time in the initial version, could be run in parallel at different stations.

For tests 100 central Au+Au UrQMD events at 25 AGeV have been simulated. A detector geometry with 2 MAPS and 8 double-sided strip detectors has been used. The efficiency and time of execution have been monitored. The processor with two cores Pentium D 3.0 GHz with 2 MB L2 cache has been used for tests.

Efficiency is defined as the number of reconstructed tracks assigned to generated particles divided by the number of all reconstructable tracks. Reconstructable tracks are those, which have momentum greater than 0.1 Gev/c and intersect the sensitive regions of at least four consecutive stations. A reconstructed track is assigned to a particle, if at least 70% of its hits have been caused by it. If more then one track are assigned to the particle, all additionally reconstructed tracks are regarded as clones. A reconstructed track is called ghost, if it is not assigned to any particle.

The efficiency of reconstruction (see Figure 1) is similar to the efficiency of the initial version. Clones and ghost level are about 3.5%.

Timing results are shown in Table 1. For comprehensive analysis of the package CPU and real times were measured. The CPU time is a sum of working times of all cores. The real time is the time spent by CAT on the track fit execution. For separation of the parallelization one from the optimization speed up CAT was run both on one core and on two cores. Parallelization gives the speed up factor of 1.2 only,

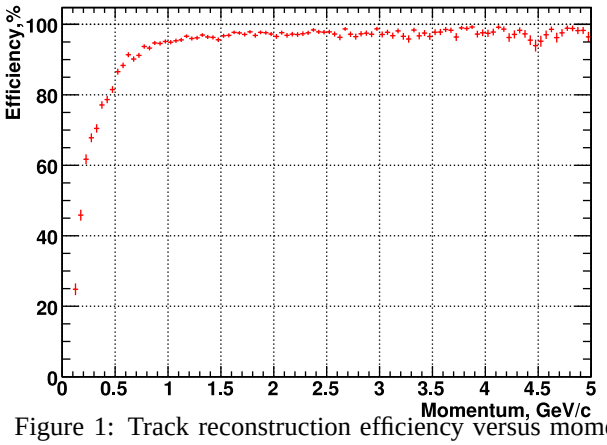

Figure 1: Track reconstruction efficiency versus momentum

	w/o TBB	with TBB	
		1 core	2 cores
CPU time [μs/track]	575	278	321
Real time [μs/track]	576	286	233

Table 1: Execution time of initial and obtained versions of CAT

while on the two-core processor the speed up factor of 2 is expected. This can be explained by the dependence at data level of the tasks executed in parallel. Also the additional overhead for the parallelization control could give a certain influence on the speed of CAT. The overhead can be extimated as 15%.

The algorithm optimization gives the additional speed up factor of 2 (see Table 1).

Also some additional tuning of the algorithm parameteres has been done, that reduced time per event to 120 ms. Thus, the total speed up of factor 5 has been achieved.

Further optimisation and parallelization of the Cellural Automaton based track finder will be investigated.

References

[1] I. Kisel, Event reconstruction in the CBM experiment, Nucl. Instr. and Meth. A566 (2006) 85-88.

[2] ITBB Reference Manual, `http://www.intel.com` .

Results from first beam tests for the development of a RICH detector for CBM

J. Eschke[1], K. Todoroki[2], and C. Höhne[1]

[1]GSI, Darmstadt, Germany, [2]University of Tokio, Japan

A key observable of the CBM physics program is a precise measurement of low-mass vector mesons and charmonium in their leptonic decay channel. In CBM, electrons will be identified using a gaseous RICH detector combined with several TRD detectors positioned behind a system of silicon tracking stations [1]. The concept of the RICH detector foresees an array of Multianode Photomultipliers (MAPMTs) as photodetector.

First beam test data for Cherenkov light detection with a 64 channel Hamamatsu H8500 MAPMT were recorded in August/September 2009 at GSI. Figure 1 shows the beam test set up. A 2 GeV proton beam was used to produce Cherenkov photons in a 8 mm thick plexiglass radiator. The signals of the MAPMT were attenuated by a factor of 40 in order to be compatible with the self triggered readout electronics based on the *n-XYTER* ADC chip which originally has been developed for signals from Silicon sensors [2].

A clear separation of the ADC signals of uncorrelated, low amplitude *noise* events from signals of Cherenkov photons with higher amplitude was achieved by a cut on the time difference between the beam counter coincidence and the hits in the MAPMT (Figure 2).

Figure 3 shows the event integrated signal of the projected ¼ Cherenkov ring. On average 3.52 hits were recorded per beam event. This number agrees well with an estimate taking into account the number of produced Cherenkov photons, geometrical losses, transmission losses and the quantum efficiency and collection efficiency of the MAPMT.

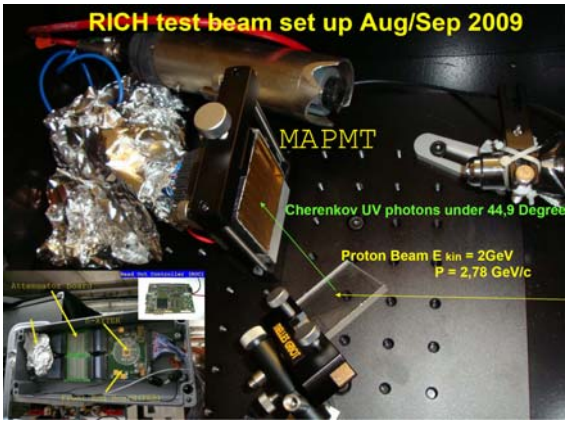

Figure 1: Test beam set up for detection of Cherenkov photons produced by a 2 AGeV Proton beam in a 8 mm plexiglass radiator.

Conclusions

The results of this beam test demonstrate that the self triggered *n-XYTER* ADC chip readout electronics is suited for the readout of the Hamamatsu H8500 MAPMT even with the currently needed attenuation of the primary PMT signals. It could be demonstrated that this MAPMT is able to detect single Cherenkov photons which can be well separated from noise using available timing information on the event.

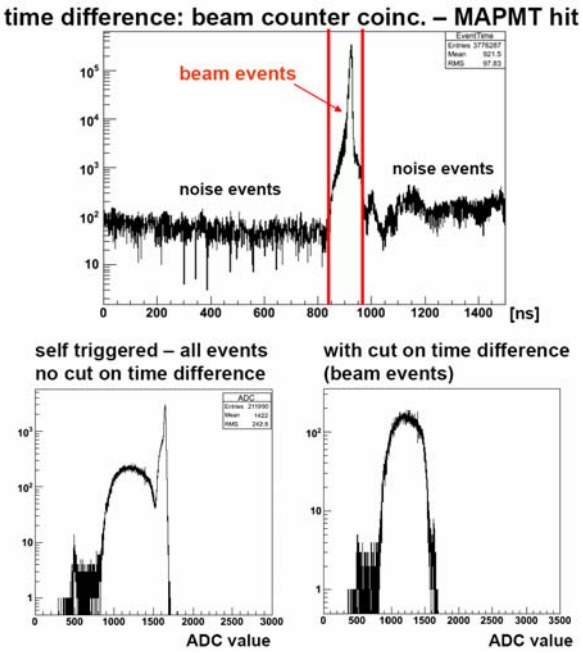

Figure 2: Time difference between beam counter coincidence and MAPMT hits (upper fig.). The selection of events within the indicated lines removes uncorrelated "noise" events (pedestal peak) in ADC spectra (lower figures, note the inverted ADC scales).

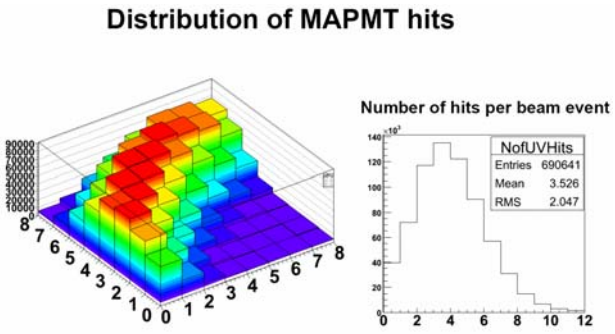

Figure 3: 1/4 Cherenkov Ring as detected with a 64 channel Hamamatsu H8500 Multianode Photomultiplier.

References:

[1] C. Höhne, CBM-RICH layout optimization, CBM Progress Report 2007

[2] A.S. Brogna et al., NIM A 568 (2006) 301–308

Fast parallel ring reconstruction algorithm for the RICH detector in the CBM experiment*

S. Lebedev[1,2], C. Höhne[1], and G. Ososkov[2]
[1]GSI, Darmstadt, Germany; [2]JINR, Dubna, Russia

Very fast event reconstruction is extremely important for the CBM experiment because of the huge amount of data which has to be handled. Fast algorithms require less computer power and becomes possible to use them in the online reconstruction. In this contribution, the fast parallel ring recognition algorithm for the CBM RICH detector is presented.

Modern CPUs have two features, which enable parallel programming. First, the SSE technology allows using the SIMD execution model. Second, multi core CPUs enable the use of multithreading. Both features were implemented in the parallel ring reconstruction algorithm.

RICH ring reconstruction in CBM [1] consists of two stages: 1) a local search of ring-candidates, based on the Hough Transform (HT) method; 2) a global selection algorithm, which compares all ring-candidates and selects only good rings, rejecting clone and fake rings.

In order to use parallel features, the ring reconstruction algorithm was significantly modified. It was found that 99% of the calculation time is consumed in the local ring-candidate searching. This part was optimized in several ways, which include combinatory and mathematic optimization of the HT, software optimization, memory usage optimization etc.

Then, the algorithm was SIMDIzed by changing the data representation from scalar to vector form. The idea is to calculate ring 4 parameters (x,y,r) from triplets in parallel by packing 4 scalar hit parameters into one vector.

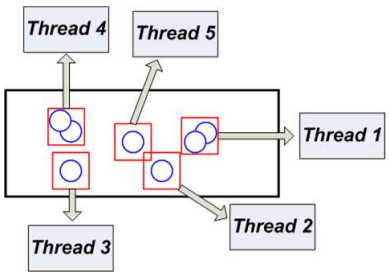

Figure 1: Sketch to illustrate the approach for many independent local ring-candidate reconstructions in the photodetector plane.

Multithreading parallelization of the Hough Transform algorithm was on different levels. Two parts of the RICH photodetector are completely independent because they are physically separated. The ring reconstruction procedure can thus be executed for each photodetector in parallel in two different threads. Furthermore, localized Hough Transform enables many independent local ring-candidate reconstructions in the photodetector plane (see Figure 1). Third, hits can be divided into several groups for independent HT execution for each group in parallel.

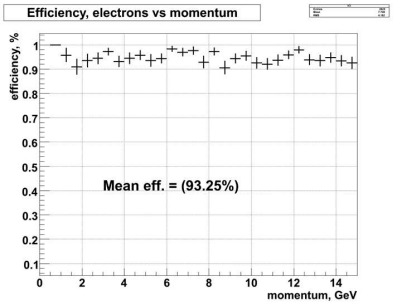

Figure 2: Efficiency for the reconstruction of primary electron rings in central Au+Au collisions at 25 AGeV beam energy.

In order to test the parallel ring reconstruction algorithm, central UrQMD Au+Au collisions at 25 $AGeV$ beam energy with 10 embedded primary e^+ and e^- were simulated. A computer with Core2Duo processors at 2.13 GHz was used for timing tests. The comparison of the initial serial scalar version and the parallel version of the ring finding shows that the reconstruction efficiency is the same for both versions with 93%, the number of fake rings is 3.5 per event, the number of clone rings is around 1 per event. The efficiency in dependence on momentum is shown in Figure 2. A speed up of a factor 55 is achieved by the optimization of the algorithm. Using SIMDization and multithreading the speed of the algorithm was increased further by a factor of 2. In total a speed up factor of 107 was achieved (from 750 ms/event to 7 ms/event) for the optimized parallel version in comparison to the initial algorithm. Larger speed up factors from multithreading are expected when using modern many core CPUs.

Table 1: Time per one event for different versions of the ring reconstruction algorithm.

	Time per event, ms	Speedup
Initial version	750	-
Optimization	13.6	55
Parallelization	7	1.95

References

[1] S. Lebedev et al., CBM Progress report 2008, p. 84.

* Work supported by BMBF.

Possible start version of the CBM muon detector system at SIS100*

A. Kiseleva† [1], C. Höhne[1], E. Kryshen[2], A. Lebedev[1,3], M. Ryzhinskiy[2], and P. Senger[1]
[1]GSI, Darmstadt, Germany; [2]PNPI, Gatchina, Russia; [3]JINR-LIT, Dubna,Russia

The CBM muon detection system (MuCh) was optimized for nucleus-nucleus collisions at $SIS300$ beam energies (see [1]). We have investigated the possibility to simplify the setup for measurements of J/ψ mesons in proton-nucleus collisions at $SIS100$ beam energies. Therefore, the performance of the muon detection system has been studied as function of the number of the detector stations for J/ψ measurements in $p + Au$ collisions at 25 AGeV. The simulations are based on a segmentation of the detector layers into pads with a minimum size of 0.28×0.28 cm^2, and a maximum size of 4.48×4.48 cm^2, corresponding to a total of 560 000 channels. For full track reconstruction the LIT global tracking package [2] is used. In order to study the sensitivity of the reconstruction algorithm on the number of the detector stations, we removed the hits in each station from the track finding procedure. The signal-to-background (S/B) ratio and the J/ψ meson reconstruction efficiency or the full and for the reduced systems are shown in fig.1: 1-6 means that hits of all 6 stations are used by the reconstruction procedure; 2-6 means that the hits of the first station were removed from the reconstruction; 3-6 means that the hits of the two first stations were not used in reconstruction, etc.

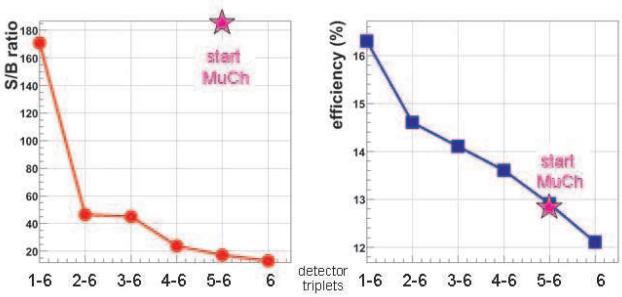

Figure 1: Signal-to-Background (S/B) ratio and reconstruction efficiency for J/ψ mesons from $p + Au$ collisions at 25 AGeV for full (1-6) and for the reduced muon systems (for explanation see text). The stars show results of the reconstruction for the start version of the muon system (see fig. 2).

The results of the simulations show a fast decrease of the S/B ratio (by more than a factor of 40) when removing the first station from the track finding procedure (see left panel of figure 1). This finding demonstrates that the first detector station is very important for background suppression. The reconstruction efficiency of the J/ψ mesons decreases linearly from 16% up to 12% when decreasing the number of stations (see right panel of figure 1).

A possible star version of the CBM muon detector system to be used for proton-nucleus collisions at $SIS100$ energies is shown in figure 2. This setup consists of 2 iron absorber layers (thickness 20 cm and 205 cm) and 2 detector stations with 3 detector layers each. The results of the track reconstruction based on this start version are depicted in figure 1 (star symbols): the J/ψ reconstruction efficiency (right panel of figure 1) is about 13% (to be compared to 16% for the full detector system with 6 stations), but the S/B ratio as high as for the setup equipped with 6 detector stations (left panel of figure 1). These results demonstrate that a start version of the muon detection system can be built with 2 detector stations only: a highly granulated detector triplet based on GEM technology after the first absorber, and a large-area low-granularity detector triplet after the second absorber. For the second triplet, either the first TRD station or straw-tube detectors can be used. Both options are under investigation.

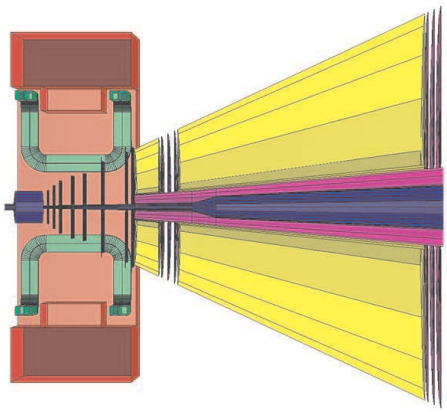

Figure 2: Reduced version of the muon system for measurements at $SIS100$.

References

[1] A. Kiseleva, et al., Optimization of the CBM muon detection system, GSI Scientific Report 2008.

[2] A. Lebedev et al., Status of the global track reconstruction algorithms for the CBM experiment at FAIR, GSI Scientific Report 2009.

* Work supported by EU/FP6 HADRONPHYSICS
† a.kiseleva@gsi.de

Muon simulations based on a realistic CBM muon detector system*

A. Kiseleva† [1], C. Höhne[1], E. Kryshen[2], A. Lebedev[1,3], M. Ryzhinskiy[2], and P. Senger[1]
[1]GSI, Darmstadt, Germany; [2]PNPI, Gatchina, Russia; [3]JINR-LIT, Dubna,Russia

The CBM muon detection system is designed to measure muon pairs from the decay of vector mesons ($\rho, \omega, \phi, J/\psi$) produced in heavy-ion collisions. At FAIR energies the muon momenta can be rather low, therefore, we developed a muon detection concept which a variable definition of absorber thickness according to the muon momentum was been developed. The reconstruction strategy was described in [1].

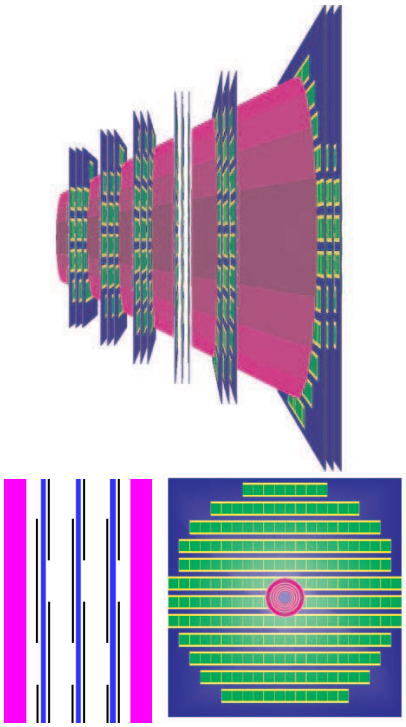

Figure 1: The modular design of the muon system: top - total system, bottom left - the side wiew of one gap between two absorbers with 3 detector layers, bottom right - the front view of one detector layer with detector moduls.

The actual design of the muon detector system consists of 6 hadron absorber layers (iron plates of thickness 20, 20, 20, 30, 35, 100 cm) and 15-18 gaseous tracking chambers located in triplets behind each iron slab. The geometry of the muon system is presented in figure 1: the side view of the full system (top), the side wiew of one gap with detector layers (bottom left), and the side view of one detector layer with detector moduls (bottom right). The modular design of the muon system was described in detail in [2].

* Work supported by EU/FP6 HADRONPHYSICS
† a.kiseleva@gsi.de

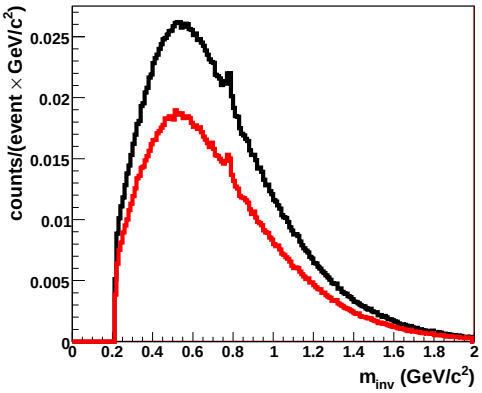

Figure 2: Invariant mass spectra of reconstrcucted muon pairs from central Au+Au collisions at 25 AGeV. Black line - without clustering, red line - with clustering.

For the simulations we used a segmentation of the detector layers into the pads. The minimum size of the pads was 0.28×0.28 cm^2, maximum - 4.48×4.48 cm^2, corresponding to 560 000 channels in total. We use a simple model of clustering which was explained in [3]. LIT tracking [4] is used for track finding in MuCh. Results for the ω-meson from central Au+Au collisions at 25 AGeV are the folloing: signal-to-background ratio is 0.062 (0.059) and ω reconstruction efficiency 1.8% (1.2%) without (with) clustering. The losses in the ω reconstruction efficiency are due to the efficiency of the clustering procedure. These losses of hits also increase the number of ghost tracks, and as a result the signal-to-background ratio decreases. Invariant mass spectra of reconstrcucted muon pairs are shown in fig.2.

The next step of the muon simulations is the implementation of a realistic detector response based on the results of the detector prototype tests.

References

[1] A. Kiseleva, et al., Muon measurements at different beam energies in CBM, GSI Scientific Report 2008.

[2] E. Kryshen, et al., Detaild geometry for MUCH tracker and FEE requirements, CBM Status Report 2008.

[3] E. Kryshen, et al., Digitization and hit finding in the CBM muon detector, CBM Status Report 2007.

[4] A. Lebedev et al., Track reconstruction in the MUCH and TRD detectors of CBM, GSI Scientific Report 2008 and CBM Status Report 2008.

Fast parallel tracking algorithm for the muon detector of the CBM experiment

A. Lebedev[1,2], C. Höhne[1], I. Kisel[1], and G. Ososkov[2]
[1]GSI, Darmstadt, Germany; [2]JINR, Dubna, Russia

The tracking algorithms of the CBM experiment have to process terabytes of input data produced in particle collisions. Therefore, the speed of the tracking software is extremly important for data analysis. In this contribution, a fast parallel track reconstruction algorithm for the muon detector (MUCH) which uses available features of modern processors is presented. These features comprize a SIMD instruction set (SSE) and multithreading. The first one allows to pack several data items into one register and to operate on all of them in parallel thus achieving more operations per cycle. The second feature enables the routines to exploit all available CPU cores and hardware threads.

MUCH track reconstruction in CBM is based on track following and Kalman Filter methods using reconstructed tracks in the STS as seeds. In order to use SIMD and multithreading the tracking algorithm has been significantly modified. The changes include necessary modifications in the track propagation and track fitting in order to optimize and SIMDize the algorithm. The optimization include several steps. First, the access to the magnetic field was optimized using a local approximation of the field by polynomials. It was found to be sufficient for the track propagator to use a 2D polynomial of the fifth order to approximate the field in the planes of each station. The field behavior between stations is approximated by a straight line. Track parameters taken with the polynomial approximation of the magnetic field are as precise as those calculated using the full magnetic field map. Second, a simplified detector geometry and an optimized geometry navigation algorithm were developed. The simplified geometry is created by converting the detailed Monte-Carlo detector geometry into a reduced one, which only consists of planes perpendicular to the beam direction. The navigation in such a simplified geometry has been significantly optimized. Then, the algorithms were SIMDIzed by changing the data representation from scalar to vector form, therefore, after packing the correspondent four scalar track parameters from different tracks into vector one can propagate and fit four tracks in parallel.

The track finder algorithm was also significantly modified to use a SIMDized track propagator and track fitter. The multithreading capabilities have also been implemented to the tracking algorithm.

The track fitter algorithm has been tested using simulated muon tracks which have been transported through the CBM setup using GEANT3. Table 1 shows the computational times and speed up factors for the track fitter algorithm in the muon detector for two computers: 1) PC1 with an Intel Core 2 Duo processor at 2.26 GHz and 2) PC2 with a 2×Core i7 processors at 2.66 GHz. For PC1 an acceleration of factor 60 is achieved by the substantial optimization of the algorithms described above. For PC2 the gain is even more with a factor 92. Changing the data representation from the scalar to the vector (SIMD) format results in a 3 times faster algorithm. Running several threads of the SIMDized track fitter routine in parallel gaines speed up of 1.8 for the 2 core PC1 and 8.8 for the 8 core PC2. In total a speed up factor of 324 (from 1100 μs/track to 3.4 μs/track) is achieved for the PC1 computer and a factor of 2400 (from 1200 μs/track to 0.5 μs/track) for the PC2 computer.

	PC1: Core 2 Duo		PC2: 2×Core i7	
	Time	Speedup	Time	Speedup
Initial	1100	-	1200	-
Optimization	18.4	60	13	92
SIMDization	6.2	3	4.4	3
Multithreading	3.4	1.8	0.5	8.8

Table 1: Speedup of the track fitter algorithm. Time is shown per track in μs.

	PC1: Core 2 Duo		PC2: 2×Core i7	
	Time	Speedup	Time	Speedup
Initial	636	-	730	-
Optimization	10.2	62	7.2	101
SIMDization	6.4	1.6	4.9	1.5
Multithreading	4.2	1.5	1.5	3.3

Table 2: Speedup of the track finder algorithm. Time is shown per event in ms.

In order to test the parallel tracking algorithm, central Au+Au collisions at 25 AGeV beam energy were simulated with UrQMD and propagated through the CBM setup using GEANT3. In addition 5 μ^+ and 5 μ^- were embedded in each event at the primary vertex. The comparison of the initial serial scalar version and the parallel version of the tracking shows that on account of a minor loss in the momentum integrated track reconstruction efficiency (from 94.7% to 94.0%) the parallel tracking algorithm is much faster (see Table 2). A speed up of 62 is achieved for PC1 by optimization of the algorithm and the use of the optimized Kalman filter routines. For PC2 the speed up is even more 101. SIMDization and multithreading give less speed up factors than for the track fitter, which can be explained by the fact that some parts of the track finder are not completely SIMDized and parallel. In total, the parallel tracking algorithm is 151 times faster than the initial serial scalar algorithm (from 636 ms/event to 4.2 ms/event) for the PC1 computer and 487 times faster (from 730 ms/event to 1.5 ms/event) for the PC2 computer.

Progress with performance simulations of the CBM Silicon Tracking System*

A. Kotynia[1] and J.M. Heuser[2]
[1]Univ. Frankfurt, Germany; [2]GSI, Darmstadt, Germany

Efficient charged particle tracking and high momentum resolution are central performance requirements of the CBM Silicon Tracking System (STS). The aim of the ongoing layout studies is to design a highly granular and low-mass detector system which can track up to 1000 charged particles that are typically generated in one central Au+Au collision at 25 GeV/u projectile energy. A low-mass detector is crucial to achieve a momentum resolution down to 1%. Progress has been made with optimizations of the detector geometry and with the implementation of realistic detector response functions.

Detector layout studies

The STS comprises eight tracking stations located 30, 35, 40, 50, 60, 75, 95 and 100 cm downstream of the target. The stations have a modular structure and are constructed from 300 μm thick double-sided silicon microstrip sensors. Groups of sensors (sectors) are individually read out with electronics located at the perimeter of the stations. Signals from the sectors are sent through thin aluminum-polyimide micro-cables to the front-end electronics (Fig. 1).

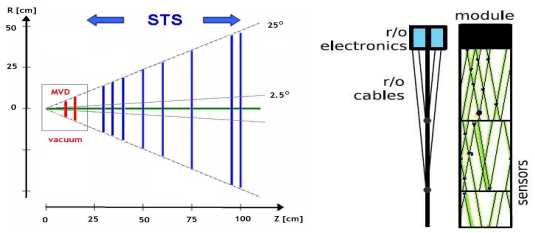

Figure 1: Left:Schematical layout of the STS. Right: One module with read-out electronics.

Three variations of this layout have been studied.

1. Following a modified arrangement of the Micro Vertex Detector (MVD) with its detector stations at 5 and 10 cm distance from the target, it is possible to place the first STS station at 20 cm. In order to have enough space for mechanical support structures, the distance between the STS stations should not be less than 7 cm. Taking this into account, the STS stations have been redistributed to the z positions 20, 27, 34, 44, 60, 75, 90, 100 cm. This results in an increased track finding efficiency (+2%), together with a momentum resolution decreasing from 1.37% to 1.12%.

2. Due to the fact that the current track reconstruction software requires four consecutive hits in the STS, a geometry with one additional station has been studied as well. Besides the expectation one more station does not improve the tracking results significantly. The efficiency increases by about 1% but the momentum resolution worsens from 1.12% to 1.20%.

3. In the tracking modules detectors with a width of 6 cm and a strip pitch of 60 μm are applied. The strip length has been matched to a maximum occupancy of less than 5% what results in a vertical size of one sector between 2 to 18 cm. The strips on the front side are tilted by $7.5°$ and on the back side by $-7.5°$ creating a stereo angle of $15°$. Every strip can cross between 100 and 800 strips on the opposite side of a sector. This results in a large number of fake or combinatorial hits. To reduce this effect, a special geometry with shorter strips has been prepared. The strip lengths vary between 1 cm in inner parts of the tracking stations and 6 cm in their outer parts. In such a geometry, the number of fake hits is reduced by a factor of two, from 5.7k to 2.7k per central event.

Performance studies

The performance of the STS has been evaluated with realistic detector response functions implemented. Signal sharing between strips together with charge collection inefficiency and Lorentz shift due to the presence of the magnetic field, channel dead time, and single-channel inefficiencies are present in the simulations. For more details see [1]. The efficiency of the cluster finding method only depends on the particle's incident angle. For angles below $20°$ the hit finding efficiency drops from 98% for ideal digitization to 95% in the realistic case.

Next steps

In order to improve the hit finding efficiency, we consider tilting the outer parts of all STS stations by $20°$ around the vertical axis. This should assure hit finding efficiencies above 95% for all parts of the tracking stations.

References

[1] A. Kotynia, J.M. Heuser and W. Müller, "Simulation of realistic detector responce in the CBM Silicon Tracking System", GSI Progress Report 2009

* Supported by EU/FP7 HadronPhysics2

Simulation of realistic detector response in the CBM Silicon Tracking System*

A. Kotynia[1], J.M. Heuser[2], and W. Müller[2]
[1]Univ. Frankfurt, Germany; [2]GSI, Darmstadt, Germany

The Silicon Tracking System of the CBM Experiment consists of eight tracking layers of silicon detectors. Each layer is an array of vertical modules containing 300 μm thick double-sided silicon strip sensors. The strip pitch is 60 μm on both sides. The sensors are segmented into 1024 strips per side. On either side the strips are tilted by +7.5° or -7.5° with respect to the vertical edge, creating 15° stereo angle between the opposite sides. This allows reconstructing multiple hits from the same sensor at the expense of a poorer spatial resolution in the vertical direction, keeping high resolution in horizontal direction for better reconstruction of the particle momenta.

Detector response simulations

The simulations which have been developed include the complete chain of physical processes caused by a charged particle traversing the detector – from charge creation in the silicon to the digitized output signals. Fig. 1 illustrates the simulated track originating from a minimum ionizing particle in the silicon detector, where every point along the track represents a charge packet. The track is constructed using finite steps to exploit fine granularity in the energy deposition. In the second phase, the charge packets are collected on the strips. A random noise sample is added to the charge signal, according to a Gaussian distribution whose standard deviation should be considered as an equivalent noise charge of the detector system.

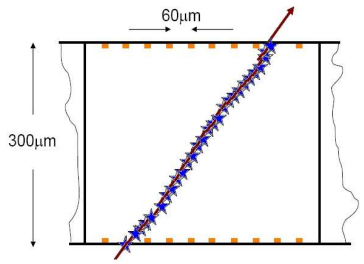

Figure 1: Simulated track of a minimum ionizing particle in the silicon detector (arrow). The orange rectangles represent the read-out strips.

The presence of a magnetic field in the region where the detectors operate influences the collection of the charge on the strips. Due to the Lorentz force on the charge carriers, electrons and holes produced along the track of a crossing particle are collected at an angle ϑ_L (Lorentz angle) with respect to the track. In our STS configuration ϑ_L is 1.5° for holes and 7.5° for electrons. For a more detailed description of the Lorentz force see [1].

The center-of-gravity algorithm (1) allows to obtain the position of the incident particle in the sensor. Using this method, it is possible to estimate the particle position as the weighted average of the position x_i of the n strips included in one cluster with the S_i being the corresponding signals:

$$x = \frac{\sum_{i=1}^{n} S_i x_i}{\sum_{i=1}^{n} S_i} \quad (1)$$

This procedure has been performed independently for both sensor sides. Two clusters found on opposite sides are associated with a particle hit, under the condition that the fired strips on one side have a point of intersection with the fired strips on the other side. This method results in strong dependance of the hit finding efficiency on the particle crossing angle, which is presented in Fig. 2 together with the distribution of cluster sizes in the first STS station. The results were obtained with a noise width of 0.5 and a threshold of 4k electrons.

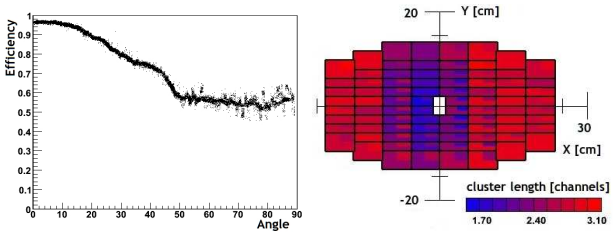

Figure 2: Left: Hit finding efficiency as a function of the particle crossing angle. Right: Number of fired strips per cluster on first STS station.

Single channel inefficiencies occurs as a result of the readout electronic's dead time. According to the newest predictions for the actual behaviour of the STS prototype readout electronics, the channel dead time significantly depends on the pulse amplitude and varies between 100 and 1000 ns. Moreover, the measurements of the pulse length have been done for three settings "fast", "mid" and "slow" corresponding to the discharge time. Those settings result in different noise values. Preliminary studies of the hit finding efficiency show that for the "fast" setup in the inner parts of stations one and two 6% of the hits are lost, while for the outer parts of the stations the number of lost hits drops down to 1%. The influence of this effect on the track reconstruction is to be studied further.

References

[1] *An algorithm for calculating the Lorentz angle in silicon detectors*, Nuc. Instr. Meth. A497 (2003) 389-396

* Supported by EU/FP7 HadronPhysics2

Optimization of the CA Track Finder for the STS Geometry with Sensors Overlapping

D. Golubkov[1], I. Kisel[2], A. Kotynia[2], I. Rostovtseva[1], and Y. Zaitsev[1]
[1]ITEP, Moscow, Russia; [2]GSI, Darmstadt, Germany

Our previous work on adaptation of the Cellular Automaton (CA) track finder [1] to the realistic STS geometry with overlapping sensors allowed to recover the high tracks-finding efficiency [2] which it has had for the simplified STS description with sensors of each station arranged at the same Z position (the "same-Z" geometry).

Below we report on a detailed study of the behaviour of the track finder for the realistic STS geometry that addressed the problem of an increased number of clone and ghost tracks relative to the same-Z geometry.

In the realistic STS geometry the sensors overlap, the hits within the same station have different Z coordinates, and also the detector contains more material. A larger number of hits (both true and fake) is produced in the sensor overlap regions giving more than 1 hit per track per station, additional hits also coming from the increased number of delta electrons.

To reduce the combinatorics we optimized the X- and Y-windows used in the track candidate search based on the pull distributions, Fig. 1.

The main component of the clones turned out to consist of short pieces of long MC tracks, broken due to hits, which did not fit into the Y-window at the step of the doublet creation. These broken tracks ($\sim 4\%$) become effectively lost for analysis, since one of the pieces has low spatial accuracy, and the other has bad momentum resolution. From our studies we found that the increase in the number of clone tracks is not connected to the inhomogeneity of the magnetic field, but to the increase in the amount of multiple scattering; the main contribution to ghost tracks originates from the large hit density due to fakes (after an artificial removal of fakes, the ghost rate $\sim 4-5\%$ decreases down to $\sim 0.2\%$). If some hit occurs within about 5σ of the error ellipse, then at the level of the track finder it is practically equivalent to the true hit. A fake hit can be picked up instead of the true hit which reduces the efficiency of the hit assignment.

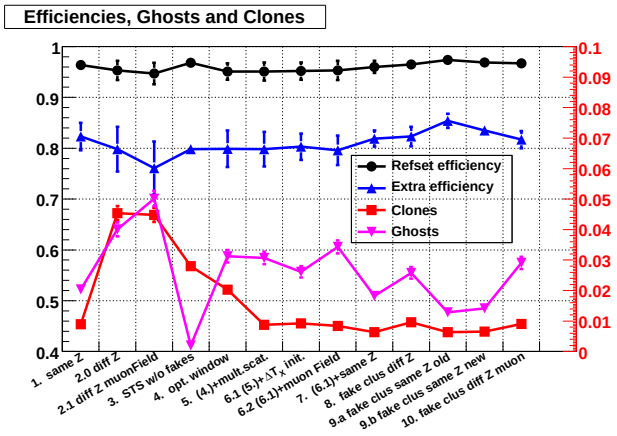

Figure 1: The track reconstruction efficiency, ghost and clone rates at the different steps of the study. The results were obtained using an MC sample of central Au+Au collisions at 25 AGeV.

To improve the quality of the hit-to-track assignment it is planned to develop a procedure similar to the outlier removal to be applied during the track fit. To estimate the possible increase in efficiency which can be achieved with such a procedure, we modified the track efficiency calculation by considering all hits within 5σ to belong to the track, even if the track finder picked up a fake hit in that plane. After such a "fake clusterization" procedure the number of tracks in which 100% of hits belong to the same MC track increased by $\sim 19\%$, but the relative percentage of ghosts and clones did not change significantly. This indicates that the remaining ghost are mainly fakes (i.e. tracks consisting of a random combination of fake hits), and a cut on the fit χ^2 might be useful for their suppression. It would be also helpful to further optimize the STS geometry and reduce the combinatorics and the number of fakes, probably by re-optimization of the lengths and stereo-angles of the strips.

To summarize, the following modifications were implemented and included in the `cbmroot` to decrease the clones and ghosts: more accurate account for multiple scattering optimization of the X- and Y-windows for track candidate search based on pulls and the initial value of ΔT_x in singlets.

With the described modifications the problem with clones was solved ($\sim 0.8\%$ of clones as in the same-Z geometry). The number of ghosts has been reduced too, but for further reduction more studies are necessary (track fit, outlier removal, STS geometry optimization).

References

[1] I. Kisel, Event reconstruction in the CBM experiment. Nucl. Instr. and Meth. A566 (2006) 85–88.

[2] D. Golubkov *et al.* Cellular automaton track finder in realistic STS detector geometry, CBM Progress Report, p. 76, GSI, Darmstadt, 2008.

Results of a Hough Tracker implementation for CBM

C. Steinle[1], A. Kugel[1], and R. Männer[1]
[1]University of Heidelberg, Department of Computer Engineering V, 68159 Mannheim, Germany

The customized Hough transform is a global method for track finding, which transforms all STS detector hits into a parameter space according to the components of the track momentum p (θ, $-q/p_{xz}$, m). As the direct implementation of this three dimensional Hough space requires a huge amount of memory, this situation is avoided by the decomposition of the Hough space into several two dimensional layers, where the number of parallel computed ones can be adjusted to the existing hardware resources. In addition to this, the goal of the implementation is to process the tracking with maximum speed, which means in detail the processing of one detector hit per clock cycle. Thus the complicated calculations of the customized Hough transform according to the real detector geometry and the real magnetic field are implemented with look-up tables (LUTs), which can be calculated offline by any sufficiently precise algorithm.

Since the first approach for the application of the customized Hough transform to the CBM experiment, the usage of special parallel hardware is suggested to practically and applicably fulfil the speed requirement for a tracking decision system, which is able to cope with 10^7 interactions per second. As such an implementation is obviously quite complicated to build it from scratch, three different levels have been developed, which become faster and thus more complex.

So at the first level, a C++ software implementation package for the CBMROOT framework is designed to simulate the efficiency behaviour of the customized Hough transform. For this purpose it is clear that it is not important to make use of any hardware specific instruction sets, but rather poor, because the package should run possibly on every imaginable computational platform. Hence substantiating the most abstract algorithm description, it is obviously the slowest implementation.

While improving this implementation, the second level is at first thought to be only a rapid prototyping system for a conceivable multi-chip platform [1], which forms actually the third level. But during the development of this second level implementation, the Sony Playstation III with its Cell BE is realized to be also completely operational [2], because it delivers the same output data based on the same input data than the CBMROOT package:

Coming finally to the third level, it should be at first mentioned here that this implementation is just preliminary. That means that there is no prototype, but all necessary concepts are proven to be generally operational by the HDL simulator MODELSIM and the assumed timing behaviour is evaluated by CBMROOT framework simulations. As the parallelism level of a FPGA is exhaustive and in particular the level of a multi-chip platform, the results of just three implementations are presented here, because they are of special interest. The first one can be characterized by using just a single chip, the second one by being the fastest possible implementation and the third one by realizing a good trade-off between timing performance and hardware requirement.

Architecture	Time for a single event	Required platforms for CBM
PC: P4@3GHz and 2GB RAM; not optimized CBMROOT simulation	4.0 s	10,000,000
Playstation III: CellBE@3.1GHz, 256MB RAM and 256kB LS; vectorized, 6SPUs	21.5 ms	53,750
1 FPGA: xc5vlx110-ff1760-3@125MHz; implementing 1 histogram layer	752.2 μs	1,881
15 FPGAs: xc5vlx110-ff1760-3@250MHz; implementing all histogram layers	62.8 μs	157
3 FPGAs: xc5vlx110-ff1760-3@250MHz; implementing 14 histogram layers	88.5 μs	222

Table 1: Result summary for all implementations

Table 1 summarizes the results for all introduced implementations with regard to the time consumption for a single event and based on this the number of required platforms to fulfil the CBM requirements.

As the presented results are quite satisfying with regard to the timing behaviour, the next step is obviously given by the realization of a FPGA platform prototype. In addition to this, the efficiency of the algorithm can be possibly improved by the usage of more appropriate LUTs and the application of successive decision units.

References

[1] C. Steinle, A. Kugel and R. Männer, “Implementation of a Hough Tracker for CBM”, CBM Progress Report 2007, May 2008.

[2] C. Steinle, A. Kugel and R. Männer, “Implementation of a Hough Tracker for CBM”, CBM Progress Report 2008, February 2009.

Operation and performance of the CBM Silicon Tracking reference telescope*

V. Friese[1], J.M. Heuser[1], V. Kleipa[1], S. Linev[1], W. Müller[1], W. Niebur[1], C.J. Schmidt[1], A. Kotynia[2], A. Lymanets[2], A. Wilczek[3], and B. Bozsogi[4]

[1]GSI, Darmstadt, Germany; [2]University of Frankfurt, Germany; [3]University of Silesia, Katowice, Poland; [3]Eotvos Lorand Univ., Budapest, Hungary

A reference tracking telescope consisting of three stations based on double-sided silicon microstrip detectors has been constructed and tested in a 2 GeV proton beam experiment at GSI. This proof-of-principle device designed for charged particle track measurement with high spatial resolution closely integrates silicon sensors with self-triggering front-end electronics. Each station features the full readout of a *CBM02B2* prototype detector with 2×256 strips of orthogonal orientation and 50 μm strip pitch. Four self-triggering n-XYTER readout chips have been directly wire-bonded to the detector.

Operation of the tracking stations

In the experiment the data streams from several detector systems have been combined using the Data Acquisition Backbone Core framework [1]. An online monitor based on the Go4 system [2] has been used to control the data quality by representing raw spectra (e.g. ADC distributions, channel occupancies) as well as an elementary analysis of e.g. time correlations. The online histograms provide feedback for the correct adjustment of the readout electronics. The ADC spectrum in each channel contains a noise peak and a signal distribution created by the beam particles. By setting the threshold in the chip above the noise most of the registered hits become associated with the incident beam.

Also the stability of the detector settings has been monitored. Temperature stability turned out to be most important for particle detection with constant performance. The tracking stations dissipate up to 20 W (current of up to 4 A at 5 V) and thus must be cooled. The boards were sandwiched between aluminum plates through which chilled water was circulated. Initially, due to periodic switching of water chiller, the temperature of all three tracker stations exhibited sinusoidal time dependence with a period of $\sim$20 minutes and a full swing of $\sim 3\,^{\circ}C$ (see Fig. 1 left). Observed temperature variation causes a drift of baseline in the read-out chip, revealing its high temperature coefficient. The right panel of Fig. 1 shows time dependence of baseline position as a result of temperature variation. The peak-to-peak amplitude of the baseline drift comprises 200 ADC counts, exceeding the signal amplitude of a beam particle. The cooling system was exchanged with more stable device and, in addition, an on-line amplitude calibration method was implemented. The high temperature coefficient of the front-end chip will be addressed in the upcoming n-XYTER engineering run.

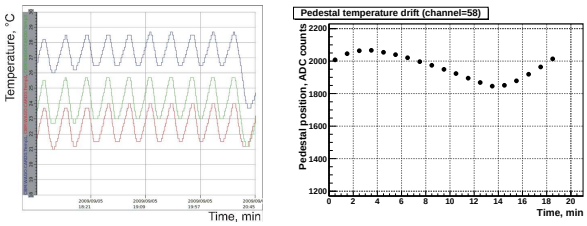

Figure 1: Temperature oscillations tracking stations (left). Pedestal drift in a front-end chip (right).

Offline performance analysis

Advance tools for offline analysis have been developed. As a first step the raw data files are converted to root files. After such conversion, it is possible to use the current STS digitization and STS hit finding algorithm, developed for the full CBM setup. The hit finding tools include charge sharing beetween neighbouring strips, which provide position resolution better than 15 μm [3]. As an example of the hit distribution the beam profile reconstructed in one of the detector stations is shown in Fig. 2.

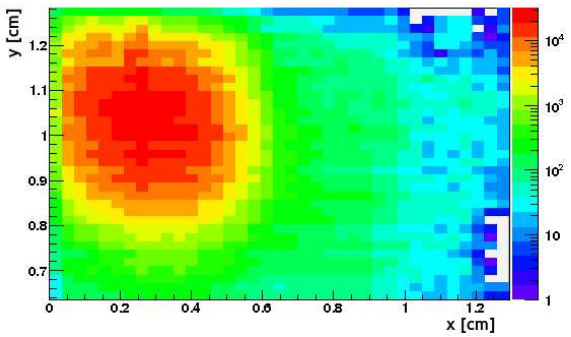

Figure 2: Beam spot reconstructed in a tracking station.

References

[1] Data Acquisition Backbone Core, http://dabc.gsi.de

[2] GSI Object Oriented On-line Off-line system, http://go4.gsi.de

[3] A. Kotynia et al., *Simulation of realistic detector response in the CBM STS*, GSI Progress Report 2009

* Supported by EU/FP7 HadronPhysics2

Microstrip detector design optimization for the CBM Silicon Tracking System*

S. Chatterji and J.M. Heuser
GSI, Darmstadt, Germany

We are using the SYNOPSYS [1] package for three-dimensional TCAD simulations to optimize various design parameters of the Double Sided Silicon Strip Detector (DSSD) under development for the CBM Silicon Tracking System.

Three-dimensional device simulations

Building on the experience with two-dimensional simulations in PISCES [2], we developed a three-dimensional grid in TCAD which approximates all the features of our existing prototype detector, like the strip pitch of 50 μm, strip width of 20 μm, strip stereo angle of $\pm 7.5^\circ$ with *AC* coupling. A part of the modeled detector is shown in Fig. 1, zooming in on a n-strip and its neighbouring p-stops. The x (horizontal) axis points along the width and pitch of the strips, the y axis along the lenght of the strips and z (vertical) axis along the wafer thickness. The $\pm 7.5^0$ stereo angle of the strips is better recognized from Fig. 2 which shows a two dimensional projection (x-y plane) of the grid.

We have simulated transients by passing Minimum Ionizing Particles (MIP) at various angles through the detector. Fig. 3 shows in the left graph the transient charge generated by the passage of the MIP. Many device parameters can be extracted from the simulation. Examples are interstrip capacitances and resistances relevant e.g. for an understanding of the cross talk between channels. The right graph of Fig. 3 shows the interstrip admittance as a function of the applied bias voltage. The value of interstrip resistance comes out to be around 10-20 GΩ which is as per the expected value.

Comparison with measurements

At present the simulations represent existing detector designs. We have started to verify the calculations with measurements of our prototype detectors. The simulation tools will then be used to optimize the next generation of CBM DSSDs already during the design phase.

References

[1] http://www.synopsys.com/home.aspx, http://home.comcast.net/ john.faricelli/tcad.htm

[2] S. Chatterji et al., GSI Report 2008-1 14

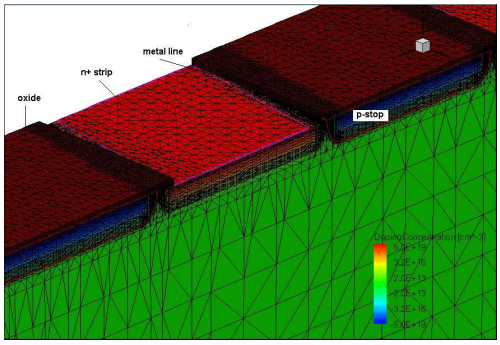

Figure 1: Three dimensional grid of the simulated DSSD.

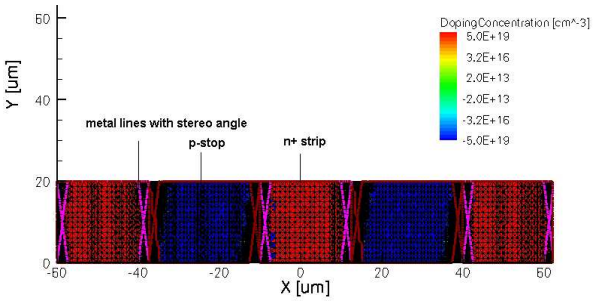

Figure 2: 2-dim. projection of the 3-dim. DSSD grid.

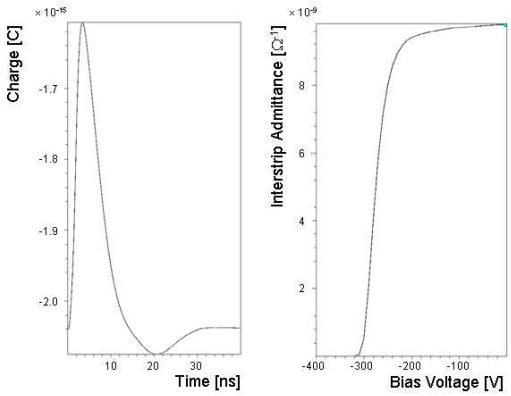

Figure 3: Transient charge generated by passage of MIP through the simulated grid (left). Simulated interstrip admittance versus bias voltage (right).

* Supported by EU/FP7 HadronPhysics2

Simulation study of radiation damage in double-sided silicon microstrip detectors for the CBM Silicon Tracking System*

S. Chatterji and J.M. Heuser
GSI, Darmstadt, Germany

We started TCAD simulations last year to understand the radiation damage in Double Sided Silicon Strip Detectors (DSSD) for the CBM Silicon Tracking System. We used the public domain versions from Stanford namely SUPREM for Process Simulation and PISCES for device simulation [1]. The results were reported in the GSI Scientific Report 2008 [2]. Now we are using the three-dimensional TCAD simulation package from Synopsys [3] which we procured through the Europractise Software Service. Synopsys has several subpackages for three-dimensional simulations like Sentaurus Process, Sentaurus Device, Workbench, TecPlot, Inspect etc.

Two- and Three-dimensional simulations

Fig. 1 shows the two-dimensional grid of the DSSD. There are three n-strips on the front side seperated by p-stops, and three p-strips on the back side. It is also possible to simulate transients like passage of Minimum Ionizing Particles (MIPs) through the device. One can see a very dense mesh in the middle of the grid which is required to correctly simulate the passage of the MIP. It is also very important to give a fine mesh at the junction curvatures and at interfaces. This is seen in Fig. 2. We apply a negative bias on the backside and ground the n-strips in order to reversely bias the detector. We have found that the peak electric field occurs at the junction curvature as can be seen from the left panel of Fig. 3. The right panel shows that p-stops are indeed able to isolate the adjacent n-strips under depleted condition. The extension of the studies with a three-dimensional implementation of the detector is illustrated in [4].

Studies of radiation damage

We are ready to simulate the radiation damage in the DSSD by changing the effective substrate concentration using the Hamburg model [5] and also by changing the surface oxide charge.

References

[1] http://home.comcast.net/ john.faricelli/tcad.htm

[2] S. Chatterji et al., GSI Report 2008-1 14

[3] http://www.synopsys.com/home.aspx

[4] S. Chatterji et al., *Microstrip detector design optimization for the CBM Silicon Tracking System*, GSI Progress Report 2009

[5] Nucl. Instr. Meth. Phys. Res. A439 (2000) 282-292

* Supported by EU/FP7 HadronPhysics2

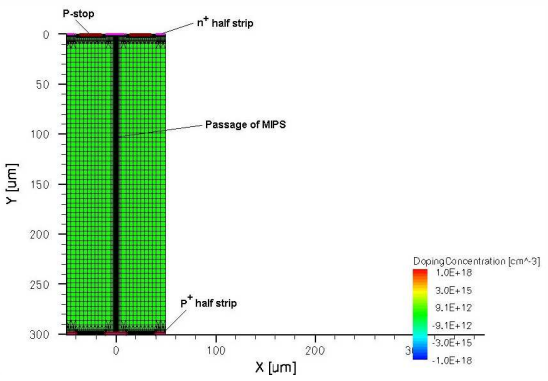

Figure 1: Two-dimensional grid of the simulated DSSD.

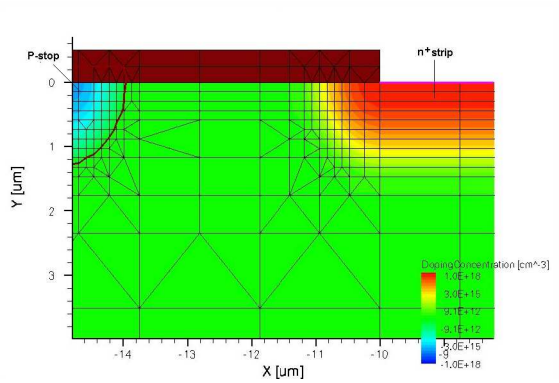

Figure 2: Zoomed frontal view of the simulated DSSD.

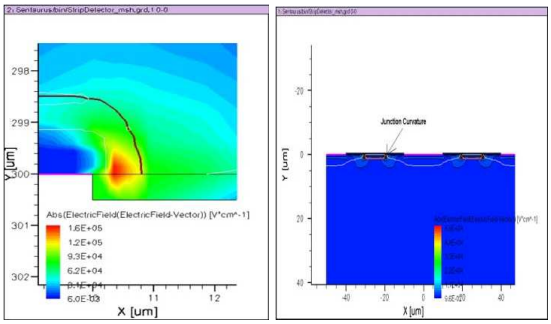

Figure 3: Electric field distribution at the curvature of one of the p-strips (left). Role of p-stops in isolating the adjacent n-strips in non-depleted condition (right).

Progress with the development of double-sided microstrip detectors for the CBM Silicon Tracking System*

J.M. Heuser[1], L. Long[2], M. Luleich[2], H. G. Ortlepp[2], and R. Röder[2]
[1]GSI, Darmstadt, Germany; [2]CiS Forschungsinstitut für Mikrosensorik und Photovoltaik GmbH, Erfurt, Germany

The second prototype of a full-size double-sided silicon microstrip detector for CBM's Silicon Tracking System has been developed in cooperation of GSI and CiS. Its dimensions and contact pattern are compatible with the construction of a low-mass demonstrator tracking module by the CBM-MPD STS Consortium [1]. Further activities concern the preparation of a new technology wafer for the exploration of a variety of sensor design improvements towards improved high signal efficiency after high radiation exposure.

Full-size prototype detector CBM03

Based on the first prototype *CBM01* [2] and experience with technology wafer *CBM02* [3], the new design *CBM03* realizes a large double-sided detector with the strips under a stereo angle on both sides. This design is favoured for aspects of the module assembly but requires interconnecting the short corner strips on both sides through lines on a second metal layer to read out the detector from two edges only. The detector matches in its outer dimensions and the layout of its readout pattern with another prototype detector with shorter strips, designed within the CBM-MPD STS Consortium as one of three possible detector types for the CBM Silicon Tracking System. The *CBM03* design has the following features:

- n-type Si material
- double-sided segmentation into strips
- 1024 strips per side
- stereo angle ± 7.5 degree
- 58 μm strip pitch
- AC-coupled readout
- 1 DC pad and 4 AC pads per strip
- poly-silicon resistor plus punch-through biasing
- p-spray insulation on the ohmic side
- two metal layers per side
- 10 guard rings
- outer dimension 6.2 cm by 6.2 cm

The wafer requires 19 masks for production. Processing started early 2010 and the delivery of a batch is expected by Summer 2010.

* Supported by EU/FP7 HadronPhysics2

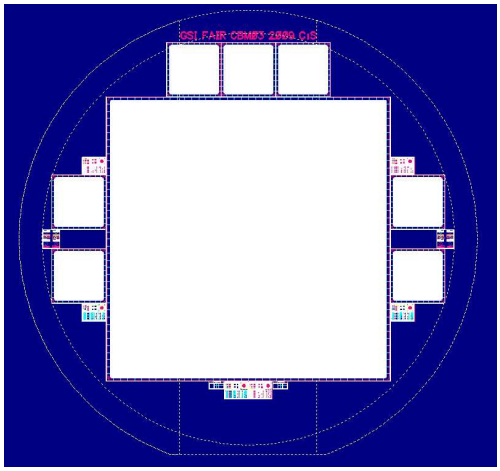

Figure 1: Layout of the *CBM03* wafer (4" diameter) with the main detector in the center and various test structures.

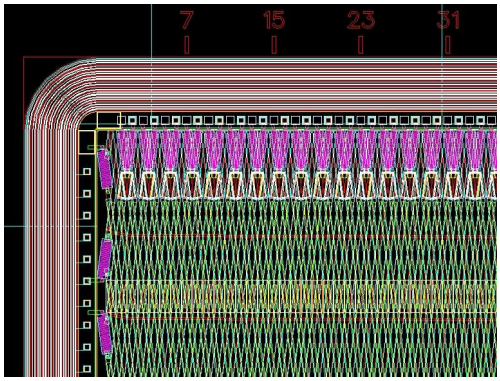

Figure 2: Design of the *CBM03* main detector with strips under ± 7.5 degree stereo angle and double-metal interconnections of the corner strips.

Preparations for a second technology wafer

Various design parameters are the target of a forthcoming second technology wafer. The research project of CiS will develop and implement innovative structures to improve the detectors' radiation tolerance and charge collection efficiency after exposure to high particle fluence as expected in the CBM experiment.

References

[1] http://sunse.jinr.ru/projects/sts/abstract_sts.html
[2] J.M. Heuser et al., GSI Report 2008-1 9
[3] J.M. Heuser et al., GSI Report 2009-1 10

Construction of a reference telescope from prototype components of the CBM Silicon Tracking System*

J.M. Heuser[1], V. Kleipa[1], W. Müller[1], W. Niebur[1], C.J. Schmidt[1], C. Simons[1], and A. Lymanets[2]
[1]GSI, Darmstadt, Germany; [2]Univ. Frankfurt, Germany

A reference tracking telescope has been developed and constructed in preparation of in-beam tests with forthcoming prototype modules of the CBM Silicon Tracking System. A first test in a 2 GeV proton beam took place at GSI in Fall 2009 [1].

Assembly of a tracking station

A tracking station is realized on an 8-layer printed circuit board that features the full readout of a *CBM02B2* [2] double-sided prototype silicon microstrip detector with 2×256 orthogonal strips of 50 μm pitch (Fig. 1). Four self-triggering n-XYTER [3] readout chips have been directly wire-bonded to the detector. The detector is glued into a squared opening in the board resting on a machined-in balcony structure of about 100 μm width. Two chips read out one detector side. The 10 cm by 10 cm board also houses the external *ADC* converter and *DC* power converters. It is connected to a CBM readout controller [4] with two high-density flat/twisted-pair cables. The detector bias is provided through a coaxial cable.

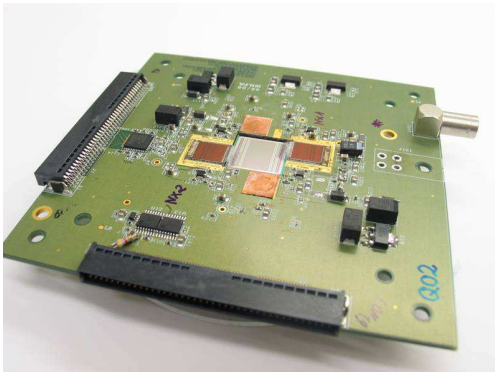

Figure 1: A reference tracker board comprising a double-sided *CBM02B2* prototype detector wire-bonded to four n-XYTER readout chips, two per side.

The four readout chips dissipate up to 20 W. The tracker board has therefore to be cooled to avoid excessive temperatures of chips and silicon detector that would result in unstable operation, high leakage current and noise, particularly in a concealed space like in an experimental setup. On the tracker board, the readout chips are brought in thermal contact with a copper inlay reaching to the back side of the board. The board is then sandwiched between two aluminum plates with built-in water cooling pipes as shown in Fig. 2. A compact object is created.

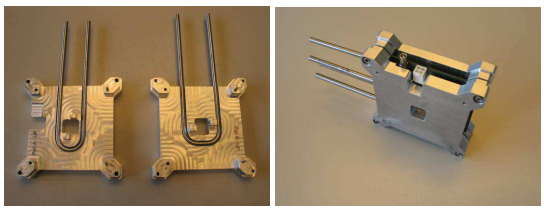

Figure 2: A tracker board mounted between cooling plates.

Three tracker boards have been mounted in an aluminum shielding box. They were then connected to the low and high-voltage supplies, the control and readout system as well as the water cooling and temperature monitoring system. The completed setup as operated in the laboratory and on the beam line is shown in Fig. 3.

Setup of a reference tracking telescope

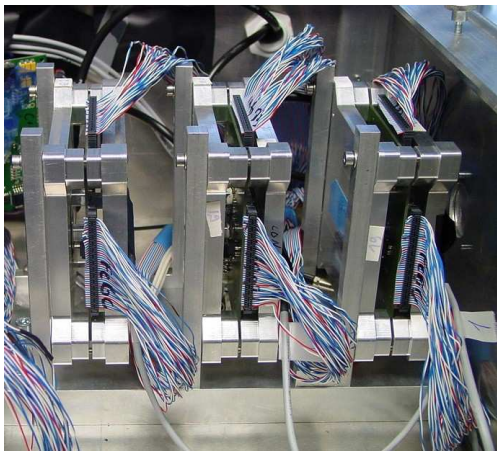

Figure 3: Three tracking stations on the beam line.

References

[1] V. Friese et al., *Operation and performance of the CBM Silicon tracking reference telescope*, GSI Progress Report 2009
[2] J.M. Heuser et al., GSI Report 2009-1 10
[3] GSI Report DOC-2007-Mar-137 49
[4] GSI Report DOC-2007-Mar-137 53

* Supported by EU/FP7 HadronPhysics2

Development of ultra-thin cables for the CBM Silicon Tracking System*

V.M. Borshchov[1], J.M. Heuser[2], Yu.A. Murin[3], O.M. Listratenko[1], M.A. Protsenko[1], I.T. Tymchuk[1], Y.Y. Kostyshyn[1], Y.A. Shulenko[1], A.M. Steblina[1], and the CBM-MPD STS Consortium

[1]State Enterprise Scientific Research Technological Institute of Instrumental Engineering (SE SRTIIE), Kharkov, Ukraine; [2]GSI, Darmstadt, Germany; [3]Joint Institute for Nuclear Research (JINR), Dubna, Russian Federation

Three types of demonstrators for studies of the readout of silicon microstrip detectors with ultra-light cables were developed by participants of the CBM-MPD STS Consortium [1] and manufactured in SE SRTIIE, Kharkov, Ukraine. The cables were made on the basis of adhesive-less aluminium-polyimide foiled dielectrics and assembled using a "chip-on-flex" technology.

Demonstrator 1-a

Demonstrator 1-a (Fig. 1) is a cable with connectors at both ends that attaches to the already existing Demonstrator 0-b [2] built around the double-sided prototype detector CBM01B2. Its purpose is to investigate the effect of the cable length on the signal transmission. Three sets of multilayer cables were designed and manufactured, with lengths of 10 cm, 20 cm and 30 cm. Their main features are:

- 2 signal layers, 1 shielding layer, 1 mesh-spacer;
- signal layers: foiled dielectric FDI-A-24 (aluminium/polyimide 14 μm/10 μm); shielding layer: FDI-A-50 (aluminium/polyimide 30 μm/20 μm); mesh-spacer: 50 μm Kapton, 50% fill factor;
- 64 traces per signal layer, $\sim$100 μm pitch.

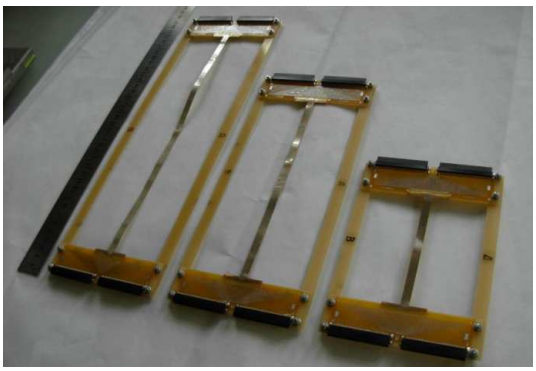

Figure 1: Multilayer analog cables.

During the manufacturing process all cables were tested for shorts/breaks/resistance of the traces using specialized automated test equipment.

Demonstrator 1-b

Demonstrator 1-b (Fig. 2) extends the application of the developed cables to a new object. The cables are connected through tab-bonding to the double-sided prototype detectors CBM02B2. They permit the readout of all 2$\times$256 orthogonal strips of the detector. The demonstrator has been manufactured in three specimen with different cable length.

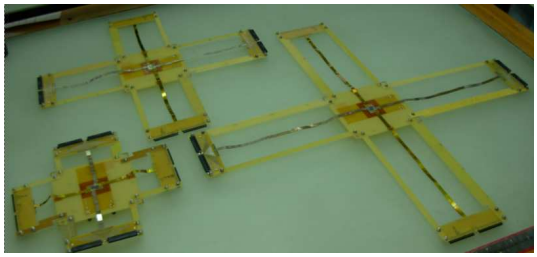

Figure 2: Demonstrators 1-b.

Demonstrator 1-b'

Demonstrator 1-b' (Fig. 3) is a subsequent development of demonstrator 1-b and realizes the first prove-of-principle object to study the concept of the planned CBM silicon tracking modules. It is built around the full-scale double-sided prototype detector CBM01 [3] and realizes the readout of 2$\times$128 strips (1/8th of all detector channels).

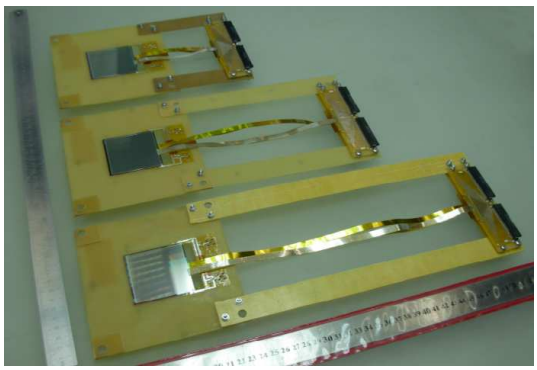

Figure 3: Demonstrators 1-b'.

Various tests planned with the demonstrators in the laboratory and with beam will yield important feedback for the determination of technical requirements of the components for the CBM STS detector modules.

References

[1] http://sunse.jinr.ru/projects/sts/abstract_sts.html
[2] V.M. Borshchov et al., GSI Report 2009-03 12
[3] J.M. Heuser et al., GSI Report 2008-1 9

* Supported by EU/FP7 HadronPhysics2

Construction and test of the demonstrator of the CBM-Micro-Vertex-Detector*

M. Deveaux[1], S. Amar-Youcef[1], J. Baudot[2], N. Bialas[1], N. Chon-Sen[2], H. Düring[1], I. Fröhlich[1], M. Goffe[2], J. Michel[1], C. Müntz[1], C. Schrader[1], P. Scharrer[1], S. Seddiki[1,2], J. Stroth[1], and T. Tischler[1]

[1]Goethe University Frankfurt/Main, Germany; [2]Institut Pluridisciplinaire Hubert Curien, Strasbourg, France

Reconstructing open charm with the CBM-experiment requires a vertex detector with outstanding rate capability, spatial resolution and low material budget. The MVD-demonstrator project studied the feasibility of building such a detector.

The CBM-experiment aims to explore the properties of hadronic matter in the region of highest baryonic densities. One of the major probes of the experiment are open charm particles, which are produced close to the kinematical threshold at CBM beam energies (10-40 AGeV). Reconstructing those rare and short lived ($c\tau \sim 100\ \mu\mathrm{m}$) particles calls for a vacuum compatible vertex detector with an outstandingly high spatial resolution ($\lesssim 5\ \mu m$) and very low material budget ($\lesssim 0.3\ \mathrm{X}_0$). To match those requirements, we aim to build an actively cooled detector based on ultra light and highly granular Monolithic Active Pixel Sensors (MAPS).

The MVD-demonstrator project [1] aimed to study the integration of up to four MIMOSA-20 sensors into a detector ladder. MIMOSA-20, which was designed by IPHC Strasbourg, provides a pixel matrix with 640×320 pixels with $30 \times 30\ \mu\mathrm{m}^2$ pitch. The chip is readout within $2.2\ \mathrm{ms}$ via two serial analog outputs submitting each $50\ \mathrm{Mpixel/s}$. Slow control is done via a JTAG interface. Sensors thinned down to $50\ \mu\mathrm{m}$ were successfully operated conjointly with the PLUME-collaboration [2] but not chosen for the MVD-demonstrator for reasons of risk management. Due to a (meanwhile solved) problem in the chip production, the noise of the MIMOSA-20 sensors used was increased to a disappointing value of $\sim 23\ \mathrm{e}^-\ \mathrm{ENC}$.

The demonstrator was built by wire bonding a three layer flexprint cable top of two sensors. Two of the objects obtained were glued on the opposite faces of a cooling support formed from the highly heat conductive TPG and the ultra light and stiff carbon foam RVC. This support is to transport the heat of the sensors towards a liquid cooled heat sink located outside the acceptance of the future MVD. The sensor control was performed by a dedicated add-on board of the HADES-TRB2, which hosts among others four 12-bit ADCs sampling the analogue data stream of the sensors, a VIRTEX4 FPGA and an 1 GB SDRAM module.

The demonstrator was intensely tested in laboratory. Vacuum compatibility to fairly below $10^{-6}\ \mathrm{mbar}$ was demonstrated with the vacuum vessel of the IKF technology lab. The cooling concept of the ladder was validated despite the disappointing performances of the rather simplistic heat sink. First attempts to operate MIMOSA-20 via the flex print cables showed an unusually high noise of 45 e^- ENC, which could be reduced to the expected $\lesssim 23\ e^-$ ENC with an FPGA-based common mode filter.

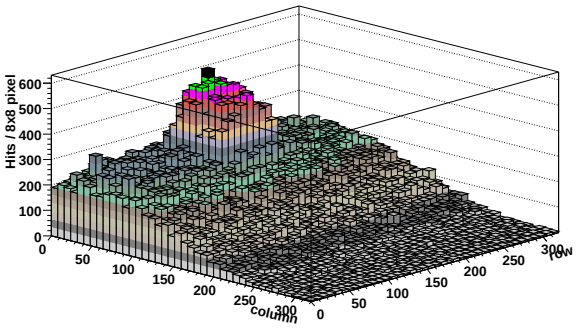

Figure 1: *Number of hits as function of the pixel coordinate as recorded in beam with the CBM-MVD demonstrator.*

The demonstrator was tested with $\sim 120\ \mathrm{GeV}$ pions at the CERN-SPS. Two single sided MVD-demonstrators were operated with continuous read out. Trigger signals and additional time stamps obtained from the IPHC TAPI beam telescope were encoded into their data stream and allow for an offline synchronization with data obtained from this telescope. The readout clock of the demonstrators was set to $20\ \mathrm{Mpixel/s}$ (corresponding to $5.5\ \mathrm{ms}$ readout time), which reduced the data rate of the demonstrators from $2.4\mathrm{Gbit/s}$ to $960\ \mathrm{Mbit/s}$.

According to our data analysis, the good noise performances observed in the laboratory could be reproduced in the beam. Moreover, we observed the shadow of the trigger scintillator (see figure 1), which is located on top of a background formed from untriggered particle hits. A preliminary evaluation of the spatial resolution (σ) of the demonstrator was carried out by correlating the hits observed in both stations. We measured $\sigma \lesssim 5.6\ \mu\mathrm{m}$ which, probably due to the increased noise of MIMSOA-20, does not fit the ultimate resolution ($\sim 2\ \mu\mathrm{m}$) expected for this sensor. However, the results match the requirements of CBM, which validates the concept of the MVD-demonstrator.

References

[1] S. Amar-Youcef et al., "R&D for the demonstrator of the CBM-Micro-Vertex-Detector", GSI Scientific Report 2008, FAIR-Experiments-18

[2] http://www.iphc.cnrs.fr/plume.html.

* Work supported by BMBF (06FY1731), GSI F&E and HIC for FAIR

Development of very light pixel arrays based on fast and radiation tolerant CMOS sensors for the CBM vertex detector*

M. Winter, for the Strasbourg team[1] and M. Deveaux, for the Frankfurt team[2]
[1]Institut Pluridisciplinaire Hubert Curien, Strasbourg, France; [2]Goethe University, Frankfurt/Main, Germany

The Micro-Vertex Detector (MVD) of the CBM experiment requires very light detector stations equipped with highly granular and thin pixel sensors adapted to hostile running conditions. CMOS pixel sensors of the MIMOSA series are being developed for several years in ordre to match the challenging specifications of the MVD. Breakthroughs were achieved in 2009, which concern the fast sensor read-out architecture and its non-ionising radiation tolerance. A significant step was also made towards very light sensor arrays.

Full scale sensor with zero-suppression

MIMOSA-26, the first full scale sensor featuring fast read-out with integrated zero-suppression, was fabricated and tested extensively. It is composed of 1152 columns read out in parallel, each made of 576 pixels (18.4μm pitch) and terminated with a discriminator. The discriminator outputs are processed through an integrated zero-suppression logic. The 665,000 pixels of the sensor cover an active area exceeding 1×2 cm^2 and are read out in $\sim 110\mu s$. More than 30 chips were characterised. A fabrication yield of $\sim$ 90% was measured. The total sensor noise (N) was evaluated to 13-14 e$^-$ENC.

6 sensors were assembled in a telescope configuration and installed on a $\sim$ 100GeV particle beam at the CERN-SPS. A detection efficiency of $\gtrsim$ 99.5% was measured with discriminator threshold values ($\sim$ 5 N) high enough to maintain the rate of noise fluctuations above threshold around 10^{-4} (typically 40 to 80 pixels per frame). These performances validate the architecture for its extension to shorter read-out times like those required for the MVD.

Non-ionising radiation tolerant sensor

A new fabrication process was investigated in 2008 with the MIMOSA-25 prototype, featuring a high resistivity epitaxial layer. The latter could thus be depleted, resulting in substantial charge collection efficiency and non-ionising radiation tolerance improvements. The sensor, which features 20μm pitch pixels, was studied with $\sim$ 100GeV particles at the CERN-SPS, before and after irradiation with $\sim$ 1MeV neutrons. The result of the study is summarised in figure 1, which displays the signal-to-noise ratio (SNR) of the cluster seed pixels before and after an exposure to a fluence of $3\cdot10^{13}$ n$_{eq}$/cm^2.

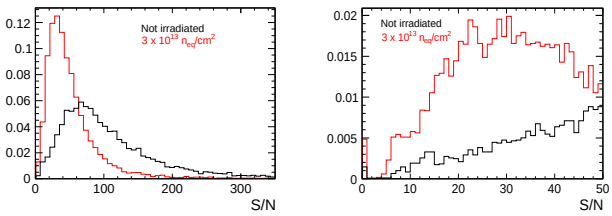

Figure 1: SNR of MIMOSA-25 before (black lines) and after (red lines) irradiation (fluence of $3\cdot10^{13}$ n$_{eq}$/cm^2). The right figure is a zoom of the left one.

The SNR before irradiation ($\sim$ 60-65) is more than twice higher than in case of a usual, low resistivity, epitaxial layer. After an exposure equivalent to $3\cdot10^{13}$ n$_{eq}$/cm^2, the SNR is still $\sim$ 30-35, translating into a detection efficiency of $\sim$ 99.5%. A fluence of $\gtrsim 10^{14}$ n$_{eq}$/cm^2 is therefore likely to be tolerable, which would well fullfil the MVD specifications.

3D integrated technologies

The performances of CMOS sensors are expected to still improve with vertical integration technologies. First prototypes were designed and fabricated in a 2-tier, 130 nm, process. Several different chips were realised, with expected read-out times of a few μs. One of them is foreseen to be interconnected with a sensing tier featuring a depleted epitaxial layer as for *MIMOSA-25* (see previous section). The chips are currently being manufactured and will be tested during 2010.

Ultra-light pixelated ladders

The development of very light sensor arrays was initiated via the Hadron Physics 2 project. It aims at unsupported, flexible, sensor rows featuring a material budget of $\lesssim$ 0.15% of radiation length. The concept consists in assembling a row of $\sim 35\mu m$ thin pixel sensors on a very thin flexible cable and in wrapping the device in a very thin polymerised film. These rows would next be mounted on the mechanical (and cooling) support. The first prototype, which should allow commissioning the procedure, is being fabricated.

References

[1] M. Winter et al., 2008 GSI annual report.

[2] M. Winter et al., DESY PRC report, Novembre 2009.

*Work supported by EU within the projects EUDET (FP-6) and Hadron Physics 2 (FP-7).

Dark rates of irradiated Monolithic Active Pixel Sensors*

M. Deveaux[1], D. Doering[1], M. Domachowski[1], S. Ottersbach[1], J. Stroth[1], and F. M. Wagner[2]

[1]Goethe University Frankfurt/Main, Germany; [2]Forschungsneutronenquelle Heinz Maier-Leibnitz(FRM-II), TU München, Garching, Germany

Due to the high collision rates foreseen, the vertex detector of Compressed Baryonic Matter experiment will be exposed to very high radiation doses. We studied, if the damage caused by this radiation might provoke a crucial increase in the dark rate of the detector.

The Compressed Baryonic Matter (CBM)-experiment aims to explore the properties of hadronic matter in the region of highest baryonic densities. One of the major probes of the experiment are open charm particles, which are produced close to the kinematical threshold at CBM beam energies (10-40 AGeV). Reconstructing those rare and short lived ($c\tau \sim 100\ \mu\mathrm{m}$) particles calls for a vacuum compatible vertex detector with an outstanding spatial resolution ($\lesssim 5\ \mu m$) and very low material budget ($\lesssim 0.3\ \mathrm{X}_0$). To match those requirements, we aim to build an actively cooled detector based on ultra light and highly granular Monolithic Active Pixel Sensors (MAPS).

Within one year of operation, the sensors will be exposed to very high radiation doses of $\gtrsim 10^{13}\ \mathrm{n_{eq}/cm^2}$ and $\gtrsim 3\ \mathrm{Mrad}$. The question how to extend their radiation tolerance to those values triggered a common R&D program of the IPHC (Strasbourg), GSI and the Goethe University Frankfurt/Main. In the context of this program, we observed that non-ionizing radiation damage causes Random Telegraph Signal (RTS) [1]. This non-gaussian noise was found to dominate the dark rate of the detector, which remains only tolerable if the detector is moderately cooled. This conclusion was so far restricted to sensors which were exposed exclusively to non-ionizing neutron radiation. The question, if the predicted additional ionizing doses would worsen the situation remained to be studied.

This study was performed with MIMOSA-18 sensors obtained from IPHC Strasbourg. The sensors host four matrices with 256×256 SB-pixels and $10\ \mu\mathrm{m}$ pixel pitch each, which are read out within $6.5\ \mathrm{ms}$. They were irradiated with fission neutrons at the MEDAPP facility of the FRM-II reactor. Moreover, some of the chips were exposed to a dose of $\sim 10\ \mathrm{keV}$ X-rays at the irradiation facility of the Karlsruhe Institute of Technology. After the irradiations, we compared the dark rates of non-irradiated sensors with the ones of sensors irradiated with either $1.3 \times 10^{13}\ \mathrm{n_{eq}/cm^2}$ or $200\ \mathrm{krad}$. Moreover, a sensor being consecutively irradiated with both, $1.3 \times 10^{13}\ \mathrm{n_{eq}/cm^2}$ or $200\ \mathrm{krad}$ was available. The moderate ionizing dose was chosen as MIMOSA-18, which was initially designed for other purposes, does not feature radiation hardened pixels.

The sensors were tested by measuring their dark rate as a function of the temperature. We counted a false hit if a pixel indicated a signal above $150\ \mathrm{e^-}$ ENC in the absence of a particle source. This value represents a limit up to which a MAPS detector should still be reasonably efficient. The temperature was measured at the cooling support of the test cards used. Cross checks suggest that, despite a bias by several $^\circ\mathrm{C}$ towards room temperature, the true chip temperature was well reproduced.

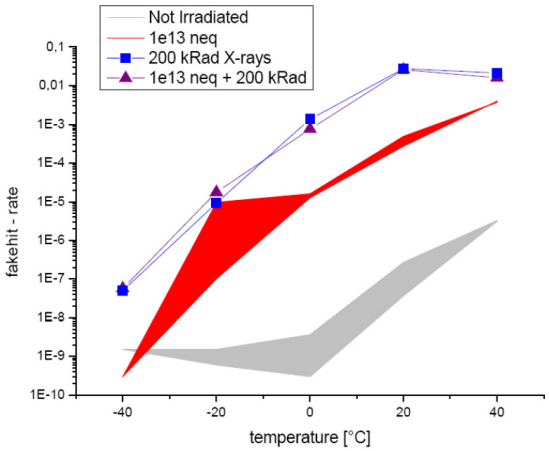

Figure 1: *Dark rate of irradiated MIMOSA-18 sensors as function of radiation dose and temperature.*

The results of our measurements are displayed in Figure 1. It is shown that irradiation increases the dark rate of the sensors at all temperatures. Unlike our initial assumptions this holds in particular for ionizing irradiation which increases the dark rate by several orders of magnitude with respect to the one of the non-irradiated chip. However, a cooling to $-20\ ^\circ\mathrm{C}$ is sufficient to dim the dark rate to an acceptable value below 10^{-4}. We believe that the foreseen improvements in terms of readout speed will further reduce the dark rate as the faster sampling acts as a high pass filter which partially suppresses RTS.

We intend to use the results obtained as input for the MVD-digitizer [2]. This will allow for a detailed simulation study of the impact of the effects observed on CBM.

References

[1] M. Deveaux et al., "Radiation hardness studies on Monolithic Active Pixel Sensors", GSI Scientific Report 2008, FAIR-Experiments-19

[2] C. Dritsa et al., "Detector response simulation of the CBM Micro Vertex Detector", GSI Scientific Report 2008, FAIR-Experiments-21

* Work supported by BMBF (06FY1731), GSI F&E and HIC for FAIR

Materials' properties of wavelength shifting films for the CBM-RICH detector - thickness dependence and efficiency *

P. Koczon[1], A. Braem[2], C. Joram[2], M. Dürr[3], and C. Höhne[1]

[1]GSI, Darmstadt, Germany; [2]CERN, PH Department, Geneva, Switzerland; [3]Hochschule Esslingen, Fakultät Angewandte Naturwissenschaften, Germany

P-terphenyl (PT) and tetraphenyl-butadiene (TPB) have been investigated as possible wavelength shifting materials for use in Ring Imaging Cherenkov (RICH) detectors. Wavelength shifting films made out of these organic molecules absorb light in the UV region and re-emit fluorescence photons at larger wavelength. Used on top of photomultiplier tubes (PMT), they therefore can enhance the quantum efficiency of the PMTs in the UV region. For an application in Cherenkov counters, gain factors for the number of measured photoelectrons for a cutoff wavelength of 200 nm ($E_{\max} = 6.2$ eV) are 1.71 ± 0.17 for PT and 1.27 ± 0.13 for TPB compared to a PMT with borosilicate windows. See [1] for a summary of these results.

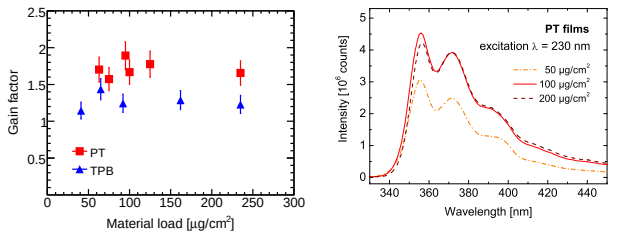

Figure 1: Left: Gain factor versus material load for a cutoff energy $E_{\max} = 6.2$ eV ($\lambda_{\max} = 200$ nm). Right: Photoluminescence spectra of PT films with different material load. See Fig. 2 for corresponding film thickness.

These investigations were continued by evaluating quantum efficiencies and gain factors for PT and PTB films of different thickness, see Fig. 1 (left). No significant dependence on the applied material load in the coating process was found in the evaluated range. This insensitivity to the material load is clearly a plus for the application in a RICH detector. With many hundreds of PMTs to be coated, there is no need for a restrictive thickness control. To better understand the thickness dependent results of the measured quantum efficiency, fluorescence measurements and scanning electron microscopy were performed with films grown on glass substrates similar to those on the PMT windows. Measurements of fluorescence intensity as a function of wavelength with excitation at 230 nm are shown in Fig. 1 (right) for PT-films of different thickness. A pronounced increase in intensity can be observed for the 100-μg/cm^2-film when compared to the 50-μg/cm^2-film, while the intensities of the 100-μg/cm^2-film and 200-μg/cm^2-film are

* Work supported by BMBF. We acknowledge M. v. Stenis (CERN) for coating the PMTs and test samples with PT and TPB, and Dr. J. Kraut (Esslingen) for taking the SEM images.

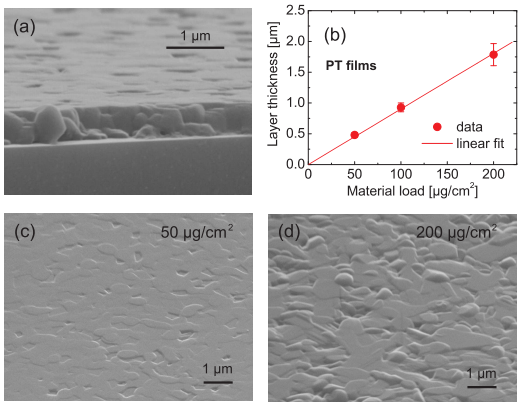

Figure 2: (a) SEM side-view of a 0.5-μm-PT-film on glass, viewing angle 80° off normal. (b) Dependence of layer thickness as measured by means of SEM as a function of material load during the evaporation process. (c) and (d) SEM bird's eye view of the layers' surface (60° off normal) for the 0.5-μm-PT-film and 2-μm-PT-film, respectively.

almost identical. Obviously, the PT-film with a thickness of 100 μg/cm^2 absorbs already almost all of the incoming photons. As a consequence, the efficiency of the PMTs is not increased with increasing film thickness. For the 50-μg/cm^2-film, however, a lower fluorescence intensity is observed. This indicates only a fraction of the available UV photons is absorbed. It suggests that for less material load than shown in Fig. 1 (left, PT) the quantum efficiency and gain factor will drop.

SEM images of PT films are shown in Fig 2. The side view in Fig. 2(a) indicates a rather smooth film growth and only minor formation of larger crystals. The measured thickness of each film is plotted against the material load applied during the evaporation process in Fig. 2(b). The thickness of the layers follows linearly the applied material load corresponding to a density of $\rho = (1.12 \pm 0.10)$ g/cm^3 which is slightly below the reported density of PT of ρ=1.23 g/cm^3. With increasing film thickness, a more pronounced formation of micro-crystals is observed which results in a higher surface roughness. However, the increased surface roughness and correlated increase in light scattering for the thickest layer shows, if any, only a small effect in the fluorescence spectrum.

References

[1] P. Koczon, C. Höhne, M. van Stenis, A. Braem, C. Joram, FAIR-EXPERIMENTS-16, GSI Scientific Report 2008.

Development and Test of a Real-Size Prototype for the CBM TRD*

C. Bergmann[1], M. Klein-Bösing[1], D. Emschermann[1], J. P. Wessels[1], M. Petriş[2], V. Simion[2], M. Petrovici[2], and C. Höhne[3]

[1]Institut für Kernphysik, Münster, Germany; [2]NIPNE, Bucharest, Rumania; [3]GSI, Darmstadt, Germany

The Compressed Baryonic Matter (CBM) experiment at FAIR at the GSI is a dedicated heavy-ion experiment. It is designed to study strongly interacting matter in ultrarelativistic heavy ion-collisions and to explore the QCD phase diagram of nuclear matter. CBM consists of several detectors, one of them the Transition Radiation Detector (TRD) providing particle tracking and electron identification. We have constructed a TRD prototype (395.5 $\times$ 106 mm) based on a symmetric arrangement of two MWPCs with a common, central pad readout electrode made from kapton foil (25 μm) coated initially with 20 nm chromium and afterwards with 200 nm aluminum on both sides. The prototype is designed to feature a two-dimensional position reconstruction in one detector layer with a Position Resolution (PR) of 300-500 μm and a pion suppression factor of the order of 100 at 90% electron efficiency for the whole TRD. The double-sided read-out pad plane concept with a gas volume of 12 mm thickness, an anode wire separation of 3 mm, and an anode cathode gap of 3 mm is retained from the previous small prototype [1] due to a good performance of electron/pion separation and PR shown by these prototypes in test beams. The two-dimensional track position reconstruction is reached by subdividing the 36 rectangular pads (each 10 $\times$ 80 mm) into 2 $\times$ 36 triangular pads with independent read-out channels for two pads back-to-back on opposite sides of the pad plane. The cluster position was reconstructed in two different coordinate-systems a and b by using a weighted (w) and an unweighted (uw) displacement d of the cluster position relative to the center of the pad group with maximum charge, based on the Pad Response Function (PRF) [1] for signals measured on eight adjacent pads (see Fig. 1). The second coordinate system

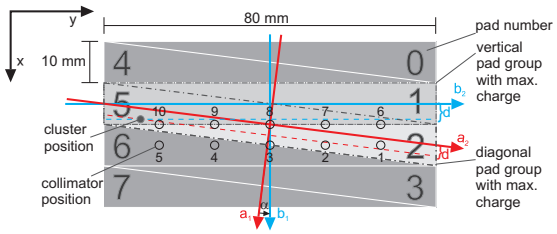

Figure 1: Sketch of the eight used pads, collimator positions 1 - 10 and wire positions

b is shifted by half a pad width and rotated by α relative to a. The PR and the energy resolution (FWHM/Energy) has been examined using a collimated ^{238}Pu (20.2 keV photons) and an ^{55}Fe (5.9 keV photons) source at 10 collimator positions. The energy resolution of the prototype is $26.5 \pm 4.9\%$ for the ^{55}Fe source and $21.7 \pm 5.5\%$ for the ^{238}Pu source. The position resolution of the real-size prototype cannot be determined by a source measurement of one single prototype due to the unknown absolute position of the initial photon. The PR is correlated with the deviation of the reconstructed coordinate from the collimator coordinate and the deviation of the measured collimator diameter from the reconstructed diameter. The increasing deviation for collimator position 3, 4, and 5 is due to the small number of pads used for this measurement. Therefore, data efficiency (ratio of reconstructed events to all measured events) decreases and only events inducing maximum charge on pad two or five can be reconstructed. The reconstructed x-coordinates and collimator diameter show a good agreement with the expected values for all reconstruction methods (see Fig. 2). The reconstructed y-coordinates and collimator diameter deviate from the theoretical values because of the diagonal shift generated by the non-gaussian shape of the PRF and the accumulation of reconstructed clusters next to the wire positions due to the electric field characteristic perpendicular to the wire direction. The absolute PR will be measured at a cosmics or test beam run using a silicon tracking detector, scheduled for 2010. The PR in y-direction of the real-size prototype is given by the wire distance divided by $\sqrt{12}$ because the measured clusters are located in the avalanche region volume surrounding the anode wires. Thus, other pad and chamber geometry options have to be checked.

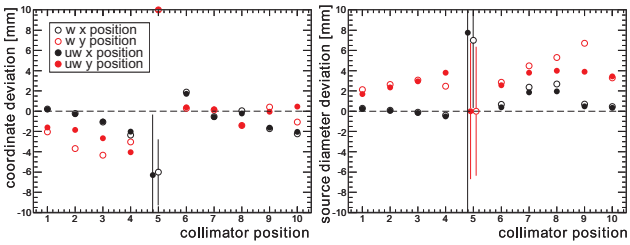

Figure 2: Reconstructed position spectra are fitted to a Gaussian distribution to determine collimator position (left) and diameter (right).

References

[1] M. Klein-Bösing et al., "Position resolution of a high efficiency transition radiation detector for high counting rate environments", Nucl. Instr. Meth. Phys. Res. A 585 (2008) 83-87

* Work supported by BMBF and the HadronPhysics2 project financed by EU-FP7.

TR-Efficiency Studies for the CBM Transition Radiation Detector*

P. Reichelt† [1], H. Appelshäuser[1], and M. Hartig[1]
[1]Institut für Kernphysik, Goethe-Universtität, Frankfurt am Main, Germany

In the CBM experiment at FAIR, a Transition Radiation Detector (TRD) is foreseen for tracking and electron/pion discrimination. A thin gas volume without drift region is considered in order to have sufficiently fast readout for the intended high collision rates. This however compromises the TR-photon absorption efficiency, which is essential for electron identification. In this report, we discuss an approach of increasing the yield of TR-photons by selecting suitable materials for the readout pads of the detector, from which photons can be re-emitted.

Measurement of TR-photons

As an electron passes through the radiator of the TRD, transition radiation photons can be produced and emitted in forward direction, thus entering the gas volume of the detector. The probability of such photons being absorbed depends on the mass attenuation coefficient of the corresponding material and its density and thickness. The remaining photons reach the readout structure of the detector, which is typically coated with copper. During tests with ALICE-TRD chambers [1] it was found that a portion of these photons causes ionization of the copper and that the subsequent emission of a secondary photon into the gas volume contributes to the TR-signal. Figure 1 shows the simulated energy distribution of detected photons in Xenon gas[1] for a $5\ \mu\mathrm{m}$ copper coating. The energy of directly

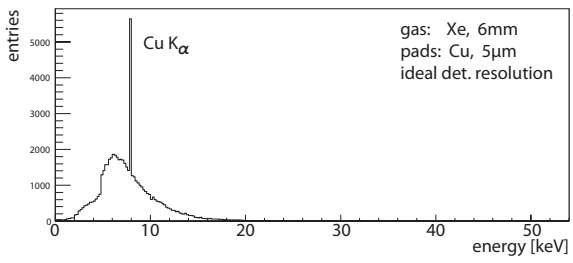

Figure 1: Simulation of a TR-spectrum as measured with a TRD using copper readout pads.

absorbed photons is $\mathrm{E}_{\mathrm{direct}} = 38.8\,\%$ of the total produced TR-spectrum and the energy from secondary photons is $\mathrm{E}_{\mathrm{pads}} = 3.3\,\%$. To compare the portion of $\mathrm{E}_{\mathrm{pads}}$ for different materials, values for thicknesses close to a radiation length of $10^{-3}X_0$ are composed in Table 1. The last columns show the results for two different TR-sprectra as produced by electrons with 2 and $10\ \mathrm{Gev}/c$. In both

Element	Thickness	$\mathrm{E}_{\mathrm{pads}}$ ($2\ \mathrm{Gev}/c$)	$\mathrm{E}_{\mathrm{pads}}$ ($10\ \mathrm{Gev}/c$)
Cr ($Z = 24$)	$22\ \mu\mathrm{m}$	$3.4\,\%$	$2.3\,\%$
Fe ($Z = 26$)	$18\ \mu\mathrm{m}$	$4.3\,\%$	$3.3\,\%$
Cu ($Z = 29$)	$15\ \mu\mathrm{m}$	$4.4\,\%$	$4.0\,\%$
Ga ($Z = 31$)	$25\ \mu\mathrm{m}$	$4.0\,\%$	$3.9\,\%$
Rb ($Z = 37$)	$90\ \mu\mathrm{m}$	$1.8\,\%$	$2.3\,\%$

Table 1: Contribution of secondary photons for different materials and electron momenta.

cases copper is best, while the distribution shifts to heavier elements at higher electron momenta. Elements with significantly different Z do not have their K-lines in the energy range of the TR-spectrum and are not useful.
The photon yield can still be improved by increasing the thickness of copper and we found that it saturates at $\mathrm{E}_{\mathrm{pads}} = 4.7\,\%$ when implementing a $20\ \mu\mathrm{m}$ layer.

Multiple layers

Another way to enhance the number of secondary photons is to arrange layers of the above materials in such an order, that the K-line energies and mass attenuation coefficients reduce the transmission of photons into deeper layers. Figure 2 shows the resulting photon yield that is higher than the exponential distribution of a single material. However, the photons from iron and chromium are

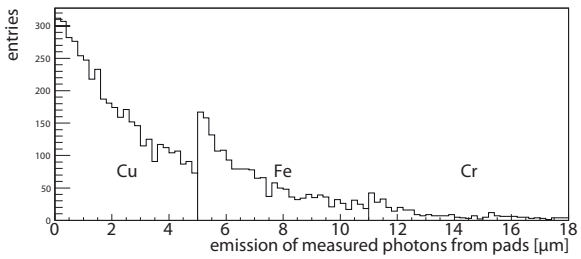

Figure 2: Origin of secondary photons (0 = pad surface).

less energetic and reduce the benefit so that practically a single copper layer proves to be the most efficient coating.

References

[1] P. Reichelt: *Bestimmung der Gasverstärkung der ALICE-TRD-Auslesekammern*. Bachelor Thesis Goethe-Universität Frankfurt (2008).

* Work supported by BMBF and GSI
† preichelt@ikf.uni-frankfurt.de
[1]Data reported here is based on a thickness of $6\ \mathrm{mm}$ for the gas layer.

Progress in the simulation of Multi-strip RPCs

D. Gonzalez-Diaz[1], G. Kornakov[2] for the CBM-TOF group
[1]GSI, Darmstadt, Germany; [2]USC-LabCaF, Santiago, Spain.

Timing Resistive Plate Chambers in multi-strip configuration, pioneered by the FOPI collaboration [1], are planned for covering the low-granularity part of the CBM-TOF wall. A recent experiment at GSI cave-B has shown that, with an adequate optimization of the strip layout and readout, the multi-strip concept is sound in terms of timing and efficiency, and well suited for a multi-hit environment. The progress since previous discouraging attempts [2] has been made possible through a combined effort of detector design in conjunction with sophisticated simulations [3].

The newly developed RPC-simulation package is by now based on a (1+1+1) factorization of the original 3D problem. Signal formation (across the gas gap) is treated first; signal induction (across the strip) is calculated in a second step by using weighting field techniques. Finally, the propagation along the strip up to the amplifier is calculated by resorting to the HF-solver APLAC [4].

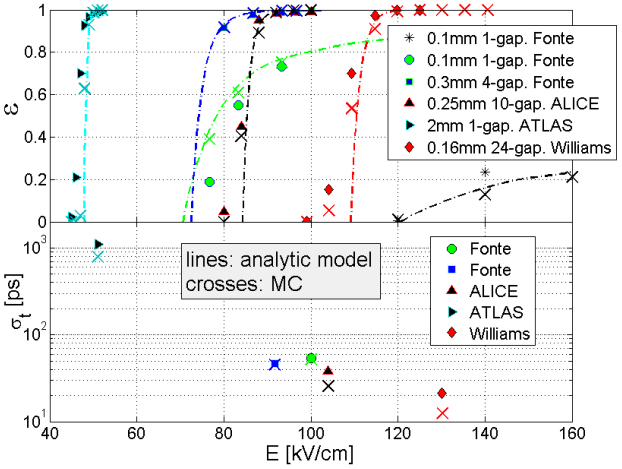

Figure 1: Efficiency and resolution for various RPCs.

We have made substantial progress in the first part of the problem (signal formation) during the last months: the simulation is based on a microscopic image of the avalanche, parameterized through a computationally-inexpensive algorithm and driven by recent measurements of the parameters of the electron swarm [5]. The results for efficiency and resolution are shown in Fig. 1 for wide-strips/pads of various remarkable world-wide efforts. Results from the simulation are shown (crosses) together with analytical formulas (dot-dashed lines), when available. The simulation relies at present on only one free parameter, a sort of shape-independent equivalent charge-threshold Q_{th}=10-100fC, not always known or available. This single quantity is used by detector developers to characterize the complex amplifier+discriminator response. This assumption seems to work according to our simulations with remarkable accuracy, despite Q_{th} being an 'effective' value.

With the signal generation under control it is possible to explore the multi-strip response by including the induction and propagation processes. Fig. 2 shows the most characteristic observable, the efficiency as a function of the transverse coordinate for a previous attempt [2] (left) and preliminary results from the recently developed prototypes in [6] (right). Although in both cases the transverse profile is dominated by a rather large width of the trigger system (2 cm), the shear cross-talk shows up as a flat background independent from the transverse coordinate, visible once the trigger position is far away from the strip under study: previously observed cross-talk at the level of 80-90% has been now reduced to much more respectable 1-3% levels.

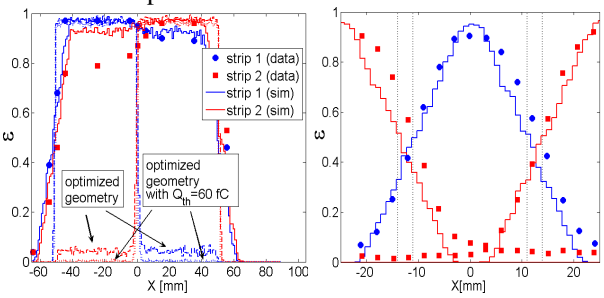

Figure 2: Efficiency vs trigger position across the strips for [2] (left) and for an optimized structure from [6] (right). Lines are the results from simulation.

Much progress has been done in the analytical understanding of cross-talk,, that is shown to be reducible to a 2-strip situation in many typical cases, characterized by 2 dominant modes (or propagation velocities) as:

$$I_{tr}(t) = \frac{T}{2}\frac{I_{v1}(t)+I_{v2}(t)}{2} + \frac{Z_m R_{in}}{(Z_c + R_{in})^2}\frac{I_{v2}(t)-I_{v1}(t)}{2}$$

$$I_{ct}(t) = \frac{Z_m R_{in}}{(Z_c + R_{in})^2}\frac{I_{v1}(t)+I_{v2}(t)}{2} + \frac{T}{2}\frac{I_{v2}(t)-I_{v1}(t)}{2}$$

References

[1] A. Schuettauf et al., NIM A 3(2009)679.
[2] A. Blanco et al., NIM A 485(2002)328.
[3] A. Berezutskiy et al, GSI report 2008, FAIR-EXP-23.
[4] http://web.awrcorp.com/Usa/Products/APLAC/
[5] E. Basurto et al., Proc. to 28th ICPIG, Prague, 2007.
[6] Y. Sun et al., also on this book.

Performance of Long-strip MRPC for CBM-TOF*

Y. Sun[1], C. Li[1], Z. Tang[1], and L. Xu[1]
[1]USTC, Hefei, China

The CBM-TOF wall will be used for Hadron identification with accurate Time-of-Flight measurement and large area coverage. Multi-gap Resistive Plate Chamber (MRPC), which has excellent performance and relatively low cost per channel, is a good candidate for CBM-TOF. Concerning the outer part of the TOF wall, long-strip pattern (with 25 cm, 50 cm and 100 cm strip length, respectively) is enough to satisfy the experimental multiplicity requirement.

In the long-strip design of MRPC, the cross-talk is critical to the detector performance. A test was carried out between August and September 2009 at GSI to test the performance of Long-strip MRPC prototypes.

The MRPC module has ten gas gaps of 250 μm, arranged in two stacks. Normal floating glass of 700 μm thick is used as resistive plate. The High-Voltage (HV) electrodes, on the outer surface of each glass stack, are made by Licron spray with surface resistivity of ~40 MΩ/□. The readout structure of the prototype is schematically shown in Figure 1. The readout strips are 50 cm long, 2.5 cm wide and with 0.6cm gaps between them. The signals are read out from both ends of each strip.

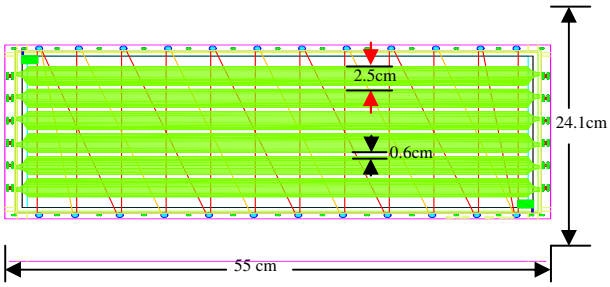

Figure 1: Readout structure of the Long-strip MRPC.

The test was performed at GSI in Cave-B behind the FOPI experiment, using the secondary beam of 3.5 GeV/*c* protons bumped into a lead target. The trigger area of 4 cm × 2 cm (along and across the MRPC strips, respectively) is defined by two scintillators, which are read out from both ends by 4 PMTs offering the reference time with ~63 ps σ time resolution.

The efficiency and time resolution the MRPC at different HV is shown in Figure 2. At working voltage around ±7 kV, the time resolution of 60 ps σ can be achieved with detecting efficiency over 97%.

In the cross-strip scanning test, the efficiency of each strip is shown in Figure 3. The gentle incline at the strip edge mainly comes from the 2 cm wide trigger width. When triggered on the center of a strip (strip 4 in this case), the efficiency of nearby strip is mainly from cross-talk contribution. The test result of 3% gives the upper limit of the cross-talk probability. The real cross-talk should be less than this value because 1/3 of these signals have a valid charge recorded, indicating that they possibly come from charge sharing with the neighbor strip or double-hits within the same primary collision.

At the same time, the efficiency drop between strips is observed to be less than 1%.

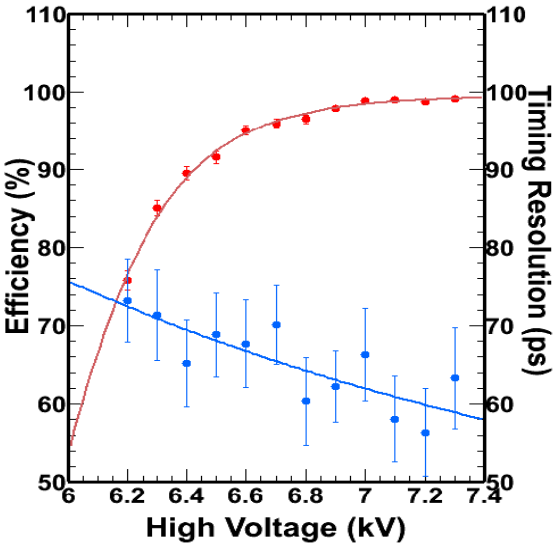

Figure 2: The efficiency and time resolution vs. the HV.

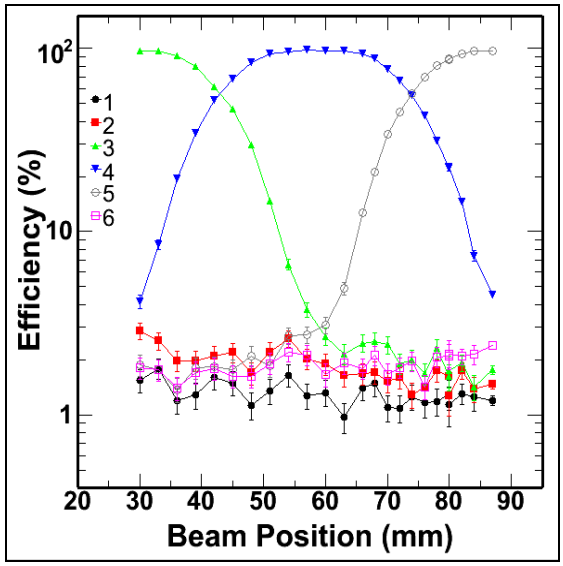

Figure 3: The efficiency of each strip at different trigger positions.

The data will be further analysed with the silicon tracking system which is available at the late stage of the test in order to reconstruct the intrinsic strip-profile.

* Work supported by National Natural Science Foundation of China (10875120).
#cee@aps.anl.gov

A prototype of high rate MRPC for CBM-TOF

Yi Wang[a], Jingbo Wang[a],Xianglei Zhu[a], Yuanjing Li[a], Jianping Cheng[a], Nobert Herrmann[b], Ingo Deppner[b], Yapeng Zhang[b], P. Loizeau[b], P. Senger[c],D.Gonzalez-Diaz[c]
[a]Tsinghua University, China; [b] University Heidelberg, Heidelberg, Germany; [c]GSI, Damstadt, Germany

Multi-gap Resistive Plate Chambers (MRPCs) are planar gaseous detectors made with resistive electrodes. Such detectors have a good time resolution, a high efficiency and a relatively low cost. These excellent characteristics make MRPCs favorite detectors for high-granularity large-area time of flight (TOF) systems in modern nuclear and particle physics experiments, such as STAR, ALICE, FOPI, HADES and HARP [1].

The TOF wall of CBM, used for hadron identification, is proposed to be assembled with MRPCs [2,3]. However, new materials should be investigated in order to adapt MRPCs to the high-rate environment foreseen, with fluxes up to 20 kHz/cm^2. The use of electrodes made of low resistivity glass is an inspiring way of improving the MRPC rate capability. A kind of low resistive glass (with bulk resistivity of about $10^{10}\Omega$ .cm) has been developed to assemble 'a high rate MRPC' prototype. Presently, the glass biggest dimension is 30cm*30cm, with 0.7mm thickness. 50cm*50cm glass is being developed to fit to the outer part of the wall.

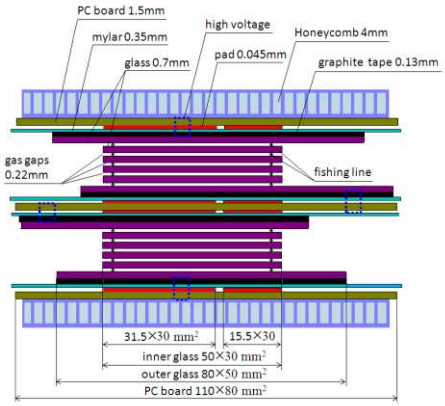

Fig.1 Structure of high rate pad readout MRPC

Fig.1 shows the structure of the high rate MRPC. It is mirrored and consists of 10 gaps. The gap width is 0.22mm. The beam test was performed with 2.5 GeV protons at GSI-Darmstadt. The prototype shows

This work is supported by the National Natural Science Foundation of China under Grant No. 10620210287, 10610285, 10675072 and 10775082. This study is also supported by the Ministry of Science and Technology under Grant No. 2008CB817707.

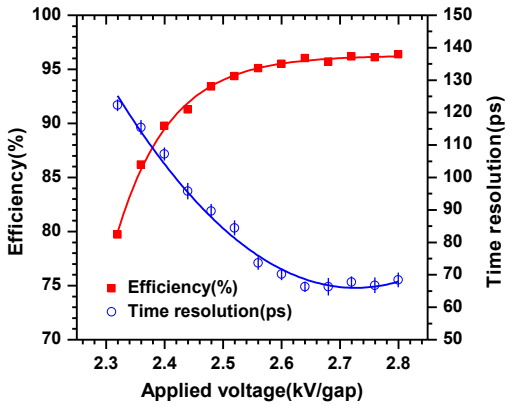

Fig.2 Efficiency and time resolution as a function of high voltage at a rate of about 3KHz/cm^2

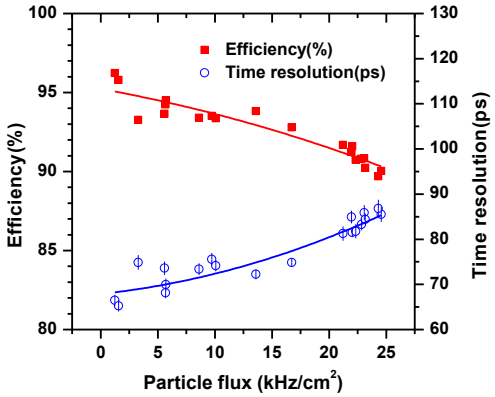

Fig.3 Efficiency and Time resolution as a function of particle flux at an applied voltage of 2.6kV/gap.

a promising performance: efficiencies above 90% and time resolutions below 90ps were obtained for a particle flux up to 25 kHz/cm^2, as is shown in Figs.2 and 3. When the particle flux increases every 5 kHz/cm^2, the efficiency decreases by 1% and the time resolution deteriorates by 4 ps. All of these performances can meet the requirement of CBM-TOF.

References

[1] A. Akindinov et al., Nucl. Instr. Meth. A 602 (2009) 709–712.
[2] L.Lopes et al., Nucl. Instr. and Meth. A 533(2004)69-73.
[3] CBM collaboration. The CBM experiment at GSI/FAIR, 3-200

CLOSY: A very Precise Clock Generation for Timing Measurements and Synchronization of the CBM ToF Wall

K. Koch
GSI, EE-Department, Darmstadt, Germany.

***Abstract*–A new electronics for precise clock generation and distribution has been designed for the CBM ToF-wall. The main card (CBM-CLOCK-SYTEM) is based on a frequency synthesizer chip to create two independent output frequencies that are phase coupled. An additionally downstream fast CPLD creates a synchronization signal, which is needed as a periodically epoch marker for the system.**

Introduction

In the concept of the CBM-Time of Flight (ToF) detector readout two phase coupled high-performance frequencies are needed [1]. One is directly used for time measurements with an event driven TDC (FEET-board, GET4 TDC chip) [2, 3], the other for synchronous data transportation reasons (Read Out Controller board, ROC) [4]. The front-end boards with the GET4 TDC chip have a clock requirement of about 160 MHz with very low jitter, less than 5 ps sigma. The ROC board has a need for a 250 MHz clock, but with less strict demands due to jitter.

Circuitry

Based on a programmable any-rate XO (Silicon Laboratories, Si570) a low jitter synthesizer and jitter cleaner (Texas Instruments, CDCL6010) and a fast CPLD (Xilinx, XC2C32A) an impedance controlled six layer board has been developed that delivers two phase coupled signals (250 MHz and 156.25 MHz) and an additional synchronization signal (SYNC) (see Fig. 1).

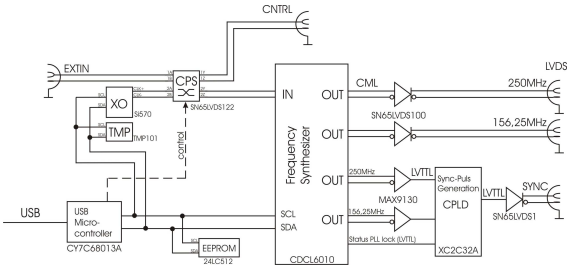

Figure 1: Simplified schematic of CLOSY2 (CPS: cross-point switch, TMP: temperature sensor).

Inside of the frequency synthesizer an integrated jitter cleaner with the option of a narrow external PLL loop filter also offers the opportunity of using a non optimal external clock source relating to incoming jitter.

To define the suitable output frequency, a rational fraction of 5/8 from 250 MHz (156.25 MHz) would be a good choice to get a fixed frequency relation concerning to the requirement of the TDC chip and the ROC board.

Results

Best results will be obtained with an oscillator clock frequency of 312.50 MHz (Jitter measurement at CNTRL output: $\sigma_{TIE} \sim 2.7$ ps, $\sigma_{Period} \sim 3.7$ ps).

The outputs then show much better results than the above-mentioned requirements (see Table 1).

output freq.	method	@CLOSY2	20 m distance
156.25 MHz	TIE	3.2 ps	4.2 ps
	Period	2.3 ps	3.1 ps
250.00 MHz	TIE	4.0 ps	6.0 ps
	Period	4.2 ps	5.4 ps

Table 1: Sigma values of timing jitter (TIE: time interval error, output signal at CLOSY2 and 2 times cascading over 20 m distance, XO frequency = 312.50 MHz).

Conclusion

The clock system is ready to be used in the CBM ToF environment with very good parameters exceeding the requirements. The essential control parameters are easy configurable via USB or over a boot sequence stored in an EEPROM on board. The CPLD is also reprogrammable in the case of other frequency ratios or delaying the SYNC signal.

Above all, CLOSY could be deployed in other physics experiments as well as laboratory equipment with the need of precise phase coupled clocks.

References

[1] W.F.J.Müller, V.Friese: CBM Progress Report 2008, GSI Report , Darmstadt, Germany, 2009, (http://www.gsi.de/documents/DOC-2009-Feb-233-1.pdf)

[2] H.Deppe, H.Flemming: Development of High Resolution ASICs for CBM-ToF, GSI Scientific Report 2007, p.250 (http://www.gsi.de/informationen/wti/library/scientificreport2007/PAPERS/INSTRUMENTS-METHODS-44.pdf) (1997) 56.

[3] H.Flemming, H.Deppe: Development of High Resolution TDC ASICs at GSI, Nuclear Science Symposium Conference Record, 2007 IEEE.

[4] S.Manz: Status of the Read Out Controller for the FEET Boards, 13. CBM Collaboration Meeting, March 9-13, 2009, GSI Darmstadt (http://www.gsi.de/documents/DOC-2009-Mar-97-1.pdf).

Progress in the development of a multi-purpose chip for the CBM experiment at FAIR.

H.K. Soltveit[1], J. Stachel[1], and M. De Gaspari[1,2]
[1]Physikalisches Institut, Universität Heidelberg, Germany; [2]CERN, Switzerland

A first prototype of a 10-bit pipeline ADC clocked at 40 MHz designed in IBM 130 nanometer process was submitted in March 2009 [1] . The chip came back June 2009 and was successfully tested at CERN during June/July 2009. Close to simulated values are achieved, and the most encouraging is an Effective Numbers Of Bits (ENOB) of 9.1 [2].

The next step in the development phase, is to integrate this ADC with an earlier developed Charge Sensitive Amplifier (CSA) in the same technology. The CSA is fully programmable, can handle both polarities and incorporates a third order shaper with programmable shaping time. The CSA is fully tested and shows a very good correlation between simulated and measured values. The most promising is the Equivalent Noise Charge (ENC) of about 270e at 10pF [2]. The integration of the 16 channel prototype consisting of the CSA and the ADC its ongoing at CERN since last quarter of 2009 [2], and it is expected to be submitted mid 2010.

In parallel a read-out ASIC in IBM 130 nm technology is under development. The motivation for going to 130 nm CMOS technology is to achieve a lower material readout, higher speed at less power, and better radiation hardness performance. A block diagram of the chip is shown in Figure 1. This ASIC is intended to have a total of 128 channels. The chip can be masked in groups of 16 channels (16-32-64 and 128). Depending on the segmentation needed it would include different features depending on the needs of the different detectors. Key features of the chip include analog pulse height, sparse readout, high resolution timestamp and selectable segmentation. Each of the 128 channels consists of a low noise CSA with selectable gain and dual polarity capability. To achieve fast counting at short peaking time, the CSA is followed by a pole zero cancellation circuit, which reduces pulse pileup for high input signal rates. The signal will then be split in order to feed an energy and a timing branch, each of them producing sparsified pulse trains. To ensure a good energy resolution and peak position stability at high count rate a baseline restorer is under development to eliminate the baseline shift. The possibility to select different gains in the preamplifier and the wide range of peaking times is to provide a versatile preamplifier potentially suitable for several of the proposed CBM detectors (RICH, ECAL, STS,TRD) and potentially also PANDA. To generate a logic signal that reports the arrival time of a particle at the detector, a discriminator will be used.

The pipeline ADC is an often used architecture for data conversion scheme which requieres a compromise between speed and accuracy. In this context a programmable (8-12) bit pipeline Analog-to-Digital Converter (ADC) with an adaptable sampling rate from 5-80 MHz is under development.

The chip will provide analog and binary readout information. For every event above a given energy level (the threshold is internally /externally adjustable) the ASIC stores the channel number, amplitude and the event time in digital form. The readout is data driven, so when data are available they are sent off-chip.

The chip has a low noise differential analog output to preserve its low noise high energy resolution capability. A sparse readout mode is available for reading out only the channels, which contain data. Power consumption is adjustable. Also full or partial power down is available on a channel-by-channel basis.

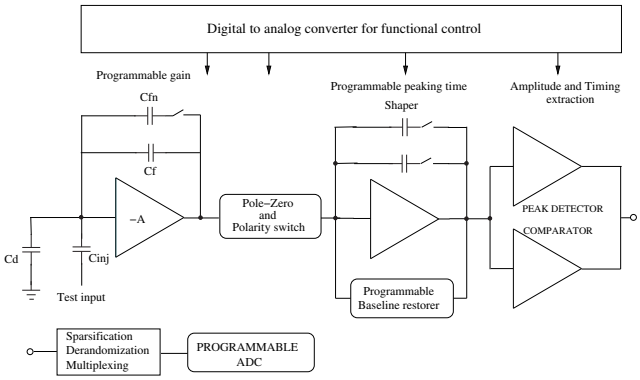

Figure 1: A simplified schematic of the chip.

To bias and to control the chip, a bandgap circuit ensures the stability versus changes in supply voltage and temperature for all the requested references in the analog core. The chip will be fully programmable through an I2C interface. The back-end readout circuitry will be responsible for output of the data. R&D is ongoing. Several readout schemes are under evaluation to find the optimum readout for all potential applications. The design of this chip has a modular approach, therefore each block could be used as an individual component as well.

References

[1] H.K.Soltveit et al., GSI Annual Report 2008, p 31

[2] H.Franca, Massimiliano De Gaspari and L Musa, Private communication

Characterization of the n-XYTER chip and preparations for the engineering run

C.J. Schmidt[1], M. Höhl[1], V. Kleipa[1], W. Müller[1], H.K. Soltveit[2], and A. Lymanets[3]
[1]GSI, Darmstadt, Germany; [2]Phys. Inst. Univ. Heidelberg, Germany; [3]Univ. Frankfurt, Germany

The n-XYTER ASIC, developed and prototyped by the EU-FP6 NMI3 DETNI collaboration in 2006, has undergone extensive testing and evaluation during the past years at GSI. This 128 channel ASIC [1] realizes a self triggering front-end readout architecture that will as such uniquely serve the CBM collaboration to prototype a purely data driven detector readout chain. CBM intends to employ this readout chain early on in detector prototyping and system development and study the implications of such change in readout paradigm.

During 2009 the mixed signal chip underwent detailed investigations on the chips performance and various mechanical, electronic and software integration aspects. In parallel it was integrated into the novel, dedicated data driven CBM readout chain and DAQ under development. Chip performance became for the first time experimentally accessible in all depth with the successful smooth realization of the entire chain, in which every single link was new and marginally tested.
With the data chain operative and versatile test and control software available, finally pulse hight spectra could be taken. To this end the chip was connected to a small dc-coupled strip detector of 300 μm wide and 10 mm long strips. The strips, wide compared to the 50.7 μm strips of the CBM prototypes, would reduce the probability of events sharing charge among neighboring channels. With this setup, an enclosed ^{241}Am gamma source was employed to generate signals in the sensor. This source provides several predominant gamma lines that generate below one MIP equivalent charge signals with reasonable detection efficiency in the 300 μm thick sensor. This source thus almost perfectly matches the needs for this chips evaluation. Using the 26.3 keV (7.2 ke in Si) together with the 59.5 keV gamma line (16.3 ke in Si) for gain calibration, 460 ENC could experimentally be confirmed on the latter line, which is in agreement with simulation considering a detector capacitance on the order of 6 pF but unprecisely known.

Chip testing was particularly intensified and extended to the study of the multi-channel spread of analogue parameters among the 128 input channels. These activities were performed in view of a larger production run for this ASIC targeted to improve the chips availability for neutron scattering detector applications on one hand and on the other hand for detector prototyping within CBM and eventually beyond within FAIR. In this production run and with the preparatory engineering work realized at Physikalisches Institut Heidelberg, the most severe drawbacks encountered in the current realization are being addressed and will be corrected. These are:

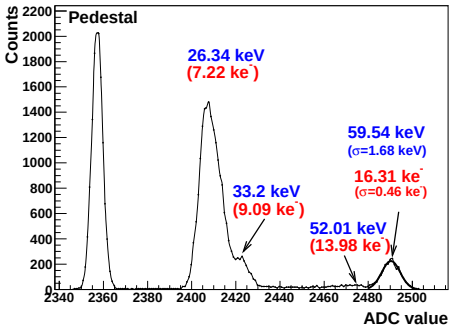

Figure 1: ^{241}Am gamma spectrum measured with the n-XYTER chip in self triggered mode on a 300 μm Si-strip detector. Several characteristic lines are seen, the rightmost one corresponding to 59.5 keV. The fit of a gausian to it reveals a resolution of 460 ENC. The pedestal was additionally added through a random trigger in the n-XYTER test trigger mode, which may be employed for an alternative, triggered operation of the chip.

- extermination of an observed severe temperature coefficient of up to 4%/K in the analogue baseline.
- annihilation of several layout related deficiencies potentially causing powering problems and consequently an observed and undesired channel to channel base line shift across the chip.
- reduction of the observed channel to channel base line spread that effectively reduces the dynamic range.
- improvement of in-channel as well as inter channel cross talk.
- implementation of an optional reduction in gain by about a factor of 4 in order to enhance the dynamic range.

A more in depth report on these submission preparations is published elsewhere in this annual report. We expect to have the n-XYTER available in sufficiently large numbers in spring this year. Automated extensive per chip characterization and tests are planned for this production batch.

References

[1] NIM A, 568 (2006) 301-308

Readout of the Hamamatsu H8500-03 MAPMT with the n-XYter chip*

P. Koczoń, C. Höhne, C. Schmidt, and W.F.J Müller

GSI, Darmstadt, Germany

Abstract: Hamamatsu Multi Anode Photomultipliers H8500-03 are currently foreseen as photodetector for the CBM-RICH. To operate the H8500-03 with the n-XYter chip, which is a prototype of a future CBM data acquisition readout, the photomultiplier signals have to be strongly attenuated. An attenuator in form of a charge divider has been developed and tested. After laboratory tests, a readout system based on the n-XYter could be succesfully operated in a test-setup during a proton beam time of the FOPI experiment at GSI.

Readout of the Hamamatsu H8500-03

In the CBM-RICH detector a photodetector plane based on Hamamatsu H8500-03 is foreseen for Cherenkov light detection [1]. To encounter the high interaction rates and thus data flow, front-end electronics with self triggered readout chips is planned. At present, readout electronics is based on a first version of the n-XYter chip [2]. It has a dynamic range of 125000 e^- while typical photomultipliers have a gain of 10^6. As temporary solution a charge divider has been developed which accomodates the MAPMT signals to the n-XYter input (Fig. 1). A simple resistor - capacitor circuit with an attenuation factor of 50 has been built and tested. The signal amplitude is reduced while the shape is hardly deteriorated. The control of the n-XYter chip as well as further data processing is done with Readout Controller (ROC) and a data aquisition (DABC) system developed for CBM [3] running on a standard Linux PC.

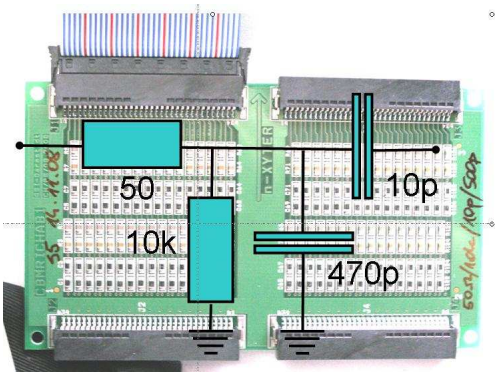

Figure 1: Charge divider

Experimental setup

The readout system has been tested in the lab with a LED driven by a pulse generator. The mapping of the 8×8 pixel surface of the MAPMT to the n-XYter channels has been verified with a pinhole mask. The setup has also been tested during a proton beamtime of the FOPI experiment. It comprised a plexiglass block of dimensions (8cm $\times$ 8 cm $\times$ 6 cm) placed directly in front of the MAPMT, which was installed in 3 cm radial distance from the beam axis while the plexiglass extended into the beam. Protons of 3.5 GeV kinetic energy crossing the plexiglass produced Cherenkov photons. A coincidence of two crossed scintillator detectors of 5 mm width each placed in front of the plexiglass radiator to detect protons delivered a trigger signal. It was recorded as so called AUX signal by the ROC-DABC and used as event trigger in the offline data analysis.

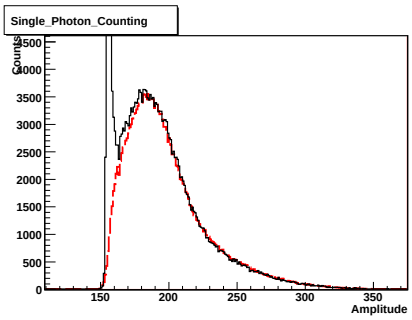

Figure 2: Single photon amplitude distribution measured with H8500-03 (data for only one pad is shown): Thermal electrons and noise (solid black line), single photons (red dashed line). Distributions have been normalised to each other.

Results

DABC System has proven its ability to stand up to $3{\cdot}10^5$ Hz trigger rate. This rate was limited by the bandwidth (8MB/s) od the used Ethernet connection. It could be demonstrated that the H8500-03 MAPMT with strongly attenuated output signals and n-XYter readout is able to register single Cherenkov photons. Fig. 2 compares the amplitude distribution from one selected MAPMT pixel for noise (solid line) and requiring beam coincidence (dashed line). Single photon counting is clearly demonstrated as the amplitude distributions of thermal electrons and electrons from Cherenkov photons show the same shape.

References

[1] C. Höhne at al., Nucl. Instr. Meth. A 595 (2008) 187.

[2] A.S. Brogna et al., Nucl. Instr. Meth. A 568 (2006) 301.

[3] http://cbm-wiki.gsi.de/cgi-bin/view/DAQ/WebHome, http://dabc.gsi.de/

* Work supported by BMBF

Optical Communication Tests with Active Buffer Board

W. Gao[1], A. Kugel[1], A. Wurz[1], G. Marcus[1], M. Stapelberg[1], and R. Männer[1]
[1]Department of Computer Science V, ZITI, University of Heidelberg, Mannheim, Germany

Introduction

The Active Buffer Board (ABB) is the transfer unit in the CBM DAQ sub-system. It receives CBM events, performs local buffering and formatting and forwards them to the host PC via the PCIe channel. Based on the development of the ABB-v1 (with Virtex 4 FPGA), the ABB-v2 (AVNET Virtex 5 board) is successfully equipped with optical link functions. Also, 3 traffic classes, DAQ (data acquisition), CTL (control) and DLM (deterministic latency message) are defined. To access these traffic classes, a software interface is built. A multi-threaded higher level software supports the interleaved data and control accesses. As shown in figure **??**, the ABB communicates with the DCB (data combining board) or the ROC (read-out controller) over fibre. Commissioning DAQ chain tests show good channel performance. [1]

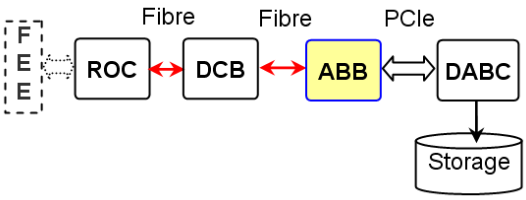

Figure 1: ABB in DAQ test chain

Firmware

To the ABB-v2 board, HDL development on the Virtex 5 FPGA (XCV5LXT110) involves the DMA engine and the link protocol module, as well as the new traffic classes processing. An efficient transfer of data from the FEE (front-end electronics) to the host over optical links is possible in this way.

A FIFO structure has been carefully designed, where the incoming DAQ packets are buffered. We have two options for this buffer, one is a 128KB internal Block RAM FIFO, the other is a 256MB external DDR SDRAM FIFO. The buffer is written and read asynchronously, which demands special treatment for the data count, especially for the larger DDR FIFO version. Otherwise the software would run into a time-out DMA status or even crash. CTL messages are important in coordinating the data flow between the front-end and the back-end. New logic design reserves buffers both for outgoing and incoming CTL messages, because in the link protocol, CTL messages can be delayed for some cycles, which is different from DLM messages. Control/Status register pairs are set to the PCIe DMA logic related to the optical link and the traffic class buffers. They enable the software to access the new firmware components.

A link protocol module has been developed by CAG Group, Uni. Heidelberg. It manages the high-speed transfer over optical channels and multiplexes the traffic classes on a single link after arbitration. [2]

A data generator inside the ABB board is implemented to emulate the link behaviour in the ABB stand-alone (internal loop-back) test. It helps also to source the pseudo-DAQ data packets in the performance test.

Software

The new software development aims at a continuous data transfer under multiple traffic classes.

Functions for CTL message sending and receiving are built into a new software component, the ABB Daemon, which enables the ABB board to communicate with the FEEs via DCB or ROC over optical links. Multiple CTL messages can be merged. The command carried in the CTL message can be successfully acknowledged by the receiver. The DMA targeted to the FIFO-structure data source is upgraded and verified. The PCI driver has been updated with functions corresponding to the new traffic patterns. The ABB Daemon provides a serialization of CTL and DAQ packets from the ABB while allowing concurrent access from multiples threads/applications.

Tests of traffic classes

All new features of the ABB-v2 have been proven reliable. CTL message tests have been well proceeded because they are the management for almost all DAQ activities. Application-level tests for CTL message latencies result in 0.138 ms for write-read and 0.053 ms for read. DLM messages have been very fundamentally tested and they are supposed to be further accomplished in terms of the protocol. When 2 ROCs are connected, DMA performance in transferring DAQ packets is about 300 MB/s.

References

[1] W. Gao, et al. Active Buffer for DAQ in CBM Experiment. IEEE-RT'09 Conference Record. 2009.

[2] F. Lemke, et al. A Unified Interconnection Network with Precise Time Synchronization for the CBM DAQ-System. IEEE-RT'09 Conference Paper. 2009.

Prototype Results of an Optical Communication Network for the CBM DAQ-System*

F. Lemke, S.Schenk, and U. Bruening[1]
[1]University of Heidelberg, Mannheim, Germany

Introduction

For the CBM Data Acquisition (DAQ) System a specific protocol has been developed considering the special demands of limited area for hardware, radiation tolerance, support for different types of network traffic and the need of synchronization mechanisms. Within the CBM network only a single bidirectional fiber link is used for the three network traffic classes: Data Transport Messages (DTM), Detector Control Messages (DCM), and Deterministic Latency Messages (DLM). DTMs are optimized for data transfer from the detector frontend to the backend computing cluster. The DCM class provides a higher fault tolerance level to guarantee the delivery of control messages. DLMs are used for precise time synchronization. The CBM DAQ protocol fulfills all requirements mentioned before and was implemented for the usage within the Field Programmable Gate Arrays (FPGA) of all developed readout chain boards. The chain, developed by several groups, consists of Read-Out-Controller (ROC) boards interfacing and initializing the front-end electronics and building link-packets, Data-Combiner-Boards (DCB) combining data streams from multiple ROCs, and finally Active-Buffer-Boards (ABB) for receiving, buffering and reorganizing the data. The ABB also writes the data via PCI express to the memory of the back-end node.

Prototype Setup and Measurements

All presented measurements and results in [1] and within this section are prototype build-ups consisting of DCBs V1.3 shown in figure 1, also known as the HTX-Board, the Avnet ADSAES-XLX-V5LXT as ABBs and ROC boards, which are also called SysCore Board V2. The preferred combinations for conducted tests were ABB - 2ROCs and ABB - DCB - 2ROCs, because they are sufficient to prove the concepts and to declare them as suitable for a final build. Due to given data rates, the ROC-DCB-ABB chain is currently running with 2.5 Gbps optical links. This link speed can be increased with feasible design changes by at least a factor of two, if necessary. During the first tests with the prototype systems test pattern generators were used to create random sized data and control packets. Data streams included periodically embedded DLMs. After successful tests with different setups, the optical protocol was combined with logic of the ROC and ABB development groups. In the next step a complete readout chain was tested under real usage conditions. It was possible to use control messages to read and write registers within the ROC and to control initializations required by ROC logic. Also a data stream of a detector readout was activated and written into main memory of the computing node for further processing. The theoretical peak bandwidth utilization of the protocol for each link is over 240 MB/s, which is more than 95 percent of the maximum possible bandwidth of 250 MB/s considering 8b/10b coding on a 2.5Gb/s link. Measurements for data bandwidth utilization show that we can reach more than 220 MB/s, which is over 90 percent of the possible protocol bandwidth. The message based precise time distribution requires deterministic latency within the DAQ system. Besides special synchronization mechanisms implemented in hardware, a recovered receive clock has to be used for sending messages. The clock's jitter must be less than 40 ps peak-to-peak to guarantee correct transceiver operation. Therefore a jitter cleaner device presented in figure 2 was developed. Deterministic latency has been proven in multiple long-term lab tests and DLMs were successfully sent.

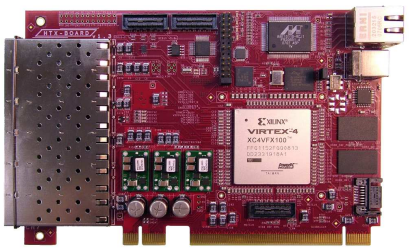

Figure 1: Data Combiner Board V1.3

Figure 2: Jitter Cleaner Extension Board V1.0

References

[1] Frank Lemke, David Slogsnat, Niels Burkhardt, Ulrich Bruening, "A Unified Interconnection Network with Precise Time Synchronization for the CBM DAQ-System", 16th IEEE NPSS Real Time Conference 2009 (RT 09), May 10-15, Beijing, China.

* Work supported by GSI, BMBF FAIR-CBM 06MN229I

Status of FAIR SIS100 and HEBT

P. Spiller, U. Blell, L. Bozyk, H. Eickhoff, E. Fischer, E. Floch, F. Hagenbuck, P. Hülsmann, M. Kauschke, A. Krämer, D. Krämer, H. Klingbeil, J. P. Meier, C. Mühle, P. Puppel, N. Pyka, S. Ratschow, H. Ramakers, H. Reich-Sprenger, M. Schickert, J. Stadlmann, H. Welker

GSI Darmstadt, Germany

MODIFICATIONS IN THE SIS100 CRYOMAGNETIC SYSTEM

With the goal to built and procure the first preseries unit of the cryomagnetic system of SIS100, the design of the dipole module has been modified and completed. In context with the completion of the design of the dipole module, the overall lattice cell has been optimized with respect to the cryostat interfacing. All cryostat distances could be equalized with the advantage that all connecting cryostats and their heat shields are now the same. The longer distance between the two dipoles of each lattice cell improves also the accommodation of the slightly elongated dipole chamber and the connecting beam line bellows. In order to maintain the acceptance of SIS100, the horizontal aperture of the elongated vacuum chamber has been increased from 115 to 120 mm. The new distance enables an installation of the adsorption pumps for hydrogen pumping, which are foreseen in each second lattice cell, in between the dipole magnets.

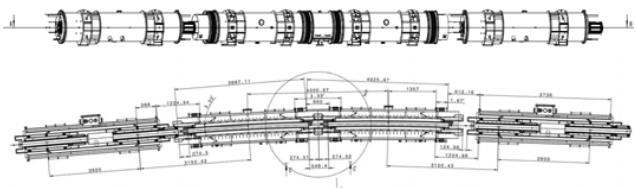

Figure 1: Modified SIS100 lattice providing equalized cryostat distances between the dipole- and quadrupole modules.

The preseries dipole magnet itself will feature a new coil design with half of the number of turns and a new high current cable which is being operated at twice the current of the available prototype dipole magnets (~ 13 kA). In order to minimize the cross talk between the bus bars at the higher operation currents and to account for the increased distances between the magnets, the design of the bus bar system had to be modified. The preseries dipole module will also address the question of the chamber cooling. A chamber temperature below 12 K is needed for an effective pumping of heavy residual gas components which are the main origin of ionization beam loss in SIS100. Therefore, two chamber types, one with active cooling by means of cooling tubes and one with contact cooling will be built and tested with the preseries dipole.

MODIFICATIONS IN THE FAIR HEBT SYSTEM

In the frame of the progressing building and civil construction planning, a number of modifications in the FAIR HEBT system were implemented. For a more effective radiation shielding the beam transport system in front of the machine setting dump has been deflected down. The proton beam line has been adapted to the space requirements of the PANDA building and the beam line passing the pbar target towards the NESR, has been rearranged to accommodate radiation shielding for the Super-FRS. In the frame of a new modularization of the FAIR project, several options were studies to accommodate a new APPA target area. Presently, in close interaction with the users, the beam line system is being optimized for the experiment equipment and needs. A slight increase of the distance between the CBM building and the Super-FRS has been proposed, which would allow a later extension of the FAIR facility to the East. For the civil construction planning, major assumptions have been made for the transportation, installation and maintenance of accelerator components. The cross sections of all tunnels, the routes of transportation, the major transportation equipment and cranes were specified and summarized in a HEBT building specification document. The document does also contain the required floor space areas in the HEBT supply buildings, which were changed and optimized drastically in comparison to the former building layout.

The design of the FAIR HEBT system, accounting for all major accelerator components as simplified 3D CATIA models, has been continued and completed for all beam line sections. Major collisions have been identified and removed in an interactive process between the engineering- and ion optical designers.

SIS 100 Main Magnets: Test Results and Operation Parameters *

E. Fischer †[1], P. Schnizer[1], A. Mierau[1], A. Bleile[1], P. Akishin[2], C. Heil[4], H. Khodzhibagiyan[2], R. Kurnyshov[3], B. Schnizer[4], P. Shcherbakov[5], C. Schroeder[1], A. Stafiniak[1], and S. Y. Shim[1]

[1]GSI, Darmstadt, Germany; [2]JINR, Dubna, Russia; [3]Elektroplant, Moscow, Russia; [4]TUG, Graz, Austria; [5]IHEP, Protvino, Russia

Introduction

The FAIR accelerator complex will consist of several accelerator rings. The SIS100 synchrotron, the core component of this facility, will be the world's second large scale synchrotron using superconducting magnets (dipoles: maximum field 2 T, repetitions frequency 1 Hz) targeted for accelerating high current ion beams (Uranium up to U^{28+}).

Based on thorough R&D [1], first full scale magnets were built [2, 3] with the first dipole already extensively tested and its operation parameters measured, including: the magnetic field [4, 5, 6] and the AC losses [7].

Magnetic Measurement to Elliptic Multipoles

The overall length of the magnet on the test bench of 7 m, its medium size aperture of $115\,mm \cdot 60\,mm$ as well as the anticryostat, providing room temperature access to the magnets aperture, led to developing a "mole" [8]. (A "mole" is a rotating coil probe system with all auxiliary instruments working within the magnetic field). The main challenges were caused by the fast magnetic field changes; thus all used material had to be non magnetic and of a high electric resistance.

Elliptic coordinates $x = e\cosh\eta\cos\psi$, $y = e\sinh\eta\sin\psi$ match naturally the elliptic aperture of the vacuum chamber. The field $\mathbf{B} := B_y + iB_x$ can be described within the whole ellipse using

$$\mathbf{B}(\eta + i\psi) = \frac{\mathbf{E}_0}{2} + \sum_{q=1}^{M} \mathbf{E}_q \frac{\cosh[q(\eta + i\psi)]}{\cosh(q\eta_0)}, \quad (1)$$

with $\eta_0 = \tanh^{-1}(b/a)$ the reference ellipse and a, b its half axes; $e = \sqrt{a^2 - b^2}$ [9]. An analytic transformation allows to transform $\mathbf{E}_q$ to the classical multipoles $\mathbf{C_m}$. These are given by $\mathbf{B(s)} = \sum_{n=1}^{\infty} \mathbf{C_n} \left(\frac{\mathbf{s}}{R_0}\right)^{n-1}$ with $\mathbf{B(s)} = \mathbf{B}\,(x + \mathtt{i}y) = B_y + \mathtt{i}B_x$, x, y the Cartesian 2D coordinates and R_0 the reference radius. The relative multipoles $\mathbf{c_n}$ are $\mathbf{dec_n} = b_n + \mathtt{i}a_n = C_n/C_m$ with C_m the main multipole (m = 1 dipole).

In the measurement the rotating coil probe is placed at different lateral positions but with a remaining overlap at the field is measured independently. The field deviation is measured with a higher accuracy than the average value, thus in the evaluation procedure the overlap region is used to subtract the difference between the averaged value (in the order of 100 ppm) and then the elliptic multipoles (1) are calculated. The measured and calculated normal sextupole b_3 and dekapole b_5 are given in Fig. 1.

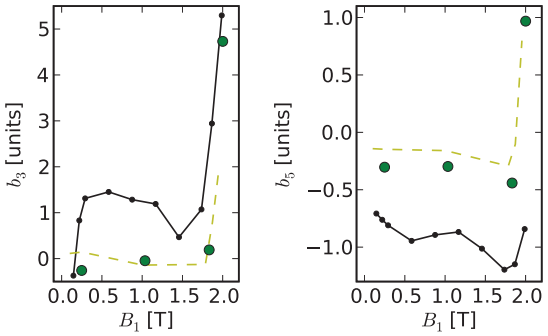

(a) b_3 (b) b_5

Figure 1: The calculate and measured higher order multipoles versus the main field. black line – measured, yellow line – TOSCA, green line – ANSYS.

AC Losses

As the magnets are fast ramped eddy currents and hysteresis heat up the magnets. Due to thermodynamic limitations, described by the Carnot process, as well as the technological achievable cryoplant efficiency, 250 W have to be paid for 1 W created in magnet at 4.2 K.

Therefore the AC loss in the magnet must be fully understood and well described. The magnet was measured (with and without installed vacuum chamber) in continuous triangular cycles with different ramp rates $dB/dt = \dot{B}$ and maximum fields B_{max} [7].

Based on the measurement results, the power loss in a triangular cycle can be modelled by

$$P_{\wedge} = q_h(B_{max})f + q_e(B_{max})f^2 \quad f = 1/\tau_{\wedge} \quad (2)$$

with

$$q_h = h_a\,B_{max} + h_b\,B_{max}^2 \quad (3)$$

$$q_e = \begin{cases} 0 & B_{max} < B_{th} \\ e_a\,(B_{max} - B_{th})^2 & B_{max} \geq B_{th} \end{cases} \quad (4)$$

B_{th} is the threshold field (see Table 1) and $\tau_{\wedge}$ the cycle period. B_{th} describes that the eddy currents are mainly created in the yoke when the ends start to saturate as predicted

* Work supported by the EU FP6 Design Study (contract 515873 - DIRAC secondary beams) and the BMBF

† e.fischer@gsi.de

Table 1: AC loss model coefficients

Component	h_a	h_b	e_a	B_{th}
Magnet	7.6	8.3	15.5	0.95
Vacuum Chamber	3.7	-1.3	8.0	0.2
Total	10.3	8.3	15.5	0.4

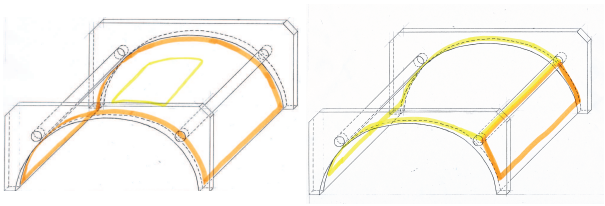

Figure 2: Eddy currents across the tube (left) and across the vacuum tube as well as the short circuits by the ribs.

by calculations. The expected power, dissipated in an arbitrary cycle, can be estimated using the above equations with the parameters in Table 1 [7].

Vacuum chamber

As high charge state ions (Uranium up to U^{28+}) will be transported in SIS100, the vacuum has to be better than 10^{-12} mbar.So the vacuum chamber has to fulfil antagonistic specifications: a cold surface, used as an cryogenic adsorption pump, to obtain a vacuum pressure below 10^{-12} mbar, minimise eddy currents induced due the ramping field and sustain a pressure difference of 1 bar [10].

FEM codes can calculate the magnetic field as well as the eddy currents in the magnet vacuum chamber assembly but will always only provide a single number. Therefore an analytical model was developed based on the following assumptions: the dipole field is prefect, the eddy currents do not disturb the external field, and the vacuum chamber specific conductivity σ is uniform. Different current loops were considered (see Fig. 2) and their resistance next to the seen Flux was calculated. Formulae were derived for the eddy currents induced in the elliptic vacuum chamber itself, which have to be evaluated numerically. The eddy current calculated for the cooling loop was found to be $\approx 1.1\,W$ versus 3 W found by FEM calculations. This fact can be explained; which is that the FEM model took a fair amount of solder into account, missing in the analytical calculation.

Outlook

The built and tested magnet verified that the 2 layer design coil can not provide 1 Hz but only 0.3 Hz and thus the curved single layer coil, using a high current cable, was correctly chosen as the dipole for the SIS 100. In order to describe its magnetic field with the same quality as for a straight magnet local toroidal multipoles were developed [11].

Further investigations will be made on a conduction cooling scheme for the vacuum chamber. i.e. a design, where the chamber is cooled contacting it to the magnet's coil and yoke [12], as it simplifies the overall cooling scheme of SIS100.

The high current cable can also be used for the quadrupole reducing the pole turns from six to two [6]. The final choice has to be made considering all its impacts: required cooling power and hydraulic limits, lattice layout and the economical benefits of using the same cable for all main magnets.

References

[1] E. Fischer *et al*, Critical mechanical structure of superconducting high current coils for fast ramped accelerator magnets with high repetition rates in long term operation. EUCAS09, September 2009, Dresden.

[2] G. Sikler *et al*, "Fabrication of a prototype of a fast cycling superferric dipole magnet" PAC09, May 2009, Vancouver, MO6PFP043

[3] E. Fischer *et al*, "Fast ramped superferric prototype magnets of the FAIR project, first test results and design update" PAC09, May 2009, Vancouver, MO6PFP065

[4] E. Fischer *et al*, "Measured and calculated field properties of the SIS100 magnets described using elliptic and toroidal multipoles". PAC09, May 2009, Vancouver, TH5PFP057

[5] A. Mierau *et al*, "FEM analysis of fast ramped superconducting synchrotron magnets and comparison to experimental results", EMF, May 2009, Mondovi.

[6] E. Fischer *et al*, "Superconducting SIS100 prototype magnets design, test results and final design issues" MT21, October 2009, Hefei, 2AO-5.

[7] E. Fischer *et al*, "Thermodynamic properties of fast ramped superconducting accelerator magnets for the FAIR project", CEC/ICMC 2009, June 2009, Tuscon

[8] P. Schnizer *et al*, "Commissioning of the mole for measuring SIS100 magnets and first test results" MT21, October 2009, Hefei, 2KP-15.

[9] P. Schnizer, B. Schnizer, P. Akishin, and E. Fischer, Nuclear Instruments and Methods A, 607(3):505 – 516, 2009.

[10] E. Fischer *et al*, "Impact of the beam pipe design on the operation parameters of the superconducting magnets for the SIS100 synchrotron of the FAIR project", EUCAS09, September 2009. Dresden

[11] P. Schnizer, B. Schnizer, P. Akishin, and E. Fischer, Int. J. Comp. Math. Elec. Eng., 28(4):1044 – 1058, 2009,

[12] E. Fischer, J. Macavei, A. Mierau, "Designkonzept für eine Vakuumkammer mit Kontaktkhlung" MT-INT-EF-2009-001, Internal Note, GSI, 2009

Transient Eddy-Current Simulations of the Full-Size SIS-100 Dipole using a Parallelized Simulation Tool*

S. Koch§[1] and T. Weiland[1]

[1]Technische Universitaet Darmstadt, Institut fuer Theorie Elektromagnetischer Felder (TEMF), Schlossgartenstrasse 8, 64289 Darmstadt, Germany

Introduction

The calculation of the eddy-current losses in the SIS-100 dipole magnet by numerical methods is very time-consuming, in particular when the full-length geometry is considered. Parallelization strategies in combination with higher-order finite element methods provide a significant reduction in the required computational time.

Computational Model

For the sample geometry of the SIS-100 dipole [1] including end plates as well as brackets made from stainless steel shown in Fig. 1, transient eddy-current simulations are carried out. The coil current is varied according to cycle 2c reported in [2], whereas the amplitude is chosen such that the magnetic flux density reachs 2 T in the aperture.

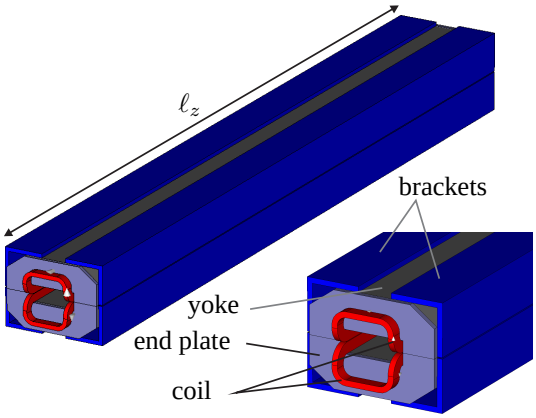

Figure 1: CAD model of the full-length SIS100 dipole ($\ell_z = 2.8$ m) containing yoke, end plates and brackets ensuring mechanical stability. The model uses a low coil in order to reduce the eddy-current losses in the end regions.

Results

The time-integrated eddy-current losses are reported in Table 1 for the respective parts of the magnet assembly together with the computational time required for the simulations. Whereas the losses in the stainless steel parts exhibit merely a negligible dependence on the discretization level, the losses in the yoke, forming the major contribution, vary by 1%. The distribution of the component of the magnetic flux density normal to the end plates, which is responsible for the eddy currents in the lamination, is shown in a 2D cut in Fig. 2 at the maximum excitation level.

Table 1: Eddy-current losses in the separate parts of the yoke assembly for two different levels of discretization both using FE shape functions of second order ($p = 2$).

Discretization	433 246 **dofs**	791 072 **dofs**
yoke	12.97 J	12.73 J
end plates	1.19 J	1.18 J
bracket	1.95 J	1.95 J
total	16.11 J	15.85 J
simulation time	20.0 h	36.0 h

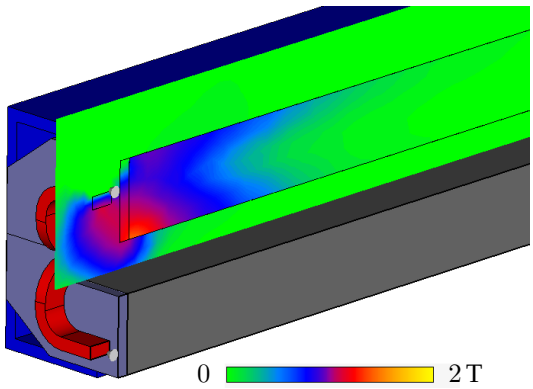

Figure 2: Magnitude of the normal component of the magnetic flux density responsible for the eddy-currents at the end regions in logarithmic color scale at $t = 0.82$ s.

Conclusion

Using parallelized simulation codes, the full-length geometry of the SIS-100 dipole together with additional parts of the magnet assembly can be considered in eddy-current simulations. Thanks to the speed-up in parallel computations, the simulation time is kept at a reasonable level.

References

[1] E. Fischer, H.G. Khodzhibagiyan, and A.D. Kovalenko, "Full size model magnets for the Fair SIS100 synchrotron", IEEE Trans. Appl. Supercond., 18(2):260263, June 2008.

[2] "FAIR Baseline Technical Report", March 2006, http://www.gsi.de.

* Work supported by GSI, Darmstadt under contract DA-WEI1.

§ koch@temf.tu-darmstadt.de

Simulation of Dynamic Vacuum Effects using the StrahlSim Code

P. Puppel[1,2], P. Spiller[1], U. Ratzinger[2], and L. Bozyk[1,3]
[1]GSI, Darmstadt, Germany; [2]Goethe-Universität, Frankfurt a.M.; [3]Technische Universität Darmstadt

Introduction

The StrahlSim code simulates the charge exchange beam loss and the generated dynamic vacuum in heavy ion accelerators. Intermediate charge state ions are exposed to a high probability of charge exchange due to interactions with residual gas particles. Ions which underwent a charge change will be deflected differently with respect to the reference ion in dispersive elements and may be lost on the vacuum chamber where an energy-dependent gas desorption takes place. The pressure rise in the accelerator due to this desorption process depends on the intensity of the ion beam and is referred to as dynamic vacuum. The StrahlSim code is a unique tool that combines systematic and dynamic beam loss mechanisms, vacuum gas composition and vacuum pumping systems of an accelerator and accounts for the relevant ionization and electron capture cross sections at the actual beam energy. StrahlSim allows to estimate the transmission of heavy ion beams and to calculate the pumping power needed to stabilize the dynamic vacuum.

Beam Loss Simulations

Machine experiments done in October 2009 led to a new world record of accelerated U^{27+}-ions [1]. The machine settings used have been taken over in the StrahlSim simulations. As there are no cross sections available for charge exchange processes of U^{27+}, the simulations were conducted with U^{28+} (which has similar cross sections). Fig. 1 compares the simulation results with five measured cycles. Injection losses, which induce a pressure bump inside the ring, were chosen such that the experimental data are reproduced. Apparently not all particles lost during injection lead to a pressure rise affecting the beam. The simulation with StrahlSim confirms the expected improvement of the vacuum system, which has been achieved by the NEG coated vacuum chambers and the ion catcher system [1].

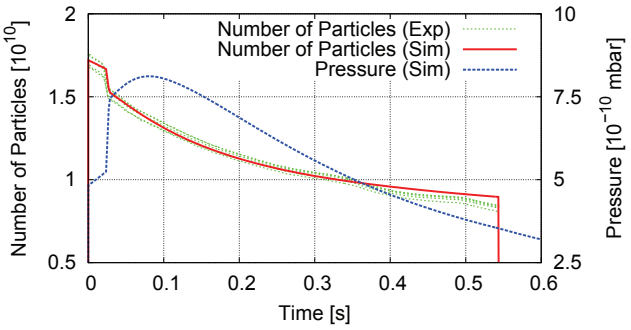

Figure 1: Measured number of U^{27+} particles in SIS18 cycles in comparison to StrahlSim simulations with U^{28+}-ions (which have similar cross sections).

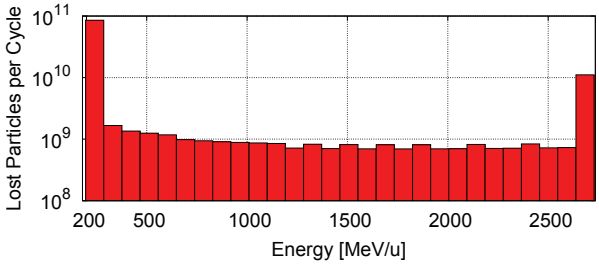

Figure 2: Histogram of lost U^{28+} particles in SIS100 as a function of the actual particle energy in cycles with fast extraction. The ionization beam losses depend on initial systematic losses which initiate the dynamic vacuum process.

StrahlSim can also be used to provide valuable input for estimations of machine related quantities. Fig. 2 for example shows the number of lost particles as a function of the energy of U^{28+}-ions during a specific SIS100 cycle with fast extraction. Beam losses during injection and losses induced by nonlinear dynamics and RF capture have been considered [2]. These studies were input for radio protection calculations.

Extension of StrahlSim

StrahlSim is being extended to provide time dependent longitudinal pressure profiles. For SIS18 we expect insight into the pressure rise during injection and its propagation along the circumference for the rest of the cycle. For SIS100 the pumping speed needed in the dipole and quadrupole magnet chambers will be estimated considering the real loss positions with respect to the properties of the pumping surfaces.

Acknowledgements

We would like to thank V. Shevelko and T. Stöhlker for providing ionization cross sections for interactions of intermediate charge state heavy ions with residual gas particles. This work is supported by HIC for FAIR.

References

[1] P. Spiller et al., "Status of the SIS18 Upgrade Program and Progress in Acceleration of Intermediate Charge State Heavy Ions", GSI Scientific Report 2009.

[2] P. Spiller, "Beam Loss in SIS18/100/300/HEBT", GSI, Darmstadt, December 2009.

A Test Stand to Measure Desorption of Cryogenic Surfaces

H. Kollmus[1], M. Wengenroth[1], Th. Hackler[1], M. Bender[1], D. Severin[1], A. Krämer[1], E. Mahner[2], and H. Reich-Sprenger[1]

[1]GSI, Darmstadt, Germany; [2]CERN, Geneva, Switzerland

Ion induced desorption is a serious intensity limitation for high current, low charge state heavy ion accelerators like SIS18 and SIS100. Whereas room temperature desorption was intensively investigated in the last years [1, 2], there is only one measurement for molecular desorption of a cryogenic surface in the relevant energy regime [3]. Since SIS100 is a cryogenic, super-conducting machine, desorption yield data for cryogenic surfaces in the relevant temperature regime are required. Therefore two test stands where taken in operation at CERN and GSI in 2009. First GSI results will be presented.

Experimental Setup

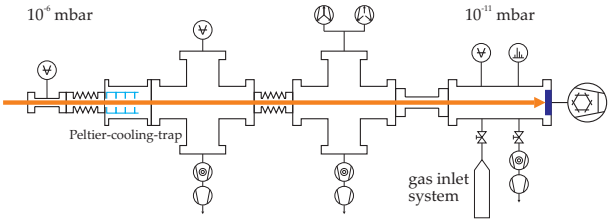

Figure 1: Schematic drawing of the experimental setup at GSI.

The setup, which is located at the HLI-UU beam line, is sketched in Fig. 1. It consists basically of a differential pumping stage with a Peltier-cooling-trap to separate the accelerator vacuum system, which operates at the HLI in the 10^{-6} mbar regime, from the test chamber, which operates in the 10^{-11} mbar regime. The Peltier-cooling-trap has a working temperature of about 235 K and traps hydrocarbons (m/q > 38) from the HLI vacuum environment. Downstream the cooling-trap there are two pumping stages connected by a well known conductance to the test chamber. The target is mounted on the second stage of a cryo-pump and the temperature can be varied from 8 - 80 K. The target material is copper and was delivered by CERN in order to have similar prepared targets for GSI and CERN experiments. In the last pumping post there is in addition a scintillation screen in order to control and adjust the beam size. The test chamber is equipped with an extractor gauge to measure the total pressure and a residual gas analyzer to measure the partial pressure distribution during ion irradiation. Additionally a gas inlet system is realized, in order to be able to freeze out a dedicated amount of gas onto the cryogenic surface. This enables to measure the desorption yield as a function of the amount of pumped gas and allows to simulate long term operation and aging effects.

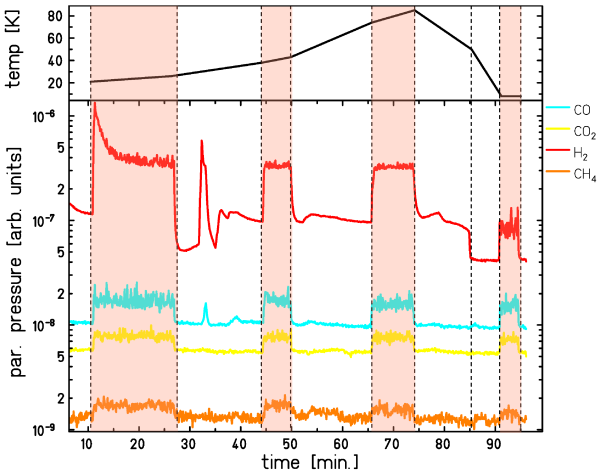

Figure 2: Commissioning results for desorption from cryogenic surfaces: partial pressure distribution for H_2, CO, CO_2 and CH_4 for different surface temperatures.

First Results

After setting up the experiment a first commissioning run was performed in autumn 2009 using 1.4 MeV/u Ca^{10+}, with a repetition rate of 1 Hz, a bunch length of 5 ms and a current of $1.5 \cdot 10^{11}$ particles per second. One exemplary result is shown in Fig. 2. Here, the partial pressure distribution for H_2, CO, CO_2 and CH_4 under ion irradiation is shown for different surface temperatures. The light red areas indicate beam on target, the fluctuations in between are caused by thermal desorption due to temperature adjustment. A significant hydrogen desorption is observed for the first shots on the 20 K copper target. In the following the pressure increase for all four gases stays nearly constant independent on the target temperature up to 80 K, except for the very last irradiation at 8 K. Here, during cool-down a significant decrease in the hydrogen partial pressure was observed at 50 K and the hydrogen desorption at 8 K is on the level of the hydrogen background at the higher temperatures. More sophisticated experiments using different ion species and impact energies are scheduled for 2010.

References

[1] E. Mahner, Phys. Rev. ST Accel. Beams 11, 104801 (2008)

[2] H. Kollmus et al., Vacuum **82** (2007) p. 402

[3] E. Mahner et al., American Institute of Physics, CP733, High Intensity and High Brightness Beams, edited by I. Hofmann, J.-M. Lagniel, and R.W. Hasse (2005) p. 219

Investigations of the vacuum conditions inside the SIS100 dipole vacuum chamber during magnet ramping

St. Wilfert, A. Krämer, T. Hackler, M. Wengenroth, and H. Reich-Sprenger
GSI, Darmstadt, Germany

Abstract

More than 45% of the cryogenic beam pipes in the arches of the future SIS100 will be formed by dipole magnets. As usual in superconducting machines, the inner surface of all cold vacuum chambers, also including the dipole chambers, will be used as an effective cryopump to generate low beam pipe pressures. However, since the dipole magnets have to be rapidly ramped at high repetition frequencies, eddy current-induced heating of the chambers could become a serious problem with regard to their pumping behaviour. With exceeding a critical wall temperature of 15K, previously pumped gas could desorb from the walls in a pressure rise during ramping. Up to now it was not clear which concrete consequences would have the magnet ramping on the vacuum quality inside the dipole chambers. The article presents first experimental results on measurements of the chamber temperature and partial pressure evolution during magnet operation.

Experiments and results

The measurements were carried out using the BNG magnet [1]. The used dipole chamber [2] is shown schematically in Fig. 1. The wall temperatures *T*01, *T*02,… were measured at four selected chamber positions (see Fig. 1,2). A quadrupole mass spectrometer installed outside the magnet was used for residual gas analysis.

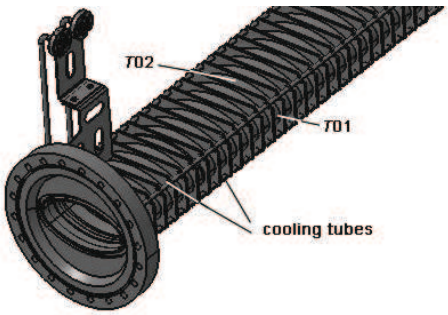

Figure 1: Prototype of the dipole chamber with LHe-cooling tubes installed inside the BNG magnet

The tests were carried out under real operating conditions using several relevant magnet ramping cycles for future SIS100 operation. Detailed parameters of all cycles can be found in [3]. Here, only one critical cycle is considered more closely. This cycle corresponded nearly to the real cycle 2c, which causes the second highest eddy current losses of all cycles. The results obtained with this cycle are depicted in Fig. 2. The measurements show that the chamber responds immediately to magnet ramping with an increase in temperature. The dipole chamber walls heat up from 5…6.8K to maximum temperatures of 12…14K. At these temperatures, only He and H_2 are released from the chamber walls. All other residual gases remain stuck to the cold walls. Helium desorbs completely from the walls, indicating that He can not be removed by wall-pumping during machine operation. Therefore, auxiliary pumps are needed for He. In contrast, H_2 desorbs intensively only after ramping start. After passing a short-term maximum the hydrogen partial pressure declines again to twice the initial value. From this finding it can be concluded that even under dynamic conditions a certain fraction of hydrogen can be pumped by the walls.

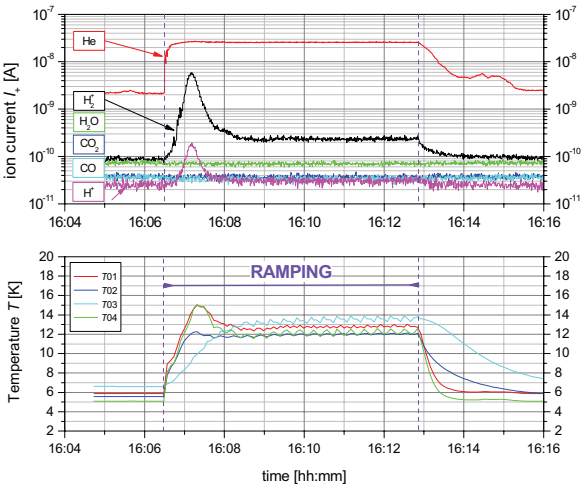

Figure 2: Chamber temperatures and partial pressure conditions during magnet ramping

Conclusions

Since the chamber temperature does not exceed 15K during magnet operation, the design concept of the tested dipole chamber with supplementary LHe cooling tubes has been proved to be suitable for SIS100 machine.

References

[1] E. Fischer, et al., IEEE Trans. Applied Superconductivity, 18(2) (2008), 260 - 263
[2] S. Y. Shim et al., Proc. ICEC, 22-ICMC (2008), 705-710
[3] E. Fischer, et al.: “Thermodynamic properties of fast ramped superconducting accelerator magnets for the FAIR project”, CEC/ICMC 2009, June 2009, Tuscon

Development of a Cryocatcher Prototype for SIS100*

L. Bozyk[1,2], D. H.H. Hoffmann[1,2], H. Kollmus[1], and P. Spiller[1]
[1]GSI, Darmstadt, Germany; [2]TU Darmstadt, Germany

Introduction

The central accelerator SIS100 of the FAIR-facility will provide high intensity ion beams. In order to reach the FAIR goals for heavy ion intensities, intermediate charge stats are used. Thereby intensity losses due to stripping processes can be avoided and the limit by space charge can be shifted to higher number of particles. However, such ions can be further ionized by collisions with residual gas molecules and get lost after the next dipole group. At the region of impact a local pressure bump is created by ion stimulated desorption which increases again the probability for further ionization.

The ion optical lattice of SIS100 has been designed such, that stripped beam ions are not lost uncontrolled on the beam pipe, but at defined highly localized positions in the cryogenic arcs [1]. This loss distribution allows the installation of an efficient ion catcher system with a dedicated low desorption yield surface for lost ions. Almost 100% of U^{28+}-ions which loose an electron can be caught by this catcher system.

Design of the Cryocatcher

The cryogenic environment around the catcher acts as a powerful cryo pump. The cryocatcher itself will be kept at a higher temperature to avoid freezing out of gases on the area of ion impact which would result in a higher desorption yield.

In figure 1, the design of the cryocatcher is sketched. Its distance to the revolving beam is chosen such that it does not define the accelerator's aperture while the catching efficiency is maximal. For the prototype two different geometries are foreseen: A block catcher as indicated in the figure, similar to the ion catchers installed in SIS18 and a wedge catcher with a stair like structure. This catcher provides a perpendicular surface for incident ions and it shields the desorbed molecules from the revolving beam.

The ion catcher is thermally and mechanically hooked up in a dome whose top is connected to the surrounding cryostat's thermal shield. In this way, the ion catcher's temperature is stabilized. The dome keeps the temperature gradient between the ion catchers temperature (50-80 K) and the cold chamber wall (5 K) stable and provides a thermal resistance to keep the heat load onto the 5 K level small. The outside of the chamber is coated with 2 mm copper to provide a uniform low temperature distribution. Together with the inner secondary chamber sheets, a big pumping surface emerges. The chamber coating is connected via flexible copper straps to the liquid helium supply.

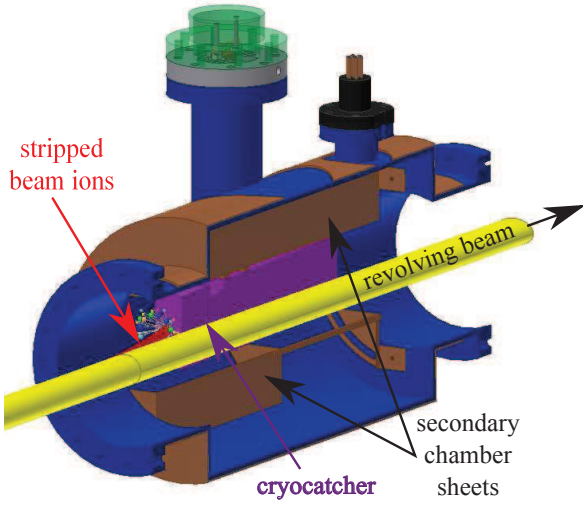

Figure 1: Illustration of the working principle and the design of the cryocatcher (purple): Vacuum chamber in blue, surrounding copper coating in brown, revolving beam in yellow, ionized beam ion trajectories in red, desorbed gases as colored balls, cold surfaces (secondary chamber plates) in brown.

The prototype is located inside a small cryostat which will be mounted in an experimental cave at GSI. The setup will be connected to an existing warm beam line through a cold warm transition.

Testing of the Prototype Cryocatcher

Heavy ion beams will be used to expose the setup to realistic conditions. The pressure rise during ion bombardment inside the vacuum chamber will be measured while varying different parameters like the ion catchers temperature and its coverage by residual gas molecules. The results are important input parameters for the simulation of SIS100 with StrahlSim [2, 3].

The construction and test of the cryocatcher prototype at GSI is a workpackage of the EU-FP7 project COLMAT. The tendering process for construction and manufacturing has been started. The test setup is expected to be completed in the middle of 2010. A beamtime request has already been submitted.

References

[1] P. Spiller et al, Proc. of ICFA04 (2005)
[2] C. Omet et al, New Journal of Physics 8, 284 (2006)
[3] P. Puppel et al, this annual report

* Work supported by EU (FP7 project COLMAT) and FIAS

Numerical calculation of ring coupling impedance for synchrotron accelerators SIS-18 and SIS-100*

L. Hänichen[1], O. Boine-Frankenheim[2], W.F.O. Müller[1], and T. Weiland[1]

[1]Technische Universität Darmstadt, Institut für Theorie Elektromagnetischer Felder (TEMF), Schlossgartenstrasse 8, 64289 Darmstadt, Germany; [2]GSI, Darmstadt, Germany

Introduction

Coupling impedances are the source of coherent instabilities and corresponding beam intensity limits for the operation of high current accelerators such as the SIS-100 synchrotron for the GSI FAIR project. The impedance contributions caused by the multiple types of beamline components need to be determined for stability studies. The coupling impedances are defined as follows:

$$Z_{||}(\omega) = \frac{1}{q^2}\int d^3x E \cdot J_{beam}, \qquad (1)$$

$$Z_{x,y}(\omega) = \frac{i}{q^2\Delta}\int d^3x \rho_{x,y} \cdot (E_{x,y} \mp vB_{y,x}), \qquad (2)$$

where E is the longitudinal electric field and $E_{x,y}$ and $B_{y,x}$ are the transverse electric and magnetic fields excited by the beam.

Main objectives

Coupling impedances can be determined in three ways: through bench measurement [1, 2], (semi-)analytically [3] or numerically by solving a discretized form of Maxwell's equations. The analytical method is typically limited to geometries that exhibit symmetry. Reference examples for beamline components have been chosen such as resistive pipe, step transition and ferrite yoke. For these examples the obtained numerical solutions have been compared with analytical expressions. A bench setup for beam coupling impedance measurement is subject for discussion.

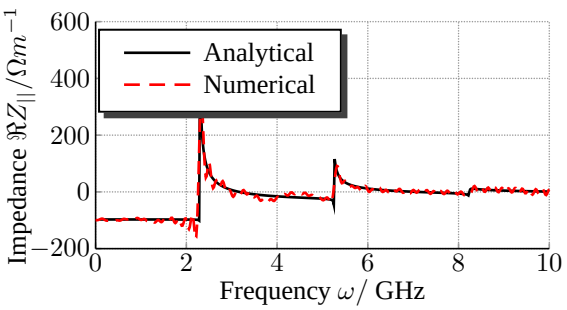

Figure 1: Real part of the coupling impedance for a step-in transition with step ratio p=0.2.

Numerical results

This problem can either be adressed in the time domain using FDTD 3D wake field solvers or in frequency domain, making use of the time harmonic description of a circulating point charge. Figure 1 compares the numerical and analytical results for a step transition.

Bench measurement requirements

The method in [1] is based on a high relativistic beam which EM field is purely transverse and similar to a TEM wave. Thus the energy loss of the TEM wave corresponds to the energy lost by the beam. This coaxial wire method has been practiced many times, however, its applicability for non-relativistic heavy ion beams has to be studied.

Summary and Outlook

Impedance calculation for exemplary geometries has been carried out using CST PARTICLE STUDIO®. For a frequency range up to several GHz, time domain wake codes are convenient to use. If the frequency decreases, the length of the exciting bunch increases and so does simulation time. At this point the time domain approach reaches its limitations. For capturing hysteresis effects of ferrite yokes, an alternate frequency domain solver as introduced in [4]. All recent results are summarized in [5]. Future work will account for low β beams and seek for opportunities to include this in eventual bench measurements.

References

[1] M. Sands and J. Rees, "A Bench Measurement of the Energy Losses of a Stored Beam to a Cavity.", SLAC report, 1974, Stanford.

[2] F. Caspers, "Bench methods for beam-coupling impedance measurement.", Lecture Notes in Physics, 1992, Geneva.

[3] A. M. Al-Khateeb, O. Boine-Frankenheim and R.W. Hasse "Comparison of the longitudinal impedance from different source terms.", Nucl. Instruments and Meth. in Physics Res. A, 2008.

[4] B. Doliwa, H. DeGersem and T. Weiland, "Numerical calculation of coupling impedances for kicker modules.", FAIR report, 2006, Darmstadt.

[5] L. Hänichen, O. Boine-Frankenheim, A.M. Al-khateeb, W.F.O. Müller and T. Weiland "Application of time and frequency domain methods for coupling impedance calculation.", Proceedings of the ICAP, 2009.

* Work supported by GSI under contract DAWEI2.

Technical Studies for a Radiation Hard Slow Extraction System of SIS100

N. Pyka[1], U. Blell[1], E. Mustafin[1], C. Mühle[1], M. Petryk[1], I. Petzenhauser[1], A. Smolyakov[1, 2], and P. Spiller[1]

[1]GSI, Darmstadt, Germany, [2]ITEP, Moscow, Russia

Slow extraction of SIS100 generates unavoidably beam loss in a local area of the extraction straight section. This beam loss is mainly originated by the interaction of the beam ions with the wires of the electrostatic septum. Where in case of intermediate charge state operation, the beam ions are fully stripped and consequently deflected against the beam pipe by the next quadrupole system. A further challenge is the high specific energy deposition of heavy ion beams of high intensities in the wires of the electrostatic septum (~Z^2) which may lead to a temperature rise up to the limit of mechanical stability. Therefore, developments for a radiation hard electrostatic septum and warm quadrupole doublet are being conducted.

Energy deposition in the electrostatic septum

In the process of slow extraction, unavoidably beam loss is generated by the interaction of beam ions with the wires of the electrostatic septum, see figure 1. At the extraction of partially stripped ions (e.g. U^{28+}, green) the charge state is further enhanced by the interaction process up to the equilibrium charge state at the relevant beam energy (typically fully stripped, e.g. U^{28+} => U^{92+}). The fraction of beam ions interacting with the wires (purple) is lost by its strongly mismatched magnetic rigidity to a large extent in the following quadrupole doublet[1, 2]. The energy deposition of heavy ions in the septum wires has been determined with the ATIMA and FLUKA codes[2]. With uranium at an energy of 2.7 GeV/u, the energy deposition in a Tungsten wire of Ø25 µm amounts to 108 MeV per lost ion. The range of the U ions is 27 mm in a Tungsten plate at this energy.

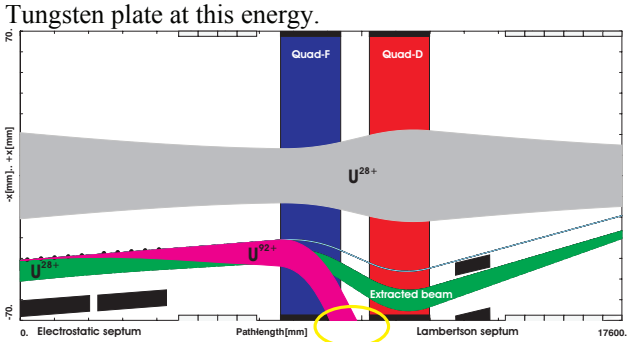

Figure 1: Beam loss of a U^{28+}-beam due to charge increase in the wires of the electrostatic septum. As a consequence of the energy deposition, the warm (not cryogenic) post quadrupole doublet is foreseen.

Figure 2 shows the maximum beam loss as a function of the jump length and wire thickness. In order to assure a non-critical operation temperature, the intense beam of SIS100 requires a rather thin wire (Ø25 µm in comparison with Ø100 µm of the SIS18 septum wires) of a W-Re alloy. A typical step width for the extracted particles is 8-12 mm. The smaller wire diameter allows for a smaller step width. A large Re fraction (~25%) in the alloy assures the necessary ductility and stability of the wires in the temperature range of operation. In order to pull a wire in case of a break quickly from the HV area, a spring has to keep the wires under a defined tension. In this way it can be avoided that a wire touches the cathode and produces short-circuits which may degrade the surface quality of the cathode. The most suitable tension for the thin wires at their expected operation temperature is being investigated experimentally.

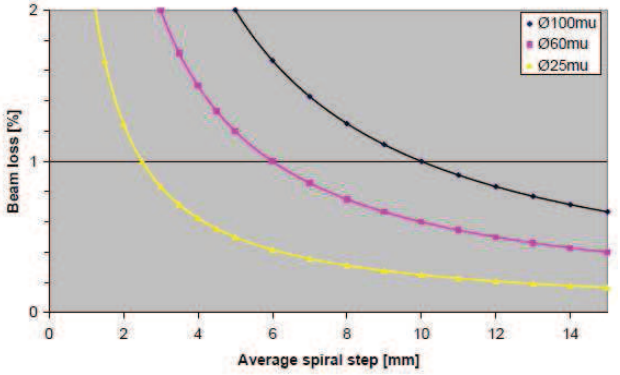

Figure 2: Maximum beam loss at an electrostatic septum wire as a function of the step width at slow extraction.

Warm quadrupole magnets following the electrostatic septum

Due to its large stopping power, uranium ions at 2.7 GeV/u are stopped within a range of 51 mm in an iron target, or here in the quadrupole chamber and yoke. The radiation behind the interaction zone is dominated by neutrons[3] which transport most of the energy. We estimate a total beam loss due to slow extraction of up to 5% during normal operation[1]. This represents at maximum a total energy of 2.6 kJ of a uranium beam with $5x10^{11}$ ions. Hence, in order to avoid quenching of superconducting magnets, radiation hard warm quadrupoles will be used here. A split-coil construction will be investigated with a gap in the yoke in the horizontal plane. Such a design would allow dumping the ions in an adjacent radiation protection installation. Thereby, the lifetime of these magnets may be considerably increased.

References

[1] FAIR Technical Design Report SIS100 (2008) 29
[2] A. Smolykov et al, EPAC08-THPP102 (2008) 3602
[3] O. Yordanov et al, Nucl. Instr. and Meth. in Phys. Res. B240 (2005) 863

Test Set-up of a Bipolar SIS100 Kickersystem

K. Samuelsson[1, 2], U. Blell[1], P. Spiller[1], J. Florenkowski[1], I. Petzenhauser[1] and V. Hinrichsen[2]
[1]GSI, Darmstadt, Germany; [2]TU Darmstadt, Darmstadt, Germany.

Introduction

SIS100 is one of the main accelerators planned for the FAIR project. The extraction kicker system of SIS100 enables bipolar kicks and can be used for fast extraction- and emergency dumping. A test set-up for the final power stage of the corresponding pulse power generator, including its load is being prepared. This project is based on the findings and suggestions of [2] and [3].

Motivation

Since bipolar kicker systems with a similar electrical configuration have so far not been realized elsewhere, a potential cross-talk between the two Thyratrons switches must be experimentally investigated. The pulse will be generated at a large distance from the kicker magnet and is transported to the kicker by means of a transformer, for potential detachment, and a transmission line. Therefore, it is necessary to verify the theoretically expected pulse shape at the kicker magnet. The test set-up shall also clarify which placements and configurations of the end resistors are most favorable. For cost reasons, the performance of the two Thyratrons CX2004X and CX1171 will be compared. CX1171 is the cheaper one, but CX2004X shows a higher hold-off voltage.

Set-up of a bipolar pulse power generator

Figure 1 shows the principal configuration of the planned test set-up.

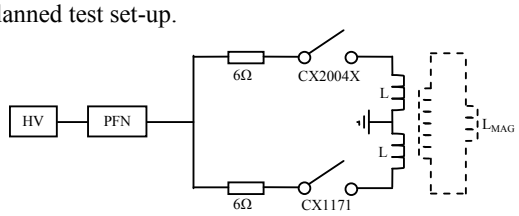

Figure 1: Principal test set-up

An eight-cell PFN, with an impedance of 6Ω, will be charged up to voltages between 10 kV and 80 kV. With triggering of one of the two Thyratrons, the PFN can be discharged with a pulse duration of 7µs over an end resistance of 6Ω. These parameters can be found in Table 1. The parameters correspond to the final design of the bipolar kicker of SIS100 with one exception: The final PFN will be constructed of 22 cells instead of 8. This change has only an influence on the quality of the discharge pulse. For the test set-up the quality is not of interest, only the pulse length is important which will not differ in both configurations. In Figure 2a simulations of the current pulse from the eight-cell PFN are shown. In the first seven cells C=80nF and L=2.9µH and in the last cell L=4µH.

The additionally added inductances L represents approximately the primary side of a pulse transformer, which is used in the kicker circuit for potential detachment. The parts of the secondary side, which are shown in Figure 1 with a doted line, will not be considered in this set-up.

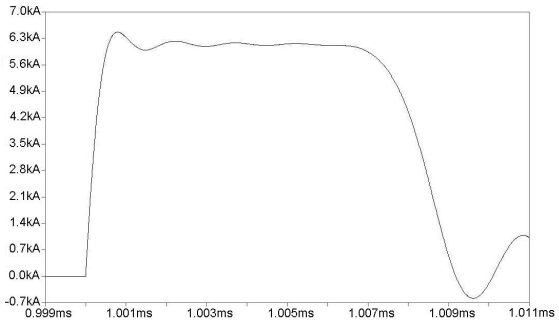

Figure 2: Simulation of PFN pulse form.

The first part of the test will focus on the cross-talk between the Thyratrons. Therefore at this stage the impedances L will be ignored. Cross-talking here implies that both Thyratrons become conductive, although only one was trigged. This results in two pulses which cancel each other. If cross-talking occurs, suitable counter measures should be developed within this project.

In the second part of the testing, the transfer of the pulse to the kicker magnet L_{MAG} will be in the focus (see Figure 1). Here, the impedances L must be considered, since they represent the primary side of the transformer which detaches the magnet potential from the PFN.

Technical specifications

Table 1: Main electrical parameters of the bipolar emergency/extraction kicker system of SIS100

Max. voltage	70 kV
Max. magnet current	5833 A
Characteristic impedance	6 Ohm
Rise- and falling time	800 ns
Max. pulse length	7.0 µs
PFN(final set-up)	N=22
PFN (test set-up)	N=8

References

[1] P. Spiller et al., "Technical Design Report on the SIS100 Synchrotron", p. 141.
[2] T. Wietoska, "Optimierung der Ansteuerung von Ablenkmagneten in Teilchenbeschleunigern unter besonderer Berücksichtigung halbleiterbasierter Lösungen", D17 Darmstädter Dissertation, Darmstadt, 2008
[3] PPT Design Studie, internal communication

Design and Tests of the SIS100 BPM Prototype

P. Kowina, M. Freimuth, and J. Macavei
GSI, Darmstadt, Germany

Design Considerations

All Beam Position Monitors (BPMs) of the superconducting SIS100 synchrotron will be installed inside the cryostats of the quadrupole doublets. As discussed in [1,2] only a solution based on ceramics is able to withstand the temperature changes between room temperature and liquid helium temperature and to fulfill the tight requirements of mechanical stability and reproducibility [1] (see Fig. 1). The Al_2O_3 ceramic pipe with an inner diameter of 135 mm and a wall thickness of 4 mm is metalized on the inner side with a 40 μm MoMn layer. The electrode- and guard ring pattern is formed by cutting grooves into the metalized layer. The configuration of the electrodes and guard rings was optimized using FEM simulations as described in [1, 3]. The ceramic pipe is fixed only on one side to a rigid plate being a part of the joke of the prescending quadrupole magnet. This allows precise and mechanically stable positioning of the BPM with respect to the center of the quadrupole. To compensate different contraction coefficients of the materials used in the BPM design the opposite side of the ceramic pipe slides on the inner part of the BPM chassis on CuBe contact ribbons.

Production of SIS100 BPM Prototype

Prior to the production of the SIS100 BPM prototype the feasibility of the manufacturing process had been verified. The main challenge was the pattern forming in the metal layer coating the inner ceramic wall. The precision of the cuts results directly in the later linearity and accuracy of the beam position determination. Therefore, to reach the required accuracy of the beam position determination [1], the tolerance of cut widths and parallelism of their edges should not exceed $\pm 0,1$ mm. For the given electrode pattern the only applicable technique is blasting of the metalized surface. Two methods of blasting were compared. The first attempt was to locally remove the metalized layer

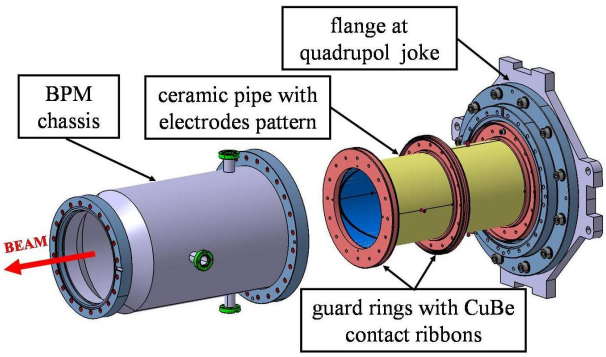

Figure 1: Design of the SIS100 BPM. For better visualization the BPM chassis was moved out in beam direction.

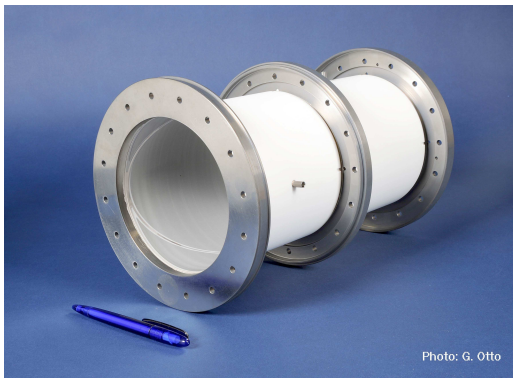

Figure 2: Prototype of the interior part of SIS100 BPM.

by blasting trough a nozzle mounted on a mechanized support. Unfortunately, the capability of this method could only be proven on samples in the shape of a half cylinder. For the treatment of a ceramic tube the blast head had to be positioned through the side opening. This would have required a development of a dedicated tooling and would have severely increased the costs of the prototype fabrication. Instead, an alternative method was used for the production of a second sample with an electrode pattern similar to the final one. In this case a mask was used to cover the parts of the metalization that should not be removed during blasting. Here the blast head was introduced from one side of the pipe. The global symmetry of the pattern was positively verified by measurements of the electrodes capacity with respect to ground potential as defined by guard rings. The cut widths and their parallelism were investigated by profile measurements. For this purpose the fragment of sample was cut to fit into the profile measurement device. A mean deviation of the cut widths in the order of $\pm 0,2$ mm was observed. However, for the production of the prototype shown in Fig. 1 these problems were eliminated by extending the blasting duration and better mask positioning. The improved method of mask blasting was chosen as less expensive and satisfying all requirements for the metalization process and realization of the electrode pattern.

Further developments for the SIS100 prototype will include production of the BPM chassis (see Fig. 2) and integration of signal feed-throughs. All components will be tested under cryogenic conditions using a cryogenic test setup that was successfully commissioned in January 2009.

References

[1] P. Kowina et al., *Proc. EPAC'06*, Edinburgh, p.1022 (2006).
[2] P. Kowina et al., *Proc. DIPAC'09*, Basel, p.35 (2009).
[3] P. Kowina et al., *Proc. DIPAC'07*, Venice, p.96 (2007).

Cryogenic Tests of Matching Transformers for SIS100 BPM

M. Freimuth, W. Kaufmann, P. Kowina, and H. Rödl
GSI, Darmstadt, Germany

Introduction

The optimization presented in this contribution was focused on the coupling path of the synchrotron Beam Position Monitors (BPM) to low noise amplifiers with 50 Ω input impedance. As already discussed in [1], only a solution based on matching transformers (MT) can meet the requirements of reflection-free signal transfer through the long lines without loading the capacitive BPM by 50 Ω. Transformers based on Vitroperm-500F toroidal cores were chosen due to their high permeability and high saturation magnetic induction B_s [2]. Since the MTs will be installed inside the insulation vacuum of the SIS100 cryostat [3], they have to be suitable for cryogenic temperatures. To improve rf-features, i.e. linearity and resonance-free transmission, the MT PCB have to be designed carefully. The performance of the MTs was tested in liquid Nitrogen and liquid Helium using a new cryogenic test setup that was successfully commissioned in January 2009.

Investigations on Coupling Transformers

The transmission function is the most important MT parameter and can be determined by a vector network analyzer with the scattering parameter S_{21}. For the new MT with optimized PCB-layout the transmission is very linear over a broad frequency range exceeding significantly the required bandwidth. This can be seen in Fig. 1 where the frequency dependence of S_{21} measured at different temperatures is shown. The table in Fig. 1 summarizes the useful MT bandwidth (defined as the frequency range, in which the S_{21} variation is smaller than $\pm 0.1\,dB$). Since the bandwidth grows with decreasing temperature the new MT based on a Vitroperm-500F core can be successfully used in the cryogenic environment. The high linearity of the MT transmission can be deteriorated, mostly at lower frequencies, by core saturation that occurs for the highest expected BPM signal amplitudes. First investigations of the former

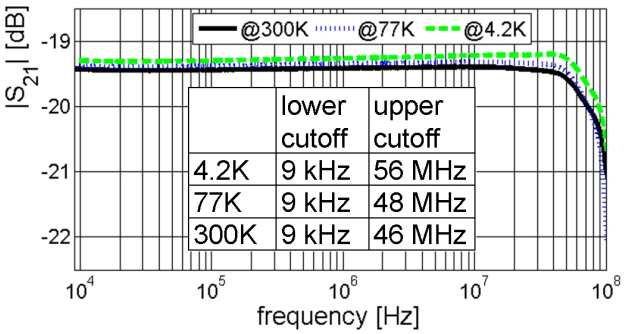

Figure 1: Transfer function of the newly designed MT at different temperatures. MT-core dimensions $\varnothing_A$:22 mm $\varnothing_i$: 10.5 mm h = 10 mm and winding ratio 18:2.

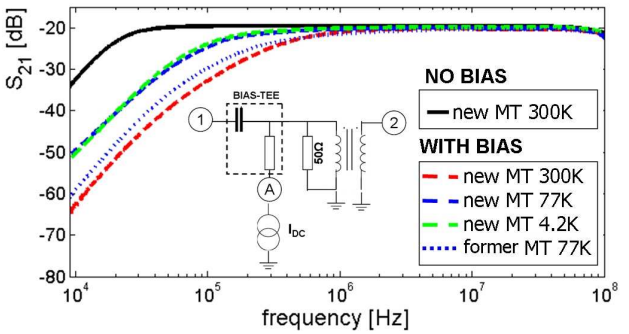

Figure 2: Transfer functions measured with and without DC bias at different temperatures, see text.

MT type had shown strong saturation effects ranging from 40 dB at 100 kHz down to 5 dB at 1 MHz [4], respectively. Even though, the deviation in the order of few dB might seem negligible, it exceeds the allowed value by almost two orders of magnitude [3]. To reduce the saturation influence on the transfer function, the new MT toroidal cores have a larger cross section than the previous design [4]. To simulate the core saturation the primary MT winding was biased with DC current via BIAS-TEE using a setup schematically shown in Fig. 2. The solid line in this figure presents the transmission function without DC bias and corresponds to that in Fig. 1. The additional low frequency limitation is caused by the high pass characteristics of the BIAS-TEE. The dashed lines show the transmission at the bias current of 450 mA which is equivalent to the highest expected signal amplitude of 1.8 kV [3]. Note, that the saturation effects at the low temperatures (77 K and 4.2 K) are much smaller than at room temperature due to the temperature dependency of the saturation polarization. This tendency, observed already for other nanocrystalline alloys [5], is advantageous when MTs are operated at cryogenic conditions. Moreover, the newly designed MTs, with the larger toroid cross section, are by a factor of two less bias sensitive in comparison to the preliminary used cores (doted line). To minimize the offset of the BPM position determination the MTs have to be pairwise balanced within 0,1 dB. Therefore, the geometry of windings will be stabilized using Staycast epoxy. The choice of the epoxy material used for this purpose was verified under cryogenic conditions.

References

[1] J. Schölles,et.al., DIPAC 2003.
[2] http://www.vacuumschmelze.de.
[3] P. Kowina,et.al.,EPAC2006.
[4] P. Kowina,et.al.,GSI Scientific Report 2007.
[5] R. Grössinger,et.al.,Advanced Engineering Materials - Volume 5 Issue 5, Pages 285 - 290,Wiley, 2008.

Damage Assessment for the SIS100 and the LHC Beams*

N.A. Tahir[1], A. Shutov[2], I.V. Lomonosov[2], P. Spiller[1], and A.R. Piriz[3]
[1]GSI, Darmstadt, Germany; [2]IPCP, Chernogolovka, Russia; [3]UCLM, Ciudad Real, Spain

For the design of the SIS100, the potential destruction at an accidental impact and total loss of the SIS100 beam has been studied and compared with the LHC beam. These studies have been performed to determine the requirements for a suitable machine protection system for the SIS100. The beam–matter interaction of the SIS100 and the LHC beams are quite different. Due to the higher effective charge Z^2, the stopping power of a single heavy ion is in general stronger and the range much shorter than of a Proton. However, the LHC beam as a whole carries a tremendous total energy (362 MJ). A full perpendicular impact of an SIS100 and an LHC beam on any accelerator component with a typical size as given by the regular lattice and the beam emittance has been studied. Previous simulations

Table 1: Main Beam Parameters

	LHC	SIS100
Ion Species	Protons	Uranium
Total Number of Particles	$3.2\text{x}10^{14}$	$5\text{x}10^{11}$
Total Number of Bunches	2808	8
Bunch Length (ns)	0.5	190
Bunch Separation (ns)	25	270
Beam Duration (μs)	89	3.4
Particle Energy (TeV)	7	0.6426
Gaussian Profile [σ (mm)]	0.2	3.376
Specific Energy Deposition (kJ/g)	25.0	2.2

have shown that [Tahir et al., PRE 79 (2009) 046410 and LPB 27 (2009) 475] the energy deposited by few tens of bunches in solid targets will severely damage the target. The LHC protons will penetrate up to 35 m in solid copper and up to 10 m in solid carbon.

In the present contribution we report numerical simulations of the hydrodynamic and thermodynamic response of a solid cylindrical copper target that is facially irradiated with the SIS100 beam. The target has a length of 6 cm and a radius of 2 cm, respectively. The simulations have been carried out using a 2D hydrodynamic code, BIG2. In Fig. 1 we present the specific energy distribution in the target at the end of the SIS100 beam. It is seen that the maximum specific energy deposition in the Bragg peak region is 2.2 kJ/g. The corresponding temperature distribution is plotted in Fig. 2 that shows a maximum temperature of the order of 4200 K which is high enough to evaporate the target material. The density distribution is presented in Fig. 3 that shows that in the density along the axis has been signif-

* Work supported by the BMBF and EU project EuCARD: Colmat

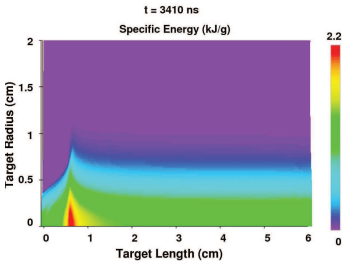

Figure 1: Specific energy deposition at the end of the pulse.

icantly reduced and has a minimum value of about 6 g/cm^3 at the location of the Bragg peak. This is due to the radially outgoing shock wave that is generated by the high pressure (12 GPa) produced by the energy deposited by the first three bunches.

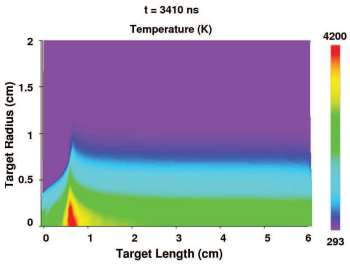

Figure 2: Temperature distribution at the end of the pulse.

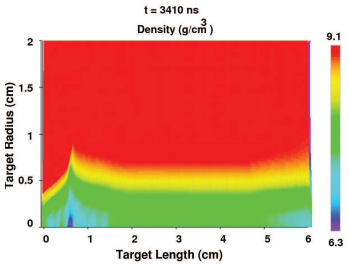

Figure 3: Density distribution at the end of the pulse.

It is thus concluded that like the LHC beam, the SIS100 beam will also cause considerable damage to the equipment in case of an accidental release of the particles.

Electron Cloud Studies for SIS-18 and for the FAIR Synchrotrons

F. Petrov[2], O. Boine-Frankenheim[1], and T. Weiland[2]
[1]GSI, Darmstadt, Germany; [2] TU-Darmstadt, TEMF, Darmstadt, Germany

Introduction

Electron clouds (EC) generated by residual gas ionization pose a potential threat to the stability of the circulating heavy ion beams in the existing SIS-18 synchrotron and in the projected SIS-100. The electrons can potentially accumulate in the space charge potential of the long bunches. As an extreme case we study the accumulation of electrons in a coasting beam under conditions relevant in the SIS-18.

Previous studies of EC in coasting beams [1] used Particle-In-Cell (PIC) codes to describe the generation of the cloud and the interaction with the ion beam. PIC beams exhibit much larger fluctuation amplitudes than real beams. The fluctuations heat the electrons. Therefore the obtained neutralization degree is strongly reduced, relative to a real beam. That is why it is important to develop a new model of EC generation in FAIR synchrotrons.

Model and Results

Our PIC code is using ionization cross sections given by expressions proposed in [2]. These cross sections have higher values than those used in [1] and give good agreement with experimental ones. We assume that the beam propagates in a drift section inside a cylindrical beam pipe. In order to account for the beam induced heating of electrons we add a Langevin term to the electron equation of motion. The code was benchmarked with the simple analytical model proposed in [3] for Ar^{18+} and U^{73+} coasting beams. For thick beams filling the pipe the agreement is good. However, the model used in [2] does not include electron space charge and overestimates value of neutralisation degree (η) for SIS-18 conditions.

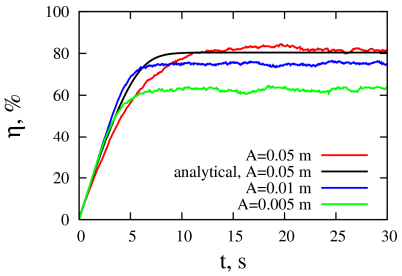

Figure 1: η evolution for a 11.4 MeV/u Ar^{18+} coasting beam with 10^{10} ions as a function of the beam radius A. The black curve shows the result of the analytical model for a thick beam filling the pipe.

In order to solve this problem the analytical theory was extended to include space charge. In this modified model η does not exceed 100% however it stays at level of 80% like in the PIC simulation (Fig. 1). The saturation time varies from 2 to 5 s for U^{73+} and Ar^{18+} correspondingly. Our study confirms that the final neutralisation degree does almost not depend on the type of ion species.

The effect of transverse Schottky beam fluctuations on the electron concentration was studied. The electrons where excited by a Schotty side-band overlapping with the electron frequency distribution (Fig. 2). Preliminary studies indicate that the EC build-up is insensitive to this perturbation. We also studied the effect of electron reflection and secondary emission at the beam pipe.

For coasting beams the EC concentration showed to be independent of the reflection from the wall and of the secondary emission yield (SEY) due to the low impact energy of the electrons.

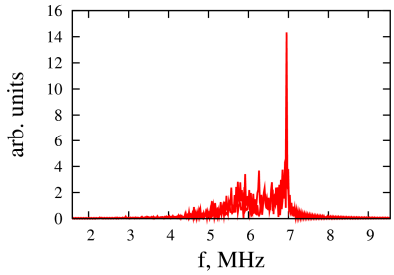

Figure 2: Electron transverse oscillation spectrum for a 11.4 MeV/u U^{73+} beam with A = 0.03 m and 10^{10} ions.

Discussion and Outlook

It is shown that the EC concentration in coasting beams may reach significant values in SIS-18. However, the maximum values for η will be lower due to the growing two-stream instability [4]. The instability threshold will be reached for a neutralization degree of a few percent. This is why detailed analytical and numerical studies of the instability threshold η are presently being performed. A key quantity is the transverse impedance of the EC. The impedance obtained from PIC simulations will be compared to the expression given in [4]. This impedance as well as the predicted neutralization degree will be verified in upcoming SIS-18 machine experiments. The bunching of the beam may also cause to a significant decrease in η. At the same time SEY will start playing a role.

References

[1] G. Rumolo et al, Proceedings of EPAC 2004, Lucerne, Switzerland, p 1963-1965
[2] I. Kaganovich, E. Startsev, R. Davidson, N. J. Phys. 8 (2006) 278
[3] P.Zenkevich, N. Mustafin, O. Boine-Frankenheim, Proceeding of Ecloud 2002, CERN, April 2002, Yellow Report CERN-2002-001
[4] K. Ohmi, T. Toyama, M. Tomizawa, Proceedings of 2003 PAC, p.3083-3085

Shielding Calculations for the SIS 100/300

K. Vogt and G. Fehrenbacher
GSI, Darmstadt, Germany

Introduction

The planned new Heavy Ion Synchrotron SIS 100/300 for the FAIR Project will consist of two separate tunnels. In addition to the tunnel where the beam lines itself will be situated, there will be an additional tunnel, for maintenance and supply purposes. This maintenance tunnel is desired to be accessible for technical personnel also during beam operation.
Therefore, from the radiation safety point of view, not only the activation of the soil and ground water surrounding the tunnels needs to be considered [1], but also the prompt dose rates resulting from the operation of the accelerator, especially in the maintenance tunnel. In order to estimate the dose rates, Monte Carlo calculations have been performed using the computer code FLUKA [2,3].

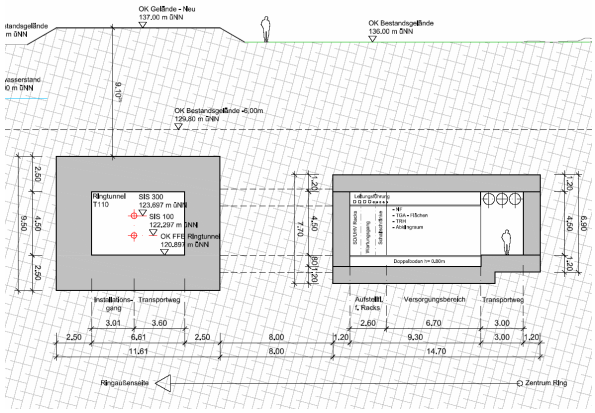

Figure 1: SIS 100/300 cross sectional area

In Fig. 1, a cross sectional cut of the SIS 100/300 is shown. The beam tunnel on the left side and the maintenance tunnel on the right side are separated by 8 meters of soil. For technical reasons, numerous shafts connecting both tunnels are needed. In order to reduce the amount of radiation transported through these shafts they are not horizontal but diagonal (see Fig.2).

Results

The results of the FLUKA calculations are presented in Figs. 2 and 3. Shown are the dose rates in Sv/h produced by a point like beam loss of 10^{10} U-238 ions per second, with an energy of 2.7 GeV/u. The shaft connecting both tunnels has a cross sectional area of about one square meter and is assumed to be empty. It can be seen that the dose rates in the supply tunnel in some places reach levels of more than 10 µSv/h, which is far above the preliminary design goal of less than 0.5 µSv/h.
It can also be seen that these high dose rates originate from the exit of the connecting shaft.

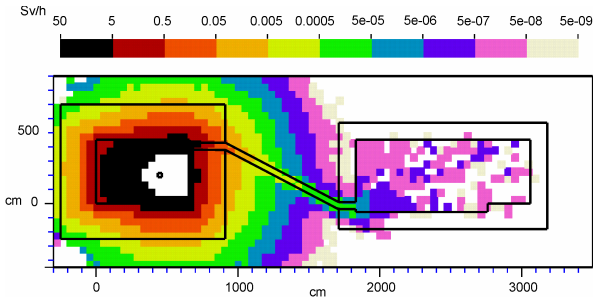

Figure 2: Dose rates calculated by FLUKA for the design of Fig. 1

As a consequence of these results, it was recommended to build an additional vertical concrete wall of 50 cm thickness in the maintenance tunnel, behind the shafts exit, in order to provide additional shielding against the emerging radiation. In order to reduce construction costs, it was also desired to reduce the distance between both tunnels. Therefore additional FLUKA calculations have been performed including the wall and only 6 meters of soil between the tunnels (Fig. 3). In this scenario, dose rates behind the wall are less than 2.5 µSv/h in all places.

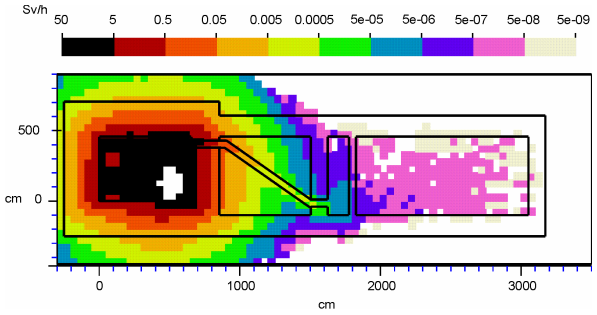

Figure 3: Dose rates calculated by FLUKA for the modified design

References

[1] K. Vogt, G. Fehrenbacher, and M. Haida, GSI Scientific Report 2008, p.100
[2] A. Fassò, A. Ferrari, J. Ranft, and P.R. Sala, CERN-2005-10 (2005), INFN/TC_05/11, SLAC-R-773.
[3] FLUKA: http://www.fluka.org

Developments for Stochastic Cooling in the Collector Ring

F. Nolden[1], R. Hettrich[1], U. Jandewerth[1], W. Maier[1], C. Peschke[1], P. Petri[1], and M. Steck[1]
[1]GSI, Darmstadt, Germany

The collector ring CR is a storage ring in the framework of FAIR which serves mainly for stochastic precooling of fresh antiproton (pbar) and rare isotope (RI) beams. These beams have different velocities (pbar: 0.97 c, RI: 0.84 c) and are cooled using different optical settings of the storage ring with different betatron amplitudes in the pick-ups and kickers. Here we discuss the final optimization of the pick-up electrodes [1] and tests with the prototype pick-up tank [2]. For details, the reader should consult the references.

Measurements of the final version of the slotline pick-up, the aluminum body and the combiner plate were performed. The frequency and phase behaviour of the measured transmission between the slotlines and our near field probe has reached an optimum. This design can now be transferred directly to aluminum oxide ceramics in order to fullfil the vacuum requirements. Preliminary mechanical prototyping was performed in collaboration with industry with satisfactory results. It is planned to manifacture and test a full ceramic pick-up module in 2010.

To accommodate beams with different velocities, a velocity switch circuit was developed, which adjusts the signal path lengths to the actual beam velocity.

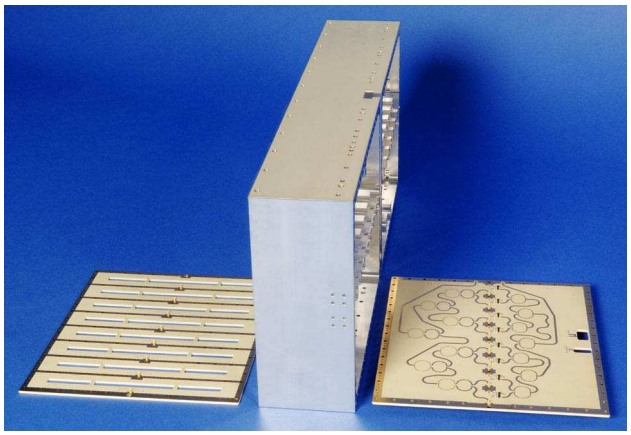

Figure 1: Slotline electrode and combiner boards with aluminum case

The prototype pick-up tank was equipped with two linear motor drives in order to perform motion tests. There is a delicate balance of mechanical forces inside the drive. The pressure difference to vacuum is compensated by appropriate spring forces which decrease the maximum motor force. Simultaneous motion of the two drives was realized. Accelerometers measure the acceleration of the movable parts in three dimensions. The parameters of the servo control for the linear motor were tuned to minimize residual accelerations which might be harmful to the sensitive microwave parts at low temperature inside the tank.

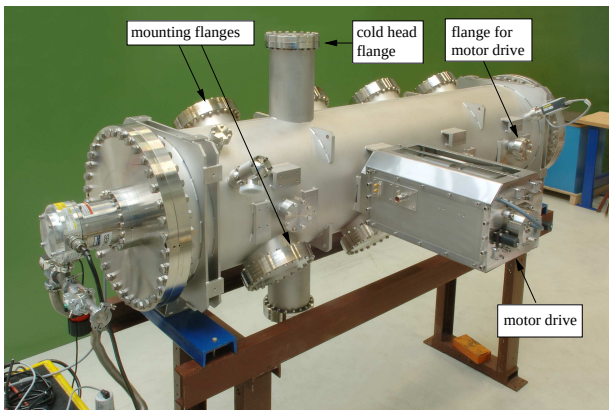

Figure 2: Prototype tank with motor drive

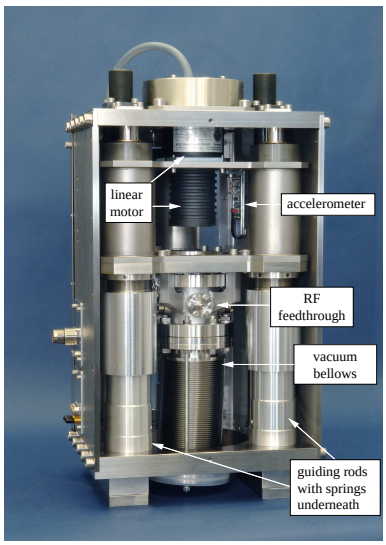

Figure 3: View into motor drive unit

The design of the interior parts of the tank was nearly completed. The pick-ups will be cooled by helium cold heads to temperatures near 20 K in order to enhance the signal to noise ratio of the pick-up signal. The cold parts are shielded from the room temperature surroundings by means of a gilded copper cylinder which is kept at a temperature of 80 K. The gold surface is 4 μm thick and has an extremely low thermal emissivity.

References

[1] C. Peschke et al., Prototype Pick-up Module for CR Stochastic Cooling at FAIR, Proc. Cool09, to be published

[2] F. Nolden et al., Prototype Pick-up Tank for CR Stochastic Cooling at FAIR, Proc. Cool09, to be published

Stochastic Cooling System for Antiproton Accumulation in the RESR

C. Dimopoulou, A. Dolinskii, T. Katayama, S. Litvinov, F. Nolden, C. Peschke, M. Steck[1], and D. Möhl, L. Thorndahl[2]

[1]GSI, Darmstadt, Germany; [2]CERN, Geneva, Switzerland.

The main purpose of the RESR storage ring in the FAIR project is the accumulation of high intensity antiproton stacks, mainly for the HESR storage ring, but also for the deceleration in the NESR storage ring which provides antiprotons for low energy experiments in the FLAIR experimental area. The high efficiency of antiproton production required for high luminosity experiments in the HESR is achieved by combining the large acceptance Collector Ring (CR) with the accumulator ring RESR. The first ring after the antiproton production target (CR) can be designed for large acceptance and for operation of a dedicated stochastic pre-cooling system. Concerning the accumulator ring RESR, this concept results in moderate requirements for the acceptance needed for injection of the secondary beam and gives more freedom for the design of an ion optical lattice which supports the accumulation process. First considerations to use a barrier bucket system for the accumulation revealed problems at high intensity operation of the stochastic cooling system, when up to 1×10^{11} antiprotons are accumulated. Consequently, it was decided to design a system for longitudinal accumulation similar to the one of the AA ring [1] at CERN or the FNAL Accumulator Ring [2].

The ion optical lattice of the RESR provides the large momentum acceptance necessary for the accumulation by coordinated longitudinal manipulations with the rf system and the stochastic cooling system. Main feature of the RESR lattice is a large flexibility in the choice of the transition energy (variable in the range $3.3\leq \gamma_t\leq 6.4$ for a fixed position of the cooling pick-ups and kickers) which is achieved by tuning of the focussing magnets. Additional ring lattice requirements come from the stochastic cooling system. The electrodes should be installed in positions with small vertical beta function. Electrodes with a small vertical gap have a high sensitivity for the beam and a small extension of the field in radial direction. This allows precise control of the electric field with a radial distribution matched to the requirements of accumulation.

The accumulation technique involves the injection of the pre-cooled antiproton bunches from the collector ring CR on an inner orbit with a momentum offset of $\Delta p/p$ = -0.8 % with respect to the central orbit. The fresh batch is accelerated by rf to the deposit orbit ($\Delta p/p$ = 0.0 %) close to the central orbit. On the deposit orbit, the combined action of two tail cooling systems acts on the beam driving the particles with an exponentially decreasing gain to an outer orbit. The particles finally end on the core orbit which has a momentum offset $\Delta p/p$ = +0.8 % relative to the central orbit. At the core position an intense stack of up to 1×10^{11} antiprotons is built up and finally cooled by the core part of the stochastic cooling system. The tail cooling systems operate in the frequency band 1-2 GHz, the core cooling system in the band 2-4 GHz. For transfer, an adjustable fraction of the stack is decelerated with rf to the injection orbit and extracted to the subsequent ring.

The effect of the stochastic cooling system on the antiprotons was studied with two different simulations codes using the Fokker-Planck equation in longitudinal phase space [3][4]. The main goal was the optimization of the system parameters for the required fast longitudinal momentum change. Important parameters are the geometry of the electrode system, the required rf power, special delays and filters to shape the correction signal. The effect of the various parameters on the cooling performance was studied and optimized with the simulation code.

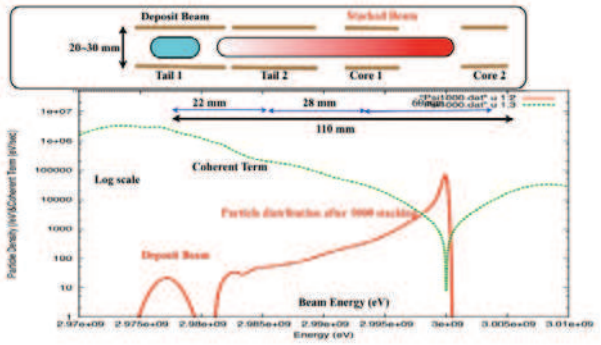

Figure 1: Radial arrangement of tail and core electrodes of the stochastic accumulation system and particle momentum distribution of the stack after 1000 injections.

The radial arrangement of the electrodes and the expected stack distribution according to the simulations are shown in Fig. 1. Because of the small emittance of the pre-cooled antiprotons (ε_v = 5 mm mrad) and of the small vertical beta function at the electrode position ($\beta_v\leq$ 4 m) the vertical gap can be as small as 20 mm. The electrodes could be of Faltin type [3]. Assuming a pre-cooled bunch of antiprotons injected every 10 s from the CR, the longitudinal distribution of the antiprotons after one thousand injection and stacking cycles was calculated. The accumulation system forms a dense core which contains a fraction of more than 90 % of the particles in a momentum window $\Delta p/p = \pm 2.5\times10^{-4}$. The accumulation scheme also works for moderate changes of the input parameters.

References

[1] H.Koziol, S.Maury, CERN-PS 95-15 (AR/BD) 1995.
[2] R. Pasquinelli et al., Proc. of PAC'87, p. 1132.
[3] D. Möhl, L. Thorndahl, GSI internal report.
[4] T. Katayama, GSI internal report.

Simulation of the Antiproton Yield for a Pulsed pbar Target

K. Knie[1], P. Sievers[2], V. Gostishchev[1] and M. Steck[1]
[1]GSI, Darmstadt, Germany; [2]CERN, Geneva, Switzerland

At FAIR antiprotons will be produced by a 29 GeV proton beam impinging on a ~10 cm long metal target [1]. As a consequence of the production of a proton-antiproton-pair, the antiproton beam is highly divergent. The angular distribution for 3 GeV antiprotons peaks at nearly 100 mrad with respect to the beam axis. In order to collect the antiprotons efficiently, a strong focusing device right after the target is indispensable. In our case, it will be a magnetic horn [2], which is capable to focus pbars with angles up to 80 mrad. It will be located ~20 cm behind the target.

At such a close distance from the focusing device, however, the target geometry deviates notedly from the ideal, point-like geometry, which results in a reduced collection efficiency. For this reason, it has been proposed to lead a high current (a few 100 kA) in the direction of the beam axis through the target. This current induces a circular magnetic field which focuses the antiprotons already in the target. At CERN, first experimental tests indicated an increase of the pbar yield by about 50 %. However, the targets were not able to withstand a continuous operation with high beam intensities [3].

In this work we simulated the antiproton yield* by means of the Monte-Carlo code FLUKA [4]. To capture 3 GeV antiprotons with angles up to 80 mrad (i.e. those antiprotons, which will be focused by the magnetic horn) in the target, about 500 kA are necessary, independently of the target radius r_t. As the temperature increase per pulse scales with r_t^{-4}, we have chosen a relatively large r^t = 6.5 mm for our first simulation. The results are depicted in fig. 1. In the 4th panel one can clearly see the focusing effect for antiprotons. However, the primary beam is defocused by the same field, thus no improvement of the yield can be achieved, as can be seen in the blue circles of fig. 2. It is obvious, that the amount of this defocusing depends on the size of the primary beam. Here, the beam particles were homogeneously distributed on a disc with r = 1 mm, which should be a realistic assumption for high intensity proton beams at FAIR.

A further simulation was performed for a Cu target with r_t = 1.5 mm, embedded in a container of a low Z material. The advantage of this setup is that antiprotons with higher angles will leave the Cu region and travel through an area with drastically reduced self absorption. In addition, a simulation with a reduced current of 150 kA was performed, which nevertheless corresponds to a temperature increase of more than 400 K during one 20 µs pulse, thus a very elaborate cooling system would be required. Whereas the advantage of the reduced self absorption can clearly be seen (see red triangles in fig. 2), the antiproton yield cannot be significantly increased by pulsing.

*the number of antiprotons, which will reach the collector ring divided by the number of primary protons

One can summarize that in all of these realistic simulations, pulsing of the target did not result in a significantly increased antiproton yield.

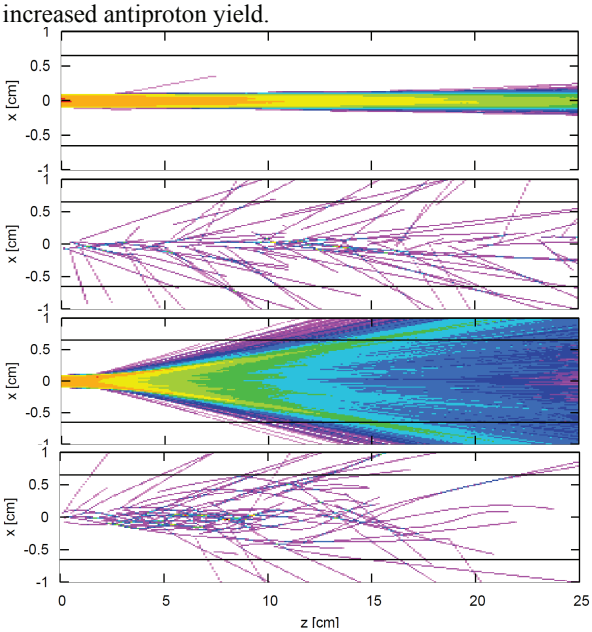

Figure 1: Particle distributions in a Cu target with a radius of 6.5 mm. Top to bottom: primary protons, not pulsed; antiprotons, not pulsed; primary protons, 500 kA pulse; antiprotons, 500 kA pulse;

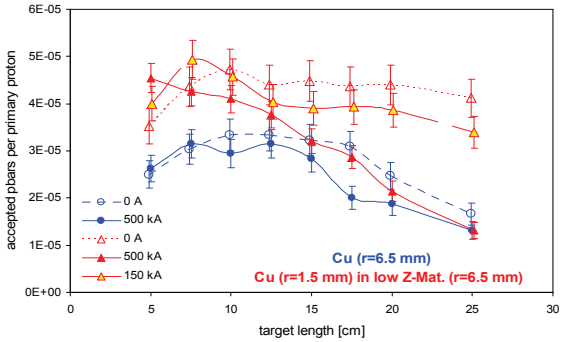

Figure 2: Antiproton yield as a function of the target length. The error bars correspond to the statistical error.

References

[1] GSI Scientific Report (2007) 59.
[2] D. Boimond et al., CERN/PS 94-02 (AR) (1994)
[3] T.W. Eaton et al., IEEE Transactions on Nuclear ScienceNS-32, No. 5, (1985)
[4] A. Fassò, A. Ferrari, J. Ranft, and P.R. Sala, CERN-2005-10 (2005), INFN/TC_05/11, SLAC-R-773.

Status of the FAIR Proton Linac

L. Groening[1#], W. Barth[1], R. Brodhage[2], G. Clemente[1], R. Gobin[3], H. Podlech[2], U. Ratzinger[2], G. Schreiber[1], W. Vinzenz[1]

[1]GSI, Darmstadt, Germany; [2]IAP, University of Frankfurt a.M., Germany; [3]CEA/Saclay, Gif-sur-Yvette, France.

Introduction

The FAIR proton linac has to provide the primary proton beam for the production of antiprotons. It will deliver a 70 MeV beam to the SIS18 with a repetition rate of 4 Hz. The room temperature linac will be located north of the existing UNILAC complex. Its conceptual layout is shown in Fig. 1 and its main beam parameters are listed in Tab. 1. An up-date of the Technical Report has been issued in Decembre 2009 [1].

Tab. 1: Main parameters of the proton linac for FAIR.

Final energy	70 MeV
Pulse current	70 mA
Protons per pulse	$7{\cdot}10^{12}$
Repetition rate	4 Hz
Trans. beam emittance	4.2 µm (tot. norm.)
Rf-frequency	325.224 MHz

Collaboration with France

The linac will be designed constructed, and commissioned within a bilateral French/German collaboration. France took responsibility for the Source&LEBT set-up, the magnets for the inflection into the transfer channel to the synchrotron, and for the BPM/phase probe devices. Additional French participation is currently under discussion. Work packages have been defined including time schedule, budgets, and manpower requirements.

Source and LEBT

The front-end system will be based on the design for IFMIF project [2] aiming to deuteron beams. Adoption of the layout for a 100 mA proton beam is progressing and first results of beam dynamics simulations are available. The construction of the solenoids with integrated steerers has started and delivery is expected within 2010. First commissioning of the front-end system is foreseen in 2011 at CEA/Saclay.

BPM / Phase Probes

The combined BPM / phase probe devices still require R&D lasting until end of 2010. A preliminary layout of the geometry is available but considerable efforts are required to estimate and mitigate the impact of primary rf-power to the bunch signal quality. The probes are to be installed within the end-tubes of the rf-cavities together with quadrupole triplets. Mayor efforts on the engineering design are imposed by the manifold of interfaces overlapping at the corresponding sections of the linac.

Rf-Cavities

The construction of a prototype cavity has been started (Fig. 2) at the Goethe University of Frankfurt. It is foreseen to be used at the operating linac for acceleration from 11.7 to 24.4 MeV.

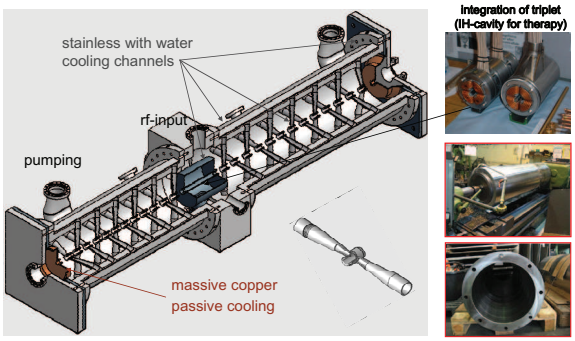

Figure 2: Prototype cavity of the proton linac.

Delivery of the cavity is expected in Spring 2011 followed by testing until late 2011. Rf-testing requires a dedicated Rf-test-stand. The klystron is already on-site, the power converter is tendered, and the missing components are to be tendered in the forthcoming months.

Beam dynamics simulations starting from the source's plasma knee up to the injection into the synchrotron demonstrated that final beam emittances are about 25% below the design value. These simulations included also a benchmarking campaign of three codes on the beam dynamics inside the 4-rod RFQ.

References

[1] *Technical Report "Proton Linac"*, Vers. Dec 2009, GSI Darmstadt, Germany, (2009).

[2] R. Gobin et al., Proc. 13th ICIS Conf., Gratlinburg, U.S.A. (2009).

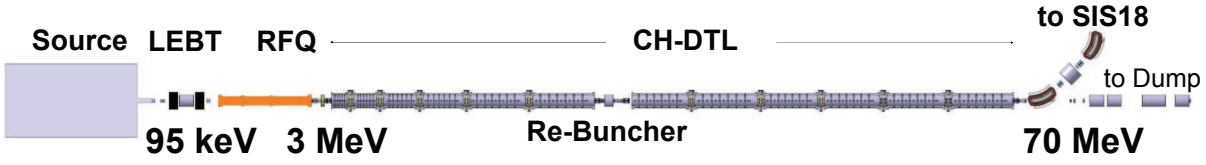

Figure 1: Conceptual layout of the FAIR proton linac.

#la.groening@gsi.de

Prototype construction of the second cavity for the FAIR proton linac.

R. Brodhage[1], U. Ratzinger[1], G. Clemente[2], S. Minaev[1], L. Groening[2], H. Podlech[1], and R. Tiede[1]
[1]IAP, University of Frankfurt, Germany; [2]GSI, Darmstadt, Germany

For the 70MeV, 35mA proton injector for FAIR a beam dynamics design based on a CH-DTL was developed successfully during the last years. This report will focus on the prototype construction of the second coupled cavity for the proton injector for FAIR. The main changes from the original layout will be presented as well as most recent developments in tuning and manufacturing.

Introduction

The linac is medchanically grouped in two tanks, having lengths of about 9m and 12m respectively. In between there will be a diagnostics section affording two lenses and one rebuncher to get a safe beam transport.

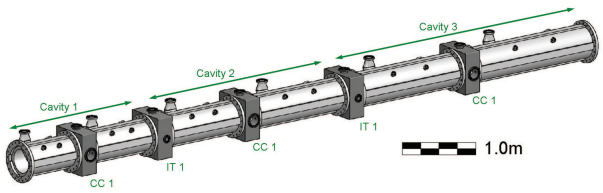

Figure 1: Outer view of the 35MeV p-linac section

The coupled prototype cavity

The low energy section consists of 13 gaps, followed by the coupling cell and by the 14 gap high energy section. The whole cavity has an inner length of about 2.8m.

Mechanical Design

As pointed out before three cavities will mechanically form one tank of about 9m. The prototype cavity probes the second cavity of the low energy section. This concept leads to tight tolerances with respect to the plane orientation of the end flanges as well as with respect to their transverse positioning against the beam axis. To avoid mechanical deformation by gravity the linac will be placed on a rail system with flexible supports - as applied on the GSI Unilac. Alternatively, each tank could be mounted on a robust support and then be aligned via a 3-point adjusting device with respect to the beam axis.

The acceleration sections of the cavity contains no screwed connections. Therefore a Q-value within 5% of the theoretical value is expected. This was demonstrated successfully by the 8-cell prototype

Status of Cavity Construction

The Construction process of the prototype cavity started in the end of 2008. At this time the outer tanks for the first and second part of the coupled cavity were ordered and shortly after the tanks were delivered to NTG (Neue Technologien GmbH).
NTG then milled the tanks from the outside, cut the tanks to a specified length and drilled eight centering drillings in each of the face sides.
These centering drillings were needed by company Wuesthoff, that drilled the longitudinal cooling channels along the tank walls. After the cooling channels were drilled, the tanks were transported back to the NTG for further treatment.

In the next months the holes for the drifttube structure will be drilled and the flanges for vacuum and diagnostics will be attached.

Gap voltage tuning by inductive tuners

Because the tuning of a coupled cavity showed to be more difficult than expected, new tuning techniques were investigated.

The possibilities of capacitive and inductive tuners at different positions inside the cavity were tested and it was found, that in some bad cases it is not possible to tune the cavity only by tuners. The 1:2 scaled model has the opportunity to change the drifttube lengths, which then was used to finally get a flat voltage distribution.
For this reason it was decided, that during the manufacturing process of the original prototype it would be good to also have the opportunity to change slightly the drifttube lengths. The solution for this problem is the production of dummy stems from aluminum. These aluminum stems will be attached to the cavity temporarily to measure the voltage distribution.

References

[1] G. Clemente, H. Podlech, U. Ratzinger, R. Tiede, S. Minaev, "HIPPI-Relevant Activities at IAP-Frankfurt on the Development of the Room Temperature CH-DTL", CARE-Report-2008-014-HIPPI

[2] R. Brodhage, U. Ratzinger, S. Minaev, G. clemente, H. Podlech, R. Tiede, "Status of the Prototype Construction of the second cavity for the FAIR proton linac", IAP-ACCC-260609

Optimization of the Slow Extraction Process from SIS300

A. Saa-Hernandez*[1,2], P. Spiller[1], U. Ratzinger[2], N. Pyka[1], G. Franchetti[1], and A. Dolinskii[1]
[1]GSI, Darmstadt, Germany; [2]IAP, Frankfurt, Germany

The Facility for Antiproton and Ion Research (FAIR) will house its two superconducting synchrotrons in the same tunnel. This singular feature results in non-standard phase-advances per FODO cell for SIS300 while SIS100 is based on standard design rules. A lattice with 'out of phase' elements is in general more prone to excite unwanted resonances. These resonances may eventually lead to coupling of the horizontal and vertical planes, reduction of the dynamic aperture (DA) and overall particle loss, unless a careful optimization of the sextupole strengths is performed. This important task has been realized by following the work on driving modes (also hamiltonian terms) from Bengtsson [1] and Streun [2]. The excitation of the different resonances driven by the chromatic and resonant sextupoles, together with the amplitude-dependent tune-shift coupling coefficient (α_{xy}), can be thus quantified and conveniently minimized by just resorting to an adequate functional. The lattice optimization as presented in this work has been carried out by requiring slow extraction to perform at high efficiency, the latter being evaluated through simulations realized with the code Elegant [3].

The studies on beam dynamics performed using the initial SIS300 lattice showed a small DA for particles with non-zero vertical amplitudes (y) or angles (y'). Those particles could not be extracted, as shown in Fig 1-left. The results for the 1^{st} order geometric terms of the driving modes showed that the contribution from the chromatic sextupoles, ideally zero, was not negligible. Additionally, the resonant sextupoles, which should only excite the extraction resonance, $3Qx$, excited the coupling resonance $2Q_y + Q_x$ by one order of magnitude more. Similarly, the coupling coefficient, α_{xy}, was as well one order of magnitude bigger than the horizontal term α_{xx}.

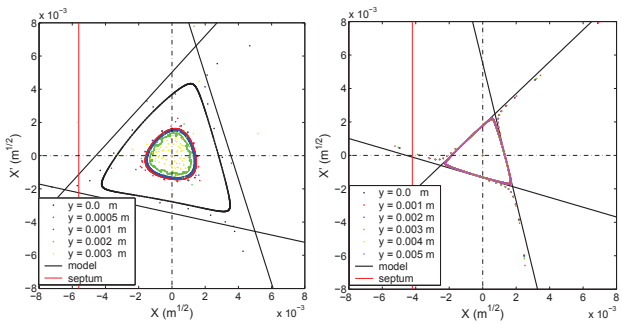

Figure 1: Phase-space plots for on-momentum particles at the entrance of the septum showing the characteristic triangular shape of slow extraction. The tracking simulations are compared with the 1D-analytical model from Pullia [4], before (left) and after (right) the optimization process.

A functional was built having the strengths of the sextupoles as main variables, and whose optimization guaranteed the following requirements to be satisfied:

- Correction of the horizontal chromaticity to fulfill the Hardt condition (i.e. removal of the momentum dependence at the entrance of the septum in order to decrease the particle loss).
- Minimization of the unwanted resonances:
  $h_{21000}(Q_x) \rightarrow 0$; $h_{10110}(Q_x) \rightarrow 0$
  $h_{10200}(Q_x + 2Q_y) \rightarrow 0$; $h_{10020}(Q_x - 2Q_y) \rightarrow 0$
- Excitation of the 3^{rd} integer resonance for extraction. The value needed depends on the tune distance (ε) and on the emittance (ε_x) of the beam:
  $h_{30000}(3Q_x) \rightarrow 2\varepsilon/(3\pi\varepsilon_x/4\sqrt{3})$
- Minimization of the detuning coupling term:
  $\alpha_{xy} \rightarrow 0$
  The vertical chromaticity does not play any role and can be freely chosen.

A new working point, corresponding to a phase advance per FODO cell of $\psi_x = 79.9°, \psi_y = 78.3°$ was used, in order to generate a dispersion function with dispersion-free straight sections. By placing there the resonant sextupoles their contribution to the chromaticity is canceled. Additionally the chromatic sextupoles were repositioned with proper phase advances to avoid the excitation of resonances. After the redesign process the DA increased by more than one order of magnitude in the vertical axis. Tracking simulations performed on the new lattice of SIS300 show that all particles can be now extracted independently from their vertical amplitude as seen in Fig 1-right. The slow extraction efficiency of a uniformly distributed beam with an emittance of 2/1 mm·mrad (horizontal/vertical planes respectively) has a value of 92.02% for the optimized SIS300 lattice. The calculation was repeated for the case in which the chromaticity was not corrected to fulfill the Hardt condition. In this situation the slow extraction efficiency was reduced to a value of 75.95%

References

[1] J. Bengtsson. SLS Note 9/97, 1997.
[2] A. Streun. Lectures at CAS, Zeuthen 2003.
[3] M. Borland. APS LS-287, 2000.
[4] M. Pullia. PhD thesis, October 1999.

* a.saahernandez@gsi.de

R&D for SIS 300 magnets at INFN in 2009

P. Fabbricatore[1], S. Farinon[1], R. Muenich[1], F. Alessandria[2], G.Bellomo[2], M.Sorbi[2], G.Volpini[2] and U.Gambardella[3]

[1]INFN Genova, Genova, Italy; [2]INFN- LASA, Milano, Italy; [3]INFN Laboratori di Frascati, Italy

Three sections (Genova, Milano and Frascati) of Italian Institute for Nuclear Physics (INFN) are working since four years for developing a fast cycling superconducting magnet for FAIR-SIS300. This R&D is aimed at building a model for the superconducting dipole synchrotron SIS300 of the facility FAIR. The complex of activities is regulated by a Memorandum of Understanding signed between INFN and FAIR at the end of 2006 with an initial forecast of total expenditure of 4.8 M€ and a temporal plan of 4 years. The activity is in an advanced stage of its development and it is moving towards its completion in late 2010. Over the last year (2009) important objectives have been achieved [1,2,3]:

1) The finalization in May of the conceptual design and the project engineering (following a dedicated technical review held in November 2008).

3) The development of an innovative low-loss superconducting cable (July 2009). The conductor critical current density was measured to be 2400 A/mm^2 at 4.5K and 5 T (result on extracted stands). With respect to the specification we have a 10% degradation causing a stability margin of 0.8 K wrt 1.0 K designed. The n-value is 34, the effective filament diameter 3 μm and the twist pitch 6 mm. These results were considered very good in view of the ac operating conditions.

4) The design of the horizontal cryostat (see Fig.1) hosting the dipole at GSI (May 2009) has been finished and the contract awarded to a company (October 2009).

5) The start of the model cold mass construction at ASG Superconductors (this is actually the heart of the program) scheduled to be completed by April 2010. Within November 2009 both poles were completed (Fig.2) and the main components (collars and poles) were ready (Fig.3).

Fig.1: The horizontal cryostat enclosing the cold mass. This cryostat will be connected to the GSI facility for the final magnet test.

Fig.2: The two complete poles, after curing and impregnation of the coil ends

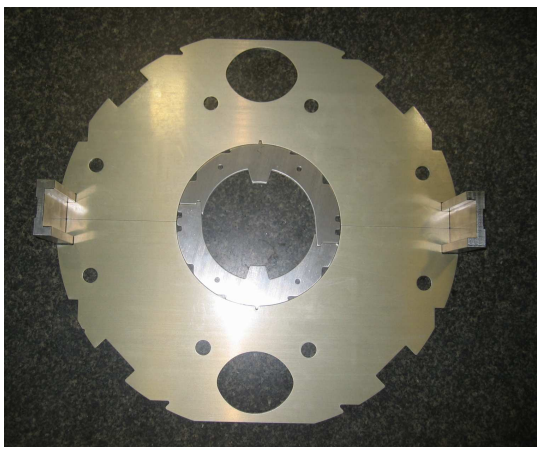

Fig.3: Collars and iron yoke laminations

References

[1] The transverse resistivity in S/C multifilament wires studied through ac susceptibility measurements Fabbricatore P, Farinon S, Incardone S, et al. JOURNAL OF APPLIED PHYSICS Volume: 106 Issue: 8 Article Number: 083905 2009

[2] Electromagnetic Design of the Coil-Ends for the FAIR SIS300 Model Dipole Sorbi M, Alessandria F, Bellomo G, et al. IEEE TRANSACTIONS ON APPLIED SUPERCONDUCTIVITY Volume: 19 Issue: 3 Pages: 1131-1135 Part 2 2009

[3] A Model Dipole for FAIR SIS300: Design of the Mechanical Structure Farinon S, Fabbricatore P, Musenich R, et al. IEEE TRANSACTIONS ON APPLIED SUPERCONDUCTIVITY Volume: 19 Issue: 3 Pages: 1141-1145 Part 2 2009

SIS 300 R&D at IHEP in 2009

A. Ageyev, I. Bogdanov, S. Kozub, V. Pokrovsky, P. Shcherbakov, V. Sytnik, L. Tkachenko, S. Zintchenko, V. Zubko
Institute for High Energy Physics (IHEP), Protvino, Russia

In 2009 R&D work for SIS 300 at IHEP concentrated on the following points:

1) In the frame of a collaboration between IHEP (Protvino, Russia) and GSI (Darmstadt, Germany) IHEP developed, produced and tested a superconducting model dipole. The main parameters of the dipole are a two-layer coil, 100 mm inner coil diameter and 1 m length. The magnet is designed for 6 T central magnetic field with a 1 T/s operating field ramp rate. The nominal operating current of 6720 A (6 T central magnetic field) was reached after the third quench and critical current of 7738 A (6.8 T central magnetic field) was reached after the eighteenth quench. The critical current of the dipole did not reduce up to ramp rate of 1300 A/s (1.15 T/s). AC losses for different magnetic field cycles were measured too. The results of the magnet tests were presented at MT 21 [1]. The magnet was delivered to GSI in May 2009.

2) In the frame of collaboration in the FAIR project IHEP also has finished the design of a fast cycling quadrupole, which will be assembled together with corrector magnets in an united cryostat. The quadrupole creates a 45 T/m central gradient in 105 mm aperture [2]. A possible simple quench protection scheme was developed, too.

3) Engineering drawings of the tooling for the production of a SIS300 prototype quadruple were developed and manufacture of the tooling was begun. This quadrupole is intended as the main unit for the SIS 300 ring. Its 1-layer is divided in three blocks and will be wound with a cored 19 strands cable.

4) The cabling machine at IHEP was modernized and 35 m of cable with 19 superconducting strands and a 316 L stainless steel core was produced by IHEP (Fig.1). The SC wire of 0.825 mm diameter for the cable was produced by Bochvar institute. The cable will be used for the manufacture of a trial winding of the SIS300 prototype quadruple in the beginning of next year.

5) A device for magnetic measurements of the SIS300 prototype quadruple was developed.

6) The local cryogenic system of SIS300 was calculated. A report on the system calculation will be presented soon.

7) The conceptual Design Report on the SIS300 prototype quadruple has been completed.

8) Designs of chromaticity sextuple, resonance sextuple, steering magnet and multiple corrector for the SIS 300 were developed [2].

Fig.1. Cored cable with 19 superconducting strands and stainless steel core for the trial winding of SIS300 prototype quadruple.

References

[1] SIS 300 dipole model, S. Kozub, I. Bogdanov, V. Pokrovsky, A. Seletsky, P. Shcherbakov, L. Shirshov, V. Smirnov, V. Sytnik, L. Tkachenko, V. Zubko, E. Floch, G. Moritz and H. Mueller, to be published in IEEE J. Applied Superconductivity

[2] Development of Quadruple, Steering and Corrector Magnets for the SIS 300, L. Tkachenko, I. Bogdanov, S. Kozub, P. Shcherbakov, V. Sytnik, A. Tchikilev, V. Zubko, to be published in IEEE J. Applied Superconductivity

A model-based development approach for multi-cavity RF control systems*

C. Spies[†1], P. Zipf[1], A. Guntoro[1], P. Surapong[1], M. Glesner[1], and H. Klingbeil[‡2]
[1]Technische Universität Darmstadt, Darmstadt, Germany; [2]GSI, Darmstadt, Germany

Abstract: We present a model-based approach for developing digital RF system components for the FAIR project. A simplified simulation model of a synchrotron and its longitudinal beam dynamics has been developed. This model can now be used to determine design parameters and to verify control concepts. An implementable solution can be determined by refining the model iteratively.

Introduction

In the area of RF control especially, digital controllers are more versatile than analog ones and able to perform complex control tasks with little hardware complexity. GSI's RF department therefore aims to use digital control throughout the FAIR project.

The different RF control systems in a synchrotron interact in a complex manner. In the SIS100 synchrotron, a fiber optical network will link the spatially distributed digital RF controllers, and their clocks will be synchronised by the BuTiS system [1] in order to let changes become effective simultaneously. Calculating the stability limits of such a complex system analytically is very difficult, if not impossible. Instead, we developed a simplified system-level simulation model.

Model Structure

We use Ptolemy II [2] for modeling and simulation. The model is built up hierarchically. Its basic structure is shown in figure 1. The longitudinal beam dynamics are specified as a set of linearized ordinary differential equations. The dynamics of the individual cavities are modeled as transfer functions in the Laplace domain. Digital hardware components and the network are modeled as discrete-time blocks. The model is parametrized to allow its quick adaption to different ion types and even different synchrotrons.

Simulations

Measurements from the SIS18 synchrotron and ramps designed for the SIS100 are used as inputs to the model. This way, entire acceleration cycles can be simulated. Figure 2 shows the developing of the beam phase during an acceleration cycle for $^{20}_{10}\mathrm{Ne}^{10+}$ lasting $500\,\mathrm{ms}$ as an example for the kind of output the simulation produces.

The feasibility of synchronising multiple cavities and dampening coherent longitudinal oscillations has been demonstrated. The noise susceptibility of several control loops has been investigated using simulation experiments. First results on the bandwidth requirements have also already been reported [3].

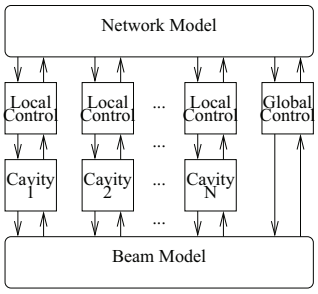

Figure 1: Basic model structure

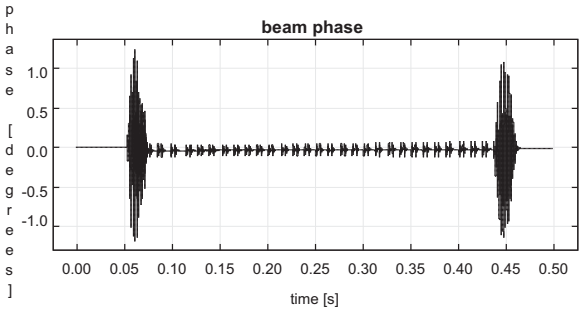

Figure 2: Beam phase (in degrees) vs. time

Future Work

After obtaining constraints for the hardware to be developed, the model can be refined iteratively in order to take implementation details into account as they become known. Every iteration can be compared against the previous one to ensure functional equivalence. The resulting hardware can then be verified by cosimulating a VHDL description with the model.

References

[1] R. Bär, "The FAIR Accelerator Control System", in: FAIR Technical Design Report, 2007.

[2] UC Berkeley, Department of EECS: The Ptolemy Project. http://ptolemy.berkeley.edu.

[3] C. Spies, P. Zipf, M. Glesner and H. Klingbeil, "Bandwidth Requirement Determination for a Digitally Controlled Cavity Synchronisation in a Heavy Ion Synchrotron Using Ptolemy II", in: IEEE Workshop on Rapid System Prototyping, pp. 196–201, 2008.

* Work supported by GSI, contract DA/GLE2
† cspies@mes.tu-darmstadt.de
‡ h.klingbeil@gsi.de

Modular RF Power Amplifier for Synchrotron RF Systems

K.-P. Ningel[1], M. Barthel[2], G. Schreiber[1], H. Klingbeil[1]
[1]GSI, Darmstadt, Germany, [2]barthel HF-Technik GmbH, Aachen, Germany

Introduction

FAIR will consist of several synchrotron and storage rings with several tens of accelerating cavities including RF power amplifiers in different power ranges. Under standardization aspects and as a cost, time and effort saving measure, a driver amplifier has been developed in a modular way in close collaboration with barthel HF-Technik GmbH. First tests and the commissioning of a first prototype in one SIS18 cavity during the summer 2009 beam time confirmed that the requirements for future applications are fulfilled.

Tasks and Requirements

In almost all FAIR RF systems, tetrodes with an output power of up to 300 kW will be used in a frequency range of 400 kHz to 5.4 MHz. These final amplifiers must be equipped with driver amplifiers in a wide spread power range up to 2.5 kW. Avoiding a variety of different types of amplifiers from different suppliers, a modular concept of a common controller unit with integrated 4 stage-combiner has been developed, that allows to combine 1, 2, or 4 identical 700 W amplifiers to resulting output powers of at least 500W, 1kW, and 2kW, respectively (see Fig. 3). This standardized concept minimizes the efforts in stock-keeping, the amount of spare parts as well as maintenance aspects. The design and specification of each power amplifier stage focuses strongly on high precision in linearity, stability, frequency and phase response over the required frequency range. Regarding the phase response, only a uniformly continuous variation is acceptable without having any negative influence on the cavity synchronization [1, 2].

The 2 kW versions cover nearly all applications for accelerating cavities. For single applications with higher required RF power, a combination of more output stages will be specified in the near future.

Results and Technical Data:

Frequency range:	0.3...6 MHz ± 0.5dB see Fig. 1
Input:	50Ω, 0dBm @ rated power, VSWR: 1.1 typ.
Output:	2200 W max. @ 50Ω load, CW operation
Max. Distortion:	-40 dB typ. at rated power and 1st harmonic
Rise/Fall/Settling Time:	50nsec, 10nsec, 5 µsec
Linearity:	±0.8 dB, 2...2000W, 0.3...6MHz

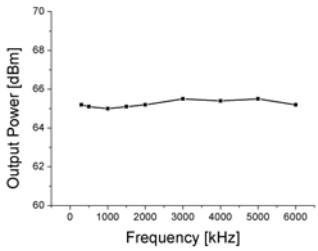

Fig. 1: Frequency response at full load

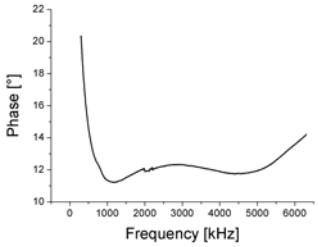

Fig. 2: Phase response at full load: Differential phase deviation of 0.4° / 10kHz for 0.3...6MHz, (0.04° / 10kHz for 0.7...6MHz, resp.); a range change-over of the measuring setup is responsible for the phase jump @ 2 MHz.

Fig. 3: Photo of the new 2kW RF Driver Amplifier consisting of a master controller with integrated combiner (uppermost crate) and four identical 700W power amplifiers.

References

[1] H. Klingbeil et al., "A Digital Beam-Phase Control System for Heavy Ion Synchrotrons", IEEE Trans. Nucl. Science, vol.54, pp. 2604-2610, 2007

[2] H. Klingbeil, "A Fast DSP-Based Phase-Detector for Closed-Loop RF Control in Synchrotrons", IEEE Trans. Instr. Meas., vol. 54, pp. 1209-1213, 2005

Optical Network for the FAIR RF Reference Signal Distribution

M. Bousonville
GSI, Darmstadt, Germany

Introduction

In the FAIR facility several RF cavities must be synchronised in spite of their large distance from each other.

For this purpose, two clock signals will be distributed via a star-shaped network and their delays will have to be measured and compensated [1-2]. As a result phase-synchronous reference clock signals with sub nanosecond precision will be available in all relevant buildings.

In this paper, the optical network developed for this challenge will be described. More information about the whole system can be found in [1].

Optical Network

For signal transmission, SMFs (standard single mode fibres) are used. Two clock signals are modulated onto two different optical wavelengths λ_1 and λ_2 and combined into one fibre in a multiplexer (Fig. 1). The two optical signals then pass an add/drop multiplexer, the transmission line (SMF ≤ 1 km) and an FBG (fibre Bragg grating). In the demultiplexer, the wavelengths are separated again and forwarded to two separate receiver units.

The measurement signal for determining the delay is modulated onto a third optical carrier λ_M. Via a circulator, the measurement signal is delivered to the add/drop multiplexer which combines the signals λ_1, λ_2 and λ_M. After passing the SMF, all signals meet the FBG, which represents a wavelength-selective reflector that exclusively reflects λ_M while allowing the other two signals to pass. The measurement signal now returns, is decoupled in the add/drop multiplexer and forwarded to the measurement receiver via the circulator.

Fig. 2 shows how the distribution to several points takes place. The optical signals are fed into several transmission lines via a power splitter. The attenuation of the splitter is compensated by an EDFA (erbium-doped fibre amplifier). With this approach, phase displacements in the optical transmitters no longer matter because they affect all transmission branches equally and thus do not have any influence on the reference signal synchronisation.

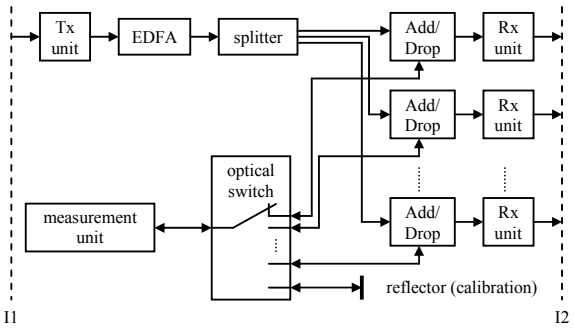

Figure 2: Star-shaped distribution.

Only one measuring unit is used to determine the signal delay (Fig. 2). By means of an optical switch, the measurement signals are switched sequentially to the different branches and a reflector for calibration. Any remaining systematic errors are, up to the FBG, of the same magnitude for all measurements and therefore irrelevant for the phase synchronisation of the reference signals. For measuring, one sinusoidal oscillation f_M after the other is modulated onto λ_M and a phase comparison of the outgoing and returning signal is performed (Fig. 1). This is done five times with frequencies between 30 kHz and 6 GHz. Based on the measured phase values, the signal delay of the clocks, taking account of dispersion, can be finally determined. The accuracy of the measurement τ_{accu} depends on the highest measurement frequency f_{max} = 6 GHz and the accuracy of the phase meter $\varphi_{accu} < 0.4°$.

$$\tau_{accu} < \frac{1}{f_{max}} \frac{\varphi_{accu}}{2 \cdot 360°} = 92.6\,fs \qquad (1)$$

References

[1] M. Bousonville „Optische Übertragung phasensynchroner Taktsignale unter Verwendung des Wellenlängen-Multiplex-Verfahrens", Doctoral thesis, TUD, 2009.

[2] P. Moritz „Technical Concept Bunchphase-Timing-System (BuTiS)", GSI Darmstadt, 2007.

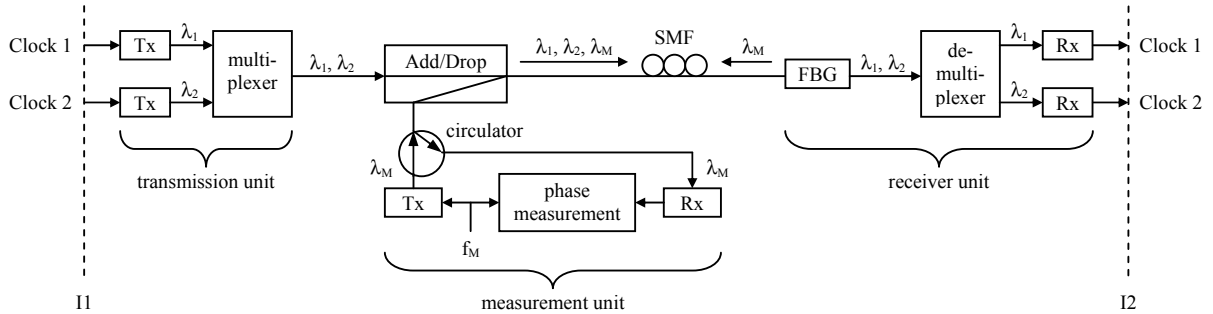

Figure 1: Configuration of one transmission branch with transmission and measurement unit.

Synchronized RF Generation in Distant Supply Rooms

M. Bousonville and H. Klingbeil
GSI, Darmstadt, Germany

Introduction

For the operation of FAIR, the generation of phase synchronous RF cavity voltages in different supply rooms will be necessary. Caused by the high masses of heavy ions, frequency ramps between 0.85 and 5.4 MHz must be provided during the acceleration. These frequency ramps will be produced by digital signal generators that work according to the DDS principle (Direct Digital Synthesis). To enable synchronous operation of the signal generators, phase-synchronous reference signals must be provided by the bunch phase timing system BuTiS [1-2]. A prototype of this timing system has successfully been tested already. Based on this, the paper at hand describes the test of the synchronous generation of frequency ramps in distant supply rooms which provides the proof of principle for the cavity synchronisation concept.

Proof of Concept

Two DDS units were provided with BuTiS clock signals via two different transmission lines (optical fibres). Without any compensation, the different signal delays of the transmission lines of 2 km and 1 m in length lead to asynchronous clock signals. Therefore, the system measured the delays and carried out phase corrections of the clock signals at the end of the transmission lines [1]. Afterwards, frequency ramps were generated in both DDS units and the phase deviation between them was measured by a DSP-System [3]. In Fig. 1, the mean phase deviation between both DDS units can be seen. The phase deviation during the frequency ramp was better than the accuracy requirement of ±1°.

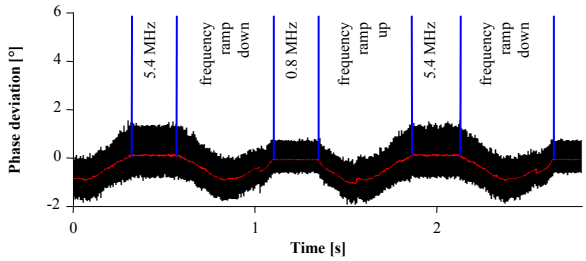

Figure 1: Synchronized frequency ramps (timing system active).

In the next step, the system stability under signal delay variations was checked. Therefore, a significant change of the delay was caused by cooling down the 2 km long transmission line to -25°C. The warming up in the laboratory with a room temperature of 27,1°C resulted in a delay change of 3.55 ns*. At the beginning of the test, the timing system was active and synchronized the phases of the clock signals. The measurement delivered a result that was similar to that seen in Fig. 1. Afterwards, the phase correction of the timing system was intentionally no longer updated to show what would happen without any active delay compensation. Since the delay in the 2 km long optical fibre had changed by 3.4 ns, the phase deviation was measured again. Now the phase deviation was beyond the tolerance limit (Fig. 2). This was caused by the delay change. Consequently, the clock signals were no longer synchronized.

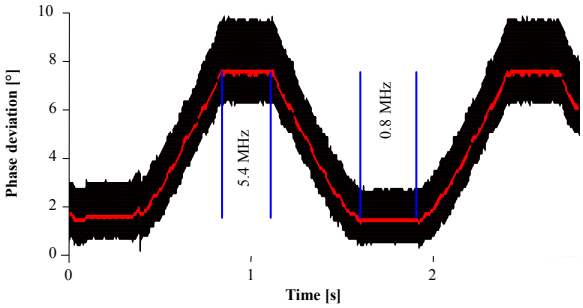

Figure 2: After 3.4 ns delay change without further correction.

After the reactivation of the phase correction update, the synchronization of the clock signals and thus the synchronization of the frequency ramps were re-established (Fig. 3). The difference between Fig. 2 and 3 shows the necessity of active delay compensation.

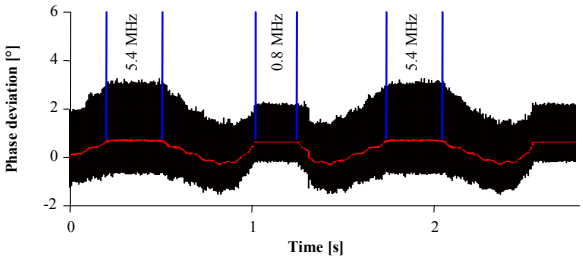

Figure 3: After 3.4 ns delay change with correction.

This test confirmed the concept of synchronized RF generation in distant supply rooms.

References

[1] M. Bousonville, et al. „Universal Picosecond Timing System for the Facility for Antiproton and Ion Research", APS, PRST-AB, Vol. 12, Issue 4, 2009.
[2] P. Moritz „Technical Concept Bunchphase-Timing-System (BuTiS)", GSI Darmstadt, 2007.
[3] H. Klingbeil, "A Fast DSP-Based Phase-Detector for Closed-Loop RF Control in Synchrotrons", IEEE Trans. Nucl. Sc., Vol. 54, No. 3, June 2005, pp. 1209-13.

* Total delay ≈ 9.83 µs at -25°C.

Development of a fast Closed Orbit Feedback by DELTA-COSY-GSI Collaboration*

G. Schünemann[1], P. Hartmann[1], D. Schirmer[1], P. Towalski[1], T. Weis[1], S. Khan[1], J. Dietrich[2], V. Kamerdzhiev[2], M. Schwickert[3], P. Forck[3], and P. Kowina[3]

[1]DELTA, TU University of Dortmund; [2]FZ Jülich, Jülich, Germany; [3]GSI, Darmstadt, Germany

Achieving high beam currents in accelerator facilities requires a stable beam orbit to minimize beam losses and activation of material. This applies to electron machines as well as to present hadron machines. To achieve a stable orbit, a fast orbit feedback (FOFB) is required. The GSI (SIS18, HESR), Forschungszentrum Jülich (COSY) and DELTA, like many others, face this general problem with machine specific differences. In general a FOFB consists of a classic control loop. On the input side fast orbit measurement takes place, a correction is then calculated utilizing correction&filtering algorithms. Using dedicated corrector magnets the calculated magnetic field is then applied to the particle beam. We propose a FPGA-based system for data processing to realize a fast orbit feedback system with a correction bandwidth of over 100 Hz.

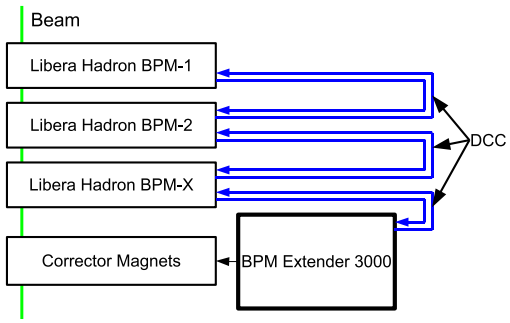

Figure 1: Fast orbit feedback system. Additional bus participants (BPMs/correctors) can be connected if needed.

Collaborative Development

In the framework of an BMBF-Project of joined research in conjunction with additional funding by the FZ Jülich, a FOFB system is being developed by DELTA, FZ Jülich and GSI. Even though a complete control loop system for electron accelerators is commercially available (Libera Electron, Libera Brilliance [1]), the "Libera Hadron", as installed in SIS18, is supplied with basic functions only. A recent development at DELTA resulted in an FPGA-based orbit measurement system for Electron Beam Position Monitors (Bergoz-BPMs [2]) called the BPM-Extender. This development allows a mixture of Libera Electron/Brilliance-BPMs and Extender-BPMs as orbit measurement devices for electron machines. An orbit correction algorithm utilizing the Extender has been implemented [3] and successfully commissioned. The excellent performance of the local orbit feedback at DELTA showed the feasibility of this approach. The collaboration of DELTA, FZ Jülich and GSI strives for a further development towards a fast global orbit feedback for electron- as well as hadron accelerators. As a first step a global fast orbit feedback for DELTA will be realized. A prototype of a fast orbit feedback for hadron machines is currently being assembled at DELTA. Once enough experience has been gained, this will be transfered to a local fast orbit feedback at COSY (FZ Jülich). The results will then be utilized for the development of a global fast orbit feedback for SIS18.

System Details

Figure 1 shows the general layout using Libera Hadron BPMs for position measurement. The analog data are transferred to the ADC-part of the Libera Hadron for fast digitization (125 MSa/s). A digital bunch recognition algorithm is applied to extract the beam position [4]. After position evaluation and further data reduction, the data are passed over to the Diamond Communication Controller (DCC), a specialized software for position data distribution [5]. The communication is split into time frames during which the data distribution takes place. Once the position data of all BPMs are collected by the Extenders during one time frame, a correction is calculated using a SVD matrix inversion method and applied to the particle beam using power supplies connected to fast correction coils. Currently the development and testing of the Extender is nearly finished with only minor tasks to complete. Two prototypes have been built, 25 are due to be built, for the DELTA FOFB as well as the COSY and SIS18 feedbacks, as soon as final testing is finished. In parallel the Libera Hadron test bench is being assembled at DELTA.

References

[1] Instrumentation Technologies, `http://www.i-tech.si`

[2] Bergoz Instrumentation, `http://www.bergoz.com`

[3] P. Towalski et al., DIPAC 2009, Basel, CH, MOPD13, p. 74.

[4] K. Lang et al., PCaPAC2008, Ljubljana, SI, TUP002, p. 79.

[5] I.S. Uzun et al.,ICALEPCS 2005, Geneva, CH, PO2.030-2.

* Work supported by BMBF, FKZ 06DO9055I and Forschungszentrum Jülich, contract no. COSY/FAIR-114

Development of FAIR superconducting magnets and cryogenic system*

D. Acker, A. Bleile, E. Fischer, E. Floch, O. Gumenyuk, G. Hess, M. Kauschke, F. Klos, Th. Knapp, H. Leibrock, J. Macavei, F. Marzouki, A. Mierau, J.P. Meier, G. Moritz, C. Muehle#, H. Mueller, I. Pschorn, P. Schnizer, C. Schroeder, S.Y. Shim, A. Stafiniak, K. Sugita, F. Walter, B. Weckenmann, M. Weipert, Y. Xiang
GSI, Darmstadt, Germany

Introduction

R&D continued during 2009 for FAIR superconducting magnets, for the main dipoles, quadrupoles, the correctors, and the corresponding cryogenic distribution / cryostat system as well. Full size models and prototype constructed in 2008 were tested at GSI and in other institutes.

Superconducting Magnets

Rapidly-Cycling Magnets for SIS 100

The first full size dipoles were built and tested [1]. These model tests show that the predictions established on Nuclotron model magnets are correct and thus the curved single layer magnet was the appropriate choice for the main dipole [2]. The generated AC losses were measured and a model built allowing calculating the expected loss of the dipole for any arbitrary cycle just with a few parameters [2]. Its predicted field quality matches the measured ones nicley.

These results reassure that it is necessary to build the SIS100 main dipole based one a coil design with a high current cable and a single layer coil, which will provide the magnet with sufficient cooling power so that it will be able to provide even the triangular cycle [2].

This magnet has to be procured and tested. Prototype wires and cable pieces with a CuMn interfilamentary matrix were developed in frame of an INTAS project for the required high current Nuclotron cable [3].

An analysis of the source of the AC losses revealed that significant loss occurs in the nose of the stainless steel endplate, supporting the Rogowsky profile. A field analysis showed that the integral field strength non linearity is dominated by the non linearity of the B-H curve along the load line and thus a rectangular magnet end should be considered [2].

The high currenct cable, required for the main dipole, was used as basis for a 2 turn quadrupole design. This design allows constructing a G11 coil reinforcement structure and profiting from the R&D made for the dipole[2].

Rapidly-Cycling Magnets for SIS 300

The 6 T dipole prototype of IHEP (Protvino) was delivered to GSI. It will be tested at GSI in 2010. IHEP this year produced cable for a main quadrupole prototype and continued the design work for the corrector. For further details see the contribution of A. Ageyev et al [4].

The R&D for the curved 4.5 T dipole at the Italian National Institute of Nuclear Physics INFN (DISCORAP-project) has well advanced in the last year [5]. The cable was delivered, the coils are produced, the collar laminations stamped and also the stamping of the yoke laminations is nearly finished. A completion of the cold mass is foreseen for spring 2010. Details on the progress of the project can be found in the presentation of P. Fabbricatore [6].

Magnets for the Super-FRS

• Superferric dipole

The FAIR China Group, consisting of three collaboration partners Institute of Modern Physics (IMP Lanzhou), CAS; Institute of Plasma Physics (ASIPP, Hefei), CAS, and Institute of Electric Engineering (IEE, Beijing), CAS developed in cooperation with GSI a prototype of super-conducting dipole magnets for the Super-FRS. The cold tests of the superconducting magnet have been successfully performed by IMP in Lanzhou [7]. The maximum required magnetic flux density of 1.6 Tesla was reached for a current of 233 A, which agrees well with the 230 A computed during the design phase. IMP built a search coil system to measure the integral field homogeneity at different currents in the midplane with a radius shift of ±190 mm in 5 mm steps. The relative field homogeneity is within the required limits of $\pm 3 \cdot 10^{-4}$. Special quench tests are planned for the summer 2010.

• Superconducting Multiplets

Several meetings with representatives from CEA, France, CIEMAT, Spain and GSI took place to discuss different design studies for the Super-FRS Multiplets which will be built within cooperation between CEA and CIEMAT as In Kind Contribution for FAIR [8].

Quench and Electrical Systems

Complete quench studies were performed on: the SIS100 dipole (single layer), the SIS100 chromaticity sextupoles, and the Super-FRS quadrupoles designed by CIEMAT. The heat exchange to the He bath during a quench was computed for the Super-FRS dipole. Complete quench measurement and analysis were performed on the SIS100 full-size dipole built by BNG. Other works related to quench protection and detection are: computation and measurement of bus bar self and mutual inductances, specification guidelines and computations for wires

* Work supported by EU, EURONS contract No. 506065 and by INTAS, project Ref. Nr. 06 - 1000012 – 8865.

#C.Muehle@GSI.DE

and cables, computation and measurement of magnet inductances.

Cryogenics

The cryogenic system for FAIR was adapted to the new building layout which is now proposed by the planners. The length of helium transfer lines is reduced by introducing one more distribution box into the system. Beside this the helium storage is optimized to fit more smoothly into the landscaping of FAIR. In addition the safety aspects of the transfer lines combining helium and electrical supply come more into focus due to the accident at LHC in 2008. As the layout of buildings was changed seriously, the question of radiation protection at the feed in of the helium transfer lines into experimental areas was raised more than before.

To the design of the cryogenic system, the local supply for the Super-FRS has been much more detailed, e.g., 3D layout for cryogenic feedbox including warm gas management and instrumentation; the control logic related with different operation modes and the trip scenarios of magnets and cryogenic facilities, and the simulation of over pressure by quench in a prototype dipole [9].

The control system for the FAIR wide cryogenic system is again approached and the working scheme for the design phase fixed with the accelerator controls department.

Cryostats

SIS 100 Cryostats

The first two full length model dipole cryostats, designed and built by BNG and BINP, respectively, were taken into operation at the GSI magnet test facility. A measurement of structural stability of the BNG model cryostat was performed and shall be evaluated in 2010. A test setup for position stability of cold masses in the cryostats was applied to the BNG cryo-magnetic-module (CMM) and first results [10] are under discussion. The first version of a beam pipe cold-warm-transition was taken into operation and was optimised in terms of thermal coupling of its interception flange. The optimised design, which shall be realised within a pre-series version of the dipole CMM is expected to undercut the tolerable heat loads to the cryogenic surrounding. The development of a pumping cold warm transition (CWT) for installation in the quadrupole doublet CMMs was started.

The specifications for the pre-series dipole CMM were completed in 2009 and a call for tender shall be carried into execution in the 1st quarter of 2010.

A conceptual design and first stability calculations for the missing dipole cryostats were performed by Cracow University of Technology (CUT). The development includes the support structures and their reaction under forces induced by failure modes [6],[11].

Based on modifications in the SIS 100 lattice structure it was possible to unify the distances in between CMMs. Unified connection cryostat structures were established in the planning of the ring assembly.

SIS 300 Cryostats

The design of the first model cryostat for a short dipole was finished at INFN [5] and the production shall be established in 2010.

References

[1] E. Fischer et al., “SIS 100 Main Magnets: Test Results and Operation Parameters“ , this annual report
[2] E. Fischer et al, “Superconducting magnets for SIS100”, IEEE T. Appl. Supercon, to be published
[3] L. Potanina et al., “Superconductor wire and cable development for FAIR”, this annual report
[4] A. Ageyev et al., “SIS 300 R&D at IHEP in 2009”, this annual report
[5] P. Fabbricatore et al, Technical Design Report of a Superconducting Model Dipole for FAIR SIS300, Genova, Italy, 2009
[6] P. Fabbricatore et al., “R&D for SIS 300 magnets at INFN in 2009”, this annual report
[7] H. Leibrock et al., "Prototype of the Superferric Dipoles for the Super-FRS of the FAIR-Project", Proceedings of MT-21, Hefei, China, October 2009
[8] "Super-FRS: Multiplet Design Meeting", https://indico.gsi.de/conferenceDisplay.py?confId=494
[9] Y. Xiang et al., "Conceptual Design of Cryogenic Facilities for Super-FRS of FAIR", Proceedings of MT-21, Hefei, China, October 2009
[10] Metronom Automation GmbH, Messbericht Transfermessung Messung im warmen und kalten Zustand, Mainz, Germany, 2009
[11] M. Sitko, B. Skoczeń, REPORT Thermal and Structural Optimization of the MDC Support Plate, Cracow University of Technology, Cracow, Poland, 2009

Superconductor wire and cable development for FAIR*

L. Potanina[1], V. Pantsyrny[1], A. Shikov[1], N. Salunin[1], I. Gubkin[1], V. Korpusov[1], H. Khodzhibagiyan[2], A. Kovalenko[2]

[1]Bochvar Institute, Moscow, Russia; [2]JINR, Dubna, Russia

The project **"Research and development of new design superconducting NbTi wire with low AC losses intended for use in magnet systems of SIS100 and SIS300 synchrotrons of FAIR Accelerator Facility**" was completed in 2009.

NbTi wire with a filament size of 2.5-3.5 μm, a high enough critical current density [J_c up to 2700 A/mm^2 at 5 T, 4.2 K], a Cu/non Cu ratio of 1.3-1.8 and a filament twist pitch as small as possible without degradation of the critical current density is of ultimate interest for the FAIR synchrotrons SIS100 and SIS300. Such a wire with thin filaments should contain a resistive inter-filament matrix (e.g. Cu-0.5%Mn) to reduce the inter-filament coupling current loss and oxygen free copper outside and inside the filamentary region to provide the required stabilization. Because of the very small size and huge number of stacking elements in the billets for the production of such a wire, significant problems could be expected using a single stacking approach for the mass production.

The main objectives of this work were the development of superconducting NbTi wires of new design, using a double stacking approach in billet design, which is more convenient for industry, and also the fabrication and testing of experimental prototype wires and model cables based on these wires.

It was decided to fabricate experimental wires with diameters of 0.825 mm, 0.79 mm and 0.5 mm with J_c (5T) ~ 2500 A/mm^2, Cu/non Cu ~ 1.38 and filament diameter 3±1 μm. The wires were fabricated at the experimental workshop of the Bochvar Institute (VNIINM). In October 2008 long length samples of the wires were delivered to JINR (Dubna, Russia) and IHEP (Protvino, Russia) for the fabrication of model cables.

Results

1. Experimental 0.5 mm, 0.79 mm and 0.82 mm wires were successfully fabricated and fully characterized [1,2].

2. A wide database on J_c and AC loss data was obtained for the wires with 3-4 micrometer filaments and Cu-0.5% Mn inter-filament matrix. From this J_c=2550 A/mm^2 (4.2K, 5T) can be fixed as minimum value of J_c in the specification of the wires for SIS100 and SIS300 FAIR magnets.

3. As for the hysteresis losses in the wires, the best results are about 30 mJ/cm^3 at the field amplitude of ± 3 T.

4. Model cable samples were fabricated at JINR and AC losses were measured. Compared to the Nuclotron wire and cable, a loss reduction of a factor 4 is possible for a SIS100 prototype dipole due to use of the improved fine filament wire and a shorter winding length.

4. A double stacking approach is more favourable for the 0.79 – 0.825 mm wires. Difficulties during wire production have been clearly identified and can be avoided in future. The heat treatment can be further optimised. Less filament distortion and smaller twist pitches are possible with machines available at a new production plant.

5. Next step should be the verification and improving of these results by producing the wires at the new plant.

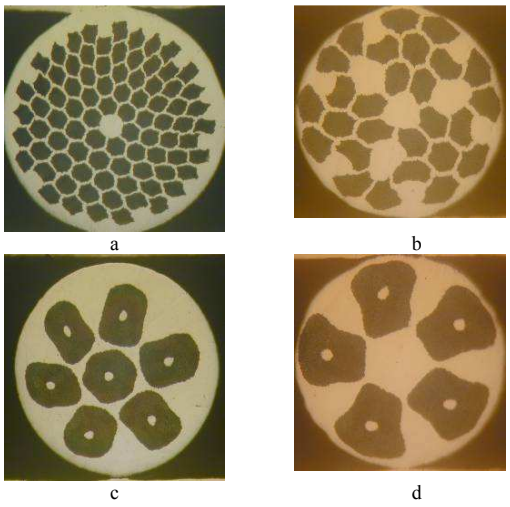

Fig.1. Cross sections of the wires: a, b - double stacked wires, c, d – single stacked and cold bonded wires.

References

[1] V Pantsyrny, L Potanina, A Shikov, H Khodzhibagiyan, V Drobin, A Kovalenko, N Vladimirova, E Fischer, "Design and Study of New Cables for Superconducting Accelerator Magnets: Synchrotron SIS 100 at GSI and NICA Collider at JINR", EUCAS 2009 (Dresden, Germany) –,

[2] L. Potanina, V. Pantsyrny, A. Shikov, N. Salunin, I. Gubkin, V. Korpusov, H. Khodzhibagiyan, A. Kovalenko, E. Fischer, H. Mueller, G. Moritz, "Experimental Results on the Development of Superconducting NbTi/Cu-Mn/Cu Wires for Magnet Systems of SIS100 and SIS300 Synchrotrons of FAIR", to be published in IEEE Journal of Appl. Superconductivity.

* Work supported by INTAS, project Ref. Nr. 06 - 1000012 – 8865.

An Improved Cryogenic Current Comparator for FAIR*

R. Geithner[1], W. Vodel[1], P. Seidel[1], R. Neubert[1], H. Reeg[2], and M. Schwickert[2]
[1]Institut für Festkörperphysik, Friedrich-Schiller-Universität Jena, Germany; [2]GSI, Darmstadt, Germany

A unique feature of the upcoming FAIR facility will be the availability of high energy, high intensity beams of ions and rare isotopes. Nevertheless, the transport of slow extracted beams in the HEBT sections demands for non-intercepting online detection of nA-beam currents. To this end an improved LTS SQUID based cryogenic current comparator (CCC) is presently developed in collaboration with FSU Jena and MPI-K Heidelberg [1].

Measurement Principle and Improvements

The measurement principle of a CCC is based on the effect that for an ideal superconductor the magnetic flux is expelled from the bulk material through shielding currents on the materials surface. The magnetic field of a passing ion beam is measured by a superconducting toroid including a single winding pick-up coil with a ferromagnetic core. The coil signal is coupled into a DC SQUID and digitized [2]. In order to achieve a high current resolution in the nA-range both, the SQUID and the pick-up coil, have to be effectively shielded against external magnetic fields. A detailed investigation on noise contributions of the magnetic core material was carried out. The theoretical calculations have shown that, apart from a good attenuation of external fields, the CCC resolution strongly depends on the choice for the core material [3]. The use of a ferromagnetic core leads to a possible optimization for better noise performance (I_s: measured current, I_n: noise current) using materials with a high μ_r, as

$$B, L \propto \mu_r \Rightarrow \frac{I_s}{I_n} \propto \sqrt{\mu_r}. \quad (1)$$

Because the signal to noise ratio is proportional to the permeability of the core, magnetic materials with high permeability, especially nanocrystalline alloys such as Vitroperm [4] and Nanoperm [5], were investigated.

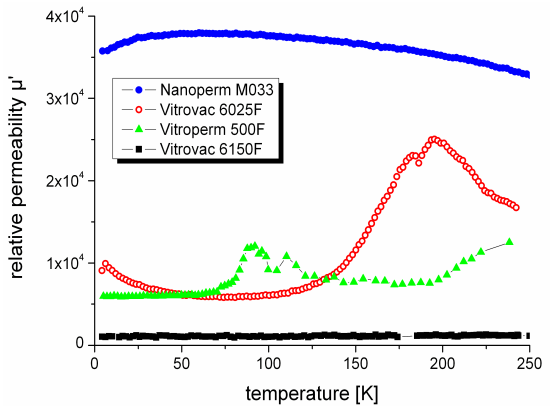

Fig. 1: Relative permeability μ_r at 100 Hz for various ferromagnetic core materials as a function of temperature

* Work supported by GSI under contract name JVODEL

Various materials have been studied with respect to their permeability as a function of temperature (down to 4.2 K) and frequency (DC to 100 kHz). Fig. 1 shows μ_r as a function of temperature at 100 Hz as measured with a purpose-built dipstick setup in a helium dewar. Nanoperm M033 achieved the highest absolute μ_r of 40,000.

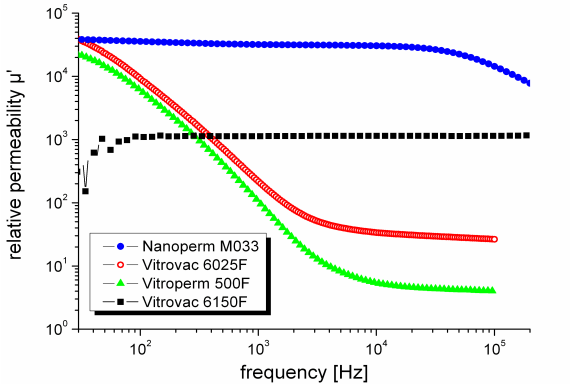

Fig. 2: Relative permeability $\mu_r(f)$, measured at 4.2 K

The frequency dependence of μ_r, as presented in Fig. 2, is very small for Nanoperm, but decreases by three orders of magnitude between 30 Hz and 10 kHz in the case of the Vitrovac and Vitroperm samples.

Outlook

The investigations have shown that the best choice for the core material is Nanoperm, due to its high permeability over a wide range of temperatures and frequencies. The next step is to manufacture a prototype coil structure and to implement it in a cryogenic system. Currently the collaboration partner MPI-K Heidelberg is working on a mechanical design for a CCC planned for installation inside the Cryogenic Storage Ring CSR, presently under construction at MPI-K. Special requirements, like e.g. a temperature stability of the CCC of 50 mK, are subject of ongoing investigations. The installation of a detector prototype inside the CSR will be an ideal test bench for the development of the FAIR CCC.

References

[1] T. Sieber et al., DIPAC2009, Basel, CH, WEOA02, p. 418.
[2] A. Peters et al., DIPAC1999, Chester, UK, PS05, p. 109.
[3] A. Steppke et al., Applied Superconductors Conf. 2008, Chicago, USA.
[4] http://www.vacuumschmelze.de
[5] http://www.magnetec.de
[6] W. Vodel et al. Proc. PAC 2009, Vancouver, CA, TH5RFP046.

First FESA Implementations for Beam Diagnostics at GSI

T. Hoffmann, H. Bräuning
GSI, Darmstadt, Germany

For the FAIR control system a new data acquisition concept is required to meet the demands of sophisticated beam diagnostics, real time performance and high level of standardization. For that purpose the Front End Software Architecture (FESA) developed at CERN was chosen [1,2]. FESA provides the tools to design and operate DAQ systems (FESA classes) based on common platforms such as PCI, cPCI and VME. It handles common tasks like multiplexing and publishing of the data to Java based GUI applications.

A complete FESA framework environment (V2.10) has now been established at GSI, which already allows developments for the existing accelerators to obtain the expertise with the development techniques and the look-and-feel of the final applications. In the last year several FESA classes were developed for general feasibility studies such as video imaging or access of PLC systems as well as fully operational tools like the beam position monitoring at the SIS18. These developments confirmed the decision for FESA at FAIR.

Fast Current Transformer

Recently a BERGOZ fast current transformer with a bandwidth of 600MHz was installed into the SIS18. The data acquisition and system control is realized with FESA. Main part of the development is the integration of a SIS3350 VME 12-Bit ADC with 500MSa/s and a high performance data throughput. To control the amplifier settings a SIS3610 VME I/O is used. A beta version is available and will be tested in the first half of 2010.

ABLASS for FAIR

The beam loss measurement and scaling system (ABLASS) [3] which mainly counts pulses from particle detectors installed in the SIS18 and HEBT, is based on an outdated OS and programming language (Kylix) and can no longer be supported. A first new implementation based on FESA with a set of Java GUI applications using the hardware of the expert version ABLAX is already operational although not all features of ABLASS have been realized yet. A real improvement within that development is the FESA filter mechanism, which allows GUIs to request only partial data, thus reducing the bandwidth required in the transfer. In addition block transfer readout of the VME modules has been implemented, which increases the sampling speed from 4 kHz to 20 kHz for a complete readout of 6 modules with 32 channels each.

PLC Access

For slow control applications such as motion control of camera lenses, voltage control and switching operations, a programmable logic controller (PLC) S7-300 from Siemens combined with dedicated I/O and relay modules was set up for testing purposes. To establish a network socket between a FESA server and the PLC the CERN IEPLC tool was used to create Step 7 source code. FESA 2.10 provides a dedicated PLC class layout for a fast design. The upcoming FESA 3 will provide access to PLCs from any FESA class.

Beam Position Monitoring

Within the upgrade program of the SIS18 the DAQ part of the existing BPM system was upgraded by using FESA on a Scientific Linux server platform (SL5, X86_64). The work was done in collaboration with Cosylab [4] in 2009. The system is now in the commissioning phase and will be operational within the first half of 2010. Details about the data acquisition are described in [5]. The BPM DAQ system can be easily expanded for later use at the SIS100 due to its modular design. The main features of the new

Figure 1: GUI of the FESA based BPM system.

BPM system are bunch-to-bunch, closed orbit, raw-data and tune measurements. Fig. 1 presents the Java based GUI as seen by the operator. The closed orbit measurement is shown.

Infrastructure

Many efforts were made in advance to be able to run FESA classes. These were among many others the connection of the GSI timing to FESA, the preparation of the diskless CPU (RIO3 + LynxOS and Intel + SL5_RT) and NFS environment, adaption of the CERN control system software such as middleware (CMW/RDA), ORACLE database and GUI development infrastructure (JDataviewer, JAPC). The release of FESA 3 is the next challenging task for the FESA teams at GSI and CERN. The authors would like to thank all members of the CERN control system group for the work done so far within the scope of this collaboration.

References

[1] M. Arruat et al., ICALEPCS 2007, Knoxville, USA, p. 310-312.
[2] T. Hoffmann, Proc. PCaPAC08, Lubliana, p.183
[3] T. Hoffmann et al., Proc. BIW06, Batavia, p.343
[4] www.cosylab.si
[5] G. Jansa et al., Proc. ICALEPCS 2009, Kobe, Japan

LSA: Towards a Setting Generation System for FAIR

D. Ondreka, J. Fitzek, R. Hellmich, M. Kirk, H. Liebermann,
R. Müller, S. Reimann, B. R. Schlei, J. Struckmeier

GSI, Darmstadt, Germany

Among other tasks, the FAIR control system will have to generate and manage consistent settings to ensure the coordinated activity of thousands of devices. At CERN, the generic framework LSA (LHC Software Architecture) [1] is used for this purpose.

At the end of 2008, a project group was initiated at GSI to evaluate the possibility of using LSA as a basis of the setting generation system for FAIR (including the existing GSI facility as injector). The main goal of the project group for the year 2009 was to set up LSA at GSI and to establish a working setting generation system using LSA, with the existing SIS18 serving as a prototype. The prototype system should then be used to analyze the usability of LSA for FAIR. [2]

The prototype system was successfully realized during the last year. When it became clear that CERN and GSI have similar requirements for extending LSA, a collaboration with CERN was established, in which the first substantial changes to LSA were already implemented. Thanks to this collaboration, there appear to be no fundamental obstacles in using LSA as basis for the FAIR setting generation system.

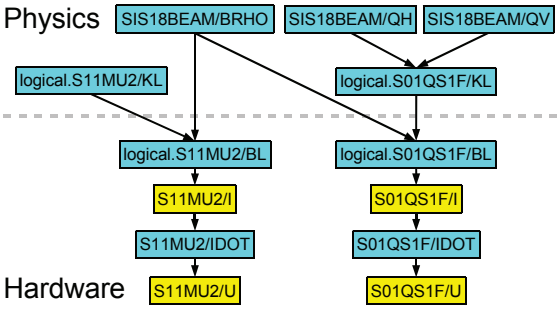

Figure 1: Part of the SIS18 parameter hierarchy.

The prototype modelling of SIS18 fell into two distinct tasks: (i) the static data, describing the physical and ion optical layout of the accelerator as well as the properties of devices (equipment models, hardware limits, calibration curves), had to be imported into the LSA database; (ii) physics parameters for operating the accelerator had to be introduced and the dependence of the hardware settings on these physics parameters had to be defined.

Filling the LSA database with the static data was non-trivial. At CERN, this import is performed by automated scripts from other data sources, such as a layout database. At GSI no such data source exists yet. Therefore, device data for SIS18 had to be collected manually from the SISMODI configuration files and calibration raw data. Likewise, data for the SIS100 were taken from the technical design report. All data were converted into a standard XML format and then imported into the LSA database using a generic import script. In a similar way, information about the control system interface of the GSI devices had to be imported from various sources, requiring a lot of manual steps.

The physical and ion optical layout of SIS18, SIS100, and beam lines was taken from MIRKO lattices, since this is a de facto standard at GSI. To ensure the long-term usability of MIRKO, the project group took the responsibility for maintaining and extending the MIRKO program according to the requirements for FAIR. As a first step, MIRKO was ported to Linux, and the possibility to export in the MADX Twiss format was implemented. The latter functionality is now extensively used to generate and import ion optical information into the LSA database. Further, it is planned to use MIRKO as an online tool in the LSA environment. In this context, the possibility to transform MIRKO into a platform independent client-server system is presently being investigated.

A parameter hierarchy for SIS18 from high level physics parameters down to hardware parameters was defined. (Cf. figure 1.) The rules for calculating hardware parameters from physics parameters were implemented independently of the present setting generation system SISMODI, but based on the experience with the setting generation system of the HIT synchrotron. A number of reference cycles were generated for SIS18, which shall be used for test runs in the near future. The hardware settings for the reference cycles were benchmarked with SISMODI. No unexpected deviations were observed.

It is emphasized that even though the SIS18 was chosen as prototype accelerator, the modelling is done in a completely generic way. In particular, the calculation rules as implemented for the SIS18 apply to any other accelerator, which has been demonstrated explicitly for the SIS100.

In 2010, the first tests of running the SIS18 with beam using LSA for setting generation are foreseen. Also, it is planned to model a simple ESR operation mode to gain experience with the use of LSA for storage rings. Further extensions of the LSA framework within the LSA collaboration are under discussion.

References

[1] Grzegorz Kruk et al, “LHC Software Architecture (LSA) - Evolution Toward LHC Beam Commissioning”, ICALEPCS’07, Knoxville, Tennessee, USA, WOPA03

[2] R. Müller et al, “Evaluating the LHC Software Architecture for Data Supply and Setting Management within the FAIR Control System”, ICALEPCS’09, Kobe, Japan, THP012

Properties of Magnetic Materials at Very High Magnetization Rates

B.-J. Lee[1], I. Petzenhauser[2], U. Blell[2], P. Spiller[2], M. Iberler[1], J. Jacoby[1] and K. Frank[3],
[1]IAP, Univ. Frankfurt, [2]GSI, Darmstadt, Germany; [3]Uni Erlangen-Nuremberg.

Introduction

For the operation of the magnetic kicker systems of the future Facility of Antiproton and Ion Research (FAIR), high voltage low pressure gas discharge switches will be needed. A problem of such switches is the lifetime reduction due to commutation losses. To reduce the losses by delaying the current flow until the voltage has dropped to a low value, saturating inductors have been tested in series with Thyratrons with good results [1]. A pseudospark switch (PSS) is under development as an alternative to Thyratrons. In contrast to Thyratrons, a PSS has a cold cathode for which it is difficult to apply such a delaying system. A certain initial strength of the current is needed to begin and develop the PSS discharge. Here we investigate the pivotal material characteristics of magnetic materials, such as B-H curve and losses, for a magnetic reversal velocity of about 30 T/µs. Finally, these materials were tested as a saturating inductor to improve the capabilities of PSS.

Experimental setup

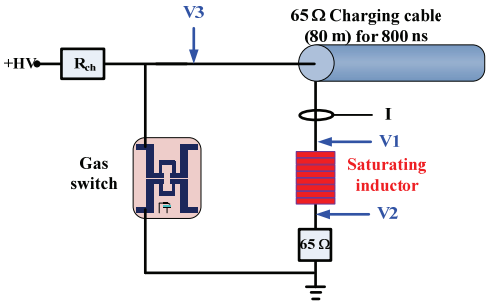

Figure 1: Experimental setup

The experimental setup used is shown in Figure 1. To gain basic data and to prove the applicability in a circuit with a pseudospark gas discharge switch, different materials were used as saturating inductors in our experiments. In total, seven different inductors are tested: Three iron based amorphous alloys (Vitroperm 500F, two FINEMET with different initial permeability), one MnZn ferrite (T38) and three NiZn ferrite (SN20, K10, CMD5005) materials. When the switch is closed, the negative pulse initiating the magnetization process leads to rapid changes of the permeability from a large value to a relatively small one. Current waveforms are measured with and without cores. The circuit provides a rectangular pulse (rise/fall time <20 ns) of 5 kV for 800 ns.

Experimental results

Cores made of iron based alloys and MnZn deteriorate the rise time of the current pulse, e.g. Vitroperm 500F, increases the rise time by a factor of 5 compared to the circuit without inductors (i.e. 20 ns to 100 ns). Due to the material characteristics (slow motion of the domain walls) these materials could not respond fast enough. Flatness and rise time are crucial in applications requiring accurate pulses for driving loads. For this reason, we focus more on NiZn ferrite. Another limiting factor for magnetic materials used in pulse power systems is losses at high magnetization rates. Core losses for different materials are measured as a function of the voltage V3. NiZn ferrites are clearly superior to MnZn (T38) ferrite showing very small losses during the magnetization. CMD 5005 shows the smallest losses.

Hysteresis loops are used to determine the magnetization behavior of the magnetic material. The data provided by the manufacturers are measured by continuous sinusoidal power sources at low frequencies. In this case, the magnetization rate for CMD 5005 is ~6 T/ms, whereas in our experiment it is 30 T/µs. This results in a rise of the remanence B_r from 0.18 T to 0.2 T. It indicates a ~17 % reduction in ΔB when a unipolar pulse is used for the magnetization without a reset system.

As shown in Figure 2, commutation losses can be reduced by more than a factor of two by saturating inductors. CMD5005 showed the best performance per unit volume.

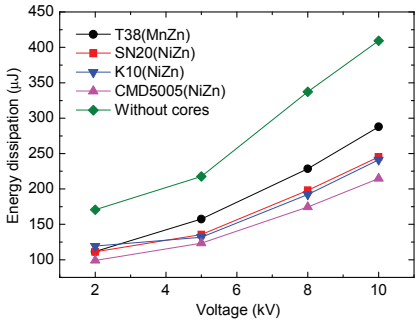

Figure 2: Commutation losses for different inductors

Conclusions

In conclusion, we found that CMD5005 was the best selection among the tested magnetic materials and it could be proven that this saturating inductor was also useful for the PSS. Based on our measurements, accurately designed saturating inductors (made of CMD5005) will be tested with a new multi-gap pseudospark switch and with a CX1671 Thyratron.

References

[1] G.D. Wait and M.J. Barnes, "Thyratron Lifetimes, a Brief Review" presented at the Modulator-Klystron Workshop at SLAC for future Linear Colliders, SLAC Report 481, Oct, 1995

Verification of Monte-Carlo Transport Codes FLUKA, MARS and SHIELD

V. Chetvertkova[1,2], E. Mustafin[1], I. Strasik[1], L. Latysheva[3], N. Sobolevskiy[3]
[1]GSI, Darmstadt, Germany; [2]Goethe University, IAP, Frankfurt am Main, Germany; [3]INR RAS, Moscow, Russia

The project "Verification of Monte-Carlo transport codes" is running at GSI as a part of activation studies of FAIR relevant materials. Checking of the electronic stopping and isotope production modules of FLUKA [1], MARS [2] and SHIELD-A [3] (with ATIMA [4] stopping module) was based on the results of irradiation of stainless steel and copper with uranium beam held in GSI in September 2004 – May 2005 [5] and the irradiation of aluminum target with argon beam done in August 2009.

The experimental setup for stainless steel and copper targets irradiated with uranium beam of 500 MeV/u and 950 MeV/u is described in [5]. In present studies we compared measured energy deposition function and stopping range with simulations done by FLUKA, MARS and SHIELD-A. The results are presented in Table 1.

Table 1. Ranges of U ions in copper and stainless steel targets.

	Range, mm			
	E = 500 MeV/u		E = 950 MeV/u	
	St.steel	Cu	St. steel	Cu
Measurement	6.0±0.2	5.5±0.2	14.4±0.4	13.1±0.4
FLUKA	6.34	5.86	15.67	14.52
MARS	6.18	5.69	14.99	13.79
SHIELD-A	6.11	5.61	14.59	13.35

One could see that FLUKA overestimates the range of uranium ions. The ranges calculated by MARS coincide with the measured ranges within the accuracy of the measurement. The best agreement of the measured and calculated ranges is given by SHIELD with ATIMA stopping module.

For checking isotope production modules the irradiation of aluminum with argon of 500 MeV/u was done. After the extraction from the synchrotron, the beam went through the vacuum window, air gap and hit the target. The target was assembled from foils (Fig.1). The geometry of the target was chosen in a way to study the depth profiles of isotopes, activated by argon beam.

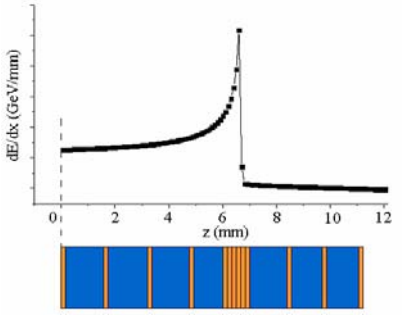

Figure 1. Range of Ar ions (500MeV/u) in Al and scheme of the target, assembled from foils

Gamma-activation analysis was performed only with thin foils. The isotopes, which were detected in aluminum target (99.2%) irradiated with argon beam of 500 MeV/u, are ^{7}Be and ^{22}Na. Comparison of measured and simulated with FLUKA, MARS and SHIELD, depth profiles is shown on figures 2 and 3.

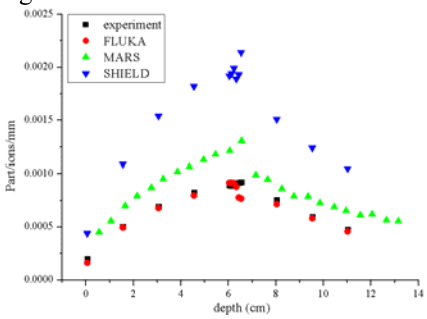

Figure 2. Depth profile of ^{22}Na in aluminum target

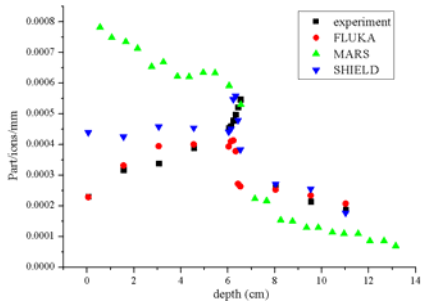

Figure 3. Depth profile of ^{7}Be in aluminum target

Discrepancies between experimental and calculated results could be explained by differences in cross-sections as well as physical models used in simulations. According to performed analysis FLUKA shows better agreement with the experiment, than MARS and SHIELD-A.

References

[1] G. Battistoni, S. Muraro, P.R. Sala et al., The FLUKA Code: Description and Benchmarking, Proc. of the Hadronic Shower Simulation Workshop 2006, Fermilab 6-8 September 2006, AIP Conference Proceeding 896 (2007) 31.

[2] N.V. Mokhov, S.I. Striganov, "MARS15 Overview", Fermilab-Conf-07/008-AD (2007); in Proc. of Hadronic Shower Simulation Workshop, Fermilab, September 2006, AIP Conf. Proc. 896, pp. 50-60 (2007)

[3] N. Sobolevsky, Modification of the Monte-Carlo particle transport code SHIELD for needs of the FAIR project, GSI internal note, ACC_THEORY-note_internal-2008-001, December 15, 2008

[4] http://www-linux.gsi.de/~weick/atima/

[5] A.A. Golubev, E. Mustafin et al, Nuclear Instruments and Methods in Physics Research B 263 (2007) 339–344

Accelerator Operation Report

W. Bayer, U. Scheeler, P. Schuett, D. Wilms
GSI, Darmstadt, Germany

This report describes the operation statistics of the GSI accelerator facility in the year 2009. The presented information is based on the data of the GSI electronic operation logbook OLOG [1] which allows for a detailed evaluation of operation statistics especially for the time-sharing operation mode of the accelerators.

General Overview

From January till October 2009 four beam time blocks were scheduled, the third one exclusively for UNILAC experiments. In total, the SIS has been operated for 4512 hours and the UNILAC for 5968 hours, which split into 5704 hours for experimental beam time and 264 hours for the commissioning of the accelerator after shutdown.

The first long shutdown period (in parallel to the UNILAC operation) lasted from April 27th till July 29th. Within this time the upgrade of the SIS vacuum system was started. Furthermore the RFQ section of the High Current Injector was upgraded. The other longer shutdown started on October 24th. It was used to continue the SIS upgrade program and to restore the damaged drift tube of the Alvarez III cavity. Due to the extensive shutdown measures about 250 hours less operation time have been scheduled compared to 2008.

Table 1: Overall beam time of the accelerator facility

	2009	2008
Integral target time for all experiments	**9201h**	10123 h
Time for retuning	**56 h**	98 h
Time of interruption	**2720h**	2312 h
Total beam time	**11978 h**	12533 h

In Table 1 the total beam time of the whole facility is shown. In total, 9201 hours of beam-on-target-time were successfully delivered to the different physics experiments, about 922 hours less than in 2008. The category 'retuning' includes the time necessary to improve the beam performance during the running experiment. The 'time of interruption' covers the categories ‘accelerator setup’ (1096 h), ‘ion source service’ (256 h) and ‘unscheduled down time’ (1368 h). These are all events which lead to a break of the running beam for the corresponding experiment. Altogether these times add up to the 'total beam time', which is bigger than the above mentioned operation time of the accelerators due to time sharing operation. The ratio between target time and total beam time (availability of the facility) decreased compared to 2008 from 81% to 77%. This is caused by an increase of time for machine setup by 2% and down time by 2%.

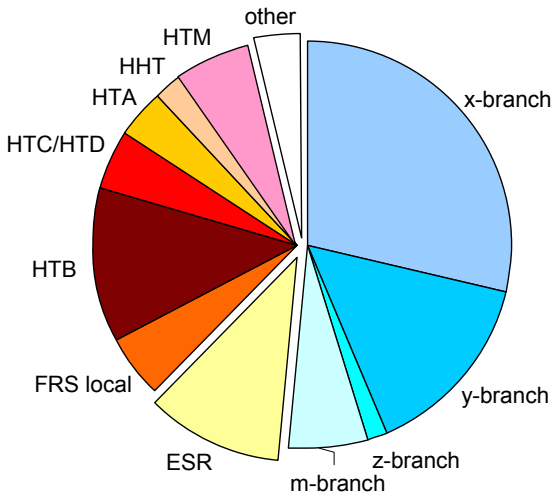

Figure 1: Distribution of target time to the different experimental areas

Figure 1 displays the distribution of target time for different experimental areas with the fraction of the 4 beam branches of the UNILAC on the right side, the ESR and the different experimental caves behind the SIS on the left side. Details corresponding to the different experimental programs are given in [2].

UNILAC Experiments

The beam time for the UNILAC experiments is shown in Table 2. Over the year, 17 different experiments were performed at the UNILAC. In total, 4880 hours of target time for physics experiments have been achieved.

A new beam branch used for Material Science experiments (1009 hours) went into operation in 2009. The other main users of the UNILAC beam were the SHIP Program (1516 hours) and Nuclear Chemistry Experiments (1835 hours).

Table 2: Beam delivered to UNILAC experiments

	Time	Fraction
Target time for experiments	4880 h	80,0%
Time for retuning	18 h	0,3%
Accelerator setup	446 h	7,3%
Ion source service	156 h	2,6%
Unscheduled down time	599 h	9,8%
Total beam time	6099 h	100%

SIS Experiments

The heavy ion synchrotron delivered beams to 26 fixed target experiments and to 7 experiments at the ESR. In total 4321 hours of target time have been achieved. The summary is given in Table 3.

In 2009 the main SIS user was FOPI. About 1250 hours of beam time were delivered to this experiment. The target time for ESR (direct beam and beam via FRS) increased to 1097 hours. For about 482 hours beam was delivered to the FRS.

Table 3: Beam delivered to SIS/ESR experiments

	Time	Ratio
Target time for experiments	4321 h	73,5%
Time for retuning	39 h	0,7%
Accelerator setup	650 h	11,1%
Ion source service	100 h	1,7%
Unscheduled down time	769 h	13,1%
Total beam time	5879 h	100%

Accelerator operation

Figure 2 shows the total beam time for all accelerated isotopes during 2009. Over the year 18 different isotopes have been accelerated. The rare isotopes (^{6}Li, ^{7}Li, ^{34}S, ^{48}Ca, ^{54}Cr) were produced by the ECR ion source, which has been operated for 4757 h. Besides Li these beams were mainly provided to UNILAC experiments. The Penning ion source was mainly used for ^{96}Ru, ^{58}Ni and ^{197}Au (in total 2632 hours of operation). The high-current ion source operation lasted for 2725 hours. Especially ^{40}Ar and proton beams were delivered from the MUCIS ion source. ^{238}U was accelerated from the MEVVA ion source for 533 hours.

Table 4: Statistics of all unscheduled down time events

	Down time	No. of events
Power supplies	339 h	303
Vacuum and structures	159 h	111
Beam diagnostics	34 h	31
Operation	37 h	37
Safety-/ Interlock system	177 h	59
Ion Sources	103 h	71
RF system	287 h	465
Controls	94 h	58
Infrastructure	69 h	27
Others /	55 h	51
Total of unscheduled down time	1354 h	1189

In Table 4 all unscheduled down time events are shown in more detail. Compared to 2008 about 200 hours less of down time events were recorded due to a decrease of breakdowns of power supplies and ion sources.

An earth leak of the main feed-in of the SIS power supplies caused a break of two days for SIS operation. The renewed control of the radiation safety system of SIS/ESR caused a lot of interruption in the first block. This system was upgraded and runs very reliably meanwhile. During commissioning for the forth block the breakdown of one drift tube cooling threatened a stop of the operation. However, a special mode of low duty cycle operation was tested successfully. This mode allowed standard beam conditions for SIS injection and the operation could be continued. For the UNILAC experiments with energies above 5.9MeV/u the duty cycle needed to be restricted. The drift tube was replaced during the subsequent shutdown.

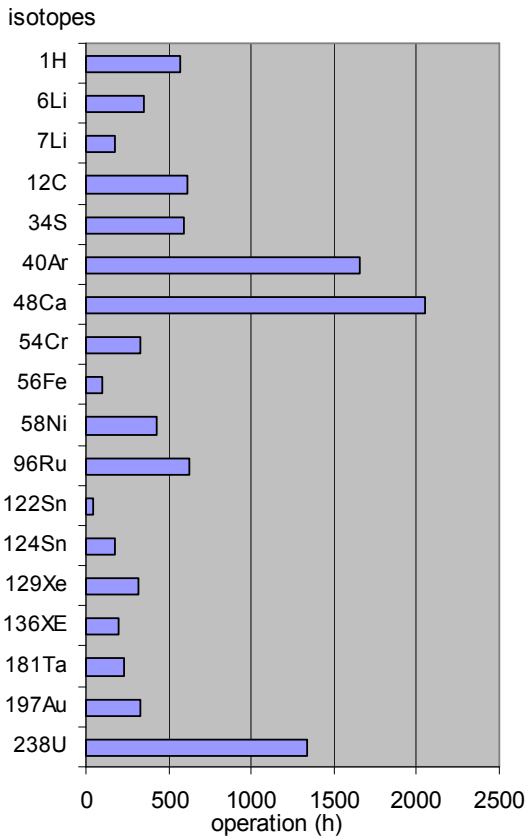

Figure 2: Total beam time for the different ion species

For accelerator experiments at the UNILAC 144 hours, at SIS 301 hours, and at ESR 95 hours beam were delivered, which is for SIS an increase by a factor of three compared to last year.

References

[1] OLOG GSI operation logbook
[2] Report of beam time coordinator, this report

Ion Source Development and Operation

P. Spädtke, B. Gutermuth, F. Heymach, R. Hollinger, R. Lang, J. Mäder, F. Maimone, K. Ochs, J. Roßbach, P. Schäffer, S. Schäffer, M. Stork, K. Tinschert, and C. Vierheller
GSI, Darmstadt, Germany

ECR Ion Sources

Regular operation of the ECR ion source (ECRIS) at the High Charge State Injector (HLI) was performed for the ion species listed in the table below:

Table 1: Ion beams delivered from the HLI in 2009.

Ion species	Auxiliary gas	Duration (days)	Analyzed intensity (eμA)
$^{1}H_2^{1+}$	—	5	150
$^{6}Li^{1+}$	He	16	30
$^{7}Li^{1+}$	He	7	20
$^{12}C^{2+}$	O_2	26	60
$^{34}S^{6+}$	O_2	27	170
$^{48}Ca^{10+}$	He	85	100
$^{54}Cr^{8+}$	He	14	60
$^{122}Sn^{17+}$	O_2	2	15
$^{124}Sn^{17+}$	O_2	8	15
$^{129}Xe^{17+}$	O_2	13	20

Besides $^{1}H_2^{1+}$, $^{7}Li^{1+}$ and $^{12}C^{2+}$, respectively, all ion species were produced from highly enriched isotopic materials.

$^{12}C^{2+}$ was provided for machine experiments and for biophysics experiments at the SIS, while a $^{129}Xe^{17+}$ ion beam was delivered for various experiments on materials research. A proton beam was generated from the $^{1}H_2^{1+}$ beam by stripping in the transfer channel in front of the SIS and was used to prepare a future high current proton experiment behind the SIS.

More than 62 % of the beam time in 2009 delivered from the ECRIS at the HLI was dedicated to the research on Super Heavy Elements (SHE). For $^{48}Ca^{10+}$ and for $^{54}Cr^{8+}$ this was performed according to the standard procedure of evaporation of the pure metals from the ECR standard oven. Applying the same procedure as for a $^{36}S^{5+}$ ion beam in 2008 [1] a beam of $^{34}S^{6+}$ ions was produced from $^{34}SO_2$ sample material with an enrichment of 99 % providing highest efficiency of beam production which was delivered for experiments on SHE.

Beams of the Sn isotopes ^{122}Sn and ^{124}Sn, respectively, were delivered for short periods to experiments behind the UNILAC.

An ion beam of $^{6}Li^{1+}$ was produced from enriched LiF sample material for an experiment on nuclear spectroscopy at the SIS, while an ion beam of $^{7}Li^{1+}$ was produced from natural LiF and was delivered to an experiment at the ESR working on an experimental test of time dilatation.

In parallel to most of the regular beam time periods for the different ion species measurements of the radiation level of neutrons and gamma rays were performed behind the IH LINAC at the HLI where the ion beam velocities are at 1.4 MeV/amu [2].

In the frame of the HLI upgrade programme in a first step the old RFQ tank was removed completely in order to investigate the ion beam properties at the entrance of the RFQ structure. During the shut down period at the end of the year a dedicated experimental analysis of the ion beam at this location was performed. Ar beams of various charge states were used as this guarantees a very stable ion beam. According to the RFQ upgrade schedule first the new RFQ tank will be installed including a four–rod structure for an ion input velocity of 2.5 keV/amu. Later on it is intended to replace the rod structure by a new one for an ion input velocity of 4.0 keV/amu which will be suitable for a superconducting ECR ion source. Therefore Ar^{q+} ion beams (q = 5, 7, 8, 9, 11) at ion beam velocities of 2.5 keV/amu and 4.0 keV/amu, respectively, were investigated.

For beam characterization standard measurements of the emittance in vertical and in horizontal direction were performed using a slit–grid device [3]. In addition two–dimensional images of the beam profile were recorded using viewing targets as described in [4]. These investigations confirm that the internal complex structure of the ion beam from an ECRIS which was observed along the low enegy transport line (LEBT) up to the analyzing plane of the dipole magnet in previous experiments at the ECR Injector Setup (EIS) [4] is further transported to the location of the RFQ entrance. Furthermore it could be demonstrated that the two–dimensional profile of the beam is influenced by the respective settings of ECRIS and LEBT as well as it is depending on the respective charge state (see Figure 1). More detailed analysis of the data is in progress.

At the EIS the work on an adaptation of the mechanical support system in order to handle both, GSI's conventional ECRIS CAPRICE as well as the superconducting MSE-CRIS [5] was completed. All measures to improve the cooling of the beam line as well as for the vacuum chamber of the dipole spectrometer were finished. Finally the reinstallation of the CAPRICE ECRIS was accomplished

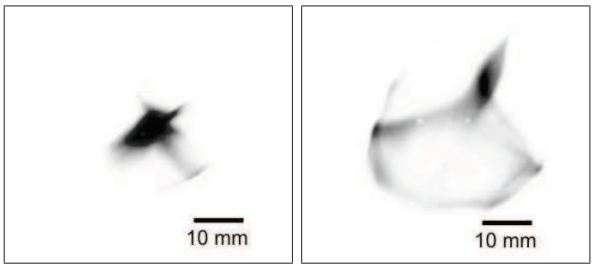

Figure 1: Two–dimensional ion beam profiles of Ar^{8+} ion beams at the location of the RFQ entrance for different settings of the LEBT.

and the instrumentation, the infrastructure and the controls of the test bench were functional in late 2009.

In order to establish a standard procedure for the production of ^{50}Ti beams from highly enriched materials a test series was started at the EIS to investigate different types of evaporation ovens.

High Current IS and Penning IS

The PIG source has been used for regular operation of the accelerator. No specific development was necessary to satisfy the beam time requirements.

Table 2: Ion beams delivered from the PIG Injector in 2009.

Ion species	Auxiliary gas	Duration (days)	Analyzed intensity (eμA)
$^{40}Ar^{+,2+}$	-	16	150 ... 400
$^{56}Fe^{3+}$	Ar	3	150
$^{58}Ni^{2+,3+}$	Ar	13	10 ... 100
$^{96}Ru^{2+}$	Ar	22	25
$^{136}Xe^{3+}$	-	8	90
$^{197}Au^{8+}$	Ar	12	250
$^{238}U^{4+,10+}$	Ar, Xe	25	10 ... 100

For the planned Li-experiment the PIG source has been tested with a specific alloy as sputter electrode which provided good experience in earlier times with an axial PIG ion source. The used PIG at GSI however has a radial extraction, which is a substantially different plasma confinement. At the test bench for the PIG source we could demonstrate a high fraction of Lithium in the beam, comparing the ratio of mass 14 N^{1+} and mass 7 (N^{2+} and Li^{1+}). Whether meta-stable ions are in the beam at all or what the percentage of meta-stable ions in the beam is could not determined due to missing diagnostic elements.

The new MUCIS has been set into operation very successfully for a long period Ar beam time. With this ion source, designed in 2008 it was possible to increase the extractable ion current by 10% at even lower arc power, which indicates a better plasma confinement. Main differences to the existing version of this source is an enlarged discharge chamber, a coaxial cathode holder, and an improved magnetic flux distribution. The higher efficiency of the ion source results in a longer life time of the filaments.

Table 3: Ion beams delivered from the High Current Injector in 2009.

Ion species	Auxiliary gas	Duration (days)	analyzed intensity (emA)
$^{1}H_3^+$	-	23	0.5
$^{40}Ar^+$	-	24	20
$^{181}Ta^{3+}$	Ar	9	11
$^{238}U^{4+}$	-	36	15

To increase the intensity for very light ions, molecules can be extracted instead of the desired element in atomic form. This increases the available extraction voltage, and as long the particle density within the plasma is high enough, the extracted current will increase according Child's law. At the gas stripper the molecule will brake apart and all residual electrons will be removed, which triples the intensity for H and D when $^{1}H_3^+$, respectively $^{2}D_3^+$ is extracted from the source.

The high current uranium beam time of September and October was very successful from the ion source point of view. The maximum analyzed beam intensity was 20 emA for $^{238}U^{4+}$ before entering the rf-accelerator with a repetition rate of 1 Hz and 1 ms pulse length.

The new ion source service station for radioactive elements has been taken into operation. Service of ion sources is now made within a glove box to avoid any contamination of service personal with radioactive isotopes. Ion source replacements (Mevva, Varis, PIG) have been done without any failure.

References

[1] K. Tinschert, R. Lang, J. Mäder, J. Roßbach, P. Spädtke, A. Yakushev, Proc. 18^{th} Int. Workshop on ECR Ion Sources, Chicago, 2008, 92

[2] M. Wengenroth, F. Becker, G. Fehrenbacher, Ch. Pöppe, K. Tinschert, R. Becker, this report

[3] W. Barth et al., this report

[4] P. Spädtke, R. Lang, J. Mäder, J. Roßbach, K. Tinschert, Proc. 18^{th} Int. Workshop on ECR Ion Sources, Chicago, 2008, 194

[5] K. Tinschert et al., GSI Report 2008-1, 85

The role of the electromagnetic field on the ECRIS beam production

F. Maimone, R. Lang, J. Mäder, J. Roßbach, P. Spädtke, K. Tinschert
GSI, Darmstadt, Germany.

In order to increase the beam intensity on the target it is mandatory to better understand the plasma generation, the beam extraction and the beam transport. It is well known that the plasma properties and the beam creation are modified by the microwave frequency and power. In this report we investigated how the ions beam generation in an ECR ion source is affected by the electromagnetic field excited inside the plasma chamber. For this purpose simulations and related experiments have been performed with the CAPRICE ECRIS [1].The injection flange of the ion source consists of a copper matching box where the WR62 waveguide line connects the Klystron generator and the source. The electromagnetic wave is transmitted into the plasma chamber through a coaxial line. In order to realize an impedance matching inside the copper box a movable plunger is present. This structure modification determines a volume change which affects the electromagnetic field inside the matching cube and inside the plasma chamber. This effect has been simulated with CST Microwave Studio [2]. A horizontal cut view of the matching box and of the plasma chamber together with the electric field excited inside is shown in figure 1. The hole and the shape of the plasma electrode have not been taken into account and a closed cylindrical plasma chamber filled with a medium with electric permittivity ε_r (ε_r=1) has been considered in the simulation. In the upper figure the plunger of 46 mm diameter located in the upper wall is moved 3.5 mm outside of the inner wall, in the middle and in the lower figures it is moved 0.5 mm and 4.5 mm inside, respectively.

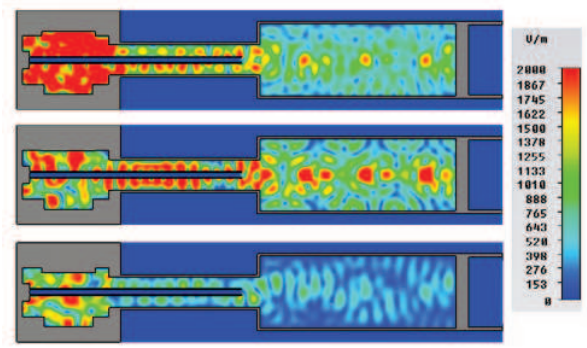

Figure 1: Electric field amplitude for three different matching box settings.

The electromagnetic field distribution excited inside the plasma chamber completely changes. The same effect is expected when the chamber is filled by a homogeneous isotropic plasma. In order to analyze the effect of the field modification, when the matching box structure changes, on the plasma properties and then on the particle beam production, a beam viewer has been installed in the low energy beam transport line (LEBT) of the high charge state injector (HLI) behind the solenoid UN4M01 focusing the selected charge state [3]. The experimental setup and the instrument characteristics are described in [4]. Using a $^{40}Ar^{5+}$ beam, the microwave power has been varied and the position of the matching plunger has been changed. For both cases the charge state distribution (CSD) and the beam shape have been analyzed. Since no significant variations on the CSD have been detected when varying the microwave power in a small range of values, the position of the matching piston has been adjusted of around 1 mm. The analysis of the CSD shows that its maximum shifted from $^{40}Ar^{8+}$ to $^{40}Ar^{5+}$ and the beam current of $^{40}Ar^{5+}$ increased by 7.4% without changing the forward power (≈ 60 W). The $^{40}Ar^{5+}$ beam shapes recorded on the viewing target are shown in figure 2. Since the beam shape presents evident variations, the beam emittance will change. The results of the simulations and of the measurements carried out with the viewing targets at the HLI revealed how the ERCIS performances are affected by the different electromagnetic field patterns excited inside the plasma chamber due to a different matching. It has to be pointed out that the analysis was carried out by keeping constant the microwave frequency at 14.5 GHz in the simulator setting parameters and during the experiment. If the microwave frequency is varying, different modes can be excited inside the plasma chamber and several simulations in the 14-15 GHz frequency range have been also carried out. The effect of a microwave frequency change in a narrow range on the source performances in terms of beam current and beam shape has been analyzed in the ECR Injector Setup (EIS) [5] test bench in 2007 [6]. Further investigations covering a wider frequency range are planned using improved diagnostics.

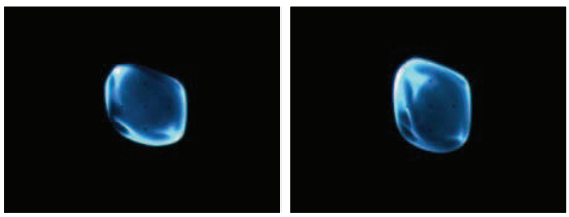

Figure 2: $^{40}Ar^{5+}$-beam on the viewing target (left: initial plunger position; right: optimized plunger position).

References

[1] D. Hitz et al., Proc. 11th Int. Workshop on ECRIS, Groningen 1993, KVI-Report 996 (1993) 91
[2] Computer code CST Microwave Studio, Computer Simulation Technology, Darmstadt, Germany
[3] H. Schulte et al., Rev. Sci. Instrum. 63 (1992) 2883
[4] J. Mäder *et al.*: GSI Report, August 2009
[5] K. Tinschert et al., Rev. Sci. Instrum. 69 (1998) 709
[6] L. Celona *et al.*: Rev. Sci. Instrum.,79, 2008

UNILAC Status and Developments

W. Barth, L. Dahl, P. Gerhard, L. Groening, M. Maier, S. Mickat, M.S. Kaiser, H. Vormann, S. Yaramishev, GSI, Darmstadt, Germany

Status of Operation

For further biology experiments under therapy conditions a carbon beam from the Electron Cyclotron Resonance (ECR) ion source was accelerated via the high charge state injector (HLI) in the UNILAC for the SIS-injection (2 weeks) [1]. Additionally UNILAC experiments used the beam from the HLI with a duty factor of up to 30 %. Furthermore the ECR source was in operation for the production of various isotopes (3H, ^{6}Li, ^{7}Li, ^{34}S, ^{48}Ca, ^{54}Cr, ^{122}Sn, ^{124}Sn,^{136}Xe) as well. During a four weeks block with sulphur beam and a two weeks block of chromium beam at the beginning of 2009 experiments for the Super Heavy Element synthesis (SHE) were supplied. Besides ^{48}Ca was used for two weeks at the SHIPTRAP. Dominantly during two long runs of six weeks ^{48}Ca-beam could be delivered to the TASCA-Separator for chemistry experiments. Additionally ion beams with different Zinc isotopes were used for the UNILAC-experiment X7 at low beam energy. The ECR-beam (3H, ^{6}Li, ^{7}Li) was also injected into the SIS 18 for high energy fixed target experiments as well as for ESR-experiments. The Penning (PIG) ion source provided ^{40}Ar, ^{56}Fe, ^{58}Ni, ^{96}Ru, ^{136}Xe, ^{197}Au and ^{238}U beams with medium intensity, especially for high duty factor experiments with heavy ions at UNILAC-beam energies. Mainly the heavy ions were delivered especially for the material research experiments at the new M-branch and at X0. Light ions as well as heavy ions from the PIG were accelerated via High Current Injector (HSI) in the UNILAC with short pulses for the SIS 18. The MUlti Cusp Ion Source (MUCIS) provided beams for different high-energy experiments with high intensities (H_2, ^{40}Ar). The Metal Vapour Vacuum Arc (MEVVA) ion source delivered ^{181}Ta and ^{238}U beams for SIS-injection. After a long time of absence the UNILAC was in operation for five weeks for uranium machine studies as well as for a week block of regular uranium beam experiments. Heavy ion machine experiments in preparation for the UNILAC as an injector for FAIR were performed additionally with tantalum (medium intensity) and high current argon beams.

Shutdown Working

During shutdown time new power supplies for the Alvarez 2a, 2b, 3 and 4 inner tank quadrupoles were installed, enabling stronger beam focussing in the whole poststripper section. The Alvarez tank revision program starting in the winter shutdown 08/09 was finished for tank no. 1. Furthermore an advanced chemical rinsing procedure was successfully tested and applied for the cooling system of the drift tubes and tank mantle of ALVAREZ 1 and 2, due to a critical occlusions with ferric oxide particles. The chemical rinsing will be extended to the other tanks in the next years. The defective cooling resulted in a overheating of one A3-drift tube and its quadrupole. Accordingly after a long time of beam operation with limited duty factor and reduced focussing strength, a new drift tube was successfully installed in the wintershutdown 09/10. Design and fabrication of the drift tube and the quadrupole was completely accomplished in the GSI-workshops. Additionally another three defective tank quads inside ALVAREZ were detected. An advanced repair program is already scheduled. But for all that the UNILAC operated with high reliability. [1]

UNILAC-Upgrade Measures

Fig. 1: The new RFQ for the HLI (left) and the HSI-RFQ with newly installed electrodes (right).

Different UNILAC-upgrade projects were planned and accomplished in essence:

- HSI-RFQ-Upgrade for FAIR [2]
- Preparation of the HSI-LEBT-Upgrade for FAIR [2]
- Beam investigations at the High Current Test Bench with a sc-solenoid
- High Current beam diagnostics for the FAIR-UNILAC-Upgrade: Mounting of additional BIF-stations in the UNILAC and the transfer line to the SIS18
- Commissioning of a 8 kW-rf-amplifier prototype and the first delivery of the batch fabrication
- HLI-RFQ-Upgrade [3]

Machine Experiments

11 days of machine experiments were performed with an high current argon beam mainly for commissioning of the upgraded HSI-RFQ. Two days with a tantalium beam and one days with uranium beam were accomplished for recommissioning of the UNILAC with low charged heavy ion beams from the MeVVa-ion source. Finally in december the ECR ion source delivered argon beam for one week of experiments in the HLI-LEBT in preparation of the HLI-RFQ-upgrade [3].

References

[1] U. Scheeler et. al., Accelerator Operation Report, (this report)
[2] H. Vormann, et. al., HSI Frontend-Upgrade, (this report)
[3] P. Gerhard, et. al., Status of the HLI-RFQ-Upgrade (this report)

Annual neutron doses in the UNILAC experimental hall

Ch. Pöppe[1], G.. Fehrenbacher[1]
[1]GSI, Darmstadt, Germany

Introduction

GSI has the obligation to verify that the accelerator operation is in compliance with the radiation protection ordinance and that the conditions given in the permissions of the authority (HMUELV) are fulfilled. For this purpose, dose measurements must be performed. From these dose measurements the annual dose values are derived for various radiological areas at the UNILAC and the experimental hall. The assumed definition of the different kind of radilogical areas (controlled, area, survey area and free accessible areas) must be checked or – if neccessary – conformed.

Method of measurement

The overall dose values outside the shielding of the accelerators and experimental areas consist in most cases of neutron and photon radiation.
The GSI's Safety and Radiation Protection division provided thermoluminescence detectors (TLD, type 6776) for the dose measurements. The TLD cards consists of two ^{6}LiF (sensitive for n- and γ -radiation) and two ^{7}LiF (sensitive for γ-radiation but not for n-radiation) elements and were mounted in moderator spheres (diameter: 30 cm) made from polyethylene (PE). The TLDs are sensitive to neutrons with energies from the thermal range up to the highest energies. The advantage of this system is that the dose reading is independent on the spill structure of the beam, i.e. there are no dead time effects etc. in contrary to the active systems.

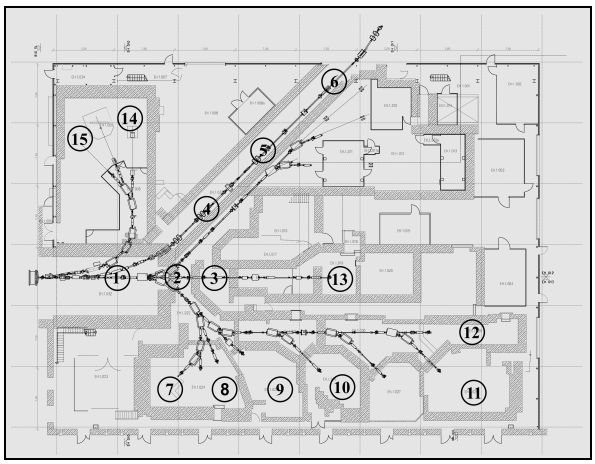

Figure 1: Measurement positions of the neutron doses in the UNILAC experimental hall.

Annual doses in 2008 and 2009

Figure 1 shows the downstream part of the UNILAC, a part of the TK and the experimental areas with the positions of the neutron detectors. The detectors are placed on the roof of the caves.
It can be seen (Tab. 1) that the dose values 2008 are in the range of 0.01 mSv/a up to 7 mSv/a. The largest dose values are measured at X1, X0 and Y7. All these locations are not accessible during experiment operation. In case of X1 it is sometimes necessary that the area around the cave must be declared as a temporarily controlled area because the dose rates are higher than 3 µSv/h (threshold dose rate value for the definition of controlled areas).
In 2009 the range of the values reach from 0.07 up to 0.71 mSv/a. In comparison to the annual values of 2008 the dose values are generally lower, on average by a factor of 1.4 if the dose values at X1 are not taken into account. At the area X7 experiments are carried out with ion beams which have energies below the nominal Coulomb threshold energy. During recent experiment periods it turned out that during the preparatory beam operation for the experiment substantial dose rates can occur (use of illumination targets etc.). Therefore additional shielding measures will be installed in the year 2010.
In 2010 an elaborate dose survey program is planned for both the assessment of the annual exposure using the TLD's as well as detection of the peak dose rates focused on the areas X1, X7, X8 and Y7 with rem counters.

Table 1: Measured Neutron doses in the UNILAC experimental hall outside the shielding, the positions are shown in Fig. 1

		Neutron - Dose H*(10) [mSv]	
Position	**Area**	**2008**	**2009**
1	end of UNILAC	0.19	0.12
2	end of UNILAC	0.15	0.16
3	end of UNILAC	0.30	0.21
4	TK	0.01	0.15
5	TK	0.01	0.15
6	TK	0.01	0.09
7	X 1	7.00	0.12
8	X 2,3	0.37	0.12
9	X 4	0.29	0.22
10	X 6	0.35	0.28
11	X 8	0.52	0.71
12	X 0	1.44	0.38
13	Y 7	1.25	0.41
14	M 1	-	0.08
15	M 3	-	0.07

References

[1] T. Radon, G. Fehrenbacher,, Ch. Pöppe, J. Sauer, and M. Wengenroth, GSI annual report 2008

SIS18 Status Report

P. Spiller, R. Balss, O. Boine-Frankenheim, U. Blell, Y. El-Hayek, H. Eickhoff, G. Franchetti, P. Hülsmann, M. Kirk, H. Klingbeil, H.G. König, H. Kollmus, U. Laier, C. Mühle, A. Parfenova, D. Ondreka, H. Ramakers, H. Reich-Sprenger, M. Schwickert, J. Stadlmann, H. Welker

GSI Darmstadt, Germany

INTRODUCTION

Beside the main upgrade program dedicated to the acceleration of low charge state heavy ions for FAIR [1], several measures have been initiated and completed which improve the beam performance for the running experimental program. The machine development program for high intensity operation and nonlinear dynamics studies has been intensified [2, 3, 4, 5].

TRANSFER OF UNILAC BEAMS

Low energetic (4 MeV/u) Xe-beams from the UNILAC could be transferred without acceleration through SIS18 to the ESR. By means of a slightly modified tune, setting of horizontal steerer magnets and switched-off bumper magnets, the UNILAC beam could be guided directly from the injection channel towards the extraction channel to the high energy beam transport system. SIS18 has only been used as a transport system and the UNILAC beams could be sent to the ESR [6] for potential use at the HITRAP experiment.

BEAM LOSS AT MULTITURN INJECTION

Depending on the emittance of the injected UNILAC beam and the actual settings of the injection devices, beam loss of the order of typically 30% is unavoidable during the transverse multi turn injection process. In order to minimize the multi turn injection losses, the scraper system in section 6 and 7 of the transfer channel may be used to cut of the tails of the injected beam. Precondition is an imaging optical system in between the scrapers and the injection septum, including three turns of revolution. Such an optical setting could be realized by means of emittance measurements with an updated MIRKO model of the beam transport and injection system. In the frame of machine experiments, it could be demonstrated that the beam intensity may be maintained in the SIS after cutting 25 % percent of the total intensity of the injected beam [7].

BEAM OPTICS STUDIES

The development of the Nonlinear Tune Response Matrix method (NTRM) for the reconstruction of nonlinear field errors was continued. The first attempts have been performed to reconstruct the natural sextupolar field components of the ring's main dipoles. The β-functions of the machine were systematically measured to determine the tune response of quadrupole and sextupole magnets [8]. According to the carried out measurements and simulations, the β-functions may be affected by the CO induced β-beating. The initial CO distortion in the presence of sextupoles leads to a β-beating via the feed-down of quadrupolar components. The uncontrolled β-beating, affects the nonlinear field error reconstruction and may also affect the efficiency of the multiturn injection and slow extraction. Therefore, it is important to correct the CO at the best in order to keep the β-functions symmetric. The new SISMODI closed orbit correction software was tested. However, the horizontal CO correction suffers from missing bipolar power converters.

BUNCH COMPRESSION

The first bunch compressor cavity based on magnetic alloy ring cores as inductive load has been installed in the SIS18 synchrotron and commissioned with beam [9]. The new cavity provides a compression voltage of up to 40 kV in Rf pulses with a length of 500 ns. So far, one of the Fe-loaded acceleration cavities with a maximum voltage of 14 kV, has been used for compression for e.g. plasma physics experiments. Although the implementation of the new cavity in the accelerator control system was not completed, first compression experiments could be performed on the injection plateau and at final energy. The experiments at final energy were partly performed in combination with one of the Ferrit-loaded acceleration systems.

BUNCH TRIMMING

For a further reduction of the pulse length on the target and especially for a removal of the leading and following beam tails, the extraction kicker system may be used. This method is based on the fact that the acceptance angle of the extraction channel is a small fraction of the total kick angle. By igniting the kicker after the leading tail and shortening before the following tail, only the core of the bunch is extracted. However, the particles of the tails are dumped and distributed in the synchrotron. It could be shown, that by means of the extraction kicker trimming, the core of a compressed bunch may be cut out and pulse lengths of a few ten nanoseconds may be achieved on the target (Figure 1). See also [10].

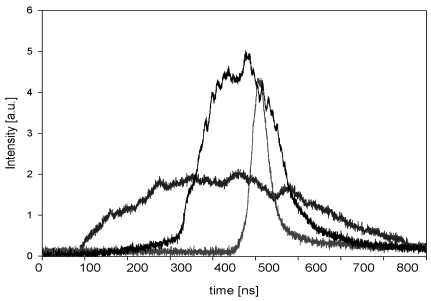

Figure 1: Intensity profiles of extracted single bunches measured with the fast transformer in TE1, without compression (long), with compression (medium) and with compression and extraction kicker trimming (short peaked).

REFERENCES

[1] P. Spiller et al, this annual report
[2, 3, 4, 5] S. Appel, G. Franchetti, S. Sorge, this annual report
[6] J. Stadlmann, internal note,
www.gsi.de/beschleuniger/sis18/einstellung_steuerung.html
[7] Y. El-Hayek, Masterthesis, GSI Master 2009-01 (2010)
[8] A. Parfenova et. al., internal note,
https://www.gsi.de/documents/DOC-2009-Nov-94-1.pdf.
[9] P. Hülsmann et al, Proc. of the EPAC04, Lucerne (2005)
[10] A. Tauschwitz et al, this annual report

A High-Speed Data Converter for Digital Control of Synchrotron RF Cavities

Shahab Sanjari[1], Martin Kumm[2], Harald Klingbeil[1], and Bernhard Zipfel[1]
[1]GSI, Darmstadt, Germany; [2]University of Kassel, Germany

Introduction

In order to provide synchrotron RF cavities with proper high frequency signal, several closed-loop control systems are required. This might be achieved using analogue or digital electronics. The main advantages of a digital approach are reconfigurable modules that build up the control loop. The topology used for the digital synchronisation of the radio frequency cavities of the GSI SIS18 heavy ion synchrotron, is based on a modular concept [1]. The use of field programmable gate arrays (FPGA) facilitates high–speed data processing of different interfaces such as high–speed optical links. For these FPGA modules a still growing software component library written in VHDL language is established. The components are stored in a version control system so that multiple developers can work on the same project using a well defined network on chip architecture [2].

As an extension to the digital modules, a data converter was designed in 2006 as an interface between analogue and digital world. A revision of the board then improved the signal to noise ratio with a spurious free dynamic range of at least 50 dBc [3]. The latest revision of this board utilises an Altera® Cyclone® III FPGA (Figure 1). The board includes two 14–bit analogue to digital converter channels each with a sampling rate of up to 120 MSPS, and two 14–bit digital to analogue converters each with a sampling rate of up to 210 MSPS. The sampling rates can be varied during the operation. Low pass filters, high speed operational amplifiers and 45 dB digitally controlled variable gain amplifiers are available in the signal path. Each analogue input path can be calibrated digitally by voltage reference ICs using an analogue switch. The circuit is built on a 10 layer circuit board with elaborate grounding and signal distribution.

Automatic Gain Control

For the beam phase measurement in the digital control loop, an automatic gain controller was developed using the converter board. The algorithm is based on an existing solution that uses a fast on–off digital controller (M. Kumm 2003). The converter board showed considerable improvements in the recovery time after sudden changes in the amplitude of the input signal, so that it is now manufactured in quantity for this purpose.

Other Applications

The converter board is being continuously used in newly designed modules. In 2007 it was used to realise a digital offset local oscillator which is now available as a serially manufactured device [4]. In 2009 a digital phase and amplitude detector was realised [5].

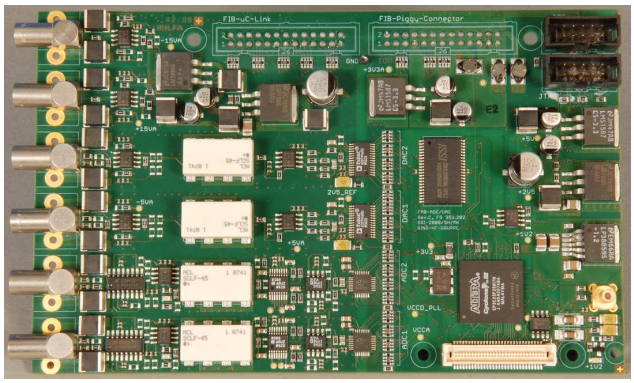

Figure 1: The converter board, Photo: G. Otto, GSI.

Using various algorithms, the board can be used as a signal generator or processor. The available high speed converters allow sampling at intermediate frequency (IF) which together with appropriate signal processing algorithms make (de)modulation and filtering more accessible in digital domain [6].

References

[1] H. Klingbeil, B. Zipfel, M. Kumm and P. Moritz, “A digital beam-phase control system for heavy-ion synchrotrons”, IEEE Transactions on Nuclear Science, vol 54, pp 2604–2610, 2007.

[2] U. Fischer, “Entwurf und Implementierung eines echtzeitfähigen Network-on-Chip für den Einsatz in zeitkritischen Regelungsaufgaben”, Diplomarbeit at Fachhochschule Fulda, Januar 2005, Fulda.

[3] M. S. Sanjari, “Hardware and Software Implementation of a Radio Frequency High-Speed Data Conversion Unit for Digital Control Systems”, Bachelor Thesis at the Technische Universität Darmstadt, October 2006, Darmstadt.

[4] M. Kumm, “FPGA-Realisierung eines Offset-Lokaloszillators basierend auf PLL–und DDS–Technologien”, Diplomarbeit at Technische Universität Darmstadt, July 2007, Darmstadt.

[5] T. Wollmann, “Entwurf und Implementierung eines digitalen Phasen- und Amplitudendetektors für eine HF-Beschleunigerkavität”, Diplomarbeit at Technische Universität Darmstadt, September 2009, Darmstadt.

[6] M. Kumm and M. S. Sanjari, “Digital Hilbert Transformers for FPGA-based Phase-Locked Loops”, International Conference on Field Programmable Logic and Applications, 2008.

Beam Response on Base-Band Tune Measurement System

U. Springer[1,2], P. Forck[1], P. Hülsmann[1,2], P. Kowina[1], and P. Moritz[1]
[1]GSI, Darmstadt, Germany; [2]Goethe University, Frankfurt, Germany

For high current operation of SIS18 precise control of the tune value is required. It is measured by excitation of coherent betatron oscillations and turn-by-turn position determination using a Beam Position Monitor (BPM). In order to define the working area of this Tune Measurement System using direct digitized BPM data, the influence of beam excitation on emittance must be evaluated. The beam width and beam loss were measured along with the frequency spectrum obtained out of BPM data.

An example of such investigations is shown in Fig. 1 using a beam with the following conditions: $7 \cdot 10^9$ Ar^{18+} were accelerated from 11.4 to 300 MeV/u within 254 ms. The beam was excited using band limited noise excitation centered on expected betatron sidebands in order to actuate a coherent betatron motion [1, 2, 3]. The bandwidth was set broad enough to cover the expected range of tune variation whereas the level of excitation was altered. The BPM data are directly digitized and post-processed offline [4]. To obtain the horizontal and vertical beam envelope, and thus beam emittance, the Ionization Profile Monitor (IPM) installed at SIS18 was used [1, 5]. Moreover data from the DC Current Transformer (DCCT) was analyzed to obtain the amount of beam loss.

The measurements were performed with the given beam parameters 250 ms after ramp start just before reaching flattop. As the measurement system is considered to display the tune with a ms time resolution work during complete acceleration, all beam losses introduced by the beam excitation during acceleration are included. The tune value is obtained from SIS18 section 5 turn-by-turn position data by Fourier Transformation. The Signal/Noise ratio presented in Fig. 1 is calculated by integrating the tune peak in the Fourier amplitude spectrum divided by the corresponding part of spectrum of equal width outside the resonance. For each data point in Fig. 1(top) 26 spectra were averaged and their fluctuations are represented in the error bars. For the DCCT data an average of 100 measurements is taken. The beam width is determined from transverse profiles recorded by the IPM using an average over 60 measurements.

It was observed that a S/N ratio of about 3 is enough to achieve stable measurements, meaning that the evolution of tune can be reconstructed each 512 turns all along the ramp. For this S/N an Exciter Power of about 2 W is needed. On the other hand no significant beam loss exceeding 2 % was observed for excitation levels up to 10 W. An alteration in beam profile was measured exceeding 8.5 W. A working area providing sufficient signal strength for tune determination and low transverse emittance enlargement thus could be defined between 2-8.5 W of Exciter Power. The results may be scaled (dep. on Z, A, E) for other ion species and energy ranges.

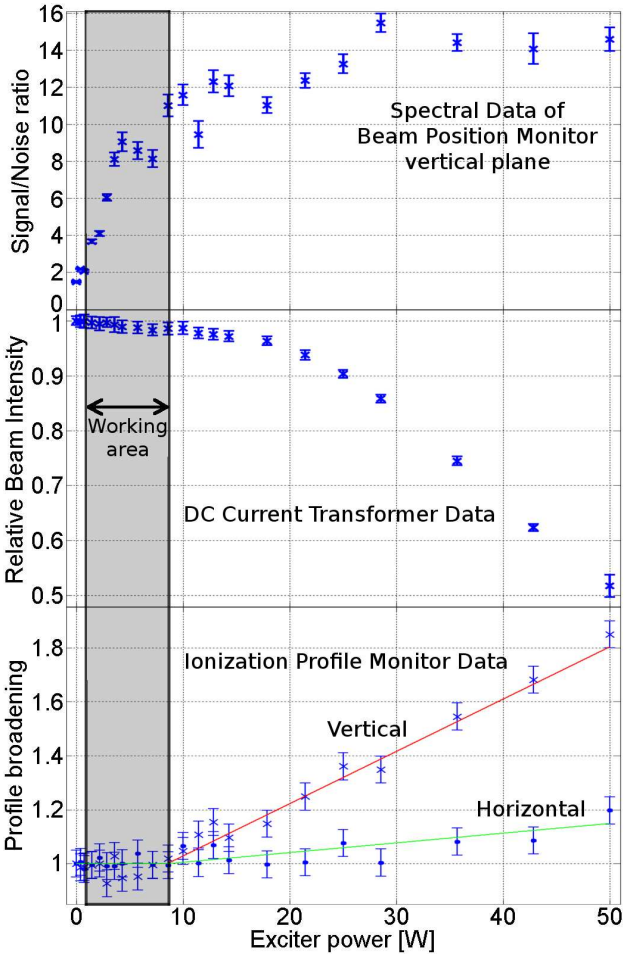

Figure 1: The influence of beam excitation using band limited noise is shown using BPM (upper part), DCCT (middle) and IPM data (lower part). For measurement parameters see text.

References

[1] U. Rauch et al, “Baseband Tune Measurements at GSI SIS-18 using Direct Digitized BPM signals”, Proc. DIPAC’09, Basel, Switzerland

[2] K. Blasche et al,“SIS Status Report”, GSI Scientific Report 2000, p.184

[3] U. Rauch, et al, “Base-Band Tune Measurements at SIS-18 using Direct Digitized BPM signals”, GSI Scientific Report 2008, p.122

[4] U. Rauch et al, “Investigations on BaseBand Tune Measurements using Direct Digitized BPM Signals”, Proc. of 5th CARE-HHH-ABI Workshop, Chamonix, Dec. 2007, p.58

[5] T. Giacomini et al,“Development of Residual Gas Profile Monitors at GSI”, Proc. of 11th Beam Instrumentation Workshop BIW’04, Knoxville, USA

Dose Survey at SIS and following Experimental Areas

T. Radon[1], G. Fehrenbacher[1], G. Freml[1], Ch. Pöppe[1], and J. Sauer[1]
[1]GSI, Darmstadt, Germany;

Introduction to GSI monitored areas

The experimental halls at GSI outside the shielding of the caves and accelerators are declared as surveyed or monitored areas. These areas are to be found around controlled areas which are on GSI premises for example the experimental caves. It is obligatory to install surveyed areas if the annual dose can exceed 1mSv per year. It is mandatory to guarantee that the dose in these areas does not exceed 6 mSv per year which is at the same time the lower border of the effective dose per year for which a controlled area has to be set up.

Neutron dose measurements

Neutron doses provide the largest proportion of the total effective dose around the accelerator facilities and experimental areas of the high energy part of GSI. Thus the measurement of the neutron dose is the crucial part in the annual dose inspection. We focus here on the measurement of the neutron doses by a passive detection system[1] and as a complement the neutron dose has been measured by an active dosimeter [1]. The passive detector system is based on thermoluminescence which makes it a reliable tool for dose measurements even for beams with complex spill-structures. Some of the detectors of the active system belong to the interlock chain which prevents the primary or secondary beams to enter the corresponding area in case of a dose rate transgression.

Measurements in 2009

Figure 1 shows the SIS and the following experimental areas together with the position of the active (larger squares) and passive (smaller squares) neutron detectors. It is noticeable that the annual dose values are largest in the vicinity of the SIS extraction area, the HHD beam dump and the FRS target area. Similar to last year[2] these areas had to be declared as controlled area as the corresponding dose rate of 3 µSv/h was transgressed for certain primary beams in order to keep the annual dose limit. The dose values of the active and passive system can hardly be compared due to their different positions including different heights in the experimental halls. However both systems reliably demonstrate the higher dose values in the region mentioned before. A further increase in the primary beam intensities will require an improvement of the shielding in this area.

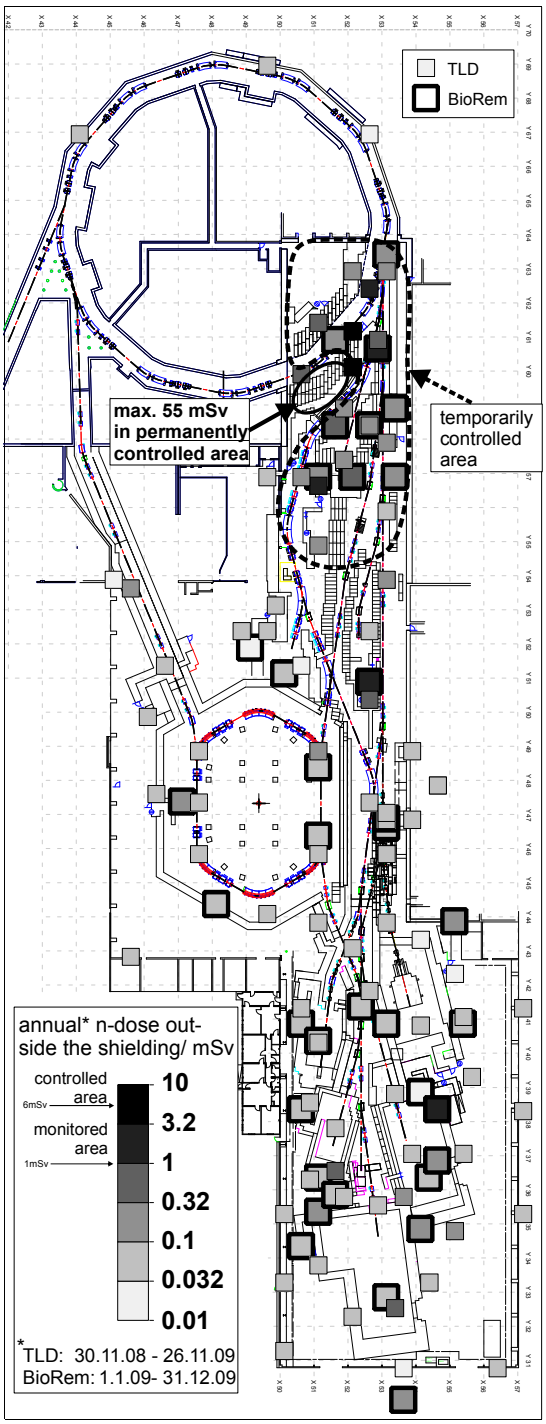

Figure 1: Dose map of the high energy beam facilities at GSI. The annual dose measured with active (larger squares) and passive (smaller squares) dosimeters is shown. Values below 10 µSv were not taken into account.

References

[1] F. Gutermuth, T. Radon, G. Fehrenbacher, and J.G. Festag, Kerntechnik (2003), 68, 4, pp. 172-179.
[2] T. Radon, G. Fehrenbacher, Ch. Pöppe, J. Sauer, and M. Wengenroth, GSI-report 2008, p. 129.

ESR Operation and Development

C. Dimopoulou, A. Dolinskii, O. Gorda, V. Gostishchev, R. Hettrich, C. M. Kleffner, S. Litvinov, F. Nolden, P. Petri, U. Popp, I. Schurig, M. Steck
GSI, Darmstadt, Germany

In the framework of machine developments at the ESR two new modes of operation were tested. After first unsuccessful attempts to demonstrate the slow extraction of a decelerated beam, the slow extraction test was performed at higher energy. The main advantage is a much shorter cycle time allowing faster variation of parameters and easier diagnostics in the HITRAP linac. With improved orbit corrections and after careful tuning of quadrupole and sextupole magnets the resonant extraction of a cooled bare argon beam at an energy of 100 MeV/u could be demonstrated. The extraction was performed by tuning the main quadrupoles such that the tune was close to the third order resonance $Q_x = 2.333$, subsequent slow linear variation of two sextupoles shifted the beam tune across the resonance. Particles which are excited to large betatron amplitude enter the electrostatic septum which deflects them into the extraction channel. Extraction times up to 10 s could be achieved easily. The required magnet setting for the resonant extraction is thus known and can be applied, if slow extraction of bare decelerated ions is needed in the future.

The second new mode followed a request to have shorter cycle times for HITRAP commissioning with a 4 MeV/u beam delivered to the HITRAP linac. It resulted in tests of the direct transfer of a Unilac beam using SIS and ESR as single pass beamlines. Although this transfer was tried out several times with different ion species, all tests resulted in beam loss after the first dipole magnet in the ESR. The tests were seriously hampered by the fact, that no diagnostics are available to detect the low energy beam in the ESR during a single pass, neither destructively nor non-destructively. Various problems of this mode could be identified. The power converters of the beam line magnets between SIS and ESR were not foreseen to operate at such low magnetic rigidity. The focussing of the beam through SIS and the beamline is different from normal operation and the beam could not be matched to the standard ESR optical setting. At the location of the main beam loss, the electrodes of the stochastic cooling system limit the acceptance, even further impeding the passage of the unmatched beam.

The HITRAP commissioning was regularly continued in two blocks of about five days with bare nickel and xenon beams decelerated in the usual way from 400 to 4 MeV/u. Up to 2×10^7 nickel ions could be decelerated to 4 MeV/u with an efficiency of 15 % for the deceleration in the complex deceleration cycle. For xenon, limited by the shorter lifetime in the residual gas, 2×10^6 ions could be decelerated, the total cycle time could be reduced to 45 s.

Various experiments were performed at the internal target of the ESR. A nuclear physics experiment used $^{94}Ru^{44+}$ ions decelerated from 100 to 10 and 9 MeV/u and a dense hydrogen target. The reaction products of the (p, γ) reaction were studied with particle detectors installed in a section with large dispersion behind the target. Several high charge states (89+, 90+, 91+) of uranium and different energies in the range 120 to 400 MeV/u were used in an atomic physics experiment at the internal target.

The experiment on time dilatation with precision laser spectroscopy of lithium ions was continued. A half life of the 59 MeV/u Li^{1+} beam of 60 s confirmed that the problem with a tiny leak in the ultrahigh vacuum system of the ESR, which had hampered the experiment in previous years [1], has been solved.

The mode for the production of rare isotope beams right in front of the ESR, tested before [1], was used for an experiment of dielectronic recombination of cooled lithium-like uranium. A beam of helium-like $^{237}U^{90+}$ at 186 MeV/u was produced in a 10 mm thick beryllium target from a 381 MeV/u primary $^{238}U^{73+}$ bunch of up to 2×10^9 ions. The helium-like charge state injected and stored close to the central orbit was used to breed lithium-like uranium ions by capture of electrons from the comoving high intensity electron beam (electron current 450 mA). After 2-5 minutes $1 - 2 \times 10^5$ helium-like ions had captured one more electron circulating on an orbit radially further outside. These comoving $^{237}U^{89+}$ ions were then moved to the central orbit by ramping all magnets of the ring to a higher field with a field increase of about 1 %. During this manipulation the electron cooling was continued at fixed energy. Finally, the selected particles circulated on the central orbit, whereas most other beam components, which were injected together with the wanted particles, were removed by inserting fast scrapers from inner and outer side into the ring acceptance. The lithium-like charge state was then used for measurements of dielectronic recombination spectra by scanning the energy of the comoving electron beam thus varying the relative velocity between ions and electrons. This measurement cycle was repeated for $^{236}U^{89+}$ and $^{238}U^{89+}$ in order to detect small shifts of resonant lines for different isotopes.

For future experiments with single or few ions a new Schottky noise pick-up based on a pill box type cavity with a resonant frequency around 250 MHz has been designed and constructed. The stainless steel body was copper plated at GSI. A quality factor of around 1000 should considerably increase the signal to noise ratio compared to the existing broad band Schottky pick-up. The cavity will be tested and prepared for installation in the ESR early 2010.

References

[1] C. Dimopoulou et al., GSI Report 2009-1.

Improved Isochronous Mode of the ESR

S. Litvinov[1], C. Dimopoulou[1], A. Dolinskii[1], Yu. Litvinov[1,2], F. Nolden[1], M. Steck[1], and H. Weick[1]
[1]GSI, Darmstadt, Germany; [2]MPI-K, Heidelberg, Germany

In the isochronous ion-optical mode of a storage ring the revolution time of circulating ions is independent of their velocity, and depends on their mass-over-charge ratio only. This mode is the basis for the Isochronous Mass Spectrometry (IMS). This experimental technique for direct mass measurements of a large variety of short-lived exotic nuclei has been developed at the FRS-ESR facility at GSI [1]. Improved isochronicity of the ESR as well as the ion-optical matching of the FRS-ESR has been calculated.

Ion-Optical Calculation

The isochronous mode has been originally calculated using the five ESR quadrupole families [2]. The main peculiarity of this optics is the large negative dispersion in the straight sections ($D\approx$-8 m) whereas the FRS is an achromatic system at the last focal plane before the injection into the ESR. This leads to a large dispersion mismatch. Additionally, there is a mismatch in the transverse phase space. These effects induce incorrect betatron and dispersion motions in the ring, and, therefore, strongly reduce the transmission of the ions into the ESR. A careful ion-optical matching had been required and was achieved for the first time by adjusting the 11 quadrupoles of the FRS, which allowed to increase the transmission by a factor of 10 [3].

Besides the transmission, the erroneous dispersion motion causes an additional time spread of the circulating ions. Moreover, the non-achromatism of the ESR itself brings a supplementary uncorrectable first-order transverse contribution to the revolution time. These contributions are the largest at the first revolutions and average out after many turns. For example, after the first 100 revolutions the calculated $\Delta m/m \sim 1\cdot 10^{-5}$ (1σ) is for a momentum deviation of 0.12% (mismatched dispersion) and $2\cdot 10^{-5}$ (1σ) for a horizontal emittance of 5 mm mrad (non-achromatism).

In order to make the ESR achromatic, to facilitate the FRS-ESR matching and to improve the isochronicity of the ESR, it was proposed to recalculate the isochronous optics. The new mode has been designed using 10 quadrupole families, since the 20 ESR quadrupoles are connected to the power supplies in pairs. The calculation has been performed with the ion-optical code GICOSY [4]. The dispersion function of both isochronous settings is illustrated in Fig. 1. It can be seen, that the "new" dispersion function is smaller on average, which allows to increase the momentum acceptance of the ESR by about 25%. Additionally, a smaller dispersion ($D\approx$-5 m) at the position of the time-of-flight (TOF) detector shall increase its efficiency.

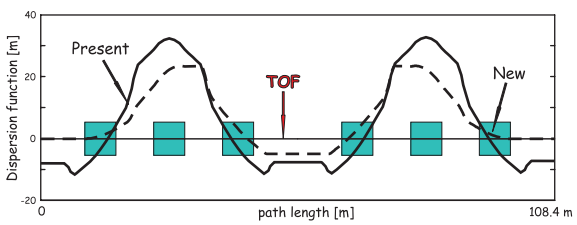

Figure 1: Calculated dispersion functions for the present (solid curve) and the new (dashed curve) isochronous optics. The position of the TOF detector is indicated with an arrow. Grey squares represent the dipoles.

The 8 ESR sextupoles are connected independently to the corresponding power supplies. The sextupoles have been employed for the second-order corrections (isochronicity, natural chromaticities) in calculations of both optical modes. The optimized modes have been further used in the Monte-Carlo simulations.

Monte-Carlo Simulation

The simulations have been performed with the program MOCADI [5]. We have simulated 10^5 ions circulating for 100 turns in the ESR. The corresponding results are presented in Fig. 2.

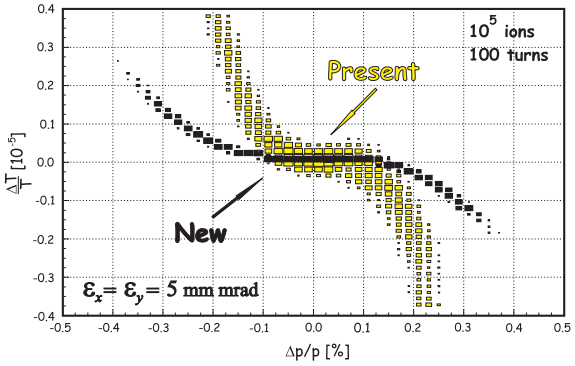

Figure 2: The variation of the revolution time as a function of the momentum deviation for the present and the new isochronous optics.

The high-order aberrations play a significant role for particles with large momentum deviations. In a region of $\Delta p/p = \pm 0.1\%$ the mass resolution in the new mode is about $2\cdot 10^{-7}$. This is one order of magnitude improvement compared to the present mode. Even for almost zero momentum deviations, the time spread due to different transverse motion is significant in the present optics, and is improved in the new mode (achromatism of the ESR).

References

[1] M. Hausmann, et al., Nucl. Instr. Meth. A 446, 569 (2000).
[2] A. Dolinskii et al., Proceedings of EPAC, 596-598 (1996).
[3] S.Litvinov, et al., GSI Scientific Report 2007, p. 212 (2008).
[4] H. Wollnik, et al., AIP Proceedings 177, 74 (1988).
[5] N. Iwasa et al., Nucl. Instr. Meth. B 126, 284-289 (1997).

The new ProfileView Software for Beam Induced Fluorescence Monitors

R. Haseitl, F. Becker, P. Forck, and T. Hoffmann
GSI Accelerator Beam Diagnostics, Darmstadt, Germany

System Setup

GSI accelerators are currently equipped with four Beam Induced Fluorescence (BIF) monitors. They determine the transverse beam profiles without beam disturbance by detecting the fluorescence light generated by excitation of a working gas (N_2) with the passing ion beam. Therefore, they are well suited to observe the beam at multiple positions simultaneously [1].

The fluorescence photons are detected by two microchannel plate (MCP) based image intensifier systems using FireWire CCD cameras to determine the horizontal and vertical beam profile. Each camera lens has a remote controllable iris to adjust the number of photons hitting the photo cathode of the intensifier system. Irises and MCP amplification are controlled by an Ethernet connected DAC electronics. Additionally, each BIF monitor comprises a pressure control unit to inject defined gas pressures into the beam pipe and a timing decoder to trigger the cameras and the MCPs.

Software Design

The software for the system consists of a server part written in LabView [2] and a client part written in C++. The server part is running on a powerful Windows PC (2.66 GHz, Quad Core CPU). The image data is read out from the cameras and pre-processed according to the user settings (e.g. image rotation, mirroring, projection calculation). The resulting data is then forwarded via the network to a client PC running the C++ application called ProfileView. In daily operation, only the projections are sent via the network and displayed in the graphical user interface. Additionally, unompressed raw images can be transmitted for storage and offline analysis. The network load of a 20 Hz data stream of one BIF monitor rises considerably from 0.8 MBit/s (projections only) to 110 MBit/s when both, projections and raw images, are requested. For network communication, standard TCP/IP sockets over a gigabit Ethernet connection are used.

Supplemental hardware devices are controlled by ProfileView via Ethernet. Critical systems, like MCP or pressure control, are implemented using separate threads for each device. Therefore, extensive calculations in the main event loop of the application will not block the communication with these devices. If the connection to the MCP amplification device is lost, the hardware sets all voltages to a "save value" to prevent damage of the system. To avoid accidental flooding of the beam pipe with gas, pressure values are double-checked by ProfileView and the pressure hardware prior to valve regulation. The network connection to the timing generator is established on demand and closed after the successful dispatch of the command. ProfileView uses the Qt C++ libraries [3] to achieve platform independence and is executable on both, Windows and Linux computers. Using the Linux X-technology, the graphical user interface shown in Fig.1 can be beamed to any of the terminals in the GSI main control room. Additional information on the software architecture can be found in [4].

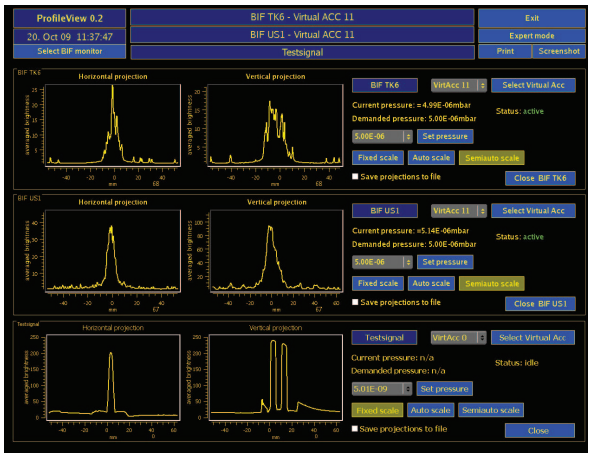

Figure 1: Screenshot of the ProfileView software, showing two active BIF monitors (TK6, US1) and a test signal.

User Experience and Outlook

ProfileView is used for the commissioning of the recently installed BIF monitors in 2009. During 2010 a final number of seven BIF monitors will be set up at GSI. First experiences show a good performance of the system. The ability to view multiple BIF images simultaneously and to store their raw data is a great benefit e.g. for beam alignment procedures and quality assurance. User requests for additional functionality have been collected and will be implemented in the next version of ProfileView.

References

[1] F. Becker, et al., "Beam Induced Fluorescence Monitor for Transverse Profile Determination", DIPAC'07, Venice, (2007).

[2] Company National Instruments, www.ni.com

[3] Company Nokia, http://qt.nokia.com/

[4] R. Haseitl, et al., "ProfileView - A Data Acquisition System for Beam Induced Fluorescence Monitors", DIPAC'09, Basel, (2009).

Imaging-Spectroscopy for BIF-Monitors in Rare Gases and Nitrogen

F. Becker*[1], P. Forck[1], R. Haseitl[1], B. Walasek-Hoehne[1], P.A. Ni[2], and D.H.H. Hoffmann[3]
[1]GSI, Darmstadt, Germany; [2]LBNL, Berkeley, CA 94720, USA; [3]IKP, TU-Darmstadt, Germany

For transverse profile determination a non-intercepting Beam Induced Fluorescence (BIF)-monitor was developed. The BIF-monitor detects fluorescence light emitted by residual gas molecules after atomic collisions with beam ions [1]. Using an imaging spectrograph the spectral response was mapped and associated with the corresponding gas transitions in helium, argon, krypton, xenon and nitrogen. Spectrally resolved beam profiles were obtained from the spectrographic images simultaneously. The present study with 5 MeV/u proton, S^{6+} and Ta^{24+}-ions reproduced the results of earlier studies with a 95 keV proton beam [2]. Moreover, the camera system connected to the spectrograph was image intensified, to provide single photon detection in order to resolve even weak transitions [3].

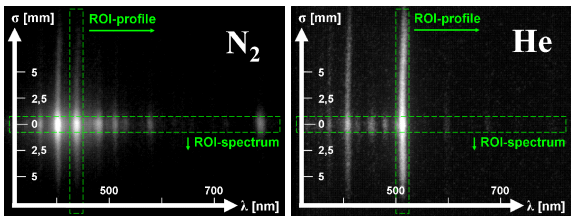

Figure 1: Fluorescence images of $3{,}2 \cdot 10^{11}$ S^{6+} ions with E_{kin} = 5.16 MeV/u in 10^{-3} mbar N_2 (left) and He (right) for 5 ms pulse duration at GSI-UNILAC.

The fluorescence light emitted by the residual gases was imaged with a chromatically corrected quartz-lens (UV-VIS) to the adjustable entrance slit of an imaging spectrograph [3]. A holographic grating with 285 grooves/mm provides 1.5 nm spectral resolution. The spatial resolution was determined to be 40 μm/pixel. Exemplarily for other gases, fluorescence images for a S^{6+}-beam in N_2 and He are shown in Fig. 1. In order to purify the gas atmosphere, the chamber was evacuated to the base pressure of 10^{-8} mbar and carefully flushed with each gas species before taking spectral data.

Beam profiles obtained for N_2, Ar, Kr and Xe show reasonable profile widths and correspond well with each other. He however is the only gas that generates significantly broadened profiles, see Fig. 2. All fluorescence spectra were calibrated and transitions could be identified with the help of spectroscopic databases [3]. Furthermore, results from spectroscopy show that rare gases have only 25% of the induced light yield (normalized with respect to the differential energy loss) achieved in nitrogen, [3]. Additionally, the fluorescent light of N_2 is concentrated in a few transitions, see Fig. 3. Thus N_2-gas seems to be the best choice and is therefore used at 7 BIF-stations along the UNILAC, which are currently installed and commissioned.

* frank.becker@gsi.de

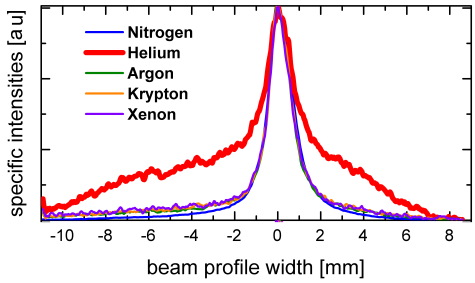

Figure 2: Beam profiles of S^{6+} ions in different purified gas-species at 10^{-3} mbar, for beam parameters see Fig. 1.

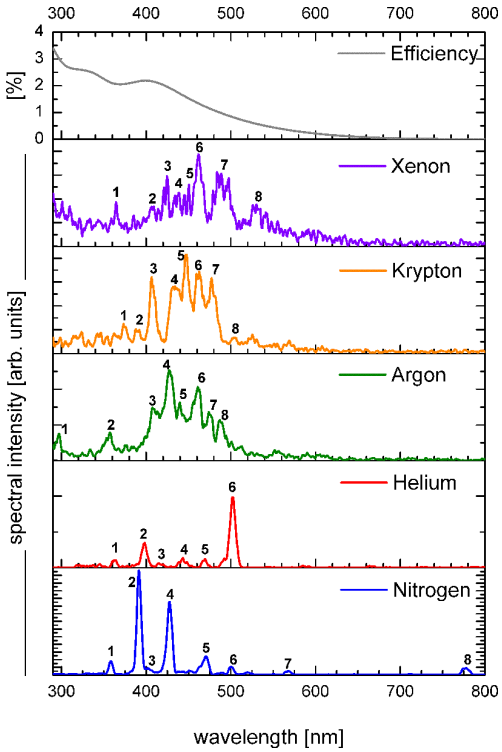

Figure 3: Fluorescence spectra of different working gases, induced by the S^{6+}-beam described in Figure 1. The indexed transitions can be found in [3].

References

[1] P. Forck and A. Bank, *Residual Gas Fluorescence for Profile Measurements at the GSI UNILAC*, EPAC'02, 2002, Paris, p. 1885-1887

[2] P. Ausset, S. Bousson, D. Gards, A. C. Mueller, B. Pottin, R. Gobin, G. Belyaev and I. Roudskoy, *Optical Transverse Beam Profile Measurements for High Power Proton Beams*, EPAC'02, 2002, Paris, p. 1840-1842

[3] F. Becker, C. Andre, F. M. Bieniosek, P. Forck, R. Haseitl, A. Hug, P. A. Ni, D. H. H. Hoffmann, B. Walasek-Hoehne, *BIF-Monitor & Imaging Spectrography of Different Working Gases*, DIPAC'09, 2009, Basel, p. 161-163

Charge-Frequency-Converter (QFW) Test Board and Results

H. Flemming**, S. Löchner**, H. Reeg*, **M. Witthaus***, GSI, Darmstadt, Germany

Overview

GSI Beam Diagnostics department recently started investigations on an economic solution for profile grid electronics. The front-end amplifiers and control devices presently used are outdated, very expensive and important parts, like low noise amplifiers, have long delivery times and/or have been discontinued by the manufacturer.
For the FAIR beamlines, around one hundred profile grid systems will be needed. The QFW CMOS-ASIC (Charge-Frequency-Converter [1][3]), developed by the Experiment Electronics department (EE) is a very promising candidate for a new design of the profile grids, due to it's high dynamic range without the need for any range switching.
After first tests with the 4-channel QFW module [2], it was decided to develop a new board, more related to practice and with additional electronic features (Fig. 1).

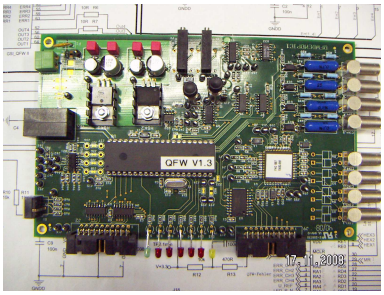

Fig. 1: New QFW-board with PIC micro-controller, display LEDs, current divider, LVDS-/LV-TTL-drivers.

Hard- and Software

The experimental board shown in Fig. 1 consists of:

- 4-channel QFW II
- current divider (for extended measuring range)
- LVDS- or LV-TTL outputs drivers
- power-supply for external devices (+3.3V/+5V)
- ICD-interface
- two precision voltage sources
- micro-controller Microchip® PIC 18FL4520
- several LEDs, hex-switch and two push-buttons

This board was designed in order to check the QFW in different operational modes, thus enabling measurements in the experimental areas of GSI. It was negotiated between Bio-Physics dept. and EE to add a selectable current divider onto the board, making it possible to measure currents up to 20 mA, of course dependent on the values of the circuit elements. Free-programmable LEDs, push buttons, a hex-switch and several I/O channels allow for adoption of the board to different measurement tasks.

*Beam Diagnostics ** Experiment Electronics

Output pulses and overload-bits are fed to their connector plugs through LVDS- or LV-TTL-drivers.
The micro-controller software was programmed in assembler via Microchip MPLAB®. The hex-switch allows changing range and polarity. After Power-On or Reset with the related buttons, the micro-controller transfers the necessary instructions to the QFW interface, whereupon operation starts.

Measurement Results

The QFW was tested under different conditions. At first the agreement with the results from the QFW datasheet and jitter behaviour was checked, and then tests under different ambient temperatures and different levels of X-radiation were carried out (see [4] for more information).
A jitter around 0.1 ppt or better at each particular current value was detected by using an HP time interval analyser 5372A.
The linearity of the frequency outputs fulfils the requirements for future profile grid electronics. Also the frequency deviation between each channel and a reference signal was investigated. This deviation is better than 1 % Full Scale.
The temperature behaviour studies were performed in a climatic exposure cabinet. Many measurement series were done between 0°C and 50°C. The results show a deviation of 0.7 % only, with respect to the 20°C reference.

Presently, all these results show that the QFW ASIC can be used in a new design for profile grid electronics. Additional comprehensive tests are in progress.

Outlook

A new QFW board equipped with 8 ASICs will be developed in 2010, in collaboration with the EE department. This prototype will be controlled by an existing FPGA-I/O VME board (VUPROM) .
A LabVIEW program will control the measurements. First beam tests of the prototype will be performed with a 2x16-wire profile grid in an experimental beamline at GSI. The board will also be used for further characterisation of the QFW ASIC.

References

[1] H. Flemming, QFW II Preliminary Datasheet, GSI, 2008
[2] H. Flemming, QFW Module Preliminary Datasheet, GSI, 2007
[3] H. Flemming, E. Badura, A High Dynamic Charge to Frequency Converter ASIC, GSI Scientific Report, 2004
[4] S. Löchner, Total Ionising Dose Studies of the QFW ASIC, GSI Scientific Report, 2009.

Temperature and Spectroscopic Studies on Inorganic Scintillating Materials

E. Gütlich[1,2], W. Ensinger[2], P. Forck[1], K. Gütlich[1], R. Haseitl[1], and B. Walasek-Höhne[1]
[1]GSI, Darmstadt, Germany; [2]Technical University Darmstadt, Darmstadt, Germany

At the GSI UNILAC scintillating screens are used for transverse beam profile monitoring. For high current beam operations inorganic scintillators were investigated and numerical analysis of the recorded images was performed.

The light yield, imaged beam width and higher statistical moments show strong dependence on the scintillating materials deployed [1, 2] and their temperature. Detailed temperature studies were carried out using a Ni layer (as a heating loop) sputtered on the backside of the ZrO_2 screen. Additionally, the spectral response of the materials was mapped for different temperature levels (RT-300^{o}C), using a spectrometer.

During the measurements, heating power was kept constant but the temperature of the sample was increasing due to the energy deposition of the impinging ion beam. As shown in Fig. 1 the light yield and imaged beam width for ZrO_2 irradiated by the proton beam increase with temperature, except the initial phase which is difficult to interpret. In the temperature range from 125 - 250^{o}C, the light yield increases by the factor of 4 and the imaged beam width by 1.5. These results clearly point out that the temperature of the scintillators is critical for high current operations.

Spectra of the scintillation light show a temperature dependance [3] as depiced in Fig. 2. For the broad band at 480 nm a slight shift to higher wavelengths is observed during the heating process. The bands around 400 and 725 nm are affected by the temperature, as well. For the spectra obtained with the proton beam, a sharp line around 515 nm occurred which is not observed for Ta^{24+} beam. Additionally, this line is not influenced by the change of screen temperature (Fig. 2).

Several scintillating materials like Al_2O_3, $Quartz$ etc. were investigated under various beam conditions (H^+ as well as heavy elements up to U^{28+}). Different readings of the imaged beam width for various materials were found. Further more, spectroscopic studies on different materials show a significant dependence of the spectra on the used ion species. A detailed discussion of these topics can be found in [3] and will be further investigated.

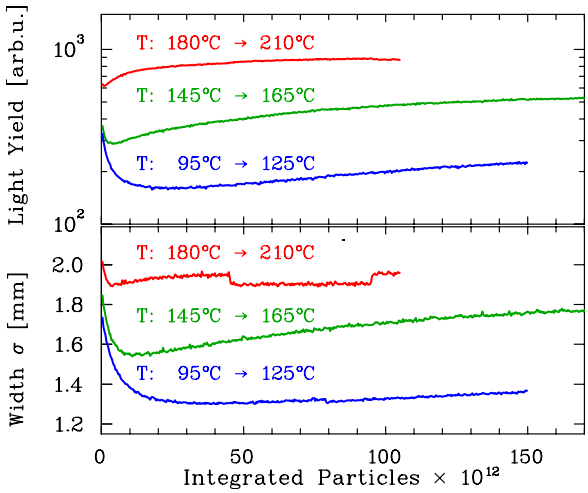

Figure 1: Temperature dependence of light yield and beam width for ZrO_2. Parameters of H^+ beam: 300-500 macro-pulses of 4 ms lenght, 2 Hz repetition rate with $3.5 \cdot 10^{11}$ ppp at 4.8 MeV/u.

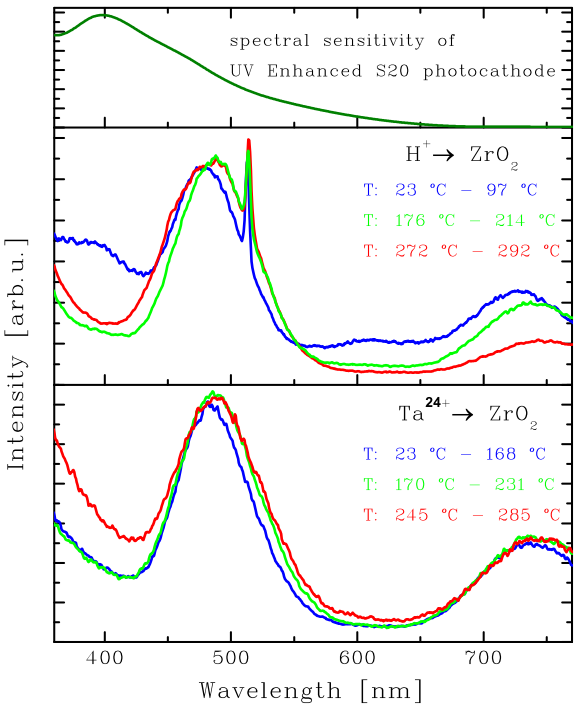

Figure 2: Scintillation light specra of ZrO_2 for irradiation with H^+ (for the beam parameters see Fig. 1.) and Ta^{24+} (beam parameters: 1 Hz repetition rate with $8.8 \cdot 10^9$ ppp in 100 μs pulse length at 11.4 MeV/u. The spectra are averaged over 1000 images and are not corrected for photocathode (top) and spectrometer efficiency.

References

[1] E. Gütlich et al., "Scintillation Screen Investigations at UNILAC", 2007/2008 GSI Scientific Report, pp. 105/pp. 126.

[2] E. Gütlich et al., "Scintillation Screen Investigations for High Current ion Beams at GSI-LINAC", BIW'08, Lake Tahoe, May 2008, p. 100, http://www.jacow.org/.

[3] E. Gütlich et al., "Scintillation screen investigations for high current ion beams", SCINT'09, Jeju, June 2009, IEEE Transactions on Nuclear Science, accepted for publication in June 2010 issue.

Transversal Beam Dynamics Calculations for HITRAP

J. Pfister [1,2], G. Clemente[2], F. Herfurth[2], O. Kester[3], and U. Ratzinger[1]

[1]IAP, University of Frankfurt, Germany; [2]GSI, Darmstadt, Germany; [3]NSCL, East Lansing, MI 48824, USA

Until 2008 several transversal and longitudinal beam dynamics simulation codes have been used for the calculation of the transversal beam behavior in the HITRAP decelerator and its connected beamlines. Since simulations are an essential support during commissioning, the aim of this project was to be able to simulate at least the complete beam from the exit of the ESR through different optical elements including the transversal effect of the Double-drift buncher as well as the first deceleration stage (IH-structure) shown in fig. 1 using only one code. This should result in a fast code for transversal optimization down to the RFQ, which can be used online during commissioning.

Elements taken into account are two big dipoles and

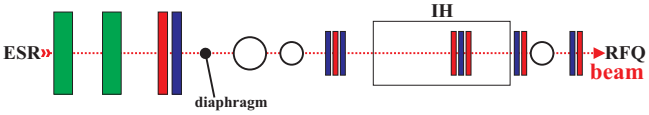

Figure 1: Schematic of transversal optical elements: dipoles (green), quadrupoles (red,blue), buncher (circles) and IH-cavity (square).

a strong quadrupole doublet already used in the old reinjection line. Furthermore new quadrupole triplets and doublets as well as the double-drift buncher and the IH-structure were installed in the linear deceleration beamline.

The problem has been approached using the COSY Infinity software [1]. Algorithms for transversal influence of an acceleration gap have been developed and extensively tested and compared with LORASR calculations. A matrix routine together with the knowledge of accelerating fields and phase relations in each gap of bunchers and IH-structure has been implemented.

Since the complete transversal beam dynamics can be calculated within this code without interchanging data to other codes an easy-to-use simulation tool including the deceleration from 4 MeV/u down to 500 keV/u and injection into the RFQ was achieved. It can be used for optimization of the transversal beam properties.

An essential, but also critical part in the beamline is a diaphragm (see fig. 1, length 150 mm with inner diameter 12 mm) inserted during and is staying there since the first beamtime in May 2007 in between the ESR extraction beamline and the HITRAP linear decelerator for vacuum decoupling. This was not foreseen in the TDR [2] and makes beam transport more difficult.

Studies which were carried out in 2009 show that this makes an efficient transversal focusing into the IH-structure impossible and then causes beam losses in the intertank section resp. at RFQ injection due to too big RF defocusing in the IH. At least 25% of the particles will be lost with the presently possible magnet gradients. Fig. 2(a) shows best possible beam transport from the IH to the RFQ using the current intertank setup including the permanently installed diaphragm in front of the first buncher. Phase space distributions and acceptance of the RFQ are compared in figs. 2(b) and (c).

Simulated beam transport from the ESR to the IH has

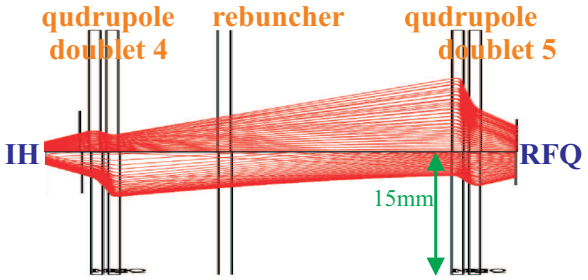

(a) intertank beam transport

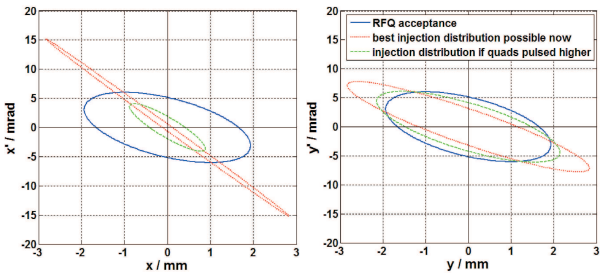

(b) horizontal phase space (c) vertical phase space

Figure 2: (a) Beam transport from IH to RFQ and injection with diaphragm and current setup, (b) and (c) Best possible phase space distributions and RFQ acceptance.

been experimentally proven. It shows discrepancies of only up to a few percent, which is caused by the measurement error of the beam diameter.

This problem could be solved by an adjusted intertank section. If the two doublets could be pulsed to higher gradients no physical adjustement would be necessary reaching a transversal transmission of 98%. The corresponding phase space is also shown in fig. 2 and compared to the RFQ acceptance.

References

[1] K. Makino and M. Berz, “COSY INFINITY version 8”, Nucl. Instrum. Methods A 427 (1999) 338-343.

[2] T. Beier, L. Dahl, H.-J. Kluge, C. Kozhuharov und W. Quint, “HITRAP Technical Design Report”, Gesellschaft für Schwerionenforschung mbH, Darmstadt (2003).

Founded by BMBF06FY160I and HITRAP-IH-Struktur
j.pfister@gsi.de

Investigation of the Beam Quality from High Current Ion Sources on HOSTI

A. Adonin, R. Hollinger, and P. Spädtke
GSI, Darmstadt, Germany.

With the coming FAIR project at GSI the requirements for beam brilliance for heavy ion beams provided by the high current injector will increase, especially for uranium ions. To perform and to demonstrate the required improvements the high current test injector (HOSTI) has been built up. The main purpose of HOSTI is an optimization of the experimental setup of a high current ion source and the post acceleration gap to increase the beam brilliance [1].

The investigations have been performed in two stages [2]. The first stage of investigations includes the measurements of the transversal ion beam emittance with slit-grid scanner installed directly behind the post acceleration gap. The measurements were performed with a singly charged Ar-beam provided by MUCIS with fixed ion velocity of 2.2 keV per nucleon (actual requirements of existing RFQ). During this stage the beam emittance has been investigated as a function of the following parameters: ratio between extraction ($U_{ext.}$) and post acceleration (U_{PA}) voltages at fixed ion energy; width of the high voltage gap in the post acceleration system; emission current density of the ion source; ion beam current in the beamline.

For the second stage of the measurements the superconducting solenoid (built by Cryogenic LTD) was installed directly behind the post acceleration gap. The solenoid represents a two-magnet system with the main coil in the middle and two serially connected compensation coils positioned symmetrically at each end of the main coil.

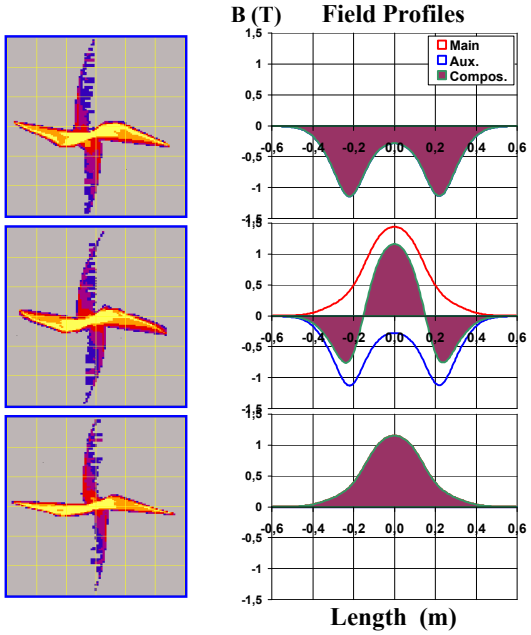

Figure 1: Influence of the longitudinal profile of the solenoid field on the beam emittance.

During the second stage the influence of the solenoid field with different focusing strength and various profile shapes on the beam emittance was investigated [2]. Of particular interest were the measurements with variation of the longitudinal field profile keeping the same focusing strength. In Fig.1 the emittance pictures and the field profiles for three drastically different solenoid field shapes: only compensation coil, main and compensation coils and only main coil are shown.

In addition we measured the real space profile of the ion beam. Measurements were performed using the viewing screen installed on the same position as the scanner slit with 45 degrees to the ion beam axis. The beam profile has been investigated as a function of various settings of the ion source, post acceleration system as well as the solenoid field. As a main result of these measurements it was shown that the structure of the ion beam after extraction is conserved and there is no full homogenization of the ion distribution in the post acceleration gap. Thereby with adjustment of certain parameters it is possible to reproduce the image of the extraction electrode on the viewing screen (several meters behind the gap) (Fig.2).

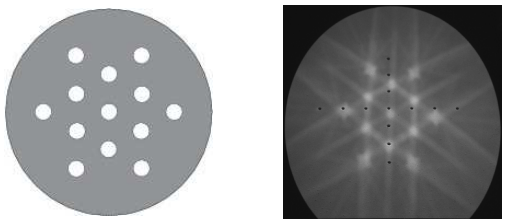

Figure 2: (left) electrode shape of 13-hole extraction system; (right) reflected image of the extraction electrode.

From these investigations the following conclusions can be drawn:

– the superconducting solenoid is suitable for transporting and focusing the high current heavy ion beam with the required parameters;
– we could not observe any reasonable growth of the beam emittance due to solenoid focusing;
– the strong magnetic field of the solenoid does not disturb the space-charge compensation of the ion beam and does not produce any additional optical aberrations;
– we did not observe any appreciable influence of the longitudinal magnetic field profile on beam emittance beside different focal length;
– the beam profile measurements provided simultaneously with emittance measurements can give necessary information about the ion distribution.

References

[1] R. Hollinger, M. Galonska, F. Heymach, K.D. Leible, K. Ochs and P. Spädtke: *High Current Ion Source Development and HOSTI*, GSI Scientific Report 2005, ISSN 0174-0814.

[2] A. Adonin, R. Hollinger, P. Spädtke: *Measurements of Transverse Ion Beam Emittance Generated by High Current Ion Sources at the GSI Test Injector Facility HOSTI*, Proceedings of the 13th International Conference on Ion Sources, Gatlinburg, USA, September 2009.

HSI-Frontend Upgrade

W. Barth, L. Dahl, M.-S. Kaiser, A. Kolomiets*, S. Mickat, S. Minaev*, W. Vinzenz, H. Vormann, S. Yaramyshev
GSI, Darmstadt, Germany; *ITEP, Moscow, Russia.

Overview HSI-Frontend Upgrades

To fulfil the requirements of FAIR (15 emA of U^{28+} with min. 70 µs pulse length to be injected into SIS18), the UNILAC has to be upgraded in several sections: the LEBT [1], the HSI-RFQ [2], the Alvarez main accelerator [3], and high current beam diagnostics [4].

Corresponding to the requirements of FAIR, the High Current Injector HSI has to deliver 18 mA U^{4+} at HSI output. This cannot be achieved with the RFQ and the LEBT as existing up to 2008. Therefore a three-step upgrade of this HSI-Frontend is scheduled: The RFQ-Upgrade has been realized in 2009, the LEBT-upgrade I (quadrupole quartet and switching magnet) is foreseen for 2010, followed by LEBT-upgrade II with an additional linear source branch (Compact LEBT), as a part of the FAIR-UNILAC upgrade.

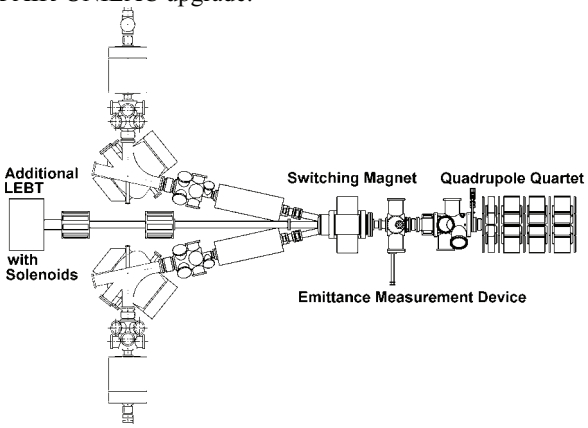

Figure 1: HSI-Frontend upgrade, including new ion source terminal and Compact LEBT.

HSI-RFQ Upgrade

In a prior upgrade of the HSI-RFQ (2004), a modified input radial matching section (IRM) was installed, resulting in significantly increased high current transmission, confirmed by simulations [5].

In 2009, the HSI-RFQ has been upgraded again, now with a completely new beam dynamics design of the new electrodes [2]. With an enlarged aperture and higher voltage (155 kV instead of 125 kV at Uranium level, but max. surface peak field held lower than the old design), the acceptance is increased. With an improved IRM design the emittance in the radial matching section is keeping small.

A constant average aperture, transverse electrode vane shape and carrier ring dimension along the whole RFQ was chosen from simulations to meet the resonance frequency and a flat voltage distribution. After machining and reassembly of the RFQ, first measurements during the RF tuning period confirmed the predicted properties. As expected from the comparison of simulations and measurements of existing resonator sections, only six fixed plungers were needed.

Besides mechanical modifications, the power supply for the RF transmitter has been equipped with bigger capacitors, to provide for the higher total RF power and for acceptable reliability. RF conditioning took only four days to reach the argon level (104 kV, 330 kW), and three more weeks to reach uranium level (155 kV, 1.2 MW). Conditioning for uranium level was proceeded for additional six weeks, until the necessary RF-power decreased (1.0 MW).

HSI-RFQ	New Design	Existing Design
Electrode voltage / kV	155	125
Average aperture radius / cm	0.6	0.5245 – 0.7745
Electrode width / cm	0.846	0.9 – 1.08
Maximum field / kV/cm	312.0	318.5
Modulation	1.012 – 1.93	1.00 – 2.09
Synch. Phase, degrees	-90^0 - -28^0	-90^0 - -34^0
Minimum aperture radius, cm	0.410	0.381
Number of cells with modulation	394	343
Length of electrodes, cm	921.74	921.74

Table 1: Design parameters of the HSI-RFQ.

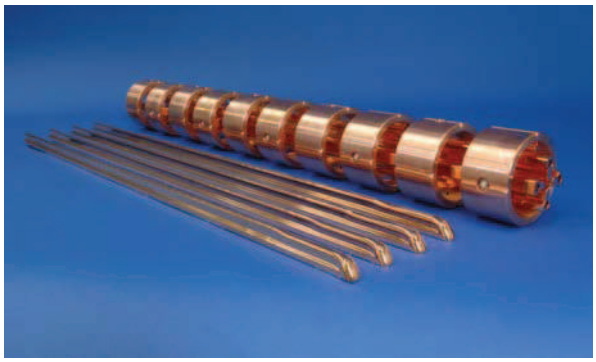

Figure 2: New RFQ electrodes, with new IRM.

Electrodes and carrier rings fabrication, assembly	July 2008 - April 2009
RF tuning (prelim. assembled)	May 2009
Re-assembly in beamline	June 2009
Beam-commissioning with argon	July 2009
Beam-commissioning with uranium, routine heavy ion high current operation	since September 2009

Table 2: RFQ upgrade schedule.

Beam-commissioning started in July 2009 with Ar^{1+}. For this an emittance measurement device was installed behind the RFQ. Transmission measurements showed a gain of 50 % compared to the previous RFQ-design: After

optimization up to 85% of 12.5 mA input beam current were transported and accelerated through the quadrupole quartet and the new RFQ.

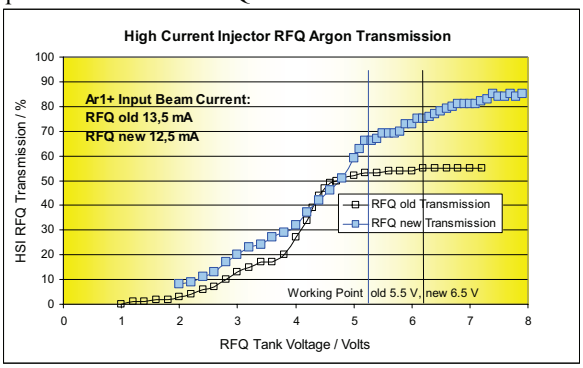

Figure 3: Measured transmission of the HSI-RFQ.

As a consequence of the increased acceptance the measured RFQ emittance is larger. Compared to the results of the initial RFQ-commissioning in 1999 a two times higher transverse beam emittance was confirmed by high current beam emittance measurements.

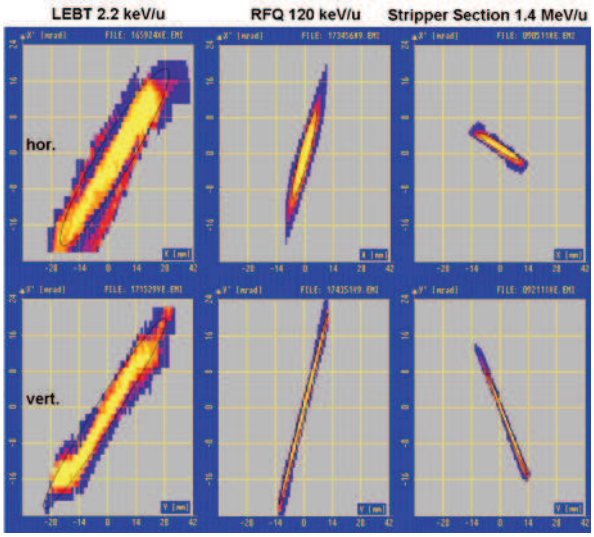

Figure 4: Ar^{1+} high current HSI-emittances.

Re-commissioning of the complete HSI (incl. reassembled Superlens and IH) with Ar^{1+} showed the correct RFQ beam energy of 120.5 keV/u. The measured beam current of 8.5 mA Ar^{1+} behind the HSI (at 1.4 MeV/u, stripped 13mA Ar^{10+}) is a new world record, exceeding the old HSI record of 8.0 mA, even despite a lower input current (13 mA instead of 16 mA).

Measurements with high current U^{4+}-beam in September/October 2009 gave maximum transmission values of 80% through the quadrupole quartet and the RFQ (input beam current 6 mA U^{4+}, LEBT settings optimized for max. transmission), resp. 70 % (input beam current 11 mA). The transmission is higher than predicted from simulations with measured LEBT particle distributions, because the beam with big radius and divergence is not caught fully on the emittance grids.

	U^{4+}		Ar^{1+}	
	2004	2009	2004	2009
inp. beam curr. /mA	8.5	10	8	13
ε_x/mmmrad (90%,4*rms)	140	130	110	190
ε_y/mmmrad (90%,4*rms)	125	100	150	130
X/Y / mm	±20/28	±24/20	±20/28	±28/28
X'/Y' / mrad	±12/20	±12/25	±18/15	±16/20

Table 3: Measured transverse emittances before QQ.

	U^{4+}		Ar^{1+}	
Beam current/ Transmission	before upgrade	2009	before upgrade	2009
Before QQ	12.4 mA	11 mA	13.5 mA	12.5 mA
Behind RFQ	7.9 mA	7.5 mA	7.6 mA	9.5 mA
Transm. RFQ	64 %	70 %	56 %	85 %
Behind HSI	6.6 mA	6 mA	5.9 mA	8.5 mA
Transm. HSI	50 %	60 %	44 %	56 %

Table 4: HSI max. high current transmission.

High current requirements for the HSI cannot be fulfilled with the existing LEBT. For this an upgrade of the LEBT is in preparation for 2010.

HSI-LEBT Upgrade

In the existing LEBT the switching magnet, the emittance measurement device and the quadrupole quartet will be replaced. Wider aperture diameters behind the switching magnet (150 mm instead of 100 mm) will allow the optimization of the beam matching to the RFQ. The ceramic vacuum chamber for the new switching magnet is designed (DN100CF vac pipe for the straight branch, aperture 104 mm), a redesign of the magnet is in preparation. Vacuum chambers and grids for the new emittance measurement device are delivered (64 wires, 0.1 mm diameter, 0.8 mm distance, 80 mm length), ordering of the slits (water cooled, 0.1 mm slit width, 80 mm length) and grids (47 wires each plane, 2 mm distance) on the basis of design studies is finished. The new quadrupole quartet (l_{eff} 1st quadrupole 76 mm, 2nd to 4th 225 mm each) will be delivered in August 2010. A steerer device, a beam current transformer and a vacuum valve will be replaced by larger ones.

Compact LEBT

Further improvements of the beam brilliance cannot be reached with the existing ion source branches. Therefore an additional straight-line branch with two superconducting solenoids is planned. One solenoid of this type (200 mm warm bore diameter, max. 4 T, vacuum tube aperture diameter 180 mm) has already been delivered and tested successfully at the GSI high current ion source test bench.

References

[1] L. Dahl et al., proc. Linac 2006, p. 183,
[2] A. Kolomiets, W. Barth et al., proc. Linac 2008,
[3] L. Groening et al., Phys. Rev. ST Accel. Beams **11** 094201, (2008)
[4] A. Peters, P. Forck et al., proc. Linac 2004, p.13.
[5] W. Barth et al, proc. Linac 2004, p. 246

Status of the HLI-RFQ Upgrade

P. Gerhard*[1]
[1]GSI, Darmstadt, Germany

Introduction

The high charge state injector HLI at the UNILAC provides mainly beams for the super heavy element research (SHIP, TASCA). High average beam intensities, i.e. high duty factors, are prerequisite. Fed by an ECR source, the HLI meets the requirements well. Additionally, it is also used for rare isotope beams.

The HLI–linac comprises a radio frequency quadrupole (RFQ) and an IH structure. While the high charge state of the ions from the ECR source facilitates the acceleration, the existing RFQ was figured out to be a bottleneck concerning high duty factor operation. Therefore it was decided four years ago to replace it by a new RFQ. This measure is part of an upgrade program including a second, new 28-GHz superconducting ECR ion source [1].

Design of the new RFQ

The new RFQ has to accelerate ions with $A/q \leq 6$ in cw operation. The design goal was to enable this with the existing rf power amplifier ($\leq$70 kW average power). For A/q up to 8.5 the duty cycle is limited to 50%. More details are given in tab. 1. The RFQ structure is shown in fig. 1.

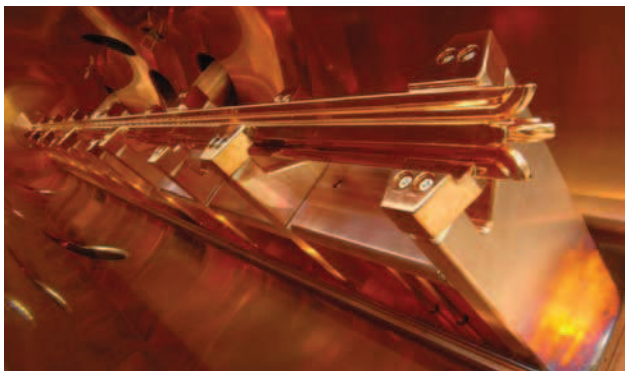

Figure 1: New RFQ during final assembly (courtesy of G. Otto, GSI).

* p.gerhard@gsi.de

Property	Value
Injection / extraction energy [keV/u]	2.5 / 300
RF frequency [MHz]	108.48
A/q (cw / max.)	$<$ 6.0 / 8.5
Power (avg. / max.) [kW]	70 / 140
Intervane voltage (cw / max.) [kV]	55 / 78
Design acceptance [π mm mrad]	$\geq$ 200

Table 1: Design properties of the new HLI RFQ [2].

Assembly & rf commissioning

In February 2009 the RFQ tank was copper plated at GSI. The milling of the electrodes at the company NTG lasted until July. The production of the RFQ was completed by copper plating of the electrodes in the GSI workshop. Assembly, alignment and rf tuning took place at IAP in Frankfurt. Final assembly (water cooling, vacuum and alignment measurements) followed after delivery to GSI. The electrodes had to be realigned. Afterwards the RFQ was transferred into the rf test bunker for first high power rf tests. Within short time reasonable rf power could be applied to the tank until contact springs at the tuning plates burnt down. All springs were renewed and enhanced, and the electrodes were realigned again. In December the RFQ was mounted in the HLI bunker for further rf tests.

Beam dynamics measurements

While the RFQ was under test, the HLI beam line was prepared for the new RFQ. After the old RFQ was removed, an emittance measurement device was installed and extensive emittance and beam profile measurements were performed. These data will be used to calculate the beam dynamics for the new RFQ. Measured emittances are shown exemplary in fig. 2. Beam commissioning of the RFQ and final (re-)commissioning of the HLI with the new accelerator are scheduled for February and March 2010 respectively.

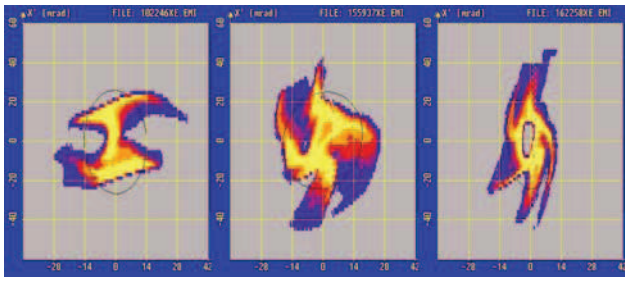

Figure 2: Measured beam emittances of Ar^{7+}@2.5 keV/u (left, middle) and Ar^{8+}@4 keV/u (right) in front of the RFQ.

References

[1] P. Gerhard et al., Status of the UNILAC–Upgrade programme for the heavy element research at GSI–SHIP, EPAC'08, Genoa, June 2008, THPP021, p. 3416 (2008)

[2] A. Schempp, M. Vossberg, Design, production and tests of the HLI 4-rod radio frequency quadrupole accelerator, Conceptual Design Report (2008)

Measurement of Space Charge Driven Resonances in the UNILAC Alvarez DTL

L. Groening[1], I. Hofmann[1], W. Barth[1], W. Bayer[1], G. Clemente[1], L. Dahl[1], P. Forck[1], P. Gerhard[1], D. Jeon[2], M.S. Kaiser[1], M. Maier[1], S. Mickat[1], T. Milosic[1], D. Uriot[3], and S. Yaramyshev,[1]
[1]GSI, Darmstadt, Germany; [2]ORNL, Oak Ridge, TN, U.S.A., [3]CEA/Saclay, Gif-sur-Yvette, France

Last years experiments aimed to the investigation of resonant transverse emittance growth for high intensity beams. The driving force is the self field of the beam's space charge.

The first resonance is driven by similar beam envelope phase advances in the transverse and longitudinal dimension [1]. First theoretical investigations date back to 1992 and avoiding this resonance is a design rule for all high intensity linac projects. Experimental confirmation was not achieved world-wide due to the leak of diagnostics, machine control, and beam matching. For a given experimental set-up the longitudinal phase advance σ_l is constant and the resonance is probed by varying the transverse phase advance $\sigma_\perp$ using the quadrupole strength. Figure 1 plots the measured transverse emittance at the DTL exit as a function of the phase advance ratio. Additionally, results from computer simulations are shown being in good agreement with the measured data as well as with the underlying theoretical concepts. A detailed description of the experiment can be found in Ref. [2].

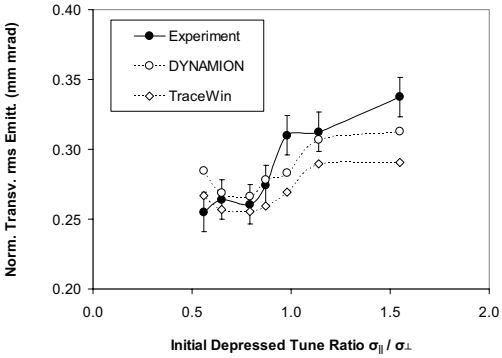

Figure 1: Emittance as function of phase advance ratio.

The second resonance is purely transverse and it is driven by the octupolar component of the polynom describing the beams transverse charge density. The corresponding field term scales as an octupole, namely $\approx r^3$. This field component acts to the periodically focused beam as a perturbation and it is resonantly excited if the transverse phase advance becomes equal to 360°/(3+1), i.e. 90°. This resonance has been predicted about three decades ago [3]. Recent simulation studies [4] revealed that this resonance dominates the well-known envelope instability occurring at 90° as well [5]. Moreover, they revealed that this resonance might be measured using the UNILAC's Alvarez DTL.

Figure 2 shows the measured emittance at the DTL exit as a function of the transverse phase advance. The predicted resonant increase at about 90° was observed and has been confirmed with three different simulation codes. A characteristic feature of an octupolar resonance is the formation of four arms in the phase space distribution. This four-fold filamentation was measured as well at the UNILAC and it is displayed in Fig. 3.

The described experiments (see [6] for details) are the first successful validation of resonant emittance growth in a linear accelerator world-wide. Since resonant phenomena along a linac are tiny perturbations, it requires a very stable and reliable operation of the UNILAC. The same applies to the diagnostic components.

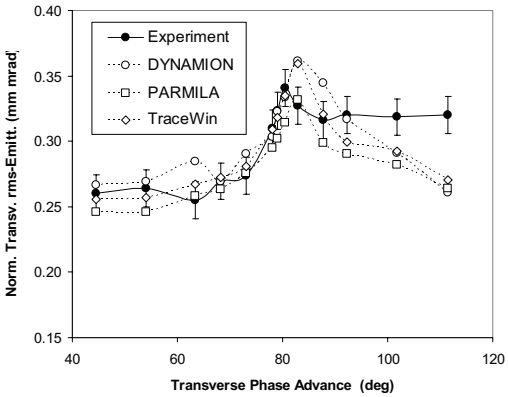

Figure 2: Emittance as function of transverse phase advance.

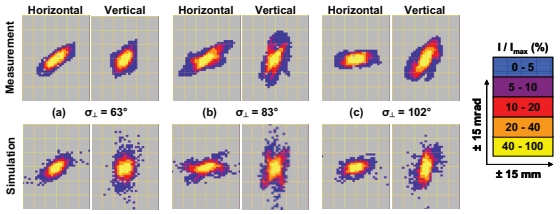

Figure 3: Phase space distributions at DTL exit.

References

[1] I. Hofmann et al., PRL **87**, 034802 (2001).
[2] L. Groening et al., PRL **103**, 224801 (2009).
[3] I. Hofmann et al., AIP Conf. Proc. No. 642, p. 248, (2002).
[4] D. Jeon et al., PRST-AB **12**, 054204 (2009).
[5] I. Hofmann et al., Part. Accel. 13, 145 (1981).
[6] L. Groening et al., PRL **102**, 234801 (2009).

Measurement of the Longitudinal Phase Space at UNILAC

T. Milosic[1], P. Forck[1], and D. Liakin[1,2]
[1]GSI, Darmstadt, Germany; [2]ITEP, Moscow, Russia

To deliver the required currents for FAIR an important goal is to improve the matching into the Alvarez section of the UNILAC. Besides simulated phase space data, crucial information about the beam parameters is provided by diagnostic devices. While there are several standard methods to access the four-dimensional transverse phase space information, the longitudinal degree of freedom is as important but an unequally more demanding measurement task.

The current approach is based on the time-of-flight (TOF) measurement of single particles between two detectors (see Fig. 1), and constructing the longitudinal phase space via 2-dim histogramming using the arrival times at both detectors and UNILAC rf reference [1]. The energy information is extracted from the TOF between a MCP and a diamond detector, whereas the arrival time at the diamond with respect to the rf serves as a direct measure of the relative phase location between particles. Imposed by the limited distance (800 mm) between these detectors, a time resolution of only several tens of picoseconds is mandatory to resolve an rms energy spread of about 1% at 1.4 MeV/u. The TDC and discriminators are capable to provide a time resolution of about 50 ps rms. Additionally, signals from the diamond and MCP suffer from a broad pulse height spectrum and varying pulse shapes that significantly degrade time resolution.

While the vertical projection of the longitudinal phase space distribution yields trustworthy bunch structure information, the limited energy resolution affects the measured size of the phase space, which results in an enlarged emittance ε and decreased covariance. Therefore the related correlation as described by the Twiss parameter $\alpha = -cov\left(\frac{\Delta E}{\langle E \rangle}, t\right)/\varepsilon$ is smaller than expected from simulations and a plausible machine operation mode. To

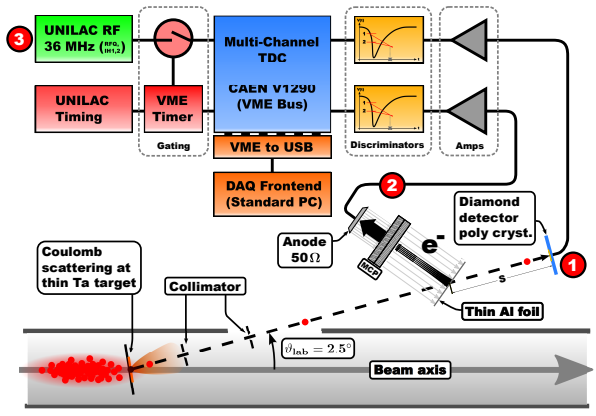

Figure 1: Single particles are detected indirectly at the MCP module (2) and directly at the diamond detector (1) whereas the UNILAC rf serves as timing reference (3).

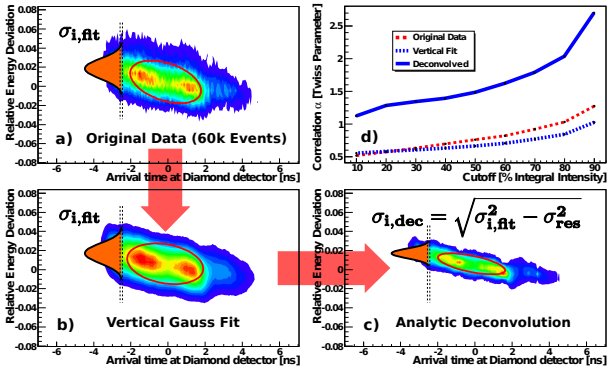

Figure 2: **a**) Plain data from DAQ. **b**) Reconstructed phase space using Gaussian fits to energy degree of freedom. **c**) Analytic deconvolution with $\sigma_{i,dec} = \sqrt{\sigma^2_{i,fit} - \sigma^2_{res}}$ for each vertical slice i (see text). **d**) Correlation α for original, fitted and deconvolved phase space vs. integral cutoff levels.

improve the systematic energy broadening, deconvolution methods were investigated in order to disentangle the error contribution from the original phase space data. In Fig. 2 an example of the original and deconvoluted data is shown from a high current Argon beam (6.5 mA) recorded during the *HIPPI* campaign at GSI [2]. Statistical noise, off-center vagabonding particles and the intrinsic low count rates are severe issues concerning a deconvolution approach. Furthermore, no pulse response is available from experimental data due to the lack of a monochromatic beam. Thus the pulse response is deduced from a consideration of error contribution based on a Gaussian model denoted by σ_{res}. This permits us to perform an analytic deconvolution of the energy information when vertical slices are also fitted with an Gaussian parameterization as depicted in Fig. 2. A consistent deconvolution of the energy distribution is achieved even for noisy data. Moreover, the *correlation* α changes significantly and approaches the expected value.

As an alternative to the TOF measurement preliminary investigations of the calorimetric properties of a monocrystalline diamond detector have been performed using an Am-243 source. Preliminary analysis shows an energy resolution of about 1% for α particles at several MeV. The detector has been installed and will be tested soon.

References

[1] T. Milosic, P. Forck, D. Liakin, “Longitudinal Emittance Measurement using Particle Detectors”, DIPAC’09, Basel, May 2009, p. 330.

[2] High Intensity Pulsed Proton Injectors (HIPPI), Joint Research Activity (JRA3) in the framework of CARE.

Emittance Exchange due to Linear Coupling by Skew Quadrupole in SIS-18

W. Daqa[1,2], I. Hofmann[1,2], V. Kornilov[1], J. Struckmeier[1,2], and O. Boine-Frankenheim[1,3]
[1]GSI, Darmstadt; [2]Johann Wolfgang Goethe University, Frankfurt; [3]TU-Darmstadt, Darmstadt

For high current synchrotrons and for the SIS18 operation as booster of the projected SIS100 it is important to improve the multi-turn injection efficiency. This can be achieved by coupling the transverse planes with skew quadrupoles, which can move the particles away from the septum. Linear betatron coupling due to skew quadrupole components in SIS18 including space charge effect was studied in an experiment using different diagnostic methods during the crossing of the difference coupling resonance.

As an extension of previous study of linear coupling [1], we considered space charge effects in our measurement in August 06, 2009. We used $^{40}Ar^{18+}$ coasting beam at injection energy 11.35 MeV, where the horizontal beam size was chosen such that $\epsilon_x \leq A_y/2$, where A_y is the vertical acceptance at injection, with $\epsilon_x/\epsilon_y \approx 5$. The beam intensity was controlled via the UNILAC so we had $N_p \approx 2.0\times10^9 - 1.5\times10^{10}$. The horizontal tune was set on $Q_x = 4.26$, then we performed a static vertical tune scan $Q_y = 3.20 - 3.36$ using SISMODI software. We switched on one skew quadrupole installed in the first sector of the SIS-18 lattice (S01KM3QS) with different strengths and tested its effect on the difference coupling stop band width for low and high intensity beam. Using a residual gas monitor we measured the RMS transverse emittance exchange. We concluded an overestimation of the transverse beam sizes which could be a result of the abrasion of the MCPs in the RGM. The actual beam size was corrected to $\sigma_x = \sigma_{x\text{meas}}/1.21$ and $\sigma_y = \sigma_{y\text{meas}}/1.26$ to fulfill the invariance condition $\epsilon_x + \epsilon_y$ =constant. In figure (1), we show the case with the natural coupling due to random roll errors in the normal quadrupoles. The large tune shift of the resonance center is due to systematic deviations in SISMODI software.

We simulated the emittance exchange, where a KV particle distribution was generated and tracked in SIS18 triplet linear lattice using PARMTRA, which is a code developed at GSI [2]. The linear coupling was introduced by one skew quadrupole (thin lens) with a strength equivalent to the natural coupling strength. The RMS transverse emittances were computed turn by turn. Then we considered the averaged value to obtain figure (2). Space charge effects are: broadening the stop band width; reduction of the maximum emittance transfer (depending on the skew quadrupole strength); shifting of the resonance center above the single particle resonance as $\epsilon_x/\epsilon_y > 1$ [3]; and modification of the exchange curve so it becomes asymmetric.

The coupled tunes were measured from Gaussian fitting of the Schottky noise spectrum where we identified the side bands for the coupled motion. To estimate the number of turns for exchange from the measured beam loss we increased the injected turns, then we fixed the working point and changed the skew quadrupole strength. Therefore, we used the fast current transformer. The results can be used for further investigation on how to use linear coupling to improve the machine injection efficiency.

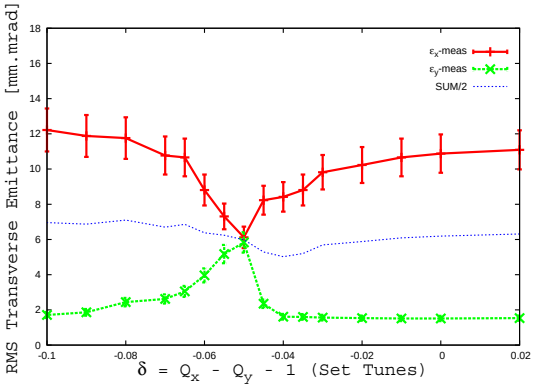

Figure 1: Emittance exchange measurement (06Aug2009) using residual gas monitor (RGM). The incoherent tune shift are $\Delta Q_x = -0.02, \Delta Q_y = -0.05$ with natural skew strength $k_{sq} = k_0$

.

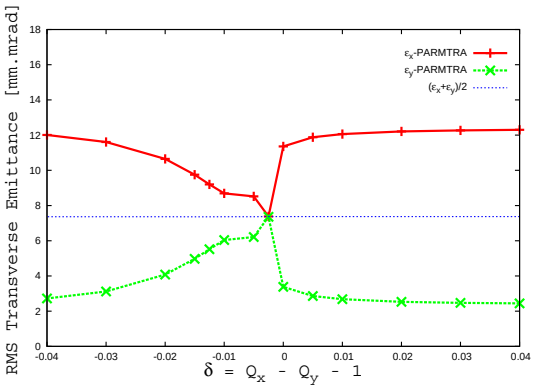

Figure 2: Emittance exchange simulation using PARMTRA. The incoherent tunes shift are $\Delta Q_x = -0.020, \Delta Q_y = -0.047$ with external skew quadrupole strength $k_{sq} = 5 \times 10^{-3}$ m^{-1}

.

References

[1] W. Daqa , V. Kornilov, I.Hofmann, O. Boine-Frankenheim, Acc-note-2009-003, GSI-Darmstadt.

[2] J. Struckmeier, GSI-ESR-87-03, GSI-Darmstadt.

[3] M. Aslaninejad and I. Hofmann, Phys. Rev. STAB, **6**, 124202 (2003).

Simulation and observation of the space charge induced multi-stream instability of linac micro bunches in the SIS-18 synchrotron

S. Appel[1], O. Boine-Frankenheim[2], and Th. Weiland[1]
[1]TEMF, TU Darmstadt, Germany; [2]GSI, Darmstadt, Germany

For the upgrade of the SIS-18 synchrotron it is of importance that the initial momentum spread of the injected coasting beam does not exceed the limit set by the rf bucket area. The lower limit is determined by microwave instabilities which cause a sudden increase of the momentum spread below a threshold momentum spread.
For a coasting Ar^{18+} beam in the SIS-18 the measured momentum spread as a function of the number of injected turns is shown in Fig.1. The momentum spread has been obtained from different Schottky bands.
During the transverse multi-turn injection the SIS-18 is filled with micro bunches from the UNILAC linac at 36 MHz. For low beam intensities the micro bunches debunch within a few turns and form a coasting beam with a Gaussian-like momentum spread distribution. With increasing intensity we observe a few 100 turns after injection persistent current fluctuations and an accompanying pseudo-Schottky spectrum.
The Schottky spectrum should be used to routinely measure the momentum spread (see Fig.1) and revolution frequency directly after injection. Therefore is is important to understand the origin of the pseudo-Schottky spectrum.
In [1] it is shown that the multi-stream instability induced by the space charge impedance leads to phase space turbulence with strong coherent fluctuation. The dispersion relation is

$$-i\frac{qI_0\eta}{2\pi\gamma\beta^2mc^2}\frac{Z_{sc}}{n}\frac{n^2\omega_0^2}{M}\sum_{j=1}^{M}\frac{1}{(\omega-kv_j)}=1, \qquad (1)$$

from which the critical number of filaments results as

$$M_{thr}=\frac{32}{\pi U_{sc}} \qquad (2)$$

where Z_{sc} is the space charge impedance, v_j the velocity of the jth filament, U_{sc} the space charge parameter and σ the momentum spread.
The saturation of the instability causes persistent current fluctuations with a broad frequency spectrum. Such a fast transition to a broad frequency spectrum was observed in the SIS-18 shortly after injection of $N = 10^9$ Ar^{18+} ions (Fig. 2) as well as in simulations. The transition occurs exactly after M_{thr} filaments have been generated.
A simulation code has been developed which reproduces the important aspects of the observed instability, like the threshold number of filaments and the broadness of the spectrum after saturation. The code will be used to estimate the effect of other ring impedances on the beam momentum and on its spread.

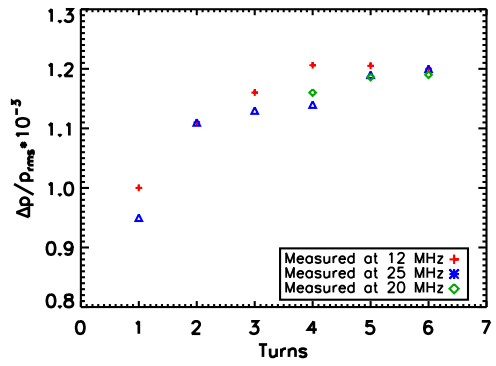

Figure 1: Rms momentum spread as a function of the number of injected turns measured from different Schottky bands. Approximately 10^9 Ar^{18+} ions are injected per turn. A possible reason for the obtained increase are microwave instabilities.

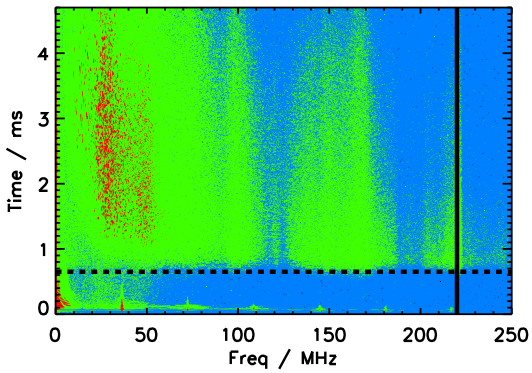

Figure 2: Measured frequency spectrum from $N = 10^9$ Ar^{18+} ions injected into SIS-18. The dashed line indicates the duration after which the broad frequency spectrum develops in the simulation. The solid line present the SIS-18 beam pipe cut-off frequency.

In addition the minimum momentum spread achievable in SIS-18 as well as the characteristics of the pseudo-Schottky noise will be analyzed using the code together with the experimental data.
Experiments with the new SIS-18 broadband current transformer a planed for the upcoming beam times.

References

[1] I. Hofmann, GSI Note March 1989
[2] S. Appel et al., DPG-Tagung München 2009

High intensity resonance driven beam loss and emittance growth in the SIS18 synchrotron

G. Franchetti, O. Chorniy, I. Hofmann, W. Bayer, F. Becker, O. Boine-Frankenheim, P. Forck, T. Giacomini, M. Kirk, T. Mohite, C. Omet, A. Parfenova, P. Schütt, GSI, Darmstadt, Germany

In this report we give a short summary of the results of the S317 experiment which took place in SIS18 in the years 2006-2008. A longer report is to be found in a future journal publication [1]. This experiment had the goal to study experimentally the long term effects arising in a high intensity bunch stored in a synchrotron. This type of effects are of relevance in the SIS100 U^{+28} scenario [2] where high intensity bunches have to survive for a storage time of 1 second. The beam physics explored derives from the combination of space charge and synchrotron motion during the long term storage in presence of lattice nonlinearities, which creates a challenge on beam dynamics and computer code prediction necessary for FAIR verification studies. The study of the high intensity effects required the excitation of a controlled resonance and the preparation of a high quality beam, together with the analysis of the transverse and longitudinal profile with time. Transverse profiles are measured with the intra-beam profile monitor (IPM) [3], while the longitudinal profile is measured with a beam position monitor. By using the beta functions at the position of the IPM, $\beta_x = 6.28$ m, $\beta_y = 7.8$ m, and the measured beam distribution, the transverse rms emittances are calculated. Previous studies in SIS18 (see Ref. [4]) provided an experimental resonance chart, which reveal several 2nd and 3rd order resonances excited by machine errors. From this study we set the resonance $3Q_x = 13$ as the reference resonance for the experimental scans. In the S317 campaigns an ion beam of $^{40}A^{18+}$ was used. After injection the beam is left to coast for 100 ms as prior to being bunched (via an external RF cycle) in 10 ms with a final RF voltage of 4 kV. This bunch, characterized by a bunching factor $B_F = 0.37$ and $(\delta p/p)_{rms} = 1.3\times10^{-3}$, is stored for 0.9 seconds, then adiabatically de-bunched in 100 ms (before a final bunching with acceleration and extraction). Under this operational scheme we explored the beam response as a function of Q_x. The average peak space charge tune-shift directly measured from the IPM data yields $\Delta Q_x \simeq -0.04$, and $\Delta Q_y \simeq -0.06$. In Fig. 1a we show the experimental finding. The red stripe marks the position of the beam loss stop-band measured with a low intensity coasting beam. We find as in the CERN-PS experiment that a region of beam loss (red curve) is located on the right side of the resonance. For a comparison of the two experiments see in Ref. [5]. In absence of beam loss ($Q_x \sim 4.3425$) an emittance growth is observed (Fig. 1a black curve): this result is consistent with trapping/scattering regimes discussed in [5]. The green curve shows the relative bunch rms length, which becomes shorter closer to the maximum beam loss at $Q_x = 4.3365$. In Fig. 1b are shown the simulation result from the computer modeling of the S317. We retrieve the

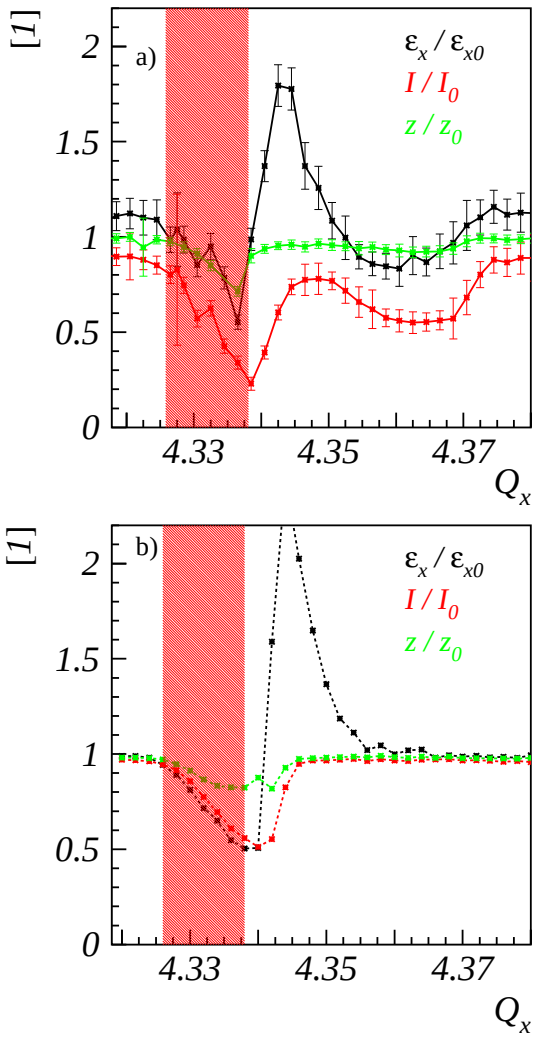

Figure 1: Experimental transverse-longitudinal beam response to the long term storage as function of working points around the third order resonance (top); Simulation results of the experiment (bottom).

essential feature of the emittance increase and beam loss as well as of the bunch shortening. Due to the unavoidable uncertainties in the experimental data, the simulations underestimate the long term beam loss and overestimate the emittance increase. The understanding of the single RF high intensity beam behaviour set the ground for experimental studies with dual RF for mitigating trapping/scattering negative effects. We thank the support of P. Spiller.

References

[1] G. Franchetti *et al.*, submitted to Phys. Rev. ST-AB.
[2] P. Spiller *et al.*, Proc. of EPAC 2008, p. 298, MPOC100.
[3] T. Giacomini *et al.*, Proc. of BIW, Knoxville, USA, 2003.
[4] G. Franchetti, P. Schütt, *et al.*, GSI-Acc-Note-2005-02-001.
[5] G. Franchetti, *et al.*, Proc. of PAC 2009.

Status of the SIS 18 Vacuum Upgrade*

M.C.Bellachioma, M.Bender, J. Cavaco, H. Kollmus, A. Kraemer, J. Kurdal, and H. Reich-Sprenger
GSI, Darmstadt, Germany.

In the context of the technical developments for the construction of the Facility for Antiproton and Ion Research at GSI, an intensive programme for the vacuum upgrade of the existing heavy ion synchrotron (SIS 18) was started in 2005, with the aim to improve the beam lifetime and the beam intensity. To reach these purposes the installation of NEG coated dipole and quadrupole chambers was foreseen, and additionally to overcome the dynamic vacuum instability a collimation system equipped with thin film coated absorbers was designed and commissioned.

The production of the thin film getter was carried out in two cylindrical magnetron sputtering facilities described in details in Ref. [1]. The surface chemical composition and the good activation behaviour of the produced thin films (≈ 1µm thick) were proved at CERN and at the Magdeburg University by X-ray Photoelectron Spectroscopy (XPS). Considering that the vacuum chambers mounted in accelerators undergo several venting-activation cycles, a deep investigation on the NEG ageing was performed last year at GSI by Elastic Recoil Detection Analysis (ERDA) [2]. In each activation cycle an identical quantity of oxygen is dissolved in the film bulk. However heating at temperatures lower than 250°C (as performed for the GSI coated chambers) does not allow a uniform oxygen concentration to be reached in the film and, as a consequence, oxygen atoms are settled in the film to form a concentration profile with the maximum close to the surface (see fig.1) which finally leads to accelerated performance degradation. The film degradation can be also explained in terms of C accumulation on the surface; in effect this element needs a higher heating temperature to be dissolved in the film bulk [3]. An abrupt reduction of the pumping speed was observed for thin coatings (0.25µm) after about 12 cycles when heating at 200°C [4].

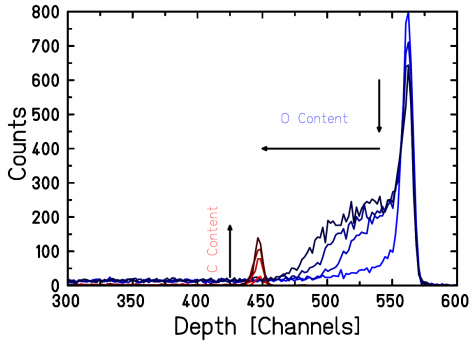

Figure 1: The number of activation cycle is plotted from light to dark colour, carbon in red and oxygen in blue.

* Work supported by EU design study, DIRAC-PHASE-1 RP6 SIS18-2 contract No. 515876.

In parallel to the production and characterisation of the thin film getters an ion catcher system was designed and commissioned to guarantee that the loss of the charge exchanged particles behind the dipole chambers of the SIS 18 occurs on a low desorbing material and in a high pumping environment (assured by a NEG thin film). Lowest desorption was observed for gold coated copper targets, where a thin nickel film between copper and gold avoid diffusion of the materials into each other during the standard UHV bakeout. For this purpose a Ni film thickness around 200nm is sufficient [2, 5].

Initially two geometries were realized: a wedge and a block shaped absorber. The first one, which separates the region where the losses occur from the circulating beam, has the disadvantage that the particles hit the absorber under grazing incident causing high desorption. The second one, which can be placed in the correct position by a linear motion feedthrough guarantees instead perpendicular incident with the disadvantage of an open geometry. Experiments have shown [5] that the block shaped absorber has a lower desorption yield on the level of 25 molecules per incident ion. Therefore it represents the favourite solution for the ion catcher system.

At the end of 2008 two ion catcher prototypes, 14 coated dipole chambers and one quadrupole chamber were implemented in the SIS18. First experiments to evaluate the vacuum upgrade achievement showed a clear improvement in achievable U^{28+} beam lifetime caused by the upgraded UHV system [6].

During the 2 upgrade shutdowns in 2009 all the remaining coated dipole and quadrupole (except for the one in S11) chambers and ten ion catcher were mounted in the accelerator. In summary, during the upgrade shutdowns from 2006 to 2009 24 dipole magnet chambers, 11 long quadrupole chambers, 5 short quadrupole chambers, 10 collimator chambers and 5 straight vacuum chambers were replaced by NEG-coated UHV chambers, which corresponds to app. 65% of the SIS 18 circumference. Commissioning of the UHV system upgraded will be performed in the beginning of 2010. Detailed measurements of the improved performance will follow in 2010.

References

[1] M.C.Bellachioma et al., Vacuum 82 (2008), p.435-439.
[2] M.C.Bellachioma et al., Proceedings of PAC09, Vancouver, BC, Canada.
[3] P.Chiggiato and P.Costa Pinto, Thin Solid Film 515, (2006), p.382-388.
[4] P.Chiggiato et al., unpublished, to be submitted to J.Vac.Sci.Technol. A.
[5] Kollmus et al., this GSI Annual Report
[5] G.Weber et al., Phys.Rev.STAB, 12, 084201 (2009).

Measurement of the acceptance of SIS-18 by means of a transverse RF beam excitation

S. Sorge, G. Franchetti, and A. Parfenova, FAIR-AT, GSI, Darmstadt, Germany

INTRODUCTION

We present the results of a measurement of the acceptance of SIS-18. The need for such an experiment particularly arises from the usage of the GSI synchrotron SIS-18 as a booster within the FAIR project [1, 2] including regular high-current operation. In this regime, an uncontrolled beam loss in the pipe can lead to vacuum degradation and irradiation of the machine. A precise knowledge of the acceptance will help to optimise SIS-18 to reduce particle loss.

Several experiments, which used diffusion, had been performed at different accelerators to measure the acceptance or the dynamic aperture. Here, the time required for the beam edge to reach the aperture was measured, see e.g. [3, 4]. Unfortunately, the estimation of this time is unprecise because a detailed knowledge of the initial beam size is necessary which translates in a large uncertainty in the derived acceptance. In order to avoid this uncertainty we study the evolution of the particle loss after the beam edge has reached the aperture.

METHOD

To determine the acceptance ϵ_{lim} of SIS-18, we excite a coasting heavy ion beam using the BTF exciter leading to an increase of the transverse beam width. When the beam width exceeds the limiting aperture, particle loss starts to occur. It can be shown that after a certain time the beam shape and the particle loss do no longer depend on the initial conditions. From this moment, the beam current will follow an exponential decrease entirely determined by the machine parameters and the excitation. This decrease can be modelled using a tracking algorithm. Here, we use the lattice parameters based on a MAD-X calculation and a realistic RF signal of the BTF exciter,

$$U(t) = U_a \sin(2\pi f_C t + \phi_0(t)), \qquad (1)$$

[5], where f_C is the carrier frequency being adjusted to the fractional part of the betatron frequency. ϕ_0 is a phase jumping between the values $0, \pi$ with a probability of $50\ \%$ and the time $T_S = 1/f_S$ between two possible jump times. f_S is the half width of the corresponding power spectrum.

Within a trial-and-error procedure, we calculate the particle loss where ϵ_{lim} is varied until a computed curve is found which fits well the measured one.

PARAMETERS USED AND RESULTS

The experiments were done with a Ta^{61+} beam initially consisting of 10^9 ions at the extraction energy $E = 100\ \mathrm{MeV/u}$. The working point was $(\nu_x, \nu_y) = (4.17, 3.29)$. An RF signal with an amplitude voltage $U_a = 28\ \mathrm{V}$ was applied. For technical reasons, only a vertical excitation and so, the measurement of the vertical acceptance, was possible. Measurements with $f_S = 0.01/T_0$ and $f_S = 0.005/T_0$, respectively, were performed. The resulting values for the vertical acceptance were $\epsilon_{lim} = 46\ \mathrm{mm\ mrad}$ and $\epsilon_{lim} = 45\ \mathrm{mm\ mrad}$, respectively [6]. A measured curve and a calculated one for the larger width of the exciter spectrum are shown in figure 1. Within an

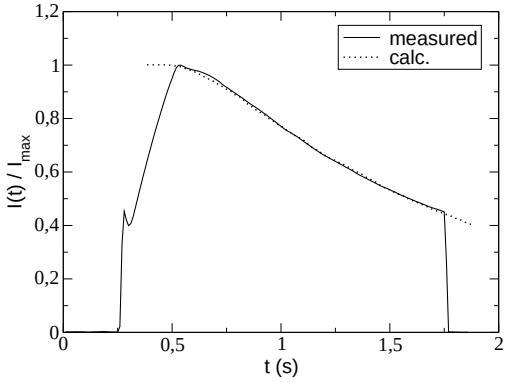

Figure 1: Normalised current measured and calculated for $E = 100\ \mathrm{MeV/u}$, $U_a = 28\ \mathrm{V}$, $f_S = 0.01/T_0$, and $\epsilon_{lim} = 46\ \mathrm{mm\ mrad}$.

error analysis, the maximum uncertainty for ϵ_{lim} has been estimated to $13\ \%$.

REFERENCES

[1] P. Spiller and G. Franchetti, "The FAIR accelerator project at GSI", NIM A 561 (2006) 305-309.

[2] "An International Accelerator Facility for Beams of Ions and Antiprotons", Conceptual design report, GSI Darmstadt, May 2006, Section 3, "The Facility",

`http://www.gsi.de/GSI-Future/cdr`.

[3] X. L. Zhang, V. Shiltsev, and C. Y. Tan, "Tevatron admittance measurement", Proc. of 2005 Particle Accelerator Conference, Knoxville, Tennessee

[4] X. Altuna *et al.*, "The 1991 dynamic aperture experiment at the CERN SPS", AIP Conf. Proc., No. 255, p. 355 (1991)

[5] M. Kirk and P. Moritz, "Noise excitation parameters for the SIS-18 RF-KO excitation", GSI internal note, GSI 2006

[6] S. Sorge, G. Franchetti, and A. Parfenova, "Measurement of the acceptance by means of a transverse beam excitation with RF noise", submitted to Phys. Rev. ST-AB.

Status of the SIS18 Upgrade Program and Progress in Acceleration of Intermediate Charge State Heavy Ions

P. Spiller, U. Blell, L. Bozyk, H. Eickhoff, P. Hülsmann, H. Klingbeil, H. Kollmus, P. Puppel,
H. Ramakers, H. Reich-Sprenger
GSI Darmstadt, Germany

INTRODUCTION

In order to reach the desired FAIR [1] intensities for heavy ions, SIS18 has to be operated with intermediate charge states [2,3]. Operation with intermediate charge state heavy ions at the intensity level of about 10^{11} ions per cycle has never been demonstrated elsewhere and requires a dedicated upgrade program. Such an upgrade program dedicated to the goal of minimizing the ionization beam loss [4] and stabilizing the dynamic residual gas pressure has been defined in 2005. So far, a major part of this upgrade program has been realized and a significant increase of the accelerated number of intermediate charge state heavy ions could be reached.

STATUS OF THE UPGRADE PROGRAM

Six major tasks of the upgrade program have been summarized and are realized in the frame of an EU FP6 funded construction program [5]. The tasks and their present status are summarized in Table 1.

Table 1: The six upgrade tasks of the EU FP6 funded SIS18 construction program and their present status.

New injection system for injection of U^{28+} beams at 11.4 MeV/u with larger acceptance, diagnostics and protection equipment [6]	Completed
New NEG coated dipole and quadrupole chambers for strong distributed pumping	Completed
Ion catcher system for ionization beam loss to minimize the effective gas desorption [7]	Completed
New h=2 acceleration cavity for fast acceleration in a two harmonic bucket	Ongoing
New TK stripper system for high charge state operation	Completed
Fast residual gas profile monitor for turn by turn beam profile measurements	Ongoing

The new power grid connection of the GSI pulse power network, which has been completed in 2006, enables ramping of SIS18 with high ramp rates without constrains. High ramp rates are significantly contributing to the goal of minimizing the ionization beam loss and stabilising the dynamic residual gas pressure at intermediate charge state operation.

STATUS OF INTERMEDIATE CHARGE STATE, HEAVY ION OPERATION

First experiments with high intensity, intermediate charge state heavy ion beams have been performed in 2001. At this time, most of the injected 10^{10} U^{28+}-ions have been lost by ionization in the residual gas within a few hundred milliseconds (Figure 1). Fast pressure bumps initiated by initial systematic beam loss, drove a strong residual gas pressure dynamic, which itself has amplified this loss process. Meanwhile, the ionization beam loss could significantly been reduced and acceleration and extraction of about 10^{10} ions has been demonstrated with U^{27+} and Ta^{24+} ions. Figure 1 shows the intensity profile in an acceleration cycle with U^{28+} and U^{27+} beams in 2001 and 2009.

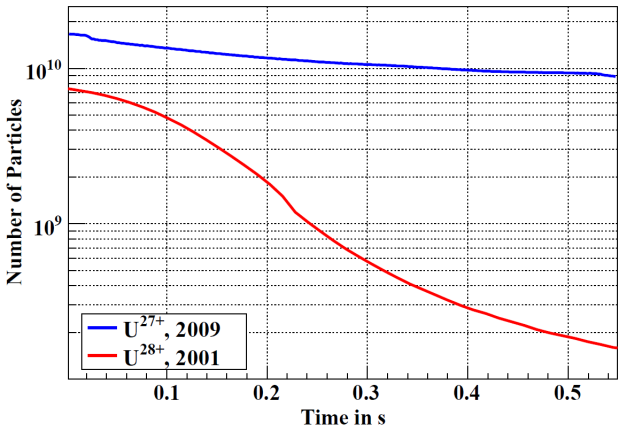

Figure 1: SIS18 acceleration cycle with intermediate charge state Uranium ions in 2009 and 2001. Beam loss by ionization, which is by far the dominating loss mechanism, could be significantly reduced and the number of extracted ions increased by a factor of 70.

The following measures have contributed to this progress:

- Injection at higher energy (11.4 MeV/u instead of 7.1 MeV/u with lower ionization cross section.
- Acceleration with higher ramp rates (4 T/s instead of 1.3 T/s) and correspondingly shorter cycle times
- Careful optimization of the acceleration cycle in terms of systematic beam loss at multi turn injection and RF capture loss
- At the time of the machine experiments the UHV upgrade and the set-up of the scraper system was only partially completed and have to a certain extend contributed to the stabilization of the vacuum pressure.

Further improvement has been achieved in the time averaged number of accelerated heavy ions. While the progress in accelerated Ta-ions per cycle could only be achieved with breaks of 9 seconds in between two cycles, the breaks at the Uranium run could be reduced to one second only.

REFERENCES

[1] P. Spiller, "FAIR at GSI", Proc. of HB2006, (2006)24
[2] P. Spiller et al, Proc. of PAC09 (2010)
[3] C. Omet et al, Proc of PAC07 (2008)1416
[4] G. Weber et al, Phys RevSTAB.12,084201 (2009)
[5] Description of work, DOW_CNI-515876_20050705
[6] U. Blell et al, Proc. of PAC07 (2008)167
[7] C. Omet et al, New Journal of Physics 8 (2006)284

Beam Tests of the Novel Ionization Profile Monitor*

T. Giacomini[1], C. Böhme[2], J. Dietrich[2], P. Forck[1], S. Kamerdzhiev[2], G. de Villiers[3]
[1]GSI, Darmstadt, Germany; [2]COSY, Jülich, Germany, [3]iThemba Labs, South Africa

The new Ionization Profile Monitor IPM is intended to provide fast and reliable non-destructive beam profile measurements at the existing synchrotron and storage ring as well as the future FAIR machines [1]. It will provide two different readout techniques, a fast readout mode on a turn-by-turn basis with 1 mm resolution and, secondly, a high resolution mode of 100 Profiles/s with 0.1 mm resolution. The new IPM will be able to detect both, ions and electrons. The ionisation products are guided by a transverse electric field to a position sensitive MCP-PS detector (Multi-Channel-Plate plus Phosphor Screen). For the high spatial resolution mode residual gas ions are detected, while detection of electrons is required to allow for fast turn-by-turn profile measurements.

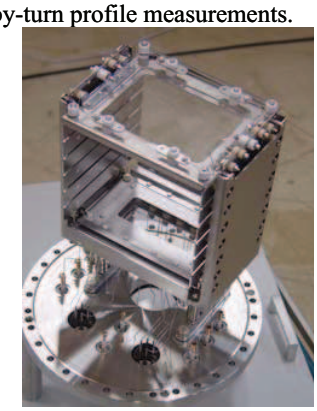

Figure 1: Photograph of the electrical field box

Fast mode measurements are performed using a multichannel photomultiplier. To overcome distortions of the measured profiles due to the space charge effect during residual gas electron detection, a guiding magnetic field in parallel to the electric field is necessary. Fig. 1 shows the design of electrical field box of the IPM prototype for one beam plane built at GSI and installed for tests in the COSY facility in Jülich. The device showed excellent performance, for details see [2]. The test installation in Jülich is not equipped with a magnet; hence only ion detection technique can be applied.
The CCD cameras are read out by a LabView server application running on a PXI-based front end which is remote controlled by a PC client program. Both, the server and client applications were developed by a commercial partner. The data acquisition system produces permanently beam profiles from beam injection until extraction with 50 profiles per second. Additionally, pre-processed data, like profile integral, beam position and beam width are presented to the user. As an example for the COSY test measurements Figure 2 shows the fast evolution of the horizontal profile of a polarized proton beam during injection and acceleration.

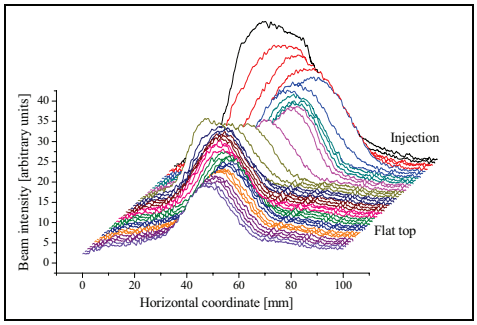

Figure 2: Evolution of the horizontal proton beam profile injection to acceleration to 1.343 GeV/c, $3 \cdot 10^9$ polarized protons, time span 2 s.

The design and calculations of this particular magnet device were another important step within the IPM project. The magnet openings are as large as 540 mm because the magnetic field is applied outside of the vacuum tank. Due to the restricted space in the SIS the device length was limited to 2.5 m. The need of corrector magnets lead to the configuration shown in Figure 3. The inner magnets are the main dipoles the outer magnets are the correctors as required for a closed beam bump.

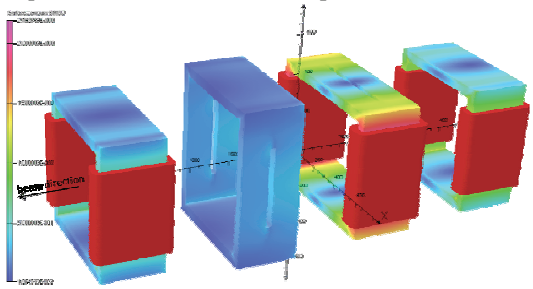

Figure 3: Magnet Design, 2 Main Dipoles, 2 Correctors

Outlook

The assembling process starts in January 2010 and insertion into SIS18 is planned for winter 2010. The magnetic system is presently being designed in collaboration with iThemba LABS, South Africa. A slightly different IPM version without magnetic field will be inserted into ESR in June 2010.

References

[1] M. Schwickert et al., "Beam Diagnostic developments for FAIR", Proc. DIPAC09, Basel (2009).
[2] T. Giacomini et al., "Development of a residual gas profile monitor with high resolution and fast readout", Proc. BIW04, Knoxville (2004).

* *Work supported by EU, EURONS contract No. 515876.*
#*cee@aps.anl.gov*

Chemical stripping of bulk saturated NEG coatings

M. Wengenroth[1], H. Kollmus[1], M. C. Bellachioma[1], S. Sievers[2], J. Conrad[2], M. Bender[1], and H. Reich-Sprenger[1]
[1]GSI, Darmstadt, Germany; [2]TU, Darmstadt, Germany

Introduction

In the recent years the installation of non-evaporable getter (NEG) coated dipole and quadrupole chambers at the GSI heavy ion synchrotron (SIS 18) have been carried out and ware completed in January 2010. The NEG coated chambers was part of different upgrade activities of the existing UHV system [1]. Those non-evaporable thin film getters, consisting of Ti–Zr–V, are deposited onto the vacuum chambers using three magnetron sputtering facilities built at GSI, each fulfilling different geometric shapes and dimensions. A detailed description of the production and the functional principle is given in Ref [1]. In brief, after coating and activation a highly chemical reactive surface is present in the vacuum system getting dissociated residual gas components by means of oxidation, nitration and carbonisation of the surfaces metallic constituents. The capacity of the NEG surface is approximately one monolayer for CO and CO_2 (10^{15} particles per cm^2). In the environment of the SIS18 the operation time of an activated NEG surface is typically longer compared to the venting cycle time due to maintenance. The live time capacity of a 1 µm NEG thin film is limited to 30 – 50 reactivations [2].

After the bulk of the NEG film is completely saturated, it has to be stripped of the vacuum chamber before applying new NEG coating. Industrial stainless steel pickling utilizing solutions containing nitric and hydrofluoric acid similar to buffered chemical polishing (BCP) [3] has proven to work on thick walled chambers (>2 mm) [4] but is not feasible for delicate dipole and quadrupole chambers of only 0.3 mm wall thickness because of non-uniformities especially at welded joints. Therefore, an alternative method was proven and will be described in the following.

Experimental procedure

Briefly, the chemical material removal is obtained by an oxidation of the metallic constituents through the nitric acid and the dissolution of these oxides by the hydrofluoric acid. Performing those steps sequentially will considerably reduce the risk of damaging a delicate chamber permanently. Accordingly NEG coated samples have been treated at the cleaning facility for superconducting niobium RF cavities of S-DALINAC (Superconducting Darmstadt Linear Accelerator). The oxidation is done by immersing the samples into nitric acid (65 %) for 5 minutes followed by the removal of the oxides by immersing into hydrofluoric acid (40 %) for 1 minute. Five coated samples have been treated employing the above sequence one to five times.

Measurements

The results of the etching were investigated using proton Rutherford Backscattering Spectroscopy (RBS) at the ion beam analysis department of the Forschungszentrum Dresden-Rossendorf and shown in Fig. 1, were the energy distribution of the backscattered protons is displayed. Highest proton energies are achieved for collision with Zr and only observed for the untreated sample (compare red line in Fig. 1). This means that after the first treatment the approx 1 µm NEG film was already completely removed.

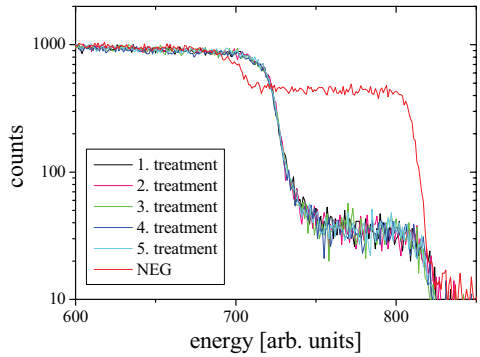

Figure 1: The energy distribution of the backscattered protons shows the highest energies from collisions with Zr only for the untreated NEG sample.

Conclusion

A method of stripping a saturated NEG film from thin wall chambers has been proven. Nevertheless, nitric and especially hydrofluoric acid can't be handled without introducing certain safety measures.

References

[1] M.C. Bellachioma, et al., Vacuum **82** (2008), p. 435
[2] P. Chiggiato and P. Costa Pinto, Thin Solid Films **515** (2006) p. 382
[3] B. Aune, et al., Phys. Rev. ST-AB, **3**, 092001 (2000)
[4] M. Wengenroth, Internal Report (2009)

Acknowledgements

The authors would like to thank M. Brunken of the S-DALINAC accelerator group for his support and R. Grötzschel (FZ Dresden-Rossendorf) and W. Assmann (LMU Munich) for performing the RBS analysis at the FZ Dresden-Rossendorf.

Linac Commissioning at the Italian Hadrontherapy Centre CNAO

B. Schlitt[1], A. Reiter[1], G. Breitenberger[1], J. Cavaco[1], G. Clemente[1], M. Hörr[1], N. Kischnik[1], C. Kleffner[1], M. Maier[1], G. Schulz[1], W. Vinzenz[1], H. Vormann[1], E. Bressi[2], M. Pullia[2], E. Vacchieri[2], S. Vitulli[2], A. Pisent[3], P. Posocco[3], C. Roncolato[3], C. Biscari[4]

[1] GSI, Darmstadt, Germany; [2] CNAO, Pavia, Italy; [3] INFN/LNL, Legnaro, Italy; [4] INFN/LNF, Frascati, Italy

Introduction

The Centro Nazionale di Adroterapia Oncologica (CNAO) presently under commissioning in Pavia, Italy, will be the first Italian centre for the treatment of deeply sited tumours with proton and carbon ion beams [1]. The 7 MeV/u, 216.8 MHz injector linac is a copy of the linac at the Heidelberg Ion-beam Therapy centre (HIT) and consists of a 4-rod type RFQ and of an IH-type drift tube linac, both designed by GSI and IAP Frankfurt [2]. In 2004, a collaboration between CNAO and GSI was established for delivery and commissioning of the CNAO linac and for delivery of complete beam diagnostics systems by GSI [3, 4, 5]. Linac installation and commissioning in Pavia were performed in collaboration by CNAO, GSI, and INFN during 2008/09 [6, 7, 8]. GSI coordinated and supported installation and tests of all linac components and technical subsystems, performed commissioning of the LLRF systems as well as RF tests and conditioning of the resonators. Linac beam commissioning was supervised by GSI. During beam commissioning periods, 3 – 4 GSI employees worked permanently at CNAO for accomplishment of the linac shifts. Overall, in 2009 twelve GSI employees worked ~95 weeks at CNAO in Pavia.

Linac Commissioning

Table 1: Commissioning schedule and milestones

May 08 – Jan 09	Ion sources & LEBT	Final installation & commissioning
Nov 08 – Jan 09	RFQ	RF conditioning & tests
Feb – Mar 09		Installation & RF conditioning at final position
Mar – Apr 09		Beam commissioning
Apr – Jun 09	IH linac	Installation & RF conditioning
Jun – Jul 09		Beam commissioning
Jul – Nov 09	MEBT, Debuncher	Final installation, RF tests & conditioning
Nov – Dec 09	Linac, MEBT	Beam tests, linac operation training
Dec 09	Synchtrotron	First turn in synchrotron

The layout of the injector including two ECR ion sources and LEBT is shown in Fig. 1. After completion of ion sources and LEBT commissioning in January 2009 [7], the RFQ and thereafter the IH linac were commissioned during 2009 (Table 1), both with H_3^+ and C^{4+} ion beams. Final acceptance tests of all linac RF amplifiers as well as commissioning and beam tests of MEBT components delivered by GSI (debuncher resonator and BD devices) were performed during autumn 2009. The first turn in the synchrotron was achieved in December. The complete linac is shown in Fig. 2.

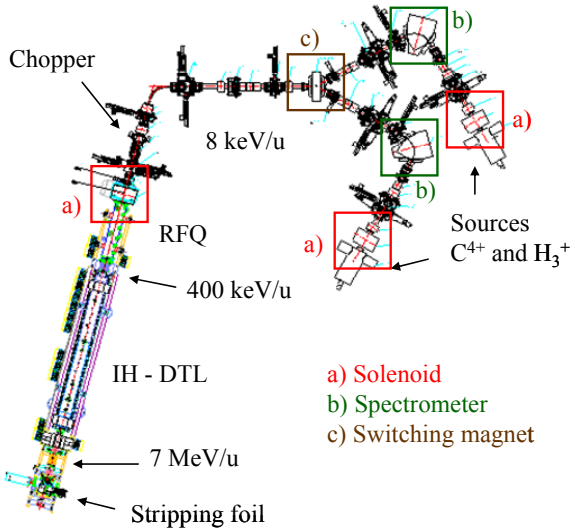

Figure 1: Layout of the CNAO injector

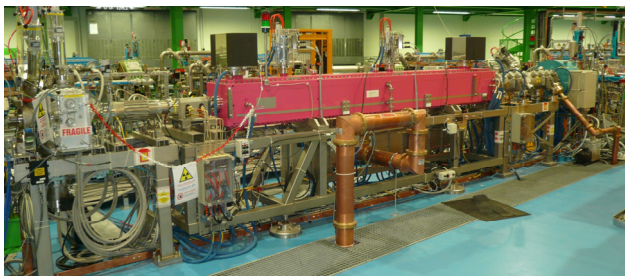

Figure 2: Complete linac with RFQ (right), IH linac (center), and stripper section (left)

Three different beam diagnostics test benches were used behind LEBT, behind RFQ, and behind the stripper section, respectively, and allowed for beam current, profile, and emittance measurements [7, 8]. For RFQ and IH linac commissioning the test benches were designed and prepared by GSI. They comprised an emittance measurement device loaned from GSI as well as a set of three phase probes for accurate time-of-flight beam energy measurements.

RFQ

As an example Fig. 3 shows the beam energy measured behind the RFQ vs. tank voltage for different ion beams. The required injection energy for the IH linac of 400 keV/u is reached for all ion species around the same RFQ working point – corresponding to a RF pulse power of 195 – 200 kW. Different LEBT beam energies and steerer settings were investigated to optimize RFQ injec-

tion. Finally, the design value of 8.0 keV/u was kept. Transmissions along the RFQ up to 60 % were reached for H_3^+ as well as for C^{4+} beams for matched injection. For a detailed summary of RFQ commissioning results see Ref. [8].

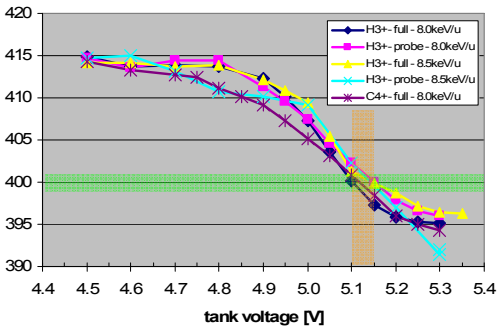

Figure 3: RFQ output beam energy in keV/u as function of the scaled tank voltage for different ion beams

IH Linac

More than 140 measurement series including numerous amplitude and phase scans were performed with the IH linac. Different LEBT beam energies, RFQ settings, and IH tank plunger configurations were investigated. The linac was optimized with respect to high beam transmission, minimum beam emittances and optimized bunch signal amplitudes. For the final setting, the measured linac beam energy amounts to 7.2 MeV/u at a RF pulse power of 910 – 930 kW.

Table 2: Typical beam currents and linac transmission

Ion Species	Beam Current / µA			Linac Transmission
	LEBT	Linac	Stripped	
C^{4+} / C^{6+}	~170	~80	115	48 %
H_3^+ / p	1100	400	1200	39 %
	710	307	900	46 %

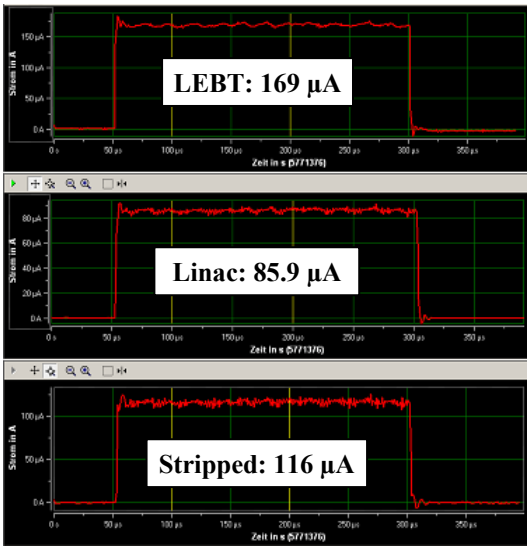

Figure 4: Measured C^{4+} / C^{6+} beam pulses

Table 2 summarizes typical beam currents achieved at the LEBT upstream of the solenoid focusing into the RFQ, behind the IH linac, and behind the stripping foil. Fig. 4 shows examples of measured beam pulses. A total linac transmission (incl. solenoid, RFQ, and IH linac) up to 48 % was achieved, meeting the design beam currents behind the stripper (100 – 120 µA for C^{6+} and 700 µA for protons) and even exceeding them.

The quadrupole settings behind the linac were optimized to achieve minimum beam diameters at the stripping foil in order to reduce emittance growth effects in the foils. Measured beam emittances for the final settings are listed in Table 3 and are shown in Fig. 5. Twiss parameters are similar in both transverse planes.

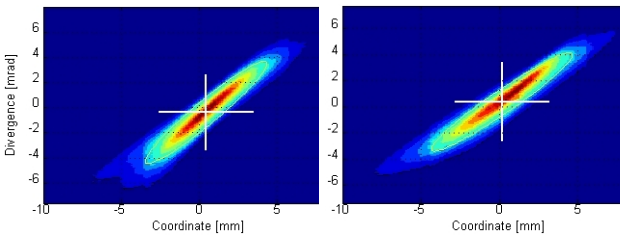

Figure 5: Hor. (left) and ver. (right) proton beam emittances measured ~1 m behind the stripping foil

Table 3: Measured beam emittances (4 × rms for 90 % of the beam current) behind the stripping foil and emittance growth in the foil

Ion Species	$\varepsilon_{4\times\text{rms},90\%}$ / π mm mrad		Emittance Growth	
	horizontal	vertical	hor.	ver.
C^{6+}	3.6	3.0	6 %	6 %
protons	4.7	4.7	15 %	40 %

Summary and Outlook

Commissioning and beam tests of all components delivered and supervised, respectively, by GSI were accomplished successfully in 2009. Design beam currents were achieved and even exceeded; the measured beam emittances agree well with expected values. Finally, twenty CNAO operators, engineers and physicists were trained in linac operation by GSI in November 2009 – marking the end of the GSI services fixed in the CNAO-GSI contract.

Acknowledgements

The authors wish to thank the numerous GSI colleagues involved in this project over the past years. Their efforts are greatly acknowledged. Many thanks to all CNAO and INFN collaborators for the fruitful cooperation, the cordial atmosphere and the great hospitality at CNAO.

References

[1] S. Rossi, EPAC 2006, p. 3631.
[2] B. Schlitt, LINAC08, p. 720.
[3] B. Schlitt et al., GSI Scientific Report 2006, p. 383.
[4] A. Reiter et al., EPAC 2006, p. 1028.
[5] H. Vormann et al., EPAC08, p. 1833.
[6] B. Schlitt et al., GSI Scientific Report 2008, p. 409.
[7] E. Bressi et al., PAC09, TU6PFP005.
[8] P. Posocco et al., HIAT09, in print.

Influence of an electrostatic LEBT chopper on linac beam parameters at CNAO

B. Schlitt[1], A. Reiter[1], S. Vitulli[2]
[1] GSI, Darmstadt, Germany; [2] CNAO, Pavia, Italy

Introduction

The Centro Nazionale di Adroterapia Oncologica (CNAO) located in Pavia, Italy, will be the first Italian facility for hadrontherapy of deeply sited tumours [1]. The accelerator consists of a RFQ and of an IH-type drift tube linac, both delivered by GSI [2], followed by a synchrotron built by CNAO.

In the low energy beam line (LEBT), an electrostatic chopper horizontally deflects the DC ion source beam via an electric field across two parallel plates at opposite potential. The field is generated by a dual-polarity high voltage module (max. ±5 kV). When triggered, a fast HV switch allows a beam pulse of adjustable length to pass into the RFQ. Within about 1 µs the potential across the plates drops to a few Volt and, after a defined down-time, is restored with a similar time constant.

Unlike the Heidelberg facility HIT, CNAO has not foreseen a chopper behind the linac. Hence, chopper disturbances on the ~20 µs pulse can not be corrected for and might affect the multi-turn synchrotron injection. Studies of chopper effects on the beam are subject of this article.

Ion Source Beam Measurements

Due to the small RFQ aperture radius of ~3 mm, correct beam injection into the RFQ is very critical. During LEBT commissioning a profile grid monitored the beam 280 mm behind the injection solenoid for the RFQ.

At DC chopper voltages below 300 V, a 1st series of profiles resulted in a linear displacement coefficient of ~0.05 mm/V at grid position. Hence, at the RFQ injection plane 48 mm behind the solenoid, the measured residual 6 V across the chopper plates cause a small offset only.

In a 2nd experiment the chopper was operated in pulsed mode. 11 µs beam pulses, initially set outside the profile grid amplifier integration window, were shifted by –1 µs between measurements in order to analyse variations between incremental beam portions. Within the first two microseconds the beam position at the profile grid changed by ~0.3 mm in either plane and then gradually drifted about 0.5 mm before it reached a stable value.

Linac Beam Measurements

After the linac was put into operation, phase probes and profile grids measurements mainly with 7 MeV/u H_3^+ or proton beams complemented the LEBT investigations. The phase probes were equipped with wide-band amplifiers to resolve the 216.8 MHz rf micro-structure and delivered information on the longitudinal bunch distribution.

Macro-Pulse Structure

Fig. 1 shows phase probe signals of a 1 µs beam pulse for two of the investigated chopper operating values. The probe is installed behind the RFQ tank. Signal rise- and fall-time can be estimated to be ~200 ns and <100 ns, respectively. Hence, only a small 300 ns fraction of the macro-pulse is affected by the chopper switching process compared to the ~2.2 µs revolution period at synchrotron injection. The effective pulse length decreases slightly at higher voltages, in the present case from 1.1 µs to 0.9 µs. Similar results hold for the phase probes behind the linac.

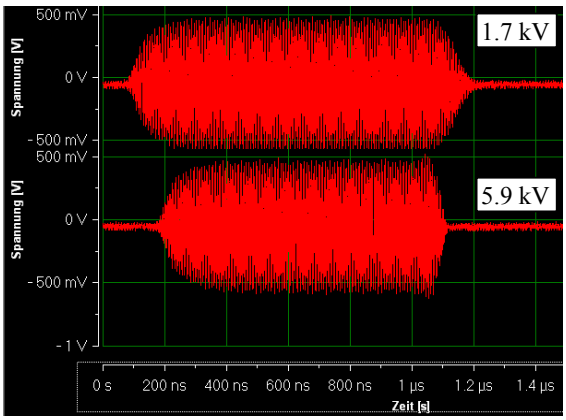

Figure 1: Phase probe signals for a 1 µs chopper window and deflection voltages of 1.7 kV and 5.9 kV.

MEBT Beam Profiles

Between linac and synchrotron five profile grids are installed. Variations of beam distributions were investigated for pulse lengths of 2 µs and 25 µs. Online data measured in the final straight section are compared in Fig. 2. The markers indicate beam position (yellow) and width (red). On average beam position and width changed by less than 0.5 mm. Hence, no disturbing effect is expected for the synchrotron multi-turn injection process.

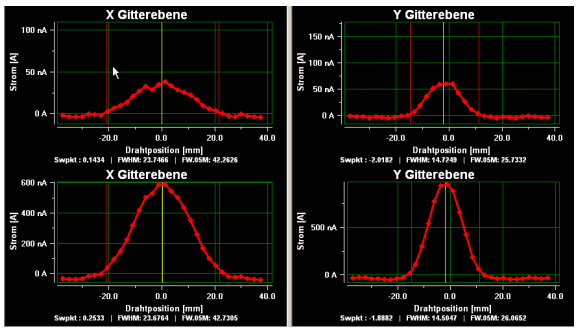

Figure 2: Beam profiles for chopper windows of 2 µs (top) and 25 µs (bottom).

References

[1] E. Bressi et al., PAC09, TU6PFP005.
[2] B. Schlitt et al., this report.

The status of the cw-LINAC-demonstrator

S. Mickat[1], W. Barth[1], L. Dahl[1], A. Jankowiak[2], M. Kaiser[1], H. Podlech[3], U. Ratzinger[3]
[1]GSI Helmholtzzentrum für Schwerionenforschung, Darmstadt, Germany
[2]KPH Institut für Kernphysik, Universität Mainz, Germany
[3]IAP Institut für Angewandte Physik, Universität Frankfurt, Germany

Introduction

In June 2009 the Helmholtz-Institute Mainz (HIM) was founded. The research activities of HIM are supported by the integrated department of accelerator physics and integrated detectors (ACID) [1]. Within the scope of ACID a collaboration of the Institute of Applied Physics of University Frankfurt (IAP) and the GSI acceleration division is established. Its longterm task should be the design and the realisation of a superconducting cw-LINAC in parallel to the existing UNILAC at GSI. Such a machine is highly desirable with respect to the progress in the field of Superheavy Elements (SHE), because the UNILAC at GSI is limited in providing a proper beam for SHE and in fulfilling the requirements for FAIR simultaneously.

In a first step a prototype of such a superconducting cw-LINAC as a demonstrator is financed by HIM. The aim is a full performance test of the demonstrator with beam at the GSI high charge injector (HLI) in 2012.

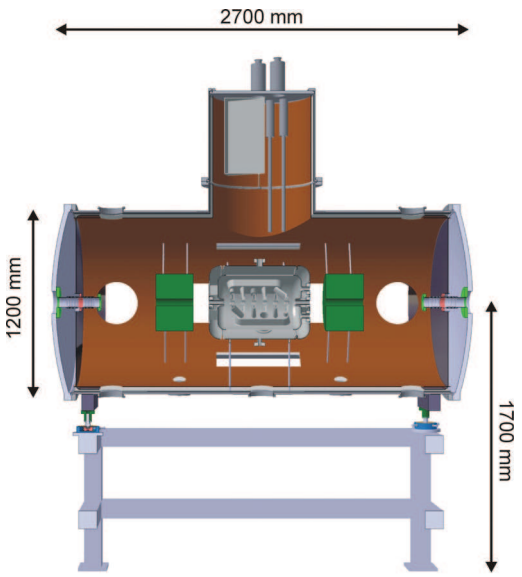

Figure 1: A draft of the superconducting cw-LINAC demonstrator is shown. The cavity embedded by two solenoids is mounted in a cryostat.

cw-LINAC Demonstrator

The proposed cw-LINAC should comprise 9 superconducting CH-cavities operated at 217 MHz with high luminosity [2]. The required input parameters match the conditions at the GSI HLI injector with its ECR source and energies of 1.4 MeV/u. The output energy range is from 3.5 to 7.5 MeV/u. The energy spread should be kept at about ±3keV over this whole range. The demonstrator is the first section of the proposed cw-LINAC consisting of a superconducting CH-cavity embedded by two superconducting solenoids. The components should be mounted in a cryogen environment operating at temperatures of 4.4 Kelvin (fig. 1).

Projectstatus and -schedule

Presently the tendering of the solenoids, the cavity, the cryostat and the rf-amplifier is in preparation. The technical design is a challenging task regarding to the cold-warm-bridges, the support-system and the high requirements of shielding external and internal magnetic stray fields for example. The delivery and the following complex assembly of the components under cleanroom conditions to a well-working system are expected in 2011. First rf-tests of the system should take place at IAP then.

For full performance tests with beam a test station at the HLI injection line is favoured. The mid-term goal is to connect the demonstrator straight ahead to the HLI in 2012 (fig. 2). Successful tests would be the first stage towards a cw-LINAC in parallel to the UNILAC.

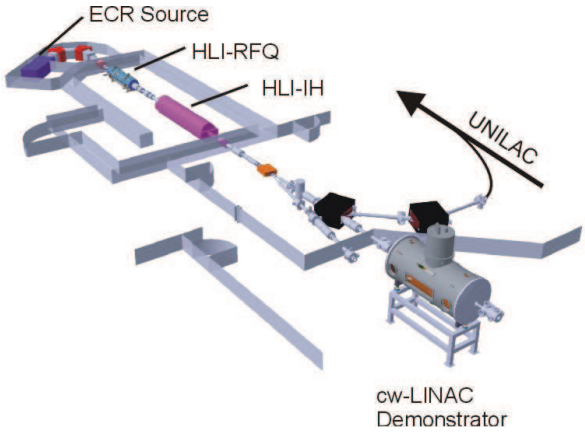

Figure 2: A general drawing of the HLI injector at GSI is shown. In straightforward direction the cw-LINAC demonstrator should be mounted.

References

[1] Stöcker H., Krausch G., Maas F., Proposal for the Establishment of a Helmholtz Institute: "Helmholtz Institute Mainz" – Structure, Symmetry and Stability of Matter and Antimatter (2009)

[2] Minaev S. et al., Superconducting, energy variable heavy ion linac with constant β, multicell cavities of CH-Type, Phys. Rev. ST Accel. Beams 12, 120101 (2009)

Superconducting CH-Cavity Development for Ion Linacs*

M. Busch† [1], H. Podlech[1], U. Ratzinger[1], and W. Barth[2]

[1]Institut für Angewandte Physik, Goethe Universität, Frankfurt, Germany; [2]GSI, Darmstadt, Germany

Abstract

At present 3 prototype CH-cavities are under design and / or construction at velocity ranges from $\beta = 0.05$ up to $\beta = 0.45$ to further improve and explore the capabilities of that novel type of multi-cell superconducting cavity.

CH-Cavity Design

A 325 MHz, 7 cell, $\beta = 0.15$ CH-cavity has been designed and is currently under construction at Research Instruments (see fig. 1)[1]. The most important changes in

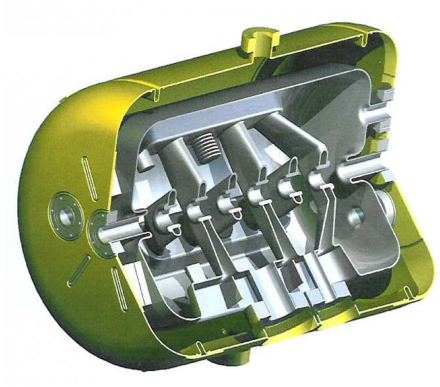

Figure 1: RF design of the 325 MHz sc CH-cavity.

comparison to the previously built 360 MHz CH-prototype are: inclined end stems, additional flanges at the tank caps for cleaning procedures , slow / fast bellow tuner inside the cavity and large power coupler due to changed stem geometry. Inclined end stems lead to a more homogeneous field distribution along the beam axis compared with straight stems because the volume for the magnetic field in this area and therefor the inductance is increased. The longitudinal dimensions of the cavity can be reduced by about 20%-25% since an extended end cell is not needed for field flattening. Additional flanges at the tank caps provide a convenient way to process the cavity surface chemically. For the tuning of the cavity three types of tuners are foreseen: 4 static tuners with a diameter of 40 mm and a height of up to 60 mm to adjust the frequency after fabrication. They are positioned between the stems and the height is fixed after adjustment. Furthermore there will be two bellow tuners (a fast and a slow one) inside the cavity. They will be placed on the girder between the stems and will be driven by a piezo. The slow tuner adjusts the frequency after cooling the cavity down, while the fast one regulates the

* Work supported by BMBF 06FY9089 I

† busch@iap.uni-frankfurt.de

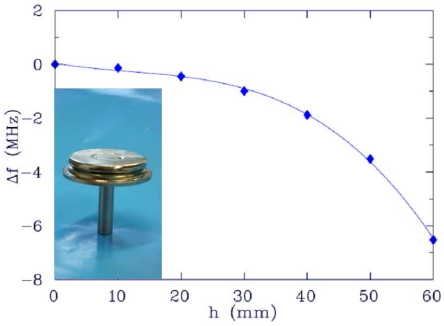

Figure 2: Tuning range of the fast bellow tuner.

frequency during beam operation. The desired frequency shift for each one is $100 - 130 Hz/\mu m$ (see fig. 2).

Applications to GSI-FAIR

The design effort for a cw operated, s.c. heavy ion linac for nuclear chemistry and SHE-production has started. The linac will be used for the production of super heavy elements. It has to provide ion beams with an A/q of up to 6 and energies up to 7.3 AMeV. Above an energy of 3.5 AMeV the linac is fully energy variable. The front end will be the existing high charge injector (108.408 MHz, 1.4 AMeV) which is presently being upgraded for the required duty cycle. The main acceleration of approximately 35 MV will be provided by 9 CH-cavities operated at 216.816 MHz (see fig 3)[2]. The 7-cell, 325 MHz cavity shown in

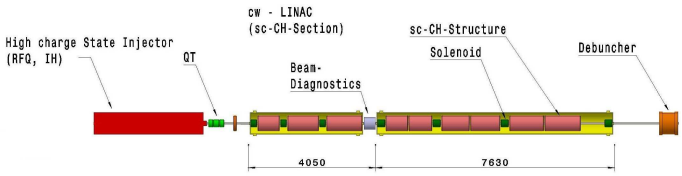

Figure 3: Schematic overview of the cw heavy ion linac.

fig. 1 is suited to be tested with a pulsed, intense ion beam from the Unilac.

References

[1] M. Busch et al., “Recent Superconducting CH-Cavity Development”, PAC 2009, Vancouver, Canada.

[2] S. Minaev et al., ”A Superconducting Energy Variable Heavy Ion Linac with Constant Beta, Multi-Cell Cavities of CH-Type, Phys. Rev. STAB 12, 120101.

High Voltage Pulse Generator for an ExB Chopper System*

C. Wiesner#, L. P. Chau, H. Dinter, M. Droba, N. Joshi, O. Meusel, I. Müller and U. Ratzinger
Institut für Angewandte Physik, Goethe-Universität, Frankfurt/Main, Germany;

Introduction

High intensity beams which are increasingly needed for a variety of applications pose new challenges for beam chopping. Long drifts must be avoided due to space charge constraints. The duty cycle for electrostatic beam deflection must be minimized in order to reduce the risk of voltage breakdowns. Beam dumping outside the transport line is preferable in order to avoid high power deposition and uncontrolled production of secondary particles at the slit or other vulnerable beamline components.

ExB Chopper System

An ExB chopper system for intense proton beams of up to 200 mA and repetition rates of up to 250 kHz is under development at IAP. It will be tested and installed in the low energy section of the Frankfurt Neutron Source FRANZ [1] with beam energies of 120 keV.

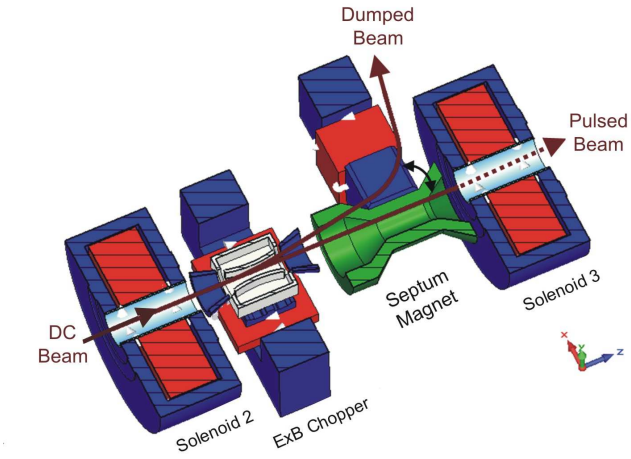

Figure 1: Scheme of the ExB Chopper System.

The chopper consists of a Wien filter-type ExB configuration, where the electric field can be pulsed and is followed by a static septum magnet [2]. As pulsing of the magnetic deflection field is not possible with a repetition rate of 250 kHz due to high power consumption, a pulsed electric field (fig. 3) is generated between two deflector plates located inside the dipole gap. It compensates the magnetic deflection and is thus creating a 100 ns proton pulse in forward direction for injection into the first accelerator structure.

High Voltage Pulse Generator

The electric field will be driven by a High Voltage Pulse Generator shown in fig. 2. It uses fast MOSFET technology in the primary circuit while the high voltage is provided in the secondary circuit around a ferrite transformer core.

Figure 2: High Voltage Pulse Generator.

Two pulses of more than 5 kV of positive and negative voltage, respectively, are required to charge both deflector plates symmetrically. Voltage pulses of ±5.8 kV with a repetition rate of 250 kHz were achieved (fig. 3). In addition post-pulse oscillations were minimized by reducing parasitic capacitances and by installing diodes as well as ohmic resistances.

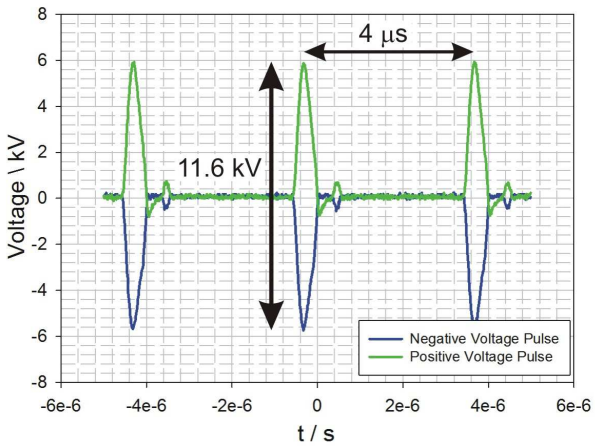

Figure 3: Measured Voltage Pulses.

References

[1] O. Meusel et al., "Injector Development for High Intensity Proton Beams at Stern-Gerlach-Zentrum", LINAC'08, Victoria, BC, Canada, September 2008, MOP002, p. 49-51.

[2] C. Wiesner et al., "Chopper for Intense Proton Beams at Repetition Rates up to 250 kHz", PAC'09, Vancouver, BC, Canada, May 2009, TU6PFP088.

* Work supported by BMBF – 06FY9089I and LOEWE-HIC for FAIR.

#wiesner@iap.uni-frankfurt.de

Space Charge Lens for Focusing Uranium Beams*

K. Schulte, M. Droba, O. Meusel, J. Pfister, and U. Ratzinger
IAP, Goethe University Frankfurt, Germany

Introduction

Space charge lenses (SCL) are a promising concept for the focusing of ion beams. The confined homogeneous electron cloud induces a linear radial electric field that provides a strong attracting force on the beam particles and hence a linear transformation in the transversal phase space. Furthermore focusing is independant from the ion mass and the trapped electron cloud compensates the space charge forces of the positively charged beam.

A new experiment is under construction which will test the performance of the SCL in the case of low energy heavy ion beams like $^{238}U^{4+}$.

Space Charge Lens

A new SCL [1] has been designed for the possible application at the HSI-Upgrade (GSI) [2] as a focusing element. The numerical simulations are used to prepare beam transport experiments at GSI using a $^{238}U^{4+}$-beam with aa beam energ of 2.2 AkeV.
Figure 1 shows the final layout of the new device.

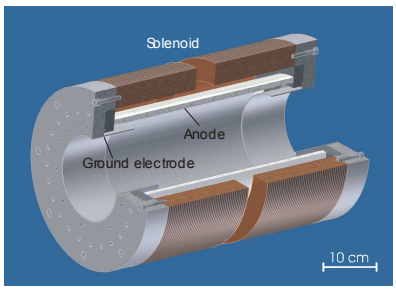

Figure 1: Design of the new space charge lens.

The total length of the proposed space charge lens will be 0.47 m and the longitudinal confinement of the electrons will be provided by an anode with radius r_A = 0.085 m. For focusing heavy ions like U^{4+} a self electric field produced by the trapped electrons of about $E_{r,max}$=140 kV/m is needed.

Preliminary Experiment and Diagnostic

The mapping quality of the space charge lens depends on thermodynamic properties and the homogeneity of the non neutral plasma [3]. Therefore one concern by using SCL is the investigation of the plasma parameters.

An experiment (Figure 2) was constructed to investigate the time evolution of the non neutral plasma and to carefully determine the special operation modi for its application at GSI.

* Funded by BMBF06FY9089I, Primärstrahlerzeugung für FAIR, HITRAP-IH-Struktur

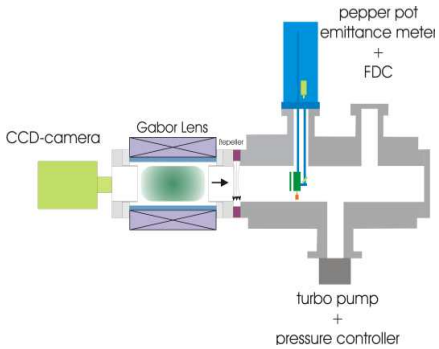

Figure 2: Experimental set-up.

Besides a well-proven SCL the experimental set-up consists of a CCD camera, a Faraday cup, and a pepper pot emittance meter to analyze the phase space distribution of residual gas ions and electrons. These residual gas ions are produced by collisions between the trapped electrons within the SCL and the residual gas. In the case of thermalisation electrons are also able to escape from the lens volume. Therefore the diagnostic measurements yield information about the confined non neutral plasma state.

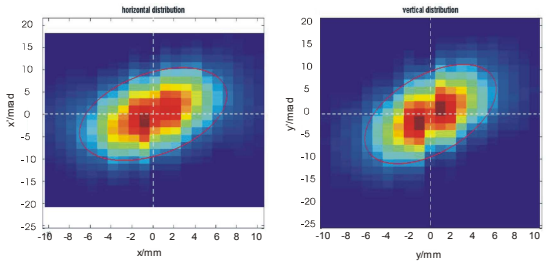

Figure 3: An example of the phase space distribution of residual gas ions.

The next step will be the construction of the new SCL, the further diagnostic of the non neutral plasma and the preparation of possible beam transport experiments at GSI.

References

[1] K. Schulte, et al., “A Space Charge Lens for Focusing Heavy Ion Beams”, GSI Scientific Report, 2008.
[2] P. Spädtke and R. Hollinger, et al., REVIEW OF SCIENTIFIC INSTRUMENTS 76, 063307 (2005)
[3] K. Schulte, “Research of diagnostic techniques on a nonneutral plasma”, Diploma thesis, IAP, 2008, http://publikationen.ub.uni-frankfurt.de/volltexte/2009/6244/.

Status report on the Frankfurt 200 mA proton source

J. Sun[1], W. Schweizer[1], K. Volk[1]
[1]IAP, Frankfurt, Germany

A remarkable progress on the 200 mA 120 keV high current proton source for FRANZ (Frankfurt Neutron Source at the Stern Gerlach Centre) was achieved till end of 2009. Figure 1 shows a technical cross-section of the source. Principally, the source is composed of the Frankfurt Volume Source plasma generator and equipped with a new pentode extraction system. The plasma generator has a maximum input power of 8 kW with a total arc current of 100 A and an arc voltage of 80 V. The plasma confinement is achieved by a solenoidal magnetic field with a maximum flux density of 40 mT. Also included in the design is a filter magnet which generates a transversal magnetic field in front of emission aperture.

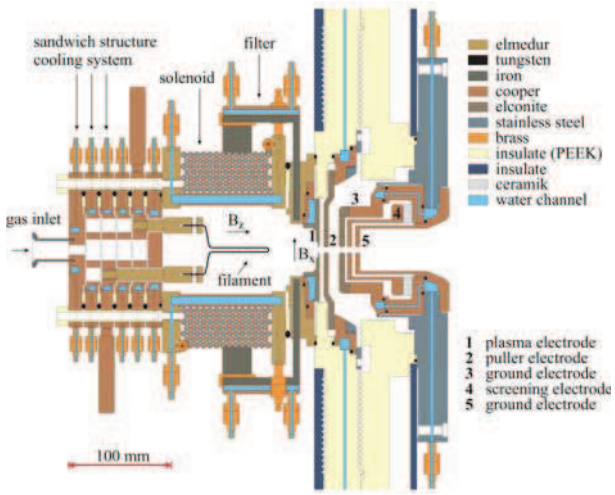

Figure 1: Cross-section of the 200 mA proton source.

The first measurements were performed for testing source characteristics and to evaluate the total beam current and the relative fraction of protons. An exemplary measurement can be seen in Figure 2.

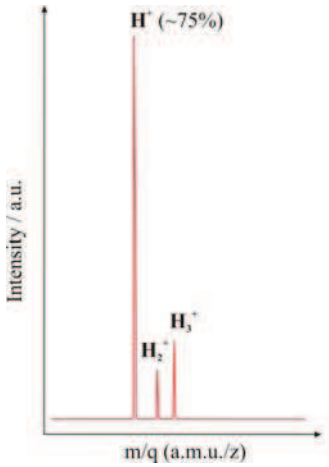

Figure 2: Measured beam fraction at a 25 mA total beam current.

A pentode extraction system has been designed for the FRANZ project with a single hole aperture of 5 mm radius. The application of a pentode extraction system enables not only decoupling of beam parameters from the beam energy but also allows a pulsed operation mode. With an optic fibre controlled high voltage switcher it is possible to adjust and optimize the repetition rate and pulse length to aim for a higher field strength resulting in higher peak current and less sparking between plasma and puller electrode. Furthermore, the pulsed operation mode relaxes the thermal loading for the whole extraction system and beam transport section. The operation time can be consequently extended. The very first pulsed beam is displayed in figure 3.

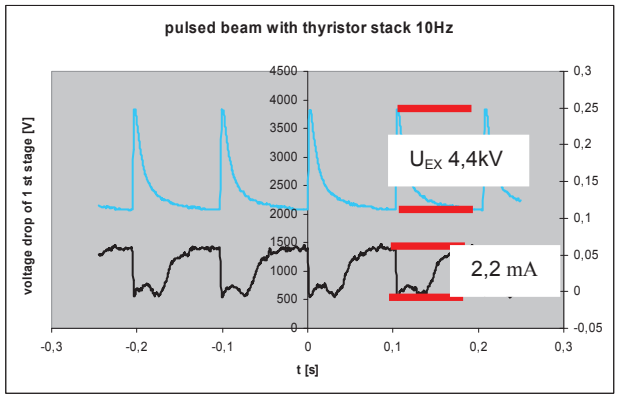

Figure 3: Beam pulse from Frankfurt volume source in pulsed extraction operation mode.

A reliable switch system has been interdisciplinary developed and successfully tested. Current beam sensor using parallel flux gating principle is chosen for comprehensive investigation on the pulsed beam. Intensive investigation on soft magnetic material for flux gate sensors has been accompanied. This helps for optimized operation parameters for detecting beam pulse [1] with sufficient resolution under current operation environment.

Pulsed pentode extraction system opens new perspective in terms of operation mode extraction system, it brings also further topic with itself, which are relevant for a study of dynamic behaviour of plasma meniscus, sparking from Hz till kHz range, beam noise. All these topics associated with pulsed extraction mode will sustain more innovative development of extraction system.

[1] B-J. Lee et al.: “Properties of magnetic materials at very high magnetization rates”.

Neutron streaming though the RF waveguide ducts of SPL*

E. Kozlova[1], T. Radon[1], T. Otto[2], and G. Fehrenbacher[1]
[1]GSI, Darmstadt, Germany; [2]CERN, Geneva, Switzerland

Introduction

Presently a new accelerator complex is being planned at CERN, which will replaced the ageing Proton Synchrotron (PS). A high-power160 MeV H^- linac (Linac 4) will replace the present 50 MeV proton linac injector [1], a 5 GeV Superconducting Proton Linac (SPL) will replace the 1.4 GeV PS Booster (PSB) [2] and a 50 GeV synchrotron (PS 2) will replace the 26 GeV PS [3]. A tentative layout of the planned accelerators, integrated into the CERN accelerator complex, is shown in Fig. 1.

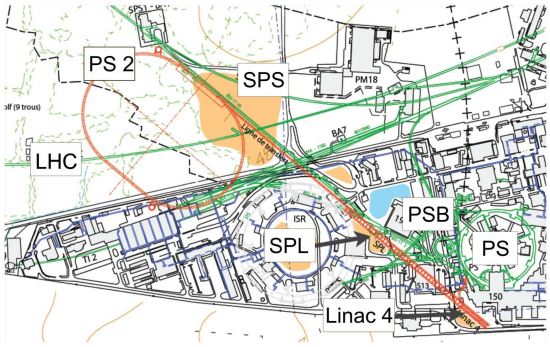

Figure 1: Layout of the LHC injectors at present and in the future.

In this paper some radiological aspects are discussed concerning the propagation of neutrons through the waveguide ducts from the SPL tunnel to the surface. Injected 160 MeV H^- ions from the Linac 4 into the SPL will be accelerated up to 4-5 GeV. The SPL tunnel will be situated in the earth at a depth between 20 and 30 meters. The expected uncontrolled losses are 1 W/m at each section of the SPL. Thus the radiobiological study has been started with the estimation of the dose rate level at the surface at the exit of the waveguide, coursed by uncontrolled losses in the SPL.

Prompt dose calculations

The calculations of the prompt dose rate were performed by using the Monte Carlo code FLUKA. The first calculation was done for a proton beam energy of 5 GeV. The total length of the SPL is 550 meters, for the calculation 100 meters were taken. Along 100 meters three waveguide ducts (shaft) will be situated. The target in which the beam is lost was assumed by a 0.02 × 0.02 × 100 m^3 iron block placed at the beam height. The dose rate was calculated from the superposition of 11 sources, which were equally distributed all over the target. In Fig. 2 the radiation streaming in the SPL tunnel and in one of the shafts is presented. The most conservative case is for the shaft number 3 which is shown in the lower part of Fig. 2. Without implementing any waveguides in the calculations the dose rate on ground level is less than 50 µSv/h. The inclusion of the waveguides in the ducts will further reduce the dose rate at the surface. This will be one of the future radiation protection studies for the SPL.

The same calculations were performed for the beam energy of 1 GeV. Assuming in this case also the beam losses of 1 W/m it was found out that the dose rate at ground level is by a factor of 3 higher than for the beam energy of 5 GeV. This lower energy is overcompensated by the higher intensity.

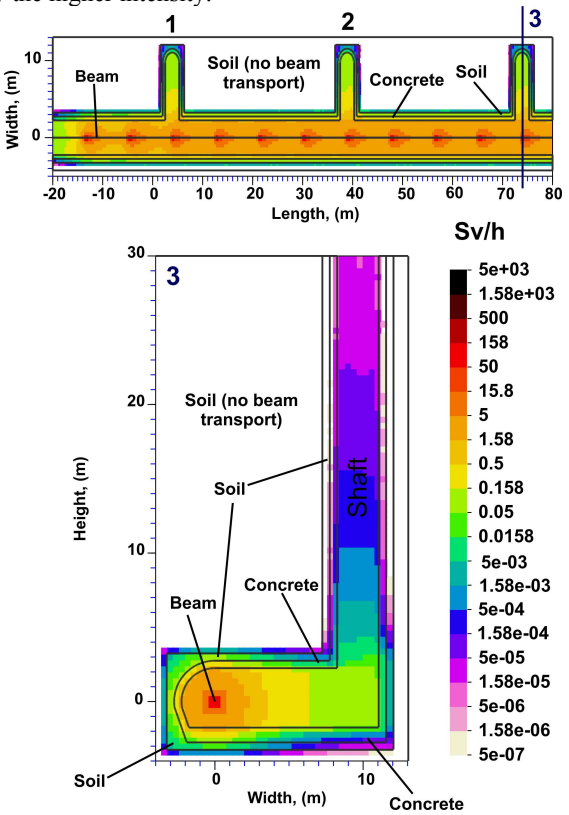

Figure 2: Neutron streaming through three waveguide ducts of SPL. Uncontrolled losses are assumed to be 1 W/m. The primary beam energy is 5 GeV. The importance biasing technique was used to improve the transport of the neutrons. The beam transport in the soil was switched off.

* Work supported by FP7 under the Grant Agreement No. 212114 (SLHC-PP).

References

[1] E. Mauro and M. Silari, "Radiation protection studies for a high-power 160 MeV proton linac", Nucl. Instrum. Methods Phys. Res. A, 605, 2008, p. 249.
[2] https://twiki.cern.ch/twiki/bin/view/SPL/SplWeb.
[3] https://paf-ps2.web.cern.ch/paf-ps2.
[4] www.fluka.org.

Residual dose rate calculation for an injection absorber of 4 GeV H^- injection in the PS 2 accelerator project*

E. Kozlova[1], T. Radon[1], T. Otto[2], and G. Fehrenbacher[1]
[1]GSI, Darmstadt, Germany; [2]CERN, Geneva, Switzerland

Introduction

The PS 2 accelerator is proposed to replace the existing PS complex, to provide more reliable operation and improved basic beam parameters for the foreseen LHC luminosity upgrade. In the projected PS 2 accelerator various beam dumps will absorb beams. One of the beam absorber, which has been study in the present work, will serve for stopping of unstripped H^0/H^- ions. It is planned to strip the coming from SPL to SP 2 H^- ions by using a charge-exchange H^- system. After a 500 μg/cm^2 foil 95 % of stripped H^+ ions will be accelerated in the SP 2 and the unstripped H^0/H^- ions will be dump. The beam load for the H^- dump is 6.4x10^{19} particles per year at the energy of 4 GeV [1, 2].

The beam dump design

As the starting point the design of the H^- injection dump like in the Project X at Fermilab is studied [3]. The same parameters and materials were taken for the SP 2 beam dump. In Fig. 1 schematic geometry of the dump is shown.

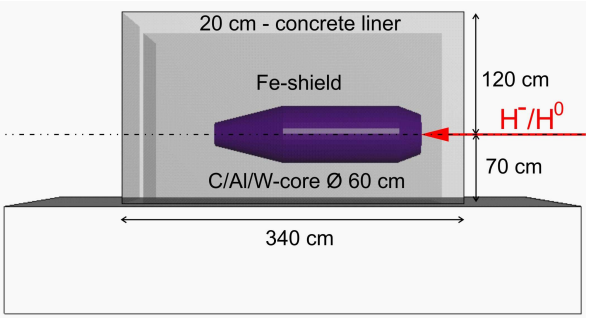

Figure 1: Geometry of the beam dump. The inner core consists of graphite, aluminium and tungsten. The core is surrounded by iron shielding. The outer layer of the shielding is concrete.

Residual dose calculations

The design goal of the beam absorber is after irradiation and 8 hours of cooling, to have in the close vicinity of the absorber the residual ambient dose rates is not higher than 10 μSv/h. For the optimization the Monte Carlo code FLUKA [4] was used. First of all, the geometry, as it is shown in Fig. 1, was taken for the calculation. The beam is assumed as a pencil beam. The intensity is 6.4E10^{19} protons uniformly distributed during 8 months of operations. The irradiation period is 10 years of operation, each of 8 months of beam operation and 4 months of shutdown. The dose is scored for 5 different cooling down periods after the last 8 months of irradiation: 8 hours, 1 day, 1 week, 1 month and 4 months. First calculations have shown that for reaching of our design goal the sizes of the dump had to be modified: the height of the iron part had to be increased by 20 cm, the width had to be 40 cm wider on each side; the tungsten core had to be shortened by 20 cm. The last result of the optimization is presented in Fig. 2. The residual dose rate after 8 hours of cooling is already below 10 μSv/h. Only at the beam entrance of the dump the dose rate is above the limit. It can be solved by closing the entrance after the shut down.

* Work supported by FP7 under the Grant Agreement No. 212114 (SLHC-PP).

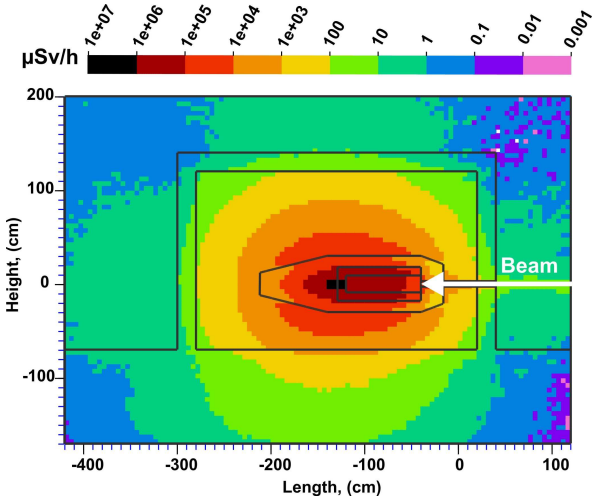

Figure 2: Plot of the residual dose rate after the irradiation period described in the text and a cooling time of 8 hours.

Conclusions

First results of the beam dump design are presented in this paper. The next steps of the study are estimation of the activation for the dump components like air, soil and ground water.

References

[1] B. Goddard et al, "4 GeV H^- charge exchange injection into the PS 2", AB-Note-2008-034, Geneva, September 2008.
[2] T. Kramer et al, "Design considerations for the PS 2 beam dumps", AB-Note-2008-035, Geneva, September 2008.
[3] http://projectx.fnal.gov.
[4] www.fluka.org.

Production and decay of element 114: high cross sections and new nucleus ^{277}Hs*

Ch.E. Düllmann[1,#], D. Ackermann[1], M. Block[1], W. Brüchle[1], H.G. Essel[1], J.M. Gates[1,2], W. Hartmann[1], F.P. Heßberger[1], A. Hübner[1], E. Jäger[1], J. Khuyagbaatar[1], B. Kindler[1], J. Krier[1], N. Kurz[1], B. Lommel[1], M. Schädel[1], B. Schausten[1], E. Schimpf[1], J. Steiner[1], A. Gorshkov[2], R. Graeger[2], A. Türler[2], A. Yakushev[2], K. Eberhardt[3], J. Even[3], D. Hild[3], J.V. Kratz[3], D. Liebe[3], J. Runke[3], P. Thörle-Pospiech[3], N. Wiehl[3], L.-L. Andersson[4], R.-D. Herzberg[4], E. Parr[4], J. Dvorak[5,6], P.A. Ellison[5,6], K.E. Gregorich[5], H. Nitsche[5,6], S. Lahiri[7], M. Maiti[7], J.P. Omtvedt[8], A. Semchenkov[8], D. Rudolph[9], J. Uusitalo[10], M. Wegrzecki[11]

[1]GSI, Darmstadt, Germany; [2]TU Munich, Garching, Germany; [3]Johannes Gutenberg-University of Mainz, Germany; [4]University of Liverpool, UK; [5]LBNL Berkeley, CA, USA; [6]UC Berkeley, CA, USA; [7]SINP, Kolkata, India; [8]University of Oslo, Norway; [9]Lund University, Sweden; [10]University of Jyväskylä, Finland; [11]ITE, Warsaw, Poland

Introduction

Discoveries of new superheavy elements (SHE) were reported from FLNR, Dubna, Russia [1], including observations of element 114 isotopes produced in ^{48}Ca+^{242,244}Pu reactions. Successful independent studies of some of the reactions studied in Dubna were reported [2,3], most recently also the observation of one atom each of ^{286,287}114 produced in the ^{48}Ca+^{242}Pu reaction at LBNL [4]. Predictions on the existence of an "island of stability" in the region of SHE have substantiated, despite the small number of observed events in every confirmation experiment. All successful confirmation experiments reported cross sections lower than those from FLNR by factors of two or more. Nevertheless, these cross sections are unexpectedly high compared to extrapolations from lighter systems [5], and intriguingly constant over a large range of $112 \le Z \le 118$. A thorough understanding of the underlying production mechanism is still missing; location and extension of the "island of stability" in the region of spherical SHE is still far from being established. To help shedding more light on these problems, a ^{48}Ca+^{244}Pu experiment was performed at the gas-filled TransActinide Separator and Chemistry Apparatus (TASCA) [6,7], which was optimized for the study of ^{48}Ca-induced fusion reactions with actinide targets. TASCA's efficiency for this nuclear reaction type is currently unsurpassed.

Experimental

The UNILAC accelerated a pulsed ^{48}Ca beam (~$2 \cdot 10^{12}$ s^{-1}), which passed through $^{244}PuO_2$ targets (average thickness: 438 μg/cm^2 ^{244}Pu). Beam energies inside the targets were 241.3-246.2 MeV (E*=39.8-43.9 MeV; hereafter referred to as 42-MeV run) and 236.4-241.0 MeV (E*=36.1-39.5 MeV; 38-MeV run). $2.44 \cdot 10^{18}$ (42-MeV run) and $1.15 \cdot 10^{18}$ (38-MeV run) projectiles passed through the targets. Nuclear reaction products entered TASCA, operated in "high transmission mode" [7], and were separated in 0.8 mbar He gas. The detection system consisted of a Multi Wire Proportional Counter (MWPC) and a focal plane detector box (FPDB). The FPDB consisted of a Double Sided Silicon Strip Detector (DSSSD; pitch size: 1 mm; 144 vertical / 48 horizontal strips) and Single Sided Silicon Strip Detectors (SSSSD) mounted perpendicular in the backward hemisphere of the DSSSD [8]. The MWPC provided a signal for ions recoiling from the target and allowed distinguishing these from radioactive decays of species implanted in the DSSSD. The energy resolution of the FPDB was 25 keV FWHM for 8.1 MeV α-particles fully stopped in the DSSSD and 170 keV for α-particles that deposited a fraction of their energy inside the DSSSD and the remainder in the SSSSD. The detection efficiency was 72% for α-particles and 100% for SF. The efficiency for focusing element 114 EVRs into the DSSSD was (60±6)% [9]. Data acquisition was triggered by events registering more than 300 keV in the DSSSD or more than 500 keV in a SSSSD. More details are given in [10,11].

Results

We searched [12] for decay chains from ^{288,289}114 exhibiting the decay patterns as published in [1]. Afterwards, upon identification of a chain, additional α-particles occurring in the same pixel as the chain were searched for, in between registration of the EVR and the terminating SF. Based on the event rate only 0.02 (^{289}114) and 0.05 (^{288}114) random chains from unrelated background events were expected. The search yielded nine EVR-α-SF chains (^{288}114) and four EVR-α-α(-α)-SF chains (^{289}114). Ten chains were measured in the 42-MeV run and three chains in the 38-MeV run (Figs. 1 and 2). The agreement of our data (Table 1) with that of [1] is good in all cases except for chain #9. The data measured for the EVR, the first, and the second α-particle suggest assigning chain #9 to $^{289}114 \rightarrow ^{285}112 \rightarrow ^{281}$Ds. ^{281}Ds then decayed by emission of a (8.727±0.025)-MeV α-particle 5.688 s after the decay of ^{285}112, during the beam-off period, where background is low. ^{281}Ds has undergone SF in all ten previously observed decays [1] with $T_{1/2} = 11.1^{+5.0}_{-2.7}$ s. Based on background rates, the probability to register

* Work supported by the BMBF (06MT247I, 06MT248, 06MZ223I); the GSI-F&E (MT/TÜR, MZJVKR); the Swedish and Norwegian (177538) Science Councils; the US DOE (DE-AC03-76SF00098; DE-AC02-05CH11231; NNSA Fellowship); the Govt. of India (TADDS).

#c.e.duellmann@gsi.de

an α-like event with properties as exhibited by the observed one is only 0.1%. We thus assign it to a so far unobserved α-branch in ^{281}Ds. Considering this α-decay and the thirteen measured SF decays from [1] and our work, an α-decay branch b_α of 9^{+16}_{-7} % results after correcting for detection efficiency differences for α-decay and SF. The chain was terminated 4.5 ms later by SF of the new nucleus ^{277}Hs.

The B•ρ of element 114 EVRs in 0.8 mbar He was measured to (2.29±0.11) T•m.

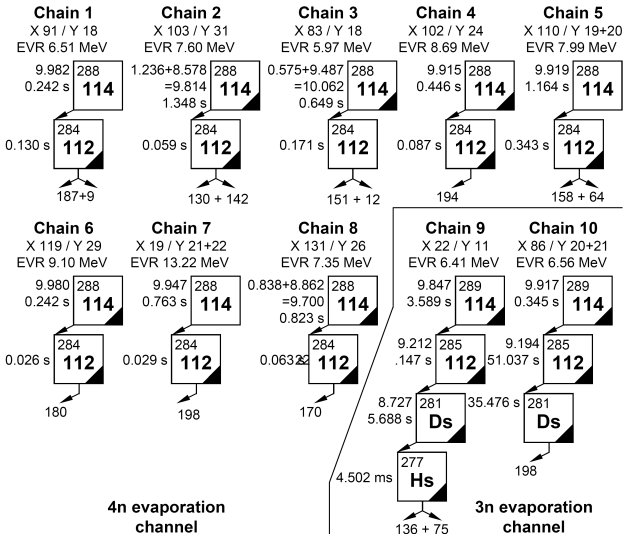

Figure 1: Decay chains assigned to ^{288}114 (chains 1-8) and ^{289}114 (chains 9, 10) observed during the 42-MeV run. A black triangle in the lower right corner of a box indicates that the beam was off at the time of the event.

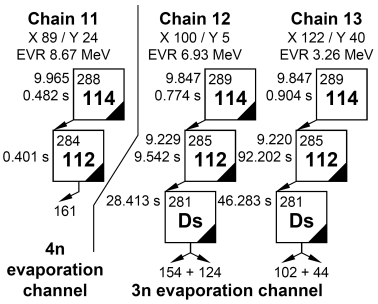

Figure 2: Same as Figure 1, but showing decay chains observed during the 38-MeV run.

Table 1. Decay properties (this work combined with [1])

Isotope	Decay	$T_{1/2}$ (this work)	$T_{1/2}$ (combined)
^{289}114	α	$0.97^{+0.97}_{-0.32}$ s	$2.1^{+0.8}_{-0.4}$ s
^{288}114	α	$0.47^{+0.24}_{-0.12}$ s	$0.69^{+0.17}_{-0.11}$ s
^{285}112	α	30^{+30}_{-10} s	29^{+11}_{-6} s
^{284}112	SF	101^{+50}_{-25} ms	99^{+24}_{-16} ms
^{281}Ds	SF/α:91/9	20^{+20}_{-7} s	13^{+5}_{-3} s
^{277}Hs	SF	3^{+15}_{-1} ms	3^{+15}_{-1} ms

Discussion

Z=108 is a deformed proton shell closure in N~162 isotopes. The observed ^{277}Hs lifetime is short compared to half-lives of the Hs isotopes near the deformed N=162 shell closure, indicating reduced shell stabilization in the N=169 nucleus ^{277}Hs. Macro-microscopic model predictions of $T_{1/2}$(SF) for the neighboring isotopes are 46 ms (^{276}Hs) and 0.98 ms (^{278}Hs), the geometric mean being 6.7 ms [13]. This is similar to our observed lifetime. The odd neutron is expected to hinder SF decay significantly. Thus, the drop in $T_{1/2}$(SF) when increasing N above 162 may be more severe than suggested by [13]. ^{275}Hs (N=167) decays by α-particle emission with $T_{1/2}$=0.19 s [1]. The experimental trend with prevalent α-decay in Hs isotopes with N=157-167, but predominant SF in lighter as well as in heavier isotopes is close to that in [10], which suggests dominant α-decay from N=154 to N=166 but SF for N>168. This indicates that stability vanishes rapidly with increasing distance from N=162.

Measured cross sections for element 114 isotopes in the 38-MeV run were $8.0^{+7.4}_{-4.5}$ pb (3n channel) and $2.8^{+4.2}_{-2.1}$ pb (4n channel), and in the 42-MeV run, $3.5^{+3.3}_{-2.0}$ pb (3n channel) and $9.8^{+3.9}_{-3.1}$ pb (4n channel). Error bars include statistical uncertainties only (68.3% confidence level); the systematic uncertainty is estimated to 14%. In contrast to any other confirmation experiment, we confirm the large cross sections as reported from FLNR [1]. In fact, our measured cross sections are higher than those reported from the DGFRS. These high cross sections call for investigations of the details of the production mechanism. Production rates that follow from these values encourage using this nuclear reaction to produce relatively long-lived isotopes of element 114, in particular for envisaged chemical investigations [14] or for γ-spectroscopic studies that allow shedding light on the nuclear structure in this SHE region and may facilitate unique Z identification.

We thank the ECR and UNILAC staff for excellent ^{48}Ca beams and H. Brand and the GSI EE department, the machine shop staff at the institute of radiochemistry, TU Munich, and V. Gorshkov for technical support.

References

[1] Yu.Ts. Oganessian, J. Phys. G 34 (2007) R165.
[2] S. Hofmann, EPJA 32 (2007) 251.
[3] R. Eichler et al. Nature 447 (2007) 72.
[4] L. Stavsetra et al., PRL 103 (2009) 132502.
[5] S. Hofmann, Lect. Notes Phys. 264 (2009) 203.
[6] M. Schädel, Eur. Phys. J. D 45 (2007) 67.
[7] A. Semchenkov et al., NIM B 266 (2008) 4153
[8] A. Gorshkov et al., in preparation for NIM A.
[9] K.E. Gregorich et al., GSI Sci. Rep. 2006 (2007) 144.
[10] Ch.E. Düllmann et al., submitted to PRL.
[11] J.M. Gates et al., in preparation for PRC.
[12] H.G. Essel et al., this Scientific Report.
[13] R. Smolanczuk, PRC 52 (1995) 1871.
[14] A. Yakushev et al., this Scientific Report.

The Performance of TASCA in the ^{48}Ca+^{206,207,208}Pb Reactions

J. Khuyagbaatar[1], M. Schädel[1], D. Ackermann[1], Ch.E. Düllmann[1], E. Jäger[1], F.P. Heßberger[1], A. Semchenkov[1,2], A. Gorshkov[2], R. Graeger[2], A. Türler[2], A. Yakushev[2], K. Eberhardt[3], J. Even[3], J.V. Kratz[3], L.-L. Andersson[4], D. Rudolph[4] for the TASCA Collaboration

[1]GSI, Darmstadt, Germany; [2]Technical University München, Garching, Germany; [3]University of Mainz, Mainz, Germany; [4]Lund University, Lund, Sweden

The gas-filled recoil separator TASCA (**T**rans**A**ctinide **S**eparator and **C**hemistry **A**pparatus) was installed in a dipole-quadrupole-quadrupole configuration (DQQ) at the UNILAC at GSI [1-3]. An extensive commissioning program [4] was carried out at TASCA studying a large number of experimental parameters and nuclear reactions. Depending on the polarity of the quadrupole magnets TASCA can be operated in two modes: the so called High Transmission Mode (HTM) and the Small Image Mode (SIM). Dispersion values of 9 and 1 mm per one percent change of $B\rho$ were calculated for the HTM and SIM, respectively [3]. Ion optical calculations of the HTM and SIM were performed using Monte-Carlo simulations [5].
Important characteristics of TASCA in both modes were investigated using ^{48}Ca+Pb reactions and a 16-strip 80x35 mm^2 large position-sensitive silicon-strip detector based focal plane detector (FPD). Optimal magnetic settings and gas pressures were established by centering spatial distributions of α-decaying evaporation residues in the FPD. Transmission measurements were performed with targets of well determined thicknesses.

HTM:

Measured spatial distributions of ^{254}No ions are shown in Fig. 1 for different helium gas pressures and a constant dipole magnet setting of $B\rho$=2.08 Tm. Solid curves show the calculated [5] distribution of ^{254}No ions in the FPD of TASCA at different gas pressures. Well centered distributions were observed in the range of 0.8 to 1.0 mbar pressure range. These distributions are in very good agreement with the calculated ones. However, at lower and higher gas pressures the ^{254}No distributions are horizontally shifted off-center. This means that the deflection angle of ^{254}No in the dipole magnet is changing. This is related to a change of average charge of ^{254}No ions. Such an effect was observed also at the Dubna gas-filled separator and it was explained with so-called "density effect" [6].
An average value of (57±5) % for the transmission of No isotopes synthesized in ^{48}Ca on $^{206-208}$Pb reactions was deduced using the cross-section data for fusion-evaporation reactions from [7]. This value is in good agreement with the calculated value of about 52 % for the HTM of TASCA.

SIM:

To find optimal settings for the quadrupole magnets in the SIM is more difficult than for the HTM. Various settings for the quadrupole focusing were tested to obtain best values. A 40-mm diameter image size was taken as a "reference" best value. Again, deviations between this optimized result, which is in agreement with theoretical calculations, and distributions obtained at pressures lower than the optimal He pressures were observed.
A transmission of (35±5) % was deduced at optimized SIM settings for the reaction ^{48}Ca+^{208}Pb. This value is in good agreement with calculated values.

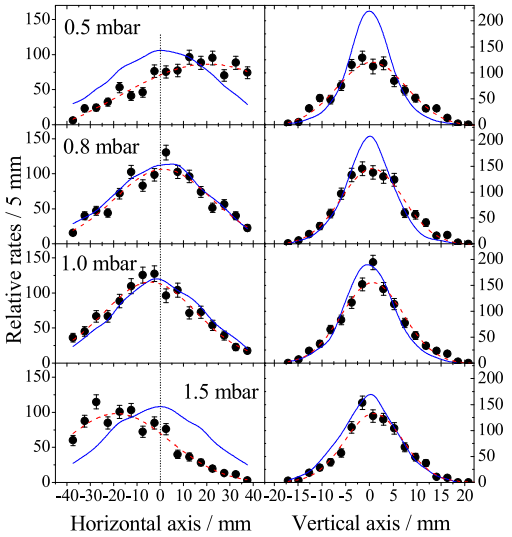

Fig 1: Spatial distributions of ^{254}No ions in the FPD at different pressures of the He filling-gas. TASCA was operated in HTM. Dashed lines show the Gaussian fit.

Pure hydrogen and He-H_2-mixtures were used as filling gases in both modes as well. The optimal magnetic settings and gas pressures were investigated and the corresponding average charges of nobelium ions were determined. Within a 10% uncertainty, the measured transmissions for He, H_2 and mixtures of both gases were identical. When pure H_2 and a mixture of He and H_2 were used, we observed a better background suppression of target-like ions as compared with pure helium.
More detailed information on the TASCA performance in ^{48}Ca+Pb reactions and average charges of the nobelium ions in various gases will be given in [8].

[1] M. Schädel, Eur. Phys. J. D 45 (2007) 67. See also www.gsi.de/TASCA.
[2] M. Schädel, J. Nucl. Radiochem. Sci. 8 (2007) 47.
[3] A. Semchenkov et al., NIM B 266 (2008) 4153.
[4] M. Schädel et al., GSI Sci. Rep. 2008 (2009) 138.
[5] K.E. Gregorich et al., GSI Sci. Rep. 2006 (2007) 144.
[6] Yu.Ts. Oganessian et al., PRC 64 (2001) 064309.
[7] Yu.Ts. Oganessian et al., PRC 64 (2001) 054606.
[8] J. Khuyagbaatar et al., to be published.

Cross-sections for production of neutron deficient Sg - isotopes in reactions $^{54}Cr + ^{206,207,208}Pb$

F.P. Heßberger[1,2], S. Antalic[3], B. Streicher[1,4], B. Sulignano[5,1], D. Ackermann[1], M. Block[1], S. Heinz[1], S. Hofmann[1,6], J. Khuyagbaatar[1], B. Kindler[1], I. Kojouharov[1], B. Lommel[1], R. Mann[1]

[1]GSI-Helmholtzzentrum für Schwerionenforschung, Darmstadt, Germany; [2]Helmholtz - Institut Mainz, Mainz, Germany, [3]Comenius University Bratislava, Bratislava, Slovakia , [4]University of Groningen, The Netherlands, [5]CEA Saclay, Gif-sur-Yvette, France, [6]Goethe-Universität Frankfurt, Frankfurt, Germany

Due to low cross-sections for the production of heaviest nuclei the choice of the optimum reaction for specific nuclides is crucial for nuclear structure investigations based on α-γ-decay spectroscopy, which demand maximum numbers of observed events. Following previous decay studies of ^{255}No [1] and ^{257}Rf [2] an experiment to investigate ^{259}Sg, the next heavier N=153 isotone, for which only rough decay properties were known so far [3], was performed at SHIP in March 2009. The most efficient way to produce neutron deficient isotopes of seaborgium is employing reactions of ^{54}Cr with Pb - isotopes. Excitation functions for ^{54}Cr + ^{208}Pb [2] and ^{207}Pb [4] had been measured previously. The results are displayed in fig. 1.

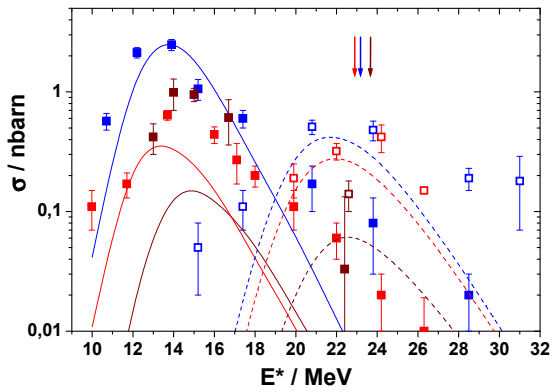

Figure 1: Excitation functions for the reactions ^{208}Pb(^{54}Cr,xn)$^{262-x}$Sg (blue symbols), ^{207}Pb(^{54}Cr,xn)$^{261-x}$Sg (red symbols), ^{206}Pb(^{54}Cr,xn)$^{260-x}$Sg (wine symbols) (x=1,2). The full symbols represent the 1n - channels, the open symbols the 2n - channels. The lines represent the results of HIVAP calculations (full line = 1n channel, dashed line = 2n channel) for the corresponding systems. The arrows denote the positions of the Bass model fusion barriers [5] for the respective target - projectile combinations.

HIVAP [6] calculations using parameterisations to reproduce the 1n and 2n cross-sections for the reaction ^{54}Cr + ^{208}Pb were performed. Evidently this parameterisation satisfactorily reproduces also the 2n cross-sections for ^{54}Cr + ^{207}Pb, while the 1n cross-section is underpredicted by roughly a factor of two. Going from ^{207}Pb to ^{206}Pb HIVAP predicts a decrease by roughly factors of 2.5 and 4 for the 1n and 2n cross-sections, respectively, and in addition a shift of the excitation energy for the 1n cross-section maximum by ≈1.5 MeV towards higher values. Since the thus expected cross-section of ≈150 pb for ^{259}Sg is only about a factor of two lower than the measured value for the reaction ^{207}Pb(^{54}Cr,2n)^{259}Sg and an astonishing high cross-section of ≈320 pb was obtained for the reaction ^{208}Pb(^{54}Cr,1n)^{259}Sg [7] it seemed valuable to test the reaction ^{206}Pb(^{54}Cr,1n)^{259}Sg as an alternative way of production. The result is shown in fig. 1 (wine symbols). A cross-section of ≈1 nb was measured for ^{259}Sg, which is even about 50% higher than the 1n cross-section using the more neutron rich target isotope ^{207}Pb. Differences of the 2n cross-section are less dramatic. One data point, close to the expected [6] maximum was taken. We obtained σ(2n) = 0.14±0.04 nb at E^* = 22.5 MeV, which is roughly a factor of two higher than the predicted value and a factor of two lower than the 2n cross-section for the reaction ^{54}Cr + ^{207}Pb. This more 'regular' behavior does not suggest an enhanced stability of ^{259}Sg against prompt fission during the deexcitation process. The production ratios σ(^{260}Sg,2n) / σ(^{259}Sg,2n) ≈ 1.7 and σ(^{260}Sg,1n) / σ(^{259}Sg,1n) ≈ 0.6 do also not suggest a reduction of the SHIP transmission for ^{260}Sg due to a short-lived isomeric state decaying during the separation process. It rather hints at a strong nuclear structure influence of the target nucleus on the fusion probability at energies far below the fusion barrier, established at E^* = 23.2±0.5 MeV for the three systems. More detailed measurements of excitation functions will show if this is just a local effect connected with the specific projectile or a more general phenomenon. In the latter case, only slightly decreasing 1n cross-sections going from ^{208}Pb to the lighter isotopes ^{206}Pb or even ^{204}Pb, would not only give new insight into the process of 'cold' fusion, but also enhance our chances of continuing our program on detailed nuclear structure investigations of nuclei in the vicinity of the N = 152 subshell towards isotopes of elements above seaborgium (Z=106).

References

[1] F.P. Heßberger et al., EPJ A 29, 165 (2006)
[2] B. Streicher, PHD, Comenius University Bratislava, 2006, and to be published
[3] F.P. Heßberger et al. EPJ A 41, 145 (2009)
[4] B. Sulignano, PHD, Johannes-Gutenberg Universität Mainz, 2007
[5] R. Bass, Nucl. Phys. A 231, 45 (1974)
[6] W. Reisdorf, Z. Phys. A 300, 227 (1981)
[7] C.M. Folden III et al. Phys. Rev. C 79, 027602 (2009)

Study of ^{240}Cf and new isotope ^{236}Cm

J. Khuyagbaatar[1], F.P. Heβberger[1], S. Hofmann[1], D. Ackermann[1], V.S. Comas[2], S. Heinz[1], J.A. Heredia[2], B. Kindler[1], I. Kojouharov[1], B. Lommel[1], R. Mann[1], K. Nishio[3] and A. Yakushev[4]
[1]GSI Helmholtzzentrum für Schwerionenforschung, Darmstadt, Germany, [2] Institute for Technologies and Applied Sciences, Habana, Cuba, [3]Japan Atomic Energy Agency (JAEA), Tokai, Japan, [4]Institut für Radiochemie, Technische Universität München, Garching, Germany

Decay properties of neutron-deficient isotopes of actinide elements provide valuable information on the nuclear mass surface close to the proton drip line, on nuclear structure of deformed heavy nuclei and on fission properties far from stability. However, detailed experimental data on decay properties of neutron-deficient nuclei in the region of Z>96 are still scarce due to low production rates.

Recently, attempts were carried out to investigate the decay properties of neutron-deficient isotopes of fermium [1]. Due to this renewed interest on decay properties of neutron-deficient isotopes we aimed to study the decay of the isotope ^{240}Cf at SHIP by measuring simultaneously α decay and spontaneous fission.

The isotope ^{240}Cf was first identified in [2] by α decay. Spontaneous fission of this isotope was measured in [3] and a fission branching of ≈0.02 was deduced. However, in [3] only fission events were measured. Therefore, the estimated fission branching and deduced partial spontaneous fission half-life was based on a calculated total production cross-section in the fusion-evaporation reaction ^{208}Pb(^{34}S,2n)^{240}Cf [3]. Consequently, this important decay property was relatively uncertain. In addition, an α decay branching of ^{240}Cf being close to one would open a possibility to search for the so far unknown isotope ^{236}Cm using the α-α and α-SF correlations.

The reactions ^{36}S(^{207}Pb,3n) and ^{36}S(^{206}Pb,2n) were used for production of ^{240}Cf. Beam energies were at E_{lab}=170.3 and 163.3 MeV, respectively. Corresponding α decay spectra measured in the energy region (6500–7700) keV are shown in figs. 1a and b. The strongest line, observed at an energy of (7585±20) keV was attributed to ^{240}Cf according to the literature data [2]. In the reactions ^{36}S(^{206}Pb,2n)^{240}Cf and ^{36}S(^{207}Pb,3n)^{240}Cf, a total number of ≈70 and ≈770 α decay events were observed, respectively, having full energy release in the focal plane detector. A so far unknown α line at E=(6954±20) keV was observed in both irradiations during the beam-off periods.

To assign this line we performed a position and time correlation analysis (see fig. 1c). The scatter plot marks events which are in delayed coincidence within a position window of ±0.3 mm and within a time window of 25 min. The scatter plot clearly reveals a cluster of events at parent-daughter energies of 7585 and 6954 keV, respectively. In addition to these events we observe correlations to known α decays of ^{232}Pu, ^{228}U, ^{224}Th and ^{220}Ra. Therefore, we unambiguously assign the group of events at (7585±20) and (6954±20) keV to ^{240}Cf and to the new isotope ^{236}Cm, respectively.

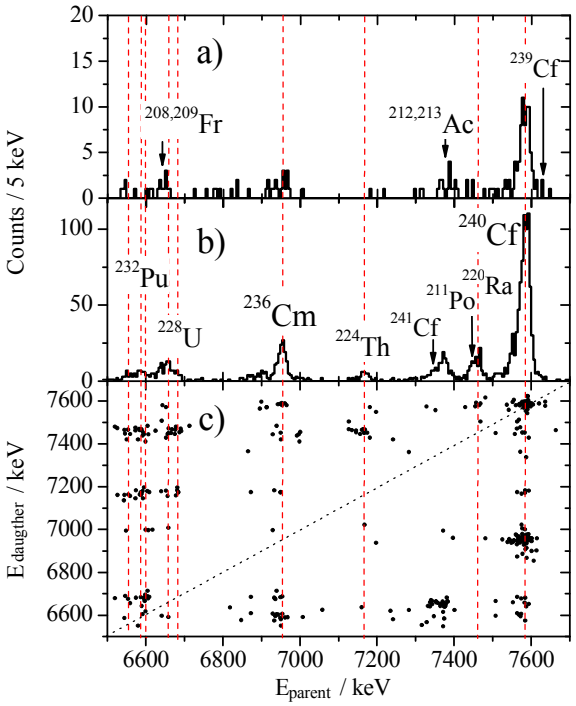

Fig 1: Alpha spectra taken during the beam-off periods in irradiations of ^{206}Pb with ^{36}S at E_{lab}=163.6 MeV (a) and of ^{207}Pb with ^{36}S at E_{lab}=170.3 MeV (b). Two dimensional α-α correlation plot (c). Dashed lines mark the energies of α decays of ^{240}Cf and its decay products. See text for details.

A half-life of (590±70) s was extracted for ^{236}Cm from the time distribution of the correlated events. An α branching of (0.18±0.02) was determined on the basis of the observed α decays for ^{240}Cf and ^{236}Cm.

A total 22 spontaneous fission events was observed during the beam-off periods. They were assigned to the decay of ^{240}Cf, and a fission branching of (0.015±0.002) was deduced.

The results of our work improve significantly the literature data. More detailed information will be given in [4].

References

[1] J. Khuyagbaatar et al., Eur. Phys. J. A **37**, 177 (2008) and GSI Scientific Report 2008, 136 (2009).
[2] R.J. Silva et al., Phys. Rev. C **2**, 1948 (1970).
[3] Yu.A. Lazarev et al., Phys. Rev. C **588**, 501 (1995).
[4] J. Khuyagbaatar et al., to be published.

The capture process and first steps to cold fusion

S. Heinz, V. Comas, S. Hofmann, D. Ackermann, J. Heredia, F.P. Heßberger, J. Khuyagbaatar, B. Kindler, B. Lommel, and R. Mann
GSI, Darmstadt, Germany

The synthesis of heavy elements in cold fusion reactions using lead and bismuth targets reveals maximum cross-sections for central collisions at energies below the barrier predicted by the Bass model. The two-centre shell model [1] gives an approach to explain fusion at such low energies. It assumes that the nucleons move in a potential which is formed by combining the potentials of the individual nuclei. In central collisions at near-barrier energies the relative velocities and angular momenta are small and the valence nucleons can move between the reaction partners as soon as the outer orbits come into contact. We investigated the applicability of the two-centre shell model by following the capture process and first steps to the compound nucleus in the superheavy system ^{64}Ni + ^{207}Pb (Z_{proj} + Z_{target} = 110). This was done by studying transfer products with proton numbers beyond the target proton number, which have been created under the same kinematical conditions which result in maximum yields of fusion products, namely, in central collisions and at near-barrier energies.

The experiment was performed at the velocity filter SHIP [2] which allows the detection of reaction products at angles of (0 ± 2)°. We measured at beam energies of 4.80, 5.00, 5.20, 5.40, 5.53 and 5.92×A MeV. We detected several transfer products with proton numbers 84 ≤ Z ≤ 88 via their α-decays. Figure 1c shows the excitation functions representatively for the isotopes ^{211}Po, ^{212}At, ^{213}Rn, ^{213}Fr and ^{214}Ra (Z = 84 to 88). The excitation functions for isotopes with Z = 84, 85 and 86 are rather narrow (FWHM = 15 MeV) with maxima located below the Bass barrier (arrows). They are comparable to those from cold fusion reactions leading to superheavy elements after one-neutron evaporation (figs. 1a and b). At low energies fusion or transfer is hindered by the Coulomb barrier while towards higher energies other evaporation or fission channels open and lead to the decrease of the yield. The location of the maxima corresponds to a distance of ≥ 14 fm between the nuclear centres, which just allows for the contact of the surfaces. According to the two-centre shell model this is sufficient to start the exchange of valence nucleons between the cores. For transfer products with Z > 86 the maxima of the excitation functions are located at higher energies and their half-widths are larger which points to higher excited primary products in comparison to the previous case. They are comparable to fusion excitation functions for evaporation channels with more than one nucleon. If and to what extent also the occupation of specific neutron and proton shells influences the capture process will be subject to future experiments.

All observed transfer products originate from deep inelastic reactions. This is reflected by the total kinetic energies

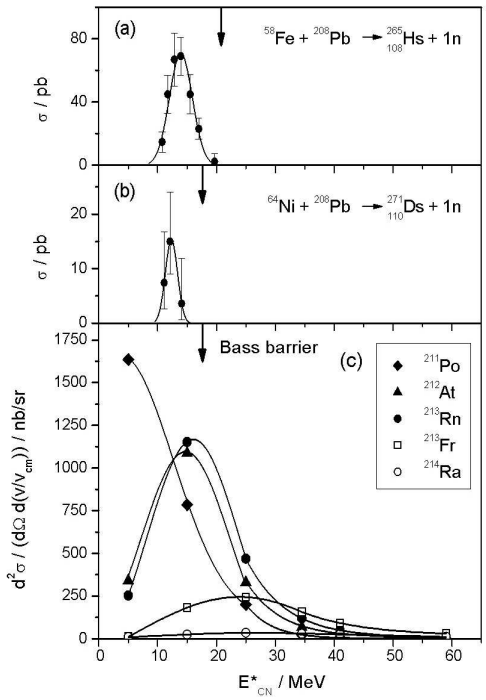

Figure 1. Excitation functions for 1n evaporation channels in the cold fusion reactions ^{58}Fe + ^{208}Pb and ^{64}Ni + ^{208}Pb (a, b) and for different isotopes produced in transfer reactions in ^{64}Ni + ^{207}Pb collisions (c). The energy scale on the abscissa gives the excitation energy of the compound nuclei ^{266}Hs and ^{271}Ds.

in the exit channel, which are independent of the bombarding energy and have values slightly below the Viola energy.

The massive transfer of nucleons, which we observed at very low beam energies, has also an applicatory aspect. The low beam energies lead to transfer products at low excitation energies. This enhances their survival probability against particle evaporation and fission. Therefore, such transfer reactions could be used to create new isotopes of heavy nuclei, especially on the neutron-rich side of the nuclear chart.

References

[1] D. Scharnweber, W. Greiner, and U. Mosel, Nucl. Phys. A 164, 257 (1971).
[2] S. Hofmann and G. Münzenberg, Rev. Mod. Phys. 72, 733 (2000).

Mass transfer and nuclear interaction times in deep inelastic U + U collisions

S. Heinz[1], C. Golabek[2], W. Mittig[2], F. Rejmund[2], and A.C.C. Villari[2]
[1]GSI, Darmstadt, Germany, [2]GANIL, Caen, France

In heavy ion collisions at Coulomb barrier energies a di-nuclear system (DNS) can be formed when the cores come into contact. This enables the exchange of nucleons which is usually accompanied by the dissipation of kinetic energy. During this time the nuclei stick together. We investigated ^{238}U + ^{238}U (Z = 184) collisions at the VAMOS spectrometer at GANIL at five beam energies in the interval (6.09 − 7.35)×A MeV. At 6.09×A MeV the Coulomb barrier is not reached at all mutual orientations of the deformed uranium nuclei. The spectrometer covered the angles (35 ± 5)°. We observed a massive transfer of nucleons resulting in reaction products far from the entrance channel. Only nuclei lighter than uranium were observed. The transfer was correlated with a large energy dissipation of up to several 100 MeV. Fig. 1 shows the total kinetic energy (TKE) in the exit channel as a function of the detected fragment mass for all beam energies.

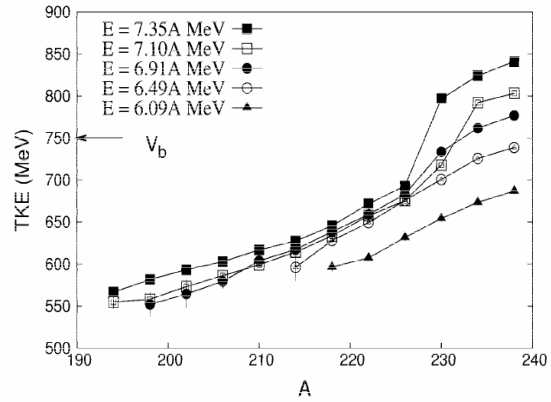

Figure 1. Total kinetic energy of (quasi-)elastic and deep inelastic reaction products from ^{238}U + ^{238}U collisions at different beam energies. V_b denotes the Coulomb barrier of the exit channel for spherical nuclei.

Two regions can be distinguished. For 225 < A < 238 TKE is strongly beam energy dependent like expected for elastic and quasi-elastic reactions. For A < 225 the correlation between TKE and A becomes linear and for the four highest energies TKE is nearly independent of the bombarding energy. This is characteristic for deep inelastic reactions where all kinetic energy is damped leading to the re-separation of the di-nuclear system with the Coulomb barrier of the exit channel. In all cases the observed TKE is below the Coulomb barrier for spherical nuclei, which is about 750 MeV for all observed exit channels. At all beam energies the deep inelastic region is entered at the same TKE of 690 MeV. This reflects that massive transfer is only starting when the di-nuclear system reaches a certain deformation and provides a sufficiently strong neck. Fig. 2 shows the mass distributions for deep

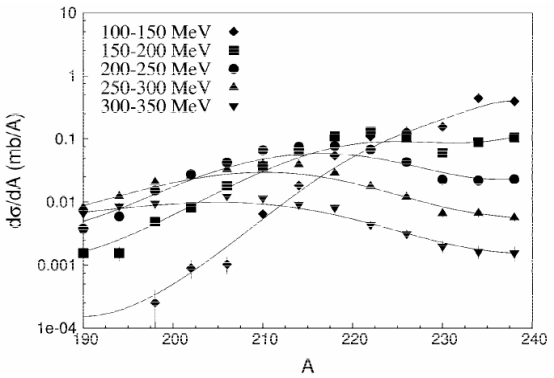

Figure 2. Mass distribution of deep inelastic reaction products from ^{238}U + ^{238}U collisions at 7.35×A MeV for different windows on TKEL.

inelastic products for different windows on the total kinetic energy loss (TKEL) for the beam energy 7.35×A MeV. With increasing TKEL the maximum of the distribution shifts towards lower masses and its width increases. We attribute the shift mainly to sequential fission of the excited primary reaction products, which affects with increasing excitation energy also the nuclei lighter than uranium.

Our results show the characteristics of a diffusion process as origin of the observed nuclei. Therefore, we applied the diffusion model [1] to derive values for the underlying nuclear interaction times T_{int}. According to this model T_{int} increases linearly with the variance of the mass distribution. We deduced the respective values for T_{int} for the TKEL windows given in Fig. 2. Predominantly, the deep inelastic events result from reactions where T_{int} is not longer than 2×10^{-21} s. The longest time delay of 8×10^{-21} s we obtain for events with TKEL = (300 – 350) MeV. This converts to a differential cross-section of 400 μb/sr for the covered angular range and corresponds to a fraction of 3% of all deep inelastic transfer products with TKEL ≥ 100 MeV.

We observed no nuclei heavier than uranium due to fission of these products. Moreover, the high background in the region 238 < A < 260 set a lower cross-section limit of 1 mb. Nevertheless, the large nucleon transfer also observed at the lowest beam energies could open a way to produce neutron-rich heavy nuclei in the region of Z > 100, which are not accessible in other reactions. Especially at low beam energies the excitation energy of the fragments is moderate, which increases their survival against sequential fission.

References

[1] C. Riedel and W. Nörenberg, Z. Phys. A 290, 385 (1979).

Towards a direct mass measurement of ^{255}Lr at SHIPTRAP

M. Dworschak[1], D. Ackermann[1], K. Blaum[2,3], M. Block[1], C. Droese[4], S. Eliseev[2], E. Haettner[1,5], F. Herfurth[1], F.P. Heßberger[1], S. Hofmann[1], J. Ketelaer[6], G. Marx[4], D. Nesterenko[7], Yu. Novikov[1,7], W.R. Plaß[1,5], A. Popeko[8], D. Rodríguez[9], C. Scheidenberger[1,5], L. Schweikhard[4], P. Thirolf[10], and C. Weber[10]

[1]GSI, Darmstadt; [2]MPI-K Heidelberg; [3]Universität Heidelberg; [4]Universität Greifswald; [5]Universität Gießen; [6]Universität Mainz; [7]Petersburg Nuclear Physics Institute; [8]JINR, Dubna; [9]Universidad de Granada; [10]LMU München

The mass of a nuclide is a fundamental parameter. It provides information about the nuclear binding energy and is thus crucial for nuclear structure and reaction studies. Compared to the indirect mass determination via decay energies, a method in which the mass can be directly obtained is favorable since it is independent of a detailed knowledge of nuclear level schemes. Especially in the region of transuranium nuclides direct mass measurements are desirable to check the information on the binding energy which is presently based on spectroscopic data.

The Penning-trap mass spectrometer SHIPTRAP [1] is presently the only facility where direct measurements on transfermium nuclides can be performed. After the first successful experiments on three nobelium isotopes (Z=102) [2] the focus was set on extending direct mass measurements to higher Z. For the next step the isotope ^{255}Lr was selected, which is of specific interest since its mass, as well as that of its daughter nuclide ^{251}Md, are presently only estimated from systematic trends. Furthermore, two low-lying levels decaying by α emission have been observed. The excitation energy of the isomeric state could not be determined so far but has to be settled at $E_{exc} < 50keV$. A direct mass determination would thus provide more information on ground state masses and would hence be another anchorpoint in an odd-even α-decay chain.

The nuclei investigated at SHIPTRAP were produced by fusion-evaporation reactions and were separated from the primary beam by the velocity filter SHIP [3]. ^{255}Lr was produced in the reaction ^{209}Bi(^{48}Ca,2n)^{255}Lr at a primary beam energy of 4.55 MeV/u with a cross section of about 200 nb. This corresponds to a rate of about 0.3 ions per second measured at a position-sensitive silicon detector in front of SHIPTRAP. The reaction products with kinetic energies of about 40 MeV were decelerated in degrader foils and were stopped in a gas cell at 50 mbar helium. The lawrencium atoms were extracted from the gas as singly and doubly charged ions.

After the extraction from the gas cell the ions were cooled and accumulated in an RFQ structure and then ejected as a short ion bunch. Subsequently, the ions were injected into a double Penning trap system, which is consisting of a preparation trap and a measurement trap, placed in a 7T magnet. In the latter the mass was determined by measuring the cyclotron frequency ν_c of the ions using a time-of-flight cyclotron-resonance-detection technique.

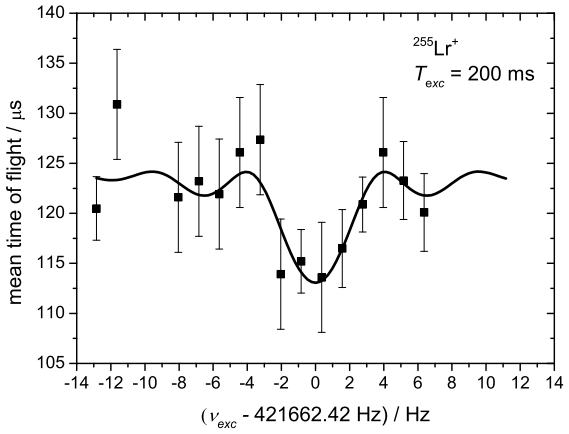

Figure 1: Time-of-flight resonance of ^{255}Lr$^+$. The solid line is a fit of the theoretical line shape to the experimental data points.

Altogether around 30 ^{255}Lr$^+$ ions were detected in about 30 hours measurement time and the time-of-flight resonance shown in Fig. 1 was obtained. ^{255}Lr is thus both, the heaviest radionuclide and the one with the lowest production rate ever studied in a Penning trap.

The SHIPTRAP measurements on nobelium and lawrencium are first steps away from the well-studied region of known masses towards direct mass measurements of superheavy nuclides. Further improvements of the experimental setup will pave the way to address nuclides with even lower production rates. One goal is to fix the endpoints of α-decay chains originating from superheavy nuclei that currently are not connected to the area of known nuclei. This will open up new perspectives for the identification of long-lived elements on the predicted island of stability.

References

[1] M. Block *et al.*, Eur. Phys. Jour. D 45 (2007) 39.

[2] M. Block *et al.*, Nature, in print (2010).

[3] G. Münzenberg *et al.*, Nucl. Instr. Meth. 161 (1979) 65.

TRAPSPEC – Towards Isotope-Selected Decay Spectroscopy *

D. Rudolph[1], M. Block[2], F.P. Heßberger[2,3], D. Ackermann[2], L.-L. Andersson[4], M.L. Cortes[5,*], C. Droese[6], M. Dworschak[2], M. Eibach[7,8], U. Forsberg[1,*], P. Golubev[1], R. Hoischen[1,2], J. Ketelaer[7], I. Kojouharov[2], J. Khuyagbaatar[2], D. Nesterenko[2,9], H. Schaffner[2], S. Stolze[10,*], and the SHIPTRAP collaboration[1]

[1]Lund University, Sweden; [2]GSI Helmholtzzentrum, Darmstadt, Germany; [3]HIM, Mainz, Germany; [4]University of Liverpool, UK; [5]Universidad Nacional, Bogotá, Colombia; [6]Universität Greifswald, Germany; [7]Universität Mainz, Germany; [8]Universität Heidelberg, Germany; [9]PNPI, St. Petersburg, Russia; [10]University of Jyväskylä, Finland

Contemporary nuclear structure studies aim at nuclei far from the line of stability. While the neutron-rich outskirts of the chart of nuclides can only be reached by fragmentation or fission of relativistic heavy-ion beams, fusion-evaporation reactions may still compete on the neutron-deficient side, but continue to remain the only reliable way to produce superheavy elements (SHE). With production cross-sections in the regime of μb down to pb, however, preparing isotopically clean and thus unambiguous identification of decay products becomes ever more essential: Even in the focal planes of velocity and/or A/q recoil separators, the needles of interest are usually hidden in the hay stack of isobaric analogues (neutron-deficient nuclei) and/or inevitable background (SHE).

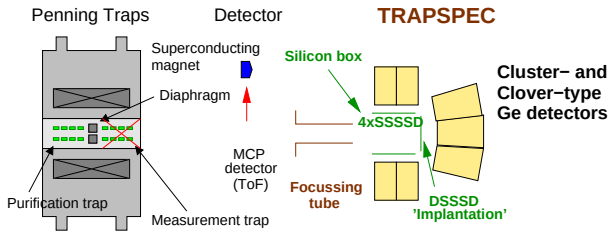

Figure 1: Schematic view of the rear section of SHIPTRAP and the TRAPSPEC extension.

Figure 1 provides a sketch of the GSI-unique opportunity for isotopically pure decay spectroscopy of exotic neutron-deficient isotopes and/or SHE. The price to pay is the efficiencies to stop and extract ions in the SHIPTRAP gas-cell [1]. Instead of invoking mass measurements with the second penning trap and the MCP time-of-flight detector at the SHIPTRAP exit, the nuclei in either ground or metastable states of interest are extracted from the purification trap with tiny kinetic energies through a focussing tube (-300 V) into a silicon box surrounded by composite germanium detectors. This 'TRAPSPEC' arrangement is basically identical to the succesfully commissioned TASISPEC set-up developed for SHE-spectroscopy behind TASCA [2, 3].

In 2009 TRAPSPEC was commissioned with the reaction ^{170}Er(^{48}Ca,5n)^{213}Ra [4]. One VEGA-Clover and one EUROBALL-Cluster Ge-detector were used in conjuction with four single-sided Si-strip box detectors (SSSSD) and one double sided Si-strip implantation detector (DSSSD). Following the unexpected experience of actually being able

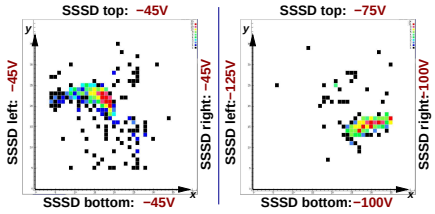

Figure 2: DSSSD position distribution of ^{213}Ra α-decays with two different sets of bias voltages on the four SSSSDs.

to steer the ^{213}Ra nuclei with the detector bias applied to the Si box detectors (Fig. 2), a transport efficiency of essentially 100 % from the nominal MCP spot onto the TRAPSPEC DSSSD was achieved. This led to the prompt α-$\gamma(\gamma)$ coincidence spectra displayed in Fig. 3, acquired within only 12 hours of parasitic beam time ($\overline{I}_{beam} \sim 30$ pnA). The spectra are in line with Ref. [4], even providing one 110-218 keV coincidence event.

Scaling roughly the numbers by taking the 130 α-γ coincidences of the 215-keV peak in Fig. 3, comprehensive decay spectroscopy on the level of some 20 nb should be straightforward with the complete TRAPSPEC set-up.

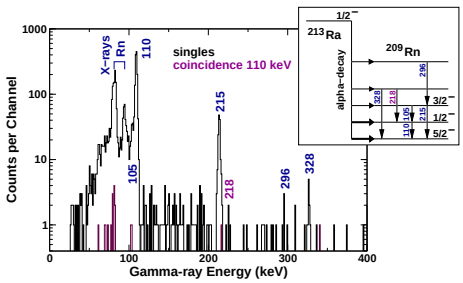

Figure 3: Gamma-ray spectra in prompt coincidence with observed ^{213}Ra α-decays. Black: Total projection. Magenta: Coincidence with the 110-keV ground-state transition in ^{209}Rn. The inset provides a simplified sketch of the decay scheme [4].

References

[1] J.B. Neumayr *et al.*, Nucl. Instr. Meth. B **244**, 489 (2006).

[2] L.-L. Andersson *et al.*, GSI Scientific Report 2008, p. 142; ibid, 2009.

[3] L.-L. Andersson *et al.*, submitted to Nucl. Instr. Meth. A.

[4] P. Kuusiniemi *et al.*, Eur. Phys. J. A **30**, 551 (2006).

* Supported by the 2009 GSI Summer Student Program.

TASISpec – Heading towards its first experiment.

L.-L. Andersson[1], D. Rudolph[2], D. Ackermann[3], Ch.E. Düllmann[3], K. Eberhardt[4], J. Even[4], U. Forsberg[2], J. Gellanki[2], J. Gerl[3], P. Golubev[2], R. Hoischen[2,3], R.-D. Herzberg[1], F.P. Heßberger[3], E. Jäger[3], J. Khuyagbaatar[3], I. Kojouharov[3], J.V. Kratz[4], J. Krier[3], N. Kurz[3], E. Merchán[3], W. Prokopowicz[3], M. Schädel[3], H. Schaffner[3], B. Schausten[3], E. Schimpf[3], A. Semchenkov[5,6], A. Türler[5,7], H.-J. Wollersheim[3], A. Yakushev[5], and P. Thörle-Pospiech[4]

[1]University of Liverpool, Oliver Lodge Laboratory, Liverpool L69 7ZE, United Kingdom; [2]Department of Physics, Lund University, S-22100 Lund, Sweden; [3]GSI Helmholtzzentrum für Schwerionenforschung GmbH, D-64291 Darmstadt, Germany; [4]Universität Mainz, D-55128 Mainz, Germany; [5]Technische Universität München, D-85748 Garching, Germany; [6]University of Oslo, 0315 Oslo, Norway; [7]Paul Scherrer Institute, 5232 Villigen, Switzerland

TASISpec (*TA*sca *S*mall *I*mage mode *Spec*troscopy) [1, 2] is a Si and Ge detector setup optimised for particle-γ-X-ray coincidence spectroscopy of superheavy elements in conjunction with the TASCA separator [3]. The detection system consists of 192 Si strips distributed over one double sided silicon strip detector (DSSSD) and four single sided silicon strip detectors (SSSSD). The DSSSD is the focal plane detector into which the residual nuclei are implanted and their subsequent decay products such as fission fragments or α particles are detected. The SSSSDs form a "box" upstream from the DSSSD and they are used to detect α particles which have escaped detection in the DSSSD, conversion electrons (CE) and possibly the second fission fragment. A seven-crystal Ge cluster detector is mounted directly behind the DSSSD and four clover detectors are mounted behind the four SSSSDs. The complete setup is thus composed of a total of 23 Ge crystals.

The setup is constructed to enable multi-coincidence spectroscopy such as α-γ-CE and α-γ-γ with unprecedented γ-ray efficiency and thus reveal essential information necessary to build reliable level schemes for superheavy elements.

During 2009 a thorough evaluation of the commissioning experiments was performed [2]. This involved amongst others detection efficiencies and implant-decay correlation times. As an example, the decay of ^{253}No has been explored. The half life of the ground state was previously determined to $T_{1/2} = 1.56(2)$ min [4]. In the present analysis the half life is determined to $T_{1/2} = 1.61(21)$ min where the uncertainty originates mainly from the small number of α particles, which could be included in the analysis. In Fig. 1 the DSSSD hitpattern is shown. It shows the pixels in which the 8.0 MeV α particles relating to the decay of the ground state of ^{253}No were detected. As can be seen in this figure the implants are nicely focused into a very narrow spot. Since the half life of ^{253}No is rather long the pixels in the very centre of the focal spot where the implantation rates are at its highest, were excluded when determining the half life. This minimises the risk of random correlations between the incoming evaporation residues and the α particles.

In a commissioning run in July 2009 was the reaction ^{208}Pb(^{48}Ca,$1n$)^{255}No applied to explore the benefits gained from the usage of pulse-shape electronics. Pulse shape analysis could yield particle identification due to distinct ionisation schemes in the semiconductor material for different incidenting particles, like e.g. α particles and CE.

In the beginning of 2009 TASISpec was granted beamtime for its first main beam experiment. The experiment is scheduled for spring 2010 and will aim to explore K-isomers in ^{253}No in detail.

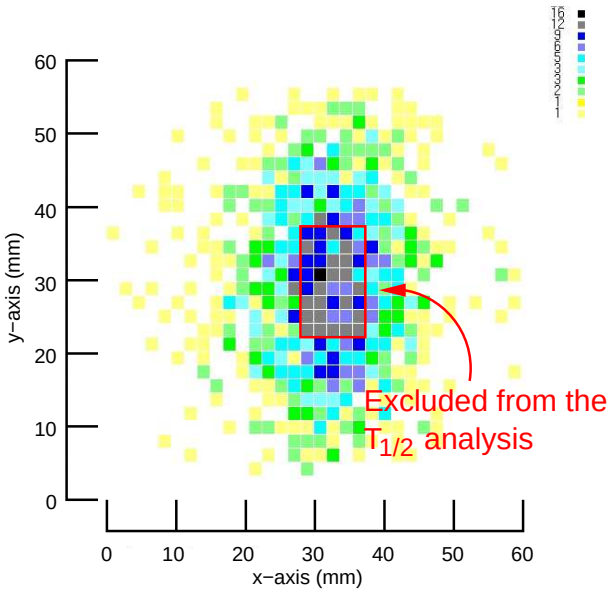

Figure 1: The position of the detected ^{253}No correlated alpha particles in the DSSSD. On the x and y-axis the size of the DSSSD is indicated.

References

[1] L. -L. Andersson *et al.* GSI Scientific report 2008. `http://www-wnt.gsi.de/kernchemie/images/PDF_2008/NUSTAR-SHE-11.pdf`

[2] L. -L. Andersson *et al.*, submitted to Nucl. Instrum. Meth.

[3] A. Semchenkov *et al.*, Nucl. Instrum. Meth. Phys. Res. B **266**, 4153 (2008).

[4] R.-D. Herzberg *et al.*, Eur. Phys. J. A (2009).

A new TASCA focal plane detector setup and DAQ system*

A. Gorshkov[1#], J.M. Gates[1,2], R. Graeger[1], A. Türler[1†], A. Yakushev[1], D. Ackermann[2], W. Brüchle[2], Ch.E. Düllmann[2], H.G. Essel[2], E. Jäger[2], J. Khuyagbaatar[2], I. Kojouharov[2], J. Krier[2], N. Kurz[2], M. Schädel[2], B. Schausten[2], E. Schimpf[2], J. Dvorak[3,4], L.-L. Andersson[5], D. Rudolph[6], M. Wegrzecki[7]

[1]TU Munich, Garching, Germany; [2]GSI, Darmstadt, Germany; [3]LBNL, Berkeley, CA, U.S.A; [4]University of California, Berkeley, CA, U.S.A.; [5]University of Liverpool, UK; [6]University of Lund, Sweden; [7]ITE, Warsaw, Poland

During the TASCA commissioning phase competitive tests of two types of focal plane detectors for TASCA – a Position Sensitive Silicon Stripe Detector (PSSSD) and a Double Sided Silicon Strip Detector (DSSSD) - have been performed. The DSSSD proved to be more reliable and more sensitive for the detection of decay chains due to the high granularity of the DSSSD; moreover the position resolution of the DSSSD is independent of implantation position and deposited energy [1, 2]. The new TASCA focal plane detector setup consists of a Multi Wire Proportional Counter (MWPC) and a Focal Plane Detector Box (FPDB). The implantation detector of the FPDB consists of two side-by-side mounted 300 μm-thick DSSSDs with an active size of 72x48 mm^2 each mounted on a PCB frame. Eight 500 μm-thick Single Sided Silicon Strip Detectors (SSSSD) of the same size form a backward array – a four-sided box with an open side of 144x48 mm^2 and a depth of 72 mm (Fig. 1) [3]. The DSSSD comprises 144 vertical strips on the front side and 48 horizontal strips on the back side, each with 1 mm pitch size. Spectrometric signals are read out from the front and back sides. They provide implantation and decay energies and (x,y) coordinates with a position resolution of 1 mm. While the registration efficiency from the back side is almost 100%, the one from the front side is about 90% due to a gap of 100 μm between the strips. Each SSSSD has 8 strips with an active area 5.7x72 mm^2 without position resolution. The energy resolution in the DSSSD was ≤25 keV (FWHM) for 8.1 MeV α-particles measured with implanted ^{254}No depositing their full energy in the DSSSD and 170 keV for reconstructed α-particles that deposited a fraction of their energy inside the DSSSD and the remainder in the SSSSD. The average detection efficiency of the FPDB for α-particles emitted from a nucleus implanted in the active area of the DSSSD is 72%. Two additional SSSSDs are mounted behind the implantation detector and serve as a punch-through veto detector for light fast ions. The punch-through detector together with the MWPC serves for discriminating between ions recoiling from the target, radioactive decays of implanted species, and fast light ions. A cluster Ge-detector consisting of seven crystals was installed ~30 mm behind the FPDB for γ-ray measurements in coincidence with α- or SF decays.

In total 640 spectrometric channels (320 for the α-particle branch and 320 for the SF branch) are required to readout the FPDB. To minimize the total number of ADC channels, 8-channel dual-range amplifiers with integrated multiplexers were built. 40 analog output signals from the α-particle branch and 40 ones from the SF branch are connected to inputs of three V785 32-channel peak sensing ADCs (CAEN). 40 digital 3-bit outputs from the amplifiers with address codes of the fired strips are stored in four SIS 3820-3600 32-channel I/O VME registers (Struck GmbH). Analog signals from Ge-detectors are digitized in the SIS 3302 8-channel 100 MS/s 16-bit flash ADC (Struck GmbH). The amplifiers have a logical trigger output with adjustable discriminator level. All trigger outputs from the amplifiers are collected by "OR" in a CAMAC Common Trigger module. When a processed common trigger signal is accepted by a VME trigger module TRIVA5, the amplitudes of all fired ADC channels, the status of all registers, and time stamps are read out by a RIO4 (CES) frontend VME controller using the MBS software package. The total readout dead time was about 50 μs; a shorter dead time of ~30 μs was measured without Ge-detectors reading. Visualization as well as on-line and off-line analysis was performed using the software package GO4 [4].

The new detector setup and new DAQ system have been successfully used during the experiment on the synthesis of element 114 performed at TASCA in 2009 [5].

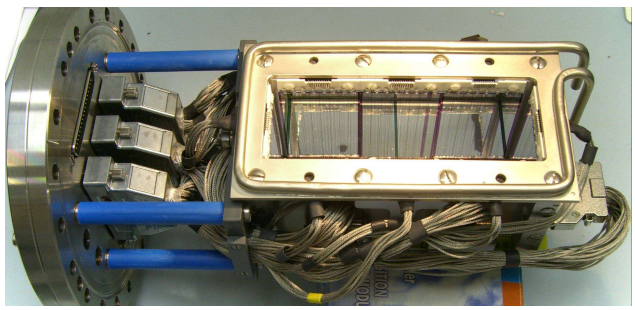

Figure 1: The new DSSSD-based TASCA FPDB.

References

[1] A. Gorshkov et al., GSI Sci. Rep. 2008, p. 140,
[2] A. Gorshkov et al., Phys. Rev. C, to be submitted.
[3] A. Gorskov et al., NIM A, to be submitted.
[4] H.G. Essel et al., GSI Sci. Report 2009, p. ???
[5] Ch.E. Düllmann et al., GSI Sci. Report 2009, p. ???

* Work supported by the BMBF (06MT247I, 06MT248); the GSI-F&E (MT/TÜR).

†Current address: Bern University & PSI Villigen, Switzerland
#alexander.gorshkov@radiochemie.de

COMPACT Coupled to TASCA for Element 114 Chemistry*

A. Yakushev[1#], J.M. Gates[1,2], A. Gorshkov[1], R. Graeger[1], A. Türler[1†], D. Ackermann[2], M. Block[2], W. Brüchle[2], Ch.E. Düllmann[2,3], H.G. Essel[2], F.P. Heßberger[2,3], A. Hübner[2], E. Jäger[2], J. Khuyagbaatar[2], B. Kindler[2], J. Krier[2], N. Kurz[2], B. Lommel[2], M. Schädel[2], B. Schausten[2], E. Schimpf[2], K. Eberhardt[4], M. Eibach[4], J. Even[4], D. Hild[4], J.V. Kratz[4], L.J. Niewisch[4], J. Runke[4], P. Töhrle-Pospiech[4], N. Wiehl[4], J. Dvorak[5,6], H. Nitsche[5,6], J.P Omtvedt[7], A. Semchenkov[7], U. Forsberg[8], D. Rudolph[8], J. Uusitalo[9], L.-L. Andersson[10], R.-D. Herzberg[10], E. Parr[10], Z. Qin[11], M. Wegrzecki[12]

[1]TU Munich, Garching, Germany; [2]GSI, Darmstadt, Germany; [3]Helmholtz Institute Mainz, Germany; [4]University of Mainz, Germany; [5]LBNL, Berkeley, CA, U.S.A; [6]University of California, Berkeley, CA, U.S.A.; [7]University of Oslo, Norway; [8]Lund University, Sweden; [9]University of Jyväskylä, Finland; [10]University of Liverpool, UK; [11]IMP, Lanzhou, P.R. China, [12]ITE, Warsaw, Poland

The unambiguous identification of new superheavy elements (SHE) is a very difficult task for both, physicists and chemists due to very low production rates, absence of a link to known isotopes, and unknown chemical, and decay properties. Chemical studies of SHE are of great importance because they can identify the proton number of the studied isotopes. Coupling of chemistry setups to physical recoil separators allows chemical experiments with extremely high sensitivity due to a strong suppression of unwanted byproducts in the preseparator [1]. At GSI, the new gas-filled separator TASCA has been put into operation in 2008. It is designed specifically for chemical studies of transactinides produced in nuclear fusion reactions of ^{48}Ca beams with actinide targets [2].

The highest cross section for SHE formation was observed in the reaction ^{48}Ca+^{244}Pu [3,4] leading to element 114 (E114). First attempts to chemically identify E114 were performed by a PSI-FLNR-LLNL collaboration in Dubna, and an unexpectedly low adsorption enthalpy of element 114 on gold was reported [5], in contradiction with theoretical predictions of the trend in the binding energy, E_b, Pb>>E114>Hg>E112 [6]. These studies were performed without preseparation, and the relatively high counting rate from unwanted byproducts led to controversially discussed results. An attempt to observe E114 in the chemistry experiment after preseparation failed [7].

A chemistry experiment with E114 was carried out at TASCA in 2009. Because the lifetimes of even the longest-lived E114 isotopes, ^{288,289}114, are short [4], TASCA was operated in the Small Image Mode (SIM) [2], which focuses fusion products into a small area of about ~30x40 mm^2. The lower transmission efficiency of SIM (~35%) compared to HTM (~60%) is compensated by the smaller volume of the Recoil Transfer Chamber (RTC), which allows a faster transport of products to a detection setup. During the experiment on the synthesis of ^{288,289}114 [4], the operation of TASCA in SIM was successfully tested with a focal plane detector. A beam dose of $0.98 \cdot 10^{18}$ ^{48}Ca ions at E*(^{292}114)=42 MeV was acquired and two ^{288}114 decay chains were observed. In the preparation of the experiment two RTCs made of Teflon™ were tested: a "small" one with a volume of 14 cm^3 and a "large" one with 29 cm^3. Transport times and yields to COMPACT [8] were optimized for both chambers with short-lived Hg and Pb isotopes produced with ^{40}Ar and ^{48}Ca beams. Transport times of 0.6 s and 0.8 s were measured at a gas flow rate 1.3 l/min for the "small" and "large" RTC, respectively. Three different He/Ar gas mixtures with ratios of 30:70, 50:50, and 70:30 were explored. The last one was selected for the E114 chemistry experiment. Two similar COMPACT detectors connected in series were used; each detector consisted of 32 pairs of 1x1 cm^2 PIN diodes covered with a 35-nm thick gold layer. The first detector, kept at the room temperature, was connected directly to the RTC exit via a 2-cm long Teflon™ tube. The second detector, connected via a 30-cm long Teflon™ capillary, was placed downstream of the first one; a temperature gradient from +20 to −162 °C was applied along it. The use of two detectors in series allows detecting species in a wide range of volatilities – from the non-volatile Pb to the noble gas Rn (Fig. 1). With this setup the adsorption enthalpy of short-lived ^{288,289}114 on gold was measured with relatively high efficiency under background-free conditions. The data are under evaluation.

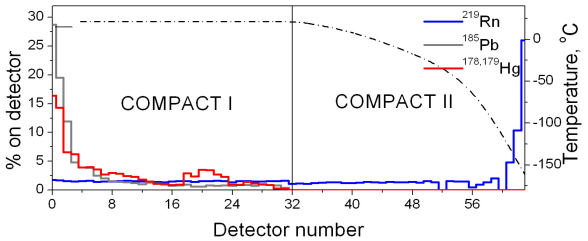

Figure1:Pb, Hg and Rn distributions in COMPACT.

References

[1] Ch. E. Düllmann, Eur. Phys. J. D **45**, 75 (2007).
[2] A. Semchenkov et al. NIM B **266**, 4153 (2008).
[3] Yu. Oganessian, J. Phys. G **34**, R165 (2007).
[4] Ch. E. Düllmann et al. This report, p.???(2010).
[5] R. Eichler et al. Radiochim. Acta, accepted (2009).
[6] V. Pershina et al. J. Chem. Phys. **131**, 084713 (2009).
[7] D. Wittwer et al. Nucl. Instr. Meth. B **268,** 28 (2010).
[8] J. Dvorak et al. Phys. Rev. Lett. **97,** 242501 (2006).

* Work supported by the BMBF (06MT247I, 06MT248); the GSI-F&E (MT/TÜR).

†Current address: Bern University & PSI Villigen, Switzerland
#alexander.yakushev@radiochemie.de

Pilot-Test Experiment with Os of a SISAK Setup for Hs-Chemistry Studies

F. Samadani[1], J. Alstad[1], F. Schulz[1], J. Nilssen[1], J.P. Omtvedt[1], H.B. Ottesen[1], S. Qureshi[1], Ch.E. Düllmann[2], J.M. Gates[2], E. Jäger[2], J. Khuyagbaatar[2], J. Krier[2],M. Schädel[2], B. Schausten[2], K. Eberhardt[3], J. Even[3], D. Hild[3], J.V. Kratz[3], Ch. Roth[3], N. Wiehl[3], A. Türler[4], A. Yakushev[4]

[1]University of Oslo, Norway, [2]GSI, Darmstadt, Germany, [3]Johannes Gutenberg-University of Mainz, Germany, [4]TU Munich, Garching, Germany

A liquid-liquid extraction system for investigating chemical properties of element 108, hassium, was developed [1] using γ-emitting ^{181}Os produced at the Oslo Cyclotron Laboratory (OCL). The system is targeted for the fast solvent extraction system SISAK [2] and based on OsO_4 reacting with NaOH. Such an experiment would be the first attempt to study Hs in the liquid phase. Successful Rf and Db experiments [3-5] performed at LBNL in Berkeley indicate that SISAK with its liquid scintillation detectors is sensitive enough to detect Hs, even though the Hs cross section is ~3 orders of magnitude lower.

The first investigation of the reaction between HsO_4 and NaOH was performed in a gas phase experiment [6]. The interaction of HsO_4 appeared somewhat weaker with NaOH than that of OsO_4, in fair agreement with theoretical predictions [7]. The liquid-liquid extraction Hs-experiment proposed in the work presented here is based on results from this gas-phase experiment. In aqueous solution, it is assumed [1] that the reactions occurring are:

$$OsO_4(aq) + NaOH(aq) \leftrightarrow Na[OsO_4(OH)](aq) \quad (1)$$

$$Na[OsO_4(OH)] + NaOH \leftrightarrow Na_2[OsO_4(OH)_2] \quad (2)$$

$$OsO_4(aq) \rightarrow OsO_4(org) \quad (3)$$

The distribution ratio between NaOH solution and toluene, which was selected as organic phase because it is also suitable as solvent for the liquid scintillation detection used by SISAK, is given by:

$$D = \frac{[OsO_4]_{org}}{[OsO_4]_{aq} + [OsO_4(OH)]^- + [OsO_4(OH)_2]^{2-}} \quad (4)$$

which can be rewritten as:

$$D = \frac{K_D}{1 + K_1[OH^-] + K_1K_2[OH^-]^2} \quad (5)$$

where K_1, K_2 and K_D are equilibrium constants for reactions (1), (2), and (3), respectively. Experiments were performed in Oslo, utilizing manual extractions and SISAK on-line measurements to carefully study the behavior of Os in this chemical system, see Samadani et al. [1] for details. The results are summarized in Fig. 1.

Based on the results from Oslo a "proof-of-principle" experiment with α-decaying Os isotopes was performed at GSI: the full SISAK setup [8], as it would be used for a Hs experiment with double α-detector arrays to simultaneously measure both phases (for the aqueous phase done indirectly, after a second extraction step) was set up and tested. $^{40}Ar^{11+}$ ions from the UNILAC irradiated a ^{nat}Ce target in the gas-filled separator TASCA (TransActinide Separator and Chemistry Apparatus) producing $^{172-175}$Os.

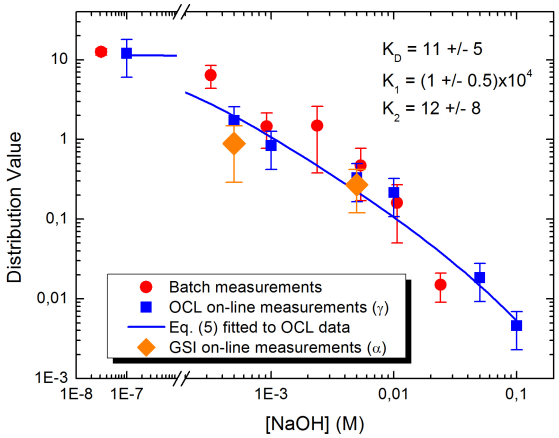

Figure 1: Comparison of data from OCL and GSI, together with fit of eq. (5) to OCL data.

In the separator focal plane a Recoil Transfer Chamber (RTC) was mounted. It was flushed with a He/O_2 gas mixture, which passed an oven (run at 600°C) mounted at the exit of the RTC to ensure fast and complete oxidation of Os. The volatile osmium tetroxide was transported to SISAK by the He/O_2 gas and dissolved in NaOH solution. After extraction into toluene the α-activity was measured in on-line flow cells by liquid scintillation detection. This was the first SISAK experiment behind TASCA. Results from this run using α-decaying ^{172}Os agree well with those of γ-measurements obtained in Oslo, as shown in Fig. 1. This successful experiment proved that the system is suitable for studying Hs.

References

[1] F. Samadani et al., "Development of a SISAK extraction system for chemical studies of element 108, hassium", submitted to Radiochim. Acta.

[2] J.P. Omtvedt et al., J. Alloy Comp. **271-273**, 303 (1998).

[3] J.P. Omtvedt et al., Journ. Nucl. Radiochem. Sciences, **3**, 121 (2002).

[4] L. Stavsetra et al., Nucl. Instrum. Method Phys. Res. Sect. A, **543**, 509 (2005).

[5] J.P. Omtvedt et al. "Detection of ^{258}Db with the SISAK Liquid Scintillation Detection System", manuscript in preparation for Radiochim. Acta.

[6] A. von Zweidorf et al., Radiochim. Acta, **92**, 855 (2004).

[7] V. Pershina, Radiochim. Acta, **93**, 373-376 (2005).

[8] J.P Omtvedt, et al., Eur. Phys. J. D, **45**, 91 (2007).

Theoretical Investigations of Trends in Volatility of the Heaviest Elements

V. Pershina[1], A. Borschevsky[2], J. Anton[3], and T. Jacob[3]
[1]GSI, Darmstadt, Germany; [2]School of Chemistry, Tel Aviv University, Israel; [3]Institut für Elektrochemie, Universität Ulm, Germany

Elements 112 through 118 are expected to be very volatile. Early extrapolations of the sublimation enthalpies, $\Delta H_{sub}=\Delta H_f(g)$, of the solid state in groups 12 through 17 have indeed shown the lowest ΔH_{sub} for the heaviest elements in each group of the elements, respectively [1,2]. (The gas-phase chemistry experiments give ΔH_{sub} as a measure of volatility of an element using measured ΔH_{ads} on metal surfaces and an assumed linear correlation between these values [3]). The reason for the high volatility is strong relativistic effects on the valence electrons of these elements.

It was also recognized that linear extrapolations of properties within the chemical groups should be made cautiously due to increasing (non-linearly with Z) relativistic effects. Thus, relativistic calculations are nowadays a must for reliable predictions of properties of the heaviest elements. Since ΔH_{sub} should be related to the interaction energy of an atom with itself, we have performed a systematic calculations of the M-M dissociation energies (D_e) for the entire 6p and 7p rows of the elements and compared them with the known values of $D_e(M_2)$ and ΔH_{sub} in groups 13 through 18.

For the calculations of the electronic structures of M_2 (M = Hg/112, Tl/113, Pb/114, Bi/115, Po/116, At/117, Rn/118), we have used our 4*c*-DFT method [4] proven to be a reliable tool in predicting binding energies and bond lengths. Very large optimized basis sets were used including 5g virtual atomic orbitals. Results of the calculations are summarized in Table 1.

Table 1. Optimized bond lengths R_e (in Å) and dissociation energies D_e (in eV) in M_2 (M = Tl/113 through Rn/118)

M_2	R_e	D_e	M_2	R_e	D_e
Tl_2	3.185 3.00*	0.47 0.42*	$(113)_2$	3.613	0.06
Pb_2	2.97 2.93*	1.18 1.17*;0.83*	$(114)_2$	3.49	0.13
Bi_2	2.685 2.6596*	2.23 2.05*	$(115)_2$	3.072	0.82
Po_2	2.813 -	2.15 1.94*	$(116)_2$	3.238	1.34
At_2	3.041 -	1.02 0.87±1.3*	$(117)_2$	3.524	0.77
Rn_2	-	unbound	$(118)_2$	4.498	0.012

* Experimental values; $R_e(Tl_2)$ is questionable.

Good agreement with experiment was obtained for the lighter homologs of the heaviest elements. The Rn dimer was obtained unbound, so that calculations with even larger basis sets could follow.

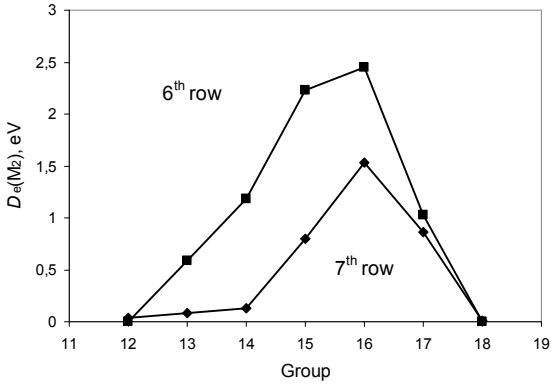

Figure 1: Calculated binding energies in group 12 through 18 homonuclear dimers.

Fig. 1 shows that $D_e[M_2]$ of the 7p elements are much smaller than $D_e[M_2]$ of the 6p homologs in groups 13 through 16. This is due to the fact that bonding in the lighter M_2 is due to the participation of both the $np_{1/2}$ and $np_{3/2}$ AOs, while the contribution of the former one is drastically diminished in the heaviest homologs (it practically forms a closed-shell). A remarkable fact is that the difference in D_e between the 6th and 7th row elements diminishes with the group number from group 15 on and gets even reversed in group 18: thus, element 118 is stronger bound to itself than Rn.

A good correlation between $D_e(M_2)$ and $\Delta H_f(g)$ was found for groups 13 through 17. On their basis, the following ΔH_{sub} for the heaviest elements were obtained: 145 kJ/mol for element 113, 70 kJ/mol for element 114, 164 kJ/mol for element 115, 101 kJ/mol for element 116, and 92 kJ/mol for element 117. These values are close to those obtained via linear extrapolations of $\Delta H_f(g)$ in the groups [1,2]. Extensive cluster calculations should be performed to confirm the predicted values.

References

[1] O.L. Keller *et al*. J. Phys. Chem. 74, 1127 (1970); *ibid*, 78 (1974) 1945.
[2] B. Eichler, Kernenergie, 10 (1976) 307.
[3] B. Eichler, R. Eichler, In: "The Chemistry of Superheavy Elements", Kluwer, 2003, Ed. M. Schädel, p. 205.
[4] J. Anton, B. Fricke, E. Engel, Phys. Rev. A, 69 (2004) 012505.
[5] H. Rossbach and B. Eichler, Akademie der Wissenschaft der DDR, Report No. ZFK-527, 1984.

Theoretical Investigations of Trends in Adsorption of the Heaviest Elements on Gold

V. Pershina[1], A. Borschevsky[2], J. Anton[3], and T. Jacob[3]
[1]GSI, Darmstadt, Germany; [2]School of Chemistry, Tel Aviv University, Israel; [3]Institut für Elektrochemie, Universität Ulm, Germany

Elements 112 through 118 are expected to be very volatile due to strong relativistic effects on their valence electrons. Their volatility is to be studied via the gas-phase thermochromatography technique by measuring the adsorption enthalpy, ΔH_{ads}, on gold plated detectors located along the chromatography column (see results for elements 112 and 114 [1,2]). The obtained ΔH_{ads} is then related to the sublimation enthalpy, ΔH_{sub}, of macroamounts using a linear correlation between these values [1].

Results of our extended cluster calculations [3] have shown that ΔH_{ads} of group 12 and 14 atoms M adsorbed on gold surface can reliably be predicted on the basis of knowledge of binding energies (D_e) of gold dimers, MAu: the difference in D_e(M-Au$_n$), where $1 \le n \le 120$, between the adatoms M is kept almost constant independently of the gold cluster size and adsorption position. Accordingly, in this work, we try to estimate ΔH_{ads} of the 7p elements and their 6p homologs, as well as trends in the chemical rows, on the basis of the calculated D_e(MAu), where M = Tl/113, Pb/114, Bi/115, Po/116, At/117, Rn/118.

The calculations were performed with the use of our fully relativistic 4*c*-DFT method [4] proven to be a reliable tool in predicting binding energies and bond lengths. Very large optimized basis sets including 5g virtual AOs were used. Results of the calculations of the bond lengths (R_e) and D_e are summarized in Table 1.

Table 1. Optimized bond lengths R_e (in Å) and dissociation energies D_e (in eV) in MAu (M = Hg/112 through Rn/118)

MAu	R_e	D_e	MAu	R_e	D_e
HgAu	2.67	0.06	112Au	2.73	0.51
TlAu	2.668	2.72	113Au	2.716	1.83
PbAu	2.64	2.15	114Au	2.88	0.73
BiAu	2.638	2.43	115Au	2.892	2.44
PoAu	2.631	2.29	116Au	2.867	2.17
AtAu	2.644	1.97	117Au	2.835	1.87
RnAu	3.023	0.23	118Au	3.003	0.66

The calculated D_e are depicted in Fig. 1 together with the measured $-\Delta H_{ads}$ of Hg, Tl and Pb on gold; $-\Delta H_{ads}$ of element 112 (measured [1]) and 4*c*-DFT predicted for elements 113 and 114 [3]; as well as the calculated $-\Delta H_{ads}$ for Hg through Po and for elements 112 through 116 using semi-empirical models [5]. The obtained D_e(MAu) indicate that there should be no decrease in the binding energies with gold from Bi to element 115, and a very little decrease from Po and At to elements 116 and 117, respectively. Moreover, the trend in D_e gets reversed for RnAu and 118Au, in line with the expected higher reactivity of element 118 in comparison with Rn. Thus, taking into account our experience for groups 12 - 14 [3], one can expect that $-\Delta H_{ads}$ of Bi through Rn and elements 115 through 118 should follow the trends found for the D_e(MAu) of these elements (Fig. 1).

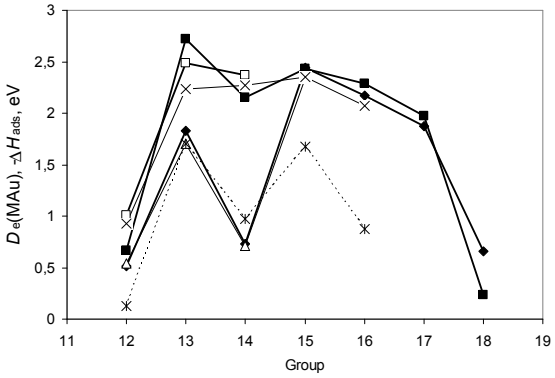

Figure 1: Binding energies: filled squares – calculated here D_e(MAu) (M = Hg through Rn), and filled rhomboids – D_e(MAu) (M = elements 112 through 118); open squares – measured $-\Delta H_{ads}$ of Hg, Tl and Pb on gold; open triangles - $-\Delta H_{ads}$ of element 112 (measured [1]) and elements 113 and 114 (4*c*-DFT predicted [3]); crosses – calculated $-\Delta H_{ads}$ for Hg through Po, and stars – for elements 112 through 116 [5].

The expected high $-\Delta H_{ads}$ of elements 115 through 117 are in contrast with the results of the semi-empirical calculations [5]: the latter show a decrease in $-\Delta H_{ads}$ from the 6p to 7p elements in groups 15 – 17, similar to that in groups 13 and 14. The present results also mean that the linear correlation between $-\Delta H_{ads}$ and ΔH_{sub} used in [1] is questionable: the estimated (via a linear extrapolation in the groups) ΔH_{sub} of elements 115 - 117 [6] are much smaller than ΔH_{sub} of Bi through At. Extensive cluster calculations are needed to confirm these conclusions.

References

[1] R. Eichler, *et al*. Nature, Letters, 447 (2007) 72.
[2] A. Yakushev, Presentation at the 7th Workshop on the Chemistry of the Heaviest Elements, Mainz, 2009.
[3] V. Pershina, J. Anton, T. Jacob, J. Chem. Phys. 131 (2009) 084713.
[4] J. Anton, *et al.,* Phys. Rev. A, 69 (2004) 012505.
[5] H. Rossbach and B. Eichler, Akademie der Wissenschaft der DDR, Report No. ZFK-527, 1984.
[6] B. Eichler, Kernenergie, 10 (1976) 307.

Theoretical Investigations of Chemical Reactivity of Element 113

J. Anton[1], V. Pershina[2] and T. Jacob[1]
[1]Institut für Elektrochemie, Universität Ulm, Germany; [2]GSI, Darmstadt, Germany

The heaviest element identified chemically is Z=112. Using the gas-phase thermochromatography technique, its volatility, i.e., the adsorption enthalpy, ΔH_{ads}, on gold plated detectors located along the chromatography column was investigated and compared to that of Hg [1]. Very recently, results of the first chemical studies on element 114 using the same technique were reported [2,3]. Both elements, 112 and 114, were shown to be very volatile which is explained by their closed, $7s^2 6d^{10}$, and quasi-closed, $7s^2 7p_{1/2}^2$, shells, respectively. Element 113 (having the $7s^2 7p_{1/2}$ ground state) is to be studied next. It is expected to be also volatile and relatively inert, though less than 112 and 114, due to the relativistic stabilization of the 7s and $7p_{1/2}$ electrons. Feasibility experiments have already been conducted for its lighter homolog, Tl [4]

Earlier, we have predicted ΔH_{ads} of elements 112 and 114 on inert and gold surfaces by performing 4*c*-DFT calculations for the atoms adsorbed on very large gold clusters [5]. We have also predicted ΔH_{ads} of element 113 on inert surfaces using result of accurate *ab initio* Dirac-Coulomb atomic calculations [6]. It was shown that element 113 should be well transported through the Teflon capillaries from the target chamber to the chemistry setup.

In this work, we study reactivity of element 113 and Tl on the basis of the calculations for their M_2 and MAu dimers: it was shown that binding energies in MAu are directly related to ΔH_{ads} of M on gold [5]. In addition, we study the stability of hydroxides that can be formed in the oxygen atmosphere over the gold surface.

For the calculations, we have used our 4*c*-DFT method [7]. Very large optimized basis sets were used. Results of the calculations for M_2, MAu and MOH (M = Tl and element 113) are given in Table 1 [9].

Table 1. Optimized bond lengths R_e (in Å), dissociation energies D_e (in eV) and vibrational frequencies w_e (in cm^{-1}) for M_2, MAu and MOH (M = Tl and element 113)

Molecule	R_e	D_e	w_e
Tl_2	3.185	0.479	67
$(113)_2$	3.613	0.058	25
TlAu	2.668	2.669	141
113Au	2.716	1.825	144
TlOH	2.176	3.680[a]	547
113OH	2.282	2.424[a]	519

[a] with respect to the MOH = M + OH decomposition

The potential energy curves for TlAu and 113Au are shown in Fig. 1. One can see a decrease in D_e of 0.84 eV from TlAu to 113Au with a respective bond lengthening of 0.048 Å, similar to that of Tl_2 with respect to $(113)_2$ (of 0.42 eV), and that of the simple hydrides and fluorides of these elements, found in other calculations.

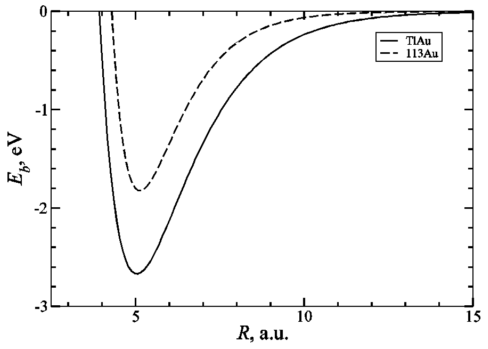

Figure 1: Calculated binding energies in TlAu and 113Au.

Using the difference in D_e between MAu and 113Au, one can estimate $-\Delta H_{ads}(113)$ on a gold surface with respect to the measured $-\Delta H_{ads}(Tl) = 240 \pm 5$ kJ/mol [4]. Thus, one can expect that element 113 will adsorb on gold at about 0.84 eV (82 kJ/mol) lower energies than Tl. This gives a preliminary value of $\Delta H_{ads}(113) = -158.6$ kJ/mol, which is very close to -164.4 kJ/mol predicted with the use of adsorption models and extrapolation of properties in group 13 [8]. According to the results, the sequence in the volatility of the heaviest elements should be 112 > 114 > 113.

The data of Table 1 also indicate that the M-OH bonds should be stronger and shorter than the M-Au ones. This explains why Tl reacts preferentially with OH and not with gold in the oxygen atmosphere. The same is expected for element 113 forming a stronger 113-OH bond than the 113-Au one. The $-\Delta H_{ads}(113OH)$ on gold is expected to be lower than $-\Delta H_{ads}(113)$.

References

[1] R. Eichler *et al.* Nature, Letters, 447 (2007) 72.
[2] R. Eichler, Abstract of the NRC7 International Conference, Budapest, 24-29 August 2008.
[3] A. Yakushev, Presentation at the 7th Workshop on the Chemistry of the Heaviest Elements, Mainz, 2009.
[4] S. König, *et al*., PSI Annual Report 2005, 2006, p. 5.
[5] V. Pershina, J. Anton, T. Jacob, J. Chem. Phys. 131 (2009) 084713.
[6] V. Pershina, A. Borschevsky, E. Eliav, U. Kaldor, J. Phys. Chem. A 112 (2008) 13712.
[7] J. Anton, *et al*., Phys. Rev. A, 69 (2004) 012505.
[8] H. Rossbach and B. Eichler, Akademie der Wissenschaft der DDR, Report No. ZFK-527, 1984.
[9] V. Pershina, J. Anton, T. Jacob, Chem. Phys. Lett. 480 (2009) 157.

Electron Affinity of Element 114, with Comparison to Sn and Pb

A. Borschevsky[1], V. Pershina[2], E. Eliav[1], and U. Kaldor[1]
[1] School of Chemistry, Tel Aviv University, Israel; [2] GSI, Darmstadt, Germany

Knowledge of the electronic structure and properties of element 114 is important for its chemical identification. By comparing its behaviour with that of the lighter group 14 homologues, its position in the periodic table can be confirmed.

In this work, we investigate the electron affinity (EA) of element 114, together with its lighter homologues in group 14, Sn and Pb [1]. Electron affinity is important for calculations of chemical potential, μ, and electronegativity, χ, which, in turn, reflect chemical reactivity of the element under study.

The calculations were performed in the framework of the projected Dirac-Coulomb-Breit Hamiltonian,

$$H_{DCB} = \sum_i h_D + \sum_{i<j} (1/r_{ij} + B_{ij}), \quad (1)$$

where

$$h_D = c\vec{\alpha}\cdot\vec{p} + \beta c^2 + V_{nuc}\,. \quad (2)$$

Here, V_{nuc} is the nuclear attraction operator, and α and β are the four-dimensional Dirac matrices. The nuclear potential, V_{nuc}, takes into account the finite size of the nucleus, modelled as a uniformly charged sphere. The two electron terms include the nonrelativistic electron repulsion and the Breit term, B_{ij}, and are correct to the second order in the fine structure constant.

Electron correlation is taken into account using the Fock space (FS) [2] and mixed sector intermediate Hamiltonian (MSIH) [3] coupled cluster (CC) methods, which are considered to be one of the most powerful tools in quantum chemistry.

Two types of the basis sets were used in the calculations, that of Faegri [4] and the even tempered universal basis set of Malli *et al*. [5]. For each of the elements under study, both types of the basis sets were extended to convergence. The size of the model spaces used was gradually increased in order to obtain convergence of the results.

The calculated electron affinities of Sn and Pb are shown and compared with experiment [6] in Table 1.

Table 1. Electron affinities of Sn, Pb, and element 114 (in meV).

Method	Sn		Pb		Element 114	
	I	II	I	II	I	II
FSCC	736	735	247	245	No EA	No EA
MSIH	1085	1072	383	363	No EA	No EA
Exp. [6]	1112		364			

I- Faegri basis set; II – Malli basis set.

The FSCC EA values are about 35% too low, while the MSIH results are within 5% of the experiment. This is due to the possibility of employing large and flexible model spaces within the MSIH framework. Good agreement with experiment, as well as the very small differences between the results for the two types of the basis sets, confirm the convergence of the MSIH calculations.

The same methods were used to estimate the electron affinity of element 114. All the calculations have given negative electron affinities. Thus, the very good agreement of the MSIH EAs of Pb and Sn, and the converged exhaustive calculations for element 114, lead to the conclusion that element 114 will not bind an extra electron.

This prediction is in accord with the trend in the EAs of group 14 elements. The EAs of the group 14 elements go down monotonically, as is shown in Fig. 1. The decrease is enhanced for Pb by the relativistic destabilization of the $6p_{1/2}$ orbital. As is shown by the dashed line in Figure 1, an extrapolation of the line from Sn to Pb crosses the *x* axis well before Z=114. In fact, an even steeper decrease may be expected for element 114, which should exhibit stronger relativistic effects than Pb. This supports our prediction that no electron binding will occur in element 114.

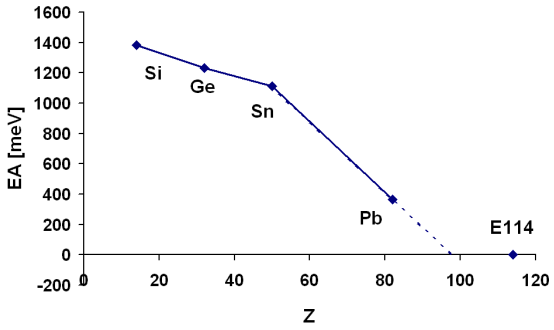

Fig. 1. Electron affinities of group 14 elements. The dashed line is an extrapolation from Sn and Pb.

References

[1] A. Borschevsky, V. Pershina, E. Eliav, and U. Kaldor. Chem. Phys. Lett. 480 (2009) 49.
[2] E. Eliav, U. Kaldor, and Y. Ishikawa, Phys. Rev. A 49 (1994) 1724.
[3] A. Landau, E. Eliav, Y. Ishikawa, and U. Kaldor, J. Chem. Phys. 121 (2004) 6634.
[4] K. Faegri, Theor. Chim. Acta 105 (2001) 252.
[5] G.L. Malli, A.B.F. Da Silva, Y. Ishikawa, Phys. Rev. A 47 (1993) 143.
[6] H. Hotop, W.C. Lineberger, J. Phys. Chem. Ref. Data 4 (1975) 539, *ibid*, 14 (1985) 731.

^{244}Pu-targets for production of element 114 at TASCA*

K. Eberhardt[1,#], J. V. Kratz[1], J. Runke[1], Ch. E. Düllmann[2], B. Lommel[2] and M. Schädel[2]
[1]Institut für Kernchemie, Johannes Gutenberg-Universität Mainz, Germany; [2]GSI, Darmstadt, Germany

Introduction

In a series of recent experiments at TASCA, production and decay as well as chemical properties of element 114 have been investigated using the ^{244}Pu(^{48}Ca,3/4n)-reaction leading to ^{288,289}114 [1,2]. Because the ^{244}Pu target material is available only in very limited amounts, the target preparation technique should give high yields. Easy and complete recovery of the target material is another prerequisite [3]. Thus, we have chosen Molecular Plating (MP) onto 2 µm thin pinhole-free titanium foils as the target preparation technique. At TASCA, a rotating target wheel is used composed of three banana-shaped target segments with an active target area of 1.44 cm^2 each. The rotating target is confined in a nearly closed container in order to protect the beam line as well as the separator against contamination in the case that a target gets destroyed.

^{244}Pu target production and characterization

For the production of one target segment by MP about 1 mg of ^{244}Pu in the form of its nitrate is dissolved in a small volume (100-200 µl) of nitric acid in a Teflon™ beaker and mixed with a surplus of isopropanol (800 µl). The mixture is then transferred into the electrochemical deposition cell (EDC) made of Teflon™ which is subsequently filled up with isobutanol to a total volume of 16 ml [4]. MP is carried out by applying a voltage of 150-200 V at a maximum current density of about 1.2 mA/cm^2. After 5-6 hours plating time, deposition yields up to 90 % are achieved. The backing foils are produced by cold rolling at GSI [5]. They should be pinhole-free and are pre-cleaned with isopropanol, 6 M hydrochloric acid and water. Prior to use, the foil integrity is checked by optical microscopy to ensure that the backing is pinhole-free. The average foil thickness is determined by weighing, whereas the homogeneity of the foil thickness is checked by α-particle energy-loss measurements. For a target backing foil with a nominal thickness of 2.2 µm deviations are in the order of ± 0.2 µm.

The target thickness is determined by two independent methods: (i) *α-particle spectroscopy*. After the deposition is completed, the target is dismounted from the EDC, dried under an infrared lamp and measured with a surface barrier α-detector at a distance of about 30 cm. (ii) The Pu-content of the solution in the EDC is determined by *Neutron Activation Analysis*. Subsequent to MP an aliquot of the supernatant solution in the EDC (1 ml) is irradiated for 2 h in the TRIGA Mainz research reactor with a thermal neutron flux of 7 x 10^{11} cm^{-2}s^{-1}. Here, 10.5 h-^{245}Pu is formed via the reaction ^{244}Pu(n,γ)^{245}Pu. The Pu content of the irradiated solution is determined by means of γ-spectrometry using the prominent γ-lines resulting from the ^{245}Pu decay at 327 keV, 308 keV, and 560 keV, respectively [3]. Table 1 comprises all ^{244}Pu-targets produced for TASCA so far.

Table 1: ^{244}Pu-targets for TASCA

Target#	Thickness [µg/cm^2]
08-395	401
08-482	502
08-485	490
08-486	390
08-487	472
09-562	673
09-594	724
09-623	790
09-624	785

The homogeneity of the Pu-layer is checked with radiography [6] using a commercial radiographic imager (FLA 7000 from FUJIFILM Corp.). Figure 1 shows a picture of a target segment. Here, the brown layer indicates the Pu-oxide deposit. Also shown is a 3-dimensional plot of the activity distribution. With this technique it could be shown that the active target area is completely covered and, in addition, that Pu is homogeneously distributed over the entire target area. From this one can conclude that variations in target thickness are in the order of about 15%.

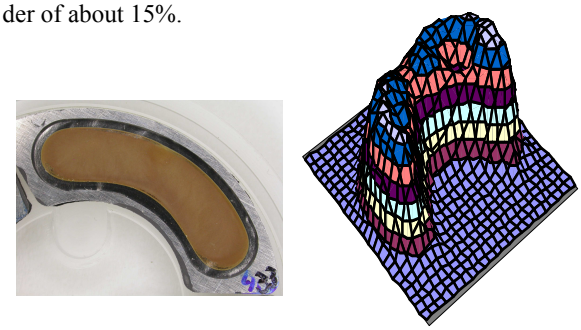

Figure 1: ^{244}Pu target segment (the brown layer indicates the Pu-oxide deposit) and corresponding plot of the activity distribution as obtained by radiographic imaging.

References

[1] Ch. E. Düllmann *et al.*, contribution to this report.
[2] A. Yakushev *et al.*, contribution to this report.
[3] J. Runke *et al.*, contribution to this report.
[4] K. Eberhardt et al., NIM A 590 (2008) 134
[5] B. Lommel et al., NIM A 590 (2008) 141
[6] D. Liebe et al., NIM A 590 (2008) 145

*Supported by the GSI F&E (MZJVKR).
#klaus.eberhardt@uni-mainz.de

Recovery of ^{244}Pu from irradiated targets for production of element 114*

J. Runke[1,#], K. Eberhardt[1], J. V. Kratz[1], Ch. E. Düllmann[2] and M. Schädel[2]
[1]Institut für Kernchemie, Johannes Gutenberg-Universität Mainz, Germany; [2]GSI, Darmstadt, Germany

The ^{244}Pu targets [1] (PuO_2 electrodeposited on Ti backing) were irradiated during recent bombardments with $^{48}Ca^{10+}$ ions to produce $^{288,\ 289}$114 [2,3]. During these bombardments with up to 3.6 x 10^{18} ions, targets and backings underwent changes that made reprocessing and production of new targets for forthcoming experiments desirable.

Figure 1: Teflon vessel.

Recovery of ^{244}Pu from one arc-shaped segment was accomplished as follows: The Al-target frame was inserted into a Teflon vessel containing a cavity into which the frame could be inserted, see Figure 1. With a sharp knife, the target was cut out of the frame, the frame was removed, and the target together with the Ti backing was dissolved in hot conc. HCl. The dissolution of the Ti backing was incomplete. The central part of the backing that had received the highest beam intensity did not dissolve. The resulting solution with the remainder of the undissolved Ti was evaporated to near dryness, transferred into a 10 ml measuring flask and filled with 8 M HCl. An aliquot of that solution was removed, evaporated to dryness, and the α-particle activity was determined. The total activity was used for yield determination. The results indicate that more than 80 % of the Pu had been recovered.

*Sponsored in the frame of a GSI R&D project (MZJVKR).
runke@uni-mainz.de

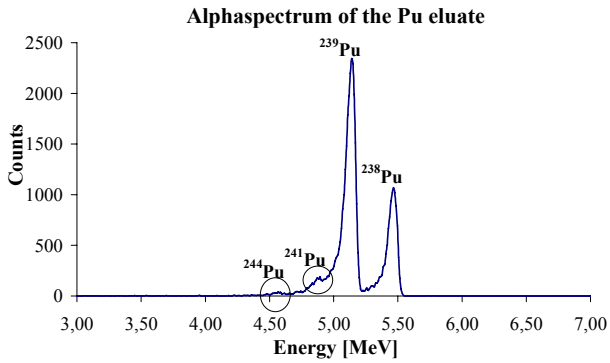

Figure 2: Alphaspectrum of the Pu eluate.

The Pu/Ti solution in 8 M HCl was transferred to a AG 1x8 anion-exchange column (3 x 50 mm), and was washed subsequently with 10 x 1 ml of 8 M HCl to remove the Ti and the ^{241}Am from the column. Then, the Pu was eluted from the column in 8 x 1 ml of 0.5 M HCl. Figure 2 shows the spectrum of α particles of an aliquot of the eluate. Due to the isotopic composition of the plutonium (97.9 % ^{244}Pu, 1.3 % ^{242}Pu, 0.7 % ^{240}Pu, < 0.1% other), the main α activities are associated with ^{238}Pu and ^{239}Pu. 100 µl of that solution was removed, filled up to 2 ml and was irradiated with thermal neutrons in the TRIGA reactor at the Institute of Nuclear Chemistry at the University of Mainz at 100 kW together with a second reference sample containing 9.62 µg ^{244}Pu for 6 h. After a decay time of 18 h, both samples were assayed for the 327.6 keV γ-activity of ^{245}Pu at a Ge detector, see Figure 3. The activation analysis showed a ^{244}Pu recovery of 89 %.

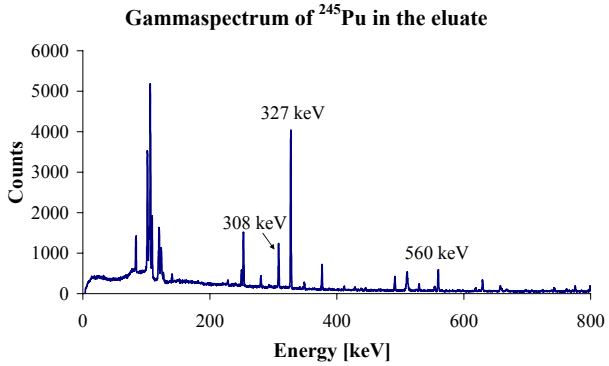

Figure 3: Gammaspectrum of ^{245}Pu solution.

References

[1] K. Eberhardt *et al.*, contribution to this report.
[2] Ch. E. Düllmann *et al.*, contribution to this report.
[3] A. Yakushev *et al.*, contribution to this report.

Investigation of New Isotopes produced with a High-Intensity Uranium Beam

J. Kurcewicz[1], S. Pietri[1], F. Farinon[1,2], H. Geissel[1,2], C. Nociforo[1], A. Prochazka[1,2], H. Weick[1], P. Allegro[3], J. Benlliure[4], G. Benzoni[5], M. Bunce[6], M. Bowry[6], P. Boutachkov[1], J.Gerl[1], M. Górska[1], A. Gottardo[7], N. Gregor[1], R. Janik[8], R. Knöbel[1], I. Kojouharov[1], T. Kubo[9], Yu. A. Litvinov[1,10], E. Merchan[1], I. Mukha[1], F. Naqvi[1,11], B. Pfeiffer[1], M. Pfützner[12], W. Plaß[2], M. Pomorski[12], Zs. Podolyak[6], P. Regan[6], B. Riese[1], M.V. Ricciardi[1], H. Schaffner[1], C. Scheidenberger[1,2], B. Sitar[8], P. Spiller[1], J. Stadlmann[1], P. Strmen[8], B. Sun[2,13], I. Szarka[8], H. Takeda[9], I. Tanihata[14], S. Terashima[9], J.J. Valiente-Dobón[7], J.S. Winfield[1], M. Winkler[1], H.-J. Wollersheim[1], Ph. Woods[15]

[1]GSI, Darmstadt, Germany; [2]JLU Giessen, Germany; [3]USP, Sao Paulo, Brazil; [4]USC, Santiago de Compostela, Spain; [5]INFN-Universita di Milano, Italy; [6]University of Surrey, Guildford, UK; [7]LNL-INFN Legnaro, Italy; [8]Comenius University, Bratislava, Slovakia; [9]RIKEN Nishina Center, Wako, Japan; [10]MPI-K, Heidelberg, Germany; [11]IKP, Köln, Germany; [12]IEP, Warsaw, Poland; [13]Beijing University, China; [14]Osaka University, Japan; [15]University of Edinburgh, UK

The experiment was performed at the SIS synchrotron of GSI Darmstadt, which delivered a 1 *A* GeV ^{238}U beam in spills lasting 0.5-2 s with a repetition period of 2–4 s. The beam impinged on a 1.6 g/cm^2 thick beryllium target placed at the entrance to the Projectile Fragment Separator (FRS) [1]. The primary beam intensity was about 2*10^9 ions/spill. The reaction products were separated by the FRS operated in the standard achromatic mode. The FRS, combining two stages of magnetic selection and an energy loss in two degraders located at the first (S1) and second (S2) focal plane, allows a full identification of reaction products with respect to their nuclear charge *Z* and mass *A*. After the first magnetic selection and the S1 degrader, reaction products are slowed down in a thick aluminium degrader located at the intermediate focal plane. A second magnetic selection is applied to the ions leaving the S2 degrader. To decrease the abundance of not-fully stripped ions, a niobium and iron foil strippers were placed behind the target and the degrader, respectively.

The time-of-flight measurement was performed between two pairs of plastic scintillator detectors, one located in the intermediate focal plane and the other one at the final focus. The typical flight time was around 160 ns.

Four TPC detectors, two placed at the intermediate and two other located at the final focal plane provided tracking information (position and angle of ions).

At the exit of the spectrometer, two ionization chambers (MUSIC) were mounted with a 104 mg/cm^2 copper strippers placed in front of each. The MUSIC detectors delivered the energy loss signal of fragments, thus providing the information about their atomic number.

The implantation point located at the final focal plane was surrounded by the RISING germanium detector setup [2] composed of fifteen Euroball cluster of seven crystals, used in 4π configuration. The isomer tagging technique was applied in order to facilitate the identification of the reaction products as seen, for example, in Figure 1.

In this experiment several *Bρ* settings of the FRS were used, which were chosen to yield optimum beam intensities for neutron rich Dy, Os, Hf, Pt and At isotopes. A preliminary identification spectrum of ions registered in the ^{226}At setting at the final focal plane of the FRS is shown in Figure 2. From the online spectra we could positively identify new isotopes in the Tl-Ra region, while having hints of new isotopes in the other regions. A more detailed analysis is ongoing.

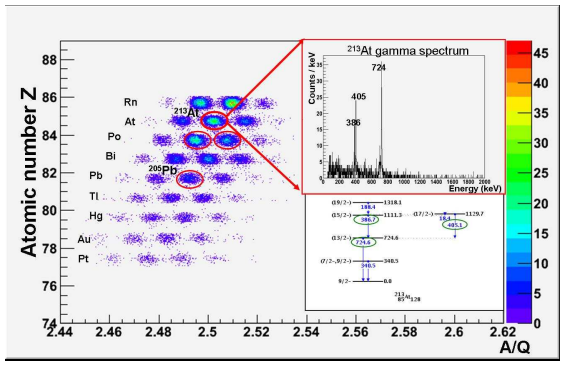

Figure 1 Identification spectrum obtained at the final focal plane (S4) of the FRS for the ^{205}Pb setting. The figure inlets show the gamma spectrum registered within 100 μs after the implantation of the ^{213}At and the decay scheme of ^{213}At.

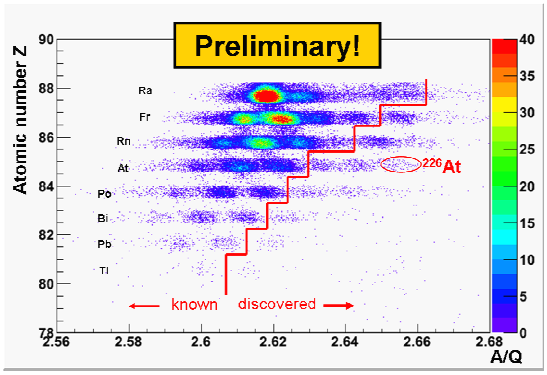

Figure 2 Preliminary identification spectrum of ions registered at the last focal plane (S4) of the separator. The FRS *Bρ* setting was optimised for ^{226}At. The red line indicates the limit of the previously observed nuclei.

References

[1] H. Geissel et al. NIM B 70, (1992) 286
[2] S. Pietri et al. NIM B 261, (2007) 1079

Spectroscopy of neutron-rich lead nuclei

G. Benzoni[1], J.J. Valiente-Dobón[2], R. Nicolini[1], A. Gottardo[2], A. Bracco[1], F.C.L. Crespi[1], F. Camera[1], A. Corsi[1], S. Leoni[1], B. Million[1], O. Wieland[1], D.R. Napoli[2], E. Sahin[2], S. Lunardi[3], R. Menegazzo[3], D. Mengoni[3,4], F. Recchia[3], P. Boutachkov[5], L. Cortes[5], C. Domingo-Prado[5], F. Farinon[5], H. Geissel[5], J. Gerl[5], N. Goel[5], M. Gorska[5], J. Grebosz[5], E. Gregor[5], T. Haberman[5], I. Kojouharov[5], N. Kurz[5], C. Nociforo[5], S. Pietri[5], A. Prochazka[5], W. Prokopowicz[5], H. Schaffner[5], A. Sharma[5], H. Weick[5], H-J. Wollersheim.[5], A.M. Bruce[6], A.M. Denis Bacelar[6], A. Algora[7], A. Gadea[7], M. Pfützner[8], Zs. Podolyak[9], N. Al-Dahan[9], N. Alkhomashi[9], M. Bowry[9], M. Bunce[9], A. Deo[9], G.F. Farrelly[9], M.W. Reed[9], P.H. Regan[9], T.P.D. Swan[9], P.M. Walker[9], K. Eppinger[10], S. Klupp[10], K. Steger[10], J. Alcantara Nuñez[11], Y. Ayyad[11], J. Benlliure[11], E. Casarejos[11], R. Janik[12], B. Sitar[12], P. Strmen[12], I. Szarka[12], M. Doncel[13], S. Mandal[14], D. Siwal[14], F. Naqvi[15,5], T. Pissulla[15], D. Rudolph[16], R. Hoischen[16,5], P.R.P. Allegro[17], R.V. Ribas[17], and Zs. Dombradi[18]

[1]Università degli Studi e INFN sezione di Milano, Milano, I; [2]INFN-LNL, Legnaro (Pd), I; [3]Università di Padova e INFN sezione di Padova, Padova, I; [4]University of the West of Scotland, Paisley, UK; [5]GSI, Darmstadt, D; [6]Univ. Of Brighton, Brighton, UK; [7]IFIC, Valencia, E; [8]University of Warsaw, Warsaw, Pl; [9]Universiy of Surrey, Guildford, UK; [10]TU Munich, Munich, D; [11]University of Santiago de Compostela, Santiago de Compostela, E; [12]Comenius University, Bratislava, Sk; [13]Univ. Of Salamanca, Salamanca, E; [14]Univ. of Delhi, Delhi, IND; [15]IKP Koeln, Koeln, D; [16]Lund University, Lund, S; [17]Univ. Of Sao Paulo, Sao Paulo, Br; [18]ATOMKI, Debrecen, H.

Introduction

The experiment described in this report aims at studying the shell evolution along Z=82.

The region of heavy Pb isotopes presents high-spin isomers, which involve the high-j orbitals, $\nu i_{11/2}$, $\nu g_{9/2}$, $\nu j_{15/2}$. The spectroscopic information derived from these isomeric states reflects the underlying microscopic nuclear structure. Previous to this experiment, the most n-rich lead isotope studied was ^{212}Pb, in which hints of an isomeric 8^+ state were found [1].

This experiment, performed in September 2009, also aimed at measuring β-decay half lives, which are particularly needed for r-process calculations, as an essential test to validate the nuclear and β decay models away from stability [2].

Experimental Details

The nuclei of interest were produced following projectile fragmentation of ^{238}U primary beam at 1 GeV/u, impinging on a Be target, 2.5 g/cm^2 thick. The ^{238}U beam was provided by the SIS synchrotron with an intensity of 1.5-2.0$\times 10^9$ ions/spill. Fragmentation reaction products were separated using the FRagment Separator (FRS) [3], operated in monochromatic mode with an aluminium wedge degrader in the intermediate focal plane (S2). In order to decrease the contaminations due to the population of nuclear species close to the primary beam an additional aluminium degrader, 2 g/cm^2 thick, was placed after the first bending dipole of the FRS (S1).

The RISING stopped beam set-up [4] has been used, with the addition of an active stopper consisting of DSSSD [5], allowing to study ion-β-γ correlations.

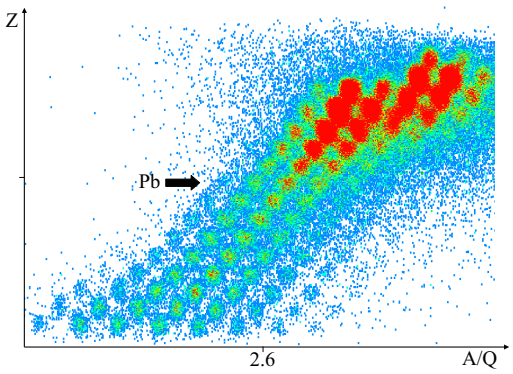

Figure 1: Z vs. A/Q plot for the ^{215}Pb setting. Pb isotopes are highlighted.

Two different settings were used in the present experiment: the first one centred around ^{215}Pb and the second around ^{217}Pb, in order to populate more exotic nuclei.

Figure 1 shows an example of a Z vs. A/Q identification plot for the ^{215}Pb setting, where Pb, Tl and Bi isotopes are, in particular, recognizable. New isomers have already been identified.in many Pb and Bi isotopes. Data analysis is ongoing.

References

[1] M. Pfutzner et al., Phys. Lett. **B 444** (1998) 32-37.

[2] I.N. Borzov. Phys. Rev. **C67** (2004) 025802.

[3] H. Geissel et al., Nucl. Instr. Meth. **B70** (1992) 286.

[4] S. Pietri et al., Nucl. Instr. Meth. **B 261** (2007)1079 .

[5] R. Kumar et al., Nucl. Instr. Meth.**A 598** (2009) 754.

Total fission cross section of ^{181}Ta + ^{1}H at 1, 0.8, 0.5 and 0.3 GeV studied in inverse kinematics.

Y. Ayyad[1], J. Benlliure[1], E. Casarejos[1], H. Álvarez[1], A. Bacquias[2], A. Boudard[2], T. Enqvist[3], V. Foehr[3], A. Kelic[3], K. Kezzar[1], S. Leray[2], C. Paradela[1], D. Pérez-Loureiro[1], R. Pleskac[3], and D. Tarrío[1]

[1]GENP, Univ. de Santiago de Compostela, Spain; [2]CEA-Saclay,Gif sur Yvette, France; [3]GSI, Darmstadt, Germany

Total fission cross-sections provide valuable information on the dynamics of the fission process [1] but they are also fundamental data of interest in a wide range of applications. Despite that interest the available experimental information is scarce considering the many combinations of nuclei and energies involved. Moreover, state-of-the-art models show discrepancies with the data at different energies. One of the most demanding application of this type of data are related to accelerator-driven-systems and nuclear waste incineration. The spallation data related to proton-induced reactions in different materials, provide clue information about the spallation target efficiency, and structural- and general-related parameters. In this context, it was soon recognized the importance of measuring key cases that would provide both: direct information on the nuclei of interest, and also to serve as benchmark data to test the simulation codes based on related models.

The experimental setup was mounted behind the FRS. The liquid hydrogen target (85 mg/cm^2) was surrounded by two Multi Sample Ionization Chamber (MUSIC) in order to identify the reactions produced in the hydrogen. Two scintillator paddles mounted one on top of the other provided , not only the fission trigger but also an energy loss measurement.In a second step a 'twin' ionization chamber and a ToF-wall detector would allow to identify in charge the residues. Only by using the information of the first part of the setup we have already accessed to the total fission cross-section.

The analysis was performed selecting the region of data that correspond to fission events in the MUSIC spectrum, separating ^{181}Ta ions from other species, applying the condition in the two paddles scintillators plot where the energy loss provides the charge distribution region of differents reactions and the clear selection of the fission events, and normalizing to the beam counting and target thickness. Special attention was paid to the evaluation of the fission background since the fission channel, contributes less than 1% to the total reaction cross section. The two scintillators, allow to further study the background that partially overlaps the fission region. This is actually the most important part of the analysis in order to guaranty the final quality and accuracy of the measurement.

The preliminary values of total fission cross-section of ^{181}Ta + p at different energies are the following: 18.49 $\pm$ 3.93 mb at 1 GeV, 11.40 $\pm$ 1.85 mb at 800 MeV, 5.14 $\pm$ 1.36 mb at 500 MeV and 2.79 $\pm$ 1.39 mb at 300 MeV. In figure 1 we compare the measured cross sections with sevaral model calculations. The dashed line represents a widely-used systematics on previously measured data [3]. As can be seen, this systematics clearly over-predict the data obtained in this work, in particular for the lowest energies. The two other lines correspond to microscopic calculations obtained with the intra-nuclear cascade model (INCL v4.1) coupled to de-excitation code (ABLAv3p). The dotted line represents a calculation where the fission probability is calculated according to the statisticl model of Bohr and Wheeler while the calculation described by solid line includes a dynamical description of the fission probability where a nuclear dissipation parameter reduces the fission flux across the barrier. Both calculation provide very different predictions of the total fission cross sections, while the statistical calculation (dotted line) clearly overestimate the fission cross section, the dynamical model of the fission width provide a reasonable good description of the measured data. This work confirms then the validity of the dynamical description of fission at high excitation energies as previously stated [2].

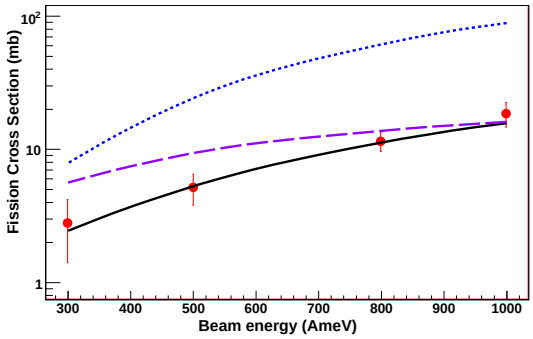

Figure 1: Experimental Results vs Simulation. Solid Circle: This work - Solid line: Simulation (dissipation) - Dotted Line: Simulation (statistical) - Dashed Line: Prokofiev Systematics

References

[1] B. Jurado et al Phys. Rev. Lett. 93(2004) 072501.

[2] J.Benlliure et al Nucl. Phys. A 700 (2002) 469.

[3] A.V. Prokofiev Nucl. Inst. Meth. A 463 (2001) 557.

Total interaction cross sections of medium mass nuclei

D. Dragosavac[1], H. Álvarez-Pol[1], J. Benlliure[1], B. Blank[2], E. Casarejos[1], V. Föhr[3], M. Gascón[1], W. Gawlikowicz[4], A. Heinz[5], K. Helariutta[6], A. Kelić[3], S. Lukić[3], F. Montes[3], D. Pérez-Loureiro[1], L. Pieńkowski[4], K-H. Schmidt[3], M. Staniou[3], K. Subotić[7], K. Sümmerer[3], J. Taieb[8], A. Trzcińska[4], and M. Veselsky[9]

[1]USC, Santiago, Spain; [2]CENBG, Gradignan, France; [3]GSI, Darmstadt, Germany; [4]Uni. Warsaw, Poland; [5]Yale Uni., USA; [6]Uni. Helsinki, Finland; [7]Inst. Vinča, Serbia; [8]CEA/DAM, France; [9]SAS, Bratislava, Slovakia

The radial distribution of protons and neutrons are fundamental properties of nuclei directly related to the nucleon-nucleon interaction that sometimes manifest in abnormal phenomena such as the proton or neutron haloes or the neutrons skins. Moreover, we know that nuclear radii can also help to constrain the equation of state (EOS) of nuclear matter, in particular the symmetry term, at subsaturation density [1].

Total interaction cross sections of relativistic projectiles can give access to matter radii for a large variety of nuclear species [2-4]. In this work we have performed systematic measurements of total interaction cross sections for long isotopic chains of medium-mass nuclei covering the radial evolution of the matter distribution with neutron excess.

The experiment was performed at GSI Fragment Separator (FRS) [5]. Beams of ^{238}U and ^{132}Xe around 1 A GeV were used to produce by fission and fragmentation reactions medium-mass nuclei ($46 < Z < 55$) covering long isotopic chains (e.g.^{111}Sn to ^{136}Sn). The first section of the FRS provides the separation and identification of the cocktail beam of exotic projectiles coming from the production target placed at the entrance of the FRS. The second section was used to separate and identify the residual nuclei produced in the interaction of the cocktail beam species with the beryllium interaction target placed at the intermediate-image plane of the separator. Both sections of the spectrometer were equipped with time-projection chambers, ionization chambers and plastic scintillators for measuring the magnetic rigidity, atomic number and time-of-flight of the transmitted nuclei [6,7].

The two reaction mechanism used for producing nuclei far from stability made it possible to cover long isotopic, isotonic and isobaric chains of medium-mass nuclei. Then, total interaction cross sections were determined using the transmission method, counting the number of projectiles impinging the interaction target and the number of projectiles arriving to the final image plane of the spectrometer. The measured values were corrected by the optical transmission of the ions, detection efficiency and interaction in other layers of matter than the target by using the measurements without interaction target. Using this method we could determine total interaction cross sections for more than 150 different medium-mass nuclei with an accuracy mainly limited by statistics for the most exotic species.

Figure 1 shows the measured total interaction cross sections for the 23 tin isotopes produced in this experiment. These cross sections are compared with the predictions obtained with a Glauber-model calculation using the optical limit approach and two parameter Fermi distributions to describe the radial distribution of protons and neutrons [8]. In this case the half-density radius and the surface thickness parameter of the Fermi distributions were obtained from the droplet model of Myers [9].

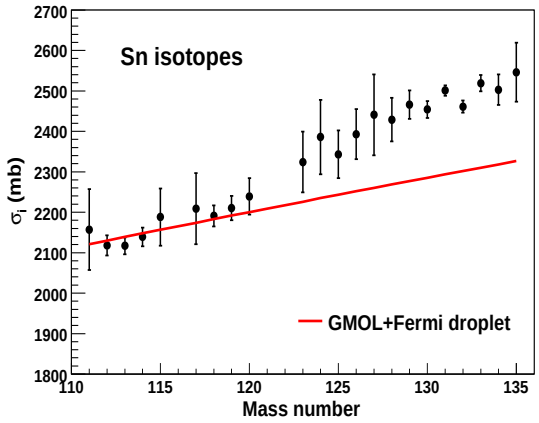

Figure 1: Total interaction cross sections for tin isotopes compared to model calculation.

The total interaction cross sections for the most neutron-deficient tin isotopes increase smoothly with the mass but for the most neutron-rich isotopes this increase is much stronger. This result would indicate that the spatial extension of the most neutron-rich tin isotopes is wider than predicted, and could be signature for a skin structure in those nuclei.

References

[1] A.W. Steiner et al., Phys. Rep. 411 (2005) 325
[2] A. Ozawa et al., Nucl. Phys. A 709 (2002) 32
[3] A. Khouaja et al., Nucl. Phys. A 780 (2006) 1
[4] N. Aissaoui et al., Phys. Rev. C60 (1999) 034614
[5] H. Geissel et al., Nucl. Instr. and Meth. B 70 (1992) 286
[6] J. Benlliure et al., Phys. Rev. C 78 (2008) 054605
[7] J. Pereira et al., Phys. Rev. C 75 (2006) 044612
[8] P.J. Karol, Phys. Rev. C 11 (1975) 1203
[9] W.D. Myers and K.-H. Schmidt, Nucl. Phys A 410 (1983) 61

Improved modelling of helium and tritium production for spallation targets

S. Leray[1], A. Boudard[1], J. Cugnon[2], J.C. David[1], A. Kelić-Heil[3], D. Mancusi[2], M.V. Ricciardi[3]
[1]CEA/Saclay, Irfu/SPhN, Gif-sur-Yvette, France; [2]FIPA, University of Lige, Belgium; [3]GSI, Darmstadt, Germany

Reliable predictions of light-charged particle (LCP) production in spallation reactions are important to correctly assess gas production in spallation targets. In particular, He production yield is important for assessing damage in the window separating the target and the accelerator vacuum, and tritium is a major contributor to the target radioactivity. Up to now, the models available in the MCNPX transport code, including the widely used default option Bertini-Dresner and the INCL4.2-ABLA combination of models, were not able to correctly predict light-charged particle yields. Here, we present the work done recently on both the intranuclear cascade model INCL4.5 [1] and on the de-excitation model ABLA07 [2] to improve the LCP prediction, in particular tritium and helium.

In LCP energy spectra, two different components are generally observed: a low-energy isotropic peak coming from the evaporation stage, and a high-energy forward-peaked tail, coming from initial reaction stage. The contribution of the latter in the production cross sections of tritium and ^{3}He is far from being negligible. This is why a coalescence mechanism leading to LCP emission has been implemented into INCL (first in ref. [2], later in ref. [1, 3]). The cluster emission mechanism is based on surface coalescence in phase-space i.e. on the assumption that a cascade nucleon ready to escape at the nuclear surface can coalesce with other nucleons close enough in phase space and form a cluster. All possible clusters up to a given mass number are formed and the priority is given to the one with the lowest excitation energy per nucleon. The selected cluster is emitted only if it succeeds to go through the Coulomb barrier. In INCL4.5 clusters up to mass 8 are considered.

In the original version of ABLA only nucleons and alphas could be evaporated. The new version [2] now allows the evaporation of all the types of light charged particles from p to ^{4}He and also of intermediate mass fragments. It uses improved parameterizations of inverse reaction cross sections and barriers of potential in order to better reproduce experimental particle energy spectra. A simultaneous break-up (multifragmentation) mechanism has been added for systems overcoming a certain limiting temperature. The fission part has also been modified.

In figure 1, the experimental light composite particle energy spectra [5] for the reaction p+Ta at 1.2 GeV are compared with the results obtained with INCL4.5-ABLA07. The dashed curve shows the contribution coming from the coalescence process in INCL4.5. It is evident that the combination of the two new models is rather successful and represents a definite improvement compared to the former models, which did not evaporate tritium and ^{3}He and were unable to account for the high energy tail of the particle spectra. A more detailed description of this work can be found in ref. [6]. Comparisons with many more experimental data and with other available models are also presented there.

This work was partly supported by the FP6 Euratom project EUROTRANS/NUDATRA, EC contract number FI6W-CT-2004-516520.

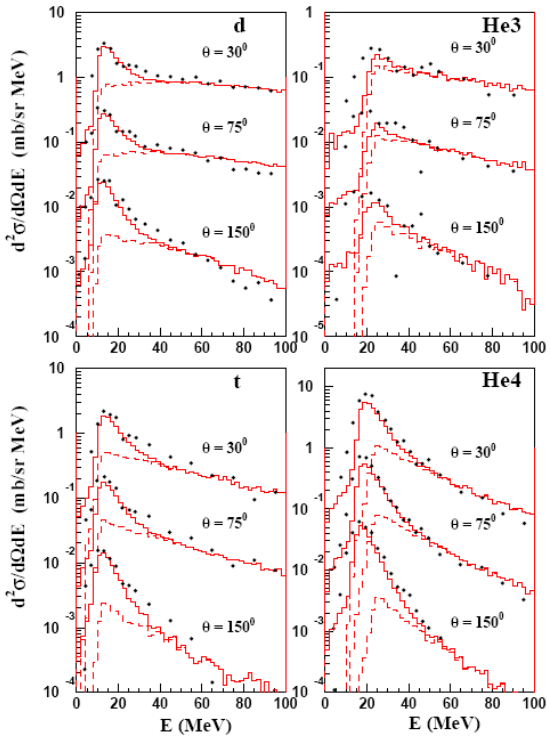

Figure 1: Light composite particle double-differential cross sections in the p+Ta reaction at 1.2 GeV [5] compared with the results of INCL4.5-ABLA07. Each successive curve, starting from the smallest angle, is scaled by a multiplicative factor of 10^{-1}. The contribution due to the coalescence process in INCL4.5 is given by the dashed line.

References

[1] A. Boudard and J. Cugnon, Proc. of the ICTP-IAEA Advanced Workshop on Model Codes for Spallation Reactions, ICTP Trieste, Italy, 4-8 February 2008.
[2] A. Kelic, M.V. Ricciardi and K.-H. Schmidt, Proc. of the ICTP-IAEA Advanced Workshop on Model Codes for Spallation Reactions, ICTP Trieste, Italy, 4-8 February 2008.
[3] A. Boudard et al., Nucl. Phys. A 740, 195 (2004).
[4] J. Cugnon *et al.*, Proc. of the International Topical Meeting on Nuclear Research Applications and Utilization of Accelerators, 4-8 May 2009, Vienna.
[5] C.M. Herbach *et al.*, Nucl. Phys. A 765, 426 (2006).
[6] S. Leray et al., Nucl. Inst. Meth. B. In press.

S304: Measurement of the spallation of ^{136}Xe in inverse kinematics at 1 GeV per nucleon

J.-É. Ducret[1], T. Aumann[2], Y. Ayyad[3], S. Bianchin[2], O. Borodina[2,4], A. Boudard[1], C. Caesar[2], E. Casajeros[3], B. Czech[5], T. Gorbinet[1], S. Hlavac[6], N. Kurz[2], C. Langer[2], T. Le Bleis[2], A. Le Fèvre[2,6], S. Leray[1], J. Lukasik[5], P. Pawlowski[5], S. Pietri[2], C. Rappold[2,8], M.-D. Salsac[1], T.R. Saito[2,4], H. Simon[2], M. Veselsky[6], and O. Yordanov[9]

[1]IRFU, CEA-Saclay, F91191 Gif sur Yvette, France; [2]GSI, Darmstadt, Germany; [3]University of Santiago de Compostella, Spain; [4]Institut für Kernphysik, University of Mainz, Germany; [5]Institute of Nuclear Physics, Polish Academy of Sciences, Krakow, Poland; [6]Institute of Physics, Slovak Academy of Sciences, Bratislava, Slovakia; [7]Subatech, Nantes, France; [8]IPHC, Strasbourg, France; [9]Institute of Nuclear Research & Nuclear Energy, Bulgarian Academy of Sciences, Sofia, Bulgaria

A few years ago, a program of spallation experiments in inverse kinematics was undertaken in GSI with extensive measurements of spallation-residue production cross-sections at FRS on systems ranging from $^{56}Fe + p$ to $^{238}U + d$ at energies from 250 to 1500 MeV per nucleon with highly-resolved mass - charge identification & centre-of-mass longitudinal velocity reconstruction [1]. In 2000, new experiments began with the detection in coincidence of the produced light & heavy fragments & neutrons [2]. These experiments were aiming at understanding in detail the spallation mechanism, with emphasis either on the fission channels of spallation [3] or on the de-excitation mechanisms as a function of the mean excitation energy of the projectile (i.e. of the projectile size) [2, 4]. Our first results were published in 2008 [5] for the $^{56}Fe + p$ reaction at 1 GeV per nucleon, where we could distinguish between different decay channels of the excited projectile & where we studied the production of fragments ($Z \geq 3$) as a function of the excitation of the projectile in a model-independent way. The experiment S304 [4] is aiming at such a coincidence measurement on $^{136}Xe+p$ & $^{28}Si+p$. We did our ^{136}Xe run in April 2009, in Cave C.

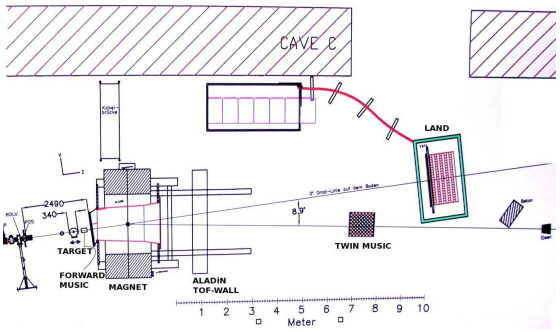

Figure 1: Sketch of the S304 Set-up in Cave C.

Our set-up is sketched on Fig. 1. The beam diagnostics of Cave C were used. The projectile residues of charge $Z \geq 15$ were detected in a Multiple Sampling Ionisation Chamber (MUSIC) set between the target & the ALADIN magnet entrance & in a (TWIN) MUSIC behind. The neutrons were detected in LAND & the lighter charged fragments in the highly-segmented ALADIN TOF WALL, installed at the exit of the magnet. A charge spectrum (up to $Z = 14$) of one scintillator is shown on Fig. 2.

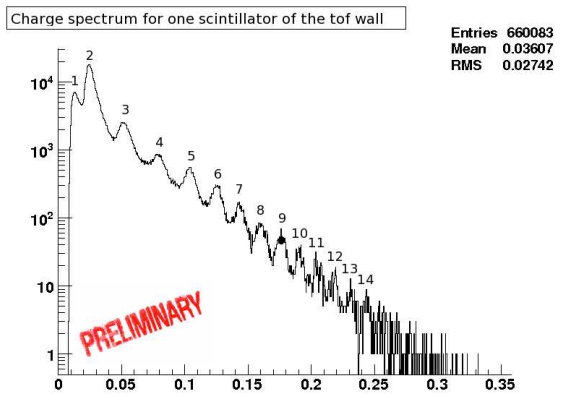

Figure 2: Charge spectrum of one scintillator of the ALADIN TOF WALL.

We used two different targets: a new thin-wall liquid-hydrogen target built on purpose in Saclay & a ^{12}C target, which will permit to study two reactions, $^{136}Xe + p$ & $^{136}Xe + ^{12}C$, at a beam energy of 1 GeV per nucleon. The experiment ran well with very stable beam conditions & high statistics of events were recorded. The data analysis is currently running, with the aim of producing our first results by the end of 2010. Emphasis is made on the understanding of LAND to reconstruct the expected high neutron multiplicities.

References

[1] C. Villagrasa-Canton *et al.*, Phys. Rev. C **75**, 044603 (2007) & references therein.

[2] J.-É. Ducret *et al.*, exp. S248, GSI-EA (2000)

[3] A. Boudard *et al.*, exp. S293, GSI-EA (2005)

[4] J.-É. Ducret *et al.*, exp. S304, GSI-EA (2005)

[5] É. Le Gentil *et al.*, Phys. Rev. Lett. **100**, 022701 (2008)

High-Precision Momentum Measurements of Projectile Fragments in ^{112,124}Sn+^{112,124}Sn Collisions at 1 *A* GeV*

V. Föhr[1], A. Bacquias[2], V. Henzl[3], A. Kelić-Heil[1], M.V. Ricciardi[1], K.-H. Schmidt[1] for the CHARMS collaboration

[1]GSI, Darmstadt, Germany; [2]CENBG, Bordeaux-Gradignan, France; [3]MSU, East Lansing, MI 48824, U.S.A.

The longitudinal re-acceleration phenomenon of the fragmentation residues, was observed originally in the projectile fragmentation of uranium [1,2] at the Fragment Separator (FRS), GSI Darmstadt. According to transport calculations [3], this phenomenon is related to the participants blast, and the longitudinal momenta of the surviving residues can give a direct access to the momentum-dependent properties of the nuclear mean field (MF), little affected by the uncertainties in nuclear incompressibility [3]. After this first experimental observation, a set of experiments was carried out at the FRS. The aim was to explore the dependence of the reacceleration phenomenon on the initial beam energy, on the system size, as well as the importance of the isospin effects on the evolution and strength of the participants' blast. The dependence on the initial beam energy and on the size of the system was pursued by studying the reactions ^{197}Au+^{197}Au and ^{197}Au+Al at 500 and 1000 *A* MeV [4] at the FRS, GSI.

This work is devoted to study the importance of the isospin effects. To this purpose the fragmentation of two systems, ^{112}Sn+^{112}Sn and ^{124}Sn+^{124}Sn at 1000 *A* MeV, whose *N/Z* ratio is 1.24 and 1.48 respectively, was studied. If there are sensible effects of the momentum on the isospin dependence of the MF (as it is expected in this energy regime [5]) one could expect sensible differences [3] for the momentum transfer to the spectators, that would be detectable in the mean longitudinal velocity of fragments from systems with different isospin content.

The experiment was performed using the high-resolution magnetic spectrometer, the FRS, at GSI. The 1 *A* GeV ^{112}Sn and ^{124}Sn beams impinged on two thin targets of ^{112}Sn and ^{124}Sn, respectively. The magnetic rigidity of each projectile-residue could be measured with high precision by determining the deflection in a magnetic dipole field. This gave a measure of the longitudinal momentum – and hence on the longitudinal velocity – with a uncertainty of ± $5\cdot10^{-4}$ once the product is identified in mass and atomic number. Details of the experimental set-up and the detector equipment, as well as a description of the analysis method can be found in ref. [1,2,4,6].

To give an idea of the precision of the method, in figure 1, as an example of longitudinal velocity distribution, we present the measured spectra of two fragments, ^{65}Zn and ^{82}Sr. The velocity is given in the frame where the beam is at rest. The mean values of the velocity distributions of fragmentation residues as a function of their mass number are shown in figure 2. Statistical uncertainties are not shown in order not to overload the figure. They correspond to the fluctuations of the points. The absolute uncertainty amounts to less than 0.03 cm/ns for each system, independently.

With increasing mass loss, the velocities first decrease as expected from previously established systematics [6], described bye the dashed line, then level off, and finally increase again, the same tendency as observed in ref. [1,2,4]. The discussion on the physical results and the comparison of the experimental results with theoretical predictions is still in progress.

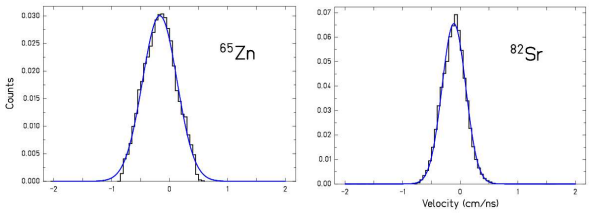

Figure 1: Example of longitudinal velocity spectra for two final fragments: ^{65}Zn and ^{82}Sr.

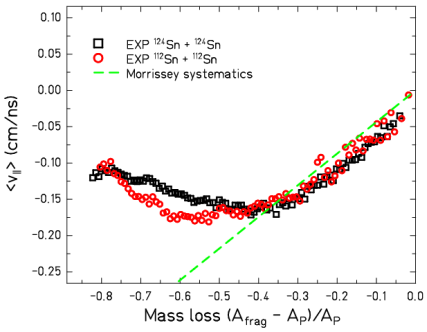

Figure 2: Measured mean value of the longitudinal velocity as a function of the mass of the fragments produced in the reactions ^{112,124}Sn+^{112,124}Sn at 1 *A* GeV. The dashed line gives the prediction of the Morrissey's systematic [7].

References

[1] T.Enqvist *et al.*, Nucl. Phys. A658 (1999) 47.
[2] M.V.Ricciardi *et al.*, Phys. Rev. Lett. 90 (2003) 212302
[3] L.Shi, P.Danielewicz and R.Lacey, Phys. Rev. C64 (2001) 034601.
[4] V. Henzl, PhD Thsis, TU Prague, Czech Rep., 2001.
[5] V.Greco *et al.*, Phys. Let. B 562 (2003) 215.
[6] V. Föhr, PhD Thesis, Univ. of Jyväskylä, Finland, in prepapartion.
[7] D. J. Morrissey, Phys. Rev. C 39 (1989) 460.

* This work forms part of Ville Föhr 's PhD thesis.

Origin of the even-odd effect in the yields from high-energy reactions

M. Valentina Ricciardi[1], Karl-Heinz Schmidt[1]and Aleksandra Kelić-Heil[1]
[1]GSI, Darmstadt, Germany

In 2004, the analysis of experimental production cross-sections of relatively light nuclei produced by fragmentation in the reaction ^{238}U+Ti at 1 *A* GeV revealed a very strong and complex even-odd staggering [1]. The experiment was performed at the FRS, at GSI, Darmstadt. It was concluded that structural effects cannot be attributed to the surviving of nuclear structure of the colliding nuclei, as in low-energy fission; the structures appear as the result of the condensation process of heated nuclear matter while cooling down in the evaporation process [1].

Here, we want to discuss which kind of staggering we have to expect in the cold final products due to the influence of an evaporation cascade starting from hot pre-fragments. After their formation, the initial pre-fragments are definitely free of any even-odd structure, because there is no pairing above the critical pairing energy. The number of available states from a certain total excitation energy of the decaying system is essentially determined by a mostly structureless level density above a fictive liquid-drop ground state. This structureless cloud in *N* and *Z* rains down in excitation energy and in nucleon number due to evaporation. This process is essentially deterministic, because in most cases one particle dominates and the variation of the kinetic energy of the emitted particle is small compared to the binding energy. In this way, a well-defined 3-dimensional subspace of the *N, Z ,E** initial production cloud ends up in a certain fragment. As a consequence, *the final yields will be modulated by the range of excitation energy below the lowest particle threshold*. In order to visualise this idea, in figure 1 we present the lowest particle threshold for each nuclide, calculated as the minimum value between the proton and neutron separation energies. The data are taken from ref. [3].

Recently, we performed a new systematic analysis of the even-odd effect over a large range of nuclear reactions, nuclear systems and energies. It is impressive how the staggering of the lowest particle threshold, shown in figure 1, is consistent with the even-odd staggering in the yields of ref. [1] and all other analysed data.

Hereafter, among all new analysed data, we focus on the reaction ^{56}Fe+Ti at 1 *A* GeV [2], where it was possible to extend the measurement of production cross sections down to Li isotopes. The kinematical properties of the light products (IMF) indicate that they are produced in multifragmentation events, as a consequence of a thermal instability. We will consider two possible scenarios at freeze-out. In the first scenario, the IMFs are essentially produced in their ground state; the yields are governed by Boltzmann statistics under certain conditions. This implies that the essential parameter related to the yields is the binding energy of the respective IMF. In the second scenario, the fragments at freeze-out are essentially produced with excitation energies above the critical pairing energy and will undergo the de-excitation process; the essential parameter related to the yields is the lowest particle threshold of the respective IMF. In figure 2, the measured IMF cross sections from ref. [2] are compared to the extra binding energy due to pairing (obtained by subtracting a calculated LD part from the values of ref. [3]) and to the lowest particle separation energy. The results indicate clearly that assuming that IMFs are produced cold at freeze-out is wrong, even for very light IMFs such as Li isotopes. So, it is dangerous to extract fundamental properties of hot nuclear matter assuming that the population at freeze-out is given by the Boltzmann factor. The situation is even more severe when these methods are extended to treat even heavier final fragments. It was recognized previously that the determination of the freeze-out temperature with the isotopic yield thermometer might be disturbed by the evaporation process [4]. Several authors investigated this problem by means of nuclear models and proposed suitable corrections to this effect. Our analysis on the fine structure observed in the yields indicates in a model-independent way the dominant role of the evaporation process.

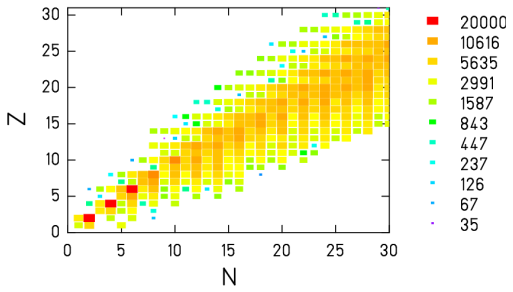

Figure 1: Lowest particle threshold (in keV).

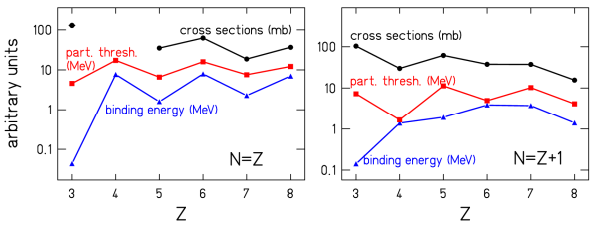

Figure 2: Staggering in the lowest particle threshold (MeV) and in the binding energies (MeV) compared to measured fragmentation cross sections (mb).

References

[1] M.V. Ricciardi et al., Nucl. Phys. A 733 (2004) 299.
[2] P. Napolitani et al., Phys. Rev. C 70 (2004) 054607.
[3] G. Audi, A. H. Wapstra and C. Thibault, Nucl. Phys. A729 (2003) 337.
[4] M. B. Tsang *et al.*, Phys. Rev. Let. 78 (1997) 3836

Properties of the ^{7}He ground state from ^{8}He neutron knockout*

Yu. Aksyutina[1,2], H.T. Johansson[2], T. Aumann[1], K. Boretzky[1], M.J.G. Borge[3], A. Chatillon[1], L.V. Chulkov[1,4], D. Cortina-Gil[5], U. Datta Pramanik[6], H. Emling[1], C. Forssén[1], H.O.U. Fynbo[7], H. Geissel[1], G. Ickert[1], B. Jonson[2], R. Kulessa[8], C. Langer[1,9], M. Lantz[2], T. Le Bleis[1,9], K. Mahata[1], G. Münzenberg[1], T. Nilsson[2], G. Nyman[2], S. Paschalis[10], W. Prokopowicz[1], R. Reifarth[1,9], A. Richter[11], K. Riisager[7], G. Schrieder[11], H. Simon[1], K. Sümmerer[1], O. Tengblad[3], H. Weick[1], and M. Zhukov[2]

[1]GSI, Germany; [2]Chalmers University of Technology, Sweden; [3]CSIC Madrid, Spain; [4]RRC Kurchatov Institute Moscow, Russia; [5]University of Santiago de Compostela, Spain; [6]SINP Kolkata, India; [7]Aarhus University, Denmark; [8]Jagellonian University Krakow, Poland; [9]University of Frankfurt, Germany; [10]University of Liverpool, United Kingdom; [11]Technische Universität, Darmstadt, Germany

Neutron-knockout reactions with a 240 MeV/u ^{8}He beam in a liquid-hydrogen target have been studied in an experiment at the ALADIN-LAND setup. The detection of ^{6}He in coincidence with a neutron permits to reconstruct the relative-energy of the unbound ^{7}He system using the relativistic equation:

$$E_{fn} = |P_f + P_n| - M_f - m_n, \qquad (1)$$

where $P_f(P_n)$ is the fragment (neutron) four-momentum and $M_f(m_n)$ is the mass of the fragment (neutron).

A previous measurement of ^{7}He, performed with a carbon target, showed a spectrum which could not be described as a single Breit-Wigner resonance [1, 2]. The deviation from the Breit-Wigner shape was tentatively interpreted as corresponding to the first excited state in ^{7}He with possible spin-parity $1/2^{-}$. The present experiment was performed at the same setup, but with a hydrogen target. The obtained relative-energy spectrum of ^{6}He +n is shown in Fig. 1 (upper panel). It can be described by single Breit-Wigner resonance at an energy above the neutron-decay threshold E_r = 0.387(2) MeV with Γ = 0.190(6) MeV. No excited states are observed.

The difference between results of the two experiments may originate in a eventual target dependence. Hydrogen is the simplest nuclear probe, while the carbon nucleus exhibits a complex structure and may affect the reaction mechanism. One possible explanation is multiple scattering, which can play a role even at relativistic energies and is more pronounced in the case of the carbon target. A second possibility is, that an excited state with a $^{6}\mathrm{He}(2^{+}) + \mathrm{n}$ structure was observed on the carbon target. Such state, however, cannot be excited in a single-step process on a hydrogen target.

The spectroscopic factor for the ^{6}He(0^{+})+n configuration was obtained as ratio of the observed reduced width and the single-particle reduced width, $S_n = \gamma^2_{obs}/\gamma^2_{sp}$. In order to perform a model-independent analysis, the single-particle reduced width was taken from the ^{5}He spectrum obtained in Ref. [1]. Its ground state represents an ideal case of a single-particle $p_{3/2}$ state. However, the low-energy part of the spectrum shows a deviation from a pure Breit-Wigner shape. In the reanalysis, performed in Ref. [3] a contribution from s-wave scattering was suggested. This permits to separate the contribution from the s-wave component and to extract the single-particle width for the p-state. The obtained γ^2_{sp} value for ^{5}He was scaled to the mass of ^{7}He. The deduced spectroscopic factor S_n=0.61 disagrees with the assumption of a single-particle structure of the ^{7}He ground state and suggests configuration mixing.

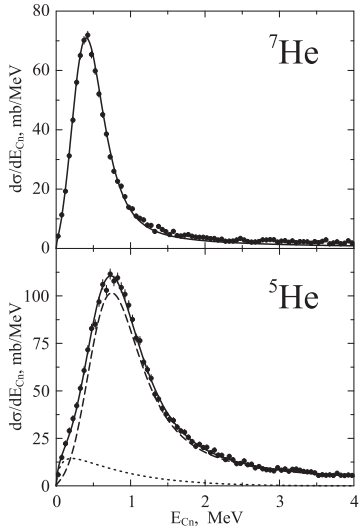

Figure 1: Relative-energy spectrum of ^{6}He+n, obtained after one neutron knockout in hydrogen target [3] (upper panel) and the relative-energy spectrum of ^{4}He+n [1], obtained with a carbon target (lower panel).

References

[1] K. Markenroth et al., Nucl. Phys. A 679 (2001) 462

[2] M. Meister et al., Phys. Rev. Lett. 88 (2002) 102501

[3] Yu. Aksyutina et al., Phys. Lett B 679 (2009) 191

*This work was supported by the Alliance Program of the Helmholtz Association (HA216/EMMI)

Three-body correlations as a key to the structure of ^{10}He*

H.T. Johansson[1], Yu. Aksyutina[1,2], T. Aumann[2], K. Boretzky[2], M.J.G. Borge[3], A. Chatillon[2], L.V. Chulkov[2,4], D. Cortina-Gil[5], U. Datta Pramanik[6], H. Emling[2], C. Forssén[1], H.O.U. Fynbo[7], H. Geissel[2], G. Ickert[2], B. Jonson[1], R. Kulessa[8], C. Langer[2,9], M. Lantz[1], T. Le Bleis[2,9], K. Mahata[2], G. Münzenberg[2], T. Nilsson[1], G. Nyman[1], S. Paschalis[10], W. Prokopowicz[2], R. Reifarth[2,9], A. Richter[11], K. Riisager[7], G. Schrieder[11], H. Simon[2], K. Sümmerer[2], O. Tengblad[3], H. Weick[2], and M. Zhukov[1]

[1]Chalmers University of Technology, Sweden; [2]GSI, Germany; [3]CSIC Madrid, Spain; [4]RRC Kurchatov Institute Moscow, Russia; [5]University of Santiago de Compostela, Spain; [6]SINP Kolkata, India; [7]Aarhus University, Denmark; [8]Jagellonian University Krakow, Poland; [9]University of Frankfurt, Germany; [10]University of Liverpool, United Kingdom; [11]Technische Universität, Darmstadt, Germany

The results of an experiment with a relativistic ^{11}Li beam, with energy of 280 MeV/u, impinging on a liquid hydrogen target are discussed. Proton knockout from ^{11}Li leads to the formation of the unbound ^{10}He system, followed by its subsequent decay. The experimental setup, consisting of the neutron detector LAND, the dipole spectrometer ALADIN and different types of tracking detectors, allows to reconstruct the momentum vectors of all decay products measured in coincidence. The properties of the unbound nucleus ^{10}He are investigated by determining the relative-energy spectrum as well as by studying the angular and energy correlations between the decay products. The relative-energy spectrum allows to observe resonances and determine their position and width, while three-body correlations provide information about their structure.

The obtained relative-energy spectrum in the $^{8}\mathrm{He}+\mathrm{n}+\mathrm{n}$ system can be affected by the initial correlations in the ^{11}Li ($^{9}\mathrm{Li}+\mathrm{n}+\mathrm{n}$) projectile. This leads to two possible alternative interpretations that are shown in Fig. 1. The spectrum can be described either as a ground-state resonance superimposed to the correlated background explained in the beginning of this paragraph, Fig. 1(a), or as a ground-state resonance overlapping with an excited state, Fig. 1(b).

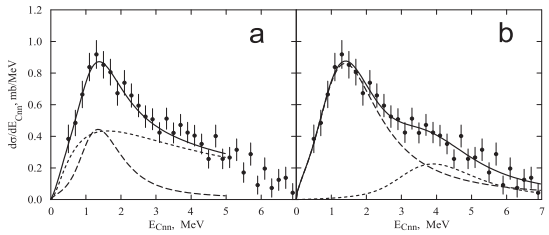

Figure 1: Two interpretations of the relative-energy spectrum of ^{10}He.

The correlations between the decay products of ^{10}He permit to give a preference to the latter version. A convenient description of the three-body system is achieved in terms of so-called Jacobi momenta. One of them, $\mathbf{q}_{12}$, is the relative momentum between two particles, core-n or n-n, while the second connects center of mass of this system to the third particle – $\mathbf{q}_{3-12}$. After integration over all possible orientations of the three-body system, the correlations can be described by three variables: the angle θ between Jacobi momenta $\mathbf{q}_{12}$ and $\mathbf{q}_{3-12}$, the total relative energy E_{Cnn} in the three-body system and the fractional energy $\varepsilon_{12} = \mathbf{q}_{12}^2/E_{Cnn}$ in a particular pair of particles.

The obtained distributions, corresponding to the relative-energy interval 0 – 3 MeV are shown in Fig. 2. The

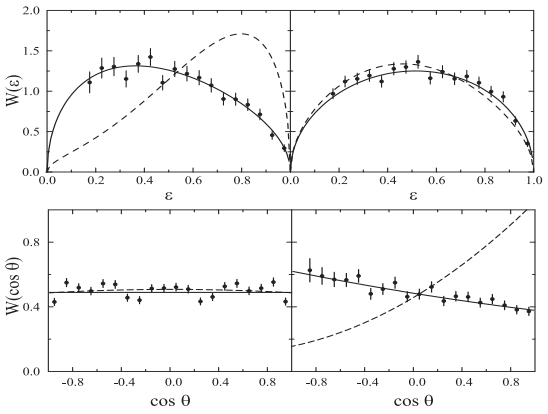

Figure 2: Energy and angular correlations in $^{8}\mathrm{He}+\mathrm{n}+\mathrm{n}$ system in the relative-energy interval 0 – 3 MeV.

dashed line corresponds to predicted correlations using a ^{11}Li wave-function [1] as correlated background. The solid line represents a fit assuming a spin-parity of $\mathrm{I}^{\pi} = 0^{+}$. The difference between experimental and theoretical distribution demonstrates the effect of the final-state interaction leading to the $^{10}\mathrm{He}$ ground state. The correlations observed for $3 < E_{Cnn} < 7$ MeV give a more evident picture and can be described assuming $I^{\pi} = 2^{+}$. Eventually, the experimental spectrum is interpreted as 0^{+} $^{10}\mathrm{He}$ ground state and an 2^{+} excited state.

References

[1] N. Schulgina et al., Nucl. Phys. **A825**(2009)175.

*This work was supported by the Alliance Program of the Helmholtz Association (HA216/EMMI)

One nucleon knockout reactions from light carbon isotopes*

V. Volkov†[1], T. Aumann[2], J. Enders[1], F. Farinon[2], H. Geissel[2], M. Holl[1], N. Iwasa[5], R. Janik[6], R. Krucken[4], P. Maierbeck[4], C. Nociforo[2], A. Prochazka[2], C. Rodriguez-Tajes[3], H. Simon[2], B. Sitar[6], P. Strmen[6], K. Summerer[2], H. Weick[2], and J. Winfield[2]

[1]Technische Universitat Darmstadt, Germany; [2]GSI, Darmstadt, Germany; [3]Universidad de Santiago de Compostela, Spain; [4]Technische Universitat Munchen, Germany; [5]Tohoku University, Japan; [6]Univerzita Komenskeho, Bratislava, Slovakia

Knockout of single nucleons from beams with intermediate to relativistic velocities is widely used to elucidate the single-particle structure of nuclei, in particular for rare isotopes, see Ref. [1]. It has been argued [2] that nucleon knockout reactions provide access to absolute spectroscopic factors. Measured spectroscopic factors $C^2_{\rm exp}$ are smaller than those predicted within a shell-model calculation, $C^2_{\rm th}$. The quenching factor $R_s = \sigma_{\rm exp}/\sigma_{\rm th} = C^2_{\rm exp}/C^2_{\rm th}$ from relativistic appears to approach unity for small binding energies of the knocked-out nucleon, whereas for deeply bound nucleons significant quenching $R_s \ll 1$ is observed, see [3].

Experiment S341 studied, among others, the inclusive knockout reactions ^{9}Be(^{12}C,^{11}C)X, ^{9}Be(^{11}C,^{10}C)X, ^{9}Be(^{10}C,^{9}C)X, and ^{9}Be(^{9}C,^{8}B)X, thereby covering a large range of binding energy difference values. The reactions with residues ^{9}C and ^{8}B benefit from the fact that the ground state is the only bound state in these nuclei. The reactions ^{9}Be(^{12}C,^{11}C)X and ^{9}Be(^{9}C,^{8}B)X have been carried out before and may serve for benchmarking the experiment.

The experiment used an incident ^{12}C beam from the SIS at 1670 MeV/nucl. impinging on a 4 g/cm^2 beryllium sheet at the FRS target position. At the intermediate F2 focus of the FRS, a 4.9 g/cm^2 Be target served as secondary break-up target after charge identification in a preceding scintillator. The outgoing residues were tracked using time-projection chambers (TPC). To maximize transmission, the reaction residues were detected at the third FRS focus F3 using TPC tracking and scintillation detectors for charge identification and time-of-flight measurement.

The ongoing data analysis resulted in preliminary cross sections between 21(2) mb (for (^{10}C,^{9}C)) and 51(4) mb (for (^{12}C,^{11}C)). Using the Glauber model for describing the reaction and shell-model predictions for the spectroscopic factors from the Cohen-Kurath p-shell interaction, we extract the following preliminary reduction factors: 0.55(5) for (^{12}C,^{11}C), 0.33(5) for (^{11}C,^{10}C), 0.47(6) for (^{10}C,^{9}C), and 0.79(7) for (^{9}C, ^{8}B). With the exception of the unexpectedly low value for the (^{11}C,^{10}C) reaction, the preliminary results support the trend of Ref. [3] and are in agreement with previous data.

* Work supported by GSI research and development program DA PIET and BMBF, contract 06DA9040I

† v.volkov@gsi.de

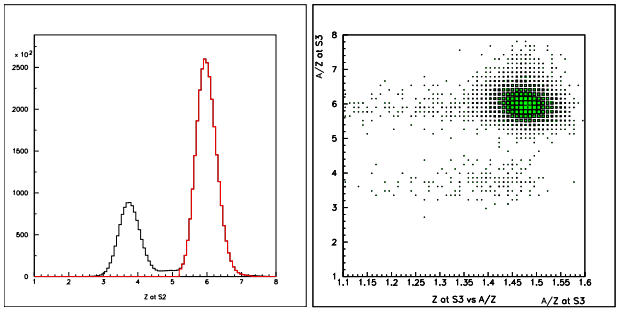

Figure 1: Charge identification at F2 (left) and mass to charge ratio identification at F3 (right)

It has been argued that the reduction of spectroscopic strength originates from correlations that are not accounted in conventional shell-model calculations. While, e.g., the Cohen-Kurath value for the spectroscopic factor amounts to 1.73, within the Green's function Monte-Carlo approach a value of 1.04 is obtained [4] so that with respect to that model the quenching factor would be much closer to unity. We note that Timofeyuk suggested recently [5] how contributions from excluded model spaced in shell-model calculations with limited model space could be accounted for.

References

[1] P. G. Handen, J. A. Tostevin, Annu. Rev. Nucl. Part. Sci. 53, 219 (2003)

[2] B. A. Brown et al., Phys. Rev. C 65, 061601(R) (2002)

[3] A. Gade et al., Phys. Rev. C 77, 044306 (2008)

[4] R. B. Wiringa, private communication

[5] N. K. Timofeyuk, Phys. Rev. Lett. 103, 242501 (2009)

Two-Nucleon Knockout Reactions from ^{11}C *

M. Holl[1], T. Aumann[2], D. Cortina-Gil[3], J. Enders[1], F. Farinon[2], H. Geissel[2], N. Iwasa[5], R. Janik[6], R. Krücken[4], P. Maierbeck[4], C. Nociforo[2], A. Prochazka[2], C. Rodriguez-Tajes[3], H. Simon[2], B. Sitar[6], P. Strmen[6], K. Sümmerer[2], V. Volkov[1], H. Weick[2], and J. Winfield[2]

[1]Technische Universität Darmstadt, Germany; [2]GSI, Darmstadt, Germany; [3]Universidad de Santiago de Compostela, Spain; [4]Technische Universität München, Germany; [5]Tohoku University, Sendai, Japan; [6]Univerzita Komenskeho, Bratislava, Slovakia

Two-nucleon knockout reactions of the more deficient nucleon species have the property to proceed as an almost completely direct process which makes them interesting for nuclear spectroscopy [1]. The FRS experiment S341 studied, amongst other things, an example of such a reaction, the two-neutron knockout reaction from ^{11}C. For this reaction the momentum distribution was measured as well as the reaction cross section.

If one compares the cross sections obtained experimentally to those calculated by the theory described above, one often observes that the experimental values are significantly lower. As a measure of these deviations one can define a reduction factor by taking the ratio of the experimentally and theoretically found spectroscopic factors or, in the case of a knockout reaction, by taking the ratio of the experimental and theoretical cross sections [1, 2].

The ^{11}C beam was created by a particle beam of 1670 AMeV ^{12}C hitting a 4 $\frac{\mathrm{g}}{\mathrm{cm}^2}$ production target placed at the entrance of the FRS. It then impinged on a 4.8 $\frac{\mathrm{g}}{\mathrm{cm}^2}$ beryllium target at F2. The incident beam was identified using only the atomic mass obtained from the energy loss in a plastic scintillator in front of the target. The residues of the collision were identified using two scintillators at F3 which were used to measure the energy loss of the particles as well as their time of flight.

TPCs and multiwire chambers at F2 and F3 were used to measure the positions of the ions, and to reconstruct their momentum distribution. The position distribution at F3 was tracked back to the focal plane and is hence proportional to the parallel momentum. Since the FRS was used in a non-achromatic mode it was necessary to correct the momentum distribution of the reaction residues for the influence of the reactions in the production target. This was done by substracting the momentum spread of the incoming beam.

The reaction cross section was measured to be σ = (2.89 $\pm$ 0.12) mb. Together with a theoretical cross section of 4.55 mb [3] this corresponds to a reduction factor of R_s = 0.63 $\pm$ 0.03. The position distribution of the detected ^{11}C at F3 is shown in figure 1. The function fitted to the experimental data is a convolution of a Gaussian with the response function of the spectrometer. The width of the momentum distribution of the reaction residues was found to be $\sigma_p = (133 \pm 7)\frac{\mathrm{MeV}}{\mathrm{c}}$. This corresponds well with a knockout of two single, strongly bound nucleons and supports that the the two-neutron knockout ^{11}C proceeds as a completely direct reaction.

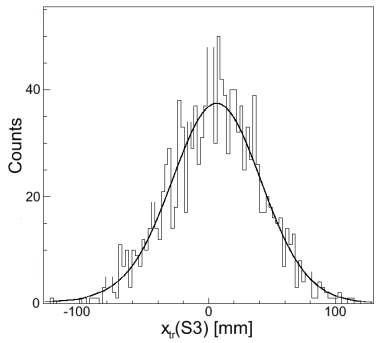

Figure 1: The position distribution at F3 for ^{9}C.

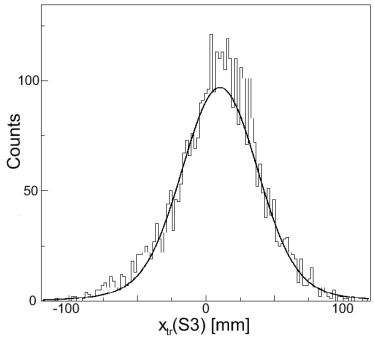

Figure 2: The position distribution at F3 for ^{9}Be.

The two-proton knockout from ^{11}C was also examined. Here a significant contribution from indirect reaction processes is expected. In agreement with this expectation, a significantly larger reaction cross section of σ = (8.36 $\pm$ 0.41) mb was measured (preliminary). The position distribution of the detected ^{11}C at F3 is shown in figure 2. The width of the momentum distribution was found to be $\sigma_p = (135 \pm 8)\frac{\mathrm{MeV}}{\mathrm{c}}$.

References

[1] P.G. Hansen, J.A. Tostevin, Annu. Rev. Nucl. Part. Sci. 53 (2003)

[2] A. Gade et al., Phys. Rev. C 77 (2008)

[3] J.A. Tostevin, private communication

*Work supported in part by the GSI Research and Development Program (DA PIET) and by the BMBF (06DA9040I)

Study of ^{27,28}Ne via one-neutron knockout reactions

C. Rodríguez-Tajes* for the S245 collaboration[1]

[1]USC (Spain), IEM CSIC (Spain), GSI (Germany), TUM (Germany), Chalmers (Sweden), CERN (Switzerland), Saint Mary's (Canada)

The proximity of neutron-rich neon isotopes to the *island of inversion* has motivated several experimental studies in the last years. The description of the results obtained for the most exotic nuclei requires SDPF-M calculations, which allow the mixing sd and pf configurations. This is the case for the 3/2$^-$ level of ^{27}Ne at 765 keV and the first excited state of ^{28}Ne, located at 1293 keV, with $I^\pi = 2^+$. Experimental evidences that show the importance of intruder states in the ground-state configuration of ^{28}Ne have also been found [1].

In the work presented here, the ground state of ^{27,28}Ne was explored by means of one-neutron knockout reactions in a beryllium target at relativistic energies. In the high energy regime, stripping reactions dominate the process and the measurement of the longitudinal-momentum distribution of the A-1 fragment can be used to identify the orbital angular momentum of the removed neutron inside the projectile. This interpretation assumes that the target is transparent to the A-1 fragment and is commonly known as the transparent limit of the Serber model [2].

The experiment was performed in the Fragment Separator (FRS), at GSI. A fully ionised ^{40}Ar primary beam was accelerated up to 700 MeV/nucleon and directed towards a beryllium target located at the entrance of the FRS, where a cocktail of exotic neutron-rich projectiles, with Z = 6-13 and N = 9-22, was produced via fragmentation reactions. The identification and selection of the projectiles were performed in the first stage of the FRS. Then, the one-neutron knockout reaction took place at the intermediate focal plane, in a 1720 mg/cm^2 beryllium target, and the second part of the FRS was dedicated to the analysis of the resulting knockout fragments. The different detectors included in this experimental setup allowed a clean determination of the reaction channel, based on the identification of both the projectile and the A-1 fragment.

The longitudinal-momentum distribution of the fragments was measured by Time Projection Chambers. The interpretation of this observable was carried out with the help of a simple theoretical model that takes into account the fact that only the outer part of the wave function is sampled with this technique by using the asymptotic form of the wave function and including a lower cut-off on the impact parameter [3]. The ground-state structure of the ^{27,28}Ne projectiles was descibed as the contribution of two different $core(I^\pi, E) \otimes neutron(l)$ configurations, where I^π and E refer to the spin-parity and to the excitation energy of the core and l is the orbital angular momentum of the copupled neutron. On this basis, an admixture of two different functions, each representing a $core \otimes neutron$ configuration, was used to fit the measured momentum distributions. The results obtained with this procedure are displayed in Fig. 1. A major $l = 2$ component was expected due to the population of the $0d_{3/2}$ neutron orbital at N = 17. However, the analysis of the momentum distributions clearly contradicts this hypothesis, showing that these nuclei are dominated by $s_{1/2}$ neutrons coupled to an excited core. In particular, it was found that excited core states contribute with probabilities of 64 ± 12 and 81 ± 9 % to the ground state of ^{27}Ne and ^{28}Ne, respectively.

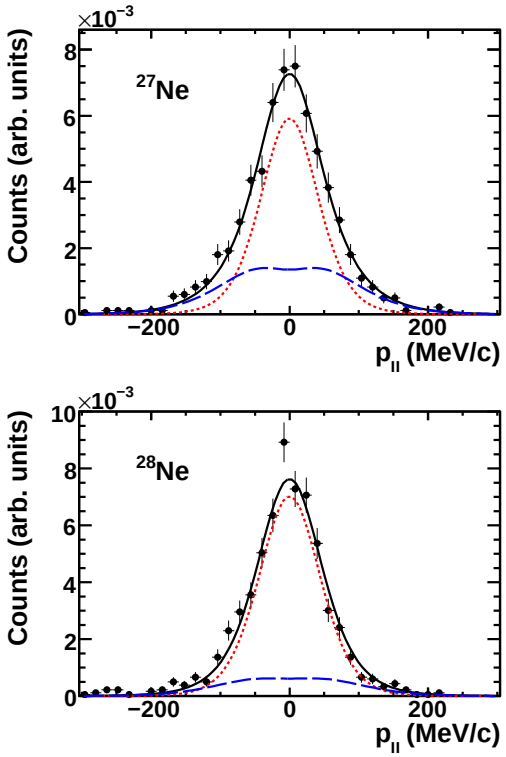

Figure 1: Inclusive momentum distribution of ^{26,27}Ne after one-neutron knockout of ^{27,28}Ne (normalised to unity). The solid lines represent the fit to the experimental data. The dotted (dashed) lines correspond to the calculated $l = 0$ ($l = 2$) contributions.

References

[1] J. R. Terry et al., Phys. Lett. B 640 (2006) 86.

[2] R. Serber, Phys. Rev. 72 (1947) 284.

[3] M. Smedberg, PhD thesis, Chalmers tekniska höskola och Göteborgs universitet (1998).

* carme.rodriguez@usc.es

One-Neutron-Knockout Reactions on Scandium Isotopes*

S. Schwertel[†1], R. Gernhäuser[1], P. Maierbeck[1], R. Krücken[1], T. Kröll[1], H. Alvarez-Pol[2], F. Aksouh[3], T. Aumann[3], K. Behr[3], E.A. Benjamim[2], J. Benlliure[2], V. Bildstein[1], M. Böhmer[1], K. Boretzky[3], M.J.G. Borge[4], A. Brünle[3], A. Bürger[5,6], M. Caamano[2], A. Chatillon[3], L.V. Chulkov[3], D. Cortina-Gil[2], J. Enders[7], K. Eppinger[1], T. Faestermann[1], J. Friese[1], L. Fabbietti[1], M. Gascon[2], H. Geissel[3], J. Gerl[3], M. Gorska[3], P.G. Hansen[†8], B. Jonson[9], R. Kanungo[3,10], O. Kiselev[3], I. Kojouharov[3], A. Klimkiewicz[3], T. Kurtukian[2], N. Kurz[3], K. Larsson[3,9], T. Le Bleis[3], K. Mahata[3], L. Maier[1], T. Nilsson[7], C. Nociforo[3], G. Nyman[9], C. Pascual-Izarra[4], A. Perea[4], D. Perez[2], A. Prochazka[3,11], C. Rodríguez-Tajes[2], D. Rossi[3,12], H. Schaffner[3], G. Schrieder[7], H. Simon[3], B. Sitar[11], M. Staniou[3], K. Sümmerer[3], O. Tengblad[4], H. Weick[3], and S. Winkler[1]

[1]TU München, Physik-Department E12, Garching, Germany; [2]USC, Santiago de Compostela, Spain; [3]GSI, Darmstadt, Germany; [4]CSIC, Madrid, Spain; [5]CEA, Saclay, France; [6]ISKP, Bonn, Germany; [7]TU Darmstadt, Germany; [8]MSU, East Lansing, USA; [9]Chalmers University of Technology, Göteborg, Sweden; [10]St. Mary's University, Halifax, Canada; [11]Comenius University, Bratislava, Slovakia; [12]Johannes Gutenberg Universität, Mainz, Germany

It is known for many years that the structure of nuclei far away from the valley of stability changes. E.g. there is a new shell closure predicted for N = 34 in ^{54}Ca [1]. In recent years knockout reactions have proven to be important tools for investigations of the structure of light exotic nuclei. An experiment extending this method to medium-mass nuclei with energies of about 400 MeV was performed with the fragment separator (FRS) at GSI.

The FRS was operated in the dispersion matched mode where the dispersion of the first half is cancelled by the dispersion of the second half and the momentum transfer can be measured directly. A 500 AMeV ^{86}Kr beam was fragmented on a 1625 mg/cm^2 ^{9}Be production target. The knockout target (1720 mg/cm^2 ^{9}Be) was located at S2. Because of the high acceptance of the FRS, mother and daughter nuclei of one-neutron knockout reactions in the isotopes ^{51,52,53,54,55}Sc were transported with high efficiency. The fragments were identified before and after the knockout target. So the one-neutron-knockout reaction can be measured for each isotope.

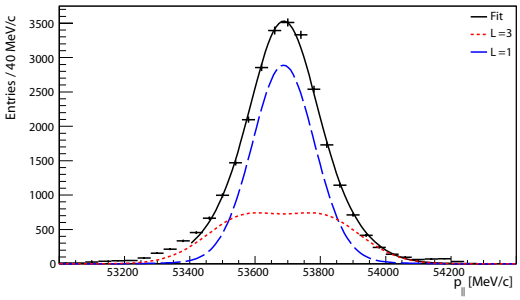

Figure 1: Longitudinal momentum distribution of the reaction ^{53}Sc → ^{52}Sc with a fit function and its contributions from different orbital angular momenta including the expected resolution.

In ^{51,52,53,54,55}Sc single neutrons will be knocked-out mostly from the $f_{7/2}$, the $p_{3/2}$, $p_{1/2}$ (^{54,55}Sc) or $f_{5/2}$ orbitals. Fig. 1 shows the longitudinal momentum distribution for the reaction ^{53}Sc → ^{52}Sc. The continous line is a fit, which consists of a L = 1 and a L = 3 part. In dashed and dotted these parts are shown according to their contribution to the fit. For this reaction an inclusive knockout cross section of 101(15) mbarn was determined with an assignment of 65(10) mbarn to L = 1 and 36(15) mbarn to L = 3. Fig. 2 shows the measured (stars) and calculated (squares) [2] inclusive cross sections for all isotopes (left) and for knockout of a L = 3 neutron (right).

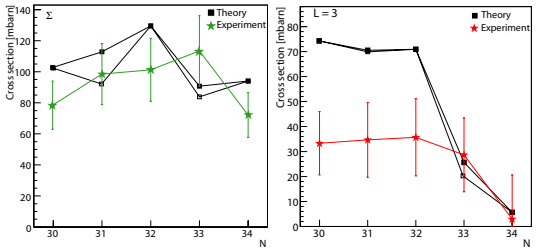

Figure 2: Knockout cross sections for one-neutron removal from L = 1 and L = 3 orbital (left) and from L = 3 orbital (right) vs. neutron number for experiment (stars) and theory (squares), respectively.

The experimental and theoretical inclusive cross sections are consistent as well as the cross sections for knockout of a L = 1 neutron. For L = 3 neutrons we observe good agreement for ^{55}Sc and ^{54}Sc, but for the other isotopes there is a discrepancy of a factor of about two. A reason could be that the actual spectroscopic strength is different than expected from theory as collective excitations are not taken into account. This could lead to lower cross sections.

The decrease of the L = 3 cross section for N = 34 shows that the $f_{5/2}$ orbital is relatively high above the $p_{1/2}$ orbital. This confirms that the residual interaction GXPF1A [3], which results in this orbital order and in a shell closure for this neutron number, describes the data very well confirming findings in different measurements [4].

References

[1] M.Honma et al., Phys. Rev. C 65, 061301,2002
[2] T. Otsuka and J.A. Tostevin, private communication
[3] T.Otsuka et al., Phys. Rev. Lett. 87,08502, 2001
[4] P.Maierbeck, PhD Thesis, 2009

* Work supported by GSI, BMBF, DFG (Exc. Clust. 153-Universe), and EU (RII3-EURONS 506065)

† sabine.schwertel@ph.tum.de

Electromagnetic Excitation of Neutron-Rich Ni Isotopes *

T. Le Bleis[1,2,3], D. Rossi[4], P. Adrich[1], F. Aksouh[1], H. Alvarez-Pol[5], T. Aumann[1], J. Benlliure[5], M. Boehmer[6], K. Boretzky[1], E. Casarejos[5], M. Chartier[7], A. Chatillon[1], D. Cortina-Gil[5], U. Datta Pramanik[8], H. Emling[1], O. Ershova[1,3], B. Fernandez-Dominguez[7], H. Geissel[1], M. Gorska[1], M. Heil[1], H. Johansson[1,9], A. R. Junghans[10], A. Klimkiewicz[1,11], O. Kiselev[1,4], J.V. Kratz[4], N. Kurz[1], M. Labiche[12], R. Lemmon[13], Y. Litvinov[1], K. Mahata[1], P. Maierbeck[6], T. Nilsson[9], C. Nociforo[1], R. Palit[14], S. Paschalis[7], R. Plag[1,3], R. Reifarth[1,3], H. Simon[1], K. Sümmerer[1], A. Wagner[10], W. Walus[11], H. Weick[1], and M. Winkler[1]

[1]GSI, Darmstadt, Germany; [2]IPHC, Strasbourg, France; [3]Univ. Frankfurt, Germany; [4]Univ. Mainz, Germany; [5]Univ. Santiago de Compostela, Spain; [6]TU Munich, Germany; [7]Univ. Liverpool, UK; [8]SINP Kolkata, India; [9]Chalmers Göteborg, Sweden; [10]FZ Dresden Rossendorf, Germany; [11]Jagiellonian Univ., Krakow, Poland; [12]Univ. Paisley, UK; [13]Daresbury, UK; [14]TIFR Mumbai, India

As a response to an external electromagnetic field, a nucleus can be collectively excited to a Giant-Resonance state. The Giant Resonances, and in particular the isovector Giant Dipole Resonance (GDR), have been extensively studied both theoretically and experimentally in stable nuclei. In the early 1990s, theoretical studies predicted the presence of low-lying dipole strength below the GDR region in isospin-asymmetric nuclei. This new dipole mode, usually referred to as Pygmy Dipole Resonance (PDR), has been attributed to the oscillation of a neutron- or a proton-skin against an isospin-saturated core [1]. More recently, experimental developments allowed the investigation of the dipole response of short-lived nuclei. In particular, neutron-rich Sn isotopes were studied using heavy-ion-induced electromagnetic excitation at relativistic energies in inverse kinematics at the LAND-R^{3}B setup at GSI. The differential cross section $d\sigma/dE^*$, which is obtained from invariant-mass reconstruction, shows the presence of low-lying strength in the dipole response that cannot be explained by the GDR alone, and which has been associated with the Pygmy Resonance mentioned above [2].

In order to study the dipole response of neutron-rich Ni isotopes including ^{68}Ni, a similar experiment has been performed by the LAND collaboration using the Coulomb excitation technique. The neutron-evaporation channels have been investigated and the strength distribution was obtained. Measurements were performed with three different targets (C, Sn and Pb) in order to distinguish electromagnetic and nuclear-induced excitations. A measurement without target yielded the background contribution. While electromagnetic excitation occurs at impact parameters larger than the sum of the radii of the colliding nuclei, the nuclear contribution stems from a narrow impact-parameter range close to the grazing impact parameter b_c. This determines the target dependence of the nuclear cross section σ_N scaling basically with the sum of the two radii, i.e., $\sigma_N \propto A_T^{1/3} + A_P^{1/3}$. In addition to this 'black-disc' approach, we have considered a model taking into account the transparency of the nuclei for an impact-parameter range Δb, yielding $\sigma_N \propto \left[b_c - \frac{\Delta b}{2}\right]\Delta b$. Here, we adopt the parametrization of b_c based on empirical nuclear densities and Eikonal calculations, which has been checked against measured cross sections for electromagnetic dissociation of stable nuclei [3]. The charge dependence of the electromagnetic contribution $\sigma_C \propto Z_T^\alpha$ was determined from a semi-classical calculation resulting in, e.g., $\alpha = 1.61(2)$ for the $1n$ cross section of ^{68}Ni. Fits to the obtained cross sections with the three targets show that both models lead to the same results. It is then possible to determine the nuclear component of the interaction with Pb using the results obtained on C, e.g., $\sigma_N^{Pb} = 1.57(20)\sigma^C$ for ^{68}Ni.

The preliminary analysis of both integrated and differential cross sections for electromagnetic dissociation of $^{67-69}$Ni shows that the cross sections cannot be explained only by the excitation of the GDR with parameters from various systematics. In particular, a larger cross section in the low-energy part of the spectrum is observed, which can be described by the addition of extra dipole strength exhausting 5 to 10% of the energy-weighted sum rule. The comparison of our result, which refers to the dominant neutron-decay, with a recent (γ, γ') measurement for ^{68}Ni [4] yields a decay branching ratio of about 3% for the gamma back-decay of the Pygmy resonance in this nucleus.

Although the analysis is still on-going, we can say in summary that evidence for the presence of a low-energy component in the dipole-strength distribution of neutron-rich Ni isotopes has been obtained indicating, a systematic nature of the PDR mode.

References

[1] N. Paar *et al.*, Rep. Prog. Phys. 70 (2007) 691 and references cited therein.

[2] P. Adrich *et al.*, Phys. Rev. Lett. 95 (2005) 132501. A. Klimkiewicz *et al.*, Phys. Rev. C 76 (2007) 051603(R).

[3] T. Aumann *et al.*, Phys. Rev. C 51 (1995) 416; C.J. Benesh *et al.*, Phys. Rev. C 40 (1989) 1198.

[4] O. Wieland *et al.*, Phys. Rev. Lett. 102 (2009) 062502.

*This work is supported in part by BMBF grant 06MZ2221, by the HGF Young Investigators Project VH-NG-327, and by the Alliance Program of the Helmholtz Association (HA216/EMMI).

Gamow-Teller decay of the $T_Z = -1$ ^{62}Ge nucleus*

E.Grodner[1,2], A.Gadea[1,3], A.Algora[3], M.Gorska[4], G de Angelis[1], J.J.Valiente-Dobón[1], J.Grebosz[4,5], P.Boutachkov[4], L. Caceres[4], S.Pietri[4], Zs.Podolyak[6], H.Weick[4], J. Agramunt[3], L. Amon[7], E. Banioplu[7], D. Bazzacco[8], J. Benlliure[9], G.Benzoni[10], R. Burcu-Gakirli[7], A. Bracco[10], F.Camera[10], F.C.L.Crespi[10], P. Doornenbal[4], E.Farnea[8], W. Gelletly[6], H.Geissel[4], J.Gerl[4], T.Haberman[4], I.Kojouharov[4], N.Kurz[4], S.Leoni[10], S.Lunardi[8], D. Mengoni[8], F. Molina[3], A. Morales[9], B.Million[10], D.R.Napoli[1], R. Orlandi[1], Y. Okten[7], R. Page[11], D. Perez[9], F.Recchia[8], P.Regan[7], S. Rinta-Antila[11], B. Rubio[3], D.Rudolph[12], E.Sahin[1], H.Schaffner[4], B. S. Nara Singh[13], A. N. Steer[13], S.Verma[9], R. Wadsworth[13], O. Wieland[10], and H-J.Wollersheim[4]

[1]INFN-LNL, Legnaro, I; [2]University of Warsaw, Pl; [3]IFIC, CSIC - Uni. Valencia, E ; [4]GSI, Darmstadt, D; [5]IFJ PAN, Krakow, Pl; [6]Universiy of Surrey, Guildford, UK; [7]University of Istanbul, Tr; [8]Università and INFN Padova, I; [9]University of Santiago de Compostela, E; [10]Università degli Studi e INFN sezione di Milano, I; [11]University of Liverpool, U.K; [12]Lund University, S; [13]University of York, U.K.

The experiment to measure the β-decay of ^{62}Ge was performed at GSI using the *FRagment Separator* (FRS) and the *Rare Isotope Spectroscopic INvestigations at GSI* (RISING) setups [2, 1]. The fully stripped ^{62}Ge ions were produced by fragmentation of a ^{78}Kr beam with an energy of 750 $A \cdot MeV$ impinging on a ^{9}Be production target with a thickness of 4.0 g/cm^2 placed at the entrance position of the fragment separator FRS. The ^{78}Kr 750 $A \cdot MeV$ beam, provided by the GSI heavy-ion synchrotron SIS, had intensity about 4×10^9 ions per spill. The spill period was $\approx 9s$ thus providing an average primary ^{78}Kr beam intensity of $\approx 4 \times 10^8$ ions/s. The reaction products were selected in the FRS. The various FRS scintillation time-of-flight and ionization detectors were used to perform A and Z identification as well as position tracking for each individual ion [2]. At the final focal plane of FRS it was placed the RISING array in the stopped beam configuration [4] with the active implantation setup in the center of the array. RISING consist of 15 Cluster composite detectors [3] in this case mounted in a close configuration with an average 22 cm distance from the centre of the implantation detector to the front face of the Cluster detectors [4]. For the present experiment an efficiency of about 9%, for the ^{60}Co source 1.3 MeV transition, has been determined for the array. The active implantation setup for RISING [5] consisted on six 1 mm thick double-sided silicon strip detectors (DSSSD).

In a first step od data analysis the lifetime of ^{62}Ge isotope has to be extracted. This can be done from the spectrum of beta activity as a function of time. Such a spectrum contains not only^{62}Ge$\rightarrow^{62}$Ga decay events but also the activity of ^{62}Ga$\rightarrow^{62}$Zn transition making lifetime analysis difficult. To unbind the result from the decay of ^{62}Ga daughter nucleus special beta activity spectrum was constructed. In this spectrum a time distribution of the first beta decay was collected if the second one was detected. In such a way the activity spectrum got clean (only ^{62}Ge has double sequential decay) and contained only single exponential decay of the nucleus of interest. A lifetime of $\tau = 119.6(\pm 20)ms$ has been measured for the ^{62}Ge ground state.

GT transition from ^{62}Ge leads to 1^+ states of ^{62}Ga which then decay via gamma transitions to the ground state of ^{62}Ga.The gamma spectrum was constructed from triple coincidences: FRS implantation - beta - gamma. A polygon gate on Z vs A/q spectrum from FRS was set in order to select the implantation of ^{62}Ge nuclei only. Gamma quanta were registered when a beta decay was detected by silicon detectors in the given time limits after the implantation The resulting spectrum can be seen in Fig.1.

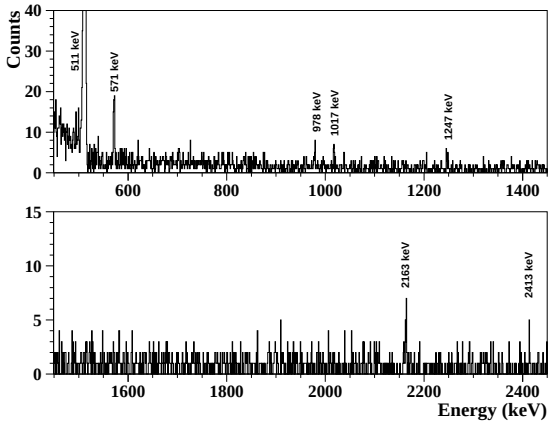

Figure 1: Gamma-ray spectrum populated in the decay of ^{62}Ge

References

[1] H. Wollersheim, *et al.*, Nucl. Instr. and Meth. **A537**, 637 (2004)

[2] H. Geissel, *et al.*, Nucl. Instr. and Meth. **B70**, 286 (1992); Ann. Rev. Nucl. Part. Sci. **45**, 163 (1995).

[3] J. Eberth, *et al.*, Nucl. Instr. and Meth. **A369**, 135 (1996).

[4] S. Pietri, *et al.*, Acta Phys. Pol. **38**, 1255 (2007); Nucl. Instr. and Meth. **B261**, 1079 (2007).

[5] R. Kumar,*et al.*, Nucl. Instr. and Meth. in press.

* Work supported by EU, EURONS contract No. 506065.

News from the S352 experiment – Isomer spectroscopy of ^{96}Ag *

P. Boutachkov[1], M. Górska[1], H. Grawe[1], N. Braun[2], T. Brock[3], A. Blazhev[2], B.S. Nara Singh[3], Z. Liu[4], R. Wadsworth[3], S. Pietri[1], C. Domingo-Pardo[1], S. Steer[5], L. Cáceres[1], T. Faestermann[6], F. Farinon[1], N. Goel[1], J. Gręboszˇ[7], R. Hoischen[1,8], I. Kojuharov[1], N. Kurz[1], C. Nociforo[1], J. Nyberg[9], A. Prochazka[1], Zs. Podolyák[5], H. Schaffner[1], P-A. Söderström[9], H. Weick[1], A. Ataç[10], L. Bettermann[2], K. Eppinger[6], T. Engert[1], F. Finke[2], K. Geibel[2], J. Gerl[1], A. Gottardo[4], C. Hinke[6], G. Ilie[2], H. Iwasaki[2], J. Jolie[2], R. Krücken[6], E. Merchán[11], M. Pfützner[12], P. Regan[5], P. Reiter[2], D. Rudolph[8], S. Rinta-Antila[13], C. Scholl[2], N. Warr[2], H-J. Wollersheim[1], and P. Woods[4]

[1]GSI, Darmstadt, Germany; [2]University of Cologne, Germany; [3]University of York, UK; [4]University of Edinburgh, UK; [5]University of Surrey, UK; [6]Technische Universität München, Germany; [7]IFJ PAN, Krakow, Poland; [8]Lund University, Sweden; [9]Uppsala University, Sweden; [10]Ankara University, Turkey; [11]Universidad Nacional de Colombia, Colombia; [12]Warsaw University, Poland; [13]University of Liverpool, UK

The S352 experiment investigated isomeric and β decay of $N \sim Z$ Cd, Ag and Pd isotopes. This study provides information on the p-n interaction and the shell evolution around the N=Z=50 shell closure [1], and it can be used as a benchmark for large-scale shell-model calculations.

The experiment was performed in July 2008 with the RISING stopped-beam setup [2, 3] at the GSI-FRS facility [4]. Fragmentation of ^{124}Xe on a ^{9}Be target was used to produce the nuclei of interest [5]. In Fig. 1 an identification plot, including the N=Z+2 nuclei ^{96}Ag, ^{98}Cd and ^{94}Pd is shown. Preliminary results on ^{94}Pd and ^{98}Cd were reported in Refs. [6] and [7, 8], respectively. In this report we present new results on ^{96}Ag.

In $^{96}_{47}$Ag$_{49}$ a microsecond isomer and two γ-ray transitions from its decay were known [9]. The new data from the S352 experiment revealed three isomers, with life times ranging from hundreds of nanoseconds to tens of microseconds. These data extend the level scheme to high-spin spherical structures, including core-excited states. The quality of the data allowed for $\gamma - \gamma$ coincidence analysis, uniquely placing the observed transitions in the ^{96}Ag level scheme. A spectrum with γ-transitions depopulating the isomers in ^{96}Ag is shown in Figure 2.

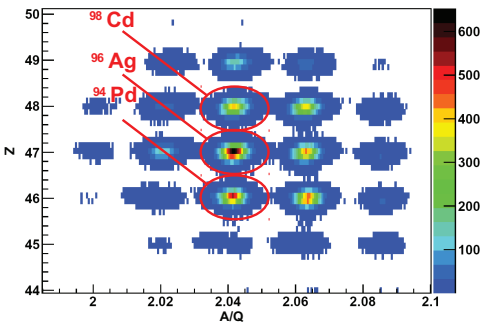

Figure 1: A Z vs A/Q identification plot of the nuclei under investigation in the S352 run. The ^{98}Cd, ^{96}Ag and ^{94}Pd nuclei are marked with red circles.

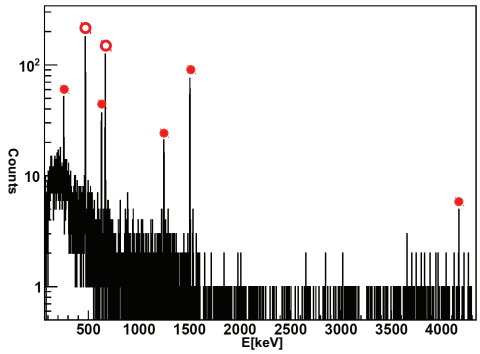

Figure 2: A preliminary γ-ray spectrum of the isomeric decays of ^{96}Ag fragments. The transitions marked with filled circles were observed for the first time in this experiment. The 470 and 668 keV transitions, marked with open circles were reported in Reference [9].

In the reported measurement, only part of the approved beam time of the S352 experiment was completed. The remaining beam time will be devoted to the completion of the original goals of the experiment. The analysis of the data for further isomeric decays and $\beta - \gamma$ correlations is currently in progress.

References

[1] H. Grawe *et al.*, Eur. Phys. J A**27**, S01, (2006) 257.

[2] S. Pietri *et al.*, Nucl. Inst. and Meth. B**261** (2007) 1079.

[3] R. Kumar *et al.*, Nucl. Inst. and Meth. A**598** (2009) 754.

[4] H. Geissel *et al.*, Nucl. Instr. and Meth. B**70** (1992) 286.

[5] P. Boutachkov *et al.*, GSI Scientific Report (2008) 149.

[6] R. Wadsworth *et al.*, Acta. Phys. Pol. B**40** (2009) 611.

[7] A. Blazhev *et al.*, J. Phys.: Conf. Ser. (2010) in press.

[8] A. Blazhev *et al.*, this Scientific Report.

[9] R. Grzywacz *et al.* Phys. Rev. C**55** (1997) 1126.

* Work supported by BMBF 06KY205I and 06MT238 (Germany), by STFC (UK) and the Swedish Science Council.

News from experiment S352 – Isomer spectroscopy of ^{98}Cd *

A. Blazhev[1], N. Braun[1], H. Grawe[2], P. Boutachkov[2], B.S. Nara Singh[3], T. Brock[3], Z. Liu[4], R. Wadsworth[3], M. Górska[2], S. Pietri[2], C. Domingo-Pardo[2], I. Kojuharov[2], L. Cáceres[2], T. Engert[2], F. Farinon[2], J. Gerl[2], N. Goel[2], J. Grębosz[5], R. Hoischen[2,6], N. Kurz[2], C. Nociforo[2], A. Prochazka[2], H. Schaffner[2], S. Steer[7], H. Weick[2], H-J. Wollersheim[2], A. Ataç[8], L. Bettermann[1], K. Eppinger[9], F. Finke[1], T. Faestermann[9], K. Geibel[1], A. Gottardo[4], C. Hinke[9], G. Ilie[1], H. Iwasaki[1], J. Jolie[1], R. Krücken[9], E. Merchan[10], F. Nowacki[11], J. Nyberg[12], M. Pfützner[13], Zs. Podolyák[7], P. Regan[7], P. Reiter[1], D. Rudolph[6], S. Rinta-Antila[14], C. Scholl[1], P-A. Söderström[12], N. Warr[1], and P. Woods[4]

[1]University of Cologne, Germany; [2]GSI, Darmstadt, Germany; [3]University of York, UK; [4]University of Edinburgh, UK; [5]IFJ PAN, Krakow, Poland; [6]Lund University, Sweden; [7]University of Surrey, UK; [8]Ankara University, Turkey; [9]Technical University of Munich, Germany; [10]Universidad Nacional de Colombia, Colombia; [11]IPHC, Strasbourg, France; [12]Uppsala University, Sweden; [13]Warsaw University, Poland; [14]University of Liverpool, UK

Studies of isomerism in the neutron-deficient $N \simeq Z$ nuclei around ^{100}Sn give important insights into the role of proton-neutron pairing, serve as testing grounds for nuclear models and give input for understanding the astrophysical rp-process [1]. In the S352 Stopped-RISING experiment the nuclei of interest were produced via the fragmentation of a ^{124}Xe beam on a ^{9}Be target, selected and identified by the FRS [2] and finally implanted into an active stopper [3]. The active stopper was surrounded by the highly efficient RISING Ge-array [4] and γ rays correlated with ion implantation and particle decays were collected.

Although only half of the approved beam time was used, several new isomeric states and γ rays in different isotopes were discovered. Preliminary results on ^{94}Pd [5], ^{96}Ag [6] and ^{98}Cd [7] were already reported at some conferences.

The preliminary results from the S352 experiment have revealed a new high-energy isomeric γ-ray transition in ^{98}Cd, which confirmed previous spin-parity assignments and enabled, for the first time, the measurement of the $E2$ and $E4$ strength for the two decay branches of the high-energy core-excited (12^+) isomer [7, 8]. Figure 1 presents a γ-ray spectrum gated on implanted ^{98}Cd ions showing the new isomeric transition. Both the γ-γ-coincidence relations as well as the halflife suggest the existence of an alternative cascade $(12^+) \rightarrow (10^+) \rightarrow (8^+)$, with a ($10^+$) state at 6585 keV, and an $E2$ character of the new 4157 keV high-energy transition (Fig. 1) [7]. This also implies an experimentally non-observed 50 keV $E2$ isomeric transition depopulating the (12^+) state and feeding the (10^+) state [7]. With this assignment from the measured halflife and the observed branching the preliminary transition strengths $B(E2; 12^+ \rightarrow 10^+) = 2.1(13)$ W.u. and $B(E4; 12^+ \rightarrow 8^+) = 3.0(10)$ W.u. are inferred [7].

The new experimental results on the (12^+) and (10^+) states in ^{98}Cd reveal problems with previous large-scale shell-model calculations [8]. Currently, two possible microscopic explanations exist [7]. The first one requires a "reversed" ordering of the neutron $d_{5/2}$ and $g_{7/2}$ orbitals above the $N = 50$ shell gap, i.e. $\nu d_{5/2}$ lies higher than $\nu g_{7/2}$, while the second explanation needs an increased strength of proton particle-hole excitations across the $Z = 50$ shell gap. Nuclear structure data on ^{98}Cd is thus of key importance since it allows the fine tuning of the effective interaction around the ^{100}Sn.

The analysis of the data for further isomeric decays and $\beta - \gamma$ correlations continues.

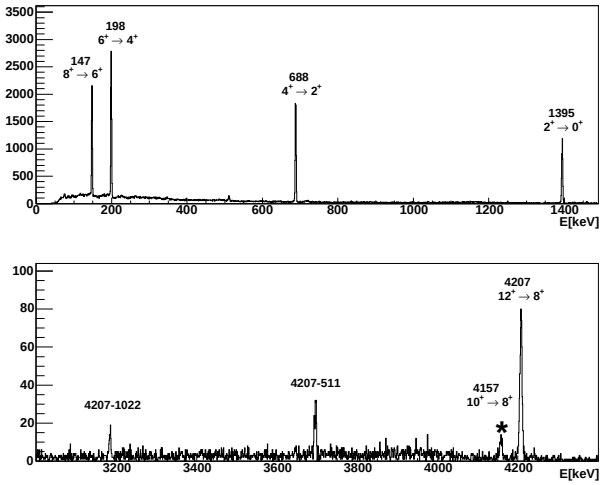

Figure 1: Preliminary γ-ray spectrum gated on implanted ^{98}Cd ions. The new transition is marked with an asterisk.

References

[1] H. Grawe *et al.*, Eur. Phys. J A**27**, S01, (2006) 257.

[2] H. Geissel *et al.*, Nucl. Instr. and Meth. B**70** (1992) 286.

[3] R. Kumar *et al.*, Nucl. Inst. and Meth. A**598** (2009) 754.

[4] S. Pietri *et al.*, Nucl. Inst. and Meth. B**261** (2007) 1079.

[5] R. Wadsworth *et al.*, Acta Phys. Pol. B**40** (2009) 611.

[6] P. Boutachkov *et al.*, this scientific report, and in preparation.

[7] A. Blazhev *et al.*, J. Phys.: Conf. Ser. (2010) in press.

[8] A. Blazhev *et al.*, Phys. Rev. C**69** (2004) 064304.

* Work supported by BMBF 06KY205I and 06MT238 (Germany), by STFC (UK) and the Swedish Science Council.

Decay Properties of ^{100}Sn *

C.Hinke[1], N.Al-Dahan[2], N.Alkhomashi[2], A.Atac[3], A.Blazhev[4], M.Böhmer[1], P.Boutachkov[5], N.Braun[4], L.Caceres[5], I.Čeliković[6], T.Davinson[7], G.deFrance[8], I.Dillmann[1], C.Domingo-Pardo[5], P.Doornenbal[9], K.Eppinger[1], T.Faestermann[1#], G.Farell[2], F.Farinon[5], H.Geissel[5], J.Gerl[5], R.Gernhäuser[1], N.Goel[5], M.Górska[5], A.Gottardo[7], H.Grawe[5], J.Grębosz[10], T.Habermann[5], R.Hoischen[5], R.Janik[11], M.Karny[12], A.Kaskas[3], I.Kojouharov[5], Th.Kröll[1], R.Krücken[1], N.Kurz[5], M.Lewitowicz[8], Y.Litvinov[5], Z.Liu[7], L.Maier[1], S.Myalski[10], F. Nebel[1], S.Nishimura[9], C.Nociforo[5], J.Nyberg[13], A.Parikh[1], S.Pietri [2,5], Zs.Podolyák[2], A.Procházka[5], P.H.Regan[2], C.Rigollet[14], H.Schaffner[5], C.Scheidenberger[5], S.Schwertel[1], P.-A.Söderström[13], S.Steer[2], K.Steiger[1], A.Stolz[15], P.Strmeň[11], H.Weick[5], H.J.Wollersheim[5], P.J.Woods[7], and the RISING collaboration

[1] TU München, [2]U of Surrey, [3]U of Ankara, [4]U of Köln, [5]GSI , [6]Inst. Vinca Belgrade, [7]U of Edinburgh, [8]GANIL, [9]RIKEN, [10]IFJ PAN Krakow, [11]U of Bratislava, [12]U of Warsaw, [13]U of Uppsala, [14]KVI - U of Groningen, [15]MSU

The analysis of the data obtained in 2008 [1] for neutron deficient nuclei produced by fragmentation of a ^{124}Xe beam has progressed. Here we concentrate on the decay properties of ^{100}Sn, of which we identified about 250 ions.

The time distribution of decay events after ^{100}Sn implantation in the same or neighbouring of the 1mm^3 pixels of the implantation detector yielded a preliminary value for the half-life of 1.16(0.20)s. This is much more precise than earlier values measured at GSI [2,3] or at MSU [4].

The β-decay of ^{100}Sn is supposed to populate essentially a single 1^+ state in ^{100}In, that is formed by coupling the $g_{9/2}$ proton hole to a $g_{7/2}$ neutron particle. In order to determine the decay energy we had placed on either side of the implantation detector 10mm of Si detectors as calorimeter. For every decay event the energies deposited in the implantation and calorimeter detectors were summed up and yielded the spectrum shown in Fig. 1. Around 200 keV there is a line originating presumably from a sum of converted transitions after electron capture decay. From the centroid of the energy distribution in the range indicated by the blue bar we determined a preliminary value for the endpoint energy of 3.15(20)MeV. There are still small corrections necessary for energy losses in the dead layers, but the quality of this result is very much improved compared to our earlier estimate based on 7 decays [2,3]. With the preliminary values for half-life and decay energy we calculate a log(ft) value of 2.54(20) which is the smallest of all known β-decays and thus ^{100}Sn shows the largest transition strength. The Gamov-Teller strength B_{GT}=11(4) shows a reduction by only a factor 1.6 compared to the value from the extreme single-particle model, where 10 protons contribute to the decay.

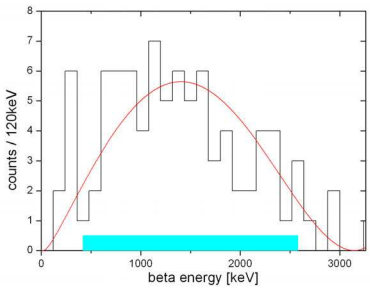

Fig. 1: β-spectrum of events following the implantation of identified ^{100}Sn nuclei. The red curve shows the calculated spectrum for an endpoint energy adjusted to have the same centroid as the measured spectrum in the range indicated by the blue bar.

With the 105 Ge-detectors of the RISING setup we measured with high efficiency for the first time the γ-spectrum after β-decay of ^{100}Sn, which is shown in Fig. 2. Besides the annihilation radiation we observe 5 lines after feeding the 1^+ daughter state(s) in ^{100}In. Shell model calculations predict a cascade of γ-transitions down to the 6^+ ground-state, but whether the observed γ-lines are all in cascade or in parallel branches, we cannot decide yet.

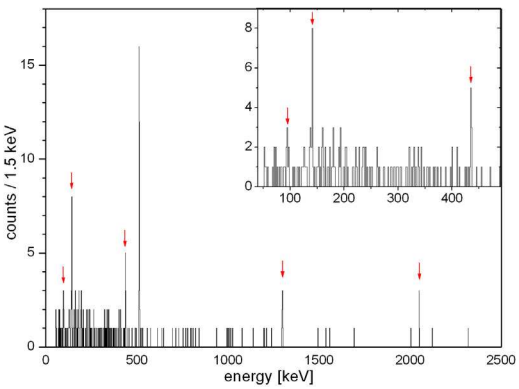

Fig. 2: γ-spectrum of events following the β-decay of identified ^{100}Sn nuclei. The low-energy part is shown enlarged in the inset.

References

[1] K. Eppinger et al., GSI Scientific Report 2008, p.147
[2] J. Friese, Proc. Hirschegg 1996, p. 123
[3] A. Stolz et al., AIP Conf. Proc. 610 (2002) 728 and T. Faestermann et al., EPJA15 (2002) 185
[4] D. Bazin et al., PRL 101 (2008) 252501

* work supported by MLL, BMBF, DFG, GSI, EPSRC, STFC(UK), and EURONS
# thomas.faestermann@ph.tum.de

Structure of excited states of ^{127}Cd

F. Naqvi[1,2], M. Górska[2], L. Cáceres[2,3], A. Jungclaus[3], M. Pfützner[4], H. Grawe[2], F. Nowacki[5], K. Sieja[5], S. Pietri[2], P.H Regan[6], D. Rudolf[7], Z. Podolyák[6], J. Jolie[1], K. Andgren[8], T. Beck[2], P. Bednarczyk[2,9], J. Benlliure[10], G. Benzoni[11], A.M Bruce[12], E. Casarejos[10], B. Cederwall[8], F. Crespi[11], P. Detistov[13], Zs. Dombrádi[14], P. Doornenbal[2], H. Geissel[2], J. Gerl[2], J. Grebosz[2,9], B. Hadinia[8], M. Hellström[7], R. Hoischen[2,7], G. Ille[1], A. Khaplanov[8], I. Kojouharov[2], M. Kmiecik[9], R. Kumar[15], N. Kurz[2], S. Lalkovski[12,13], A. Maj[9], S. Mandal[16], V. Modamio[3], F. Montes[2], S. Myalski[9], W. Prokopowicz[2], P. Rieter[1], H. Schaffner[2], G. Simpson[17], D. Sohler[14], S.J Steer[6], S. Tashenov[2], J. Walker[3], H.J Wollersheim[2], and O. Wieland[11]

[1]Institut für Kernphysik, Universität zu Köln, D-50937 Köln, Germany; [2]Gesselschaft für Schwerionenforschung(GSI), D-64291 Darmstadt, Germany; [3]Departmento de fisica Teórica, Universidad Autónoma de Madrid, E-28049 Madrid, Spain; [4]IEP, Warsaw University, PL-00681 Warsaw, Poland; [5]IReS, IN2P3-CNRS/University Louis Pasteur,F-67037,Strasbourg,France; [6]Department of Physics, University of Surrey, Guildford, Gu2 7XH, UK; [7]Department of Physics, Lund University, S-22100 Lund, Sweden; [8]KTH Stockholm,S-10691 Stockholm, Sweden; [9]The Henryk Niewodniczański Institute of Nuclear Physics, PL-31342 Kraków, Poland; [10]Universidad de Santiago de Compostela, E-175706 Santiago de Campostela, Spain; [11]INFN, Universitadegli Studi di Milano and INFN Sezione di Milano, I-20133 Milano, Italy; [12]School of Enigineering, University of Brighton, Brighton, Bn2 4GJ, UK; [13]Faculty of Physics, University of Sofia, Bg-1164, Sofia, Bulgaria; [14]Institute National Polytechnique de Grenoble, F-98026 Grenoble Cedex, France; [15]Inter University Accelerator Centre, New Delhi, India; [16]University of Delhi,New Delhi, India; [17]Institut Laue-Langevin, F-38042 Grenoble, France

The region around doubly magic ^{132}Sn has attracted intense research interest because of several features. Few valence particles/holes outside the inert core make the nuclei good candidates for studying the shell structure and residual interactions between valence nucleons in neutron rich environment. The astrophysical r-process, responsible for synthesizing heavy neutron rich nuclei in nature, follows a path along the N = 82 line up to Z = 50. To test the theoretical models explaining the r-process in this region, experimental data on the evolution of N = 82 nuclei is crucial. Therefore recently, several even mass Cd isotopes were investigated. To complete the systematics for odd heavy Cd isotopes, a detailed examination of data from the RISING experimental campaign using relativistic fragmentation of a ^{136}Xe beam performed at the FRagment Separator (FRS) at GSI was done.

Ions of ^{127}Cd were selected and identified in the FRS and were implanted in a plastic catcher, surrounded by a close geometry of 15 Ge cluster detectors from the RISING array. A single γ - ray spectrum containing five γ transitions at energies between 110 and 849 keV assigned to the decay of the isomer in ^{127}Cd is shown in Fig. 1.

Coincidence relations of observed γ transitions and intensity balance yielded the level scheme for ^{127}Cd as shown in Fig. 2. Spins and parities of the excited states were determined based on reduced transition probabilities and comparison with the systematics of known neighbouring odd-mass heavy Sn isotopes [1] . The isomerism in ^{127}Cd is attributed to a competition between M2 and E3 transitions from the $(19/2^+)$ state, formed from the coupling of $\pi g_{9/2}^{-2}$ and $\nu h_{11/2}^{-2} d_{3/2}^{-1}$. Comparison of experimental data with large scale shell model (LSSM)[2] and shell model (SM) calculations was performed . The discrepancy visible in the sequence of the $(13/2^-)$ and $(15/2^-)$ states is due to a deficiency in the quadrupole part of the interaction. Further details on experiment, analysis and interpretation will be given in the forthcoming paper[3].

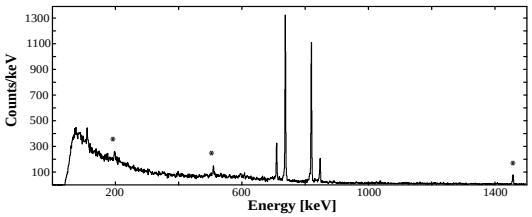

Figure 1: Single gamma ray energy spectrum of ^{127}Cd.

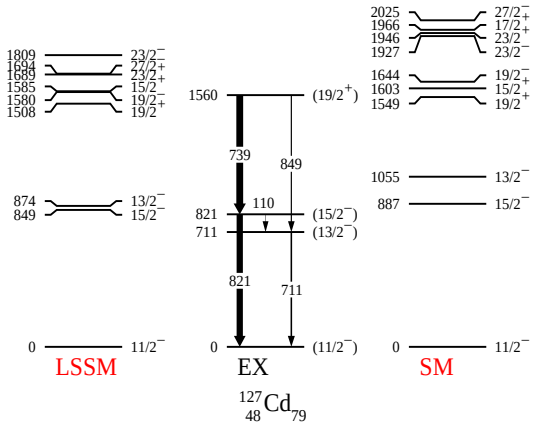

Figure 2: Level schemes of ^{127}Cd determined experimentally and calculated with LSSM and SM.

References

[1] R. Lozeva et al., Phys. Rev. C**77**, 064313 (2008).

[2] K. Sieja et al., to be published.

[3] F. Naqvi et al in preperation.

Isomeric states in ^{128}Cd

L. Cáceres[1,2], M. Górska[1], A. Jungclaus[2,3], M. Pfützner[4], H. Grawe[1], F. Nowacki[5], K. Sieja[1], S. Pietri[6], D. Rudolph[7], Zs. Podolyák[6], P. H. Regan[6], E. Werner-Malento[1,4], P. Detistov[8], S. Lalkovski[8,9], V. Modamio[2], J. Walker[2], K. Andgren[10], P. Bednarczyk[1,11], J. Benlliure[12], G. Benzoni[13], A. M. Bruce[9], E. Casarejos[12], B. Cederwall[10], F. C. L. Crespi[13], P. Doornenbal[1,14], H. Geissel[1], J. Gerl[1], J. Gręboszˇ[1,11], B. Hadinia[10], M. Hellström[7], R. Hoischen[1,7], G. Ilie[14,15], A. Khaplanov[10], M. Kmiecik[11], I. Kojouharov[1], R. Kumar[16], N. Kurz[1], A. Maj[11], S. Mandal[17], F. Montes[1], G. Martínez-Pinedo[1], S. Myalski[11], W. Prokopowicz[1], H. Schaffner[1], G. S. Simpson[18], S.J. Steer[6], S. Tashenov[1], O. Wieland[13], and H. J. Wollersheim[1]

[1]GSI, Darmstadt, Germany; [2]Departamento de Física Teórica, Universidad Autónoma de Madrid, Madrid, Spain; [4]IEP, Warsaw University, Warsaw, Poland; [5]IReS, IN2P3-CNRS/University Louis Pasteur, Strasbourg, France; [6]Department of Physics, University of Surrey, Guildford, GU2 7XH, UK; [7]Department of Physics, Lund University, S-22100 Lund, Sweden; [8]Faculty of Physics, University of Sofia, Sofia, Bulgaria; [9]School of Engineering, University of Brighton, Brighton, BN2 4GJ, UK; [10]KTH Stockholm, Stockholm, Sweden; [11]The Henryk Niewodniczański Institute of Nuclear Physics, PL-31342 Kraków, Poland; [12]Universidade de Santiago de Compostela, Santiago de Compostela, Spain; [13]INFN, Universitádegli Studi di Milano and INFN sezione di Milano, Milano, Italy; [14]Institut für Kernphysik, Universität zu Köln, Köln, Germany; [15]National Institute of Physics and Nuclear Engineering, Bucharest, Romania; [16]Inter University Accelerator Centre, New Delhi, India; [17]University of Delhi, New Delhi, India; [18]LPSC, Université Joseph Fourier Grenoble 1, CNRS/IN2P3, Institut National Polytechnique de Grenoble, F-38026 Grenoble Cedex, France

The flattening of the yrast 2^+ state systemactics from $N = 78$ to $N = 80$ in the Cd isotopic chain has awaken the interest of both experimentalists and theoreticians. Previous experimental results [1] suggest that the anomalous behavior of the $E(2^+)$ excitation energies could have its origin on the persistence of some collectivity in those very neutron-rich Cd nuclei approaching the neutron shell closure. Recent results based on isomeric decays studies in ^{130}Cd [2] and ^{131}In [3] have concluded the persistence of the $N = 82$ shell gap at $Z = 48$. Although the production cross section for ^{128}Cd, two-proton holes and two-neutron holes with respect to ^{132}Sn, is larger than the previously mentioned nuclei, its structural characteristic remained unknown up to date. In the S305 experiment performed within the RISING stopped beam campaign the decay pattern of ^{128}Cd has been unambiguously constructed based on $\gamma\gamma$ coincidence relations in conjunction with half-life analysis. The nucleus of interest was produced both by fragmentation of ^{136}Xe and fission of ^{238}U beams on a ^{9}Be target. In total 3.29×10^5 ^{128}Cd nuclei were identified. The high efficiency and granularity of the RISING HpGe array in combination with the particle detection provided by the FRagment Separator at GSI allowed to measure γ rays with 1% intensity of the main cascade crucial to unambiguously establish the decay pattern associated to ^{128}Cd. Three isomeric states have been identified at 1871 keV, 2108 KeV and 2714 KeV excitation energies. The spin and parity assignment to the levels is based on the electromagnetic transition probabilities, relative intensity balance, and inferred conversion coefficients. The experimental data indicates that the isomeric decay pattern is selective to the structure of the populated states and their leading π or ν configuration. This conclusion is further supported by comparison to large scale shell model calculations that yield an overall good agreement and additionally strengthen the spin and parity assignment. The deviation in level energies between experiment and shell model at intermediate spins reveal the need for further adjustment of the interaction that could be achieved by minor monopole corrections [4]. Further details of this work can be found in Ref. [5]

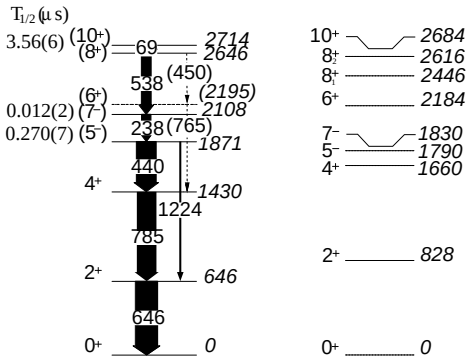

Figure 1: *Comparison of the deduced experimental level scheme for the isomeric decay of ^{128}Cd (left) with shell model calculations (right).*

References

[1] T. Kautzsch et al., Eur. Phys. J. A 9, 201 (2000).

[2] A. Jungclaus et al., Phys. Rev. Lett. 99, 132501 (2007).

[3] M. Górska et al., Phys. Lett. B 672, (2009).

[4] K. Sieja et al., unpublised.

[5] L. Cáceres et al., Phys. Rev. C 79, 011301(R) (2009).

MC Simulations for the PreSPEC campaign of AGATA at GSI

C. Domingo-Pardo[1], P. Doornenbal[2], E. Farnea[3], J. Gerl[1], E. Merchan[1], and M. Reese[4]
[1]GSI, Darmstadt, Germany; [2]RIKEN, Japan; [3]LNL, Legnaro, Italy; [4]TU-Darmstadt, Germany; [1]
and the AGATA and PRESPEC collaboration

Introduction

The next campaign of in-flight γ-ray spectroscopy experiments at the GSI Fragment Separator (FRS) will be performed, in the framework of the PreSPEC project [1], using the advanced γ-tracking array AGATA [2].

In order to exploit best its γ-efficiency and high intrinsic energy- and spatial-resolution, the geometry and the physical arrangement of this multidetector needs to be optimized according to the characteristics of the ion beam at the final focal plane of the FRS. To this aim we have performed systematic Monte Carlo calculations using the GEANT4-based AGATA code [3].

One of the main experimental constraints is the transversal spatial distribution of the FRS ion beam at the focal plane (approx. 6×4 cm^2 FWHM). Thus, the secondary beam covers an area larger than the standard AGATA pentagon holes, commonly used for the beam-pipe at other facilities like LNL [4]. According to our MC calculations, it became clear that a remarkable improvement in γ-ray sensitivity can be achieved for the setup at GSI when the standard AGATA triple cluster detectors are complemented with double cluster detectors (see Fig. 1). This conclusion has triggered the development and production of 5 AGATA double cluster detectors, which will be used for the experiments at GSI, and probably also later at GANIL.

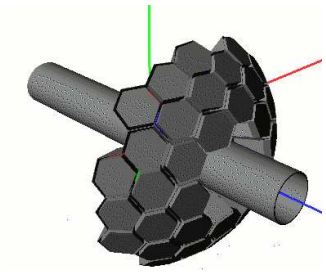

Figure 1: AGATA geometry proposed for the next fast-beam campaign at GSI. It consists of an inner ring of 5 double cluster plus an outer ring of 10 triple cluster AGATA detectors.

Estimated performance of AGATA at GSI

The performance of this setup has been evaluated on the basis of a MC study, where 1 MeV γ-rays were emitted from a nucleus at a recoil energy of $\sim$100 MeV/u or $\beta = 0.43$. A systematic study was carried out for different target-array distances in the range from 0 cm to 25 cm. For each particular experiment, the latter distance can be adjusted in such a way that efficiencies from 10% to 18% and γ-ray resolutions between 5 keV and 10 keV FWHM can be obtained. Such a performance corresponds to more than one order of magnitude improvement in terms of γ-ray sensitivity, when compared to the present existing RISING array based on Euroball cluster detectors.

Benchmark experiments

In PreSPEC, experiments with exotic nuclei will be carried out at beam energies around 100 MeV/u. The performance of the proposed AGATA geometry for a real experiment can be evaluated using the AGATA code [4] complemented with an Event-Generator [5] and a ROOT-based analysis code. Simulations of three representative types of experiments are being carried out, namely Coulomb excitation, fragmentation and plunger [6] lifetime measurements. The example shown in Fig. 2 corresponds to the simulation of the first excited states in ^{50}Fe produced after fragmentation of a ^{54}Ni-beam impinging at 120 MeV/u on a 700 mg/cm^2 Be-target.

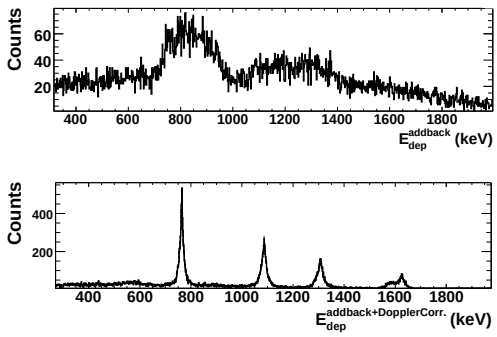

Figure 2: Raw (top) and Doppler-Corrected (bottom) γ-ray energy spectrum of the first excited states in ^{50}Fe.

References

[1] Gerl, J. March 2009 *Acta Physica Polonica B* **40**, 767.

[2] J. Gerl, W. Korten (Eds.) AGATA Technical report GSI, Darmstadt (2001).

[3] Farnea, E. August 2006 volume **853**, of American Institute of Physics Conference Series : pp. 473–478.

[4] Farnea, E. August 2009 volume **1165**, of American Institute of Physics Conference Series : pp. 390–393.

[5] Doornenbal P., Short Manual of a Geant4 Simulation Code for γ-Ray Detectors used in the RIKEN-RIBF Facility (2009).

[6] M. Reese, Simulations of PreSPEC Plunger experiments, AGATA Week, Legnaro (2010).

The HypHI Phase 0 experiment *

T.R. Saito† [1,2], S. Bianchin[1], O. Borodina[1,2], V. Bozkurt[1,3], B. Göküzüm[1,3], M. Kavatsyuk[4], E. Kim[1,5], S. Minami[1], D. Nakajima[1,6], B. Özel-Tashenov[1,3], C. Rappold[1,7], P. Achenbach[2], S. Ajimura[8], T. Aumann[1], C. Caesar[1], S. Erturk[3], T. Fukuda[9], E. Guliev[4], Y. Hayashi[10], T. Hiraiwa[10], J. Hoffmann[1], G. Ickert[1], Z.S. Ketenci[3], D. Khaneft[1,2], M. Kim[5], S. Kim[5], K. Koch[1], N. Kurz[1], Y. Ma[2,11], F. Maas[1,2], Y. Mizoi[9], M. Moritsu[10], T. Nagae[10], A. Okamura[10], W. Ott[1], J. Pochodzalla[2], A.Sakaguchi[12], M. Sako[10], C.J. Schmidt[1], M. Sekimoto[13], H. Simon[1], H. Sugimura[10], T. Takahashi[13], G.J. Tambave[4], K. Tanida[5], H. Tamura[11], M. Träger[1], W. Trautmann[1], S. Voltz[1], C.J. Yoon[5], and K. Yoshida[12]

[1]GSI,Darmstadt, Germany; [2]Johannes Gutenberg Universität Mainz, Mainz, Germany; [3]Nigde University, Nigde, Turkey; [4]KVI, Groningen, The Netherlands; [5]Seoul National University, Seoul, Korea; [6]The University of Tokyo, Tokyo, Japan; [7]Université Louis Pasteur Strasbourg, Strasbourg, France; [8]RCNP, Ibaraki, Japan; [9]Osaka Electro-Communication University, Osaka, Japan; [10]Kyoto University, Kyoto, Japan; [11]Tohoku University, Sendai, Japan; [12]Osaka University, Toyonaka, Japan; [13]KEK, Tsukuba, Japan

The HypHI collaboration has conducted the first physics production experiment, so called "Phase 0" in cave C. In the experiment, projectiles of ^{6}Li at 2 A GeV with an intensity in average of 5×10^{7} per spill (10 s spill length) were impinged in a graphite target with a thickness of 8 g/cm^2. The Phase 0 experiment was divided into two blocks; three days in August for commissioning and 11 days in October for data taking. The main goal of the experiment is to reconstruct events of light hypernuclei as $^{3}_{\Lambda}$H$\rightarrow^{3}$He$+\pi^-$, $^{4}_{\Lambda}$H$\rightarrow^{4}$He$+\pi^-$ and $^{5}_{\Lambda}$He$\rightarrow^{4}$He$+\pi^-+$p.

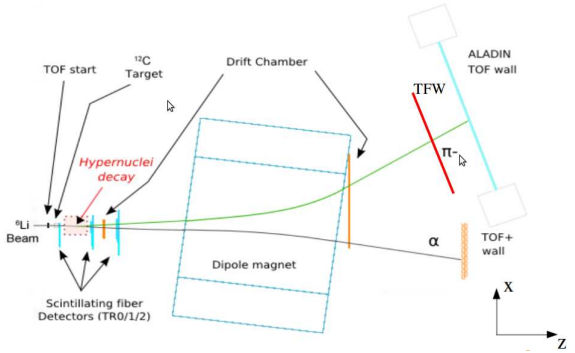

Figure 1: Experimental setup for the Phase 0 experiment

Figure 1 shows a schematic layout of the experimental setup for the October run. Beams are delivered from the left side of the figure. In front of the target, an array of plastic finger detectors, TOF-start, measures the projectiles and defines time-zero for the Time-of-Flight (TOF) measurements /cite. Behind the target, three arrays of scintillating fiber detectors (TR0, 1 and 2) were used to track charged particles in the horizontal and vertical directions [2, 3]. Between TR1 and TR2, a drift chamber was mounted for tracking charged particles. Since the drift chamber can not operate under the high beam intensity conditions, a beam killer has been developed by wrapping sense wires by teflon sheets around the beam region [4]. Behind these detectors, charged particles are separated by ALADiN dipole magnet at 0.75 T. Time and hit position of positively charged particles were measured by a TOF wall indicated as TOF+, and negatively charged particles dominated π^- are measured by two additional TOF walls referred as TFW and the ALADiN TOF wall [1]. Behind the ALADiN magnet, there is another drift chamber for tracking charged particles. For this drift chamber, a beam killer has also been implemented by connecting potential and sense wires around the beam region [4].

In the trigger level to the data acquisition system, events with secondary vertex events observed by the scintillating fiber detectors, positively charged particles with $Z = 1$ and 2 by TOF+, and negatively charged particles by TFW were selected in order to reduce the background events. Details of the trigger are found in ref. [5].

Data analysis is in progress. The current data analysis algorithm employes Hough transform and Kalman filter for the track finding and propagation [6]. Preliminary analyses have already revealed indications of Λ-hyperons and $^{5}_{\Lambda}$He [7, 8].

References

[1] S. Bianchin, O. Borodina, V. Bozkurt *et al.*, in these reports.

[2] D. Nakajima, B. Özel-Tashenov *et al.*, Nucl. Inst. Meth. A 608 (2009) 287-290.

[3] D. Nakajima, B. Özel-Tashenov *et al.*, in these reports.

[4] E .Kim, D. Nakajima, B. Özel-Tashenov *et al.*, in these reports.

[5] S .Minami, C. Rappold *et al.*, in these reports.

[6] C. Rappold *et al.*, in these reports.

[7] C. Rappold, Ph.D. thesis, Strasbourg University.

[8] D. Nakajima, Ph.D. thesis, Tokyo University.

* The HypHI project is supported by the Helmholtz Association as Helmholtz University Young Investigators Group VH-NG-239 and by DFG with the research grant SA 1696/1-1.

† t.saito@gsi.de

The HypHI project at GSI and FAIR: Genfit package for track fitting in the hypernuclei event reconstruction analysis

C.Rappold*[1,2], S. Bianchin[1], O. Borodina[1,3], V. Bozkurt[1], B. Göküzüm[1], M. Kavatsyuk[4], E. Kim[1], F. Maas[1,3], S. Minami[1], D. Nakajima[1,5,6], B. Özel-Tashenov[1], T.R. Saito[1,3], and W. Trautmann[1]

[1]GSI, Darmstadt, Germany; [2]Université de Strasbourg, Strasbourg, France; [3]Mainz University, Mainz, Germany; [4]KVI, Groningen, The Netherlands; [5]KEK, Tsukuba, Japan; [6]Tokyo University, Tokyo, Japan

The HypHI project aims to study hypernuclei by means of collisions of stable heavy ion and RI beams on stable target materials. As the first step (Phase 0), the feasibility of hypernuclear spectroscopy with heavy ion beams will be demonstrated with a ^{6}Li beam at 2 A GeV impinged on a ^{12}C target by identifying $^{3}_{\Lambda}$H, $^{4}_{\Lambda}$H and $^{5}_{\Lambda}$He hypernuclei from their mesonic decay modes. The Phase 0 experiment was performed in August and October 2009 [2].

A dedicated event reconstruction analysis has been developed in order to reconstruct hypernucleus event from the obtained data. The four-momentum of each particle is calculated by finding and fitting each possible tracks from hits collected by the tracker system [3, 4] and PID system [5]. The invariant mass method and vertex reconstruction of interested hypernuclei is performed from their respective daughter particles. Each daughter candidate is selected from the goodness of the track fitting.

A new step has been included in the track reconstruction after the satisfied implementation of track finding [6]. Possible track found by the Hough transform across the full setup is fitted with a Kalman Filter algorithm. The implementation of the algorithm has been initially based on the Genfit package provided in the PandaROOT framework. Several modifications have done to handle experimental data and the specificity of the setup of Phase 0 experiment. One of the main change includes a new propagation algorithm : a track propagation in non-homogeneous magnetic field by a analytic formula for track extrapolation [7].The new implementation of the full reconstruction analysis with the track fitting algorithm gives us the opportunity to select the goodness of the tracking within a high confidence level.

The reconstruction of hypernuclei from Monte Carlo simulations has been studied with the full event reconstruction analysis. Monte Carlo simulations have been based on a UrQMD event generator and the GEANT4 framework. 20000 $^{3}_{\Lambda}$H, $^{4}_{\Lambda}$H and $^{5}_{\Lambda}$He hypernucleus with their associated background particles from the production reaction have been used. For the background, firstly 20 million background events representing primary reaction which does not lead to any strangeness production have been used to simulate the primary reaction. This background represents $\sim$1b reaction cross section, from which all other simulation results have been scaled. Secondly, the background associating free Λ production with other possible Z=2 projectile fragments is the most crucial background since those events behave like hydrogen hypernuclei if the proton from the free Λ decay is missing.

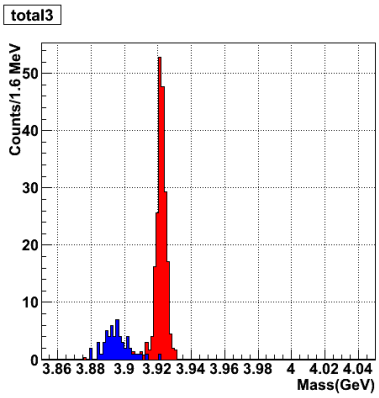

Figure 1: Invariant mass of $^{4}_{\Lambda}$H within 95 % CL. In blue : the background contribution while in red the $^{4}_{\Lambda}$H signal.

Those three different inputs have been analyzed and the resulting invariant mass of $^{4}_{\Lambda}$H from all input has been scaled to each other to match the expected cross section difference. The figure 1 is showing this scaled invariant mass spectrum, with two color codes separating the background from the signal. It shows a clear separation between background (in blue) and the hypernuclei signal (in red). The full background from primary reactions is completely rejected thanks to a secondary vertex selection. Only the free Λ background is contributing to the background shown in blue. The invariant mass resolution obtained in this way is 2.07 MeV for $^{4}_{\Lambda}$H. All other interested hypernuclei, $^{3}_{\Lambda}$H and $^{5}_{\Lambda}$He have been also studied in the same procedure.

References

[1] Proposal of the HypHI Phase 0 experiment, the HypHI collaboration.

[2] T.R. Saito *et. al.*, in these Scientific Reports.

[3] D. Nakajima *et. al.*, in these Scientific Reports.

[4] E .Kim *et. al.*, in these Scientific Reports.

[5] S. Bianchin *et. al.*, in these Scientific Reports.

[6] C. Rappold *et. al.*, GSI Scientific Report 2008, GSI, Darmstadt, 2008, p. 53.

[7] S. Gorbunov, I. Kisel, *Analytic formula for track extrapolation in non-homogeneous magnetic field*. Nucl. Instr. Meth. A 559 (2006) 148-152

* c.rappold@gsi.de

Single-Ion Decay Spectroscopy of Hydrogen-like ^{122}I Ions

F. Bosch[1], Yu.A. Litvinov[1,2], N. Winckler[1,2], D. Atanasov[3], K. Blaum[2], D. Boutin[1], C. Brandau[1], L. Chen[4], C. Dimopoulou[1], H.G. Essel[1], T. Faestermann[5], H. Geissel[1,4], I. Hachiuma[7], E. Haettner[4], M. Hausmann[8], S. Hess[1], T. Izumikawa[9], P. Kienle[5,6], R. Knöbel[1,4], C. Kozhuharov[1], R. Krücken[5], J. Kurcewicz[1], N. Kuzminchuk[4], S.A. Litvinov[1], L. Maier[5], R. Mao[10], R. Märtin[1], M. Mazzocco[1,11], G. Münzenberg[1], A. Musumarra[12,13], K. Namihira[7], C. Nociforo[1], F. Nolden[1], T. Ohtsubo[9], W.R. Plaß[1], A. Prochazka[1], R. Reuschl[1], C. Scheidenberger[1,4], D. Shubina[2], U. Spillmann[1], M. Steck[1], T. Stöhlker[1,14], B. Sun[1], T. Suzuki[7], S. Torilov[15], M. Trassinelli[1,16], S. Trotsenko[1], H. Weick[1], M. Winkler[1], D. Winters[1], and T. Yamaguchi[7]

[1]GSI, Darmstadt; [2]MPI-K, Heidelberg; [3]Uni. Sofia; [4]JLU Gießen; [5]TU München; [6]SMI Vienna; [7]Saitama Uni.; [8]MSU East Lansing; [9]Niigata Uni.; [10]IMP Lanzhou; [11]INFN Padova; [12]INFN Catania; [13]Uni. Catania; [14]RKU Heidelberg; [15]St. Petersburg Uni.; [16]CNRS, Paris

In last years' report [1] we presented preliminary results on orbital electron capture decay (EC) of hydrogen-like (H-like) $^{122}I^{52+}$ ions (see also Ref. [2]). This investigation had been motivated by the observation of time-modulated EC decays in $^{140}Pr^{58+}$ and $^{142}Pm^{60+}$ ions [3].

The data on $^{122}I^{52+}$ ions can be divided into two groups: spectra with only one EC decay within the measurement cycle and spectra with more than one EC decay. It turned out that the analysis is more complicated than the corresponding analyses on $^{140}Pr^{58+}$ and $^{142}Pm^{60+}$ ions. One of the reasons is that the strength of a Schottky frequency peak is proportional to the square of the ion's charge. Since the I ions have a lower charge compared to the Pr and Pm ions, the signal-to-noise ratio is reduced.

Two independent analyses of all data have been performed. However, the obtained decay times agree well only for the first EC decay. The decay times of the second and later decays vary strongly. Two decay times are considered agreeing if their values agree within 0.64 s. Therefore we restricted ourselves on the analysis of the data with only one EC decay. In total there are 2664 such EC decays. The histograms obtained from two analyses are illustrated in Figure 1. About 98% of all decay times from these analyses agree within 0.64 s. The distribution of decay time differences is given in the inset of Figure 2. The result of the χ^2 analysis of these histograms is illustrated in Figure 2. Both analyses show an evidence for an oscillation in the ^{122}I decay probability with a period of ≈6 s, however, at a different statistical confidence level (≈ 2.5σ and $> 5\sigma$).

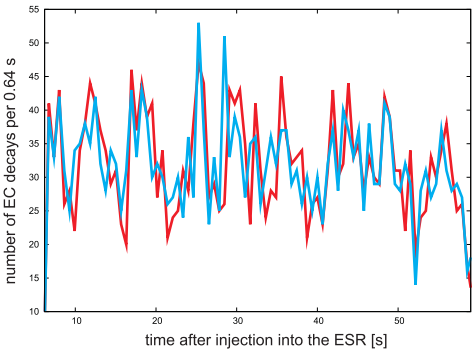

Figure 1: Histograms of the number of EC decays per 0.64 s as a function of time after injection of ions into the ESR. Two colors show two different analyses of the data. Only spectra with 1 EC decay per spectrum are considered.

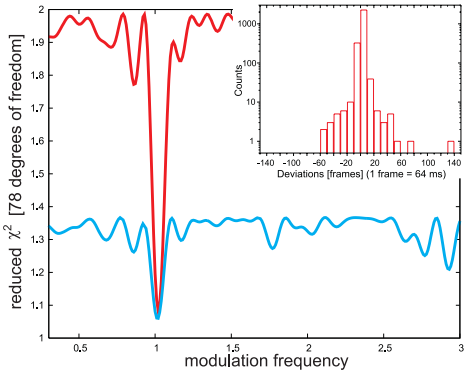

Figure 2: The χ^2 analyses of the histograms as illustrated in Fig. 1. In this analysis the minimum χ^2 is determined for the frequencies on the x-axis by varying the normalization, amplitude and phase of an oscillation (see Ref. [3]). Both analyses show an evidence for a modulation with a period of 6 s. The inset shows the distribution of time differences for the two analyses (note logarithmic scale).

A new Schottky pick-up detector has been designed and constructed. This detector shall enhance significantly the signal-to-noise ratio indispensable for our measurements with low-Z ions. The first tests of this pick-up will be performed early in 2010.

References

[1] N. Winckler et al., GSI Scient. Report 2008, **2009-01** (2009).

[2] P. Kienle, Nucl. Phys. **A827** (2009) 510c.

[3] Yu.A. Litvinov et al., Phys. Lett. **B664** (2008) 162.

Consistency of results from single- and many-ion lifetime spectroscopy

N. Winckler[1,2], F. Bosch[1], H. Geissel[1], C. Kozhuharov[1], Yu. A. Litvinov[1,2], and Z. Patyk[3]

[1]GSI, Darmstadt; [2]MPI-K, Heidelberg; [3]Soltan Institute for Nuclear Studies, Warsaw

Orbital electron capture decay of H-like ^{142}Pm and ^{140}Pr ions has been studied in ESR experiments at GSI. The experiments have been carried out in two modes. One of them was to store a large number of parent ions and to monitor continuously the number of parent and daughter ions. The other way was to inject on average 2 parent ions. In this way the decay times of each ion could be accurately determined. While the decay curves, measured with many parent ions, follow the expected exponential behavior [2, 3], a modulated in time exponential decay [1] has been observed in single-ion experiments . In this report we show that these results are consistent. Let us assume that the number of stored parent ions at time t, $N_M(t)$, decreases at a rate:

$$\frac{dN_M(t)}{dt} = -\widetilde{\lambda} \cdot N_M(t) \qquad (1)$$

where the total decay rate $\widetilde{\lambda}$ is the sum:

$$\widetilde{\lambda} = \lambda_\beta + \lambda_{EC}(1 + a\cos(\omega t + \phi)) + \lambda_{loss} \qquad (2)$$

The solution of equation (1) is:

$$N_M(t) = \quad N_M(0) \cdot \exp\left[-\lambda t(1 + \tfrac{a\lambda_{EC}}{\lambda} \cdot \tfrac{\sin(\omega t+\phi)}{\omega t})\right] \qquad (3)$$

where $\lambda = \lambda_\beta + \lambda_{EC} + \lambda_{loss}$. In the case of non-modulated EC-decay rate ($a = 0$) we find the usual solution: $N^0_M(t) = N_M(0) \cdot \exp[-\lambda t]$ The number of stored parent ions $N_M(t)$ and $N^0_M(t)$ as well as the diference $N^0_M(t) - N_M(t)$ are plotted in Fig. 1 using the experimental parameters as the example of ^{142}Pm [1, 3]. We note that the relative change has an upper bound:

$$\left|\frac{N^0_M(t) - N_M(t)}{N^0_M(t)}\right| \leq \frac{a\lambda_{EC}}{\omega} \approx 0.001 \qquad (4)$$

which clearly shows that a modulated decay term leads to a per mille effect in the evolution of the number of stored parent ions. Within experimental error bars, it is clear that oscillation cannot be seen in multi-ions experiments.

Similarly, the variation $dN_D(t)/dt$ for the daughter ions (see Fig. 2) can be written as follows:

$$\frac{dN_D(t)}{dt} = \lambda_{EC}(1 + a\cos(\omega t))N_M(t) - \lambda_{loss}N_D(t) \qquad (5)$$

The solution of this differential equation is the sum of the solution of the homogeneous differential equation, $N_D(t) = N_D(0)e^{-\lambda_{loss}t}$, with the particular solution to the inhomogeneous equation, $N_D(t) = F(t)e^{-\lambda_{loss}t}$, which is derived by mean of the "constant variation" method. One shows that, using the approximation $\frac{a\lambda_{EC}}{\lambda}\frac{\sin(\omega t)}{\omega t} \ll 1$, the solution of eq. (5) is:

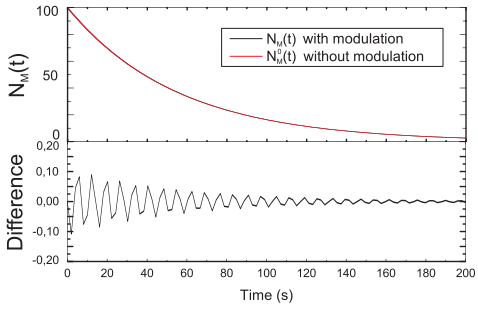

Figure 1: Decay curves of parent ions $N_M(t)$ and $N^0_M(t)$ and their difference as a function of time. The curve with the modulation term, $N_M(t)$, can hardly be distinguished from the one without modulation, $N^0_M(t)$.

$$\begin{aligned} N_D(t) = & \quad \tfrac{\lambda_{EC}}{\lambda-\lambda_{loss}}(e^{-\lambda_{loss}t} - e^{-\lambda t})N_M(0) \\ + & \quad N_D(0)e^{-\lambda_{loss}t} \\ + & \quad a\lambda_{EC}[\tfrac{\omega\sin(\omega t)-(\lambda-\lambda_{loss})\cos(\omega t)}{\omega^2+(\lambda-\lambda_{loss})^2}]N_M(0)e^{-\lambda t} \\ + & \quad \tfrac{a\lambda_{EC}(\lambda-\lambda_{loss})}{\omega^2+(\lambda-\lambda_{loss})^2}N_M(0)e^{-\lambda_{loss}t} \end{aligned} \qquad (6)$$

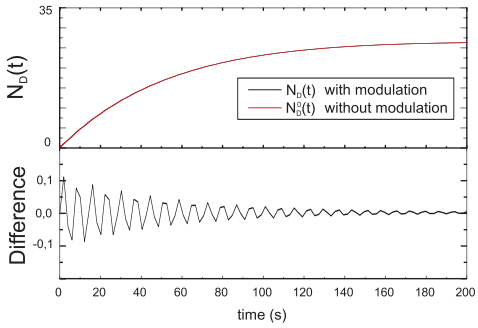

Figure 2: Growth curves of daughter ions and difference with respect to the solution with $a = 0$ as a function of time. The fit parameters were taken from [1, 3]. We also assumed $N_M(0) = 100$ and $N_D(0) = 0$.

It is therefore clear that within the achieved experimental error bars, it was not possible to observe the modulation in the many-ion experiments.

References

[1] Y. A. Litvinov et al., Phys. Lett. B664, 162 (2008).

[2] Yu. Litvinov et al., Phys. Rev. Lett. 99, 262501 (2007).

[3] N. Winckler et al., Phys. Lett. B679, 36 (2009).

Schottky Measurements of Stored Hafnium and Tantalum Isomers

M.W. Reed[1], P.M. Walker[1], K. Blaum[2], F. Bosch[3], C. Brandau[4], J.J. Carroll[5], D.M. Cullen[6], I.J. Cullen[1], A.Y. Deo[1], B. Detwiller[5], C. Dimopoulou[3], F. Farinon[3], H. Geissel[3,8], E. Haettner[8], M. Heil[3], R.S. Kempley[1], R. Knöbel[3], C. Kozhuharov[3], J. Kurcewicz[3], N. Kuzminchuk[8], S. Litvinov[3], Yu.A. Litvinov[2,3], Z. Liu[7], R. Mao[9], C. Nociforo[3], F. Nolden[3], W.R. Plass[8], A. Prochazka[3], C. Scheidenberger[3,8], M. Steck[3], T. Stöhlker[3], B. Sun[3], T.D. Swan[1], G. Trees[5], H. Weick[3], N. Winckler[3], M. Winkler[3], P.J. Woods[7] and T. Yamaguchi[10]

[1]Surrey Univ., [2]MPI Heidelberg, [3]GSI Darmstadt, [4]TU Munich, [5]Youngstown State Univ., [6]Manchester Univ., [7]Edinburgh Univ., [8]Giessen Univ., [9]IMPCAS Lanzhou, [10]Saitama Univ.

Projectile fragmentation produces highly charged ions which can be selected by the GSI Fragment Separator, injected into the Experimental Storage Ring (ESR) and electron cooled. A Schottky pickup in the ESR enables single-ion identification, with a mass/energy uncertainty of less than 50 keV. This capability has been exploited for isomer discoveries. For example, a new isomer at 103±12 keV in ^{125}Ce has been found with the ESR [1].

We now report new isomers observed in ^{184}Hf and ^{187}Ta. Figure 1 shows A = 184 (q = 72+) and A = 187 (q = 73+) spectra selected from a series of injections into the ESR, following the fragmentation of ^{197}Au beam particles. ^{184}Hf and ^{187}Ta are each seen to have two isomers, at excitation energies of about 1.5 and 2.5 MeV, in addition to their ground states and some known isobars.

While the first hafnium isomer, ^{184m1}Hf, was already known [2], with $T_{1/2}$ = 48 s, its confirmation is non-trivial since, in the ISOL experiment [2], it could have been confused with ^{184}Lu β decay. The second isomer, ^{184m2}Hf, is observed for the first time, as are both the ^{187}Ta isomers. All three new isomers have half-lives of minutes or longer. An important feature of the ESR method is that there is no upper-limit on the isomer half-life (in contrast to measurements that rely on decay radiations). Furthermore, it is notable that, with bare hafnium (72+) and tantalum (73+) ions, there is no ambiguity between the isomeric states and the less-bound isobars (lutetium and hafnium, respectively) since they cannot exist in the required charge states.

The excitation energy of the ^{184m2}Hf isomer matches well with the prediction of a spin-17 four-quasiparticle state [3]. This gives improved confidence that ^{186}Hf and ^{188}Hf will also have long-lived isomers, as predicted [3]. The m1 and m2 tantalum isomers are interpreted as three- and five-quasiparticle states respectively, and their excitation energies agree with model calculations. We also note that the mass and half-life of the ^{187}Ta ground state are obtained for the first time. Furthermore, the general quality of the data illustrates clearly the well-known feature that the Schottky analysis method requires only a single unknown ion in the ESR for positive identification, providing the mass calibration can be established from known ions.

With half-lives of minutes or longer, there is a strong possibility of β decay from the four- and five-quasiparticle isomers. Taking into account also their low production rates, these isomers probably could not have been uniquely identified in any other way than as stored bare ions.

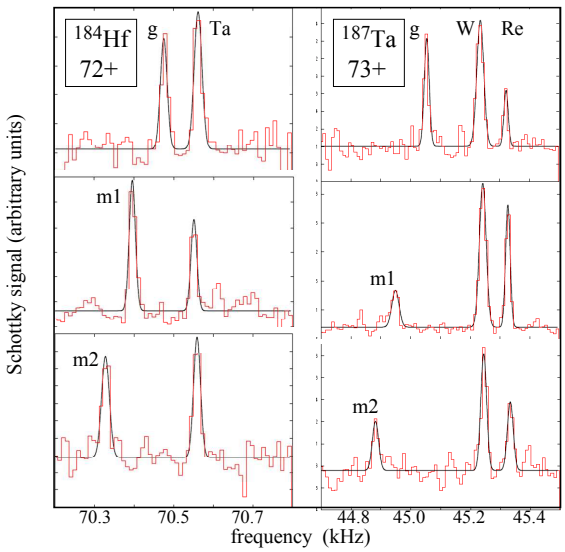

Figure 1: Examples of Schottky spectra for A = 184 and 187 isobars and isomers, for a variety of different injections in the ESR. All the illustrated isomer data correspond to single ions. (The A = 184 and 187 vertical scales differ significantly, to accommodate the multiple-ion peaks for A = 187 ground states.)

These new data establish that the existence of long-lived hafnium and tantalum isomers extends well into the neutron-rich domain. The data complement γ-ray measurements of shorter-lived A ~ 190 isomers [4], and open up to more detailed study a predicted region [5] of shape instability between well-deformed prolate and oblate collective rotation.

References

[1] B. Sun et al., Eur. Phys. J. A31 (2007) 393.
[2] K. Krumbholz et al., Zeit. Phys. A351 (1995) 11.
[3] P.M. Walker, G.D. Dracoulis, Nature 399 (1999) 35.
[4] N. Alkhomashi et al., Phys. Rev. C80, 064308 (2009).
[5] F.R. Xu et al., Phys. Rev. C62, 014301 (2000).

^{96}Ru(p,γ)^{97}Rh measurement at the GSI storage ring*

T. Aumann[1], S. Bishop[3], K. Blaum[9], K. Boretzky[1], F. Bosch[1], H. Bräuning[1], C. Brandau[1,3], T. Davinson[4], I. Dillmann[3], O. Ershova[1,5], H. Geissel[1], G. Gyürky[6], M. Heil[1], F. Käppeler[7], A. Kelić[1], C. Kozhuharov[1], C. Langer[1,5], T. Le Bleis[1,5,10], Y. A. Litvinov[1,9], G. Lotay[3], J. Marganiec[1], N. Petridis[5], R. Plag[1,5], U. Popp[1], R. Reifarth †[1,5], B. Riese[1], C. Rigollet[8], C. Scheidenberger[1], H. Simon[1], T. Stöhlker[1], T. Szücs[6], G. Weber[1], H. Weick[1], D. F. A. Winters[1], N. Winters[1], P. J. Woods[4], and Q. Zhong[1,2]

[1]GSI Helmholtzzentrum für Schwerionenforschung GmbH, Darmstadt, 64291, Germany; [2]China Institute of Atomic Energy (CIAE) 102413 Beijing China; [3]Technische Universität München, 85748 Garching, Germany ; [4]University of Edinburgh, Edinburgh, UK; [5]J.W. Goethe Universität, Frankfurt a.M, 60438, Germany; [6]Institute of Nuclear Research of the Hungarian Academy of Sciences, Hungary; [7]KIT Forschungszentrum Karlsruhe, Institut für Kernphysik, Karlsruhe, Germany; [8]Kernfysisch Versneller Instituut, Netherlands; [9]Max-Planck-Institut für Kernphysik, 69117 Heidelberg, Germany; [10]Institut Pluridisciplinaire Hubert Curien, Strasbourg, France

Introduction

The nucleosynthesis of elements beyond iron is dominated by neutron captures in the s and r processes [1]. However, 32 stable, proton-rich nuclides between ^{74}Se and ^{196}Hg cannot be formed during those processes, because they are shielded from the s-process flow and r-process β-decay chains. These nuclei are thought to be produced in the p process, where proton-rich nuclei are made by sequences of photodisintegrations and proton captures reactions and following β^+ decays on existing r- and s-seed nuclei. Rate predictions for the (p,γ) and (α,γ) reactions are very difficult since only a handful of experimental data for stable isotopes have been determined in the Gamow window of the p process so far.

Cross-section measurements on (p,γ) and (α,γ) reactions in the astrophysically interesting energy range are already very challenging on stable nuclei. Only a minute part of the nuclei involved in p-process networks, however, is stable. The majority of the isotopes crucial for the final p-abundance are unstable. The most promising approach to determine the desired reaction rates is to produce the isotopes at Radioactive Ion Beam facilities and to investigate the reactions in inverse kinematics.

In order to prove the principle of this approach, an experiment was performed at the Experimental Storage Ring (ESR) at the GSI Helmholtzzentrum für Schwerionenforschung GmbH.

Experiment and preliminary results

The pioneering experiment was performed at the Experimental Storage Ring (ESR) at GSI. Fully stripped ions of ^{96}Ru were injected into the storage ring and slowed down to 9-11 MeV per nucleon. The ^{97}Rh ions following the ^{96}Ru(p,γ) reaction at a cryogenically cooled liquid microjet hydrogen target were detected with Double Sided Silicon Strip Detectors (DSSSD) mounted inside a pocket. We could prove the feasibility of this approach and clearly detected events originating from proton captures on ^{96}Ru (see Figure 1). The analysis is still in progress, but the preliminary results show that the cross section at 11 MeV, is only slightly above the prediction from the NON-SMOKER code. The detailed analysis will eventually include a simulation of all beam line components and reaction channels. It will also be extended down to 10 and 9 MeV.

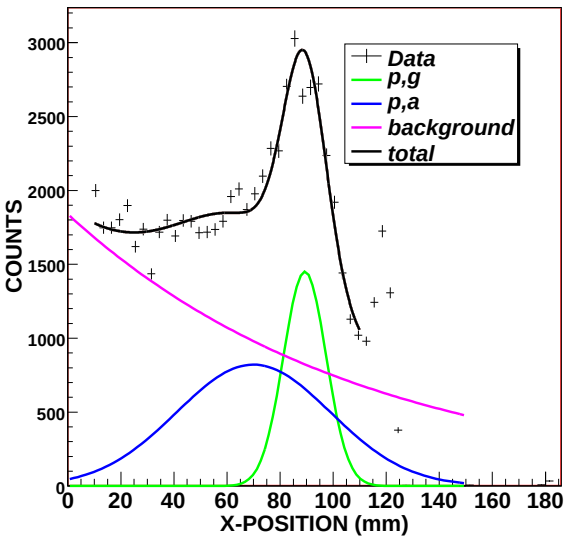

Figure 1: A fit of the experimental data neglecting the (p,n) component. The position of the primary beam is at -40 mm.

References

[1] E. Burbidge, G. Burbidge, W. Fowler and F. Hoyle, Rev. Mod. Phys. 29 (1957) 547

* Work supported by the HGF Young Investigators Projects VH-NG-327 and VH-NG-331 and the ERC grant no. 203175.

† r.reifarth@gsi.de

Direct Observation of Bound-State β^- Decay of Fully Ionized ^{205}Hg

J. Kurcewicz[1], F. Bosch[1], H. Geissel[1,2], Yu. A. Litvinov[1,2], K. Beckert[1], P. Beller[1], D. Boutin[1,2], C. Brandau[1], L. Chen[1,2], T. Faestermann[3], B. Franzke[1], M. Hausmann[4], P. Kienle[3,5], O. Klepper[1], R. Knöbel[1,2], C. Kozhuharov[1], S. A. Litvinov[1,2], L. Maier[3], M. Mazzocco[1], F. Montes[1], A. Musumarra[6], C. Nociforo[1], F. Nolden[1], W. R. Plaß[1,2], C. Scheidenberger[1,2], M. Steck[1], B. Sun[1], K. Takahashi[7], H. Weick[1], N. Winckler[1,2], and M. Winkler[1]

[1]GSI, Darmstadt, Germany; [2]JLU, Gießen, Germany; [3]TUM, München, Germany; [4]MSU, East Lansing, U.S.A.; [5]SMIsP, Vienna, Austria; [6]LNS, Catania, Italy; [7]ULB, Brussels, Belgium

The β^- decay to an electronic bound state in the daughter atom, accompanied by the emission of a monoenergetic neutrino was first observed at GSI in 1992 [1], more than 40 years after its theoretical prediction [2]. This phenomenon of minor importance for neutral atoms, might become a strong decay channel for highly ionized atoms in stellar environments. Thus the heavily altered nuclear half-lives might have a large impact on the path of the nucleosynthesis process. Here we report on the direct observation of the bound-state β^- decay of fully ionized ^{205}Hg.

The experiment was performed at the SIS synchrotron of GSI Darmstadt, which delivered a 750 A GeV ^{208}Pb beam with an intensity of the order of 10^9 ions/spill. The ions of interest ^{205}Hg^{80+} were produced in the projectile fragmentation. The 4 g/cm^2 thick beryllium target was placed at the entrance of the projectile Fragment Separator (FRS). The ^{205}Hg were selected by passing the magnetic sections of the separator and injected into the ESR storage ring, where they could remain for extended periods of time circulating with a revolution frequency of the order of 2 MHz. Both, stochastic and electron cooling were applied in order to decrease the velocity spread of the circulating ions.

The beamline of the ESR is equipped with a set of Schottky noise probes which collect the mirror charge of each passing ion, thus providing the information about its revolution frequency. The 30th harmonic of the noise signal generated in the Schottky pick-up electrodes was amplified and mixed down with a local oscillator providing a reference frequency. The difference signal in the frequency range of 0-300 kHz was digitized by using a 16-bit ADC and a Fast Fourier Transformation was applied to the data yielding revolution frequency spectra of the coasting ions. Analyzing the frequency peaks present in the subsequently accumulated Schottky spectra, a time distribution of the number of the bare Hg and the β_b-decay daughter Tl ions stored in the ESR was constructed. In general the time evolution of the number of ions of mother activity can be described by the following expression

$$N_m(t) = N_m(0)e^{-\lambda t}, \qquad (1)$$

where $N_m(0)$ is the number of stored mother ions at the beginning of the measurement and $\lambda = \lambda_{\beta_b} + \lambda_{\beta_c} + \lambda_{\text{loss}}$ is the decay constant consisting of components corresponding to continuum-state, bound-state β^--decay and non-radioactive losses in the ring, respectively. In case of the daughter activity the number of stored ions is given by

$$N_d(t) = N_m(0)\frac{\lambda_{\beta_b}}{\lambda - \lambda_{\text{loss}}}\left(e^{-\lambda_{\text{loss}}t} - e^{-\lambda t}\right) + N_d(0)e^{-\lambda_{\text{loss}}t}, \qquad (2)$$

where $N_d(0)$ is the number of daughter ions at the beginning of the measurement. Several measurements of the decay constant have been performed showing overall consistent results. The results of the analysis of the Schottky power noise spectra are shown in Fig. 1. The obtained time evolution of the number of mother and daughter ions was fitted separately for each of performed measurements using Eq.(1) and (2), respectively.

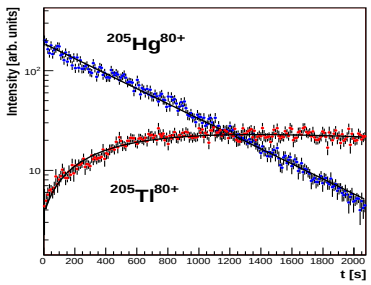

Figure 1: Time distribution of the peak intensity corresponding to number of stored ^{205}Hg^{80+} and ^{205}Tl^{80+} ions. The continuous line shows the fitted theoretical dependence given by Eqs. (1) and (2).

The average decay rates for bound and continuum state β^- decay are $\lambda_{\beta_b} = 3.7(3) \cdot 10^{-4}$ s^{-1} and $\lambda_{\beta_c} = 1.69(14) \cdot 10^{-3}$s^{-1}, respectively. The experimental values of the decay constant indicate an overall good agreement with the theoretical prediction $\lambda^{th}_{\beta_b} = 3.21 \cdot 10^{-4}$ s^{-1}, $\lambda^{th}_{\beta_c} = 2.21 \cdot 10^{-3}$ s^{-1} [3], however, showing a lower λ_{β_c} value. The aforementioned result of calculation has been confirmed by a recent theoretical work which provides for bare ^{205}Hg^{80+} the continuous β^--decay rate value of $\lambda_{\beta_c} = 2.34 \cdot 10^{-3}$ s [4].

References

[1] M. Jung et al., Phys. Rev. Lett. 69 (1992) 2164
[2] R. Daudel et al., Jour. de Phys. Rad. 8 (1947) 238
[3] K. Takahashi et al., Phys. Rev. C36 (1987) 1522
[4] M. Faber et al., Phys. Rev. C78 (2008) 061603(R)

Direct Measurement of the 4.6 MeV Isomer in Stored Bare ^{133}Sb Ions

B. Sun[1,2], R. Knöbel[3], H. Geissel[1,3], Yu. A. Litvinov[3,4], P. M. Walker[5], K. Blaum[4], F. Bosch[3], D. Boutin[3], C. Brandau[3], L. Chen[1], I. J. Cullen[5], A. Dolinskii[3], B. Fabian[1], M. Hausmann[6], C. Kozhuharov[3], J. Kurcewicz[3], S. A. Litvinov[3], Z. Liu[7], M. Mazzocco[8], J. Meng[2], F. Montes[6], G. Münzenberg[3], A. Musumarra[9], S. Nakajima[10], C. Nociforo[3], F. Nolden[3], T. Ohtsubo[11], A. Ozawa[12], Z. Patyk[13], W. R. Plaß[1,3], C. Scheidenberger[1,3], M. Steck[3], T. Suzuki[10], H. Weick[3], N. Winckler[3], M. Winkler[3], and T. Yamaguchi[10]

[1]JLU Giessen, Germany; [2]Beihang Univ., Beijing, China; [3]GSI, Darmstadt, Germany; [4]MPI-K, Heidelberg, Germany; [5]Surrey Univ., Guildford, U.K.; [6]MSU, East Lansing, U.S.A; [7]Edinburgh Univ., Edinburgh, U.K.; [8]INFN Padova, Italy; [9]INFN Catania, Italy; [10]Saitama Univ., Japan; [11]Niigata Univ., Japan; [12]Tsukuba Univ., Japan; [13]SINS, Poland

Isomer investigations were performed recently with stored ions in cooled storage rings and Penning traps, e.g. with excitation energies of 103(12) keV ($T_{1/2} > 1$ s) in ^{125}Ce [1], and of 402(5) keV ($T_{1/2} > 150$ ms) in ^{65}Fe [2]. The present work applies a novel method, namely, isochronous mass spectrometry [3], to measure mass-resolved nuclear isomers with lifetime down to a few tens of μs. The excitation energy and survival time of the isomer in ^{133}Sb are determined based on precise revolution time measurements of a few individually stored ions.

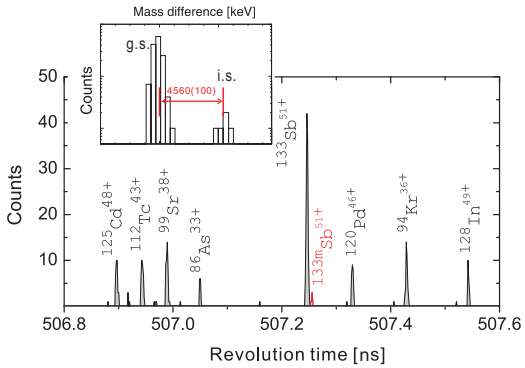

Figure 1: Part of the revolution-time spectrum including the ^{133}Sb ions in the ground and isomeric states. The identified ions with well-known masses are indicated in the spectrum. The final mass distribution for both states in the off-line analysis are shown as an inset.

In the measurement [4], neutron-rich exotic nuclei were produced by projectile fission of 411 MeV·A ^{238}U ions in a 1 g/cm^2 Be target placed at the entrance of the FRS. The energy of the primary beam was chosen such that the energy of ^{133}Sn^{50+} fragments corresponded to the relativistic Lorentz factor γ=1.41 which matches exactly the isochronous condition of the ESR. The intensity of the primary beam was about $2 \cdot 10^9$ particles per spill. The fission fragments emerged from the target mainly as bare ions. Under this condition the observed half-lives of nuclear isomeric states can be much longer if the electron conversion branch is suppressed [5]. In principle, this presents the possibility to observe bare isomers with lifetimes that would be even shorter than μs in the corresponding neutral atoms.

The uranium fission products were then separated in flight according to their magnetic rigidity and injected into the ESR. The magnetic-rigidity of the fission fragments has been determined at the focal plane S2 of the FRS, which defines precisely the velocity spread ($\Delta v/v$) of fragments to about 10^{-4} [6]. Each measurement cycle was 1 ms long which corresponded to about 2000 revolutions of the ions in the ESR. On average there was about one stored ion per injection. More than 13000 independent injections were made over four days.

Both the ground state and the isomeric state in ^{133}Sb have been produced. Due to different rest masses, they were well resolved in the experiment via the difference in their revolution times (see Figure 1). The excitation energy of 4.56(10) MeV is determined experimentally for the first time as a complement to gamma-ray experiments [7]. The survival half-live in the centre-of-mass frame of 58^{+47}_{-18} μs (1σ) enables us to conclude that at the 95% confidence level the ^{133}Sb isomer with a neutral-atom half-life of 17 μs is located above the $I^\pi = 17/2^+$, 4526 keV state, giving direct experimental evidence for the shell-model prediction of an energetically favored $I^\pi = 21/2^+$ state [7].

By employing the newly improved IMS technique it is possible to gain access to rare nuclear isomers, including those associated with highly converted decay transitions, which can be very difficult or impossible to measure by γ-ray and electron spectroscopy. This achievement has opened the way to accurate mass measurements of short-lived exotic isomeric states, which have a great potential for nuclear structure and nuclear astrophysics investigations at the future FAIR facility [8].

References

[1] B. Sun *et al.*, Eur. Phys. J. A 31 (2007) 393.
[2] M. Block *et al.*, Phys. Rev. Lett. 100 (2008) 132501.
[3] M. Hausmann *et al.*, Nucl. Instr. Meth. A 446 (2000) 569.
[4] B. Sun *et al.*, Nucl. Phys. A 812 (2008) 1.
[5] Yu.A. Litvinonv *et al.*, Phys. Lett. B 573 (2003) 80 .
[6] H. Geissel *et al.*, Hyperfine Interact. 173 (2006) 49.
[7] J. Genevey *et al.*, Eur. Phys. J. A 7 (2000) 463.
[8] C. Scheidenberger *et al.*, Hyperfine Interact. 173 (2006) 61.

Progress of nuclear physics data evaluation projects at GSI

B. Pfeiffer[1], U. Czok[2], Z. Patyk[3], C. Scheidenberger[1], and K. Venkataramaniah[4]

[1]GSI, Darmstadt, Germany; [2]II. Phys. Inst., Gießen, Germany; [3]Soltan Institute for Nuclear Studies, Warsaw, Poland; [4]Sri Sathya Sai University, Prasanthinilayam, India

To counteract the general decline of data collection and evaluation in Europe, the GSI took the initiative to participate in the *International Network of Nuclear Structure and Decay Data Evaluators* [1].

Advanced Atomic Mass Evaluation

In 2009, the screening of the literature for all nuclear data relevant for future evaluations of masses and decay properties has been continued (see Ref. [2]).
The data are now structured for input into data bases in the framework of the Advanced Atomic Mass Evaluation – AAME– project. For the mid-term future it is envisioned to make all data available via electronic media for broad dissemination of the original and the evaluated data, respectively. The creation of a web-site with interactive tools to serve the community of experimentalists, theorists, and for users in applied sciences is under development.

Atomic Mass Data Center

In close collaboration with the Atomic Mass Data Center at Orsay, these data, mainly on α, p- and β-decay as well as direct mass measurements from FRS/ERS, are added to the master files of the Future Atomic Mass Evaluation and NUBASE, which ought to replace the actual version AME03 [3] in 2013. Up till now about 500 new α-decay data points have been added. An important part of these new results have been obtained at GSI. At SHIPTRAP, not only many new α- and p-decay energies were measured, but additonal information on decay schemes could be obtained by particle-γ coincidences. The nuclear structure information allows to calculate the Q-values and by this the mass difference between mother and daughter nuclide.
The recent measurements with advanced techniques at the ridge of the valley of stability seem to indicate that the mass surface lies much higher (higher masses, less binding energy) than derived from the older data underlying the actual AME. A first overview will be presented at the International Conference for *Nuclear Data for Science and Technology – ND2010* at Jeju Island, Korea [4]. Changes at the driplines will influence astrophysical calculations as, e.g., for the rp- and r-process of nucleosynthesis.

National Nuclear Data Center

Nuclear structure information is needed for the interpretation of β- and α-decay measurements to derive correct Q-values. Lack of information on excited states of daughter nuclei led to many erronneous results, as too low Q_β-values (see previous section). Therefore, information is exchanged with the National Nuclear Data Center at Brookhaven (specialised in evaluating level schemes). For the updates of ENSDF, intermediate atomic mass evaluations are provided by the AMDC [5].
Future installations like SUPER-FRS at FAIR will make new regions of the nuclidic chart accessible to experiments and at the same time enable sophisticated studies of known nuclides. This will lead to a vast number of new nuclear structure data to be compiled and evaluated by the AMDC and NNDC. The additional amount of work requires to *globalise* the task.
To attract new collaborators from Europe for the updating of the "Evaluated Nuclear Structure Data File ENSDF", the basis for e.g. the Nuclear Data Sheets, a workshop for the training of evaluators was organized by NNDC with support from the IAEA in Bucharest: *Nuclear Structure & Decay Data Evaluators ENSDF-2009* [6].
During the workshop, the Nuclear Data Sheets for the mass A=84 were updated by the participants and have been published in November 2009 [7].
Following the participation in the Bucharest workshop, one of the authors (B.P.) was invited to present an overview of the nuclear data work at GSI [8] at the *US Nuclear Data Program –USNDP– Annual Meeting* during the *US Nuclear Data Week at BNL* [9].
The project is conducted in collaboration with ISNSM in Orsay (France), and the Institute of Modern Physics of the Chinese Academy of Sciences in Lanzhou (China). The authors thank G. Audi, D. Lunney, M. Wang, H. Geissel for valuable discussions.

References

[1] A.L. Nichols, Nuclear Physics News 19(1), 3 (2009).

[2] B. Pfeiffer et al., GSI Scientific Report 2008, NUSTAR-EXPERIMENTS 16

[3] G. Audi et al., Nucl. Phys. A 729 (2003) 3; A.H. Wapstra et al., Nucl. Phys. A 729 (2003) 129; G. Audia et al., Nucl. Phys. A 729 (2003) 337.

[4] http://www.nd2010.org

[5] G. Audi, M. Weng, D. Lunney, B. Pfeiffer, NSR Keynumber 2009AUZZ

[6] http://tandem.nipne.ro/∼workshop_ensdf/

[7] D. Abriola, M. Bostan, S. Erturk, M. Fadil, M. Galan, S. Juutinen, T. Kibedi, F. Kondev, A. Luca, A. Negret, N. Nica, B. Pfeiffer, B. Singh, A. Sonzogni, J. Timar, J. Tuli, T. Venkova, K. Zuber, Nuclear Data Sheets 110 (2009) 2815.

[8] http://www.nndc.bnl.gov/proceedings/2009csewgusndp/Thursday/usndp/Pfeiffer-USNDP.pdf

[9] http://www.nndc.bnl.gov/meetings/usndp2009/

Beryllium isotopes studied in Fermionic Molecular Dynamics

T. Neff and H. Feldmeier
GSI, Darmstadt, Germany

Fermionic Molecular Dynamics (FMD) [1] is a microscopic many-body approach using Gaussian wave packets localized in phase-space as single-particle basis states. Slater determinants projected on parity, angular and total linear momentum are used as many-body basis states. The FMD basis is very flexible and contains harmonic oscillator shell model and Brink-type cluster wave functions as special cases. The widths of the wave packets are also variational parameters which is useful for the description of halo nuclei with extended single-particle wave functions. An effective interaction derived from the realistic Argonne V18 interaction by explicitly including short-range central and tensor correlations in the Unitary Correlation Operator Method is used. A phenomenological two-body correction term is added which is fitted to binding energies and radii of closed-shell nuclei.

In recent years it has become possible to measure the isotope shifts of short-lived nuclei. With that precise and model independent measurements of the charge radii are possible. As shown in Fig. 1 the Beryllium isotopes ^{7}Be-^{11}Be measured by Nörtershäuser *et al* [2, 3] show an interesting behavior. Starting from a very large radius for ^{7}Be the charge radius decreases going to ^{9}Be and ^{10}Be and increases again when going to ^{11}Be. These pronounced changes in the charge radii are related to changes in the structure of these nuclei. Important are here clustering effects due to low cluster thresholds in ^{7}Be and ^{9}Be and the halo nature of ^{11}Be.

In a simple Hartree-Fock FMD calculation (HF) the charge radii come out to small. This is explained by intrinsic wave functions that are to compact. For light nuclei like the Beryllium isotopes it is possible to perform a real variation after parity and angular momentum projection (VAP). Here we find a more pronounced clustering and larger charge radii. The description can be improved further by including additional configurations with smaller and larger cluster separation distances. To generate such configurations we performed VAP calculations with constraints on the mean proton distance $R_{pp}^2 = \frac{1}{Z^2}\langle\sum_{i<j}^{\text{protons}}(\vec{r}_i - \vec{r}_j)^2\rangle$. The underlying assumption here is that the Beryllium isotopes can be understood as systems of ^{4}He and ^{3}He clusters and neutrons. The energy surfaces shown in Fig. 2 show shallow minima for ^{7}Be and ^{9}Be that have small cluster separation energies and a narrow minimum for ^{10}Be. In multiconfiguration mixing calculations the extended configurations show significant contributions in case of the shallow minima which explains the large charge radii. The situation in ^{11}Be is different. Here we have a very small neutron separation energy and an extended neutron halo develops. Basically the ^{11}Be structure can be explained as ^{10}Be core with an additional neutron in an extended s-orbit. Due to the motion of the ^{10}Be core with respect to the total center of mass the charge radius increases significantly in comparison to the ^{10}Be core.

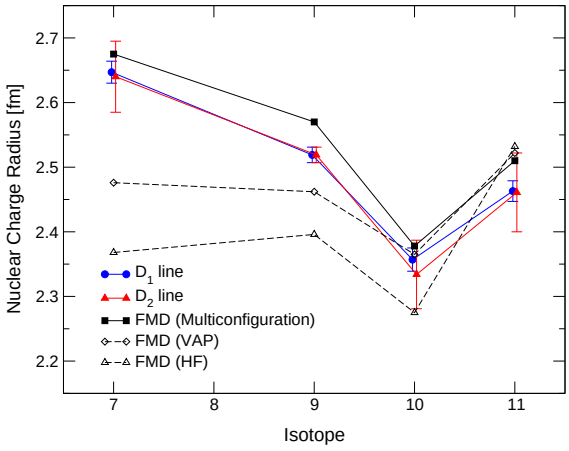

Figure 1: Experimental charge radii from two different optical transitions and FMD calculations on the Hartree-Fock level (HF), using a single optimized configuration (VAP) and multiconfiguration calculations.

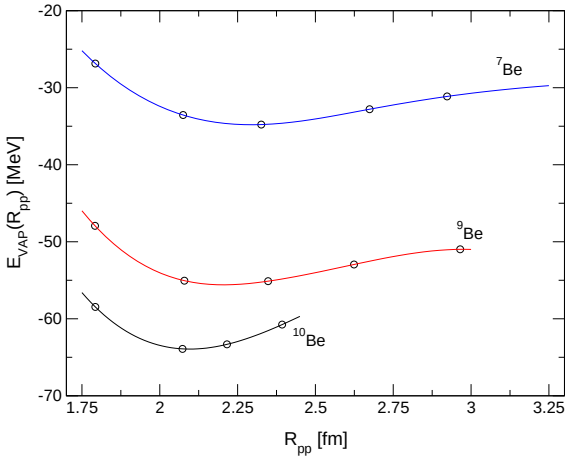

Figure 2: FMD VAP energies as a function of mean proton distance R_{pp}.

References

[1] T. Neff and H. Feldmeier, Eur. Phys. J Special Topics **159** (2008) 69.

[2] W. Nörthershäuser *et al*, Phys. Rev. Lett. **102** (2009) 062503.

[3] M. Žáková, T. Neff *et al*, submitted to J. Phys. G

Fission barriers and half-lives of super-heavy elements

J. Erler and P.–G. Reinhard

Institut für Theoretische Physik, Universität Erlangen, D-91058 Erlangen, Germany

Self-consistent mean field models have reached a high descriptive power for nuclear ground state properties and collective excitations, for reviews see [1, 2]. Their application to a fully microscopic description of fission is a very demanding task and it is only in the last years that new investigations on this topic appear, see e.g. [3, 4, 5]. We report here briefly on recent development of a fully self-consistent description of fission life-times of super-heavy elements (SHE) [6] on the grounds of Skyrme-Hartree-Fock (SHF). We start with summarizing the computational scheme [6]: The fission path is generated by quadrupole-constrained SHF whose energy expectation values yield a "raw" collective energy surface displaying a more or less large fission barrier. The collective mass and moments of inertia are computed by self-consistent cranking along the states of the path. Approximate projection onto zero angular momentum is performed and quantum corrections for the spurious vibrational zero-point energy are applied using the collective masses and widths. The collective ground state energy is computed fully quantum mechanically [7]. The tunneling rate and the repetition rates are computed by the standard semi-classical formula (known as WKB) using the quantum-corrected potential energy and collective mass; the fission life-time is finally composed from these two rates. All calculations are done in axial symmetry. Figure 1 shows results on fission barriers and lifetimes for a some SHE for which experimental data are available and for a large variety of Skyrme parameterizations (SkM* [8], SkP [9], SkI3 [10], SLy6 [11] and SV-min [12]). The SHE represent two groups, one at the lower side and another one at the limits of present days data. The span of predictions from the various Skyrme forces is huge. It is gratifying to see that the most recent parameterization SV-min which has been adjusted with a new pool of ground state data [12] performs very well for barriers and lifetimes in the lighter group (Rf, Sg, Hs). This suggests that one may use the fission properties as additional selection criterion for pinning down more precisely the most realistic Skyrme force. However, a problem appears when looking at the trend from the lighter side (Rf, Sg, Hs) to the larger SHE (Z=112, 114). All parameterizations produce a wrong trend. Barriers and lifetimes drop significantly in all SHF predictions while they stay practically constant in experiment. Possible triaxiality, ignored here, can perhaps lower the barriers by 0.5–2 MeV which does not suffice to resolve the mismatch. Altogether, we interpret these results optimistically: SHF predictions on fission stay in a reasonable range and fission data, including the unresolved trend, will help in the further development of nuclear energy functionals as SHF.

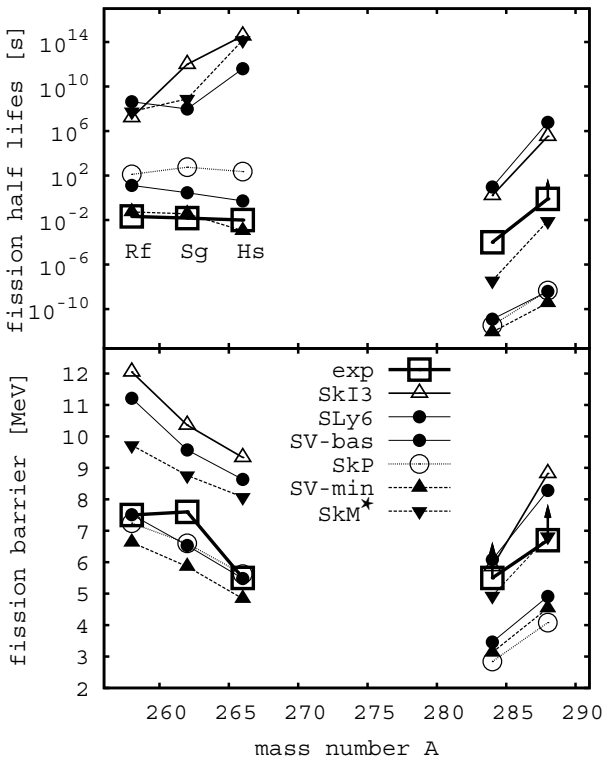

Figure 1: Fission barriers (lower) and life-times (upper) for two chains of super-heavy elements. Compared are results from a variety of Skyrme parameterizations with experimental data [13, 14, 15, 16].

References

[1] M. Bender *et al*, Rev. Mod. Rhys. **75** (2003) 121.
[2] J.R. Stone *et al*, Prog. Part. Nucl. Phys. **58** (2007) 587.
[3] Berger J.–F. *et al*, Nucl. Phys. A **685** (2001) 1c.
[4] Bürvenich T. *et al*, Phys. Rev. C **69** (2004) 014307.
[5] Warda M. *et al*, Phys. Scr. T **125** (2006) 226.
[6] Schindzielorz N. *et al*, Int. J. Mod. Phys. E **18** (2009) 773.
[7] Klüpfel P. *et al*, Eur. Phys. J. **37** (2008) 343.
[8] Bartel J. *et al*, Nucl Phys. A **386** (1982) 79.
[9] Dobaczewski *et al*, Nucl. Phys. A **422** (1984) 103.
[10] Reinhard P.-G., Flocard H., Nucl. Phys. A **584** (1995) 467.
[11] Chabanat E. *et al*, Nucl. Phys. A **627** (1997) 710.
[12] Klüpfel P. *et al*, Phys.Rev. C **79** (2009) 034310.
[13] Audi G. *et al*, Nucl. Phys. A **729** (2003) 3.
[14] Hofmann S. *et al*, Eur. Phys. J. A **10** (2001) 5.
[15] Tandel S.K. *et al*, Phys. Rev. Lett. **97** (2006) 082502.
[16] Oganessian Yu. Ts. *et al*, Phys. Rev. C **74** (2006) 044602.

Mode-coupling in a relativistic two-phonon model*

E. Litvinova[1,2], P. Ring[3], and V. Tselyaev[4]

[1]GSI Helmholtzzentrum für Schwerionenforschung, Germany; [2]Institut für Theoretische Physik, Goethe-Universität, Frankfurt am Main, Germany; [3]Physik-Department, Technische Universität München, Germany; [4]Nuclear Physics Department, St. Petersburg State University, Russia

The relativistic quasiparticle time blocking approximation (RQTBA), developed recently as a consistent combination of the covariant energy density functional theory (CEDFT) and the modern extensions of the Landau–Migdal theory of finite fermi systems, is reviewed in Ref. [1]. In the RQTBA, starting from the covariant energy functional, phonon energies and their vertices are calculated without any further parameters. They form the basis of particle-vibrational coupling leading to an energy dependence of the self-energy and an induced energy-dependent interaction in the response equation. A proper subtraction of the static phonon coupling contribution from the induced interaction avoids double counting of this contribution. Applications in spherical nuclei show excellent agreement with experimental data on nuclear spectra below 30 MeV.

The theoretical description of nuclear low-lying dipole strength remains among the most important problems in nuclear structure and nuclear astrophysics. Modern measurements of the dipole strength resolve the fine structure of the spectra below the neutron threshold. This offers exciting opportunities for microscopic nuclear structure models to describe the fine structure of the dipole spectra below the neutron threshold and to help in analyzing the experimental data.

In nuclei with pronounced isospin asymmetry the low-lying dipole strength is characterized by the pygmy resonance which is a coherent oscillation of the isospin excess against the isospin saturated core. Since the pygmy dipole mode has essentially surface nature, it mixes with other surface modes, especially with low-lying ones. This supposition has been confirmed by explicit RQTBA calculations. It has been found that the pygmy mode, arising in RQRPA as a single state or as very few low lying dipole states with isoscalar character, is strongly fragmented over many states in a broad energy region due to the coupling to phonons. As a result, some fraction of the strength is located well below the original position of the RQRPA pygmy mode. Compared to existing data, the RQTBA describes the total fraction of the dipole strength below the neutron threshold very reasonably. However, in order to account for the fine structure of the spectrum, more correlations should be included in the microscopic model. In particular, it has to reproduce the lowest dipole state in vibrational nuclei, which is identified as a member of the quintuplet $[2^+_1 \otimes 3^-_1]$.

A two-phonon version of the relativistic quasiparticle time blocking approximation (RQTBA-2) represents a new class of many-body models for nuclear structure calculations based on the covariant energy density functional [2]. As a fully consistent extension of the relativistic quasiparticle random phase approximation (RQRPA), the two-phonon RQTBA implies a fragmentation of nuclear states over two-quasiparticle and two-phonon configurations. This leads, in particular, to the splitting-off the lowest 1^- state as a member of the two-phonon $[2^+ \otimes 3^-]$ quintuplet from the pygmy dipole mode. The inclusion of the two-phonon configurations in the model space allows to describe the positions and the reduced transition probabilities of the lowest 1^- states in the tin isotopic chain as well as the low-energy fraction of the dipole strength without any adjustment procedures [2]. The model is also applied to the low-lying dipole strength in neutron-rich ^{68,70,72}Ni isotopes, see Fig. 1. Recent experimental data for ^{68}Ni [3] are reproduced fairly well.

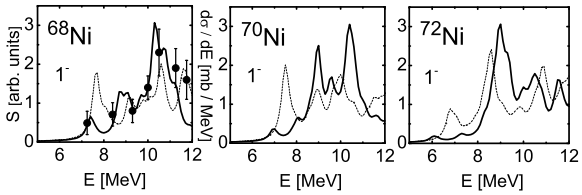

Figure 1: Low-lying dipole spectra of ^{68,70,72}Ni calculated within the RQTBA (dashed curve) and the RQTBA-2 (solid curve) with a smearing of 200 keV. Left panel contains also the data (filled circles with error bars, units on the right).

Being applied to the description of the pygmy dipole resonance, the relativistic two-phonon model provides a new quality of understanding of mode coupling mechanisms in nuclei. The method is based on Green's function techniques and can be widely applied also in other areas of quantum many-body physics.

References

[1] P. Ring, E. Litvinova, Phys. Atomic Nuclei 72, 1285 (2009).

[2] E. Litvinova, P. Ring, V. Tselyaev, arXiv:0910.4343 [nucl-th].

[3] O. Wieland *et al.*, Phys. Rev. Lett. **102**, 092502 (2009).

* Work supported by the HIC for FAIR Program.

Microscopic M1 strength functions for nuclear astrophysics

H.P. Loens[1,2], K. Langanke[1,2], G. Martínez-Pinedo[1,2], and K. Sieja[1]
[1]GSI, Darmstadt, Germany; [2]Institut für Kernphysik, TU Darmstadt, Darmstadt, Germany

The so-called Hauser-Feshbach model relies on various nuclear structure input, e.g. nuclear masses, nuclear level densities, and radiative strength-functions (RSFs). The latter are a crucial input to the description of the γ-channel that is usually dominated by E1 and M1 transitions for which one often applies analytical formulae: the E1 transitions are usually described with a Lorentzian form adjusted to the electric giant dipole resonance [1] based on experimental data. The M1 transitions one usually modeled by using either the single-particle approach, which gives an energy independent strength [5], or by a Lorentzian representing the spin-flip resonance [4].
Unfortunately all these approaches are not capable of taking into account any low-lying strength such as a Pygmy dipole resonance (PDR) or a scissors mode. For the PDR a recent study showed, that it can have a strong influence on the reaction rate needed for r-process nucleosynthesis [3]. A similar study has not been performed for M1 transitions yet. Therefore we have examined the influence of the scissors mode on theoretical (n,γ) rates with the help of a shell-model M1 strength description. Although E1 transitions usually dominate, the M1 transitions can become more important when reaching the dripline or when one parity dominates up to excitation energies of several MeV [2].

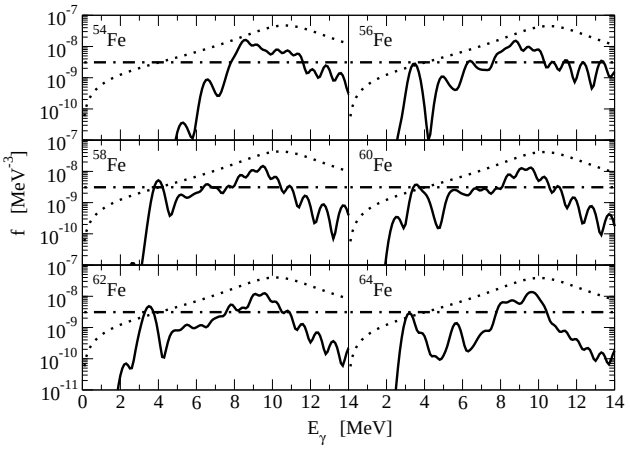

Figure 1: Different RSFs for iron isotopes from the single-particle model (dash-dotted) [5], a Lorentzian parametrisation [4] (dotted), and the shell-model (solid).

In fig. 1 we can see the RSFs for different iron isotopes. Clearly we can also see the low-lying M1 strength resulting from a scissors mode in $^{56-64}$Fe in the shell-model approach (solid line). The Lorentzian parametrisation (dotted line) gives a larger integrated strength compared to the shell-model strength.

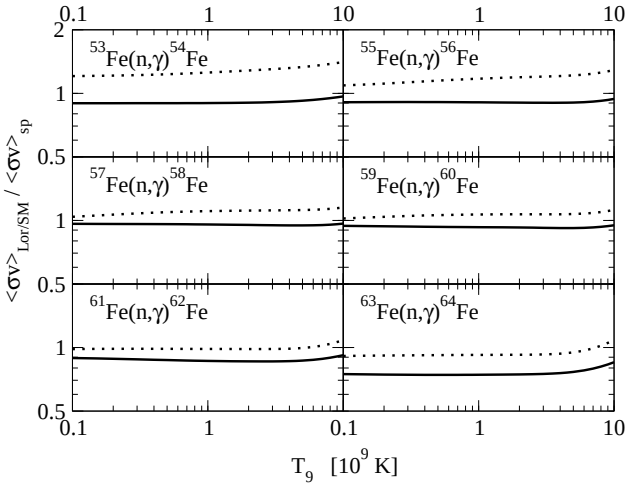

Figure 2: Ratio of reaction rates (see text for further explanation); the E1 transitions were treated identically for all reaction rates.

Fig. 2 shows the ratio of reaction-rates obtained with either a Lorentzian approach (dotted) or a shell-model approach (solid) to the single-particle approach. We can see that by going towards the neutron-dripline the overall effect from the Lorentzian approach changes: while for the radiative-neutron captures on $^{53-59}$Fe the spin-flip resonance dominates (due to the high neutron-separation energy), the Lorentzian low-energy tail for the the reactions on $^{61-63}$Fe reduces the reaction rate. The shell-model calculation generally gives lower reaction-rates compared to the single-particle approach in the relevant energy regions. Unfortunately the E1 transitions are too dominant in the reactions studied here to resolve the nuclear structure effect of a potential scissors mode. For that we will have to go to more neutron-rich nuclei closer to the dripline. Here the low neutron-separation energies may lead to a competition between E1 and M1 transitions.

References

[1] J.J. Cowan *et al.*, Phys. Rep. **208**, 1 (1991)
[2] H.P. Loens *et al.*, Phys. Lett. B **666**, 4 (2008)
[3] E. Litvinova, Nucl. Phys. A **863**, 26 (2009)
[4] RIPL-2 Handbook, http://www-nds.iaea.org/RIPL-2/
[5] J.A. Holmes *et al.*, ADNDT **18**, 305-412 (1976)

The effects of r-process heating on fall-back accretion in compact object mergers

A. Arcones *[1,2], G. Martínez-Pinedo[1], B. D. Metzger[3], and E. Quataert[3]

[1]GSI Helmholtzzentrum für Schwerionenforschung, Planckstr. 1, 64291 Darmstadt, Germany; [2]Institut für Kernphysik, TU Darmstadt, Schlossgartenstr. 9, D-64289 Darmstadt, Germany; [3]Astronomy Department and Theoretical Astrophysics Center, University of California, Berkeley, 601 Campbell Hall, Berkeley CA, 94720

Gamma-ray bursts (GRBs) are one of the most energetic explosions observed in the universe. Observations indicate that there are long-duration GRBs resulting from the deaths of massive stars and short-duration GRBs whose origin remains unknown. The most popular and well-studied engine model for short GRBs is the binary merger of two neutron stars (NS-NS) or a neutron star and a black hole (NS-BH).

Mergers result in a central compact object (neutron star or black hole) surrounding by a compact disk ($\approx 10^{-3} - 0.1 M_\odot$). The accretion timescales of the disk are similar to the duration of the burst. This favours the compact object mergers as explanation for the short GRBs. However, this scenario has become more complex with the discovery that short GRBs are often followed by a "tail" of emission (usually soft X-rays). In our work [1] we find that the heating produced by r-process (rapid neutron capture process) can produce a complete cut-off in the fall-back and for some combination of parameters this fall-back can reappear producing the observed tail in the X-ray emission. In our study

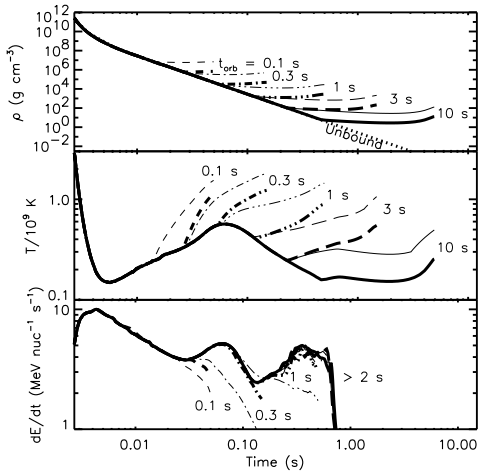

Figure 1: Density and temperature evolutions of trajectories with different orbital periods ($t_{\rm orb}$) that are given in the figures. The bottom panel shows the total r-process heating rate for the same trajectories.

we have used a merger trajectory from [2] to describe the early exponential expansion. For the later evolution, material with negative binding energy (E) and orbital period $t_{\rm orb} \propto |E|^{-3/2}$ decouples from the unbound material and follows $\dot{M} \propto t_{\rm orb}^{-5/3}$. The evolution of density and temperature is shown in the upper and middle panels of Fig. 1 for trajectories with different orbital periods as indicated in the figure. Total r-process heating rate for these trajectories appears in the bottom panel. We have used a dynamical r-process network that includes neutron captures, photodissociations, beta decays, and fission. The contribution of the r-process heating is consistently added to the entropy to determine the temperature change.

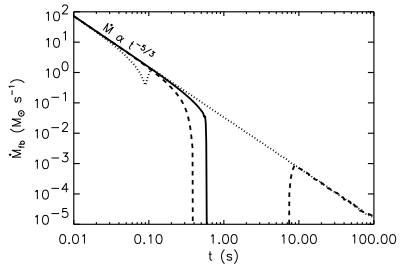

Figure 2: Fall-back rate $\dot{M}_{\rm fb}$ in NS-NS/NS-BH mergers including the effects of r-process heating. Different line styles correspond to different heating timescales: $t_{\rm heat} = 0.1$ s (dotted line), 0.86 s (dashed line), and 3 s (solid line).

In the paper [1] an analytic model has been developed to study the evolution of the fall-back material. We found that when the heating time scale (i.e., timescale for the r-process heating) gets similar to a critical orbital period, there is a cut-off in the accretion (solid curve in Fig. 2). However, material with binding energy above some critical value may remain marginally bound, thus leading to a temporal gap in the fall-back rate. This is shown in Fig. 2 by the dashed curve corresponding to a model with $t_{\rm heat} = 0.86$ s.

The heating from the r-process can change the dynamics of the fall-back accretion in compact object mergers. Including a full r-process network into merger simulations is not yet computational doable, however one has to think how to account for the contribution of r-process heating in the simulations.

References

[1] B. D. Metzger, A. Arcones, E. Quataert and G. Martinez-Pinedo "The effects of r-process heating on fall-back accretion in compact object mergers" Accepted in MNRAS.

[2] C. Freiburghaus, S. Rosswog, and F.-K. Thielemann 1999, ApJL, 525, L121

* supported by the Deutsche Forschungsgemeinschaft through contract SFB634

Thermodynamics of nuclear matter with clusters *

S. Typel[1,2,3], G. Röpke[4], D. Blaschke[5,6], T. Klähn[5,7], M. Voskresenskaya[1], and H.H. Wolter[2,8]

[1]GSI, Darmstadt; [2]Excellence Cluster Universe, Garching; [3]Technische Universität München; [4]Universität Rostock; [5]Uniwersytet Wrocławski; [6]JINR, Dubna; [7]Argonne National Laboratory; [8]Ludwig-Maximilians Universität München

The composition and the equation of state (EoS) of nuclear matter from very-low to super-saturation densities are widely discussed in several areas of nuclear physics and astrophysics. In particular, the dependence of the thermodynamical properties on the neutron-proton asymmetry, represented e.g. by the symmetry energy, is of crucial importance in heavy-ion collisions, exotic nuclei, neutron stars, and core collapse supernovae.

We investigate properties of nuclear matter at finite temperature and density, including the formation of light clusters (deuteron, triton, helion, and α-particle). The novel feature of this work [1] is to include the formation of clusters as well as their dissolution due to medium effects in a systematic way using two many-body theories: a microscopic quantum statistical (QS) approach and a generalized relativistic mean-field (RMF) model with density-dependent nucleon-meson couplings. Nucleon quasi-particle properties are determined within the RMF model from the scalar and vector self-energies. Cluster binding energies are reduced in the medium due to Pauli blocking shifts calculated in the QS approach. Both models reproduce the limiting cases of nuclear statistical equilibrium (NSE) at low densities and nuclear matter free of clusters at high densities. The treatment of the cluster dissociation is based on the Mott effect, implemented in slightly different ways in the QS and generalized RMF approaches. This leads to somewhat different results in the intermediate density range of about 10^{-3} to 10^{-1} fm^{-3} which gives an estimate of the present accuracy of the theoretical predictions.

The cluster abundances and thermodynamical properties of theses models are compared in the region of temperatures $T \leq 20$ MeV and baryon number densities from zero to a few times nuclear saturation density. The effect of cluster formation on the liquid-gas phase transition and on the density dependence of the symmetry energy is studied. We demonstrate that the parabolic approximation for the asymmetry dependence of the nuclear EoS breaks down at low temperatures and at subsaturation densities due to cluster formation. Comparison is made with other theoretical approaches, in particular those that are commonly used in astrophysical calculations. Substantial differences are found.

Conventional theoretical calculations based on mean-field approaches fail to describe the correct density-dependence of the symmetry energy in the low-density, low-temperature limit. New data from heavy-ion collisions can be used to extract the free and internal symmetry energies at subsaturation densities and temperatures below 10 MeV, see [2] for details. Figure 1 depicts the dependence of the free and internal symmetry energy on the surface velocity $v_{\rm surf}$, that is a parameter measuring the time when particles leave the source in the heavy-ion collision. The QS approach with clusters predicts symmetry energies that are in very good agreement with experimental data. It uses the nucleon self-energies from the RMF model with density-dependent couplings in a parametrized form.

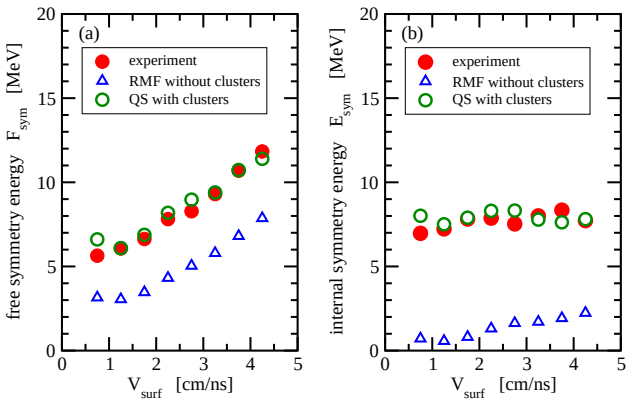

Figure 1: Free and internal symmetry energy as a function of the surface velocity. Experimental results are compared with results of theoretical calculations neglecting cluster formation (RMF) and including cluster formation (QS).

The density dependence of the nucleon-meson couplings in the RMF model is found by fitting properties of finite nuclei assuming a particular functional form [3]. It is well determined only at densities near saturation. The couplings in the limit of zero density are presently obtained from an extrapolation. Investigating the low-density limit of the generalized RMF model with clusters we find relations between the zero-density couplings and the nucleon-nucleon scattering lengths that will help to better constrain the parameters of the RMF model.

References

[1] S. Typel, G. Röpke, T. Klähn, D. Blaschke and H. H. Wolter, Phys. Rev. C **81**, 015803 (2010).

[2] J. B. Natowitz, G. Röpke, S. Typel, D. Blaschke, A. Bonasera, K. Hagel, T. Klähn, S. Kowalski, L. Qin, S. Shlomo, R. Wada and H. H. Wolter, arXiv:1001.1102 [nucl-th].

[3] S. Typel, Phys. Rev. C **71**, 064301 (2005).

* This research was supported by the DFG cluster of excellence "Origin and Structure of the Universe" and CompStar, a Research Networking Programme of the European Science Foundation.

Giant monopole resonances in an improved transport model*

T. Gaitanos, A.B. Larionov, H. Lenske, and U. Mosel
Inst. für Theor. Physik, Giessen, Germany

The nuclear giant monopole resonance (GMR or breathing mode), i.e. the collective isoscalar 0^+ excitation of a nucleus, is investigated within an improved relativistic Boltzmann-Uehling-Uhlenbeck (BUU) transport approach. The theoretical investigation and physical interpretation of the properties (centroid energies, decay modes) of this resonance is still an object of current debates [1, 2, 3]. It represents also an important tool to better understand the nuclear many-body problem. Many microscopic models have been developed for the theoretical description of the GMR. They can be divided into two groups: purely quantum mechanical approaches and semi-classical dynamical models, see the review [1, 2] for details. Here we apply a semi-classical transport approach, i.e., the relativistic Giessen-Boltzmann-Uehling-Uhlenbeck (GiBUU) model, to collective isoscalar monopol vibrations. The GiBUU transport equation is solved with the test particle *Ansatz*, where the collision integral is treated in an parallel ensemble algorithm.

The numerical treatment of the GiBUU equation for the case of small-amplitude collective vibrations excited in a finite nuclear system is not trivial. It requires a very good stability of the ground state configurations, which is difficult to reach in the spirit of the test-particle method. So far empirical density distributions have been used to initialize ground state nuclei in transport simulations, which might be not always consistent with the energy density functional used for the propagation of the system. Another well known problem is related to the calculation of Pauli blocking factors in the Uehling-Uhlenbeck collision integral for the small-amplitude Fermi surface distortions. We thus have improved the relativistic GiBUU transport model by performing Thomas-Fermi calculations with the same energy-density functional as that used in the dynamical evolution. Furthermore, the numerical treatment of the Pauli blocking factors has been carefully studied, as in detail explained in Ref. [4]. The inclusion of collisions decline the numerical propagation of nuclear ground states, however, the spurious particle emission is of the order of max. 10% for $t > 400$ fm/c. The simulation of collective vibrations is modeled by scaling all test particle coordinates such that the corresponding excitation is close to the experimental data, before the propagation starts.

The results are shown in Fig. 1. The excitation energy is close to the experimental data, and agrees also with calculations according the liquid-drop model. The situation for the width is more involved. Pure Vlasov calculations, in which only one-body friction is included and is in agreement with wall formula calculations, strongly underpredict the data.

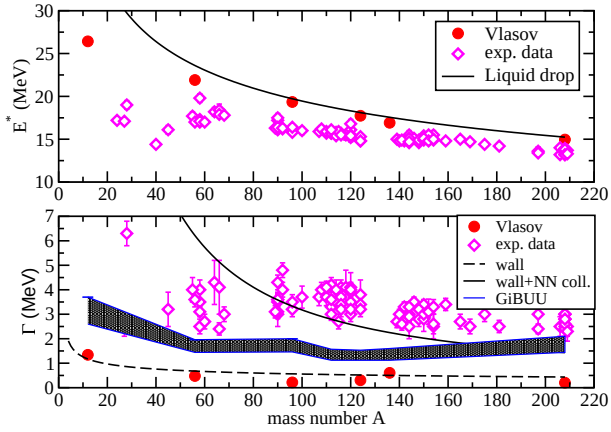

Figure 1: Excitation energy (upper panel) and width (lower panel) of the GMR as function of the mass number. Vlasov and full BUU results (filled circles and gray band, respectively) are compared with experimental data (open diamonds). The solid line in the upper panel shows liquid-drop model results. In the lower panel, the dashed line depicts the wall formula results, while the solid line shows the full width including both the wall and collisional contributions.

The inclusion of collisions improves the situation to some extend. It is worthwhile to note that similar results are obtained in recent quantal (Q)RPA calculations [3], in which only $2p2h$ configurations are accounted for. Only extended RPA models by including a coupling to more complex configurations or a coupling of $1p1h$ to phonons can explain the experimental data better.

We conclude that the present improved relativistic GiBUU transport approach is appropriate to describe the basic features of collective small-amplitude vibrations and is in satisfactory agreement with standard RPA calculations. It would be helpful to extend this study to other vibration modes such dipole and quadrupole excitations.

References

[1] J.P. Blaizot, Phys. Rep. 64 (1980) 171.

[2] S. Kamerdzhiev, J. Speth, G. Terychny, Phys. Rep. 393 (2004) 1.

[3] V. Tselyaev et al., arXiv:0912.5328 [nucl-th].

[4] T. Gaitanos, A.B. Larionov, H. Lenske, U. Mosel, in preparation.

* Work supported by DFG and BMBF.

Isospin Observables in Multifragmentation of Relativistic Projectiles*

S. Bianchin[1], A.S. Botvina[2], N. Buyukcizmeci[3], J. Łukasik[4], I.N. Mishustin[2], R. Ogul[3], C. Sfienti[5], W. Trautmann[1], and the ALADIN Collaboration[†1]

[1]GSI, Darmstadt, Germany; [2]FIAS, J.W. Goethe University, Frankfurt, Germany; [3]Selçuk University, Konya, Turkey; [4]IFJ-PAN, Kraków, Poland; [5]Catania University and INFN, Catania, Italy

Multifragmentation is a universal phenomenon occurring when a large amount of energy is deposited in a nucleus. It was observed in high energy nuclear reactions induced by hadrons and heavy ions. It is believed to be a manifestation of the nuclear liquid-gas phase transition which is also expected to occur in crusts of neutron stars and in supernova explosions. This reaction offers a unique possibility to experimentally study properties of fragments imbedded in the hot environment of other nuclear species. The ALADIN experiment S254, conducted in 2003 at SIS, was designed to study isotopic effect in projectile fragmentation at relativistic energies [2, 3]. Stable beams of neutron-rich ^{124}Sn and radioactive beams of neutron-poor ^{107}Sn and ^{124}La, delivered by the fragment separator FRS, were used. The ALADIN set up permits the nearly complete detection and identification of all particles with $Z \geq 2$ originating from the disintegration of excited projectile spectators [4]. For the analysis of the experimental data, the Statistical Multifragmentation Model (SMM, Ref. [1]) has been used. Previously, the SMM was successfully applied for the interpretation of experimental data by many groups.

By selecting a realistic ensemble of excited residual nuclei emerging after the fast dynamical stage of the reaction, it has been possible to describe important characteristics of the fragment charge distributions and correlations: cross-section and multiplicity distributions and fragment-fragment correlations within events. The analysis of isotope distributions and of the neutron contents of produced fragments as well as the isoscaling analysis [2] have shown that the properties of fragments at the breakup stage of these multifragmentation reactions are different from those of cold isolated nuclei as assumed in the standard version of the SMM [5]. In particular, the symmetry energy of fragments has to be considerably lowered in order to describe the observed neutron richness of the produced fragments. This is illustrated in Fig. 1 where the experimental yields of fragments with $7 \leq Z \leq 10$ are shown in comparison to the results of standard and modified calculations. The observed effect is attributed to the influence of the surrounding matter and possible expansion or deformation of the fragments as they form in the hot environment. This effect has far reaching consequences for astrophysical processes like supernova explosions when similar temperatures and densities can be reached [6].

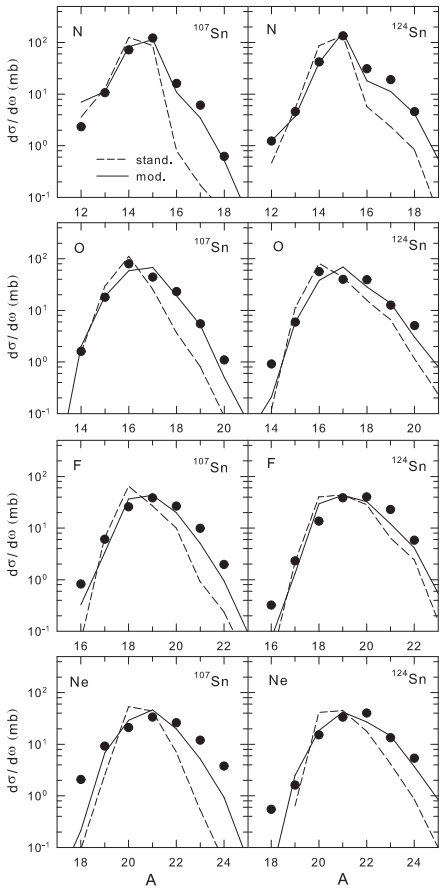

Figure 1: Isotope distributions of fragments with atomic number $Z = 7 - 10$ for ^{107}Sn (left panels) and ^{124}Sn (right panels), integrated over $0.2 \leq Z_{\rm bound}/Z_0 \leq 0.8$. The dots represent the experimental data. Normalized results from calculations with the standard ($\gamma = 25$ MeV) and modified ($\gamma = 14$ MeV) symmetry-term coefficients are shown by the dashed and solid lines, respectively.

References

[1] J.P. Bondorf et al., Phys. Rep. 257 (1995) 133.

[2] S. Bianchin et al., GSI Scientific Report 2007, p. 165.

[3] C. Sfienti et al., Phys. Rev. Lett. 102 (2009) 152701.

[4] A. Schüttauf et al., Nucl. Phys. A607 (1996) 457.

[5] N. Buyukcizmeci et al. Invited talk at NUFRA2009, Kemer, Turkey, http://fias.uni-frankfurt.de/nufra2009.

[6] A.S. Botvina and I.N. Mishustin, preprint arXiv:0811.2593 (2008).

* Work supported by EU under contract No. HPRI-CT-1999-00001.

† w.trautmann@gsi.de

Protons and deuterons from Al+Al collisions at 1.93A GeV measured by FOPI*

K. Piasecki† [1,2], N. Herrmann[1], and FOPI collaboration[1]

[1]Physikalisches Institut, Universität Heidelberg; [2]Institute of Experimental Physics, University of Warsaw, Poland

Full mapping of phase space of particles emitted from the final state of heavy-ion collisions at beam energies around 2A GeV has not yet been accomplished. This paper reports the investigation of protons and deuterons emitted from central collisions of light symmetric system of Al+Al at 1.93A GeV, done by FOPI. These particles, being the most abundant subsample of Light Charged Particles (LCP, Z$\leq$2), amount to a bulk of nuclear matter participating in the collision. Analysis of proton and deuteron phase space helps sheding light on a degree of nuclear stopping [1], and possible deviations from the ideal state of thermal equilibrium. The only published thermal model prediction for this colliding system [2] is based on an array of four yield ratios, limiting the predictive power to a coarse suggestion. Establishing the ratio of deuteron to proton yields enhances this array, which could be further on compared to the predictions of thermal models as well as the non-equilibrium transport model UrQMD [3].

The S279 experiment was carried out in August 2005 at the SIS-18. The ^{27}Al ions were hitting the ^{27}Al target, shifted 40 cm upstream from its nominal position. The CDC chamber was surrounded by the Plastic Barrel (PLB) in a version covering the polar angles between 27° and 57° with respect to the target position. Out of 290·10^6 recorded events in total, samples of 9.8·10^6 (29.5·10^6) events were selected for the analysis of protons (deuterons). For each sample, events corresponding to 20% of most central collisions were selected.

Particles were identified using standard FOPI PID techniques [4] and analysed on the $p_t - y$ (rapidity) plane. For CDC tracks matching the PLB hits, the information from both detectors was used, and for the particles emitted at polar angles larger that 57°, only the CDC information was available. The compensation of losses due to deficiency was done in two steps:

(i) losses due to cuts on mass parameter from CDC and PLB were compensated by extrapolating the gaussian-like mass distributions outside the cut bounds;

(ii) losses due to detectors, tracker algorythm, CDC-PLB matching and cuts intended to purify the sample were estimated by simulating 3·10^6 IQMD events in the GEANT environment and analysing the output with the help of the standard FOPI software.

The reconstructed $p_t - y$ phase space was first analysed in rapidity slices. The Boltzmann function

$$\frac{dN}{dp_T} = N \cdot p_T \cdot E \cdot exp(-m_T/T) \qquad (1)$$

where $m_T = (p_T^2 + m_{prot,deut}^2)^{1/2}$, was fitted to the data and the inverse slopes T were extracted. For protons (deuterons), T = 109±5 (112±8) MeV was found at the midrapidity of the nucleon-nucleon centre of mass. The rapidity distribution (see Fig. 1) was reconstructed by integrating out the fitted Eq. 1 for each rapidity bin. The integrated yield of protons (deuterons) was found to be 21.0±0.25 (4.0±0.25), and the deuteron to proton yield ratio 0.19±0.015. The above mentioned errors include the limitation of experimental and simulated statistics and inaccuracy due to extrapolation of p_T spectra, but not due to variation of cut parameters. Large abundance of deuterons relative to protons might require introducing cluster formation in the modelling of heavy-ion collisions. A careful investigation of all the systematic errors is ongoing.

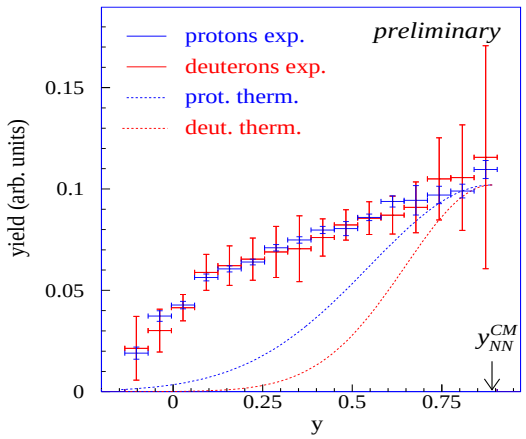

Figure 1: Rapidity distribution (normalized to unity) of protons and deuterons (solid) emitted from central collisions of Al+Al at 1.93A GeV compared to Boltzmann predictions assuming as temperatures the inverse slopes extracted from fits to p_t spectra (dashed).

References

[1] W. Reisdorf et al. (FOPI Collaboration), Phys. Rev. Lett. 92 (2004) 232301.

[2] X. Lopez et al. (FOPI Collaboration), Phys. Rev. C 76 (2007) 055203(R).

[3] S.A. Bass et al., Prog. Part. Nucl. Phys. 41 (1998) 225.

[4] B. Sikora (FOPI Collaboration), Acta Phys. Pol. B 31 (2000) 135.

* Work supported by BMBF 06HD154

† kpiaseck@physi.uni-heidelberg.de

Centrality dependence of K^+ flow in ^{58}Ni + ^{58}Ni collisions at 1.91A GeV measured with the FOPI detector *

T.I. Kang[†1,2], N. Herrmann[3], R. Averbeck[2], K. D. Hildenbrand[2], B. Hong[1], M. Kiš[2], Y. Leifels[2], K. Piasecki[3], W. Reisdorf[2], A. Schüttauf[2], and for the FOPI Collaboration[2]

[1]Korea University, Seoul, Korea; [2]GSI, Darmstadt, Germany; [3]Physikalisches Institut, Universität Heidelberg, Germany

Kaon production in ^{58}Ni + ^{58}Ni heavy-ion collisions at 1.91A GeV was measured by the FOPI collaboration at the heavy-ion synchrotron (SIS) at GSI making use of the newly installed MMRPC barrel [1]. Sub-threshold kaon production is expected to provide valuable insight into the properties of hadrons at high density [2]. The kaon-nucleon potential is expected to enhance the in-medium effective mass for K^+ and to reduce the effective mass for K^- if the system becomes more dense. Thus, the production of a K^+ will require more energy while the production of a K^- will require less energy in a dense system.

Furthermore, the repulsive kaon-nucleon potential tends to make kaons flow away from nucleons and the attractive antikaon-nucleon potential is expected to let anti-kaons flow similar to nucleons. Since the magnitude of these medium effects on charged kaons depends on the strength of the kaon-nucleon potential [2], in principle it is possible to deduce this strength from the measurement of charged kaon flow in heavy-ion collisions.

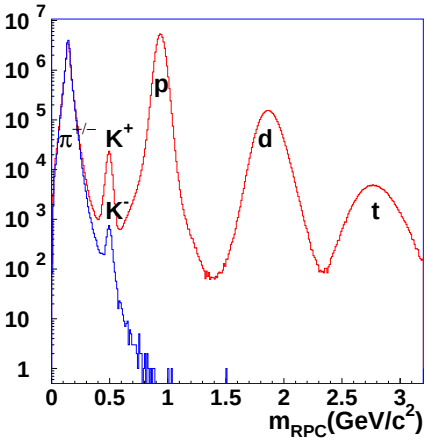

Figure 1: Reconstucted mass distribution of produced particles with $p_{lab} \leq 0.8$ GeV/c in ^{58}Ni + ^{58}Ni collisions. Positively (negatively) charged particles are shown by the red (blue) histogram.

In April 2008, the FOPI experiment has recorded 55 $\times$ 10^6 ^{58}Ni + ^{58}Ni collisions, corresponding to the most central 50 % of total geometric reaction cross section. 190,000 K^+ and 4,000 K^- are identified with a ratio of signal to background better than 9. We are able to identify K^+ up to a momentum of $p_{lab} = 1.1$ GeV/c and K^- could be separated from the background up to 0.8 GeV/c. Figure 1 shows the mass distributions of charged particles in ^{58}Ni + ^{58}Ni collisions at 1.91A GeV, demonstrating a clear separation of $\pi^{\pm}$, $K^{\pm}$, protons, deuterons, and tritons.

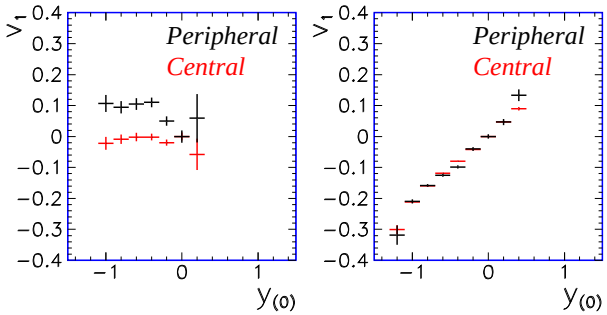

Figure 2: Directed flow parameter v_1 for K^+ (left panel) and for protons (right panel) for central ($b \leq 3$ fm) and peripheral collision ($b \sim 6 \pm 1$ fm) as a function of the normalized rapidity $y_0 = y_{lab} / y_{cm}$ - 1.

Figure 2 shows the fourier expansion coefficient v_1 for K^+ and protons for two different centrality selections, extending our previous FOPI result [4]. The values reported in Figure 2 are obtained by analyzing transverse momentum in the FOPI acceptance, upper momentum limit for kaons $p_{lab} \leq 1.0$ GeV/c for $30^o < \theta < 52^o$ (MMRPC Barrel) and 0.5 GeV/c for $52^o < \theta < 110^o$ (Plastic Barrel). While the K^+ directed flow shows a distinct dependence on the collision centrality, the proton flow is the same for central and peripheral collisions.

A detailed comparison of our data with state of the art transport models will help to disentangle the density and the momentum dependence of the kaon nucleon potential.

References

[1] A. Schüttauf *et al.*, Nucl. Phys. B Proc. Supp. 158 (2006) 52.

[2] W. Cassing and U. Mosel, Prog. Part. Nucl. Phys. 25 (1990) 235.

[3] G. Q. Li, C. M. Ko, and Bao-An Li Phys. Rev. Lett. 74 (1995) 235.

[4] P. Crochet *et al.*, Phys. Lett. B 486 (2000) 6.

* Work supported by DFG 446 KOR 113/216/0-1, BMBF 06HD190I and EU/FP6 I3 HPcontract no. R113-CT-2004-506078.

† t.i.kang@gsi.de

The ppK$^-$ Experiment at GSI *

M. Berger[1], L. Fabbietti[1], R. Münzer[1], and the FOPI Collaboration
[1]TU München - Excellence Cluster Universe, 85748 Garching

Recently, the search for deeply bound nuclear states with antikaons has attracted large interest. As it is suggested by recent results by the DISTO collaboration from a reanalysis of older data p+p reaction might be a promising tool to produce (K$^-$pp) nuclear bound states. Recent results of analysis gave an indication for the existence of this lightest kaonic bound state (Ref. [1]). New experiments have been proposed to study this kind of physics and a measurement was performed in October 2009 using the FOPI detector [2] to detect the final state particles in the reaction p+p$\rightarrow$(K^-pp) + $K^+ \rightarrow \Lambda$p $K^+ \rightarrow$ p + π^- + p + K^+. By the measurement of all charges particles the binding energy of the (K$^-$pp) could be determined by the missing mass of the K$^+$ and the invariant mass of Λp.
In the experiment in October 2009 a proton beam with a beam energy of 3.1 GeV and liquid hydrogen target with 2 cm thickness was used. To improve the tracking capability in the forward direction and reduce background events the additional detector SiΛViO (Silvion for Λ Vertexing and Identification Online) was put inside FOPI directly after the target. This detector consists of two layers of segmented silicon detectors that cover the polar region from 10° to 35°, that are used to create a trigger signal and one additional track point. The trigger signal is created by measuring the hit-multiplicity in the two layer, which should be higher in the second layer in the case of a Λ that has decayed between the two layers.
The trigger signal of SiΛViO combined with the first level

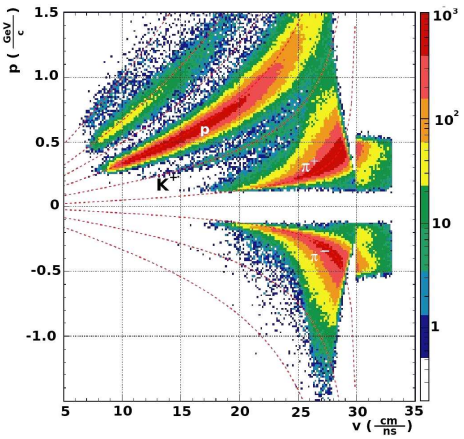

Figure 1: Momentum times charge measurement versus time-of-flight. The signal for K$^+$ could be separated up to 0,7$\frac{GeV}{c}$

Trigger condition, which requires at least 2 charged particles in the time of flight detectors, was used to generate the second level trigger (LVL2). During this measurement about 80 million second level trigger events were recorded. A crucial point for the reconstruction of the interesting decay channel is the identification of K$^+$, which is been done by time-of-flight and momentum measurement. The best time-of-flight resolution could be achieved by the Resistive Plate Chambers (RPC). Figure 1 shows the particle momentum against the particle velocity. From this picture one can see, that the separation of K$^+$ is possible up to momentum of 0.7 $\frac{GeV}{c}$.
The second crucial point is the identification of Λ-particles

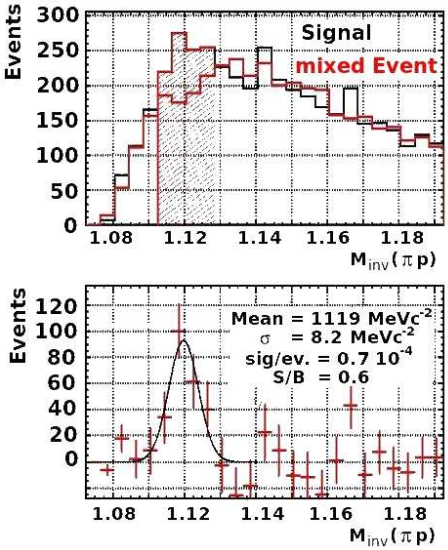

Figure 2: Invariant-mass of pπ^- emitted under small polar angles, which were detected by SiΛViO, Helitron and PLAWA

which are emitted under small polar angles. To improve the secondary vertex resolution the trackpoint in SiΛViO is used to improve the track resolution. By using geometrical and momentum cuts a first Λ signal in the invariant mass spectrum of pπ^- could be be seen. In the upper picture of Fig. 2 can see the signal together with the combinatorial background in red, calculated exploiting the mixed event technique. The difference of the both shows a peak at 1,119$\frac{GeV}{c^2}$ with a sigma of 8,2 $\frac{MeV}{c^2}$ and 0.7$\cdot$ 10^4 Λ-Hyperon per event.

References

[1] M.Maggiora, Proceedings of the 'Hypernuclear and Strange Particle Physics' conference, Tokai, 2009

[2] http://www.gsi.de/documents/DOC-2007-Mar-168-1.pdf

* Work supported by HGF and DFG-Excellence Cluster Universe

Start counter and target system for the FOPI S349 experiment*

P. Bühler[1], O. Hartmann[1], M. Schafhauser[1], K. Suzuki[1], J. Zmeskal[1], and FOPI collaboration

[1]SMI, Vienna, Austria

In summer 2009 the FOPI collaboration carried out experiment S349. This experiment aims at investigating the potential existence of the most fundamental antikaon-nucleon bound state, the K^-pp [1]. The antikaon is predicted to form nuclear bound states, because of the strongly attractive interaction between the antikaon and nucleon [2]. The verification of the existence of this bound state with a reliable experiment is of vital importance and will shed light on the nature of the $\overline{K}N$ interaction.

To investigate the properties of the system K^-pp we exploited the reaction

$$p + p \rightarrow K^+ + K^-pp \rightarrow K^+ + \Lambda + p \qquad (1)$$

at 3.1 GeV incident proton energy. In 42 shifts approximately $80 \cdot 10^6$ level 2 trigger events were acquired. The data analysis is in progress.

The experiment with a proton beam poses specific requirements to the detectors and the original FOPI setup therefore needed some modifications. The new hardware developments for this experiment include a start counter, a Beam Profile Monitor (BPM), a veto detector, a liquid-hydrogen target, and a Λ-trigger. A schematic layout of the beam line with the various elements is presented in Figure 1. The whole setup was mounted upstream of the FOPI CDC such that the target center was placed at -40 cm upstream from the CDC center.

The **Λ-trigger** is a detector system which allows to select events with Λ hyperon production on the hardware level and thus enhances the number of potentially interesting events in the acquired data. It was build at the TU Munich and has been presented in a previous report [3].

The **start counter** needed to be sensitive to MIPs and was required to provide a time resolution of around 100 ps at counting rates of up to a few times 10^6 counts per second. We used a 1 cm thick scintillating detector consisting of 5 vertically arranged, 2 mm wide segments. Each segment was readout on both ends with PMTs. Power supply boosters were used for the last three dynodes of the PMTs which helps to keep the gain high at high rates. The magnetic field strength at the location of the start counter is still around 60 mT. In order to work safely the PMTs were magnetically shielded with iron tubes and were mounted in an iron box. With this setup an intrinsic time resolution of ≈ 130 ps was achieved at a rate of up to $2 \cdot 10^6$ 1/s.

The **liquid hydrogen target system** consisted of a cryogenic cooler and a cylindrical target volume with a radius and width of 1.5 cm. For space reasons and to keep the cryogenic part outside the main magnetic field the cryogenic setup was mounted upstream, just outside of the magnet yoke of the CDC. The target volume was connected to the cold head via a thin tube, through which the liquefied hydrogen was, driven by gravity, flowing into the target volume. It took roughly 8 hours to cool down and completely fill the target volume. One filling was sufficient for the entire beam time.

The **veto detector** was located close (upstream) to the target and vetoed data acquisition when charged particles penetrated off beam-axis. It confined the cross-section of the fiducial target volume to a circle with a diameter of 1 cm. The counter consisted of two 5 mm thick layers of scintillating material which both were split into 2 segments. For readout fine-mesh PMTs were used because of the magnetic field of 0.6 T. The veto PMTs were also operated with boosters and additionally shielded with three layers of mu-metal. The veto efficiency was above 98%.

For this experiment we required the protons to be delivered with high precision onto the target. For beam tuning we needed a device which allowed to monitor the position and profile of the beam. The equipment for beam diagnostics in Cave-B is not suited for protons of 3.1 GeV. For this reason we developed a **Beam Profile Monitor (BPM)**. The BPM consist of a mesh of $16+16$ scintillating fibers which are read out by Silicon Photo-multipliers (SiPM) [4]. The active area is 3.2×3.2 cm^2. After setup of the beam the BPM was lifted out of the beam for data taking.

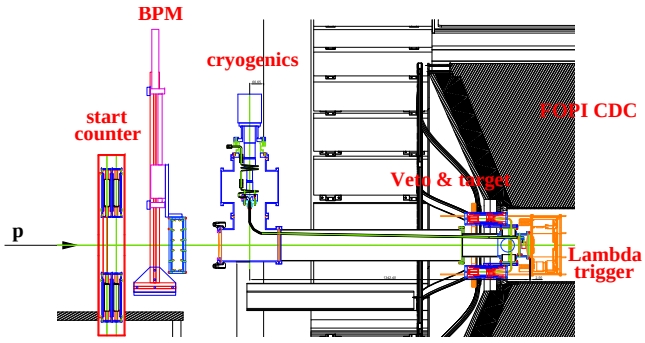

Figure 1: Layout of the beam line for the $p + p$ experiment showing the position of the start counter, BPM, veto detector, target, and Λ-trigger

References

[1] K. Suzuki *et al.*, Nucl. Phys. A 827 (2009) 312.

[2] T. Yamazaki and Y. Akaishi, Physical Review C 76 (2007) 045201.

[3] M. Berger *et al.*, GSI Jahresbericht 2008, INSTRUMENTS-METHODS-24.

[4] K. Suzuki *et al.*, Nucl. Instr. and Methods A 610 (2009) 75.

* Work supported by FWF project P21457-N16

Wavelets decomposition properties in the vicinity of Gibbs instabilities

P. Koczoń[1], S. Lebedev[1,2], and G. Ososkov[2]
[1]GSI, Darmstadt, Germany; [2]JINR, Dubna, Russland

Abstract: Applicability of the wavelet decomposition method for detection of a mass lines on some complicated background just above the reaction phase space limit has been investigated. A possibility of circumventing so-called Gibbs instability by means of artificial background prolongation is reported.

Introduction

Wavelet analysis (WA) can be used for disentangling useful signals from statistical fluctuations [1]. The decomposition can be performed in a chosen basis of wavelets (similar to Legendre polynomials analysis). For this report a set of second derivatives of Gaussian function (mexican hat shaped functions) has been used as a basis. Significant and the most interesting structures resulting from WA are usually being deformed near the edge of the analysed distribution [2]. A method of removing this Gibbs instability is reported.

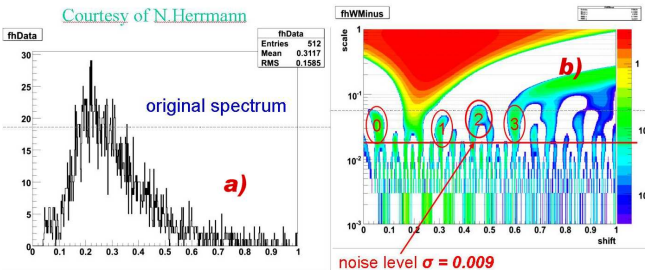

Figure 1: Invariant mass distribution to be analysed is shown in (a). The result of the wavelet analysis is presented (b). The red line marks scale limit above which searched structures (0,1,2,3) can be observed.

Invariant mass spectrum analysis

A partially resolved invariant mass distribution measured by FOPI group in one of numerous beam times has been kindly provided by Norbert Herrmann (Fig.1a). Wavelets decomposition graph is presented in Fig.1b. The largest scale parameter values (around 1) correspond to a bulk structure of the analysed distribution and are attributed to the background. The scale parameter values below 10^{-2} are interpreted as noise. The middle part (scale between 10^{-1} and 10^{-2}) shows several remarkable structures. These are usually signatures for significant, althought invisible peaks in the measured spectrum. Well visible objects 1 and 2 are attributed to hidden mass peaks, while interpretation of number 0 and 3 (towards both ends of the distribution) is not yet established, because of the deteriorating influence of Gibbs instabilities, an artefact of WA. Gibbs instabilities can be at least partially removed by an artificial extension of measured spectrum by means of, for example, symmetrization or just prolongation with flat, white-noise-like continuation avoiding an abrupt end of the distribution. The last method has been investigated by simulation using a broad Gaussian distribution with a small gaussian peak ("signal") placed on its tail and shifted in several steps. For each position of the simulated "signal" the WA has been performed and the corresponding structure in the resulting graph has been characterised by its maximum value, width, position and integral. The same procedure has been repeated for "signal" on Gaussian distribution "improved" by a white-noise pedestal. Fig.2 presents a comparison of the simulations' results.

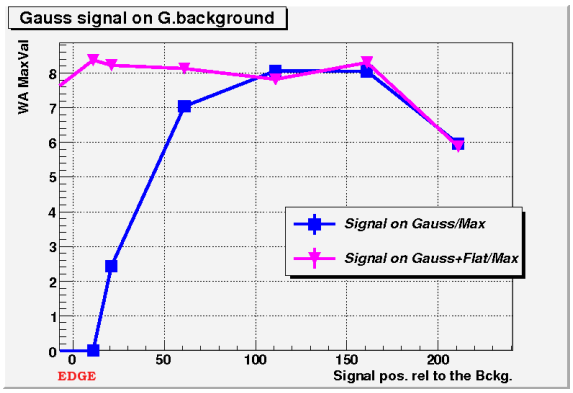

Figure 2: Wavelets Analysis results obtained with simulated input data: signal on a gaussian-shaped background distribution (blue) compared to signal on the same background, improved by introduction of the randomised pedestal (pink), where no Gibbs effect is expected. Maximum value of the resulting WA structure, corresponding to the signal strength, stays constant towards the left edge of the distribution in case of the extended distribution.

Summary

In the simulation it has been shown, that Gibbs instability occuring in the WA at edges of analysed distribution can be circumvented by introduction of a simple flat, white-noise-like pedestal underneath of the distribution to be analysed.

References

[1] http://www.amara.com/current/wavelet.html
[2] http://cnx.org/content/m10092/latest/

e^+e^- production in NN collisions at 1.25 GeV

I. Fröhlich[1], T. Galatyuk*[1], and J. Stroth[1] for the HADES Collaboration
[1]Goethe - Universität Frankfurt am Main, Germany;

Di-electron production in N+N collisions at $E_{kin} < 5$ GeV/u was studied previously by the DLS collaboration [1] and have been available for about 10 years, although with limited statistics and mass resolution. Microscopic transport calculation, hovewer, never succeeded to explain the experimental data satisfactory until a strong bremsstrahlung contribution in n+p interactions has been recently predicted within the framework of a covariant One Boson Exchange (OBE) model [2]. The authors choose the free parameters of their theory similar to the ones used in [3], but the restoration of the gauge invariance (for n+p) has been realized in a different way. This leads to different types of the form factors and quite different results. Indeed, it is found to differ by a factor of 4 for n+p interactions, but also by a factor of about 2 for p+p reactions at 1 GeV kinetic beam energy compared to the ones of Ref. [3]. As the NN bremsstrahlung process as included in the new OBE calculations from Kaptari *et al.* [2] is widely discussed in context with the interpretation of the ^{12}C+^{12}C data, we should have a closer look on the comparison of these calculations to the HADES data for p+p and n+p interactions.

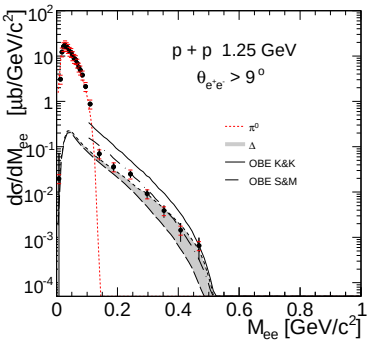

Figure 1: Invariant mass distribution of electron pairs measured in p+p reactions at a beam energy of 1.25 GeV [4]. The dashed and long-dashed lines show the contributions of π^0 and Δ Dalitz decays, respectively, in simulations using the resonance model. The enhancement due to the N-Δ transition form factor is shown as the grey area. The dashed and full lines are the results of OBE models [3] and [2], respectively.

The di-electron yield measured in p+p and n+p reactions is presented in Figs. 1 and 2, respectively. The theoretical curves show results of model calculations with the Pluto event generator [5]. At low masses a prominent $\pi^0 \rightarrow e^+e^-\gamma$ peak dominates the spectra. In the case of the p+p reaction, the region of invariant masses larger than

* Work supported by Helmholtz Alliance HA216/EMMI

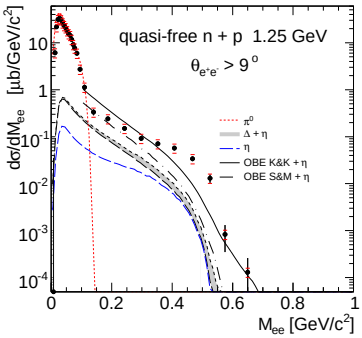

Figure 2: Invariant mass distribution of electron pairs measured in quasi-free n+p reactions at a beam energy of 1.25 GeV/u [4], same notations as in Fig. 1. Note, that the η contribution has been added to the OBE model calculations.

0.15 GeV/c^2 is well described by the simulation of the Δ Dalitz decay. A more accurate description is expected from the OBE models, since all amplitudes (graphs) involving intermediate Δ or nucleons are treated coherently. The predictions of [3] (dashed line) are in good agreement with the data, but the OBE model [2] (full line) overestimates the data. In case of n+p reaction, the resonance model simulation underestimates the measured dilepton yield. However, no satisfactory agreement is achieved either by the OBE exchange models. The yield in the high-mass region is too low and in the π^0 region the di-electron yield is unfortunately not calculated.

Our data for the invariant-mass spectrum in the reaction $np \rightarrow npe^+e^-$, extracted from the tagged subreaction in $dp \rightarrow p_{sp}npe^+e^-$, point to a shoulder at intermediate values of the di-electron invariant mass. Such a structure is hardly described within the hitherto models. As it has been shown, understanding the elementary channels remains challenging.

Acknowledgments: The authors are grateful to F. Iachello, R. Shyam, J. Van de Wiele and B. Martemyanov for the fruitful discussions.

References

[1] W.K. Wilson *et al.*, Phys. Rev. **C 57** (1998) 1865.
[2] B. Kämpfer and L.P. Kaptari, Nucl. Phys. **A 764** (2006) 338.
[3] R. Shyam and U. Mosel, Phys. Rev. **C 67** (2003) 065202.
[4] G. Agakishiev *et al.*, arXiv:0910.5875 [nucl-ex].
[5] I. Froehlich *et al.*, arXiv:0909.5373 [nucl-ex].

First ω-meson Production Cross Sections in the Leptonic and Hadronic Decay Channels in pp Collisions at 3.5 GeV*

K. Teilab[1], A. Tarantola[1,2], I. Fröhlich[1], T. Galatyuk[1,2], R. Holzmann[2], M. Lorenz[1,2], J. Markert[1,2], C. Müntz[1,2], A. Rustamov[2], H. Ströbele[1], J. Stroth[1,2], and C. Sturm[1,2]

[1]Institut für Kernphysik, Goethe-Universität, Frankfurt, Germany; [2]GSI Helmholtzzentrum für Schwerionenforschung GmbH, Darmstadt, Germany

The inclusive and exclusive ω-meson production cross sections are presented. These are analysis results of the proton-proton run performed by HADES in 2007, with a $3.5\ GeV$ proton beam on a liquid hydrogen target. The resulting e^+e^- invariant-mass spectrum is an important reference for the study of vector meson production off the nucleus, recently performed by the HADES in p+Nb reactions at the same beam energy. We observe a prominent signal at the ω mass in the invariant-mass spectrum, in Fig. 1. More than 65×10^3 pairs have been obtained in the total mass range and 250 pairs in the ω region. The ω meson peak shows a mass resolution of $15.3\ MeV/c^2$ and its pole mass has been fitted to be $0.761\ GeV/c^2$. It is shifted by $20\ MeV/c^2$ on the lower side. If we take energy loss of electrons into account, the position of the ω peak agrees with the expected value. The spectrum has been corrected by detector inefficiencies on a pair-by-pair basis, defined as the product of single-electron inefficiencies deduced from dedicated Monte-Carlo events embedded into real events [1, 2] and normalized to pp elastic scattering events, which were simultaneously measured. The preliminary ω inclusive production cross section has been extracted to be σ_ω = $0.285\ mb \pm 0.070\ mb$. Using the same

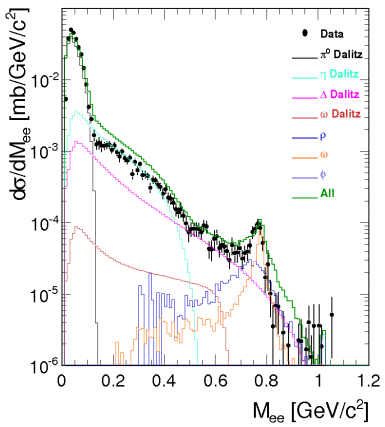

Figure 1: Invariant mass distribution of electron pairs measured in the acceptance of HADES in pp collisions at $3.5\ GeV$ beam kinetic energy. The lines show various contributions from a HSD simulation which takes all known sources into account.

data, we studied the hadronic ω-decay into three pions in the exclusive channel ($pp \rightarrow pp\pi^+\pi^-\pi^0$). The charged particles were identified through their characteristic energy deposition in the multi-wire drift chambers, whereas the neutral pion was identified by means of the missing mass method. Fig. 2 shows the invariant mass distribution of the identified 3 pions. In order to determine the true number of reconstructed ω-mesons, a PLUTO [3] simulation of the reaction $pp \rightarrow pp\omega \rightarrow pp\pi^+\pi^-\pi^0$ was done. The effects of detector efficiency and acceptance were taken into account by a full of GEANT digitization. By running through the same analysis chain as for real data, effects e.g. due to track reconstruction efficiency were also included. The shape of the ω peak as determined from the simulation is then scaled to fit the data peak, whereas the non resonant background is fitted by a polynomial function. The position and width of the simulated peak are not modified. One can see that the simulated peak fits well, which shows that detector performance is well understood. The total number of ω mesons in

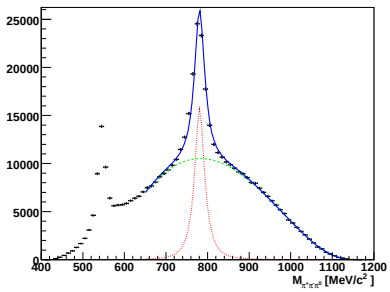

Figure 2: The invariant mass distribution of the identified 3 pions (data points). The red dashed line represents the simulated signal shape, the blue line is a fit to both the signal and background. The background function is indicated in green. The peak is positioned at $781\ MeV/c^2$ with a width of $15.4\ MeV/c^2$. (colors online)

the peak is about 62×10^3. The resulting exclusive production cross section is $0.130\ mb \pm 0.030\ mb$ to be compared to $0.285\ mb \pm 0.070\ mb$ for the inclusive cross section obtained from electron pairs.

References

[1] G. Agakishiev et al, (HADES Collab.), Phys. Rev. Lett. 98, 052302 (2009).

[2] G. Agakishiev et al, (HADES Collab.), Phys. Rev. Lett. B663, 43 (2009).

[3] I. Fröhlich et al., arXiv:0909.5373 [nucl-ex.] (2009).

* For the HADES Collaboration. This work has been supported by the BMBF (Contract Nr. 06FY171) and the Helmholtz Research School.

Exclusive ppe$^+$e$^-$ channel from p+p reaction at 1.25 GeV

W. Przygoda[1] for the HADES Collaboration
[1]Smoluchowski Institute of Physics, Jagiellonian University, 30-059 Kraków, Poland

The experimental run of p+p at 1.25 GeV took place in April 2006. The beam energy was selected below η meson production threshold in order to favour Δ(1232) production and investigate the Δ Dalitz decay: $\Delta^+ \rightarrow p\,\gamma^* \rightarrow p\,e^+\,e^-$. The identification of three particles (p, e^+, e^-) allows for the exclusive reconstruction of Δ Dalitz decay channel under two conditions: a) invariant mass $M_{ee} > 0.14\ GeV/c^2$ for rejection of the $\Delta^+ \rightarrow p\,\pi^0$ decay followed by the π^0 Dalitz decay; b) selection of the missing mass of pe^+e^-, M_{pee}^{miss}, close to the proton mass (Fig. 1) as a signature of the exclusive $p\,p \rightarrow p\,p\,e^+\,e^-$ channel identification. All spectra are normalized to the number of produced π^0 mesons (see [1]).

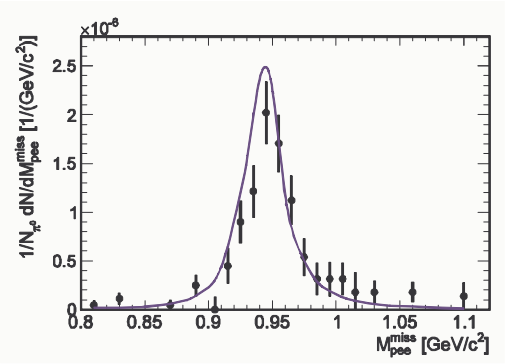

Fig. 1. (p,e^+,e^-) missing mass (for $M_{ee} > 0.14\ GeV/c^2$) compared to simulated Δ Dalitz decay channel (blue line).

In the simulation (PLUTO event generator [2], followed by the full GEANT HADES spectrometer simulation, the reconstruction and analysis) we use a resonance model [3]. Two channels (π^0 Dalitz decay and Δ Dalitz decay – with implementation of the OBE model of Delta production [4] and Delta decay model [5]) are sufficient to describe the invariant mass spectrum of e^+e^- (p-p *bremsstrahlung* is negligible). The simulation is used to apply acceptance corrections to the measured events and finally deduce the Δ Dalitz decay branching ratio. The integrated yield for $M_{ee} > 0.14\ GeV/c^2$ is not sensitive to the $N-\Delta$ transition form factor model [5], so the main model-dependent uncertainty will come from the description of the angular distributions.

The signal to background ratio for $M_{ee} > 0.14\ GeV/c^2$ ranges from 5 to 10 (CB is very low) and the number of the reconstructed signal pairs $N_{e^+e^-}^{signal} \approx 200$, after the $0.889 < M_{pee}^{miss} < 1.011\ GeV/c^2$ (3σ) selection. It is important to prove that the data reveal the Δ resonance properties despite the unavoidable smearing due to the proton not coming from the Δ decay. Firstly, the measured (p, e^+, e^-) system invariant mass and angular production distribution (Fig. 2) are in good agreement with simulation which indicates the resonant origin of the observed events.

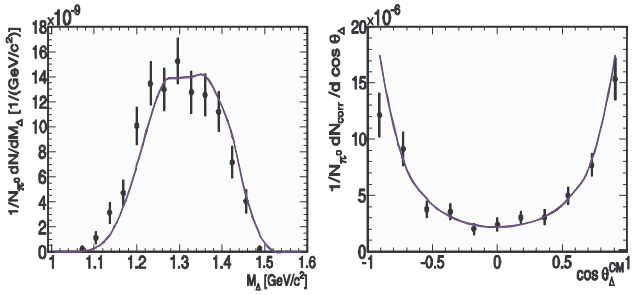

Fig. 2. (p, e^+, e^-) system invariant mass (left) and angular distribution (acceptance and efficiency corrected) in the CM rest frame (right), compared to the simulation (blue line) based on the OBE model [4].

Another useful quantity is the helicity angle - between leptons in the γ^* rest frame and the γ^* itself, when both leptons and γ^* are boosted to the Δ rest frame at first.

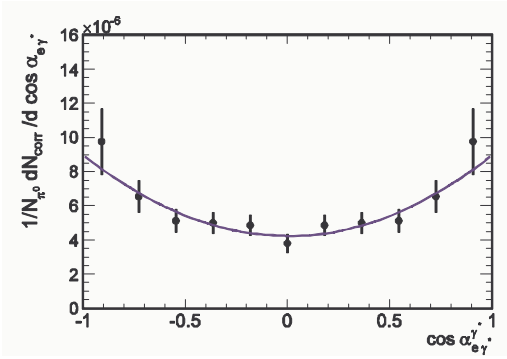

Fig. 3. Helicity angle (acceptance and eff. corrected). The blue line is a fit $\mathbf{1 + b \cdot cos^2\alpha}$, $\mathbf{b = 1.11 \pm 0.32}$.

Fig. 3 shows the (acceptance and efficiency corrected) helicity spectrum, which is anisotropic and in agreement with the $1 + cos^2\alpha$ distribution expected from the QED, when neglecting the Coulomb transition amplitude [6]. This is, again, the hint that the Δ Dalitz decay channel has been reconstructed. Also the branching ratio is in agreement with the value predicted by the QED calculations ($\sim 4 \cdot 10^{-5}$) within 9% (stat.) and less than 20% syst. (to be verified) error. The comparison of the exclusive 3-prong analysis in p+p and quasi-free n+p @ 1.25 GeV will shed more light on the nature of the e^+e^- pair excess (measured in *np*) and the role of the N-N *bremsstrahlung*.

References

[1] G. Agakishiev *et al.*, arXiv:**0910.5875** [nucl-ex]
[2] I. Fröhlich *et al.*, arXiv:**0909.5373** [nucl-ex].
[3] Z. Teis *et al.*, Z. Phys. A**356**, 421 (1997).
[4] V. Dmitriev *et al.*, Nucl. Phys. A**459**, 503 (1986)
[5] M. I. Krivoruchenko *et al.*, Phys. Rev. D**65**, 017502 (2002); M. Zetenyi *et al.*, arXiv:**0202047** [nucl-th].
[6] E.L.Bratkovskaya *et al.*, Phys. Lett. B**348**, 283 (1995).

Lepton identification using a multivariate classification method

M. Lorenz[1,2], R. Holzmann[1], K. Göbel[2], J. Markert[2], T. Galatyuk[2], J. Stroth[1,2], A. Rustamov[1], and the HADES collaboration.

[1]GSI, Darmstadt, Germany; [2]University Frankfurt, Germany

In September 2005 the HADES collaboration measured the collision system Ar+KCl at 1.76 AGeV. Compared to the previous lower multiplicity runs pp and CC, the larger data set and the search for ever smaller signals, namely the vector mesons ρ, ω and ϕ, it has become essential to extract a maximum of information from the data.

Therefore a multivariate classification method (MVA) [1] based on machine learning techniques has been applied to lepton identification [2] and finalized for the ArKCl data set during the year 2009.

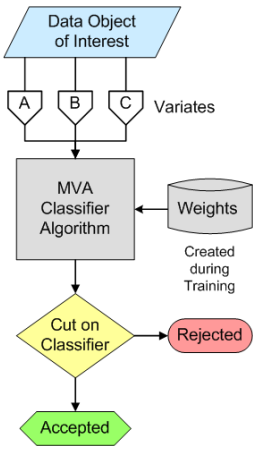

Figure 1: Schematic flow chart of the MVA method

The concept of such a multivariate classification is that instead of applying a set of boolean cuts serially to the data one feeds all cut criteria into an algorithm which provides one scalar response value, used to decide whether it is a true lepton track or not, as illustrated in picture 1. Therefore a track with a fluctuation in one of the selection criteria but with acceptable values in all other criteria will not be discarded. The processing is done in the following steps: Before analyzing the data, the algorithm has to be trained with pure signal and background samples of the data being classified. These pure samples are obtained by asking for a very precise matching of a ring in the RICH detector to a reconstructed trajectory in the spectrometer. Afterwards, different sets of variates in diverse ranges were tested as well as all provided algorithms from the toolkit for multivariate analysis (TMVA) [3], a root package from CERN and a neural network performed best.

After the training of the network, the algorithm is applied to the data selecting lepton candidates, followed by a wide cut on the RICH-MDC matching and a selection of reconstructed tracks, cleaning up those who share one or more of the same detector hit. Finally, on the pair analysis level, a condition on the opening angle of a lepton pair $> 9^o$ and on an other reconstructed track within an angle of also $> 9^o$ is asked to suppress leptons originating from conversion in the detector material.

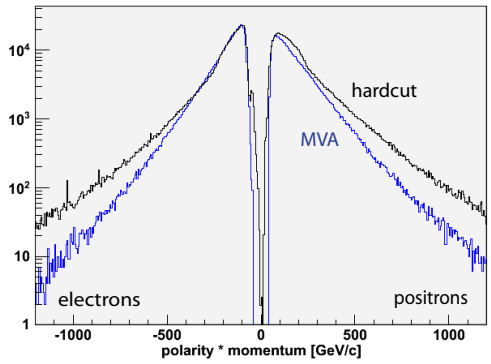

Figure 2: Momentum times polarity distributions of single leptons measured in pNb. Black line - result of the analysis of hard cuts, blue line - MVA.

Using MVA the dilepton reconstruction efficiency increased throughout the whole phase space, compared to the method of hard cuts, resulting in a factor two more reconstructed ω mesons compared to the pervious setting of the MVA network having the same signal to background ratio.

The same multivariate classification method was applied for the new p+Nb data measured in September 2008. First preliminary results show a higher purity of the single lepton sample compared to the hard cut online analysis, as one can see from the momentum distribution of leptons in figure 2.

References

[1] A. Hocker *et al.*, PoS A **CAT** (2007) 040 [arXiv:physics/0703039].

[2] S. Lang, doctoral thesis, Frankfurt (2008).

[3] http://tmva.sourceforge.net

Study of rare resonances in p+p with HADES *

E. Epple, L. Fabbietti, A. Schmah, and J. Siebenson for the HADES Collaboration
TU München - Excellence Cluster Universe, 85748 Garching

The analysis results of a high statistics proton-proton run at 3.5 GeV beam energy, measured by HADES in April 2007, will be presented. We have reconstructed the strange resonances $\Sigma(1385)^+$, $\Lambda(1405)$ and the $\Lambda(1520)$.

Reconstructing the $\Sigma(1385)^+$

The $\Sigma(1385)^+$ is produced via the following reaction

$$p+p \Rightarrow \Sigma(1385)^+ + K^+ + n \rightarrow (\Lambda + \pi^+) + K^+ + n \quad (1)$$

Events with the four detected particles K^+, π^+, p, π^-, were selected for the analysis. The particles were identified by dE/dx and mass cuts. The missing mass of all charged particles had to be within a range of 914 MeV $< MM_{K^+,\pi^+,p,\pi^-} <$ 962 MeV, to fulfill the event condition. If this was the case, a kinematic refit [1] has been applied to the data, using as a constraint that the total missing mass had to be the neutron mass. On the refitted sample a further cut was applied. Data were accepted, if the invariant mass of p and π^- was in the Λ mass region (1009.7 MeV $< M_{p,\pi^-} <$ 1119.7 MeV). Additional track cuts on the p and π^- geometry were applied to increase the Λ signal to background ratio. By combining the selected Λ and a π^+, one obtains a clear signal of the $\Sigma(1385)^+$. Figure 1 shows this signal after the subtraction of the combinatorial background. The triangles show a measurement of the $\Sigma(1385)^+$ by [2], which is in well agreement with our data.

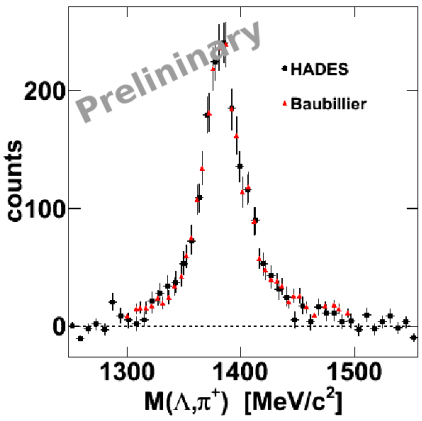

Figure 1: Invariant mass of $\Lambda\pi^+$, showing a clear signal of the $\Sigma(1385)^+$. The triangles correspond to a measurement of Baubillier [2], which is in well agreement with our data.

Reconstructing the $\Lambda(1405)$

The $\Lambda(1405)$ is produced via the following reaction:

$$p+p \Rightarrow \Lambda(1405) + K^+ + p \rightarrow (\Sigma^\pm + \pi^\mp) + K^+ + p \quad (2)$$

The analysis however is not exclusive as a nearby resonance, the $\Sigma(1385)^0$ also decays into the same particles. Both resonances are close in their mass and very broad, so that they completely overlap in the p, K^+ missing mass spectrum. The branching ratio for the decay of $\Sigma(1385)^0 \rightarrow \Sigma^\pm + \pi^\mp$ is however small compared to the $\Lambda(1405)$ decay. Thus the contribution of the $\Sigma(1385)^0$ to the p, K^+ missing mass spectrum is only a few percent and can be subtracted. Events with a p, K^+, π^+, π^-, were selected, as described above. Again a missing neutron was required from the decay $\Sigma^\pm \rightarrow n\pi^\pm$. After applying the neutron mass cuts, the remaining events were kinematically refitted, like in the $\Sigma(1385)^+$ analysis. The refitted sample was used to plot the missing mass of $p, K^+, \pi^\mp$ which shows a signal of $\Sigma^\pm$ with a signal to background ratio of about 1. For the final spectra events with a $MM_{p,K^+,\pi^\mp}$ in the $\Sigma^\pm$ mass region were used to plot the missing mass of p, K^+. Figure 2 shows the result of this analysis after subtracting the background. A clear signal of $\Lambda(1405)$ and $\Lambda(1520)$ can be seen.

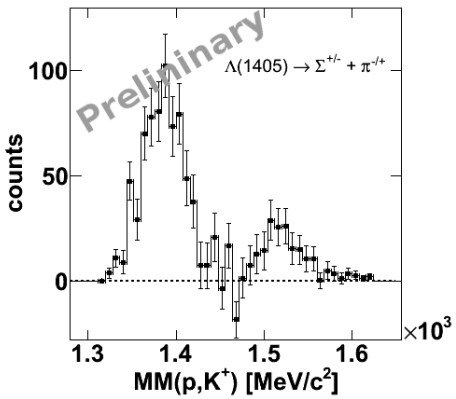

Figure 2: The missing mass of p, K^+ after the event selection and background subtraction. A clear peak of $\Lambda(1405)$ and $\Lambda(1520)$ can be seen. Not included are systematic errors.

References

[1] P. Avery, http://www.phys.ufl.edu/simavery/fitting.html

[2] M. Baubillier et al. Z.Phys. C23 (1984)213

* Work supported by HGF and DFG-Excellence Cluster Universe

Dilepton production in 1.756 GeV/u ^{40}Ar+KCl reactions*

R. Holzmann[1], M. Jurkovic[2], F. Krizek[3], and M. Lorenz[1,4] for the HADES collaboration
[1]GSI, Darmstadt, Germany; [2]TUM, Garching, Germany; [3]UJF, Rez, Czech Republic; [4]Uni Frankfurt, Germany

During the year 2009 the dielectron analysis of our 2005 ^{40}Ar+KCl run at 1.756 GeV/u has been finalized. This experiment provided data for a moderately large collision system, allowing to continue our studies of dilepton production started with the light ^{12}C+^{12}C system [1], as well as in the elementary $p+p$ and $d+p$ reactions [2]. We can now address the evolution with beam energy *and* system size of the so-called pair excess, first observed by the DLS in the mass range of 0.15 - 0.50 GeV/c^2 [3].

Spectroscopy of the vector-meson region was started with this data set as well. The reconstructed dielectron invariant-mass distribution shows for the first time at SIS energies a clear ω peak, providing thus new and valuable constraints for transport models.

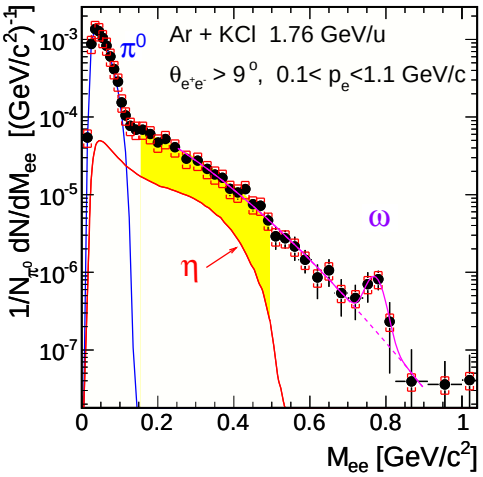

Figure 1: Reconstructed, efficiency-corrected and normalized dilepton mass spectrum in 1.756 GeV/u Ar+KCl. Lines are the π^0 and η components of the PLUTO cocktail, the shaded (yellow) area indicates the excess yield over the η. A gauss fit to the ω peak is shown as well.

In the Ar+KCl run a large statistics of 2.2×10^9 LVL1 triggered events was acquired. Fig. 1 shows the e^+e^- invariant-mass spectrum after subtraction of the combinatorial background, correction for inefficiencies, and normalization per triggered event and pion multiplicity. A total of ~90k signal pairs were reconstructed, with more than 16k pairs above the π^0 Dalitz region. A clear omega peak is visible ($\sigma_M/M = 3\%$), totalling about 40 pairs. A fit of the signal gives a LVL1 ω multiplicity of $M_\omega = 0.0067 \pm 0.0027$. Comparing this with the ϕ multiplicity of 0.00026 ± 0.00007 obtained from our K^+K^- analysis [4] we find a ϕ/ω ratio of 0.039 ± 0.017, i.e. much larger than typically observed in $p+p$ collisions.

The e^+e^- spectrum can be compared with a pair cocktail of long-lived components (those still present at freeze-out) generated with the PLUTO event generator. The simulation is based on thermal sources with their multiplicities, temperatures and anisotropies either taken from data (HADES, TAPS) or estimated with an $m_\perp$-scaling ansatz (see [1] for details). This type of calculation evidently underestimates the experimental pair yield at masses > 0.15 GeV/c^2 and the measured excess above the calculated η Dalitz is thought to quantify the radiation from the early phase of the collision. Fig. 2 shows the excess multiplicity of $0.15 < M_{ee} < 0.50$ GeV/c^2 dileptons for all collision systems studied so far by HADES and DLS, together with the corresponding neutral meson multiplicities measured by the former TAPS experiment at GSI. This systematics allows to study the beam-energy as well as the (non-trivial) system-size dependence of the electromagnetic radiation from the nuclear medium. Further progress will be made by extending next our measurements to heavy reaction systems like Ag+Ag and Au+Au.

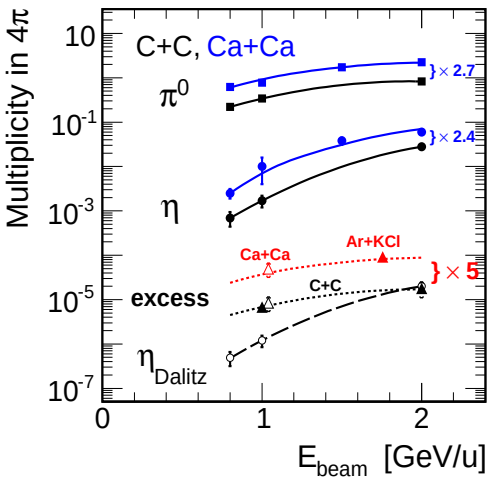

Figure 2: Multiplicity of the pair excess as function of beam energy and system size (full triangles), together with π^0 and η multiplicities from TAPS 2-photon measurements. DLS data points [3] are shown as open triangles.

References

[1] G. Agakichiev *et al.*, HADES collaboration, Phys. Lett. B 663, 43 (2008) and Phys. Rev. Lett. 98, 052302 (2007).

[2] G. Agakichiev *et al.*, HADES collaboration, arXiv:0910.5875.

[3] R. J. Porter *et al.*, DLS collaboration, Phys. Rev. Lett. 79, 1229 (1997).

[4] G. Agakichiev *et al.*, HADES collaboration, Phys. Rev. C 80, 025209 (2009).

* Work supported by the BMBF

Upgrade of the HADES Experiment*

S. Yurevich[1] for the HADES Collaboration

[1]GSI Helmholtzzentrum für Schwerionenforschung GmbH, 64291 Darmstadt, Germany;

The HADES upgrade project aims at improving the granularity of the time-of-flight (TOF) system and the data rate capability to allow for the experiments with heavy ions at SIS18 and later at FAIR. In this report, we outline the current upgrade progress of the HADES experimental setup, in particular for the installation of the RPC chambers, the new MDC, the new RICH electronics, and its data acquisition system.

The production and installation of all six Resistive Plate Chamber (RPC) [1] sextants into the HADES main frame, including the front-end electronics (FEE) and low voltage power supplies, has been finished (see Fig. 1). The installation of the DAQ-electronics has been completed for two sectors. The analysis of cosmic ray data shows an average time resolution of 80 ps (σ) and an acceptable low crosstalk. The average longitudinal position resolution is better than 10 mm (σ).

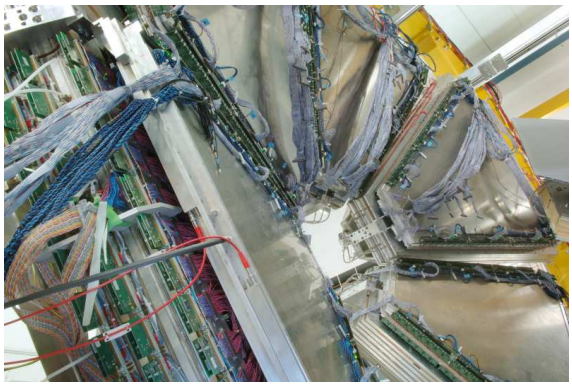

Figure 1: Installed RPC chambers.

The tracking system, consisting of 24 drift chambers is beeing upgraded with respect to (i) re-build of all 6 chambers of the first plane and (ii) replacing the copper-based digital part of the FEE by optical readout. The mounting of the newly built chambers has been finished after a comprehensive commissioning phase at the Forschungzentrum Dresden-Rossendorf.

In order to meet the requirements for heavy collision systems at FAIR, the front-end readout has been completely replaced, using optical fibres thus keeping the induced noise occupancy below 0.1 %, equivalent to one noise hit per chamber per event and an increased data taking bandwidth of the system by a factor about 50. The new readout architecture relies on new optical driver cards interfacing the existing TDC boards mounted at the detector with plastic optical fibres (POF). This work is presently being accomplished, first tests confirmed the expected noise level reduction.

The 28500 pads of the MWPC photon detector of the RICH will be equipped with new front-end electronic cards based on APV25 chips [2] with operation parameters adopted for gaseous detectors. Digitization is performed in new FPGA controlled ADC modules (ADCM) with optical fiber link to the DAQ system. The hardware production is finished and the modules are presently under test in Munich.

A general overview of the architecture of the upgraded DAQ system can be found in [3]. Its basic component is the “Trigger and Readout Board” and detector-specific AddOn-boards.

The trigger and data transport is organized by a new protocol named TRB-Net [4] which has been implemented on all the subsystems of the HADES detector. The new protocol has been successfully tested for the RICH and MDC subsystems. The coherent access over the network to the FEE cards (in particular for the MDC) allows for new monitoring methods [5].

The components of the event building system (Gigabit Ethernet, parallel event building and run control) have been implemented and tested [6]. The ethernet interface to the TRB-Net is still under test.

For the TOF detector, all AddOn boards have been produced. Currently the installation and integration of the new electronics is ongoing. The performance of the board is satisfactory. The achieved time resolution is on the level of 80 ps, which is almost by a factor of 2 better than the old electronics.

The AddOn board for the shower detector combines digital and analog electronics. A first prototype of the AddOn has been manufactured and tested in terms of electronic resolution and readout performance. The final production of all boards has been started.

In summary, we reported on the status of the HADES upgrade. We expect that the final installation and commissioning will be finished in summer 2010.

References

[1] A. Blanco *et al*, this volume

[2] M. Raymond *et al*, CERN/LHCC/2000-041, 130-134

[3] I. Fröhlich et al, IEEE Trans.Nucl.Sci. 55 (2008) 59-66

[4] J. Michel *et al*, this volume

[5] B. Milanovic *et al*, this volume

[6] S. Yurevich *et al*, this volume

* Work supported by EU grant 515876, 227431 and the BMBF

Centrality dependence of particle ratio fluctuations in Pb + Pb at 158A GeV*

H. Beck[1], C. Blume[1], J. Book[1], V. Friese[2], M. Gaździcki[1], C. Höhne[2], D. Kresan[2], M. Mitrovski[1], M. Pohl[1], R. Renfordt[1], T. Schuster[1], R. Stock[1], and H. Ströbele[1]

[1]IKF, Goethe Universtität, Frankfurt am Main, Germany; [2]GSI, Darmstadt, Germany – for the NA49 collaboration

Recent lattice QCD calculations expect a first order phase transition from hadronic to partonic degrees of freedom at finite temperature and baryon chemical potential [1]. This first order transition line ends with a critical endpoint. The search for either the first order phase transition or the critical endpoint is a challenging task in modern high energy heavy-ion physics.

Dynamical fluctuations of the K/π ratio were proposed as a signature for the first order phase transition from hadronic to partonic degrees of freedom and the critical endpoint [2]. The NA49 experiment [3] has measured the energy dependence of the K/π ratio fluctuations in central Pb+Pb collisions [4]. An increase of the fluctuations towards lower beam energies was observed. A possible explanation of this dependence was proposed in [2], namely scaling of the K/π ratio fluctuations with $1/\langle N_K \rangle$. In order to test this hypothesis one would like to measure the centrality dependence of this observable at fixed beam energy.

The measured centrality dependence of the dynamical fluctuations of the K/π ratio in Pb + Pb collisions at 158A GeV beam energy is presented in figure 1 as a function of the average number of kaons in the acceptance $\langle N_K \rangle$.

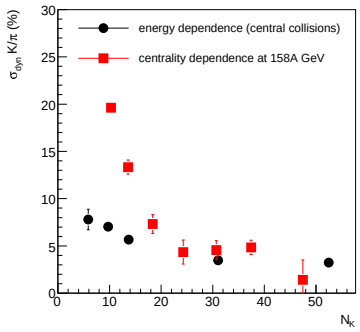

Figure 1: Dynamical fluctuations of the K/π ratio as a function of $\langle N_K \rangle$ in Pb + Pb collisions at 158A GeV beam energy (squares) and in central Pb + Pb collisions at all NA49 energies (circles).

From figure 1 one can conclude that the results of the energy and centrality dependences disagree at low number of kaons, which correspond to low centrality or low beam energy. Thus, the dynamical fluctuations are enhanced at small systems as compared to the large systems at smaller energy densities.

The situation is different in case of the p/π ratio. From the definition of the dynamical fluctuations [5] one can derive an analytical expression, which is dominated by the correlation term [5]:

$$\sigma^{p/\pi}_{dyn} \approx -\sqrt{\frac{cov(N_p, N_\pi)}{< N_p >< N_\pi >}} = -\sqrt{\frac{(< N_p >< N_\pi >)^\alpha}{< N_p >< N_\pi >}}, \quad (1)$$

Here, the covariance is parametrized by $(\langle N_p \rangle \langle N_\pi \rangle)^\alpha$. With the assumption of dominating feeddown from resonances the parameter α is expected to become 0.5.

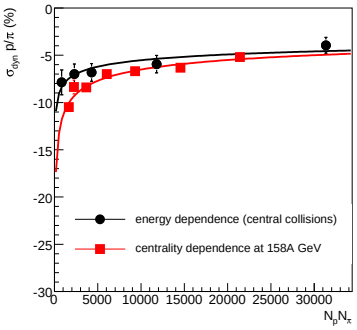

Figure 2: Dynamical fluctuations of the p/π ratio as a function of $\langle N_p \rangle \langle N_\pi \rangle$ for the energy (circles) and the centrality (squares) dependence. Solid curves show fits according to the above equation.

Figure 2 shows the dynamical fluctuations of the p/π ratio as a function of $\langle N_p \rangle \langle N_\pi \rangle$. After fitting the dependences of the p/π ratio fluctuations with equation 1, the following α parameters were obtained: $\alpha = 0.66 \pm 0.12$ for the energy dependence and $\alpha = 0.51 \pm 0.03$ for the centrality dependence. This observation strongly supports the assumption that Δ resonance decays are the dominant source of dynamical fluctuations of the p/π ratio and give a natural explanation for both, the energy and centrality dependence.

References

[1] Z. Fodor and S. D. Katz, JHEP **0404** (2004) 050 [arXiv:hep-lat/0402006].

[2] V. Koch, arXiv:0810.2520 [nucl-th].

[3] S. Afanasev *et al.* [NA49 Collaboration], "The NA49 large acceptance hadron detector," Nucl. Instrum. Meth. A **430** (1999) 210.

[4] C. Alt *et al.* [NA49 Collaboration], arXiv:0808.1237 [nucl-ex].

[5] D. Kresan and V. Friese, PoS C **FRNC2006** (2006) 017.

[6] D. Kresan, arXiv:0908.2875 [nucl-ex].

* Supported by BMBF and HQM.

Centrality dependence of K_s^0 production in Pb+Pb collisions at the CERN SPS

J. Book[1], H. Beck[1], C. Blume[1], V. Friese[2], M. Gaździcki[1], C. Höhne[2], D. Kresan[2], M. Mitrovski[1], M. Pohl[1], R. Renfordt[1], T. Schuster[1], R. Stock[1], H. Ströbele[1], and the NA49 Collaboration

[1]Institut für Kernphysik Frankfurt, Germany; [2]GSI, Darmstadt, Germany

Motivation

At high energy densities a new phase of matter, the quark-gluon-plasma (QGP), is expected to be formed. The system size dependence of strangeness production per wounded nucleon shows an increase towards larger reaction systems [1]. Also the energy dependence of K^+/π^+ has been studied and shows an anomaly at low SPS energies [2]. To cross check these results obtained for charged kaons, the K_s^0 can be studied. A comparison is possible because of the approximate isospin symmetry and strangeness conservation:

$$(K^+ + K^-)/2 \approx K_s^0 \quad (1)$$

Data Analysis

The data were measured by the fixed target experiment NA49 [3] at the CERN SPS in 2001 and 2002. A zero-degree-calorimeter (ZDC) determines the centrality of the collisions via the energy deposition of the spectators.
For the K_s^0 reconstruction by their decay topology ($K_s^0 \rightarrow \pi^+ + \pi^-$) a V^0 finding algorithm is implemented. It combines all pairs of opposite charged tracks and extrapolates them step-by-step towards the main vertex. The minimum distance of their closest approach (dca) indicates a K_s^0 candidate for which the invariant mass can be calculated:

$$m_{K_s^0} = \sqrt{(E_1 + E_2)^2 - |\vec{p_1} + \vec{p_2}|^2} \quad (2)$$

The invariant mass spectra in a given y-p_t-bin are now analysed by a fit procedure, where the background is described by a polynomial and the signal by a MC simulated line shape.
There are three types of losses, the geometrical acceptance, the reconstruction inefficiency due to the V^0 algorithm and due to the track density. To determine these losses a simulation chain has been implemented. In the first step MC K_s^0 are generated and their daughter particles are propagated through the virtual NA49 detector by GEANT. After this the data is embedded in real events to take care of track density effects. In the last step these data are reconstructed by the standard reconstruction chain and compared to real data to calculate the detection probability P_{detect}.

Results

The corrected m_t-spectra for all centrality classes are shown in Figure 1. A Boltzmann-function is used to extrapolate into unmeasured m_t-regions.

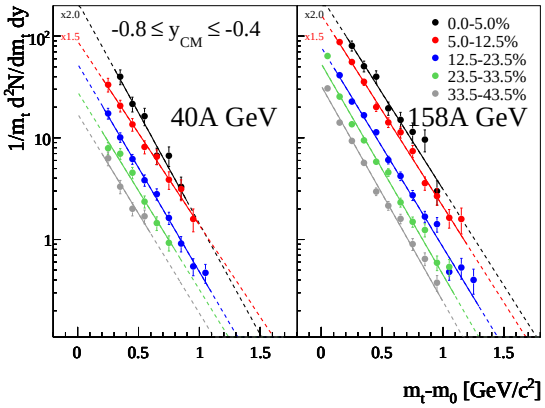

Figure 1: The corrected m_t-spectra for all centrality classes for Pb+Pb collisions.

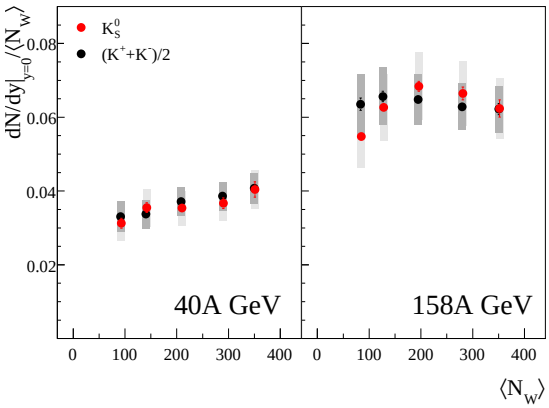

Figure 2: The yields around midrapidity ($|y| \leq 0.4$) per wounded nucleon as a function of the number of wounded nucleons for Pb+Pb reactions at 40*A* and 158*A* GeV. The systematic error is represented by gray fields.

In Figure 2 you can see a good agreement of the yields of charged kaons [4] and K_s^0 at midrapidity within the systematic errors.

References

[1] J.Rafelski & B.Müller, Phys.Rev.Lett. 48, 1066–1069 (1982)

[2] C.Alt et al. [NA49 Collaboration], Phys.Rev.C 77, 024903 (2008)

[3] Afanasiev et al. [NA49 Collaboration], Nucl. Instrum. Meth.A430, 210–244 (1999)

[4] P. Dinkelaker, PhD thesis, "Kaon and Pion Production in Centrality Selected Minimum Bias Pb+Pb Collisions at 40 and 158 A GeV", Goethe University Frankfurt, (2009)

Proton - Lambda Correlations in Central Pb+Pb Collisions at 158A GeV

H. Beck[1], C. Blume[1], J. Book[1], V. Friese[2], M. Gaździcki[1], C. Höhne[2], D. Kresan[2], M. Mitrovski[1], M. Pohl[1], R. Renfordt[1], T. Schuster[1], R. Stock[1], H. Ströbele[1], and the NA49 Collaboration

[1]Fachbereich Physik der Universität, Frankfurt; [2]Helmholtzzentrum für Schwerionenforschung (GSI), Darmstadt

Motivation

The fireball created in ultra-relativistic heavy ion collisions is thought to form a state of deconfinement: the quark-gluon plasma (QGP). The QGP is believed to have existed fractions of seconds after the big bang and proof of it's creation and properties are of general interest. Two particle correlations are widely used to investigate the dynamic evolution of the fireball. Especially pion-pion correlations allow for a multi-dimensional analysis of the parameters of the particle emitting source. Although proton-lambda correlation measurements suffer from lower statistics (thus only one-dimensionial analyses have yet been published), they provide a clean signal: only strong interaction leads to an excess of proton-lambda pairs for small momentum differences of the two particles [1]. Known parameters of the final state interaction allow us to extract source sizes from correlation measurements.

Data Analysis

The data presented in this contribution was registered with the NA49 detector at the CERN SPS. The analyzed set consists of $2.8 \cdot 10^6$ central (23.5%) Pb+Pb collisions at 158A GeV. The lambda sample was obtained by combining all oppositely charged tracks to so called V^0 vertices and then applying selection criteria to both the daughter tracks and the V^0 vertex. Identification of primary protons was performed via a measurement of the specific energy loss in the four large volume TPCs of the detector. Selection criteria were varied to estimate the systematic error. Two-track cuts were applied to avoid influences of two-particle effects like two-track resolution. Without a cut, the finite detector resolution would cause merging of close tracks, which would lower the correlation function. The raw correlation function was obtained by dividing the measured distribution of momentum differences between pairs of protons and lambdas within the same event by an equivalent distribution constructed by pairing protons and lambdas from different events. Analysis chain was exactly the same for both distributions. Corrections to the correlation function were done, which were necessary due to the imperfect particle identification and contributions of particles from decays.

Results

Figure 1 shows the corrected correlation function as a function of the momentum difference of the proton and the lambda, measured in the rest frame of the pair. The fitted

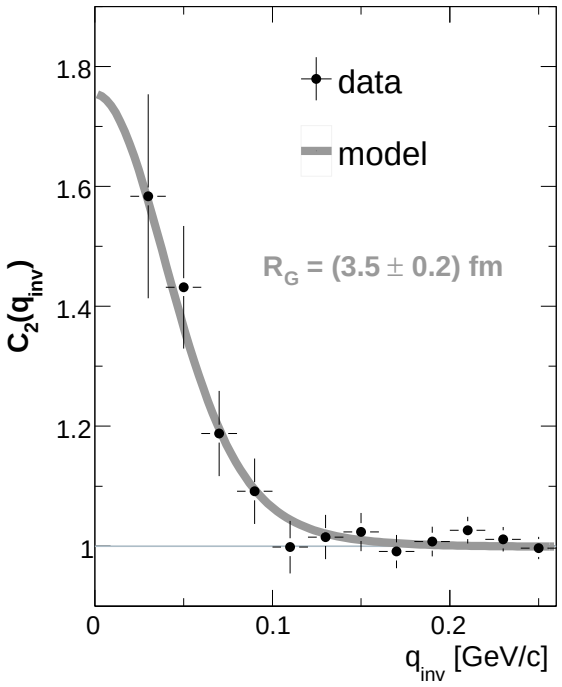

Figure 1: Corrected correlation function with fit.

model [2] uses the effective range approximation for the S-wave interaction and assumes a spherically symmetric, Gaussian shaped source with the radius parameter R_G being the σ of the spatial distribution. In the effective range approximation, the proton-lambda interaction is described by two parameters: the scattering length f_0^S and the effective range d_0^S. Here, according to [1], values of $d_0^S = 2.92$ fm (singlet), 3.78 fm (triplet) and $f_0^S = -2.88$ fm (singlet), -1.66 fm (triplet) are used.
All fits are consistent and result in a value for the radius parameter of:

$$R_G = (3.5 \pm 0.2(\text{stat.}) \pm 0.45(\text{syst.}))\ \text{fm}.$$

The STAR collaboration obtained a value for the proton-lambda system in Au+Au collisions at $\sqrt{s_{NN}} = 200$ GeV of $R_G = (2.97 \pm 0.34^{+0.19}_{-0.25} \pm 0.2)$ fm. Both measurements agree well with each other.

References

[1] F. Wang and S. Pratt, Phys. Rev. Lett. **83**, 3138 (1999).
[2] R. Lednicky and V.L. Lyoboshitz, Sov. J. Nucl. Phys. **35** (1982).

First pp collisions seen with the ALICE Time Projection Chamber

The ALICE TPC collaboration[1]

The ALICE Time Projection Chamber (TPC) is the central tracking detector of the CERN-LHC ALICE experiment [1]. First proton-proton collisions at $\sqrt{s}$=900 GeV/c were successfully recorded during the initial data taking campaign in December 2009. A typical example of tracks from a pp-event is shown in Fig. 1.

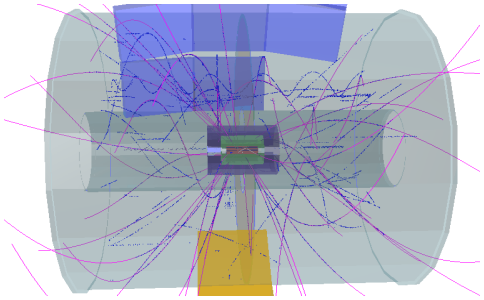

Figure 1: Clusters (blue dots) and reconstructed tracks (red lines) recorded by the TPC.

The commissioning and calibration of the TPC has been done with cosmic data, laser runs and radioactive krypton in 2008 and 2009 and is reported in detail elsewhere [2].

Collision Data

During the initial data-taking period the TPC trigger rate from the collisions of 4 on 4 counter-rotating proton bunches was up to 10 Hz. Each of the bunches containing initially up to 10^{11} protons. The trigger included both empty events and beam-gas interaction. The events size was in average of the order of 170kB owing to the excellent low noise behaviour of the TPC readout chain. The magnetic field was set to ±0.5 T and, for alignment purposes, to B=0 T.

To ensure immediate feedback on the data quality the raw data were immediately transferred to GSI, where they were reconstructed and analyzed using the entire GSI Tier 2 batch farm and the high-performance cluster with 2000 cores and 1 PB of storage on Lustre. Feedback on the detector performance was available within a few hours after the data had been recorded. All results were constantly communicated to the CERN detector control room. Thanks to the outstanding performance of the GSI computing infrastructure, the analysis chain was running uninterrupted during the complete data-taking period.

Result from Data Analyses

Fig.2 shows a dE/dx vs. momentum spectrum from pp collision at 900 GeV/c employing the calibration data from the cosmic and krypton runs. As can be seen the excellent particle separation anticipated from the cosmic runs is also manifest in the collision data, e.g., by the π/μ-separation visible at low momentum.

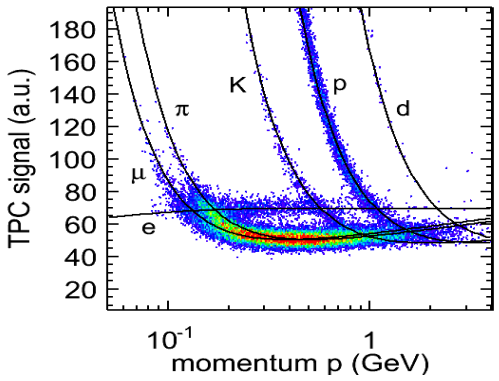

Figure 2: Particle identification the TPC.

This, together with precise tracking, readily allows reconstructing invariant mass spectra. As a further example of the TPC performance with data we show in Fig. 3 the K_0^S-invariant mass plot from the $\pi^+\pi^-$ V0 decays vertices. The narrow width and the perfect agreement with the PDG mass should be taken as certification of the readiness of the TPC for the upcoming pp and PbPb runs in 2010.

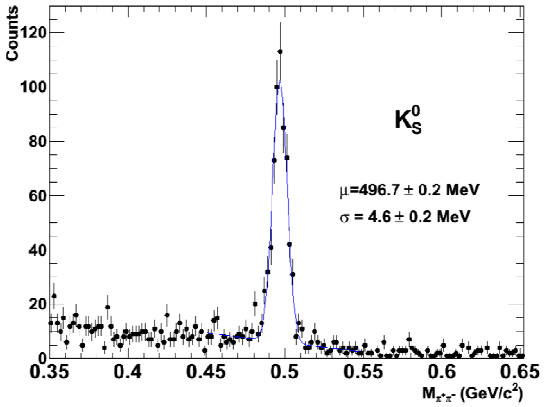

Figure 3: Reconstructed K_0^S from $\pi^+\pi^-$ V0 decays vertices.

References

[1] "The ALICE experiment at the CERN LHC", ALICE Collaboration, 2008, JINST 3 S08002

[2] "The ALICE TPC, a large 3-dimensional tracking device with fast readout for ultra-high multiplicity events", J. Alme *et al.*, 2010, e-Print: arXiv:1001.1950

[1] The list of members and institutions is available at http://www-alice.gsi.de/tpc

Photon reconstruction with conversions in ALICE

K. Aamodt[1], F. Bock[2], P. Braun-Munzinger[3,4], T. Dietel[5], P. Gonzalez[6], M. Heide[5], M. Ivanov[3,4], K. Koch[2], P. Ladrón de Guevara[6], A. Marín[3,4], M. Rammler[5], K. Reygers[2], D. Röhrich[7], E. Serradilla[6], J. Stachel[2], J.P. Wessels[5], and for the ALICE Collaboration

[1]Department of Physics, University of Oslo, Oslo, Norway; [2]Physikalisches Institut, Ruprecht-Karls-Universität Heidelberg, Heidelberg, Germany; [3]ExtreMe Matter Institute EMMI, Darmstadt, Germany; [4]GSI Helmholtzzemtrum für Schwerionenforschung, Darmstadt, Germany; [5]Institut für Kernphysik, Westfälische-Wilhems-Universität Münster, Münster, Germany; [6]Centro de Investigaciones Energéticas, Medioambientales y Tecnológicas (CIEMAT), Madrid, Spain; [7]Department of Physics and Technology, University of Bergen, Bergen, Norway

ALICE (A Large Ion Collider Experiment) is a general-purpose, heavy-ion detector designed to study the physics of strongly interacting matter and the quark gluon plasma in nucleus-nucleus collisions at the CERN LHC. The LHC started delivering collisions at the injection energy of $\sqrt{s}$ = 900 GeV/c in November 2009. During the 2009 period about 400 k pp collisions were recorded in ALICE with all detectors included. ALICE can measure photons that convert in the detector material (mainly the six ITS layers and the TPC container vessels [1]) via the measurement of the $e^{\pm}$ pair in the Central Barrel detectors. Converted photons, K^0_S, Λ and $\bar{\Lambda}$ candidates are reconstructed using a secondary vertex finder algorithm [2]. In order to select photons among all secondary vertices, first electron selection and pion rejection using the specific energy loss in the TPC are applied. Second, constraints on the reconstructed photon mass and on the orientation of the reconstructed photon momentum vector are applied using a reconstruction package for fitting decay particles [3]. Moreover, a precise calculation of the conversion point, assuming zero opening angle between the two tracks, valid only for γ conversions has been implemented. The resulting distribution of the reconstructed photon conversion points in a plane perpendicular to the beams is shown in Fig. 1. The 3D detector image obtained with this method provides an important check of the ALICE material budget and of its implementation in the current GEANT simulations. Combining two of these reconstructed photons, a clear π^0 meson peak is visible in the invariant mass spectrum (Fig. 2). The plot contains all data from the first data taking period. This method yields a very good π^0 mass resolution and very small background. With the quasi online calibration the width of the π^0 peak is 7.2±1.6 MeV/c^2. These results demonstrate that the conversion method is in ALICE a viable tool to study photon physics at the LHC. The LHC will have a long pp run during the year 2010 that will deliver enough statistics to study the transverse momentum distribution of π^0 and η mesons.

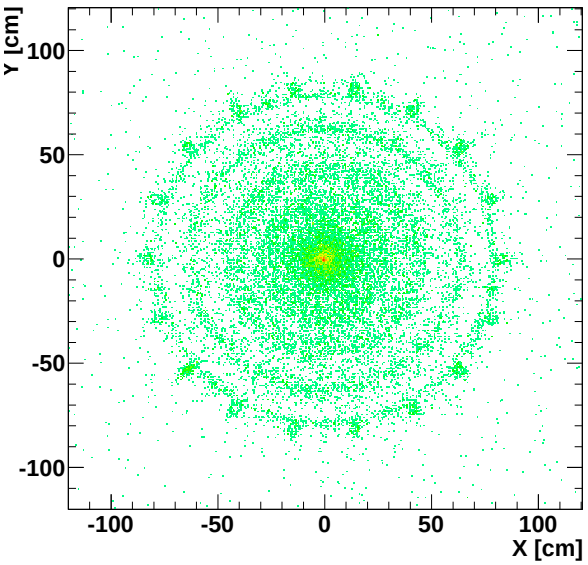

Figure 1: X vs Y distribution of reconstructed photon conversion vertices within $|\eta|$ <1.2. The different ITS layers and the TPC container vessels are clearly visible.

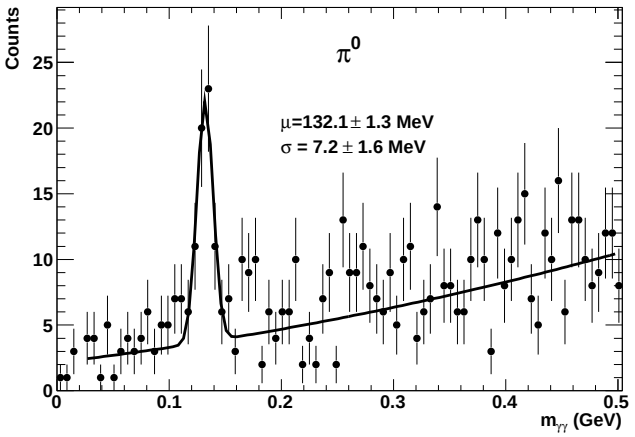

Figure 2: Invariant mass of two γ reconstructed in ALICE using the conversion method. A π^0 meson peak is clearly visible on top of the combinatorial background.

References

[1] "The ALICE experiment at the CERN LHC", K. Aamodt et al. (the ALICE Collaboration), 2008 JINST 3 S08002

[2] "ALICE: Physics Performance Report, Volume II", ALICE Collaboration et al., (2006) J. Phys. G: Nucl. Part. Phys. 32 1295-2040 doi: 10.1088/0954-3899/32/10/001

[3] "Reconstruction of decayed particles based on the Kalman filter", S. Gorbunov and I. Kisel, http://www.gsi.de/documents/DOC-2007-May-14-1.pdf

Correlation between mean transverse momentum and multiplicity in p-p collisions at $\sqrt{s} = 900\,\mathrm{GeV}$ in ALICE*

P. Luettig†[1], H. Appelshaeuser[1], H. Buesching[1], S. Schuchmann[1], and J. Otwinowski[2]
[1]Goethe University Frankfurt, Germany; [2]GSI, Darmstadt, Germany

The mean transverse momentum $\langle p_T \rangle$ of particles produced in heavy ion collisions and its event-by-event fluctuations are considered to be sensitive to critical fluctuations of the temperature of the hot and dense system created in such collisions. Fluctuations of $\langle p_T \rangle$ in proton-proton collisions are an essential reference measurement for these studies. Furthermore the mean transverse momentum in itself, and in particular its dependence on the charged particle multiplicity is an important constraint for phenomenological models to describe these collisions at high energies.

Here we report how $\langle p_T \rangle$ is extracted from the transverse momentum spectra measured by the ALICE Time Projection Chamber in the first run period of the LHC in 2009 in proton-proton collisions at $\sqrt{s} = 900$ GeV.

$\langle p_T \rangle$ vs. Charged Multiplicity

This analysis is based on the measurement of the transverse momentum (p_T) spectra of charged particles in the ALICE Time Projection Chamber (TPC) [1]. The p_T spectra of particles with $0.15\ \mathrm{GeV/c} \leq p_T \leq 10\ \mathrm{GeV/c}$ in $|\eta| < 0.8$ are used, after they are fully corrected for efficiency and contamination from secondaries.

One way to extract the mean transverse momentum $\langle p_T \rangle$ from the measured p_T-spectra is to calculate the arithmetic mean of the transverse momenta of the measured particles, $\langle p_T \rangle_{meas}$:

$$\langle p_T \rangle_{meas} = \frac{1}{N_{meas}} \Sigma p_{Ti} \qquad (1)$$

The measured mutliplicity N_{meas} is the number of particles which are used to calculate $\langle p_T \rangle_{meas}$.
Figure 1 shows the results for $\langle p_T \rangle_{meas}$ as a function of N_{meas} in the ALICE TPC. Only particles with $p_T = [0.3\ \mathrm{GeV/c}, 4.0\ \mathrm{GeV/c}]$ in $|\eta| < 0.8$ are taken into account. As observed by UA1 at the CERN proton-antiproton collider, the p_T spectrum flattens for increasing multiplicity [2]. This flattening corresponds to an increase in the mean transverse momentum as demonstrated in Figure 1.

An alternative way to extract $\langle p_T \rangle$ from the measured p_T-spectra is to find an adequate parametrization of the spectrum. By using this parametrization $\langle p_T \rangle$ can be calculated by extrapolation of the spectrum to $p_T = 0$ GeV/c.

Furthermore N_{meas} can be related to the true multiplicity N_{true} using a detailed simulation of the detector response and unfolding of the N_{meas} distribution.
Various approaches to fit the p_T spectra and to extract N_{real} by unfolding the measured distribution are recently being tested.

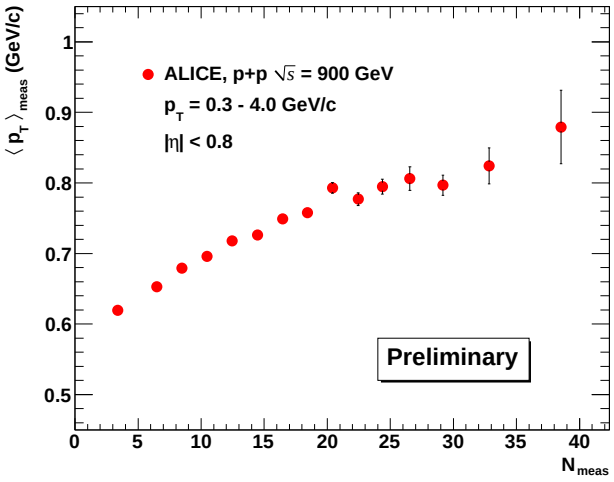

Figure 1: Measured mean transverse momentum $\langle p_T \rangle_{meas}$ in the ALICE TPC as a function of the measured multiplicity N_{meas} for particles with $p_T = [0.3\ \mathrm{GeV/c}, 4.0\ \mathrm{GeV/c}]$ in $|\eta| < 0.8$.

Outlook

As a next step, we prepare the extraction of $\langle p_T \rangle$ on an event-by-event basis and investigate its flucuation as function of the charged particle multiplicity. Such data will provide an important baseline for similar studies in heavy-ion collisions at LHC.

References

[1] ALICE-TPC Technical Design Report, CERN / LHCC 2000-001, ALICE TDR 7, 07. Jan. 2000

[2] A study of the general characteristics of proton-antiproton collisions at $\sqrt{s} = 0.2$ to 0.9 TeV, UA1 Collaboration, CERN-EP / 89-85, July 12th, 1989

* work supported by BMBF and GSI
† luettig@ikf.uni-frankfurt.de

Trigger Particle Correlations in *pp* Collisions with the ALICE Detector *

J. Ulery[1] and H. Appelshäuser[1]
[1]Institut für Kernphysik, Goethe Universtität, Frankfurt am Main, Germany

Introduction

The Large Hadron Collidor, LHC, will produce collisions of protons at energies up to $\sqrt{s} = 14$ TeV and lead ions at energies up to $\sqrt{s_{NN}} = 5.5$ TeV. These collisions can be probed with jet-like correlations. These correlations can be used to improve our knowledge of jets in relativistic collisions. In elementary collisions, jet-like correlations can tell us about how partons fragment into jets of particles. In heavy-ion collisions these correlations can provide information about how energy is lost in the medium created in these collisions.

Analysis

The analysis is performed in the ALICE Time Projection Chamber (TPC). Charged particles with intermediate or high transverse momentum (p_T) are chosen as trigger particles. This selection provides us with particles that are likely from jets. The trajectory of these particles is most likely along the jet axis. The other particles in the event are studied in their relative angles in azimuth, $\Delta\phi = \phi_{Trig} - \phi$, and pseudo-rapidity, $\Delta\eta = \eta_{Trig} - \eta$. These jet-like angular correlations can then be studied as a function of the transverse momentum of the particles.

The efficiency and acceptance of the detector is corrected using simulated events. This is done by simulated particles with an event generator, then running them through a simulation of the detector. The tracks are reconstructed from the simulated particles as if they were from real data. The trigger particle correlation from the reconstructed particles and from the originally simulated particles are compared to find the efficiency of the particle detection as a function of the relative angles between the particles. This corrects for detector effects on particle detection up to the level the detector is simulated.

The unsubtracted jet-like correlations also have an underlying event that does not have an angular correlation. Backgrounds are created through event mixing, trigger particles are mixed with associated particles from other events. The triggered events have a bias, from requiring the intermediate or high p_T trigger particle, that the events used in mixing, minimum bias, do not have. This gives a large multiplicity in triggered events. The extra particles might be from the jets we are looking at (in which case we do not want to subtract those particles) or from other sources. If the triggered events would be used instead for mixing then the multiplicity would be higher than our underlying event and be contaminated with particles from jets. The true level of the underlying event is unknown. The mixed event is normalized such that there is no yield after background subtraction between the peak, Zero Yield At Minimum assumption. This assumption can be applied to both elementary collisions and heavy-ion collisions and therefore makes it good to use for comparisons between the different collision types. A fixed location is used from the minimum to reduce additional statistical uncertainty when using a floating minimum. The minimum is determined at the lowest trigger and associated p_Ts where the peaks are the widest.

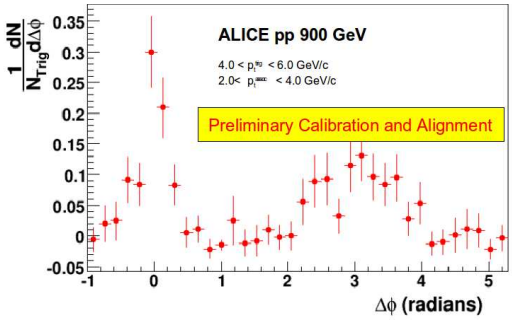

Figure 1: Preliminary Two-particle jet-like azimuthal correlation from $\sqrt{(s)} = 900$ GeV events in ALICE.

Results and Conclusions

Currently the LHC has taken data at in *pp* collisions at $\sqrt{(s)} = 900$ GeV. This data been studied with this analysis. Work is ongoing with this data set to finalize the results. The analysis has also been performed on simulated data from different event simulators of *pp* collisions at $\sqrt{s} = 900$ GeV and also at other energies. The simulated data can be used for comparisons and for corrections.

An example azimuthal correlation from the $\sqrt{s} = 900$ GeV data is shown in the figure. The peak at $\Delta\phi = 0$ is from particles near the trigger particle in angle. These particles and the trigger particle are likely from the same jet-cone. The fragmentation in this peak is biased due to our requirement of a trigger particle. The peak at $\Delta\phi = \pi$ is likely from particles in the other jet of a di-jet. The particles in this peak have an unbiased fragmentation. From studying both peaks we can observe both biased and unbiased fragmentation. Once heavy-ion data has been obtained by studying both peaks we can look at peaks with different medium modification as triggering likely biases the trigger jet to be near the outside of the medium.

* Work supported by EMMI, GSI, and BMBF

Perspectives of J/ψ $\rightarrow$e$^+$e$^-$ measurement in pp collisions at the LHC in ALICE

A. Andronic[1], I.C. Arsene[1], A. Bernhard[2], C. Blume[2], J. Book[2], P. Braun-Munzinger[1,3,4], F. Kramer[2], D. Krumbhorn[5], M. Mager[3], W.J. Park[1], and J. Wiechula[5]

[1]GSI Darmstadt, Germany; [2]J.W Goethe University of Frankfurt, Germany; [3]Technical University, Darmstadt, Germany; [4]ExtreMe Matter Institute, GSI Darmstadt, Germany; [5]University of Heidelberg, Germany

Besides being a crucial observable for the dignosis of the deconfined matter produced in high-energy nucleus-nucleus (AA) collisions (see e.g. [1] for a review), the charmonium family is also a powerful observable to test QCD models for production in pp collisions [2]. The measurement in pp is essential also as a reference for the AA data. The measurements in the new energy domain opened by the LHC are eagerly awaited for both AA and pp.

The ALICE detector, although having as primary goal the study of AA collisions, can make an important contribution in the charmonium sector also for pp collisions. We discuss here, based on simulated events, the expected performance for the J/$\psi \rightarrow e^+e^-$ measurement in the ALICE central barrel, covering $|\eta|$ <0.9. A crucial aspect of the measurement is electron identification, realized with the signal in the Time Projection Chamber (TPC) and in the Transition Radiation Detector (TRD). While the TPC covers the whole azimuthal angle, for the TRD 7 out of the 18 supermodules are presently installed.

The Level-1 trigger capability of the TRD [3] can be exploited to enhance the J/ψ statistics substantially. We first note that the maximum pp luminosity (limited by the maximum envisaged number of pile-up events in TPC of 27) in ALICE is 3·10^{30} cm^{-2}s^{-1} (240 kHz interaction rate). The maximum data taking rate envisaged for pp collisions in the central barrel of ALICE is $\sim$1 kHz. Consequently, the trigger has to provide a reduction factor of $\sim$200 to allow the sampling of rare signals over the whole available luminosity.

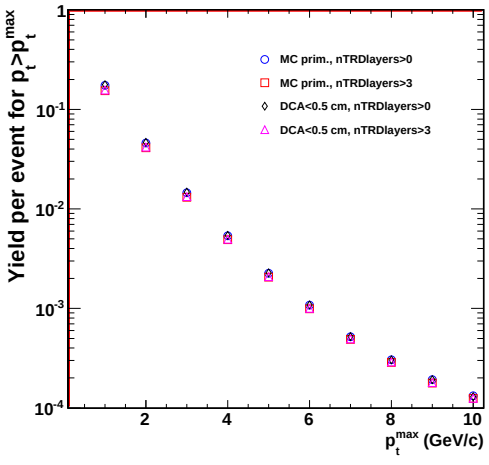

Figure 1: Abundance per event of tracks with transverse momentum larger than p_t^{max}.

In Fig. 1 we show the abundance per event of tracks with momentum larger than a given value. A trigger at 2 GeV/c, combined with a hadron rejection factor of 10-20 achievable online can provide the required selectivity at Level-1 trigger. The effect of the reduced p$_t$ resolution in the online algorithm is under study and efforts are ongoing for the implementation of such a trigger, a concept which was part of the TRD design [3]. The trigger impurity is another issue which needs careful investigations.

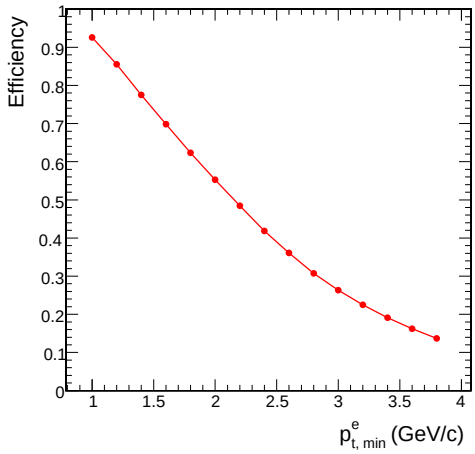

Figure 2: Efficiency of J/ψ as a function of the transverse momentum cut applied on either the electron or positron.

Such a single-leg electron trigger with a threshold in the range 2-3 GeV/c leads to a corresponding J/ψ efficiency in the range 54-26%, as shown in Fig. 2, where we show the J/ψ efficiency as a function of the single-leg cut $p^e_{t,min}$. Assuming a conservative J/ψ efficiency of 10%, for 10^7 s running time at $\sqrt{s}$=7 TeV, we can reconstruct with the present setup for the first LHC run about 10^5 J/ψ, 1500 ψ', 700 $\chi_{c1,2}$ [4] and 1000 Υ events. To achieve the partial bandwidth available to this trigger in the experiment a further selection in the High-Level Trigger system may be required.

When the TRD will be completed during the LHC shutdown period following the first physics run, the detection efficiency will increase by a factor of almost 10.

References

[1] R. Rapp, D. Blaschke, P. Crochet, arXiv:0807.2470.

[2] J.P. Lansberg, Eur. Phys. J. C 60 (2009) 693.

[3] ALICE Transition Radiation Detector Technical Design Report, ALICE TDR 9, CERN/LHCC 2001-021.

[4] P. Gonzalez et al., Eur. Phys. J. C 61 (2009) 899; Erratum ibid., C 61 (2009) 915.

Development of Analysis Methods for $J/\psi \rightarrow e^+e^-$ at ALICE

F. Kramer[1], C. Blume[1], A. Andronic[2], I.C. Arsene[2], A. Bernhard[1], J. Book[1], D. Krumbhorn[3], W.J. Park[2], and J. Wiechula[3]

[1]IKF, Goethe-Universität, Frankfurt, Germany; [2]GSI Darmstadt, Germany; [3]University of Heidelberg, Germany

ALICE is the dedicated heavy-ion physics experiment at the LHC. It is designed to provide excellent means to study the quark-gluon plasma, a deconfined state of matter assumed to be created under extreme conditions. One very promising observable therefore is the measurement of quarkonia, including the J/ψ, ψ' and the Υ states. The ALICE central barrel detectors (ITS, TPC, TRD) will reconstruct quarkonia via their decay into an electron-positron pair [1]. For this purpose the Transition Radiation Detector (TRD) [2] will provide excellent electron identification.

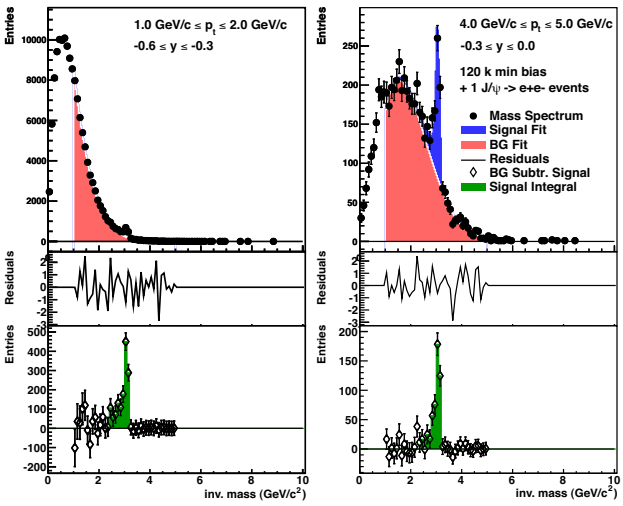

Figure 1: Fit procedure of the invariant mass distributions

Dedicated simulated and fully reconstructed data samples had been used in order to prepare for the analysis of real measurement data. At first all electron-positron pair candidates in a given event that passed a specific set of cuts are used to record an invariant mass spectrum. Different methods to extract the signal and the background contribution from that spectrum can be applied. Fig. 1 shows the result of such a fit procedure for two arbitrarily selected bins of the pair's phasespace (p_t, y). Due to energy loss of the electrons by bremsstrahlung the shape of the peak is asymmetric. The signal part had been matched by the distribution of a simulated pure signal (blue), the background (red) has been fitted with a polynomial. The difference between fit and distribution in numbers of standard deviations of the distribution are drawn in the middle boxes of the two panels. These residuals indicate that the fit procedure achieves a good representation of the simulated data. Note that the sample used for this technical study containes a minimum bias Pythia p+p simulation plus one J/ψ per event and does thus differ strongly from a real measurement sample. Studies of realistic data samples with corresponding signal to background ratios are ongoing. The lower boxes of Fig. 1 show the remaining signal after background subtraction. The integral of the peak gives the measured J/ψ yield.

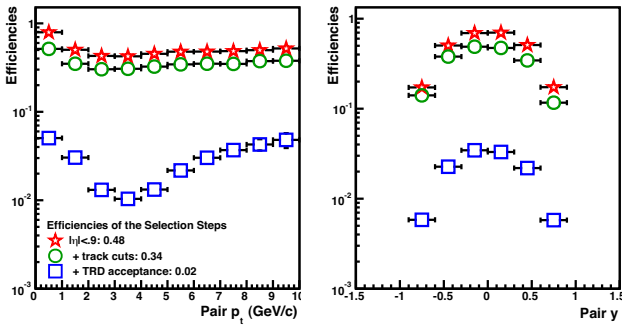

Figure 2: The efficiencies of few reconstruction steps

Since the detector does not cover the whole phasespace and each step of the reconstruction performs only with a certain efficiency, simulations have to be carried out to correct for losses due to acceptance and reconstruction efficiency. Fig. 2 shows an example of the efficiency maps of various different reconstruction steps projected along p_t (left panel) and y (right panel). Red stars represent the efficiency of measuring both J/ψ daughter tracks within the acceptance $|\eta| < 0.9$. For the distribution of the green circles the daughters also have to pass track quality cuts. The blue squares correspond to the additional requirement that both daughters hit the TRD. Since the latter is not completely installed yet the efficiency drops about one order of magnitude when giving this requirement. Such maps are later applied to the measured yields.

As presented the analysis methods for the measurement of J/ψ yields and their efficiency corrections are put in place and can be used for large sets of real data as soon produced at the LHC. Systematic error studies are ongoing.

References

[1] The ALICE Collaboration, "Physics Performance Report Volume II", CERN/LHCC 2005-030, (2005)

[2] The ALICE Collaboration, "TRD Technical Design Report", CERN/LHCC 2001-021, (2001).

A Peformance Study of Electron-Hadron Correlations with ALICE

S. Altınpınar[1]
[1]GSI, Darmstadt, Germany

Since in nucleus-nucleus collisions at ultrarelativistic energies, heavy quark pairs are produced only in hard processes at the early phase of the collision, they are especially suited to investigate the properties of the Quark-Gluon Plasma. Particularly in order to understand the energy loss of heavy quarks, traversing this medium, it is important to distinguish the contributions from charm and bottom quarks. This can be done by Angular Electron-Hadron Correlations with ALICE, an experiment at the LHC. pp collisions have to be measured as reference for nucleus-nucleus collisions. Some studies of azimuthal angle corellations of heavy quark pairs in ALICE, were done already in [1].

In this method, electrons from semileptonic decays of mesons with charm or beauty content, are correlated in azimuthal angle with hadrons originating from the same hard process. For example for a back to back process like pair creation, the electron is preferentially on the opposite side of the D^0 for charm quarks and on the same side for beauty quarks. As it is visible in the sketch in Figure 1, only for the charm case a correlation of electrons with D^0's is possible, whereas the presence of a $\bar{D}^0$ with an electron indicates as origin bottom quarks. It should be noted that certainly the charge symmetric case is considered as well.

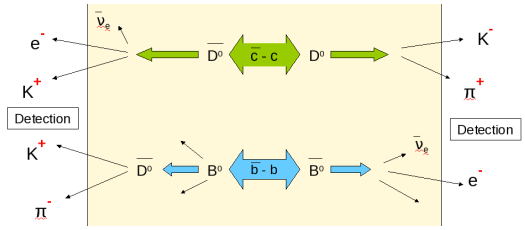

Figure 1: Example decay stems for $c\bar{c}$ and $b\bar{b}$ pairs

For this analysis, a simulation of roughly 50 million pp events at 10 TeV, produced with the Monte Carlo event generator PYTHIA, is used. On the electron side a transverse momentum selection is applied in order to minimize the non heavy quark electron impurity. In Figure 2 the correlation in azimuth between such electrons having a transverse momentum higher than 1 GeV/c and D^0 mesons is shown. Moreover the three leading order processes which are contributing to the overall correlation are indicated. It is possible to deduce from such a correlation function the relative charm and bottom contribution, by comparing the electron-D^0 correlation yield in the near- and away-side. The invariant mass distributions and reconstruction performance, categorized in transverse momentum bins are shown in Figure 3 and Table 1.

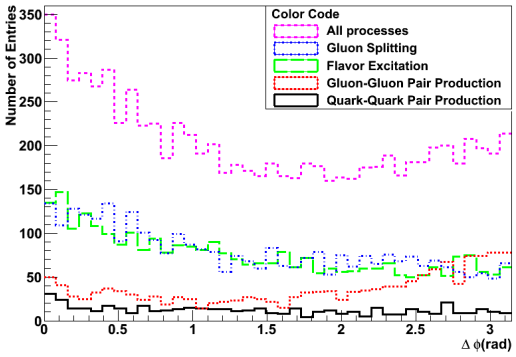

Figure 2: Azimuthal Angle Correlation of electrons and D^0 mesons

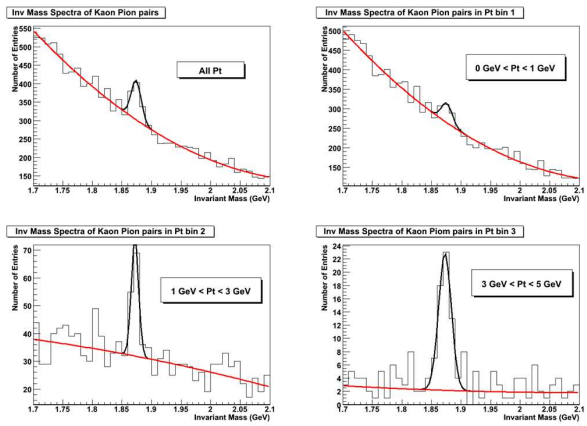

Figure 3: Invariant mass distributions of Kaon Pion pairs with $D^0/\bar{D}^0$ peaks

D^0 P_t Range	S	B	S/B	Signif. (10^9)
All (GeV/c)	154	509	0.3	6 26.8
0→1 GeV/c	78	478	0.16	3.3 14.7
1→3 GeV/c	45	39	1.14	4.9 21.9
3→5 GeV/c	38	5	8.19	5.8 25.9

Table 1: D^0 Reconstruction Performance

The correlation with reconstructed D^0 mesons (see Table 1) and electrons, yields a correlation plot with only a few entries. To obtain a correlation function, the full statistics of one year data taking at ALICE (10^9 ev.), which is corresponding to roughly 350 entries, is needed.

References

[1] ALICE Collaboration, J. Phys. G: Nucl. Part. Phys. 32 (2006) 1295

Parton and flavor discrimination using jets with ALICE at the LHC

H. León-Vargas[1], C. Blume[1], and C. Klein-Bösing[2]
[1]IKF, University of Frankfurt, Germany; [2]Institut für Kernphysik Münster, Germany

Introduction

The study of the jet cross section and that of its different components (quarks and gluons) is an important test of perturbative QCD. Using the excellent tracking and PID capabilities of ALICE, it is possible to use a combination of different tagging variables to disentangle the jets produced by quarks or gluons, and even the jets produced by heavy or light quarks. We are interested in using the tagged jets as probes of the hot and dense matter produced during heavy ion collisions. The proton-proton collisions will be used as a benchmark for the Pb-Pb collisions.
The data set used to generate the figures on this report contains 1.25 million simulated proton-proton collisions at 7 TeV from PYTHIA. We used the UA1 jet finder running over charged particles, with a cone radius of 0.4.

Quark and gluon jet tagging

The differences in the fragmentation properties of quarks and gluon jets is the basis that allows to distinguish jets produced by these two sources. For instance, the jets produced by the fragmentation of gluons are expected to contain more particles and be broader in $\eta - \phi$ space than jets produced from quarks.
Two approaches for the jet tagging are under study. The first is based on the method proposed in [1] that basically calculates the number of cells in a $\eta-\phi$ grid, which are necessary to recover a certain fraction of the jet energy. The second method uses the second moment of the jet profile in transverse momentum, as proposed in [2]:

$$\langle \delta R^2_{jet} \rangle = \frac{\Sigma_i \Delta R^2(i, jet) \times p^i_T}{\Sigma_i p^i_T} \qquad (1)$$

Where the index *i* runs over all stable charged particles and $\Delta R = \sqrt{(\Delta\eta)^2 + (\Delta\phi)^2}$. Figure 1 shows the distribution of the second moment of the jet profile for all jets in black circles, quark jets in blue crosses and for gluon jets in green triangles. The mean value of the second moment of the jet profile is higher for gluons jets than for quark jets over the whole jet p_T range studied.

B-jet tagging

Following the ideas in [3], we are also studying the possibility of tagging b-jets using the semileptonic decay channel of B mesons. B jets are selected based on the kinematic properties of the electrons relative to the jet. An example of a discriminating variable is shown in figure 2, where the red line shows the distribution obtained for b-jets, the solid black line for gluons, the dotted blue line for c-jets and the dashed black for light quarks. As one can see, the fraction of the jet energy carried by electrons is larger when the jet is originated from a heavy quark.

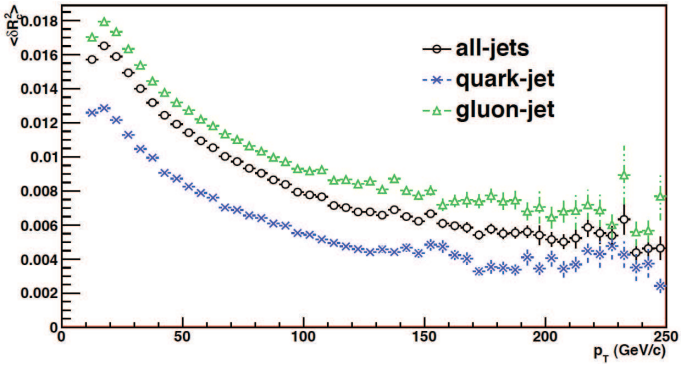

Figure 1: Discrimination of quark and gluon jets using the second moment of the jet profile.

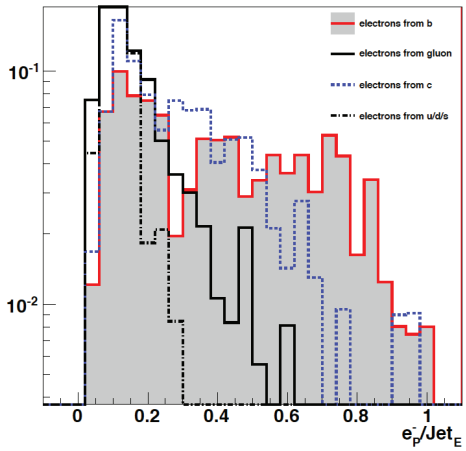

Figure 2: Ratio of the electron momentum to the jet energy for jets with energy greater than 50 GeV.

References

[1] J. Pumplin, "How to tell quark jets from gluon jets", Phys. Rev. D 44 (1991) 2025

[2] The CMS Collaboration, "Study of jet transverse structure using the second moment of the jet profile in transverse momentum in pp collisions at $\sqrt{s} = 10$ TeV", CMS PAS QCD-08-002, 2009.

[3] P. Demin, S. de Visscher, A. Bocci, R. Ranieri, "Tagging b jets with electrons and muons at CMS", CMS NOTE 2006/043.

Study on Impact Parameter of Charged Particles in ALICE
preparing for studying electrons from semi-leptonic heavy-flavor decay at LHC energies*

C. Bombonati[1], S. Masciocchi[2], K. Schweda[3], J. Stachel[3], and H. Yang[†3]
[1]INFN, Padova, Italy; [2]GSI, Helmholtzzentrum für Schwerionenforschung GmbH, Darmstadt, Germany;
[3]Physikalisches Institut, Universität Heidelberg, Heidelberg, Germany

Beauty is produced much more abundantly at LHC energies compared to RHIC energies. The increase in production, coupled with the beauty large mass, makes it an interesting observable for the physic of the ALICE experiment[1]. Semi-electronic decay of beauty mesons offers a powerful tool to study beauty production in ALICE, attributed to its high tracking resolution (ITS, TPC, TRD) and vertexing (ITS)[2]. With the high single track pointing resolution of about 50 μm at $p_T \approx 1 GeV/c$, ALICE is well suited for studying the displaced electrons from beauty mesons decay because the relatively large difference in typical decay length of beauty ($\approx$ 500 μm) and charm (up to $\approx$ 300 μm).

Results

The impact parameter projection of reconstructed tracks in the transverse plane (xy) and the z direction are defined as:

$$d_{xy} = q \cdot [R - \sqrt{(x_v - x_c)^2 + (y_v - y_c)^2}], \quad d_z = z_{track} - z_v \tag{1}$$

where q is the sign of particle charge, R and (x_c, y_c) are the radius and center coordinates of the track projection (a circle) in the transverse plane, and (x_v, y_v, z_v) the position of the collision vertex.

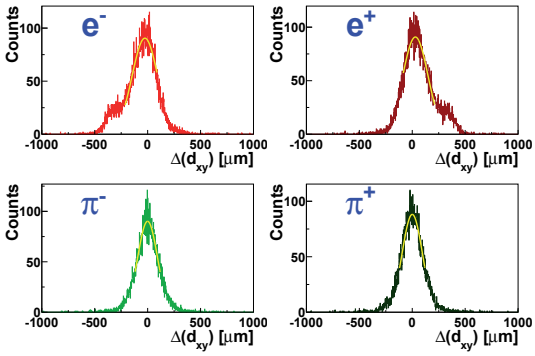

Figure 1: An example of single Gaussian fit on residuals between measured and expected impact parameter within $0.5 < p_T \leq 0.6\ GeV/c$.

This analysis is based on Monte Carlo data samples produced at the GSI[3] computing center, with 5 different particle species ($e^{\pm}$, $\mu^{\pm}$, $\pi^{\pm}$, $K^{\pm}$, $p(\bar{p})$) of flat p_T distribution within a p_T range $(0, 20]\ GeV/c$ with GEANT. Tracks are reconstructed with realistic detector geometries and detector response functions. The impact parameter of reconstructed tracks in the transverse plane and the z direction are considered separately.

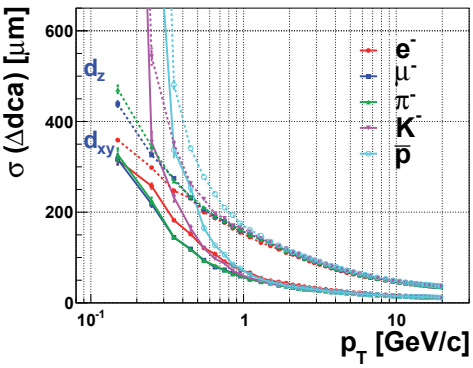

Figure 2: Momentum dependence of the impact parameter resolution for charged particles.

The residuals $\Delta(dca)$, namely the difference between the measured and expected impact parameters, are fitted with a single Gaussian function within various p_T bins, from which the resolution is obtained as the width of each Gaussian fit. As an example, figure 1 shows a typical Gaussian fit over the residuals of d_{xy} within optimal-σ range within $0.5 < p_T \leq 0.6\ GeV/c$. Residuals of $e^{\pm}$ are affected by the Bremsstrahlung processes, which appear as a shoulder-like structure on left or right (for e^- or e^+) side of the distribution, but disappear when the Bremsstrahlung is switched off. On the other hand, for the other charged particles, Bremsstrahlung effects are negligible. Figure 2 shows the transverse momentum dependence of the impact parameter resolution.

The resolutions in the transverse plane (xy) and the z direction are about 60 μm and 160 μm at $p_T \approx 1 GeV/c$ and better at higher transverse momentum respectively. The resolution of electrons and positrons in the transverse plane at low p_T is strongly affected by the Bremsstrahlung effect. These results are consistent with the earlier study[2]. High resolution in measuring the impact parameter for electrons, enables the ALICE detector to disentangle electrons produced by semi-electronic decay of beauty from charm.

References

[1] ALICE Collaboration, J. Phys. G: Nucl. Part. Phys. 30 (2004)1517-1763, 32 (2006) 1295-2040.
[2] A. Dainese and R. Turrisi, ALICE-INT-2003-28 (2003) 1-15.
[3] http://www-alice-new.gsi.de/catalog/SimProd/index.php.

*This work has been supported by the Helmholtz Association under contract numbers VH-NG-147, HA-216/EMMI and the Federal Ministry of Education and Research under promotional reference 06HD9129D.
†hongyan@physi.uni-heidelberg.de

A Linear Sigma Model with Vector Mesons and Global Chiral Invariance*

D. Parganlija†[1], F. Giacosa[1], and D. Rischke[1,2]

[1]Goethe University, Frankfurt/Main, Germany; [2]FIAS, Frankfurt/Main, Germany

The primary focus of our work has been the research of vacuum properties of the low-lying scalar, pseudoscalar, vector and axial-vector mesons (with the energies up to approximately 1.5 GeV) within a linear sigma model with global chiral invariance. As a first approximation of a larger study, we have taken into account only the mesons containing u and d quarks. All mesons in our model are quark-antiquark states due to their behaviour in the limit of large number of colours (e.g., no $qq\bar{q}\bar{q}$ states for now). Their assignment to the physical fields is straightforward in the case of pseudsosclars: pion and η_N (the latter is the non-strange contribution to the physical η meson); vectors: $\omega(782)$ and $\rho(770)$; axial-vectors: $f_1(1285)$ and $a_1(1260)$. The scalar mesons can be assigned in at least two ways: to $f_0(600)$ and $a_0(980)$ or to $f_0(1370)$ and $a_0(1450)$.

In Refs. [1, 2] we have presented the case where the scalar mesons are assigned to $f_0(600)$ and $a_0(980)$. The Lagrangian of the model is discussed and we derive the formulas for the s-wave $\pi\pi$ scattering lengths with isospin zero (scattering length a_0^0) and isospin two (scattering length a_0^2) in the $\pi\pi$ coupled channel. We also derive the decay widths for the following processes: $\rho \to \pi\pi$, $f_1 \to a_0(980)\pi$, $a_1 \to \pi\gamma$, $f_0(600) \to \pi\pi$, $a_1 \to f_0(600)\pi$ and $a_1 \to \rho\pi$ as well as the decay amplitude in the $a_0(980) \to \eta_N\pi$ channel. We have used the scattering lengths and the decay widths $\rho \to \pi\pi$, $f_1 \to a_0(980)\pi$ and $a_1 \to \pi\gamma$ to calculate the parameters of the model; the decay amplitude $a_0(980) \to \eta_N\pi$ and the decay widths $a_1 \to f_0(600)\pi$, $a_1 \to \rho\pi$ and $f_0(600) \to \pi\pi$ are then the results of the model and can be compared to the experimental data.

Our calculations have resulted in a perfect agreement with the Crystal Barrel data [3] on the $a_0(980) \to \eta\pi$ decay amplitude. Our results correspond very well to the experimental data on the a_1 phenomenology [the best results are obtained for $m_{a_1} \simeq 1180$ MeV - that is about 50 MeV smaller than the usually cited value from the Particle Data Group (PDG) [4], but this is not worrying as the data on m_{a_1} is model-dependent because the $a_1(1260)$ resonance is broad]. However, we also obtain the value of decay width $f_0(600) \to \pi\pi$ that increases very slowly with $m_{f_0(600)}$ so that even at $m_{f_0(600)} \simeq 600$ MeV one obtains only $\Gamma_{f_0(600)\to\pi\pi} \simeq 50$ MeV [unlike the result $\Gamma_{f_0(600)\to\pi\pi} = (600 - 1000)$ MeV quoted by the PDG [4]].

Therefore, assigning the scalar states of the model to the physical mesons $f_0(600)$ and $a_0(980)$ has yielded a too small value of the $f_0(600) \to \pi\pi$ decay width. Thus, we have concluded that the low-lying scalar states $f_0(600)$ and $a_0(980)$ cannot be (predominantly) $q\bar{q}$ states.

For this reason, we have also considered an alternative assignment for the scalars present in the model. In this case, the $q\bar{q}$ states are assumed to correspond to the physical states $f_0(1370)$ and $a_0(1450)$. Then we can calculate our parameters in a similar way to the previous case where the $f_0(600)$ and $a_0(980)$ mesons were assumed to be $q\bar{q}$ states, with the difference that the decay width $f_1 \to a_0(980)\pi$ cannot be used anymore for kinematic reasons and that the full decay width of the $a_0(1450)$ meson is used instead of the decay amplitude $a_0(980) \to \eta_N\pi$. The calculation of the $f_0(1370) \to \pi\pi$ decay width yields $\Gamma_{f_0(1370)\to\pi\pi} = 410$ MeV for $m_{f_0(1370)} = 1300$ MeV and $\Gamma_{f_0(1370)\to\pi\pi} = 470$ MeV for $m_{f_0(1370)} = 1350$ MeV. This result is in accordance with the experimental data from the PDG [4] stating the full width of the $f_0(1370)$ between 200 and 500 MeV [and $1200 \leq m_{f_0(1370)} \leq 1500$]. Therefore, we conclude that the scalar mesons $f_0(1370)$ and $a_0(1450)$ are (predominantly) $q\bar{q}$ states.

The role of the (axial-)vector mesons is very important in reaching the mentioned conclusions about the structure of the scalar mesons. As shown in Ref. [2], the $\pi\pi$ scattering lengths and the $f_0(600) \to \pi\pi$ decay width both correspond to the respective experimental data in the linear sigma model without (axial-)vector mesons, but the inclusion of (axial-)vectors, while still allowing for the scattering lengths to be described correctly, leads to a significant lowering of the $f_0(600) \to \pi\pi$ decay width (by approximately a factor of nine). Thus, when the (axial-)vectors are included into the model, one has to look for the $q\bar{q}$ scalar states in the energy region above 1 GeV. Then the identification of the $f_0(1370)$ and $a_0(1450)$ mesons as $q\bar{q}$ states leads to the correct value of the isoscalar decay width.

Our future work will concentrate on further investigation of the nature of the $f_0(600)$ and $a_0(980)$ mesons (possibly as $qq\bar{q}\bar{q}$ states or $\pi\pi$ molecules) and on calculations of meson properties at $T \neq 0$ in order to investigate the QCD phase diagram, the restoration of chiral invariance and deconfinement.

References

[1] D. Parganlija, F. Giacosa and D. H. Rischke, PoS **CONFINEMENT8**, 070 (2008) [arXiv:0812.2183 [hep-ph]].

[2] D. Parganlija, F. Giacosa and D. H. Rischke, arXiv:0911.3996 [nucl-th].

[3] D. V. Bugg, V. V. Anisovich, A. Sarantsev and B. S. Zou, Phys. Rev. D **50**, 4412 (1994).

[4] C. Amsler et al. (Particle Data Group), Phys. Lett. **B667**, 1 (2008).

* Work supported by the GSI F&E Project.

† parganlija@th.physik.uni-frankfurt.de

About the origin of the mass of the nucleon in a linear sigma model*

S. Gallas[1], F. Giacosa[1], and D.-H. Rischke[1,2]

[1]Institut für Theoretische Physik, Johann Wolfgang Goethe University, Frankfurt, Germany; [2]Frankfurt Institute for Advanced Studies, Johann Wolfgang Goethe University, Frankfurt, Germany

Understanding the mass of the nucleon is one of the most important issues in modern physics. Neglecting the small contribution of the explicit symmetry breaking, in the classical linear sigma model the mass of the nucleon is generated exclusively through spontaneous breaking of the chiral symmetry, leading to the appearance of a chiral condensate $\phi \sim f_\pi$, where $f_\pi = 92.4$ MeV is the pion decay constant [1]. The chiral condensate ϕ can be directly related to the fundamental quark condensate $\langle \bar{q}q \rangle$ as $\phi \simeq \Lambda_{QCD}^{-2} \langle \bar{q}q \rangle$, where Λ_{QCD} is the QCD Yang-Mills scale.

However, not only the quark condensate, but also other condensates, such as the gluon and the tetraquark ones, can contribute to the mass of the nucleon m_N and it is not yet settled which is their quantitative role [2]. A possibility to study this problem in the context of a linear sigma model goes via the so called mirror assignment, which was first discussed in Ref. [3] and extensively analyzed in Refs. [4, 5]. In this assignment, the nucleon N and its chiral partner N^* form a doublet of the chiral group. Then it is possible to introduce a chirally invariant mass term parametrized by m_0. This leads to non-vanishing masses of the nucleon and its chiral partner in the chirally restored phase where $\phi \to 0$, instead they acquire the same mass $m_0 \neq 0$. We show this in Fig. 1.

A study of the parameters using the decays $N^* \to N\pi$ and $a_1 \to \pi\gamma$ results in a value of 460 MeV for m_0 which denotes the contribution to the mass of the nucleon *not* stemming from the quark condensate [6].

The viability of our model is tested by studying the decay $N^* \to N\eta$ and pion-nucleon scattering at tree level. This can provide useful information to clarify the origin of the nucleon mass and its behavior in the chirally restored phase.

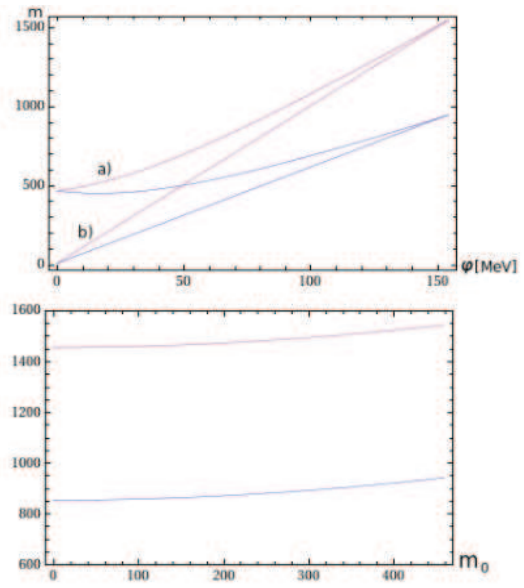

Figure 1: Upper panel: The masses of the nucleon (blue line) and its chiral partner (purple line) as a function of the quark condensate at fixed $m_0 = 460$ MeV. a) When varying ϕ from 0 to the physical value the nucleon mass goes from $m_0 = 460$ MeV to 939 MeV, thus showing that in limit $\phi \to 0$ the mass does not vanish. b) If we turn off m_0, the masses are exclusively generated by chiral symmetry breaking, thus vanishing for $\phi \to 0$. Lower panel: The chiral condensate ϕ is kept fixed to its physical value but the parameter m_0 is left free. The baryon masses are plotted as function of m_0.

References

[1] R. D. Pisarski, arXiv:hep-ph/9503330.

[2] T. D. Cohen, R. J. Furnstahl, D. K. Griegel and X. m. Jin, Prog. Part. Nucl. Phys. **35** (1995) 221.

[3] B.W. Lee, "Chiral Dynamics", Gordon and Breach, New York, 1972

[4] C. DeTar and T. Kunihiro, Phys. Rev. D **39** (1989) 2805.

[5] D. Jido, M. Oka, and A. Hosaka, Prog. Theor. Phys. **106** (2001) 873. D. Jido, Y. Nemoto, M. Oka and A. Hosaka, Nucl. Phys. A **671** (2000) 471.

[6] S. Gallas, F. Giacosa and D. H. Rischke, arXiv:0907.5084 [hep-ph]. submitted to Phys. Rev. D.

* Work supported by EU, EURONS contract No. 506065.

Correlations in Exotic Nuclear Matter

P. Konrad*[1] and H. Lenske[1,2]

[1]Institut für Theoretische Physik, Universität Gießen, Germany; [2]GSI, Darmstadt, Germany

In recent years, the interest in correlations inside nuclei became an important issue in nuclear physics. On the theoretical, side several calculations using different models including short-range correlation have been done for nuclear matter. However, there is still not much known about the role of correlations in neutron star matter containing hyperons. In our work we examined dynamical correlations in infinite nuclear and hypernuclear matter. We used a self-consistent approach to calculate the dynamical self-energy and the spectral function. The self-energy is approximated by the one-particle-two-hole (1p2h) and two-particle-one-hole (2p1h) polarization self-energy by neglecting higher order terms. For a realistic treatment of the nuclear mean-field incorporating an accurate description of finite nuclei, we used modern Skyrme parameterizations for the energy density functional. As shown by [1], dynamical correlations are more influenced by the strength of the interaction and the available phase space rather by the details of the interaction. Therefore, we assumed an energy- and momentum-independent interaction matrix element to approximate the polarization self-energies. Information on the average interaction matrix element was obtained by a weighted sum of the Landau-Migdal parameters extracted from the Skyrme energy-density functional [2].

The spectral function shows a behavior known from other many-body calculations, a sharp quasi-particle peak with a wide spectral distribution. The location of the quasi-particle peak is mainly given by the mean-field contribution of the self-energy, while the collisional part is responsible for the spectral distribution. The comparison of different Skyrme parameterizations shows that the results for the different parameterization agree very well in symmetric and asymmetric nuclear matter.

We kept the total baryon number fixed by varying the strangeness fraction to examine the influence of dynamical correlations in hypernuclear matter. Qualitatively, the results for the width, the spectral function and the momentum distribution of the nucleons and Λ-hyperons are similar to those found in nuclear matter. Quantitatively, the Λ-hyperons are less correlated since the interaction strength is reduced, while the correlations of the nucleons are of the same order as in nuclear matter. Thus Λ-hyperons show a smaller width, a sharper structure of the spectral function and a less pronounced high energy tail of the momentum distribution than the nucleons. This observation agrees perfectly well with the sharp spectral structure seen in hypernuclear spectra e.g. [3].

The situation in β-equilibrated nuclear matter is different. As seen in Fig.1, the particle width and the spectral function resemble qualitative the same properties as in nuclear matter. However, it is surprising that the width of the neutrons is about the same size as the hyperons rather the protons [2], as it can be seen in the lower panel of Fig.1. This fact can be explained by the high excess of neutrons in β-equilibrated nuclear matter, as already seen in neutron rich matter, Pauli-blocking leads to a decrease of the neutrons. This observation is confirmed when we examine the quasiparticle strength at the Fermi-edge as a function of the density. This shows that the correlations in our approach are connected directly to the abundance of the particles and the available phase space rather than the details of the interaction.

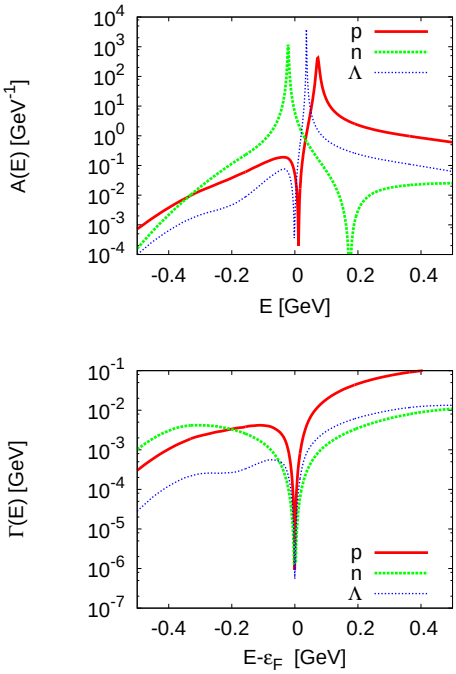

Figure 1: The spectral function A (upper panel) and the width Γ (lower panel) as function of the energy E for protons, neutrons and Λ-hyperons in β-equilibriated nuclear matter at the density $\rho = 0.48$ fm^{-3} and momentum $p' = 0.3$ GeV.

References

[1] J. Lehr, H. Lenske, S. Leupold, U. Mosel, Nucl. Phys. A703, 393-408, 2002

[2] P. Konrad, Correlations in Exotic Nuclear Matter, Dissertation, Universität Gießen, 2009

[3] H. Hotchi, Phys. Rev. C64, 044302, 2001

* Patrick.Konrad@theo.physik.uni-giessen.de

Description of Heavy Ion Reactions at GSI Energies*

Amand Fäßler[1] and Herbert Müther[1]

[1]Institut für Theoretische Physik der Universität Tübingen, D-72067 Tübingen, Germany

We have investigated the connection between different forms of the nucleon-nucleon interaction, nuclear matter and heavy-ion reactions. In particular, the dilepton and σ-meson production in the experiments FOPI and HADES at the GSI have been studied.

In [1, 2] two microscopic models, UrQMD and QGSM, have been employed to study the formation of locally equilibrated hot and dense nuclear matter in heavy-ion collisions at energies from 11.6 A GeV to 160 A GeV. Both dynamical models indicate that the state of kinetic, thermal and chemical equilibrium is nearly approached at any bombarding energy after a certain relaxation period. Equation of state has a linear dependence $P = c_s^2(\sqrt{s})e$, where c_s is the sound velocity. Change of the slope in $c_s^2(\sqrt{s})$ behavior occurs at $E_{lab} = 40$ A GeV and can be assigned to the transition from baryon-rich to meson-dominated matter. The phase diagrams in the $T - \mu_B$ plane show the presence of kinks along the lines of constant entropy per baryon which can be linked to the inelastic freeze-out in the system.

The light vector mesons ρ and ω are of particular interest since their decay to dileptons allows to probe the electromagnetic response of the nuclear medium. In heavy ion reactions dilepton pairs provide a clear view on effective degrees of freedom at high baryon density and temperature. We have determined the modification of the ρ and ω meson properties in nuclear matter within a resonance model. For both mesons a substantial broadening of the width and a significant shift of spectral strength down to smaller invariant masses are found. In a first approximation the spectral functions have been determined from vacuum resonance properties. Going beyond this approximation, the in-medium modification of the nucleon resonance widths has been included. In [3] the in-medium spectral functions of ρ and ω mesons and the broadening of nucleon resonances at finite baryon density are calculated self-consistently by combining a resonance dominance model with an extended vector meson dominance model. The dilepton spectrum is generated for the C+C reaction at 2.0A GeV and compared with recent HADES Collaboration data. The collision dynamics is described by the Tübingen relativistic quantum molecular dynamics transport model. An iterative calculation of the vector meson spectral functions that takes into account the broadening of the nucleon resonances due to their increased in-medium decay branchings converges and provides a reasonable description of the experimental data in the mass region $0.45 \leq M \leq 0.75$ GeV.

In [4, 5] production of the σ meson is investigated in the quantum molecular dynamics model for the $p+A$ reactions with the nuclei ^{12}C, ^{40}Ca and ^{208}Pb at the incident proton energies $E_p = 1.50$ GeV. The simulation results indicate a distinctive A dependence of the σ production. The σ meson production is strongly medium-dependent, and the produced σ mesons decaying in a denser medium experience a stronger mass shift towards lower masses. This mass shift is experimentally observable.

In [6] previous studies of the nuclear many-body problem have been extended, in particular with respect to the isospin dependence of the forces within the relativistic Dirac Brueckner Hartree Fock (DBHF) approach. It is found that the proton properties are sensitive to the choice of the Bonn potential for isospin asymmetric nuclear matter. Furthermore, the neutron effective mass remains practically unaffected, whereas the proton mass experiences a sizable reduction, since in neutron rich matter proton properties depend much stronger on contributions from the np channel than neutron properties. In [7] a parameterization of the density dependent meson-nucleon coupling constants has been developed (DDRMF), which is based on the DBHF calculations [6]. This model has been used to study the properties of low density matter relevant in the crust of neutron stars, in particular for the so-called "pasta-phase". At densities below 0.08 nucleons/fm^3 the DDRMF approach predicts non-homogeneous structures, which are similar (though less pronounced) to those predicted by Thomas-Fermi or Skyrme Hartree-Fock calculations for the "pasta-phase" in the crust of neutron stars.

In order to effectively perform calculations within the nuclear shell model, a quick and reliable access to the basic nuclear matrix elements is need. By using the MAPLE software in [8] analytical representations of the basic Talmi integrals are obtained for a general class of two-body operators. This allows faster calculation of matrix elements for a wide class of two-body operators, icluding those which appear in description of neutrinoless double beta decay [9].

References

[1] L. Bravina *et al.*, Phys. Rev. C **78**, 014907 (2008).

[2] E. Zabrodin *et al.*, arXiv:0902.4601 [hep-ph].

[3] E. Santini *et al.*, Phys. Rev. C **78**, 034910 (2008).

[4] P. Srisawd *et al.*, Int. J. Mod. Phys. A **22**, 6219 (2008).

[5] Y. M. Zheng *et al.*, Commun. Theor. Phys. **50**, 725 (2008).

[6] E.N.E. van Dalen, C. Fuchs, and A. Faessler, Eur. Phys. J. A **31**, 29 (2007).

[7] P. Gogelein, E. N. E. van Dalen, C. Fuchs and H. Müther, Phys. Rev. C **77**, 025802 (2008).

[8] L. Rodina, Amand Faessler, to be published.

[9] F. Simkovic, A. Faessler, H. Müther, V. Rodin and M. Stauf, Phys. Rev. C **79**, 055501 (2009).

* Work supported by the GSI Theory Project TUEMUE.

Dilepton production in neutron-proton collisions at HADES energies*

R. Shyam[1,2] and U. Mosel[1]

[1]Institut für Theoretische Physik, Universität Giessen, Germany; [2]Saha Institute of Nuclear Physics, Kolkata, India

Experiments with High Acceptance Di-electron Spectrometer (HADES) are aimed at searching for medium modifications of hadrons at moderately high temperatures ($T < 100$ MeV) and baryonic densities up to 3 times the normal nuclear matter density. Due to negligible final state interactions with surrounding medium, dileptons provide a very clean and powerful probe for this purpose.

Dilepton production was studied by the DLS collaboration at BEVALAC [1] at beam energies of 1–2 GeV/nucleon. A large dilepton excess over the "hadronic cocktail" was observed in the ^{12}C + ^{12}C and ^{40}Ca + ^{40}Ca collisions which could not be explained by theoretical models. This situation became known as the "DLS puzzle". To resolve this issue, the HADES experiment [2] has reinvestigated this reaction in ^{12}C + ^{12}C collision at similar beam energies. The remarkable fact is that the HADES data agree well with those of the DLS Collaboration. Therefore, there is no longer any question against the validity of the DLS data and the puzzle has now shifted to the theory side.

In a recent transport model calculation it has been shown [3] that if larger cross sections are used for the proton-neutron (pn) bremsstrahlung process then the excess dilepton yields observed in ^{12}C + ^{12}C collisions by both the DLS and the HADES experiments can be reproduced. Enhanced pn bremsstrahlung cross sections, however, are not in agreement with the results presented in Refs. [4] and [5] where a fully relativistic and gauge-invariant model has been employed to calculate the dilepton production in nucleon-nucleon (NN) collisions. On the other hand, calculations reported in Refs. [6] do support a larger value for this cross section. This is somewhat puzzling as the later model uses similar ingredients and the input parameters as those in Refs. [4, 5].

We have taken up a systematic investigation of the dilepton production in the NN collisions at HADES energies within our fully relativistic and gauge-invariant model. We aim at describing the recent HADES data for this reaction reported very recently in Ref. [7]. Furthermore, we would also like to understand the reason for the differences seen between the results of Refs. [4, 5] and [6] as it has important implications for a proper theoretical interpretation of the HADES ^{12}C + ^{12}C data.

In this report we examine the role of various meson exchange processes to the dilepton production in the pn collisions. In Fig. 1, we show individual contributions of the π- and ρ-exchange graphs to the invariant mass distribution of the dilepton production in the pn collisions at 1.25 GeV beam energy. Contributions of other meson exchange processes are relatively smaller. The coherent sum of the two terms is also shown there. We note that π-exchange process dominates the cross sections and more significantly it interferes destructively with the ρ-exchange terms as the coherent sum of the two diagrams is even slightly smaller than the pion-only exchange term. This result is in contrast to the observations made in Ref. [6]. This implies that a larger ρ-exchange term will lead to even smaller total cross sections.

As is shown in Ref. [8], the HADES dilepton data for pp collisions agree with the predictions of our model whereas the calculations of Ref. [6] overestimate them. We are currently carrying out investigations to explain the pn cross sections where a bump has been observed in the data in the mass region between 0.15 and 0.5 GeV/c^2.

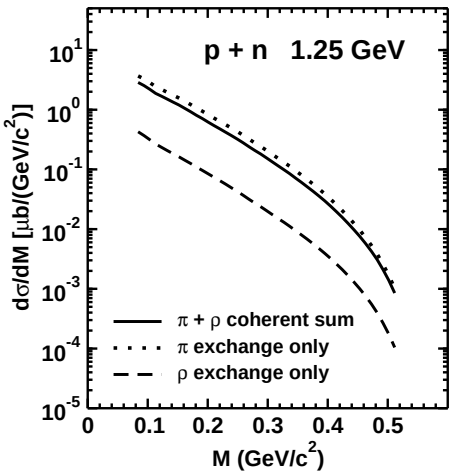

Figure 1: Contributions of π (dotted line) and ρ (dashed line) exchange diagrams to the invariant mass distribution of the dileptons produced in proton-neutron collisions at the beam energy of 1.25 GeV. Their coherent sum is shown by the solid line

References

[1] R. J. Porter *et al.*, Phys. Rev. Lett. **79** (1997) 1229.

[2] G. Agakishiev *et al.*, Phys. Lett. **B663** (2008) 43.

[3] E. Bratkovskaya and W. Cassing, Nucl. Phys. **A807** (2008) 214.

[4] R. Shyam and U. Mosel, Phys. Rev. C **67** (2003) 065202.

[5] R. Shyam and U. Mosel, Phys. Rev. C **79** (2009) 035203.

[6] L.P. Kaptari and B. Kämpfer, Nucl. Phys. **A764** (2006) 338; Phys. Rev. C 80 (2009) 064003

[7] G. Agakishiev *et al.*, arXiv:0910.5875 [nucl-ex].

[8] B. Ramstein *et al.*, arXiv:0912.2677 [nucl-ex].

* Work supported by GSI Darmstadt

Estimate of the magnetic field strength in heavy-ion collisions*

V. Skokov†[1], Yu. Illarionov[2], and V. Toneev[3]

[1]GSI, Darmstadt, Germany; [2]University of Trento, Italy; [3]JINR, Dubna, Russia

One of the most exciting signals of the deconfinement and the chiral phase transitions in heavy-ion collisions, the chiral magnetic effect, suggested in Ref. [1], predicts the preferential emission of charged particles along the direction of angular momentum in the case of the noncentral heavy-ion collisions due to the presence of nonzero chirality. This effect is because the strong magnetic field in the presence of imbalanced chirality induces a current along the magnetic field. As it was stressed in Refs. [1, 2], both the deconfinement and the chiral phase transitions are essential for the chiral magnetic effect to take place.

The effects caused by a strong magnetic field are not limited by the chiral magnetic effect [2]. They include also the induced chiral symmetry breaking, modification of the nature of the chiral phase transition (e.g. turning the crossover phase transition to the first-order one through influence on the chiral condensate), influence on the possible color-conducting phases and the pion condensate, spontaneous creation of the axial currents, and formation of the π_0-domain walls. Recently, the effect of a large magnetic field on the sound velocity of a propagating plane wave was studied.

The key quantity of these effects is a magnitude of the background magnetic field strength created in heavy-ion collisions. Early estimates of the magnetic field for RHIC energies was made in Ref. [1]. It was shown that the field may reach very high values $eB \sim 3 \cdot m_\pi^2 \sim 3 \times 10^{18}$ Gauss. In Ref. [3] we improved the previous qualitative estimate by making the quantitative calculation of the magnetic field for heavy-ion collisions at different impact parameters and different energies and studying its characteristics. The calculations were carried out within the microscopic transport model, namely the Ultrarelativistic Quantum Molecular Dynamics model (UrQMD), and were complemented by analytical considerations.

In Fig. 1, the time evolution of the magnetic field strength for SPS and RHIC energies is shown. The magnetic field is created in the noncentral Au–Au collision with the impact parameter $b = 4$ fm. The resulting field strength is averaged over 100 events to reduce statistical fluctuations.

Note that this magnetic field strength is higher by about 4 orders of magnitude than that in the surface of magnetar.

The calculated dependence of the magnetic field strength on the coordinate y parallel to the direction of angular momentum demonstrates that the field stays approximately constant up to $y \sim 5$ fm, showing the high degree of homogeneity in the central region.

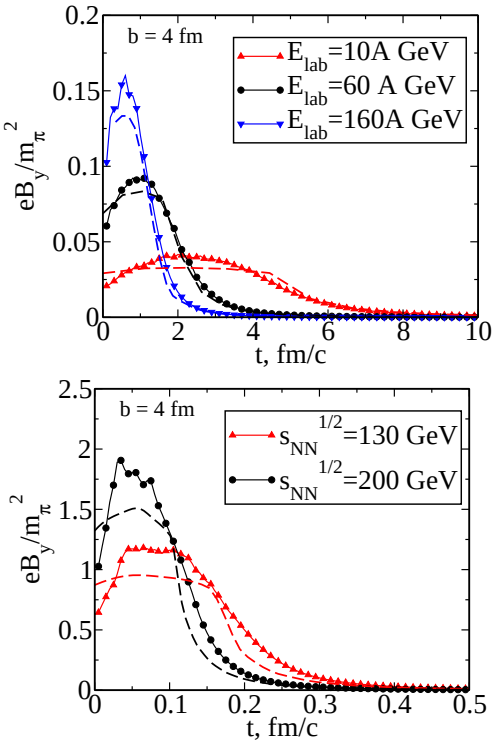

Figure 1: The time evolution of the magnetic field strength eB_y at the central point of colliding ions in Au–Au collisions with impact parameter, $b = 4$ fm, in the UrQMD model, for different bombarding energies. The magnetic field obtained by modelling the gold ions as two Lorenz contracted non-interacting uniformly charged spheres with radius $R = 7$ fm are shown by dashed lines.

We estimated the lowest bound of the maximal magnetic field strength at the LHC energy $\sqrt{s_{NN}} = 4.5$ TeV to be about $15 \cdot m_\pi^2$ in collisions of Pb–Pb ions with the impact parameter $b = 4$ fm.

References

[1] D. E. Kharzeev, L. D. McLerran and H. J. Warringa, Nucl. Phys. A **803**, 227 (2008) [arXiv:0711.0950].

[2] K. Fukushima, D. E. Kharzeev and H. J. Warringa, Phys. Rev. D **78**, 074033 (2008) [arXiv:0808.3382].

[3] V. Skokov, A. Y. Illarionov and V. Toneev, Int. J. Mod. Phys. A **24** (2009) 5925 [arXiv:0907.1396].

* Work supported by Frankfurt Institute for Advanced Studies

† V.Skokov@gsi.de

Ratio Fluctuations in Nucleus-Nucleus Collisions from Microscopic Transport Approach*

E. L. Bratkovskaya[1], M. I. Gorenstein[2,3], M. Hauer[4], and V. P. Konchakovski[1,4]

[1]Institut für Theoretische Physik, JWG Universität Frankfurt, Germany; [2]Frankfurt Institute for Advanced Studies, University of Frankfurt, Germany; [3]Bogolyubov Institute for Theoretical Physics, Kiev, Ukraine; [4]Helmholtz Research School, University of Frankfurt, Germany

Event-by-event fluctuations of the kaon-to-pion [1, 3, 4] as well as kaon-to-proton and proton-to-pion [2, 3, 4] number ratio in nucleus-nucleus collisions are studied within the statistical hadron-resonance gas model (SM) for different statistical ensembles and in the Hadron-String-Dynamics (HSD) transport approach. Substantial differences in the HSD and SM results are found for the fluctuations and correlations of the particle numbers.

It has been found that the HSD model can qualitatively reproduce the measured excitation function for the K/π ratio fluctuations in central Au+Au (or Pb+Pb) collisions from low SPS up to top RHIC energies (Fig. 1, top). Accounting for the experimental acceptance as well as the centrality selection has a small influence on $\sigma^{K\pi}_{dyn}$ and does not change the shape of the $\sigma^{K\pi}_{dyn}$ excitation function.

Thus, the HSD hadron-string model - which does not have a QGP phase transition and not explicitly includes the quark and gluon degrees of freedom - can reproduce qualitatively the experimental excitation function. In particular, it gives the rise of $\sigma^{K\pi}_{dyn}$ with lowering the bombarding energy. This fact brings to the conclusion that the observable $\sigma^{K\pi}_{dyn}$ might dominantly signal of nonequilibrium string dynamics rather than a phase transition of hadronic to partonic matter or to the QCD critical point.

The data for σ^{Kp}_{dyn} in Pb+Pb collisions at the SPS energies will be available soon and allow for further insight. A comparison of the HSD results with preliminary STAR data in Au+Au collisions at RHIC energies are not fully conclusive: σ_{dyn} from the HSD calculations is approximately in agreement with data for the K/p ratio (Fig. 1, middle), but overestimates the experimental results for the p/π ratio (Fig. 1, bottom). New data on event-by-event fluctuations in Au+Au at RHIC energies will help to clarify the situation.

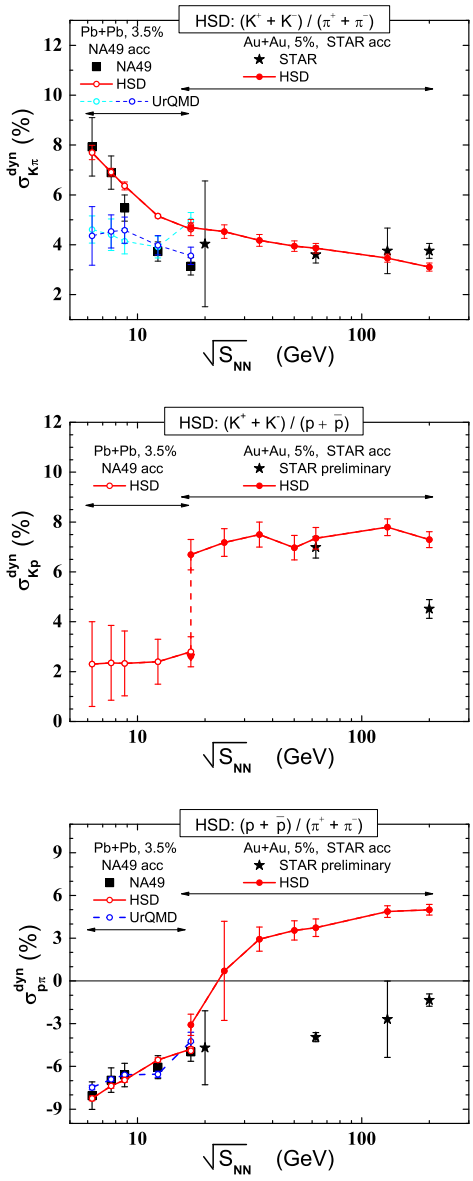

Figure 1: The HSD results for the excitation function in σ_{dyn} for the K/π, K/p, p/π ratios within the experimental acceptance (solid line) in comparison to the experimental data measured by the NA49 Collaboration at SPS and by the STAR Collaboration at RHIC. The UrQMD calculations are shown by dotted lines.

References

[1] M. I. Gorenstein, M. Hauer, V. P. Konchakovski and E. L. Bratkovskaya, Phys. Rev. C **79** (2009) 024907.

[2] V. P. Konchakovski, M. Hauer, M. I. Gorenstein and E. L. Bratkovskaya, J. Phys. G **36** (2009) 125106.

[3] V. P. Konchakovski, M. I. Gorenstein, E. L. Bratkovskaya and W. Greiner, to be printed in J. Phys. G, arXiv:1001.3085.

[4] V. P. Konchakovski, M. Hauer, M. I. Gorenstein and E. L. Bratkovskaya, arXiv:0912.5157 [nucl-th].

*Work supported by the Helmholtz International Center for FAIR within the the LOEWE program launched by the State of Hesse.

Dileptons and charm as probes of the strongly interacting quark-gluon plasma (sQGP) within the parton-hadron-string dynamics (PHSD) transport*

O. Linnyk†[1], E. L. Bratkovskaya[1], and W. Cassing[2]

[1]Frankfurt Institute for Advanced Studies, Frankfurt am Main, Germany; [2]Institut für Theoretische Physik, Universität Giessen, Giessen, Germany

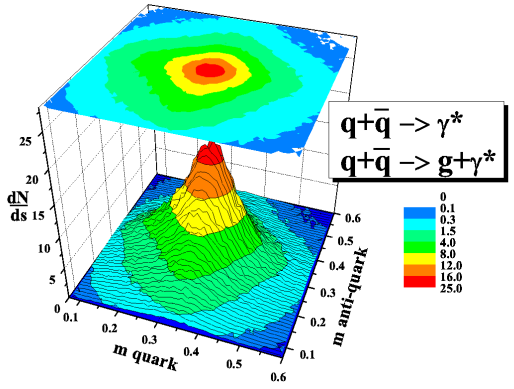

Figure 1: Multiplicity of $q+\bar{q}$ events as a function of quark virtualities.

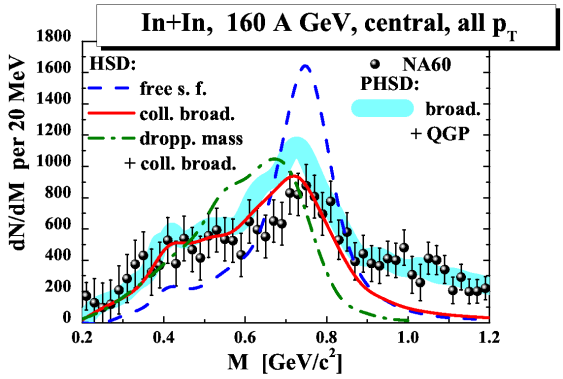

Figure 2: Spectra of dileptons at SPS energy.

Our ultimate goal is understanding the dynamical properties of the partonic phase with quarks, antiquarks and gluons as dynamical degrees of freedom (strongly interacting QGP) and the phase transition to an interacting hadronic system. During 2009 we focused on studying how the QGP phase transition influences the charm and dilepton production. The charm quark degrees of freedom are of particular importance since they are expected to be dominantly produced in the early, QGP state of the heavy ion collisions. The dileptons are well suited for an investigation of the violent phases of a high-energy heavy-ion collision, because they can leave the reaction volume essentially undistorted by final-state interactions. As 'research tools' we are using effective field theory based on the high temperature QCD and the microscopic Parton-Hadron-String-Dynamics [1] (PHSD) transport approach.

Dilepton radiation by the quasiparticles proceeds via the following elementary processes: $q+\bar{q} \to \gamma^*$, $q(\bar{q})+g \to \gamma^* + q(\bar{q})$, and $q+\bar{q} \to g+\gamma^*$. Note that in our calculations the running coupling α_S (which depends on the local energy density according to a parametrization of lQCD data) is of the order $O(1)$ and thus the contribution of the higher order diagrams is not subleading! Also, in order to make a quantitative comparison to experimental data at the realistically low photon virtuality $M \sim 1$ GeV, we have taken into account the non-perturbative spectral functions and self-energies of quarks and gluons thus going beyond the leading twist (cf. Fig.1).

In Fig. 2 we present PHSD results for the dilepton spectrum as produced in $In+In$ reactions at 158 AGeV compared to the data of the NA60 Collaboration [2]. We find that the spectrum at invariant masses below 1 GeV is well reproduced by the ρ meson yield, if a broadening of the meson spectral function in the medium is assumed. On the other hand, the spectrum at $M > 1$ GeV is shown to be dominated by the partonic sources.

At RHIC and LHC energies the radiation from QGP is expected to constitute a large contribution to the dilepton spectrum. On the other hand, at lower energies one probes the physics of the nuclear matter at extremely high baryonic densities as will be produced at the future experimental facility FAIR. The FAIR facility will allow the study of charm hadron production closer to the threshold for charm production in pp reactions so that in-medium effects might have a strong influence on the open and hidden charm production. The dilepton production at FAIR energies will reflect the properties of hadrons in the dense nuclear medium.

References

[1] W. Cassing and E. L. Bratkovskaya, *Phys. Rev.* C **78** (2008) 034919, *Nucl. Phys.* A **831** (2009) 215.

[2] S. Damjanovic *et al.*, *Nucl. Phys.* **A 783** (2007) 327c.

[3] O. Linnyk, E.L. Bratkovskaya, W. Cassing, J. Phys. G **36** (2009) 064059.

[4] E.L. Bratkovskaya, W. Cassing, O. Linnyk, Phys. Lett. B **670** (2009) 428.

[5] O. Linnyk, E. L. Bratkovskaya and W. Cassing, Nucl. Phys. A **830**, 491C (2009).

*Work supported through the "HIC for FAIR" framework of the "LOEWE" program.

† linnyk@fias.uni-frankfurt.de

In-Medium Properties of Vector Mesons in Elementary Nuclear Reactions*

J. Weil[†1] and U. Mosel[1]

[1]Institut für Theoretische Physik, JLU Giessen, Germany

While the vacuum properties of most hadrons are known to reasonable accuracy today, it is a much-debated question how these properties change in nuclear matter. In particular for the light vector mesons there have been various theoretical predictions regarding their in-medium properties.

One of the expected in-medium effects is the so-called 'collisinal broadening' of the meson spectral function, due to inleastic collisions with the hadronic medium. A second class of predictions claim that the vector meson masses will be shifted in the medium [1]. These changes of the peak mass are connected to the partial restoration of chiral symmetry in the medium and have been studied via QCD sum rules [2]. This effect has been claimed to be seen in experiments, but is still being discussed controversially.

For studying in-medium effects, the more promiment hadronic decay modes of the vector mesons suffer from the drawback that they are affected by strong final-state interaction with the hadronic medium – in contrast to the rare dilepton decay modes, which only feel the electromagnetic force. Therefore they are ideally suited to carry the in-medium information outside to the detector, undisturbed by the hadronic medium.

Although dilepton production has first been studied in heavy-ion collisions, we concentrate on elementary nuclear reactions in our work (γA, pA and πA). These have a number of advantages, in particular they involve a more sharply defined density and are simply much cleaner. This makes it easier to interpret the resulting spectra and to disentangle the various contributing channels.

Experimentally, dilepton spectra from elementary nuclear reactions are being studied e.g. with the CLAS detector at JLAB, where Bremsstrahlung photons in the energy range of about 1-3 GeV are shot on nuclei [3], or by the E325 experiment at the Japanese KEK facility, where 12 GeV protons are used as projectile [4]. Also the HADES detector at GSI has an ambitious program for measuring dilepton spectra from AA, pA and pp reactions [5]. On the side of the hadronic decays, most notably $\omega \rightarrow \pi^0\gamma$ is being investigated by the CB/TAPS group in photon-induced reactions at the ELSA accelerator [6].

For the numerical simulation of these processes we use the GiBUU transport model, which provides a unified framework for various types of elementary reactions on nuclei as well as heavy-ion collisions [7, 8, 9]. This model takes care of the correct transport-theoretical description of the hadronic degrees of freedom in nuclear reactions and all the subtleties this may involve, including the propagation, collisions and decays of particles in a nuclear environment. For the investigation of in-medium properties of vector mesons, the most crucial parts of the transport model are: 1) The production mechanisms of vector mesons on nuclei, e.g. $\gamma N \rightarrow VX$ or $NN \rightarrow VX$. 2) The description of the VN interaction, which is responsible for absorption and collisional broadening. 3) A proper off-shell treatment in the propagation of vector mesons and the handling of density-dependent spectral functions. 4) A correct description of the background processes (Dalitz decays, Bremsstrahlung, etc).

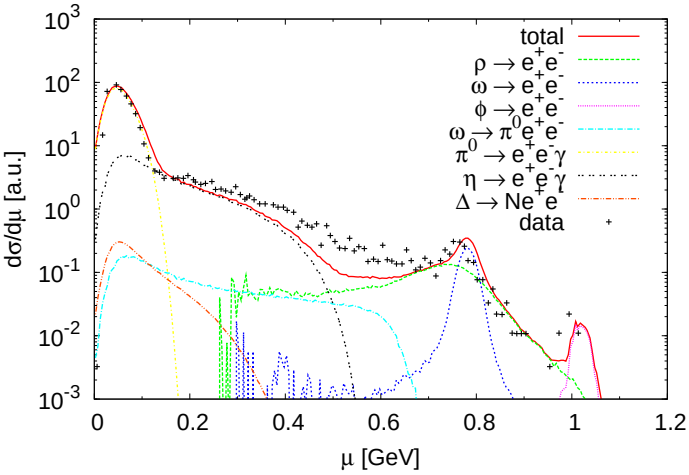

Figure 1: Dilepton spectrum for p+p@3.5GeV.

Fig. 1 shows a preliminary comparison plot of a GiBUU simulation to HADES data. The simulation results have not been corrected for the full HADES acceptance yet. Only simple kinematical cuts have been applied. Still the simulation reasonably reproduces the shape of the data over most of the spectrum, apart from a slight underestimation in the intermediate region (possibly due to the missing bremsstrahlung contribution).

References

[1] G.E. Brown, M. Rho, Phys. Rev. Lett. 66 (1991) 2720.

[2] T. Hatsuda, S.H. Lee, Phys. Rev. C 46 (1992) R34.

[3] M.H. Wood et al., Phys. Rev. C 78 (2008) 015201.

[4] M. Naruki et al., Phys. Rev. Lett. 96 (2006) 092301.

[5] I. Fröhlich et al., Int.J.Mod.Phys.A24 (2009) 317-326.

[6] M. Kotulla et al., Phys. Rev. Lett. 100 (2008) 192302.

[7] http://gibuu.physik.uni-giessen.de

[8] M. Effenberger et al., Phys. Rev. C 60(1999) 044614.

[9] P. Mühlich, U. Mosel, Nucl. Phys. A 773 (2006) 156-172.

* Work supported by DFG.

† janus.weil@theo.physik.uni-giessen.de

Pion induced coherent strangeness production*

S. Bender† [1], H. Lenske[1,2], and R. Shyam[3]

[1]Institut für Theoretische Physik, Universität Gießen, Germany; [2]GSI, Darmstadt, Germany; [3]Saha Institute of Nuclear Physics, Kolkata, India

We investigated pion induced coherent strangeness production on light (^{12}C) and medium-heavy (^{40}Ca, ^{51}V, ^{89}Y) nuclei with a covariant model. This model was based on a Lagrangian approach, where resonance excitation and decay is the driving mechanism behind the elementary process. The aim of this work was to apply this model, which was already successfully applied to strangeness production on nuclei in proton [1, 2] and photon [3] induced reactions, to pion-nucleus reactions.

Since the Λ is not subject to Pauli blocking with respect to the other nucleons, it provides an excellent probe for the interplay of single-particle and many-body degrees of freedom in nuclei. They are, therefore, a suitable choice when it comes to verify our models of these bound states and for doing spectroscopy.

The theoretical description, however, gets rather involved since one is dealing with interacting many-body systems and approximations are necessary when dealing with them. Most of the theoretical models used so far to describe the (π^+, K^+) reaction employ a non-relativistic distorted wave impulse approximation (DWIA) framework [4, 5] without resolving the production vertex. In these calculations, the Λ bound states are generated by solving the Schrödinger equation with Woods–Saxon or harmonic oscillator potentials. However, for processes involving momentum transfers of typically $300\,\mathrm{MeV/c}$ or more, a non-relativistic treatment of the corresponding wave functions may not be adequate as in this region the lower component of the Dirac spinor is no longer negligible in comparison to its upper component.

In our work [6, 7], we studied the $\mathrm{A}(\pi^+, K^+)_\Lambda\mathrm{A}$ reaction within a fully covariant model by retaining the field theoretical structure of the interaction vertices and by treating the baryons as Dirac particles. In this model, the kaon production proceeds via the collision of the projectile pion with one of the target nucleons. This excites intermediate baryon resonance states (N^*) which decay into a kaon and a Λ hyperon. The hyperon is captured in the respective nuclear orbit while the kaon rescatters onto its mass shell. The intermediate resonance states included are $N^*(1650)[\frac{1}{2}^-]$, $N^*(1710)[\frac{1}{2}^+]$, and $N^*(1720)[\frac{3}{2}^+]$ which have dominant branching ratios for the decay to the $K^+\Lambda$ channel. Terms corresponding to the interference among various resonance excitations are included in the total reaction amplitude.

We find that excitations of $N^*(1650)$, and $N^*(1710)$ resonant states dominate the cross sections for the (π^+, K^+) reaction for beam energies below $2\,\mathrm{GeV}$. Our model describes well the shapes of the experimental angular distributions [8] for the two states which corresponds to the prominent peaks in the $^{12}_{\Lambda}$C spectrum. The total cross sections show a substantial dependence on the beam energy with a distinct peak around $1\,\mathrm{GeV}$ for reactions on both ^{12}C and ^{40}Ca targets. The differential cross sections peak near zero degrees for both light mass as well as heavier targets. Thus, measurements at forward angles and at beam energies around $1\,\mathrm{GeV}$ are expected to have high yields.

The characteristic bump structures reflecting the Λ major shell orbits as seen in the spectra of the $^{51}_{\Lambda}$V and $^{89}_{\Lambda}$Y hypernuclei (see figure 1 for $^{89}_{\Lambda}$Y) were reproduced reasonably well by our model [6, 7]. However, for a quantitative description of the spectra, more realistic calculations with configuration mixed Λ particle, neutron hole states are required. Mixing of the different parity states within a given particle-hole configuration may also be needed.

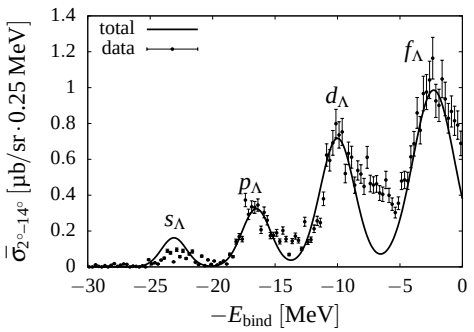

Figure 1: The excitation spectrum compared to experimental data for the $^{89}_{\Lambda}$Y hypernucleus.

References

[1] R. Shyam, H. Lenske and U. Mosel, Phys. Rev. **C69**, 065205 (2004), [arXiv:nucl-th/0308085].

[2] R. Shyam, H. Lenske and U. Mosel, Nucl. Phys. **A764**, 313 (2006), [arXiv:nucl-th/0505043].

[3] R. Shyam, H. Lenske and U. Mosel, Phys. Rev. **C77**, 052201 (2008), [arXiv:0710.4888].

[4] C. B. Dover, L. Ludeking and G. E. Walker, Phys. Rev. **C22**, 2073 (1980).

[5] H. Band$\bar{\mathrm{o}}$, T. Motoba and J. Žofka, Int. J. Mod. Phys. **A5**, 4021 (1990).

[6] S. Bender, *Pion induced coherent strangeness production on light and medium-heavy nuclei*, PhD thesis, Universität Gießen, 2009.

[7] S. Bender, R. Shyam and H. Lenske, arXiv:0910.4868.

[8] H. Hotchi *et al.*, Phys. Rev. **C64**, 044302 (2001).

* Work supported by EU, EURONS contract No. 506065.

† stefan.bender@theo.physik.uni-giessen.de

Charmonium in hot and dense medium from QCD sum rules*

Kenji Morita[1] and Su Houng Lee[2]
[1]GSI, Darmstadt, Germany; [2]IPAP, Yonsei university, Seoul, Korea

Heavy quarkonium such as J/ψ provides a probe of confinement-deconfinement transition in QCD [1, 2]. While in-medium modification of quark-antiquark potential and subsequent change of the bound state properties have been studied, we have developed a QCD sum rule approach to in-medium modification of the heavy quarkonia by utilizing temperature dependent gluon condensates [3, 4, 5]. So far analyses have been limited to pure gauge case of which lattice QCD results were used to extract gluon condensates. In this work, we first extend the framework to the full QCD case by modeling the gluon condensates of hadronic matter with a resonance gas. Then, we calculate the mass shift of J/ψ and χ_c and examine possible implication to experimental data in the context of the statistical hadronization.

The scalar and twist-2 gluon condensates, which are the lowest dimensional operators in the operator production expansion (OPE) of the heavy quark current correlator, are related to the gluonic part of the energy-momentum tensor of QCD as $G_0(T) = G_0^{\rm vac} - \frac{8}{11-\frac{2}{3}N_f} M_0(T)$ and $G_2(T) = -\frac{\alpha_s(T)}{\pi} M_2(T)$ where the M_0 and M_2 correspond to the gluonic part of the trace anomaly and symmetric and traceless part such that $M_0(T) = \varepsilon - 3p$ and $M_2(T) = \varepsilon + p$ in the pure gauge theory, respectively. One needs to subtract the quark contribution from the energy-momentum tensor to obtain the gluonic part. To carry out the subtraction, we model the gluonic part on the analogy with the case of low density nuclear matter in which the linear density approximation is used

$$M_0(T,\mu) = \sum_i \rho_i m_i^0 \quad (1)$$

$$M_2(T,\mu) = \sum_i \rho m_i A_G^i. \quad (2)$$

Here, ρ_i denotes the number density of a hadron species i with mass m_i calculated from a resonance gas model with excluded volume correction [6]. The subscript 0 in Eq. (1) means the chiral limit, which subtracts the fermionic contribution. The moment of the gluon distribution function A_G^i can be safely taken to be common value, 0.9. The excluded volume is determined by a fit to the equation of state and gluonic part of the trace anomaly measured in th latest lattice QCD [7]. The resultant gluon condensates are shown in Fig. 1.

The mass of chamonium is calculated with Borel transformed QCD sum rule as described in Ref. [8]. Possible brodening is also taken into account, but $\Gamma = 0$ is obtained in most cases after optimization. We explore various temperatures and chemical potentials inferred from statistical

* Work supported by Korean Ministry of Education

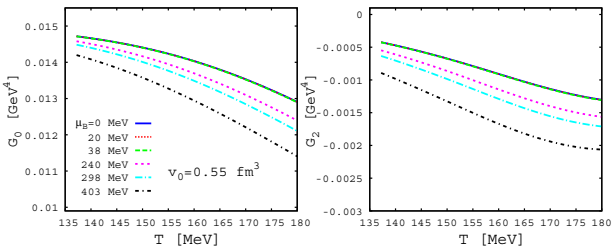

Figure 1: Gluon condensates at various chemical potentials

hadronization picture [9]. We find that the downward mass shift of J/ψ and χ_c is $-17 \sim -30$ MeV and $-40 \sim -70$ MeV in collisions with $\sqrt{s_{NN}} \geq 12$ GeV, respectively. We examine the effect of mass reduction in the statistical production of the charmonia as shown in Fig. 2. One sees the mass reduction results in notable changes in the particle ratio.

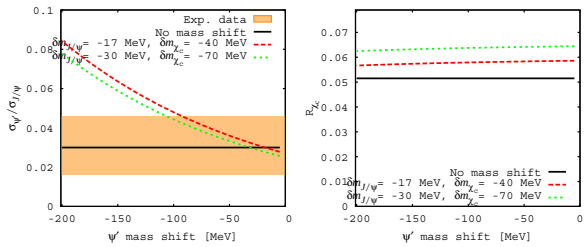

Figure 2: Particle number ratio as a function of ψ' mass shift. Left: N'_ψ/N_ψ, Right: fraction J/ψ coming from χ_c.

References

[1] T. Matsui, H. Satz, Phys. Lett. B 178 (1986) 416.

[2] T. Hashimoto, O. Miyamura, K. Hirose, T. Kanki, Phys. Rev. Lett. 57 (1986) 2123.

[3] K. Morita, S. H. Lee, Phys. Rev. Lett. 100 (2008) 022301.

[4] K. Morita, S. H. Lee, Phys. Rev. C 77 (2008) 064904.

[5] Y. Song, S. H. Lee, K. Morita, Phys. Rev. C 79 (2009) 014907.

[6] D. H. Rischke, M. I. Gorenstein, H. Stöcker, W. Greiner, Z. Phys. C 51 (1991) 485.

[7] A. Bazavov, et al., Phys. Rev. D 80 (2009) 014504.

[8] K. Morita, S. H. Lee. arXiv:0908.2856.

[9] A. Andronic, P. Braun-Munzinger, J. Stachel, Nucl. Phys. A772 (2006) 167.

Statistical hadronization of heavy flavor quarks in elementary collisions: successes and failures

A. Andronic[1], F. Beutler[6], P. Braun-Munzinger[1,2,3,4], K. Redlich[5,2], and J. Stachel[6]

[1]GSI Darmstadt, Germany; [2]ExtreMe Matter Institute, GSI Darmstadt, Germany; [3]Technical University Darmstadt, Germany; [4]FIAS, J.W Goethe University, Frankfurt, Germany; [5]University of Wrocław, Poland; [6]University of Heidelberg, Germany

We analyze recently compiled data on the production of open heavy flavor hadrons and quarkonia in e^+e^- as well as pp and p-nucleus collisions in terms of the statistical hadronization model [1].

In Fig. 1 we show a comparison of data and model prediction. for charmed and bottom hadron yields in e^+e^- annihilations at $\sqrt{s}$=91 GeV. For the model we have used the parameter set: T=170 MeV, V=16 fm^3 and γ_s=0.66, which represents the best fit of multiplicities of hadrons with lighter quarks [1].

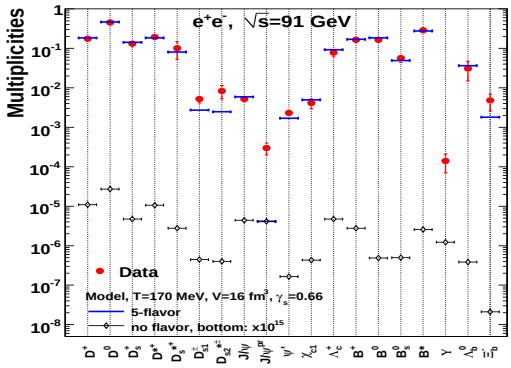

Figure 1: Multiplicities of hadrons with charm and bottom quarks in e^+e^- collisions compared to the thermal model calculations for two cases: i) the 5-flavor jet scheme (thick lines) and ii) no (net) flavor jet scheme (thin lines with diamonds). Note, for case ii) the factor 10^{15} used to scale the model calculations for bottom hadrons to fit in the plotting range.

The calculation employing the 5-flavor scheme is in very good agreement with the data. Despite this overall agreement, the exceptions are significant: the Υ meson yield is underpredicted by the model by 17 orders of magnitude, while the prompt J/ψ yield is underpredicted by almost 2 orders of magnitude. Obviously, the production of quarkonia is expected to be strongly suppressed in the statistical model. The disagreement is a consequence of the separate hadronization of the c and $\bar{c}$ quarks. The measured prompt J/ψ production in Z^0 decays (into hadrons) is about 3×10^{-4}. The thermal model predicts a prompt yield for J/ψ of 4.1×10^{-6} (1.6×10^{-7} for ψ' and 4.3×10^{-7} for χ_{c1}), identically for the two calculation schemes. Whenever the model seems to describe the yields of charmonia the measured yields are dominated by the feed down from bottom hadrons and the agreement only reflects the agreement seen for the open bottom hadrons and their branching ratios to charmonia, properly considered in the model.

The calculation employing a purely thermal ansatz underpredicts all the measurements by many oders of magnitude, while for the light quark sector the differences between calculations with a pure thermal model and with the 5-flavor quark-antiquark scheme were found to be small [1]. This reflects the fact that a negligible number of c and b quarks are formed in the fragmentation process.

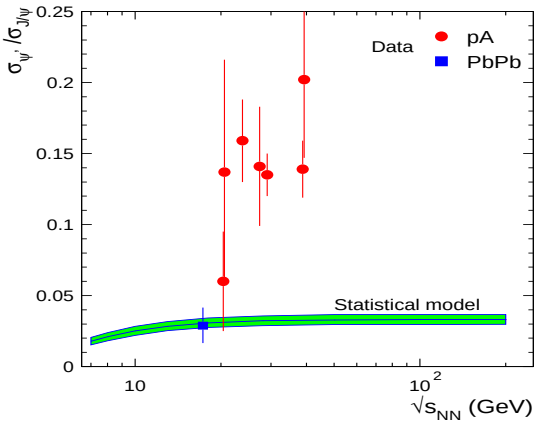

Figure 2: Production cross section of ψ' relative to J/ψ.

In Fig. 2 we show the model comparison to data for the relative production cross section of J/ψ and ψ' charmonia. The measurements in pA collisions are about a factor 4 above the model values. The relative production cross sections of charmonium states cannot be described in the thermal approach. This is in sharp contrast to the (only currently existing) measurement in central nucleus-nucleus collisions, performed at the SPS by the NA50 experiment, which is well described. We recall that it was in part the observation of this measurement that brought forward the idea of statistical production of charmed hadrons in nucleus-nucleus collisions [2]. We note that the pA data exhibit a constant $\psi'/J/\psi$ production ratio as a function of energy. In the model, the value is determined only by the temperature and this is reflected in the slight decrease of the ratio towards low energies. A constant value, also up to the LHC energies, is predicted beyond $\sqrt{s_{NN}} \simeq$20 GeV.

References

[1] A. Andronic, F. Beutler, P. Braun-Munzinger, K. Redlich, J. Stachel, Phys. Lett. B **675** (2009) 312 [arXiv:0804.4132], Phys. Lett. B **678** (2009) 350 [arXiv:0904.1368].

[2] P. Braun-Munzinger, J. Stachel, Phys. Lett. B **490** (2000) 196 [nucl-th/0007059].

The horn, the hadron mass spectrum and the QCD phase diagram

A. Andronic[1], P. Braun-Munzinger[1,2,3,4], and J. Stachel[5]

[1]GSI Darmstadt, Germany; [2]ExtreMe Matter Institute, GSI Darmstadt, Germany; [3]Technical University Darmstadt, Germany; [4]FIAS, J.W Goethe University, Frankfurt, Germany; [5]University of Heidelberg, Germany

The analysis of hadron yields measured in central heavy ion collisions from AGS up to RHIC energies has shown [2] that hadron multiplicities can be described very well with a hadro-chemical equilibrium approach which is governed by the chemical freeze-out temperature T, baryochemical potential μ_b, and the fireball volume V. The main result of these investigations was that the extracted temperature values rise rather sharply from low energies on towards $\sqrt{s_{NN}}$ $\simeq$10 GeV and reach afterwards constant values near T=160 MeV, while the baryochemical potential decreases smoothly as a function of energy. While in general all hadron yields are described rather quantitatively [2], a notable exception was up-to-now the energy dependence of the K^+/π^+ ratio which exhibits a rather marked maximum, "the horn" [3], near $\sqrt{s_{NN}} \simeq 10$ GeV [4].

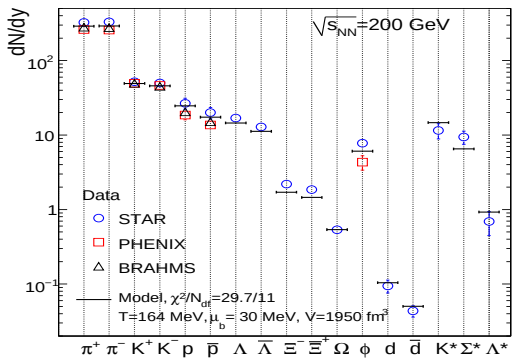

Figure 1: Experimental hadron yields and model fit at 200 GeV.

We have performed recently [1] a new analysis of hadron production in central nucleus-nucleus collisions, with the aim to explore the consequences of an improved hadronic mass spectrum in which the σ meson and many higher-lying resonances are included. An example of a fit to the data is shown in Fig. 1 for the energy of 200 GeV. The model is successful in reproducing the measurements and this applies to all energies, from 2 AGeV beam energy (fixed target) up to the top RHIC energy of $\sqrt{s_{NN}}$=200 GeV. The reduced χ^2 values are reasonable. In most cases the fit quality is improved compared to our earlier analysis [2], even though the experimental errors are now smaller. An important result of our analysis is that the resulting thermal parameters are close to those obtained earlier [2].

We employ parametrizations of T and μ_b to investigate the energy dependence of the relative production yields K^+/π^+ and Λ/π^-, shown in Fig. 2. The K^+/π^+ ratio shows a rather pronounced maximum at a beam energy

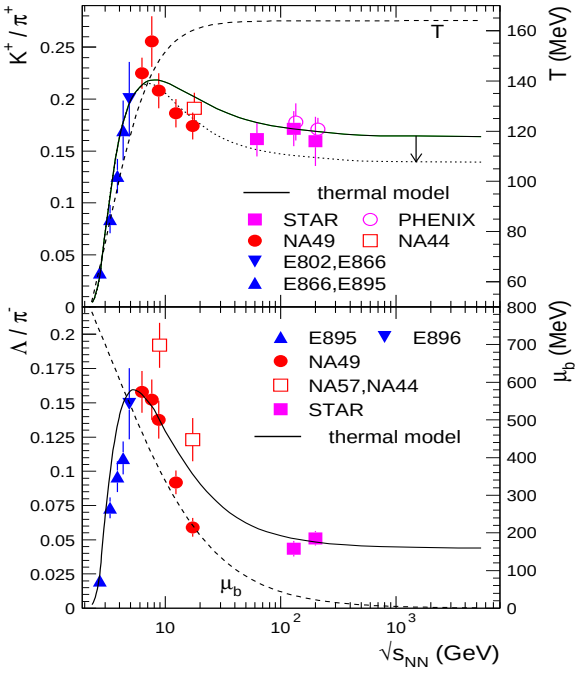

Figure 2: Energy dependence of the relative production ratios K^+/π^+ and Λ/π^-. The dashed lines show the energy dependence of T (upper panel) and μ_b (lower panel).

of 30 AGeV [4], and the data are well reproduced by the model calculations. In the thermal model this maximum occurs naturally at $\sqrt{s_{NN}}$ $\simeq$8 GeV [5]. It is due to the counteracting effects of the steep rise and saturation of T and the strong monotonous decrease in μ_b. The competing effects are most prominently reflected in the energy dependence of the Λ hyperon to pion ratio (lower panel of Fig. 2), which shows a pronounced maximum at $\sqrt{s_{NN}}$ $\simeq$5 GeV. This is reflected in the K^+/π^+ ratio somewhat less directly; it appears mainly as a consequence of strangeness neutrality, assumed in our calculations.

References

[1] A. Andronic, P. Braun-Munzinger, J. Stachel, Phys. Lett. B **673** (2009) 142 [arXiv:0812.1186], Erratum: ibid. B **678** (2009) 516; Acta Phys. Pol. **40** (2009) 1005 [arXiv:0901.2909].

[2] A. Andronic, P. Braun-Munzinger, J. Stachel, Nucl. Phys. A **772** (2006) 167.

[3] M. Gaździcki, M.I. Gorenstein, Acta Phys. Polon. B **30** (1999) 2705.

[4] C. Alt et al. (NA49), Phys. Rev.C **77** (2008) 024903.

[5] P. Braun-Munzinger, J. Cleymans, H. Oeschler, K. Redlich, Nucl. Phys. A **697** (2002) 902.

Equation of State for physical quark masses *

F. Karsch[1,2,7], M. Cheng[4], S. Ejiri[1], P. Hedge[1,6], O. Kaczmarek[7], E. Laermann[7], R. D. Mawhinney[6], C. Miao[1], S. Mukherjee[1], P. Petreczky[1,5], C. Schmidt[7], and W. Söldner[†3]

[1]BNL, Upton, NY 11973, USA; [2]Columbia University, New York, NY 10027, USA; [3]GSI, Darmstadt, Germany; [4]LLNL, Livermore, CA 94550, USA; [5]RIKEN-BNL Research Center, BNL, Upton, NY 11973, USA; [6]Stony Brook University, Stony Brook, NY 11790, USA; [7]Universität Bielefeld, D-33615 Bielefeld, Germany

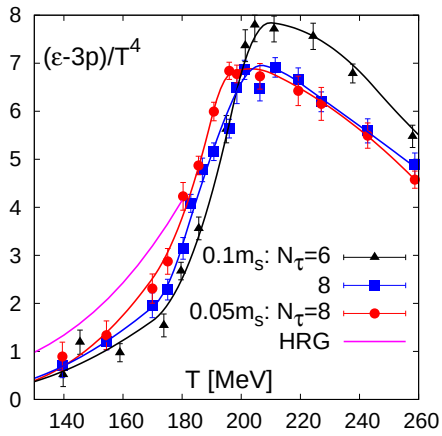

Figure 1: Trace anomaly $(\epsilon - 3p)/T^4$ calculated for physical quark mass and compared with previous calculations at larger light quark masses $m_l = 0.1m_s$ as well as with HRG model which includes all resonances up to 2.5GeV. Also shown are interpolations of the lattice data.

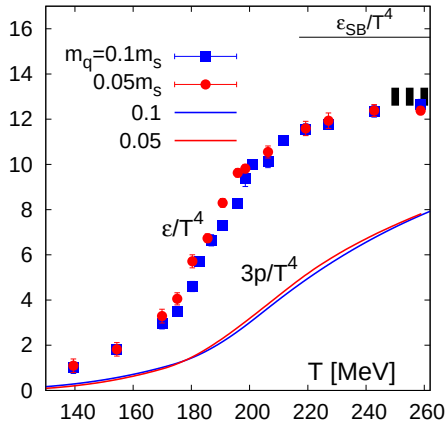

Figure 2: Energy density and three times the pressure at physical value of light quark mass and compared with previous calculations performed at $m_l = 0.1m_s$. The horizontal band shows the expected uncertainty in the energy density due to the choice of the lower integration limit.

We have calculated the QCD equation of state for temperatures corresponding to the transition region with physical mass values for two degenerate light quark flavors and a strange quark using an improved staggered fermion action (p4-action) on lattices with temporal extent $N_\tau = 8$, see Ref. [1]. We compare our results with previous calculations performed at twice larger values of the light quark masses as well as with results obtained from a resonance gas model calculation. We show that compared to the calculations performed at twice larger value of the light quark mass the transition region shifts by about 5MeV toward smaller temperatures, as can be seen in Fig. 1 where the shift below the transition region $T = 200$MeV is nicely visble. From the trace anomaly $(\epsilon - 3p)/T^4$ the energy density ε and the pressure p are calculated, see Fig. 2.

We have also calculated the renormalized Polyakov loop, subtracted chiral condensate and strangeness fluctuations in (2+1)-flavor QCD in the crossover region from low to high temperatures, see Ref. [1]. There, we also discuss the deconfining and chiral aspects of the QCD transition in more detail.

We found that thermodynamic quantities below the deconfinement transition are larger compared to the previous calculations performed at twice larger quark mass but fall below the resonance gas model result. The differences in the thermodynamic quantities calculated at $m_l = 0.05m_s$ and $m_l = 0.1m_s$ can be well understood in terms of the shift of the transition temperatures towards smaller values when the quark mass is decreased. This conclusion is also supported by the calculation of renormalized Polyakov loop, subtracted chiral condensate and strangeness fluctuations. No additional enhancement of the pressure and the energy density is seen at low temperatures. This and the deviation from the resonance gas model may be a cutoff effect due to taste violations. However, better statistical accuracy and calculations at smaller lattice spacing are needed to quantify this assertion. At temperatures above 200 MeV no quark mass dependence is seen in the equation of state.

References

[1] M. Cheng *et al.*, "Equation of State for physical quark masses," arXiv:0911.2215 [hep-lat].

* Work supported in part by contracts DE-AC02-98CH10886 and DE-FG02-92ER40699 with the U.S. DoE, BMBF under grant 06BI401, GSI under grant BILAER, EMMI under grant HA216/EMMI, and DFG under grant GRK 881. Numerical simulations have been performed on the QCDOC computer of the RIKEN-BNL research center, the DOE funded QCDOC at BNL, the apeNEXT at Bielefeld University and the BlueGene/L at the NY Center for Computational Sciences (NYCCS).

† soeldner@gsi.de

Lattice QCD with distributed GPUs

M. Bach[1,2], P. Bialas[5], O. Kaczmarek[3], F. Karsch[3], V. Lindenstruth[1,2], C. Schmidt[3], and W. Söldner[4]

[1]Frankfurt Institute for Advanced Studies, Germany; [2]Institut für Informatik, Frankfurt, Germany; [3]Universtität Bielefeld, Germany; [4]GSI, Darmstadt, Germany; [5]Jagellonian University, Krakow, Poland

Lattice QCD today is one of the big computational challenges. Amongst other subjects lattice QCD allows to study the quark gluon plasma in areas where perturbative methods fail.[2] The current algorithm of choice is the rational hybrid Monte Carlo.[1]

The Traditional Approach

Up till now Lattice QCD calculations are often performend on specialized hardware like the apeNEXT or extremely large systems like the BlueGene. These system are special, in that the single nodes are rather slow, but communication between the nodes is extremely efficient. However production of and access to this systems is expensive.

New Possibilities

In recent years multi and many core architectures have evolved, continuing an increase in single node compute power even though the race for higher clock speeds has come to a halt. Today such architectures are available in GPUs, providing an excellent ratio between arithmetical power and costs. Therefore GPUs provide an interesting platform for lattice QCD calculations.[3]

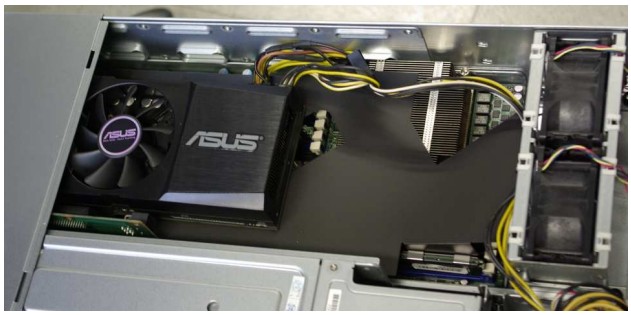

Figure 1: One of the development systems

Utilizing new Hardware

In a first step we have been able to implement a GPU based conjugate gradient solver for calculations with staggered fermions using NVIDIA CUDA. This solver is the most expensive step in Lattice QCD calculations. Our solver achieves a performance of $\approx$ 55 Gflops on one NVIDIA Tesla C1060 and $\approx$ 75 Gflops on a GTX285. A multi GPU version has been implemented which scales over multiple GPUs in a single system. This performance has only been possible by heavily optimizing the memory access patterns of the algorithm, which in its current implementation now saturates the memory bandwidth of the GPUs.

Challenges

With increasing arithmetical power of a single node the penalties of communication increasingly limit the overall performance of the algorithm. Therefore we are studying different methods in partitioning the problem and organizing the communication in ways to optimize overall algorithm performance. Key points to reach that goal are to minimize communication and parallelize communication and calculations as far as possible.

Applications and Outlook

Today the solver is used to calculate Taylor expansion coefficints of the pressure with respect to the chemical potential on a given gauge field configuration. The goal is to explore the QCD phase at nonzero baryon number density. Therefore work is ongoing in implementing a full rational hybrid monte carlo algorithm. This implementation is based on a full rational hybrid monte carlo code existing for the apeNEXT, but due to the different nature of the hardware major parts of it have to be rewritten to work efficiently.

References

[1] M. A. Clark and A. D. Kennedy, "The RHMC algorithm for 2 flavors of dynamical staggered fermions," Nucl. Phys. Proc. Suppl. **129** (2004) 850 [arXiv:hep-lat/0309084].

[2] M. Cheng *et al.*, "Equation of State for physical quark masses," [arXiv:0911.2215 [hep-lat]].

[3] M. A. Clark, "QCD on GPUs: cost effective supercomputing," PoS **LATTICE2009**, 003 (2009) [arXiv:0912.2268 [hep-lat]].

On the magnetic equation of state in (2+1)-flavor QCD*

F. Karsch[1,2,4], S. Ejiri[1], E. Laermann[4], C. Miao[1], S. Mukherjee[1], P. Petreczky[1,3], C. Schmidt[4], W. Söldner[† 2], and W. Unger[4]

[1]BNL, Upton, NY 11973, USA; [2]GSI, Darmstadt, Germany; [3]RIKEN-BNL Research Center, BNL, Upton, NY 11973, USA; [4]Universität Bielefeld, D-33615 Bielefeld, Germany

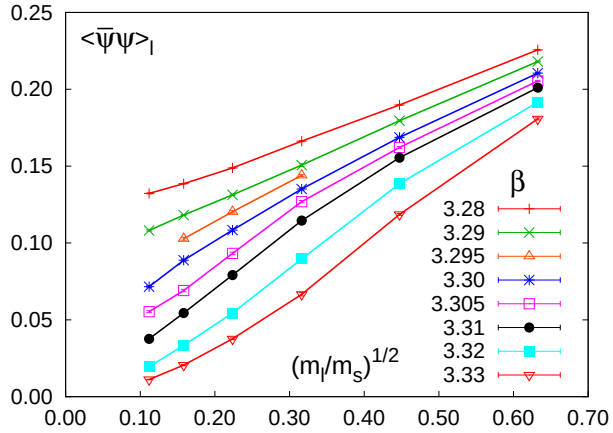

Figure 1: The light quark chiral condensate in lattice units versus the square root of the ratio of the light and strange quark masses. The condensates have been calculated on lattice of size $N_\sigma^3 \times 4$ at various values of the gauge couplings β. The spatial lattice size for the two lightest quark mass values, $m_l/m_s = 1/80$ and $1/40$, is $N_\sigma = 32$, for $m_l/m_s = 1/20$ it is $N_\sigma = 32$ for $\beta = 3.28$. In all other cases ($m_l/m_s = 1/10,\ 1/5$ and $2/5$) the spatial lattice size is $N_\sigma = 16$.

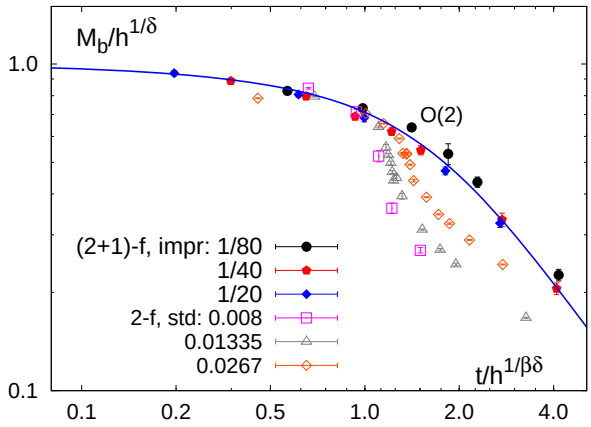

Figure 2: Scaling plot for the chiral condensate calculated with an improved staggered action in (2+1)-flavor QCD (this work) and the standard staggered action in 2-flavor QCD [2, 3]. The results are shown in a log-log plot. For the (2+1)-flavor data set labels indicate the ratio m_l/m_s, in the 2–flavor case we give the bare quark masses $\hat{m}$. Data for the lightest quark mass are from [2], data for the other two quark mass values are from [3].

A first study of critical behavior in the vicinity of the chiral phase transition of (2+1)-flavor QCD is presented [1]. We analyze the quark mass and volume dependence of the chiral condensate and chiral susceptibilities in QCD with two degenerate light quark masses and a strange quark. The strange quark mass (m_s) is chosen close to its physical value; the two degenerate light quark masses (m_l) are varied in a wide range $1/80 \leq m_l/m_s \leq 2/5$, where the smallest light quark mass value corresponds to a pseudoscalar Goldstone mass of about 75 MeV. All calculations are performed with staggered fermions on lattices with temporal extent $N_\tau = 4$. For an overview of the data see Fig.1.

We show that numerical results are consistent with $O(N)$ scaling in the chiral limit. We find that in the region of physical light quark mass values, $m_l/m_s \simeq 1/20$, the temperature and quark mass dependence of the chiral condensate is already dominated by universal properties of QCD that are encoded in the scaling function for the chiral order parameter, *the magnetic equation of state*. This is shown in Fig.2 where we also compare to $N_f = 2$ data from earlier studies [2, 3]. Within our new study it is now possible for the first time to show strong evidince for the characteristic $O(N)$ scaling behavior.

We also provide evidence for the influence of thermal fluctuations of Goldstone modes on the chiral condensate at finite temperature. At temperatures below, but close to the chiral phase transition at vanishing quark mass, this leads to a characteristic dependence of the light quark chiral condensate on the square root of the light quark mass, as can be seen in Fig.1.

* Work supported in part by contracts DE-AC02-98CH10886 with the U.S. DoE, BMBF under grant 06BI401, GSI under grant BILAER, EMMI under grant HA216/EMMI, and DFG under grant GRK 881. Numerical simulations have been performed on the BlueGene/L at the NY Center for Computational Sciences (NYCCS) which is supported by the U.S. DoE and by the State NY as well as the QCDOC computer of USQCD.

† soeldner@gsi.de

References

[1] S. Ejiri *et al.*, "On the magnetic equation of state in (2+1)-flavor QCD," Phys. Rev. D **80** (2009) 094505 [arXiv:0909.5122 [hep-lat]].

[2] C. W. Bernard *et al.*, "Critical behavior in N(t) = 4 staggered fermion thermodynamics," Phys. Rev. D **61**, 054503 (2000).

[3] M. D'Elia, A. Di Giacomo and C. Pica, "Two flavor QCD and confinement," Phys. Rev. D **72**, 114510 (2005).

The Functional Renormalization Group and $O(4)$ scaling*

B. Stokić[1], B. Friman[1], and K. Redlich[2,3]

[1]GSI, Darmstadt, Germany; [2]ITP, University of Wroclaw, Poland; [3]IKP, TU Darmstadt, Germany

In this work [1] we use the FRG method in the quark–meson model to explore the universal properties of the chiral phase transition. We go beyond previous RG studies of this model and analyze the critical region in the broken and in the symmetric phase close to the critical point and discuss the scaling functions for different physical quantities as well as the magnetic equation of state [2]. In this report we only show a few illustrative examples.

The FRG equation for the effective action reads [3]

$$\partial_k \Gamma_k[\Phi,\psi] = \frac{1}{2}\mathrm{Tr}\left\{\partial_k R_{kB}\left(\Gamma^{(2)}_{kB}[\Phi,\psi]+R_{kB}\right)^{-1}\right\} - \mathrm{Tr}\left\{\partial_k R_{kF}\left(\Gamma^{(2)}_{kF}[\Phi,\psi]+R_{kF}\right)^{-1}\right\}, \quad (1)$$

where $\Gamma^{(2)}_{kB}$ and $\Gamma^{(2)}_{kF}$ denote the second functional derivatives of the effective action $\Gamma_k[\Phi,\psi]$ with respect to the field variables. The fields Φ and ψ in Eq. (1) denote bosonic and fermionic fields, respectively.

In order to exhibit the scaling behavior of the susceptibilities for a non-vanishing explicit symmetry breaking term $h \neq 0$, we introduce the ratios

$$R^h_{\chi_{\pi,\sigma}} = \frac{t}{\chi_{\pi,\sigma}}\frac{\partial \chi_{\pi,\sigma}}{\partial t} \quad (2)$$

for the transverse χ_π and the longitudinal χ_σ susceptibilities. These ratios define the effective critical exponents [4].

In the top figure we show the t and h dependence of the $R^h_{\chi_\pi}$ and $R^h_{\chi_\sigma}$ in the vicinity to the critical point. In the symmetric phase, χ_π and χ_σ coincide and their critical behavior is determined by the critical exponent γ.The transition between the two regimes takes place at $z \equiv th^{-1/\beta\delta} \simeq 1$. In the broken phase, the critical exponents differ, $R^h_{\chi_\sigma} \simeq \beta(1-\delta/2)$ and $R^h_{\chi_\pi} \simeq \beta$, in complete agreement arguments based on the Widom-Griffiths form of the magnetic equation of state.

The critical exponent δ may be determined in an elegant way, by exploiting the scaling properties of the susceptibilities [5] χ_π and χ_σ. Consider the ratio

$$\Delta(t,h) = \frac{\chi_\pi^{-1}}{\chi_\sigma^{-1}} = \frac{h}{\langle\tilde{\sigma}\rangle}\frac{\partial\langle\tilde{\sigma}\rangle}{\partial h}, \quad (3)$$

which has the useful property that its value at $t = 0$ is independent of h within the scaling region. Indeed, one easily finds

$$\lim_{h\to 0}\Delta(t,h) = \begin{cases} 1, & t>0, \\ 1/\delta, & t=0, \\ 0, & t<0. \end{cases} \quad (4)$$

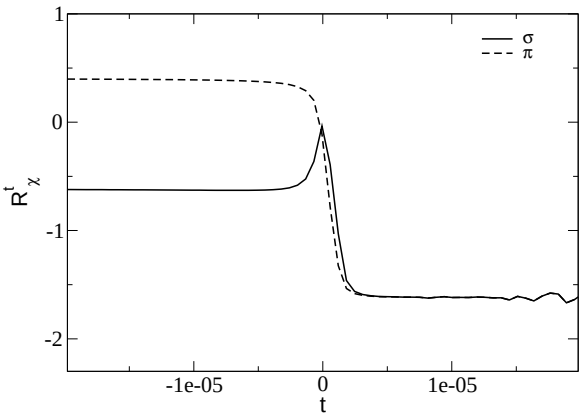

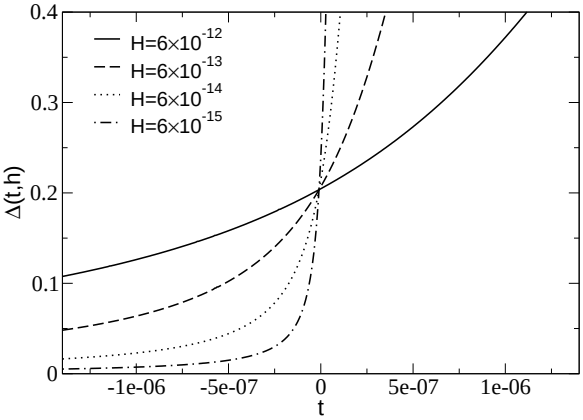

Consequently, the ratio $\Delta(t,h)$ can be used to directly extract the value of the critical exponent δ, without resorting to logarithmic fits. Moreover, this ratio simultaneously reveals the position of the critical point, since in the scaling regime, all $\Delta(t,h)$, plotted as functions of t for different h, cross at $t = 0$, as shown in the bottom figure.

References

[1] B. Stokić, B. Friman and K. Redlich, arXiv:0904.0466

[2] A. Onuki, *Phase transition dynamics* (Cambridge University Press, Cambridge, 2002)

[3] C. Wetterich, Phys. Lett. B**301**, 90 (1993).

[4] E. K. Riedel and F. J. Wegner, Phys. Rev. B**9**, 924 (1974).

[5] G. Boyd, J. Fingberg, F. Karsch, L. Kärkkäinen and B. Petersson, Nucl. Phys. B**376**, 199 (1992).

*Work supported in part by the Polish Ministry of Science, by DFG under the Mercator Programme. and by the Helmholtz Research School on Quark Matter Studies.

Isentropes near critical end point in QCD phase diagram

E. Nakano[1,2], B.-J. Schaefer[3], B. Stokic[2], B. Friman[2], and K. Redlich[2,4]

[1]EMMI; [2]GSI, Darmstadt, Germany; [3]Karl-Franzens-Universität, Graz, Austria; [4]Univ. of Wroclaw, Wroclaw, Poland

In recent decades relativistic heavy ion collision experiments have been attracted much interest. They aim at detecting quark-gluon plasma (QGP) phase, and at investigating phase structures, static and dynamical properties of QCD. Along with the experiment also theoretical studies have been done to understand physics behind data accumulated. Our present work is concerning boundaries of the chiral phase transition and its critical end point (CEP). The latter is a terminal point of the first order chiral phase transition from low temperature and high density side in T-μ phase diagram. The transition changes to crossover on the other side to the CEP. The CEP is theoretically expected from many variants of QCD effective theories, and also recently from Lattice QCD.

We have studied isentropes (contours of constant entropy S over baryon number N ratio) in QCD phase diagram, with special emphasis on those around the CEP. In the nuclear-nuclear collision experiments the net baryon number participating is fixed in the whole process, while the total entropy to be produced depends on the collision energy. The most of the entropy production would be completed in the early stage of collision, and late time evolution of the system, a fire ball expanding and cooling from QGP to hadronic phase, can be well described by ideal hydrodynamics (implying vanishing viscosities, thus no further entropy production). In the T-μ plane of the QCD phase diagram, therefore, each isentropic contour with a specific constant value of S/N corresponds to a hydrodynamic evolution of each event in relativistic heavy ion collision experiment. Since the hydrodynamic evolution describes the system across the phase boundaries, the isentropic behavior provides some clues to finding experimental signature of phase boundary and the CEP.

Recently an interesting feature of the isentropes in the QCD phase diagram had been reported in the literature [1]: the critical fluctuation implies a focusing of the isentropes toward the CEP. It means that a bunch of contours in a wide area on the crossover side focus on the CEP (the focusing effect). This is conjectured in a model system composed of a bag model on the hadronic side and a quark-gluon gas on the QGP side, which are interpolated by the 3d Ising model scaling function for the CEP. Some implications for the experiment have been reported on the basis of the focusing effect. One of our motivation is to examine if such effect really can be expected in a more rigorous way.

To this end we employ the functional renormalization group (FRG) approach to evaluate the thermodynamic potential from which entropy and baryon number ratio S/N can be derived. The beauty of the FRG is that one can systematically integrate out higher momentum contributions to the partition function, and derive a low energy effective potential by solving so-called flow equation. The FRG provides a general non-perturbative framework, and the resulting effective potential includes all effects of fluctuations beyond the mean-field approximation. We have applied the FRG to an effective model of QCD, the quark-meson model, which belongs to the same universality class of the CEP. Hence this model is capable of describing critical behavior such as isentropes near the CEP correctly with the FRG.

Here we only show our result of isentropes in the figure [2]: the solid point indicates the location of the CEP, and the contours show isentropes with different numerical values for S/N. Dashed and solid lines are from different methods to solve the flow equation. As seen from the figure isentropic contours look very smooth, and do not in any way reflect the proximity of the CEP. The conjectured focusing effect toward the CEP is not observed.

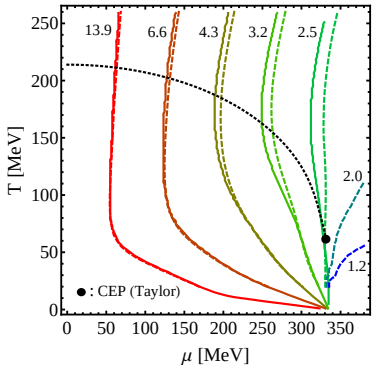

Our result can be understood in the following way: near the CEP the thermodynamic potential F can be decomposed into two parts, model dependent regular part F_r and universal scaling part F_s. F_s is responsible for singularities of thermodynamic properties, e.g., the divergence of specific heat, obtained by higher derivatives of F than 2nd order. S and N of our interest are 1st derivatives, therefore, they do not possess any singularities. Contributions to S/N from F_s become subdominant compared to those from F_r as the CEP is approached. Thus we conclude that any peculiar behavior of the isentropes, such as the focusing effect, is very unlikely.

References

[1] C. Nonaka and M. Asakawa, Phys. Rev. C71 (2005) 044904; M. Bluhm and B. Kämpfer, PoS CPOD2006 (2006) 004.

[2] E. Nakano, B.-J. Schaefer, B. Stokic, B. Friman, and K. Redlich, Phys. Lett. B682 (2010) 401.

Microscopic description of the phase transition from hadronic to partonic matter and dynamics of hadronization *

E. L. Bratkovskaya[1], W. Cassing[2], and O. Linnyk[1]
[1]Univ. of Frankfurt, Germany; [2]Univ. of Giessen, Germany

The nature of confinement and the dynamics of the phase transition from hadronic to partonic mattre is an outstanding question of todays physics. The dynamics of partons, hadrons and strings in relativistic nucleus-nucleus collisions is analyzed within the novel Parton-Hadron-String Dynamics (PHSD) transport approach, which is based on a dynamical quasiparticle model for partons (DQPM) matched to reproduce recent lattice-QCD results - including the partonic equation of state - in thermodynamic equilibrium. Scalar- and vector-interaction densities are extracted from the DQPM as well as effective scalar- and vector-mean fields for the partons. The transition from partonic to hadronic degrees of freedom is described by covariant transition rates for the fusion of quark-antiquark pairs or three quarks (antiquarks), respectively, obeying flavor current-conservation, color neutrality as well as energy-momentum conservation. Since the dynamical quarks and antiquarks become very massive close to the phase transition, the formed resonant 'pre-hadronic' color-dipole states ($q\bar{q}$ or qqq) are of high invariant mass, too, and sequentially decay to the groundstate meson and baryon octets increasing the total entropy.

The PHSD approach is applied to nucleus-nucleus collisions from 20 to 160 A·GeV in order to explore the space-time regions of 'partonic matter'. We find that even central collisions at the top-SPS energy of 158 A· GeV show a large fraction of non-partonic, i.e. hadronic or string-like matter, which can be viewed as a hadronic corona (cf. Fig. 1). Studying in detail Pb+Pb reactions from 40 to 158 A·GeV - we observe that the partonic phase has a very low impact on rapidity distributions of hadrons but a sizeable influence on the transverse mass distribution of final kaons due to the repulsive partonic mean fields. Furthermore, we find a significant effect on the production of multi-strange antibaryons (Fig. 2) due to a slightly enhanced $s\bar{s}$ pair production in the partonic phase from massive time-like gluon decay and a larger formation of antibaryons in the hadronization process.

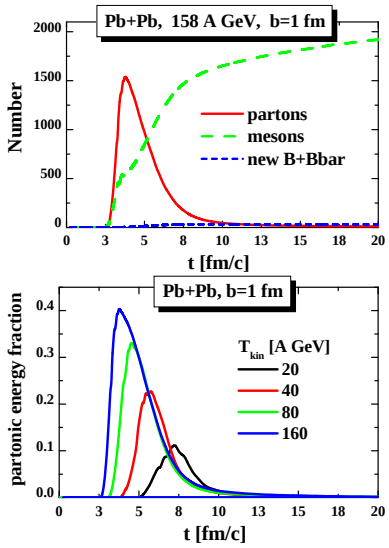

Figure 1: Top: The number of produced partons, mesons and newly produced baryon + antibaryons as a function of time for Pb+Pb at 158 A·GeV (for b=1fm). Bottom: The partonic energy fraction as a function of time for impact parameter b = 1 fm for Pb+Pb at 160, 80, 40 and 20 A·GeV.

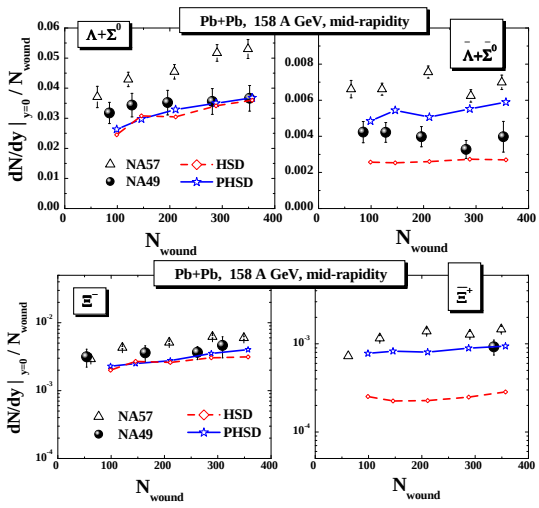

Figure 2: Top: The multiplicities of $(\Lambda + \Sigma^0)/N_{wound}$ (l.h.s.) and $(\bar{\Lambda} + \bar{\Sigma}^0)/N_{wound}$ (r.h.s.) as a function of the number of wounded nucleons for Pb+Pb collisions at 158 A·GeV at mid-rapidity from PHSD and HSD in comparison to the experimental data from the NA57 and NA49 Collaborations. Bottom: The multiplicities of Ξ^-/N_{wound} (l.h.s.) and $\bar{\Xi}^+/N_{wound}$ (r.h.s.) vs N_{wound} for Pb+Pb collisions at 158 A·GeV at mid-rapidity.

References

[1] W. Cassing and E.L. Bratkovskaya, Nucl. Phys. **A831** (2009) 215.

[2] W. Cassing and E.L. Bratkovskaya, Phys. Rev. **C 78** (2008) 034919.

[3] W. Cassing, E.L. Bratkovskaya, Y.-.Z. Xing, Prog. Part. Nucl. Phys. **62** (2009) 359-364.

*Work supported by the Helmholtz International Center for FAIR within the the LOEWE program launched by the State of Hesse.

Polyakov–Nambu–Jona-Lasinio Models and QCD Phase Diagram *

T. Hell, M. Cristoforetti, B. Klein, and W. Weise
Physik-Department, TU München, D-85747 Garching, Germany

Strongly interacting matter under extreme conditions is a topic of continuing interest, both from the point of view of ultrarelativistic heavy-ion collisions and lattice QCD. In our work we use approaches based on the time-honored Nambu–Jona-Lasinio model in order to investigate the nature of the different phases of QCD matter at finite temperatures and densities. From hadron spectroscopy it is well-known that the chiral symmetry of the QCD Lagrangian is spontaneously broken, manifested in mass gaps between, e. g., the vector and pseudovector mesons. When dealing with two light up- and down quarks ($m_u \approx m_d \sim \mathcal{O}(10\,\mathrm{MeV})$ plus one heavy strange quark ($m_s \sim \mathcal{O}(100\,\mathrm{MeV})$ one has to additionally include the anomalous breaking of the axial $\mathrm{U}(1)$ symmetry. This last point is particularly important in order to describe the mass splitting between the eta- and the eta-prime meson. The NJL model and a nonlocal version of it, both used in our work, can account for this symmetry breaking pattern.

The thermodynamical description of NJL type models does not inlcude the important feature of confinement. This can be introduced by implementing the Polyakov loop $\langle\Phi\rangle$ as the proper order parameter for the confinement-deconfinement transition. The resulting models are of the Polyakov-loop extendend NJL (PNJL) type [1, 2, 3]. Finite temperature and finite density phenomena are described by standard means of thermal field theory.

The nonlocal approach leads the phase diagram shown in Fig. 1. It shows the low-density behavior expected from lattice QCD calculations: namely a crossover region that terminates at a critical point located at $T_{\mathrm{CEP}} \approx 170\,\mathrm{MeV}$ and $\mu_{\mathrm{CEP}} \approx 180\,\mathrm{MeV}$ which marks the endpoint of the following first order transition line. From our investigations of the phase diagram we conclude that the location of the critical point is sensitive to the strength of the axial-$\mathrm{U}(1)$ breaking.

A better understanding of the mechanism at the origin of these transitions requires the investigation of fluctuations beyond mean field in the PNJL model. By performing numerical simulations of the thermodynamics using standard Monte-Carlo techniques we can perform this improvement [4]. The relevance of fluctuations on the thermodynamics is particularly evident looking at the flavor non-diagonal second derivative of the thermodynamic grand canonical partition function with respect to quark chemical potentials. The PNJL mean field calculation predicts a vanishing coefficient, whereas fluctuations (primarily of pionic origin) are at the origin of a non-zero value of this flavor off-diagonal susceptibility, χ_{ud}. In Fig. 2 the good agreement between lattice data and the Monte-Carlo calculation (MC-PNJL) clearly shows the role of such fluctuations in the model.

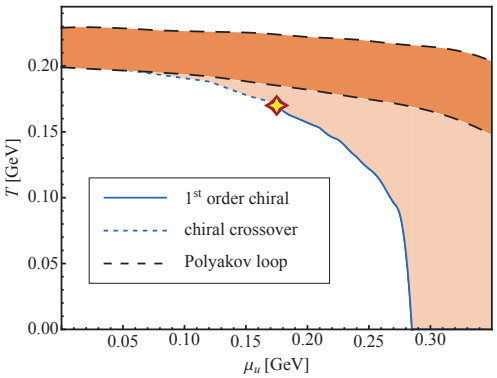

Figure 1: Phase diagram for $N_{\mathrm{f}} = 3$ flavors calculated using the nonlocal PNJL model [1, 2]. The solid line shows the first-order chiral transition (the star denotes the critical end point). The dotted line marks the (chiral) crossover transition while the dashed lines correspond to the deconfinement transition region.

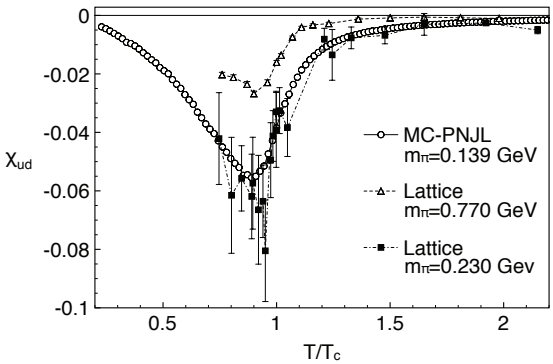

Figure 2: Temperature dependence of the second order flavor off-diagonal susceptibility in the Monte-Carlo approach to the PNJL model [4] in comparison with two-flavor lattice data.

References

[1] T. Hell, S. Rößner, M. Cristoforetti and W. Weise, arXiv:0911.3510 [hep-ph] (2009).

[2] T. Hell, S. Rößner, M. Cristoforetti and W. Weise, Phys. Rev. **D79**, 014022 (2009).

[3] S. Rößner, T. Hell, C. Ratti and W. Weise, Nucl. Phys. **A814**, 118 (2008).

[4] M. Cristoforetti, T. Hell, B. Klein and W. Weise, in preparation.

* Work supported in part by GSI, BMBF, and by the DFG Excellence Cluster "Origin and Structure of the Universe".

Nuclear energy density functional from chiral pion-nucleon dynamics

N. Kaiser and W. Weise
Physik-Department, TU München, D-85747 Garching, Germany

The nuclear energy density functional is the many-body method of choice in order to calculate the properties of medium-mass and heavy nuclei in a systematic manner. Parameterized (non-relativistic) Skyrme functionals as well as relativistic mean-field models have been used widely and successfully for such nuclear structure calculations. A complementary approach based on chiral effective field theory attempts to constrain the form of the nuclear energy density functional by many-body perturbation theory and the underlying two- and three-nucleon interactions. In particular, the long- and medium-range 1π- and 2π-exchange dynamics should be included and its role for nuclear many-body systems should to be explored systematically.

A tool for constructing an explicit (and numerically tractable) nuclear energy density functional is the density matrix-expansion. It removes the non-local character of Fock contributions by mapping them onto a generalized Skyrme functional with density dependent couplings. Recently, Gebremariam, Duguet and Bogner [1] have developed via phase-space averaging techniques an improved density-matrix expansion for spin-unsaturated nuclei:

$$\sum_\alpha \Psi_\alpha(\vec r-\vec a/2)\Psi^\dagger_\alpha(\vec r+\vec a/2) = \frac{3\rho}{ak_f}\, j_1(ak_f) - \frac{a}{2k_f}\, j_1(ak_f)\Big[\tau - \frac{3}{5}\rho k_f^2 - \frac{1}{4}\vec\nabla^2\rho\Big] + \frac{3i}{2ak_f}\, j_1(ak_f)\, \vec\sigma\cdot(\vec a\times\vec J)\,, \qquad (1)$$

with $j_1(ak_f)$ a spherical Bessel function. Here, $\rho(\vec r\,) = 2k_f^3(\vec r\,)/3\pi^2$ denotes the nuclear density and $\vec J(\vec r\,)$ is the so-called spin-orbit density. The Fourier transform of eq.(1) to momentum space defines a "medium insertion" which allows to calculate the nuclear energy density functional:

$$\mathcal{E}[\rho,\tau,\vec J] = \rho\,\bar E(\rho) + \Big[\tau - \frac{3}{5}\rho k_f^2\Big]\Big[\frac{1}{2M} + F_\tau(\rho)\Big] + (\vec\nabla\rho)^2\, F_\nabla(\rho) + \vec\nabla\rho\cdot\vec J\, F_{so}(\rho) + \vec J^{\,2}\, F_J(\rho)\,, \qquad (2)$$

in a diagrammatic way. Our calculation [2] treats all effects from 1π-exchange, iterated 1π-exchange, and irreducible 2π-exchange with intermediate Δ-isobar excitations, including Pauli-blocking corrections up to three-loop order.

Fig. 1 shows the strength $F_\nabla(\rho)$ of the surface-term $(\vec\nabla\rho)^2$. The dashed line corresponds to the truncation to 1π- and iterated 1π-exchange, whereas the full line includes in addition the 2π-exchange and the associated three-body contributions. Taking the band spanned by phenomenological Skyrme forces as a benchmark one can conclude that chiral pion-nucleon dynamics reproduces well the strength of the surface-term in the density region $\rho_0/2 < \rho < \rho_0 = 0.16\,\mathrm{fm}^{-3}$ mainly relevant for nuclei.

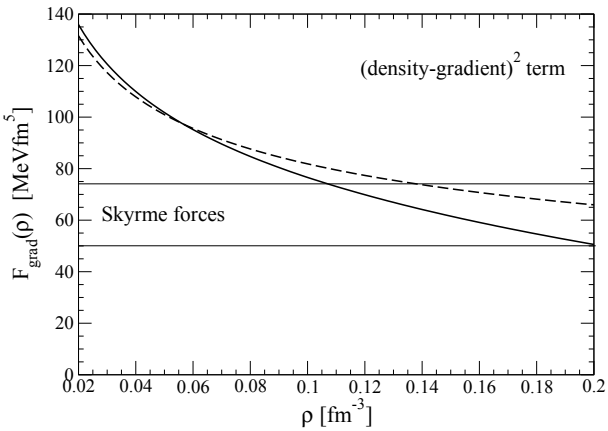

Figure 1: Strength $F_\nabla(\rho)$ of the surface-term $(\vec\nabla\rho)^2$.

The strength $F_{so}(\rho)$ of the spin-orbit coupling term $\vec\nabla\rho\cdot\vec J$ (see Fig.2) receives contributions from iterated 1π-exchange (of the "wrong sign") and from three-nucleon interactions mediated by 2π-exchange with virtual Δ-excitation (of the "correct sign"). In the region around $\rho_0/2 \simeq 0.08\,\mathrm{fm}^{-3}$ where the spin-orbit interaction in nuclei gains most of its weight these two components tend to cancel, thus leaving room for the short-range nuclear spin-orbit interaction. The latter is represented either by contact-terms or by Lorentz scalar and vector mean-fields.

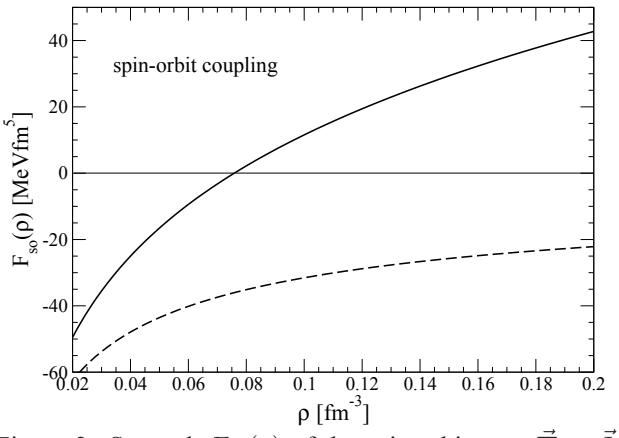

Figure 2: Strength $F_{so}(\rho)$ of the spin-orbit term $\vec\nabla\rho\cdot\vec J$. Dashed curve: iterated 1π-exchange. Full curve: including three-body contributions mediated by 2π-exchange.

References

[1] B. Gebremariam, T. Duguet, S. Bogner, nucl-th/0910.4979.

[2] N. Kaiser and W. Weise, nucl-th/0912.3207; Nucl. Phys. A (2010) in print; and references therein.

Structure of the rho meson and the pion form-factor

S. Leupold[1]
[1]Institut für Theoretische Physik, Universität Giessen, Germany

From the electromagnetic form factor of the pion and from the decay modes of the τ lepton involving two or three pions one can see that the isovector–vector quark current couples strongly to the ρ meson whereas the isovector–axial-vector current couples strongly to the a_1. Therefore such reactions provide excellent access to studies of the properties of (axial-)vector mesons. It has been shown recently [1] that the τ decay data, where the a_1 meson shows up as a bump in the three-pion spectral information, can be well understood by the assumption that initially a ρ-π pair is produced which dynamically generates a resonant state in its rescattering process. In the following it is demonstrated with the same method that the ρ *cannot* be understood as a dynamically generated state of π-π scattering. In other words, while the a_1 meson seems to have a hadronic substructure, the ρ meson appears to be dominantly a quark-antiquark state. For further details and references see [2].

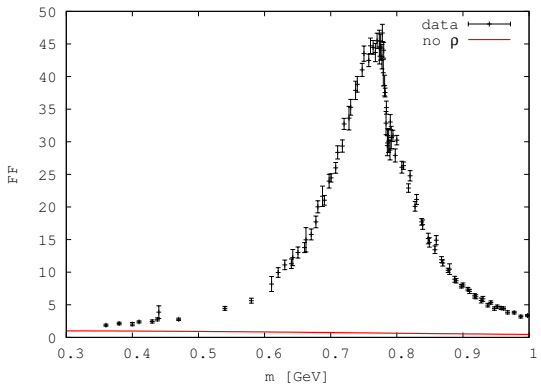

Figure 1: Pion form-factor without an elementary vector meson.

The (time-like) form factor of the pion can be deduced from the reaction $e^+e^- \to \pi^+\pi^-$. This reaction is described within a Bethe-Salpeter approach which allows for the rescattering of the pions. For the construction of the scattering kernels the very same logic as in [1] is applied: If there is an elementary resonance in the kinematical region of interest the corresponding s-channel diagram is included in the kernel. All other interactions are smooth functions of the center-of-mass energy $m = \sqrt{s}$. These non-resonant interactions are approximated by the respective lowest-order terms of chiral perturbation theory. It is an important aspect that these interactions are fixed model-independently. Two scenarios are studied: One without and one with an elementary vector meson. In both cases the pion-pion and pion-photon interactions from lowest-order chiral perturbation theory are taken into account. As a consequence, in the first scenario the production of pions happens only directly from the virtual photon which couples to the pion charge. In this scenario the pions rescatter by the point-like interaction of the non-linear sigma model. There are essentially no free parameters in this case once the renormalization of the appearing loops is settled. The result is shown in figure 1. Obviously this scenario is not compatible with the data; the final-state interaction between the pions is not sufficient to provide enough binding for the appearance of a dynamically generated resonance. This is different from the axial-vector channel where the lowest-order chiral interaction is strong enough to generate the a_1. For the second scenario, where an elementary resonance is included, there are additional processes where the photon can transform into the elementary ρ meson which only then couples to the pions and/or where the pions rescatter via the formation of a ρ meson. In this scenario there are naturally free (resonance) parameters: the mass of the vector meson and its couplings to the photon and to two pions. These ingredients are sufficient to explain the data for the form factor of the pion as can be seen from figure 2.

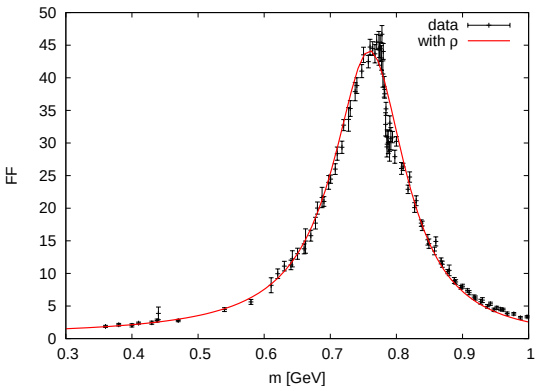

Figure 2: Pion form-factor including in the kernels an elementary vector-meson resonance.

The presented work is of high relevance for the physics at FAIR: Tools to distinguish between dynamically generated and preformed states are of utmost importance to identify and analyze exotic states at $\bar{\text{P}}$ANDA. In addition, the understanding of vector-meson properties is a key ingredient to explore the in-medium changes of hadrons which could be observed with HADES and CBM.

References

[1] M. Wagner and S. Leupold, Phys. Rev. D **78** (2008) 053001, Phys. Lett. B **670** (2008) 22.

[2] S. Leupold, Phys. Rev. D **80** (2009) 114012 .

A New Approach to the Gluon Structure Function

D. Grünewald*[1], E.-M. Ilgenfritz†[2], and H.J. Pirner‡[3]

[1]Institut für Theoretische Physik, Heidelberg, Germany; [2]Institut für Physik, Berlin, Germany, and Institut für Theoretische Physik, Heidelberg, Germany; [3]Institut für Theoretische Physik, Heidelberg, Germany, and Max-Planck-Institut für Kernphysik, Heidelberg, Germany

In Euclidean lattice simulations, using the operator product expansion the lowest moments of the meson and nucleon structure functions have been evaluated. On the other side, Loop-loop correlation functions of tilted Wegner-Wilson loops can be related to the gluon distribution function of a color dipole which consists of a static quark and antiquark pair connected by a Schwinger string. In the work presented here we have used an alternative approach based on light cone dynamics with constituents moving along the light cone, as suggested by the picture of Feynman scaling. In the light cone approach the non-perturbative QCD vacuum structure is hard to achieve within the Fock representation of free fields acting on a trivial vacuum. Therefore, in recent papers [1, 2] we have developed a near-light-cone (nlc) approach in which we exploit the lattice formulation, benefitting from simplifications emerging in the light cone limit. In Ref. [2] we have used the variationally optimized ground state wave functional of Ref. [1] to determine the gluon distribution function of a color dipole. The present report gives a short review of the main results obtained in this approach.

The gluon structure function $g(x_B)$ is the probability that a gluon carries a fraction x_B of the longitudinal momentum of the fast moving hadronic target. In light cone coordinates, it is given by the Fourier transform of the matrix element of the two-point operator $G_{lc}(z^-, \vec{z}_\perp\,; 0, \vec{z}_\perp)$ of longitudinally separated gluon field strength operators $F^b_{-k}(0, \vec{z}_\perp)$ and $F^a_{-k}(z^-, \vec{z}_\perp)$ in a hadron state $|h(p_-, \vec{0}_\perp)\rangle$. The hadron $|h(p_-, \vec{0}_\perp)\rangle$ is centered in transversal configuration space at $\vec{b}_\perp = \vec{0}_\perp$ and carries a longitudinal momentum p_-. A Schwinger line in the adjoint representation, running along a light like path is inserted between the gluon field strength operators. The importance of the Schwinger lines along the light cone is demonstrated e.g. in the loop-loop correlation model where hadron-hadron scattering cross-sections are calculated from Wegner-Wilson loop correlation functions. The eikonal phases arising from the strings along the x^-- direction describe so–called "final state" interaction effects which distinguish structure functions from parton probabilities.

We are using near-light-cone coordinates which allow us to implement light front quantization as a limit of equal time quantization.

We impose the quark dynamics of the color dipole externally. Since the total hadron longitudinal momentum is given by the sum of the momenta of its constituents, the typical mean gluon momentum is taken from experiment. The gluon string momentum p^S_- results from the difference of hadron momentum and quark and the antiquark momenta. At the input scale $Q^2 \approx \pi^2/a_\perp^2 = 1.5\,\mathrm{GeV}^2$, we use the *MRST*-parameterization and assign a mean momentum fraction $p^S_- = 0.38\,p_-$ to the gluon system, i.e. we ascribe this momentum p^S_- to the gluons.

The n-link distribution function is given by the product of a splitting function $P_{n\to n-1}$ multiplying the gluon distribution function with $n-1$ links. The one-link distribution is calculable directly from the lattice. The theoretical gluon structure function for a $n = 4$ link dipole is compared with the *MRST* and the *CTEQ* gluon distribution function at $Q^2 = 1.5\,\mathrm{GeV}^2$ as functions of the gluon fractional momentum $x_B = p^g_-/p_-$. The first moment of the lattice gluon distribution function has been fixed in this calculation to the value $\langle x_B\rangle = 0.38$ at $Q^2 = 1.5\,\mathrm{GeV}^2$. We choose four links to be consistent with the size of a proton and the relation $\left\langle R^2_\perp\right\rangle = \frac{n\,a_\perp^2}{2}$ and a transversal lattice spacing of $a_\perp \approx 0.65$ fm. Within the systematic uncertainty, the lattice gluon distribution function agrees with the phenomenological *MRST*-gluon distribution function.

References

[1] D. Grünewald, E.-M. Ilgenfritz, E. V. Prokhvatilov, and H. J. Pirner, "Formulating Light Cone QCD on the Lattice", Phys. Rev. D 77 (2008) 014512.

[2] D. Grünewald, E.-M Ilgenfritz, and H. J. Pirner, "Gluon Structure Function of a Color Dipole in the Light-Cone Limit of Lattice QCD", [arXiv:0908.0715 [hep-th]].

* d.gruenewald@tphys.uni-heidelberg.de

† ilgenfri@physik.hu-berlin.de

‡ pir@tphys.uni-heidelberg.de

Non-Abelian vortex strings in QCD

E. Nakano[1], M. Eto[2], T. Matsuura[3], and M. Nitta[4]

[1]EMMI, GSI, Darmstadt, Germany; [2]RIKEN, Saitama, Japan; [3]ECT*, Trento, Italy; [4]Keio Univ., Kanagawa, Japan

Let us start with defining the Non-Abelian vortex to be discussed below, whose stability is guaranteed by non-trivial 1st homotopy class

$$\Pi_1[G/H] = Z \tag{1}$$

where Z is the additive group (in general not necessary to be Z), and we have supposed the symmetry of the system G breaks down to H. The 'non-Abelian' implies that the coset space G/H be more complex than usual $U(1)$ case. The vortex is a one-dimensionally extended object at spatial dimension $d > 2$, it therefore looks like a string, we call it non-Abelian vortex string (NAVS).

We have studied 'Semi-Local' NAVS under a spontaneous symmetry breaking within a general Ginzburg-Landau theory: $G = U(1)_{\rm B} \times SU(N)_{\rm color} \times SU(N)_{\rm flavor}$ down to $H = SU(N)_{\rm C+F} \times Z_N$. The case with $N = 3$ corresponds to Color-Flavor-Locked (CFL) phase of color superconductor in high density QCD. In this case the vortex string possesses properties of both local gauge color flux and the global baryon-number $U(1)_{\rm B}$ superfluid vortex. The most fundamental vortex solution is of the form of the order parameter Φ, in the cylindrical coordinate,

$$\Phi(r,\theta) = \{e^{i\theta} f(r), g(r), g(r)\} \tag{2}$$

where profile functions satisfy $f(0) = 0, g(0)' = 0$ and $f(\infty) = g(\infty) = \Phi_0$ with Φ_0 being the vacuum expectation value. The above vortex solution looks as if one vortex with $1/3$ tension is embedded only in the first component. This is because the Z_3 in the H provides warp points in the coset space $G/H = U(3)$, see the figure, which makes a segment from cross to cross be a non-trivial loop. Here the most interesting is that the advent

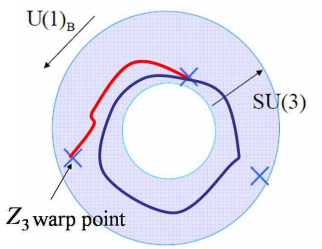

of the NAVS further breaks the symmetry: $H \to H' = SU(N-1) \times U(1)$, and thus there appears a Nambu-Goldstone mode, so-called 'orientation mode' associated with the coset space $H/H' \simeq \mathbf{C}P^{N-1}$. The orientation mode represents a vector like symmetry corresponding to degrees of freedom to assign the embedded vortex to a specific component in the multi-component order parameter.

We have evaluated the interaction between two 'Semi-Local' NAVS with arbitrary relative orientation (see the left in the figure) within the Abrikosov method, and found that the static force between two straight NAVS's is independent from the relative orientation at a long distance, and becomes an universal repulsion. This is due to the color gauge symmetry which can align the relative orientation at a longer distance over vortex core size. This result clearly shows that the usual $U(1)_B$ vortex string, which has been believed to appear in the CFL phase, is indeed unstable against the decay into $N(=3)$ semi-local NAVS's, see the right in the figure. Our previous works on the NAVS have

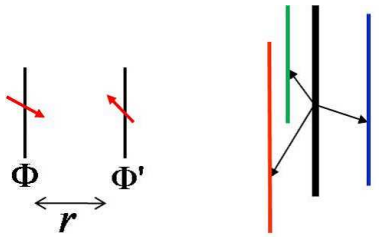

been applied to compact star physics for inner structure with quark matter core [1].

We have also constructed the low energy effective action for the orientation mode in $\mathbf{C}P^2$, and evaluated the Kähler class (this corresponds to the pion decay constant in chiral models) numerically in the background non-Abelian vortex solutions with various setups [2].

We have also studied the global NAVS associated with chiral symmetry breaking in a general Sigma model [3]: $G = SU(N)_{\rm L} \times SU(N)_{\rm R} \times U(1)_{\rm A}$ down to $H = SU(N)_{\rm L+R} \times Z_N$. The order parameter is transformed as $\Phi \to e^{i\alpha} U_L \Phi U_R^\dagger$. The vortex structure is very similar to the semi-local one discussed above, except that all the symmetries are global. We have evaluated the interaction between two NAVS's with arbitrary relative orientation in the similar manner to semi-local case, then found that the static force at a long distance does depend on the relative orientation as $\sim (1 + \cos\alpha)/r$ unlike the semi-local case: α is a relative angle between the two orientations, and the force vanishes when the orientation is opposite $\alpha = \pi$, while the most repulsive when the orientation aligns $\alpha = 0$. This feature provides important basis to determine the structure of multi-vortex-string systems, such as vortex lattice.

References

[1] D. M. Sedrakian, K. M. Shahabasyan, D. Blaschke and K. M. Shahabasyan, Astrophysics **51**, 544 (2008).

[2] M. Eto, E. Nakano, and M. Nitta, Phys. Rev. D80 (2009) 125011; Nucl. Phys. B821 (2009) 129.

[3] E. Nakano, M. Nitta, and T, Matsuura, Phys. Lett. B672 (2009) 61.

The GSI Mass Storage

H. Göringer, M. Feyerabend, S. Sedykh
GSI, Darmstadt, Germany

Overview

The GSI mass storage systems provide safe, reliable, and redundant long term storage of all user and experiment data. Fast and highly parallel access to the data is available 24 hours a day and 7 days a week.

Backup/Archive functionalities are provided with the commercial Tivoli Storage Manager (**TSM)**.

Experiment data storage is performed with **gStore,** the GSI made client server system. Design principles and functionality are described in more detail in several previous reports (e.g. [1]) and in a paper [2].

gStore Status and Enhancements

At the end of 2009 about 440 TB of experiment data were available with gStore. Thereof 330 TB were stored in the IBM 3592 Automatic Tape library (ATL). The remaining 110 TB are raw data copies. They are stored in a new IBM 3584-L23 ATL installed in 2009 in the BG2 building, some 100 m remote from the computing center. This prevents from loss of valuable raw data not only in case of media damage but also in case of a larger disaster in the computing centre.

Used and available storage capacities of gStore components and the high performance **lustre** data file system (see [3]) are summarized in table 1.

storage resource	used	max
IBM 3494 ATL	330 TB	1.6 PB
IBM 3584 ATL (raw data copy)	110 TB	160 TB
overall data mover disk cache	< 90%	50 TB
lustre disk cache	~80%	1.0 PB

Table 1: Status GSI Mass Storage December 2009

The overall I/O bandwidth amounts to 800 MB/s between data mover disk cache and tape, and up to 900 MB/s between disk cache and lustre or other user storage. In total 1.6 million files (390 TB) have been moved in 2009.

Backup Enhancements

The migration of backup/archive data from LTO tape media has been completed in 2009. All data are stored now on modern IBM 3592 tape media in the IBM 3494 ATL. The two older L700 StorageTek ATLs handling LTO1 tape media (capacity 70 TB) and LTO2 tape media (capacity 140 TB) are now out of operation.

We have started to store copies of all backup/archive data additionally in the remote 3584 ATL in BG2 for potential disaster recovery.

Online Migration of Experiment Data

During data taking by experiments the data from the event builders must be copied for long term storage as fast as possible to gStore write cache. In addition they must be available as soon as possible for monitoring. This is realized now by gStore utilizing the **lustre** file system available at GSI (see figure 1).

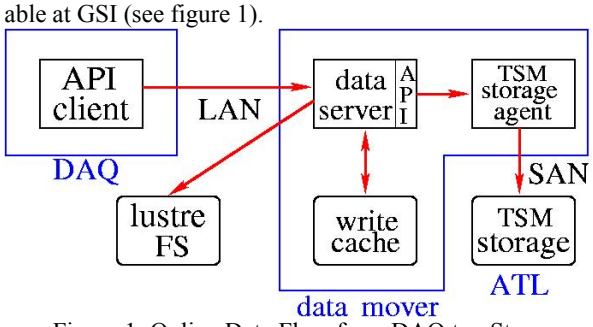

Figure 1: Online Data Flow from DAQ to gStore

For this purpose the gStore API client offers a new interface developed in close cooperation with the Hades DAQ group. It is available now in the Hades DAQ system (see [4]) and in MBS V6. The data buffers sent from the event builders to gStore data movers are written to gStore write cache **and** to lustre, either in parallel (buffers) or sequentially (files), depending on the selected operation mode. There are some more user options to control the data flow, e.g. the fraction of files to be copied to lustre, or the maximum number of files to be written to a lustre path before automatic creation of a new path.

Migration to tape takes place automatically after the copy to lustre is finished. In any case the first data buffers of a file are available in lustre for monitoring and online analysis very quickly.

The new functionalities have been tested successfully with several parallel test data streams from the Hades DAQ. The gStore hardware will be upgraded in the first half of 2010 to enable – in addition to the normal operation - the support of up to 10 parallel input data streams providing overall 250 MB/s over weeks. This will match the maximum capacity of the new Hades DAQ system which will be in operation at the next major Hades beam time expected in autumn 2010.

References

[1] H.Göringer et al: The GSI Mass Storage System, GSI Report 2009-1, p. 262

[2] Experiences with gStore, a scalable mass storage system with tape backend. J.Phys.: Conf. Ser. 119 Volume 119 (2008) 052018 (7pp)
see also: http://www-aix.gsi.de/computing/expdv/gStoreChep07JournalofPhysics.pdf

[3] W. Schön et al: High Performance Computing, this Report

[4] S. Yurevich et al: The Hades Event Building System, this Report

Grid Activities at GSI*

M. Al-Turany, M. Dahlinger, S. Daraszewicz, P. Malzacher, A. Manafov, A. Montiel Gonzalez, V. Penso, C. Preuss, K. Schwarz, F. Uhlig, and M. Zynovyev
GSI, Darmstadt, Germany

This article describes the work of the GSI Grid Group with the aim to enlarge and operate an ALICE tier2 centre within the global environment of the LHC Computing Grid and to prototype a possible FAIR grid environment.

ALICE tier2 centre

The deployment of the ALICE tier2 centre has been finished in time for the startup of the Large Hadron Collider at CERN. The focus of the work moved to operating and upgrading the new infrastructure.

The available disk space is distributed among an xroot[1] cluster (300 TB) and Lustre[1] (700 TB). The xroot cluster is configured as a Grid Storage element, while Lustre is used for local data storage.

The CPU has been increased up to 2400 cores corresponding to about 3300 KSI2K. Throughout the whole year GSI participated in all centrally managed ALICE production and data analysis activities. The overall job share of GSI and Forschungszentrum Karlsruhe has been 13% of all ALICE Grid jobs worldwide. The contribution of GSI, including local activities, comprises about 20% of the global ALICE Tier2 capacity.

By running local and Grid jobs, as well as interactive PoD sessions, the compute farm is well utilised all the time.

For PROOF[1] analysis a transition of the GSI Analysis Facility GSIAF[1] from a static cluster with xroot processes being tightly integrated into the system to PROOF on Demand (PoD[1]) has been done.

The whole infrastructure of the ALICE tier2 centre is monitored in detail by using MonaLisa[1].

Due to the LHC startup in autumn 2009 the ALICE tier2 centre met it's first "real data" challenge. The main tasks of a tier2 centre are Monte Carlo simulations and individual data analysis. Additionally, during the startup period alignment and calibration runs have been processed for the detector components TPC and TRD. The raw data have been transferred in real time to GSI, while the results had been made available via the central calibration data base on the Grid.

The EGEE project

GSI is participating in EGEE III as partner of the distributed Swiss German Regional Operations Centre (ROC) and the German Joint Research Unit (JRU). Within EGEE[1] the main tasks of GSI are to operate a functioning Grid site and to support users and applications from ALICE and FAIR. In this context GSI participated also courses in interactive data analysis in the GridKa School 2009[1] .

D-Grid

During this year the HEP Community Grid within the D-Grid project came to an end and the final report has been submitted. In work package 3 distributed analysis tools have been developed at GSI. Within this context the PoD utilities have been released.

Also significant amounts of compute resources have been bought from D-Grid fundings to enlarge the local cluster (storage and cpu). To be able to use the resources with D-Grid methods also after the end of the project the machines have been equipped with supported middleware including Globus Toolkit 4 and added to the D-Grid information system.

Preparation for FAIR tier0

PANDA-Grid[1] has been extended to 19 sites. In a third data challenge the full chain of simulation, digitization, reconstruction, and data analysis has been exercised. The jobs have been computed on 12 sites with GSI and Dubna being the largest contributors. Currently 3 universities from the Philippines are participating in PandaGrid. During an international Grid conference in Bohol/Philippines, the contact between Philippine and European Grid experts has been established.

The central Grid services for CBM have been set up at GSI. First small productions have been running successfully at GSI using the CBM Grid infrastructure.

The collaboration between ALICE and the FAIR experiments intensified significantly. Since the common software stack used by all experiments is quite large there have been many areas identified, especially in software development, where synergy effects are being experienced. Successful collaborative work has been shown in the development of the Virtual Monte Carlo (VMC)[1] interface, the development of the experiment frameworks AliRoot and FAIRRoot[1] as well as in the context of Grid computing. Recent success stories are the fact that the cmake based build system has been taken over by the AliRoot/ROOT team, the development of the AliEn[1] - Oracle interface as well as the prototyping of an inter VO[1] Grid interface.

* Work supported by BMBF - Förderkennzeichen 01AK802G (D-Grid), 06GSI0011I (ALICE-Tier2), and PHL08/001 (Integration philippinischer und südostasiatischer Rechenzentren in das FAIR-Projekt) - and European Commission - contract number INFOSO-RI-031688 (EGEE II) and INFSO-RI-222667 (EGEE III)

[1] a list of related links: http://wiki.gsi.de/cgi-bin/view/Grid/Links

PROOF on Demand*

P. Malzacher, A. Manafov, V. Penso, C. Preuss, and K. Schwarz
GSI, Darmstadt, Germany

The Parallel ROOT [1] Facility, PROOF [2], is an extension of ROOT enabling interactive analysis of large sets of ROOT files in parallel. PROOF on Demand, PoD [3], is a set of utilities, which allows starting a PROOF cluster at user request on any resource management system. Installation is simple and doesn't require administrator privileges, and all the processes run in user space. PoD gives users, who don't have a centrally-administrated static PROOF cluster at their institute, the possibility to enjoy the full power of interactive analysis with PROOF.

Overview

PoD is a set of utilities, scripts, and configuration files. It provides a possibility to set up a PROOF cluster dynamically on Grid and batch systems. It consists of the following main components:

- pod-agent, a lightweight, standalone C++ daemon. Responsible to control the cluster of PROOF workers and optionally acts as package forwarder when there is a firewall between server and workers. Also pod-agent has a number of additional useful features which help to start, to process, and to control a PROOF interactive analysis.
- pod-console, a standalone C++ application. It provides a GUI and aims to simplify the usage of pod-agent and PoD configuration files. It is a PoD management console.
- PoDWorker script, a generic job script, executed on remote machines.
- PoD utilities, these are default job scripts for plug-ins, a number of configuration files and helper utilities.

Use Case

The main use case of PoD is to set up a distributed PROOF cluster on the Grid and/or local resource management system. The first thing, a user has to do, is to start the server side processes on a central machine; in terms of PoD it is a user interface machine. The next step is to submit PoD jobs to worker nodes. As soon as a job arrives at a remote worker node, it automatically configures the environment and starts all needed client services including an xrootd worker and a pod-agent in client mode. In case the pod-console is used as session management tool, each new connection is immediately reflected in the GUI. When the instantiated PROOF workers of all submitted PoD jobs are connected, or when the user is satisfied with the number of connected worker processes, the PROOF analysis can be processed as if on a native PROOF cluster. The user then starts a ROOT session, e.g. on the private laptop, and connects to the PROOF master, registers the data, and runs the analysis script. Since PROOFAgent can manage disconnects, the user can also disconnect from ROOT, restart the ROOT session, and reconnect to the same PROOF cluster without having to resubmit the PoD jobs.

Summary

The main features of PoD:

- One click installation. The process of installation of PoD is fully automated and in user space.
- Easy to use. PoD provides a simple graphics user interface in order to simplify access to its functionality.
- It works out of the box. The PoD distribution contains everything users need to just immediately start using PoD right after the installation.
- Supports different job submission front-ends. Pod-console supports job manager plug-ins, therefore it is very easy to extend PoD to support different kinds of resources. PoD currently supports gLite [4] and LSF [5]. In future versions more plug-ins will be implemented, such as SSH [6] and PBS [7].
- PoD supports reconnections. This is an essential feature of PoD. Whatever happens with the ROOT/PROOF analysis sessions, even a crash, users don't need to resubmit PoD jobs. PoD will automatically refresh the environment and reconnect its workers.

References

[1] An Object Oriented Data Analysis Framework (ROOT) http://root.cern.ch
[2] The Parallel ROOT Facility (PROOF) http://root.cern.ch/drupal/content/proof
[3] PROOF on Demand (PoD) http://pod.gsi.de
[4] gLite http://glite.web.cern.ch/glite/
[5] Load Sharing Facility (LSF) http://www.platform.com/
[6] Secure Shell (SSH) http://www.openssh.com/
[7] Portable Batch System (PBS) http://www.pbsgridworks.com

* Work supported by BMBF - Förderkennzeichen 01AK802G (D-Grid),

FairRoot framework: GPUs for event reconstruction

M. Al-Turany[1] and F. Uhlig [1]
[1]GSI, Darmstadt, Germany

In the last few years, the graphics processor units (GPUs) have moved away from the traditional fixed-function 3D graphics pipeline toward a flexible general-purpose computational engine. Moreover they are getting cheaper and more powerful [1]. The GPU is especially well-suited to address problems that can be expressed as data-parallel computations i.e. the same program is executed on many data elements in parallel. Because the same program is executed for each data element, there is a lower requirement for sophisticated flow control; and because it is executed on many data elements and has high arithmetic intensity, the memory access latency can be hidden with calculations instead of big data caches

Hardware

In this work a Tesla c1060 card is used (240 cores at 1.3 GHz, 4 GBytes GDDR3 memory and PCIe x16 System Interface) [2] . This card was used inside a PC with 2.5 GHz Intel Xeon Quad-Core and 16 GB memory. The Tesla products are intended for the high performance computing, the main difference between Tesla products and ordinary video cards is the lack of ability to output images to a display. The primary function of Tesla products are to aid in large scale calculations for professional and scientific fields, with the use of CUDA.

Track fitting with CUDA

The track fitting was compared in four different modes: GPU Float: The algorithm is implemented for GPU in single precision accuracy. GPU Double: The algorithm is implemented for GPU in double precision accuracy. CPU : original algorithm. GPU Emulation: The GPU implementation runs on the CPU in GPU emulation mode. The results obtained from the different runs are summarized in table.1.

Mode/(Track/event)	50	100	1000	2000
GPU (Emu)	6.0	15.0	180	370
CPU	3.0	5.0	120	220
GPU (Double)	1.2	1.5	3.2	5.0
GPU (Float)	1.0	1.2	1.8	3.2

Table 1: Results: Time in ms needed to fit the corresponding number of tracks using the different algorithms and/or mode

The comparison between GPU and CPU time is summarized in figure 1. from this figure one can see that one can gain almost a factor 70 in this example. However using the

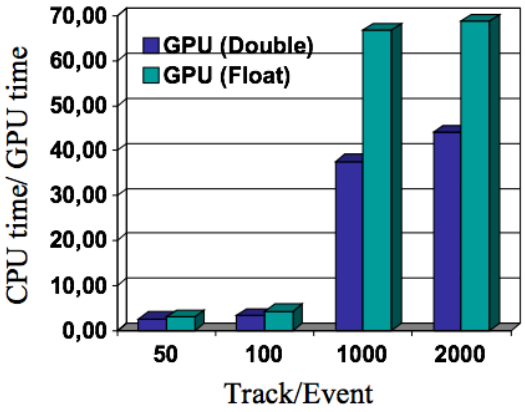

Figure 1: Ratio between time needed on CPU to the time needed by GPU for track fitting

"CUDA Occupancy Calculator" (i.e. a programmer tool that allows you to compute the multiprocessor occupancy of a GPU by a given CUDA kernel [3]) we found that in this example we are using only 25 % of the hardware, which explain the difference between double and float calculations. i.e. using the full capacity of the Tesla card one expect to have about a factor ten in performance between float and double (see Reference [2]).

Conclusion

In contrary to GPGPU, which usually means, writing software for a GPU in the language of the GPU CUDA permits working with familiar programming concepts while developing software that can run on a GPU, Moreover CUDA compile the code directly to the hardware (GPU assembly language, for instance), thereby providing great performance. Using GPUs for track fitting one can win orders of magnitudes in performance compared to the CPUs, however one has to determine how to divide the data into smaller chunks for distribution among the thread processors (GPUs)

References

[1] CUDA, Supercomputing for the Masses, http://www.ddj.com/hpc-high-performance-computing/

[2] Tesla C1060 Computing Processor, http://www.nvidia.com/object/product_tesla_c1060_us.html

[3] NVIDIA http://developer.nvidia.com/object/cuda.html

Status of the HLT-RORC and the Fast Cluster Finder*

T. Alt[1] and V. Lindenstruth[1]

[1]Frankfurt Institute of Advanced Studies, Goethe-Universität Frankfurt, Germany

The ALICE HLT-RORC is a FPGA based PCI-X card which receives the data via optical links from the ALICE detector and transfers it into the memory of the HLT computing farm. Furthermore the use of programmable logic allows to implement some of the detector specific analysis algorithms in hardware which gives a significant speedup in processing time. For the ALICE TPC the first step of the tracking, the Fast Cluster Finder, has been realized in the FPGA.

H-RORC

The HLT-Read Out Receiver Card (RORC) is a PCI-X card which receives the data from the detectors with dedicated optical interfaces (DIUs), formats and transmits it via DMA into the main memory of the hosting node. The card supports up to 2 DIU cards and provides 4 independent DMA channels. Two of the channels are used for the raw data, while the other two can be used for preprocessed data. The total maximum transfer rate is about 900 MByte/s. The framework inside the FPGA provides standardized interfaces for detector specific algorithms. In case of the ALICE TPC this algorithm is called Fast Cluster Finder, which is the first step in tracking. The Fast Cluster Finder is based on the software cluster finder.

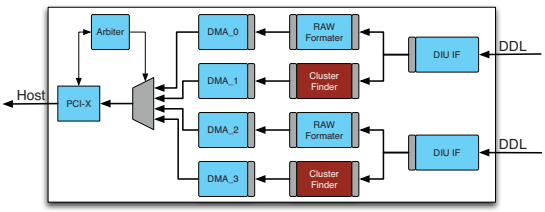

Figure 1: H-RORC FPGA Framework

Status of H-RORC

- 250 H-RORCs installed in the HLT
- Continuous operation since 2007
- All cards operate stable

Fast Cluster Finder

The Fast Cluster Finder is the first step in the tracking of the TPC. It calculates the center of gravity of the charge distribution generated by a traversing, charged particle in the TPC. The clusters are then used as seeds for the tracker.

* Work supported by BMBF.

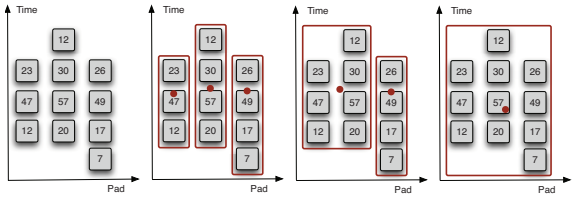

Figure 2: Example of clusterfinding for one cluster. First the cluster candidates are calculated (red dots) for each pad in time direction, then neighboring pads are searched for adjacent candidates, which are merged (red square)

Implementation of the algorithm

The algorithm consists of several modules (Fig.3) which process the raw TPC data. The channel extractor extracts the channels from the data stream and applies the gain calibration for each channel. The channel processor handles the single channels (pads) and calculates the cluster candidates in time direction. This information is passed to the channel merger which searches for matching candidates on adjacent channels and merges them into a cluster. For the found clusters the FP division unit calculates then the center of gravity in pad and time direction and the deviation.

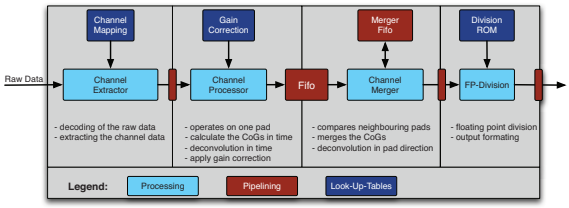

Figure 3: Block diagram of the Fast Cluster Finder

Status of the Fast Cluster Finder

- Algorithm fully implemented and integrated
- 216 Fast Cluster Finder for the ALICE TPC
- Tested and verified with generated and simulated data
- Benchmarking and testing with real data ongoing
- Processing time for 10 tracks in a TPC sector ∼65 us
- Processing time for 200 tracks in a TPC sector ∼750 us

Go4 Analysis Framework v4.4

J. Adamczewski-Musch[1], H.G. Essel[1], and S. Linev[1]
[1]GSI, Darmstadt, Germany

Overview

Go4 (**G**SI **O**bject **O**riented **O**nline **O**ffline) is established as standard GSI analysis framework for several experiments of atomic and nuclear structure physics, e.g. FRS, SHIP, TASCA, and RISING. Go4 is based on ROOT (root.cern.ch) and can be downloaded under GPL from the Go4 homepage go4.gsi.de. At GSI, Go4 is installed and maintained on the public linux cluster.

A new release Go4 v4.4 was published in 2009, which can be built either with Qt3 or native Qt4 (Nokia) graphics libraries, respectively.

The new version runs on Linux and Solaris, and has been ported to Windows (XP and W7) with full GUI support.

More than fifty modifications have been made compared to v4.0 enhancing performance and interactive operation, less than 10% concerning bug fixes. A standard analysis executable is provided which can replace the main programs of most of the applications. New functions to automatically restore or create analysis objects like histograms are available. The tools to install, build, and run Go4 are improved considerably. All modifications are downwards compatible. No application code needs to be changed.

GUI improvements (Qt4)

Because Qt3 will not be supported anymore in the near future, it was necessary to port the Go4 GUI to the current Qt version 4. Early Go4 versions 4.x were built on the Qt3 compatibility mode libraries of Qt4. Qt3 could only be used with Go4 v3.x. The new Go4 v.4.4 is adapted and linked to the native Qt4 libraries, but can also be built with old native Qt3 libraries.

New standard executable

Up to now a Go4 application had to provide a main program, commonly named *MainUserAnalysis*. Parts of this program had to be kept unchanged to be callable from the framework. Other parts were free to implement application specific code. This mixture made problems when the framework changed.

Therefore there is now a standard executable *go4analysis* maintained as part of the framework. Application specific code for setup can be moved from existing main programs to the application analysis (subclass of *TGo4Analysis*). The main programs can then be discarded. User arguments from the command line are passed as argument vector to the application analysis constructor. Through this mechanism user argument lists can be used as before. A standard argument list is evaluated by *go4analysis*. Invoking *go4analysis* from shell with optional arguments one can steer the analysis and manage the analysis steps.

Restoring and creating objects

Analysis objects like histograms can be stored in ROOT files and restored from these files on next startup. Up to now the application code had to check if a histogram or parameter had been restored by the framework or had to be created. Now there is a set of new API functions doing this implicitly: when the object cannot be restored from a file it is created. For histograms, arguments can be specified for the lettering saving some lines of codes needed previously.

New applications

Go4 has been used for on-line monitoring during a CBM test beam [1]. Connected to the data acquisition system (based on DABC [2][3]) the detector performance could be checked on-line. Figure 1 shows a screen shot from two detectors, RICH and STS.

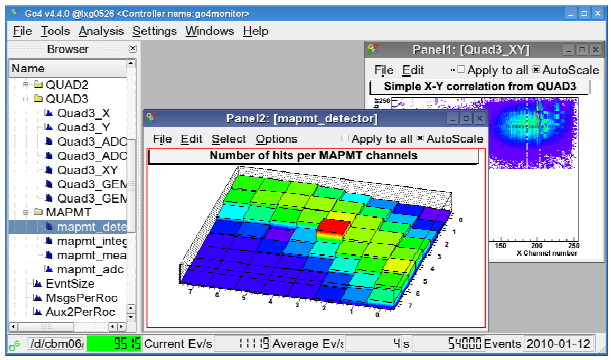

Figure 1: Go4 used as on-line monitor for the CBM test experiment. In front a quarter of a Cherenkov ring (RICH), in background the beam spot (STS).

A new Go4 application for on-line and off-line analysis of the TASCA experiment 114 was written and used during the summer beam time (www-win.gsi.de/tasca09).

References

[1] P. Senger, "Successful beam test of prototype detectors for CBM and PANDA", FAIR newsletter 14, page 5

[2] J. Adamczewski, H.G. Essel, N. Kurz, S. Linev, "Data Acquisition Backbone Core DABC", IEEE Trans.on Nucl. Science, Vol.55, No.1, pp. 251-255, February 2008.

[3] J. Adamczewski, H.G. Essel, N. Kurz, S. Linev, "Data Acquisition Backbone Core DABC", Journal of Physics: Conference Series 119 (2008) 022002

Go4 Analysis for TASCA

H.G. Essel[1], J. Dvorak[3,4], J.M. Gates[1,2], A. Gorshkov[2], and A. Yakushev[2]
[1]GSI, Darmstadt, Germany; [2]TU Munich, Germany; [3]LBNL Berkeley, CA, USA; [4]UC Berkeley, CA, USA

Go4 [1] (go4.gsi.de) is established at GSI as standard analysis framework. It is based on ROOT (root.cern.ch) providing full access to ROOT functionality. Getting data on-line from the GSI standard DAQ system MBS [2] or processing data files produced by MBS is fully supported. At GSI, Go4 is installed and maintained on the public Linux cluster. In addition, it can be downloaded and installed on any Linux or Windows machine. For the new TASCA [3] and COMPACT [4] experiments (www-win.gsi.de/tasca09) a new analysis package has been developed based on Go4. It can be used for calibration, on-line monitoring, and final analysis.

The analysis is separated in four processing steps. This makes the analysis faster, and the data sets smaller. The processing of the first two steps, *Unpack* and *Calibration*, has to be done only once or at least rather seldom. The *Checker* step has to be processed eventually more often because here the events are tagged and discarded. The *Analysis* step does the detailed chain search and might be repeated very often. Each step optionally can store its output events to a ROOT file which can also be processed by standard ROOT macros without the Go4 analysis program. The analysis layout is shown in figure 1. The

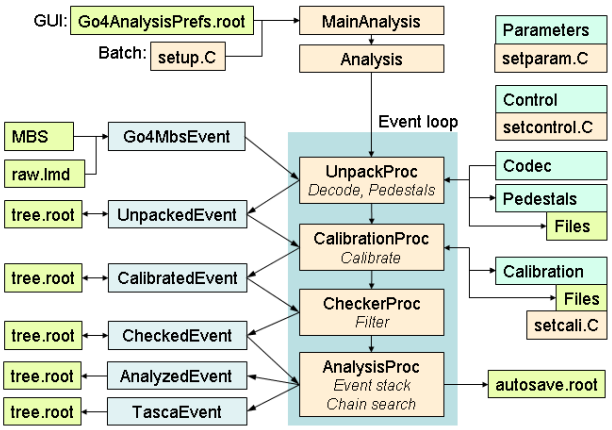

Figure 1: TASCA analysis layout

left column shows the event data objects stored/retrieved to/from files. The middle column shows the processing functions of the event loop steps. The right column shows utility objects, macros and files used by the functions. In the *setcontrol.C* macro the execution of the steps, file writing, and histogramming can be switched on or off.

Unpacker step unpacks raw events from LMD files or MBS. Function *Unpack* uses a *Codec* object to decode multiplexed detector channels and fills the data fields of *UnpackedEvent*. *Codec* also keeps the mapping tables. Unpacked events contain full data arrays, the time stamps, multiplicities and detector hit lists.

Calibrator step calibrates all data fields. It gets *UnpackedEvent* from *Unpack* step or from file. *CalibratedEvent* contains the detector hit lists, but not the arrays.

Checker step checks events. It gets *CalibratedEvent* from *Calibrator* step or from file. *CheckedEvent* is similar to *CalibratedEvent* but keeps in addition the event identification tag Evr, Alpha1, Alpha2, Alpha3, Fission1, Fission2, or Back. Events without tag are discarded.

Analysis step gets *CheckedEvent* from *Checker* step or from file and builds event stack. If an analysis start condition is fullfilled, the event stack is analyzed backwards looking for possible decay chains. Chain candidates are stored in a plain ROOT tree from *TascaEvent* events tagged as chain members together with a chain number.

Data	Files	Type	GBytes	Time
Raw	956	LMD	400	25h
Calibrated	167	ROOT	54	2h
Checked	5	ROOT	3	10m

The table shows the amount of data generations and time to produce the next generation. The unpacked data keep the full detector arrays, the calibrated data only hit indices and values. This reduces the event size considerably.

A second independent off-line analysis code was developed to verify correctness of the data analysis. This code written in C and ROOT allowed for detailed event identification, for correlation search between the events, as well as for studying of statistical data properties. Results of the independent data analysis were found to be in complete agreement with the results obtained with GO4 analysis.

Both analysis programs have been used for the TASCA element 114 run, results are in [5].

References

[1] J. Adamczewski, M. Al-Turany, D. Bertini, H.G. Essel, S. Linev, “Go4 online monitoring”, IEEE Trans.on Nucl. Science, Vol.51, No.3, June 2004, pp 565-570

[2] H.G. Essel, J. Hoffmann, N. Kurz, W. Ott, “The general purpose data acquisition system MBS”, IEEE Trans.on Nucl. Science, Vol.47, No.2, April 2000, pp. 337-339

[3] A. Gorshkov et al., “A new TASCA focal plane detector setup and DAQ system”, GSI Sci. Report 2009

[4] A. Yakushev et al., “COMPACT Coupled to TASCA for Element 114 Chemistry”, GSI Sci. Report 2009

[5] Ch.E. Düllmann et al., “Production and decay of element 114: high cross sections and nucleus ^{277}Hs”, GSI Sci. Report 2009

A novel FRS Data Acquisition

C. Nociforo[1] and N. Kurz[1]
[1]GSI, Darmstadt, Germany

In the experiments involving the use of in-flight radioactive beams the selectivity and the detection of the rare products are very demanding. Using faster processing and data acquisition (DAQ) is also important and can be crucial for the realization of those experiments that otherwise may require a non realistic beam time.

In particular, here we concern with experiments which can be performed at the GSI Fragment Separator (FRS) [1], where the count rate is limited to 10^6 pps due to an event-by-event basis detection. Depending on the reaction channel the number of parameters involved can change up to a factor 100. This is strictly connected to the used detectors and their electronics. Until now the FRS standard DAQ was working under the GSI Multi-Branch-System (MBS) [2] in the so called single event mode. The data sender is a RIO-3 CES (800MHz) processor which is located in the FRS VME crate. In this case, each event (i.e. VME ADC, TDC, QDC signals) is read out at each accepted trigger as 34 words. During this period, typically 120 μs, the DAQ is busy and any other trigger is rejected. This fixes the dead time.

Recently we have considered the use of a more efficient read out in BLock Transfer mode (BLT), which is supported by the VME Caen modules. A BLT read out of 32x34 words takes place and allows to read all events stored in the buffer (multi event mode). Whenever the buffer is empty a Bus error is generated.

Test results

This mode was recently tested online at different particle rates and compared with the standard one. The test was performed in August 2009 during the FRS000 beam time. A $^{238}U^{73+}$ beam at 750 MeV/u was delivered by the SIS18 with a spill length of 2 s. A Cu target of 90 mg/cm2 thickness was used at the entrance of the FRS to produce fragments which are then separated at the FRS mid-focal plane (S2) according their magnetic rigidity. The FRS standard equipments, i.e. scintillators, Time Projection Chambers and MUSIC detectors, were used for getting the particle identification (PID) on an event-by-event basis. The trigger was provided by the signal released by the particles counted by the scintillator and sent to the two different DAQ. The same number of VME boards were adopted in each DAQ. In particular we used ADCV795, QDCV792 and TDCV775 for detecting signals. The latter were all equally split and sent to the same number of modules. The signals of both DAQ were digitalized and registered on disk. The trigger rate was increased up to 20 kHz by varying the FRS acceptance opening the slits or increasing the intensity of the primary beam.

The two DAQ were compared on the basis of their live time, defined as the ratio between the number of the accepted and free triggers. The result is shown in Fig. 1 as a function of the particle rate. The new DAQ is more effective compared to the standard one starting from around 400 Hz. A gain factor equal to two was reached at about 4 kHz. The measured dead time at 10 kHz was equal to 48%.

The multi-event DAQ was running in stable condition giving an adequate PID. The next step will be to include the scaler Caen V830 into the new read out. Preliminary tests have given promising results.

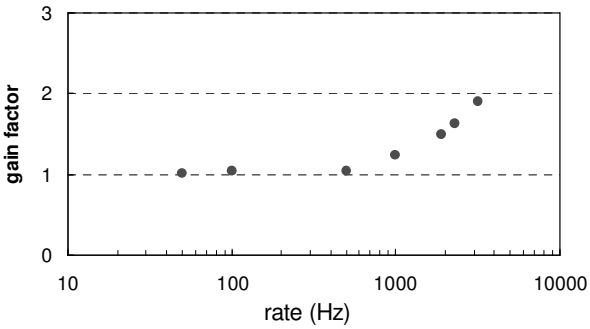

Figure 1: Gain factor of the FRS multi-event DAQ mode in respect to the standard one as a function of the particle rate.

Summary

A novel FRS DAQ based on a BLM mode was tested at the FRS. Its use can be adopted alternatively in those experiments which require the use of standard FRS equipments and an higher rate. A gain factor up to two was experimentally achieved. We would like to emphasize that this value could be still improved by using a RIO-4 CES processor. In fact another gain factor of two was already observed coupling this unit to the standard FRS single-mode DAQ. Thus in total a gain factor of approximately four may be achieved in future compared to the present situation.

References

[1] H. Geissel et al, Nucl. Inst. Meth. B 70 (1992) 286.
[2]GSI-Multi Branch System http://www.w2k.gsi.de/daq/.

Time Resolution of Diamond Detectors for Relativistic Ions and Protons*

E. Berdermann[1], M. Ciobanu[1], M. Henske[1], M. Kiš[1,2], W. Koenig[1], M. S. Rahman[1], M. Träger[1]
[1]GSI, Darmstadt, Germany, [2]IRB, Zagreb, Croatia

The high pair production energy of diamond (ε_{Dia}= 12.84 eV) is a challenging material property in timing measurements of relativistic light ions and Minimum Ionizing Particles (MIPs). The low amount of generated charge (Q_G) predicts reduced detection efficiency of assemblies, readout with broadband Front End Electronics (FEE). Eqs. (1) and (2) describe the time resolution σ_t and the Signal-to-Noise ratio (S/N), respectively [1]:

$$\sigma_t = \frac{N}{dV/dt} = \frac{\sqrt{k \cdot T \cdot (F-1) \cdot C_D}}{2.28 \cdot Q_C(e,h) \cdot BW_A} \quad (1)$$

$$S/N = Q_C(e,h) / \sqrt{k \cdot T \cdot (F-1) \cdot C_D} \quad (2)$$

with k, the Boltzmann constant; T the temperature; Q_C, the collected charge; C_D the detector capacitance; F and BW_A the noise factor and bandwidth of the FEE.

Accordingly the task is to maximize Q_C and BW_A and heights on the input impedance of a Diamond Broad band Amplifier (DBA: 50Ω, 2.5pF, 2.3GHz), generated from ions of same velocity 1GeV/A in diamond sensors of different Charge-Collection Efficiency (CCE = Q_C/Q_G) and thickness d_D = 50–400 µm (indicated by the line colours). Dot electrodes of 3 mm in diameter were assumed, and a thickness and quality dependent FWHM of the signals. The horizontal lines indicate the (rms) noise amplitude of the DBA (solid line) and its 3σ deviation (dashed line), which is at least the amplitude required for good detection efficiency and time resolution with this FEE.

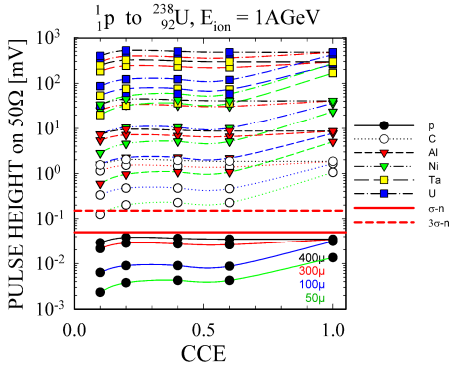

Figure 1: Expected amplitudes on 50 Ω vs. the CCE of diamond sensors of different d_D (line colours) (see text).

The data show that for Z > 6, polycrystalline diamond plates of $d_D \geq 50$µm and CCE ≥ 0.2 are feasible, whereas MIP timing with DBA like FEE is prevented even for best single-crystal CVD Diamond sensors of CCE ~ 1.

Extended simulations confirm the best time resolution for low-capacitance broadband assemblies where both C_D and parasitic capacitances C_P are ≤ 1pF; degradation up to a factor of three appears for $C_P \geq 2$pF.

* Supported by EC Projects RII3-CT-2004-506078 and MC-PAD

Recent Results with ^{6}Li Ions of 1.8 AGeV

We tested the intrinsic time resolution of scCVDD quadrant sensors for relativistic ^{6}Li ions with two setups each consisting of two d_D = 400µm (Setup 1, top left) and 100 µm thick samples (Setup 2, bottom left), respectively. The corresponding single-sector capacitances were $C_{D\text{-}1S400}$ = 0.2 and $C_{D\text{-}1S100}$ = 0.9 pF. The modular Setup 1 was readout via capacitive buffers for each sector followed by modified FEE-1 cards [2] implemented as a 2nd stage analogue processing (MOS-follower; 1MΩ, 2.1pF, 1GHz). In Setup 2, the diamond sensors were mounted on the FEE boards with each sector wire bonded to an active impedance transformer of C_i = 0.2 pF. Subsequently, the signals were shaped with an external booster amplifier [3]. The best proton result with the former 'low-Ci BBA' used for the HADES Start Detector (SD) was σ_{intr} = 117 ps [3].

The time-difference spectra obtained with both setups are shown on the corresponding right graphs of Fig. 2. Note that for Setup 1 the data analysis is preliminary and incomplete. Resolutions σ_t = 77 ps (σ_{intr} = 55 ps) achieved by selecting prompt time coincident events of high signal amplitudes. No walk correction is performed at present. In contrast, the Setup 2 data are walk corrected and processed under the condition that no neighbour sectors have fired. Due to the new transistor implemented (SiGe:C; BFR705L3RH) an excellent σ_{intr} = 32ps with a pure diamond contribution of 21ps was achieved. Further improvement is expected by readout micro-patterned SDs with broadband ASICs (PADI [1]) modified for higher sensitivity (to be tested in spring 2010).

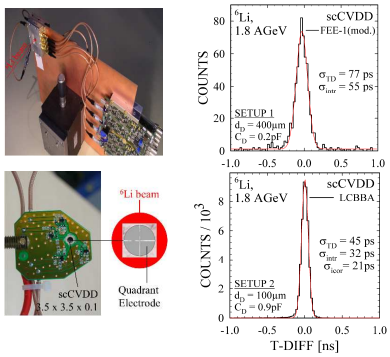

Figure 2: (left) The tested Setups, 1 (top) and 2 (bottom). (right) Time-difference spectra of two opposite sectors.

References

[1] E. Berdermann, M. Ciobanu* et al., Proc. IEEE NSS-MIC, Orlando, 2009, Conference Record.
[2] M. Ciobanu et al, IEEE Trans. on NS, Volume 54, Issue 4, Pages:1201 – 1206, August 2007.
[3] J. Pietraszko et al., subm. to NIM A, November 2009

Some Numerical Investigation of High Energy Electron Cooling*

G. Zwicknagel
Institut für Theoretische Physik, Universität Erlangen, Germany

The theoretical description of electron cooling is usually based on cooling force models which are derived assuming quasi-stationary conditions, i.e. a continuous flux of electrons colliding with the ions and a Debye-screened interaction [1, 2, 3]. But this assumption will become questionable in a high energy cooling scenario, as at the planed HESR. Here the interaction time during which ion and electron beams are merged in the cooler might be too short to reach this regime. The related lack of time to built up the screening will enlarge the interaction range and thus increases the cooling force logarithmically with the increasing screening length λ. Less obvious is the influence of now also occurring incomplete ion-electron collisions which we therefore investigated by Classical Trajectory Monte Carlo (CTMC) simulations (see [4]).

Some first results are given in Fig.1 and 2, where we show the proton-electron velocity transfer $\Delta v_{r\|}$ parallel to the magnetic field (and beamline) which converts into the parallel cooling force after averaging over the electron distribution. It is shown here as a function of the proton-electron relative velocity $v_{r\|}$ in units of the thermal parallel ion velocity $v_{th\|}$ and the maximum interaction time τ_{max}, i.e. the time the beams are merged, in units of the inverse plasma frequency ω_p^{-1} (all quantities refer to the cm-frame of the ion beam). The parameters of the electron beam are close to the HESR design with $T_{e\perp} = 0.1$ eV, $T_{e\perp} = 0.1$ meV, $n_e = 2 \cdot 10^6$ cm^{-3}, $B = 0.48$ T, and $\omega_p \approx 8 \cdot 10^7$ s^{-1}. For the CTMC simulations a Debye-screened interaction with $\lambda = 5 \cdot 10^{-4}$ m has been used.

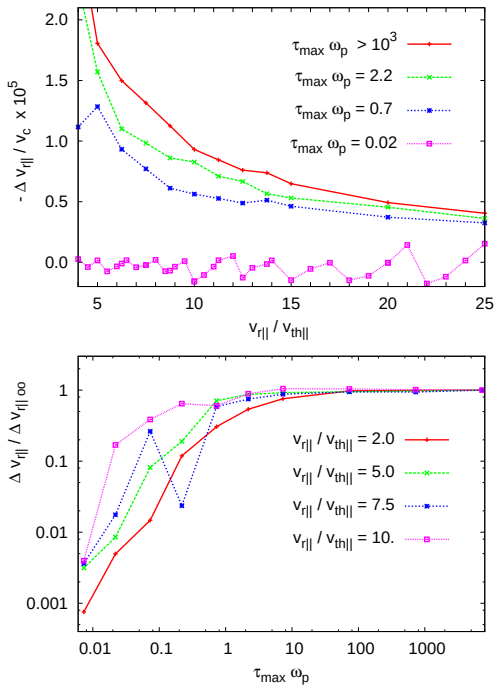

Figure 1: Velocity transfer $\Delta v_{r\|}$ of protons moving with $v_{p\perp} = 0.5\, v_{th\|}$ in a beam of monoenergetic electrons. Upper part: as function of the relative velocity $v_{r\|}$ for different interaction times τ_{max}. Lower part: as function of τ_{max} for different $v_{r\|}$ now normalized to $\Delta v_{r\|\infty}$ for infinite τ_{max}. Here $v_c = (e^2/4\pi\varepsilon_0 m_e \lambda)^{1/2}$.

Considering only the effect of incomplete collisions we find that the velocity transfer and thus the cooling force starts to decrease as soon as the interaction time τ_{max} gets smaller than about 10 ω_p^{-1} and will go down to around 1% and less of its value in a stationary scenario for $\tau_{max} \ll \omega_p^{-1}$.

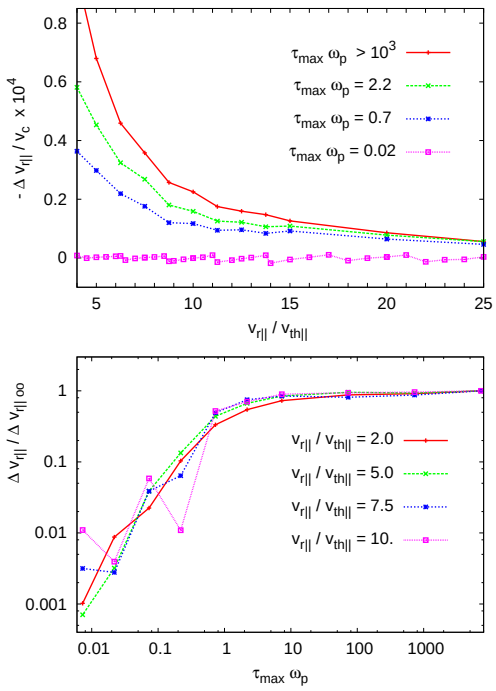

Figure 2: Same as Fig.1, but now for $v_{p\perp} = 5.0\, v_{th\|}$

References

[1] BETACOOL: http://lepta.jinr.ru/betacool/betacool.htm; A.O. Sidorin *et al.*, NIMA **558**, 325 (2006)

[2] I.N. Meshkov: Phys. Part. Nuclei **25**, 631 (1994)

[3] H. Poth: Phys. Reports **196**, 135 (1990)

[4] H. Nersisyan, C. Toepffer, G. Zwicknagel, *Interactions Between Charged Particles in a Magnetic Field* (Springer, Berlin Heidelberg New York 2007)

*Work supported by the BMBF (06ER145)

Generation of shielding data for neutron radiation produced by heavy ions

G. Fehrenbacher[1], T. Radon[1]
[1]GSI, Darmstadt, Germany

Introduction and Method

The aim of this work is the provision of attenuation data for normal concrete on the basis of double differential source distributions (solid angle, energy) of released neutron radiation. For this purpose attenuation data for mono-energetic neutron radiation were computed using the radiation transport code FLUKA[1] employing a special shaped concrete shielding from 1.5 m to 8 m in an energy range from 100 keV to 3 GeV, see Fig. 1.

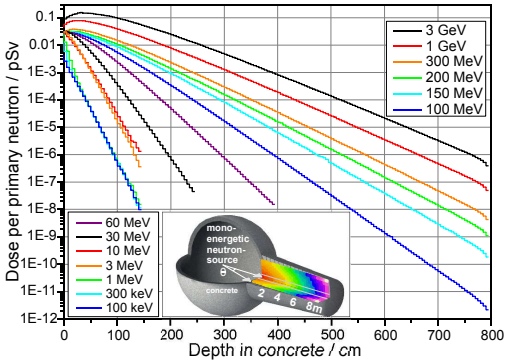

Figure 1: Attenuation curves of mono-energetic primary neutrons in the energy range from 100 keV to 3 GeV derived from MC-calculations with FLUKA. The neutrons were virtually transported through 8 m of concrete, see insert.

Measured [2,3] or calculated double differential neutron yields, see Fig. 2 serve as source terms (Eq. 1). These are then being folded with the (interpolated) mono-energetic attenuation curves, see Eq. 2. In this way the total dose as a function of the shielding thickness for each angular range is provided.

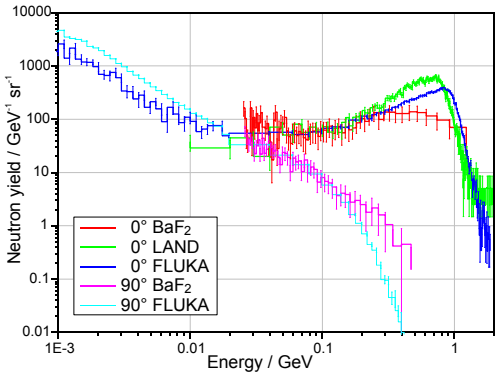

Figure 2: Source distributions of neutron spectra (0° and 90°) obtained by measurements and calculations.

$$N(E,\vartheta,\theta) = \iint \frac{\partial^2 N(E,\vartheta)}{\partial E \partial \Omega} d\Omega dE \qquad (1)$$

$$H_{tot}(x,\vartheta,\theta) = 2\pi(1-\cos\theta)\cdot \cdot \sum_{E=100keV}^{3GeV} \left(\frac{H_{mono}(x,\theta)}{N_{mono}(E)} \cdot \frac{\partial^2 N(E,\vartheta)}{\partial E \partial \Omega} \right) \qquad (2)$$

Results

In Fig. 3 the resulting attenuation curves are shown, based on the source distributions from Fig. 2. Due to the strong forward production of the neutron radiation the dose values and the depth dose curves are significantly higher for the 0°. The LAND related attenuation curve (0°) gives the highest dose values. This can be explained by the largest portion of neutrons near the peak at 600 MeV. Due to the lowest fraction of high energy neutrons (E_n > 300 MeV) from the BaF_2 measurements the resulting attenuation curve comes to the lowest dose values. An analogous explanation can be applied for the 90° direction. In order to show how the method proposed works a complete MC calculation i.e. the creation of neutrons and their transport through the concrete was performed. The agreement of these "full FLUKA" curves with the separately performed yield and transportation FLUKA calculations is better than 30%.

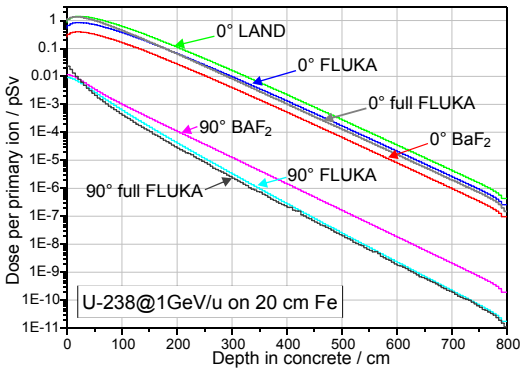

Figure 3: Resulting neutron dose attenuation data derived from the spectra of Fig. 2 and the mono-energetic neutron attenuations from Fig. 1.

References

[1] A. Ferrari, P.R. Sala, A. Fassò, and J. Ranft, "FLUKA: a multi-particle transport code", CERN 2005-10 (2005), INFN/TC_05/11, SLAC-R-773.

[2] K. Gunzert-Marx, T. Radon, G. Fehrenbacher, F. Gutermuth, D. Schardt, PoS, Internat. workshop on fast neutron detection (FNDA2006) 057, p 2, 2006.

[3] O. Yordanov, K. Gunzert-Marx, P. Adrich, T. Aumann, K. Boretzky, H. Emling, G. Fehrenbacher, F. Gutermuth, H. Iwase, H. Johannson, K. L. Jones, A. Kovalov, T. Radon, D. Schardt, Nuclear Instruments and Methods B 240 (2005) 863.

Atomic and Accelerator Physics in the QUASAR Group*

S.Artikova[2], R. Boll[1,2], J. Egberts[2], J. Gerlach[1,2], J. Harasimowicz[1,2,6,7], M. Holzscheiter[2], A. Intermite[1,2,6,7], A. Jeff[3,6,7], T. Junginger[2,3], K.-U. Kühnel[1,2], A. Papash[1,2,4], M. Putignano[1,2,6,7], C. Schömers[2,5], M.R.F. Siggel-King[6,7], M. Sapinski[3,6,7], M. Schuh[2,3], S. Sellner[1,2], S. Tegami[1,2], G. Wall[6,7], and C.P. Welsch[6,7,#]

[1]GSI, Darmstadt, Germany; [2]Max Planck Institute for Nuclear Physics, Heidelberg, Germany; [3]CERN, Geneva, Switzerland; [4]JINR, Dubna, Russia; [5] HIT, Heidelberg, Germany; [6]Cockcroft Institute, Warrington, UK; [7]University of Liverpool, Liverpool, UK

The QUASAR group combines developments in accelerator sciences with measurements on quantum systems, with a particular interest in antimatter research. The group focuses on the development of the key elements of a future ultra-low energy storage ring at the facility for low energy antiproton and ion research.

Since its start in 2008 the group substantially broadened its R&D program, has been collaborating with HIT and CERN on medical accelerators, is pursuing research into superconducting linacs, and is developing beam instrumentation for high energy accelerators.

THE USR

The Facility for Antiproton and Ion Research (FAIR) at GSI will include a dedicated facility for research with low energy antiprotons in the keV regime or even at rest, named FLAIR [1]. The deceleration of antiprotons to a final energy of 20 keV (and even down to 1 keV) will be realized in a dedicated electrostatic Ultra low energy Storage Ring (USR) [2].

The use of electrostatic elements has the significant advantage that, as compared to their magnetic counterparts, high field homogeneity in combination with a fast ramping of the fields over a wide range is possible. In addition, remanence and hysteresis effects do not occur in electrostatic elements. As the ring aims to be a multi-user facility, high luminosity, low emittance and low momentum spread of the beam together with a flexible beam shape are required. External experiments for precision studies, for example trap experiments, will form an integral part of FLAIR and the USR will provide fast and slow extraction, for the first time in an electrostatic storage ring.

In order to match the requirements from the envisaged experiments, different modes of operation are foreseen for the USR: deceleration and e-cooling, fast and slow extraction [3] and an ultra-short bunch mode for in-ring experiments as developed by the group in 2008 [4]. This allows for an optimization of the beam shape, size and dispersion for the respective experiment.

Split-Achromat Lattice

The modified layout of the USR Lattice is based on a split–achromat geometry which gives the necessary flexibility to satisfy the wide range of experimental requirements.

Fig.1 shows the new layout of the storage ring, which now has a circumference of 42.6 m, i.e. almost unaltered geometrical dimensions as compared to [2]. Four 4 m long straight sections are used to accommodate the so-called Reaction Microscope (ReMi), the different RF systems for the short bunch operation mode [4,5], the electron cooler, the decelerating drift tube, and the elements for fast/slow extraction [3]. One of the straight sections is kept free for a possible inclusion of a merged positron ring, see [1]. Five electrostatic quadrupoles, two 8^o and two 37^o electrostatic deflectors form an achromatic 90^o bend. A drift space of 1 m between the 8^o and the 37^o deflectors is left to allow for the detection of neutral particles leaving the ring after the ReMi under an opening angle of $\pm 0.7^o$.

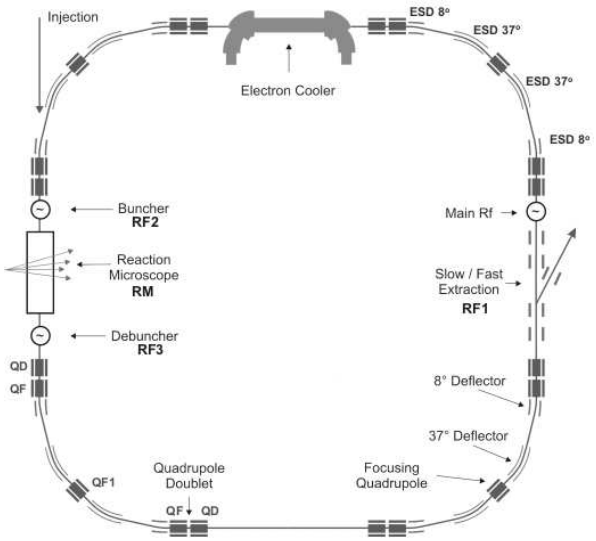

Figure 1: Overview of the USR layout.

The quadrupole QF1 in the middle of each bending section is used to provide both a round beam mode for collision experiments as well as achromatic conditions D=D'=0, if required. The dispersion function can be modified in a wide range from +60 cm down to values of –50 cm. The geometrical parameters of the electrostatic deflectors (central radius and distance between electrodes) and electrostatic quadrupoles (effective length and inscribed aperture) were defined by taking into account the possibility to extract neutral particles after the ReMi, to operate with a beam with a normalized 4rms emittance

* Work supported by GSI/HGF under contract VH-NG-328, EU contracts PITN-GA-2008-215080, PIIF-GA-2009-234814, and the Gentner program.
#carsten.welsch@quasar-group.org

as large as 1–2π mm·mrad and an upper voltage limit of ±20 kV on the deflectors and ±10 kV on the quadrupole electrodes.

Fringe fields near the ends of electrostatic elements can have negative effects on the stored beam and even lead to unwanted coupling effects between different optical elements [6]. Therefore grounded shields are foreseen at the entrance and exit regions of all deflectors, the quadrupoles, and between two individual elements of a quadrupole doublet. The 8° cylinder deflectors have a central bending radius of 2 m, a plate distance of 120 mm, and maximum voltages of ±18 kV. The main 37° deflection is realized by a deflector with a central radius of 1 m, a gap of 60 mm, and maximum voltages of ±18 kV.

The aperture radius of the electrostatic quadrupoles is 100 mm and their effective length 200 mm. The voltages that are required on the three quadrupoles to focus a 300 keV antiproton beam are U_1=-6.1 kV, U_2=+4.4 kV, and U_3=+6.35 kV.

Beam Extraction

Extensive computer simulations of the extracted beam were undertaken using the codes MAD-X, OPERA3D and SIMION, based on preliminary studies [3]. All design parameters were reviewed during the optimization process. Elements for fast and slow extraction are co-located in one of the USR's straight sections. Two electrostatic sextupoles and an RF "knock out" cavity, which will excite radial beam oscillations, are located in another ring section. Four bump electrodes will be used to shift the orbit towards an electrostatic septum that is tilted to the axis by 6^o. This combined extraction scheme will provide beams with most different time structures, through one common extraction line, to external low energy experiments.

Presently, these results are being combined with studies on the effects of space charge and fringe fields on the dynamic aperture of the USR. This will give rise to an improved understanding of the beam dynamics of electrostatic rings and help optimizing their performance.

Beam Instrumentation

A wide range of diagnostic devices has been investigated for the USR. These will be used for different stages of machine development and most of them can be used for monitoring more than one beam parameter. A compact Faraday Cup was designed and built; it will be used for tests with low intensity beams early in 2010 [7]. An electrostatic pick-up for the non-destructive measurement of the beam position was developed and is presently being manufactured. And in close collaboration with INFN-LNF, measurements were carried out on the characteristics of scintillating screens at very low beam energies and intensities. These studies will not only provide the basis for beam profile measurements in the USR, but in all low energy beam lines at FLAIR.

An alternative approach to measure the transverse beam profile in an almost non-destructive way is to use a neutral curtain-shaped supersonic gas jet target. This approach is more sensitive than those based on residual gas because the higher gas density in the curtain increases the ionisation rate. The atoms or molecules in the supersonic jet can be efficiently evacuated, due to the high directionality of the particles in the jet, in order to keep the required ultra high vacuum elsewhere in the storage ring. Numerical studies were undertaken with GDT to improve on the understanding of the gas jet dynamics [8]. Based on these studies, the mechanical design of the monitor was finalized [9] and most components have been ordered. The system will be setup early in 2010 with first test anticipated in the summer.

MEDICAL ACCELERATORS

The use of particle accelerators for medical applications has become increasingly important with dedicated facilities being built up around the world. In close collaboration with the Heidelberg Ion Therapy centre (HIT), the group contributed to the design of a novel magnet-current based beam extraction system for medical synchrotrons [10]. This included the installation of a magnet test stand and detailed investigations into the characteristics of commercial hall probes [11].

Since summer 2009 the group has been carrying out studies on the biological effects of antiprotons. Measurements were made at CERN in September and are being analyzed. Whilst this research is presently based at CERN, it is an integral part of the FLAIR experimental program and thus directly builds up on the group's USR activities.

SUPERCONDUCTING LINACS

The QUASAR group is contributing to an international effort in optimizing superconducting cavities for future high current accelerators. This technology has been successfully exploited in large scale accelerator projects, such as CERN-LEP, JLAB-CEBAF, and ONL-SNS. In addition, it was selected for future projects such as DESY-XFEL, HIE-ISOLDE and studies, such as the CERN-SPL, which will push the limits of this technology even further.

In close collaboration with CERN, the effects of higher order modes (HOMs) on the SPL particle beam were studied and upper limits for the damping requirements were defined: Even when using ten times the design current, simulation results in the transverse plane showed that a Q_{ex} of 10^6 - 10^7 is acceptable [12]. Future studies will now concentrate on analysing the effects of chopping on the longitudinal plane and of alignment errors in both planes.

To perform RF measurements on superconducting samples, a Quadrupole Resonator at CERN was successfully refurbished with the aim to characterize new materials for high gradient cavities. In first measurements at 400 MHz, the surface resistance for temperatures down to 5 K and the maximum RF field on the attached sample were determined. For a second series of measurements shielding of the ambient magnetic field and pumping of the helium bath was applied, allowing measurements at temperatures

down to 3.3 K. The penetration depth and the thermal conductivity of the attached sample were measured [13].

BEAM INSTRUMENTATION FOR HIGH ENERGY ACCELERATORS

The detection and possible control of the beam halo is of utmost importance for high energy accelerators, where unwanted particle losses lead to an activation or even damage of the surrounding vacuum chamber. Additionally, low energy machines such as the USR, are concerned in minimizing the number of particles in the tail region of the beam distribution. One option for monitoring the beam halo is to use light generated by the beam, either through synchrotron radiation, optical transition radiation, or luminescent screens. In this case, a special detection technique is required to allow for high dynamic range measurements. A CID camera, characterized in lab experiments, was shown to have a very high dynamic range of more than 10^7 [14]. In addition, a flexible "core masking technique" proved to be a reliable and comparably cheap method for measurements with a dynamic range of up to 10^6 [15]; this technique is presently being applied at UMER for studies with beam.

In addition, the group carried out characterization studies of Si-PMTs for use as beam loss monitors in combination with optical fibres and started work on the design of a longitudinal beam profile monitor for the LHC.

DITANET

The Marie Curie Initial Training Network DITANET covers the development of advanced beam diagnostic methods for a wide range of existing or future accelerators, utilising electrons or ions. It is the largest-ever EU funded training network in this field and brings together research centres such as GSI, CERN and DESY, universities, and private companies. It was initiated and is coordinated by the QUASAR group leader. Most positions within the network were filled in 2009 and the respective research projects started successfully.

An international school on *Beam Diagnostics* was organized at Royal Holloway, University of London between 30/03/09-03/04/09. The School, combined with the first DITANET annual meeting, brought together over 70 researchers. It started with an introduction to accelerator physics and the definition of particle beams, and then covered instrumentation for basic beam measurements, such as beam energy, beam current and transverse beam profile. Later in the week more advanced topics, e.g. the monitoring of the machine tune or electron cloud diagnostics were presented. A particular highlight of the school was a dedicated industry session where lecturers from associated partners Thermo Fisher Scientific, TMD, Thales, ViALUX, and Instrumentation Technologies gave insight into their cutting edge R&D activities.

A topical workshop was held in Hirschberg/Großsachsen on November 23rd - 25th on *Low Energy, low intensity diagnostics*. A particular focus was the instrumentation requirements of FAIR with discussion of state-of-the-art beam diagnostics used at storage ring and cyclotron facilities around the world.

ACKNOWLEDGEMENTS

The QUASAR Group is grateful for the fruitful collaboration with our partners at CERN (E. Bravin, B. Dehning, F. Gerigk, T. Lefèvre, W. Weingarten), HIT (E. Feldmeier, A. Peters, R. Steiner), INFN-LNF (L. Cosentino, P. Finocchiaro, A. Pappalardo), Thermo Fisher (T. Chapman, M. Pilon), U Maryland (R. Fiorito, R. Kishek), and our colleagues at the Cockcroft Institute.

The generous support of the Helmholtz Association of National Research Centres (HGF) under contract number VH-NG-328 and of the GSI Helmholtz Centre for Heavy Ion Research GmbH is acknowledged, as well as the support by the EU under contracts PITN-GA-2008-215080 and PIIF-GA-2009-234814. Finally, the authors would like to thank the MPI-K for hosting the QUASAR group.

REFERENCES

[1] C.P. Welsch, et al., ”An ultra-low-energy storage ring at FLAIR”. Nucl. Instr. and Meth. A **546** (2005) 405–417

[2] C.P. Welsch, et al., "Present status of the USR Project", Hyperfine Interact. **194** 1-3 p. 137-143 (2009)

[3] P. Schmid, et al., "Preliminary Design of an Extraction Scheme for the USR", Hyperfine Interact. **194** 1-3 p. 183-187 (2009)

[4] A.I. Papash, C.P. Welsch, “On the Possibility of Realizing Shortest Bunches in Low-Energy Storage Rings”. Physics of Particles and Nuclei Letters, Vol. **6**, No. 3 (2009)

[5] A. Papash, C.P. Welsch, "An Update of the USR Lattice: Towards a True Multi-User Experimental Facility", Proc. Part. Acc. Conf., Vancouver, Canada (2009)

[6] C.P. Welsch et al., ”An Electrostatic Quadrupole Doublet with an Integrated Steerer”, Proc. EPAC, Lucerne, Switzerland (2004)

[7] J. Harasimowicz, et al., "Beam Diagnostics for the USR", Proc. Part. Acc. Conf., Vancouver, Canada (2009)

[8] M. Putignano, et al., "Design of a Nozzle-Skimmer System for a Low Perturbation Ionization Beam Profile Monitor", Proc. DIPAC Workshop, Basel, Switzerland (2009)

[9] M. Putignano, et al., "A fast, low perturbation ionization beam profile monitor based on a gas-jet curtain for the ultra low energy storage ring ", Hyperfine Interact. **194** 1-3 p. 189-193 (2009)

[10] A. Peters, et al., "Magnetic Field Control in Synchrotrons", Proc. Part. Acc. Conf., Vancouver, Canada (2009)

[11] C. Schömers, "Investigations into the magnetic field control in normal-conducting synchrotrons", Diploma Thesis, Heidelberg (2009)

[12] M. Schuh, et al., "Higher Order Mode beam break up limits in the Superconducting Cavities of the SPL", Proc. SRF Workshop, Berlin (2009)

[13] T. Junginger, et al., "RF Characterization of Superconducting Samples", Proc. SRF Workshop, Berlin (2009)

[14] J. Egberts, et al., "Flexible Core Masking Technique for Beam Halo Measurements with High Dynamic Range", Proc. DIPAC Workshop, Basel, Switzerland (2009)

[15] J. Egberts, "Investigations on transverse beam profile measurements with high dynamic range", Diploma Thesis, Heidelberg (2009)

Single Event Effect Studies on the 180 nm UMC process with the GSI Heavy Ion Microprobe

S. Löchner*[1], B.E. Fischer[2], B. Merk[2], and K.-O. Voss[2]
[1]GSI Darmstadt, Experiment Electronics; [2]GSI Darmstadt, Material Research

Introduction

For the future experiments at the new FAIR accelerator facility radiation damages to electronic components are an important issue. In this regard, the ASIC design group of the GSI Experiment Electronics department has launched a research project for the characterisation of Single Event Effects (SEE) on the 180 nm UMC process, including the development of an ASIC called *GRISU*[1].

SEE is the term for effects in semiconductor devices triggered by a single ionising particle in contrast to effects triggered by a damage accumulated by many particles. A good choice to test these effects is the irradiation with heavy ions. Several irradiation tests with different heavy ions were performed at the X6 testing site. The beam was widened so that the entire *GRISU* chip has been irradiated at the same time[1].

First results showed that some digital storage cells were more sensitive to SEU than expected from simulation. To clarify and understand this unexpected high sensitivity the *GRISU* chip was irradiated with the sub-micron resolution beam of the heavy ion microprobe at the X0 testing site.

Single Event Effect Studies with a Single Heavy Ion Hit Microprobe

Briefly, the microbeam is situated at the end of the GSI heavy ion linear accelerator. The ions entering the microbeam line through object slits are focused down to a focal spot of about 500 nm in diameter by means of magnetic quadrupole lenses. Deflecting magnets, situated in front of the focusing lenses, are used to move the beam spot in the focal plane[2].

In May 2009 a *GRISU* chip was irradiated with a carbon microbeam with an energy of 4.8 MeV/u. This corresponds to a Linear Energy Transfer (LET) of approximately 2.25 MeV cm^2 mg^{-1}. In total five different test structure areas were irradiated. The ASIC has been scanned over $80 \times 80\,\mu\mathrm{m}^2$ for the first three SEE tests and $20 \times 20\,\mu\mathrm{m}^2$ for the last two tests.

As an example of these test results an inverter chain of different transistor sizes is depicted. The layout overlay picture of the irradiated area and the observed Single Event Transient (SET) events are shown in Fig. 1. Each red circle represents a SET event. The circle centre points to the measured origin by the microbeam DAQ system whereas the radius represents the 3σ position accuracy of 612 nm. For inverter chain no. 4 and 5 SET events were measured

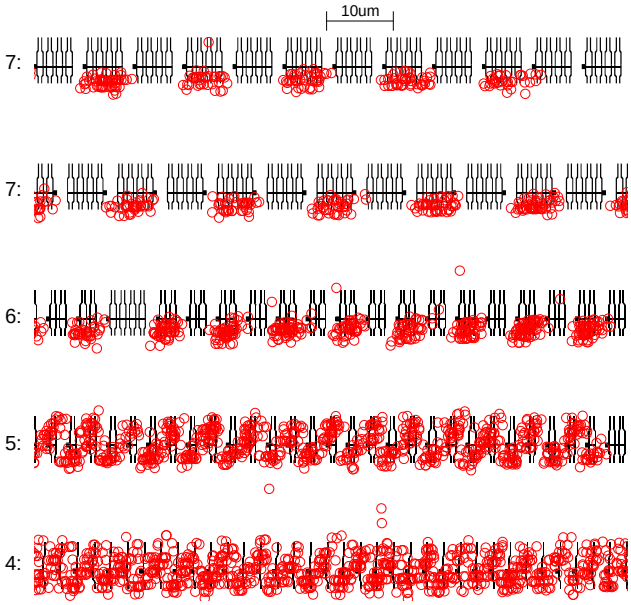

Figure 1: Overlay of inverter chain test structure layout and position of SET events. The radius of the circle is equivalent to 3σ position accuracy or approx. 600 nm.

for NMOS transistors (lower layout part in each row) as well as for PMOS transistors (upper layout part). However for inverter chain no. 6 and 7 SET hits were only measured for NMOS transistors. The explanation for this is that the node capacitances of these PMOS transistors are larger compared to the smaller NMOS.

Results

The first measurement showed that the microbeam setup is a powerful tool for spatially resolving SEE investigations. However the number of events for a closer statistical analysis as well as the resolution must be increased for closer investigations of the 180 nm process, especially for the study of some special memory structures on the *GRISU* chip.

References

[1] S. Löchner, "Radiation Studies on the UMC 180 nm CMOS Process", GSI Scientific Report 2009

[2] B.E. Fischer, "The Scanning Heavy Ion Microscope at GSI", Nuclear Instruments and Methods in Physics Research, Section B, 10-11, 693-696 (1985)

* s.loechner@gsi.de

Diamond surfaces investigated by atomic force microscopy*

S. Wetzel#, R. Lovrincic, and A. Pucci
Kirchhoff Institut für Physik, Universität Heidelberg, Germany

The surface roughness of single crystal diamonds produced by chemical vapour deposition (CVD) on diamond-seed substrates and treated with different surface polishing techniques, such as ion-beam polishing and resin-wheel-polishing was studied by atomic force microscopy (AFM). Knowledge on surface roughness is important for the production of single-crystal diamond detectors, since the quality of metallic contacts on the diamond depends on it significantly. Different to silicon wafers, the production of diamond wafers with the same crystalline quality in the bulk and especially on the surface is still impossible because of the very special diamond-growth process and the high challenges in polishing diamond. The production process of single-crystal CVD diamonds (scCVDD) and especially different surface finishing techniques are still under development [1]. This makes it necessary to characterize the diamonds concerning their surface roughness before any layer deposition for research purposes. AFM measurements are particularly suited to probe the surface morphology of insulating samples. Here some examples are shown; for other examples and various details see Ref. [1, 2]. In our previous studies on the growth of chromium and aluminum on scCVDD (C(100)) [1, 3, 4, 5] the diamond-surface quality was carefully checked before further cleaning steps (to control surface layers) and metal deposition. We always used the best available substrates.

The AFM measurements were performed with a *Multimode* scanning probe microscope (*Veeco SPM*) in tapping-mode. Images were recorded with a size of (4 × 4) μm^2 and a resolution of 512 × 512 points at different positions on each side of the wafer. For further illustration of obtained data, the selection of details, and roughness analysis, the free software *Gwyddion* [6] was used. The samples of this article had been produced by *Diamond Detectors Ltd.*.

The AFM images of Fig. 1 show the typical defects of polished surfaces. The two images were taken on the front and on the backside, respectively, of a scCVD diamond slab with a thickness of 500 µm. In contrast to the front side that shows a rather smooth surface typical for ion-beam polishing [2], on the backside many defects and scratches can be seen. It should be mentioned that the two sides have a different history. One side results from laser cutting from the seed, the other side from the as-grown surface. From the AFM data a RMS roughness of 1.4 nm and 3.1 nm for the front and for the backside, respectively, follows, proofing the clearly different roughness of the two surfaces, which is a major problem in device fabrication with two equivalent metal electrodes.

The authors gratefully acknowledge the fruitful cooperation with Eleni Berdermann and thank *Element Six* and *Diamond Detectors Ltd.* for the excellent diamond materials they have provided.

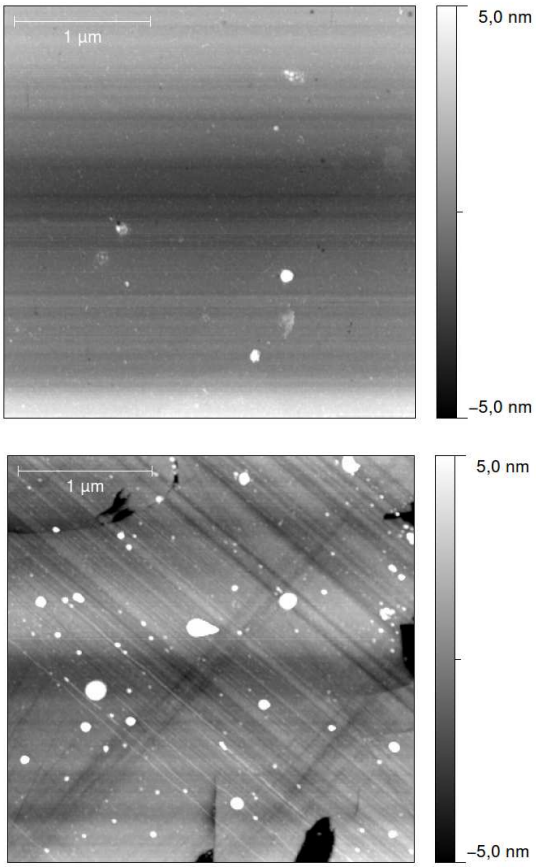

Figure 1: (3 × 3) μm^2 images from a 500 µm thick scCVDD are shown, one from the frontside (top) and a second one from the backside (bottom). Height scale is given on the right of each picture. Scanning in horizontal direction.

* Work supported by EU, project RII3-CT-2004-506078 and RII3-CT-653 227431.
# swetzel@kip.uni-heidelberg.de

[1] R. Lovrincic, thesis, Ruprecht-Karls-Universität Heidelberg 2009.
[2] E. Berdermann, et al., Diamond & Related Materials (2009), in press.
[3] R. Lovrincic and A. Pucci, Phys. Rev. B 80 (2009) 205404.
[4] R. Lovrincic and A. Pucci, GSI Scientific Report 2007, p. 207.
[5] R. Lovrincic, S. Noebel, and A. Pucci, GSI Scientific Report 2008, p. 248.
[6] *Gwyddion* - Free SPM data analysis software www.gwyddion.net

First Results of CVD-Diamond Detectors Grown on Large Iridium Substrates*

E. Berdermann[1], M. Ciobanu[1], S. Dunst[2], M. S. Rahman[1], M. Schreck[2], and M. Träger[1]
[1]GSI, Darmstadt, Germany, [2]Universität Augsburg, Germany

A promising course for large-area 'quasi' single-crystal CVD diamond (scCVDD) is the heteroepitaxial growth on the multilayer structure Ir/YSZ/Si(001) [1] - as developed at the University of Augsburg on 4inch wafers. Key issue is the similarity of the lattice constants of diamond (d_{Dia} = 3.567 Å) and Iridium (d_{Ir} = 3.834 Å).

Figure 1 shows characterization results of two Diamond-on-Iridium (DoI) samples compared to commercial scCVDD and polycrystalline CVD-diamond (pcCVDD) detectors [2]. DoI549a (top- and central-right data) is a polished freestanding film of 230µm thickness, where a 30µm layer has been removed from the nucleation side. The thickness of DoI724b (bottom left and right data) was optimized for Transient-Current Technique (TCT) measurements with ^{241}Am-α-particles: an iridium mesh was added in the depth of the α-range providing $d_D \approx 12\mu m$.

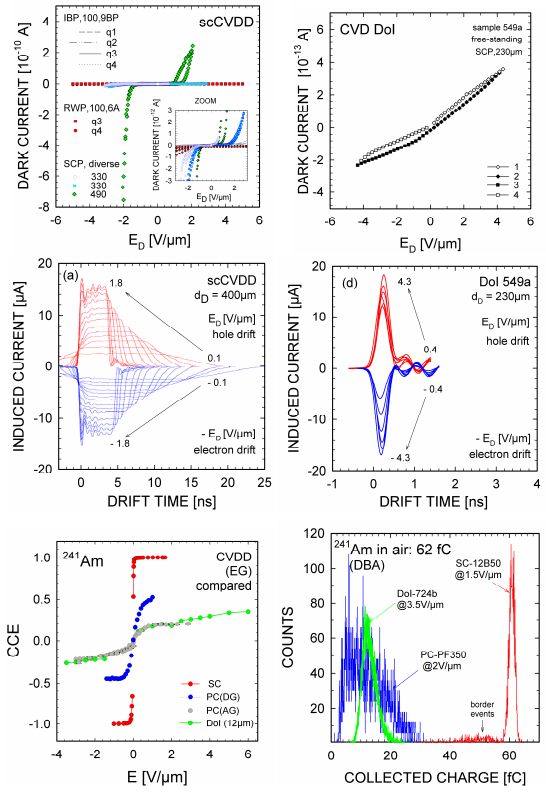

Figure 1: Characteristics of early DoI samples compared to scCVDD and pcCVDD: (top) $I_{dark}(E_D)$ curves; (central) TCT for internal E_D profile, charge-drift, and trapping; (bottom-left) Charge-Collection Efficiency (CCE) vs. E_D; (bottom-right) Collected Charge distributions.

The unexpected low dark current of DoI films is discussed in the next section. The triangular TCT signals (Fig. 1, central-right) demonstrate significant trapping of the excess charge in the vicinity of generation. The charge losses are due to the high dislocation density of present DoI CVDD [2]. In contrast, the trapezoidal signals of defect free scCVDD samples (Fig. 1, central-left) confirm a homogeneous internal field and full drift of the ionized charge to the opposite electrode. The CCE ≈ 0.4 measured for DoI724b (Fig.1 bottom-left) is presently as high as of 'as grown' (AG) pcCVDD. However, the energy resolution (Fig.1, bottom right) is significantly better, even compared with 'detector grade' (DG) pcCVDD, confirming homogeneously distributed dislocations. The amplitudes of the TC signals are similar to those of best scCVDD sensors (Fig.1, central-right and left plots). Excellent heavy-ion timing at ion rates >> 10^9ions/s is expected by minimizing detector and stray capacitances.

Electrical Conduction

We studied the dark current behaviour of DoI549a in the electric field range - 4.3 ≤ E_D [V/µm] ≤ 4.3 at temperatures from 300 K to 673 K. Two types of sandwich electrodes were tested (in vacuum): a) both sides ohmic (i.e. Ti-Pt-Au metallization); b) one side blocking (pure Al), second one same as a). As in previous studies of scCVDD [3] we found the IV characteristics of DoI films up to T = 400 ^{0}C independent of the contact metal. However, the high activation energy of 1.53 eV extracted from Arrhenius plots suggests minor contribution of the bulk defects to the dark current and points to an 'interface-controlled' conduction mechanism. We applied dedicated fitting to the data, due to which eventually pure field emission (Fowler-Nordheim) or pure trapping-detrapping (Poole-Frenkel) conduction could be excluded, while a mixing of various processes appears most likely, with Schottky Emission the dominant mechanism at temperatures 472 K - 672 K and fields E_D >1 V/µm. Similar barrier heights $\Phi_b \approx (1.72 \pm 0.01)$ eV have been estimated for both electrode types. The studies are ongoing.

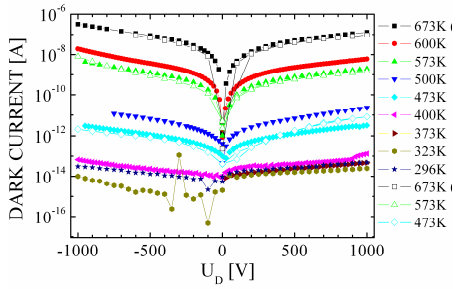

Figure 2: $I_D(U_D)$ at high temperatures. a) solid symbols: ohmic/ohmic b) open symbols: ohmic/blocking contacts.

References

[1] S. Gsell et al., Appl. Phys. Lett. 84 (2004) 4541
[2] E. Berdermann *et al,* Diam. Relat. Mater. (2009), doi:10.1016/j.diamond.2009.11.019
[3] M. Pomorski, *PhD thesis,* Univ. of Frankfurt (2008)

*Supported by EC: Projects HadronPhysics2 and MC-PAD.

An RFQ Cooler – Mass Filter – Buncher System for Experiments with Fusion-Evaporation Products*

E. Haettner[1,2], U. Czok[1], T. Dickel[1], H. Geissel[1,2], W. Kinsel[1,2], F. Lautenschläger[1], M. Petrick[1], W. R. Plaß[1,2], T. Schäfer[1], C. Scheidenberger[1,2], R. Thöt[1], and J. Werner[1]

[1]Justus-Liebig-Universität Gießen, Germany; [2]GSI, Darmstadt, Germany

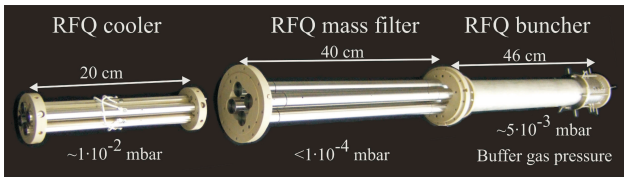

Figure 1: Photo of the RFQ cooler – mass filter – buncher system. The gas pressures (He) are chosen such that buffer gas cooling is effective in the RFQ cooler and the buncher, but that the performance of the mass filter is not compromised.

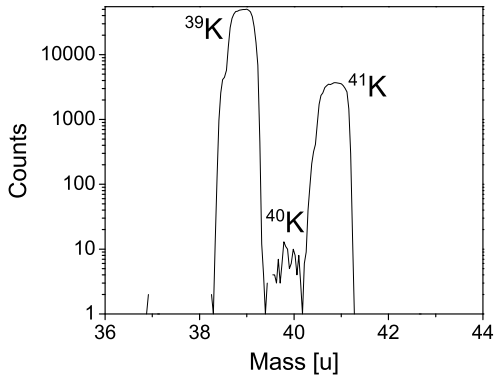

Figure 2: Separation of $^{39-41}$K isotopes in the mass filter. The different intensities correspond to the natural abundances of the isotopes.

At the Penning trap facility SHIPTRAP mass measurements of transfermium elements as well as nuclides in the vicinity of the proton drip-line have been performed [1, 2]. Going towards even more exotic proton-rich elements, the SHIPTRAP experiment is hampered by the abundant unwanted reaction products. In order to quickly identify the ions produced, to select the nuclei of interest out of all fusion products and to increase the sensitivity of the experiment, an RFQ mass filter has been developed in a matched combination with an RFQ cooler and RFQ buncher.

Instrumental developments. The RFQ cooler, mass filter and buncher have been designed [3, 4] and built, see figure 1. The mass filter is constructed out of round rods with a diameter of 18 mm and uses Brubaker lenses [5] at its entrance and exit. Special care has been taken to assure that the cooler and mass filter have the best possible alignment, in order to avoid a degradation in resolution and transmission. A control system for operation of the mass filter at a fixed working point (mass selection), in 1D scanning mode (acquisition of mass spectrum) or 2D scanning mode (mapping of stability diagram) has been developed. The RF voltages are generated by high-quality resonance circuits. Since the RF amplitude is easily affected by e.g. temperature changes and the stability of RF amplitude has a direct impact on the achievable resolution and transmission, an effort has been made to stabilize the RF voltages to the 0.1 % level. Electronic circuits for precise measurement of the RF amplitude has been developed, and a PID controller has been implemented to the control program.

The RFQ buncher consists of a 40 cm cooling section, in which the axial field is created by additional DC rods [6], and a trapping section consisting of 5 segments. These allow the user to increase the efficiency by implementing a pretrap.

Experimental results. The cooling properties of the RFQ cooler have been investigated and found to be in agreement with theory. An longitudinal energy spread of less than 0.2 eV can be obtained.

The mass resolution of the mass filter as a function of transmission has been measured and the stability diagram of the mass filter has been mapped. A mass resolving power (FWHM) of 60 with 90 % transmission and a resolving power of 150 at a transmission of 65 % have been reached for the cooler – mass filter – combination. The separation and supression of neighboring masses was investigated using a potassium ion source. A supression of neighboring mass lines by a factor of 10^4 was demonstrated, see figure 2.

Outlook. The commissioning of the complete RFQ system is scheduled for the first half of 2010. The system will extend the reach of SHIPTRAP to very proton-rich nuclides such as the N=Z nuclides ^{80}Zr and ^{84}Mo, which can be produced at SHIP with sufficient rates but so far cannot be separated effectively from other more abundant reaction products.

References

[1] C. Rauth *et al.*, Phys. Rev. Lett., 100, 012501 (2008).

[2] M. Block *et al.*, Nature, in print (2010).

[3] E. Haettner *et al.*, GSI Scientific Report 2007 (2008) 210.

[4] J. Werner, Bachelor Thesis, JLU Gießen, 2008.

[5] W.M. Brubaker, Adv. in Mass Spectrom., 4 (1968) 293.

[6] A. Loboda *et al.*, Eur. J. Mass Spectrom. 6 (2000) 531.

* Work supported by the BMBF under contract No. 06GI185I.

Ion-Optical Studies for an ESR In-Ring Spectrometer Mode

C. Brandau *[1,2], Th. Faestermann[1], R. Krücken[1], P. Egelhof[2], H. Geissel[2,3], R. Gernhäuser[1], N. Kalantar-Nayestanaki[4], S.A. Litvinov[2], L. Maier[1], Ch. Scheidenberger[2,3], M. Steck[2], H. Weick[2], and the EXL collaboration

[1]TU München; [2]GSI Darmstadt; [3]Universität Gießen; [4]KVI Groningen, Netherlands

Complementary to classical single-pass arrangements the use of storage rings for nuclear reaction studies offers some decisive advantages [1]. The circulating ions repeatedly interact with the target atoms at a high frequency (1-3 MHz) and thus provide a reasonable luminosity even at small numbers of projectile ions and/or low target densities. The stored ion beam is electron cooled, possesses very small emittances and a well-defined sharp initial momentum,—ideal prerequisites for high-resolution particle spectroscopy. It is thus appealing to utilize the storage ring bending dipoles as a magnetic spectrometer in order to identify recoil nuclei and to measure their momentum distributions. An optimal momentum resolution can be achieved if either an ion optical image between the reaction volume (internal target) and the detector position behind the first dipole exists or if the reaction products are tracked one-by-one on their flight path. The two approaches can be used exclusively but ideally they are applied complementarily to each other. We have investigated both possibilities for the present ESR, i.e., development of a new ion optical setting ("spectrometer mode") as well as the design of a tracking system that can be operated under the strict UHV vacuum conditions and that is non-destructive for the circulating primary beam. Ideally, such a detector consists of as little material as possible in order to minimize straggling. This excludes the use of standard vacuum pockets with entrance and exit windows. We therefore are considering a thin-foil detector, where secondary electrons are guided with the aid of a longitudinal magnetic field towards a micro channel plate. The arrangement is similar to the one described in [2] but with the B-field provided by a set of Helmholtz coils located outside the vacuum.

In the following we discuss the possibility of a new ion optical setting for the ESR in more detail. The task to calculate such a new mode is challenging since the ESR has never been designed under the premise of the use as a momentum spectrometer. Type and position of the ion optical elements and detector pockets are pre-determined and cannot be changed. At the same time, a circular accelerator such as a storage ring requires a multitude of boundary conditions with respect to injection and stable orbiting of the beam to be fulfilled [3]. Figure 1 presents horizontal and vertical plane of one quarter of the ESR for a potential spectrometer mode candidate. Ion trajectories starting at the internal gas-jet target are displayed that indicate the image from jet to detector. Reaction products in a cone of ± 15 mrad in horizontal and ± 2 mrad in vertical direction can be guided to the detector whereas the small angle in vertical direction is mainly given due to the height of the dipole gap. The dispersion at the position of the particle detector $\Delta x/\Delta(B\rho)/(B\rho) = 9.9\mathrm{cm}/\%$ is roughly 50 % higher than the one in the ESR standard setting. Accordingly, the momentum acceptance of the ring is reduced from $\pm 1.5\%$ to about $\pm 1.0\%$. A tilt of the image plane by 16.9° due to chromatic abberation is inevitable and cannot be corrected for using the existing hexapole magnets. Albeit large at first sight this tilt does almost not hamper the momentum resolution. It can be fully avoided if detectors/detector pockets are mounted under the same angle. The main downside of the new setting is the large septum and kick angles during injection of the beam which are 1.5 times higher than for the present standard mode. This might limit the maximum magnetic rigidity of the injected particles and/or reduce their intensity. The present calculations are a very encouraging start to further fine-tune the settings, work towards ion-optical test experiments in 2010—and on success—to prepare a first proof-of-principle run soon afterwards.

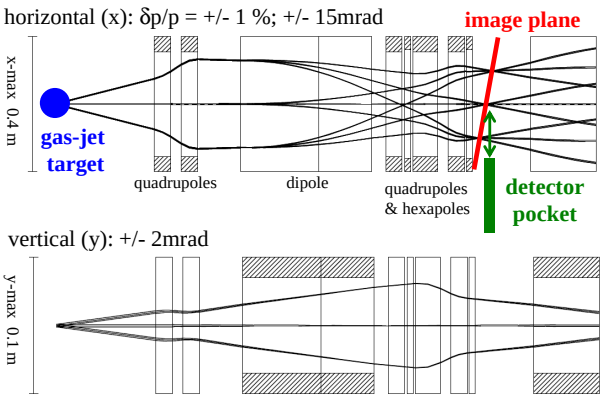

Figure 1: Ion trajectories in the new ESR "spectrometer mode" for one quarter of the ring. The new setting features an image of the reaction volume at the internal jet target at the position of the particle detector. Due to chromatic aberration the image plane is tilted by 16.9°.

References

[1] EXL Letter of intent/Technical Report on http://www.gsi.de/fair/experiments/NUSTAR/Proposals.htm

[2] D. Shapira et al., NIM A **454** 409 (2000).

[3] H. Wiedemann, "Particle Accelerator Physics", 3rd edition, 2007, Springer Verlag, Berlin, Heidelberg, New York.

* C.B. acknowledges support by GSI Darmstadt (F&E) under contract number TM/KRUE.

Drift chambers for the HypHI project

E. Kim*[1,2], D. Nakajima[1,3], B. Özel-Tashenov[1,4], S. Bianchin[1], O. Borodina[1,5], V. Bozkurt[1,4], B. Göküzüm[1,4], S. Kim[1], Y. Ma[5,6], S. Minami[1], C. Rappold[1,7], and T.R. Saito[1,5]

[1]GSI, Darmstadt, Germany; [2]Seoul National University, Seoul, Korea; [3]Tokyo University, Tokyo, Japan; [4]Nigde University, Nigde, Turkey; [5]Mainz University, Mainz, Germany; [6]Tohoku University, Sendai, Japan; [7]Strasbourg University, Strasbourg, France

The HypHI project aims to perform the precise hypernuclear spectroscopy with stable heavy ion beams and rare isotope beams at GSI and FAIR in order to study hypernuclei at extreme isospin and measure hypernuclear magnetic moment directly [1]. As the first experiment of the HypHI project, the Phase 0 experiment was performed in August and October 2009 to demonstrate the feasibility of the experimental methods with ^{6}Li beams at 2 A GeV impinging on a ^{12}C target [2].

In the experiment, two drift chambers from KEK were installed for tracking charged particles. The small drift chamber was placed between scintillating fiber detectors (TR1 and TR2) [3], and the big drift chamber was placed behind the ALADiN magnet. The component plane, active area and drift length of the chambers are listed in Table 1.

Chamber	Active area [cm^2]	Plane	Drift length [mm]
Small	24(W)×14(H)	xx' (vertical)	2.5
		uu' (-15^o)	2.5
		vv' (15^o)	2.5
Big	120(W)×90(H)	XX' (horizontal)	4.5
		YY' (vertical)	4.5
		U (45^o)	9.0

Table 1: Specifications of drift chambers.

The gas mixture for both chambers was Ar (70 %) + CO_2 (30 %) at atmospheric pressure. In the small chamber, the high voltages were 1.53 kV for potential wires and 1.42 kV for cathode planes. In the big chamber, 2.20 kV (XY) and 2.43 kV (U) for potential wires and 1.48 kV (XY) and 1.59 kV (U) for shields were applied.

These chambers are designed to be operated up to 10^5 particles per second per wire. However, since these drift chambers were located on the beam axis and ^{6}Li beams with an intensity of 10^7 particles per second were used in the experiment, an insensitive area for the beam particles was implemented for both drift chambers with different techniques.

For the small chamber, the sense wires in the beam region (1.5 cm $\times$ 1.5 cm) were wrapped with teflon sheets (refer to Figure 1). Before the experiment, the insensitivity in that region was studied with ^{90}Sr β-source. It showed a total efficiency with all six planes of 2.2 $\times$ 10^{-4} and an efficiency per plane of 0.25 $\pm$ 0.04. In addition, another method by attaching mylar tapes on the cathode planes was applied to improve the insensitivity.

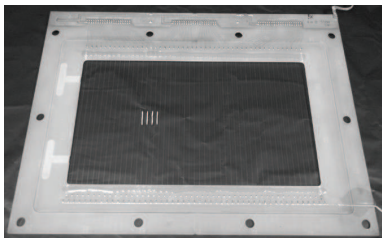

Figure 1: Taflon-wrapping to make the sense wire insensitive in the small chamber

For the big chamber, the beam region was made insensitive by connecting the sense wires and the potential wires to remove the electric field around the sense wires. With these techniques, both of the drift chambers have been operated with an beam intensity of up to 5×10^6 per second.

Logic signals from the discriminators of the drift chambers are to the newly developed universal logic modules VUPROM2 [4], and time information were recorded with a granularity of 2.5 ns.

References

[1] T.R. Saito *et al.*, Letter Of Intent of HypHI.

[2] T.R. Saito *et al.*, Proposal of the HypHI Phase 0 experiment, submitted to G-PAC 33

[3] D. Nakajima, B. Özel-Tashenov *et al.*, in these reports.

[4] S. Minami *et al.*, GSI Scientific Report 2007, GSI, Darmstadt, 2008, p223.

* e.kim@gsi.de

Scintillating fiber detectors for HypHI Phase 0 experiment *

D. Nakajima[†1,3], B. Özel-Tashenov[‡1], S. Bianchin[1], O. Borodina[1,2], V. Bozkurt[1], B. Göküzüm[1], M. Kavatsyuk[4], E. Kim[1,5], S. Minami[1], C. Rappold[1,6], T.R. Saito[1,2], P. Achenbach[2], J. Hoffmann[1], K. Koch[1], N. Kurz[1], F. Maas[1,2], W. Trautmann[1], and S. Voltz[1]

[1]GSI, Darmstadt, Germany; [2]Mainz University, Mainz, Germany; [3]Tokyo University, Tokyo, Japan; [4]KVI, Groningen, The Netherlands; [5]Seoul National University, Seoul,Korea; [6]Strasbourg University, Strasbourg, France

The first step of the HypHI project (Phase 0) has been performed in order to demonstrate the feasibility of precise hypernuclear spectroscopy with heavy ion induced reactions. In the experiment, light hypernuclei such as ${}^{3}_{\Lambda}$H, ${}^{4}_{\Lambda}$H and ${}^{5}_{\Lambda}$He are produced by induced reaction of ^{6}Li at 2 A GeV on a ^{12}C target, and the hypernuclei events are reconstructed by observing π^- decay channels by means of the invariant mass spectroscopy [1, 2]. In the Phase 0 experiment, three sets of two dimensional Scintillating fiber (SciFi) detectors ,TR0xy, TR1xy and TR2xy, are used to track charged particles behind the carbon target. They are also used to produce secondary vertex triggers to the data aquisition system [3]. Figure 1 shows the schematic layout

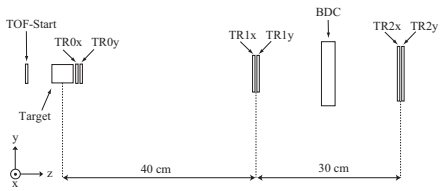

Figure 1: The schematic layout of the detector system in upstream of the spectrometer

of the experimental setup in front of the ALADiN magnet. TR0 is mounted right behind the graphite target, and TR1 and TR2 placed with distances of 40 cm and 70 cm, respectively, from the target. Each set consists of x and y plane for the horizontal and vertical tracking. In between TR1 and TR2, a drift chamber with six layers (BDC) was mounted to solve a stereo ambiguity in track finding process. Readout of scintillating photons is performed with H7260KS MOD (Hamamatsu) 32 channel multi-anode photomultiplier tube (PMT), which is an improved version of the commercial PMT H72690. It has grids in the glass window in front of the photo-cathode to separate each channel in order to reduce cross talks, and has booster cables in the last three dynode stages to stabilize the voltage under high beam intensity[4]. Analog signals from PMT are processed by a double-threshold discriminators (DTDs) from the MAMI KaoS collaboration to create LVDS logic signals. The timing information of leading- and trailing- edge of the LVDS logic signals were recorded by VUPROM2 which is a newly developed VME logic module with a FPGA running at 400 MHz. In addition, charge information of TR0 was stored by charge sensitive analog-to-digital converters (QDCs) to distinguish particles with different charges, Z = 1, 2 and 3, from their energy deposition in order to reduce background events [1].

A group of neighboring fired channels are clustered and hit position is calculated from the center of gravity of the hit cluster. The position resolution is defined as a width of the residual distribution, which is the distribution of distance between measured hit positions and track position extrapolated by the other detector. Figure 2 shows the residual hit position distribution at TR1 for the tracks extrapolated by TR0, TR2 and BDC for particles with Z = 1. Although further calibration has to be carried out, a position resolution of $\sim$ 0.47 mm in σ for particles with Z = 1 has been already achieved, which is close to the expected resolution[4]. For particles with Z = 2 and 3, position resolutions of 0.56 mm and 0.28 mm in σ have been achieved.

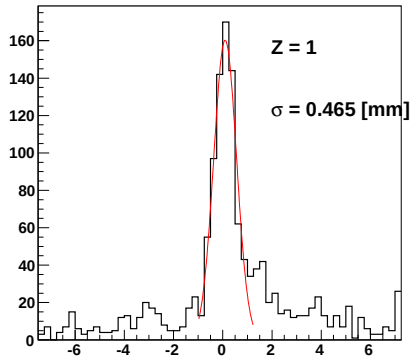

Figure 2: The residual distribution of the hit position at TR1 from the track extrapolated by TR0 and TR2 for particles with Z = 1.

References

[1] T.R. Saito *et al.*, Letter Of Intent of HypHI.

[2] T.R. Saito *et al.*, in these reports.

[3] S. Minami *et al.*, in these reports.

[4] D. Nakajima and B. Özel-Tashenov *et al.*, Nucl. Inst. Meth. A 608 (2009) 287-290

* The HypHI project is supported by the Helmholtz Association as Helmholtz University Young Investigators Group VH-NG-239 and by DFG with the research grant SA 1696/1-1.

† d.nakajima@gsi.de

‡ b.oezel@gsi.de

Performance of the trigger system at the HypHI Phase 0 experiment

S. Minami*[1], C. Rappold[1,2], S. Bianchin[1], O. Borodina[1,3], V. Bozkurt[1,4], B. Göküzüm[1,4], J. Hoffmann[1], M. Kavatsyuk[5], E. Kim[1,6], N. Kurz[1], D. Nakajima[1,7], W. Ott[1], B. Özel-Tashenov[1,4], T. Saito[1,3], and W. Trautmann[1]

[1]GSI, Darmstadt, Germany; [2]IPHC, Université Louis Pasteur,Strasbourg, France; [3]Institut für Kernphysik, Johannes Gutenberg-Universität, Mainz, Germany; [4]Nigde University, Nigde Turkey; [5]KVI, Groningen, The Netherlands; [6]Seoul National University, Seoul, Korea; [7]The University of Tokyo, Bunkyo, Japan

The first experiment of HypHI project, phase 0, has been performed at October 2009 to detect hypernuclei produced by a 2.0 *A* GeV ^{6}Li beam impinging on a ^{12}C target, by identifying the mesonic decay modes, $^{3}_{\Lambda}$H $\rightarrow ^{3}$He + π^-, $^{4}_{\Lambda}$H $\rightarrow ^{4}$He + π^- and $^{5}_{\Lambda}$He $\rightarrow ^{4}$He + p + π^- [1]. A high intensity beam of 10^6 $\sim 10^7$ particles per second and a target with a thickness of 8 g/cm^2 were used to overcome small production cross sections expected to be of the order of 0.1 μb. The challenge of the trigger system was to derive a fast trigger signal with a event rate up to 3 kHz under the experimental conditions.

Table 1: The conditions for the each trigger, the minimum-bias trigger (MBT), the reaction trigger (RT), the hypernuclear trigger(HT) and the He hypernuclear trigger (HeHT).

Trigger		MBT	RT	HT	HeHT
Vertex	Mul.$\geq$1			on	on
	Mul.$\geq$2				on
TR012	Mul.$\geq$1	on	on	on	on
TR1	Mul.$\geq$2		on	on	on
TOF+	Mul.$\geq$1		on	on	on
	Mul.$\geq$1 for He			on	on
TOF-	Mul.$\geq$1			on	on
TOFs	Mul.$\geq$1	on	on	on	on
	Mul.$\leq$2			on	on
Scaling factor		1.5×10^{-5}		1	
Mixed Trigger 1		on	on	on	
Mixed Trigger 2		on	on		on

The main feature of the trigger system is to select events with decay vertices located 20 cm in average behind the target (Vertex)[2]. It has been realized by applying sophisticated coincidence conditions to three layers of the fiber detector, TR0, TR1 and TR2 [3] using 38 VUPROMs [4]. The all three decay modes are associated with a pion and a helium, which was also utilized by requesting larger energy deposit by a helium on positive side of the TOF wall (TOF+) and at least one hit at negative side (TOF-)[5]. Furthermore, the TOF start counter[5] participated in the trigger system to define the beam and to veto events with more than 2 particles due to high beam intensity (TOFs). The conditions applied for the each detector are summarized in Table 1. The data have been stored with 2 types of the mixed trigger. One is for all decay modes with some calibration data (Mixed Trigger 1) and the other is focused on the He hypernuclei with higher beam intensity requesting 2 tracks from decay vertices (Mixed Trigger 2). The trigger rate by 'Mixed Trigger 1' gave typically the rate of 2.6 kHz with the beam intensity of 3.2×10^{6} per second and that by 'Mixed Trigger 2' gave 0.66 kHz with the beam intensity of 8.2×10^{6} per second.

The figure 1 shows the hit position distribution along the y-axis on TR2. The trigger system judged the hits plotted in the dashed histogram as ones by particles from the target, while the hits in the filled histogram as ones from decay vertices. It is appropriate that the peak by the Li beam is counted as the particles from the target. The decisions by the trigger have been compared with offline analysis applying the same coincidence matrix used for trigger. The results show that 79 % of trigger decision are consistent and 0.75 % are inconsistent. There are 20 % cases difficult to judge because of lacking information at intermediate stage of coincidence, however it is enough to conclude that there were no mistakes one might expect, i.e. the order of channels, the coincidence matrix, cabling and timing. The trigger system has achieved the experimental request and been successfully operated during the Phase 0 experiment.

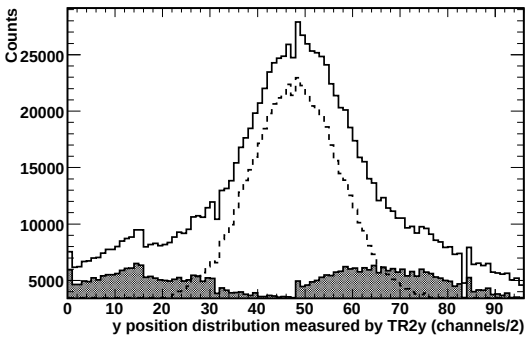

Figure 1: The hit position distribution along the y-axis on TR2, all hits (the solid histogram), particles scattered from the target (the dashed histogram), particles from the decay vertices (the filled histogram).

References

[1] T.R. Saito *et al.* in these reports.

[2] S. Minami *et al.* GSI Scientific report 2008 p51

[3] D. Nakajima, B.Özel-Tashenov *et al.* Nucl. Inst. Meth. A 608 (2009) p287

[4] J. Hoffmann *et al.* GSI Scientific report 2007 p256

[5] C. Rappold *et al.* GSI Scientific report 2007 p221

[6] S. Bianchin *et al.* GSI Scientific report 2008 p233

* s.minami@gsi.de

Performance of the time-of-flight detectors for the HypHI Phase 0 experiment

S. Bianchin[1], O. Borodina[1,2], V. Bozkurt[1,3], B. Göküzüm[1,3], M. Kavatsyuk[4], E. Kim[1,5], S. Minami[1], D. Nakajima[1,6], B. Özel-Tashenov[1,3], C. Rappold[1,7], T.R. Saito[1,2], and W. Trautmann[1]

[1]GSI, Helmholtz Center for Heavy Ion Research, Darmstadt, Germany; [2]Johannes Gutenberg Universität Mainz, Mainz, Germany; [3]Nigde University, Nigde, Turkey; [4]KVI, Groningen, The Netherlands; [5]Seoul National University, Seoul, Korea; [6]The University of Tokyo, Tokyo, Japan; [7]Université Louis Pasteur, Strasbourg, France

The HypHI phase 0 experiment of the HypHI project [1], performed in October 2009 at GSI, is devoted to demonstrating the feasibility of a precise hypernuclear spectroscopy by using heavy ion reactions.
In the Phase 0 experiment, we concentrate on studying light hypernuclei such as ${}^{3}_{\Lambda}$H, ${}^{4}_{\Lambda}$H, ${}^{4}_{\Lambda}$He produced by collisions of a ^{6}Li beam at 2 AGeV with an intensity of 10^7 particles per second on a thick carbon target (8g/cm^2).

The experimental setup of the phase 0 experiment consists of the large acceptance dipole magnet ALADiN, the start detector in front of the target, three arrays of scintillating fiber tracking detectors [2], the ALADiN and the LAND time-of-flight walls used for the detection of π^- and the TOF+ wall devoted to the detection of positively charged particles. In addition, two drift chambers from KEK are placed in front of and behind the magnet in order to increase the tracking redundancy [3].
For the purpose of this report, only the results obtained for the time-of-flight detectors designed and built by the HypHI collaboration , namely the TOF+ wall and the start detector, are discussed.

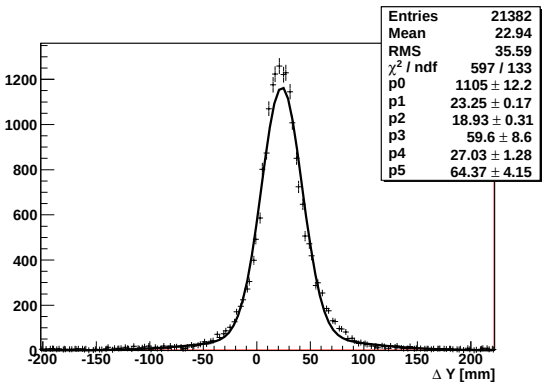

Figure 1: Y position difference between two overlapping bars of the TOF+ wall. The shift of the peaks from zero is due to a lack of absolute position calibration.

The TOF+ wall [4] consists of two layers of 16 plastic scintillator bars read on both sides by photomultiplier tubes. The active area of this detector is about 1 m^2. A hole (7.5 x 6.5 cm^2) has been arranged to allow the passage of the beam through the detector.
Due to the overlap between the two layers of scintillating plastic detectors, the X position resolution (perpendicular to the beam direction in the bending plane) is 15 mm. The Y position resolution deduced from coincidences between two overlapping bars (Fig. 1) is about 31 mm (FWHM) for one bar.
The time resolution for each bar is determined by measuring the time of flight between two overlapping bars. The time resolution after walk corrections is ~ 300 ps (FWHM) (Fig. 2).
The start detector allowing a precise measurement of the time of flight of the particles produced by the decay of hypernuclei consists of 10 scintillating plastic fingers read on both sides by photomultiplier tubes [5]. The observed time resolution of the start counter for ^{6}Li is ~ 300 ps (FWHM).

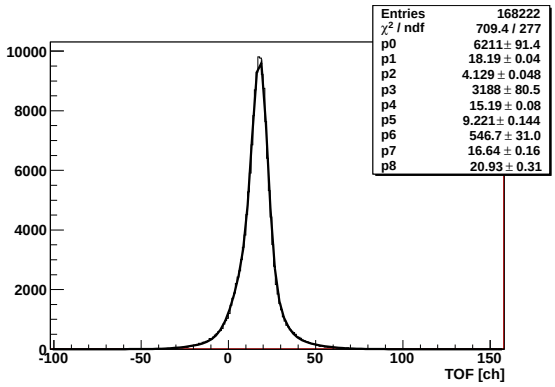

Figure 2: Time of flight measured between the two overlapping bars. The histogram is fitted by a function which is the sum of three gaussians.

References

[1] T.R. Saito *et al.*, Proposal of the HypHI Phase 0 experiment, submitted to the G-PAC 33 with a realization as S319.

[2] D. Nakajima, B. Özel-Tashenov *et al.*, in these reports.

[3] E. Kim *et al.*, in these reports.

[4] C. Rappold *et al.*, GSI Scientific Report 2006, p. 222.

[5] S. Bianchin, O. Borodina *et al.*, GSI Scientific Report 2008, p. 233.

Recent detector developments at the FRS

A. Ay[1], K.-H. Behr[1], A. Brünle[1], F. Farinon[1], H. Geissel[1], R. Janik[2], C. Karagiannis[1], A. Kelić-Heil[1], A. Kratz[1], J. Kurcewicz[1], I. Mukha[1], C. Nociforo[1], S. Pietri[1], A. Prochazka[1], M. V. Ricciardi[1], C. Scheidenberger[1], B. Sitar[2], P. Strmen[2], I. Szarka[2], S. Terashima[1], H. Weick[1], J.S. Winfield[1], M. Winkler[1], and I. Wischert[1]

[1]GSI, Darmstadt, Germany; [2]Comenius University, Bratislava, Slovakia

The GSI projectile Fragment Separator (FRS) [1] has proved to be a versatile and powerful tool for production of exotic isotopes. Several crucial experiments have been performed and many milestones of the nuclear physics have been reached over the last 20 years FRS is running. Nevertheless operation of such facility requires continuous improvement and development. In this contribution we report on recently performed test experiments focused on detectors development. Three such test were performed in 2009 namely in March ($^{96}Ru^{42+}$+^{9}Be@500 MeV/u), August ($^{56}Fe^{25+}$ + ^{9}Be @350 MeV/u) and October ($^{238}U^{92+}$ + ^{9}Be @750 MeV/u). In parallel to the detector development explained below, other NUSTAR detector systems were either tested or commissioned during those runs [2].

MUSIC

The multiple sampling ionisation chamber (MUSIC) [3] is a standard detector used for almost all experiments performed at the FRS. The energy loss signal of the fragments is used for the reconstruction of their atomic number. In the recently performed experiment the energy loss signal of the Uranium fragments registered at the last focal plane (S4) of the FRS was detected using MUSIC filled with CF_4 or P10 gases. The data were recorded applying the $B\rho$ setting of the FRS optimised for yielding high beam intensity of ^{205}Pb. In case of P10 filling gas the width of the energy loss signal distribution decreases for the heaviest species by a factor of 0.6 comparing to the standard CF_4. Thus one of two different running modes can be chosen for measurement involving the heaviest Uranium fragments depending if good signal resolution or high loads handling is of greater importance.

Several improvement to the standard velocity calibration has been made yielding a more reliable charge reconstruction.

Scintillators

Together with the information used from the ionisation chambers, to achieve full fragment identification in mass and atomic number the velocity of the fragment needs to be measured through the FRS. This is done by a time-of-flight (ToF) measurement between the second (S2) and fourth focal plane (S4). The normal system composed of two plastics (BC420) with fast PMT cannot assure a perfectly clean identification for the higher masses (see identification spectrum of Uranium fragments [4]). To improve this several tests were performed during the FRS000 beam time blocks. As a first step the ToF was duplicated in order to increase the resolution by the inverse of the square root of two. In addition BC422Q plastics were tested. They exhibit a faster time signal albeit suffer from larger light attenuation. No improvement were seen with this type of material. The faster timing were cancelled by the smaller light yield due to the larger detector size needed to cover the focal plane, and the high light attenuation of those materials. A linear REPIC photo transmitter/receiver, allowing the transfer of PMT signals from the focal planes to the Messhütte, through optical fibers was tested as well.

TPC

The Time Projection Chamber (TPC) became a standard tracking detector for the FRS. Up to now TPCs were used only in air but it is foreseen for a vacuum use as well. We have developed and successfully tested a TPC modified version for vacuum together with a new calibration scintillator for vacuum. We have developed a new calibration procedure with a software coincidence between calibration scintillators and the master trigger, which allows a faster TPC online calibration.

DAQ

A novel FRS DAQ based on a multi-event DAQ mode was tested at the FRS. A gain in data flow processing up to the factor of 2 was experimentally achieved for a count rate reaching about 3000 events/s. This result can be still improved after the upgrade of the VME send processor to the newer RIO-4 release version. For a more detailed description of the recent developments of the FRS DAQ system see Ref. [5].

Summary

Several improvements of the standard FRS detectors, operation modes, calibration procedures and data acquisition system have been achieved in the lately performed test experiments. The recent developments are first of all a basic step towards the studies of the most exotic nuclei being a more and more challenging experimental task [4]. They can also be considered important preparatory work for the Super-FRS at FAIR.

References

[1] H. Geissel et al. NIM B 70, (1992) 286.
[2] R. Hoischer et al., this report.
[3] R, Schneider, A. Stolz http://www-w2k.gsi.de/frs/technical/FRSsetup/detectors/music.asp
[4] J. Kurcewicz et al., this report.
[5] C. Nociforo et al., this report.

Development and test of Isomer TAGging detector

F. Farinon[1,2], I. Kojouharov[2], C. Nociforo[2], S. Pietri[2], K-H. Behr[2], A. Brünle[2], H. Geissel[1,2], C. Karagiannis[2], J. Kurcewicz[2], A. Prochazka[1,2], M.V. Ricciardi[2], C. Scheidenberger[1,2], H. Weick[2], J.S. Winfield[2], and M. Winkler[2]

[1]Justus-Liebig-Universität Giessen, Germany; [2]GSI, Darmstadt, Germany

ITAG (Isomer TAGging detector) is a composite detector developed for isotope identification by isomer tagging at the FRagment Separator (FRS) facility [1]. It is placed at the final focal point of FRS and detects γ-rays emitted from isomeric decay of fragments implanted into its stopper. The on-line analysis recognizes the γ-lines pattern, allowing to identify the isomers and later all the secondary fragments.
ITAG consists of two movable Germanium (Ge) detectors mechanically cooled, two plastic scintillators and an exchangeable passive stopper (Fig. 1). The whole system can be lift up from the beam line to protect the detectors from radiation damage. As further protection, the Ge crystals are shielded by a 50 mm thick lead layer. The Ge crystals are mounted on moving tables to get as close as possible to the stopper maximizing the photopeak efficiency, that ranges from 0.4% at 90 mm to 0.2% at 150 mm for γ-rays of 1.3 MeV. Each Ge-crystal was installed in a specially developed cryostat [2] based on electromechanical cooling engine X-Cooler II produced by ORTEC [3]. The cooling system was tested by scanning the whole volume of the crystal with collimated γ-sources. The energy resolution (FWHM $\approx$1.2 keV at 60 keV) was found to be constant and in good agreement with the expectation, proving the uniformity of temperature and sufficient cooling.
The plastic scintillators (BC400, 1 mm thickness) are used to count the particles and to control their implantation in the stopper. The second scintillator acts as veto detector.

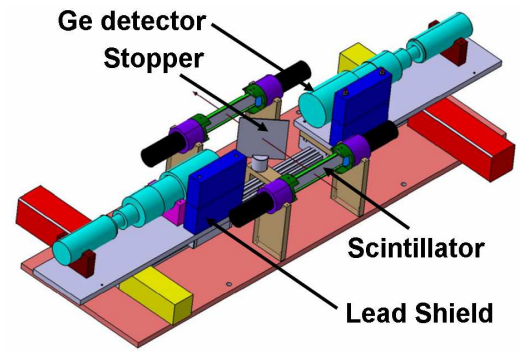

Figure 1: Schematic drawing of ITAG detector.

During an FRS000 experiment, a primary $^{96}Ru^{42+}$ beam at an energy of 500 MeV/u and a maximum intensity of $\sim 10^5$ ions/s impinged on a 2.5 g/cm^2 Be target. The FRS was used in achromatic mode and optimised for the transmission of ^{94}Ru ions. The ions were slowed down and implanted into the 3 mm thick Al stopper of ITAG. The identication of the reaction products was performed using the standard time of flight and energy loss techniques [4] and the ITAG. The time difference between an ion passing the first scintillator and its γ decay was measured using a $Time\text{-}to\text{-}Analog$ Converter (TAC). Figure 2 shows the on-line analysis steps: the selection of a fragment in the identification matrix (A); a selected fragment γ-energy and time correlation matrix (B); the energy (C) and time (D) projection of this matrix after removing of the prompt flash (x-rays emitted during the implantation phase) and comparison of eventually gamma lines and half-lifes obtained with the known ones. Two isomers (^{90}Mo and ^{92}Tc) were identified using this procedure and the results are listed in the table below. After its commisioning the ITAG is now available as a standard FRS detector for future experiments.

	Production	γ-counts	γ-lines (MeV)	$T_{1/2}$ (μs)
^{92}Tc	1.3×10^5	95	214.2 ± 2.9	1.04 ± 0.3
^{90}Mo	8.6×10^4	180	809.9 ± 3.0 947.7 ± 3.0 1053.9 ± 3.1	1.13 ± 0.16

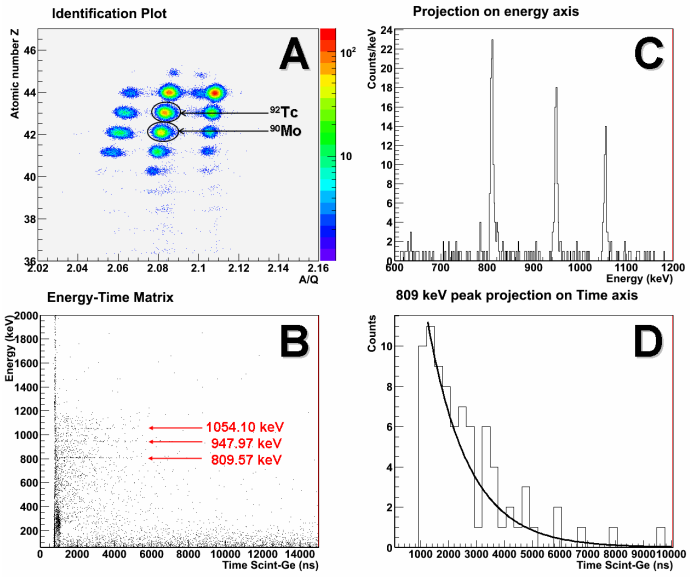

Figure 2: On-line analysis steps: identification matrix (A); ^{90}Mo γ-energy and time correlation matrix (B); ^{90}Mo gamma lines (C) and ^{90}Mo half-life (D).

[1] H. Geissel et al., NIM B70, 286-297 (1992).
[2] I. Kojouharov et al., GSI Scientific Report 2008, 235.
[3] ORTEC *X-Cooler II*. http://www.ortec-online.com.
[4] B. Voss et al., Nucl. Inst. Meth. A364 (1995) 150.

Scanner for gamma-ray detectors

N.Goel, C.Domingo-Pardo, T.Engert, J.Gerl, I.Kojouharov and H.Schaffner
GSI, Darmstadt, Germany

The core principle of segmented detectors like AGATA [1], GRETA [2], that will be used in future for 4π gamma detection arrays, is the application of the concept of pulse shape analysis (PSA). The key ingredient for this analysis is a data base containing pulses for all the interaction points inside the segmented detector. A full 3D scanning of the detectors, which experimentally determines pulse shapes for every given position inside the active volume, is therefore needed.

Novel Scanner Principle

We proposed and implemented a first detector scanner based on the principles of pulse shape comparison (PSC) [3] and positron annihilation correlation (PAC) [4].

Description of the PSC technique:

A 1MBq ^{22}Na source is placed between the position sensitive detector (PSD) and the Germanium detector which we want to scan. The PSD system is built with a LYSO crystal and a large area position sensitive photomultiplier tube (PSPMT) from Hamamatsu. The performance of PSPMT was studied in detail [5]. The trajectories of γ-rays entering the germanium volume are defined by the 2D PSD. This allows creating a "collimation-free" scanner, where many lines across the detector or even the whole detector can be scanned simultaneously. For the position a) in figure 1, a data base containing pulse shapes for all the trajectories coming inside the coincidence cone of the Ge and the PSD is recorded. The (x,y) coordinates measured in the PSD provide the trajectories of γ-rays. Now for the second set of measurement corresponding to the position b) in figure 1, the PSD and ^{22}Na are rotated together along the axis of the Ge detector. In figure 1, it is shown that they are rotated by 90^{o}. Again a data set containing the pulse shapes and the (x,y) coordinates given by the PSD for this configuration is recorded. Now if we compare these two data sets, the only case in which a signal of one set is identical to the signal of the other set is when the two signals correspond to the crossing point of two lines inside the coincidence cone. In this way, it is possible to obtain a data base containing the pulse shape for each crossing point. The (x,y,z) coordinates of the crossing point are determined from the two γ-ray trajectories measured via the PSD with an accuracy of 1mm [5]. The main feature of the PSCS is that it allows to obtain the pulse shape database for a HPGe detector much faster as compared to other conventional scanning methods [6].

The pulses for a particular interaction point are selected on the basis of a χ^2 comparison test. The pulses along one selected trajectory are compared to the pulses in perpendicular trajectory. Only those pair of pulses are selected which are below a sufficiently small χ^2 value. The pulse which is associated to a particular point is then the average of ~ 200 pulses, which are below the stringent χ^2 threshold value.

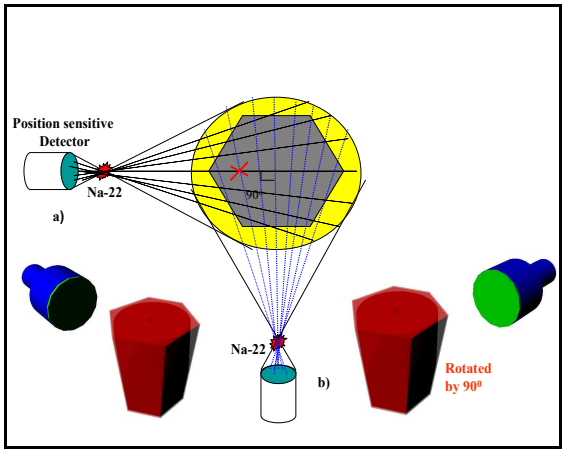

Figure 1: Pulse shape comparison scan of germanium (a) Pulse shapes recorded for the collimation lines coming inside the coincidence cone of PSD and germanium, (b) Source and PSD moved together by an angle of 90^{0} and again a data set of pulse shapes is measured.

References

[1] J.Gerl and W.Korten, AGATA Technical Proposal for an Advanced Gamma Tracking Array for the European Gamma Spectroscopy community, (2001).

[2] I.Y. Lee et.al, "GRETINA: A gamma ray energy tracking array", Nuclear Physics A, vol. 520, pp. 255-259, Nov 2004.

[3] F.C.L. Crespi et.al, "A novel technique for the charac terisation of a HPGE detector response based on pulse shape comparison", Nuclear Instruments and Methods in Physics Research A, vol. 593, pp. 440-447, Aug 2008.

[4] J.Gerl et.al "High-resolution gamma back scatter imaging for technical applications", Nuclear Instruments and Methods in Physics Research A, vol. 525, pp. 328-331, 2004.

[5] C. Domingo-Pardo, N. Goel, J. Gerl, T. Engert, I. Ko jouharov, H. Schaffner, I. Masahiro, "A position sen sitive γ- ray scintillator detector with enhanced spatial resolution, linearity and field of view", IEEE Transac tions on Medical ImagingVolume 28, Issue 12, Dec. 2009.

[6] M. Descovich et.al, "The position response of a large volume segmented germanium detector", Nuclear In struments and Methods in Physics Research A, vol. 553, pp. 512-521, 2005.

Surface characterisation and treatment evaluation of HPGe- detectors

T. Engert[1,2], I.Kojouharov[1], M. Krause[1], O.Picht[1], K.O. Voss[1],
M. Rauber[1], J.Gerl[1], P.Nolan[2], Th. Krings[3]
[1]GSI, Helmholtzzentrum für Schwerionenforschung GmbH, Germany;
[2] University of Liverpool, UK; [3] SEMIKON Detector GmbH, 52428 Juelich, Germany

Germanium-detectors are the most sensitive high-resolution γ detectors available and are the instrument in nuclear structure physics which allows important information about the structure of atomic nuclei to be obtained. The development of HPGe detectors often requires sophisticated crystal shapes in order to achieve optimal performance. The HPGe crystal treatment technology is mature [1], however is more suited to standard commercial type of detectors rather then research type one. The reported work is motivated by the needs for a new mechanical treatment procedure within the manufacturing methods in order to obtain better quality of the Germanium surfaces and increased cost-efficiency enabling complicated shapes to be produced.
Seven conservative produced germanium crystals with different surface qualities due to varying mechanical treatment were employed for the characterisation of their surfaces in the treatment technology. However, the characterisations have been carried out with a Atomic Force Microscope, a Profilometer, a Field Emission Scanning Microscope and a Electron Probe Micro Analyser.

Germanium treatment and shaping tests with a new ultrasonic grinding machine have been carried out and the results have shown very fine surface structures with tight tolerances of 2 µm. Qualitatively the degree of roughness achieved is a factor of 3.9 times better than with standard grinding techniques, while being a factor of 1.8 times better compared to standard lapping processes. This kind of sophisticated mechanical treatment allows also complicated shapes to be achieved. On the basis of these characterisation and ultrasonic treatment results a novel type of planar Ge-detector have been developed and are shown in Figure 1.

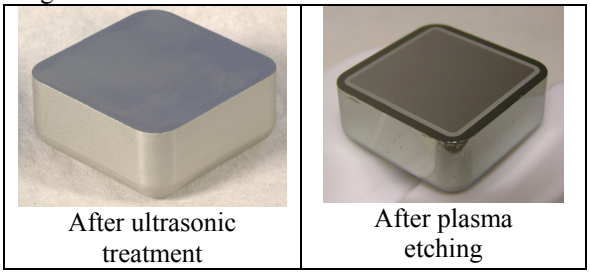

After ultrasonic treatment | After plasma etching

Figure 1: High-purity germanium crystal

For the first leakage current and spectroscopic test in this development stage, the detector was mounted in a multifunction cryostat and tested.

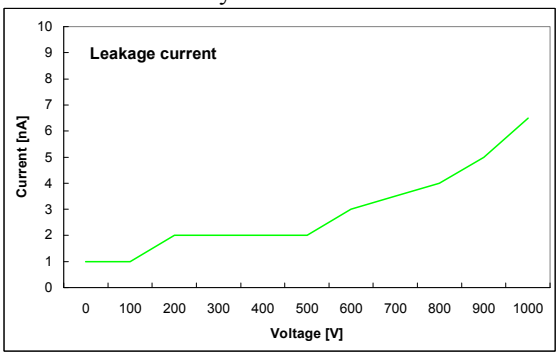

Figure 2: Leakage current characteristic

The current-voltage line shows that the depletion voltage of this detector is at 500 V. The plateau of the detector is located between 200V and 500V. Based on this configuration of crystal and cryostat, a spectroscopic test was performed, although not following the IEEE-standards.

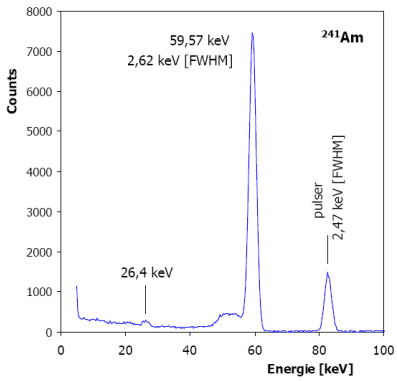

Figure 3: Spectroscopic test

The first test of the detector shows good spectroscopic results with a ^{241}Am source and a pulser, for a bias voltage of 400V. This test was enough to demonstrate that ultrasonic-grinding as a mechanical treatment can be used in the detector development process for further novel types of HPGe detectors.

References

[1] GeLab at GSI, I.Kojouharov, T.Engert, J.Gerl, Gamma Net, Padova, 10-11.05.2007

Surface projection of HPGe- detectors

T. Engert[1,2], I.Kojouharov[1], J.Gerl[1], D. Lehmann[1], P.Nolan[2]
[1]GSI, Helmholtzzentrum für Schwerionenforschung GmbH, Germany;
[2] University of Liverpool, UK

Several encapsulated single Germanium detectors have been mounted in one unit and integrated in a cryostat, in order to build efficient spectrometers to detect γ radiation emitted by nuclei excited in nuclear reactions. This kind of crystal encapsulation offer advantages compared to standard set-up of HPGe- detectors.
The basic aim of the following work is to develop a new capsule technology, in particular concerning the high-vacuum tightness and the temperature influence during the CO_2 welding procedure. The difficulty is the complexity of the detector and the germanium crystal respectively which reacts very sensitive to external influences. Consequently there is a risk that the germanium is no longer suitable for a detector because of an incorrectly employed manufacturing process. Another difficulty is the wall thickness and the material of the capsule as well as the complicated geometric shape of the detectors. To be able to understand all the circumstances of this partially complicated production, physical and economic aspects must be taken into account.

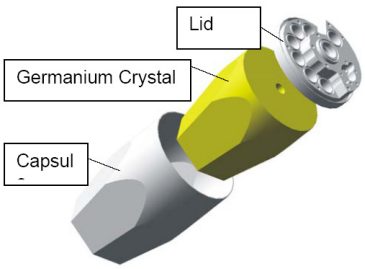

Figure 1: Encapsulated Ge-Detector

After the successful capsule/lid sealing follows the next step in the capsule development: the creation of the vacuum. The idea of the evacuation device consists of an aluminium pipe which is introduced in the lid of the capsule unit by a traditional welding method. At the other end of the pipe the evacuation of the air can take place by using a vacuum pump. After arriving the desired vacuum ultrasonic welding is used for crimping this aluminium pipe at a certain point in order to reach high vacuum tightness. For this purpose, 15 aluminium pipes were used with a special inside diameter and a special wall thickness. With the help of ultrasonic welding was closed the aluminium pipes, which was filled with helium gas inside. The result of the subsequent tests with a leak detector presented a 100% tightness of the sample.

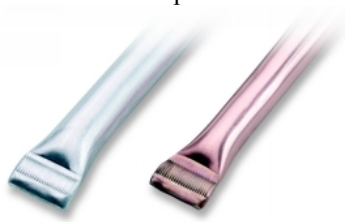

Figure 2: Ultrasonic welded copper and aluminium capillary pipes.

Further experiments were conducted with the welded pipes two hardness tests:
- The vacuum pipes were dipped in liquid nitrogen periodically (x20).
- The vacuum pipes were heated also periodically (x20) in a blast furnace.

After this experiment, were the pipes again by vacuum tested, and these tests were also successfully completed.

Another significant characteristic of the encapsulation technology is the use of an internal getter element to have a high vacuum over a longer period. The task of a getter in this closed high vacuum system is the bonding of the rest gas particles. For this purpose, gas particles are connected a chemical bond with the atoms of the getter surface or the gas particles be retained by sorption. The integration of such getter element in a detector system has proven with the previously encapsulated semiconductor detectors in the past [1]. Therefore, to fix such getter element in this system, a constructive, economic and physically meaningful solution has been searched. In this case, the problems were the lid material aluminium, the activation of the getter with current, the capacity of the getter element and the specific place in the capsule unit. A getter element are selected with this specification and integrated into the lid of the capsule unit.
On the basis of these results a novel type of encapsulated Ge-detector are planned.

References

[1] CTT, Entwicklung eines Germanium-Cluster-Detektors für das Gamma-Spektrometer EUROBALL, Dr. Köster Verlag Berlin, Diss. 1995, ISBN 3-89574-113-2

Performance tests of the AGATA Real time PSA*

M. Schlarb[1], R. Gernhäuser[1], R. Krücken[1], and the AGATA collaboration
[1]Physik-Department E12, TU München

The Advanced Gamma Tracking Array (AGATA) is a $4\,\pi$-detector of 36-fold segmented germanium crystals. Detailed simulations of a typical reaction and the associated detector pulse shapes [1] were performed to investigate its capabilities using a recently developed real time pulse shape analysis (PSA) method.

The test environment

We selected a $^{48}Ti(d,p)^{49}Ti$ reaction in inverse kinematic as a typical experiment. The beam energy was $100\,MeV\,(\beta \sim 0.06)$[2]. In order to maximize the Doppler-shift of the emitted γ-rays, one AGATA triple cluster was mounted at $90°$ to the beam axis and at a distance of 11 cm to the target. This requires a precise reconstruction of the interaction locations for an accurate Doppler correction. For this purpose a PSA is performed, using a direct comparison between the simulated experimental pulse shapes and basis signals for the detectors. PSA can be implemented either by an extensive search doing a full χ^2-comparison to all data sets in the signal basis (XGS) or by using an intelligent and much faster algorithm like the *fully informed particle swarm* (FIPS) described below.

The fully informed particle swarm

FIPS is an iterative algorithm mimicking the behavior of a flock of birds looking for food [3]. It consists of a swarm of abstract particles with each one representing a potential solution, i.e. the γ-rays interaction location(s). Each particle moves with a velocity $\vec{v}$ at iteration $q+1$ given by:

$$\overrightarrow{v^{q+1}} = \chi \cdot \left\{ \overrightarrow{v^q} + \sum_{n=1}^{N_i} \varphi \cdot r \cdot \left(\overrightarrow{P_i^q} - \overrightarrow{X^q} \right) \cdot 1/N_i \right\}. \quad (1)$$

Here $\chi < 1$ prevents an exponential growth of $\vec{v}$, φ is a tuning parameter for convergence and $r \in \{0,1\}$ is a random number. The particles current position is given by $\overrightarrow{X^q}$ and $\overrightarrow{P_i^q}$ is the best position found by neighbor i so far. The sum runs over all members of the particles static neighborhood defined before the algorithm starts.

Results

The simulated experimental data was time aligned with the basis signals using a neural network [1] and a PSA was performed using both XGS and FIPS. Since XGS searches the complete signal basis only events with one hit segment can be analyzed in real time. FIPS, by comparison, is capable of reconstructing events with up to three hit segments. For these events no γ-tracking was conducted but the interaction with the highest energy was deemed to be the first interaction. The obtained energy resolution of the line at $1382\,keV$ will be used as a measure for the performance. Figure 1 shows the obtained spectra together with the uncorrected spectrum. XGS achieves a very good energy resolution of $2.8\,keV$ but takes too long ($25\,ms$). This is a factor of 2.5 above the limit of $10\,ms$ for AGATA. FIPS, by contrast, is not just a lot faster ($2.2\,ms$ on average) but also significantly improves AGATA's sensitivity. The latter is due to the more complex events which can be included in the analysis without adversely affecting the energy resolution ($3.4\,keV$).

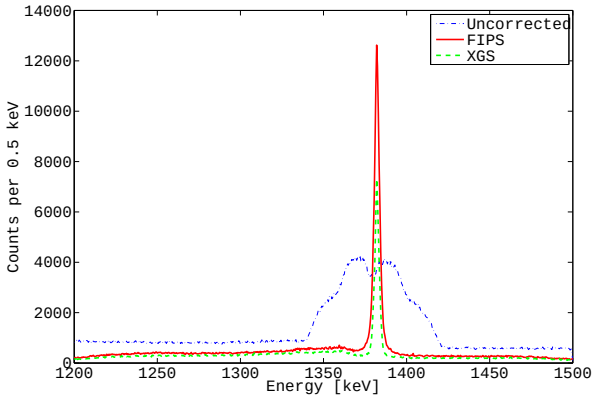

Figure 1: γ-ray spectrum of the simulated experiment. The uncorrected spectrum is given by the dash-dotted line, the Doppler-corrected spectra after PSA with XGS and FIPS are shown in dashed and solid lines respectively.

We have shown that it is possible to perform a real time PSA for AGATA and to obtain a very good energy resolution when using the FIPS algorithm. Its performance is independent of the γ hit multiplicity and it offers a higher sensitivity than XGS due to the larger portion of events which can be analyzed.

*The work was funded by BMBF(06MT238),EURONS(T-J02-3), DFG (Exz-Clust 153-Universe).

References

[1] M. Schlarb, PhD Thesis, 2009, Technische Universität München.

[2] F. Recchia et al., Nucl. Instr. and Meth. A, **604**, 2009, p. 555-562.

[3] R. Mendes, J. Kennedy and J. Neves, IEEE Trans. on Evolutionary Computation, **8**, 2004, p. 204-210.

Ultra-Fast Timing with Plastic Scintillators

R. Hoischen[1,2], S. Pietri[1], W. Prokopowicz[1], H. Schaffner[1], J. Gerl[1], H.J. Wollersheim[1], N. Kurz[1], P. Golubev[2], and D. Rudolph[2]

[1]Helmholtzzentrum für Schwerionenforschung GmbH, D-64291 Darmstadt, Germany; [2]Department of Physics, Lund University, S-22100 Lund, Sweden

As precursor to HISPEC, the upcoming PreSPEC campaign incorporates the commissioning of the first version of the LYCCA (Lund-York-Cologne-CAlorimeter) detector system called LYCCA-0. The LYCCA detector is a Time-of-Flight (ToF), ΔE, E set-up designed to unambigiously identify nuclear reaction products by their mass A, and charge Z. To achive this goal up to masses around $A = 100$, the total time resolution of the ToF measurement should be on the order of 100 ps FWHM or better [2]; comprised of 50 ps and 80 ps FWHM for the start and stop detctor, respectively. Mainly two timing options are deemed viable; polycrystaline CVD diamond detectors and fast plastic scintillators. In the LYCCA-0 set-up the diamond detectors will be tested as ToF-start detector, while a large-area fast plastic scintillator will give the ToF-stop signal.

This report is an update of last year's article [1], and as such outlines the continued development of a prototype scintillation detector for the LYCCA-0 system, and the tests performed to establish its performance - both via simulations and in-beam tests at the FRS [3]. The LYCCA-0 ToF-stop detector will have to cover an area of about 25x25cm^2. The most convenient way to achieve this coverage is to use a large plastic membrane read-out from four or more sides. Early tests performed on such a system with four large active-area photomultiplier tubes (PMT) indicated a good performance of around 80 ps FWHM. Further tests and simulations, shown in Fig. 1a, established that increasing the number of PMTs reading out the scintillator membrane improves time resolution, as expected from a purely statistical viewpoint. At the forseen membrane size, a BC-420 membrane would outperform a BC-422Q (quenched) plastic membrane, see Fig. 1b, although the latter has a significantly faster rise-time and thus, a better intrinsic time resolution. In all laboratory tests and the test experiment mentioned below, the raw signals were processed by Phillips Scientific constant fraction discriminators before being fed into a 21-bit CAEN V1290A Multihit TDC with 25 ps per step via GSI NIM-ECL converters.

To prove the system's performance under realistic circumstances, an in-beam test was conducted with a ^{238}U beam during the FRS000 [4] experiment in the S2 area of the FRS. The prototype detector shown in Fig. 1c features a round 27 cm in diameter and 1 mm thick BC-420 membrane, read out by 32 small and fast Hamamatsu R7400U PMTs mounted perpendicular to beam direction.

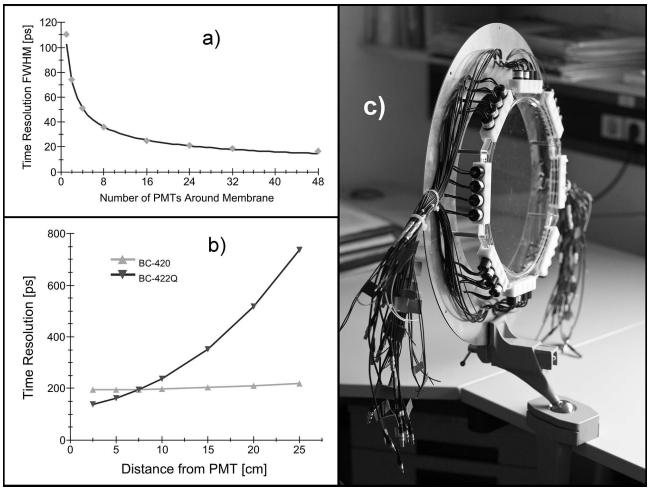

Figure 1: **a)** The addition of more identical PMTs for read-out of the scintillator membrane increases the possible time resolution by a factor $\sqrt{N}$, this trend is here shown as the solid line. A saturation effect might be visible beyond 32 PMTs. **b)** Comparing scintillator performance of two different plastics as a function of the distance to the site of photon production. **c)** The LYCCA-0 ToF-stop scintillation detector prototype.

The experimental data is still being analysed, while first rough approximations indicate a time resolution of well below 50 ps FWHM. In a previous in-beam experiment another R7400U system was tested at higher beam intensities and showed no signs of signal deterioration at particle rates of up to 100 kHz. An updated prototype version of the current detector will be tested at the FRS in an upcoming LYCCA-0 commissioning experiment in early summer 2010 at GSI.

References

[1] R. Hoischen *et al.*, GSI Scientific Report 2008.

[2] The LYCCA Technical Design Report. Can be found at: http://wwwnsg.nuclear.lu.se/lycca/lycca-TDR.pdf

[3] H. Geissel *et al.*, Nucl. Instr. Meth. B70, 286 (1992).

[4] K.H. Behr *et al.*, GSI Scientific Report 2009.

Development and tests of a new low-energy neutron detector for the R^{3}B-setup*

C. Langer† [1,2], A. Couture[3], M. Csatlós[4], M. Heil[1], A. Krasznahorkay[4], R. Plag[1,2], R. Reifarth[1,2], F. Tovesson[3], and the R^{3}B-Collaboration

[1]GSI Helmholtzzentrum für Schwerionenforschung GmbH, 64291 Darmstadt, Germany; [2]J.W. Goethe Universität, 60438 Frankfurt a.M., Germany; [3]Los Alamos National Laboratory, Los Alamos, New Mexico 87545, USA; [4]Institute of Nuclear Research of the Hungarian Academy of Sciences, H-4001 Debrecen, P.O. Box 51, Hungary

Introduction

Studies of (p,n)-reactions in inverse kinematics are a powerful tool for nuclear physics. Collective phenomena, like spin-flip and isospin-flip giant resonances, as well as the so-called neutron-skin of exotic nuclei can be studied. β-decay half lifes and Gamow-Teller strength for nuclei far off stability are rarely measured yet, but are needed for astrophysical network calculations for the different nucleosynthesis processes.

(p,n)-reactions in the R^{3}B-target allow to extract these information for exotic nuclei. Therefore a detector system with high angular granularity and a good time resolution is needed to resolve the time of flight from the target to the detector and the angle of the emitted neutrons sufficiently.

Development and Tests

The detector consists of plastic scintillator material with a size of 10x45x1000 mm. The detector bar is wrapped with a special VM2000 multilayer reflector foil. At both ends a fast PM-tube with an active divider is attached. Silicon grease of high viscosity is used for the light coupling. Two different PM-tubes are tested in order to reach the lowest possible detection threshold: Hamatsu R2059 and Photonis XP2262.

The response of the detector to γ-rays was studied in Debrecen and Frankfurt. Several γ-sources were used as well as an α-source for charged particles. A measurement performed with a ^{60}Co source shows a time resolution of 0.8 ns and hence a position resolution of around 6 cm for a single detector. At Debrecen, a very weak ^{252}Cf source was used to perform a first test of the neutron detection efficiency. The source was mounted at a distance of 1 m to the detector. A PM-tube, attached to the source, produced a start trigger by detecting the spontanous fission fragments emerged from the source.

Another efficiency study was performed at the Los Alamos Neutron Scattering Center (LANSCE) in New Mexico, USA. A white neutron spectrum is produced by a spallation process. Protons of 800 MeV and with a high current of up to 135μA are impinging on a water-cooled tungsten target and are creating a neutron beam with high flux at energies from the thermal region up to several hundreds of MeV.

In order to avoid the strong interaction of our detector with high energy primary neutrons and γ's, originating from the protons hitting the tungsten target, the detector was placed at a distance of 1 m outside the primary neutron beam. Instead, a fission chamber with a thin ^{235}U foil was situated at flight path 5 at a distance of 9 m viewing a lower tier moderator. Primary neutrons triggered fission events in the ^{235}U foil and the secondary fission neutrons were then used to calibrate the neutron efficiency of the plastic bars. Since the fission cross-section of ^{235}U is high at low incident neutron energies a huge amount of fission neutrons were produced. The fission chamber started the time-of-flight measurement for the secondary fission neutrons to reach the detector. The read-out gate was opened in a time window from 2 ms to 5 ms after the primary neutrons were produced in the spallation target.

First results

The measurements with the γ-sources prove that the detector is working according to our expectations and the results could be reproduced with GEANT3 and GEANT4 simulations (see Figure 1).

The comparison between the two different PM-tubes used in these testruns shows no significant difference in the detection threshold. The efficiency studies and the analysis of the experiment at LANSCE are still ongoing.

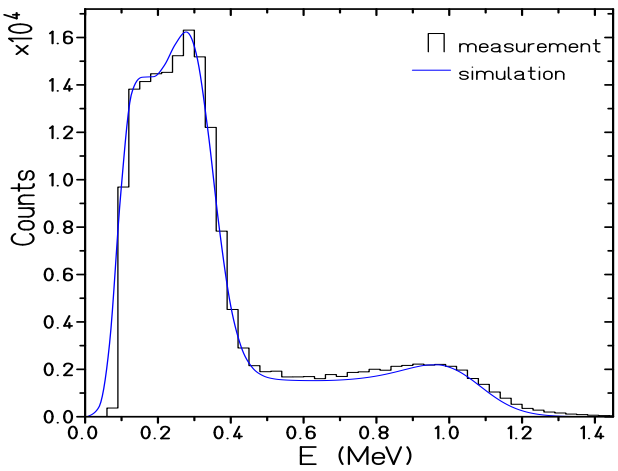

Figure 1: ^{22}Na simulation (blue solid line) compared to a measurement (black) taken with one detector bar.

*This project is supported by the HGF Young Investigators Project VH-NG-327.

† c.langer@gsi.de

Heading towards FAIR: upgrades on the R³B-CaveC electronics.

C. Caesar, J. Frühauf, J. Hoffmann, H. Johansson*, K. Koch, N. Kurz, C. Langer, W. Ott, H. Simon, for the R³B collaboration.
GSI, Darmstadt, Germany, *Chalmers Technical University, Göteborg, Sweden.

The FAIR/R^{3}B experiment will require global time resolutions with a r.m.s. of about 50ps. The precursor setup R³B-CaveC provides an ideal testing ground for novel electronics systems, used under realistic experimental conditions. The Tacquila system, originally developed for the FOPI experiment, exhibits both an excellent time and suitable energy resolution, which shall be used to replace the outdated FASTBUS readout system for the current LAND detector.

A newly developed R^{3}B-specific version of the Tacquila board provides in addition to the original version a 17th channel and a clock counter. This enables time measurements in excess of the 25ns provided by the original system. Furthermore, a new LAND front-end card (LANDFEE2, see Figure 1) has been developed, providing an amplification stage, and a splitter and discriminator. The full system consists in addition of a piggy-back QDC and the Triplex LAND control and trigger board, which is currently under design. This card will be controlled via I^{2}C from the Tacquila main board and provide individual thresholds, a multiplexer chain for monitoring individual channels, and the necessary facilities to build triggers from a multiplicity signal, an analog sum over the channels and a common or, respectively. The Tacquila board is connected to a SAM5 module [1] via GTB and read out using the MBS [2] data acquisition system. The data is analyzed online and offline using CERNs Root package coupled to the UCESB [3] unpacker.

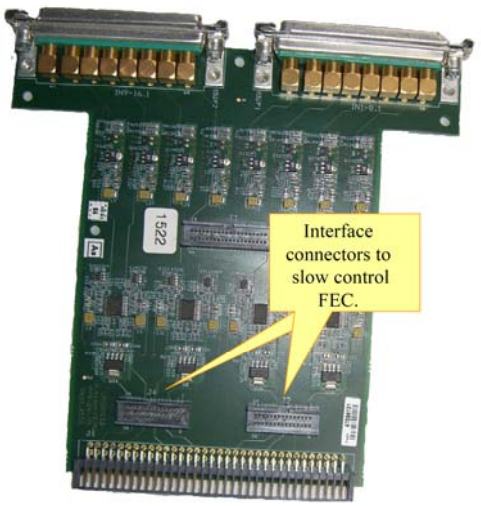

Figure 1: Novel Tacquila Frontend Card (FEC) for LAND including discriminators with individual thresholds, provided via an interface connector.

The time on the Tacquila board is measured with respect to a 40 MHz clock. A campus wide clock distribution system, using precision oscillators with laser fibres, called BuTiS [4] will be used for bunch timing purposes in the FAIR accelerator complex. In the course of its development this system will be utilized as source for clock signals for our experiments, providing phase-controlled clock signals between the FRS and CaveC. A test system, consisting of two copper-coupled BuTiS oscillators, two discriminators, and a modified CLOck SYnchronization board, developed for the CBM experiment, has been used as clock input for two independent Tacquila systems in order to derive the uncertainty in the relative timing introduced by the distribution system. The CLOSY board is acting as clock divider from 100 MHz to 40 MHz for this application. The relative uncertainty, using a single signal source as input on a channel on each board through the clock was determined to contribute with 17ps r.m.s. only. The advantage of such a scheme is that only a clock signal has to be transferred between different experimental facilities located far from each other (see Figure 2), and that the precision of the analogue time measurement via a time-to-amplitude converter ASIC is independent of the covered range for the time measurement.

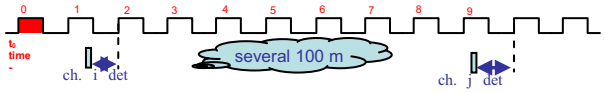

Figure 2: Distributed time measurement vs. clock.

The trigger decision, dead time blocking and priority encoding, which is currently done hardware wise via NIM modules is currently implemented in software using the VULOM [1] module. The on-board Xilinx FPGA features in its current programming [5] scalers, dead-time locking and priority encoding, logic matrices for coincidences and configurable downscale for the individual triggers, together with a pulser output used for calibration purposes.

[1] http://www.gsi.de/informationen/wti/ee/elekt_entwicklung/VME.html.
[2] http://www-win.gsi.de/daq/.
[3] http://fy.chalmers.se/~f96hajo/ucesb/.
[4] P. Moritz, GSI scientific report 2006, FAIR-ACCELERATORS-20, and Physical Review Special Topics - Accelerators and Beams **12** (2009), 042801.
[5] http://www.gsi.de/onTEAM/source/informationen/wti/ee/elekt_entwicklung/trigger_LAND.pdf

R3BRoot: a ROOT based Simulation and Analysis framework for R3B

Denis Bertini for the R3B Collaboration[1]
[1]GSI, Darmstadt, Germany

Introduction

R3BRoot is a versatile and fully ROOT based framework aiming for the simulation and analysis of the R3B experiment [1]. In particular for the simulation part it uses FairRoot [2] base class library as a layer upon ROOT and the Virtual Monte Carlo [3].

The R3B experiment

The aim of the R3B international collaboration is to develop and construct a versatile reaction setup with high efficiency, acceptance, and resolution for kinematically complete measurements of reactions with high-energy radioactive beams. The setup will be located at the focal plane of the high-energy branch of the Super-FRS [4].

Structure of the Framework

The structure of the framework is presented schematically in Fig. 1. The main class *FairRunManger* handles the overall program flow and the communication between different modules, namely *Geometry Interface*, *RunTime DataBase* , *Event Generators*, *IO Manager* and the *Virtual Monte Carlo*. The latter is an interface to differents Monte Carlo engine (Geant3, Geant4 and Fluka) allowing the user to choose at runtime which of these engine to use for the simulation.

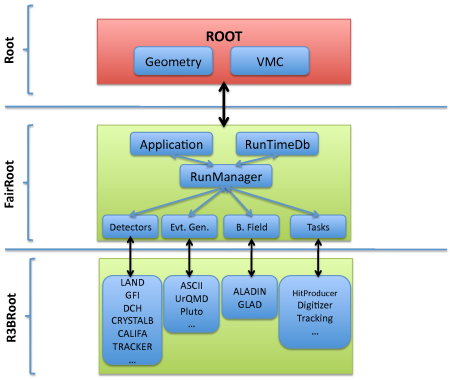

Figure 1: The R3BRoot Framework

R3B Simulation

R3BRoot uses the ROOT Geometry Modeller to uniquely describe the R3B detector geometry for all Monte Carlo engine. Currently all detectors of the R3B experiment are described in R3BROOT. Common Event Generators like UrQMD, EvtGen and dedicated ones can be used as an input to the *Run Manager* class.

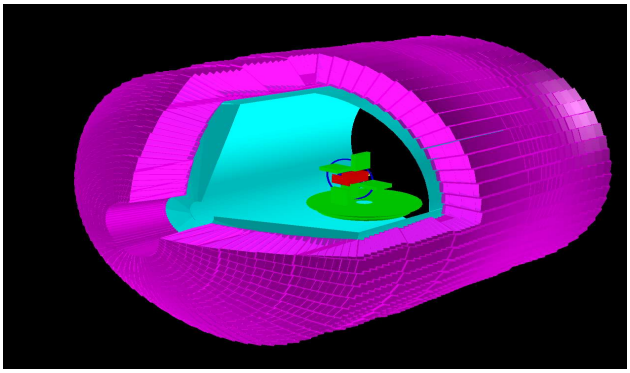

Figure 2: Inner Tracker and Calorimeter in R3BRoot.

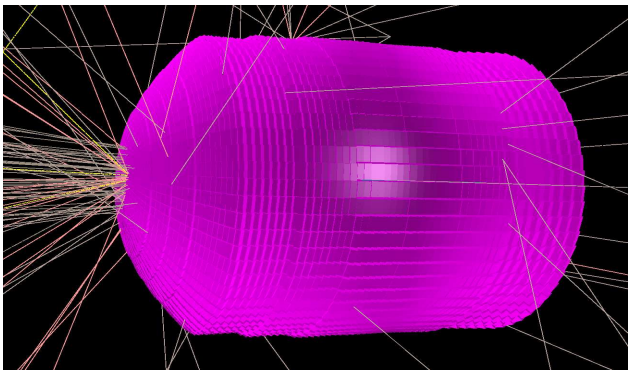

Figure 3: Inner Tracker and Calorimeter with tracks visualisation.

Conclusion

The R3BRoot is a versatile and portable framework for the R3B experiment. The description of detector components and the tools for the reconstruction is in progress.

References

[1] http://root.cern.ch

[2] The Fair Simulation and Analysis Framework, Journal of Physics: Conference Series **119** (2008) 032011

[3] The Virtual Monte Carlo, I. Hrivnacova , Computing in High Energy and Nuclear Physics, 24-28 March 2003, La Jolla California.

[4] http://www.gsi.de/forschung/kp/kp2/collaborations/R3B/

Large Area High Rate Diamond Tracking Detectors for R^{3}B*

S. Schwertel[†1], R. Gernhäuser[1], R. Krücken[1], O. Lepyoshkina[1], and S. Winkler[1]
[1]TU München, Physik-Department E12, Garching

Introduction

Diamond is radiation hard and shows fast signal collection. This makes it an ideal material for in beam tracking detectors as they are required for the R^{3}B experiment. In several tests using highly ionizing heavy ions the radiation hardness was verified up to a dose of 2.5 $\times$ 10^{13} ions/cm^2 and a time resolution of $\sigma\tau \approx 60$ ps [1] was measured on small sample detectors made of 100 μm PC (polycrystalline) CVD (chemical vapour deposition) diamond.

Highly Segmented Diamond Detectors

Beam detectors for the R^{3}B experiment have to be thin in order to minimize multiple scattering and secondary reactions and have to cover quite large areas of 50 $\times$ 50 mm^2. This size only can be realized by using PC CVD diamond, which is available in thin layers (d $>$ 50 μm) and areas up to 6".

A detector of thickness of d = 100 μm and a position resolution of 200 μm would fulfill the requirements for the R^{3}B tracking. The final detector will have 200 μm pitch in x and 1 to 2 mm in y direction.

The disadvantage of PC diamond is the reduced and non-isotropic charge collection efficiency, which is typically 10 to 30 %. Due to the large energy loss this is not a limiting factor in case of heavy ions. But the internal structure of the PC CVD material, which grows in narrow columns of a typical size of a few 10 μm might reduce the charge collection to zero between the metallized segments.

To test this, SNAKE [2], the superconducting nanoscope for applied nuclear physics at the Munich Tandem accelerator was used. The samples were 10 $\times$ 10 mm^2 diamonds, which were segmented in 64 metallized strips with Al of width 110 μm and a pitch of 140 μm. These samples were scanned point by point in steps of 2 μm in x- and 3 μm in y-direction and the signal amplitudes were recorded for each position.

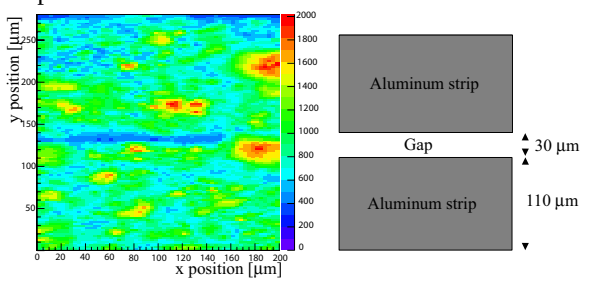

Figure 1: Left: Amplitude map of two highly segmented strips. Right: Schematic of segmentation.

The lefthand side of Fig. 1 shows the amplitude map of this measurement. Nicely the different grain sizes inside the material could be seen. Also a significant signal drop is located between two strips which is only 15 to 20 μm wide, whereas the gap is 30 μm as shown on the righthand side of Fig. 1. This means a smaller gap of about 15 to 20 μm (according to the crystallite size) should result in full efficiency. This highly segmented metallization is possible by using the same lithographic technics and was already applied for a medium-size prototype (25.4 $\times$ 25.4 mm^2) used in the beam test performed at the ALADIN/LAND setup.

A 300 μm thick, medium-size prototype with a segmentation of 128 microstrips (190 μm pitch, 30 μm gap) on the frontside (x-direction) for position measurement and 16 strips (1.5 mm pitch, 50 μm gap), on the backside (y-direction) has been produced. This prototype was tested in the S327 test experiment using a 600 AMeV ^{12}C beam with a diameter of about 5 mm. The detector was mounted in the beamline between the scintillator for the start signal for TOF measurement and the position sensitive diode in front of the target.

To provide self triggering and a maximum efficiency, the backside signals were read by charge-integrating preamplifiers, followed by shapers.Timing filter amplifiers and a constant fraction discriminator were used for triggering.

The frontside strips were read-out by two APV25 chips [3]. Both chips are connected to the GSI MBS readout via a GTB bridgeboard [4], on which four ADCs are located.

The measured signal of the beam is clearly separated from the noise. A correlation with existing beam tracking detectors shows an efficiency of 93 % as expected from the measurements described before and a nice position resolution of 200 μm, which fulfills the requirements of the R^{3}B experiment.

Summary and Outlook

The APV25 chip readout shows good performance. For parallel measurement of position and time, further development of new electronics is required. This is one of the next steps. Large area detector material (50 $\times$ 50 mm^2) was delivered and is ready for production. Still the material treatment before metallization is an important issue for detectors of good performance and low leakage current under irradiation. Beside the standard cleaning methods we are currently investigating a precoating with a thin layer of carbon from a laser plasma. First tests showed very promising results of this method.

References

[1] S. Schwertel, PhD thesis TU München, 2009
[2] G. Datzmann, NIM B 210(2003)
[3] M. Raymond et. al., Proceedings of 4th workshop on electronics for LHC experiments,2000
[4] M. Böhmer, PhD thesis TU München, 2006

* Work supported by GSI, BMBF (06MT9156), DFG (Exc. Clust. 153-Universe)
† sabine.schwertel@ph.tum.de

Geiger APDs as possible Photon Counter for Cherenkov Detectors*

B. J. Roy[1,2], H. Orth[1], C. Schwarz[1], A. Wilms[1], J. Schwiening[1], and K. Peters[1]
[1]HAD-1, GSI, PlanckStr.1, Darmstadt - 64291, Germany; [2]Also at NPD, BARC, Mumbai -400 085 India

Geiger APDs, also called Silicon photomultiplier (SiPM), are very new type of photon counting devices that show great promise to be used as detection device in combination with scintillators/Cherenkov radiators. SiPM is an avalanche photo-diode operated in limited Geiger mode. They have been considered as potential readout devices for DIRC counter of the PANDA detector which is one of the large experiment at FAIR- the new international facility to be built at GSI, Darmstadt. It is essentially an opto-semiconductor device with excellent photon counting capability and possesses great advantages over the conventional PMTs because of low voltage operation and insensitivity to magnetic fields. A SiPM consists of a matrix of micro cells, typically between 100 and 10000 per mm^2. Each micro cell acts as digital device where the output signal is independent of the number of photons absorbed. When all the cells are connected in parallel, the SiPM becomes an analog device thereby allowing the number of incident photons to be counted.

Different types of SiPM manufactured by Hamamatsu and Zecotek with different sizes of pixels and active area have been tested by us using the set-up at GSI and Goethe University, Frankfurt. A list is provided in Table 1.

Table 1: SiPM details: MPPC1 and MPPC2 are from Hamamatsu and MAPD3N is from Zecotek.

Device	Active Area [mm^2]	Pixel size [μm]	Pixel Density [1/mm^2]
MPPC1	(1x1)	100	100
MPPC2	(1x1)	25	1600
MAPD3N	(3x3)	7	15000

In fig.1 and Fig.2, we plot the photon detection efficieny (PDE) distribution as a function of the wavelength λ for Zecotek make MAPD3N and Hamamatsu make MPPC. It is to be noted that the present data for MPPC shows much broader distribution extended over larger wavelength range as compared to the report of Hamamatsu. Temperature dependence of dark current and radiation hardness study are being planned. For radiation hardness study we may use the APSARA reactor at Mumbai and for temperature dependence study, a Peltier cooling device is being developed at GSI.

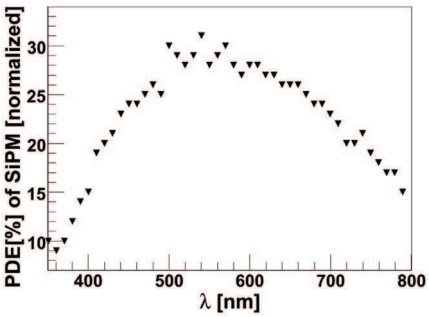

Figure 1: Photon detection efficiency distribution of MAPD3N as a function of wave length normalized with data from ref.[1] at λ = 450 nm.

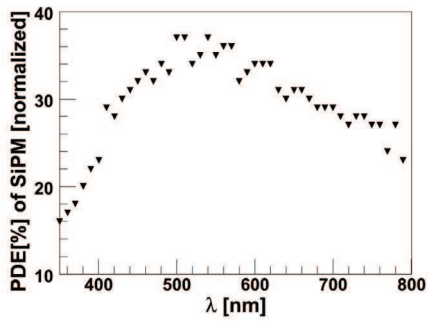

Figure 2: Photon detection efficiency distribution of MPPC normalized with data from ref.[2] at λ=450 nm.

References

[1] D. Renker, PSI (private communication).

[2] N. Anfimov, Dubna (private communication).

* Work supported by HIC4FAIR.

Development of a GEM-TPC prototype and its integration in FOPI*

M. Berger[1], F. Cusanno[1], L. Fabbietti[1], and the GEM-TPC Collaboration
[1]TU München - Excellence Cluster Universe, 85748 Garching

The use of GEM foils for the amplification stage of a TPC instead of a conventional MWPC allows one to bypass the necessity of gating, as the back drift is suppressed thanks to the asymmetric field configuration. This way, a novel continuously running TPC, which represents one option for the $\overline{\text{P}}$ANDA [1] central tracker, can be realized. The continuous readout of the central tracker is necessary due to the feature of the beam. In 2009 the design and the assembling for the readout plane (see Fig. 1) of a GEM-TPC prototype has been finished. The 702 mm long drift cages are under construction. The drift volume will have an internal diameter of 105 mm and an external diameter of 300 mm. The readout plane consists of a four layer PCB with 10296 pads. To obtain a more uniform charge distribution on the pads, it has been decided to use hexagonal pads, where the distance to the neighboring pads is equal in every direction. Furthermore the readout plane will be

Figure 1: The readout plane, seen from the side of the connectors.

equipped with 6 uniform distributed temperature sensors. For the uniformity of the field lines ending at the readout plane, grounded copper areas were added at the edges of the active area. The design and testing of the front-end cards, which will be equipped with the AFTER [2] chip, is completed, the cards mass-production is currently ongoing.

The GEM-TPC prototype will be commissioned in the FOPI apparatus at GSI, therefore the TPC data acquisition system has to be integrated in the MBS framework used for the FOPI DAQ. The diagram of the integration is shown in Fig. 2. The Trigger Control System module (TCS) of the

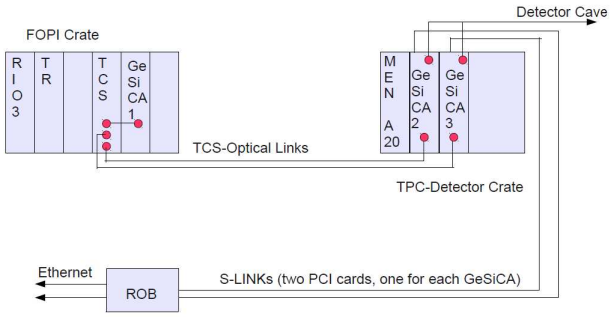

Figure 2: The scheme of the integration of the GEM-TPC DAQ in FOPI.

GEM-TPC [4] is installed in a FOPI crate. It gets control signals from FOPI and sends out triggers to the GEM-TPC readout modules (GeSiCA) accordingly. TCS also sends out to the FOPI system its deadtime signal. An additional GeSiCA (GeSiCA1) has been installed in the FOPI crate, in order to read the "time-stamps" from the event headers via the MBS CPU (RIO3). Dedicated VME scripts have been adapted for the RIO CPU in order to operate TCS and GeSiCA in the FOPI crate.
The readout of the signals from the GEM-TPC has been operated in a separate VME crate, managed for the first time by a MEN A20 CPU [5]. The proper VME drivers for the MEN A20 module were selected, tested and installed and the mySQL-based config_server [4] was adapted as well. A data-sender code has been implemented in the spill-buffer computer (ROB) operating the readout via HOLA S-Link [3]. The data-sender, based on TCP protocol, sorts out the data from the GEM-TPC event buffer to a data-receiver computer in MBS. Then the data-receiver merges the events with the data from the other detector in the FOPI event builder. The synchronization of the events is based on event number and spill number "time-stamp".

References

[1] The $\overline{\text{P}}$ANDA Collaboration, Technical Progress Report for PANDA, GSI 2005.

[2] P. Baron *et al.*, IEEE Trans. Nucl. Sci. **55** (2008) 1744.

[3] O. Bozle et al, The S-LINK Interface Specification, ECP-Division CERN, Geneva, Switzerland, 27 March 1997, also at http://hsi.web.cern.ch/HS/s-link/

[4] B. Grube, A Trigger Control System for COMPASS and a Measurement of the Transverse Polarization of Λ and Ξ Hyperons from Quasi-Real Photo-Production, PhD thesis, Technische Universität München, January 2006.

[5] http://www.men.de/products/vmebus.html

* Work supported by HGF and DFG-Excellence Cluster Universe

A Generic Monitoring System for HADES and FAIR Experiments *

B. Milanovic[1], U. Brinkschulte[1], I. Fröhlich[1], J. Michel[1], J. Stroth[1,2], and M. Traxler[2]
[1]Goethe University Frankfurt, Germany; [2]GSI, Darmstadt, Germany

The running DAQ upgrade for the HADES detector is nearly finished. In order to supply the new electronics with a suitable monitoring facility and to prepare for the upcoming FAIR experiments, a versatile monitoring network has been designed [1]. The HADES detector comprises a large variety of different sub-systems. However, a unification of the system bus using General-Purpose Trigger and Readout Boards (TRBs) and/or the TRBnet protocol has been successfully implemented [2]. The readout electronics, some front-ends, network hubs, as well as some data processing nodes now rely on FPGA chips [3]. Due to its generic nature, the monitoring system can be implemented on any FPGA chip. Therefore, internal hardware states of nearly every DAQ component can be monitored, reaching in some cases even into the front-end electronics (FEE), as shown in figure 1.

The monitoring system supports all currently used subdetectors. It has been designed resource friendly and highly customizable in order to suit upcoming FAIR detectors as well. Since all detector data needs to pass readout nodes and network hubs before getting used for trigger analysis and event reconstruction, the monitoring system integrated on these chips gains direct access to all digitized detector data. After defining the monitoring signals, which are a subset of all data packs, they are forwarded to the monitoring system over an internal interface. The system then buffers the signals directly on the FPGA chips using either simple register cells or adaptable FIFOs. The buffering process, which additionally timestamps the data allows three different timer domains for appropriate signal synchronization. Each FIFO gathers the data automatically with a preset frequency until it gets full. Furthermore, a ringbuffer mode is supported preventing the FIFO from getting full at the cost of storing only the newest data signals. It is possible to change FIFO properties in order to store any desired monitoring signal by choosing the correct depth, width, frequency, timer and data splitting method. Data packs stored inside are actually composed of three parts: raw data, timestamp and the current event number.

The readout of the monitoring signals is performed over a designated TRB residing anywhere in the optical network. The TRB runs a monitoring server application on its Linux system. The server can send instructions through the entire TRBnet using the optical link and command every monitoring chip to send its FIFO and register contents. Moreover, the server is connected to one or more monitoring clients over Ethernet and thus represents the bridge between the user and the monitoring facility. Any user that gains access to the clients can in this way send instructions to the server obtaining appropriate monitoring signals and visualizing them locally using EPICS [4]. The compatibility with the EPICS API has been demonstrated.

One huge advantage of the presented system is that every client automatically reconstructs the entire monitoring setup. Besides the system itself, the FPGA chips additionally contain a simple ROM module which stores the entire monitoring setup on that particular chip. Whenever a client connects to the server, all ROMs are read out in advance providing the client with all the necessary data regarding FIFO properties, register numbers and addresses. Such approach allows changes in one system without affecting the entire monitoring network.

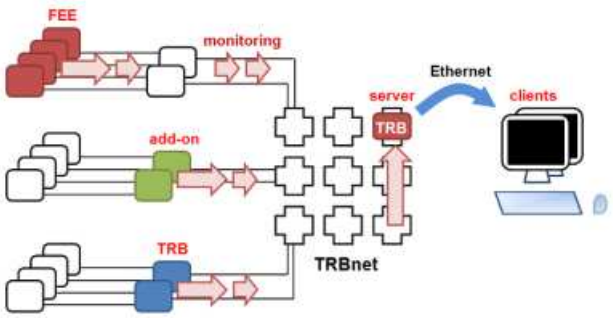

Figure 1: An exemplary monitoring scheme. The monitoring system can be integrated either on front-ends, TRBs or TRB add-on boards (e.g. readout boards and hubs).

References

[1] B. Milanovic, Development of a Real-Time General Purpose Online Monitoring System for HADES and FAIR Experiments, diploma thesis, Goethe University, Frankfurt 2009.

[2] J. Michel, Development of a Realtime Network Protocol for HADES and FAIR Experiments, diploma thesis, Goethe University, Frankfurt 2008.

[3] M. Palka et al, "The new data acquisition system for the HADES experiment", Nuclear Science Symposium Conference Record, NSS 08. IEEE, pages 1398 –1404, 2008.

[4] Experimental Physics and Industrial Control System, "http://www.aps.anl.gov/epics/".

* Work supported by EU (CNI contact No. 506065), BMBF and HIC-for-FAIR

Status of the HADES RPC Time of Flight wall*

The HADES RPC group

The production, delivery to GSI and test of the six RPC sextants, FEE and LV power supplies were concluded during 2009.

The production of 1122 cells [1] and the assembly of the last two sextants (S4 and S1) were finished. Additionally, cosmic ray tests were performed on sextants S1, S2, S4 and S6 prior to delivery to GSI. The FEE, which is subdivided in two parts, preamplificator plus comparator -daughter board (DB)- and signal gathering, power supply distribution and control -motherboard (MB) - [2], was produced and successfully tested (around 900 DB boards -four FEE channels each- and 130 MB). Twelve custom made LV power supplies [3] were also produced and tested.

All parts were delivered and set up together with the final DAQ by midyear to start the final ground cosmic ray test prior to the final installation in the mainframe of HADES.

Figure 1.a. shows the time resolution for the entire chain, cell + FEE + DAQ. All channels have a resolution under 100 ps except 36 channels with a resolution of around 120 ps. This degradation will vanish once the integral nonlinearity, which affects the DAQ, is corrected. It is shown an average resolution of 79 ps (74 ps if the DAQ-affected channels are not taken into account). It was also measured a crosstalk on the few % level and moderate timing tails along with an average longitudinal position resolution better than 10 mm sigma. Out of a total of 1116 cells, 1115 are operative along with all 2232 FEE channels.

By the end of the year, all sextants were successfully installed in the mainframe of HADES together with the HV and LV systems. DAQ was installed in two sectors.

References

[1] D. Belver et al. NIMA Vol 602, Issue 3, May 2009, 697-690.

[2] D. Belver et al. NIMA Vol 602, Issue 3, May 2009, 788-791.

[3] A. Gil et al. IEEE Trans. Nucl. Sci. 56 382-387, 2009.

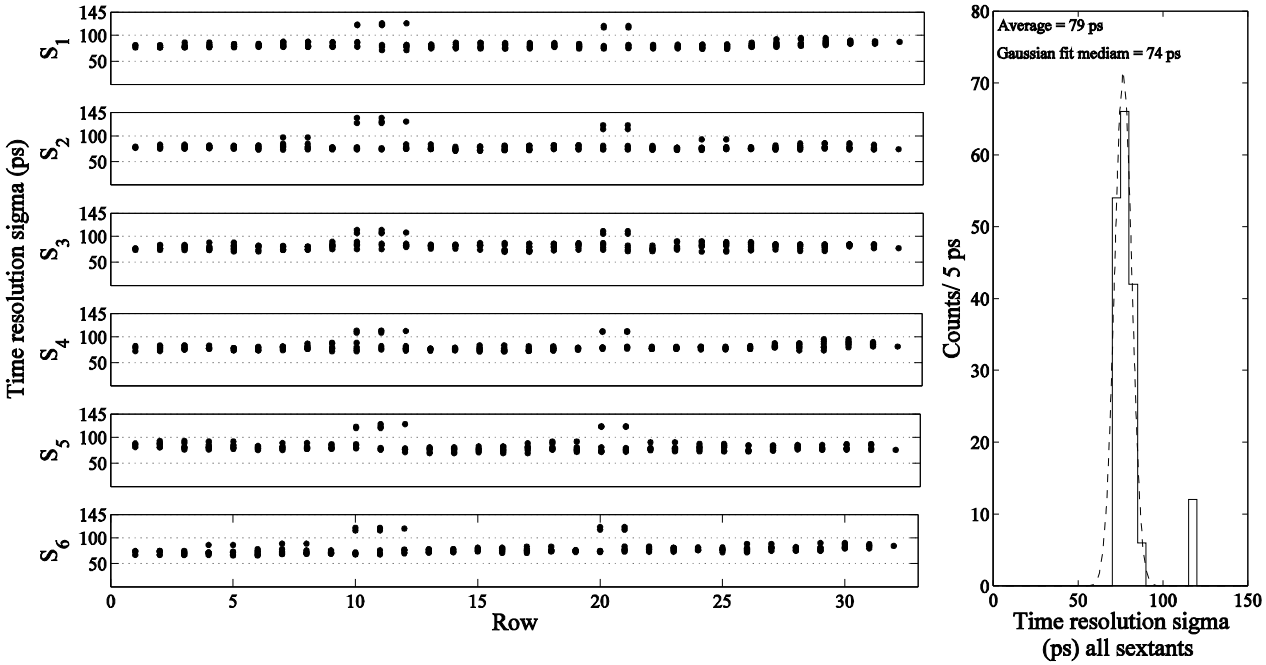

Figure 1.a Time resolution for all cells and sextants showing an average of 79 ps (Figure 1.b). All cells are under 100 ps except for 36 channels were the resolution is around 120 ps. This degradation will vanish once the integral nonlinearity, which affects the DAQ, is corrected.

* This work was supported by EC DIRAC RII3-CT-2005-515876 and MEC grants FPA1006-09154 and .FPA2006-12120-CO3-02

The HADES Event Building System*

S. Yurevich[1], M. Böhmer[2], G. Korcyl[6], J. Michel[3], J. Stroth[3,1], and M. Traxler[1]

[1]GSI Helmholtzzentrum für Schwerionenforschung GmbH, 64291 Darmstadt, Germany; [2]Technische Universität, 80333 München, Germany; [3]Institut für Kernphysik Goethe-Universität, 60486 Frankfurt, Germany; [6]Jagiellonian University, 30-059 Krakow, Poland

The upgraded HADES experiment will perform the measurements with heavy collision systems (up to Au+Au) at SIS18 and then will move to the upcoming FAIR accelerator complex. The HADES Data Acquisition System combines readout electronics and TRB-Net [1] with off-the-shelf computers in a parallel architecture interconnected with Ethernet. The complete data-flow breaks down into the following elements: from the Front-Ends the data is transported over TRB-Net via optical 2 Gb/s links to HUB2-AddOn boards where the data is packed in a special HADES data format and sent to the Event Builders (EB) over Gigabit Ethernet (GbE). Event Builders merge subevents from the different detector subsystems to a complete event and write the event to a mass storage system. Detailed description of the HADES DAQ is given in [2] and the HADES upgrade report can be found in [3].

The major task of the DAQ is to read the data from the detectors with rates up to 250 MB/s sustained and to cope with the trigger rates up to 100 kHz. The FPGA-based implementation of GbE in the HUB2-AddOn board provides the ability to send the data gathered from the Front-Ends much faster taking use of the standard GbE infrastructure. The GbE VHDL entity creates the transport queues consisting of subevents and sends the queues in UDP packets via optical fibers to the EBs. The maximum size of the queue can be set by the user. The logic will buffer the incoming data until the size is met. A connection between the HUB and the GbE-switch is established by an autonegotiation feature. GbE together with TRB-Net logic uses about 20 % of resources of Lattice FPGA (LFE2M100) and 34 % of available memory blocks, being a lightweight add-on to the existing functionality and therefore can be integrated in all subsystems.

To accumulate large amount of the data a parallel event building concept is used. In the Front-End Electronics (FEE) the data are packed in queues and sent to a number of EBs using a round robin approach. Because the subevent sizes differ among detector subsystems by a factor of 10, the EB stores subevents in the buffers of variable size improving the efficient use of memory. The advantage offered by parallel event building is that it can adapt to any data rate by adding more event builders (load sharing). When using 10 EBs at 20 kHz LVL1 trigger rate, the data rate will decrease down to some 25 MB/s per EB resulting in an event rate of 2 kHz per EB. The parallel event building scheme has been tested with 90 data sources and 2 event builders. It has shown a stable operation even with the data rates exceeding the expected by a factor of three. Furthermore, several schemes of mass storage can be used in parallel: direct recording of the data stream to the tape via the RFIO mechanism [4], writing the data to the local hard disks on the EB (160 TB available), transmitting the data via a high speed link to the Lustre distributed files system [5]. To manage parallel data streams to the mass storage systems the fast 10 Gb/s connection is used. Several event building processes will run on one server equipped with 12 cores, 44 TB hard disk space, 64 GB memory, 10 Gbps PCI Express NIC. Four servers will be connected to a 10 Gbps switch (see Fig. 1).

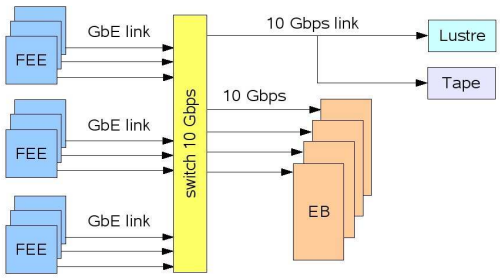

Figure 1: The event building system.

The distributed event building requires a central monitoring system. A slow control interface based on the EPICS software and graphical user interface for the monitoring of a number of EBs have been implemented and tested. To achieve synchronization of the event building processes and to provide communication between them a master/slave model has been implemented where a master EB controls all slave EBs. All the important information will be saved in the Oracle data base via a client application running on each EB server.

References

[1] J. Michel et al, "The New HADES Data Acquisition Network", this volume

[2] M. Palka et al, Proceedings of IEEE NSS, October 2008, Dresden, Conference Record N06-6

[3] S. Yurevich et al, "Upgrade of the HADES Experiment", this volume

[4] H. Göringer et al, this volume

[5] W. Schön et al, this volume

* Work supported by EU grant 515876 and 227431

The New HADES Data Acquisition Network*

J. Michel[1], M. Böhmer[3], I. Fröhlich[1], G. Korcyl[4], M. Palka[4], J. Stroth[1,2], A. Tarantola[1], and M. Traxler[2]

[1]Institut für Kernphysik, Goethe-Universität Frankfurt, Germany; [2]GSI, Darmstadt, Germany; [3]Technische Universität München, Germany; [4]Jagiellonian University, Krakow, Poland

In the framework of the current upgrade of the HADES DAQ and Trigger System the complete data acquisition network and read-out scheme has been redesigned. As described in [1], the hardware is based on front end boards equipped with FPGAs and optical transceivers. In total, the complete network will contain over 530 FPGAs and about the same number of optical transceivers. On this optical network, data is transported using a dedicated network protocol. Details about this Trigger and Readout Board Network (TrbNet) can be found in [2]. A unified front-end has been designed to simplify accessing the network, including features for distributing trigger information, data read-out and monitoring.

In the new DAQ network, distributing triggers is a three-step process. First, the central trigger system (CTS) sends a timing trigger pulse over dedicated PECL or LVDS connections to all subsystems. This pulse is followed by a LVL1 trigger being sent over the optical network. Here, all information like trigger number and trigger type as well as reliability features to check data integrity are included. The last step is the response of each front-end board to notify the CTS that the event has been successfully stored in internal memories.

The user-interface is kept very simple: All information is given to the user on separate ports along with a trigger strobe. The reply to the CTS is then generated automatically, hidden from the user. All the user has to do is setting one signal to start sending the answer.

The data read-out is done independently from the trigger logic using the same optical links. Here, the CTS sends a request to all front-ends requiring data of a specific event. The data is then equipped with a fixed data header (DHDR) containing the event information and data length as well as the network address of the front-end. In the network hubs, data from several front-ends are merged to a single data stream based on the information given in the DHDR.

Afterwards, data has to be forwarded to the Event Builders (PCs) collecting data from all subsystems and writing them to storage memory. Due to the huge amount of data (250 MByte/s), data has to be distributed to several PCs. In [3] the HADES event building system is described in detail.

The interface between DAQ electronics and the Eventbuilder system is done using optical Gigabit Ethernet links [1]. In the FPGAs on TrbNet hubs data is converted to UDP packets using the standard HADES event data format.

Our standardized interface for all subsystems also contains extensive features for status monitoring and controlling of all data acquisition hardware. Basic functions like various read/write - registers are provided by the interface. More elaborate functions like memories and fifos, can be connected using a data bus and a 16bit wide address space. Environmental status information like temperature and voltages can be easily monitored and settings for the front-end electronics can be altered dynamically. Network management features like a DHCP-like assignment of addresses are also included.

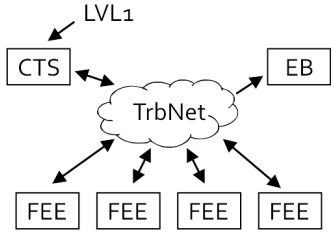

Figure 1: A schematic view of the HADES DAQ network including the central trigger system (CTS), Eventbuilders (EB) and Frontends (FEE).

For this interface a complete monitoring system with many different options has been developed [4]. With this system, each sub-detector has its own custom-made monitoring features but the interface is kept standardized throughout all detectors.

So far, the network protocol has been implemented on all subsystems of the HADES detector. Commissioning of the new read-out hardware of the RICH detector has been completely based on this network setup and has been finished successfully. The newly installed MDC electronics has also been commissioned using the TrbNet design.

The CBM-MVD collaboration plans to use TrbNet for the read-out of the micro vertex detector of the CBM experiment at FAIR. The adaption of the protocol to a token-ring-like network structure is being considered as well.

References

[1] S. Yurevich et al., this volume.

[2] J. Michel, "Development of a Realtime Network Protocol for HADES and FAIR Experiments", diploma thesis, Univ. Frankfurt 2008. [GSI-Doc: DOC-2008-Oct-34-1.pdf]

[3] S. Yurevich et al., The HADES Event Building System, this volume.

[4] B. Milanovic et al., this volume.

* Work supported by EU grant 515876 and BMBF

Development of a large-scale VUPROM system as tracking trigger for the KAOS spectrometer

A. Esser*[1], S. Sánchez Majos[1], P. Achenbach[1], S. Minami[2], J. Pochodzalla[1], and T. R. Saito[1,2]

[1]Inst. für Kernphysik, Joh. Gutenberg-Universität, Mainz, Germany; [2]GSI, Darmstadt, Germany

The VME Universal Logic Modules VULOM and VUPROM were developed at the Experiment Electronics Department of GSI for general purpose logic operations. During the last 2 years, first modules were applied as tracking triggers in experiments at GSI and at the Mainz Microtron MAMI [1]. A large-scale VUPROM system with several thousand input channels is now in operation for the triggering of the hadron arm as well as the electron arm of the KAOS spectrometer at MAMI.

The KAOS spectrometer is maintained by the A1 collaboration with a focus on the study of $(e, e'K^+)$ coincidence reactions. For its electron arm tracking system two vertical planes of fibre arrays (x- and θ-plane), each covering an active area of $1600 \times 300\,\mathrm{mm}^2$ with 2 304 read-out channels, are operated close to zero degrees scattering angle and in close proximity to the electron beam.

A sophisticated trigger logic implemented in VUPROM modules was developed in order to to minimize accidental trigger rates in the electron arm instrumentation.

The trigger must satisfy the following requirements:
(i) detection of signal clusters in each detector plane;
(ii) reconstruction of particle tracks through both planes;
(iii) acceptance test for all reconstructed particle tracks;
(iv) expandability to build a missing-mass trigger by combination with the hadron arm trigger;
(v) on-line access and control of trigger parameters.

The hardware set-up comprises 37 VUPROM modules with 256 I/O channels each. Each 6U VME module is equipped with a Virtex-4 FPGA chip, capable of operating at 400 MHz. This set-up allows easy reprogramming via VMEbus. Furthermore, output and control information is accessible during trigger operation.

The modules are arranged in 4 stages. In the first stage signal clusters are detected, and the position information is passed on to the next stage. The signals from both planes are processed separately in the first and the second stage, which consists of 6 modules with the purpose of reducing the number of channels, and providing the same position information on several outputs.

In the third stage the position information from the first stage of the x-plane and the second stage of the θ-plane are checked for temporal coincidences and used to perform an acceptance test for the reconstructed tracks.

The last stage consisting of a single module receives the information of accepted trajectories from the third stage and produces the trigger output signal.

Due to the geometrical arrangement of the fibres, a particle hit always causes a cluster of correlated signal in neighbouring channels [2]. Signal clusters are identified by requesting a signal in n neighbouring channels within a given time period. By requesting the absence of a signal in the next higher and lower channel, it is guaranteed that the found cluster is exactly of the size n. Short pulses which are the result of different delays in the input signals are suppressed by a pulse-width discriminator. An upper and lower boundary for the accepted cluster sizes is specified. Clusters with a size above the given upper boundary are vetoed to reduce background from scattered particles, hitting the detector planes under large angles with respect to the normal on the detector plane. The position of each cluster is transmitted to the next stage by setting one bit in an 32-bit wide output bus.

Table 1: Measured trigger rates in the electron arm of the KAOS spectrometer during beam-tests at MAMI in 2009.

	trigger rate (kHz)
raw signal rate	1120 ± 30
clusters in x	47.0 ± 0.2
clusters in θ	37.3 ± 0.2
x OR θ	83.9 ± 0.3
x AND θ	0.49 ± 0.02
random coincidences	0.140 ± 0.001

For performing the acceptance test, the allowed combinations of hit positions in both planes are stored in a binary matrix. This matrix is externally computed. An output signal is produced when a cluster is found on both detector planes and the corresponding matrix element is non-zero. Each VUPROM in the third stage evaluates a range of 384 channels of the x-plane and up to 1 536 channels of the θ-plane. This set-up was chosen to cover the angular acceptance known from simulations with the highest possible granularity. The position resolution for the acceptance test is 6 channels in the x-plane (4.98 mm) and 12 channels in the θ-plane (9.96 mm).

The trigger for the electron arm was successfully tested during two beam-times in July and August 2009. Raw signal rates of several MHz were observed, measured trigger rates are shown in Table 1.

References

[1] S. Minami *et al.*, GSI Scientific Report (2007) p. 223; S. Minami *et al.*, GSI Scientific Report (2008) p. 52; S. Sánchez Majos *et al.*, GSI Scientific Report (2007) p. 170.

[2] P. Achenbach, L. Nungesser, J. Pochodzalla, Nucl. Inst. Meth. in Phys. Res. **A 591**, (2008) 406.

* aesser@kph.uni-mainz.de

Prototype aerogel Čerenkov counter for kaon/pion separation*

L. Debenjak[1,2], P. Achenbach[†2], J. Pochodzalla[2], T. R. Saito[2,3], and S. Širca[1]

[1]JSI, Ljubljana, Slovenia; [2]KPH, Joh. Gutenberg-Universität, Mainz, Germany; [3]GSI, Darmstadt, Germany

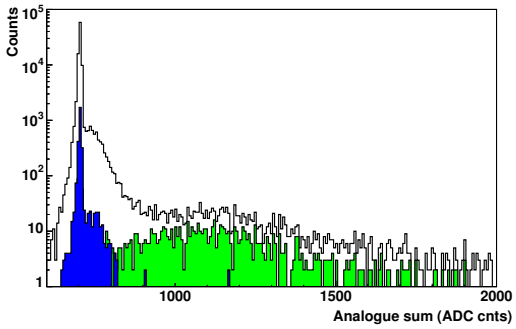

Figure 1: The analogue sum spectrum of both PMTs for events identified by the detector package of the spectrometer as pions (green) and protons (blue). The unshaded spectrum corresponds to all particles entering the Čerenkov counter. Protons were below the Čerenkov light emission threshold.

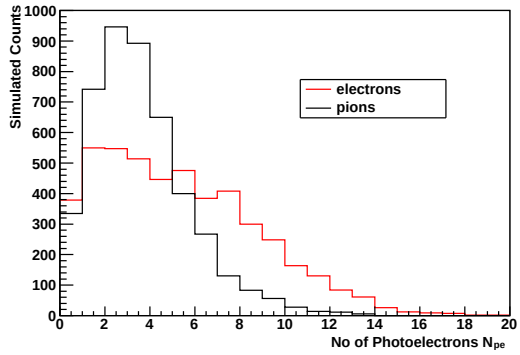

Figure 2: Simulated distribution of photoelectrons for the set-ups discussed in Table 2.

For hypernuclear experiments, which are currently performed at GSI (HypHI) or proposed for FAIR (PANDA) and for MAMI (A1), an unambiguous kaon identification is essential. An aerogel Čerenkov counter was designed for the KAOS spectrometer at the Mainz Microtron MAMI for the discrimination between kaons and pions of momenta $p \geq 1\mathrm{GeV}/c$.

Before the construction of the final detector a smaller prototype has been built, mounted inside the KAOS spectrometer, and tested. The prototype consisted of a $20\times10\times10$ cm^3 light collection box with a single layer of aerogel of active area 20×10 cm^2. The inner walls were covered by Millipore paper and the photons were detected by two 2" PMTs, attached on opposite sides. Different refractive indices and thicknesses of the aerogel, geometries of the light collection box (*e.g.* including or excluding mirrors) and momenta of the incoming particles were studied.

Table 1: Measured detection efficiencies, ϵ, for electrons and pions at various momenta, p. In one set-up the light collection box included mirrors.

p (MeV/c)	particles	mirrors	ϵ (%)
380–530	electrons	no	88
620	pions	no	90
480	pions	yes	65

Table 2: Mean number of photoelectrons measured with different set-ups and compared to simulations.

p (MeV/c)	particles	mirrors	$N_{\mathrm{pe}}^{\mathrm{exp}}$	$N_{\mathrm{pe}}^{\mathrm{simul}}$
380-530	electrons	no	4.2	4.8
480	pions	yes	3.6	3.4

We used aerogel with $n = 1.07$ made by Chiba U., Japan, which provides separation of pions and kaons in the momentum range $p \approx 365$–$1300\,\mathrm{MeV}/c$ [1]. The detector was exposed to various particle types, such as electrons, pions and protons. In Fig. 1 a representative spectrum is shown for events identified by the detector package of the spectrometer as pions and protons.

The detection efficiency was determined by the ratio of events with a Čerenkov signal above a given detection threshold to the number of events reconstructed to be passing the volume of the counter. Results for different set-ups tested during several beam-times are shown in Table 1. When testing with pions, the prototype was rotated towards the incoming particle direction.

The performance of the prototype detector was also studied with the simulation package Litrani. The number of photoelectrons, N_{pe}, predicted by the simulation was compared to number of photoelectrons seen in the actual experiments as shown in Table 2. The simulated distribution of photoelectrons for these set-ups is shown in Fig. 2.

Since the results from the experiments and the simulations are in fairly good agreement we can trust our simulations to predict and optimize the light yield of aerogel Čerenkov counters to be used in future hypernuclear experiments.

References

[1] L. Debenjak *et al.*, GSI Scientific Report 2008, (2009) p. 253.

* Financed partly by the European Union, European Social Fund

† patrick@kph.uni-mainz.de

Preparation for the n-XYTER engineering run.

H.K. Soltveit[1]

[1]Physikalisches Institut, Universität Heidelberg, Germany

During 2009 a comprehensive study and extensive simulation of the n-XYTER prototype ASIC have taken place at Physikalisches Institut in Heidelberg. The n-XYTER chip is realized in 0.35 μm CMOS technology. It has a 50 μm inter-channel pitch and it is capable of both time and amplitude measurement of arbitrary polarity charge pulses delivered by the detector. As a 128-channel, data-driven readout chip it is now being used as a prototype readout chip for several experiments at the Facility for Antiproton and Ion research (FAIR) and neutron scattering. An explanation of the chip architecture can be found in [1].

From the test results and simulation studies, it became apparent that the n-XYTER chip needed some improvements to ease its operation in FAIR detector prototypes. The main problems seen in the tests and simulation that make the circuit tedious to operate, are the relatively high temperature sensitivity, the recently seen large voltage drop of the baseline over the chip and the large adjacent channel to channel variation, also of the baseline, of up to 400 mV [2]. The voltage drop over the chip consist of two contributions. The first contribution is a uniform voltage shift (increase) over the chip from channel 0 to channel 63 of about 300 mV, and nearly the same decrease in the DC level from channel 64 to channel 127. A decrease in the DC-level with an increase in the number of active channels is also seen in test. The reasons are here the IR-drop and non-matched layout. The second contribution is the difference in the DC-level of about 400 mV seen between adjacent channels. Possible reasons for this difference are currently under investigation.

The n-XYTERs temperature sensitivity has been found to be a combination of several sources. The main source is the tracking circuit, a scaled version of the preamplifier, implemented to bias the resistor R_d in the Pole-Zero network with the same DC-level as the input of the preamplifier. The drawback is that the tracking circuit is also seen by the fast and the first slow shaper inputs, both with different gain and PMOS as input transistors. The consequence is that the tracking circuit provides a temperature sensitive offset voltage at the shaper input, that is amplified by the shaper closed loop gain, contributing significantly to the voltage shift at the output of the shaper. To eliminate this effect, the tracking circuit is removed and the bias voltage will be externally supplied. Otherwise a redesign would have been necessary.

A second source were the bias voltage generators for the shapers used to set their appropriate output DC-level. They are not matched to the shapers they should supply, causing a further increase in the temperature sensitivity. The temperature sensitivity of the channels has been reduced from about 30 mV/^{o}C and 50 mV/^{o}C for a typical process parameter simulation in the timing and energy channels, respectively, to a few mV/^{o}C for the worst case process simulation.

The Peak-Detector and Hold (PDH) circuit has also gone through some design changes due to its high sensitivity to input offset voltage, giving different peak amplitudes for equal input signals.

Most of the problems seen in the test should already have been noticed by the designers responsible of the full chip integration and of the implementation of the new features in the n-XYTER when doing simulations.

Moreover, the Opto-process C35B4C01 employed in the previous submission is not the optimum process for a mixed-mode circuit as the n-XYTER. This can make the n-XYTER circuit vulnerable to substrate noise and to crosstalk generated in the digital part of the chip. Normally used protection techniques, as for example guard rings and the use of distance between components to shield the analog part from the digital substrate have barely an effect in CMOS technology with a low ohmic substrate. Such problems are expected to be much reduced with the use of the high ohmic substrate in the C35B4M3 process target in the engineering run.

The circuit was originally designed to handle an input charge of maximum 20 fC and with a gain of about 55 mV/fC and 27 mV/fC for the timing and energy channel, respectively. In the engineering run of the n-XYTER a second gain is implemented, having the possibility to set the gain to 47 mV/fC and to 8 mV/fC for both signal polarities to expand the dynamic range. This required some design modifications of the first shaper in the energy channel. Minor changes are also done on the fast-shaper (monitoring channel) to improve the driving capabilities.

Status

The n-XYTER, both in its previous and modified version has gone through an extensive simulation with process parameters to make the engineering run of the n-XYTER more robust. Many design and layout related problems have shown up, been understood and fixed. At the moment of writing this report, the large adjacent channel to channel DC-level variation is not fully understood. To ease the bonding of the n-XYTER, a re-structuring of some of the pads is also in progress. The submission of the improved version of the n-XYTER is foreseen when all tests and simulations are done and understood.

References

[1] A.Brogna, et al., Nucl.Instr. and Meth. A 568 (2006) 301.

[2] C.J. Schmidt,. Private communication

Enhancements of the Front-End-Electronics Communication Software*

R. Keidel† [1], S. Bablok[1,2], and E.S. Conner[1]

[1]ZTT, University of Applied Sciences, Germany; [2]Institutt for Fysikk og Teknologi, Universitetet i Bergen

The InterComLayer (ICL) of the Front-End-Electronics communication (FeeCom) chain has been redeveloped and enhanced to adapt to the requirements which have arisen during daily usage by the pertinent detectors in ALICE. A major focus has been set on transfer performance and priority hierarchy imposed by the data transported. Transparency of the redesign to the underlying detectors has been achieved.

Software Architecture

The FeeCom chain consists of three layers: the Fed-Client as dedicated DIM module in the PVSS on the supervisory layer, the ICL located on the control layer and the FeeServers connected to the Front-End-Electronics (FEE) operating on the field devices.

The ICL acts as distributor and collector for the system. It distributes commands issued from the supervisory layer to the FeeServers running on the field layer and collects their data and answers before relaying them further to the PVSS. Preparation of command data inside the ICL is achieved via access to the Configuration Database and detector-specific CommandCoders (CoCo) of the respective detectors. Data exchange is performed over well-defined APIs (Application Programmers Interface; FED-API (Front-End-Device - API), FEE-API, CoCo-API) [1] [2]. Data transport between the different layers employs Distributed Information Management (DIM) as the underlying protocol [3].

Redesign of the InterCom Layer - ICL 2.0

The implementation of the ICL 2.0 has been written in Java thereby allowing for a higher degree of platform independence. Modules and frameworks, which are still written in C++, (i.e. CoCo and DIM) are attached to the ICL via JNI (Java Native Interface) [4], thereby making the Java implementation transparent to the other parts of the setup. With the redesign of the ICL 2.0 a greater granularity of the application has been achieved. Separate agents take care of their assigned tasks:

- **Control Agent** (**CA**): Relays commands to the underlying field devices and keeps track of pending acknowledgements (including ICL configuration commands as well).
- **Monitoring Agent** (**MA**): Collects values published by the FeeServers and delivers them to the PVSS.
- **Messenger**: Handles the delivery and persistence (local storage) of FeeServer and ICL log messages.

A sketch of the assembly with the agent redesign of the ICL 2.0 is shown in figure 1. All afore defined interfaces are reused in the implementation to ensure7 downward compatibility of the software. With the new design the differentiation between detector-specific and detector-independent tasks is maintained.

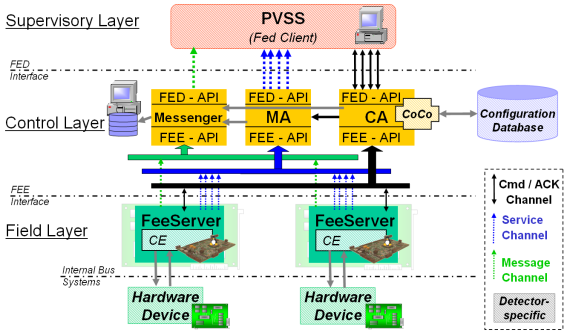

Figure 1: Three layers of the FeeCom chain with the agent redesign in the ICL 2.0. The agents (Messenger, Monitoring Agent (MA) and Control Agent (CA)) take care of their specific tasks.

Summary and Outlook

The reimplemented ICL will fit smoothly in the existing setup of the FeeCom chain allowing transparent use of the ICL 2.0 for the involved detectors. With the usage of Java a port of the system to different platforms can be easily achieved. The higher granularity of the ICL grants more fail safety and system stability, as well as allows for clearer separation of the involved tasks.

References

[1] R. Keidel, et al: Front-End-Device Application Programming Interface, GSI Scientific Report 2008 (Instruments-Methods-39), GSI Report 2009-1, May 2009, Editor: K. Groe

[2] S. Bablok: Heterogeneous Distributed Calibration Framework for the High Level Trigger in ALICE, PhD Thesis, University of Bergen (Norway), printed by Allkopi, February 2009, ISBN: 978-82-308-0740-8

[3] C. Gaspar, M. Doenszelmann, Ph. Charpentier: DIM, a Portable, Light Weight Package for Information Publishing, Data Transfer and Inter-process Communication, Presented at: International Conference on Computing in High Energy and Nuclear Physics 2000, Padova (Italy), February 2000

[4] http://java.sun.com/docs/books/jni/

* Work supported by GSI; Vorhaben: ALICE Softwareanwendung zur Modellierung von Prozesssteuerungsschnittstellen / EPICS; WOKEI

† keidel@fh-worms.de

Design and Implementation of an Universal Read Out Controller

N. Abel[1], S. Manz[1], and U. Kebschull[1]

[1]Kirchhoff Institute of Physics, Heidelberg University, Heidelberg, Germany

Introduction

Since 2007 our contribution focused the Silicon Tracker's FEE (Front End Electronic), consisting of the nXYTER, an ADC (Analog Digital Converter) and a ROC (Read Out Controller) [1]. The implementation of the nXYTER specific ROC has been done very successfully, as the beam tests in September 2008 [3] and September 2009 [2, 4] proved. Our first ROC setup consisted of the nXYTER readout logic and a PPC based Ethernet transport logic. This setup is called the nXYTER Starter Kit, which turned out to be very helpful in small laboratory setups, where physicists need quick access to the nXYTER and its measured data. The Ethernet interface keeps the communication effort as simple as possible, since every common PC supports it.

However, in the final experiment thousands of ROCs will be used. In this setup Ethernet will not be an option any longer. This is primarily caused by the galvanic isolation coming with fiber optics and by the fact that the certain ROCs are synchronized via Deterministic Latency Messages (DLMs), which by definition depend on optical fiber [5]. Thus, a second transport logic, the Optical Transport, has been implemented. In our first concept, the Optical Transport was planned to fully replace the Ethernet transport. Due to the usefulness of the Starter Kit this plan has been altered. Today, we fully support both, Ethernet and Optical Fiber, as two equal solutions.

The Universal ROC

While our first setup solely focused on the nXYTER, today we are also designing and implementing readout logic for the FEET chip [8] and the TRD chip *(in planning stage)*. To keep the re-usability as high as possible, we did split the ROC into two fully independent modules: the readout logic (RL) and the transport logic (TL). Both are connected to each other via a standard bus for slow control and via a FIFO for the hit data transport (see figure 1). This internal interface is common for all transport modules and all readout modules. Therefore the development of the modules can be done independently.

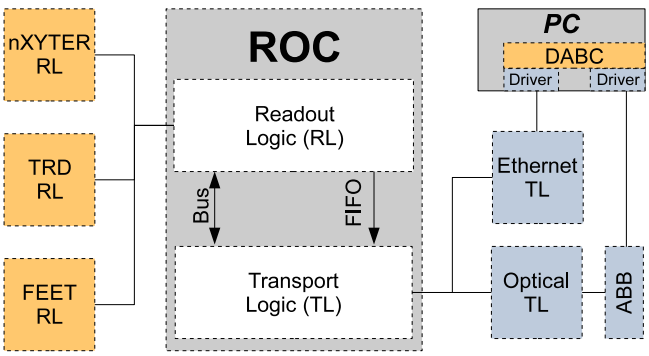

Figure 1: The unitized layout of the Universal ROC

The strict separation of the chip into RL and TL also influences the software on the PC. At this, RL and TL can be seen as two different layers. A change from Ethernet to Optic causes the change of the whole communication setup. Of course fiber cables instead of Ethernet cables have to be used. But more important, there is no fiber port on the PC. Therefore the ABB board (which in short acts as an adapter from fiber to PCIe [6]) has to be used. This leads to the utilization of completely different drivers. However, the overlying DABC software [7], which implements slow control and data taking, has not to be changed at all. Using encapsulation, it does not even have to notice the change from Ethernet to Optic. On the other hand a change of the RL from nXYTER to FEET only influences the control software and does not require any changes on the driver software.

In conclusion the modularization of the Read Out Controller and the consequential separation of the control software into different layers, enables us to provide an Universal ROC, which offers quick access to a long-run tested transport logic. This leads to a significant increase of stability and reliability compared to a development from the scratch. Beyond that, the modularization concept allows us to easily add a new readout logic for further FEE setups.

References

[1] N. Abel et. al, "Development of the Read Out Controller for the nXYTER Front End Board", GSI Progress Report 2007, Darmstadt, Germany

[2] B. Bozsogi, "Test of CBM Silicon Tracking Detectors in a proton beam at GSI", Student Report, 2009, Budapest, Hungary

[3] cbm-wiki.gsi.de/cgi-bin/view/Beamtime/BeamTimeGsiSep2008

[4] cbm-wiki.gsi.de/cgi-bin/view/Beamtime/BeamTimeGsiAug2009

[5] F. Lemke et. al, "A Unified Interconnection Network with Precise Time Synchronization for the CBM DAQ System", IEEE NPSS Real Time Conference, 2009, Beijing, China

[6] W.gao et. al, "Improved Active Buffer Board of CBM", GSI Scientific Report 2008, Darmstadt, Germany

[7] Linev et. al, "Software development for CBM readout controller board", GSI Progress Report 2008, Darmstadt, Germany

[8] Sebastian Manz, "GET4 readout chain", CBM Collaboration Meeting, 2009, Split, Croatia

A Wide Applicable TDC with Event-Driven Readout

H. Deppe[1] and H. Flemming[1]
[1]GSI, Experiment Electronics, Darmstadt, Germany

Introduction

2009 the GSI ASIC desgin group presented the first prototype of the event-driven TDC ASIC GET4. This ASIC was originally designed for the CBM Time of Flight subdetector system but its excellent time resolution and the triggerless operation make this chip to a good TDC candidate for other detectors especially in the FAIR environment.

TDC Overview

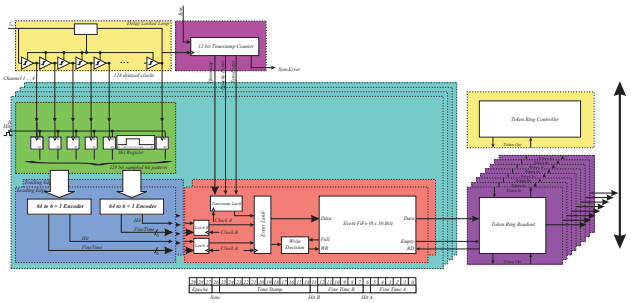

Figure 1: Block diagram of the GET4 TDC ASIC.

Figure 1 shows a block diagram of the GET4 ASIC. Main part of the time measurement system is the time core with an 128 stage Delay Locked Loop (DLL). Each of the four channels has an 128 bit hit register which is clocked by the timing signals of the DLL, four data encoders and two derandomization units. The readout of the data is done by a token ring based readout logic.

The time resolution of the TDC is given by the delay of one DLL delay element. The theoretical value is

$$\sigma_{th} = \frac{1}{\sqrt{12}} \frac{1}{128} T_{cyc} \qquad (1)$$

With a design clock frequency of 156.25 MHz the theoretical limit is $\sigma_{th} = 14.4$ ps. The splitting of the 128 bit hit register into two parts with separate data encoders makes GET4 able to cope with a burst hit rate of 312.5 MHz. The GET4 detects leading and trailing edges for time over threshold calculation.

Test Results

Figure 2 shows time measurements between channel 0 and channel 2 of the GET4 TDC. The measured correlated time resolution is 34.3 ps which leads into an uncorrelated time resolution of 24.2 ps. The histogram also shows that

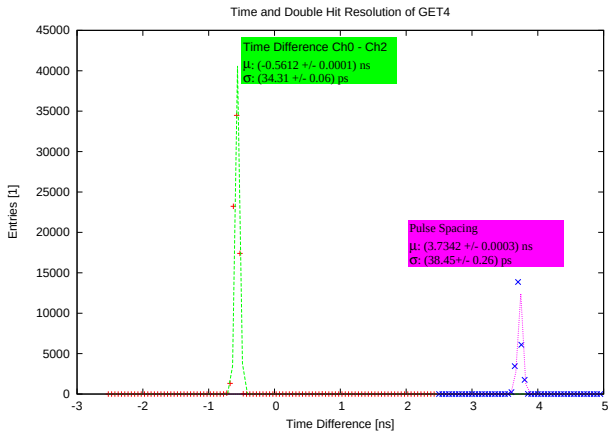

Figure 2: Histogram for time resolution and double pulse resolution determination.

the TDC can resolve double hits with ≤ 3.7 ns puls spacing. Beyond that it could be shown that GET4 is able to measure puls widths below 1 ns.

Evaluation board FEET-TDC

For detector and FEE developments an evaluation board with two GET4 ASICs on board was designed. This board with the two ASICs on the left side is shown in figure 3.

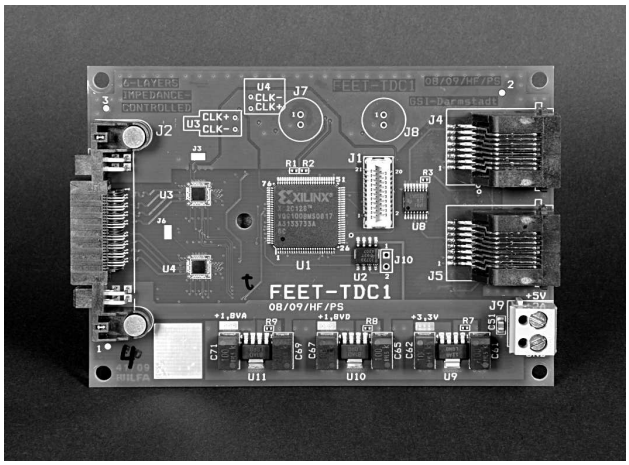

Figure 3: Picture of the FEET TDC pc-board (courtesy of G. Otto).

References

[1] H. Deppe and H. Flemming, The GSI Event-driven TDC with four Channels GET4, Nuclear Science Symposium Conference Record, 2009 IEEE

Development of a High-Resolution (< 10 ps RMS) 32-channel TDC in a Field-Programmable-Gate-Array*

E. Bayer[1,#], M. Traxler[1]
[1]GSI Helmholzzentrum, Darmstadt, Germany.

Time to Digital Converters (TDCs) are widely used in many scientific applications. At GSI high-resolution ASIC-TDCs and commercial modules are utilized in Time of Flight detectors. Two methods used in high-resolution applications – the Vernier and the tapped delay line (TDL) method – have been successfully implemented in FPGAs, e.g. a FPGA-TDC with 17 ps time resolution has been described recently in [1]. The advantage of a FPGA implementation is the less complex, less expensive and less time consuming design process as well as the flexibility and adaptability of the FPGA-TDC design to special needs of the current application. These facts motivated us to explore the performance of a TDC implementation in a FPGA.

TDC-Design

A 32-channel TDC based on the TDL method was implemented on a Virtex-4 FPGA. In this method standard chain structures in a FPGA – the carry chains – are used as a delay chain for time stretching purposes. The intrinsic delay of a cell in the chain determines the achievable time-resolution of the time interpolation. In our target device the maximum delay of a cell is 45 ps. Some methods were proposed to improve the resolution of the TDC beyond its cell delay. A promising method, called the Wave-Union method, introduced in [2] for an Altera device, was adapted to the Xilinx Virtex FPGA architecture.

Measurements

In our measurements we determined the time difference of two rising edges which were fed into two different TDC channels. The time delay between the edges was varied by using different cable delays or with Tektronix Data Timing Generator DTG5078. In a TDC channel the time difference between the asynchronous input and the next rising edge of the system clock was measured and time stamped. The measurement data was combined with a channel number and stored in a FIFO. A bin-by-bin calibration and the analysis was performed offline. Several series of tests were performed to derive the achieved time resolution and the impact on it due to the temperature and supply voltage variations. All tests were accomplished with a 200 MHz system clock.

To characterize the influence of the system clock (accuracy and jitter) on the measured RMS value three measurement series were performed. Several measurements with increasing time difference were made with both edges within a system clock period (Figure 1a), within few periods and with a time difference about 1 µs respectively. A typical distribution of 500k time measurements for one fixed time delay is shown in Figure 1b.

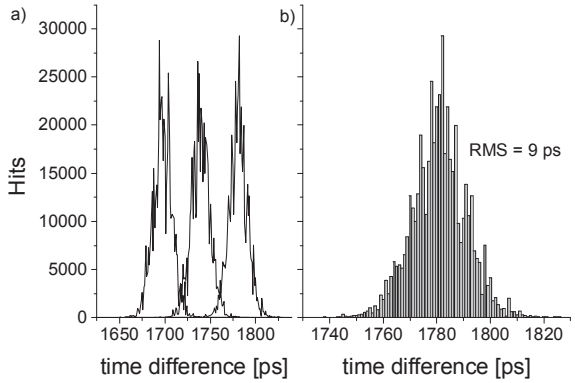

Figure 1: a: Tree different delays (incr. 40 ps) within a clock period. b: Typical distribution of 500k hits.

In the first two measurement series the RMS value was 9 ps. So the resolution of a single channel is $9/\sqrt{2} \approx 7$ ps. Due to the limited accuracy of the system clock additional 2 ps were added in the third series (long period measurement).

The performance of the TDC was also examined under varying environment conditions. In the temperature test setup the temperature of the FPGA was increased from 30 °C to 85 °C. With increasing temperature a deformation of the calibration look-up-table was observed. This results in a worsening of the RMS value if a table beyond the 5 °C temperature region is used. However, the change of the temperature has no influence if the table is updated often enough.

In the voltage test setup the supply voltage was varied within the allowed voltage range of the FPGA-core from 1.15 V to 1.25 V. We observed a 50 ps shift in the measured mean caused by the reduction of the intrinsic offset between the signal runtimes to the carry chains. Under normal conditions this effect was not observed with the used voltage regulator (DC/DC converter).

References

[1] C. Favi; E. Charbon: A 17ps Time-to-digital Converter Implemented in 65nm FPGA Technology, IEEE ISFPGA, February 2009.

[2] J. Wu, Z. Shi: The 10-ps wave union TDC: Improving FPGA TDC resolution beyond its cell delay, IEEE Nuclear Science Symposium Conference, 19-25 Oct. 2008.

* Work supported by EU FP6 grant, contract number 515876 and EU FP6 grant RII-CT-2004-506078.
# eugen.bayer@gmx.de, e.bayer@gsi.de

Design and performance of a fully differential Multigap RPC *

I. Deppner[†1], N. Herrmann[1], M. Ciobanu[2], D. Gonzales-Diaz[2], K.D. Hildenbrand[2], M. Kis[2], Y. Leifels[2], P.-A. Loizeau[1], and Y. Zhang[1]

[1]Physikalische Institut Uni. Heidelberg, Heidelberg, Germany; [2]GSI, Darmstadt, Germany

In the current design of the CBM experiment, hadron identification is based on the Time-of-Flight measurement provided by a wall of Multi-gap Resistive Plate Chambers (MRPC). Due to a lower rate the outer most part can be covered with float glass MRPCs in a multi-strip configuration.

In order to study possible configuration of such systems, a prototype of a Multi-strip MRPC with fully differential readout was developed (see Fig.1). The active area of the

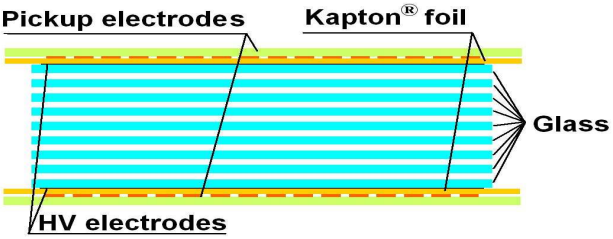

Figure 1: MRPC layout

prototype is 28 x 16.5 cm^2. Its active volume is subdivided by nine 0.55 mm thick float glass plates. The space between the glass plates is ensured by 220 μm thick fishing lines. The bottom and top plates are covered by conductive layers (surface resistivity 100 MΩ/cm^2) to form electrodes to which High Voltage of $\pm$10.5 kV and $\pm$11.5 kV is applied. Therefore the el. field in between the electrode equals to 120 kV/cm and 130 kV/cm. The two outermost plates (PCB 4mm) serve as support for the MRPC and contain also the readout strips which have a width of 7 mm. The relatively big distance between the strips is 3 mm and leads to an reduced cross talk. This strip configuration together with the total number of gaps was simulated to have the impedance of 100 Ω. A good impedance matching with the front-end electronics [1] is necessary to reduce signal reflections in the counter. Measurements with an reflectometer show a real impedance of about 80 Ω. Another advantage of the purposed strip configuration is that the strip width is comparable with the cluster size of an avalanche, which was shown to be approximately 7 mm at a field of 108 kV/cm [2], therefore charge sharing can only happen between two strips. Due to the totally symmetric layout of the counter the signal is fully differential which minimize the common mode pickup noise in the preamplifier. For signal amplification and discrimination we use the so called PADI 2 [1] with time-over-threshold function. The LVDS timing output signals from PADI are fed into an expansion card for the high timing resolution system (TACQUILA) [3], which allows time over threshold functionality for TACQUILA.

The described setup was tested in August 2009 with a 3 GeV proton beam in cave B. Using the tracking information from silicon detectors the efficiency for different strips and different positions perpendicular to the strip (y-position) could be determined with accuracy of 1 mm (see fig. 2). The efficiency of each individual strip shows a plateau of 6 mm in the overlap region of the strip in the order of 95%. It drops slightly towards the side of the strip, but in the middle of the gap between the strips it still amounts to be about 80%. The total efficiency of the RPC is over all about 95%. In addition the average cluster size

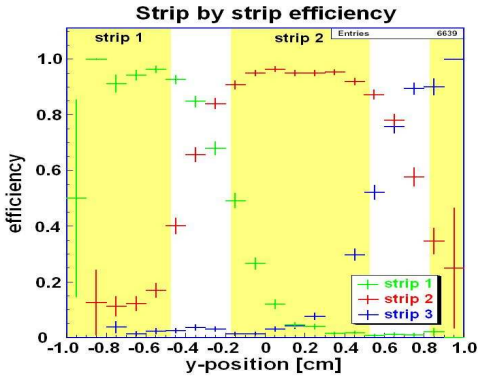

Figure 2: Strip by strip efficiency: the yellow area depict the position of the strips.

of the signals was determined. That is the average number of strips which fire for a single avalanche. At 11 kV the cluster size was found to be 1.2 strips which means that in most of the cases only one strip fires. Three strip events were found with a probability of about 2% allowing to estimate the total cross talk in this configuration to below 3%.

References

[1] M. Ciobanu, N. Herrmann, K.D. Hildenbrand, M. Kis, A. Schüttauf, " PADI, a fast Preamplifier - Discriminator for Time-of-Flight measurements", IEEE NSS, Dresden, (2008), 2018-2024

[2] I. Deppner, N. Herrmann, R. Averbeck, C. Ciobanu1, K.D. Hildenbrand, T.I. Kang, M. Kis, Y. Leifels, K. Piasecki, A. Schüttauf, D. Gonzalez Diaz, and the FOPI Collaboration " Characterisation of FOPI narrow strip RPCs", CBM Progress Report 2008

[3] K. Koch, E. Badura, " High resolution double-hit timing and time over threshold measurement feasibility for the TACQUILA system", IEEE NSS,Honolulu, HI, (2007), Volume: 1, 320-321

* Work supported by BMBF 06HD190i

† deppner@physi.uni-heidelberg.de

An algorithm for offline correction of the walk effect

H.T. Johansson[1] and Yu. Aksyutina[2]
[1]Chalmers University of Technology, Göteborg, Sweden; [2]GSI, Darmstadt, Germany

The walk effect, i.e. the dependence of a time signal on its amplitude, can lead to a significant worsening of the time resolution for a detector signal. Walk is inevitable in measurements where the time signal is produced using a leading-edge discriminator. Using a CFD supposedly should solve the problem, but any improper adjustment of the CFD can worsen the walk. Here an algorithm for offline determination of the walk effect from collected physics data is presented.

The time, t, measured by a single detector channel can be viewed as

$$t = t_0 + f(e), \tag{1}$$

where t_0 is the real time of event appearance and $f(e)$ the function containing the amplitude dependence of the measured time. Thus, to perform the walk correction, the function $f(e)$ has to be determined and corrected for. In case of events where known t_0 are available, the function $f(e)$ can be easily determined [1].

For the case with unknown t_0, events with special properties can be used. The present algorithm uses data from events where it can be expected (often by geometry) that some relationship between real times should exist. These can be either the four times of two simultaneously fired neighbouring paddles in case of the LAND and TFW detectors or a single scintillator foil viewed by four photomultipliers, such as the POS detectors. Assuming that signals with the above mentioned properties are produced by the same particle, the condition for calculated mean times

$$\frac{t_{01}+t_{02}}{2} - \frac{t_{03}+t_{04}}{2} = C \tag{2}$$

has to be fulfilled. Here, the times t_{01} and t_{02} (t_{03} and t_{04}) belong to opposite photomultipliers. The constant C is calibrated to vanish by later calibration steps and is not relevant for this paper.

Different flight paths of the particle through the two paddles cause different energy deposition. Although the energies measured in one paddle are correlated, the finite energy resolution makes them different enough to be used as independent. In case of the POS detector, all four energies are correlated but due to small detector size the light attenuation is comparable with resolution. Therefore, they also can be treated as independent.

By introducing a value

$$dt = \frac{t_1+t_2}{2} - \frac{t_3+t_4}{2}, \tag{3}$$

where t_1, t_2, t_3 and t_4 are measured times, the combination of Eq. 1 and Eq. 2 leads to

$$dt(e_1,...) = \frac{f_1(e_1)+f_2(e_2)}{2} - \frac{f_3(e_3)+f_4(e_4)}{2} + C. \tag{4}$$

Accordingly, the function dt is affected by the walk effect in all four detector channels. If one applies narrow gates on e_2, e_3 and e_4 then corresponding functions can be treated as constants and eq. 4 is simplified to $f_1(e_1) = dt(e_1) + C_1$, where C_1 includes all constant offsets. By looping over e_1 the corresponding function is determined. By moving the gates over the whole ranges of e_2, e_3 and e_4 a set of curves $f_{1,j}(e_1) = dt_j(e_1) + C_{2,j}$ is obtained, where the constant C_2 depends on the gate positions. The curves cover partial energy ranges. They are subsequently merged into one energy-dependent function. A walk curve obtained for one of the POS detector channels is shown in Fig. 1.

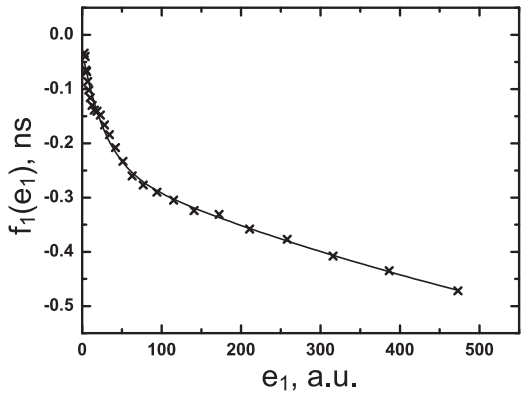

Figure 1: Walk curve obtained for one POS channel.

Once the functions $f_i(e_i)$ have been obtained, corrections can be tested for the data after the TDC slopes, prior to subsequent calibration procedures.

The presented method has been applied to the POS, TFW and LAND detectors during analysis of the S245 experiment. Due to lack of statistics for LAND and TFW the results have so far not been useable. For these detectors an alternative data collection using only two or three signals is under investigation. Curves obtained for the POS detectors were successfully applied and although gaining a small resolution improvement from $\sigma = 196$ ps to $\sigma = 192$ ps, the method works and should be very helpful in the future, when leading edge discriminators will be used in R^3B setup.

References

[1] L. Heilbronn, Y. Iwata, H. Iwase, Nucl. Instr. Meth. **A 522** (2004) 495.

Correcting integral non-linearities of the TACQUILA board

M. Kiš[1,2], R. Averbeck[1], M. Ciobanu[1], I. Deppner[2], Y. Leifels[1], N. Herrmann[2], K.D. Hildenbrand[1], and FOPI Collaboration[1]

[1]GSI, Darmstadt, Germany; [2]Physikalisches Institut, Heidelberg, Germany

The MMRPC ToF Barrel [1] was installed in FOPI towards the end of 2007; since then we have performed a few production runs in which the new detector has shown to be a valuable tool. The ToF resolution of about 95 ps has been achieved in all runs after consistent implementation of necessary corrections. Here we present the correction of integral non-linearities also known as "wiggle"-correction.

The timing electronics for the MMRPC Barrel (so-called TACQUILA board [2]) was developed by the DVEE department of GSI, which also designed the TAC chip used on the board. The measurement is performed in a common-stop mode with a distributed 40 MHz clock system as reference. The TAC ASIC has an timing resolution of about 10 ps and it features a very good linearity. However, one can still find small deviations that can be corrected. These so-called integral non-linearities are illustrated in Fig. 1. The top panel (a) shows raw spectra of the time difference.

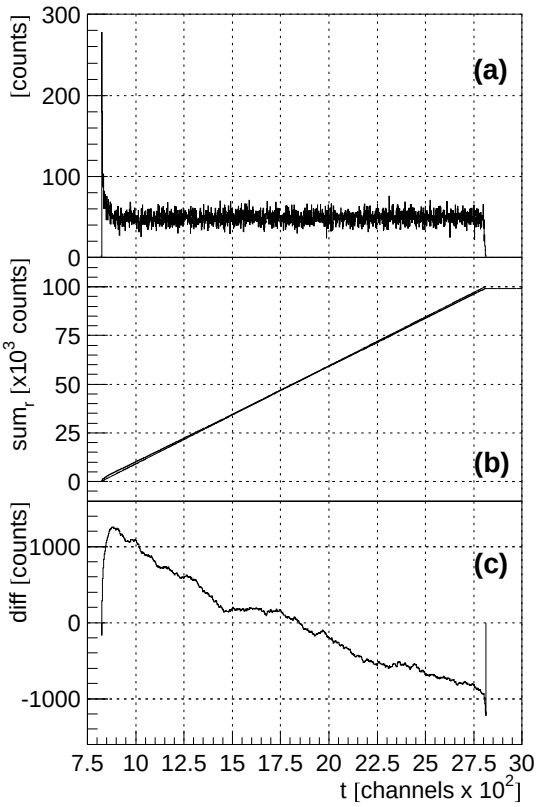

Figure 1: See text for details.

Apart from beginning and end of the spectra which are influenced by an interference, the measurement appears to be fully random since there is no correlation between physical events and the reference (clock) signal. Nevertheless, if one subtracts a linear fit of the cumulative sum of the spectra (panel b), the result (panel c) indicates a systematic non-linear behavior ("wiggle") which can be corrected.

It is known that the integral non-linearities in the case of our TAC chips are strongly dependent on temperature. Therefore a very robust cooling system for electronics was installed. In addition the calibration is performed in regular intervals. On the other hand during regular runs one cannot obtain enough statistics in order to perform a precise correction for each channel as shown in Fig. 1. Therefore, since the behavior of TAC chips is similar, the correction is performed by averaging over the 16 channels of a single TACQUILA board. The result of such a correction is

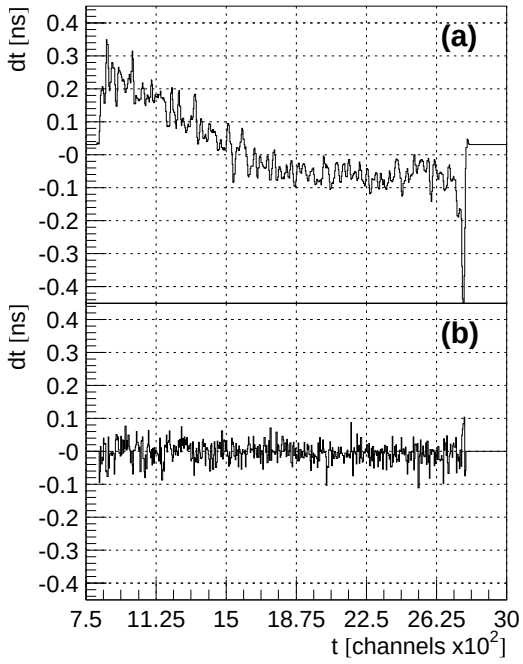

Figure 2: See text for details.

in Fig. 2, where a time difference spectra before and after correction (upper and lower panel) is shown. The corrections are applied to all RPCs of the Barrel as a last correction, bringing the overall ToF resolution from about 100 to 95 ps.

References

[1] A. Schüttauf et al., Nucl. Phys. B (proc.Supp.) 158 (2006) 52

[2] K. Koch et al., IEEE Trans. Nucl. Sci. 52 (2005) 745

Radiation Studies on the UMC 180 nm CMOS Process

S. Löchner*[1]
[1]GSI, Darmstadt, Germany

Introduction

Radiation damages to electronic components are an important issue for future FAIR experiments. One of the preferred technology for ASIC developments at GSI is the 180 nm UMC CMOS process. In this regard the ASIC design group of the GSI Experiment Electronic department has been launched a research project in 2007, including the development of an ASIC called *GRISU*. The main goal is the characterisation of Single Event Effects as well as Total Ionising Dose effects on the 180 nm UMC process.

Single Event Effect Studies

Single Event Effect (SEE) is the main generic term for effects in semiconductor devices triggered by the impact of ionising particles. Within the SEE there are more detailed types of effects. Of great interest are the so-called Single Event Upset (SEU) and Single Event Transient (SET) effects.

A good choice to test these effects is the irradiation of the semiconductor devices with heavy ions. Therefore the *GRISU* test chip has been particular designed to monitor these effects during irradiation. For a complete characterisation it is also necessary to measure the impact of ionising particles at different Linear Energy Transfer (LET) levels.

The irradiation tests of the *GRISU* were performed at the GSI linear accelerator (UNILAC) in cave X6. The coverage of the large LET range was obtained with different heavy ions and energy absorption in air. An overview of the 2008 and 2009 available ions and the resulting energy and LET parameters are given in Table 1.

Heavy ion	Energy [MeV/AMU]	Energy [MeV]	LET [MeV cm^2 / mg]
C-12	0...10.4	0...125	1...5
Ar-40	0...9.0	0...360	10...19
Ni-58	0...7.9	0...458	15...32
Ru-96	0...7.3	0...691	30...49
Xe-132	0...7.3	0...969	40...60

Table 1: Energy and LET range for the heavy ions available at the various beam test.

Exemplarily the overall cross section test results versus LET is shown in Figure 1 for a minimum sized inverter. The critical Linear Energy Transfer (LET_{crit}) as well as the maximum cross section ratio are extracted from the test results for each test structures. Furthermore the sensitivity against SEU for different types of flip-flop and memory cells have been tested.

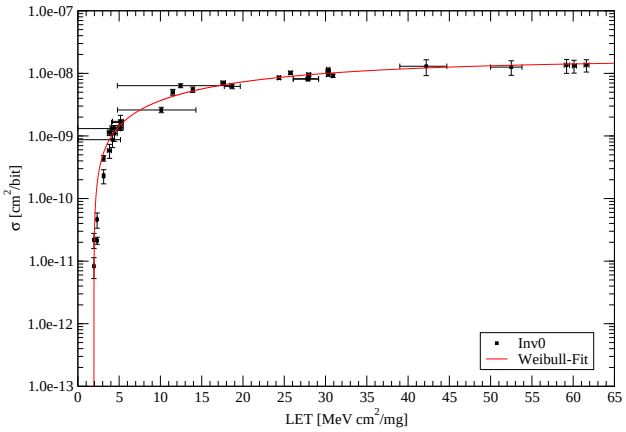

Figure 1: Weibull fit of the SET cross section of a minimum sized inverter.

Total Ionising Dose Studies

A Total Ionising Dose (TID) test was performed at the X-ray irradiation facility of the IEKP [1] / FZK [2]. In total 8 *GRISU* test chips have been irradiated. Table 2 summarises the different dose rates and accumulated doses.

The transient and output characteristics of discrete MOSFET transistors as well as threshold voltage and leakage currents were measured for different accumulated dose levels. Immediately after irradiation the annealing of the chips were measured. Finally, all chips showed a very good annealing performance. After four weeks leakage current has settled back to the initial value.

Number of chips	Dose rate [krad/h (SiO_2)]	Accumulated dose [krad (SiO_2)]
1	20	320
2	40	400...480
4	80	640...960
1	196	600

Table 2: Summary of irradiated *GRISU* chips, dose rates and accumulated doses of the TID test.

References

[1] Institute of Experimental nuclear Physics (IEKP), University of Karlsruhe (TH) http://www-ekp.physik.uni-karlsruhe.de

[2] Forschungszentrum Karlsruhe (FZK) http://www.fzk.de

* s.loechner@gsi.de

Total Ionising Dose Studies of the QFW ASIC

S. Löchner*[1], H. Flemming[1], and M. Witthaus[2]
[1]GSI Darmstadt, Experiment Electronics; [2]GSI Darmstadt, Beam Diagnostic

Introduction

In 2004 the ASIC design group of the GSI Experiment Electronics department (EE) has developed a full custom designed Application Specific Integrated Circuit (ASIC) called *QFW*[1]. This chip, based on a former development of a charge to frequency converter [2], provides a dynamic range of more than 7 decades without any range switching (1 pA. . . 10 μA respectively 10 pA. . . 100 μA).

A typical application for which the chip can be used is the signal readout of ionisation chambers or multi wire detectors. Therefore, for a good readout performance the *QFW* chip has to be mounted maybe very close to the GSI accelerator or near the beam pipe somewhere in the experiments. In these environments there are often very harsh radiation conditions to the semiconductor devices. Special effects like the Total Ionising Dose (TID) play a very important role and therefore prior to the selection of a chip must be carefully tested. In cooperation with the GSI Beam Diagnostic group a research project has been launched 2008 for testing to test these TID effects of the *QFW* ASIC.

Total Ionising Dose Studies

In July 2009 a Total Ionising Dose test was performed at the X-ray irradiation facility of the Institute of Experimental Nuclear Physics (IEKP)[3] at Forschungszentrum Karlsruhe (FZK)[4]. In total two *QFW* test chips mounted on the *QFW* board of the Beam Diagnostic group [5] have been irradiated. A picture of the test setup inside the irradiation chamber is shown in Fig. 1. During the beam tests the X-ray operation settings were held constant at 60 kV and 30 mA tube current. In order to change the irradiation dose rate the distance between X-ray source and test setup could be changed.

Measurements and Results

The first chip was irradiated up to 3.2 kGy (SiO_2), the second chip up to a total dose of 17.2 kGy (SiO_2). For all four channels of the *QFW* chip the current to frequency characteristic was measured for positive as well as negative test currents. The lower limit for the injected currents was 50 pA, the upper limit 10 μA respectively 100 μA.

Both chips were fully functional after irradiation with X-rays. The measured increase of leakage current was in the order of 70 pA per kGy (SiO_2), constant over the complete dynamic range of the *QFW*. Only one channel of one chip showed a significant higher increase in leakage current. After a total dose of 6 kGy (SiO_2) the average increase of leakage current of this channel was 1940 pA per kGy (SiO_2).

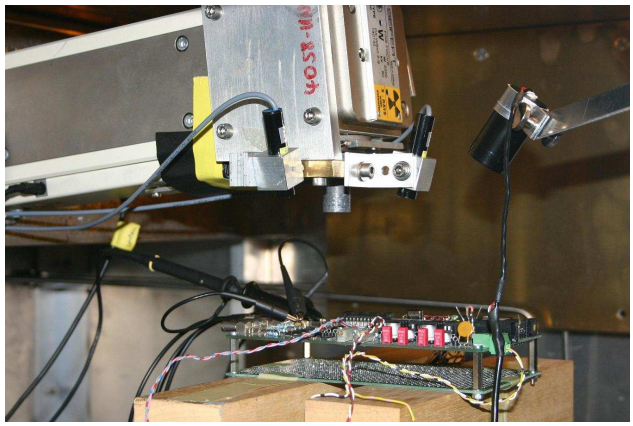

Figure 1: *QFW* test setup inside the X-ray irradiation chamber. The collimator output of the X-ray tube is shown at the top, underneath one of the both test PCB with a *QFW* chip is located.

Immediately after irradiation the annealing of the induced leak currents was observed. After two months of annealing at room temperature no leakage currents were measured for both chips.

Summary

The first Total Ionising Dose test of the *QFW* has shown that the chip can withstand higher radiation doses, although it was not designed for it. The chip also showed a very good annealing performance after the X-ray beam was switch off. It is therefore highly unlikely that failures due to TID effects will occur during normal beam operation conditions.

References

[1] H. Flemming and E. Badura "A high dynamic charge to frequency converter ASIC", GSI Scientific Report 2004

[2] E. Badura, "Vorrichtung und Verfahren zum Umwandeln von Ladungsfluss in ein Frequenzsignal", EP 1 031 040 B1

[3] Institute of Experimental Nuclear Physics (IEKP), University of Karlsruhe (TH), Karlsruhe, Germany http://www-ekp.physik.uni-karlsruhe.de

[4] Forschungszentrum Karlsruhe (FZK), Karlsruhe, Germany http://www.fzk.de

[5] M. Witthaus et al., "Charge-Frequency-Converter (QFW) Test Board and Results", GSI Scientific Report 2009

* s.loechner@gsi.de

Design and implementation of a data transfer protocol via optical fibre

S. Minami*[1], J. Hoffmann[1], N. Kurz[1], and W. Ott[1]

[1]GSI, Darmstadt, Germany

There have been development of the new electronics equipped with the small form-factor pluggable (SFP) transceivers for the data transfer via optical fiber, i.e. PEXOR (a PCIe card) [1], VULOM5 (a VME module) [2], FEBEX (a front-end board with pipeline ADC) [3] and EXPLODER (a front-end board with 32 LVDS I/O) [4]. A new protocol, GOSIP (**G**igabit **O**ptical **S**erial **I**nterface **P**rotocol) has been designed to provide communication between the electronics via optical fibre, primarily for the multi branch system (MBS), standard data acquisition system at GSI.

Table 1: An example of the structure of the packet for the address mode write request to be sent from the master to the slave. The values in the third column are the case for the write access with the value 0x01FEDCBA to the memory at the address of 0x7654321 of the 8th slave module.

	8 bit width data		example	
0	Reserved	Packet Type	0x0	0x6
1	Address Length	Data Length	0x4	0x4
2	Address 0		0x21	
3	Address 1		0x43	
4	Address 2		0x65	
5	Address 3		0x87	
6	Data 0		0xBA	
7	Data 1		0xDC	
8	Data 2		0xFE	
9	Data 3		0x01	

It is a master and slave protocol to control the busy of the communication safely. One SFP port of a master is capable to control multiple slaves if the slaves have 2 SFP ports. The slaves can be cascaded the way that the secondary SFP port of the slave at upstream to be connected with the primary SFP port of the slave at downstream. The chain of the slaves need to be initialized by 'initialization' packet and will be assigned the module ID number starting from 0x00 to the number or the slave modules. The module ID occupied 8-bit of address space in 32-bit address space that the memory with the size of 16 Mbytes can be mapped for the each slave modules. There are 2 modes of data transfer, 'address mode' and 'block mode'. 'Address mode' supports read and write memory access to the slave specified by 24-bit-wide memory address and 8-bit-wide slave module ID. 'Block mode' provides fast readout of large size of data from all the slave memory. It transfers data with the size of pre-set size from the pre-set base address and its successive addresses. The slaves can have 2 pre-set base address for double buffering to reduce dead-time. The example of the packet structure of the address mode and the block mode are shown in Table 1 and Table 2, respectively. The both modes are initiated by the master which send a 'request' packet to the slave and the slave examines the 'packet type' if it indicates 'initialization', 'address mode' or 'block mode'. If it is for 'address mode', and the address points to itself, the slave will send 'reply' packet to the master. If the address dose not match the slave, then the 'request' packet will be passed to the next slave until the address matches one slave or it reaches the last slave. The slave modules pass the packet sent from other slave modules at downstream without checking and the master receives either 'reply' packet to the correct 'request' or the original 'request' if the address dose not match any slaves. In the case of 'block mode', the slave received the 'request' packet starts transfer of the 'reply' packet with the data. When it finishes to send its own data, it passes the 'request' packet to the slave at downstream until the last slave. The last slave return the 'request' packet back to upstream.

The protocol has been implemented using Verilog HDL, currently supports the communication between PEXOR and FEBEX or PEXOR and EXPLODER.

Table 2: An example of the structure of the packet for the block mode read reply from the slave to the master. Data size (DS) to be transferred are specified in 4×8-bit fields, Data Size 0,1,2 and 3. The values in the third column are for the case to send the data, 0x01FEDCBA, with the size of 0x00000004 bytes taken with the trigger whose flag is 0x01 from the 8th slave module.

	8 bit width data		example	
	Reserved	Packet Type	0x0	0x8
1	Header Length	Data Size Length	0x3	0x4
2	Header 0 (Trigger)		0x01	
3	Header 1 (Slave ID)		0x08	
4	Header 2 (SubMemory ID)		0x01	
5	Data Size 0		0x04	
6	Data Size 1		0x00	
7	Data Size 2		0x00	
8	Data Size 3		0x00	
9	Data 0		0xBA	
10	Data 1		0xDC	
11	Data 2		0xFE	
⋮	⋮			
DS+8	The last Data		0x01	

References

[1] J. Hoffmann *et al*. GSI Scientific Report 2008, p275

[2] http://www.gsi.de/informationen/wti/ee/elekt_entwicklung/vulom5.html

[3] http://www.gsi.de/informationen/wti/ee/elekt_entwicklung/febex.html

[4] http://www.gsi.de/informationen/wti/ ee/elekt_entwicklung/exploder.html

* s.minami@gsi.de

Charge Breeding with the SPARC-EBIT

A. Thorn*[1], A. Sokolov[2], G. Vorobyev[2], F. Herfurth[2], O. Kester[3], W. Quint[2], F. Ullmann[4], and G. Zschornack[1]

[1]Institut für Angewandte Physik, Technische Universität Dresden, Germany; [2]GSI, Darmstadt, Germany; [3]NSCL/MSU, East Lansing, USA; [4]Dreebit GmbH, Dresden, Germany

Highly charged ions (HCIs) are an important tool in various fields of basic and applied physical research. However, in many cases the species of interest cannot be produced directly by a primary ion source. Therefore, charge breeding, i.e. the conversion of singly charged ions to highly charged ions, is an essential part of projects such as nuclear or astrophysical experiments with post accelerated beams of radioactive ions [1] or precise nuclear mass measurements with ions stored in penning traps [2].

At GSI's HITRAP facility [3] HCIs up to U^{92+} can be provided using an accelerator complex to strip electrons off the initially low charged ions at high velocities. In case the beam from the accelerator structure is not available, tests can be run using a compact room-temperature electron beam ion trap, the SPARC-EBIT [4], which was designed to produce HCIs from gaseous materials injected through a needle valve. To broaden the range of particles which can be fed to the source we have investigated its abilities as a charge breeder.

The setup for the charge breeding experiments includes a surface ion source for the creation of the singly charged alkali metal ions. The measurements presented in this paper were performed using potassium. These primary ions are guided straight towards the SPARC-EBIT where the charge breeding process takes place. It can be divided into three phases: K^{1+} injection, breeding, and re-extraction of a pulse of highly charged ions from the EBIT. During the re-extraction phase a quadrupole bender mounted in between the two ion sources is switched from ground to high voltage to bend the ion trajectories by 90 degrees and send the pulse towards the multi passage spectrometer (MPS) where it can then be analyzed by magnetic A/q separation.

A typical A/q spectrum of charge bred potassium measured with the MPS is presented in figure 1. The source parameters given in the picture were found to be optimal for continuous potassium ion injection. After a breeding time of $t_{\mathrm{breed}} = 3$ s the charge state distribution has reached its equilibrium. Since the electron beam energy of the EBIT was set close to the ionization energy of the K-shell, helium-like potassium shows the highest relative abundance in the spectrum. Bare potassium ions have been detected, though only in small amounts. Further on, it was discovered that an injection time of $t_{\mathrm{inj}} = 20$ ms at the beginning of the breeding time, t_{breed}, is sufficient to achieve the maximum ion output for high charge states. The capture efficiency during the measurement resulted in $\approx 2 \cdot 10^{-4}$. Breeding efficiencies for different charge states

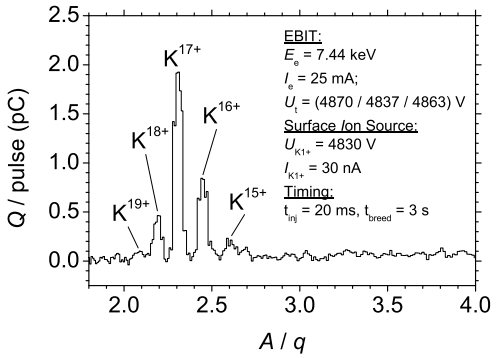

Figure 1: Charge state distribution after $t_{\mathrm{inj}} = 20$ ms and $t_{\mathrm{breed}} = 3$ s. The experimental parameters given in the picture are the electron beam energy, E_{e}, as well as the electron current, I_{e}, of the EBIT, the drift tube voltages, U_{t}, the K^{1+} ion acceleration potential, U_{K1+}, and finally the K^{1+} current, I_{K1+}, measured on a Faraday cup in front of the EBIT entrance.

are presented in table 1.

The activities will be continued with studies of advanced charge breeding techniques [5] using high-Z elements.

Table 1: Charge breeding parameters for various potassium ion charge states q including the breeding time at which q represents the maximum of the charge state distribution, t_{breed}, the maximum number of K^{q+} ions per pulse, $N_{K^{q+}}$, the relative abundance of the charge state q, $N_{K^{q+}}/N_{\mathrm{K}}$, and the breeding efficiencies, $\varepsilon_1 \rightarrow q$.

q	t_{breed}(ms)	$N_{K^{q+}}(10^5)$	$\frac{N_{K^{q+}}}{N_{\mathrm{K}}}$	$\varepsilon_{1\rightarrow q}(10^{-5})$
9	50	2.4 ± 0.5	29 %	6.3 ± 1.6
14	300	2.7 ± 0.5	32 %	7.2 ± 1.8
17	1000	5.6 ± 1.1	45 %	15.3 ± 3.8

References

[1] D. Habs et al.: Hyperfine Interactions 129 (2000) 43–66

[2] J. Dilling et al.: Int. J. Mass Spectrom. 251 (2006) 198

[3] F. Herfurth et al.: Int. J. Mass Spectrom. 251 (2006) 266

[4] B.E. O'Rourke et al.: J. Phys. Conf. Ser. 163 (2009) 012103

[5] O. Kester et al.: J. Phys. Conf. Ser. 2 (2004) 107

* a.thorn@fzd.de

Design and Implementation of the Read Out Controller for the GET4 TDC of the CBM ToF Wall Prototype

S. Manz[1] and U. Kebschull[1]

[1]Kirchhoff Institute for Physics, Heidelberg University, Heidelberg, Germany

Introduction

The Time of Flight detector of the CBM experiment will assemble about 12 500 GET4 ASICs [1]. Those chips give a very precise timestamp (resolution better than 25 ps) to detected hits and then deliver the data (24 bits/hit) via a serial LVDS link to the Read Out Controller (ROC). At the moment, the FPGA of one ROC interfaces up to 14 GET4 chips. However, the current hardware allows up to 28 GET4 chips and even more should be possible with the new generation of ROCs. In addition to the combination and synchronization of the data from all GET4 chips into one data stream, the ROC has to provide a control interface for all the chips.

Modular Design

The GET4 readout chain is one of several readout chains needed for the experiment, all with similar requirements. Therefore we implemented a modular system which separates the readout logic from the transport logic. Much functionality can be reused and only the interface to the frontend electronics needs to be exchanged. In addition, this modular approach allows an efficient development of the firmware by more than one designer. The GET4-ROC is developed as a readout logic module in the "Universal ROC" design. More details concerning the "Universal ROC" design can be found in [2].

Readout Logic

Until now a basic readout module for the GET4 chips has been developed. Figure 1 shows an overview of the ROC. First the serial data is sampled and deserialized. Then the decoded data is combined into a single data stream. At the moment a simple round robin algorithm is implemented. This stage also performs very basic message building. For future versions a slightly more complex token ring readout in combination with improved message building is planned. The sampling on the data ports can be switched off by a configurable mask register (e.g. to avoid ghost data from unconnected ports).

The ROC also needs to provide a control interface to the GET4 chips and to the ROC itself. Single commands can be send via transport logic to the ROC. In case of a command for the GET4 chips, this command is passed to the GET4-boards (the so called FEET boards) via a serializer. On default, the command is sent to every connected FEET board. To address only specific boards the control path implements a configurable mask register as well.

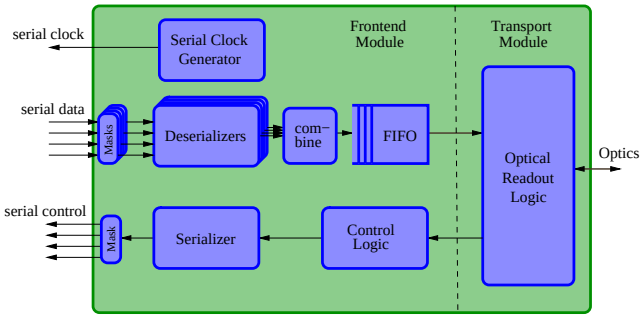

Figure 1: Block diagram of the ROC's functionality.

Transport Logic

At the moment there are two transport logic modules available to connect the ROC to a DAQ-PC, Ethernet and optics (see [3] for details concerning the optics). While Ethernet is better tested and a convenient solution for small setups, some features only come with the optics module. Those features are a high bandwidth (current hardware: ca. 230 MB/s) for the data readout and deterministic latency messages for synchronisation. However the optical readout chain requires an additional PCIe card, the ABB [4].

Future Prospects

The current version of the GET4 readout module provides a basic interface. The module is usable, however it is not feature complete. Besides the improvement of many smaller details, the features that will be developed in 2010 are a proper synchronization technique and simple data processing tasks.

References

[1] H. Flemming and H. Deppe, "GET4 TDC ASIC", GSI internal report, March 2009

[2] N. Abel, S. Manz and U. Kebschull, "Design and Implementation of an Universal Read Out Controller" GSI Scientific Report 2009, Darmstadt, Germany

[3] F. Lemke et. al, "A Unified Interconnection Network with Precise Time Synchronization for the CBM DAQ System", IEEE NPSS Real Time Conference, 2009, Beijing, China

[4] W. Gao et. al, "Improved Active Buffer Board of CBM", GSI Scientific Report 2008, Darmstadt, Germany

Usage of DABC in software development for CBM DAQ

S. Linev[1], J. Adamczewski-Musch[1], and H.G. Essel[1]
[1]GSI, Darmstadt, Germany

CBM readout controller

The CBM readout controller board (ROC) was developed to control nXYTER-based [1] front-end electronics and deliver data from the nXYTER to a PC via Ethernet. A first version of PC software libraries (ROClib [2]) for communication with the ROC was implemented.

Then a significant redesign of this software was required because new ROC firmware will support various kinds of front-end electronics and optic transport from ROC to PC. It was necessary to separate the communication (transport layer) from the device-specific controlling and configuration (application layer).

Data transport

The application layer together with communication interfaces is kept in ROClib. An abstract *roc::Board* class defines the interface for communication and data transport. The transport layer was removed from ROClib and implemented as plug-ins of the Data Acquisition Backbone Core (DABC) [3], a general purpose data acquisition framework. DABC had already been used with the previous ROClib for building DAQ applications for ROCs.

The UDP transport between ROC and PC was reimplemented with the powerfull DABC socket handling classes, allowing to handle several socket connections in one thread.

Several firmware and software components were developed at Uni Heidelberg for the optic transport from ROC to PC via a PCIe board (AVNET-board). This consists of a linux driver for the board, a user-space library (mprace) and a special daemon application. Appropriate DABC *device* and *transport* classes were implemented on top of this software.

Introducing a communication layer interface in ROClib allows to develop application software which is fully independent from the communication implementations like the DABC plug-ins.

Control interface

To control and configure different front-end electronics connected to the ROC, a control-space access interface was defined in ROClib. It consist of a single operation - *noper*, which is just a list of *put* and *get* register operations, implemented in the DABC plug-ins. Based on such interface, a number of device-specific classes were implemented in ROClib to configure ADCs, nXYTERs, I2C bus and other components.

Data format

All data taken from one kind of front-end are packed in messages of fixed length. Message format and even message size depend on the connected electronics, firmware version and the kind of the connection. To handle all possible formats a class *roc::Message* was introduced. It provides a convenient way to access the data fields for any supported message type.

User tools

The transport and control classes are used in several applications:
rocutil - command-line tool for device configuration;
rocGui - Qt4-based configuration GUI;
go4monitor - go4-based [4] program for taking and displaying data from a single ROC.

Test beamtime 2009

During September beamtime up to 6 ROCs reading data from different detectors were running in parallel. They delivered up to 30 MB/s to a single PC running the DABC data acquisition, which sorted and stored the data to list-mode data files. At the same time data was monitored online by several *go4monitor* applications, connected to the DABC application through standard GSI data channels.

Status and outlook

The developed software allows to configure and run ROCs in different environments. DABC is used as core framework for the implementation of ROClib software. A succesfull beamtime was operated with a DABC-based DAQ system in September 2009. The development of the optic transport via PCIe board is mostly finished. Information and latest news on cbm-wiki.gsi.de

References

[1] A.S. Brogna et al., “N-XYTER, a CMOS read-out ASIC for high resolution time and amplitude measurements on high rate multi-channel counting mode neutron detectors”, Nucl. Instrum. Methods A 568 (2006), pp. 301-308

[2] N. Abel et al., “Software development for CBM readout controller board”, GSI Scientific Report 2008, p. 228

[3] J. Adamczewski, H.G. Essel, N. Kurz, S. Linev, “Data Acquisition Backbone Core DABC”, Journal of Physics: Conference Series 119 (2008) 022002

[4] J. Adamczewski, M. Al-Turany, D. Bertini, H.G. Essel, S. Linev, “Go4 online monitoring”, IEEE Trans.on Nucl. Science, Vol.51, No.3, June 2004, pp 565-570

Development of a GEM-TPC for PANDA *

X. Zhang[†1], C. Höppner[1], B. Ketzer[1], I. Konorov[1], and M. Vandenbroucke[1]

[1]Physik Department, Technische Universität München, 85748 Garching, Germany, for the GEM-TPC Collaboration

The PANDA (AntiProton Annihilations at Darmstadt) experiment is an internal target experiment at the High Energy Storage Ring (HESR) for antiprotons at the new Facility for Antiproton and Ion Research (FAIR) at Darmstadt, Germany. A Time Projection Chamber (TPC) is proposed as the central tracker due to its excellent tracking and particle identification capabilities [1]. A spatial resolution of $\sim$150 μm in the rφ projecton and $\sim$1 mm in z, resulting in a momentum resolution of the order of a few percents over a range of 0.1 to 8 GeV, and a low material budget are needed by the rich physics program of PANDA.

The continuous antiproton beam structure at HESR, however, makes the use of a traditional ion gate, normally used to avoid space charge accumulation, impractical. Due to their intrinsic ion backflow suppression, the use of GEM (Gas Electron Multiplier) structures [2] for gas amplication opens up the possibility to operate the TPC in an ungated mode without accumulating excessive space charge.

A small GEM-TPC was built and characterized with cosmic muons [3]. The test chamber of 20 cm diameter and 8 cm drift length, operates with an Ar/CO_2 (70/30) gas mixture. On the readout plate, an active area of $10\times10\,cm^2$ was filled with rectangular pads of $0.8\times6.0\,mm^2$ and covered by 3 GEM foils for electron amplification. An average resolution of 200 μm had been achived using the PASA-/ALTRO [4] readout electronics.

To perform a complete characterization of the test chamber, we set up a tracking telescope on the electron accelerator ELSA in Bonn, Germany. The test bench consists of four single silicon strip detectors and 4 GEM planes, triggered by four plastic scintillators with $2\times2\,cm^2$ active area.

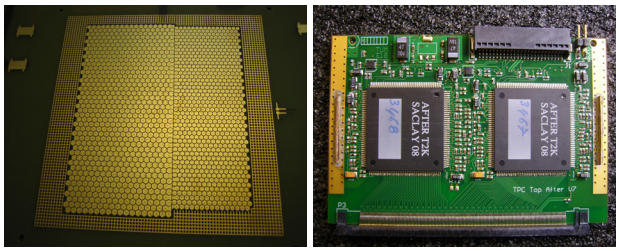

Figure 1: Photographs of the new readout plane (left) and the Front-end Electronics (FE) card (right) which holds four AFTER chips.

* Supported by the 6th Framework Program of the EU (Contracts No. RII3-CT-2004-506078, I3 Hadron Physics, and No. 515873-DS, DIRAC-secondary-Beams), the German Bundesministerium für Bildung und Forschung, the Maier-Leibnitz-Labor der LMU und TU München, and the DFG Cluster of Excellence "Origin and Structure of the Universe".

† xzhang@e18.physik.tu-muenchen.de

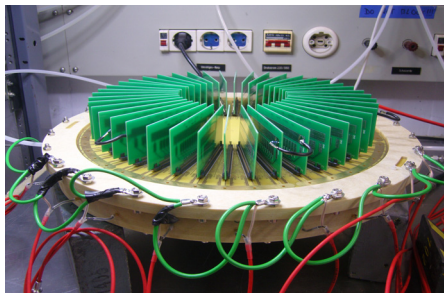

Figure 2: The GEM detector of the GEM-TPC prototype with 42 FE cards (See Fig. 1).

In addition, the TPC test chamber was upgraded before its installation in the test setup. The readout plane was changed from rectangular pads to hexagnal pads of 1.25 mm and 1.5 mm outer radius, respectively(See Fig. 1). Another main improvement is the use of a new readout based on the AFTER (Asic For TPC Electronic Readout) chip developed by CEA Saclay for the T2K experiment [5]. This 72 channels ASIC contains an analog memory, based on a switched capacitor array of 511 cells which can be read by a custom-made ADC sampling at 10 to 50MHz. The full front-end electronics reaches a good noise performance of 800 e^- at an input capacitance of 10 pF. The tracking telescope was successfully commissioned in December 2008 and has started to record data. First signals have been observed in the GEM-TPC. The texternal tracking and the very good noise performance of the readout electronics will allow a precise measurement of spatial resolution, drift velocity and charge accumulation inside the TPC. These properties will be further investigated with larger GEM-TPC prototypes (30 cm of diameter, 73 cm of drift length) currently built for the FOPI experiment at GSI and Crystal Barrel at ELSA. Fig. 2 shows its GEM detector which is being tested in our lab.

References

[1] Technical Progress Reports for PANDA, 2005, http://www-panda.gsi.de/archive/public/panda_tpr.pdf.

[2] F. Sauli, GEM, Charge transfer and charge broading of GEM structures in high magnetic fields, Nucl. Instr. Meth. A386 (1997) 531.

[3] Q. Weitzel et al., Development of a High-Rate GEM-Based TPC for PANDA, IEEE Nucl. Sci. Symp. Conf. Rec. (2007).

[4] L.Musa et al., The ALICE TPC Front End Electronic, Proceedings of the IEEE Nucl. Sci. Symp., Portland (2003).

[5] P. Baron et al., AFTER, an ASIC for the readout of the Large T2K Time Projection Chambers, Nuclear Science, IEEE Transactions on Vol. 55, Issue 3, (2008).

Readout Chain for the PANDA EMC*

Peter Wieczorek[1] and Jan Hoffmann[1]
[1]GSI, Experiment Electronics, Darmstadt, Germany

Introduction

The developed Front End Board with optical link EXtension (FEBEX) is designed for parallel analogue signal readout. The input stage of the board consists of 12 bit sampling ADCs. With the implemented FPGA a pulseshape analyse is destined. The FEBEX - board is used for a matrix readout of the preamplifier shaper ASICs (APD PANDA Front End Link (APFEL)) which are developed by the EE ASIC group for the electromagnetic calorimeter (EMC) of the PANDA experiment[1].

Preamplifier shaper ASIC APFEL

The charge sensitive preamplifier and shaper ASIC APFEL developed for the EMC of the PANDA experiment is optimised for the readout of avalanche photo diodes (APD) with a capacitance of 300 pF. It is able to cope with an event rate of 300 kHz. At the forseen operation temperature of T= $-20°$C and a detector capacitance of 300 pF an equivalent noise charge (ENC) of 4334 e^- $\pm$ 28 e^- was measured. Together with the maximum input charge of 6 pC this leads to a dynamic range of over 10 000. The power consumption is 49.5 mW / channel. These results of the preamplifier shaper ASIC are in excellent agreement with simulations and fulfil the given requirements[1].

FEBEX - Board

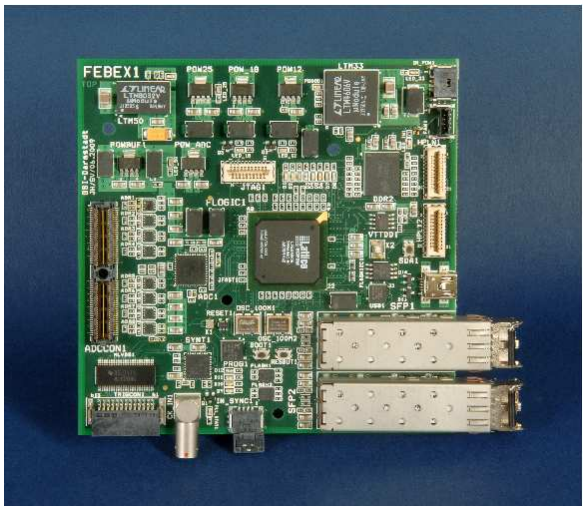

Figure 1: Picture of the FEBEX - board[2] (courtesy of G. Otto).

Figure 1 shows the FEBEX - board. The input side comprises 8 differential analogue inputs which are connected to the ADCs. The used ADC has an input range of $\pm$ 1 V with a resolution of 12 bit and a sampling rate of 65 MS/s. An implemented FPGA is forseen for pulseshape analysis. The data transfer is done over an optical link[2].

ASIC Matrix readout

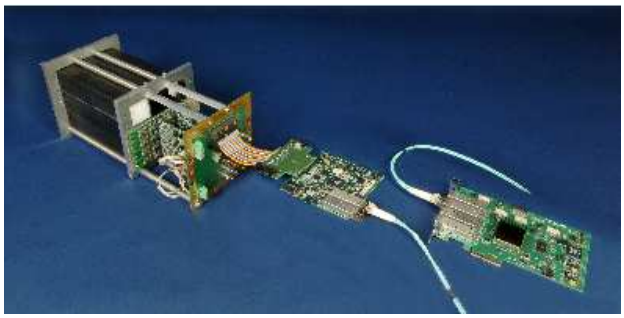

Figure 2: Picture of the matrix readout (courtesy of G. Otto).

In the end of 2009 first electronic tests were successful completed. In the next step a matrix of 16 lead tungstate crystals will be assembled. Each crystal will be equipped with an APD detector which is read out by the charge sensitive preamplifier shaper ASIC.

The differential analogue output signals of the ASIC are digitised by the FEBEX - board. Afterwards the data collection will be done over an optical link to the GSI Multi Branch System (MBS)[3]. The overview of the mounted setup is shown in figure 2. For the visualisation of the data the GSI Objected Oriented On - line Off - line system (Go4) will be used[4].

The in figure 2 presented setup is prepared for the cosmic radiation measurements which are scheduled in March. During the next year more detailed beam tests are intended.

References

[1] P. Wieczorek and H. Flemming, "Low noise preamplifier ASIC for the PANDA EMC", GSI Scientific Report 2006, June 2007 p. 4.

[2] J. Hoffmann, GSI: http : //www.gsi.de/informationen /wti/ee/elekt_entwicklung/febex.html

[3] N. Kurz, GSI: http : //www − win.gsi.de/daq/

[4] J. Adamczewski - Musch, GSI: http : //www − win.gsi.de/go4/

* Work supported by EU (contract number: RII3-CT-2004-506078)

The PANDA GEM-TPC prototype*

B. Voss, R. Arora, M. Henske, V. Kleipa, J. Kunkel, C.J. Schmidt, S. Schwab, D. Soyk, J. Weinert
GSI, Darmstadt, Germany.

A Time-Projection Chamber (TPC) [1] is an ideal candidate for the central tracking device inside the target spectrometer of PANDA@FAIR due to its excellent tracking performance and particle identification capabilities, combined with a small material budget. Its operation in the antiproton storage ring HESR at a 'standard' rate of $2{\cdot}10^7$ pp-bar annihilations per second, however, requires a continuous sampling of incoming signals leading to event mixing. The use of GEM technology for charge amplification provides the means to achieve the required resolution and to suppress the accumulation of space charge in the drift volume. We currently foresee 3 stages with 8 cake-like sectors per foil in CERN 'standard' configuration (Cu/Kapton® 5/50µm thickness and double-conical hole pattern 50/70/140µm $\varnothing_{Cu}/\varnothing_K$/distance). The leakage current at 550V has been measured to be (3.1±1.8) nA for 10 foils with a maximum value of 6.3 nA which is very well acceptable.

For in-lab tests, a pad plane with ~10000 hexagonal pads as shown in fig. 1 has been built. Its shape conforms to the design values within an accuracy of well below 0.1mm. It features common electrical support, coding of the front-end boards and a variety of sensor controls.

For test purposes it is foreseen to read out the detection systems using a future version of the data driven XYTER ASIC offering 128 ch/chip of charge sensitive amplifiers, fast (30 ns) & slow (150 ns) shapers, a peak detector, 1 ns time stamping and a de-randomizing, sparsifying 32 MHz token-ring readout. The measured noise value of σ~425e$^-$@5..10pF is close to the design-value of 370e$^-$@10pF / 550e$^-$@20pF and sufficient for the PID by the TPC. The current version AMS-CMOS-0.35µm technology needs 21 mW/ch of power requiring an effective cooling system to get rid of ~0.5 kW heat dissipated. For this purpose, a heat-piping system (see fig. 2) with a minimized number of joints is operated with liquid coolant HFE7100 under ~4 bar overpressure and turbulent flow of ~3 l/h.

Most of the ongoing work is now focussing on the construction and testing of the field-defining system (see fig. 3). Its length has been extended to 702 mm to cope with the needs of the crystal-barrel experiment at ELSA /Bonn. The simulations show that a strip width and gap of the staggered strip-lines of 1 mm and 0.5 mm, respectively, keep the field inhomogeneities in the vicinity of the walls in an acceptable range. The GEM-TPC prototype will be tested early 2010 at CB@ELSA and FOPI@GSI

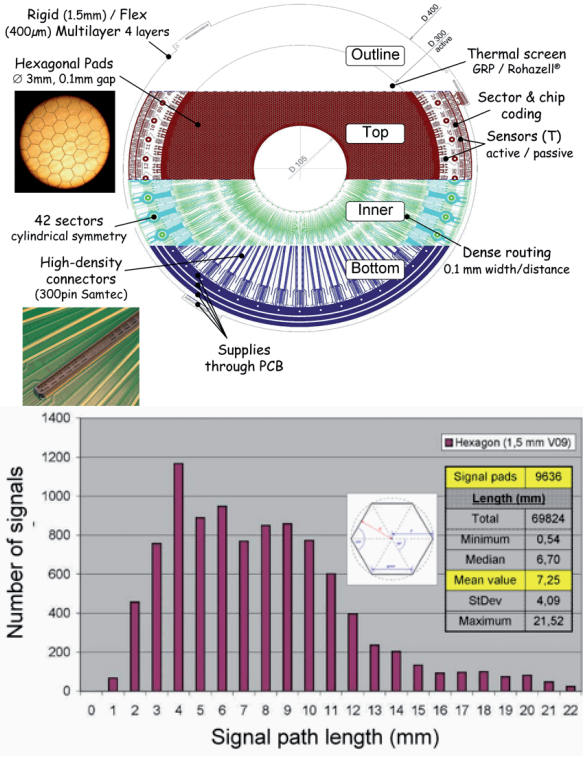

Figure 1: Features and characteristics of the pad plane.

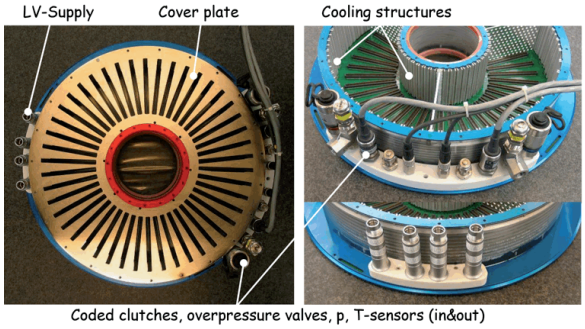

Figure 2: Details of the heat piping system.

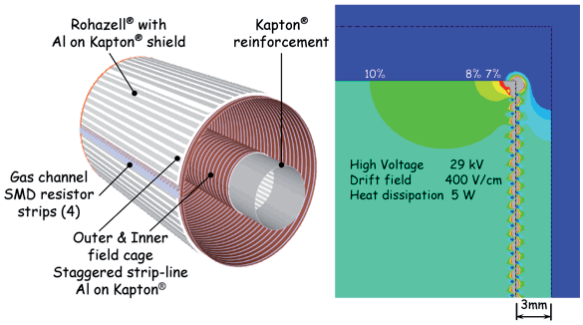

Figure 3: Design and simulation details of the field-cage.

References

[1] Voss B. et al., GSI Scientific Report 2008, GSI Report 2009-1, p.238.

* Work supported by the EU 7th framework program (I3HP2).

The GEM-Discs for the PANDA experiment*

B.Voss, J. Kunkel, R. Karabowicz
GSI, Darmstadt, Germany.

The Setup

In the PANDA experiment particles emitted at angle below 22° may not be fully covered by the Central Tracker in the target spectrometer. They will be tracked with a set of up to four large-area planar gaseous micro-pattern detectors based on GEM foils as amplification stages [1]. A sketch of their design is shown in fig. 1.

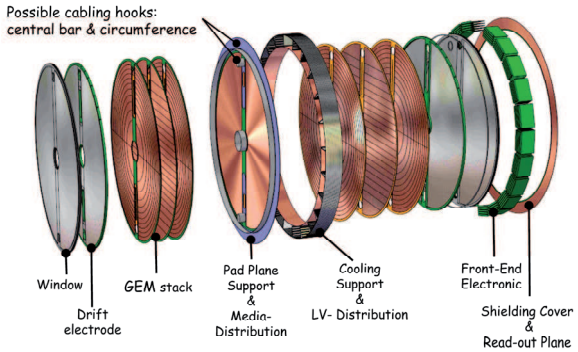

Figure 1: Sketch of the build-up of a single GEM-Disc.

In order to optimize the acceptance, these GEM-Trackers have to be of large diameters Ø0.9m (2x), 1.12m and 1.48m and will be placed 0.81m, 1.17m, 1.53m and 1.89m downstream of the target, respectively. The current design assumes up to four double planes with two projections per plane. With the envisaged position resolution of 0.1mm the system promises sufficient momentum resolution and a double track resolution of 10mm and 5°, respectively, in the range of forward angles of 4-5 up to 18-20° (depending on the available space).

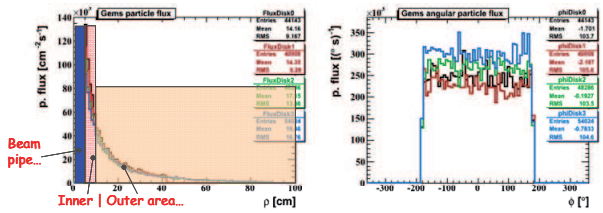

Figure 2: Simulation of the particle flux.

The chambers have to sustain a high counting rate of particles peaked at the most forward angles due to the relativistic boost of the reaction products as well as due to the small angle pp-bar elastic scattering. According to simulations [2] of the particle flux as shown in fig. 2 for the envisaged luminosity, the expected hit rate in the first chamber is about $8*10^4 cm^{-2}s^{-1}$ in the vicinity of the 6.5 cm diameter beam pipe. The track length to be recorded inside the active volumes of the detectors will be 0.5-8mm (mean 1.3-1.6mm) in radial and 0-0.8°(mean 0.15°) in angular direction. The expected cluster sizes are <1mm (single HIT cluster to be avoided). Thus the design of the read-out structures, the so called 'pad planes', are purely driven by the required resolution, not by particle occupancy. Patterning structures under investigation are strips (circular/polar+radial and Cartesian) as well as pixels of regular-polygon shapes and hybrid structures. A stable operation at design luminosity for 10 years lifetime (100 krad) and a maximal degradation of track efficiency <2%/layer is required. Moreover, the chambers have to work in the 2T magnetic field produced by the solenoid.

* Work supported by the EU 7th framework program (I3HP2).

The Detector Control System

A system for control and operation is set up currently dealing with 47 entries/parameters in ≈2000 channels (see fig. 3). Hard- and software limits are applied to the parameters under supervision, e.g. overall status, temperatures, pressures, flow of media, voltages, currents, aging and 'special events' (e.g. sparks). The dense and compact system is modular, expandable and flexible with local intelligence and pre-processing of the sensor signals. Its failsafe operation provides hierarchical interlocking and archiving under EPICS. It has to cope with various hardware, information pathways, communication protocols (I^2C, SPI, CAN, Ethernet TCP/IP) and deals with information for device configuration, -operation, -control & -monitoring and supplemental ambient & operational conditions. All electronics involved and installed '*in situ*' has to be radiation tolerant, aging resistant and insensitive to magnetic fields. The communication is performed via LWL.

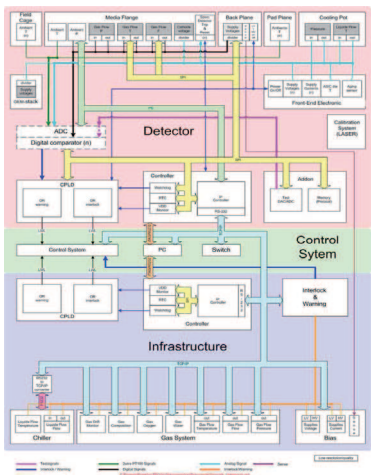

Figure 3: Sketch of the Detector Control System.

References

[1] Voss B. et al., GSI Scientific Report 2008, GSI Report 2009-1, p.242.
[2] Karabowisz R. et al., contribution to this report

Performance of the ALICE TRD with first LHC collisions

The ALICE TRD collaboration*

In December 2009 a milestone of the ALICE Transition Radiation Detector (TRD) [1] was marked when the detector was turned on to record tracks of particles produced by first stable beams in collision at the Large Hadron Collider. We report here the performance of the detector during the ensuing data taking period of 2 weeks.

Of the 18 TRD supermodules, 7 are currently installed in the ALICE setup. Assembly and testing is ongoing for the rest, envisioned to be installed during the next LHC shutdown period end of 2010. The LHC provided beams at the injection energy of 450 GeV per beam, with bunch intensities of up to 10^{10} protons. Triggering with the Silicon Pixel Detector and the V0 detector, ALICE acquired about $2.5{\cdot}10^5$ events with a good collision vertex. About 90% of the 210 individual chambers in the TRD recorded data at their nominal settings. Chamber calibration [2] was performed both online and based on a dedicated reconstruction pass performed at GSI.

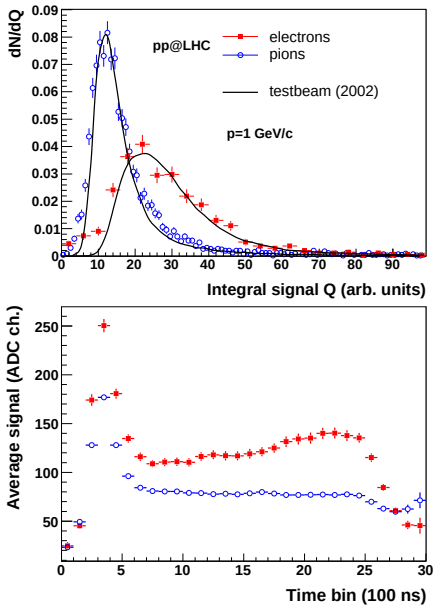

Figure 1: Integral charge deposit (top) and average signal as a function of time (bottom) for pions and electrons of 1 GeV/c.

In Fig. 1 we show for all chambers the integral charge deposit per chamber for pions and electrons as well as the average signal as a function of drift time. For these studies an electron-enriched sample is selected employing reconstructed photon conversion candidates, while the pions are selected from reconstructed K^0_s mesons. Cuts in the dE/dx signal of the TPC were additionally employed. Good agreement with data measured earlier in testbeams is observed. The TR signature of electrons, manifested in the average signal increase at late drift times is also evident.

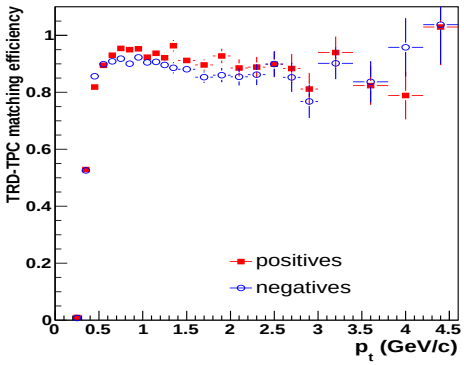

Figure 2: TRD-TPC track matching efficiency as a function of transverse momentum.

In Fig. 2 we show the track matching efficiency between the TRD and TPC, demonstrating the good performance of the detector and reconstruction algorithm.

An important prerequisite for global tracking is to properly account for the actual positions of the involved detectors. The relative alignment between the TPC and TRD was studied using cosmic muons collected within four months prior to the LHC startup. Without alignment, the residual distance between the TRD tracklets and the TPC tracks extrapolated to the TRD (dashed histogram in Fig. 3) indicates that the TRD supermodules were displaced by up to 1-2 cm with respect to the TPC. Applying the alignment parameters deduced from the cosmic muon tracks for the reconstruction of the pp collisions leads to the drastically reduced residuals shown as the solid histogram in Fig. 3.

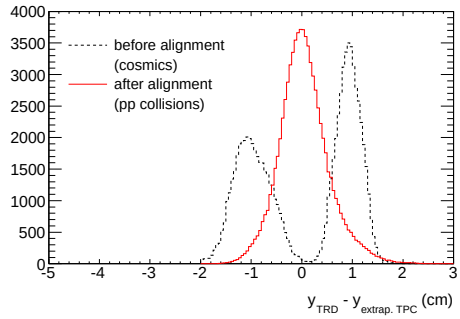

Figure 3: The $r\phi$ position residuals of the TRD w.r.t. extrapolated tracks from the TPC.

References

[1] ALICE Transition Radiation Detector Technical Design Report, ALICE TDR 9, CERN/LHCC 2001-021.

[2] R. Bailhache et al., this Report.

*The list of members and institutions is available at http://www-alice.gsi.de/trd

Gain Calibration of the ALICE TRD with Krypton (^{m83}Kr)

M. Al Helwi[1], A. Andronic[3], Y. Pachmayer[1], N. Pitz[2], C. Garabatos[3], K. Schweda[1,3], J. Stachel[1], and J. Wiechula[1]

[1]University of Heidelberg, Heidelberg, Germany; [1]University of Frankfurt, Frankfurt, Germany;
[3]GSI Helmholtz Centre for Heavy Ion Research, Darmstadt, Germany

The Transition-Radiation Detector (TRD) of ALICE at the LHC is designed for electron identification, charged particle tracking and providing a fast trigger. The TRD consists of 18 super-modules with 540 readout drift chambers filled with Xenon gas. The large active area of roughly 700 m^2 is covered by about 1.2 million readout channels. Traversing charged particles ionize the gas along their path creating secondary electrons. These electrons drift in a uniform field of 700 V/cm over 3 cm before being amplified. In order to guarantee a high quality of the collected data a uniform gain is essential. The gain contains both gas and electronics response which may vary throughout the detector.

These gain parameters can be determined with a dedicated calibration run using Krypton. During the run, the radioactive ^{m83}Kr was distributed homogeneously in the TRD volume by the gas circulation system.

This method allows a pad per pad calibration of the 7 TRD-super-modules installed in ALICE during the 2009 data and calibration run. The radioactive ^{83}Rb decays to metastable ^{m83}Kr by β-decay. ^{83}Rb is solid and therefore it allows to be placed into the gas stream via a by-pass line.

The gaseous ^{m83}Kr disperses throughout the entire TRD gas volume. It has a lifetime of 2,64h, which is short enough to ensure the chamber to be operated normally once a few lifetimes passed after cutting off the Krypton supply to the chamber. Thus no disposal of radioactive gas is necessary. On the other hand, it is long enough to be distributed in all chambers resulting in a sufficient number of decays. The metastable ^{m83}Kr decays through emissions of electrons with kinetic energies corresponding to the expected energy deposition of particles produced in heavy ion collisions (Fig.1).

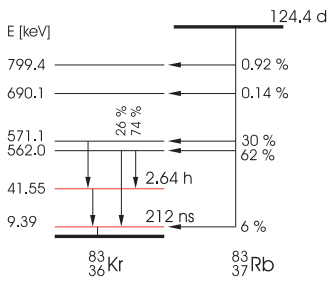

Figure 1: ^{83}Rb and ^{83}Kr energy level scheme. This figure has been taken from [1]

The Krypton data taking started on the 31^{st} of August 2009 and ended on the 25^{th} of September 2009. In this period of time about 800 million events were taken with different high voltage (1450 V, 1470 V) and magnetic field settings (0 T, 0.2 T, 0.5T). Approximately five Krypton decays per event are expected. The size of the raw data was circa 30 TB which was reduced to circa 10 TB after reconstruction.

A cluster finder algorithm that reconstructs the energy deposition in TRD from the ^{m83}Kr decays was developed. Furthermore, cuts to significantly reduce noise were implemented. Figure 2 shows the Krypton energy spectrum for

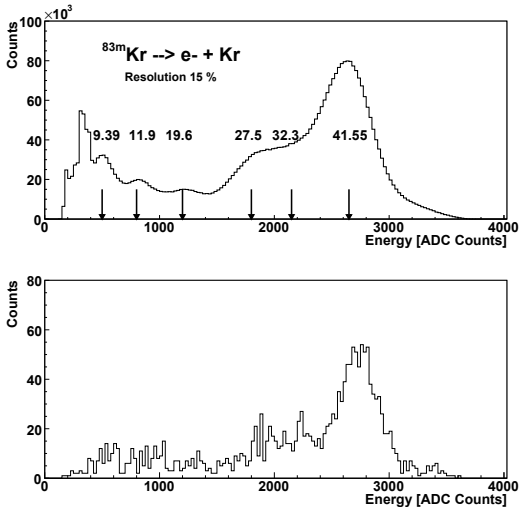

Figure 2: caption: Top: Experimental Krypton spectrum of a single TRD chamber, the arrows shows the energy in keV. Bottom: Experimental Krypton spectrum for a single pad.

one chamber with 2304 $pads$ and for one pad using approximately 10% of the statistics.The peak around ADC channel #2700 correspond to electron energies of 41.55 keV. Since this is the most likely decay channel, this peak will be used for the calibration. The other peaks provide information for cross checks.

The final goal is to provide pad by pad gain tables to be uploaded in the TRD front end electronics for data taking.

References

[1] T. Eggert, "Calibration methods of the STAR-FTPC", STAR Experiment at Brookhaven National Laboratory, USA.

Acknowledgement: This work has been supported by the Helmholtz Association under contract numbers VH-NG-147, HA-216/EMMI and the Federal Ministry of Education and Research under promotional reference 06HD9129D.

Status of the Pretrigger System for the ALICE Transition Radiation Detector *

J. Lehnert[1], B. Doenigus[2], J. Klein[3], T. Krawutschke[4], K. Oyama[3], R. Schicker[3], S. Schmiederer[3], K. Schweda[3], and J. Stachel[3]

[1]Institut für Kernphysik, Univ. Frankfurt; [2]GSI Helmholtzzentrum für Schwerionenforschung, Darmstadt, Germany; [3]Physikalisches Institut, Univ. Heidelberg ; [4]Fachhochschule Köln

The Transition Radiation Detector (TRD)[1] of the ALICE experiment at the CERN Large Hadron Collider (LHC) provides electron identification and tracking in the central barrel as well as fast triggering (6 μs). The front-end electronics (FEE) consisting of 75000 multichip modules has a total power consumption of less than 65 kW by keeping the digital electronics in a low power mode after processing each event. A fast wakeup signal for the FEE is needed to capture the TRD drift signals over the full time range and to ensure a low data processing latency. This pretrigger signal has to be generated within 400 ns after an interaction, more than 1 μs ahead of the ALICE Level0 (L0) trigger. It is based on the signals from the fast ALICE subdetectors TOF, V0 and T0, or alternatively derived from the LHC bunch counter (BC).

The pretrigger system[2] consists of a number of specific hardware components (see Fig.1) which are mounted inside the L3 magnet close to the respective detectors to minimize signal propagation delays. For the TOF detector, a single field programmable gate array(FPGA), the TLMU, evaluates 576 digital bits from the entire barrel region and provides trigger signals for configurable multiplicity conditions or geometrical correlations.

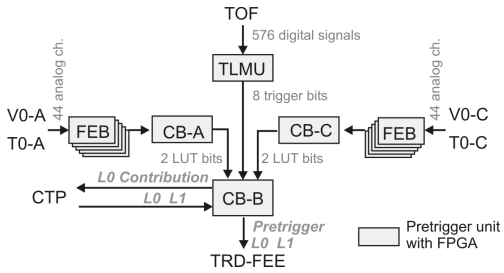

Figure 1: Schematic overview of the pretrigger system.

For the V0 and T0 detectors, preamplified analog signals from 44 channels on each side of the interaction point are discriminated in 5 front-end boxes (FEBs) and used as input to three stages of look up tables implemented in FPGAs. Their signals are combined in one control box on each side (CB-A and CB-C). One central trigger box (CB-B) processes trigger signals from each side of the forward detectors, from the TLMU and the central ALICE trigger processor. The CB-B provides event-synchronous alignment of signals from the different sources, combines them into a trigger decision and generates a pretrigger signal for the TRD FEE (see Fig.2). The CB-B also generates a contribution for the ALICE L0 trigger.

In 2009, the full pretrigger hardware and improved code versions of the most critical FPGA designs were commissioned. Tests were performed with the individual detectors either with cosmics (TOF) or with LED/laser pulsers (V0,T0), and the whole pretrigger functionality including communication with CTP and FEE was established.

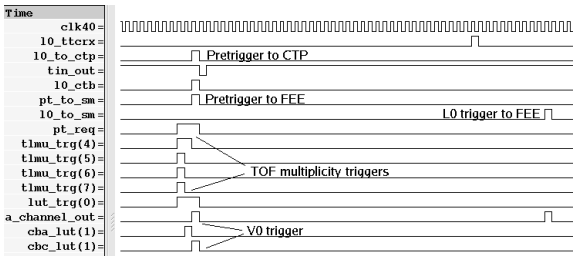

Figure 2: Screenshot from CB-B internal timing analyzer for single p+p collision.

The TRD pretrigger system was operational during the data taking period of ALICE with p+p collisions in the end of 2009. For the initial accelerator conditions with only 2 or 4 bunches in each beam, a BC trigger was used. The BC trigger on the filled bunches is internally generated in the CB-B and synchronized with the accelerator bunch clock. This trigger on each potential interaction allows pretrigger operation without any potential efficiency loss due to the detectors used in the pretrigger. With the periodic BC trigger, pretrigger rates up to 300 kHz were reached, limited only by the FEE power consumption. A V0 based pretrigger was evaluated, which is needed for more than 16 bunches per beam. A pretrigger should be generated for each L0 trigger, and a preliminary analysis of the data shows a V0 pretrigger efficiency >99% with respect to the V0 based ALICE L0 trigger. The pretrigger system was also operational with a setup including both TOF and V0 pretrigger. More detailed investigations are needed in order to estimate the performance of this setup.

For the run period in early spring 2010, optimizations of pretrigger settings and more detailed investigations of pretrigger efficiency under various conditions are foreseen and the full pretrigger DCS functionality will be implemented.

References

[1] ALICE Transition Radiation Detector Technical Design Report, ALICE TDR 9, CERN/LHCC 2001-021.

[2] S. Schmiederer, Diploma Thesis, Heidelberg 2009

*This work has been supported by the Helmholtz Association under contract numbers VH-NG-147, HA-216/EMMI and the Federal Ministry of Education and Research under promotional reference 06HD9129D.

Calibration of the ALICE Transition Radiation Detector with the First Proton Beam Data*

R. Bailhache[†1], F. Kramer[1], T. Bird[2], A. Andronic[3], I. Arsene[3], C. Blume[1], J. Book[1], and H. Appelshäuser[1]

[1]Geothe-University, Frankfurt, Germany; [2]University of Southampton, United Kingdom; [3]GSI, Darmstadt, Germany

The ALICE Transition Radiation Detector (TRD)[1] is a gaseous detector for electron identification, charged particle tracking, and triggering. When a charged particle crosses the gas volume it ionizes the gas along its path and electrons drift in a uniform field of 700 V/cm over 3 cm before being amplified. To optimize the detector performance, the drift velocity of the electrons and the amplification factor have to be corrected for variations of the temperature, pressure, and gas composition.

In December 2009 the 7 TRD supermodules installed in the ALICE setup took data together with the other detectors during the crossing of the first proton beams in the LHC. About 10 % of the 210 TRD chambers were for technical reasons not operated with their nominal anode or drift voltage and therefore ignored by the calibration procedure.

In the future, the calibration constants will be calculated during data taking with the High Level Trigger cluster[2]. The procedures have been partially tested with cosmic-rays data. A dedicated reconstruction pass performed at GSI was used to determine the calibration constants.

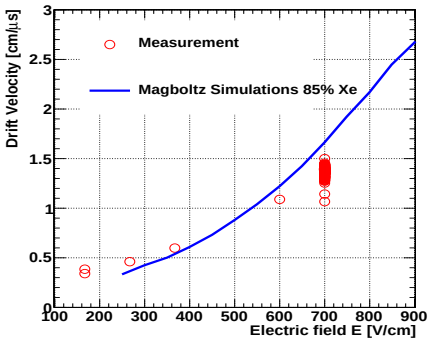

Figure 1: Drift velocity as function of the drift voltage in the chambers compared to Garfield simulations.

Fig. 1 shows the drift velocity of each chamber as function of their electric drift field for the run 104892. The results are compared to Magboltz simulations done for the corresponding gas mixture (Xe,CO_2(15 %)) at 1000 mbar.

The amplification factor was determined for each chamber. The variations of the temperature, pressure, and gas composition produce an overall shift of the gas gain. After normalization the gains can be compared from one run to another to estimate the accuracy of the gain calibration chamber by chamber. With the statistics available, an accuracy of about 5 % has been reached. Fig. 2 shows the gas gain for two different runs. In run 104892 some chambers with reduced anode voltage and therefore lower gain have been calibrated as well.

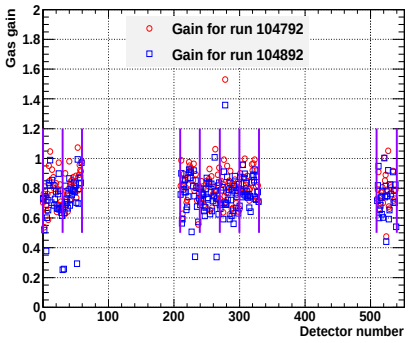

Figure 2: Gas gain for runs 104792 and 104892.

The gas gain and drift velocity constants found there were used to adjust the anode and drift voltages of the chambers to equalize their response. A first look at run 105160, taken after the High Voltage (HV) adjustment, shows a smaller dispersion of the chamber gain factors (8 % against 14 %).

Furthermore, the procedures for storing the detector configuration and status [3] have been extended. In addition to the front end electronics also the global tracking unit (GTU) is now read out twice for each run via the DIM protocol [4]. New methods have been put in place to assure that data has been transmitted correctly. The central communication proxy has been included into the standard alarm system for immediate reaction upon an error. The output, which is stored in the ALICE offline calibration database, is now read and used during data reconstruction.

References

[1] ALICE Transition Radiation Detector Technical Design Report, ALICE TDR 9, CERN/LHCC 2001-021.

[2] T.Rascanu et al., GSI Scientific Report 2009.

[3] F.Kramer et al., GSI Scientific Report 2008, Instruments-Methods-49, 269

[4] C. Gaspar et al., “DIM”, International Conference on Computing in High Energy and Nuclear Physics (Padova, Italy, 1-11 February 2000).

* Work supported by BMBF and GSI

† rbailhache@ikf.uni-frankfurt.de

Implementation of the ALICE TRD into the High-Level-Trigger*

T. Rascanu † , H. Appelshäuser, A. Arend, R. Bailhache, H. Büsching, J. Ulery
for the ALICE collaboration, Institut für Kernphysik, Goethe - Universität Frankfurt am Main, Germany

In this report, we describe the development, optimization and implementation of ALICE Transition Radiation Detector (TRD) [1] specific components into the High Level Trigger (HLT) [2] of the experiment.

The TRD High Level Trigger components

The ALICE High Level Trigger is a high performance computer cluster which provides the possibility of an online analysis of detector data from the ALICE experiment at the CERN LHC. With this online analysis it is possible to distinguish rare and interesting physics scenarios from frequently occurring and well known events. It also enables the various subdetector systems to perform online calibration, monitoring, and quality assurance. The HLT framework handles data transport and provides the infrastructure to integrate detector specific components.

The current TRD specific analysis chain in the HLT is laid out as follows: The TRD cluster and track finding components (*AliHLTTRDClusterizerComponent* and *AliHLTTRDTrackerV1*) derive directly from the offline analysis components [3]. They have been modified and optimized in terms of processing rates to the requirements of the HLT online analysis system. The calibration component (*AliHLTTRDCalibrationComponent*) has been adapted from the offline calibration procedure. The monitoring components for quality assurance (*AliHLTTRDClusterHistoComponent* and *AliHLTTRDTrackHistoComponent*) have been specifically designed for the HLT-TRD. The analysis chain is depicted in Figure 1. The trigger component *AliHLTTRDTriggerClusterMulticity* is the first approach to determine a trigger decision based on TRD information.

Current status

The HLT-TRD components have successfully been integrated into the High Level Trigger framework. During the data taking of the ALICE TRD in the year 2009 the components have intensively been tested in several scenarios (cosmic runs, data taking with krypton gas for calibration, and during the first pp-collisions). The stability and reliability of the software has been demonstrated. By using the designated HLT-TRD hardware infrastructure an overall event processing rate of more than 900 Hz was achieved for real pp-collision data in the complete chain. This event processing rate is the result of an intense optimization cycle containing a renewed memory allocation scheme, improved raw data reading patterns of the components, refined design of the core analysis components (cluster finding and tracking) and other minor optimizations.

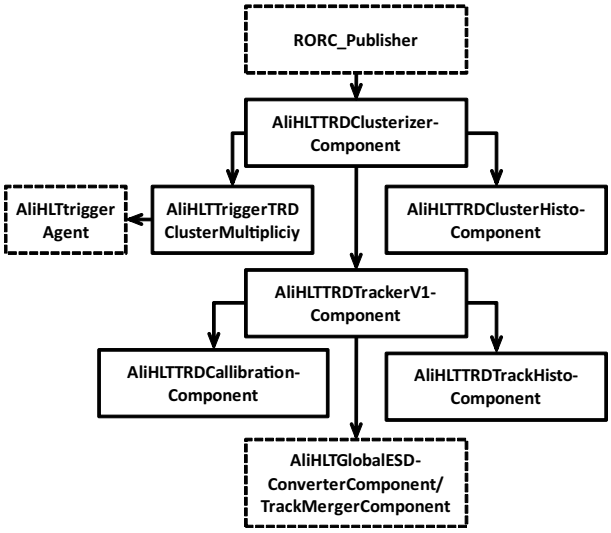

Figure 1: Data flow scheme for the HLT-TRD-Components. Dashed boxes represent components of the HLT framework.

Outlook

The ALICE HLT-TRD is ready for the upcoming data taking period at LHC with pp-collisions. Further efforts will focus on the implementation of particle identification, the development of further trigger scenarios (high p_T charged particle trigger and dilepton trigger) and on the optimization of the existing components with respect to the requirement of the scheduled PbPb-collisions.

References

[1] ALICE TRD, *Technical Design Report 9*, CERN / LHCC, 2001-021.

[2] ALICE Collaboration, *Technical Design Report of the Computing*, CERN / LHCC, 2005-018.

[3] M. Ploskon et al., *ALICE Higl-Level Trigger: Implementation of TRD-specific components*, GSI Ananual Report (2007) 184.

* Work supported by BMBF and GSI
† rascanu@ikf.uni-frankfurt.de

PID and Trigger Studies for the ALICE-TRD *

C. Klein-Bösing[†1,2], B. Albrecht[1], J. Anielski[1], B. Bathen[1], T. Dietel[1], D. Emschermann[1,3], H. Gatz[1], M. Heide[1], M. Kalisky[1], J. Klein[2], F. Poppenborg[1], M. Rammler[1], E. Sicking[1], M. Walter[1], M. Wilde[1], A. Wilk[1], J. P. Wessels[1], and U. Westerhoff[1]

[1]Institut für Kernphysik, University of Münster, Germany; [2]ExtreMe Matter Institute EMMI, GSI Darmstadt, Germany; [3]Physikalisches Institut, University of Heidelberg, Germany

The Transition Radiation Detector (TRD) has been designed for electron/pion separation and charged particle tracking within the ALICE experiment at the LHC [1]. In addition, the TRD electronics allow to provide a fast trigger decision (within 6 μs), e.g., on high-momentum electrons or jets [2]. This fast decision is based on the reconstruction of track segments (tracklets) by the 4 CPUs in each Multi-Chip Modules (MCM) of the TRD readout electronics.

To test the performance of the trigger, the MCM can be emulated in software, using real or simulated charge deposit as input. Here, the use of simulations as input allows, e.g., to directly validate the tracklet reconstruction by the MCM. This is illustrated in Fig. 1, where the resolution of the tracklet reconstruction for the y position and the inclination of the tracklet is given. For normal incidence a resolution of $\sigma_y \approx 170$ μm and $\sigma_{dy/dx} \approx 9$ mrad is reached.

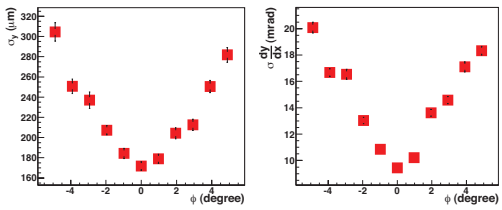

Figure 1: Width of the residuals between the tracklet information of the MCM and the true track parameters for different inclinations of the tracklet. Left: Resolution in y direction. Right: Resolution of the tracklet slope.

The separation of electrons and pions using the TRD is vital for precision measurements of quarkonia within ALICE. In order to reach the design goal of a pion rejection factor of 100 for electrons with momenta above 1 GeV/c at an efficiency of 90%, neural network techniques have been employed successfully in the analysis of TRD test beam data [3]. Neural networks allow to fully exploit the temporal structure of the charge deposit in the TRD, with the characteristic transition radiation for electrons at late times [4]. The PID performance for electrons has also been verified for the implementation of the TRD in the ALICE simulation framework (Fig. 2). Simulations allow to evaluate the PID capabilities for particle species not available in the test beams and with the expected particle abundances. Particles other than electrons can only be discriminated via their energy loss due to ionisation. As seen in Fig. 2 the TRD can nevertheless provide good identification of protons below 1.5 GeV/c and enhance the purity of proton and kaon samples at momenta above 4 GeV/c, where the TRD-PID reduces the contamination by roughly 50%. The poorer performance in case of muons is explained by the fact that the background under realistic conditions mainly consists of pions, which show only little difference in the energy deposit in the detector. The performance in the kaon identification can be understood by the poor rejection of pions as well as protons in the background.

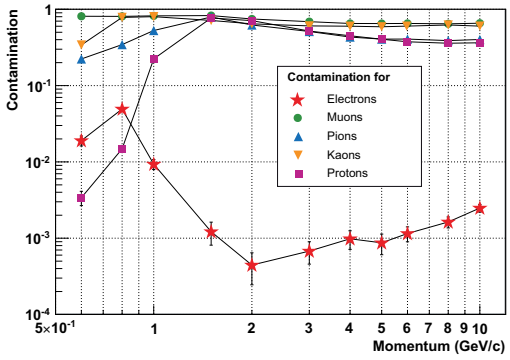

Figure 2: Remaining fraction of contamination in different identified particle samples selected with the TRD using neural networks. The particle abundances have been simulated for $p + p$ collisions at 10 TeV, the particle efficiency is 90%.

Currently, the results from the PID studies with neural networks are used for the implementation of electron PID in the ALICE-TRD trigger logic. In addition, the particle identification with real collision data at $\sqrt{s} = 900$ GeV is pursued, using topological cuts on so-called V^0s (e.g., photon conversions, λ and K^0 decays) and the PID information from other detectors to select reference data of identified particles for the TRD with high purity.

References

[1] ALICE TRD Collaboration, Transition Radiation Detector Technical Design Report, CERN/LHCC 2001-021 (2001).

[2] V. Angelov, NIM A 563, 317 (2006).

[3] C. Adler, NIM A 552, 516 (2005).

[4] A. Andronic, GSI Scientific Report 2007, 237 (2007).

* Work supported by GSI, BMBF, and Helmholtz Alliance HA216/EMMI.

† Christian.Klein-Boesing@uni-muenster.de

Analysis of ALICE TRD testbeam data at the PS-accelerator at CERN*

M. Kliemant[1], H. Appelshaeuser[1], and M. Hartig[1]
[1]IKF, UNI Frankfurt, Germany

The Transition Radiation Detector (TRD) is one of the main detectors in the ALICE experiment, the dedicated heavy ion experiment at the Large Hadron Collider (LHC) at CERN Ref. [1]. This detector consists of 18 super modules, each of them containing 30 TRD chambers. Each detector has a 4.8 cm thick radiator, which is attached to a gas chamber with a 3 cm long drift region and a 0.7 cm amplification gap.

In November 2007 a test of one fully integrated TRD super module(final electronics and cooling set-up) at the CERN PS - accelerator with a mixed electron - pion beam (1, 2, 4 and 6 GeV/c) was performed.

With this data set it is feasible to investigate the PID and tracking performance of the detector. The major aspect is to improve the electron PID performance.

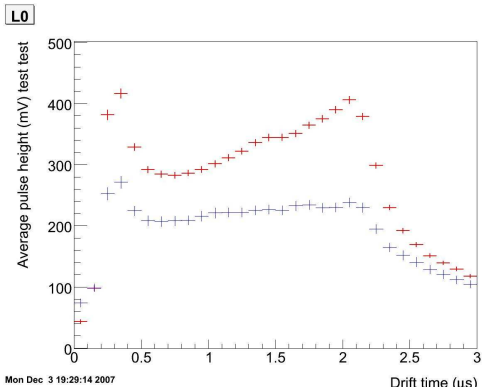

Figure 1: Average TRD signal for pions(blue) and electrons(red). The electrons have a larger dE/dx lost so the detected charge is in all time bins larger for electrons. At time bins between 18-23 we can see the characteristic tr signal for electrons.

To separate electrons from pions it is possible to use two different informations from the TRD detector. First, the different overall dE/dx of charged particles with different masses defined by the Bethe Bloch energy loss.

$\frac{dE}{dx} = \frac{4\pi n z^2}{m_e c^2 \beta^2} \cdot (\frac{e^2}{4\pi\epsilon_0}) \cdot [\ln(\frac{2m_e c^2 \beta^2}{I \cdot (1-\beta^2)}) - \beta^2]$

Second, the additional transition radiation signal from the electrons which happens most likely in the gas near to the radiator so we expect an additional signal at late time bins. This explains the overall average pulse height of electrons compared to pions, combined with a continuous increase of the electron pulse height towards large drift times see Fig. 1. In the normal 1d likelihood calculation we use just the total deposited charge and combine the information from six layers and get as an result the overall probability of a track to be an electron or pion. With the average charge spectra we calculate the likelihood as follows:

$L = \frac{P_e}{P_e + P_\pi}$

with

$\prod_{i=1}^{N} P_\pi = P(X_i|\pi)$ for the pion probability and

$\prod_{i=1}^{N} P_e = P(X_i|e)$ for the electron probability.

The product is running over the six layers , N.

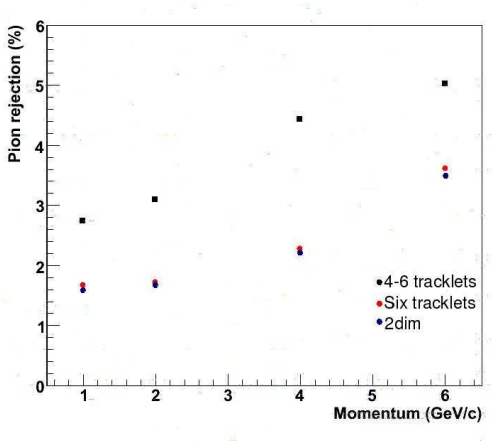

Figure 2: Pion rejection for different momenta (1-6 GeV). In black and red 1d likelihood method for different quality cuts. In blue 2d likelihood compared to test beam data from 2004 in green.

To improve the results we can go a step further and use the second information that we expect a high charge signal in late time bins. In the 2d likelihood method we use now the position of the maximum time bin and do the same calculations and combine the information from six layers like before with the 1d likelihood method. Finally, to check our analysis we can combine the 2d likelihood PID information with the Pb-glass and Cerenkov detector PID information and get a value for the pion efficiency Fig. 2. This is in agreement with further test beam data from 2004.

References

[1] ALICE TRD, Technical Design Report 9, CERN/LHCC 2001-021.

[2] R. Bailhache and C. Lippmann [ALICE TRD Collaboration], Nucl. Instrum. Meth. A **563** (2006) 310.

[3] A. Wilk [ALICE TRD Collaboration], Nucl. Instrum. Meth. A **563** (2006) 314.

*This work is supported by BMBF FSP201, the GSI F&E and the Helmholtz Gemeinschaft

Status of the ALICE TRD Global Tracking Unit*

F. Rettig[†1,2], S. Kirsch[2,3], J. de Cuveland[2], and V. Lindenstruth[2]

[1]Kirchhoff-Institut für Physik, Universität Heidelberg, Germany; [2]Frankfurt Institute for Advanced Studies, Goethe-Universität Frankfurt, Germany; [3]CERN, Geneva, Swiss

The Transition Radiation Detector (TRD, [1]) of the ALICE experiment at the LHC is designed to provide Level-1 trigger contributions on various signatures, like high-p_t electron/positron pairs or jets. Short track segments calculated by more than 65 500 multi-chip modules of the front-end electronics are sent to the Global Tracking Unit (GTU, [2]) via 1 080 optical links. The GTU performs a three-dimensional reconstruction of tracks with $p_t > 2$ GeV within less than 1.6 μs. The GTU hardware consists of 109 dedicated FPGA-based processing nodes forming a three-level hierarchy.

Operation at CERN

In 2009 the GTU was in continuous operation providing read-out and generation of trigger contributions of the TRD. The cosmic trigger was used to gather high-quality alignment data for all seven supermodules installed.

Stable and reliable interoperation with the ALICE CTP and DAQ systems has been proven in long cosmic and calibration data-taking sessions as well as during the ALICE early partition runs – preparatory tests for first collision.

Finally, during data taking with first collisions at the end of the year stable operation was shown continuously.

Track Reconstruction

Detailed timing simulations of the track reconstruction hardware prove that the design specifications are met. For highest multiplicities the tracking time stays below 1.6 μs Careful revision of the FPGA designs reduced the ressource utilization in the Virtex-4 FX100 devices to 85% including the full tracking and trigger logic.

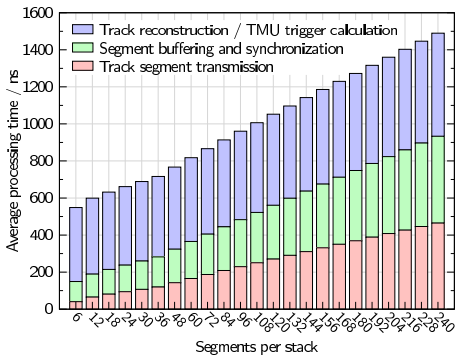

Figure 1: Time consumption of the on-line tracking [3].

Commissioning and Technical Advances

In order to operate the GTU within the ALICE/TRD DCS framework, a hierarchical system for monitoring and control has been developed. A master process controls the server processes on each of the DCS boards and interacts with the configuration database and the higher level control systems. Hardware parameters of interest are published by the system and a PVSS interface has been implemented.

As last part of the installation the optical cabling has been finalized. Custom optical fibre bundles (Fig. 2) satisfy both the needs for reliable and tight packing as well as accessibility of the electronics hardware. All fibres were produced, those for the present segments are installed.

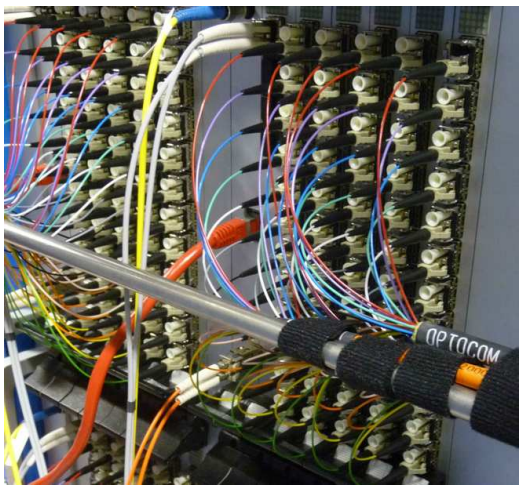

Figure 2: Custom optical fibres connecting two GTU segments with TRD supermodules.

Major technical advancements include the utilization of both embedded PowerPC cores in each of the FPGAs. Control and monitoring tasks previously occupying logic ressources is now absorbed by flexible embedded software.

One core runs an embedded Linux 2.6 kernel that will be used for high-level monitoring and control. SDCard-based storage and ethernet connectivity is under development.

References

[1] ALICE TRD Technical Design Report, ALICE TDR 9, CERN/LHCC 2001-021

[2] F. Rettig, et al., Proceedings 2008 International Conference on Field Programmable Logic and Applications, (2008)

[3] J. de Cuveland, A track reconstructing low latency trigger processor for high-energy physics, Dissertation, (2009)

* Work supported by BMBF FSP201

† rettig@kip.uni-heidelberg.de

ALICE TPC Online Tracking on GPU

D. Rohr[1], S. Gorbunov[1,2], and M. Kretz[1]

[1]Kirchhoff Institute for Physics, University of Heidelberg, Germany; [2]FIAS, Frankfurt, Germany

ALICE Online Tracker

For the ALICE High Level Trigger a fast tracking algorithm was developed by Sergey Gorbunov based on the Cellular Automaton method and the Kalman filter [1], that is currently installed in the HLT. For an efficient handling of upcoming lead-lead collisions in 2010 with a tremendous increase of clusters and tracks, possibilities for a better usage of parallelism and many core hardware were analyzed. The tracker itself was designed with parallel approaches in mind. A SIMD approach was realized by Matthias Kretz [2] in his diploma thesis and further the tracker was adopted to run on the NVIDIA CUDA framework [3].

Modern Many-Core Processors

With the race for higher and higher clock frequencies having reached an end, state of the art CPUs improve in efficiency and multi-core capabilities. Graphics cards have been designed using such approaches for many years now, and just recently started to offer support for execution of general purpose code in high level languages. The GT200b chip used consists of 30 cores, providing 8 ALUs and 16kb of fast shared memory per core. For reasons such as memory latencies there should be about 256 threads running on each core, to reach a good GPU utilization.

GPU Tracker

For fully exploiting the GPU's processing power many changes hat to be applied to the tracker. Major challenges hereby have been an efficient usage of the several heterogenous memory types on the GPU as well as a good overall utilization of all cores. In the later case different tracks lengths turned out to be a problem, that was solved by introducing a scheduler that dynamically distributes the workload among cores and threads. Utilization raised from 19% (Fig. 1) to 62% (Fig. 2). The implementation of simultaneous processing of multiple sectors allows the use of a processing pipeline where data processing and data moving to- and from the GPU overlap.

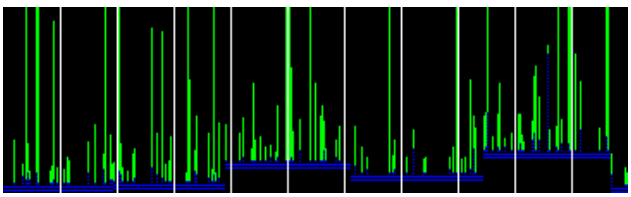

Figure 1: Tracklet Constructor without scheduling [1]

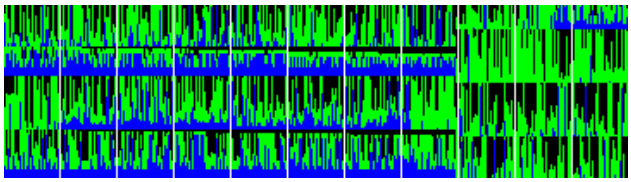

Figure 2: Tracklet Constructor with dynamic scheduling [1]

Performance

Out of the several steps involved in the tracking algorithm three have a non negligible runtime. Fig. 3 shows a performance comparison of the GPU tracker with the CPU version running on an Intel Nehalem 3.2 GHz. It demonstrates that performance for two of these three steps improved significantly. Although there is some drawback during initialization and output of the tracks, caused by GPU-Host synchronization and PCIe transfer, a complete tracking run using simulated data of a central lead-lead event was accelerated by a factor of 3.3.

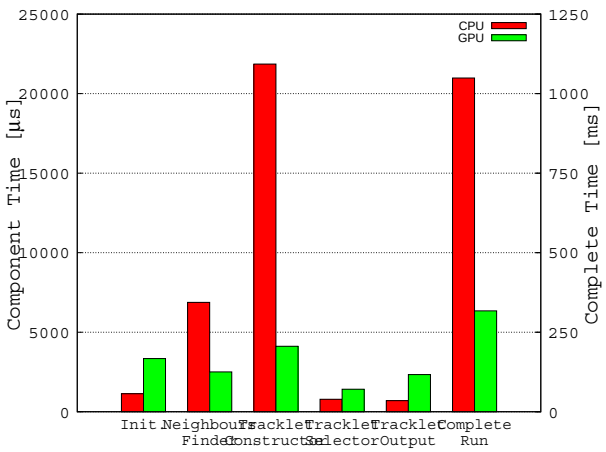

Figure 3: GPU Tracker Performance

References

[1] S. Gorbunov, Matthias Kretz, David Rohr "Fast Cellular Automaton tracker for the ALICE High Level Trigger", GSI Scientific Report 2009

[2] M. Kretz, "Efficient Use of Multi- and Many-Core Systems With Vectorization and Multithreading"

[3] NVIDIA CUDA Reference Manual, http://developer.download.nvidia.com/compute/cuda/2_3/toolkit/docs/CUDA_Reference_Manual_2.3.pdf

[1]Colors stand for: black: idling, color: working., y-axis: time, x-axis: thread

Fast Cellular Automaton tracker for the ALICE High Level Trigger

S. Gorbunov[1,2], M. Kretz[2], D. Rohr[2] for the ALICE collaboration
[1]FIAS, Frankfurt, Germany; [2]KIP, Heidelberg, Germany

The core of the event reconstruction in ALICE is the reconstruction of particle trajectories (tracking) in TPC detector, the main tracking detector of the experiment. For this propose a fast on-line algorithm has been developed. It reconstructs all types of data including physics events, cosmics and special calibration events.

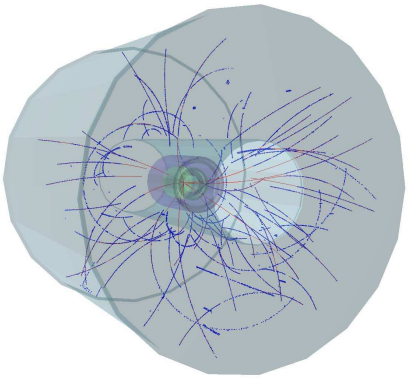

Figure 1: Real proton-proton event, reconstructed in HLT

The algorithm combines a Cellular Automaton method [1], which is used for a fast pattern recognition, and the Kalman filter method [2], which performs a fit of found trajectories and the final track selection. The algorithm has proved its high performance (99.9% for the proton-proton events and 95.8% for the central Pb-Pb collisions) in comparison with the off-line reconstruction (99.9% and 98.5% correspondingly). In addition to the the high efficiency, the on-line reconstruction is an order of magnitude faster than the off-line analysis: 19.6ms (pp) or 17.6s (PbPb central) in comparison with 66.0ms or 160.1s for the off-line.

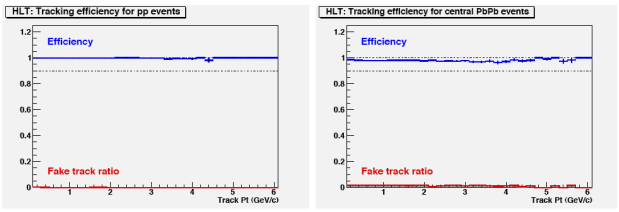

Figure 2: Reconstruction performance for p-p (left) and central Pb-Pb (right) events

Due to the large combinatorial background the key issue is the dependence of the reconstruction time on the number of tracks to be reconstructed. Figure 3 shows that the HLT tracker requires 130 us per track independent of the detector occupancy.

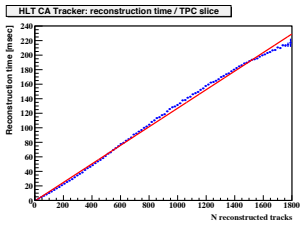

Figure 3: Reconstruction time on CPU

An important feature of the algorithm is an ability to use GPU hardware accelerators, giving another order of magnitude speed-up for the on-line data processing. The GPU accelerators allow to perform a fast reconstruction of heavy ion collisions where a track density is very high.

The first GPU implementation of the algorithm was developed for the NVIDIA graphic card. In addition, the algorithm was adopted for the upcoming Intel Larrabee graphic card. For this propose the code has been vectorized [3] , implying a detailed investigation of the SIMD instructions and development of general vector classes.

The GPU tracker is integrated to the High Level Trigger framework and will be used for the on-line data processing in the ALICE experiment.

References

[1] I. Kisel, V. Kovalenko, F. Laplanche et al. (NEMO Collaboration), Cellular automaton and elastic net for event reconstruction in the NEMO-2 experiment. Nucl. Instr. and Meth. A387 (1997) 433-442.

[2] R. Frühwirth et al., Data analysis techniques for high-energy physics. Second edition, Cambridge Univ. Press (2000).

[3] S. Gorbunov, U. Kebschull, I. Kisel, V. Lindenstruth and W. F. J. Mller, Fast SIMDized Kalman filter based track fit. Comp. Phys. Comm. 178 (2008) 374-383.

First proton-proton collisions in the ALICE High-Level Trigger

J. Thäder[1] for the ALICE HLT Collaboration
[1] Frankfurt Institute of Advanced Studies, Goethe-Universität Frankfurt, Germany

Introduction

The High-Level Trigger (HLT) [1] of the ALICE experiment (A Large Ion Collider Experiment) [2] at the LHC, CERN is designed to reduce the readout data from 25 GB/s to 1.25 GB/s. A large high performance PC cluster has been built to reconstruct and analyse the collision data on-line and allow advanced trigger algorithms to decide on-line if a given event should be rejected or permanently stored.

ALICE Commissioning

During the commissioning of the ALICE experiment, the HLT itself was already used in a production state. The HLT was performing full on-line reconstruction of cosmic particles as well as beam splashes during LHC injection tests. Fast on-line reconstruction algorithms for the central barrel detectors as well as the muon arm have been run. In the ALICE cosmics data-taking campaign, the HLT was successfully running a cosmics trigger based on the on-line reconstructed data, to enhance the L0 cosmic triggers and reduce the amount of stored raw data

First Collisions at LHC

On November 23rd, 2009 450 GeV protons where collided in inside the ALICE detector for the first time. The High-Level Trigger was running on-line reconstruction algorithms for Inner Tracking System (ITS). In order to get a fast estimate of the beam position, the vertex position was reconstructed on-line from data of the Silicon Pixel Detector (SPD) as shown in figure 1 [3].

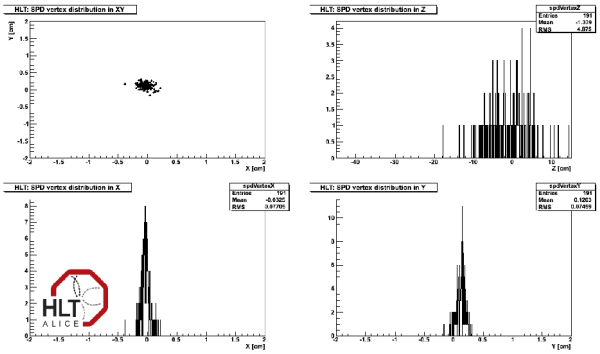

Figure 1: The first on-line reconstructed vertex position by the ALICE HLT, showing counter clockwise from bottom left the distributions in x, y, z and the x-y plane.

When LHC achieved stable beam conditions on December 6th, 2009 the HLT was running full on-line reconstruction of the central barrel detectors and the muon arm for the first time. Figure 2 shows an the first on-line reconstructed proton-proton collision in the HLT.

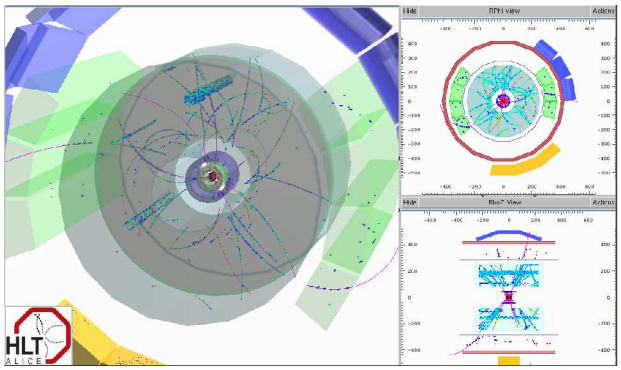

Figure 2: The first on-line proton-proton collision in the full ALICE detector, on-line reconstructed by the HLT.

In the following ALICE pp data-taking, the HLT was not only performing full on-line reconstruction, but also finding of primary and secondary vertices. Invariant mass distributions of Λ^0 and K^0_s (see figure 3) have been on-line calculated to improve the on-line quality assurance.

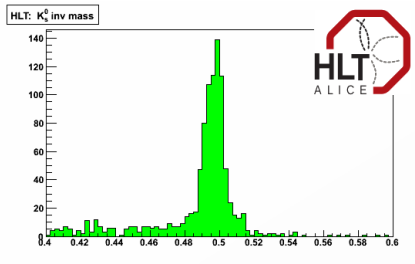

Figure 3: The first on-line calculated invariant mass distribution of K^0_s mesons by the ALICE HLT.

Acknowledgements

We thank the Norwegian research council and the German BMBF for their financial support. Further we thank and congratulate the whole ALICE collaboration to achieve the first data-taking of the ALICE detector.

References

[1] Technical Report ALICE TDR 10, CERN/LHCC 2003-062 (2004)
[2] K. Aamodt et al. The ALICE Collaboration, The ALICE Experiment at the CERN LHC. JINST **3** S08002, 259pp. (2008)
[3] K. Aamodt et al. The ALICE Collaboration, First proton--proton collisions at the LHC as observed with the ALICE detector: measurement of the charged particle pseudorapidity density at sqrt(s) = 900 GeV. Eur. Phys. J. C **65**, 111-125 (2010)

Measurement of the linear polarization of the high energy end of electron-nucleus bremsstrahlung*

R. Märtin[1,2], R. Barday[3], J. Enders[3], M. Hegewald[1], Y. Poltoratska[3], U. Spillmann[1], G. Weber[1,2], and Th. Stöhlker[1,2]

[1]GSI Helmholtzzentrum für Schwerionenforschung GmbH, Darmstadt, Germany; [2]Physikalisches Institut, Universität Heidelberg, Heidelberg, Germany; [3]Institut für Kernphysik, Technische Universität Darmstadt, Darmstadt, Germany

Bremsstrahlung is one of the basic photon-matter processes occurring in collisions of electrons with atoms and ions. Bremsstrahlung in electron-atom collisions has been the object of extensive experimental and theoretical studies [1]. These studies focused on the angular dependence of the intensity distribution of the bremsstrahlung, as well as on its linear polarization [2]. Another production mechanism of primary bremsstrahlung is the collision of ions with atoms. Here, the electrons of the target atom are inelastically scattered off the projectile's nucleus Coulomb field. Of special interest is the bremsstrahlung production in the domain of strong, unpertubated Coulomb fields, such as they prevail in few-electron, high-Z projectiles [3].

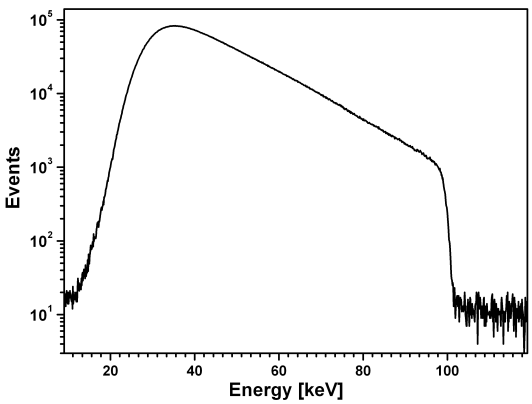

Figure 1: Bremsstrahlung distribution of 100 keV electrons impinging on a carbon target ($210\frac{\mu g}{cm^2}$) recorded with the Si(Li)-Polarimeter at 60° observation angle.

At the polarized electron source of the TU Darmstadt [4] we studied the linear polarization and the bremsstrahlung spectral distribution for an electron-atom collision system. The injector for polarized electrons, the S-DALINAC Polarized INjector SPIN, provides the possibility to perform experiments with different settings of the electron spin. The longitudinal polarized electron beam is produced at the 100 keV polarized electron source by illumination of the GaAsP photocathode with circularly polarized light. The electron spin can be rotated up to 360° and any spin orientation can be obtained. Furthermore the electron source can provide an unpolarized electron beam, too. Gold and carbon targets of different thicknesses were bombarded with electrons of different spin orientation. Fig. 1 shows the bremsstrahlung spectral distribution for a carbon target. For X-ray detection and polarization analysis we used an array of standard Ge(i) detectors and a novel type Si(Li) Compton-Polarimeter, respectively. The analysis is focused on the comparison of the linear polarization of bremsstrahlung photons induced by unpolarized and transversaly polarized electrons. Of special interest is a possible tilt of the polarization axis, which should occur for the case of a spin-polarized electron beam. Fig. 2 shows the scattering distribution of the Compton scattered photons, which indicates a linear polarization of about 88%.

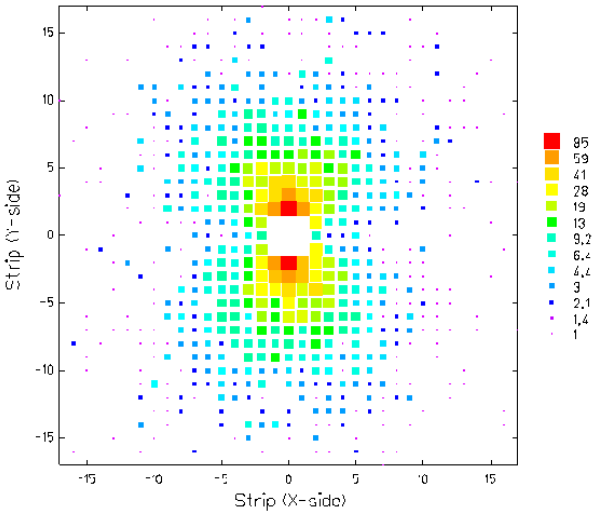

Figure 2: Position distribution of the Compton scattered bremsstrahlung X-rays with respect to the double-sided segmented detector under 60°.

In addition, we measured the bremsstrahlung produced in collisions of highly charged uraniums ions with H_2 and N_2 at different beam energies. These experiments were performed at the ESR gasjet target at GSI and allow the comparison of the characteristic properties of the bremsstrahlung produced in different collision systems as well as the study of electron screening effects.

References

[1] H.W. Koch and J.W. Motz, Rev. Mod. Phys. 31, 920-955 (1959)

[2] W. Nakel, Physics Reports 243, 317-353 (1994)

[3] T. Ludziejewski et al., J. Phys. B 31, 2601-2609 (1998)

[4] C. Heßler, Conf. Proc. EPAC08, 1482-1484 (2008)

* Work supported by DFG through SFB 634

Angular distribution and linear polarization of Bremsstrahlung arising from ion-atom collisions*

G. Weber[1,2], H. Bräuning[1], S. Hess[1,3], S. Geyer[1,3], R. Märtin[1,2], R. Reuschl[1,4], U. Spillmann[1], A. Surzhykov[1,2], S. Trotsenko[1], D. Winters[1], and Th. Stöhlker[1,2]

[1]GSI, Germany; [2]Physikalisches Institut, Universität Heidelberg, Germany; [3]Institut für Kernphysik, Universität Frankfurt, Germany; [4]Institut des NanoSciences de Paris, Université Pierre et Marie Curie-UPMC, France

Bremsstrahlung is one of the basic photon-matter processes occuring in collisions of electrons with atoms and ions. Ion-atom collisions in ion storage rings provide an unique tool to study this process under single-collision conditions in the domain of strong, unpertubated Coulomb fields, such as it prevails in few-electron, high-Z projectiles. Of special interest is the high energy limit of the Bremsstrahlung distribution as it is closely related by means of continuity over the ionization threshold to the radiative electron capture (REC) process [1, 2]. The latter can be seen as the inverse process of photoionization and has been the object of extensive experimental and theoretical studies during recent years [3]. In this work we aim to extend our well-established experimental technique for investigations of the REC process to precise measurements of the angular distribution and linear polarization of the Bremsstrahlung high-energy limit.

The experiment was performed at the internal gasjet target of the ESR by interacting bare uranium and xenon ions with a H_2 target at energies of 96.6 MeV/u and 150.25 MeV/u, respectively. The emitted x-ray photons were detected by an array of standard solid state X-ray detectors at 35°, 60°, 90°, 120° and 150° and a novel-type Si(Li) Compton polarimeter at 90° with respect to the ion beam axis. The down-charged ions were separated from the main beam by a dipole magnet and afterwards detected by a particle detector located at the outer site of the ring.

In Fig. 1 the 90° X-ray spectrum stemming from the collision of U^{92+} with H_2 is displayed. A coincidence technique between the down-charged particles and the detected X-rays allowed to discriminate the photons connected to REC events from the non-coincident Bremsstrahlung contribution. In Fig. 2 the preliminary experimental Bremsstrahlung distribution for 90° and 150° is compared to predictions by Jakubassa [4]. While the total intensity differs by about 40 % the overall shape of the experimental distribution is reproduced by theoretical data. In addition, the degree of linear polarization of the $Xe^{54+} \rightarrow H_2$ Bremsstrahlung high energy limit was obtained at an observation angle of 90° by means of Compton polarimetry. The preliminary value of 75 ± 5 % is in agreement with the theory value of 77.5 %.

Summarizing, in the presented experiment we studied the angular distribution as well as the linear polarization of the Bremsstrahlung high energy limit arising from collisions of bare, heavy ions with a H_2 target. Detailed analysis of the obtained data is still ongoing.

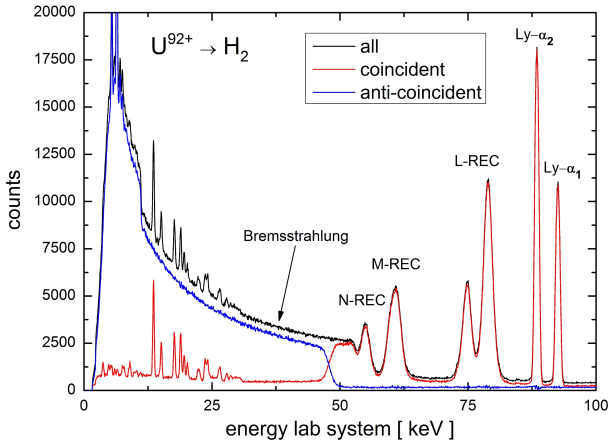

Figure 1: X-ray spectral distribution recorded at the 90° detector. Applying a coincidence technique allows to discriminate the events connected to the REC process from the non-coincident Bremsstrahlung distribution.

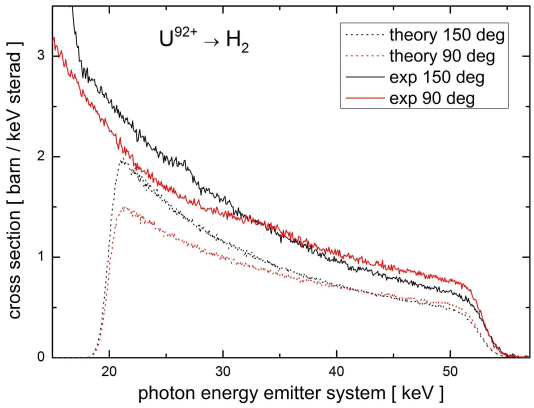

Figure 2: Bremsstrahlung distribution recorded at 90° and 150° in comparison to theoretical predictions by Jakubassa [4]. The data is displayed in the emitter system.

References

[1] T. Ludziejewski et al., J. Phys. B 31, 2601-2609 (1998)

[2] D. H. Jakubassa-Amundsen, J. Phys. B 40, 2719-2737 (2007)

[3] J. Eichler and Th. Stöhlker, Phys. Rep. 439, 1-99 (2007)

[4] D. H. Jakubassa-Amundsen, private communication

*Work in part supported by the Helmholtz Gemeinschaft under the project VH–NG–421

Accurate spectroscopy of excited levels in He-like uranium*

M. Trassinelli[1,2], A. Kumar[2,3], H.F. Beyer[2], P. Indelicato[4], R. Märtin [2,5], R. Reuschl[1,2], Y.S. Kozhedub[6], C. Brandau[2], H. Bräuning[2], S. Geyer[2], A. Gumberidze[2], S. Hess[2], P. Jagodzinski[7], C. Kozhuharov[2], D. Liesen[2], U. Spillmann[2], S. Trotsenko[2], G. Weber[2,5], D.F.A. Winters[2,5], and Th. Stöhlker[2,5,8]

[1]Institut de NanoSciences de Paris; CNRS and UPMC; 75015 Paris,France; [2]GSI Helmholtzzentrum für Schwerionenforschung GmbH, 64291 Darmstadt, Germany; [3]Nuclear Physics Division, Bhabha Atomic Research Centre, 400085 Mumbai, India; [4]Laboratoire Kastler Brossel, ENS; CNRS; UPMC; 75005 Paris, France; [5]Physikalisches Institut, Universität Heidelberg, 69120 Heidelberg, Germany; [6]Department of Physics, St. Petersburg State University, St. Petersburg 198504, Russia; [7]Institute of Physics, Jan Kochanowski University, 25406 Kielce, Poland; [8]Helmholtz Institut Jena, Friedrich-Schiller Universität, 07743 Jena, Germany

X-ray spectroscopy in heavy few-electron ions allows for sensitive tests of quantum-electrodynamic effects in strong Coulomb fields. It opens new perspectives to study the simplest many-body systems such as He-like uranium. However, almost no experimental information is available for high-Z He-like ions. Recently we have obtained the first identification of the intra-shell $1s2p\,^3P_2 \rightarrow 1s2s\,^3S_1$ transition in He-like uranium by an highly accurate measurement [1, 2, 3]. For this purpose, we used a standard Ge(i) solid-state detector and a new Bragg spectrometer specially designed for accurate spectroscopy of fast ions. The two instruments are complementary: The Ge(i) detector has a high detection efficiency and covers a wide spectral range with a moderate spectral resolving power. The Bragg spectrometer offers high resolution but limited spectral range. The measurement was conducted at the ESR storage ring at GSI. The spectrometer and the solid-state detector were mounted at the ESR gas jet target at an observation angle of 90° and 35° with respect to the beam. Excited He-like ions were produced via electron capture in the interaction of the stored H-like beam with a nitrogen gas target. The accurately measured $1s^22p\,^2P_{3/2} \rightarrow 1s^22s\,^2S_{1/2}$ transition [4] from Li-like uranium (obtained from the interaction of the stored He-like beam with the nitrogen gas jet target) was used as references. By utilizing the Doppler shift, the beam energy was adjusted (43.55 MeV/u H-like U and 32.60 MeV/u He-like U) to have a transition energy of 4308 eV in the laboratory frame for both cases. The use of the emission from moving Li-like U ions as reference drastically reduced systematic uncertainties due to the unprecisely known observation angle [2].

For the transition in He-like uranium, a total number of about 300 counts in an effective acquisition time of ~ 24 hours was accumulated (see Fig. 1). For the Li-like ions, about 160 counts in ~ 5 hours were recorded. The two intra-shell transitions have been identified unambiguously with the Ge(i) detector and the Bragg spectrometer. From the analysis of the Bragg reflection position, the energy of the $1s2p\,^3P_2 \rightarrow 1s2s\,^3S_1$ transition was measured to be [3] $E = 4509.71 \pm 0.99$ eV. The main sources of uncertainty are: the spectral line asymmetry (0.89 eV), due to the a non-uniform x-ray reflectivity over the crystal surface, the low statistic (0.48 eV) and the calibration line accuracy (0.21 eV). Other systematic uncertainties, including those originating from the beam velocity, are negligible. Our value is in agreement with the most accurate theoretical predictions ([3] and references therein) and the obtained accuracy is at the edge of the sensitivity for two-electron QED contribution, 0.76 eV in such an atomic system. In future experiments, therefore, improved and verified analyzer crystals together with an extended measurement time will allow for more stringent tests of the two-electron QED contributions in heavy highly charged ions.

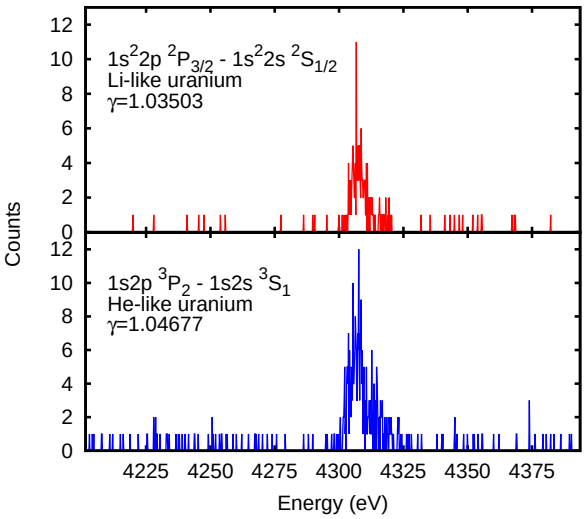

Figure 1: X-ray spectra of the $1s2p\,^3P_2 \rightarrow 1s2s\,^3S_1$ He-like (top) and $1s^22p\,^2P_{3/2} \rightarrow 1s^22s\,^2S_{1/2}$ Li-like uranium transitions obtained with the Bragg spectrometer.

References

[1] M. Trassinelli *et al*, GSI Scientific Report 2007, p. 272

[2] M. Trassinelli *et al.*, J. Phys. CS, **163**, 012026 (2009).

[3] M. Trassinelli *et al.*, Eur. Phys. Lett., **87**, 63001 (2009).

[4] P. Beiersdorfer, *et al.*, Phys. Rev. Lett. **71**, 3939 (1993).

* Work supported by EU, EURONS contract No. 506065, A. von Humboldt Foundation and DAAD contract number A/05/52927.

Photorecombination of In-flight Synthesized Uranium Isotopes

C. Brandau *[1,2,3], C. Kozhuharov[2], A. Müller[3], S. Schippers[3], D. Banas[4], L.A. Bernstein[5], D. Bernhardt[3], F. Bosch[2], F.J. Currell[6], C. Dimopoulou[2], A. Gumberidze[2,7], M. Heil[2], R. Krücken[1], Yu.A. Litvinov[2,8], M. Lochmann[2,9], R. Märtin[2], W. Nörtershäuser[2,9], F. Nolden[2], B.E. O'Rourke[2,6], D. Schneider[5], H. Simon[2], U. Spillmann[2], Z. Stachura[10], M. Steck[2], Th. Stöhlker[2,11], G. Weber[2,11], M. Wiedeking[5], D. Winters[2], and A. Wolf[8]

[1]TU München; [2]GSI, Darmstadt; [3]Universität Gießen; [4]JKU, Kielce, Poland; [5]LLNL, Livermore, CA, USA; [6]Queen's University, Belfast, U.K.; [7]EMMI, Darmstadt; [8]MPI-K, Heidelberg; [9]Universität Mainz; [10]IFJ, Kraków, Poland; [11]Universität Heidelberg

In 2009 we conducted an experiment on photorecombination (PR) with the three uranium isotopes A=236, 237, 238. The measurements strongly benefited from the experience we had obtained for heavy Li-like radioisotopes in a preceding two-day test run in 2008 [1, 2]. The primary objective of these studies is the measurement of isotope shifts and hyperfine effects to the resonant contribution of PR, i.e., in dielectronic recombination (DR). Isotope effects on DR resonances were previously studied with stable isotopes, e.g., hyperfine quenching of metastable states [3], hyperfine effects [4] and nuclear size contributions [5]. With the new DR experiments with unstable nuclei at the ESR we have broadened the spectrum of physics issues that can be addressed employing this atomic physics tool. High-Z exotic ions with nuclear lifetimes down to $\sim$ 30 s can now be studied. The tightly-bound electrons of highly-charged ions provide ideal probes for fundamental nuclear properties such as size, spin and magnetic moment. In return, the impact of the nucleus on atomic lifetime and structure is a vital topic in heavy ion atomic physics.

The procedure for the preparation of Li-like radioisotope beams for PR studies in the ESR is described in [1, 2]. Here we focus on details specific for the present experiment. The naturally abundant ^{238}U (primary beam) was chosen as the reference isotope. The uranium isotopes A=236 and A=237 were synthesized in-flight in a 1 cm (1.85 g/cm^2) beryllium plate and separated in the ESR. The Li-like charge state was obtained from charge state breeding of the initially injected He-like ions. For the ^{238}U reference isotope we applied the same procedure as for the unstable isotopes in order to have identical experimental conditions. For the measurement, the ion beam intensities were typically a few 10^5 Li-like radioisotopes per injection. Experimental data have been taken in the center-of-mass energy interval of 0 to 20 eV. For Li-like uranium, resonant DR structures belonging to both $2s \rightarrow 2p_j$ ($j = 1/2$ and $j = 3/2$) intra L-shell excitations can be found in that range. The respective resonance groups partially overlap. Figure 1 shows results from a preliminary analysis for the energy range 8 to 11.5 eV. The resonances of the A=236 isotope are shifted with respect to the ones of ^{238}U and show the same shape. Both ions posses even-even nuclei with nuclear ground state spin $I = 0$.

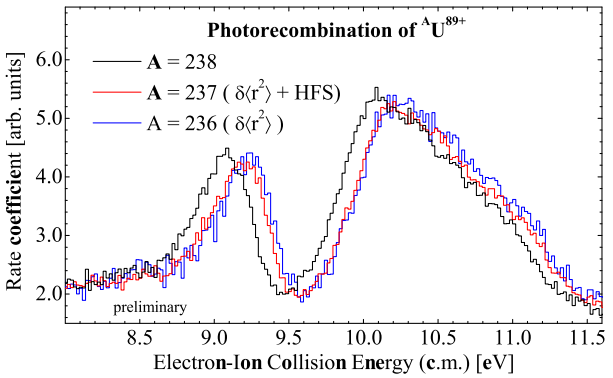

Figure 1: Isotope shifts ($\delta\langle r^2\rangle$) and hyperfine effect (HFS) in dielectronic resonances of $^{A}U^{89+}$ with A=238 (black), 237 (red), 236 (blue). The resonant capture proceeds via the autoionizing states $^{A}U^{88+}(1s^2\,2p_{1/2}\,20l_{j'})^{**}$ and $^{A}U^{88+}(1s^2\,2p_{3/2}\,5l_{3/2})^{**}$.

Thus, there are no magnetic hyperfine effects. The energy shift δE is solely due to different nuclear sizes ($\delta\langle r^2\rangle$). In contrast, the isotope A=237 has $I = 1/2+$ (the magnetic moment is unknown) and features hyperfine splitting. In the storage ring heavy highly charged ions are usually in their hyperfine ground states. The energy shift of $^{237}U^{89+}$ comprises the volume shift and, additionally, a contribution by the hyperfine lowering of the $2s_{1/2}$ level. Please note that the slope of the high-energy tail of the second resonance group (10 - 11.5 eV) differs from the ones for A=236 and A=238; again as a result of the hyperfine interaction ($2p_{1/2}$ and $2p_{3/2}$ states). A detailed analysis of the experimental data is currently being performed. For a more quantitative evaluation of the measurement with respect to the nuclear physics properties further theoretical support is needed.

References

[1] C. Brandau, et al., J. Phys.: Conf. Ser. **194** 012023 (2009).

[2] C. Brandau, et al., Hyperf. Int. in print.

[3] S. Schippers, et al., Phys. Rev. Lett. **98** 033001 (2007).

[4] R. Schuch, et al.: Phys. Rev. Lett. **95** 183003 (2005).

[5] C. Brandau, et al., Phys. Rev. Lett. **100** 073201 (2008).

*C.B. acknowledges support by GSI Darmstadt (F&E) under contract number TM/KRUE.

X-ray spectroscopy of collisions between $^{96}Ru^{44+}$ ions and H_2 clusters

Natalya Winters[1,2], H. Bräuning[1], R.E. Grisenti[*1,3], M. Heil[1], C. Kozhuharov[1], N. Petridis[1,3], R. Reifarth[† 1,3], M. Steck[1], G. Weber[1,2], D.F.A. Winters[1,2], and Th. Stöhlker[1,2]

[1]GSI Darmstadt, Germany; [2]Heidelberg University, Germany; [3]Frankfurt University, Germany

In the Experimental Storage Ring (ESR) one can store intense beams of heavy, highly charged ions at relativistic velocities for extended periods of time. At the internal (gas jet) target, the high ion number ($\sim 10^8$) and ion frequency ($\sim$ MHz) inside the ring make it possible to investigate atomic collision processes with small cross-sections. There are capture, excitation, and ionization processes, where capture processes can be radiative or not. Radiative Electron Capture (REC) [1] is of interest because it is 'time-reversed photoionization'. The projectile ion captures an electron from a target atom into a strongly bound state, and the released binding energy is carried away by a high-energy photon (*e.g.* K-REC photon). In Non-Radiative Capture (NRC), the projectile captures a target electron into a high-lying state, which then cascades down to the ground state. In the final decay steps a high-energy photon can be emitted (*e.g.* Kα photon). We want to exploit these processes and learn if they take place in the single- or multiple-collision regime. By varying the target area density, signatures of multiple electron capture can appear in the x-ray spectra.

In March 2009, we contributed to an experiment of Heil *et al.* [2] that looked at proton capture (p-process) from H_2 by $^{96}Ru^{44+}$ ions during 9-11 MeV/u collisions.

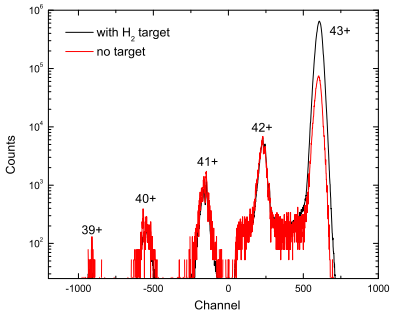

Figure 1: Positions of down-charged ^{96}Ru ions (at 11 MeV/u) on the MWPC. Switching on the H_2 target (black data) leads to an enhancement of the Ru^{43+} peak. The red data represents the residual gas contribution.

The target was generated by a novel cryogenic cluster source [3], which created an average target area density of 5×10^{12} 1/cm^2. At this density the jet produces ($\sim$ 30 nm size) clusters of atoms rather than molecules. The x-rays from the ion-target collisions were detected under 35° and 90° by means of two germanium detectors. The down-charged projectile ions were detected by a multi-wire proportional counter (MWPC) placed after the target. We could separate 5 charge states of Ru by positioning the MWPC inside the dipole magnet of the ESR.

The red data (H_2 off) in figure 1 shows evidence for (multiple) electron capture into H- to B-like Ru ions, which can only occur due to collisions with the main residual gas constituents H_2 and N_2 (pressure $\sim 10^{-10}$ mbar). Switching on the H_2 target (black data) only leads to an enhancement of the 43+ peak via single electron capture. This implies that every Ru ion interacts only with one H-atom in the cluster, *i.e.* we have single-collision conditions.

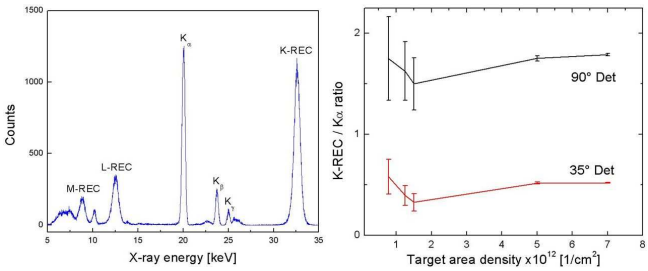

Figure 2: Left: X-ray spektrum from Ru^{44+} on H_2 at 11 MeV/u. Under 90° detection, the K-REC and Kα peak are strong. Right: K-REC/Kα peak ratio plotted versus the target area density (for both detectors).

In figure 2 (left panel) a typical x-ray spectrum, recorded by the 90° detector, is shown. The K-REC (33 keV) and Kα (20 keV) peaks are clearly dominant. Multiple electron capture processes can affect the neutralization dynamics and cause a change in the K-REC/Kα peak ratio. We analyzed this ratio as a function of target area density for both detectors. From figure 2 (right panel) we conclude that there is no clear influence of the target area density on the peak ratio.

For next studies, heavier target gases (*e.g.* Ne, Ar, Kr and Xe), which have many electrons available for capture, will be used. These gases can form larger clusters (up to $\sim 1\mu$m in size), which could open up the multi-collision regime. Since REC cross-sections increase with target atomic number (Z_T), experiments will be faster (higher rates). Multiple electron capture could then also be observed directly.

References

[1] J. Eichler and Th. Stöhlker, Phys. Rep. **439**, 1 (2007).

[2] M. Heil *et al.*, GSI beamtime application (2008).

[3] M. Kühnle, N. Petridis, R.E. Grisenti, *et al.*, Nucl. Instr. Meth. Phys. Res. A **602** 311 (2009).

* Work supported by the Helmholtz Association (VH-NG-331).

† Work supported by the Helmholtz Association (VH-NG-327).

Electron- and Proton-Impact Excitation in Stored Hydrogenlike Uranium Ions

D.B. Thorn[1], A. Gumberidze[1], S. Trotsenko[2,3], D. Banaś[4], H. Beyer[2,3], W. Chen[2], R.D. DuBois[1], S. Geyer[2,5], R. Grisenti[*2,5], S. Hagmann[2], M. Hegewald[2,5], S. Hess[2,5], C. Kozhuharov[2], R. Märtin[2,6], I. Orban[7], N. Petridis[2,5], R. Reuschl[8], A. Simon[9], U. Spillmann[2], A. Surzhykov[†2,6], M. Trassinelli[8], G. Weber[2,6], D.F.A. Winters[2,6], N. Winters[2,6], D. Yu[10], and Th. Stöhlker[2,3,6]

[1]ExtreMe Matter Institute/GSI, Darmstadt; [2]GSI, Darmstadt; [3]Helmholtz Institute Jena; [4]Jan Kochanowski University, Kielce, Poland; [5]Frankfurt University; [6]Heidelberg University; [7]Stockholm University, Sweden; [8]Institut des NanoSciences de Paris, France; [9]Jagiellonian University, Krakow, Poland; [10]Institute of Modern Physics, Lanzhou, China

At GSI we have studied, for the first time, the effect of electron-impact excitation in heavy highly charged ions (HCI) undergoing collisions with neutral atoms. Electron-impact excitation (EIE) of bound electrons is one of the most fundamental excitation processes. In particular, it is responsible for the vast majority of x-ray radiation produced in high energy density physics experiments and at laboratory fusion devices. In addition, QED effects are predicted to affect the EIE process through the generalized Breit interaction [1]. Most EIE measurements have thus far only been performed at electron beam ion trap facilities with low- to mid-Z ions [2]. To study EIE in the heaviest HCI possible, intense HCI beams are needed because the impact excitation cross-sections are typically under one barn. The only excitation studies that have thus far been performed have used multi-proton gases or solids in an effort to have reasonable x-ray yields [3].

In a recent (Sept. 2009) ESR experiment, we looked for EIE effects in relativistic collisions between H-like uranium ions and hydrogen and nitrogen targets. The target gases were produced by a cryogenically cooled liquid micro-jet, achieving densities of $\sim 10^{13}$ cm^{-2}. At energies of 100, 220 and 400 MeV/u, x-ray spectra from uranium ions were recorded to investigate the produced excitation lines ($1s \rightarrow 2p_{3/2}$) Ly-α_1 and ($1s \rightarrow 2p_{1/2}$) Ly-α_2. These energies were below, at, and above the EIE threshold of ~ 200 MeV/u. We used four HP-Ge detectors, mounted at different angles around the interaction region, and a novel 2D-Si(Li) polarimeter.

Electron and proton impact excitation processes both lead to the emission of Ly-α_1 and Ly-α_2 radiation. However, since excitation by the nuclear field scales as Z_T^2, whereas EIE scales as Z_T, different targets can be used to disentangle both excitation mechanisms. Changes caused by the target can then be studied via the Ly-α_1/Ly-α_2 peak ratio, and as a function of the projectile energy. For instance, at higher energies, *i.e.* above the EIE threshold, excitation for collisions with nitrogen atoms is mainly due to protons. But for collisions with hydrogen atoms, the proton and electron contribute equally to the excitation.

Preliminary data from the experiment are shown in Figure 1, where the Ly-α_1/Ly-α_2 peak ratio is plotted against the observation angle in the lab, for two targets (H_2 and N_2). The fits are Legendré polynomials that are known to describe the angular distribution for electric dipole transitions. In addition, the proper Lorentz transformation from the moving into the laboratory frame has been considered. The shape of the angular distribution of Ly-α_1 radiation (normalized to the isotropic Ly-α_2 distribution) does not seem to be affected by the target (H_2 or N_2). However, the data for H_2 gas are lower than those for N_2.

To understand these effects and to disentangle the EIE contribution to the excitation, polarization analysis and data taken below and at the electron excitation threshold are currently under evaluation. To fully quantify the electron and proton impact processes, new calculations involving alignment (as described in Ref. [4]) are needed.

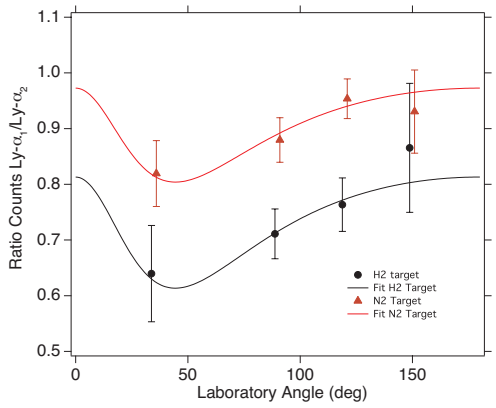

Figure 1: Preliminary data: Ly-α_1/Ly-α_2 peak ratio versus observation angle, for 400 MeV/u U^{91+} ions. The black circles are U^{91+} on H_2 data, the red triangles are from U^{91+} on N_2. The solid lines are fits to the data (see text).

References

[1] C.J. Fontes, D.H. Sampson and H.L. Zhang, Phys. Rev. A **49**, 053704 (1994).

[2] H. Chen and P. Beiersdorfer, Can. J. Phys. **86**, 55-71 (2008).

[3] T. Ludziejewski, Th. Stöhlker, H. Beyer *et al.*, Nucl. Instr. Meth. Phys. Res. B **154**, 204 (1999).

[4] A. Surzhykov, U.D. Jentschura, Th. Stöhlker *et al.*, Phys. Rev. A **77**, 042722 (2008).

[*] Work supported by the Helmholtz Association (VH-NG-331).
[†] Work supported by the Helmholtz Association (VH-NG-421).

Population Mechanisms of the $[1s_{1/2}2p_{3/2}]\ ^1P_1$ state of He-like Uranium Ions

S. Salem[1,2], Th. Stoehlker[1,3], A. Braeuning-Demian[1], A. Gumberidze*[1], and A. Surzhykov†[3]
[1]GSI, Darmstadt; [2]IKF, Frankfurt Univ.; [3]Heidelberg Univ., Germany

The investigations of the atomic structure of He-like ions probe the understanding of the interplay of relativistic effects on the dynamics of the simple atomic few-electron systems. For two-electron high-Z ions, the formation of the excited states can be studied by the observation of the radiative decay of the excited levels to the ground state. This study can be done via different processes which give information about the population mechanism of the excited L-shell levels [1, 2].

For He-like uranium the energy difference between the two-components of the $K_{\alpha 1}$ line, the $^1P_1$ and $^3P_2$ states, is around $64\ eV$. Up to now, this energy could not be resolved experimentally due to the limited energy resolution of the germanium detectors.

To populate the $^1P_1$ state, two processes were studied, namely, the excitation of K-shell in He-like uranium ions and the electron capture into H-like uranium ions. For this, the measurements have been carried out using the internal gas-jet target of the experimental storage ring ESR at GSI. The x-ray emitted during the collisions of U^{90+} and U^{91+} with N_2 atoms were detected at different observation angles with respect to the beam direction.

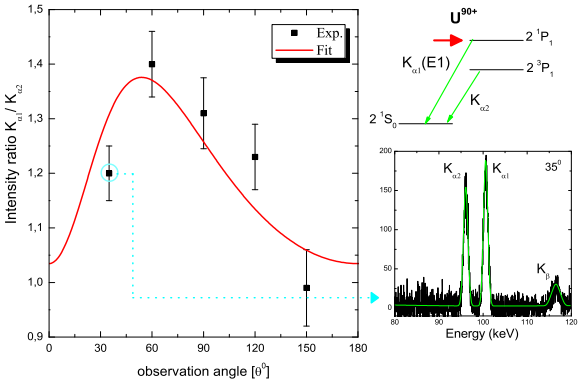

Figure 1: Angular distribution of the $K_{\alpha 1}/K_{\alpha 2}$ intensity ratio, in the laboratory frame, as observed for collision of U^{90+} with N_2 gas target. The solid line depict the fit result to the experimental data (see eqn. in ref.[3]).

The experimental data obtained for the direct K-shell excitation of He-like uranium ions, 220 MeV/u U^{90+} $\rightarrow$ N_2, are plotted in figure 1. As can be seen, the behavior of the $K_{\alpha 1}/K_{\alpha 2}$ intensity ratio is similar to that of a pure electric dipole (E1) contribution, namely, $^1P_1$ state for the $K_{\alpha 1}$ transition. This suggests that the single excitation process is a highly selective mechanism for the population of the $^1P_1$ state in the He-like uranium ions.

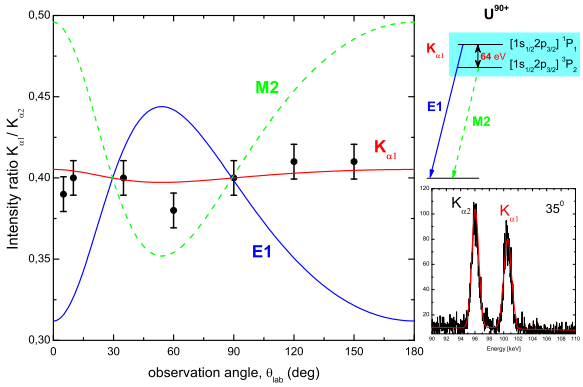

Figure 2: Angular distribution of the $K_{\alpha 1}/K_{\alpha 2}$ intensity ratio as a function of the observation angle. The experimental data for 220 MeV/u $U^{91+} \rightarrow N_2$.

For the $K_{\alpha 1}$ transition caused by electron capture into initially H-like uranium ions, the experimental results obtained are shown in figure 2. The intensity ratio in figure 2 shows an isotropic behavior. The interpretation of this behavior is due to the superposition of the $^1P_1$ and $^3P_2$ states even these individual components are strongly anisotropic. The experimental proof of this behavior agrees reasonably well with the theoretical calculation based on the Multi configuration Dirac-Fock (MCDF) approach [4, 5]. The experimental results shown in figure 2 confirm the theoretical treatment of the two-step electron capture and decay process which have been considered to describe the formation of the excited states.

References

[1] Th. Stoehlker et al., *Hyperfine Interact.* **146-147**, (2003) 97.

[2] A. Gumberidze et al., *Hyperfine Interact.* **146-147**, (2003) 133.

[3] S. Salem et al., *GSI Report 2009-1*(2008), p. 283.

[4] A. Surzhykov et al., *Phys. Rev. A* **74**, (2006) 052710.

[5] A. Surzhykov et al., *Eur. Phys. J. D* **46**, (2008) 27.

* The ExtreMe Matter Institute EMMI at GSI
† surz@physi.uni-heidelberg.de

Behaviour of mylar foils under bombardment by energetic heavy ions studied by fast electron emission measurements with the modified ARGOS detector

E. de Filippo[1], S. Hagmann[2,3], H. Rothard[4], I. Lombardo[1], E. La Guidara[1], F. Amorini[1], F. Rizzo[1], G. Politi[1], E. Geraci[1], P. Russotto[1], G. Cardella[1]

[1]INFN Sez. Catania, Italy, [2]Inst. f. Kernphysik, Univ. Frankfurt, [3]GSI, Darmstadt, [4]CIMAP-Ganil, Caen, France

Fast electrons produced by bombarding thin, conducting foils with very energetic heavy ion beams have recently been the object of accurate studies [1]. In the forward direction the velocity spectra present two main components: the convoy cusp with ELC (electron loss to continuum) and ECC (electron capture to the continuum) at $v_{eletcron}=v_{projectile}$ and binary encounter (BE) electrons which when observed at $\theta_{lab}\cong 0^0$ have around twice the beam velocity $v_{projectile}$ (see Fig. 1).

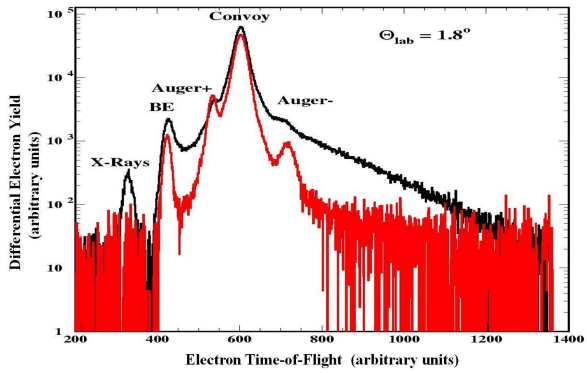

Fig. 1: Time-of-flight (TOF) spectra of fast electrons emitted at θ_{lab}=1.8° for 40.3 AMeV $^{107}Ag^{30+}$ ions on solid C (red) and Au (black) conductive targets. Binary encounter (BE), convoy- and in-flight-emitted Auger electron (forward emission, "Auger+", backward emission, "Auger-") peaks are indicated. The *convoy* peak corresponds to electrons of 22.1 keV (for details see [1]).

Experiments involving *insulating solid targets* are indeed exceedingly rare. Therefore, we performed several experiments at the superconducting cyclotron (CS) at LNS, Catania with insulating polypropylene and mylar targets (in addition to the measurements with conducting targets such as C, Ni, Au). The foils where ~100 μg/cm^2 thick, and some of them where coated on one surface with a thin gold layer of ~10 μg/cm^2 ("Mylar-Au" target). Current intensities were systematically varied for the same beam from about 10 pA up to some hundred pA. Some of the ARGOS scintillation detectors were modified (no aluminized mylar covering) in order to decrease significantly the detection threshold to below 10 keV electron energy. We observe that both convoy and BE electrons emerging from the target are slowed down remarkably and their time-of-flight increases as the time elapses, until a charge break-down occurs. This velocity difference is attributed to the charging-up induced positive target potential and therefore allows a quantitative analysis of the nature of the periodic discharge. Positive potentials as high as 9-12 kV have been seen [2].

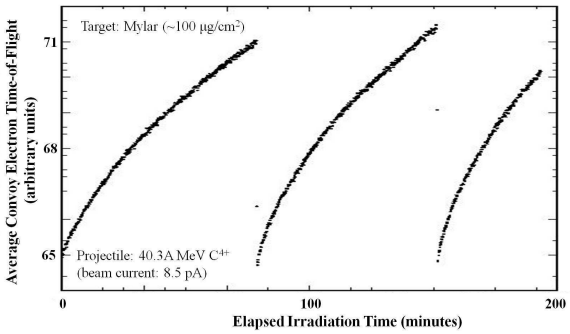

Fig. 2: Convoy–electron time-of-flight as a function of elapsed time for a beam current of 8.5 pA, for 40.3AMeV C^{4+} impinging onto an insulating Mylar target.

Some preliminary results for reaction 40 AMeV $^{12}C^{4+}$ + Mylar are shown in Fig. 2. The observation angle is 1.8°. Convoy-electron time-of-flight is reported as a function of the elapsed time T for a beam current, ~ 8.5 pA. The behaviour of *t* as a function of the elapsed time shows a regular pattern, indicating that the target surface charges-up and then the charge abruptly breaks-down incessantly, with a "period" strongly dependent on the current value.

A maximum positive potential of almost 7 kV can be easily deduced for the target surface before breakdown. The average convoy electron yield is decreasing as the target charges up, as a function of the elapsed time, i.e. scattering into larger angles increases. The width of the average convoy electron peak as a function of the elapsed time increases. For the composite Au-Mylar target a shift is only observed for convoy electrons detected in the forward direction when the Au-Mylar target was positioned with Au facing the incoming beam. In this case, the beam is entering first the Mylar and then the Au layer on the exiting surface, that is then conductive and at the ground potential, V = 0. This shows that the Au layer acts as a conductive layer screening the interior potential of the Mylar target. A detailed analysis relating observed breakdown potentials to properties of the solid is in progress.

S.H. and H.R. thank INFN and LNS for travel support.
In Memoriam Gaetano Lanzanò.

References

[1] G. Lanzanò et al., Nucl. Instr. and Meth. in Phys. Res. B256 (2007) 510-514.
[2] G. Lanzanò et al., Radiation Effects & Defects in Solids 162 (2007) 303-318.

Low-Energy Electrons Emitted in Collisions of Protons and H_3-Molecules with Thin Carbon Foils*

C. Kozhuharov† [1], M. Durante[1,2], S. Hagmann[1,3], G. Kraft[1], M. Krämer[1], and N. Lineva[1,4]

[1]GSI, Darmstadt, Germany; [2]Technische Universität, Darmstadt, Germany; [3]Goethe Universität, Frankfurt am Main, Germany; [4]Brunel, Offenbach am Main, Germany

Detailed knowledge of low-energy electron emission in collisions of swift ions with solids and gases is very important for the modeling of the dose distributions and track structures at small distances ($\leq$20 nm) in mixed radiation fields, particularly for the Local Effect Model, LEM, developed and used at GSI for the prediction of ion radiation effects in ion radiotherapy and related fields. We have, therefore, launched a project aimed at systematic investigations of the energy and angular distributions of low-energy (sub-keV) electrons emitted from solids. In our previous report[1], we described briefly the method developed by us to account for the properties of the solid-state targets, both bulk and surface, i.e. for the inherent inhomogeneity of the thickness and for the surface roughness. Our investigations have demonstrated how important it is to incorporate realistic parameters with respect to the targets, since the complex effects do not scale linearly. Ibidem [1], we have discussed the measured spectra of electrons emitted in collisions of 3.6 and 11.4 MeV/u carbon ions impinging on thin C, Ni, Ag, and Au targets within the framework of simple conventional theories, and we have compared our results[3] with dedicated Monte Carlo simulations by utilizing the TRAX software package[2]. We have shown how important it is to account for the projectile electrons and to have detailed knowledge about the instantaneous charge state of the projectile within the target material.

In order to test our methods, we complemented our investigations by experiments with the simplest ion projectiles: protons (i.e. H^+, no projectile electrons) as well as the simplest H_3-molecule impinging on a thin carbon foil. Fortunately, the H_3-molecule, which is abundantly present in the interstellar matter, is also produced in the1+ charge state in the GSI ion sources. We chose the same relative velocity for both projectiles. The thin carbon target foil was the one investigated with the electron beam.

Figure 1 shows the total energy spectra for both projectiles. The electron yields are multiplied with the electron energy; this is actually the way the spectra are measured, since $\Delta E/E$ is a constant of the electron spectrometer. The individual steps of the scanned spectra are dead time corrected and normalized with the respective Faraday cup currents. For the latter, the H_3-molecule is treated as if three separate protons are stopped in the Faraday cup. This assumption is based on measurements of the H_3 dissociation after passing thin carbon foils, which revealed that only small fractions of the molecules (in the order of a few percent) will stay in non-dissociated states [5]. The presence of undissociated molecules should therefore only slightly reduce the ratio of the cross sections for the two projectiles. The fact that the ratio is not unity and slightly increases with the electron energy supports the emphasis that we put previously [1] on the inclusion of the projectile electrons and on the knowledge of the instantaneous charge state. Clearly visible in the spectra are two structures that belong to the KLL-Auger lines of carbon and oxygen. The C-line originates from the target surface and from the adsorbed carbon; the O-line originates entirely from the adsorbed oxygen molecules. Note the similarity of the long low-energy tails of the lines that can be explained by the back-diffusion of the Auger electrons.

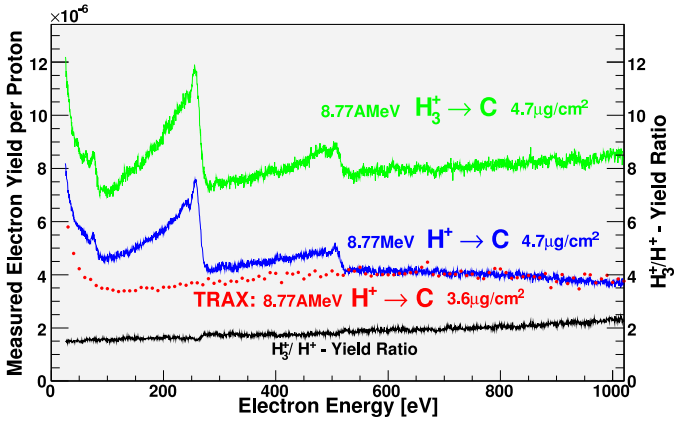

Figure 1: Energy spectra of electrons emitted in the collision systems of 8.77 AMeV H^+ and 8.77 AMeV H_3^+ projectiles impinging on a 4.7 $\mu g/cm^2$ C-Target. Also shown is the ratio of the two cross sections. We compare the measured spectra for the proton projectile with dedicated TRAX simulations for a 3.6 $\mu g/cm^2$ effective thickness.

References

[1] N. Lineva et al. GSI Annual Reports 2007 and 2008

[2] M. Krämer Nucl. Instr. Meth. B **105** (1995) 14

[3] N. Lineva et al. Nucl. Instr. Meth. B **267**(2009)801 http://dx.doi.org/10.1016/j.nimb.2009.02.038

[4] N. Lineva, PhD Thesis, TU Darmstadt, 2008 http://www.gsi.de/documents/DOC-2008-Aug-25-1.pdf

[5] Y. Suzuki et al. Phys. Rev. A **50** (1994) 3533

* Work supported by ESA: AO-08-IBER code 22

† c.kozhuharov@gsi.de

A new test of Time Dilation at ESR using fast $^7Li^+$-ions*

B. Botermann[1,2], T. Kühl[1], W. Nörtershäuser[1,2], T. Stöhlker[1], C. Geppert[2], G. Huber[2], S. Karpuk[2], C. Novotny[2], D. Bing[3], D. Schwalm[3], A. Wolf[3], G. Gwinner[4], T. W. Hänsch[5], S. Reinhardt[5], and G. Saathoff[5]

[1]GSI Helmholtzzentrum für Schwerionenforschung, Darmstadt, Germany; [2]Johannes Gutenberg Universität Mainz, Germany; [3]MPI für Kernphysik, Heidelberg, Germany; [4]University of Manitoba, Winnipeg, Canada; [5]MPI für Quantenoptik, Garching, Germany

One of the fundamental principles in modern physics is Local Lorentz Invariance (LLI), which describes spacetime symmetry in the theories of the electromagnetic, the strong and the weak force as well as the local part of general relativity. Time dilation is one of the well known consequences of LLI and Special Relativity (SR), respectively, and can be probed by experiment. Such a test can be performed by simultaneous excitation of an electric dipole transition of fast moving ions. The presented experiment uses $^7Li^+$ ions, stored at the experimental storage ring (ESR) with an velocity of 33.8 % of the speed of light. The schematic setup is shown in figure 1.

In the used experiment geometry the wavelengths of the excitation lasers ($\lambda_{a,p}$) and the wavelength of the dipole transition of metastable $^7Li^+$ ions at rest (λ_0 = 548,5 nm) have to obey

$$\frac{\lambda_a \cdot \lambda_p}{\lambda_0^2} = 1 \tag{1}$$

if SR is valid, here λ_a (λ_p) denotes the wavelength of the laserbeam which is aligned antiparallel (parallel) to the flight direction of the ions. In test theories [1, 2] hypothetical deviations from SR can be addressed by a dimensionless parameter $\varepsilon(\beta^2)$ added to eq. (1)

$$\frac{\lambda_a \cdot \lambda_p}{\lambda_0^2} = 1 + \varepsilon(\beta^2). \tag{2}$$

By using the Einstein clock synchronisation the experiment is not sensitve to the one-way speed of light and therefore the parameter $\varepsilon(\beta^2)$ is only dependent on orders of β^2.

Due to the relativistic time dilation, the wavelengths of the exciting lasers have to obey $\lambda_{a,p} = \lambda_0 \cdot \gamma \cdot (1 \pm \beta)$, where $\gamma = (1-\beta^2)^{-1/2}$ is the well-known Lorentzfactor and $\beta = v/c$ is the velocity of the ions in terms of the speed of light. With this setup the frequencies of the lasers can by fixed down to 1 MHz which corresponds to a relative accuracy of $\Delta\nu/\nu = 10^{-9}$.

During the beam time in February 2009 the transition frequencies ν_a and ν_p of the moving ions have been determined to an overall accuracy of $\Delta\nu/\nu = 10^{-8}$ which is a factor 10 more accurate than the previous experiment at GSI [3]. This leads to an upper bound for the parameter $\varepsilon(\beta^2)$ of

$$\varepsilon(\beta^2) < 1,6 \cdot 10^{-8}. \tag{3}$$

*This work was supported by the Helmholtz Association under Contract No. VH-NG-148 and by the BMBF under Contract No. 06MZ9179I.

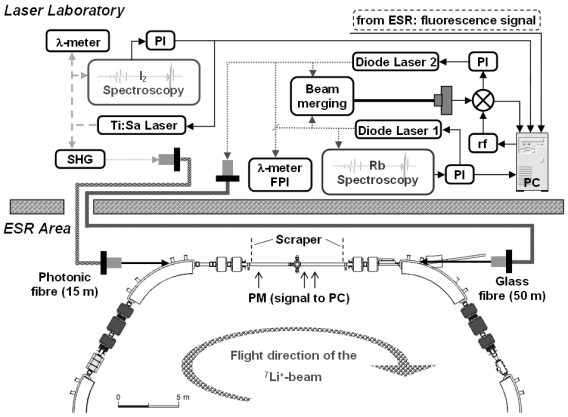

Figure 1: Schematic setup of the laser spectroscopy experiment for a test of time dilation at ESR. The laserlight for the antiparallel excitation (λ_a = 780 nm) of the lithium ions is provided by a diode laser, while the light for the parallel excitation (λ_p = 386 nm) is generated by a frequency-doubled Ti:Sa laser. The wavenlengths of both lasers are stabilised to well known transitions in atomic rubidium and molecular iodine using freqency modulation spectroscopy.

In the photon sector of the Standard Model Extension [4] $\varepsilon(\beta^2)$ can be expressed by an expansion in terms of β^2 with a coefficent κ_{tr}

$$\varepsilon(\beta^2) = 2 \cdot \kappa_{tr} \cdot \beta^2 + O(\beta^4). \tag{4}$$

This parameter is interpreted as vacuum birefringence and the presented experiment gives an upper limit for deviations from zero of

$$\kappa_{tr} < 7,05 \cdot 10^{-8}. \tag{5}$$

This is comparable with the most stringent previous test [5]. Within the uncertainties of the experiment, no deviations from SR are found. In upcoming beam times, we expect to reduce the upper bound of κ_{tr} by a factor of 10.

References

[1] R. Mansouri et al., General Relativity and Gravitation **8**, 515 (1977)

[2] V. Kostelecký et al., Physical Review D **39**, 683 (1989)

[3] C. Novotny et al., Physical Review A **80**, 022107 (2009)

[4] M. Tobar et al., Physical Review D **71**, 025004 (2005)

[5] S. Reinhardt et al., Nature Physics **3**, 861 - 864 (2007)

Precision Laser Spectroscopy of Beryllium*

M. Žáková[1], Z. Andjelkovic[1], J. Krämer[1], A. Krieger[1], R. Neugart[1], D. Tiedemann[1], Ch. Geppert[1,2], W. Nörtershäuser[1,2], R. Sánchez[1,2], T. Neff[2], K. Blaum[3], D.T. Yordanov[3], M. Kowalska[4], M.L. Bissell[5], G.W.F. Drake[6], F. Schmidt-Kaler[7], Z.-C. Yan[8], and C. Zimmermann[9]

[1]Universität Mainz, Germany; [2]GSI, Darmstadt, Germany; [3]MPI Heidelberg, Germany; [4]CERN, Geneva, Switzerland; [5]University of Leuven, Belgium; [6]University of Windsor, Canada; [7]Universität Ulm, Germany; [8]University of New Brunswick, Canada; [9]Universität Tübingen, Germany

The neutron-rich beryllium isotopes exhibit a halo structure. The matter distribution of such isotopes is significantly larger than that of their neighboring isotopes due to a very low-density tail in the matter distribution. Important information about the nuclear structure of a halo nucleus can be obtained by measuring its nuclear charge radius, i.e. the size of the proton distribution. The difference of the mean-square nuclear charge radii between two isotopes $\langle r^2\rangle_A$ and $\langle r^2\rangle_{A'}$ is related to the isotope shift (IS) of an atomic transition as follows

$$\langle r^2\rangle_A - \langle r^2\rangle_{A'} = (\mathrm{IS} - \mathrm{MS})/C_{\mathrm{FS}}. \qquad (1)$$

For light elements, like beryllium, the mass shift (MS) has to be calculated together with the field shift constant (C_{FS}) at least with a relative accuracy of 10^{-5}. It is also required to measure the IS at the same level of accuracy.

We have recently performed high-resolution collinear laser spectroscopy on a fast beryllium ion-beam and measured the IS in the $2\,S_{1/2} \rightarrow 2\,P_{1/2}$ (D_1) and $2\,S_{1/2} \rightarrow 2\,P_{3/2}$ (D_2) transitions of $^{7,10,11}Be^+$ with respect to $^9Be^+$. Here, we present the results of IS measurements in the D_2 transition and the extracted charge radii. The complete laser system was built and tested at GSI and the university of Mainz. The measurements were performed at the radioactive beam facility ISOLDE/CERN. The beryllium isotopes were laser ionized, mass separated, accelerated and delivered to the COLLAPS beamline. The ions were overlapped with two laser beams, one of them propagating in the beamline collinearly and the other anticollinearly to the ion beam. The lasers were frequency stabilized to an iodine hyperfine transition and to a frequency comb, respectively. Scanning across the resonances was performed with the so called Doppler tuning. More details about the experiment are reported in [1, 2]. The absolute transition frequency (ν_0) was determined from the centers of gravity ν_c and ν_a in the collinear and anticollinear spectrum, respectively, according to $\nu_0 = \sqrt{\nu_c \times \nu_a}$. The centers of gravity were calculated from the individual peak centers and the corresponding hyperfine splitting and a relative accuracy of 2×10^{-9} was reached. IS were extracted from the difference in the absolute transition frequency of two isotopes. The final charge radii of 2.637(55), 2.339(53) and 2.463(62) fm for ^{7,10,11}Be [2] were determined by using mass shift and field shift constant calculations [4, 5] and the reference charge radius $r_c(^9\mathrm{Be})$=2.519(12) fm obtained from electron scattering. As depicted in figure 1, the charge radii from the D2 line are in a very good agreement with the charge radii obtained from the D_1 line [1], but with larger uncertainties due to the unresolved hyperfine structure in the $P_{3/2}$ state. The experimental data are compared to nuclear calculations and the trend of charge radii is well reproduced, especially by new Fermionic Molecular Dynamics calculations [2]. The charge radii are decreasing from ^{7}Be to ^{10}Be, which is assigned to clustering. A significant increase between ^{10}Be and ^{11}Be is mainly due to the halo neutron which moves the ^{10}Be core around the center of mass. According to the comparison with fragmentation experiments and the nuclear calculations, core polarization contributions are expected to be very small. From the IS in the D_1 and D_2 transitions we extracted splitting isotope shifts of -5.1(2.2), 3.5(2.4) and 3.6(2.5) MHz for ^{7,10,11}Be, respectively. These are consistent with theoretical calculations [4, 5] and provide a valuable check of the beryllium experiment.

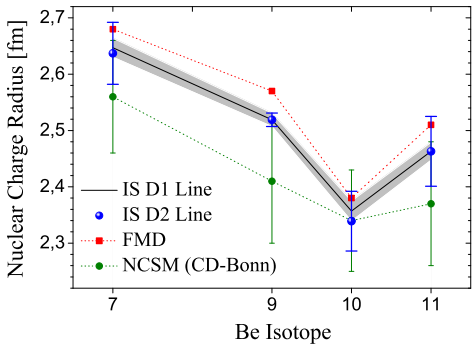

Figure 1: Experimental charge radii from the isotope shift measurements in the D1 line [1] (grey area indicates the uncertainties) and D2 line [2] compared with theoretical predictions from Fermionic Molecular Dynamics [2] and No Core Shell Model with the CD-Bonn potential [3].

References

[1] W. Nörtershäuser *et al.*, PRL 102 (2009) 062503.

[2] M. Žáková *et al.*, submitted to J. Phys. G: Nucl. Phys. (2010).

[3] C. Forssen *et al.*, Phys. Rev. C 79 (2009) 021303.

[4] Z.C. Yan *et al.*, PRL 100 (2008) 243002.

[5] M. Puchalski, K. Pachucki, Phys. Rev. A 79 (2009) 032510 and private communication.

* Work supported by the Helmholtz Association (VH-NG-148), BMBF (06TU263I, 06MZ215, 06UL264I) and the EU (FP-6 EU RII3-CT-2004-506065). M.K. was supported by the EU (MEIF-CT-2006-042114).

Nuclear structure studies with the ISOLTRAP Penning trap mass spectrometer

Ch. Borgmann*[1], G. Audi[2], D. Beck[3], K. Blaum[1], Ch. Böhm[1], M. Breitenfeldt[4], R. B. Cakirli[5], R. F. Casten[6], S. Eliseev[1], D. Fink[1], S. George[1], F. Herfurth[3], A. Herlert[7], A. Kellerbauer[1], H.-J. Kluge[3], M. Kowalska[7], S. Kreim[1], D. Lunney[2], E. Minaya-Ramirez[2], S. Naimi[2], D. Neidherr[8], Yu. Novikov[9], M. Rosenbusch[4], S. Schwarz[10], L. Schweikhard[4], and K. Zuber[11]

[1]MPI für Kernphysik, Heidelberg, Germany; [2]CSNSM-IN2P3-CNRS, Orsay, France; [3]GSI, Darmstadt, Germany; [4]Ernst-Moritz-Arndt-Universität, Greifswald, Germany; [5]Istanbul University, Turkey; [6]Yale University, New Haven, USA; [7]CERN, Geneva, Switzerland; [8]Johannes Gutenberg-Universität, Mainz, Germany; [9]PNPI, St. Petersburg, Russia; [10]Michigan State University, East Lansing, USA; [11]Technische Universität Dresden, Germany

In 2009, successful measurements on the masses of $^{122-124}$Ag, $^{64-66}$Mn and $^{96-97}$Kr were performed at the triple-trap mass spectrometer ISOLTRAP [1], which lead to new insights in different fields of nuclear structure.

The determination of the neutron-rich silver masses, clarified the previously observed, unexpected behaviour of the two neutron separation energies (S_{2n}) of this isotopic chain. Now, the trend in S_{2n} values is as expected for spherical nuclei. By measuring the masses of neutron-rich manganese nuclides, we aimed at investigating the behaviour around $N = 40$, since a sub-shell closure has been under discussion in this region. The new data for $^{64-66}$Mn show no hints for a shell closure any more. In the case of ^{66}Mn we had the additional difficulty of a very short half-life of 64.4 ms. A time-of-flight ion cyclotron resonance for ^{66}Mn is shown in Figure 1.

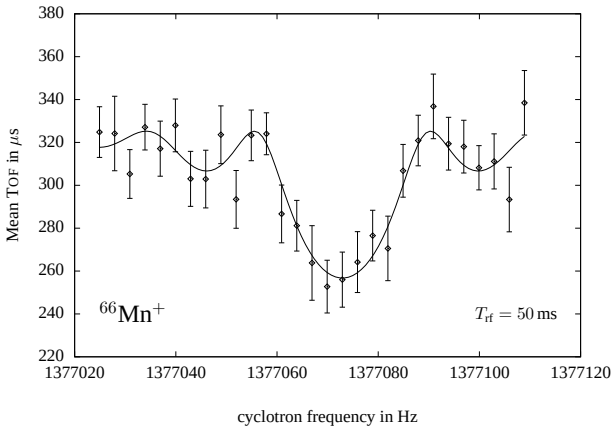

Figure 1: Time-of-flight ion-cyclotron resonance of ^{66}Mn. With this measurements, a new half-life record was established at ISOLTRAP. The solid line is a fit of the theoretically expected line shape to the data points.

The new krypton masses indicate the end of a quantum phase transition region: For higher Z, a sudden deformation occurs around $N = 60$. With our newly measured masses of $^{96-97}$Kr, however, there is no deformation visible for krypton from the two-neutron separation energies, making the krypton chain the end of the deformation region. This region is presently also under investigation using decay spectroscopy, which should shed more light on the region.

In 2009, we completed the analysis of the $^{136-146}$Xe data [2]. The results confirm the correlation between a unique behaviour of the residual proton-neutron interaction – reflected in the double differences of binding energies ($\delta V_{\rm pn}$) – and octupole deformation, previously observed by us for $^{223-229}$Rn [3]. Moreover, the analysis of the mass data for $^{99-109}$Cd has been completed as well and their influence on the rp process (rapid proton capture) has been investigated [4]. Finally, the analysis of the Q-value measurements of ^{194}Hg decaying into ^{194}Au makes ^{194}Hg a possible candidate to determine a new lower limit for the electron neutrino mass of a few eV in combination with modern calorimeter experiments.

The main technical developments in 2009 focussed on the trap-assisted decay spectroscopy system and on the laser ablation ion source. The β- and γ-detection system coupled to a tape-transport station will be used to assist mass measurements by decay spectroscopy. This year, a test run was successfully performed with ^{80}Rb, checking thoroughly e. g. ion transfer, implantation into the tape and detection efficiency. The laser ablation carbon cluster source was further developed in order to obtain a reliable source for online runs: A more suitable laser was implemented with modified laser optics. Together with an improved extraction region this led to a gain in emittance as well as higher stability and quality of the beam.

In 2010, we are going to implement a fourth trap into our system. This trap will serve as a very fast time-of-flight separator using electrostatic mirrors. With this technique we aim for an enhanced isobaric separation, mainly for cases with strong contaminations like ^{130}Cd.

References

[1] M. Mukherjee et al. Eur. Phys. J. A 35, 1 (2008)

[2] D. Neidherr et al., Phys. Rev. C 80, 044323 (2009)

[3] D. Neidherr et al., Phys. Rev. Lett. 102, 112501 (2009)

[4] M. Breitenfeld et al., Phys. Rev. C 80, 035805 (2009)

* christopher.borgmann@cern.ch

This work was supported by the German Federal Ministry for Education and Research (BMBF) through grants 06GF151 and 06MZ215, the Max-Planck Society, and the Helmholtz Association for National Research Centers (VH-NG-037).

Accuracy studies and first mass measurements at TRIGA-TRAP*

C. Smorra[1,2], D. Beck[3], T. Beyer[2,4], K. Blaum[2,4], M. Block[3], K. Eberhardt[1], M. Eibach[1,2], F. Herfurth[3], J. Ketelaer[5], Sz. Nagy[3,4], W. Nörtershäuser[1,3], D. Renisch[1], and J. Runke[1]

[1]Institut für Kernchemie, Johannes Gutenberg-Universität, Mainz, Germany; [2]Ruprecht Karls-Universität, Heidelberg, Germany; [3]GSI Helmholzzentrum für Schwerionenforschung GmbH, Darmstadt, Germany; [4]Max-Planck-Institut für Kernphysik, Heidelberg, Germany; [5]Institut für Physik, Johannes Gutenberg-Universität, Mainz, Germany

Introduction

At present atomic masses are obtained with the highest precision by measuring the cyclotron frequency of a stored ion in a Penning trap [1]. TRIGA-TRAP at the research reactor TRIGA-Mainz is so far the only Penning trap mass spectrometer installed at a nuclear reactor, which provides short-lived neutron-rich radionuclides in the mass region $80 < A < 140$ by thermal-neutron induced fission. The goal of TRIGA-TRAP is to perform mass measurements on these nuclides in order to contribute to improvements of nuclear structure studies, nucleosynthesis calculations and the predictive power of nuclear mass formulas [2].

Results

At TRIGA-TRAP the time-of-flight ion cyclotron resonance (TOF-ICR) method is routinely used to determine cyclotron frequencies of ions produced by offline ion sources. A laser ablation ion source [3] provides carbon clusters $^{12}C_n^+$ as reference ions for mass calibration and to study systematic uncertainties of the mass spectrometer. One systematic uncertainty due to non-linear magnetic field fluctuations depends on the time elapsed between two measurements Δt. The magnitude of this effect was determined in a long-term measurement of the cyclotron frequency of C_{20}^+ to be

$$\frac{\Delta\omega_{ref}}{\omega_{ref}} = 4 \cdot 10^{-11}/\text{min} \cdot \Delta t \qquad (1)$$

A trap misalignment leads to a systematic uncertainty in the mass calibration which increases with the mass difference of the ion of interest to the reference ion ($m - m_{ref}$). This so-called mass-dependent systematic effect was investigated by the determination of well-defined frequency ratios r of carbon cluster ions over a broad mass-range. About 70 frequency ratio measurements yield

$$\frac{\Delta r_m}{r} = 1.8(1) \cdot 10^{-9}/\text{u} \cdot (m - m_{ref}) \qquad (2)$$

as the result for the mass-dependent systematic effect at TRIGA-TRAP. After including these two systematic effects the residual relative systematic uncertainty of the measurements was found to be $2.5 \cdot 10^{-8}$ [4].

Ions for a mass measurement of ^{197}Au have also been produced with the laser ablation ion source using a gold foil as target. The literature value of the mass of ^{197}Au listed in the atomic-mass evaluation (AME) 2003 [5] was confirmed with the TRIGA-TRAP mass spectrometer. The frequency ratio to C_{16}^+ was determined with a precision of 6.9 keV ($\delta m/m = 3.7 \cdot 10^{-8}$). A cross-check with C_{15}^+ has been performed at the same time to ensure the accuracy of the measurement. The results of the measurements are shown in Fig. 1.

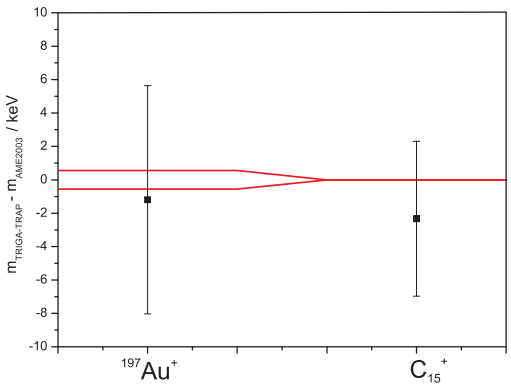

Figure 1: Results of the mass measurement of $^{197}Au^+$. The red lines represent the uncertainty of the literature values in [5], and the data points the results of TRIGA-TRAP.

Outlook

Further offline mass measurements on lanthanoids and actinoids will be performed in 2010. Concerning the online coupling to the TRIGA reactor, a gas-jet system is being connected to an ECR ion source to transport and ionize the radionuclides. An RFQ buncher is being installed to provide cooled ion bunches for high-precision mass measurements on neutron-rich fission products.

References

[1] K. Blaum, Phys. Rep. 425, 1-78 (2006).
[2] J. Ketelaer et al., Nucl. Inst. Meth. 594, 162-177 (2008).
[3] C. Smorra et al., J. Phys. B 42, 154028 (2009).
[4] J. Ketelaer et al., Eur. Phys. J. D, submitted (2009).
[5] G. Audi et al., Nucl. Phys. A 729, 337-676 (2003).

*The financial support from the Helmholtz Association for National Research Centers (HGF) under Contracts VH-NG-037 and VH-NG-148, the Max-Planck society, the 'Bundesministerium fr Bildung und Forschung' under contract 06MZ91721, and the 'Stiftung Rheinland-Pfalz fr Innovation' under contract 961-386261/854 is acknowledged. Sz. Nagy acknowledges support from the Alliance Program of the Helmholtz Association (HA216/EMMI).

Double Ionization Dynamics Studied with Four-Body Dalitz Plots

D. Fischer[1], M. Schulz[2], K. Schneider[1,3], M. F. Ciappina[4], T. Kirchner[5], A. Kelkar[1,3], X. Wang[1,3], S. Hagman[6], M. Grieser[1], K.-U. Kühnel[1], R. Moshammer[1], and J. Ullrich[1]

[1]MPI für Kernphysik, Heidelberg, Germany; [2]Missouri S&T Rolla, USA; [3]Extreme Matter Institute EMMI, GSI, Darmstadt, Germany; [4]Institute of High Performance Computing, Singapore; [5]York University, Toronto, Canada; [6]GSI, Darmstadt, Germany

The dynamics of double ionization (DI) of helium by ion impact has attracted widespread interest in the last decades, in particular, as electron-electron correlation effects play a much more important role than in single ionization (SI). Kinematically complete studies of DI, i.e. experiments recording the full momentum vectors of all involved particles, are very demanding due to the relatively small cross sections and the high-dimensional final momentum space. In order to obtain results with satisfying statistical quality, many events need to be collected and long measuring periods were required in earlier experimental runs. Here we report on a study of double ionization with the TSR in-ring Reaction Microscope at MPIK, which was earlier operated at the ESR [1]. Due to the high luminosity achievable in storage rings, data could be obtained in a short time for projectile ions ranging from 6MeV protons to 158 MeV Au^{33+} (c.f. [2]).

Fully differential cross sections (FDCS) extracted from such measurements provide the most sensitive test for theory. However, they have the drawback that they typically cover only a tiny fraction of the total cross section and thus elucidate the collision dynamics only for very specific kinematical conditions. Recently, we demonstrated that four-body Dalitz (4-D) plots are a powerful tool to present data of in double ionization [3] without loss of any part of the total cross section. By using a tetrahedral coordinate system it has become possible to present measured data as a function of all four fragments simultaneously.

In Fig. 1 4-D plots are shown for double ionization of helium in collisions with 158 MeV Au^{33+}. The front and bottom planes of the tetrahedron represent the ejected electrons, the backplane the He^{2+} nucleus, and the right plane the projectile. The distance from a given data point to the four planes provides a set of the squared momenta of each particle normalized to the sum of these squared momenta for all four particles [3]. In the case of the projectile, the momentum transfer is used. In the upper diagrams only the transverse momentum components in the scattering plane (defined by the initial and final projectile momenta) are used. In the lower line only the longitudinal components (i.e. along the projectile beam axis) are considered. The numbers in the upper left diagram label the 6 intersection lines between adjacent tetrahedron planes.

In the transversal direction (Fig. 1 a) the dominant feature is a strong maximum at intersection line 6, which is at a zero distance to the two electron planes. Thus, the electron momenta are negligible in this region and momentum is transferred predominantly between the projectile and the He nucleus. In the longitudinal direction (Fig. 1 d) binary interactions are much less important. A detailed analysis of this plot shows [2] that the "shoe-tongue-like" distribution is a signature of the strong post-collision interaction (PCI) between one (or both) electrons and the highly charged and relatively slow projectile ion.

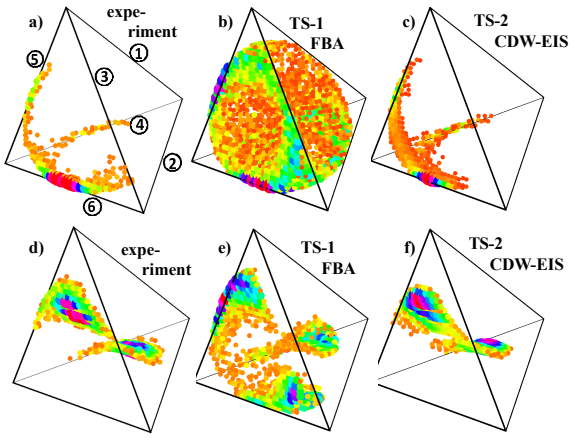

Figure 1: Experimental and theoretical 4-D plots for He double ionization by 158 MeV Au^{33+} impact (see text).

In Fig. 1b) and e) a first-order calculation is shown, i.e. here the projectile knocks out only one electron directly described in the First Born Approximation (FBA); the second electron is ejected through electron-electron correlation (TS-1). In Fig. 1c) and f) the results of an uncorrelated calculation are plotted, where both electrons are ejected by two independent interactions with the projectile (TS-2). This process is modelled by convoluting the FDCS for single ionisation of He and He^+ obtained in a continuum-distorted-wave—eikonal-initial-state (CDW-EIS) calculation. Our TS-2 model additionally accounts for the post-collision interaction [2] and qualitatively reproduces the data very well.

It should be noted, that the models presented here are relatively simple but they mark the beginning of a potentially fruitful development. We are currently working on more sophisticated models which include several double ionization mechanisms simultaneously and treat them coherently. Analyzing the 4-D plots for the individual components appears to be a powerful tool to test new models in great detail.

References

[1] K.-U. Kühnel, et al., GSI Sci. Rep. 2007, p. 276.
[2] D. Fischer, et al., Phys. Rev. A 80, 062703 (2009).
[3] M. Schulz et al., J. Phys. B 40, 3091 (2007).

Young–type interferences in the two–photon decay of heavy helium–like ions*

A. Surzhykov[†1,2], A. Volotka[3], Th. Stöhlker[1,2], and S. Fritzsche[‡1,4]

[1]GSI, Darmstadt, Germany; [2]Universität Heidelberg, Germany; [3]Technische Universität Dresden, Germany; [4]University of Oulu, Finland

The characteristic photon emission from highly–charged, heavy ions has been in the focus of experimental studies at the GSI facility for many years [1]. Apart from the one–photon bound–bound transitions, the two–photon decay of metastable ionic states has attracted much interest since it may reveal unique knowledge on the *complete* spectrum of high–Z ions, including the negative continuum of Dirac's relativistic equation. Up to the present, most two–photon studies were focused on the total as well as energy–differential decay rates [2]. Much less attention, in contrast, has been previously paid to the angular and polarization correlations between the emitted photons. Owing to recent progress in x–ray detector design, however, measurements on the γ–γ correlations in the two–photon decay of highly–charged ions are likely to be carried out in the next few years and will provide more insights into the electronic structure of such heavy atomic systems.

In order to support future coincidence experiments, we have recently applied the second–order perturbation theory based on Dirac's equation to investigate the $\gamma - \gamma$ *angular correlations* in the decay of few–electron systems [3]. Special attention in our theoretical analysis has been paid to helium–like ions which are the most suitable candidates for the two–photon studies in high–Z domain. Singly–excited states $1s2s\ ^{1,3}S_J$ and $1s2p\ ^{1,3}P_J$ of these ions can be efficiently populated in relativistic atomic collisions [4, 5] and may stabilize via two–photon emission. Apart from the well established $1s2s\ ^1S_0 \to 1s^2\ ^1S_0$ transition, recent interest has been focused also on the $1s2p\ ^3P_0 \to 1s^2\ ^1S_0$ (two–photon) decay whose properties are expected to be sensitive to quantum electrodynamics (QED) and parity non–conservation (PNC) phenomena in atomic systems. Fig. 1 displays the angular correlation function for this decay of helium–like xenon Xe^{52+} and uranium U^{90+} ions and for the equal energy sharing between the two photons: $E_{\gamma_1} = E_{\gamma_2}$. As seen from the figure, the emission pattern is strongly anisotropic: photons are more likely to be emitted back–to–back while the correlation function vanishes identically for opening angle $\theta = 0°$. Such a behaviour of the two–photon (angular) correlation function is caused by the interference between *two* pathways that appear for each allowed multipole term of the $1s2p\ ^3P_0 \to 1s^2\ ^1S_0$ transition. For instance, the leading E1M1–M1E1 decay proceeds either via (virtual) intermediate $n\ ^3S_1$ or $n\ ^3P_1$ states, thus given rise to a "double–slit" picture. By taken into account such a Young–type interference effect in the leading (E1M1) decay channel a simple analytical expression has been derived for the $\gamma - \gamma$ correlation function [3]:

$$W_{E1M1}(\theta) \propto \sin^4(\theta/2)\,. \qquad (1)$$

This angular distribution is modified, of course, by the higher (non–dipole) terms in the expansion of the electron–photon interaction. The contribution from these terms becomes more pronounced for the back–to–back photon emission where they lead to about a 30 % enhancement of the emission yield. As seen from the figure, such a enhancement remains almost constant along the helium isoelectronic sequence due to similar ($\propto Z^{12}$) scaling of the transition rates of the leading E1M1 and the (next order) E2M2 decay channels. Our calculations clearly indicate, therefore, the importance of higher multipole effects for the proper analysis of the photon–photon correlations not only in high–Z domain but also for medium–Z ions.

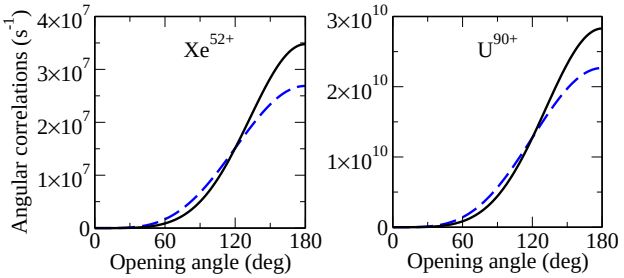

Figure 1: Angular correlation function for the $1s2p\ ^3P_0 \to 1s^2\ ^1S_0$ two–photon decay of helium–like xenon Xe^{52+} (left panel) and uranium U^{90+} (right panel) ions. Calculations obtained within the dipole E1M1 approximation (dashed line) are compared with those including all the allowed multipoles (solid line). Results are presented for equal energy sharing between the photons.

References

[1] S. Fritzsche, P. Indelicato, and Th. Stöhlker, J. Phys. B: At. Mol. Opt. Phys. **38**, S707 (2005).

[2] A. Kumar *et al.*, Eur. Phys. J. Special Topics **169**, 19 (2009).

[3] A. Surzhykov *et al.*, Phys. Rev. A (2010) submitted.

[4] J. Rzadkiewicz *et al.*, Phys. Rev. A **74**, 012511 (2006).

[5] A. Surzhykov *et al.*, Phys. Rev. A **77**, 042722 (2008).

* Work supported by Helmholtz Association and GSI under the project VH–NG–421.

† surz@physi.uni-heidelberg.de

‡ Support by GSI under the project KS-FRT.

Dominance of the Breit interaction in the x-ray emission of highly-charged ions following dielectronic recombination

S. Fritzsche*[1,2], A. Surzhykov†[2,3], and Th. Stöhlker[2,3]

[1]Frankfurt Institute for Advanced Studies; [2]GSI, Darmstadt; [3]University of Heidelberg

Highly-charged ions are found an excellent *testbed* for studying the effects of relativity and (few-) electron dynamics. Already since the early work of Gregory Breit on the fine-structure of atomic helium [1], there has been special interest to explore the relativistic contributions to the electron-electron (e-e) interaction, briefly refered as the *Breit* interaction. Today, this interaction (or at least major the parts of it) is accounted for not only in most atomic level calculations but also in hadron and heavy-ion physics as well as in quantum chemistry. Apart from level spectroscopy, the Breit interaction has been explored also for (spin-) forbidden transitions, the autoionization and recombination of highly charged ions as well as for other processes [2]. In all these examples, however, the Breit interaction usually occurs as a 'correction' to the (dominant) Coulomb repulsion, and great spectroscopic effort is required then to separate its influence from other one- and many-particle effects.

To shed further light on the Breit interaction in the presence of strong fields, we recently proposed two x-ray measurements on the angular distribution and linear polarization of the $1s2s^22p_{1/2}\ J=1 \rightarrow 1s^22s^2\ J=0$ electric-dipole (E1) emission following the dielectronic recombination of (initially) lithium-like ions. For this line, it was found that the Breit interaction among the electrons dominates the Coulomb repulsion and may even cause a *qualitative* change in the expected x-ray emission pattern for ions with $Z > 73$ [3]. Indeed, the suggested measurements are feasible with present-day x-ray detectors: While experiments on (i) the angular distribution of the $1s2s^22p_{1/2}\ J=1 \rightarrow 1s^22s^2\ J=0$ x-ray line are suitable especially for storage rings, (ii) their linear polarization can be observed at both storage rings and electron-beam ions traps (EBIT), since it requires a polarization measurement at only a single observation angle (with regard to the beam axis), and preferentially for $\theta = 90^o$.

Our analysis of the x-ray emission is based on the density-matrix theory in order to describe the sublevel population of the ions in terms of the alignment parameters $\mathcal{A}_k(\alpha_d J_d)$. For the resonant capture of (unpolarized) electrons, these parameters can be expressed by means of the (reduced) matrix elements of the e-e interaction [4]

$$V \;=\; V^{\rm C} + V^{\rm B} \;=\; \sum_{i<j} \left(\frac{1}{r_{ij}} + b_{ij} \right)$$

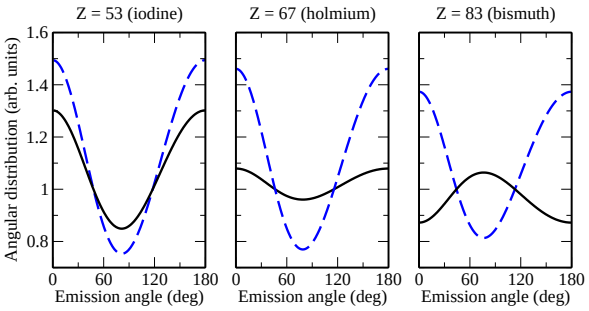

Figure 1: Angular distribution of the $1s2s^22p_{1/2}\ J=1 \rightarrow 1s^2\ 2s^2\ J=0$ dipole emission for Be-like iodine (left panel), holmium (middle) and bismuth ions (right), following the dielectronic recombination of (initially) Li-like projectiles. Calculations with only the Coulomb repulsion (blue dashed lines) are compared with a full account of the e-e interaction (Coulomb+Breit; black solid line).

which, within the relativistic theory, contains both the instantaneous Coloumb repulsion and the Breit interaction, i.e. the magnetic and retardation contributions.

Figure 1, for example, displays the large differences in the angular distribution of the considered x-ray line for calculations *with* and *without* the Breit interaction in the transition amplitues. This gives rise to a very different angular distribution of the corresponding x-ray photons. To the best of our knowledge, this is the first physics case where the incorporation of the Breit terms lead to a completely different behaviour in comparison of what is expected from the Dirac-Coulomb theory for the many-electron ions. For an increasing nuclear charge of the ions, the angular distribution of the $1s2s^22p_{1/2}\ J=1 \rightarrow 1s^22s^2\ J=0$ emission is predicted to become first isotropic for $Z \approx 73$ and becomes then more and more perpendicular to the ion beam. Both, the formation as well as the subsequent E1 decay of the $1s2s^22p_{1/2}\ J=1$ level can be well resolved with present-day (position-sensitive) x-ray detectors with a resolution of ~ 50 eV and, hence, provides a *clean and promising route* for studying the e-e interaction in relativistic collisions and the presence of strong fields.

References

[1] G. Breit, Phys. Rev. **36**, 383 (1930); *ibid.* **39**, 616 (1932).

[2] S. Fritzsche, et al., J. Phys. B **38**, S707 (2005).

[3] S. Fritzsche et al., Phys. Rev. Lett. **103** (2009) 113001.

[4] W. R. Johnson, *Atomic Structure Theory: Lectures on Atomic Physics* (Springer, 2007).

* Support by GSI under the project No. KS-FRT.

† Work supported by the Helmholtz Gemeinschaft and GSI (VH-NG-421).

Highly charged ion beam polarization and its application to the search for parity nonconservation effects in ions *

A. Bondarevskaya[1], L. Labzowsky[1,2], G. Plunien[3], D. Liesen[4], and F. Bosch[4]

[1]St. Petersburg State University, Russia; [2]Petersburg Nuclear Physics Institute, Russia; [3]Technische Universität Dresden, Germany; [4]GSI Darmstadt, Germany

The most important motivation for the production of polarized ion beams is the possibility to observe parity nonconservation (PNC) effects in hyperfine-quenched transitions in heliumlike highly charged ions (HCI), where these effects can reach an unprecedented high value for atomic physics. Their measurement also requires online-diagnostics of the degree of the ion-beam polarization. Possible schemes for such experiments as well as estimates for the magnitude of PNC effects have been recently proposed and investigated [1].

The polarization of a multi-level particle is described by the density matrix $\rho_F = \sum_{M_F} n_{FM_F} \psi^*_{FM_F} \psi_{FM_F}$ (see [2]), which turns into its diagonal form only with respect to a particular quantization axis, namely the instantaneous quantization axis (IQA). The latter concept was introduced in [1] and on its basis the conservation of the degree of polarization was proved for various magnetic fields.

In regard to the observation and measurement of the polarization of HCI in storage rings, one of such methods, up to now discussed only theoretically, is based on the dependence of the hyperfine quenching (HFQ) on the ion polarization in an external magnetic field [3]. Another possible way to control the HCI beam polarization is to observe the linear polarization in HFQ transitions of polarized ions ([1]).

The idea to determine the degree of polarization of a HCI beam by a measurement of the linear polarization of X-ray photons emitted in the process of radiative electron capture (REC) by H-like ions was discussed in [4, 5, 6]. The first measurement of the X-ray polarization in the process of electron capture by HCI with nonpolarized ions was reported in [7]. Unlike [4]-[7] we conclude that for the process we are dealing with only the alignment but not the polarization of the ions can be monitored. This finding is in agreement with the REC studies for HCI in [8].

From the existence of polarization always follows the existence of alignment, but not vice versa. Therefore from the Stokes parameter P_1 it is not possible to extract the degree of polarization λ_F. However it is possible to check, whether the polarization has taken its maximum value. The value of the Stokes parameter P_1^M, which corresponds to the maximum possible value for the nuclear polarization for the ion $^{151}_{63}\mathrm{Eu}^{61+}$ and accessable with the method of polarization as proposed in [2], is $P_1^M = -0.4$. For $n_{FM_F} = const$ we find that $P_1 = 0$, i.e. the photons are nonpolarized, if they are emitted by nonpolarized ions. What concerns the Stokes parameter P_2, in the case of a bound-bound dipole transition it appears to be $P_2^M = 0$ independent of the ion beam polarization.

An experiment with He-like Gd and Eu ions, first proposed in [9], is discussed in more details employing more accurate characteristics of ions in storage rings together with estimates for the parameters defining the feasibility of the experiment (observation time etc.) in our paper [1].

To compete with the Cs experiment, where an accuracy is of the order of 0.3% is already reached, the total observation time τ_{obs} becomes too large (of about $\tau_{\mathrm{obs}} \sim 10^{10}$s).

The way to optimize the PNC experiment with He-like HCI is to install some kind of a stripping target in the ring. In this case, the ions will be not lost and will remain in the ring. Since the process of stripping (as well as the process of dressing) is much faster than the formation process of the hyperfine sublevels, we may assume that immediately after the stripping full polarization of the nuclei will be kept. However, even for a "leakage" of ions from the ring of $\sim 10^{-3}$, the observation time for Eu^{61+} remains about 10^7s (~ 3 years), i.e. too large.

Experiments for the search of PNC effects in HCI in storage rings will become much more attractive with the modernization of the existing storage ring. This simply means the diminishing of the filling time by one order of magnitude, i.e. to $1s$ and the number of ions in the ring should also be enlarged by one order of magnitude, i.e. to 10^{11} ions. With these conditions fulfilled, the observation time for Eu^{61+} ions reduces to a realistic observation time of about 30 hours.

* Work supported by DFG and GSI.

References

[1] A. Bondarevskaya, A. Prozorov, L. Labzowsky, G. Plunien, D. Liesen and F. Bosch, (review paper prepared)

[2] A. Prozorov, L. Labzowsky, D. Liesen and F. Bosch, Phys. Lett. **B574**, 180 (2003)

[3] A. Bondarevskaya, A. Prozorov, L. Labzowsky, G. Plunien, D. Liesen and F. Bosch Phys. Lett. A **372**, 6642 (2008)

[4] A. Surzhykov, S. Fritzsche and Th. Stöhlker, Phys. Lett. A **289**, 213 (2001)

[5] A. Surzhykov, S. Fritzsche, Th. Stöhlker and S. Tashenov, Phys. Rev. A **68**, 022710 (2003)

[6] A. Surzhykov, S. Fritzsche, Th. Stöhlker and S. Tashenov, Phys. Rev. Lett. **94**, 203202 (2005)

[7] S. Tashenov, et al., Phys. Rev. Lett. **97**, 223202 (2006)

[8] J. Eichler, A. Ichihara and T. Shirai, Phys. Rev. A **58**, 2128 (1998)

[9] L.N. Labzowsky, et al., Phys. Rev. A **63**, 054105 (2001)

Coulomb glory effect in collisions of antiprotons with heavy nuclei: relativistic theory*

A. V. Maiorova†[1], D. A. Telnov[1], V. M. Shabaev[1], V. A. Zaitsev[1], G. Plunien[2], and T. Stöhlker[3,4]

[1]SPbSU, St. Petersburg, Russia; [2]TU Dresden, Dresden, Germany; [3]GSI, Darmstadt, Germany; [4]PI, Heidelberg, Germany

New facilities for antiproton and ion research at GSI will give a unique possibility to observe the Coulomb glory phenomenon predicted by Demkov and coauthors [1, 2]. The effect consists in a prominent maximum of the differential cross section (DCS) in the backward direction at a certain energy of the incident particle, provided the interaction with the target is represented by a screened Coulomb attraction potential. In our previous papers [3,4] we investigated this effect for the antiproton scattering in the framework of the non-relativistic quantum mechanics. It was shown that in collisions of antiprotons with the bare uranium the Coulomb glory is present because of the screening properties of the vacuum polarization (VP) potential. In Ref. [5] we consider collisions of antiprotons with bare uranium nuclei ($Z = 92$) in the framework of the relativistic quantum theory in the range of the antiproton kinetic energy 100 eV to 2.5 keV. To compare the results at different energies, we define the scaled DCS which is being measured in the units of the Rutherford cross section in the backward direction:

$$\frac{d\tilde{\sigma}}{d\Omega} = \left(\frac{4E}{Z}\right)^2 \frac{d\sigma}{d\Omega}. \qquad (1)$$

Now the energy domain with the largest Coulomb glory effect can be determined. In fig. 1 we show the scaled DCS at $\theta = 180^\circ$ as a function of the antiproton energy. The maximum Coulomb glory effect is reached at the antiproton energy of about 600 eV and amounts to 15.6% (fig. 1, curve (a)). The main contribution comes from the VP potential, as the DCS produced by the finite nucleus potential only (fig. 1, curve (b)) is about 10% smaller and does not exhibit a pronounced maximum. We note that the contribution from the anomalous magnetic moment to $d\tilde{\sigma}/d\Omega$ is very small ($\sim 10^{-4}$), that is in agreement with a qualitative estimate given by Milstein [6]. With the help of the optical potential method [7, 8], we have estimated the influence of the strong interaction on the Coulomb glory effect and found it negligible. In the non-relativistic limit $c \to \infty$, the present results coincide with the previous calculations [4] which are represented by curve (c) in fig. 1. It is obvious that, in accordance with the related calculations for the pure Coulomb potential [9], the relativistic corrections are very important: they are responsible for overall increase of the DCS by approximately 10% and the shift of the maximum to higher energies (from 300 eV to 600 eV). We have also estimated the significance of inelastic processes, such as the radiative recombination and annihilation of antiprotons, and found that they should not mask the Coulomb glory effect.

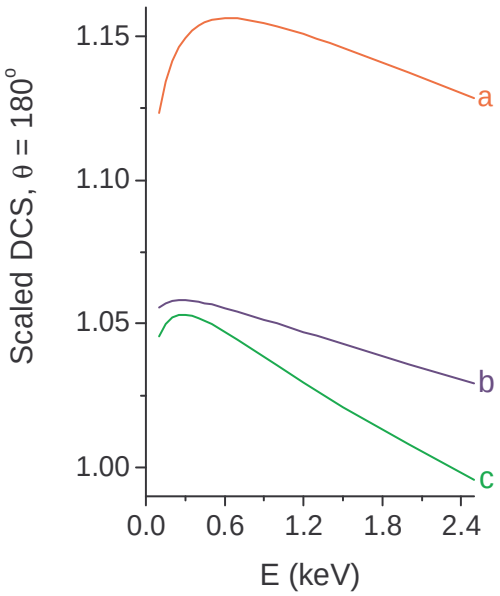

Figure 1: Scaled DCS $d\tilde{\sigma}/d\Omega$ at $\theta = 180^\circ$ as a function of the energy. (a) DCS for the total scattering potential (relativistic); (b) DCS for the finite nucleus potential only (relativistic); (c) DCS for the total scattering potential (non-relativistic).

References

[1] Yu.N. Demkov, V.N. Ostrovsky and D.A. Telnov, *Zh. Exp. Teor. Fiz.* **86** (1984) 442 (*Sov. Phys. – JETP* **59** (1984) 257)

[2] Yu.N. Demkov and V.N. Ostrovsky, *J. Phys. B* **34** (2001) L595

[3] A.V. Maiorova, D.A. Telnov, V.M. Shabaev, I.I. Tupitsyn, G. Plunien and T. Stöhlker, *Phys. Rev. A* **76** (2007) 032709

[4] A.V. Maiorova, D.A. Telnov, V.M. Shabaev, G. Plunien and T. Stöhlker, *J. Phys. B: At. Mol. Opt. Phys.* **41** (2008) 245203

[5] A.V. Maiorova, D.A. Telnov, V.M. Shabaev, V.A. Zaitsev, G. Plunien and T. Stöhlker, http://arxiv.org/ps/0912.5203

[6] A.I. Milstein, private communication

[7] C.J. Batty, E. Friedman and A. Gal, *Phys. Rep.* **287** (1997) 385

[8] A. Gal, E. Friedman and C.J. Batty, *Phys. Lett. B* **491** (2000) 219

[9] A.I. Milstein and I.S. Terekhov, *JETP* **98** 4 (2004) 687

* Work supported by DFG, RFBR, and GSI.

† maiorova@pcqnt1.phys.spbu.ru

Doubly differential cross sections for K-shell ionization by $e^{\pm}$ impact*

A.I. Mikhailov[1], A.V. Nefiodov[1,2], and G. Plunien[2]

[1]PNPI, 188300 Gatchina, St. Petersburg, Russia; [2]TU Dresden, Mommsenstr. 13, D-01062 Dresden, Germany

The single ionization of inner-shell bound electrons by lepton impact is a fundamental atomic process of particular interest. Recently, essential progress has been achieved in fragmentation experiments due to developments in many-particle imaging techniques, so-called reaction microscopes [1]. The measurements of the multiply differential cross sections become now feasible.

We have deduced the universal scaling behavior for the doubly differential cross sections of the single K-shell ionization of hydrogen-like ions with moderate values of the nuclear charge Z by electron and positron impact [2]. The study is performed to leading order of non-relativistic perturbation theory with respect to the electron-electron interaction. Accordingly, it is assumed that $1/Z \ll 1$ and $\alpha Z \ll 1$, where α is the fine-structure constant. The projectile is characterized by the energy $E = \boldsymbol{p}^2/(2m)$ and the asymptotic momentum $\boldsymbol{p}$, while the scattered particle is characterized by the energy $E_1 = \boldsymbol{p}_1^2/(2m)$ and the momentum $\boldsymbol{p}_1$. The consideration is performed within the near-threshold energy range $I \leqslant E \ll m$, where $I = m(\alpha Z)^2/2$ is the K-shell ionization potential and m is the electron mass ($\hbar = 1$, $c = 1$).

The differential cross section for the single ionization of a K-shell electron can be cast into the following form

$$\frac{d\sigma_{\rm K}}{d\varepsilon_1 d\Omega_1} = \frac{\sigma_0}{4\pi Z^4}\, G(\varepsilon, \varepsilon_1, \theta_1)\,, \qquad (1)$$

where $\varepsilon = E/I$, $\varepsilon_1 = E_1/I$, $d\Omega_1 = 2\pi \sin\theta_1 d\theta_1$, $\sigma_0 = \pi a_0^2$, and $a_0 = 1/(m\alpha)$ is the Bohr radius. The problem possesses axial symmetry with respect to the direction $\boldsymbol{p}$ of incoming particles. The scattering angle θ_1 is enclosed by the vectors $\boldsymbol{p}$ and $\boldsymbol{p}_1$. The dimensionless function $G(\varepsilon, \varepsilon_1, \theta_1)$ exhibits a universal scaling behavior, which does not depend on the particular value of Z.

For low-energy electron impact, the backward ($\theta_1 \simeq \pi$) electron scattering is more probable than the forward ($\theta_1 \simeq 0$) scattering. In particular, for $\varepsilon \lesssim 1.1$, this occurs for both slow [$\varepsilon_1 \leqslant (\varepsilon - 1)/2$] and fast [$\varepsilon_1 \geqslant (\varepsilon - 1)/2$] electrons (see Fig. 1). For $\varepsilon \simeq 1.2$, the cross sections for backward and forward scattering become to be of the comparable magnitude. The slowest electrons ($\varepsilon_1 \simeq 0$) are scattered predominantly backward, while the fastest electrons ($\varepsilon_1 \simeq \varepsilon - 1$) are scattered mainly forward. With increasing incident energies ($\varepsilon \geqslant 1.5$), the dominant contribution to the ionization cross section arises from the fast outgoing electrons, which are scattered forward at small angles θ_1. The backward scattering turns out to be increasingly suppressed. In addition, the angular distribution of the slow electrons becomes to be more isotropic.

* Work supported by BMBF and GSI

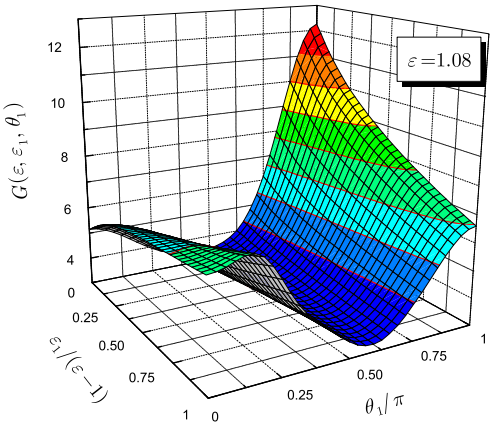

Figure 1: K-shell electron ionization by electron impact. The variable ε_1 is the energy of outgoing electron, which is detected at the angle θ_1.

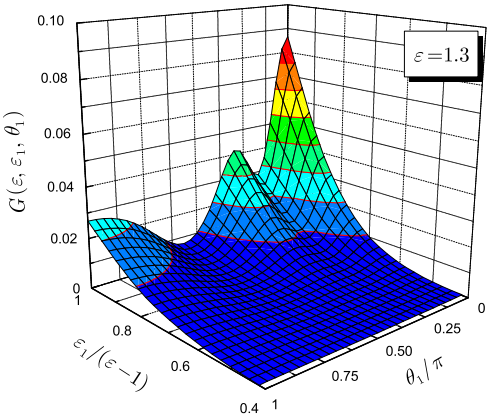

Figure 2: K-shell electron ionization by positron impact.

In the case of positron scattering, the dominant contribution to the ionization cross section arises from the fast positrons with the energies ε_1, which are close enough to the excess energy $\varepsilon - 1$. For slow collisions with $\varepsilon \lesssim 1.7$, the differential cross section contains three pronounced maxima at different scattering angles θ_1 (see Fig. 2). Increasing the incident energies up to $\varepsilon \sim 2$, the maxima coalesce near the zeroth angle, so that the positrons are preferably scattered in the forward cone ($\theta_1 < \pi/2$).

References

[1] J. Ullrich et al., Rep. Prog. Phys. 66 (2003) 1463.

[2] A.I. Mikhailov, A.V. Nefiodov, and G. Plunien, http://arxiv.org/abs/0910.5213

Hyperfine structure and g factor in heavy Li-like ions: rigorous evaluation of the screened QED corrections *

A. V. Volotka[1,2], D. A. Glazov[1,2], G. Plunien[1], V. M. Shabaev[2], and I. I. Tupitsyn[2]

[1]Technische Universität Dresden, Germany; [2]St. Petersburg State University, Russia

Investigations of the hyperfine splitting and the g factor in highly charged ions give an access to a test of bound-state QED in strongest electromagnetic fields available at present for experimental study. To date, accurate measurements of the ground-state hyperfine structure and of the g factor were performed in H-like ions. An extention of such kind of experiments to highly charged Li-like ions anticipated in the near future at the HITRAP facility at GSI [1]. This will provide the possibility to investigate a specific difference between the corresponding values of H- and Li-like ions, where the uncertainty due to the nuclear effects can be substantially reduced [2]. Achievement of the required theoretical accuracy for the hyperfine structure and for the g factor in the case of Li-like ions is a very interesting and demanding challenge for theory.

At present, the theoretical accuracy of the specific difference of the hyperfine splitting values of H- and Li-like ions and of the g factor of Li-like heavy ions is mainly limited by uncertainties of the screened QED and higher-order interelectronic-interaction corrections. The rigorous evaluation of the these corrections requires a systematic consideration in the QED framework of third-order perturbation theory terms. In a recent PRL [3] we have evaluated the complete gauge-invariant set of the screened one-loop QED corrections in the presence of a magnetic field perturbation. As the most interesting application of these results towards tests of the magnetic sector of bound-state QED, we present here our improved theoretical predictions for the specific difference between the ground-state hyperfine splitting values of H- and Li-like Bi ions and for the g factor of Li-like Pb ion.

Probing the influence of QED effects on the hyperfine splitting of highly charged ions is impeded by the uncertainty of the nuclear magnetization distribution correction [the Bohr-Weisskopf (BW) effect]. In this context, it was proposed to consider a specific difference of the ground state hyperfine splitting in H-like and Li-like ions [2]: $\Delta' E = \Delta E^{(2s)} - \xi \Delta E^{(1s)}$, where $\Delta E^{(1s)}$ and $\Delta E^{(2s)}$ are the hyperfine splittings of H- and Li-like ions, respectively. Extracting numerically the contribution of the BW effect in different terms we found that the cancellation appears with ξ chosen to be $\xi = 0.16886$ for the case of Bi. In Table 1 we present most recent result for the the energy shift $\Delta' E$ employing the most accurate value obtained for the screened QED correction. The interelectronic-interaction corrections have been evaluated to first-order in $1/Z$ within the QED perturbation theory and to higher-orders within the large-scale configuration-interaction Dirac-Fock-Sturm method.

Table 1: Individual contributions to the specific difference $\Delta' E$ for ^{209}Bi in meV.

	$\Delta E^{(2s)}$	$\xi \Delta E^{(1s)}$	$\Delta' E$
Dirac value	844.829	876.638	−31.809
Interel. inter.	−29.74(4)		−29.74(4)
QED	−5.052	−5.088	0.036
Screened QED	0.194(6)		0.194(6)
Total			−61.32(4)

Table 2: Individual contributions to the ground-state g factor of Li-like ^{208}Pb^{79+}.

Dirac value (point nucleus)	1.932 002 904
Finite nuclear size	0.000 078 58(13)
Interel. inter.	0.002 140 7(27)
QED, $\sim \alpha$	0.002 411 7(1)
QED, $\sim \alpha^2$	− 0.000 003 6(5)
Screened QED	− 0.000 001 6(1)
Nuclear recoil	0.000 000 25(35)
Nuclear polarization	− 0.000 000 04(2)
Total	1.936 628 9(28)

Similar calculations have been performed for the g factor of Li-like heavy ions. The rigorous evaluation of the screened QED correction for the case of ^{208}Pb^{79+} gives $-1.6(1) \times 10^{-6}$, where the uncertainty has been reduced by an order of magnitude in comparison with the previous value obtained with the local screening potential approach [4]. Table 2 displays the improved value for the g factor of Li-like ^{208}Pb^{79+} previously reported in Ref. [4] employing the result obtained for the screened QED correction. Further extensions of these calculations to the g factor of B-like heavy ions may serve for an independent determination of the fine structure constant from QED at strong fields [5].

The rigorous evaluation of the higher-order interelectronic-interaction correction will be the next step towards the unprecedented accuracy for the stringent test of the bound-state QED in the presence of magnetic fields.

References

[1] H.-J. Kluge *et al.*, Adv. Quantum Chem. **53**, 83 (2008).

[2] V. M. Shabaev *et al.*, Phys. Rev. Lett. **86**, 3959 (2001).

[3] A. V. Volotka *et al.*, Phys. Rev. Lett. **103**, 033005 (2009).

[4] D. A. Glazov *et al.*, Phys. Lett. A **357**, 330 (2006).

[5] V. M. Shabaev *et al.*, Phys. Rev. Lett. **96**, 253002 (2006).

* Work supported by DFG and GSI.

Performance tests of a position-sensitive planar Si(Li) detector system

U. Spillmann[1], H. Bräuning[1], S. Heß[1], G. Weber[1,2], and Th. Stöhlker[1,2,3]

[1]GSI Helmholtzzentrum für Schwerionenforschung GmbH, 64291 Darmstadt, Germany; [2]Physikalisches Institut, Universität Heidelberg, 69120 Heidelberg, Germany; [3]Helmholtz Institut Jena, 07743 Jena, Germany.

The x-ray polarimetry and spectroscopy program of the SPARC collaboration relies strongly on the availability of two-dimensional position-, time and energy sensitive Si(Li)- and Ge(i)-strip-detector systems with their excellent capabilities concerning spectroscopy and imaging as well as polarization sensitivity [1].

During the last years we have successfully applied this kind of detectors in several experiments at the ESR and at other experimental sites [2]. Analysing data taken with the Si(Li) polarimeter system it appeared that additional readout of the interaction depth would decisively suppress background events.

The Si(Li) polarimeter [3] has an active area of 64 x 64 mm^2 and is surrounded by a guard ring of roughly 7 mm width. The crystal thickness amounts to 6.65 mm. The intrinsic position resolution is given by the structure of the front and backside contact electrodes which are divided into 32 strips on each side with a pitch of 2 mm. The stripes on front side are oriented perpendicular to stripes on back. Utilizing a proper analysis algorithm the detector may be used as a 1024 pixel detector. The signals are read out by “standard” self-triggering analog NIM and VME-based electronics resulting in an energy resolution of roughly 2 keV for each strip. The setup has multi hit capability.

A more detailed investigation of the detector performance addressed the readout of the interaction depth by drift time measurements and the potentially incomplete collection of the drifting electron and holes produced as a result of the photon absorption in the detector crystal, especially if the event is detected by two neighbouring strips on the same side.

In order to measure the drift times of the generated charge in the crystal each of the 64 preamplifier got connected to its individual chain of a booster amplifier, a timing filter amplifier, a constant fraction discriminator and a TDC channel. The drift time differences between front and back have a linear dependence with the depth. Unfortunately it was not possible to irradiate the detector crystal on-edge to achieve a precise depth scan. So we were restricted to measure the attenuation of x-rays from a collimated radioactive source shining normal incident on the detector. The spectrum for the 30.8 keV line of Ba-133 is depicted in figure 1 (the coloured rectangular indicates the detector crystal). The shape of the measured intensity is declining exponentially convoluted with the time structure of the charge collection process and the time resolution of the electronics. The measured attenuation amounts to 84 percent for the complete crystal thickness. For higher energies it was found that the intensity as function of depth shows a component caused by Compton scattered photons under a very small forward angle. Due to the tiny scattering angle the energy to the recoil electron is very small and can not be discriminated within the detector resolution up to now. From the shape of the measured distribution one may estimate the position resolution for the depth to be 2.0 mm (FWHM).

In figure 2 we plot the difference versus the sum energies of two neighbouring strips on the front side of the crystal for events where both strips were involved. The 81 keV line of Ba-133 appears as a straight line. This is a proof for an excellent charge collection process at the strip contacts. Deviations from this line shape like broadening or dips would be a hint for charge traps due to electric field distortions especially in the interstrip region or crystal defects.

Improvements regarding the energy and depth resolution are a hot topic of further activities.

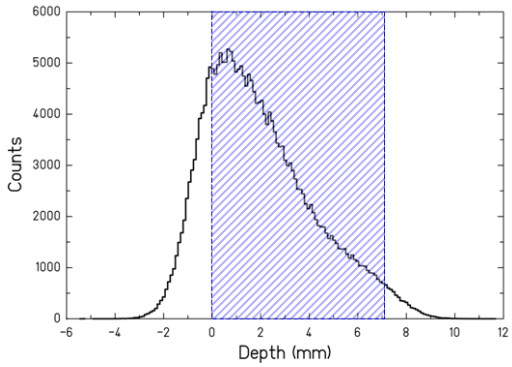

Figure 1: Depth distribution for 30.8 keV X-rays

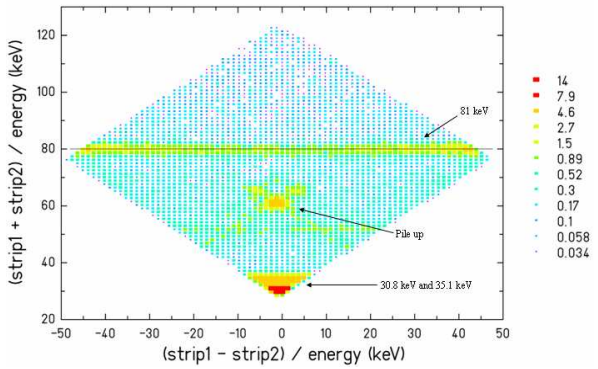

Figure 2: Energy difference versus sum of two neighbouring strips as test of complete charge collection.

References

[1] Technical Report of the SPARC collaboration www.gsi.de/fair/experiments/sparc/index_e.html

[2] see for example the reports of S. Heß, R. Märtin and G. Weber et al. within these annual reports

[3] D. Protic, Th. Stöhlker, T. Krings, U. Spillmann, IEEE TNS (2006)

Improvements of the cryogenic target beam source at the ESR

N. Petridis[1,#], U. Popp[2], A. Kalinin[1], R. Dörner[1], T. Stöhlker[2,3] and R. E. Grisenti[1,*]
[1]IKF, J.W.G.-University Frankfurt; [2]GSI, Darmstadt; [3]Physikalisches Institut, Ruprecht-Karls-University, Heidelberg.

To fulfil the requirements of future storage-ring experiments at the FAIR facility, a further development of the past internal gas jet-target source at the ESR was a crucial task. Besides a higher target area density (TAD) in the interaction region (10^{13}-10^{15} cm^{-2}), especially for the low-Z gases hydrogen and helium, a considerably small interaction length (≈ 1 mm) is mandatory.

In the last two years, we started a step-by-step exchange of the old cluster target source towards a cryogenically cooled liquid microdroplet target source. First measurements and tests were performed last year during several beamtimes [1].

The first half of 2009 was dedicated to further improvement of the internal target setup [2]. Up to this time, a continuous flow cryostat was used to cool down the source, which led to a substantially high consumption of liquid helium and an interruptive operation due to helium dewar replacement. The assembly of a new closed cycle cryostat provides a fairly good solution to both problems, but is unsuitable to helium operation. Furthermore, a tilting stage was added to the x-y-z translation stage to provide more degrees of freedom in movement. This was necessary due to recent observations of a liquid hydrogen beam done by a high-resolution shadow imaging system which is set up at Goethe-University in Frankfurt. The pictures clearly show an angular displacement that can occur during expansion of liquid H_2 through the nozzle into vacuum [Fig. 1]. The new setup affords TADs of up to 10^{15} cm^{-2}.

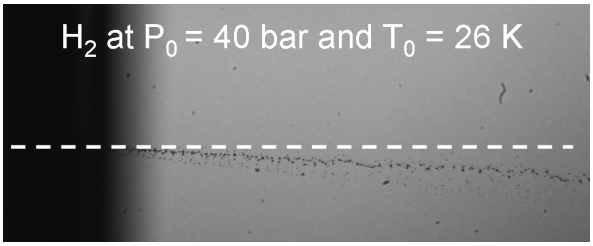

Figure 1: Picture of a liquid hydrogen microdroplet beam. A misalignment between the liquid hydrogen microdroplet beam (black dots) and its expected trajectory perpendicular to the nozzle plate (white dashed line) is shown.

An internal target with such high area densities leads to a decrease of ion beam intensity and increase of cooling time if it is not turned off during the injection and cooling cycle of the ESR. Hence, a mechanical shutter was designed and placed right in front of the source. A metal plate can now be moved into the trajectory of the microdroplet beam, enabling the possibility of switching the target on or off rapidly [3].

Unfortunately, the number of viable improvements at the target station is limited by the present construction of the inlet chamber. A different chamber geometry would open up the possibility of various advancements, e.g. variable interaction length in the overlap region. For this reason, an extensive research on a novel inlet chamber design was made which is significantly more compact and fits all requirements to implement further improvements [Fig. 2]. Moreover, both experimental environments were considered in the design process, nuclear and atomic physics.

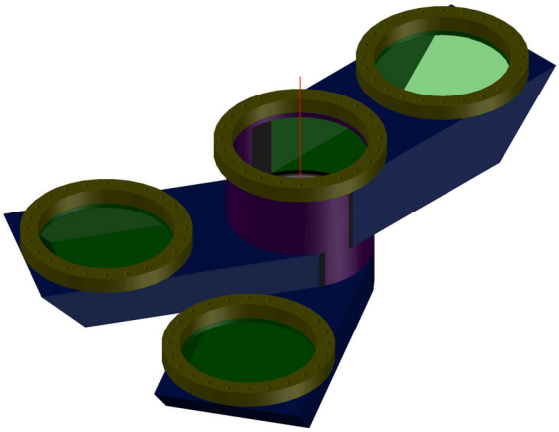

Figure 2: Preliminary Design of the target inlet chamber. Detailed simulations were performed with respect to vacuum requirements of the ESR.

During the second beamtime of the year, which took place in September, a remarkably large amount of measurements were made. The interaction between the new microdroplet target and the uranium ion beam was studied in detail by varying the parameters of the source (TAD) and the uranium ion beam (charge state, energy). We determined the impact of higher TAD on the vacuum of the interaction chamber, the momentum spread of the ion beam using schottky pickup, thus the cooling ability of the electron cooler, ionization / capture cross sections and emission of fluorescence light in the interaction point. Supplementary, we measured spectra using a neutron detector wall in 2.5 m distance from the interaction point during hydrogen and deuterium target operation. This data is currently being analyzed.

References

[1] M. Kühnel *et al.*, Nucl. Instr. And Meth. A 602 (2009) 311.
[2] N. Petridis *et al.*, "Tests with a cryogenically cooled target beam source at the ESR", GSI Scientific Report 2008, p. 292
[3] H. Baumgärtel, Bachelor Thesis, 2010

#petridis@atom.uni-frankfurt.de

*This research has been funded by the Helmholtz society under grant Nr. VH-NG-331, and by the BMBF under grant 06FY152I

A New Setup for a Search of the M1 Transition in Lithiumlike Bismuth *

M. Lochmann[1,2], C. Geppert[1], G. Huber[1], C. Novotny[1], W. Nörtershäuser[1], R. Sánchez[1,2], T. Kühl[2], T. Stöhlker[2,7], D.F.A. Winters[2,7], D. Anielski[4], V. Hannen[4], C. Weinheimer[4], A.V. Volotka[5,8], and the E083 collaboration[2]

[1]Universität Mainz; [2]GSI, Darmstadt; [3]CERN, Genf; [4]Universität Münster; [5]St. Petersburg State University; [6]Imperial College, London; [7]Universität Heidelberg; [8]TU Dresden

Motivation

Measurements of the ground state hyperfine splitting (HFS) in hydrogenlike heavy ions can be used to test QED in extremely strong electric and magnetic fields. Bismuth is the only element which has the ground state hyperfine transitions of both the hydrogen- and the lithium-like ion in a range accessible by laser spectroscopy. By comparing the values of these transition frequencies, one can eliminate the contribution of the nuclear magnetization distribution (Bohr-Weisskopf effect). Thus, tests of the QED calculations on the level of a few percent are feasible [1].

In 1993, Klaft *et al.* measured at the ESR the HFS-transition wavelength $\lambda_0 = 243.87(4)$ nm for hydrogenlike $^{209}Bi^{82+}$, i.e. with a relative accuracy of $1,6 \times 10^{-4}$ [2]. An EBIT-measurement by Beiersdorfer yielded $\lambda_0 = 1510(50)$ nm for lithiumlike $^{209}Bi^{80+}$[3], i.e. only 3 % rel. accuracy.

Setup

At the ESR, two bunches of $^{209}Bi^{80+}$ circulate with a fixed energy of ≈ 400 MeV/u, corresponding to $\beta \approx 0.7$. One serves as a "signal bunch", the other one as "reference bunch". Laser pulses of a tunable dye laser with a repetition rate of 30 Hz and a pulse energy of 100 mJ at about 630 nm are collinearly overlapped inside the electron cooler with the signal bunch. Since the transition is rather longlived ($\approx$ 80 ms), the fluorescence takes place all over the ring and can be detected on the opposite side of the ESR.

Improvements

Searches for that transition in the ESR were not successful so far. We have analyzed possible reasons why these attempts failed. We are currently developing an improved experimental setup that will overcome the shortcomings of the previous runs. It will be used in a new beamtime.

According to recent simulations, the detection efficiency of the combination of photomultipliers and the existing mirrror system was too low to produce a significient signature. To improve the signal to noise ratio considerably, a new mirror system was designed, simulated and is now being prepared at the university of Münster. The system is depicted in figure 1. A copper mirror can be moved very close to the ion beam to reflect the forwardly emitted photons onto the photomultipliers.

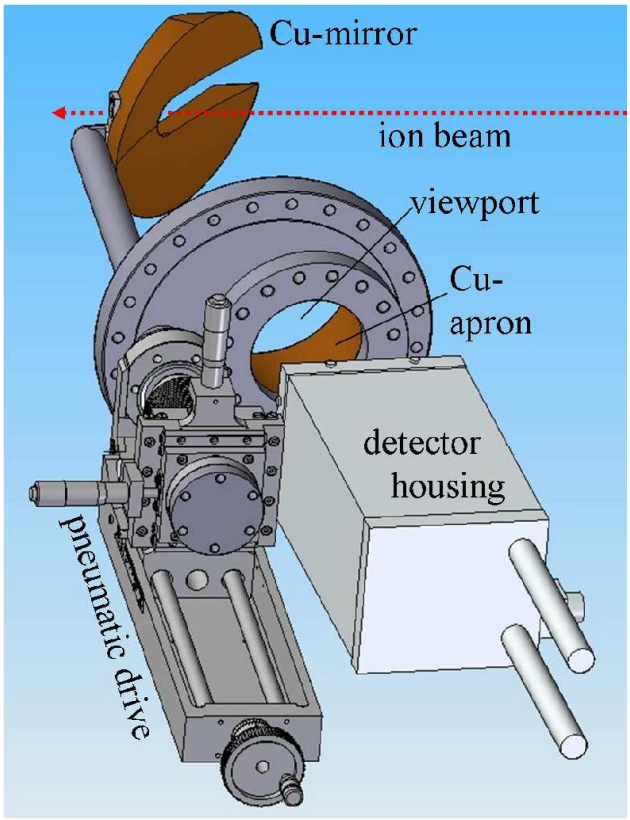

Figure 1: The new moveable mirror, which will be placed in the ESR near the gas target. When the ion beam is cold, the mirror will be centered, so the ions pass though the slit. Otherwise it is removed from the beamline.

Furthermore, a new data acquisitioning scheme, using single photon tagging, was developped. It will allow for an optimal data processing and avoid loss of information due to hardware filtering or synchronization failure. Finally, the laser system is being modernized. It will be more reliable, provide more laser power, and a better beam profile.

References

[1] V. M. Shabaev *et al.*, Phys. Rev. Lett. 86, (2001) 3959.

[2] I. Klaft *et al.*, Phys. Rev. Lett. 73, (1994) 2425.

[3] P. Beiersdorfer *et al.*, Phys. Rev. Lett. 80, (1998) 3022.

* This work was supported by the Helmholtz Association under contract No. VH-NG-148 and by the BMBF under contract No. 06MZ9179I. The Work in Münster was supported by the BMBF under contract No. 06MS9152I.

Heavy, highly-charged ions at rest - The HITRAP facility*

F. Herfurth[†1], W. Barth[1], M. Bevcic[1], M. Block[1], K. Blaum[2,3], L. Dahl[1], S. Fedotova[1], R. Fischer[1], P. Forck[1], M. Kaiser[1], O. Kester[1,4], H.-J. Kluge[1], C. Kozhuharov[1], S. Koszudowski[1], W. Quint[1], U. Ratzinger[5], A. Sauer[5], A. Schempp[5], M. Shaaban[1], A. Sokolov[1], T. Stöhlker[1,3], W. Vinzenz[1], G. Vorobjev[1], and D. Winters[1]

[1]GSI, Darmstadt, Germany; [2]MPI-K, Heidelberg, 69117 Heidelberg, Germany; [3]Ruprecht-Karls-Universität, 69120 Heidelberg, Germany; [4]NSCL/MSU, East Lansing, USA; [5]Goethe-Universität, Frankfurt, Germany

At the GSI accelerator complex, using the universal linear accelerator UNILAC and the synchrotron SIS, highly-charged ions up to U^{92+} are produced by passing a 400 MeV/u beam through a gold foil stripping off all or nearly all electrons. The HITRAP facility is built to decelerate those ions to almost rest and to provide them to the experiments [1]. First, the ions are decelerated in the experimental storage ring ESR from 400 to 4 MeV/u accompanied with stochastic and electron cooling to keep the emittance small. Then, in the HITRAP linear decelerator (figure 1) the deceleration is performed in two additional steps. An interdigital H-type (IH) structure and a radio-frequency quadrupole (RFQ) structure are operated in inverse mode to decelerate first from 4 MeV/u to 0.5 MeV/u and then further to 6 keV/u. For final cooling below one meV the ions are captured in a Penning trap. The total kinetic-energy reduction amounts then to 13 orders of magnitudes from production to final storage in the Penning trap.

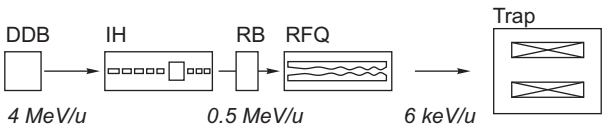

Figure 1: Schematic view of the HITRAP linear decelerator. The main components are the double-drift buncher (DDB), the interdigital H-type structure (IH), the intermediate rebuncher (RB), the radio frequency quadrupole decelerator (RFQ) and the cooler Penning trap.

After first investigations with the IH in 2008 [2] the IH structure tuning was finished in early 2009. To obtain a flat voltage distribution along the 25 decelerating gaps of the decelerator structure an additional tuning body was installed. Bead-pull measurements for various tuning bodies yielded the best position for a 85x32x37 mm copper block used for local tuning in the low energy section between gap three and four. The gap voltage distribution deviates now from the calculated values 2.3% on the high energy side and 1.3% on the low energy side if the plungers are set correctly.

The first run in 2009 took place in February, using $^{64}Ni^{28+}$ ions. The energy distribution of the beam after the IH depending on the settings of the different elements like double-drift buncher and IH radio-frequency amplitude was compared to the extensive calculations. About 12% of the beam detected after the IH was decelerated to 0.5 MeV/u.

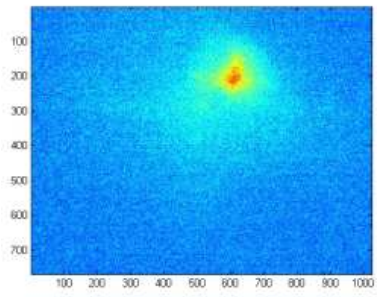

Figure 2: Ion beam after the RFQ.

The RFQ was installed and a second commissioning run took place in April. Beam was sent through the RFQ and detected on a micro-channel plate combined with a phosphorous screen (figure 2). The abundance of fast particles was very high, so that the ions seen in figure 2 are most likely at energies between 4 and 0.5 MeV/u. The first tests demonstrated the function of the micro-channel plate based diagnostics behind the RFQ even for very low intensities.

Both experiments in 2009 were preceded by great efforts to deliver ion bunches more frequently to HITRAP to speed up tuning of all parameters and hence commissioning. After some tests with a 4 MeV/u beam sent without acceleration through the heavy ion synchrotron SIS and then injected into the experimental storage ring ESR the beam will be accelerated only to 30 MeV/u for future commissioning. By saving one deceleration step in the ESR about twice as many ion pulses can be extracted per time towards HITRAP compared to the full cycle.

A new "one-shot" energy analyzer has been built and will be installed after the IH structure. Together with refurbishing steps of the RFQ structure this will allow one to advance the commissioning process towards first ions decelerated down to 6 keV/u.

References

[1] H.-J. Kluge et al., Adv. Quant. Chem. **53** (2008), 83–98.

[2] L. Dahl et al., Proceedings of the XIV Linear Accelerator Conference - LINAC08, 2008, p. 102.

* Supported by the German Federal Ministry for Education and Research (BMBF) and the research and development program (F&E) of the GSI Helmholtz centre for heavy ion research.

† F.Herfurth@gsi.de

A Pulsed Electron Source for the HITRAP Cooler Trap

C. Krantz[1], D. A. Orlov[1], A. Wolf[1], F. Herfurth[2], and O. Kester[2,3]

[1]Max-Planck-Institut für Kernphysik, Heidelberg, Germany; [2]Helmholtzzentrum für Schwerionenforschung, Darmstadt, Germany; [3]National Superconducting Cyclotron Laboratory, East Lansing, Michigan, USA

Introduction

The HITRAP Cooler Trap will store highly charged ions and cool them to a temperature of 4 K for delivery to precision experiments [1]. The trap is preceded by a decelerator complex able to slow ion bunches delivered by the ESR from a specific kinetic energy of 4 MeV/u down to 6 keV/u [2]. The Cooler Trap is designed as a 23-ring cylindrical Penning trap, providing the ability to simultaneously store positively charged ions and electrons. Application of electron cooling will decrease the thermal energy of the trapped ion bunch to 10 eV. Subsequently, electrons will be expelled from the trap in order to avoid excessive ion loss by recombination reactions [3]. The final ion temperature of 4 K will be reached by resistive cooling at the trap ring electrodes [2]. A pulsed electron source providing more than $2 \cdot 10^9$ particles per bunch has been developed at the Max-Planck-Institute for Nuclear Physics (MPIK) and will allow efficient electron filling of the Cooler Trap.

A UV-driven GaAs electron emitter

HITRAP is designed to deliver up to 10^5 bare uranium ions per duty cycle. Simulations have shown that at least 10^9 electrons are necessary in order to achieve efficient electron cooling under these circumstances [3]. The Penning trap is to be filled with electrons using a single bunch from the electron source, the latter must therefore be able to emit a rather high peak current intensity.

The electron source designed at MPIK consists of a GaAs-Cs photocathode electron emitter, featuring a quantum efficiency of (0.1…0.2) % in the ultraviolet spectrum ($\approx 240 \ldots 280$ nm). Of very compact design (c.f. figure 1), the electron gun fits into the beam diagnostic chamber on the extraction side of the Cooler Trap [4]. The GaAs-Cs photocathode will be illuminated by either a pulsed 262-nm-laser or a UV-flashlamp.

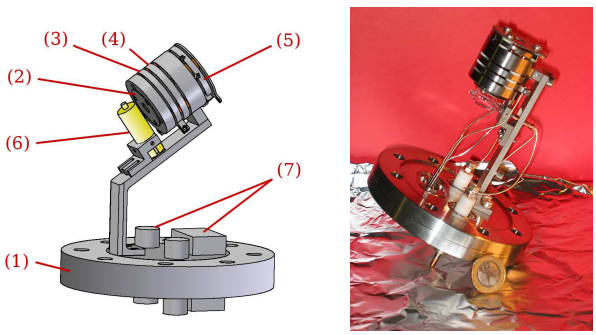

Figure 1: *Left:* Drawing of the pulsed electron source: CF-63 flange (1), GaAs-Cs photocathode holder (2), gun electrodes (3 and 4), Cs dispenser (5), radiative oven (6), feedthroughs (7). *Right:* Prototype tested at MPIK.

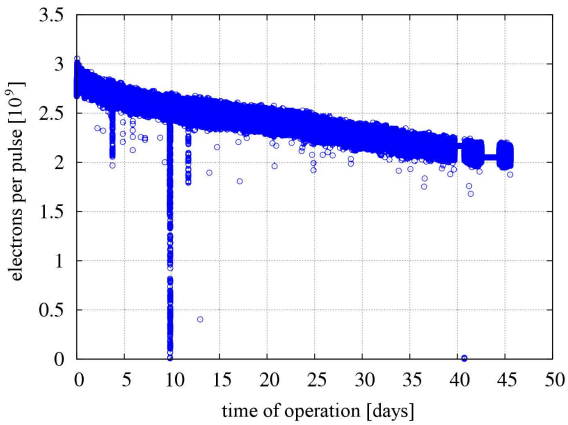

Figure 2: Long time stability of the pulsed electron source measured with a single GaAs-Cs photocathode.

Prototype tests

A prototype of the pulsed electron gun has been built and taken into operation at MPIK [4]. By illumination of the GaAs-Cs photocathode with a xenon flashlamp (*Hamamatsu L9455*) it was possible to extract up to $3 \cdot 10^9$ electrons per pulse from the source. The bunch length was defined by the time constant of the flashlamp to approximately 400 ns. The perveance of the electron gun has been measured to be of $(3.0 \pm 0.2)\,\mu$Perv.

As shown in figure 2, the pulse intensity of the source is very stable. In a long time test, electrons were extracted from the photocathode every 8 seconds for a total duration of approximately 1.5 months. During this period, the bunch intensity decreased only slightly, from approximately $3 \cdot 10^9$ to $2 \cdot 10^9$ electrons, due to degradation of the cathode quantum efficiency. The electron gun's built-in Cs dispenser allows in-situ reactivation of the photocathode without the need to open the vacuum chamber, as has also been demonstrated in operational tests of the source prototype [4].

References

[1] F. Herfurth *et al.*, Int. J. Mass Spectrom. **251** (2006), 266

[2] S. Koszudowski, dissertation, University of Heidelberg (2009)

[3] G. Maero, dissertation, University of Heidelberg (2008)

[4] C. Krantz, dissertation, University of Heidelberg (2009)

A pulsed supersonic gas jet target for HITRAP

K. Stiebing*[1], D.F.A. Winters[2,3], W. Quint†[2,3], V. Varentsov†[2,4], A. Warczak†[5], and Th. Stöhlker[2,3,6]

[1]Frankfurt University, Germany; [2]GSI Darmstadt, Germany; [3]Heidelberg University, Germany; [4]ITEP, Moscow, Russia; [5]Jagiellonian University, Krakow, Poland; [6]Helmholtz Institute Jena, Germany

Introduction

When heavy, highly charged ions (HCI) collide with target gases at low kinetic energies, target electrons are captured into high-lying atomic orbits [1]. The decay of these states can be carefully observed by means of x-ray spectroscopy [2], and compared to recent calculations. Already for light HCI, deviations between theory and experiment have been found, whereas for medium and heavy HCI (like U^{92+}) almost no experimental studies have been performed. With the aid of a pulsed supersonic gas jet target, to be operated at the HITRAP facility, these studies could be addressed. Such a gas jet target requires several powerful pumping stages for efficient differential pumping (from 10 bar to 10^{-10} mbar).

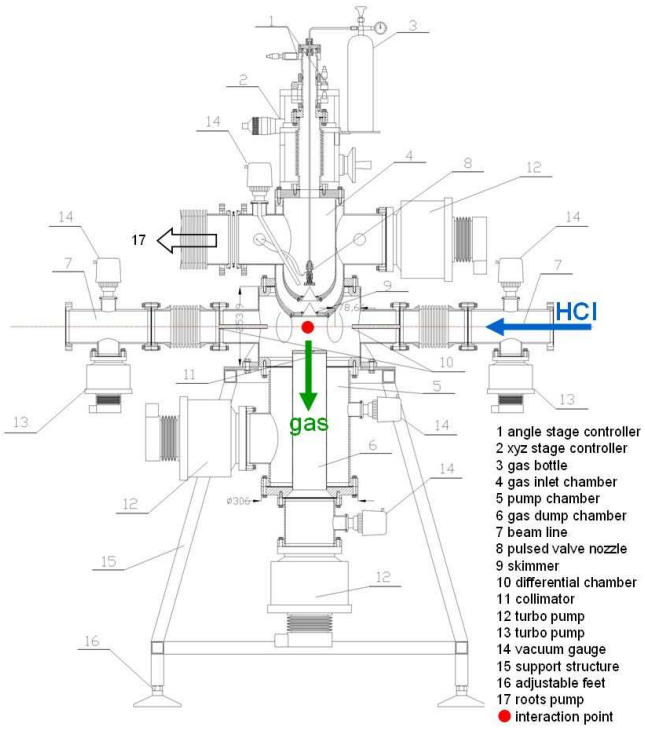

Figure 1: Schematic view of the setup around the gas jet target. X-ray detectors will be used to detect the radiation from low-energy collisions between HCI and gas atoms.

Early 2009 we submitted a proposal to the BMBF, applying for funding by the 'Förderbereich Hadronen- und Kernphysik' (within FAIR-SPARC). This proposal was accepted, and the project could start almost directly. By now, several parts of the setup have already been ordered. The construction of the setup will start in summer 2010.

Experiments at HITRAP

The HITRAP facility, which is in the commissioning phase, has been built to perform unique experiments with HCI at very low energies. The pulsed supersonic gas jet target will be one of the planned experimental setups. The ions from the HITRAP facility enter the setup from the right, see Figure 1, and interact with the gas atoms or molecules (coming from the top) produced by the jet target. Around the interaction point (red dot) an array of semiconductor (Si/Ge) detectors will be placed to perform high-precision x-ray spectroscopy. The design of the setup is compact, robust, and modular, so that different collision chambers can be mounted between the two pumping stages (gas inlet and outlet). It is essential to maintain good UHV conditions, *i.e.* the residual gas pressure should be 10^{-10} mbar or lower.

For most of the planned experiments, the cross-sections for electron capture are fairly large ($\sim 10^{-13}$ cm^2) due to the use of heavy HCI and the low collision velocities. Therefore, the gas jet target should provide area densities of the order of 10^{11} atoms/cm^2, which can easily be achieved. For the first experiments H_2 gas will be used, but other gases are also possible. It is important that the target density can be varied to ensure single-collision conditions. Several advantages / features of the gas jet are:

- compact and modular construction
- well-defined interaction zone
- large solid angle for x-ray detectors
- operation under UHV conditions ($\sim 10^{-10}$ mbar)
- pulsed mode operation (good for UHV)
- pure atomic or molecular targets

The scientific programme will firstly focus on:

- $2p \rightarrow 2s$ intrashell transitions in He-like HCI
- Total cross-sections for single-electron capture and hardness ratios (see *e.g.* [3])
- Intrashell resonant transfer excitation in Li-like HCI
- Multi-electron capture studies

References

[1] R.E. Olson *et al.*, J. Phys. B: At. Mol. Opt. Phys. **25** (1992) 2441.

[2] P. Beiersdorfer *et al.*, Phys. Rev. Lett. **85** (2000) 5090.

[3] F.I. Allen *et al.*, Phys. Rev. A **78** (2008) 032705.

* Work supported by the BMBF (06FY9098I).

† Work supported by INTAS (Ref. Nr. 06-1000012-8956).

Development of the SPECTRAP experimental setup *

Z. Andjelkovic[1], B. Sommer[2], W. Nörtershäuser[1,2], M. Vogel[5], V. Hannen[3], R. Jöhren[3], D. Church[4], S. Bharadia[5], D. M. Segal[5], R. Thompson[5], G. Birkl[6], and the HITRAP collaboration[2]

[1]Institut für Kernchemie, Johannes Gutenberg-Universität, Mainz; [2]GSI, Darmstadt; [3]Westfälische Wilhems-Universität, Münster; [4]Texas A&M University; [5]Imperial College London; [6]TU Darmstadt

The extremely strong fields that exist around the nuclei of heavy few-electron ions drastically change the properties of the electronic system such as energy level spacings, lifetimes and magnetic moments. The energies of their electric-dipole forbidden fine and hyperfine structure transitions strongly depend on the nuclear charge and shift from microwave domains in or close to the optical domain. Thus, they become accessible for laser spectroscopy and its potentially high precision. While a number of such measurements has been performed in storage rings and electron beam ion traps, the SPECTRAP experiment aims to significantly increase the accuracy by employing charged particle traps which allow to slow the ion motion nearly to rest, thus reducing Doppler effects [1].

The superconducting magnet housing the Penning trap that is to be used in the experiment (Fig. 1) was successfully tested at the beginning of the year. The coils were cooled to 4K using liquid nitrogen and helium and energized with some 30 A of current, corresponding to a magnetic field of 3 T. The observed stable operation of the magnet is a necessary condition for further development of the system and its connection to an external ion source. The beamline that will guide the ions into the magnet and the trap region was constructed separately and tested using an off-line ion source with singly and doubly charged argon ions. The whole assembly is illustrated in Fig. 1.

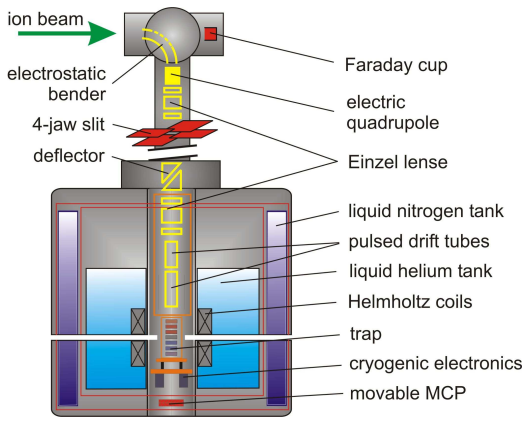

Figure 1: Overview of the superconducting magnet housing and the vertical part of the beamline.

A lot of attention was dedicated towards precision simulations of the ion-optical elements inside the beamline and the magnet housing itself, revealing the optimum operating conditions and feasibility of ion injection into the magnetic field. It was determined that magnetic field reflection does not present a problem in this arrangement because of the very length of the vertical beamline, but also that the magnetic stray field at the position of the electrostatic bender several times bigger than the earth's disrupts the ion beam, requiring anti-magnetic shielding.

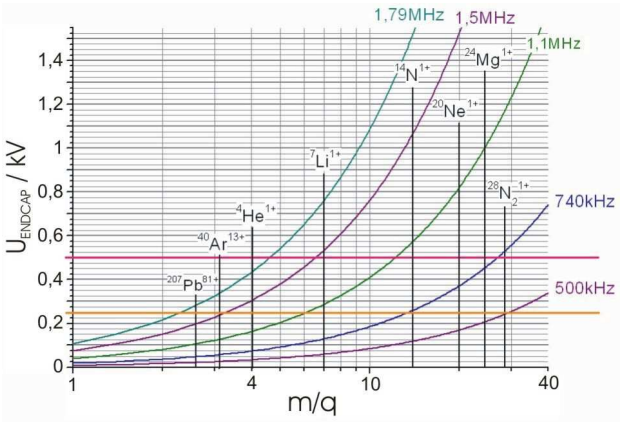

Figure 2: Graph showing different trapped ion oscillation frequencies addressable by changing the trapping voltage.

The design of the resonant electronic circuit for non-destructive ion detection was completed and awaits implementation into the system. Two resonant frequencies from Fig. 2 were chosen for two different mass to charge ratios - 740 kHz for the 20 to 40 m/q domain for lighter ions and 1.8 MHz for the 2 to 4 m/q domain where most of the highly charged ions are.

The system is expected to trap the first ions during the first half of 2010, for instance demonstrating laser cooling of singly charged species to be used for sympathetic cooling of highly charged ions. This technique would allow much lower ion temperatures than normally reachable with resistive cooling [2]. First highly charged species are expected either from the HITRAP EBIT or decelerated by the ESR at the end of the year.

References

[1] Z. Andjelkovic, S. Bharadia, B. Sommer, M. Vogel and W. Nörtershäuser, Hyp. Int. (2010) in print

[2] M. Vogel, W. Quint, J. Phys. B **42**, 15, 154016 (2009)

* Work supported by HGF under contract VH-NG-148, BMBF grant 06DA414I and the GSI F&E program.

Towards Laser Cooling of Magnesium Ions for Sympathetic cooling of Highly Charged Ions at SPECTRAP*

Radu Cazan[1,2], Christopher Geppert[1,2], and Wilfried Nörtershäuser[1,2]

[1]GSI Helmholtzzentrum für Schwerionenforschung GmbH, Darmstadt; [2]Institut für Kernchemie, Johannes Gutenberg-Universität, Mainz

Introduction

Experiments with highly charged ions (HCI), especially with H-like and Li-like ions are an excellent testing ground for quantum electrodynamics (QED) in strong electric and magnetic fields and for precise measurements of fundamental constants. At the ESR, an experiment is being prepared to search for the hyperfine transition in lithium-like $^{209}Bi^{82+}$ in order to disentangle nuclear structure from QED effects [1]. Subsequent precision laser spectroscopy measurements of these transitions are prepared by the SPECTRAP collaboration [2] as part of the HITRAP project [3]. As in most experiments with trapped ions, it is necessary to reduce the temperature of the ions in order to increase the accuracy of the measurements and to diminish the magnitude of some undesirable effects such as Doppler shifts or to extend the storage time of the ions in the trap. In the SPECTRAP experiment, resistive cooling is foreseen for first experiments. Meanwhile, we are currently setting up a laser system for laser cooling of Mg^+ ions inside the trap, with which HCI can be quickly and efficiently cooled down sympathetically.

Experimental

The laser system is composed of a 1.1 W fiber laser at 1118.54 nm and two successive second harmonic generation (SHG) ring cavities for frequency quadrupling. In the first SHG cavity, non-critical phase matching (NCPM) of a lithium triborate (LBO) crystal is used for the first stage. The 20 mm long LBO nonlinear crystal was cut for NCPM with an optimum beam waist [4] of 28 μm. Using the ray transfer matrix analysis [5] we designed a bow tie resonator that allows us to fit the oven with the crystal kept at $T = 90°$C in the middle of the short arm and to obtain the required beam waist in the crystal (see Fig. 1). The total length of the cavity is 1709 mm and has a full folding angle of 30°. The cavity length is stabilized to the laser frequency using the Hänsch-Couillaud locking scheme [6].

The second SHG cavity uses critical phase matching of a β-barium borate (BBO) crystal for doubling from 559.27 to 279.63 nm. A 7 mm long Brewster-cut BBO-crystal was used for type I CPM corresponding to an optimum beam waist of 16 μm [4]. We designed a bow-tie resonator capable of achieving a focus in the middle of the crystal with a waist of 16 μm in the vertical plane and 25 μm in the horizontal plane (see Fig. 1). The small astigmatism is introduced by the concave spherical mirrors, crystal faces and crystal axis. The full folding angle is 18.8° and the total length of the cavity is 504 mm.

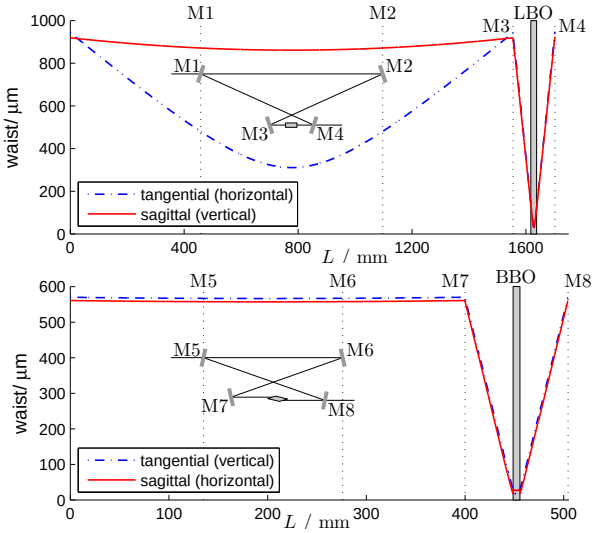

Figure 1: Beam waist inside the first (top) and the second (bottom) cavity

Results

We obtained up to 80% coupling efficiency of the fundamental laser beam into the first cavity. With an input power level of 970 mW, the maximum green output was approximately 240 mW, which is in accordance with the simulations. For the second doubler we measured a coupling efficiency of up to 75% at resonance and we were able to obtain a power level of maximum 3 mW for the 279 nm radiation with an input power level of approximately 100 mW at 559 nm. Further efforts will be made in order to optimize the locking stability of both SHG cavities and to increase the efficiency of the second SHG cavity, before the system will be used for the first time at SPECTRAP.

References

[1] V.M. Shabaev et al.: Phys.Rev.Lett. **86**, 3959 (2001)

[2] M. Vogel et al.: Rev.Sci.Instr. **76**, 103102 (2005)

[3] H.-J. Kluge et al.: Adv. Quant. Chem. **53**, 83 (2008)

[4] G.D. Boyd, D.A. Kleinman: J. Appl. Phys. **39**, 3597 (1968)

[5] T. Freeregarde et al.: Opt.Commun. **199**, 435 (2001)

[6] T.W. Hänsch, B. Couillaud: Opt.Commun. **35**, 441 (1980)

*Work supported by Helmholtz Association under Contract VH-NG-148 and by the Research Center "Elementary Forces and Mathematical Foundations" (EMG) at the University of Mainz

Characterization of detector systems for single photon counting applications in laserspectroscopy experiments at GSI*

R. Jöhren†[1], D. Anielski[1], W. Buglak[1], V. Hannen[1], M. Lochmann[2,3], W. Nörtershäuser[2,3], R. Sánchez[2,3], and C. Weinheimer[1] for the SPECTRAP collaboration

[1]WWU Münster, Institut für Kernphysik, Wilhelm-Klemm-Str. 9, 48161 Münster; [2]Johannes Gutenberg-Universität Mainz, Institut für Kernchemie, Fritz-Straßmann-Weg 2, 55128 Mainz; [3]GSI Helmholtzzentrum für Schwerionenforschung GmbH, Planckstr. 1, 64291 Darmstadt

The Institut für Kernphysik in Münster participates in the SPECTRAP experiment and related ESR measurements with the task of characterization and setup of detector systems capable of single-photon counting and suitable for use at the experiments just mentioned. The wavelengths of interest range from the UV (244 nm) to the near infrared (1550 nm).

Characterization of Avalanche Photo Diodes

Due to their high quantum efficiencies (QE) in the visible region and a QE of 20% near 1064 nm Avalanche Photo Diodes (APDs) manufactured by Radiation Monitoring Devices Inc. (RMD) [3] are a possible candidate for measurements of the hyperfine transition in $^{207}Pb^{81+}$ at SPECTRAP. The best results so far were obtained with RMD APDs of the type S0223, which have a 2x2 mm^2 active area (which is sufficiently large for SPECTRAP) and are supported by an aluminum oxide substrate material. The measurements presented in this report were performed using a cryogenic test setup which has been described in the previous GSI annual report [1]. The preamplifier board for read out of the APDs has been further optimized to an equivalent noise level below 1 keV FWHM (without detector). By measuring gain and noise as a function of bias voltage at different temperatures we determined an ideal operating point at near LN2 temperature. Two typical noise to gain ratios of the APD types S0223 (at -176 °C) and S1315 (a 13x13 mm^2 APD without substrate at -157 °C) are shown in Fig. 1. For the S0223 APD a gain of about 8000 was achieved at 1480 V bias voltage. The expected dark count rate in single photon mode was extracted by studying the noise rate at an energy corresponding to the mean energy to create an electron-hole-pair of 3.67 eV times the gain and was found to be lower than 1 Hz. A first test with actual single photons stemming from a red LED driven by 20 ns wide 800 mV pulses, showed that depending on the actual threshold value, we can indeed detect single photons at dark count rates between 10 Hz and 100 Hz.

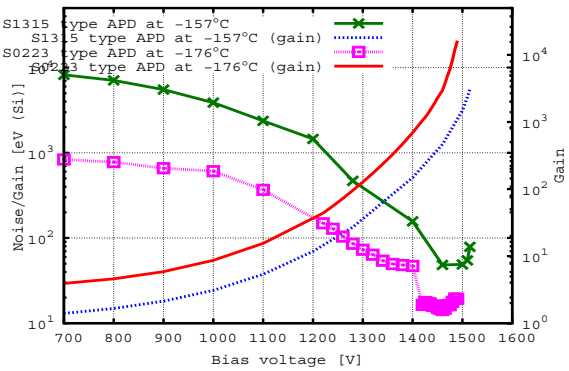

Figure 1: Noise to gain ratio of RMD type S1315 and type S0223 APDs.

Movable mirror system for ESR

For the laser spectroscopy of $^{209}Bi^{80+}$ at the ESR, described in this volume [2], a new detector setup has been developed based on a movable parabolic mirror. To optimize the setup, we have performed extensive optical simulations using the GEANT4 toolkit. While the mirror section already existing at the ESR has a signal to noise ratio of $\approx$ 10/580 for this measurement, the new setup achieves a signal to noise ratio that is 12 times better (42/200). Figure 2 shows the simulated distribution of the numbers and wavelengths of HFS photons detected with the setup.

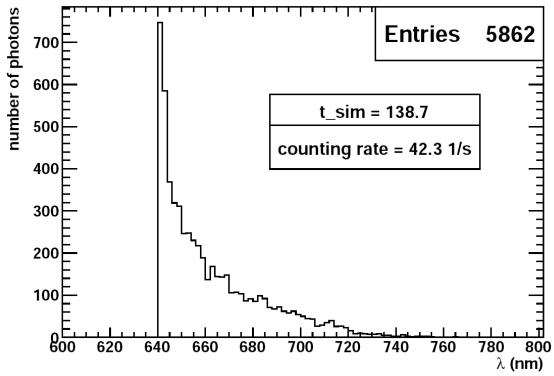

Figure 2: The Doppler-shifted wavelengths detected by the new detector system (result from simulation).

References

[1] R. Jöhren *et al.*, GSI Scientific Report 2008

[2] M. Lochmann *et al.*, this volume

[3] http://www.rmdinc.com/products/p006.pdf

* Work supported by a R&D contract with GSI

† rjoehren@uni-muenster.de

Precision Laser Spectroscopy of Forbidden Transitions in Highly Charged Ions

S. Albrecht*[1], N. Herschbach[2], G. Birkl†[1], and the SPECTRAP collaboration[3]
[1]TU Darmstadt, Darmstadt, Germany; [2]PTB, Braunschweig, Germany; [3]GSI, Darmstadt, Germany

Introduction

For extensive tests of the quantum electrodynamic theory, laser spectroscopy of highly charged ions provides an excellent test ground. In the SPECTRAP facility, systematic measurements on several species of highly charged ions will be possible with up to three orders of magnitude better spectroscopic resolution than in former experiments [1].

The setup will consist of the cryogenic Penning trap (SPECTRAP) which will be loaded by the HITRAP-facility with highly charged ions, a controllable laser and a detection system. The open-endcap cylindrical Penning trap developed in collaboration with the Imperial College London is performing tests at the Mainz University. The detectors will be provided by the University of Münster. The development of the laser system for the spectroscopy of Bi^{82+} is done at the Technical University of Darmstadt.

Setup of the Lasersystem

The required wavelength of $\lambda_0 = 243,87(4)$ nm is provided by a 975 nm diode laser which is amplified and frequency-quadrupled in two cascaded second-harmonic generation stages. This enables a wide tuning range which can be achieved modehop free over approx. 80 GHz (UV) and by manually tuning of the grating stabilized master oscillator over approx. 5 nm (UV). The master oscillator is stabilized to a resonator. This resonator is stabilized to a tunable laser system consisting of two diode lasers that can be detuned by a RF-Synthesizer with respect to a spectroscopic rubidium probe at 780 nm. This tunable offset lock allows precise control of the resonance frequency of the cavity.

The possibility of a low loss transport of the light at 243 nm may not be given so the laser source may be located beneath the trap in inaccessible area during beam time. This circumstance is taken into account by automating the tuning process as much as possible and then remotely control the laser frequency.

Characterisation of the Laser Source

For characterisation of the system, the laser frequencies of the different components were compared to atomic or molecular resonances. By multiple scans over absorption lines and successive fitting procedures the reproducibility of the system can be measured.

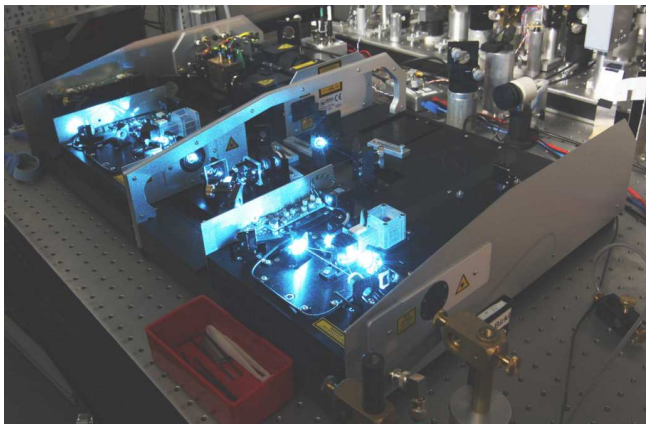

Figure 1: View of the cascaded second harmonic generation stages

Since the stabilisation of the transfer cavity is based on rubidium a comparison to other rubidium absorption lines is easy to accomplish. Measurements at 780 nm have led to values for the reproducibility of 100 kHz in the long-term regime [2].

The UV laser source can be characterised by measuring the reproducibility of one of the frequencies participating in the frequency quadrupling process. The frequency of the UV laser was changed by tuning the offset-lock at the 780 nm system and so detuning the transfer cavity. We compared the second harmonic at 488 nm to tellurium which was mapped before, so molecular resonances in the region of 420 to 540 nm are known. In a Doppler-free saturation spectroscopy a short-term ($1-2$ min) reproducibility of 1 MHz at 488 nm and long-term ($5-8$ h) reproducibility of $2-5$ MHz at 488 nm has been measured. For a test of the achievable scan range, the fundamental frequency of the UV source was locked on different cavity-fringes as reference. A spectrum with a range of approx. 400 GHz between $487,90$ nm and $487,58$ nm was measured in detail [3].

References

[1] M. Vogel, D.F.A. Winters, D.M. Segal, R.C. Thompson, Rev. Sci. Ins. **76**, 103102 (2005)

[2] S. Albrecht, N. Herschbach, G. Birkl, Verhandlungen deutsch. phys. Ges. A15.12 (2009)

[3] S. Albrecht, Master Thesis, TU Darmstadt (2009)

* Work supported by BMBF
† Gerhard.Birkl@physik.tu-darmstadt.de

Status of the *g*-Factor Experiment on Highly-Charged Medium-Heavy Ions*

S. Sturm[1], A. Wagner[†2], K. Blaum[2], W. Quint[3], B. Schabinger[1], and G. Werth[1]

[1]Institut für Physik, Johannes Gutenberg-Universität, D-55099 Mainz; [2]MPI für Kernphysik, D-69117 Heidelberg, Germany; [3]GSI, D-64291 Darmstadt, Germany

Bound-state quantum electrodynamics (BS-QED) calculations can be tested by high-precision measurements of the gyromagnetic factor (*g*-factor) of the electron bound in highly-charged ions [1, 2]. Therefore, it is planned to measure the *g*-factor of lithium- and hydrogen-like silicon and calcium in a double Penning trap setup [3]. In the last year important steps towards the final *g*-factor measurement were made by developing new detection techniques and characterizing the two traps.

Electronic feedback

The resistance of the detection circuit can be changed by feeding back the detected ion signal to the resonator. Depending on the phase-shift between signal and feedback, either a higher detection sensitivity or a cooling of the ion motion can be achieved. In the first case, the resistance is increased which implies that the quality factor of the resonator and thus the signal-to-noise ratio (SNR) are increased as well (Fig. 1). With this detection technique the measurement time can be decreased dramatically.

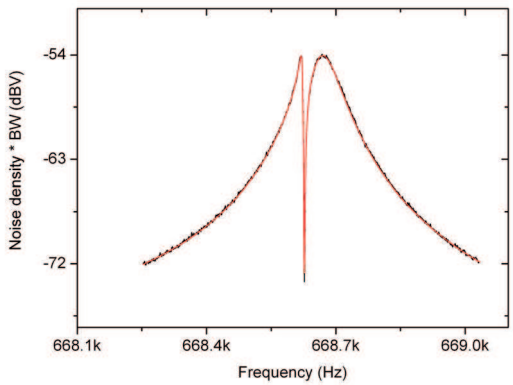

Figure 1: Signal of a single ion detected with electronic feedback.

Self-excited oscillator

Electronic feedback can also be used to create a self-excited single ion oscillator [4]. To this end electronic feedback is applied to one of the correction electrodes, generating a dipolar excitation for the trapped ion. By choosing the correct relative phase between the measured signal and the feedback it is possible to overcome damping of the tank circuit and moreover create negative damping, leading to an exponentially increasing amplitude. This amplitude is regulated to a constant value using a fast digital signal processor (DSP) and a voltage-controlled attenuator. This way it is possible to achieve a large SNR and therefore allow very fast measurements of small frequency differences as required for the detection of a spin-flip.

B_2-measurement

It is very important for the *g*-factor determination to know the magnetic field inside the traps. Therefore, its gradient was measured in both traps (see Fig. 2) by shifting the position of the ion and determining the magnetic field via measuring the free cyclotron frequency at each position. The large quadratic order term B_2 in the analysis trap originates from the ring electrode made of nickel and is required to detect a spin-flip. It results in a slightly different axial frequency for the two possible spin-directions, which is used for the spin-flip detection. In the precision trap this B_2-term is very small, which is desirable since a very homogeneous magnetic field is required for the measurement of the eigenfrequencies of the ion.

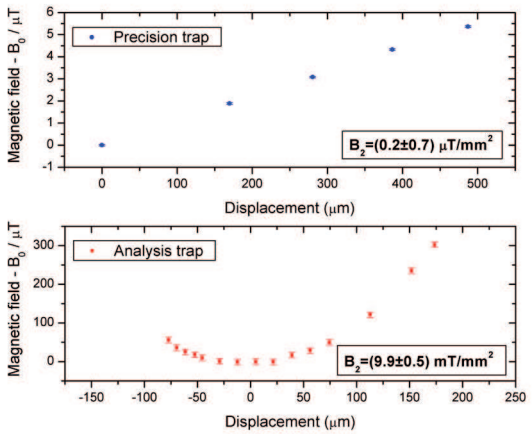

Figure 2: Magnetic field gradient in the precision trap (upper picture) and the analysis trap (lower picture).

References

[1] B. Schabinger et al., J. Phys. Conf. Ser. 163, 012108 (2009).

[2] M. Vogel et al., Nucl. Inst. Meth. B 253, 7 (2005).

[3] K. Blaum et al., J. Phys. B. 42, 154021 (2009)

[4] B. D'Urso et al., PRL 94, 113002 (2005).

* Work supported by HGF under contract VH-NG-037 and DFG under contract Vo-980-1.

† ankewag@uni-mainz.de

Bound Electron g-Factor Measurements at the HITRAP Beamline

N.P.M. Brantjes[1], D. von Lindenfels[2], W. Quint[1,2], and M. Vogel[1,3]
[1]GSI, Darmstadt, Germany; [2]Univ. Heidelberg, Germany; [3]Department of Physics, Imperial College London, UK

In the current contribution, we present recent experimental developments for bound-state QED tests and/or fundamental constants via double-resonance laser spectroscopy, in combination with trapped hydrogen-like heavy ions [1].

Figure 1: The superconducting magnet in the ESR hall.

Briefly, a mass and charge-state selected ensemble of cooled and bunched highly charged ions from the HITRAP facility will be injected into a cryogenic Penning trap designed for laser and microwave spectroscopy. The ions will remain cooled at a motional temperature of 4 K and excited by a combination of laser and microwave irradiation. The fluorescence signal will be detected axially.

In the past year we designed and produced the trap electrodes. Also, we commissioned the 7 Tesla superconducting magnet that will provide the magnetic field for the Penning trap. At the same time we made important advances to develop the detection electronics necessary to measure the g_F-Factor of a high–Z hydrogenlike ion (nucleus with spin) [2, 3, 4].

An ion in a Penning trap induces an image current on the trap electrodes. We can measure this image current in a similar fashion to what happens in a Schottky pick-up. Thus, the motional frequencies of this ion in the Penning trap can be determined. Typically the motional frequencies are between 100 kHz and 50 MHz. The magnitude of the image current induced is in fA region. Therefore, the detection circuit requires a very low signal to noise ratio. We can measure these signals with cryogenic amplification.

First the ion signal is enhanced in a LC resonator circuit. The resonator circuit should have a high Q-value, $Q = f_0/df$, i.e. a high ratio of energy stored to energy lost per cycle. For a superconducting resonator we expect values in excess of 5000 [5]. This will act as an effective parallel resistance of a few MOhm. For a fA current we now achieve a signal of approximately 10 nV. We studied the frequency behaviour of these resonators succesfully in a room temperature prototype.

In the second stage of the amplification we will use a cryogenic FET amplifier. Around 4 Kelvin the noise of such an amplifier can be as low as 1 nV. The two main challenges for the transistor are charge carrier freeze-out and pink noise. The first challenge we overcome by using GaAs based transistors instead of Si transistors. For low frequencies, the noise of a FET is dominated by the $1/f$-noise, or pink noise. Above a certain frequency, the domain boundary, white noise dominates. The domain boundary lies around 100 kHz, but can be as high as 1 MHz as well. This coincides with the motional frequencies of the ion in the Penning trap. We tested several batches of transistors and we found a transistor that matches our requirements.

In summary, we took important steps towards the development of the ion detection for the HITRAP g-Factor trap. Both the resonance circuit and the cryogenic amplifier will be ready in a few months. Also, a 7 Tesla superconducting magnet, with temporal stability of 10^{-7} per hour, was installed (Figure 1). Finally, trap electrodes with a precision of 10^{-5} meter were produced and await gold plating and assembly. First experiments are expected to take place in the course of 2010.

This work is supported by the IMPRS School on Quantum Dynamics and the EU INTAS Programme.

References

[1] W. Quint *et al.*, Phys. Rev. A **78**, 032517 (2008).

[2] V.M. Shabaev, J. Phys. B **27**, 5825 (1994).

[3] V.M. Shabaev *et al.*, Phys. Rev. A **56**, 252 (1997).

[4] D.L. Moskovkin *et al.*, Phys. Rev. A **70**, 032105 (2004).

[5] S. Ulmer *et al.*, Rev. of Sci. Instr. **80**, 123302 (2009).

Measurement of the (anti)proton *g*-factor - Status of the experiment *

H. Kracke† [1], K. Blaum[2,4], S. Kreim[1], A. Mooser[1], C. Mrozik[1], C. C. Rodegheri[1], W. Quint[2,3], S. Ulmer[1,3,4], and J. Walz[1]

[1]Institut für Physik, Johannes Gutenberg-Universität, 55099 Mainz, Germany,; [2]Ruprecht-Karls-Universität, 69047 Heidelberg, Germany,; [3]GSI, 64291 Darmstadt, Germany; [4]MPI für Kernphysik, 69117 Heidelberg, Germany

This experiment aims for the determination of the *g*-factor of a single (anti)proton stored in a cryogenic double Penning trap. Comparing the proton and antiproton *g*-factors leads to a stringent test of the CPT-symmetry in the baryon sector. The number is deduced from the measurement of the free cyclotron frequency ω_c and the larmor frequency ω_L

$$g = 2\frac{\omega_L}{\omega_c} \quad . \tag{1}$$

The cyclotron frequency is derived by application of the invariance theorem $\omega_c^2 = \omega_+^2 + \omega_-^2 + \omega_z^2$ where ω_+, ω_- and ω_z are the three eigenfrequencies of the particle in the trap [1]. These frequencies will be measured in the precision trap, which is a 5-pole cylindrical Penning trap.
The Larmor frequency will be deduced from quantum jump spectroscopy [2]. The detection of the spin state will be performed in the so called analysis trap. The central ring electrode of this trap is machined from ferromagnetic material, leading to a magnetic bottle $B(z) \propto B_2 z^2$ field in the center of the trap. This inhomogeneity couples the magnetic moment of the particle to the axial oscillation mode leading to a frequency shift which depends on the spin state of the proton.
In order to reduce electronic noise and increase the storage time of the particle in the trap, the setup is operated under cryogenic temperatures. These conditions allow for the application of superconducting detectors [3]. The detectors basically consist of a tank circuit with an inductance L, a high quality factor Q and a resonance frequency ω_0, followed by a cryogenic amplifier. On resonance the inductance of the tank circuit shorts the capacitance of the trap, resulting in an effective resistance $R_p = Q\omega L$ in parallel to the trap. Tuning the resonance frequency of the particle to the center of the detector, this resistance damps its motion with a cooling time

$$\tau = \frac{m}{Q\omega_0 L}\frac{D^2}{q^2} \quad , \tag{2}$$

where *m* and *q* are the mass and the charge of the particle and D is a geometric parameter. Cooled to thermal equilibrium with the detector, the particle acts as an ideal series tank circuit, resulting in a dip in the noise spectrum of the detector. The full width at half maximum (FWHM) of the dip is given by $\delta\nu = n/(2\pi\tau)$, where *n* is the number of stored particles. Thus, reducing the particle number results in a reduction of the FWHM in discrete steps. Figure 1 shows noise spectra of the axial detector with different particle numbers in resonance. In the last graph the FWHM of the dip is shown as a function of the particle number. These measurements were performed in the precision trap.

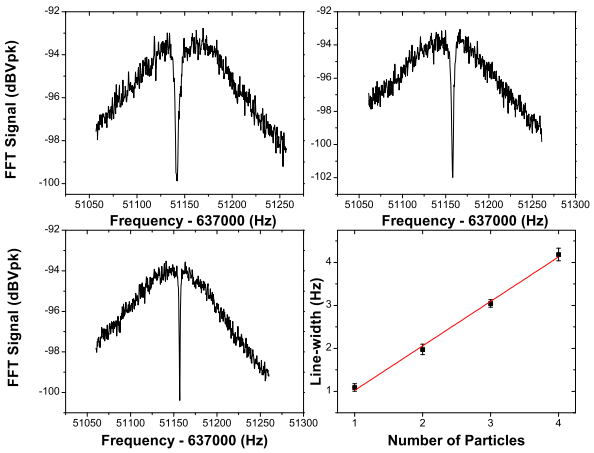

Figure 1: Noise spectra of the axial detector with different numbers of protons in resonance.

Beside the characterization and optimization of the precision trap particles were transported to the analysis trap successfully. In this trap single particle signals were detected. Furthermore the crucial technique for the resolution of an induced spin flip, the phase sensitive detection method [4], was established. Axial frequency jumps of 200 mHz were resolved in a detection time of 600 ms.
The detection of a spin flip should be possible in near future opening the way for the determination of the g-factor of the proton. Having successfully performed the experiment with protons, the apparatus will move to the FLAIR facility at GSI to conduct the same experiment with antiprotons.

References

[1] L. S. Brown, G. Gabrielse, Rev. Mod. Phys. **58**, 233 (1986)

[2] R.S. Van Dyck et al., Phys. Rev. Lett. **59**, 26 (1987).

[3] S. Ulmer et al., Rev. Sci. Inst. **80**, 123302 (2009)

[4] S. Stahl et al., J. Phys. B: At. Mol. Phys. **38**, 297 (2005)

* work supported by BMBF, HGF and DFG

† kracke@uni-mainz.de

Laser cooling of relativistic ion beams*

M. Bussmann[1], W. Wen[1,2,3], D.F.A. Winters[2,4], U. Schramm[1], W. Nörtershäuser[2,5], C. Novotny[2,5], C. Geppert[2,5], Th. Walther[6], G. Birkl[6], Th. Kühl[2], C. Kozhuharov[2], M. Steck[2], F. Nolden[2], C. Dimopoulou[2], X. Ma[3], and Th. Stöhlker[2,4]

[1]Forschunsgzentrum Dresden-Rossendorf, D-01328 Dresden, Germany; [2]GSI Helmholtzzentrum für Schwerionenforschung GmbH, D-64291 Darmstadt, Germany; [3]Institute for Modern Physics, CAS, 730000 Lanzhou, China; [4]Ruprecht-Karls-Universität Heidelberg, D-69120 Heidelberg, Germany; [5]Johannes-Gutenberg-Universität Mainz, D-55099 Mainz, Germany; [6]Technische Universität Darmstadt, D-64289 Darmstadt, Germany

Introduction

In 2004 and 2006 the feasibility of laser cooling of bunched C^{3+} ion beams with a relativistic energy of 122 MeV/u was successfully demonstrated at the ESR, GSI, see [1] and references therein. While the longitudinal momentum spread was measured to a record value of $\Delta p/p < 4\times10^{-7}$ using optical diagnostics, standard beam diagnostics such as the Schottky pickup diagnostics were limited in resolution and could only resolve momentum spreads down to $\Delta p/p \approx 10^{-6}$.

Strong momentum spread reduction in combination with strong attenuation of the Schottky signal power by 8 to 10 orders of magnitude were observed independent of the ion beam current. High-density space-charge dominated beams were routinely attained, reaching the regime of strong coupling with a plasma parameter of unity. When increasing the coupling between the ions by introducing very moderate electron cooling at currents of only a few mA, three-dimensional cooling of ion beams could be demonstrated. With such beams, high-precision laser spectroscopy of the $2S_{1/2} \rightarrow 2P_{1/2}$ and $2S_{1/2} \rightarrow 2P_{3/2}$ transition in C^{3+} at about 155 nm in the ion's rest frame, corresponding to 257 nm in the laboratory frame, resulted in a measurement challenging the best theoretical estimates in precision.

As a consequence of proving the feasibility of laser cooling of ion beams at relativistic energies, we have successfully applied for a new beam time at the ESR. In this beam time we will address some of the key questions not answered by the previous experiments. Firstly, how can we cool the hot ion beam using a laser force that has an acceptance much smaller than the initial momentum spread of the ion beam without relying on changing the bunching frequency? Secondly, how can we improve our diagnostics to determine the momentum spread of the ultra-cold ion beam? Finally, is it possible to reach strong coupling at high beam currents without relying on electron cooling?

Plans for the ESR beam time

The 2009 G-PAC granted us all requested 21 shifts for our next experiments at the ESR. For this beam time we will develop a new, all-solid-state, single-mode, single-frequency laser system that can perform a mode-hop-free frequency scan over a frequency range of several GHz. With this system it will be possible to cool the initially broad momentum distribution of the ions in the beam without initial electron cooling and scanning of the bunching frequency.

Parallel to the development of this system we are currently setting up new optical diagnostics that will allow to increase the resolution of the momentum measurement by at least one order of magnitude. With such a system it will be possible to unambiguously test for strong coupling between the ions in the beam at ultra-low temperatures and compare standard accelerator-based diagnostics with the new optical methods. We further plan to introduce fast local changes in the tune of the ESR to increase the coupling between the longitudinal and transverse degree of motion of the beam particles. A detailed discussion of the experimental setup for the next beam time can be found in [1].

Collaboration

For the upcoming beam time two new partners from Darmstadt University, namely the group of Professor Thomas Walther and Professor Gerhard Birkl, have agreed to participate in the experiment. In Professor Walther's group a new, robust, all-solid-state laser system will be developed to replace the Argon ion laser system used in the previous beam time. The seeding diode laser has already been set up, delivering mode-hop-free frequency tuning over a range of several GHz. Currently, a fibre-based amplifier system is under development that will be suitable to deliver enough power for frequency-doubling to 257 nm. The optical diagnostics will be developed by FZD in collaboration with Professor Birkl's group. Collaboration on laser cooling experiments at the CSR with the group of Professor Ma from Lanzhou, China, within the SPARC framework will complement the preparation of the laser cooling experiment at the ESR.

The plans for the ESR beam time have been presented at COOL09, Lanzhou, PEARL 2009, Dublin, SPARC 2009 Lisbon and will be presented at SNI 2010, Berlin as well as at the DPG 2010, Hannover.

References

[1] M. Bussmann et al., COOL09, August/September 2009, Lanzhou, to be published, http://www.JACoW.org.

* Work supported by GSI F&E project DRSCHR Laserkühlen

PHELIX Operation Report

V. Bagnoud[1], C. Brabetz[1,5], C. Bruske[1], U. Eisenbarth[1], J. Fils[1], S. Goette[1], T. Hahn[1], T. Kuehl[1,3], F. Knobloch[1], S. Kunzer[1], M. Kreutz[1], T. Merz-Mantwill[1], D. Reemts[1], A. Tauschwitz[1], T. Stoehlker[1,2,4]

[1]GSI, Darmstadt, Germany; [2]Helmholtzinstitut Jena, Germany; [3]Johannes Gutenberg-Universität Mainz, Germany; [4]Ruprecht-Karls-Universität Heidelberg, Germany; [5]Technische Universität Darmstadt, Germany.

General overview

PHELIX[1], a high-energy short-pulse laser, allows for combined ion-laser experiments to support the science programs of the Plasma Physics and Atomic Physics departments of GSI. 2009 was the first year of full nominal operation, in which the laser delivered high-energy pulses in the sub-kilojoule range to various target areas. In spite of its relatively low repetition rate, the 1000th documented shot* was delivered near the end of the year.

In 2009, PHELIX was used in combination with the ion beam. It was shot simultaneously with the nhelix laser to uniformly heat carbon foils to a plasma state, which was then probed using the ion beam from the UNILAC[2]. This new setup led to a significant increase in the quality of the recorded data. Other experiments were done using the laser alone to study the generation of an x-ray laser[3] at wavelengths shorter than 10 nm. In this experiment, a new setup yielded a reduction of the pump-laser energy, required to reach the lasing threshold, to values compatible with existing high repetition-rate facilities. This makes the setup ideally suited for high-average-energy short-wavelength x-ray laser systems. Another significant scientific result was obtained in proton acceleration by use of hemispherical targets[4]. Here, a significant shift of the proton spectrum to higher energies was observed.

Furthermore, about one third of the time was devoted to maintenance and improvements of the facility, which are reviewed in the last part of this report.

Operation of the laser facility

As can be seen in Figure 1, PHELIX was serving experiments (beam time and experiment setup) for more than 50% of the time. About 35% was spent for maintenance, improvements and characterization of the system (system beam time). The rest was down time.

PHELIX delivered laser pulses for eight experiments, distributed among ten beam times. For experiments conducted in the laser hall, five days of setup were usually necessary, followed by two to three weeks of beam time. These were delivered in 106 shifts, which is close to the planed 130 shifts. The difference mostly accounts for unused shifts either due to external reasons or experimental complications. For standard experiments, the number of persons required to run the facility during a shift has been reduced to two. During the year, PHELIX was available 9 hours per day for laser stand-alone experiments and 14 hours for combined laser-ion experiments.

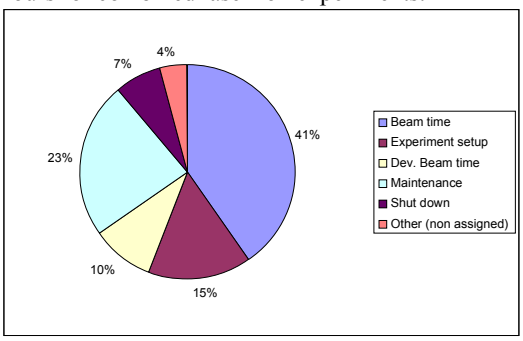

Figure 1: PHELIX usage in 2009

An internal beam time was the occasion to validate the facility at high output energies. Important aspects to be tested were the risk of a pinhole closure at the main amplifier which might occur at high energies as well as damages of optical components. For this, great care was taken in the control of the maximum beam fluence. Therefore the spatial energy uniformity (known as fill factor) of the beam was optimized at low energies in a first step. This way, we were able to safely produce the necessary output energies of 10 Joules in the pre-amplifier. We then gathered output energy data at flash lamp voltages ramping from 15.5 kV to 17 kV in steps of 500 V. At maximum voltage, the PHELIX main amplifier shows a gain of 95 and delivers 920 J. During all the shots, no signs of pinhole closure as well as the formation of damages on optical surfaces were observed.

Contribution to the experimental program

Before the year started, the plasma physics advisory committee (PPAC) had approved 88 A-graded new shifts. Out of these shifts, 50 were delivered and the rest was dedicated to B-level experiments or to the reduction of the backlog. At the end of the year, the backlog of PHELIX is constant around the 300-shift level. In September, the PPAC granted 130 new shifts with new accounting rules (2 shifts per day instead of one) that better represents reality.

In 2009 a new contract of Laserlab Europe started. Within this European Integrated Initiative, PHELIX is acting both as a contributor to joint research initiatives and as user facility for the European research community. The program supports experiments by visiting researchers from European countries. In 2009, nearly 5 weeks of

* A documented shot is a laser shot with an entry to the PHELIX log book; its parameters are usually stored by the control system.

beam time were offered in this sense, based upon an internationally open proposal system.

Improvements to the facility

Two beam times have dealt with active wavefront control which is currently the work of a diploma thesis at PHELIX. Here, we measure the wavefront of the laser beam using a Shack-Hartmann sensor and control it using a deformable mirror. The home-built control system has been developed under LabVIEW^{TM}; and in contrast to existing commercially available solutions, it can be operated on distributed computers. This allows for the measurement to be done at one location while the wavefront control with the deformable mirror is done at another place, communicating over the network.

An immediate consequence of this work has been an important increase in repetition rate for the pre-amplifier. It turned out, indeed, that the waiting time between shots could be significantly reduced from its design value of 10 minutes to a value lower than three minutes without piling up thermal effects. A second result is the successful correction of thermal aberrations that appears after the shot. At PHELIX, the shot cycle is 90 minutes, mostly limited by the cool down time of the main amplifier section. Even in such condition, a pile up of the thermal aberration appears in the course of the day. With the correction loop activated, we were able to bring the thermal aberration down to less than 0.2 λ a few minutes only after the shots. For on-shot aberrations, the correction method relies on the supposed-constant behaviour of the amplifiers. If the results are fully satisfactory at the pre-amplifier section level, see Figure 2, these obtained at the main amplifier section showed a quantitative reduction of the aberration which is promising but still deserves some attention.

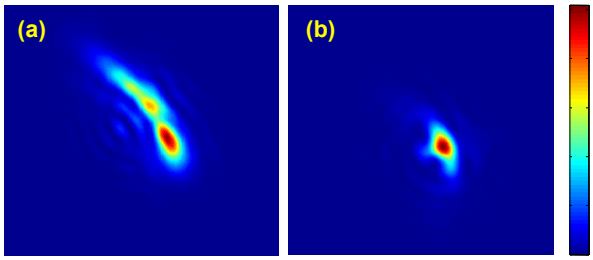

Figure 2: Far field intensity at the preamplifier stage, (a) before correction and (b) after wavefront correction

In 2009, we deployed the laser sensor after the short pulse compressor. The main challenge is the large dynamic energy range which must cover more than 5 orders of magnitude from the alignment and pre-shot checks to the on-shot measurements. Additionally, a complication arises as nonlinear effect accumulation due to the short pulse must be avoided. This difficulty is dealt with using the setup shown in Figure 3. The leaky mirror used to create the diagnostic beam has a transmission of 0.5%. Even at such low transmission values, the energy is too high to avoid nonlinear effects after the beam is down-collimated. The original solution has been to use the first internal reflection in the leaky mirror for high energy pulse diagnosis, while the direct transmission is used during the alignment phase. An immediate effect has been a better control of the laser pulse duration, even at maximum energies and a reduction of its values close to its theoretical limit.

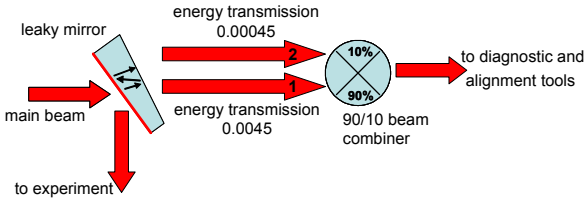

Figure 3: Intensity management scheme for the sensor

An important new diagnostic implemented in 2009 has been a back reflection diagnostic. Indeed, with a total gain up to 10^5 the laser is very sensitive to possible back reflected light coming from badly aligned optical surfaces or the experiment itself. In the beginning of 2009 we therefore installed a sensor monitoring the amount of light being reflected back, at the pre-amplifier section, consisting of a set of fast photodiodes within an optical assembly. This sensor was successfully used in one beamtime where the experiment was pushed as far as possible until the onset of a strong back-reflection.

At last, efforts to improve the temporal contrast of the laser pulse were continued. In the past, PHELIX has been plagued by a series of pre-pulses occurring nanoseconds before the main pulse. The series of optical gates (Pockels cells) has been extended to seven for the short pulse front end, together with a new low jitter trigger signal generator, which solves the issue. A second step to reduce the pulse pedestal or amplified spontaneous emission level has been started this year. A new scheme of pre-amplifier stage comprising an ultrafast OPA recently developed at the university of Rochester offers a solution for the generation of high temporal-contrast laser pulses. In this scheme, the parametric amplification factor directly translates into temporal contrast improvement for any instant located outside the temporal extension of the short pump pulse. This scheme will be used to replace the first amplifier in the short pulse front end. We developed a model using the Miro software which showed the advantages of using BBO over LBO as ultrafast OPA medium in a single stage configuration. The next steps consist in building the OPA pump line in collaboration with the Helmholtz Institute Jena and the complete OPA conversion system with a BBO crystal at PHELIX.

References

[1] V. Bagnoud et al., “Commissioning and early experiments of the PHELIX facility” Appl. Phys. B, DOI: 10.1007/s00340-009-3855-7
[2] A. Frank et al., this report
[3] D. Zimmer et al., this report
[4] M. Roth et al., to be submitted to Nature Physics

Experiments on the heating of low Z targets by means of hohlraum radiation

O. N. Rosmej[1], N. Zhidkov[2], V. Vatulin[2], N. Suslov[2], A. Kunin[2], A. Pinegin[2], D. Schäfer[3], Th. Nisius[3], Y. Zhao[4], Th. Wilhein[3], Th. Stoehlker[1]
[1]GSI, Darmstadt, Germany; [2]VNIIEF, Sarov, Russia; [3]University of Applied Science, Remagen, Germany;
[4] Institute of Modern Physics, China AS, Lanzhou

Recent progress in the design of plasma-targets for combined PHELIX laser - heavy ion beam experiments at GSI [1, 2] has been achieved by the experimental investigation of hohlraum targets irradiated with the PHELIX-Laser. In this experimental campaign we have studied the characteristics of the X-ray radiation, which occurs when the laser radiation interacts with the gold hohlraum, this investigations include the development of diagnostic techniques for measuring the electron temperature and the ionization degree of low Z foams or foils, which are inserted in the hohlraums and whichs plasma properties after laser irradiation were probed by the heavy ion beam. The laser was used at the basic frequency of 1ω with λ = 1.06 μm. The laser pulses of a duration $\tau \approx$ 1ns and energies between $E_L \approx$ 6 - 130 J were focused onto the target by a lens with 4 m focal length. The achieved diameter of the focal spot was ~∅ 300-400 μm, resulting in laser intensities up to $5 \cdot 10^{13}$ W/cm^2. In the experiments cylindrical gold hohlraum targets with a diameter 1.8 mm and 2 mm length were used. The Au-wall thickness was 10 μm, the bottom of the primary hohlraum was covered with a 0.12 μm thin gold foil in order to prevent the direct irradiation of the low Z target (0.5 - 5 μg/cm^2 CH foil or foam) placed inside the secondary cylindrical hohlraum connected to the primary one (see fig. 1).

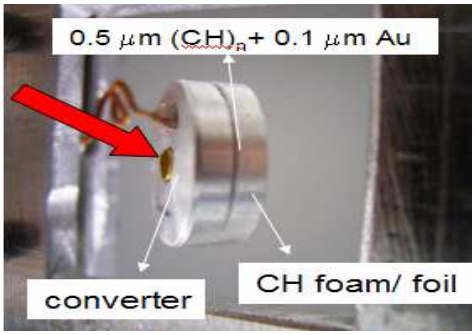

Fig.1 View of the combined hohlraum: converter and the secondary hohlraum filled with foam are divided by thin Au-layer evaporated onto the 0.5 mm polypropylene

The PHELIX- laser irradiates the wall of the primary gold cylinder through the open entrance hole with an incidence angle of 45°. Diagnostic tools were placed around the target inside a spherical vacuum chamber with a diameter of 110 cm, which could be evacuated down to P ≈ 10^{-4} mbar. In fig. 2 all diagnostic equipment used is shown: two pinhole cameras (PH) to image the hohlraum plasmas in the X-ray regime, vacuum X-ray diodes (XRD) with Carbon cathodes for time resolved measuring of the x-ray flux from the hohlraum transmitted trough the 0.12 μm Au-foil; spherically bent mica crystal spectrometers (FSSR) were used to record the radiation of the gold plasma which was generated in the laser focal spot for two photon energy ranges (1.1-1.2 keV and 2.4 - 2.5 keV). Two symmetrically placed transmission grating spectrometers (TGS) observed the X-ray radiation from the bottom of the hohlraum: TGS1 with 1000 lines/mm recorded soft X-rays in the range of 60 - 400 Å on a UF4 x-ray film and TGS2 with 10000 lines/mm was coupled to an X-ray CCD-camera for recording soft X-rays between 10 - 200 Å

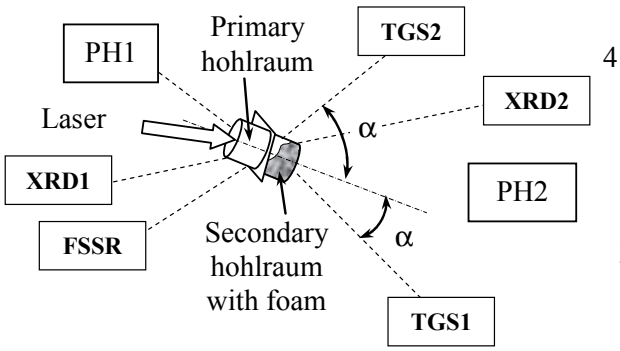

Fig. 2: Schematic set-up of the two-stage hohlraum target with different diagnostics equipment.

A restriction to laser energies up to 75 J was necessary, because at higher energies the risk existed to destroy parts of the laser system by reflection of the laser light at the hohlraum plasma back into the laser system. Estimations of the radiative temperature made for laser energy of 70 J, using measured XRD-signals (front), resulted in 35 eV. The lower level of the XRD-signals from the secondary hohlraum allows concluding that the radiative temperature there does not exceed 20 eV. During the reported experiments the possibility for diagnostic of the ionization degree of the CH-foil (foam) heated by the soft X-rays using the shift of the Carbon K-edge was demonstrated. This method will be further developed and confirmed in the next experimental campaign.

This work was performed under support of the ISTC-project #2264.

References

[1] R. Bock, D.D.H. Hoffmann et.al., PHELIX. GSI 98-10, Report, p.45
[2] V. Vatulin, E.Vasina GSI 2000-2, Report, p. 52

Time- and spectrally resolved characterisation of laser-driven hohlraum radiation

T. Heßling[1], A. Blažević[1], A. Frank[2], D. Kraus[2], M. Roth[2], G. Schaumann[2], D. Schumacher[2], and D.H.H. Hoffmann[2]

[1]GSI, Darmstadt, Germany; [2]Technische Universität Darmstadt, Darmstadt, Germany

Introduction

The measurement of the energy loss of heavy ions in plasma is one of the research activities of the plasma physics group at GSI. In addition to the recent achievements [1] in the directly heated set-up where a carbon foil is irradiated by either one or two high energy lasers, *nhelix* and PHELIX, and probed by the ion beam the indirectly heated set-up has also made significant progress. In this scheme a converter cavity, made of gold, converts the monochromatic laser light into thermal radiation at wavelengths of a few nanometres. This radiation has been characterised by an absolutely calibrated diode spectrometer as well as a XUV spectrometer [2].

Diode spectrometer

The diode spectrometer has four channels with distinct wavelengths, in which light from a diagnostic hole in the hohlraum is spectrally filtered by calibrated X-Ray mirrors and filters. The known quantum efficiency of the diodes allows to deduce the absolute radiation power and, assuming a black body, one can compare this with the predictions of Planck's radiation law. With a response time of less than a nanosecond the evolution of the temperature during the heating period of about 10 ns was recorded in various shots. Due to the strong non-linear relation of the radiation power and the temperature only temperatures above a certain threshold can be detected, as it can be seen in figure 1. Here, two typical shots are depicted, the first shows the radiation from a plane gold foil whereas the second shows the radiation from a hohlraum. The plasma from the gold foil is not thermalized and the channels exhibit different temperatures, whereas the radiation from the hohlraum shows almost equal values at all wavelengths, as expected. The maximum radiation temperature is about 35 eV.

Rowland spectrometer

The full spectrum of the thermal radiation from a laser-heated hohlraum was measured with a XUV spectrometer in Rowland geometry. In addition to the results presented last year the grating, which suffered from multiple visible diffraction orders up to the 10th, has been replaced. The new grating only shows the first diffraction order in the interesting wavelength region. The measurement of a hohlraum spectrum is depicted in figure 2 which fits best to a radiation temperature of about 32 eV.

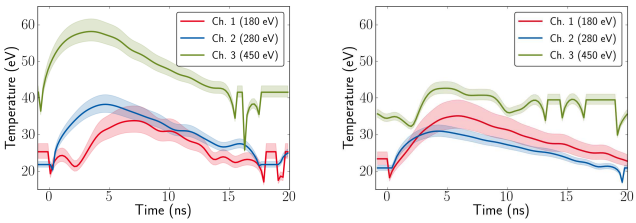

(a) Plane gold foil (b) Gold cavity

Figure 1: Measured temperatures of targets heated with a 7 ns laser pulse with energies of a) 14 J and b) 24 J.

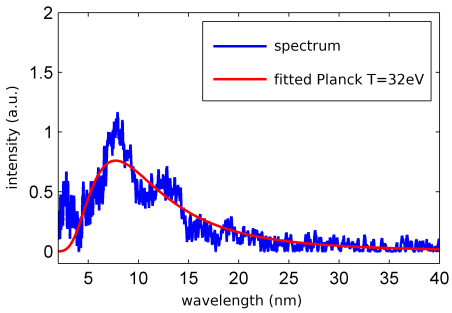

Figure 2: Measured spectrum of a hohlraum together with a fitted Planckian distribution.

Conclusions

Both diagnostics independently measured the same maximum radiation temperature. Theoretical values from a scaling law [3] predict the same temperatures of about 35 eV that were measured experimentally. With this the radiation from a single laser-heated hohlraum has been characterised completely and the next step towards indirectly heated targets will be carried out soon.

References

[1] A. Frank et al., Phys. Rev. E, **81** p. 26401 (2010)

[2] T. Heßling, PhD thesis, 2010

[3] J. Shao-En et al., Chinese Physics Letters 22 p. 2328 (2005)

Optimization of the hohlraum wall composition

E.Yu. Arapova, M.A. Barinov, M.A. Vronskii, G.V. Dolgoleva, V.F. Yermolovich
RFNC-VNIIEF, Sarov, Russia

Experimental investigations on the conversion of Nd-laser radiation (λ = 532 nm, intensity 10^{13} W/cm^2) into X-rays by irradiating gold/copper alloys have shown a dependence on the atomic percentage of gold in the alloys [1, 2]. The X-ray yield in the photon energy region up to 1 keV reaches the maximum when the alloy contains 43% of gold. For harder X-rays above 1 keV the yield decreases drastically with a higher percentage of gold in the alloy. Adding 12 % of gold into the copper of the originally investigated alloy results in a decrease by a factor of 2.1 for X-ray's above 1 keV.

The one-dimensional code SND [3] is developed for calculations of two temperature gas dynamics of plasma expansion and includes the radiation transport in a diffusion approximation. The wavelength dependent radiation diffusion in materials was used to determine the conversion of laser radiation into X-rays in AuCu alloys by variation of the gold content. The needed spectral opacities were obtained using the THERMOS code [4], which calculates spectral absorption ratios on the basis of the average atom model in the modified Hartree–Fock -Slater approximation. Fig.1 shows the curves calculated for the X-ray flux (energies up to 1 keV) emitted from a $Au_{0.43}Cu_{0.57}$ - alloy at a laser intensity of 10^{13} W/cm^2.

For a part of the X-ray spectrum the maximum yield of the radiation from the Au/Cu-alloy is higher than that from laser irradiated pure gold- or copper-targets. For example the X-ray´s yield from the $Au_{0.43}Cu_{0.57}$ - alloy at 0.15 keV, 0.3 keV and between 0.7 – 1 keV is higher than the yield from the pure gold or copper, irradiated with the same laser parameters.

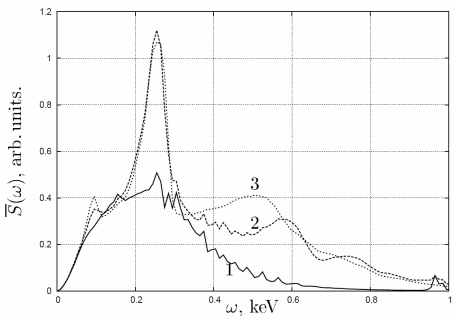

Figure 1: The calculated values of flux S(ω), ω ϵ (0,1) keV from the target: 1 - for Cu, 2- for $Au_{0.43}Cu_{0.57}$, 3 - Au.

From Fig. 1 we can conclude that the X-ray yield between 0.55 – 1.1 keV for conversion of laser irradiation at intensities of 10^{13} W/cm^2 for the considered $Au_{0.43}Cu_{0..57}$ alloy is 12 % higher than for a pure gold target and by a factor of 1.7 for a copper one.

For the X-ray energies higher than 1 keV a significant decrease in the X-ray yield is observed for alloys containing more gold, see Fig. 2.

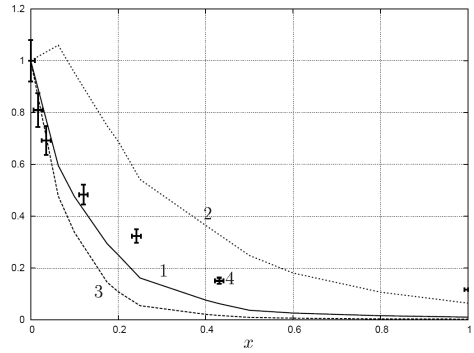

Figure 2: The calculated ratios of fluxes for the Au_xCu_{1-x}- and for the pure Au in the photon energy range of 1.15-1.6 keV: $S_{[1.15,1.6]keV}(Au_xCu_{1-x}) / S_{[1.15,1.6]keV}(Au)$

calculted for the laser intensities: 1 - $10^{13}\ W/cm^2$, 2 - $5 \cdot 10^{12}\ W/cm^2$, 3- $3 \cdot 10^{13}\ W/cm^2$.

x - atomic percentage of Au in the mixture

Numerical simulations of the experimental results on the laser radiation conversion into X-rays demonstrate the non-linear behavior of the output radiation energy (increase) within the spectral range of 0.55 - 1.1 keV and a strong decrease within the range 1.15 – 1.6 keV depending on the atomic percentage of Au in the AuCu-alloy.

The results of these investigations will be used for optimization of the hohlraum design in combined laser – heavy ion beam experiments at GSI.

This work was performed within the framework of the ISTC Project#2264.

References

[1]J. A. Chakera, V. Arora, S. Sailaja, S. R. Kumbhare, P. A. Naik, P. D. Gupta, N. K. Gupta, B. K. Godval // Applied Physics Letters v. 83, 1, 2003, pp. 27-29

[2]V. Arora, J. A. Chakera, P. A. Naik, S. R. Kumbhare, P. D. Gupta, N. K. Gupta // Journal of Applied Physics 100, 033306. 2006.

[3]G.V.Dolgoleva // VANT, Ser.: Methods and Programs for Numerical Simulation of Computational Physics Problems, 1983, Issue. 2, pp. 29- 33

[4]A.F.Nikiforov, V.G.Novikov, V.B.Uvarov, Quantum-Statistical Models of High-Temperature Plasma, Moscow: "Fizmatlit" Publishers, 2000

Energy loss of ^{48}Ca in carbon plasma created by two-sided irradiation

A. Frank[1], A. Blazevic[2], W. Cayzac[1], T. Hessling[2], J. Menzel[1], A. Pelka[1], D. Schumacher[1], T. Stöhlker[2], An. Tauschwitz[3], and M. Roth[1]

[1]TU Darmstadt, Germany; [2]GSI, Darmstadt, Germany; [3]Uni Frankfurt, Germany

The stopping power of heavy ions in matter is a field of research that has been addressed for about a century. The understanding of the interaction of charged particles with cold matter has continuously evolved, however for ionized matter it is not yet fully understood. The development of a CVD polycrystalline diamond detector [1] has lead to improved experimental data, however for the first 10 ns during the irradiation of the target by the nhelix laser system, a significant decrease in the energy loss has been observed which could not be explained at this time [2]. The most promising explanation found was that the microscopic intensity fluctuations in the 1 mm laser focus on the target generated by a RPP (Random Phase Plate) lead to huge pressure differences in the target and hence to large inhomogeneities in the target's mass distribution. The implementation of the Phelix laser at the experimental area Z6 lead to the new concept to step away from the scheme with the one sided irradiation of a thin carbon foil of $0.5\,\mu m$ thickness and to use both the Phelix and the nhelix laser to heat the target from both sides (see Fig. 1).

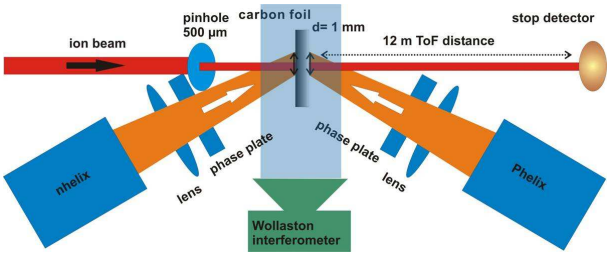

Figure 1: Experimental setup using the Phelix and the nhelix laser as well for the plasma creation.

This scheme offers several advantages. First, inhomogeneities of the ablation pressure on the target due to the laser irradiation are less important. Second, the time needed to heat the whole foil via heat conduction is reduced. And thirdly the laser energy of each laser pulse can be reduced so that the temperature of the ablated plasma is lower compared to the energy of one laser pulse from one side needed to fully heat the carbon foil to a highly/fully ionized plasma state. So, two dimensional effects of the plasma expansion which lead to a decrease of the target mass penetrated by the ion beam play a less important role. The experiment described here was carried out with laser pulses of a pulse length of 8 ns (FWHM), $E = 35\,J$ which corresponds to an average intensity of $I = 4.7 \times 10^{11}\,W/cm^2$ on the target, a carbon foil of $0.5\,\mu m$ thickness. The ion beam used here is ^{48}Ca at 4.9 MeV/u with an incident charge of 18+. The heating laser pulses of nhelix and Phelix were properly synchronized with a Δt better than 1 ns. Including the diagnostics laser of the nhelix system and the heavy ion beam four synchronized beams were included in this experimental campaign. The laser parameters were chosen according to hydrodynamic simulations [3], that the whole carbon target is fully ionized at the end of the laser pulse.

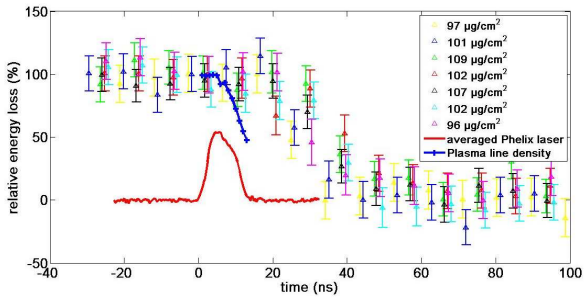

Figure 2: Energy loss of ^{48}Ca at 4.9 MeV/u.

The experimental results obtained from this experimental campaign are presented in Fig. 2. The central CVD diamond detector of the spectrometer described in detail in [4] was used as ToF detector for this experiment. The graph shows the energy loss measured in relative values, 100 % is the energy loss in the cold carbon foil. The results shown have been obtained with 7 different experiments where the timing between the laser beams and the UNILAC accelerator - which allows probing the target each 9.224 ns - was shifted to continously cover the temporal evolution of the energy loss. The corresponding temporal profiles of the Phelix laser are shown at the bottom. Mainly two facts are to be noted here. First no decrease of the energy loss during the duration of the laser pulses has been observed. However no increase as predicted for example in [2] has been measured. Second the measured energy loss remains constant over 20 ns. Since the target mass penetrated by the ion beam decreases in time (blue curve - according to RALEF-2D [3]) this corresponds to a significant increase of the projectile's energy loss in the plasma mainly arising from the more efficient energy transfer to free electrons compared to the one to bound electrons.

References

[1] F. Wamers, A. Blazevic et al, GSI annual report 2006, 277

[2] A.Frank, A. Blazevic et al, Phys. Rev. E, Vol. 81-2, 026401, 2010

[3] An. Tauschwitz, this annual report

[4] W. Cayzac, this annual report

Diagnostics of the temperature and ionization degree of low Z foams in experiments on the ion stopping in plasma.

O.N. Rosmej[1], N. Orlov[2], D. Schäfer[3], Th. Nisius[3], Th. Wilhein[3], N. Suslov[4], N. Zhidkov[4] , Y.Zhao[1]
[1]GSI, Darmstadt, Germany; [2] JIHT, Moscow, [3]University of Applied Science, Remagen, [4] VNIIEF-Sarov, Russia,

Production and investigation of plasma targets obtained by indirect heating of low Z materials is an important step in the combined laser - heavy ion beam experiments. The main goal of the reported project is a creation of dense homogeneous plasma which maintains the electron density and temperature during the heavy-ion beam – plasma interaction time of 3 ns. This goal can be achieved if low density (3 mg/cc) 500 μm thick CHO-foam (TAC) is heated by thermal hohlraum radiation of 0.3 – 1 keV photon energies. Two dimensional hydrodynamic calculations which include 2-D multi group radiation transport have shown that with the already existing PHELIX-laser beam line (300J, 1ω, 1ns, 10^{14} W/cm^2) it is possible to heat the foam target up to electron temperatures of 30-50 eV. Such plasma is expected to reveal an increased stopping power when probed with a heavy ion beam. In the expected range of electron temperatures, the conventional methods of diagnostic using characteristic self radiation of indirect heated plasma target are not applicable. The spectrum is dominated by the L-shell transitions broad due to reabsorption of the line-radiation in the optically thick plasma. For diagnostic of the electron temperature and ionization degree of the indirect heated low Z plasma target we develop a method which applies the deformation of the absorption K-edge when cold matter is heated to plasma. In cold matter, increased photo-absorption occurs when the photon energies approach the binding energy of K-shell electron in C-atom. For cold carbon the K-edge position corresponds to 285 eV of photon energy. In plasma the outershell electrons will be collisionally ionized and due to lower screening potentials in ionized atoms, the positions of the K-edges for the subsequent charge states will be shifted to the higher photon energies. According to Dirac-Fock-Slater calculations [1] for isolated carbon ions one obtains the following K-edge energies for different Carbon charge states: C^{+1}– 297.7 eV; C^{+2}- 313, 39 eV; C^{+3} -346.17 eV; C^{+4} – 380.51 eV. For ions in plasma one has to take in to account effects of plasma microfields which change the binding energies of electrons populating ground and excited ion states. For correct interpretation of experimental results the Ion Model (IM) which describes plasma radiative opacities over a wide range of densities and temperatures [2] will be used. IM includes a general set of self-consistent field equations that describe the state of the whole ensemble of plasma atoms and ions contains: (a) the Hartree-Fock equations for all atoms and ions with different electron configurations; (b) the unbound electron densities in phase space for all atoms and ions with different electron configurations; (c) the Gibbs distribution; (d) the electroneutrality condition. The results of calculations obtained by means of the IM-model for different plasma temperatures and densities can be used in order to describe the experimentally mesured deformation of the Carbon K-edge in plasma. In experiments spectra irradiated by gold hohraum plasma were measured by means of the absolute calibrated gold transmission grating spectrometer in the wavelength range of 1-20 nm [3].

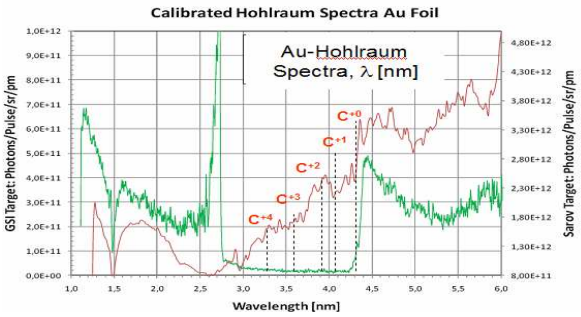

Fig.1 opacity of the 0.5 μm thick "cold" carbon filter and carbon plasma for the gold hohlraum radiation

Fig. 1 shows the spectra irradiated by the gold hohlraum plasma and recorded after transmission through the cold 0.5 μm thick Carbon filter (green) and 0.5 μm thick CH-foil (red) indirect heated with 129J 1ns PHELIX-laser pulse. The step-like form of the deformed K-edge (red) can be attributed to the presence of the carbon ions with charges up to +4. This allows an electron temperature of CH-plasma heated by the thermal hohlraum radiation not higher then 10 eV. The quantitative interpretation of this time-integrated spectrum is not possible due to fast hydrodynamic expansion of the heated foil. 1-D calculations of the hydrodynamic expansion of 3 mg/cc 500 μm thick CH-foam heated up to 10-30 eV demonstrate a promising stability of the plasma temperature and density during first 5 ns.

References:

[1]. G. Zschornack et al, Preprint ZfK-574, Rossendorf, 1986
[2]. N.Yu. Orlov "Ion model of a hot dense plasma." Laser Part. Beams 15 (1997), 627–634.
[3] T. Wilhein et al Rev. Sci. Instr. V70, N3(1999) pp. 1694-1699

Setup and commissioning of a cryogenic system for the production of targets to be used in experiments with high energy lasers and heavy ion beams *

J. Menzel[1], A. Blažević[2], D.H.H. Hoffmann[1], A. Frank[1], M. Günther[1], T. Heßling[2], M. Imran[1], A. Pelka[1], M. Roth[1], G. Schaumann[1], D. Schumacher[1], T. Stöhlker[2], and S. Udrea[1]

[1]TU Darmstadt; [2]GSI Darmstadt

The experimental investigation of the energy loss of swift heavy ions in laser produced plasmas [1] is one of the main research activities of the Plasma Physics Department at GSI.

Cryogenic systems [2] are in this context of special interest, due to the possibility to create solid state targets ($T = 4.2\,\mathrm{K}$) out of matter which is gaseous under normal conditions, especially hydrogen and deuterium. Moreover, the properties of laser produced hydrogen and deuterium plasmas are well understood theoreticaly and thus highly suitable for studying the physics of the interaction of energetic heavy ions with plasma particles.

(a) U-shape (b) O-shape

Figure 1: Solid deuterium targets with 2 mm width

Cryogenic targets with different geometries have been produced (Fig. 1). Targets with a high aspect ratio having a thickness of only a few micrometers and transverse sizes of millimeters are of special interest for the envisaged investigations. Such targets allow the generation of laser plasmas with a high degree of homogeneity, thus allowing measuring the ion energy loss under well defined conditions in fully ionized plasma.

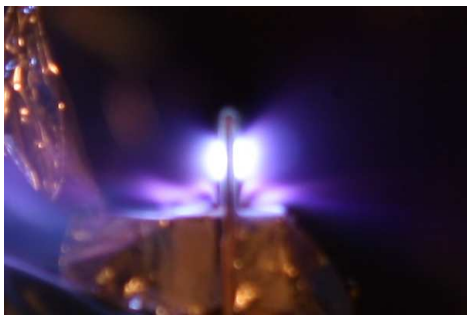

Figure 2: Deuterium plasma produced out of an solid target using the nhelix and Phelix laser systems

Solid deuterium targets have been simultaneously irradiated by the high energy laser systems nhelix and Phelix ($50\,\mathrm{J}$ in $10\,\mathrm{ns}$ @ $1064\,\mathrm{nm}$;$1053\,\mathrm{nm}$) [3] (Fig. 2). The free electron density inside the deuterium plasma has been measured for different times (Fig. 3).

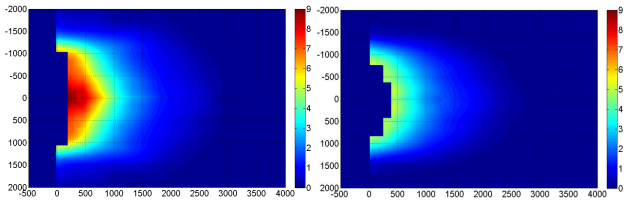

(a) $9.1\,\mathrm{ns}$ after start of laserpulse (b) $11.9\,\mathrm{ns}$ after start of laserpulse

Figure 3: Free electron density of a deuterium plasma; space in μm, electron density as colorbar in 10^{19} cm^{-3}

To measure the thickness of deuterium targets an $14\,\mathrm{keV}$ electron source with a subsequent focussing and steering system has been set up. The evolution of the thickness below $200\,\mu\mathrm{m}$ has been determined by analysing the electron scattering. A precision of $12\,\%$ has been achieved within the range of interest ($50 - 15\,\mu\mathrm{m}$) for energy loss experiments (Fig. 4).

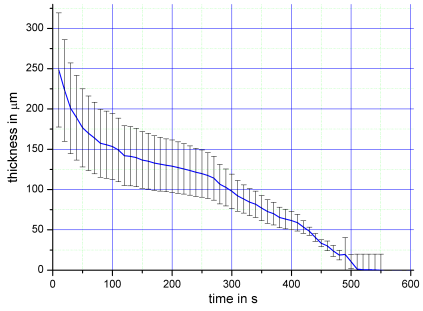

Figure 4: Evolution of the thickness of a solid deuterium target measured using electron scattering

References

[1] Frank, A. et al., Energy loss of argon in a laser-generated carbon plasma, Phys. Rev. E 81, 026401 2010

[2] Menzel, J., Setup and commissioning of a cryogenic system for the production of targets to be used in experiments with high energy lasers and heavy ion beams, Dissertation 2009

[3] Bagnoud, V. et al., Commissioning and early experiments of the PHELIX facility, Appl Phys B, 2009

* Also supported by BMBF 06DA9034 I

K-alpha backlighter optimization using high-energy picosecond laser pulses in experiments at the PHELIX laser facility*

P. Neumayer[1,2], O. N. Rosmej[1], B. Ecker[1], D. Hochhaus[1], B. Zielbauer[1], B. Aurand[1], E. Kazakov[3], Th. Kühl[1] , Th. Stöhlker[1]

[1]GSI, Darmstadt, Germany; [2]Extreme Matter Institute; [3]Kurchatov Research Center, Moscow, Russia

Development of laser driven high-brightness fast x-ray sources is a key application of the PHELIX laser for experiments in combination with the heavy ion accelerator. X-ray diagnostics of high-energy density states of matter produced with intense heavy ion beams from GSI or FAIR will require multi-keV x-ray energies to penetrate the dense plasma [1].

Recent development of backlighter sources at GSI focused on high-intensity short-pulse driven sources due to their favourable scaling to higher photon energies. When light is focused at relativistic intensities onto matter a large fraction of the laser energy is converted into super-thermal electrons which are accelerated to MeV energies. Interaction with the target material results in high-energy bremsstrahlung and characteristic line emission. Under-dense plasma formed at the front surface is heated to keV temperatures, emitting Helium-alpha and Lyman alpha radiation from highly-charged ions.

In recent experiments at PHELIX we optimized a Cu K-alpha backlighter source. Thin foils and wires with dimensions of few 10's of microns were irradiated with laser pulses of energies up to 150 J and K-alpha and hard x-ray emission was determined quantitatively as function of the laser parameters pulse duration and focal spot size over a wide range of intensities exceeding 10^{19}W/cm^2.

A variety of x-ray diagnostics was fielded in the experiments. An absolutely calibrated single-hit spectrometer gives a broad overview of the x-rays produced, from ~5 keV to over 20 keV. Fig. 1 shows a spectrum obtained from a 100 J laser shot. Up to 10^{13} Cu K-alpha photons were generated per shot, corresponding to a conversion efficiency of laser energy into line radiation of approximately 10^{-4} which is typical for this class of experiments [2]. Besides strong K-alpha emission the spectra show K-beta and He-alpha radiation.

Advanced x-ray scattering techniques [3] require a high collection efficiency of the scattering spectrometer. Highly-oriented pyrolytic graphite (HOPG) provides an exceptionally high peak reflectivity [4]. At GSI we used a 70mm large curved HOPG crystal in a van-Hamos type spectrometer. Coupled with imaging plate detectors this constitutes a highly efficient spectrometer suitable as an x-ray scattering diagnostic. The resolution is limited to E/ΔE~200 due to depth broadening and aberrations resulting from to the large mosaicity of the HOPG crystals. A much improved resolution is provided by a spherically bent Mica crystal spectrometer in Johannsen geometry. This spectrometer provides in addition 1-dimensional imaging.

The spectrum of hard x-ray bremsstrahlung was assessed using an image plate based 8-channel detector with a set of lead filters of various thicknesses. A strong dependence of the bremsstrahlung spectrum on the focused intensity was observed. While in some applications this background is detrimental, it is also a powerful backlighter for dense high-Z targets. A fitting procedure based on genetic algorithm and using Monte-Carlo simulated bremsstrahlung emission and detection allowed us to deduce the hot-electron spectra.

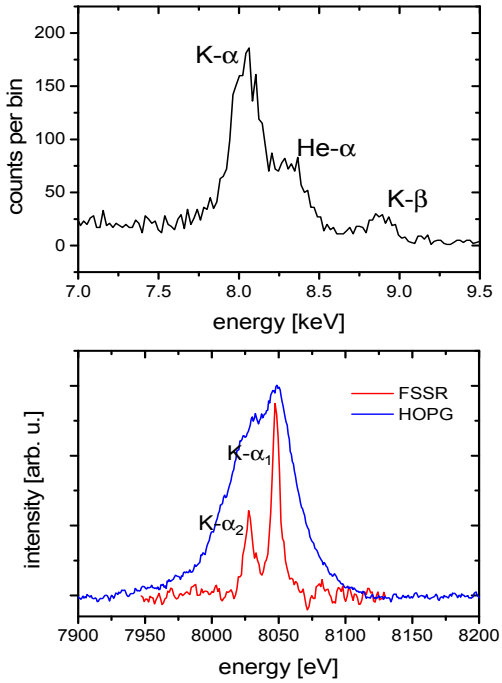

Figure 1: K-shell line emission spectra from copper irradiated with >100J of laser energy, obtained with Single-hit CCD (top) and crystal spectrometers (bottom).

References

[1] N.A. Tahir, I.V. Lomonosov, A. Shutov, V.E. Fortov, M. Geissel, A.R. Piriz, C. Deutsch and D.H.H. Hoffmann, NIM A 606, (2009) 128.

[2] H.-S. Park et al., Phys. Plasmas 13, (2006) 056309.

[3] S. H. Glenzer and R. Redmer, Rev. Mod. Phys. 81, (2009) 1625

[4] T. Döppner et al., Rev. Sci. Instrum. 79, (2008) 10E311

* This work was supported by Laserlab Europe.

Generation and tuning of high-order harmonic radiation for x-ray-laser seeding using the Phelix shortpulse-frontend

D. C. Hochhaus[1,2,3], J. Seres[4,5], B. Aurand[1,3,7], B. Ecker[1,6,7], B. Zielbauer[1,6], D. Zimmer[1,7,8], C. Spielmann[4,5], T. Kühl[1,7]

[1]GSI Helmholtzzentrum für Schwerionenforschung, Darmstadt, Germany; [2]Johann-Wolfgang von Goethe Universität, Frankfurt, Germany; [3]ExtreMe Matter Institute, Darmstadt, Germany; [4]Friedrich Schiller Universität, Jena, Germany; [5]Universität Würzburg, Würzburg, Germany; [6]Helmholtz Institut Jena, Jena, Germany; [7]Johannes Gutenberg Universität Mainz, Mainz, Germany; [8]Université Paris-Sud 11, Orsay, France

Over the last years the x-ray laser team of GSI developed a good expertise in the generation of x-ray lasers in Ni-like media using the travelling wave excitation in the in-house developed double-pulse single beam grazing incidence pumping (DGRIP) scheme [1]. Amelioration of the beam quality and the spatial coherence as well as the pointing stability of plasma-based soft x-ray lasers (XRL) has been successfully demonstrated by using high-order harmonic (HH) radiation for injection-seeding [2, 3].

The proposed usage of soft x-ray lasers at GSI (XRL) for spectroscopy of heavy ions in the experimental storage ring (ESR) and in the upcoming storage ring at FAIR (NESR) will benefit from the capability of using a seeded XRL. A successful seeding process demands amongst others a perfect spectral match between the XRL lasing transition and the seed harmonic. The pump-laser dependent HH wavelength
can be tuned by controlling the process of high-order harmonic generation in the gas medium even if the pump laser wavelength is fixed, as it is the case for the Phelix Nd:glass laser system.

In the experiments performed, we focused the 350 fs long laser pulses into a nickel tube which was connected to a pulsed gas valve delivering ms-long He, Ne or Ar gas pulses. The nonlinear interaction of the intense laser pulses with intensities of 10^{14}-10^{15} W/cm² with the gas lead to high harmonic emission in the soft x-ray regime.

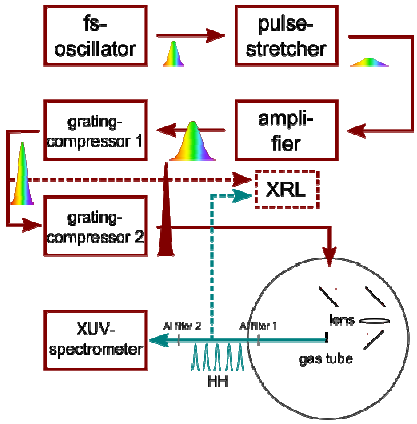

Figure 1: Schematic of the HH setup.

The HH radiation was analyzed by an in-house developed XUV-spectrometer using a flat-field grating and a XUV-charge coupled device resulting in a spectral resolution of ≈ 0.02 nm/px.

To extend the accessible XRLs for injection seeding, we mixed the Phelix frontend beam with its second harmonic to be able to create not only odd but also even order harmonic radiation up to the 59th harmonic at 17.86 nm. The lines were spectrally tuned by taking advantage of the non-adiabatic frequency shift applying quantum-path control [4].

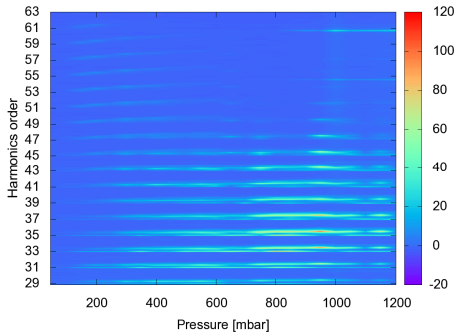

Figure 2: Broadening of the spectral coverage by the non-adiabatic blueshift

Results

We were able to extend the spectral coverage of the HH radiation created by the Phelix-fs-frontend to cover a large spectral portion of the XUV/soft x-ray regime between 18 nm and 35 nm allowing spectral overlap with many XRL transitions such as Ni-like Y (24.01 nm), Zr (22.02 nm) and Mo (18.9 nm) X-ray lasers. Ni-like Nb (20.33 nm) as well as Ne-like Mn (26.9 nm), Fe (25.49 nm), Ge (23.2 nm) and Se (20.6 nm) are in reach.

References

[1] D. Zimmer.et al., Opt. Express 16, 10398 (2008)
[2] Ph. Zeitoun et al., Nature 431, 426 ff (2004).
[3] Y. Wang et al., Nature Photonics. 2008;2(2):94-98
[4] D. C. Hochhaus et al., Appl. Phys. B (to be published)

Warp simulations for capture and control of laser-accelerated proton beams

F. Nürnberg[1,*], K. Harres[1], D.P. Grote[2,3], O. Deppert[1] , A. Friedman[2,3], B.G. Logan[2] and M. Roth[1]
[1]Institut für Kernphysik, Technische Universität Darmstadt, Darmstadt, Germany; [2]Lawrence Berkeley National Laboratory, Berkeley CA, U.S.A.; [3]Lawrence Livermore National Laboratory, Livermore CA, U.S.A.

The capture of laser-accelerated proton beams accompanied by co-moving electrons via a solenoid field has been studied with PIC simulations to compare with experimental results of a PHELIX campaign at GSI [1,2].

The main advantages of the Warp simulation suite [3] that was used, relative to envelope or tracking codes, are the possibility of including all source parameters energy resolved, adding electrons as second species and considering the non-negligible space-charge forces and electrostatic self-fields.

Energy resolved proton beam parameters measured at the PHELIX experiment and calculated with RIS (Radiochromic Film Imaging Spectroscopy [4]) are included in the simulation as source. 10^6 simulation particles (8.2×10^{12} real particles) for both species, protons and co-moving electrons, are injected and expand in a 8.6 T solenoid field.

It was observed that the influence of the electrons is of vital importance. The magnetic effect on the electrons outbalances the space-charge force. Hence, the electrons are forced onto the beam axis and attract protons (fig. 1). This proton density increase can be observed for a wide range of energies. When the beam leaves the solenoid and the field attenuates (0.3 T 5 cm behind the solenoid), the electrons start to expand and follow the protons. Additionally, a proton beam waist and an over-focusing can be seen.

Besides the energy dependent proton density increase on axis, the change in the particle spectrum (fig. 2) is also important for future applications. Protons are accelerated/decelerated slightly, electrons highly. 2/3 of all electrons get lost directly at the source, because the electron density increase on axis due to the magnetic field focussing is so high, that electrons get accelerated backwards and leave the simulation box. Because of the large beam divergence up to 50° 27% of all protons hit the inner wall of the solenoid.

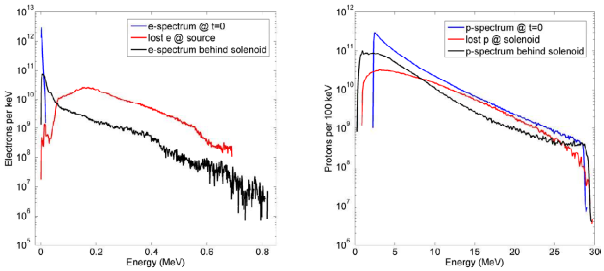

Figure 2: Electron (left) and proton (right) spectra: initial distribution, lost particles and spectrum behind solenoid.

Future studies will be optimizing the capture device and including a debunching unit. Finally, a test stand for laser-accelerated proton beams as a new particle source will be built up at GSI.

References

[1] V. Bagnoud *et al.*, Appl. Phys. **B**, DOI 10.1007/s00340-009-3855-7 (2009).
[2] K. Harres *et al.*, accepted for Plasma Phys. (2010).
[3] D.P. Grote *et al.*, AIP Conf. Proc. vol **749** issue 1 pp 55-58 (2005).
[4] F. Nürnberg *et al.*, Rev. Sci. Instrum. **80**, 033301 (2009)

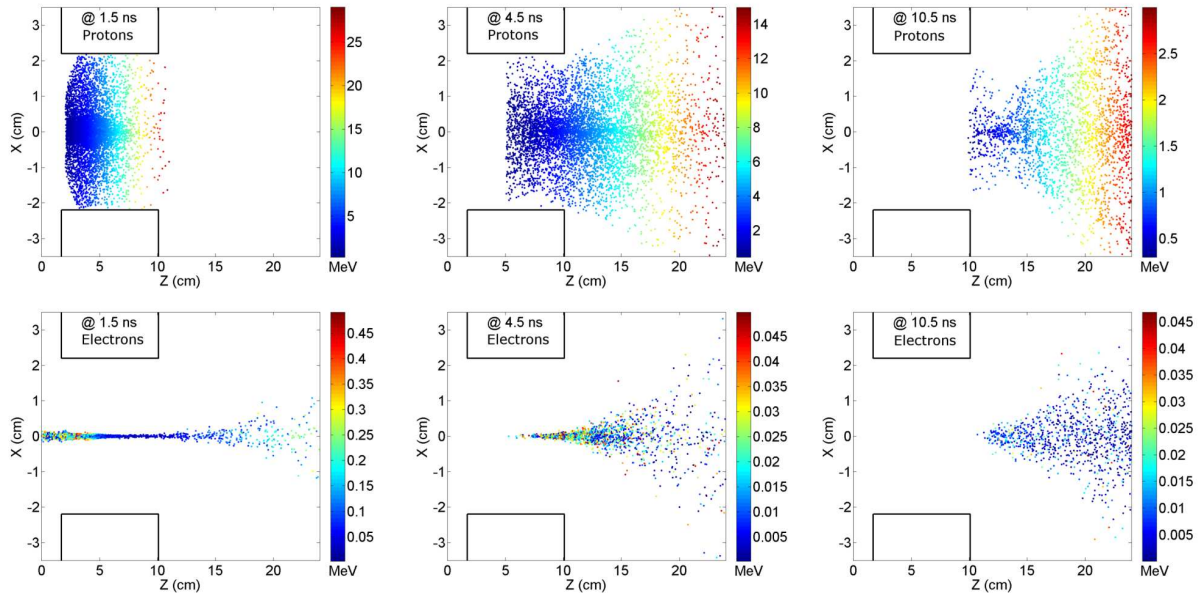

Figure 1: Snapshots of the proton (top) and electron (bottom) expansion for 3 different time steps: 1.5, 4.5 and 10.5 ns. The color scales for the particle energy (between 1.25 MeV and 29.5 MeV) were adjusted separately for a better illustration.

First nuclear activation experiments at PHELIX laser facility

M. Günther[1], K. Sonnabend[1], K. Vogt[2], V. Bagnoud[2], and M. Roth[1]
[2]GSI, Darmstadt, Germany; [1]Institut für Kernphysik, TU Darmstadt, Germany

We activated compound activation targets in conjunction with a novel nuclear pyrometry method [1] for the investigation of the high-energy electron and bremsstrahlung component in relativistic laser-plasma interactions using the PHELIX laser facility at GSI. We used the short pulse of the PHELIX laser with intensities of more than 10^{19} W/cm^2 and laser energies arround 100 J with a pulse duration of 700 fs. The activation targets contain several isotopes with different photo-neutron disintegration thresholds. In the peak intensity regime of a focused short pulse laser relativistic electrons are generated during the laser-solid interaction. These electrons are accelerated into the target. The subsequent deceleration of high-energy electrons inside the target leads to high-energy bremsstrahlung which induces photo-nuclear reactions within the target. After the activation we could reconstruct the initial photon spectrum and the angular distribution of the high-energy bremsstrahlung via a gamma spectroscopy, an autoradiography of the targets (Fig. 1) and a suited analysis method. We observed several decay lines of activated isotopes, up to (γ,5n)-reactions (Fig. 2). The nuclear pyrometry allows

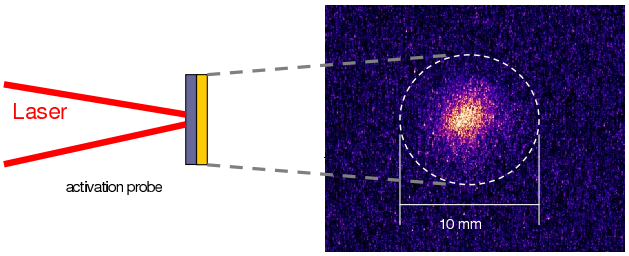

Figure 1: Left: Irradiation of an activation target by using a focused short pulse laser (schematic). Right: An autoradiograph of the activated target via Imaging Plate. This picture shows the activity distribution in the sample.

the determination of the number of bremsstrahlung photons per energy bin in a wide range of bremsstrahlung energies without any anticipated fit procedures. Furthermore, we get information about the high energetic part of the laser generated electrons concerning the spectral distribution, the average energy (temperature) and the absolute yield by using GEANT4 [2] simulations (Fig. 3). This nuclear activation diagnostic method can be used for radiation protection measurements in high-power laser applications, e.g. at the PHELIX laser. Another usage of the nuclear pyrometry method is the investigation of the relativistic laser-plasma interaction and hence the relativistic electron generation close to the interaction zone. The pyrometry is sensitive to energies above 7 MeV only. Therefore, this diagnostic is insensitive to any misleading low-energy processes. Most

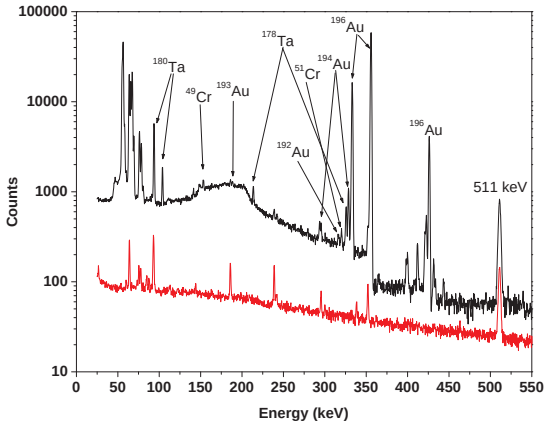

Figure 2: The gamma spectrum of an activation shot with laser energy of 118 J. The lower spectrum is background and the upper one is the decay gamma spectrum of the activated target.

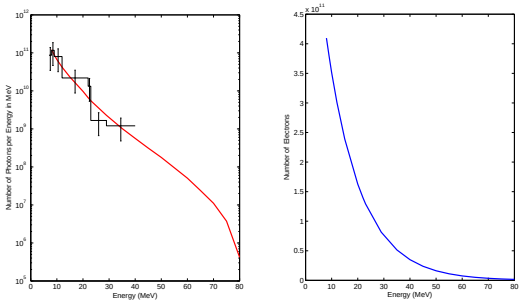

Figure 3: Left: Absolute number of bremsstrahlung photons per energy bin (stairs). The line shows the fit of bremsstrahlung spectrum using GEANT4 simulations. Right: The corresponding energy distribution of high-energy electrons. The electron distribution is Boltzmann with a temperature of k$_B$T=13 MeV.

applications depend on the relativistic electron generation, such as the laser proton acceleration [3] and laser assisted nulear physics applications [4].

References

[1] M. Günther et al., in preparation
[2] Agostinelli, S. et al., NIM A 506, 250 (2003)
[3] Hatchett, S.P. et al., Phys. Plasmas 7, 2076 (2000)
[4] Ledingham, K.W.D. et al., Science 300, 1107 (2003)

Divergence control with optimized targets for laser proton acceleration

O. Deppert[1], K. Harres[1], F. Nürnberg[1], G. Schaumann[1], M. Schollmeier[2], and M. Roth[1]

[1]Institut für Kernphysik, Technische Universität Darmstadt, Germany; [2]Sandia National Laboratories, Albuquerque NM, USA

The irradiation of thin metal foils by an ultra-intense, relativistic laser pulse leads to the generation of a highly laminar and intense proton beam accelerated from the target rear side by a mechanism called "Target-Normal-Sheath-Acceleration" [1]. This kind of acceleration mechanism strongly depends on the geometry of the target. A Gaussian-like electron sheath at target rear-side generates an electric field on the order TV/m which is responsible and formative for the acceleration of the protons. This sheath adds an energy dependent divergence to the local proton beam profile on the order of $50°$ full opening angle for a flat foil. For further applications, like the transport of the beam, it is essential to reduce the divergence in the beam profile already from the "source" of the acceleration process.

Therefore, numerical simulations were performed with the Particle-in-Cell code PSC [2] in order to analyze and optimize the proton acceleration process with respect to beam divergence. The results led to the design of different target geometries, manufactured at the target lab at TU Darmstadt. The targets consist of a hemispherical, proton focusing part and a cone-like top part for collimation, illustrated in figure 3.

Consecutive design based on PIC simulations

Based on the simulation results different target designs were compared with a reference simulation of a thin metal foil shown in figure 1. Therefore, different target parameters like the opening angle, the geometry and the length of the cone top part with its impact on the divergence could be studied. This led to a consecutive design of an optimized target which is shown in figure 3.

PIC results: flat foil at 1.6ps

Analogous to experimental data the simulation outputs an energy-over-divergence-angle distribution. For an energy interval between 14MeV and 22MeV most of the protons from the rear-side have a full opening angle between $10°$ and $30°$. For higher energies the angular distribution of the beam slightly decreases with energy down to $20°$ for 30MeV protons.

PIC results: optimized target at 1.6ps

In comparison to the results of the flat foil, the optimized target shows a completely different angular distribution. For proton energies below 10MeV the distribution is broadened with divergence angle larger $30°$. On the other hand the more interesting energy interval between 16MeV and 28MeV could be collimated down to angles smaller then $6°$. Due to strong electrostatic fields near the sharp edges

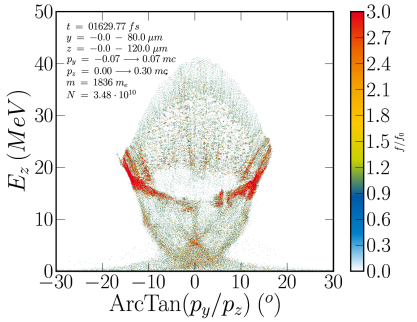

Figure 1: Reference simulation of a 3μm thin Au-foil; energy of the rear-side emitted protons over divergence angle.

of the delivery port of the optimized target the maximum proton energy is reduced to 30MeV in contrast to the flat foil with energies in the order of 40MeV.

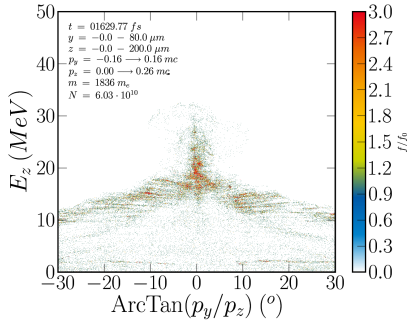

Figure 2: Simulation of an optimized hemispherical target shown in figure 3; proton energy over divergence angle.

Target fabrication

For manufacturing the sub-mm target positive forms a "micromachine" was designed. Different fabrication techniques like electroplating were used. The result is shown in figure 3.

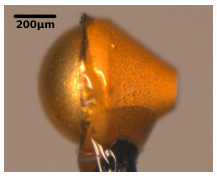

Figure 3: Optimized target for laser proton acceleration; hemispherical part (left) glued on cone top part (right); laser impinges from left.

References

[1] S.C. Wilks et al., *Energetic proton generation in ultra-intense laser-solid interactions*, Phys. Plasmas **8**, 542, 2001.

[2] H. Ruhl et al., *Classical particle simulations with the PSC code, An introduction into the PSC*, Reno USA, 2006.

[3] M. Schollmeier, *Optimization and control of laser-accelerated proton beams*, Dissertation, Technische Universität Darmstadt, 2008.

Development of a spectrometer on CVD diamond basis for heavy ion charge state measurements

W. Cayzac[1], A. Frank[1], A. Blažević[2], M. Träger[2], E. Berdermann[2], B. Voss[2], T. Heßling[2], D. Schumacher[1] and M. Roth[1]

[1]Technische Universität Darmstadt, Germany; [2] GSI, Darmstadt, Germany.

The interaction of heavy ions with hot dense laser-generated plasma, especially the energy loss of the ions, is one of the main fields of research of the plasma physics group at GSI [1]. The investigated plasma is generated by the irradiation of a thin carbon foil by intense laser beams from the *nhelix* or the PHELIX laser systems, while the heavy ions are generated by the UNILAC accelerator of GSI. The differences in the energy loss between cold matter and plasma result from two main parameters: first, the more efficient energy transfer to free electrons in the plasma and the charge state distribution of the projectile that results from the changes in the cross sections for the charge transfer processes due to the ionization of the target.

The measurement of the variation of the charge state distribution of heavy ions in plasma is the goal of this study. A spectrometer to experimentally determine this distribution was thus developed, that enables time-resolved measurements and the determination of the particle number in each charge state.

In the used experimental setup, ion beams feature 5 main charge states after exiting the plasma, that are spatially separated by a magnetic dipole at the end of a 12 m beam line. Five single detectors are thus necessary.

Due to its excellent time resolution, response speed, high sensitivity and radiation hardness, CVD diamond was chosen as detector material [2]. Simulations of the beam line properties showed that polycrystalline diamond may be used for the given application, unlike single crystal diamond. Moreover, simulations of such diamonds proved that the fluctuations in the charge collection do not exceed 5% in the experimental conditions, which makes polycrystalline diamond suitable as a detector.

Beam line simulations with Mirko [3] made it possible to find out the needed dimensions of the spectrometer. Five single detectors were thus constructed by the bonding of diamonds on ceramic boards, and positioned on a rail system (Fig.1).

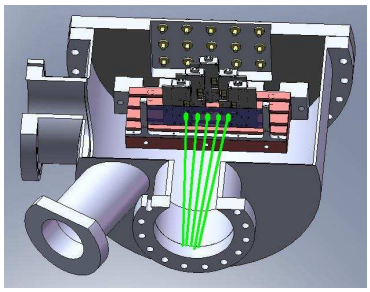

Figure 1: General view of the spectrometer, with ion beams arriving on the 5 single detectors.

$^{48}Ca^{18+}$ ions were used at an energy of 4.9 MeV/u, particle currents of 1-2 µA on the detectors and a micro bunch frequency of 108 MHz, while the 500 nm thick carbon foil was irradiated from one side by the *nhelix,* from the other side by the PHELIX laser simultaneously, with the same parameters (energy 30-40 J, pulse width of 8 ns, intensity 4×10^{11} W/cm², focus diameter 1 mm and the use of random phase plates to homogenize the laser focus profiles). The goal of this experimental scheme (setup is described in detail in [4]) is to obtain a fully ionized and homogenous plasma at the end of the laser pulses. The plasma temperature reaches 200 eV in the interaction zone with the lasers, depending on time, and the free electron density is 10^{21} cm^{-3}.

The spectrometer was successfully tested and enabled the measurement of the temporal evolution of the projectile charge state distribution after exiting the plasma (Fig.2). From 0 to 20 ns after the laser irradiation, an increase in the fraction of the 18+ charge state and a decrease of the fractions of the other charge states due to a reduction of the rates of charge transfer processes in the plasma, while from 20 to 40 ns the opposite trend is observed due to plasma expansion and cooling.

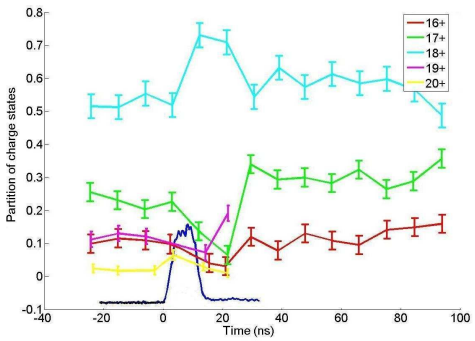

Figure 2: Example of measured charge state distribution with the 5 main charge states for ^{48}Ca ions with an incident charge state 18+. At 0 ns the lasers irradiate the target (dark blue curve). The coloured lines with error bars are the fractions of the different charge states.

References

[1] A. Frank, A. Blažević *et al.*, Phys. Rev. E, Vol. 81-2, 026401, 2010

[2] R. J. Tapper. Diamond detectors in particle physics. *Reports on Progress in Physics*, 63, August 2000

[3] B.Franczak. MIRKO, an interactive program for beam lines and synchrotrons, *Lecture Notes in Physics, Berlin Springer Verlag,* Vol.215, 1984

[4] A.Frank et al., this annual report

Lateral fast electron transport and ion acceleration in thin foils irradiated by picosecond laser pulses *

X. H. Yuan[1,5], D. C. Carroll[1], M. N. Quinn[1], X. X. Lin[2], C. Li[2] , B. Zielbauer[4], B. Aurand[4], O. Tresca[1], C. M. Brenner[1,3], R. J. Gray[1], Y. T. Li[2], D. Neely[3,1], J. Fils[4], T. Kuehl[4], M. Coury[1] and P. McKenna[1,#]

[1] Univ. Strathclyde, UK; [2] IOP, CAS, China; [3] RAL, UK; [4] GSI, Darmstadt, Germany; [5] SKLTOT, CAS, China

The transport of fast electrons in ultra-intense laser irradiated solid targets is a key issue for the fast ignition approach to inertial fusion energy and plays a crucial role in the optimization of laser-driven ion/radiation sources and study of matter in extreme conditions. Lateral spreading of the fast electron current [1, 2] can arise due to (1) fields confining electrons to a potential well on the surface giving rise to surface currents, and (2) fast electron recirculation within the target. These effects are important for fast electron transport along the inner wall of a reentry cone target and in double-cone targets for fast ignition.

We report preliminary results from an experiment using the PHELIX laser to examine the physics of lateral transport, and specifically to determine the relative importance of the two processes introduced above.

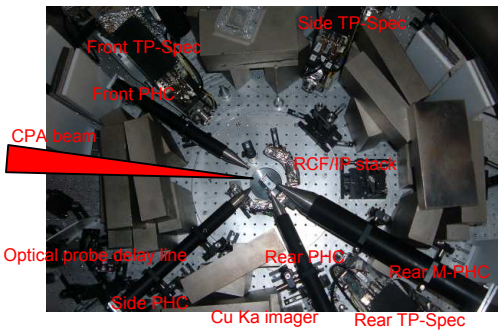

Figure 1: Experimental setup

PHELIX laser pulses, with energy of ~ 60 J on target and duration equal to 700 fs, were focussed onto foil targets to a calculated peak intensity of $1\sim2\times10^{19}$ W/cm^2. The targets were mainly Cu foils or Cu-coated metallic and insulator layered foils. The target thickness was varied in the range 20 µm to 400 µm. The target size was also varied from 5 mm x 5 mm to 0.1 mm x 0.1 mm. A range of diagnostics was used, as shown in fig 1. Five dosimetry film (RCF)/image plate (IPs) stacks surrounded the target to measure the angular distributions of emitted protons and electrons, with coarse energy resolution. Three single pinhole cameras (PHC) were located at the front, side and rear of the target to spatially image x-ray emission. One multi-pinhole camera, also located close to the rear normal direction, was used to image x-ray emission at different X-ray cut-off energies. Three Thomson Parabolic spectrometers (TP-Spec) were located along the target normal directions at both front and rear, and at 15° with respect to the target surface in the front side. These were used to determine the charge-to-mass ratio and energy distributions of ions emitted in each of these directions. A spherically bent crystal sitting below the rear single PHC was used for monochromatic imaging of Cu Kα emission.

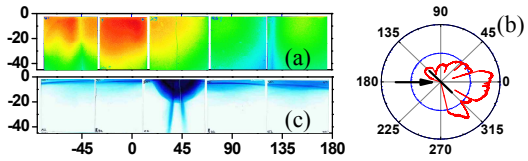

Figure 2: Angular distribution (a)-(b) Fast electrons, (c) Protons. (0°,0°) is the laser direction, and (45°,0°) is the rear normal direction of the target.

Example measurement of the spatial distribution of the fast electrons escaping the target is shown in fig. 2(a) and the polar plot fig. 2(b). Emissions peaked close to target surface are observed. Typically the beam peak direction is between laser direction and target surface. Figure 2(c) shows the corresponding spatially-resolved proton emission measurement. The highest flux and energy protons are measured along the target normal direction. However, for some conditions protons emitted from the side edge of the target with energies as high as 11 MeV have been measured. Multiple sources from both target centre and edges are then seen from TP-Spec, as shown in fig. 3(a). The X-ray pinhole cameras have revealed interesting dynamics of the fast electron currents. Figure 3(b)-(c) shows an example image of a limited mass target, with X-ray emission clearly observed at the edges of the target.

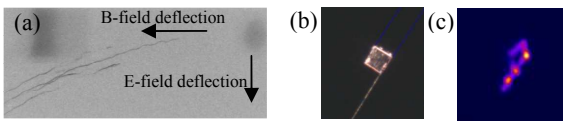

Figure 3: (a) Proton tracks from multiple sources; (b) picture of mass limited target, (c) x-ray image

A detailed analysis is underway at present to determine the sensitivity of the lateral energy transport to (1) the angle of laser incidence; (2) the lateral size of the target; (3) the thickness of the target; and (4) the conductivity of the surface layers. A full report on the results of the experiment will be presented in due course.

References

[1] P. McKenna *et al.*, Phys. Rev. Lett. **98**, 145001 (2007).

[2] Y. T. Li *et al.*, Phys. Rev. Lett. **96**, 165003 (2006).

* This work was supported by EPSRC (grant number EP/E048668/1) and LaserLab-Europe.

#p.mckenna@phys.strath.ac.uk

A 7.36 nm soft x-ray laser pumped in double-pulse single beam grazing incidence (DGRIP)

D. Zimmer*[1,2,3], D. Ros[1], V. Bagnoud[2], B. Ecker[2,3], O. Guilbaud[1], J. Habib[1], D. Hochhaus[2,3], S. Kazamias[1], B. Zielbauer[1,2], B. Aurand[2,3], P. Neumayer[2], and T. Kuehl[2,3]

[1]LASERIX-CLUPS, LIXAM UMR 8624, Université Paris-Sud 11, Bât. 350, F-91405 Orsay Cedex, France; [2]GSI Helmholtzzentrum für Schwerionenforschung GmbH, Planckstr. 1, D-64291 Darmstadt, Germany; [3]Institut für Physik, Johannes Gutenberg-Universität Mainz, Staudingerweg 7, D-55128 Mainz, Germany

We demonstrated a 7.36 nm Ni-like samarium soft x-ray laser, pumped by 36 J of a Nd:glass CPA laser. The double-pulse single-beam grazing incidence pumping (DGRIP) was applied for the efficient soft x-ray laser generation [1]. In this case the applied technique included a new single optic focusing geometry for large beam diameters, a single-pass grating compressor traveling-wave tuning capability and an optimized high energy laser double-pulse. This scheme has the potential for even shorter wavelength soft x-ray laser pumping.

A number of applications, including imaging of biological specimen and diagnostics of dense plasmas, require x-ray lasers with short wavelength and narrow bandwidth. In medical and biological research, especially attractive is the possibility to reach into the so-called "water-window", the wavelength range between the K-shell absorption edges of carbon and oxygen. A main obstacle for laser produced plasma x-ray lasers is the high pump laser energy required for the ionization and the excitation of the lasing transitions [2]. Over the last years tremendous progress was achieved towards lowering the necessary pump energy [3],[5] [8] and reaching saturated transient collisionally excited x-ray lasing down to 7 nm [4], [6], [7].

Here, we report on the application of the double-pulse single beam grazing incidence pumping (DGRIP) [10], that enables us to achieve - with a much simplified set-up - lasing down to the shortest wavelength reached to date using the transient collisional excitation scheme of laser produced plasma soft x-ray lasers [7]. The approach of [7], which used two separate laser beam lines to interact with the target, was a non-trivial complication, because of the delivery of two beams with large dimensions required by the high pump laser energy. More suitable is the approach of [8], which applied two pulses in one beam line to interact with the target. This concept was adapted in the scheme presented here, also because a similar arrangement recently proved its suitability shown by the efficient and reliable x-ray laser generation at longer wavelength [9],[10],[11]. Here the combination of a new focusing system which consists of only one 90 degrees off-axis parabola, tremendously reducing the set-up complexity compared to [8], together with a traveling-wave matching technique and the highest energy CPA double-pulse to date, short wavelength soft x-ray lasing is enabled with numerous benefits i.e. enhanced stability, reproducibility, cost decrease and improved efficiency, compared to previous experiments [7].

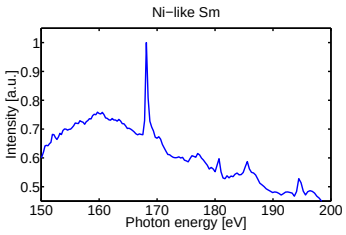

Figure 1: Ni-like Sm XRL at 168.5 eV (7.36 nm)

The generation of the Ni-like Sm x-ray laser is an important milestone for the feasibility of applying the pumping scheme also for higher pumping pulse energies, which are necessary to obtain soft x-ray laser wavelengths in the water window. With the capability of the laser facility PHELIX to bring up to 250 J double-pulse pump laser energy on the target, a Ni-like tungsten x-ray laser at 4.32 nm is conceivable. The reduction of the total pump energy below 40 J for 7 nm lasing now opens the way to take the concept to the high-repetition rate routine operation at facilities like LASERIX to optimize further the soft x-ray laser output. As an outlook the installation of a frequency doubling unit for the CPA double-pulse will provide a mixed $\omega/2\omega$ beam which might enable a more efficient laser light absorption at higher electron densities, increasing the efficiency of x-ray laser pumping, especially in the water window regime.

Acknowledgemnts to the PHELIX and LASERIX teams. Supported by Laserlab Europe. D. Zimmer is thankful for a "Bourse d'excellence d'Eiffel" grant from Égide.

References

[1] Zimmer, D. et al., submitted to Phys. Rev. A (2010)
[2] MacGowan, B. J. et al., Phys. Rev. Lett. 65, 420 (1990)
[3] Nickles, P. V. et al., Phys. Rev. Lett. 78, 2748 (1997)
[4] Dunn, J. et al, Phys. Rev. Lett. 84, 4834 (2000)
[5] Keenan, R. et al., Phys. Rev. Lett. 94, 103901 (2005)
[6] Rocca, J. J. et al., Opt. Lett. 30, 2581 (2005)
[7] King, R. E. et al., Phys. Rev. A 64, 053810 (2001)
[8] Kawachi, T. et al., Phys. Rev. A 69, 033805 (2004)
[9] Zimmer, D. et al., Opt. Express 16, 10398 (2008)
[10] Zimmer, D. et al., Opt Lett. 35, 450 (2010)
[11] Zielbauer, B. et al., Appl. Phys. B (2010)

* d.zimmer@gsi.de

Table-top high repetition rate soft x-ray laser pumped in double-pulse single beam grazing incidence (DGRIP)

D. Zimmer*[1,2,3], B. Zielbauer[1,2], M. Pittman[1], O. Guilbaud[1], J. Habib[1], S. Kazamias[1], D. Ros[1], V. Bagnoud[2], B. Ecker[2,3], D. Hochhaus[2,3], and T. Kuehl[2,3]

[1]LASERIX-CLUPS, LIXAM UMR 8624, Université Paris-Sud 11, Bât. 350, F-91405 Orsay Cedex, France; [2]GSI Helmholtzzentrum für Schwerionenforschung GmbH, Planckstr. 1, D-64291 Darmstadt, Germany; [3]Institut für Physik, Johannes Gutenberg-Universität Mainz, Staudingerweg 7, D-55128 Mainz, Germany

The paper reports on the optimization of a table-top nickel-like molybdenum transient collisionally excited soft x-ray laser (SXRL) at 18.9 nm, performed by double-pulse single beam grazing incidence pumping (DGRIP)[1]. This scheme allows for the first time the full control of the pump laser parameters including the pre-pulse duration, optimally generating the SXRL amplifier under grazing incidence. The single beam geometry of collinear double-pulse propagation guarantees the ideal overlap of the pre- and main pulse from shot to shot, resulting in a more efficient, highly stable SXRL output. SXRL energies up to 2.2 μJ are obtained with a total pump energy less than 1 J for several hours at 10 Hz repetition rate without re-alignment under once optimized double pumping pulse parameters including energy ratio, time delay, pre- and main pulse duration and line focus width.

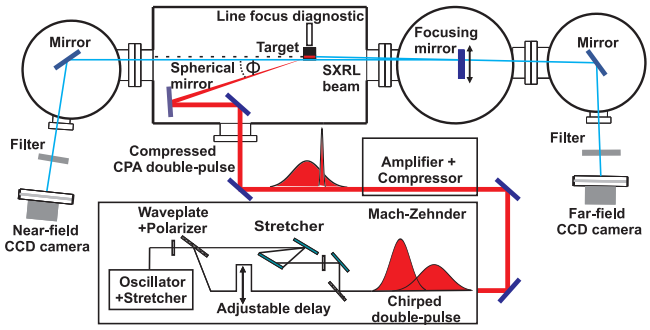

Figure 1: The insert box shows the creation of the chirped double-pulse, which is amplified and compressed. The double-pulse is then focused by a spherical mirror in a line onto the target, generating the SXRL beam propagating to the far-field diagnostic on the right or by a backreflection to the near-field diagnostic on the left.

In the laser plasma produced soft x-ray laser (SXRL) development, important steps were made to increase the efficiency of soft x-ray laser generation by introducing the transient collisional excitation scheme with traveling-wave pumping [2], non-normal incidence pumping [3] and grazing incidence pumping (GRIP) [4]. Up to now, using the suitable configuration, saturated lasing at wavelengths as low as 11 nm was observed [5], [6], enabling SXRL operation at repetition rates of 10 Hz [7]. Recently the double-pulse non-normal incidence pumping geometry joined all the important pumping principles to one more reliable and stable single beam pumping scheme [8], similar to [9], [10], [6]. In this paper an adapted version of the single beam pumping scheme in grazing incidence is carried out for 10 Hz operation, showing higher efficiency and proving its perfect suitability for high repetition rate soft x-ray lasers, and giving a promising outlook for its application in even higher repetition rate operation up to 100 Hz [11],[12].

In conclusion the introduction of the DGRIP scheme improves the efficiency and stability of table-top high-repetition soft x-ray lasers. This result shows the attractiveness of this pumping scheme for high average power operation. On one hand the low costs and the easy and rapid alignment procedure fulfill the requirements for a sophisticated installation, and on the other hand the highly stable output, compared to the jittering output of previous systems, satisfies the need for a reliable strong SXRL source. As an outlook, this system proves to be a milestone for the introduction of multiple pulse capability in Ti:sapphire CPA laser systems for future experiments.

Please find more information in [1].

References

[1] Zimmer, D. et al., Opt Lett. 35, 450 (2010)
[2] Nickles, P. V. et al., Phys. Rev. Lett. 78, 2748 (1997)
[3] Neumayer, P. et al., Appl. Phys. B 78, 957 (2004)
[4] Keenan, R.; et al., Phys. Rev. Lett. 94, 103901 (2005)
[5] Rocca, J. J. et al., Opt. Lett. 30, 2581 (2005)
[6] Gruenig, M. et al., Optics Communications 282, 267 (2009)
[7] Cassou, K.; et al., Opt. Lett. 32, 139 (2007)
[8] Zimmer, D. et al., Opt. Express 16, 10398 (2008)
[9] Kawachi, T. et al., Appl. Opt. 42, 2198 (2003).
[10] Kim, H. T. et al., Phys. Rev. A 77, 023807 (2008).
[11] Tuemmler, J. et al., Opt. Lett. 34, 1378 (2009)
[12] Furch, F. J. et al., Opt. Lett. 34, 3352 (2009)

* d.zimmer@gsi.de

On thermophysical properties of hot liquid tantalum and tungsten*

V. Ternovoi[1], S. El Moussati[2], A. Fedenev[3], A. Fertman[4], A.A. Golubev[4], D.H.H. Hoffmann[2], A. Hug[2,3], B. Ionita[2], A. Kantsyrev[4], A. Khudomyasov[4], M. Kulish[1], J. Ling[2], N. Markov[4], V. Mintsev[1], D. Nikolaev[1], A. Pyalling[1], N. Shilkin[1], V. Turtikov[4], S. Udrea[2], A. Ulrich[5], D. Varentsov[3], K. Weyrich[3], D. Yuriev[1], and Y. Zhao[6]

[1]IPCP, Chernogolovka, Russia; [2]TUD, Darmstadt, Germany; [3]GSI, Darmstadt, Germany; [4]ITEP, Moscow, Russia; [5]TUM, Munich, Germany; [6]IMP, Lanzhou, China

At the HHT area of GSI intense focused beams of energetic heavy ions are used to generate high-energy-density (HED) states in matter, or so-called warm dense matter (WDM), by their impact on solid targets. This ongoing research is currently being done in the framework of a Helmholtz-Russia Joint Research Group *"Experimental Study on WDM by Intense Heavy Ion Beams"* (HRJRG–112) with a goal to develop essential diagnostic instruments and methods for future HEDgeHOB experiments at FAIR.

Three experimental campaigns have been recently carried out at HHT with intense ($2 \cdot 10^8 - 7 \cdot 10^9$ ions/pulse) beams of $^{238}U^{73+}$ and $^{124}Xe^{48+}$ ions at 350 AMeV energy. One of the physics objectives was to study thermodynamic, transport, and optical properties of two refractory metals — tungsten and tantalum — at melting and in hot expanded liquid states. In particular, to measure electrical conductivity and to record simultaneously thermal light emission at different wavelengths and surface reflectivity of specular and diffusive types. In order to achieve a high heating uniformity, to avoid excessive boiling and hence to preserve a well-defined emitting target surface, defocused and coasting (long flat-top) beams have been used. This along with a good measurement statistics achieved by shooting many identical targets has allowed to improve the accuracy and quality of the experimental data.

One of the obtained experimental results is the dependence of temperature on the specific enthalpy $T(h)$ measured for thin tantalum and tungsten foils during quasi-isobaric heating by intense ion beams to a temperature in the range of 2000 – 6000 K. The temperature data has been recorded by a fast multi-channel optical pyrometer and the known melting temperatures T_m of Ta (3280 K) and W (3687 K) have been used for determining spectral emissivities of each target. The emissivity variation with temperature is assumed to be small for the selected wavelength channels. The specific enthalpy at the end of the melting plato h_1 has been used as a reference value for calibrating the specific energy deposition in each shot. This value has been taken as the average from previously reported experimental data that differ by less than 2.5% at this particular point. Taking the beam current profile which is also measured for each shot, the multi-channel pyrometer records are transformed this way into continuous $T(h)$ data regardless of the shot-to-shot fluctuations of the beam intensity or beam-target misalignments. The result of such processing and averaging the data from a large number of individual shots is shown in Fig. 1 together with the experimental data reported by other groups.

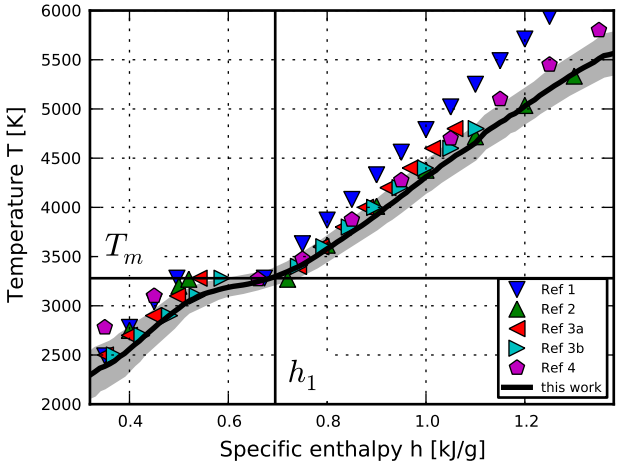

Figure 1: Temperature as a function of specific enthalpy for Ta. The solid line with its $\pm\sigma$ confidence corridor is the result of this work.

From the obtained experimental data one can determine the melting heat but with a limited accuracy due to an uncertainty in start of melting. Furthermore, the isobaric heat capacity C_p was determined for liquid Ta and W, and $C_p^{\mathrm{Ta}} = 0.284 \pm 0.025\,\mathrm{J/gK}$. This value is only slightly higher than those reported in [2,4] but differs considerably from the data in [1].

The above reported set of thermodynamic data for hot liquid Ta and W will be further enhanced when the laser backlighting ($V(T)$) and electrical conductivity ($\sigma(T)$) records which were also obtained during the experiments will be processed and analysed. A more precise physical temperature evaluation procedure may also be worked out based on the recorded reflectivity data or by fitting a temperature-dependent emissivity model to the multi-wavelength pyrometer records.

References

[1] A. Berthault et al., Int. J. Thermophysics 7 (1986) 167.

[2] G.R. Gathers, Int. J. Thermophysics 4 (1983) 149.

[3] G. Pottlacher et al., Int. J. Thermophysics 23 (2002) 1281.

[4] H. Jäger et al., Int. J. Thermophysics 13 (1992) 83.

*Work supported by HRJRG-112, INTAS 06-1000012-8707, BMBF 06DA9033-I, WTZ CHN-08/50 and FRRC.

Non-contact electrical conductivity measurements of heavy ion driven warm dense matter*

J. Ling[1], S. Udrea[1], N. Shilkin[2], S. El Moussati[1], A. Fedenev[3], A. Fertman[4], D.H.H. Hoffmann[1], A. Hug[1,3], A. Kantsyrev[4], A. Khudomyasov[4], M. Kulish[2], N. Markov[4], V. Mintsev[2], D. Nikolaev[2], V. Ternovoi[2], V. Turtikov[4], A. Ulrich[5], D. Varentsov[3], D. Yuriev[2], and Y. Zhao[6]

[1]TUD, Darmstadt, Germany; [2]IPCP, Chernogolovka, Russia; [3]GSI, Darmstadt, Germany; [4]ITEP, Moscow, Russia; [5]TUM, Garching, Germany; [6]IMP, Lanzhou, China

Characterisation of matter irradiated by intense, focused particle beams is of special interest for many research areas including nuclear (Super–FRS at FAIR) [1] and particle physics (LHC at CERN) [2]. Over the past few years, a series of measurements of the electrical resistivity of heavy ion beam generated warm dense matter (WDM) has been performed at the HHT experimental area of GSI [3]. These measurements have mostly been based on the four-point method, which gives good results, but lacks spatial resolution. Thus the development of an experimental setup for non-contact measurements by eddy currents has been initiated and first proof of principle experiments have been performed [4] with cylindrical geometry targets. These showed several technical issues that can be mitigated by planar geometry targets, requiring however a special design and higher technological effort.

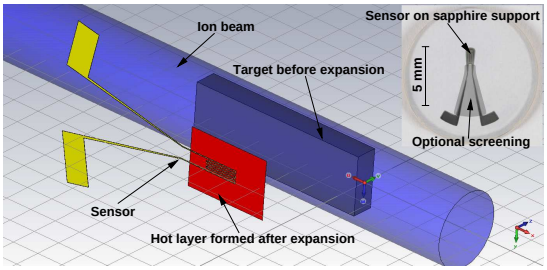

Figure 1: Principle scheme of electrical conductivity measurements using a planar geometry setup and the sensor developed for this purpose.

In this report we present the development of planar targets for non-contact measurements of the electrical conductivity of WDM and results obtained from numerical simulations and first experimental tests.

The principle of the experiment is shown in Fig. 1. A slab of the investigated material is heated by a focused, intense heavy ion beam. The heated material expands to approach the sensor for the non-contact measurement. Here a hot and relatively low density material layer builds up within few tens of nanoseconds. The layer then cools down and gains in density. If the sensor can withstand the impact with the expanding material, a conductivity measurement can be performed for all the states reached by the layer.

The sensor (see Fig. 1) has been designed as a stripline structure made of successive thin layers of titanium and gold deposited on a 1 mm thick sapphire substrate. The strip line is 10 μm thick and covered by a 2.5 μm thick sapphire layer to ensure separation from the target material. Sapphire has been the material of choice for the support and the insulating layer because of its good mechanical and thermal properties.

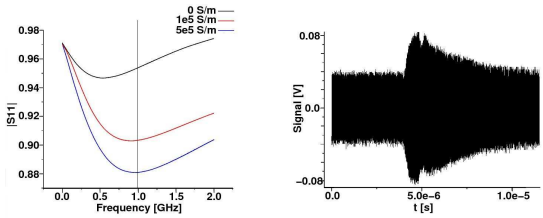

Figure 2: Amplitude of the simulated sensor S_{11} parameter; raw experimental signal obtained during first tests

The sensor acts like an antenna and is feeded by a high frequency signal up to a few GHz. The impedance of the sensor changes if a conductor is placed in its proximity. This change is used for the measurement of the electrical conductivity of the heated target material. To assess the impedance of the sensor in the presence of materials with different electrical conductivities extensive numerical simulations using CST Microwave Studio have been performed (see Fig. 2) showing that one can distinguish between them by using such a sensor.

Finally a beam time test has been performed in 2009 and one of the raw signals is shown in Fig. 2. The change of the signal amplitude following the heating and expansion of the target material is a clear sign of the presence of a conductig layer at the sensor and a therefore modified impedance. A complete analysis of the data is currently performed, and further experiments are planned for 2010.

References

[1] M. Winkler et al., GSI Report 2009-1 (2009) p. 86

[2] N.A. Tahir et al., J. Appl. Phys. 97 (2005) p. 083532

[3] S. Udrea et al., J. Phys. A: Math. Gen. 39 (2006) p. 4743

[4] S. Udrea et al., GSI Report 2009-1 (2009) p. 325

* Work supported by BMBF, INTAS and HRJRG

Spectroscopic studies on interaction of intense focused heavy ion beams with gas targets *

A. Fedenev[1], S. El Moussati[2], A. Fertman[3], A. Golubev[3], D. Hoffmann[2], A. Hug[1,2], B. Ionita[2], A. Kantsyrev[3], A. Khudomyasov[3], M. Kulish[4], J. Ling[2], N. Markov[3], V. Mintsev[4], D. Nikolaev[4], N. Shilkin[4], V. Ternovoi[4], V. Turtikov[3], S. Udrea[2], A. Ulrich[5], D. Varentsov[1], K. Weyrich[1], J. Wieser[6], D. Yuriev[4], and Y. Zhao[7]

[1]GSI, Darmstadt, Germany; [2]TUD, Darmstadt, Germany; [3]ITEP, Moscow, Russia; [4]IPCP, Chernogolovka, Russia; [5]TUM, Munich, Germany; [6]Optimare GmbH, Wilhelmshaven, Germany; [7]IMP, Lanzhou, China

It is well known that beams of energetic particles traversing gas targets may be observed in the visible spectral range due to the glow which is induced by the interaction of the projectiles with the gas atoms or molecules. However, it is by far not obvious that the spatial shape of the glow intensity represents the beam profile in a quantitative way. Therefore we are trying to find conditions where this is the case by performing spectroscopic studies of the light emitted from particle beam excited gas targets.

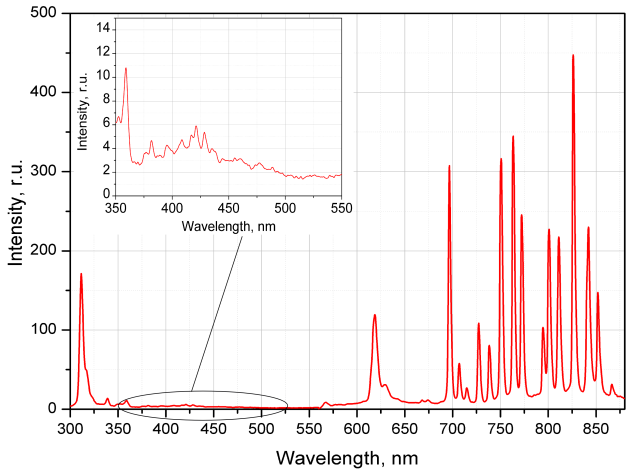

Figure 1: Ar spectrum: 300mbar, grating 150grv/mm (The instrumental response function is applied)

One concept which we follow is to use rare gases as the target material since they are chemically stable when they are irradiated. Another possible target gas is nitrogen. Emission spectra for various gas densities and beam intensities are observed. The goal is to find emission features (spectral lines or molecular bands) which are in an ideal case only emitted due to direct excitation by the projectiles and for which the emission time is short compared with the hydrodynamic expansion time of the target gas. If in addition to these conditions the light output is linear or at least quantitatively related to the flux of the projectiles it should be possible to accurately measure the beam profiles of the particle beam.

In earlier studies at the Munich Tandem accelerator we had found that argon ion lines (ArII) are only weakly excited by the secondary electrons and should fulfill most of the conditions stated above. Experiments with optical filters for the corresponding wavelength range have already been performed and an influence of the selected wavelength range on the registered beam profiles has been demonstrated [1]. The underlying spectroscopy, however, is not yet fully developed. Spectroscopic experiments have therefore been performed at the HHT target station of the SIS18 in 2009. An overview spectrum emitted from argon excited by a pulsed $350 AMeV$ ^{238}U beam with $800 ns$ pulse length and $2 \cdot 10^9$ projectiles per pulse is shown in Fig.1. The spectrum is unfortunately still dominated by impurity lines of nitrogen and OH* (see e.g. [2, 3]). The $4p - 4s$ ArI lines appear strongly in the red and near infrared. Some of the ArII lines which we had aimed at for measuring beam profiles do appear but they are very weak. It was also found that they ride on a yet unidentified continuum. The intensity of this continuum increases with pressure.

Additional experiments at the Munich Tandem accelerator in which we will compare the excitation cross sections of argon ion lines for heavy ion and electron excitation, will be carried out in March 2010.

Further spectroscopic experiments with improved gas purity at the HHT target station at GSI are planned for May 2010.

References

[1] *D. Varentsov et al.*, Transverse Optical Diagnostics for Intense Focused Heavy Ion Beams, *CPP, Volume 48 Issue 8 , p. 543 - 594 (2008)*

[2] *Herzberg G.*, Molecular spectra and molecular structure. I. Spectra of diatomic molecules, *Van Nostrand Company, Inc., Princeton, 1950.*

[3] *A. Morozov et al.*, Ultraviolet emission from argon water-vapor mixtures excited with low-energy electron beams, *Appl. Phys. Lett. Vol. 86, Issue 1, 011502 (2005)*

* Work supported by HRJRG-112, INTAS 06-1000012-8707, BMBF 06DA9033-I, WTZ CHN-08/50 and FRRC.

Contrast Improvement of Ion Bunches for Plasma Physics Experiments

A. Tauschwitz[1], U. Blell[1], B. Ecker[1], D. Hochhaus[1,3], J. Jacoby[2], P. Neumayer[1,3], J. Otto[2], P. Spiller[1], An. Tauschwitz[2,3], J. Wiechula[2]

[1]GSI, Darmstadt, Germany; [2]Univ. Frankfurt, Germany, [3]Extreme Matter Institute EMMI, Germany

Most plasma physics experiments that use ion beam heating need short bunches. To accommodate this requirement the RF system in the SIS is used to produce a single compressed ion bunch. Typical examples of such bunches were recorded in two beamtimes at the HHT experimental area in 2009 and are shown in Fig. 1. The bunch form is measured by a fast current transformer in the beamline. The bunch has a rise time exceeding 100 ns and a prepulse of typically 200ns. A reduction of the prepulse intensity and a better compression of the bunch can be achieved by careful but very time consuming optimization of the HF settings. This is not possible for the rise time which is limited to about 100 ns. Such optimized settings can usually not be preserved over an extended period of time during multi user operation of the SIS.

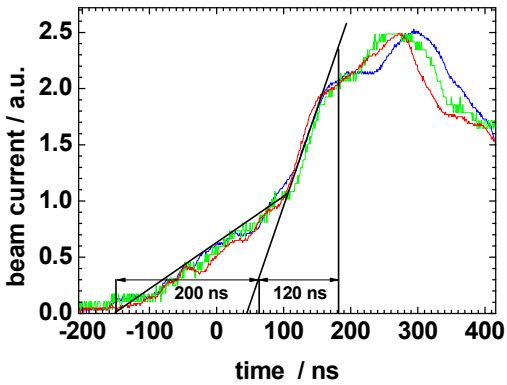

Figure 1: Typical form of bunched beams at 250 MeV/u.

A simple and reliable way to steepen the leading edge of the bunch can be achieved by use of the SIS kicker magnet. While the kicker is normally ramped up between two bunches that are circulating in the SIS the ramp can be used to cut off the prepulse and part of the rising edge of the circulating bunch. Although the electrical rise time of the kicker is 90 ns the resulting rise time of the ion bunch at the target is much shorter since the beam is deflected into the acceptance of the beam transport system only close to the flat top of the kicker current. The kicker pulse can moreover be shortened to cut additionally into the falling edge of the bunch or to shorten the flat-top length.

Fig. 2 shows typical bunches for different kick-pulse settings. Tests were done with a U^{73+} beam with 250 MeV/u and an intensity of about $3 \cdot 10^9$ ions/bunch. The measured rise time (10% to 90% of peak intensity) is below 25 ns. The slowly falling bunch slope is caused by transmission losses in the 70 m long cable between current transformer and oscilloscope. Similar losses can be expected on the rising slope which indicates that the real rise time is even faster than the measured 25 ns. To produce the longest bunch shown in fig. 2 the kick-start signal was set 130 ns earlier than for the other three bunches. In this case the rising slope is somewhat slower because the rise time of the kicker is folded with the slowly rising slope of the ion bunch.

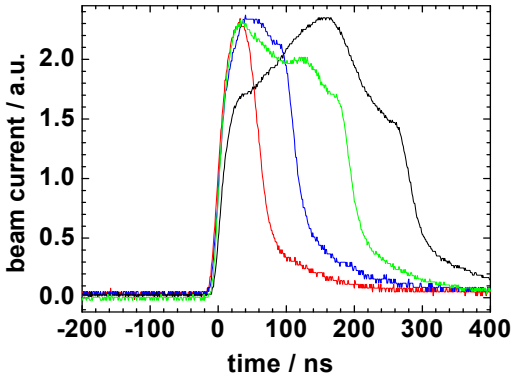

Figure 2: Ion bunches of different length produced by cutting of the circulating bunch with the kicker magnet.

An impact of the described 'bunch trimming' with the kicker on the focusability or on the spatial stability of the beam was not observed. Although a movement of the focal spot during the rising edge of the bunch is principally expected this effect could not be detected in time integrating measurements of the focal spot. Irrespectably of the kicker settings the beam was producing round holes of about 500 µm diameter in a 280 nm thick gold foil.

A high temporal contrast of the bunch is of large importance for experiments using thin targets. Examples are measurements of spectrally resolved opacities in the XUV range [1] which use target foils of few hundred nm thickness and a proposed program to measure EOS data using stacks of foil targets with few µm thicknesses [2]. The improved temporal bunch structure does not only increase the energy that can be deposited in a target before disintegration but also improves the reproducibility of experiments significantly.

References

[1] An. Tauschwitz, V.G. Novikov, A. Tauschwitz, F.B. Rosmej, J. Abdallah, E. Onkels, J. Jacoby, J.A. Maruhn, "Intense ion beams as a tool for opacity measurements in warm dense matter", Appl Phys B (2009) 95, 13

[2] An. Tauschwitz, V. Efremov, J.A. Maruhn, F.B. Rosmej, A. Tauschwitz, "Quasi-static heating of stack targets with intense ion beams for equation of state measurements", NIM B 267 (2009) 2449

Ion-optical design for PRIOR*

V. Turtikov[1], D. Varentsov[2], F. Merrill[3], A. Hug[2,4], S. Kolesnikov[5], V. Skachkov[1], S. Udrea[4], and K. Weyrich[2]

[1]ITEP, Moscow, Russia; [2]GSI, Darmstadt, Germany; [3]LANL, Los Alamos, USA; [4]TUD, Darmstadt, Germany; [5]IPCP, Chernogolovka, Russia

Proton radiography or microscopy is a novel technique for probing the interior of dense objects in dynamic experiments by mono-energetic beams of GeV-energy protons. A special system of magnetic lenses is employed for imaging and aberrations correction. Using this technique, one can measure areal density of a thick sample with sub-percent accuracy. The spatial resolution is a few micrometers over a centimeter-wide field of view, whereas the time resolution is on the nanosecond scale.

Recently an international project PRIOR (*Proton Microscope for FAIR*) [1] was started for developing of a new proton microscopy facility according to the requirements of the HEDgeHOB collaboration experiments at FAIR. The PRIOR microscope will be able to initially be fielded at GSI for testing and commissioning with the same SIS-18 proton beam as later used at FAIR. Its installation at the HHT experimental area of GSI and commissioning in static and dynamic experiments with a 4.5 GeV proton beam from the SIS-18 synchrotron is currently under discussion.

The PRIOR magnetic lens system is designed utilizing quadrupole magnets as focusing elements. The most cost effective quadrupole technology for both fabrication and operation costs are permanent magnet quadrupoles (PMQ) constructed from rare earth permanent magnet material (REPM). Having a small aperture, PMQ can reach high field gradients while maintaining high magnetization. PMQ were successfully employed in proton microscopes for 0.8 GeV proton beams at LANL [2] and at ITEP [3]. A prototype of the PRIOR PMQ with a 15 mm aperture and 238 T/m magnetic field gradient has been recently constructed at ITEP. For enlarging the field of view of the imaging optics, 30 mm aperture PMQs are also considered for PRIOR.

Table 1: Key parameters of the PRIOR proton microscope.

Parameter	*Value*
Proton energy	4.5 GeV
"Short" quadrupole length	110 mm
"Long" quadrupole length	220 mm
L1 (object to first quad)	1.0 m
L2 (first to second)	0.202 m
L3 (second to third)	0.346 m
L4 (last to image)	8.25 m
Horizontal chromatic length, C_x	2.74 m
Vertical chromatic length, C_y	2.40 m
Angular acceptance	5 mrad

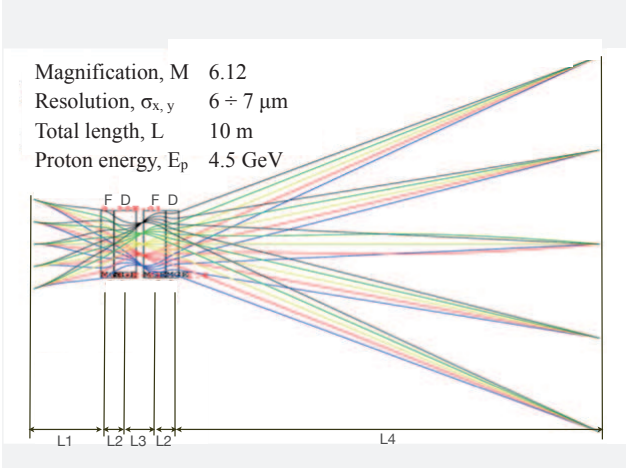

Figure 1: Ion-optical layout of the PRIOR lens system.

In order to be able to field the PRIOR setup at the HHT area, the present design study assumes the total length of the system of 10 m. COSY Infinity beam dynamics code [4] was used for optimizing the ion-optical design. The results of the simulations and the key parameters of the PRIOR setup are shown in Table 1 and Figure 1.

The spatial resolution of the PRIOR lens system for a properly matched beam has be determined as a Gaussian line spread function with an RMS of $\sigma_{x,y} = 6 - 7\,\mu\mathrm{m}$. For the angular acceptance of 5 mrad it should be possible to accurately reconstruct the areal density distributions of the targets up to $20\,\mathrm{g/cm^2}$.

Initially developed on a present GSI beam line, PRIOR can become an international user facility for proton microscopy. Such a worldwide unique proton microscope facility will provide at GSI and at FAIR a capability for unparalleled high-precision experiments with great discovery potential at the leading edges of plasma physics, high energy density physics, and materials research [5].

References

[1] PRIOR Technical Design Report, May 2009.

[2] T. Mottershead et al., Proc. PAC 2003.

[3] A. Golubev et al., Atomic Energy 104 (2008) 134.

[4] K. Makino, M. Berz, NIM A 558 (2006) 346.

[5] *1st Workshop on High Energy Proton Microscopy*, GSI, Darmstadt, Aug. 24–25, 2009, `http://www-aix.gsi.de/conferences/HEPM2009`.

* Work supported by HRJRG-112 and FRRC.

Matching the laser generated p- bunch into a CH-DTL

A.Almomani[1], M. Droba[1], U. Ratzinger[1] and I. Hofmann[2]
[1]IAP, Frankfurt University, Germany; [2]GSI, Darmstadt, Germany

Introduction

A high intensity proton beam produced by a powerful laser (PHELIX), could be injected into linac at energies of ten to several tens of MeV. A CH- structure is suggested as linac structure because of its high gradient [1, 2]. Option and the simulation tools by LORASR and LASIN are presented.

Pulsed Magnetic Solenoid

A new 3D-PIC code LASIN which was invented at IAP-Frankfurt, was used for multi-particle tracking through the solenoidal magnetic fields and its fringing fields. The magnetic solenoid of length 72 mm with inner and outer diameter 44 and 76 mm, respectively, was used. The solenoid is located 15 mm behind the target to focus and match the proton beam of energy 10 MeV into the cavity.

In order to investigate the chromatic and geometric aberrations, the simulations were done for different angles with different momentum spreads. Figure 1 shows the emittance ratio versus the momentum spread (Δp) in percent for three different opening angles. The emittance growth with momentum spread is an evidence for chromatic effect, while the geometric effect can be seen for the growth of different angles at the same momentum spread.

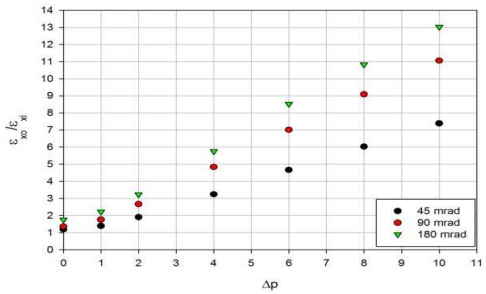

Figure 1: Emittance ratio versus Δp (%)

Prototype Cavity for High Intensity p- linac

With respect to laser accelerated beams, the capability of CH- structure linac for high current beams has been investigated. A coupled 325.244 MHz CH- cavity was simulated for 500 mA.

The design was used for FAIR proton linac which will be tested at the end 2010/early 2011[2].

Both longitudinal and transverse beam dynamics were studied by LORASR code.

The emittance growth along the structure was less than 45% in longitudinal plane and about 20% in transverse planes.

Matching into CH-DTL by Solenoid

A new design was proposed to optimize the emittance values with comparable with actual values from laser.

In this design, the magnetic solenoid was studied as a part of it. This design is operated at 325.244 MHz. It consists of 10 gaps to accelerate the proton from 10 – 17.4 MeV within 0.60 m (Figure 2). The beam parameters are summarized in table 1.

Table 1: Emittance values for the input and output distribution.

Current	Emittance	Input	Output
500 mA	ε_{tr}	0.33	0.53 mm.mrad
	ε_{long}	3.22	4.08 keV.ns

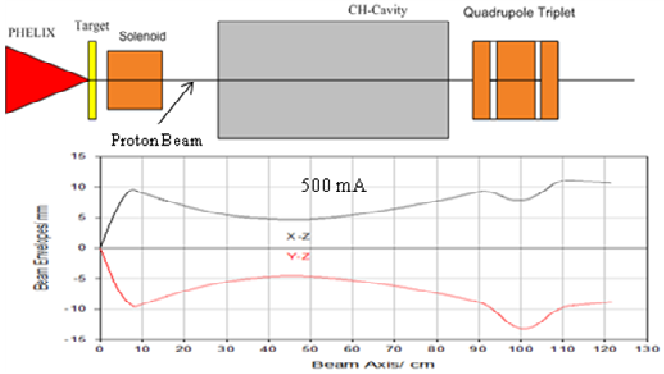

Figure2: Transverse Beam envelopes for the structure

Emittance behind the Foil

The proton pulse has a length of 500 fs which means that the emittance values are quite small (ε_{long} = 0.0193 keV.ns, and $\varepsilon_{tr.}$ = 0.099 mm.mrad) originally. For such small emittance beams, the emittance growth will be a problem especially for the longitudinal plane which may show factors of 100 and more. To reduce this growth it is better to increase the length of the proton pulse. It means that one main task of this project will be to find matching tools between the laser spot at the starting point and the injection into the cavity which is not only shape the emittance areas but also give them reasonable absolute numbers. Let's call it a well controlled emittance growth process. One way towards better matching of absolute numbers would be a significant increase in beam energy from the laser injector.

References

[1] U. Ratzinger et al., "A 70-MeV Proton LINAC for the FAIR Facility Based in CH- Cavities", Proc. of LINAC06, Knoxville, Tennessee, USA, pp. 526-530.

[2] G. Clemente et al., "Development of a Coupled CH Structure for the GSI Proton Injector", Proc. of PAC07, Albuquerque, New Mexico, USA, pp. 1428-1430.

Ponderomotive ion acceleration in dense plasmas at super-high laser intensities*

T. Schlegel† [1,2], N. Naumova[3], and V. Tikhonchuk[4]

[1]GSI, Darmstadt, Germany; [2]Helmholtz-Institute, Jena, Germany; [3]LOA, ENSTA, Ecole Polytechnique, Palaiseau, France; [4]CELIA, Université Bordeaux, France

Short laser pulses with highest intensities as proposed in the Extreme Light Infrastructure (ELI) project [1] open new prospects for the production of intense beams of energetic ions from overdense plasmas. A simple analytical model and numerical simulations demonstrate that laser pulses with intensities exceeding $10^{22}\,\mathrm{W/cm^2}$ may efficiently accelerate ions to high energies up to a few GeV. Maximum ion energy and the energy spectrum of the accelerated ions can be tuned by an appropriate choice of laser pulse intensity and duration at a given plasma density distribution. Such very intense and highly-directed particle beams may serve as drivers for isochoric heating of dense plasmas on a short time scale. Their properties also serve as the basis of the fast-ion-ignition proposal [2], where the precompressed target core should be heated to thermonuclear fusion conditions during the stagnation phase of the fusion pellet by *in situ* accelerated deuterium/ tritium ions with energies matching the fuel areal density of the core.

Under certain conditions, the ion acceleration process can be described by a quasi-stationary laser piston model [3], which was tested successfully with help of PIC simulations in strongly overdense plasmas. Equating the momentum fluxes of laser photons and plasma particles in the reference frame of the moving piston, where ions and electrons are propagating towards the piston and are being elastically reflected there with the same velocity as that of the piston, $v_f = \beta_f c$, the expression $\beta_f = \frac{B}{1+B}$ has been obtained, with $B = (I/\rho c^3)^{1/2}$ and $\rho = n_i m_i$, the plasma mass density. Relating the intensity I with the dimensionless vector potential a_0 of the incoming laser field, $I = \alpha a_0^2 n_c m_e c^3$, where $\alpha = 1$ for circularly polarized light, $\alpha = 1/2$ for linear polarization, n_c is the critical plasma density, we can also write $B = a_0\sqrt{\alpha n_c m_e/n_i m_i}$.

Since we assume that all electrons on the propagation path of the laser wave are pushed forward by the strong ponderomotive force, the laser piston may be described as a double layer consisting of an electron sheath located in the upstream region and an ion charge separation layer behind it. The peak value of the electrostatic field arising at the common boundary of both layers can be estimated theoretically as $E_{x,max} \simeq 2a_0\frac{m_e\omega c}{e}\sqrt{\frac{1-\beta_f}{1+\beta_f}}$. The ion kinetic energy equals $\varepsilon_i = m_i c^2(\gamma_i - 1) = 2m_i c^2\frac{B^2}{1+2B}$. The upper relations show that the quantities v_f and ε_i will change during the propagation of a laser pulse with varying maximum intensity or in the case of an inhomogeneous plasma. The piston slows down upon reaching plasma regions with increasing density. For a homogeneous plasma we find the reflection coefficient of the laser light in the laboratory frame, $R = (1-\beta_f)/(1+\beta_f)$, and the energetic efficiency of the laser driven ion acceleration $A = 1 - R = 2B/(1+2B)$. In case of an inhomgeneous plasma, we gain average numbers taking into account the density dependence of β_f. Obviously, the higher the piston velocity is, the more efficient is the process of energy deposition into ions. Keeping the parameter B constant means that one needs to fix a ratio $a_0^2 n_c/n_e$, where $n_e = n_i$ is assumed for simplicity. The latter expression determines a proportionality $n_e/a_0 n_c \propto a_0$, which can be directly related to the condition for overdense, non-transparent plasma $n_e/a_0 n_c \geq 1$, a necessary prerequisite for the piston regime. Therefore in order to accelerate bulk ions up to a specific energy, higher laser intensities provide better conditions in terms of keeping the plasma overcritical.

Achievable ion energies and the corresponding acceleration efficiencies in dependence on incident laser intensity are plotted in Fig. 1 for several values $n_e/a_0 n_c$. As we observed in PIC simulations, super-high intensity may sustain the plasma acceleration in the laser piston regime even for values of $n_e/a_0 n_c$ less than unity, providing simultaneously a more efficient acceleration and higher ion energies.

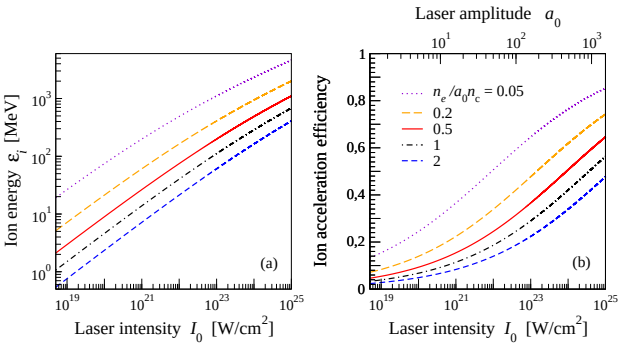

Figure 1: Laser piston model: dependencies of (a) ion (deuterium) energy and (b) ion acceleration efficiency on laser intensity for particular values of $n_e/a_0 n_c$.

References

[1] http://www.eli-laser.eu/; E. Gerstner, Nature 446 (2007) 16.

[2] N. Naumova, T. Schlegel, V.T. Tikhonchuk, C. Labaune, I.V. Sokolov, G. Mourou, Phys. Rev. Lett. 102 (2009) 025002.

[3] T. Schlegel, N. Naumova, V. T. Tikhonchuk, C. Labaune, I.V. Sokolov, G. Mourou, Phys. Plasmas 16 (2009) 083103.

* Work supported by the European Commission under contract ELI pp 212105 in the framework of the program FP7 Infrastructures-2007-1

† t.schlegel@gsi.de

Two-sided laser irradiation of thin carbon foils for ion stopping experiments

An. Tauschwitz[1,2], M.M. Basko[2,3], V.G. Novikov[4], A. Grushin[4], and J. Maruhn[2]

[1]EMMI, Darmstadt, Germany; [2]University of Frankfurt, Germany; [3]ITEP, Moscow, Russia; [4]KIAM, Moscow, Russia

We consider a C-foil irradiated from opposite sides by two laser beams. The plasma produced by the laser interaction is used for ion stopping experiments at the UNILAC accelerator at GSI. The presented calculations were done to prepare the experimental campaign in September 2009. In the experiment, the beams from the Phelix and nhelix laser systems were combined. It is assumed that the beam parameters of both lasers are identical. The laser wavelength is $\lambda = 1.064\,\mu$m. The foot-to-foot duration of the laser pulse is 13 ns. The rising and falling edges are 3 ns long, the flat top has a duration of 7 ns. The calculations were done for three different maximum laser intensities, $I_l = 2, 4$ and 6×10^{11} W/cm^2. The radial distribution of the laser intensity was approximated by a flat top 0.9 mm in diameter with Lorentzian wings. In the present simulations no account was made of focal non-uniformities (although intensity variations of some $\pm$50% on a spatial scale of 50–100 μm have actually been measured), due to which the irradiated foil may break into clumps that would eventually affect the ion stopping measurements.

The calculations were performed with the recently developed 2D radiation-hydrodynamics code RALEF-2D [1]. The code uses a second-order Godunov-like scheme on a structured adaptive quadrilateral grid. Heat conduction and radiation transport are treated on the basis of a symmetric semi-implicit method. The quasi-steady equation of radiation transport is solved by a short-characteristic method. The laser absorption is described by the Kramers formula for the inverse bremsstrahlung, ignoring refraction and reflection of the laser beam. The problem was simulated in the Cartesian (x, y) geometry rather than in the axisymmetric (r, z) geometry. The equation of state used in the simulations is described in [2]. The thermal conduction coefficient and spectral opacities have been generated by the THERMOS code [3].

In the initial state we took half of a C-foil with a total linear density $\rho x = 0.1$ mg/cm^2. The centre of the foil was placed at the origin of the coordinate system, with the y-axis treated as a reflective boundary. The laser beam is incident along the x-axis. Fig. 1 shows the specific power deposition due to the laser beam, $q_{\rm las}$, heat conduction, $q_{\rm tcn}$, thermal radiation, $q_{\rm rad}$, and their sum, q_Σ, at the laser axis for $I_l = 6 \times 10^{11}$ W/cm^2 at $t = 3$ ns. The maximum of the laser heating corresponds to the critical density. Thermal radiation carries away about 10% of the energy deposited by the laser. A 2D effect in the hydro flow causes mass reduction along the axis of the laser, which has to be taken into account in the analysis of the stopping data. In Fig. 2 the time evolution of the ion ionization degree in the centre of the foil is presented for three laser intensities. The initial peak at $t \lesssim 1$ ns is a result of shock compression. The foil is fully ionized by $t = 6.7$ ns for $I_l = 6 \times 10^{11}$ W/cm^2, and by $t = 8.9$ ns for 4×10^{11} W/cm^2. For the laser intensity $I_l = 2 \times 10^{11}$ W/cm^2 full ionization is not reached.

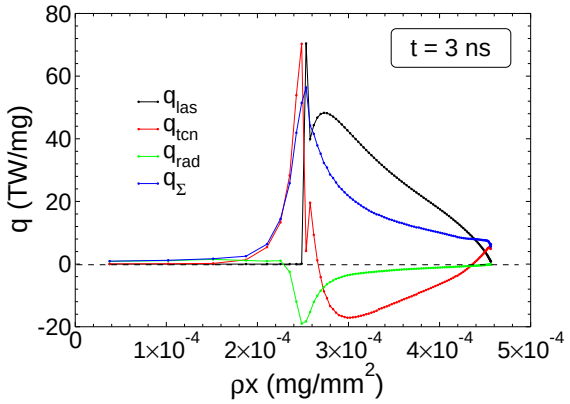

Figure 1: Specific power deposition due to the laser beam, $q_{\rm las}$, heat conduction, $q_{\rm tcn}$ and thermal radiation, $q_{\rm rad}$; $q_\Sigma = q_{\rm las} + q_{\rm tcn} + q_{\rm rad}$.

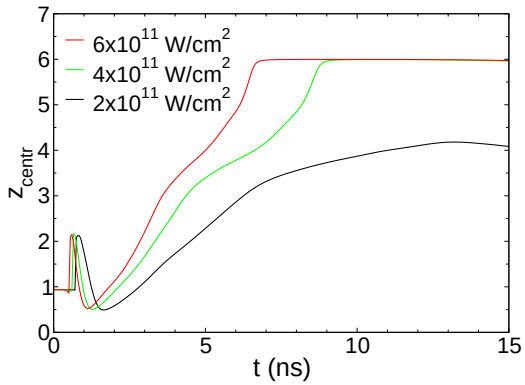

Figure 2: Ionization degree in the centre of the C-foil as a function of time; $I_l = 2, 4$ and 6×10^{11} W/cm^2.

References

[1] M.M. Basko, J. Maruhn, and An. Tauschwitz, *Development of a 2D radiation-hydrodynamics code RALEF for laser plasma simulations*, this report.

[2] M.M. Basko, Teplofiz. Vys. Temper. 23 (1985) 483 (English translation: Sov. High Temper. 23 (1985) 388).

[3] A.F. Nikiforov, V.G. Novikov, V.B. Uvarov, *Quantum-statistical models of hot dense matter: methods for computation of opacity and equation of state*, Birkhauser, 2005.

Development of a 2D radiation-hydrodynamics code RALEF for laser plasma simulations

M.M. Basko*[1,2], J. Maruhn[2], and An. Tauschwitz[2,3]

[1]ITEP, Moscow, Russia; [2]ITP, University of Frankfurt am Main, Germany; [3]EMMI, GSI Darmstadt, Germany

In 2009 a major next step was made in our effort to develop a two-dimensional (2D) radiation-hydrodynamics code for laser plasma simulations, namely, a new scheme for solving the radiation transport equation has been constructed and tested. The new code has been named RALEF-2D (Radiative Arbitrary Lagrangian-Eulerian Fluid dynamics).

The RALEF-2D code is based on the CAVEAT hydrodynamics package [1], augmented with a recently developed thermal conduction module [2]. The equation of spectral radiation transfer

$$\vec{\Omega}\cdot\nabla I_\nu = k_\nu\,(B_\nu - I_\nu) \qquad (1)$$

is solved in the quasi-static approximation, where the conduction and the radiation-coupling terms can be efficiently combined within a unified symmetric semi-implicit approach for *time* discretization of the fluid energy equation [2]. A non-trivial issue for *spatial* discretization of Eq. (1) together with the radiative heating term

$$Q_r = -\,\mathrm{div}\int_0^\infty d\nu \int_{4\pi} I_\nu\,\vec{\Omega}\,d\vec{\Omega} \qquad (2)$$

is correct reproduction of the diffusion limit on distorted non-orthogonal grids.

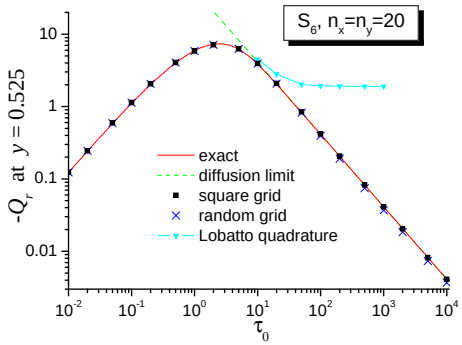

Figure 1: Radiative cooling rate $-Q_r$ at the center of a planar slab as a function of its optical thickness τ_0. The RALEF results, obtained on a 20×20 orthogonal and a 20×20 random grids, are compared with the exact solution.

In our scheme, we use the classical S_n method to treat the angular dependence of the radiation intensity $I_\nu = I_\nu(t,\vec{x},\vec{\Omega})$, and the method of short characteristics to integrate Eq. (1). The latter has a decisive advantage that every grid cell receives the same number of light rays. Correct transition to the diffusion limit, illustrated in Fig. 1 with a test problem of radiative cooling of a planar slab with a prescribed profile of the source function $B_\nu(y) = \sin(\pi y)$, $0 \le y \le 1$, is achieved by a special combination of the first- and second-order interpolation schemes in finite-difference approximation of Eqs. (1) and (2).

The capability of the RALEF code to model laser plasmas is illustrated in Fig. 2, which shows the advanced nonlinear stage of hydrodynamic instability in a thin carbon foil, irradiated by a laser pulse propagating from right to left along the x-axis. The laser intensity is ramped from zero to its maximum value of 5×10^{11} W/cm^2 within the first 3 ns, and then kept constant. An initial perturbation of the form $\delta\rho/\rho_0 = 0.05\cos(\pi y/25\ \mu\mathrm{m})$ was imposed on the foil density at $t = 0$. Here the significance of radiation transport reveals itself in the fact that the radiative heating determines the minimum length scale of the density clumps, forming due to the combined effect of the Rayleigh-Taylor instability and focal non-uniformities of the laser drive; information on the size and distribution of such clumps is important for interpretation of experiments on ion stopping in a laser plasma conducted at GSI.

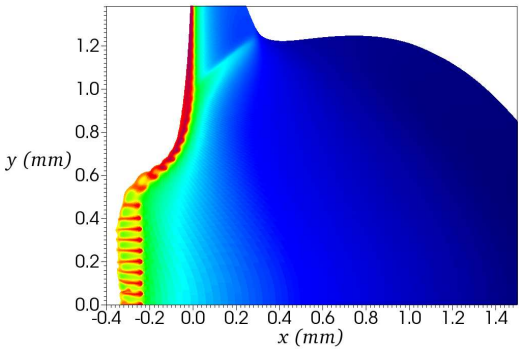

Figure 2: Density distribution at $t = 7$ ns in a carbon foil with a 5% initial density perturbation, irradiated by a 5×10^{11} W/cm^2 laser pulse.

References

[1] F. L. Addessio, J. R. Baumgardner, J. K. Dukowicz, N. L. Johnson, B. A. Kashiwa, R. M. Rauenzahn, and C. Zemach, *CAVEAT: A Computer Code for Fluid Dynamics Problems With Large Distortion and Internal Slip*, LA-10613-MS, Rev. 1, UC-905 (Los Alamos, 1992).

[2] M.M. Basko, J. Maruhn, An. Tauschwitz, J. Comput. Phys., **228** (2009) 2175.

* basko@itep.ru

Stack targets for equation-of-state measurements with heavy ion beams

An. Tauschwitz[1,2], M.M. Basko[2,3], V.P. Efremov[4], I.L. Iosilevskiy[4], S. Faik[2], A. Tauschwitz[5], P. Neumayer[1], F. Rosmej[6,7], and J. Maruhn[2]

[1]EMMI, GSI Darmstadt, Germany; [2]ITP, University of Frankfurt am Main, Germany; [3]ITEP, Moscow, Russia; [4]JIHT, Moscow, Russia; [5]GSI Darmstadt, Germany; [6]UPMC, Paris, France; [7]LULI, Palaiseau, France

Intense energetic ion beams are a promising tool for production and investigation of matter at high energy density. Using a beam from the SIS-18 a specific energy of several kJ/g can be deposited in an extended volume of condensed matter. For precise thermophysical experiments using heavy ion beams appropriate target schemes are indispensable. In this report we address a target configuration which allows direct measurements of thermophysical properties of warm dense matter without hydrodynamic recalculations. The presented experimental scheme will be realized at the current GSI synchrotron SIS-18 and the future FAIR facility in the framework of the WDM-collaboration.

Earlier it was suggested to measure equation of state data using ion beam heating of foams which are highly dispersed porous samples. The main goal is to detect the moment t_x when the pores of the heated sample close [1,2]. At the moment t_x the density is determined by the mean density of the cold sample and the enthalpy, H by the ion beam energy deposition. Hence, the caloric expansion coefficient $\alpha_p = (\partial\rho/\partial H)_p$ is obtained. Since at $t = t_x$ the heated sample is fairly homogeneous, a measurement of the surface temperature defines the thermal expansion coefficient $\alpha_p^{'} = (\partial\rho/\partial T)_p$ and the heat capacity $c_p = (\partial H/\partial T)_p$. The proposed experimental scenario can be applied, e.g. to a number of high boiling temperature metals in the temperature range of 1000–7000 K and will help to determine their critical points, which are highly uncertain for those metals [1]. Measurements with certain compounds can also confirm or disprove predicted non-congruent evaporation [1-3].

Here it is proposed to replace the complicated three-dimensional structure of a foam sample by a stack target consisting of n separated thin foils [4] as shown in Fig. 1. The gap between the foils determines the mean density of the target, $\rho_{00} = \rho_0 l_0/(l_0 + \Delta l_0)$. Similar to foam samples, the porosity of the stack target can be defined as $\rho_{00}/\rho_0 < 1$. At $t < t_x$ the foils expand quasi-statically, if the sound propagation time is short on the time scale of the energy deposition. The latter can be achieved if the foils are sufficiently thin. If the expansion is quasi-static, the density, the pressure, and the internal energy (and temperature) are constant in space. The surface velocity of the expanding foils is proportional to the foil thickness, $u_l \propto l$. When the foils merge, the launched acoustic waves increase the surface velocity of the entire target by $2u_l$, when escaping from the target surface.

The investigation of non-congruent evaporation in SiO_2 is planned for the first experiments. The evolution of the surface velocity for a stack target made of SiO_2 consisting of $n = 10$ foils is presented in Fig. 2. For the hydrodynamic calculations an energy deposition of 10 kJ/g in a 100 ns pulse is assumed. The normal density of SiO_2 is $\rho_0 = 2.2\,\mathrm{g/cm^3}$, the mean density of the stack structure is $\rho_{00} = 1.8\,\mathrm{g/cm^3}$. The initial foil thickness is $l_0 = 10\,\mu$m, the gap between the foils is $\Delta l_0 = 2.2\,\mu$m. The calculations were done using a Mie-Grüneisen equation of state with the cold curve approximated by a second order Birch-Murnaghan isotherm. The expected sharp increase of the surface velocity will help to detect the homogenization time t_x.

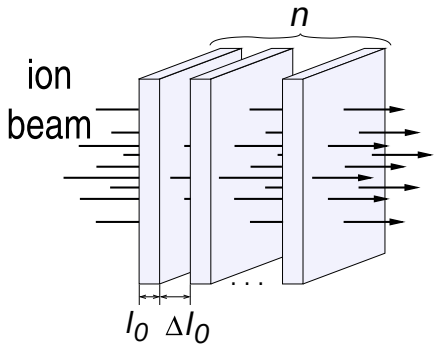

Figure 1: Stack target configuration.

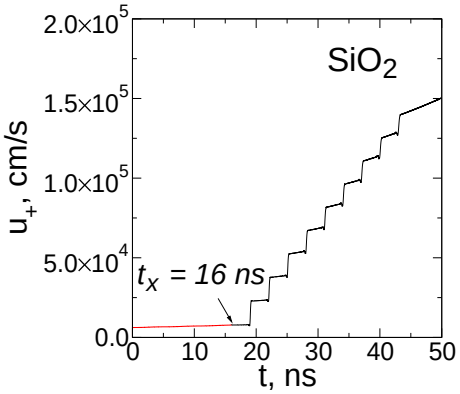

Figure 2: Surface velocity of a stack target consisting of 10 foils irradiated with an ion beam.

References

[1] I. Iosilevskiy, V. Gryaznov, J. Nucl. Mater. **344** (2005) 30

[2] I. Iosilevskiy *High Energy Density Physics with Intense Ion and Laser Beams* GSI-2007-2, May 2007

[3] I. Iosilevskiy et al., Contr. Plas. Phys. **43** (2003) 316

[4] An. Tauschwitz et al., Nucl. Instr. Meth. B **267** (2009) 2449

Planetary Physics Studies at FAIR Using LAPLAS Scheme With a Circular Beam Focal Spot: The HEDgeHOB Collaboration *

N.A. Tahir[1], A. Shutov[2], I.V. Lomonosov[2], M. French[3], N. Nettelmann[3], R. Redmer[3], A.R. Piriz[4], Th. Stöhlker[1], V.E. Fortov[2], and C. Deutsch[5]

[1]GSI, Darmstadt, Germany; [2]IPCP, Chernogolovka, Russia; [3]University of Rostock; [4]UCLM, Ciudad Real, Spain; [5]LPGP, University Paris–Sud, Orsay, France

In another contribution we presented numerical simulation results of LAPLAS implosion [1] that uses an annular beam focal spot to drive the target. In the present contribution we report similar results that have been achieved using a circular focal spot. The rest of the beam parameters and the target parameters are the same as in the other case. The transverse intensity distribution in the focal spot is considered to be Gaussian with a FWHM = 1.5 mm. Different values of the beam intensity, N, including, 10^{11}, 3×10^{11} and 5×10^{11} ions per bunch, respectively, have been considered. The results are presented in Figs. 3–1, respectively where we plot the density, temperature and pressure vs radius at the middle of the cylinder (L=3.5 mm) at the time of maximum compression in the water region. These simulations been carried out using a 2D hydrodynamic code, BIG2 [2]. For water and tungsten, we use the equation-of-state (EOS) data reported in [3] and [4], respectively.

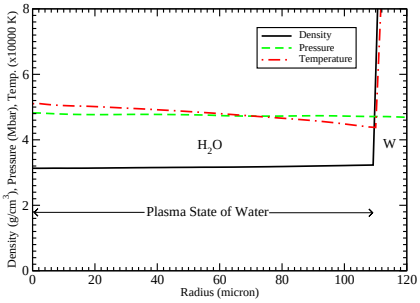

Figure 1: ρ, T and P vs radius at L = 3.5 mm in water at maximum compression using N = 5×10^{11} ions / bunch.

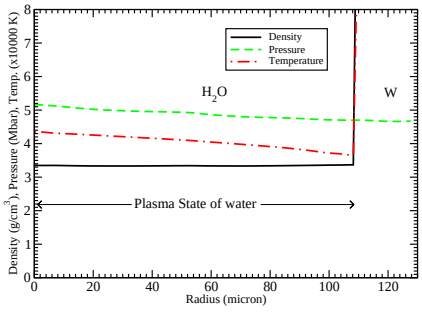

Figure 2: Same as in Fig. 1, but N = 3×10^{11} ions / bunch.

It is seen from the three figures that in case of a circular focal spot, one can only access the plasma phase of water because due to the direct heating of the sample by the ion beam, the final temperature of water is quite high. This is more clearly demonstrated in Fig. 4 where we plot the regions of the water phase diagram that can be accessed using a circular and an annular focal [5].

* Work supported by the BMBF and RFBR grant 08-02-92882-NNIO-a

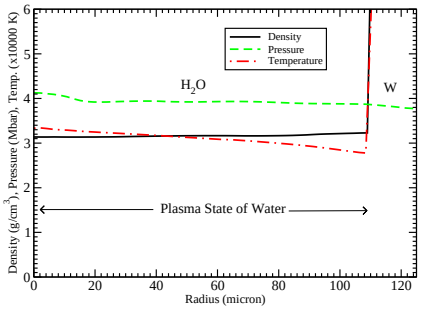

Figure 3: Same as in Fig. 1, but N = 10^{11} ions / bunch.

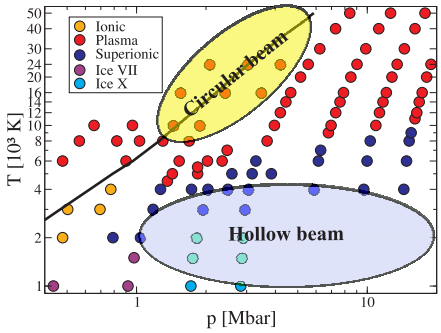

Figure 4: Each colored point corresponds to a QMD simulation in thermodynamic equilibrium. When the electronic conductivity exceeds 100/(Ohmcm) [6], the ionic (dissociated) fluid is labeled as plasma. The solid line is the principal Hugoniot curve.

References

[1] N.A. Tahir et al., PRE 63 (2001) 016402.

[2] V.E. Fortov et al., Nucl. Sci. Eng. 123 (1996) 169.

[3] M. French et al., Phys. Rev. B 79 (2009) 054107.

[4] I.V. Lomonosov, Laser Part. Beams 25 (2007) 567.

[5] N.A. Tahir et al., (2010) In press.

[6] T.R. Mattsson and M. Desjarlais, Phys. Rev. Lett. 97 (2006) 017801.

Planetary Physics Studies at FAIR Using LAPLAS Scheme With an Annular Beam Focal Spot: The HEDgeHOB Collaboration *

N.A. Tahir[1], A. Shutov[2], I.V. Lomonosov[2], M. French[3], N. Nettelmann[3], R. Redmer[3], A.R. Piriz[4], Th. Stöhlker[1], V.E. Fortov[2], and C. Deutsch[5]

[1]GSI, Darmstadt, Germany; [2]IPCP, Chernogolovka, Russia; [3]University of Rostock; [4]UCLM, Ciudad Real, Spain; [5]LPGP, University Paris–Sud, Orsay, France

The proposed LAPLAS experiment [1] will be carried out at the FAIR to study the interiors of the Giant planets in our solar system as well as the exoplanets. The beam–target geometry is shown in Fig. 1 and the target is driven by a hollow beam with an annular focal spot. In the present study the sample material is ice that is enclosed in a W shell. The target length, L = 7 mm, the radius of the sample, R_i = 0.2 mm and the outer radius of the W shell is 3 mm. The target is facially irradiated by a 1.5 GeV/u uranium beam with a duration = 50 ns. The inner radius of the annular ring, R_1 = 0.4 mm and the outer radius, R_2 = 1.4 mm. Different values of the beam intensity, N, including, 10^{11}, 2×10^{11},3×10^{11}, 4×10^{11} and 5×10^{11} ions per bunch, respectively, have been considered. Target implosion has been simulated using a 2D hydrodynamic code, BIG2 [2]. For water and tungsten, we use the equation-of-state (EOS) data reported in [3] and [4], respectively. In

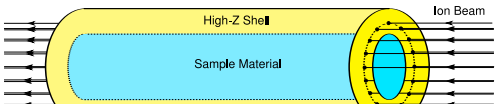

Figure 1: LAPLAS scheme using an annular focal spot.

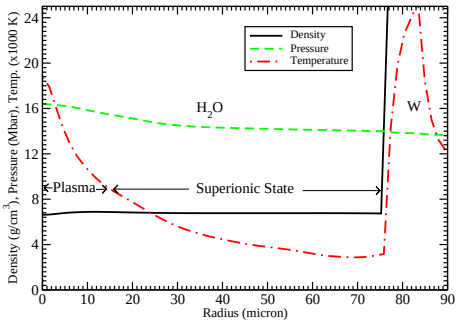

Figure 2: ρ, T and P vs radius at L = 3.5 mm in water at maximum compression using N = 5×10^{11} ions / bunch.

Fig. 2 we plot the density, temperature and pressure vs radius at the middle of the cylinder (L = 3.5 mm) in the water region at the time of maximum compression using a beam intensity of N = 5×10^{11} ions per bunch. It is seen that the radius of the sample has been reduced to about 75 micron from an initial value of 200 micron and the material is compressed seven fold (ρ = 7 g/cm^3). The pressure is on the order of 9 Mbar while the temperature is peaked towards the axis because of the cylindrical convergence of the shock. According to the model described in [3], the water within the inner 25 micron radius is in a plasma state that is surrounded by the very interesting superionic phase in which the protons become mobile in an oxygen lattice.

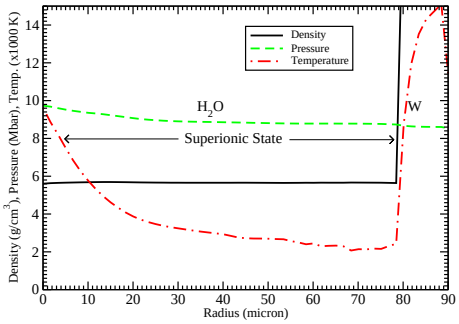

Figure 3: Same as in Fig. 2, but N = 3×10^{11} ions / bunch.

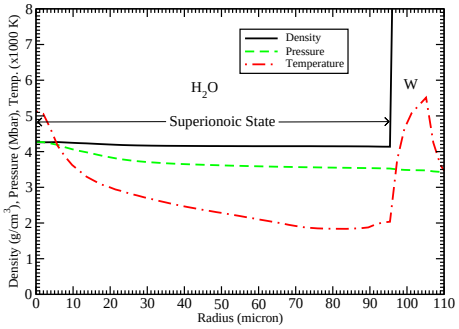

Figure 4: Same as in Fig. 2, but N = 10^{11} / ions / bunch.

In Figs. 3 and 4 we plot the same variables as in Fig. 2, but for N = 3×10^{11} and 10^{11} ions per bunch, respectively. It is seen that with lower beam intensities, the shock heating decreases and as a result the entire sample enters the superionic phase. Further details will be published in [5].

References

[1] N.A. Tahir et al., PRE 63 (2001) 016402.
[2] V.E. Fortov et al., Nucl. Sci. Eng. 123 (1996) 169.
[3] M. French et al., Phys. Rev. B 79 (2009) 054107.
[4] I.V. Lomonosov, Laser Part. Beams 25 (2007) 567.
[5] N.A. Tahir et al., (2010) In press.

* Work supported by the BMBF and RFBR grant 08-02-92882-NNIO-a

Thermo-mechanical effects induced by beam impact on LHC Phase II collimators: preliminary analysis using hydrodynamic approach *

N.A. Tahir[1], A. Shutov[2], I.V. Lomonosov[2], A. Dollocchio[3], A. Bertarelli[3], and A.R. Piriz[4]
[1]GSI, Darmstadt, Germany; [2]IPCP, Chernogolovka, Russia; [3]CERN, Geneva; [4]UCLM, Ciudad Real, Spain

Within the framework of the EuCARD project, ColMat task foresees the study of thermo-mechanical effects induced by high energy particle beam impacts on the LHC Phase II collimators. The upgrade of the LHC collimation system includes employing of metals for the jaws of secondary collimators to increase performances in terms of cleaning efficiency and to decrease impedance effects. Unfortunately, the use of high density materials like Copper, implies a reduction in the robustness of the system. Potential damages coming from a beam impact must be carefully assessed. A preliminary analysis on a simplified geometry is performed using a hydrodynamic code, BIG2 [2].

We consider a solid copper cylindrical target that is 1 m long and has a radius = 5 mm that is facially irradiated with 8 bunches of the 7 TeV/c protons where each bunch comprises of 1.15×10^{11} protons. The bunch length is 0.5 ns and two neighboring bunches are separated by 25 ns so that the total irradiation time is about 200 ns. The transverse intensity distribution in the focal spot is Gaussian with σ = 0.088 mm. The energy loss of the protons in solid copper is calculated using the FLUKA code [1] and this data is then used as input to the 2D hydrodynamic code, BIG2 [2], to study the thermodynamic and hydrodynamic response of the target. Different phases of the target material are treated using a semi-empirical equation-of-state model described in [3]. Simulations show that a specific energy of the order of 19 kJ/g will be deposited at the peak of the Gaussian distribution at about t = 200 ns, when 8 bunches have been delivered.

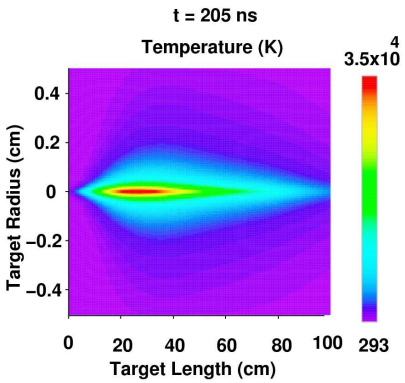

Figure 1: Temperature distribution at t = 205 ns.

In Fig. 1 is plotted the temperature distribution at t = 205 ns which shows that along the axis, the material will be heated to about 45000 K that will generate a very high pressure of the order of 35 GPa (see Fig. 2). This high pressure launches a radially outgoing shock that leads to a substantial density reduction in the central part of the cylinder, as shown in Fig. 3. It is therefore concluded that the energy deposited by 8 proton bunches from the LHC is sufficient to severely damage the target.

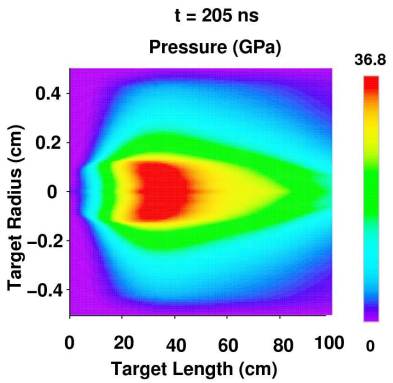

Figure 2: Pressure corresponding to Fig. 1.

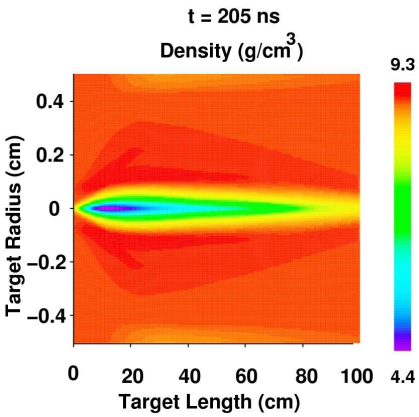

Figure 3: Density corresponding to Fig. 1.

References

[1] A. Fasso et al., "FLUKA: A Multi-Particle Transport Code", CERN-2005-10, INFN/TC-05/11, SLAC-R-773 (2005).

[2] V.E. Fortov et al., Nucl. Sci. Eng. 123 (1996) 169.

[3] I.V. Lomonosov, Laser Part. Beams 25 (2007) 567.

* Work supported by the BMBF and EU Project EuCARD: Colmat

Full Impact of the SPS Proton Beam With a Solid Cylindrical W Target: Simulations of the Future HiRadMat Facility Experiments *

N.A. Tahir[1], R. Schmidt[2], M. Brugger[2], A. Shutov[3], I.V. Lomonosov[3], A.R. Piriz[4], V.E. Fortov[3], and C. Deutsch[5]

[1]GSI, Darmstadt, Germany; [2]CERN, Geneva, Switzerland; [3]IPCP, Chernogolovka, Russia; [4]UCLM, Ciudad Real, Spain; [5]LPGP, University Paris–Sud, Orsay, France

In this contribution we present numerical simulations of full impact of the Super Proton Synchrotron (SPS) beam with a solid tungsten cylindrical target that is facially irradiated. The beam comprises of 288 bunches and each bunch is made of 1.15×10^{11} 450 GeV protons. The bunch length is 0.5 ns and two neighboring bunches are separated by 25 ns so that the total duration of the beam is about 7 μs. Transverse intensity distribution in the focal spot is Gaussian and three different sizes of the focal spot characterized by σ = 0.088, 0.28 and 0.88 mm, respectively, are considered. The energy loss of the projectile particles in the target is calculated using the FLUKA code [1] and this data is used as input to a 2D hydrodynamic computer code, BIG2 [2] to study the thermodynamic and hydrodynamic response of the target.

Energy deposited by a few tens of bunches lead to strong target heating that generates very high pressure (of the order of 30 GPa) which generates an outgoing radial shock wave. As a consequence, the density in the beam heated region decreases that leads to a longer penetration depth of the projectile particles. In Figs. 1–3 we plot the target density distribution at the end of the SPS beam (7.2 μs) for the three different sizes of the beam focal spot. It is seen that for σ = 0.088 mm, the beam penetrates up to 150 cm in solid tungsten while the range of the 450 GeV protons and the shower in solid W is about 60 cm. Figs. 2 and 3 show that the penetration depth in case of σ = 0.28 mm and 0.88 mm is 120 and 75 cm, respectively. However, the behavior is opposite in the radial direction (a larger target radius is affected in case of a beam with a larger focal spot). It is also seen that the density in the beam heated region becomes very small compared to the solid density while the simulations have shown that the temperature is very high in all the three cases (25000 – 40000 K). The target is therefore severely damaged and the beam heated region is converted into a strongly coupled plasma. An additional application of the SPS, therefore, could be to study High Energy Density (HED) physics, especially at the HiRadMat facility at CERN. Details about the calculations can be found in [3].

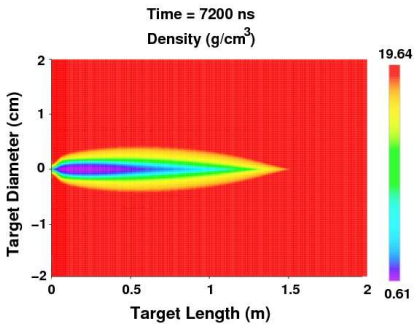

Figure 1: Target density distribution at t = 7.2 μs (end of the pulse) using σ = 0.088 mm.

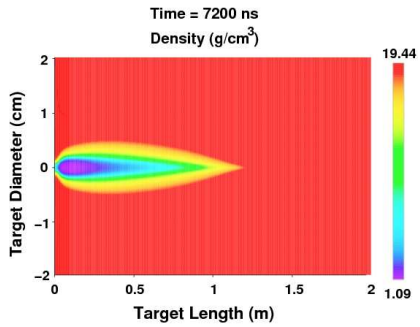

Figure 2: Same as in Fig. 1, but using σ = 0.28 mm.

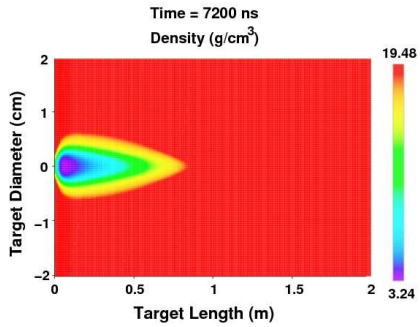

Figure 3: Same as in Fig. 1, but using σ = 0.88 mm.

References

[1] A. Fasso et al., "FLUKA: A Multi-Particle Transport Code", CERN-2005-10, INFN/TC-05/11, SLAC-R-773 (2005).

[2] V.E. Fortov et al., Nucl. Sci. Eng. 123 (1996) 169.

[3] N.A. Tahir et al., Phys. Plasmas 16 (2009) 082703..

* Work supported by the BMBF and EU Project EuCARD: Colmat

Simulations of Richtmyer–Meshkov Instability in Solids Materials *

N.A. Tahir[1], A. Shutov[2], I.V. Lomonosov[2], A.R. Piriz[3], J.G. Wouchuk[3], Th. Stöhlker[1], and C. Deutsch[4]

[1]GSI, Darmstadt, Germany; [2]IPCP, Chernogolovka, Russia; [3]UCLM, Ciudad Real, Spain; [4]LPGP, University Paris–Sud, Orsay, France

Richtmyer–Meshkov (RM) instability in solids including the influence of the constitutive properties has previously been studied analytically [1]. This problem is of particular interest to the hydrodynamic stability of the LAPLAS target [2] because the payload (cold flyer around the sample) remains in solid state and therefore it retains its material properties including yield strength which has a stabilizing effect on the target implosion. It is also important to note that no selfconsistent theory of RM instability exists, specially in the non–linear regime. One can therefore carry out dedicated experiments at the FAIR to study the problem of the RM instability in linear as well as non–linear regime.

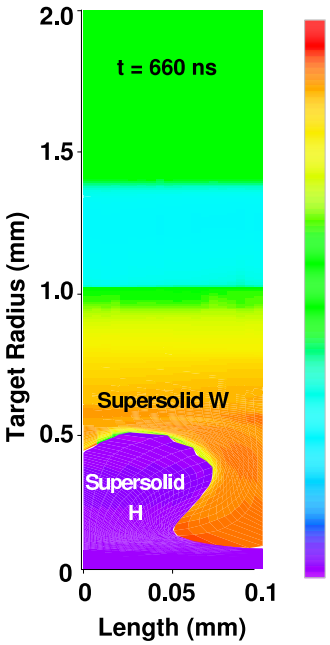

Figure 1: Density distribution at maximum compression in case of pure hydrodynamics.

We consider a perturbation with λ = 0.2 mm and an amplitude, A = 10 μm at the hydrogen–tungsten interface and simulate the implosion using a 2D hydrodynamic code, BIG2 [3]. The initial radius of the hydrogen region is 1 mm and the target is irradiated with an annular focal spot with an inner ring radius of 1.2 mm and an outer radius of 2.2 mm. The bunch length is 50 ns and it consists of 10^{11} ions of 1.5 GeV/u uranium. We study only half the wavelength ($\lambda/2$ = 0.1 mm). First we carried out simulations using pure hydrodynamic model and the results are presented in Fig. 1 where we plot the density distribution at t = 660 ns which is the time of maximum compression. It is seen that the interface is completely distorted due to the RM instability. However, this is not a correct model for the present case because payload material is in supersolid state with a temperature of about 700 K and a pressure of the order of 10 GPa during the acceleration phase. The material therefore does have solid properties although the yield strength of W is not known under these dynamic conditions. Using the values of the yield strength and the shear modulus that is known at room temperature, we carried out implosion simulations using the BIG2 version that includes an elastic–plastic model. The results are presented in Fig. 2. In this case it is seen that the interface remains stable and the RM instability does not grow at all. A detailed study has been carried out over a wide range of perturbation wavelength and amplitude and the results will be published later [4].

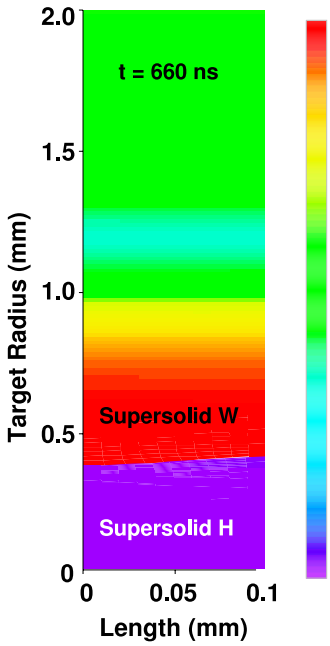

Figure 2: Same as in Fig. 1, but including elastic–plastic effects.

References

[1] A.R. Piriz et al., PRE 78 (2008) 056401.

[2] N.A. Tahir et al., PRE 63 (2001) 016402.

[3] V.E. Fortov et al., Nucl. Sci. Eng. 123 (1996) 169.

[4] N.A. Tahir et al., In Progress (2010).

* Work supported by the BMBF and RFBR grant 08-02-92882-NNIO-a

Rayleigh-Taylor instability in solids *

A. R. Piriz[1,#], J. J. López Cela and N. A. Tahir[2]
[1]Univ. de Castilla-La Mancha, Spain; [2]GSI, Darmstadt, Germany

Rayleigh - Taylor instability (RTI) in solids [1-5] is of fundamental relevance in many experiments on high-energy density physics and, in particular, for the LAPLAS experiment that we are designing in the framework of the new facility FAIR.

We have developed a model for the linear RTI in solids with elastic-plastic constitutive properties and we come up with a consistent stability criterion that shows that transition from a stable elastic regime to a plastic regime is a necessary condition for instability but not at all a sufficient one. This is done by considering a well-defined physical situation so that we can study pure incompressible RTI in a thick plate ($kh >> 1$, $k = 2\pi/\lambda$, h is the plate thickness and λ is the perturbation wave number) under a constant and uniform gravity acceleration g. The analysis is performed by means of an approximate but accurate model based on the Newton's second law that uses a Prandtl-Reuss constitutive model with the von Mises yield criterion. The study is completed by extensive two dimensional (2D) numerical simulations performed with the finite element code ABAQUS.

For constructing the model we assume a uniform thick plate of density ρ. The plate is in the plane (x, z) and it has been accelerated during a very long time until $t = 0$ by a constant and uniform pressure p_0 that represents a low density fluid accelerating the plate with an acceleration $\vec{a} = -g\,\hat{e}_y$, with $g = p_0/\rho h$. At $t = 0$ a ripple $\delta p = p_0(\xi_0/h)\sin kx$ is superposed to the uniform pressure p_0.

With the previous considerations the linear evolution of the perturbation amplitude can be well described by the following equation of motion [2]:

$$(\rho/k)\ddot{\eta} = \rho g(\eta + \eta_0) - S_{yy}\ , \qquad (1)$$

where $\eta(x,y,t) = \xi(t)\exp(ky)\sin kx$ because we assume that the perturbed velocity field can be approximated by the one corresponding to an ideal fluid. $\xi(t)$ is the instantaneous perturbation amplitude on the interface and S_{yy} represents the force per unit area due to the mechanical properties of the medium. S_{yy} is given by the normal component of the deviatoric part of the stress tensor $\sigma_{ij} - p\delta_{ij} + S_{ij}$ (p is the thermodynamic pressure and δ_{ij} is the Kronecker tensor). From the Prandtl-Reuss equations it turns out: $S_{yy} = 2kG$, for $\xi \le \xi_p$ and $S_{yy} = Y/\sqrt{3}\sin kx$, for $\xi \ge \xi_p$; where ξ_p is the value of ξ for which the elastic limit is achieved. G and Y are the shear modulus and the yield strength of the solid, respectively. Since the onset of plastic flow occurs first on the interface and then it progresses towards the plate interior its effects on the instability are not felt until it has affected a region with thickness of the order of k^{-1}. Therefore, we evaluate Eq.(1) at $y = y_p \approx k^{-1}$ and we get the equation of motion of the interface.

From the equation of motion of the interface we can be the complete solution for the instability problem. In particular we get the condition for the instability threshold (ITH): $(\rho g\xi_0/\sqrt{3}Y)_{ITH} = 1 - \sqrt{\rho g\lambda/4\pi G}$ and the condition for the elastic-plastic transition (EPT): $(\rho g\xi_0/\sqrt{3}Y)_{EPT} = (1 - \rho g\lambda/4\pi G)/2$.

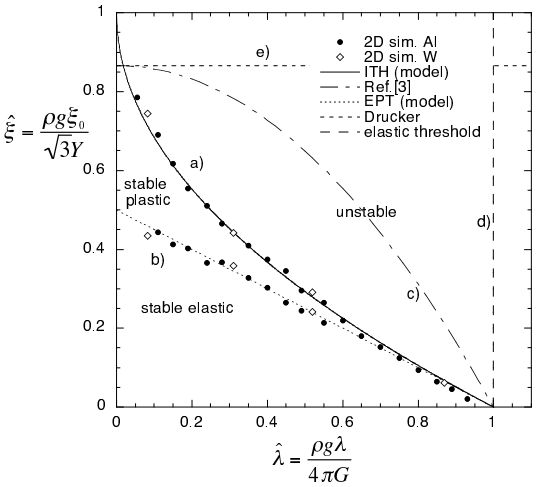

Fig.1: Instability threshold and elastic-plastic transition

In Fig. 1 we present the instability threshold [a)] and the EPT boundary [b)] together with the instability threshold derived in Refs.[4], what actually was their EPT boundary [c)]. For comparison, we show in Fig.1 the instability threshold for perfectly elastic media [d)] [4]. We also show the Drucker threshold [e)] for the instability of a perfectly rigid plastic solid [5] which is smaller than our upper limit (for $\hat{\lambda} = 0$) by a factor $\sqrt{3}/2$. Dots are the results of extensive 2D simulations performed with the code ABAQUS.

The present results have implications for the design of the LAPLAS experiment.

References

[1] J. W. Swegle and A. C. Robinson, J. Appl. Phys. **66**, 2838 (1989).
[2] A. R. Piriz, et al, Phys. Rev. E **80**, 046305 (2009)
[3] S. M. Bakharakh et al., Lawrence Livermore National Laboratory Report No. UCRL-CR-126710, 1997.
[4] A. R. Piriz et al, Phys. Rev. E **72**, 056313 (2005).
[5] }D. C. Drucker, Mechanics Today **5**, 37 (1980).

* Work supported by JCCLM and MICINN (Spain) and by BMBF (Germany).
# roberto.piriz@uclm.es

Rayleigh-Taylor instability in ablation fronts driven by ion beams *

S. A. Piriz[1], A. R. Piriz[2,#], and N. A. Tahir[3]
[1]Univ. Complutense de Madrid, Spain; [2]Univ. de Castilla-La Mancha, Spain; [3]GSI, Darmstadt, Germany

Inertial fusion directly driven by ablation induced with intense ion beams has been recently reconsidered on the basis of the relatively high hydrodynamic efficiency that can be achieved [1]. However, Rayleigh-Taylor instability (RTI) during the implosion process is still an issue of concern whose effects cannot be extrapolated from the present knowledge on RTI in ablation fronts driven by thermal diffusion that are generated in laser fusion or in indirectly driven inertial fusion [2]. For this, we have performed a linear analysis of the RTI in ablation fronts directly driven by intense ion beams [3].

We have considered the same problem as in Ref.[2] of a perturbed ablation front placed at $y=\xi(x,t)$ that separates two fluids of densities ρ_2 and ρ_1 ahead and behind the front, respectively. We assume a constant and uniform gravity g pointing in the positive $y-$axis direction, which is taken as opposite to the density gradient. We then perform the stability analysis as in Ref.[4] by describing the interface evolution by means of the Newton`s second law:

$$\frac{d[(m_1+m_2)\dot{\xi}]}{dt}=\delta\Pi_{yy}^{(1)}n_y^{(1)}+\delta\Pi_{yy}^{(2)}n_y^{(2)}\,, \qquad (1)$$

where $n_y^{(\nu)}$ ($\nu=1,2$) is the vertical component of the unit vector directed outward along the normal to the interface ($n_y^{(2)}=-n_y^{(1)}\approx 1$, and in the linear regime $n_x^{(\nu)}\approx k\xi<<1$), $\delta\Pi_{yy}^{(\nu)}=\delta p^{(\nu)}+\delta\dot{m}_\nu \mathrm{v}_\nu+\dot{m}_\nu\delta\mathrm{v}_y^{(\nu)}$ is the vertical component of the perturbed momentum flux density tensor $\Pi_{ik}^{(\nu)}$ in the fluid ν. In addition, $\delta p^{(\nu)}$, $\delta\dot{m}_\nu$ and $\delta\mathrm{v}_y^{(\nu)}$ are the corresponding perturbations in pressure, mass ablation and fluid velocity, respectively:

$$\delta p^{(\nu)}=\rho_\nu g\xi\,;\quad \delta\dot{m}_1=-\delta\dot{m}_2=\delta\dot{m}\,;\quad \delta\mathrm{v}_y^{(1)}=-\delta\mathrm{v}_y^{(2)}=\dot{\xi}\,. \qquad (2)$$

Besides, $\dot{m}=\rho_\nu \mathrm{v}_\nu$ is the ablation rate and $m_\nu=\rho_\nu/k$ is the mass of fluid ν affected by the motion of the interface due to the perturbation. Therefore, Eq.(1) reads:

$$\frac{\rho_2+\rho_1}{k}\ddot{\xi}=(\rho_2-\rho_1)g\xi-4\dot{m}\dot{\xi}-\delta\dot{m}(\mathrm{v}_1+\mathrm{v}_2)\,. \qquad (3)$$

In order to solve the previous equation we need to specify the last term $\delta\dot{m}(\mathrm{v}_1+\mathrm{v}_2)$ having the character of a surface-tension-like force. This is a reaction force due to the perturbation $\delta\dot{m}$ in the mass ablation rate that arises as the interface moves through the temperature gradient in the ablative corona. Therefore, $\delta\dot{m}$ is determined for the particular mechanism of energy deposition driving the ablation process. For obtaining it we need to take into account the fact that the ablation front is an isotherm [2] and therefore, the perturbation $\delta\varepsilon$ in the specific internal energy ε (temperature) reads: $\delta\varepsilon=-\xi\, d\varepsilon/dy$.

By assuming that all the perturbed magnitudes are of the form $\delta\varphi\propto e^{-ky}$ we can calculate $\delta\dot{m}$ provided that the particular mechanism of energy deposition is specified. For the particular case of thermal diffusion which is present in ablation driven by electromagnetic radiation we get $\delta\dot{m}/\dot{m}\approx k\xi$, and introducing it in Eq.(3) we retrieve the well known results of Ref.[2].

For the case of an ablation front driven directly by ion beams, energy is deposited in the corona plasma by classical Coulombian scattering:

$$\frac{1}{Q_b}\frac{dQ_b}{dy}=\frac{1}{E}\frac{dE}{dy}=\frac{1}{L}\,;\quad L=\frac{\alpha E^2}{\rho\Phi(\mathrm{v}_b/\mathrm{v}_{the})}\,,E=\frac{m_b\mathrm{v}_b^2}{2}\,, \qquad (4)$$

where Q_b is the energy flux of the beam, $\mathrm{v}_{the}=\sqrt{2k_BT/m_e}$, $\Phi(u)=(2/\sqrt{\pi})\left\{\int_0^u e^{-x^2}dx-ue^{-u^2}\right\}$ and $\alpha=(Am_p/Z)(m_e/m_b)/2\pi Z_b^2e^4\ln\Lambda_b$. From these equations we get $\delta\dot{m}/\dot{m}\approx -k\xi/(kL_1)^2<<k\xi$, where $L_1=[\alpha/\rho_1\Phi(u_0)](\gamma\dot{m}\varepsilon_1/\mu_b)^2$. Then, the last term in Eq.[3] can be neglected and we can get the instability growth rate:

$$\frac{\sigma L_2}{\mathrm{v}_2}=\sqrt{\frac{A_T\kappa}{Fr_2}+\left(\frac{2\kappa}{1+r_D}\right)^2}-\frac{2\kappa}{1+r_D}\,;\quad \kappa=kL_2\,, \qquad (5)$$

$$A_T=\frac{1-r_D}{1+r_D}\,;\quad r_D=\frac{\rho_1}{\rho_2}\,;\quad \rho_1=\rho(y=k^{-1})$$

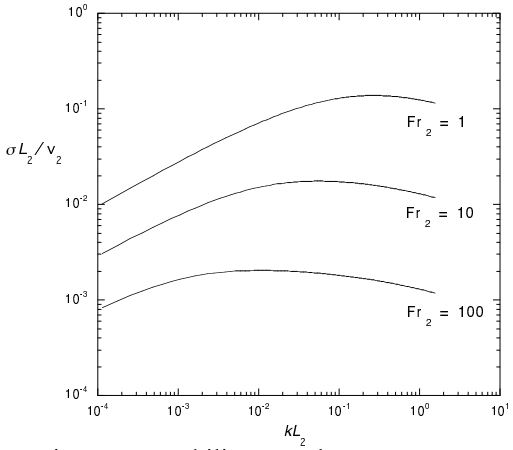

Figure 1: Instability growth rate Vs. wavenumber

As we can appreciate no cutoff wavenumber exists and the front is unstable for all values of k. However, an ablative viscous-like effect reduces the growth rate for the highest modes.

References

[1] B. G. Logan et al., Phys. Plasmas **15**, 072701 (2008).
[2] A. R. Piriz et al., Phys.Plasmas **4**,1117 (1997).
[3] S. A. Piriz et al., Phys.Plasmas **16**, 082706 (2009).

* Work supported by JCCLM and MICINN (Spain) and by BMBF (Germany).
# roberto.piriz@uclm.es

Proton Acceleration by High Intensity Laser Field. Self-Similarity Description

A. Baldin[1,2] and E. Baldina[1]

[1]Institute for Advanced Studies, Dubna Univeristy, Dubna, Russia; [2]Joint Institute for Nuclear Research, Dubna, Russia

This paper studies the specific features of energy and angular distribution of protons accelerated by high intensity ultrashort laser pulse from a dense target.

Production and acceleration of particle beams by ultrashort laser pulses with light intensities of order of 10^{20} W/cm^2 and higher is interesting both from the theoretical point of view and for practical applications, e.g., development of compact sources of quasimonoenergetic quasimonodirectional particle beams.

The self-similarity approach [1-3] developed for relativistically invariant description of multiparticle interaction in nuclear physics was used for description of the process "hardness" [4].

This method was successfully applied to the problem of positron production in collective photon field-matter interaction [5].

Here, the developed approach is applied for the analysis of energy and angular spectra of proton beams produced in the target interaction with high intensity laser fields.

The four-momentum conservation law written for the group of "coherent photons" (considered as a "big photon") and the proton in the initial and final states is used to obtain the proton cross section distributions,

$$E_\gamma + xP_1 = xP_1' + P_2 + P_3 \qquad (1)$$

where E_γ is the "big photon" energy, and the subscripts "1", "2", "3" denote the proton (which is always present in the target in the initial and final states, i.e., in both sides of Eq. (1)) and reaction products, respectively;

$$\sigma_{inv} = C_1 \exp\left(-\frac{x}{C_2}\right) \qquad (2)$$

where σ_{inv} is the invariant proton cross section and C_1 and C_2 are the constants found from normalization to experimental data.

Figure 1 shows the proton distribution in momentum-lab.angle coordinates for some assumed "big photon" energy as the example.

The specific feature of the proton beam distribution is that the maximum is rather wide both along the momentum and angle axes. Thus, for rather low-energy protons emitted from the target (average momentum of about 14 MeV/c) their angular distribution is extremely broad (practically half-space); however, the general tendency of narrowing distributions with increasing particle energy observed for antiproton production [5] can be seen here as well. Thus, for the energy of the initiating "big photon" higher by one order of magnitude (or, in other words, one order of magnitude higher light intensity) the proton distribution becomes narrower. This is especially pronounced for the angular distribution, highest-energy protons are concentrated within the twice as small angle.

Such character of the distribution is typical for particles that, unlike positrons, are initially present in the target material.

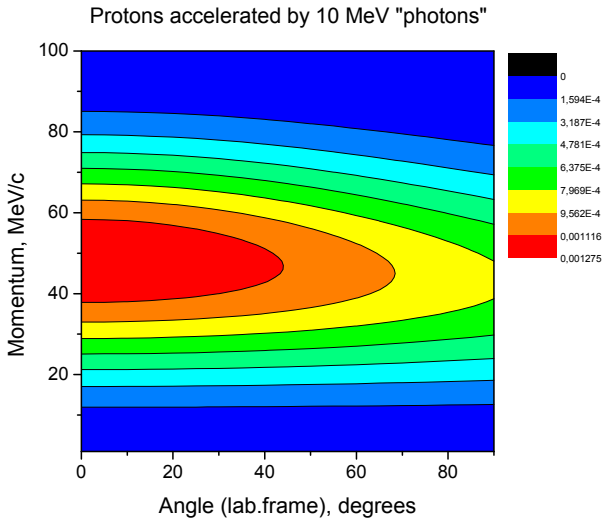

Figure 1: proton distributions in momemtum-lab.angle plane.

This method provides consistent description of initial and final states of particles interacting with (or produced by) high intensity coherent electromagnetic field. It can be used for analysis of laser driven sources of accelerated ions. Absolute calibration of the method can be performed for particular experimental conditions.

References

[1] A.A.Baldin Phys. Part. Nucl., 56 (3) (1993).

[2] A.M.Baldin, A.A.Baldin, Phys.Part.Nucl., 29 (3), (1998), p.577.

[3] A.Baldin, E. Baldina, "Self-Similarity Approach in Relativistic Nuclear Physics", GSI Report 2007-1, p.194.

[4] A.A. Baldin, E.G.Baldina, E.N.Kladnitskaya, O.V.Rogachevsky, Phys.Part.Nucl.Lett., vol. 1, no. 4(121), pp. 7-16 (2004).

[5] A.Baldin, "Collective Relativistic Phenomena with Femtosecond Laser Pulses", GSI Report 2007-1, p.306.

Directed Nuclear Radiation

A. Baldin[1,2] and E. Baldina[1]

[1]Institute for Advanced Studies, Dubna Univeristy, Dubna, Russia; [2]Joint Institute for Nuclear Research, Dubna, Russia

This paper presents the phenomenon of directed nuclear radiation based on the analysis of Lobachevsky angle of parallelism.

In spite of the wide application of Lobachevsky geometry in relativistic physics [1-3], one of its basic concepts, the angle of parallelism, has not received due interpretation. The angle of parallelism characterizes the closeness of a produced particle to the absolute in the Lobachevsky geometry. For an arbitrary distance ρ the corresponding angle of parallelism is determined as

$$\Pi_L(\rho) = 2arctg(e^{-\rho}). \qquad (1)$$

For the system of three interacting particles, the projectile and the target particles denoted by indices 1 and 2, respectively, and the particle registered in the reaction denoted by index 3, we define the following quantity:

$$\Delta_{12}^3 = 2\Pi_L(\rho) - \alpha_3. \qquad (2)$$

This quantity characterizes the closeness to the absolute for the triangle formed by the three considered particles as the vertices in the Lobachevsky rapidity space (ρ is the height of the triangle from vertex 3 onto its base which represents the relative rapidity of colliding particles, α_3 is the angle at the registered particle opposite to the base).

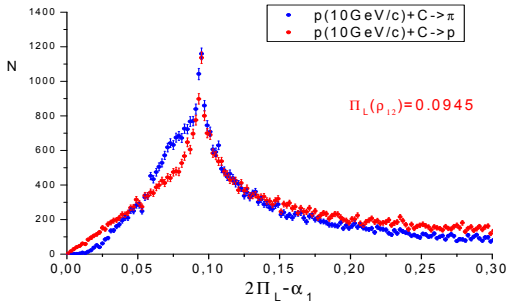

Fig. 1. Peaks in pion distributions for two reactions $p(10\,GeV/c)+C\to\pi$ and $\pi^-(40\,GeV/c)+C\to\pi$.

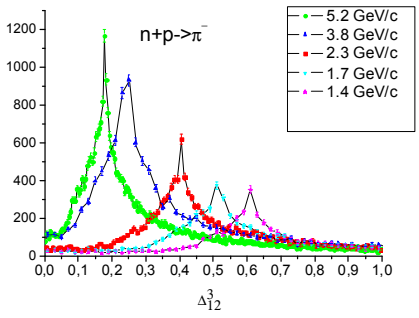

Fig. 2. Pion production in $n+p$ *reactions at different neutron momenta.*

Note that this quantity is determined from experimentally measured quantities, particle angles, momenta, and masses, and is relativistically invariant.

It was discovered that the pronounced narrow maximum of particle production is observed in experimental distributions obtained in different reactions which corresponds to the value of Δ_{12}^3 in which ρ is equal to the relative rapidity of colliding particles (see Figs. 1 and 2).

The analytical formula connecting the angle and momentum of directed nuclear radiation was found:

$$\cos\alpha_2 = \sqrt{\frac{1+th(\rho_{12})}{2}} - sh(h)\sqrt{\frac{1-th(\rho_{12})}{2}}. \qquad (3)$$

Here, the angle α_2 is the angle at the target particle (in the fixed-target case coincides with the laboratory angle of registration of particle 3). Unlike Cherenkov radiation, the angle of directed nuclear radiation decreases with increasing energy (see (3)). The angle and rapidity of directed nuclear radiation are the same for particles with different mass (pions, kaons, protons, etc.).

The angle α_3 at the registered particle is determined as

$$\alpha_3 = 2\arcsin\left\{\sqrt{\frac{1+th(\rho_{12})}{2}}\sin(\Pi(h)) - \sqrt{\frac{1-th(\rho_{12})}{2}}\cos(\Pi(h))\right\} \qquad (4)$$

This parameter can be used for selection with respect to the interaction "hardness" [4].

Note that the maximum intensity of directed nuclear radiation (peaks in Figs. 1, 2) correspond to the transverse momentum equal to the mass of the produced particle.

The predictive power of formulas (3), (4) was verified using experimental data on reactions with proton, neutron, and pion beams at different energies [5].

The introduced variable Δ_{12}^3 can be used for analysis of multiple particle production, in particular, relativistically invariant jet determination.

References

[1] A. P. Kotel'nikov, "Relativity Principle and Lobachevsky Geometry", in Collected Papers "In Memoriam N. I. Lobatschevskij", vol. 2 (Kazan, 1927), 37-64..

[2] N. A. Chernikov, Phys.Part.Nucl., 23 (5), 1187 (1992).

[3] A.A. Baldin, "Lobachevsky Space in Relativistic Nuclear Physics", in Proceedings of International Seminar "Application and Development of Ideas of Lobachevsky in Modern Physics" (25-27 February 2004, Dubna, Russia, 2004), 103-116.

[4] A.A. Baldin, E.G.Baldina, E.N.Kladnitskaya, O.V.Rogachevsky, Phys.Part.Nucl.Lett., vol. 1, no. 4(121), pp. 7-16 (2004).

[5] A.A. Baldin, “Relativistic Multiparticle Interactions in Lobachevsky Geometry. Directed Nuclear Radiation”, Proceedings of XIX International Baldin Seminar on High Energy Physics Problems (ISHEPP XIX), Dubna, Sept.29 - Oct.4, 2008/ Ed.: Sissakian A.N., V.V.Burov, A.I.Malakhov, S.G.Bondarenko, E.B.Plekhanov.- Dubna: JINR.- (JINR; E1,2-2008-188) . - Vol.1 (2008), pp.80-89.

Spatially resolved nuclear spin-relaxation in ion-irradiated LiF crystals

H. Stork[1,2], K.-P. Dinse[3], M. Ditter[1], F. Fujara[1#], W. Masierak[4], R. Neumann[5], B. Schuster[1,5], K. Schwartz[5], C. Trautmann[5]

[1]TU Darmstadt, Darmstadt, Germany; [2]Laboratoire National des Champs Magnétiques Intenses, Grenoble, France; [3]FU Berlin, Berlin, Germany; [4]Uniwersytet Kazimierza Wielkiego, Bydgoszcz, Poland; [5]GSI, Darmstadt, Germany

Within the last two years, spatially resolved Nuclear Magnetic Resonance (NMR) relaxation experiments have been introduced as a new tool for the investigation of heavy-ion induced effects in LiF [1, 2]. The NMR measurements have been accompanied by optical absorption and Electron Paramagnetic Resonance (EPR) studies [3].

To obtain spatially resolved spin-lattice relaxation rates, the irradiated crystals are moved across a magnetic field gradient which defines a sensitive volume of 10 µm width. As illustrated in Fig. 1, the signal intensity is recorded for different evolution times after saturation (due to nuclear spin-lattice relaxation) [1].

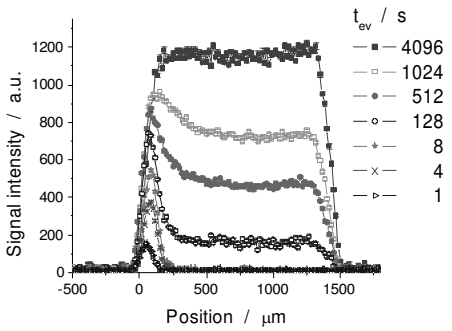

Figure 1: One-dimensional ^{19}F-NMR microimages of a LiF crystal irradiated with ^{130}Xe ions (1.44-GeV, 10^{11} ions/cm^2) for selected evolution times t_{ev}.

Figure 2 shows spatially resolved ^{19}F-spin-lattice relaxation rate profiles of crystals irradiated with ^{12}C ions of different fluences. Three depth zones can be identified: within zone 1, the spin-lattice relaxation rate profiles for the highest fluences follow the same evolution as the calculated energy loss profile [3]. The width of zone 2 varies for different irradiations and might be due to an artefact caused by random sample misalignment. In region 3, the spin-lattice relaxation is dominated by the contribution of intrinsic paramagnetic impurities in LiF.

Figure 3 presents the ion-irradiation induced spin-lattice relaxation rate T_{1rad}^{-1} (relaxation rate corrected for the rate of non-irradiated LiF) as a function of the concentration of F centers (n_F) generated at the same dose (n_F is deduced from optical absorption spectroscopy [3]). A linear correlation exists only in the regime between n_F = 3×10^{17} and 3×10^{18} cm^{-3}. For higher n_F the deviation from this proportionality is due to a change of electronic relaxation times, and for smaller n_F we ascribe the deviation to a clustering of single defects within individual tracks.

fujara@physik.tu-darmstadt.de

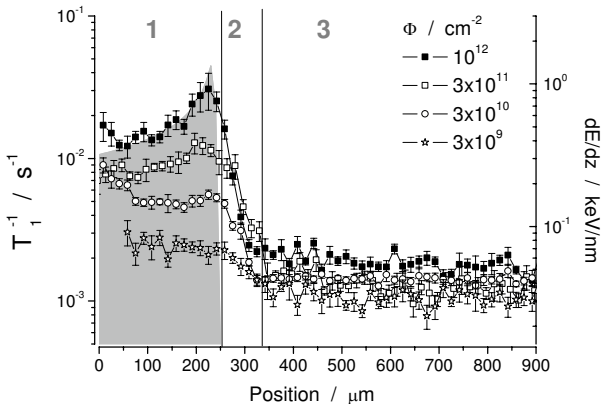

Figure 2: Position dependent ^{19}F spin-lattice relaxation rates T_1^{-1} of LiF crystals exposed to 133 MeV ^{12}C ions of different fluences Φ. The shaded region denotes the calculated [4] energy loss dE/dz (right ordinate). The abscissa is divided into zone 1 within the ion range (245 µm), a transition zone 2, and a zone 3 beyond ion range.

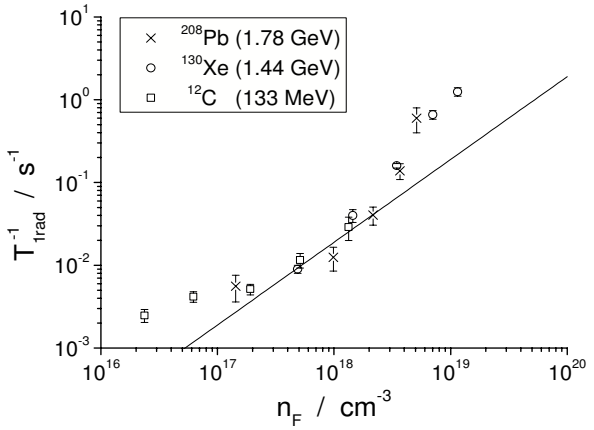

Fig. 3: Radiation induced peak ^{19}F-spin-lattice relaxation rates versus F-centre concentration n_F (deduced from optical absorption spectroscopy [3]) of LiF irradiated with various ions (continuous line indicates $T_{1rad}^{-1} \propto n_F$).

[1] H. Stork, A. Hamburger, A. Gädke, F. Fujara, K. Schwartz, J. Phys.: Condens. Matter **20** (2008) 275236
[2] H. Stork, K.-P. Dinse, F. Fujara, A. Hamburger, P. Jakes, R. Neumann, K. Schwartz, C. Trautmann, J. Phys.: Condens. Matter **20** (2008) 465215
[3] H. Stork, K.-P. Dinse, M. Ditter, F. Fujara, W. Masierak, R. Neumann, B. Schuster, K. Schwartz, C. Trautmann, submitted
[4] SRIM 2008, J.F. Ziegler, M.D. Ziegler, and J.P. Biersack (2006) http://www.srim.org/

Li colloids in heavy-ion-irradiated LiF crystals after thermal annealing

K. Schwartz[1], M.V. Sorokin[2], A.E. Volkov[2], R. Neumann[1], C. Trautmann[1]

[1]GSI, Darmstadt, Germany; [2] Russian Research Center, Kurchatov Institute, Moscow, Russia

Metallic colloids and anion clusters are damage products formed when ionic crystals are exposed to high dose (≥ 10 MGy) photon, electron, or neutron radiation [1]. Colloid formation usually requires large F-center concentrations (10^{18} - 10^{19} cm^{-3}), high F-center mobility (diffusion), and spatial separation of hole centers and F centers to prevent their recombination [1, 3]. Also, interaction of H centers by forming fluorine molecules ($H + H \rightarrow X_2$) and clusters (nX_2) is supportive to avoid annihilation [4].

In view of colloids readily formed under low ionizing radiation, it is surprising that LiF crystals irradiated at room temperature (RT) with heavy ions (up to uranium) do not show Li colloids although highly sensitive ESR spectroscopy and fluences up to 5×10^{12} ions/cm^2 (corresponding to an average dose of ~80 MGy) were applied [2]. During track formation, the local temperature around the track is probably not high enough for colloid formation. To test this hypothesis, LiF crystals were irradiated at RT with various heavy ions and subsequently thermally annealed. This post-irradiation stimulated colloid formation [1,3] was identified by means of optical absorption spectroscopy. The colloid band with maximum absorption at 440 nm was detected for annealing temperatures above 600 K, and for irradiations where the energy loss of the ions surpassed a critical value of about 10 keV/nm. Moreover, the ion fluence had to be high enough to produce F_n centers (n = 2, 3, 4).

Optical absorption spectra of colloids in LiF crystals irradiated with Xe- and U-ions are shown in Figs. 1 and 2. With increasing temperature, the intensity of the colloid absorption becomes larger, and simultaneously the F-center absorption (maximum at 248 nm) decreases.

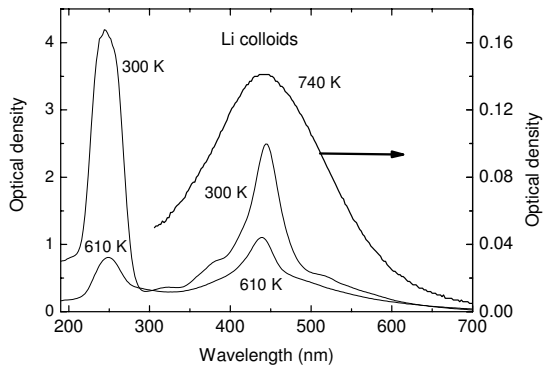

Figure 1: Optical absorption spectra of LiF crystals irradiated with 2640-MeV U ions (5×10^{10} ions/cm^2) before and after 15 min annealing at 610 K (left ordinate) and 740 K (right ordinate).

Under annealing, the initial high concentration of F centers promotes the formation of F-center clusters (nF) consisting of F centers ($v_a^+e^-$) and lithium ions (Li^+) on regular lattice positions [2]. If such clusters reach a critical size, the system collapses, the F-center electrons are captured by Li^+ ions, and Li colloid particles are created.

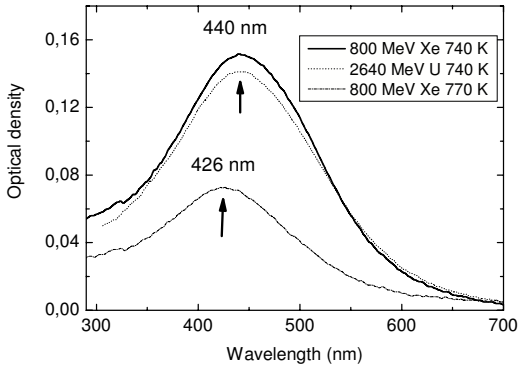

Figure 2: Optical Absorption band of Li colloids in LiF crystals irradiated with 800-MeV Xe ions (3×10^{11} cm^{-2}) and 2640-MeV U ions (5×10^{10} cm^{-2}) and annealed at 740 and 770 K (for 15 min).

For different ions but fixed annealing temperature (740 K), the absorption maximum of the Li colloids appears at 440 nm. At 770 K this maximum is shifted to 426 nm demonstrating a decrease of the colloid size (Fig. 2) [1, 3]. At these temperatures, the diffusion length for F centers is several times larger than the mean distance between the ion tracks which demonstrates that the colloid formation can involve F centers from several ion tracks. At temperatures above 800 K, the colloid band disappears and the crystal lattice seems to be completely restored.

[1] E.A. Kotomin, I. Popov, "The kinetics of radiation-induced point defect aggregation and metallic colloid formation in ionic crystals", In: *Radiation effects in solids"*, Eds. K.E. Sickafus, E.A. Kotomin, B.P. Uberuge, Springer, Amsterdam, 2007, pp. 153 - 192.

[2] C. Trautmann, K. Schwartz, J.M. Costantini, T. Steckenreiter, M. Toulemonde, Nucl. Instr. Meth. B 146 (1998) 367.

[3] A.E. Hughes, S.C. Jain, Adv. Phys. 28 (1979) 717.

[4] K. Schwartz, M.V. Sorokin, A. Lushchik, Ch. Lushchik, E. Vasil'chenko, R.M. Papaleo, D. de Souza, A.E. Volkov, K.-O. Voss, R. Neumann, C. Trautmann, Nucl. Instr. Meth. B 266 (2008) 2736.

#K.Schwartz@gsi.de

Structural modification of swift heavy ion irradiated amorphous germanium layers*

T. Steinbach[1,#], C.S. Schnohr[1], W. Wesch[1], M.C. Ridgway[2], D. Severin[3] and M. Bender[3]
[1]FSU Jena, IFK, Jena, Germany; [2] ANU, Canberra ACT 0200, Australia; [3]GSI, Darmstadt, Germany

Swift heavy ion (SHI) irradiation of conventional glasses results in non-saturable plastic flow as a consequence of the ion hammering effect [1]. SHI irradiation of amorphous Si (a-Si) at non-perpendicular incidence also leads to unsaturated plastic flow, which shows a linear dependence on the ion fluence. The positive direction of flow suggests that a liquid phase with density similar to that of the amorphous solid must exist [2]. For room temperature irradiation of a-Si to a very high fluence (~2.5×10^{15} cm^{-2}), the plastic flow is accompanied by swelling due to the formation of voids. Room temperature SHI irradiation of amorphous Ge performed at the ANU accelerator facility has shown a positive plastic flow as well, demonstrating that liquid polymorphism is common for these two semiconductors [3]. In contrast to amorphous Si, the formation of voids in amorphous germanium begins at a much lower fluence (10^{12} ions/cm^2). As a consequence of the void formation, a nonlinear plastic flow process is observed. Figure 1 shows an optical micrograph of the surface of the amorphous germanium layer with a thin quadratically shaped gold marker layer. By means of the gold squares on the samples surface the two effects, namely plastic deformation and swelling are clearly visible (see [3, 4] for more information).

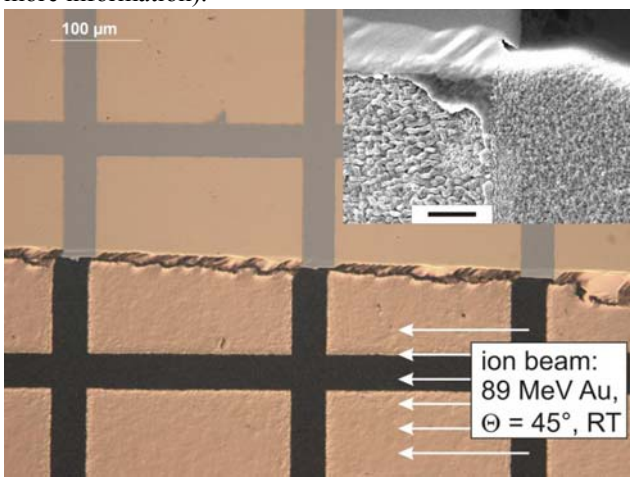

Figure 1: The optical micrograph shows plastic flow as well as swelling of an irradiated amorphous germanium layer. The irradiation was performed at room temperature using 89 MeV Au ions under an angle of $\Theta = 45°$. The inset shows the corresponding SEM image with a higher magnification (scale bar: 5 µm).

In this project, we investigated the effect of the irradiation temperature as well as the influence of higher electronic energy deposition on the void formation in a-Ge. The experiments were performed at the new M3-branch at the UNILAC. The sample was irradiated at cryogenic temperature (T = 45 K) with 1.4 GeV U-ions under 45° beam incidence. The ion flux was 4×10^9 cm^{-2} s^{-1}, the fluence ranged between 5×10^{12} and 1.5×10^{14} cm^{-2}. This first low temperature irradiation of amorphous germanium shows that in contrast to a 77 K irradiation of Si (no voids over a wide fluence range up to 8×10^{15} cm^{-2}), void formation in a-Ge was observed at a rather low ion fluence of ~ 10^{12} cm^{-2}.

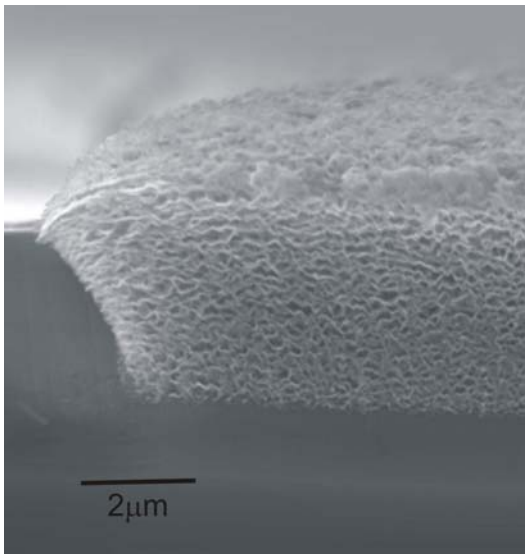

Figure 2: The cross section SEM image shows the transformation of the homogeneous a-Ge layer into a sponge-like porous germanium layer after irradiation with 89 MeV Au ions (fluence: 2.23 x 10^{14} cm^{-2}).

The mechanisms of void formation and the transformation into a sponge-like structure are not yet understood and will be subject of further investigations. For this purpose, a new target holder was constructed allowing simultaneous irradiations at room and low temperature, which enables the comparison of both samples under same irradiation conditions.

References

[1] S. Klaumünzer et al. Phys. Rev. Lett. 51 (1983) 1987.
[2] A. Hedler et al. Nat. Mater. 3 (2004) 804.
[3] W. Wesch et al., J. Phys. D: Appl. Phys. 42 (2009) 115402.
[4] T. Steinbach, C.S. Schnohr, W. Wesch, to be published.

* Work supported by BMBF, contract no. 05KK7SJ1 and DAAD, contract no. D/07/15034.
# tobias.steinbach@uni-jena.de

Stress and plastic flow in germanium during amorphization by ion bombardment*

T. Steinbach[1,#], J. Wernecke[1], W. Wesch[1], D. Severin[2] and M. Bender[2]
[1]FSU Jena, Institut für Festkörperphysik, Jena, Germany; [2]GSI, Darmstadt, Germany

This project investigates density changes and plastic phenomena in crystalline germanium (c-Ge, [100]) during the irradiation with swift heavy ions. By means of a new scanning laser reflection technique [1], the bending (curvature radius) of a freestanding germanium sample was measured as a function of ion fluence.

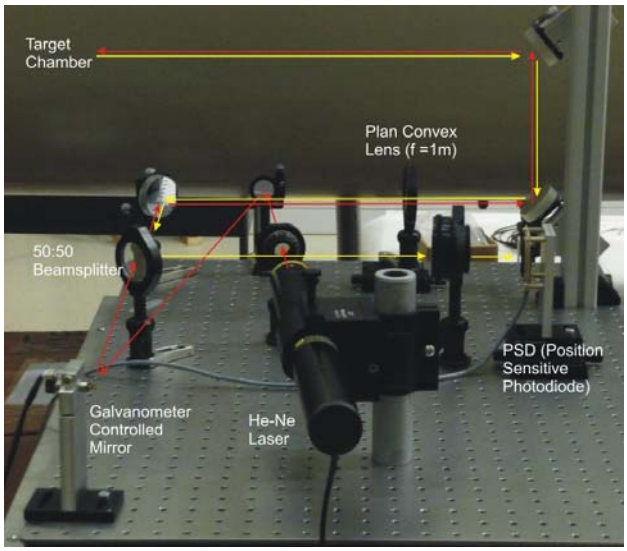

Figure 1: In-situ sample curvature measurements using a scanning laser reflection technique [1]: The image shows the horizontal path of the laser beam on the optical breadboard as well as the vertical deflection of the laser beam into the chamber. The red line indicates the primary beam, and the yellow line represents the beam reflected by the sample in the chamber.

The laser reflection system was recently installed at the newly established M3-beamline at the UNILAC (Fig. 1), providing in-situ stress measurements. The system was calibrated with a mirror of known curvature radius (R_{cal} = 5 m). One side of the bar-shaped c-Ge crystals (2 x 10 mm^2, thickness 275 µm) was mounted in such a way that the samples were quasi freestanding (see inset Fig. 2). The irradiation was performed at room temperature with 1.4 GeV Xe ions under normal incidence. At this energy, the ion range is ~66 µm. The beam flux was 2×10^9 cm^{-2} s^{-1}, and the fluence ranged between 1×10^{11} and 1×10^{13} ions/cm^{-2}. The curvature measurements were carried out in situ during short beam interruptions. These irradiation conditions lead to the formation of a buried damaged layer, i.e. stress builds up in the sample due to defect creation in the nuclear stopping regime [2].

Figure 2 shows the ion beam induced change of the in-plane stress as a function of the ion fluence. The stress state of the sample was calculated using the equation of Stoney [2]:

$$S = \int_0^{t_d} \sigma(x)dx = \frac{Y_0 t^2}{6R}, \qquad (1)$$

where t_d denotes the thickness of the damaged area, $\sigma(x)$ is the local stress in depth x, Y_0 is the Young's modulus for c-Ge, t is the thickness of the sample, and R is the radius of curvature.

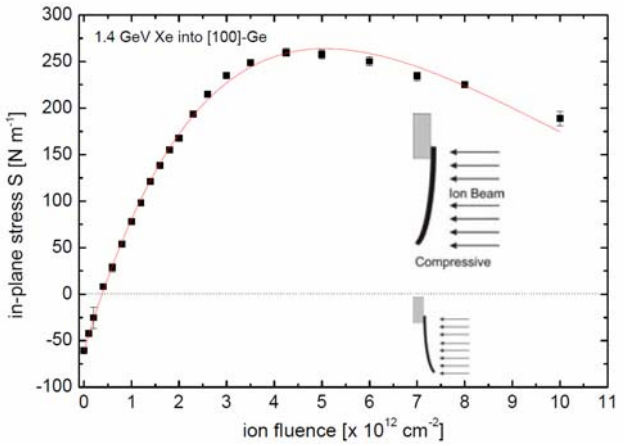

Figure 2: In-plane stress S versus ion fluence for room temperature irradiation of c-Ge with 1.4-GeV Xe ions. The inset illustrates the bending of the sample. Compressive stress ($S > 0$) corresponds to bending of the sample away from the ion beam.

The initial stress state of the sample was negative ($S < 0$). As a result of the defects formed during ion irradiation, the density is reduced leading to compressive stress ($S > 0$), i.e. the sample bends away from the ion beam. The curvature and thus the stress increases continuously with increasing fluence. For 5×10^{12} ions/cm^2, the stress reaches a maximum of 264 N/m. With further irradiation, the compressive stress state slowly decreases due to incipient plastic deformations.

References

[1] C.A. Volkert, J. Appl. Phys. 70, 3521 (1991).
[2] G. Stoney, Proc. Roy. Soc. A 82, 172 (1909).

* Work supported by BMBF, contract no. 05KK7SJ1
#tobias.steinbach@uni-jena.de

Study of Swift Heavy Ion Irradiation Effect on Yttria Stabilized Zirconia Using EXAFS Measurements

A. Iwase[1], Y. Tahara[1], and R. Neumann[2]
[1]Oasaka Prefecture University, Sakai, Osaka, Japan; [2]GSI, Darmstadt, Germany

Introduction

The reliability of sensors that are used to monitor in-situ electrochemical corrosion potential (ECP) for water condition of boiling water reactors (BWR) under an irradiation field is quite important [1]. In these sensors, the ion conductivity of yttria stabilized zirconia (YSZ) is utilized to measure the ECP. Therefore, for the accurate estimate of ECP, effects of irradiation on YSZ have to be fully understood. In this report, we show the effect of swift heavy ion irradiation on the atomic arrangement of YSZ, which has been studied by means of Extended X-ray Absorption Fine Structure (EXAFS).

Experimental procedure

Specimens used in the present study were zirconium oxide, ZrO_2, stabilized by doping 8 % Y_2O_3. X-ray diffraction measurements showed that the specimens had the fluorite type structure. Samples of 5x5x1mm^3 were irradiated at room temperature with 5.6 MeV/u (1.33 GeV) U ions at the UNILAC linear accelerator of GSI. The fluences were 5x10^{11}, 1x10^{12}, and 2x10^{12} ions/cm^2. After irradiation, EXAFS spectra were measured around the Y L3-edge at both the irradiated and unirradiated surfaces. All data were acquired using a 7-element Ge fluorescence detector.

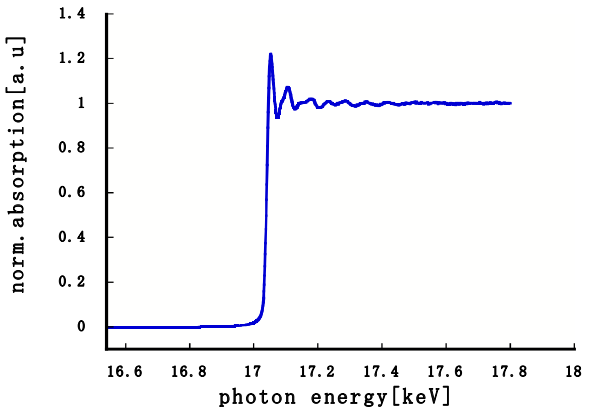

Figure 1: Normalized EXAFS spectrum measured around the Y-L3 edge of YSZ exposed to 5.6-MeV/u U ions at a fluence of 2x10^{12} ions/cm^2.

Results and Discussion

Figure 1 shows a normalized absorption spectrum. A clear EXAFS oscillation can be observed on the high-energy side of the Y L3-edge. Figure 2 illustrates the Fourier transform (FT) of the spectra for the irradiated and the rear sample side. There exist two peaks in each spectrum. The left peak corresponds to the nearest neighbours of Y atoms (O atoms), and the right to the second-nearest neighbours of Y atoms (Zr atoms).

The U ion irradiation causes the decrease in both peak heights. This result means that the coordination number for O atoms and Zr atoms around Y atoms decreases and /or that the Debye-Waller factors for Y-O and Y-Zr pairs increase by the irradiation. Such an irradiation induced local disordering of atomic arrangement around Y atoms can be found only by using EXAFS spectroscopy. The quantitative estimate to determine the values of coordination numbers and Debye-Waller factors is in progress.

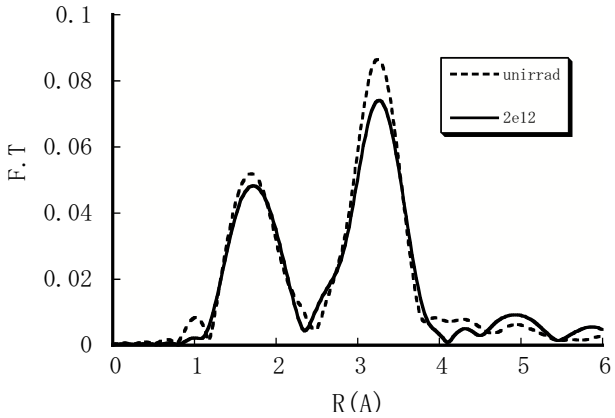

Fig. 2: FT-EXAFS spectra of YSZ: unirradiated, (dashed line), and irradiated with 5.6-MeV/u U ions at a fluence of 2x10^{12} ions/cm^2 (solid line).

References

[1] S. Hettiarachchi, Proc. 12th International Conference on Environmental Degradation of Materials in Nuclear Power System – Water Reactors, Ed. by T. R. Allen, P. J. King, L. Nelson TMS (The Minerals, Metals & Materials Society) (2005) p. 3-17.

Measurements of ion tracks in metallic glasses by small angle x-ray scattering

M. D. Rodriguez[1,#], C. Trautmann[2], B. Afra[1], R. Giulian[1], N. Kirby[3], and P. Kluth[1]
[1]Australian National University, Canberra, Australia; [2]GSI, Germany; [3]Australian Synchrotron, Clayton, Australia.

High electronic excitations provided by swift heavy ion irradiation of a solid can lead to the formation of long columnar defects along the ion trajectories. Such ion tracks have been observed in numerous insulators and a number of semiconductors. Metallic materials are in general less sensitive except a few selected metals (e.g. Bi, Zr, Ti) and various metallic glass alloys. In amorphous metals overlapping tracks produce macroscopic anisotropic growth phenomena [1]. Characterization and imaging of single ion tracks, however, is challenging and has been successful only in a few cases using chemical track etching [2] and scanning probe and transmission electron microscopy [3,4].

Small-angle x-ray scattering (SAXS) provides an suitable tool for measuring ion track properties and has previously been successfully used to measure tracks in amorphous SiO_2 [5]. Here we demonstrate that SAXS is capable of providing evidence for ion track formation and retrieving the track radii in amorphous metallic alloys.

The ion tracks were produced in amorphous $Fe_{80}B_{20}$, $Fe_{85}B_{15}$, $Fe_{81}B_{13.5}Si_{3.5}C_2$, and $Fe_{40}Ni_{40}B_{20}$ by irradiation with 11.1 MeV/u Xe ions at a fluence of 3×10^{11} ions/cm^2 at the UNILAC. The track structure was studied using synchrotron SAXS performed at the Australian Synchrotron (Melbourne). The x-ray wavelength was 1.0332 Å (~12 keV) and the distance between the sample and the CCD detector was 982 mm. Measurements as a function of angle between the x-ray beam and the sample surface (i.e. the ion tracks) show a high anisotropy of the scattering pattern which is consistent with aligned structures of high aspect ratio and gives clear evidence of the existence of tracks.

The scattering data were analysed assuming a cylindrically symmetrical density distribution consistent with continuous track formation and approximately constant energy loss throughout the sample. The simplest model that adequately reproduces the experimental data consists of a cylinder with constant density (different from that of the track surrounding matrix). Figure 1 shows the scattering intensities of the samples (symbols) and the corresponding model fits (solid lines). The track radii obtained from our analysis are summarized in Tab. 1 together with the electronic energy loss estimated using the computer code SRIM [6]. Despite the similar energy loss in all samples, our measurements reveal a considerable difference in the track radii (Δr_{max}~15Å) for the different alloys. The track radii in $Fe_{80}B_{20}$ and $Fe_{85}B_{15}$ are in excellent agreement with first calculations using an inelastic thermal spike model [7].

Further experiments for the systematic study of track formation in metallic glasses, in particular Fe-B alloys, are in progress.

#Matias.rodriguez@anu.edu.au

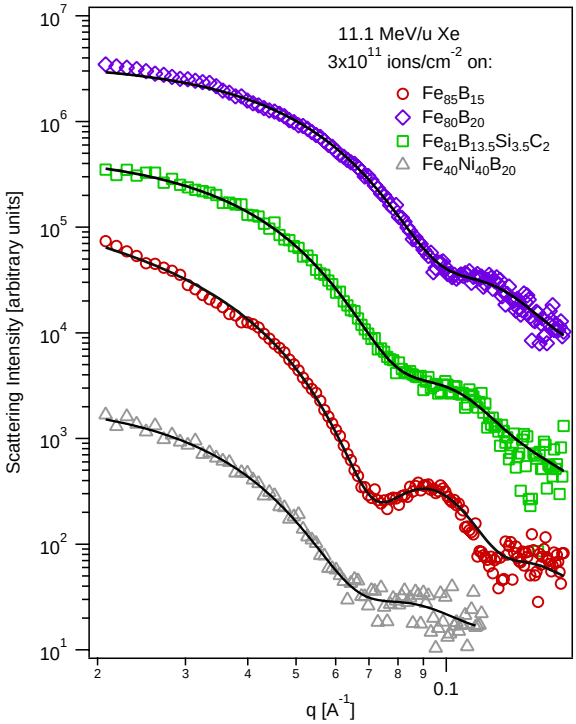

Figure 1: SAXS spectra of the metallic alloys irradiated with Xe ions. The solid lines show the corresponding fits to the hard cylinder model.

Table 1: Track radii obtained from SAXS, material densities and electronic energy loss.

Sample	r [Å]	ρ [g/cm^3]	$(dE/dx)_e$ [keV/Å]
$Fe_{80}B_{20}$	41 ± 1	7.40	3.48 ± 0.01
$Fe_{85}B_{15}$	55 ± 1	7.50	3.52 ± 0.01
$Fe_{81}B_{13.5}Si_{3.5}C_2$	51 ± 1	7.32	3.45 ± 0.01
$Fe_{40}Ni_{40}B_{20}$	59 ± 3	7.74	3.67 ± 0.01

References

[1] M.-D. Hou, S. Klaumünzer, G. Schumacher, Phys. Rev. B 41 (1990) 1144
[2] C. Trautmann *et al.*, Nucl. Instr. and Meth. In Phys. Res. B 107 (1996) 397
[3] A. Audouard, R. Mamy, M. Toulemonde, G. Szenes , L. Thomé, Europhys. Lett. 40 (1997) 527
[4] G. Rizza, A. Dunlop, G. Jaskierowicz, M. Kopcewicz, J. Phys: Cond. Matter 16 (2004) 1547
[5] P. Kluth *et al.*, Phys. Rev. Lett. 101 (2008) 175503
[6] J.F. Ziegler, M.D. Ziegler and J.P. Biersack. http: http://www.SRIM.org.
[7] M. Toulemonde. Private communication.

Swift heavy ion irradiation of diamond at high temperatures *

A.-K. Nix[1,#], U. Vetter[1], D. Severin[2], C. Trautmann[2], and H. Hofsäss[1]
[1]Universität Göttingen, Göttingen, Germany; [2]GSI, Darmstadt, Germany

Diamond to be applied in electronic devices requires doping. Ion implantation, a most suitable doping technique for many cases, has the detrimental disadvantage of producing lattice defects that need to be removed by thermal annealing. For diamond such a process requires temperatures above 1600°C and thus is unsuitable due to the risk of surface graphitization [1]. The aim of this project is to test swift heavy ion irradiation at elevated temperatures as an alternative annealing method. Ion-beam annealing of diamond was reported earlier [2], showing that the RBS channelling yield decreases after high fluence (10^{16} ions/cm^2) irradiations with MeV neon and argon ions at a temperature of 750 °C. This work investigates the possibility of ion beam annealing at lower temperatures and lower fluences by using heavier projectiles of higher energy.

In a first step, type Ia-diamonds of brownish-yellow color were pre-damaged by implanting 100-keV Ar ions of fluence 3×10^{13} and 10^{14} ions/cm^2. Channelling was avoided by slightly tilting the crystals. The mean depth of the implanted layer was 53 nm. To anneal the implantation damage, swift heavy ion irradiation experiments were performed at the new M3-branch at the UNILAC. The samples were exposed to 1.4-GeV Xe ions at 500°C using a fluence of 2.8×10^{12} ions/cm^2 (duration 1.5 h). The ions are stopped at a mean depth of 56 µm, thus far beyond the Ar implanted layer. To test the damage level, the crystals were examined by low temperature (12K) cathodoluminescence after Ar implantation and Xe-ion irradiation.

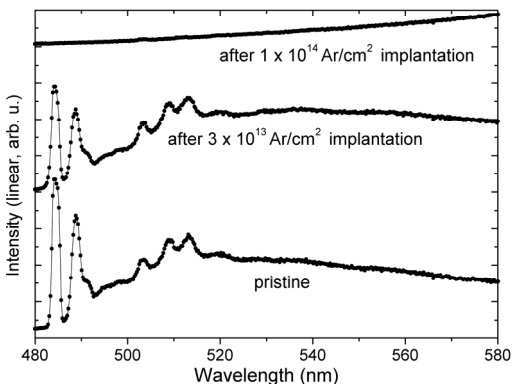

Figure 1: Cathodoluminescence of diamond before and after implantation with 100-keV Ar ions. After implantation at low fluence, the luminescence is reduced, at high fluence it vanishes completely. Spectra are shifted vertically for clarity.

The luminescence of implanted diamond is compared to untreated diamond (backside) in Fig 1. The spectrum of the pristine sample consists of five lines between 480 and 520 nm with a shoulder at 490 nm. After implantation with 3×10^{13} Ar ions/cm^2, the intensity is reduced, but the five lines are still visible, the lines at 500 nm are slightly quenched. After implantation with 10^{14} ions/cm^2, all diamond related luminescence lines disappear. The remaining intensity is due to the blackbody radiation of the filament of the electron gun. After Ar implantation and Xe irradiation at 500°C, no visible change in color was detected. Reference measurements on unimplanted diamond show that annealing diamond at 500°C for 1.5 h does not result in damage formation. Pristine diamond is not significantly affected by swift heavy ion irradiation (not shown). The high-temperature irradiation with Xe ions of diamond implanted with 3×10^{13} Ar ions/cm^2 leads to further damage (Fig 2); luminescence is hardly visible. For comparison with ion-beam irradiation, the sample implanted with 10^{14} Ar/cm^2 was only thermally annealed. Luminescence was detectable after the annealing procedure, but the intensity is low and the spectrum is dominated by black body radiation of the hot filament of the electron-gun.

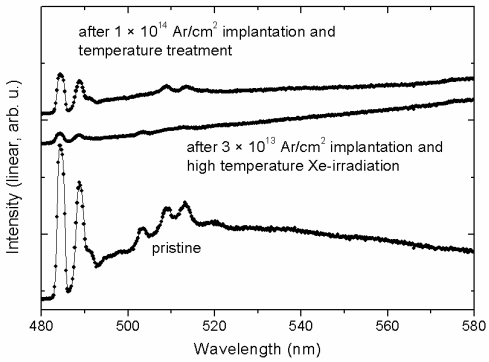

Figure 2: Cathodoluminescence of pristine and high-temperature treated/irradiated diamond. Spectra are shifted vertically for clarity.

In summary we have shown that defects in diamond, intrinsic or resulting from implantation, can be reduced by thermal annealing at 500 °C for 1.5 h. However, no annealing effect appears after irradiation with 1.4-GeV Xe ions. Further experiments are planned with heavier projectiles such as uranium or gold.

[1] A.T. Collins et al, Journal of Applied Physics 97 (2005) 083517.
[2] J. Nakata, Physical Review B 60 (1999) 2747.

* Work supported by German Federal Ministry of Education and Research
#anix@gwdg.de

Conductivity of ion tracks in doped ta-C

H.-G. Gehrke[1#], A.-K. Nix[1], J. Krauser[2], C. Trautmann[3], A. Weidinger[4], and H. Hofsäss[1]
[1]II. Physikalisches Institut, Universität Göttingen, Germany; [2]Hochschule Harz, Wernigerode, Germany; [3]GSI Helmholtzzentrum, Darmstadt, Germany; [4]Helmholtz-Zentrum Berlin für Materialien und Energie, Berlin, Germany.

In tetrahedral amorphous carbon (ta-C), swift heavy ions create electrically conducting tracks of about 8 nm in diameter. The increased conductivity along the ion path is caused by the change of a sp^3-rich to a sp^2-rich bond structure [1,2]. The individual ion track represents a nanowire embedded in the non-conducting ta-C matrix. In this work, we study the effect of doping of ta-C on the resulting track conductivity.

The dominant conduction mechanism of ion tracks in ta-C is variable range hopping [3]. The current through the unirradiated matrix is best described by a Frenkel-Poole like mechanism. The conductivity of matrix and ion tracks can be altered by changing the sp^2/sp^3 hybridisation ratio of the deposited films [4]. By increasing the amount of sp^2 bonds, the conductivity of the matrix as well as ion tracks becomes larger. However, the conductivity ratio decreases resulting in less pronounced tracks. The goal of doping ta-C is to produce highly conductive tracks while preserving the insulating property of the matrix.

The ta-C films (thickness about 100 nm) were prepared by Mass Selected Ion Beam Deposition (MSIBD) on highly doped n-Si (0.005 Ωcm). The dopants B, Fe and Cu were co-deposited using rapid switching (cycle length about 10^{15} ions) of the selected mass with concentration of 1-2 %. The irradiations were performed at the UNILAC using Au and U ions of fluences of 3×10^{10} cm^{-2}. The beam energy was about 1 GeV corresponding to a high electronic energy loss. For the electrical analysis of individual tracks we used the conductive tip of an atomic force microscope (AFM). In addition, track ensembles were measured at different temperatures (15-300 K) using macroscopic contact pads evaporated onto the film.

AFM measurements show visible tracks in all four doped systems. The average resistivity of single tracks is shown in table 1. The undoped tracks exhibit the highest resistivity. Boron slightly improves the track conductivity whereas Fe and Cu lead to significant increases in conductivity.

Table 1: Averaged conductivity of ion tracks in doped ta-C measured using the conducting tip of an AFM.

Dopant	none	B	Fe	Cu
ρ [Ωcm]	10	6.3	0.33	0.63

The measured conductivity of macroscopic contact pads on undoped ta-C films exhibits an increase in conductivity of irradiated samples by 4 orders of magnitude. At the given fluence, the tracks cover an area of only 1-2 % of the film. Assuming that only this area is changed implies an increase in conductivity of up to 6 orders of magnitude within tracks.

The conductivity of track ensembles can be estimated by the difference in conductivity before and after irradiation. To calculate the conductivity of single tracks, these values are normalized by the number of tracks covered by the contact pad. Figure 1 shows the ratio of the calculated conductivity of ion tracks and unirradited ta-C matrix as a function of temperature for Cu, Fe, and B as dopant. Doping leads to a significantly smaller conductivity contrast, except for Cu which approaches the undoped value close to room temperature.

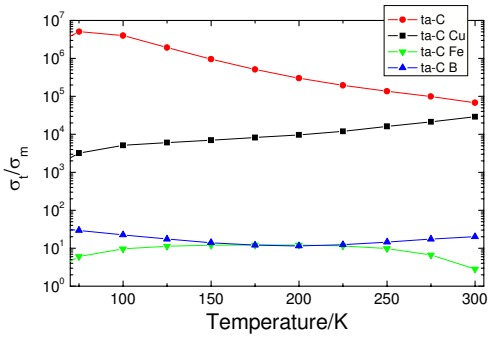

Figure 1: Ratio of track to matrix conductivity (conductivity contrast) measured on contact pads. Data is shown for doped and undoped ta-C at different temperatures.

In contrast to the AFM-deduced conductivities, the measurements using contact pads indicate similar conductivities of track ensembles independent of doping. However, doping obviously increases significantly the matrix conductivity. In the case of iron, the increase due to doping is as large as the effect of the ion irradiation. Copper dopants give the best results in terms of conductivity contrast between matrix and track. In addition, the contrast improvement with increasing temperature suggests further benefit above room temperature.

AFM measurements show that doping of ta-C improves the conductivity of tracks, whereas macroscopic measurements indicate only a significant increase of the matrix conductivity, while the track conductivity is not affected by doping. This discrepancy can be explained by the different contact resistances which might decrease the measured currents with contact pads. In addition, the extremely local AFM tip may distort the electrical field lines which force charge carriers from the matrix into the track. Hence, higher matrix conductivity leads to better track conductivity if contacted individually. B and Fe doping seems not suitable because it decreases the conductivity contrast too much, while Cu doping shows promising results for higher temperatures.

[1] M. Waiblinger et al., J. Appl. Phys. 69 (1999) 239
[2] J. Krauser et al., J. Appl. Phys. 94 (2003) 1959
[3] A.-K. Nix et al., Rev. Adv. Mater. Sci. 15 (2007) 192
[4] J.-H. Zollondz et al., Mater. Sci. Eng. 26 (2006) 1171

#hans-gregor.gehrke@phys.uni-goettingen.de

Nanoindentation of heavy ion-induced hardening of graphite

I. Manika[1], J. Gabrusenoks[1], J. Maniks[1], R. Zabels[1], M. Krause[2,3], M. Tomut[2,4,#], K. Schwartz[2], and C. Trautmann[2]

[1]Institute of Solid State Physics, University of Latvia, Latvia, [2]GSI Helmholtzzentrum, Darmstadt, Germany, [3]Technische Universität Darmstadt, Germany, [4]NIMP, Bucharest, Romania, ,

Irradiation-induced modifications of mechanical properties of graphite have been the subject of numerous studies. However, only few of them have been performed with swift heavy ions. The present work is focused on nanoindentation on isotropic fine-grained graphite exposed to swift uranium ions. This technique is well-proven for nanoscale mechanical characterization and most suitable for our graphite samples modified within a layer of only 100 μm.

Slabs of isotropic polycrystalline graphite were irradiated with ^{238}U ions of 11.1 MeV/u specific energy. The irradiations were carried out at the UNILAC, at room temperature and under normal beam incidence. We applied large fluence up to 1×10^{13} ions/cm^2 to maximize the damage. The sample thickness was in all cases much larger than the penetration depth of the ions (~97 μm).

Nanoindentation tests were performed using a MTS G200 nanoindenter with Berkovich diamond tip (R<20nm) applying the continuous stiffness mode at load resolution <50 nN, displacement resolution <0.001 nm and strain rate 0.05 s^{-1}. Hardness and Young's modulus values were deduced by averaging 10 individual tests. The distance between adjacent impressions was sufficiently large to avoid interaction of neighbouring deformation fields. In order to obtain the depth profiles of hardness and modulus, the measurements were performed on the surface of the irradiated samples as well as on cross-sections prepared by cutting the sample normal to the surface (parallel to beam incidence). The distance of the indents from the irradiated surface was measured by optical microscopy.

Figures 1 and 2 show hardness and Young's modulus data as a function of the distance from the irradiated surface (figure also contains the electronic energy-loss of the ions). Maximum irradiation effects are observed on the surface. The hardening effect shows a marked increase at a fluence of 1×10^{13} ions/cm^2, for which ion tracks strongly overlap. The hardness enhancement decreases with distance from the irradiated surface, and when approaching the projected range of the ions, the hardness falls below the value of the pristine sample.

The gain of ion-induced hardening on the graphite surface is surprisingly high (up to 500%). For comparison, ion-induced hardening of LiF, which serves as model material in many radiation damage studies, reaches a limit of only ~200 % [1]. This extra strengthening can be related to ion-induced damage leading to an increase of sp^3 bonds, bending of graphite layers, and layer interconnections via interstitial atoms. The values of Young's modulus together with Raman spectroscopy results indicate the formation of stronger chemical bonds. The process is favoured by polishing of the sample surface before irradiation, inducing a reduction of the grain size and making the very top layer of graphite more susceptible to swift heavy-ion induced damage.

Hardness values lower than those for virgin sample near the interface between irradiated and non-irradiated layer are ascribed to residual elastic stress created due to swelling of the irradiated layer. Tensile stress is known to reduce both Young's modulus and hardness.

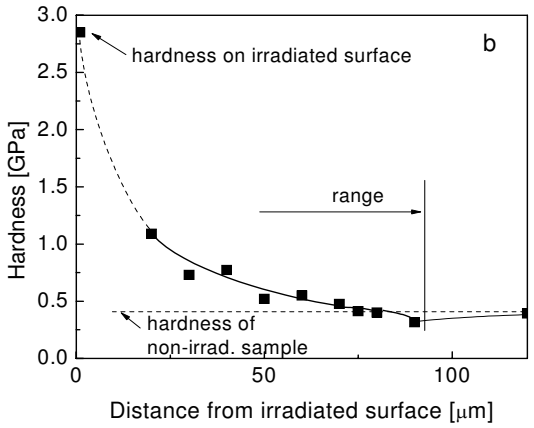

Figure 1: Hardness as a function of depth for graphite irradiated with 10^{13} U ions cm^{-2}.

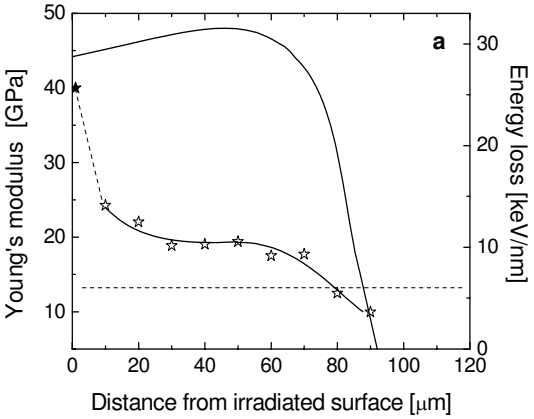

Figure 2: Depth profile of Young's modulus of graphite irradiated with 10^{13} U-ions/cm^2. The diagram displays also the electronic energy loss calculated with the SRIM code. The horizontal dotted line indicates the value of Young's modulus for pristine material.

[1] I. Manika *et al*., J.Phys. D 41 (2008) 074008.

#m.tomut@gsi.de

Microstructural Evolution of Helium-Implanted Isotropic Graphite

M. Krause[1,2,#], M. Tomut[2,3], S. Amirthapandian[4,5], C. Trautmann[2], and W. Ensinger[1]
[1]Technische Universität Darmstadt, Germany; [2]GSI, Darmstadt, Germany; [3]NIMP, Bucharest, Romania;
[4]IHFG, Universität Stuttgart, Germany; [5]MSG, IGCAR, Kalpakkam, India

The present study is motivated by the application of isotropic graphite as material for the rare isotope production target and for the beam catchers of the Super-Fragment Separator (S-FRS) of FAIR. These components have to withstand long-term beam exposure of high-energy ions at extreme flux conditions. Radiation damage and material degradation effects of concern are induced by primary beams as well as lighter ions originating from nuclear fragmentation. Among these, helium plays a special role due to its tendency to be trapped at defect sites (intrinsic as well as radiation induced defects) and to aggregate in bubbles. The accumulation between graphitic planes leads to additional swelling along the hexagonal axis of the graphite crystallites. Helium clusters at grain boundaries results in embrittlement which is in particular crucial with respect to the material response to thermal shock for extremely intense and short beam pulses (fast extraction regime). Additional damage of the graphite structure is expected when over-pressurized bubbles burst. The fraction of He retention and critical concentrations depend strongly on the type of graphite. In this study, we tested fine-grained isotropic R6650 grade (SGL Group) graphite as material selected for the S-FRS target and beam catcher.

To simulate the effect of He fragments, polished R6650 grade graphite samples were implanted with 100-keV He^+ ions, applying various fluences at room temperature. Microstructural changes, He accumulation, and swelling were investigated by profilometry, Raman spectroscopy, and scanning electron microscopy.

With increasing fluence up to 1×10^{16} ions/cm^2, Raman spectroscopy reveals milling of the graphite crystals from micrometer to nanometer size. Above this fluence, graphite is completely amorphized (Fig. 1). Also the shift of the graphite band (G-peak at 1580 cm^{-1}) as well as the area-ratio of the defect-peak (D-peak at 1355 cm^{-1}) to G-peak (Fig. 2) has a maximum at this critical amorphization fluence [1].

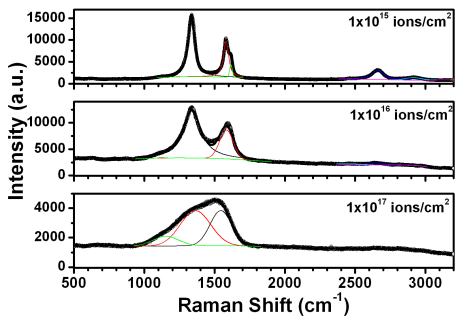

Fig. 1: Raman spectra of R6650 graphite exposed to 100-keV He^+ ions at three different fluences.

#m.krause@gsi.de

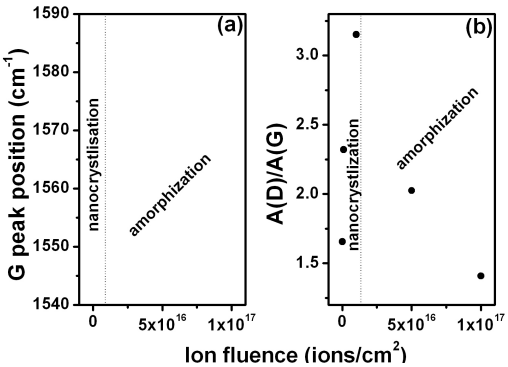

Fig. 2. Raman data as a function of fluence: (a) position of G-band and (b) ratio of area of A- to G-band.

For fluences below complete amorphization, the implanted samples the surface has a porous structure and profilometry indicates roughening rather than swelling. At a fluence of 1×10^{17} ions/cm^2, we observe burst He bubbles (it is known that amorphous carbon does not retain helium). Bunches of graphene ribbons, carbon whiskers and tubes were formed at sites of explosive release of He (Fig. 3b and 3c). The critical concentration of trapped He of this implantation experiment is ~7 at%, which is larger than the calculated value of He accumulated in the target during one year of operation (about 5 appm/year) [2]. Fig. 3d shows a magnified detail inside a burst He cavity. The structure consists of cross-linked and strongly bent, discontinuous graphitic ribbons and flakes, characteristic for "glassy" carbon.

Further annealing studies will follow the evolution of trapped He at temperatures corresponding to target and beam catchers operation.

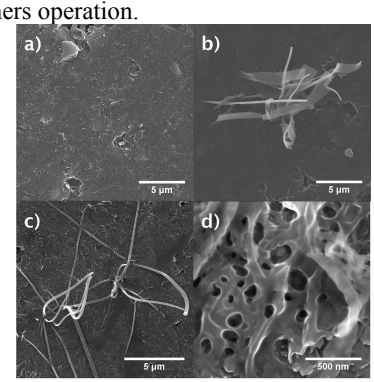

Fig. 3: Scanning electron micrographs of graphite: (a) before and (b-d) after irradiation with 100-keV He^+ of fluence 1×10^{17} ions/cm^2.

[1] J. Ferrari *et al.*, Phys. Rev. B 61 (1999) 14095.
[2] M. Tomut *et al.*, GSI Scientific Rep. 2005 (2006) 202.

Structural Modifications of $Gd_2Zr_{2-x}Ti_xO_7$ Pyrochlore Induced by Swift Heavy Ions

M. Lang[1#], F.X. Zhang[1], J.M. Zhang[1], J. Lian[2], C. Trautmann[3], W.J. Weber[4], and R.C. Ewing[1]
[1] University of Michigan, Ann Arbor, MI, U.S.A.; [2] Rensselaer Polytechnic Institute, Troy, NY, U.S.A.; [3] GSI, Darmstadt, Germany; [4] Pacific Northwest National Laboratory, Richland, WA, U.S.A.

Recently, there has been increased interest in using materials with fluorite and fluorite-related structures, such as pyrochlore, as potential host phases for the immobilization of actinides. Radiation damage from incorporated actinides can cause microstructural changes, such as macroscopic swelling, and a decrease in the chemical durability of the nuclear waste form, which may deteriorate its long-term performance. Structural modifications from alpha-decay events have been studied in great detail; whereas, the effect of energetic fission fragments on the stability of pyrochlore are for the most part unknown.

Swift xenon ions (1.43 GeV) from the UNILAC accelerator of GSI were used to systematically investigate the radiation response of pyrochlores in the $Gd_2Zr_{2-x}Ti_xO_7$ binary in the electronic energy loss regime. Ion-induced structural modifications were characterized by synchrotron x-ray diffraction (XRD), Raman spectroscopy and transmission electron microscopy (TEM).

Similar to the effects of low-energy irradiations, the composition of pyrochlore has a strong effect on the details of the ion-induced structural changes. In Ti-rich pyrochlore, amorphization is the dominant process; whereas, Zr-rich compositions transform to the disordered, defect-fluorite structure [1]. The size of individual ion tracks is deduced by either direct measurements (TEM), or indirectly from cross-section data obtained from fitting procedures (Raman, XRD). The cross-sections were calculated from the fluence-dependent growth of the amorphous phase (XRD) or decrease of the crystalline pyrochlore domains (Raman). For a given composition, each technique produces different track diameters because they probe different length-scales of the structure (Fig. 1a). The combination of different analytical techniques provides a semi quantitative track description consisting of concentric cylindrical zones [2]. Except for $Gd_2Zr_2O_7$ (not amorphizable), ion tracks in the $Gd_2Zr_{2-x}Ti_xO_7$ binary have an *amorphous core*, surrounded by a *disordered, defect-fluorite structured shell* and a *strained, defect-rich pyrochlore halo* (illustrated by concentric circles in Fig. 1). For the Ti endmember, $Gd_2Ti_2O_7$, the damage morphology and size of individual damage zones are in general agreement with the actual track structure as imaged by high-resolution TEM (Fig 1b). The complex variation in structure reflects the non-linear radial dose deposition along the path of a swift heavy ion.

[1] M. Lang, F.X. Zhang, J. Lian, C. Trautmann, Z. Wang, R.C. Ewing, J. Mater. Res. 24 (2009) 1322.
[2] M. Lang, J. Lian, J. Zhang, F.X. Zhang, W.J. Weber, C. Trautmann, R.C. Ewing, Phys. Rev. B 79 (2009) 224105.

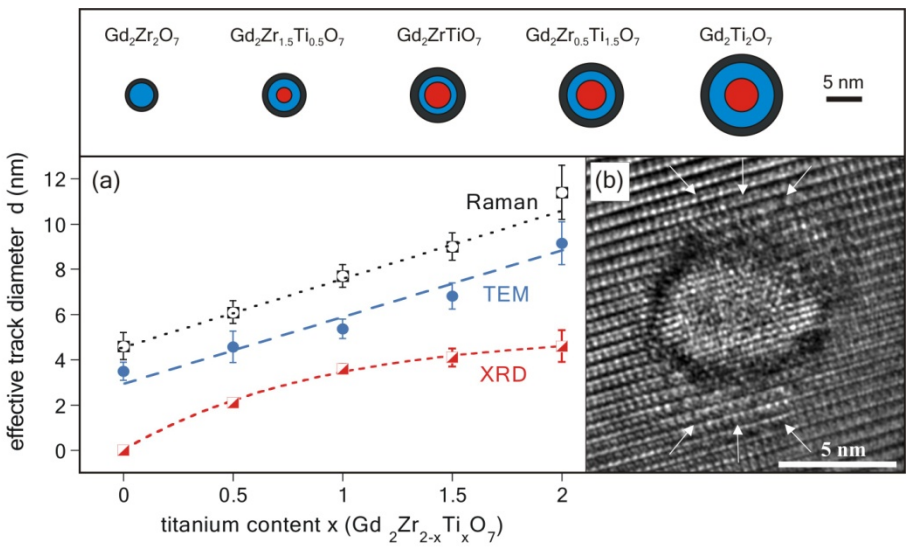

Fig 1: (a) Track diameter as a function of pyrochlore composition (Ti-content *x*). For XRD and Raman spectroscopy, the mean diameter values were deduced from damage cross-sections [2]. TEM diameters were directly measured from bright-field images (errors represent σ of 20 individual measurements). (b) High-resolution TEM image clearly shows that an individual 1.43-GeV Xe ion track in $Gd_2Ti_2O_7$ consists of concentric track cylinders containing different damage zones (schematically illustrated in inset): amorphous core, disordered defect-fluorite structured shell, and strained defect-rich pyrochlore halo [1].

mklang@umich.edu

Nanoscale Manipulation of the Properties of Solids at High Pressure with Relativistic Heavy Ions

M. Lang[1#], F.X. Zhang[1], J.M. Zhang[1], J.W. Wang[1], B. Schuster[2], C. Trautmann[2], R. Neumann[2], and R.C. Ewing[1]

[1]University of Michigan, Ann Arbor, MI, U.S.A.; [2]GSI, Darmstadt, Germany

Investigations of the properties of materials at high pressures are essential to understand the internal structure of Earth. Most recently, materials scientists have also begun to take advantage of high-pressure techniques to fabricate materials with unusual physical and chemical properties. However, a serious draw-back of these efforts is that many of the novel materials are only stable at high pressure, i.e., they rapidly transform back to the low-pressure phase on the release of pressure and cannot be examined *ex situ* or used in special applications. Here, we show that the simultaneous exposure to pressure and ion irradiation creates new possibilities for the stabilization of a new high-pressure phase to ambient conditions [1].

Swift xenon (20 GeV) and uranium (45 GeV) ions from the SIS accelerator of GSI were used to manipulate directly the nanoscale structure of a $Gd_2Zr_2O_7$ pyrochlore at high pressures (10, 21, and 40 GPa). Irradiated and non-irradiated reference samples were characterized by synchrotron x-ray diffraction (XRD) and transmission electron microscopy (TEM). Quantum-mechanical calculations of the different $Gd_2Zr_2O_7$ structure types provide the basis for a theoretical description.

Synchrotron XRD images/ -patterns of $Gd_2Zr_2O_7$ show that the initial pyrochlore (Fig. 1a) transform to the cotunnite-like high-pressure phase at pressures in excess of ~ 17 GPa (Fig. 1b). Ion-beam exposures at ~40 GPa (not shown here) and 21.5 GPa (Fig. 1c) did not result in any obvious structural modification of this phase. Although *in situ* XRD did not evidence significant radiation effects under pressure, the results are surprisingly different for the recovered samples at ambient conditions. Ten hours after release of pressure, the diffraction image and pattern of the unirradiated pyrochlore shows the typical maxima of the defect-fluorite structure (Fig. 1d); whereas, a new phase of unknown structure (denoted as "X-phase") was observed in the irradiated sample immediate (not shown here) and 50 hours after quenching (Fig. 1e). Previous studies suggest that this X-phase is an additional high-pressure phase of $Gd_2Zr_2O_7$, which is (without ion-beam exposure) apparent during pressure release below ~3 GPa, but not quenchable to ambient pressure.

The ion-matter interactions in the cotunnite-like structure have accelerated the transformation to the X-phase during pressure release and, more importantly, have triggered a remarkable stabilization of this novel structure. TEM revealed a radiation-induced, nano-crystalline texture of the irradiated pyrochlore compared with the micron-sized polycrystals of the unirradiated reference sample. The formation of these nanocrystals and effects related to surface energy plays a key role in the stabilization process, which is supported by quantum-mechanical calculations: among the different $Gd_2Zr_2O_7$ structures (pyrochlore, defect-fluorite, cotunnite-like, X-phase), the X-phase has the lowest enthalpy of formation at the nanoscale and is, thus, most stable.

Nanoscale manipulation by energetic projectiles and, in particular, the formation of radiation-induced nanocrystals is a unique tool for *in situ* modifications of the thermodynamic pathways upon pressure release. The simultaneous application of high pressure and deposition of energy at large densities provides a new strategy for the recovery of unique, high-pressure structures that are otherwise inaccessible [1].

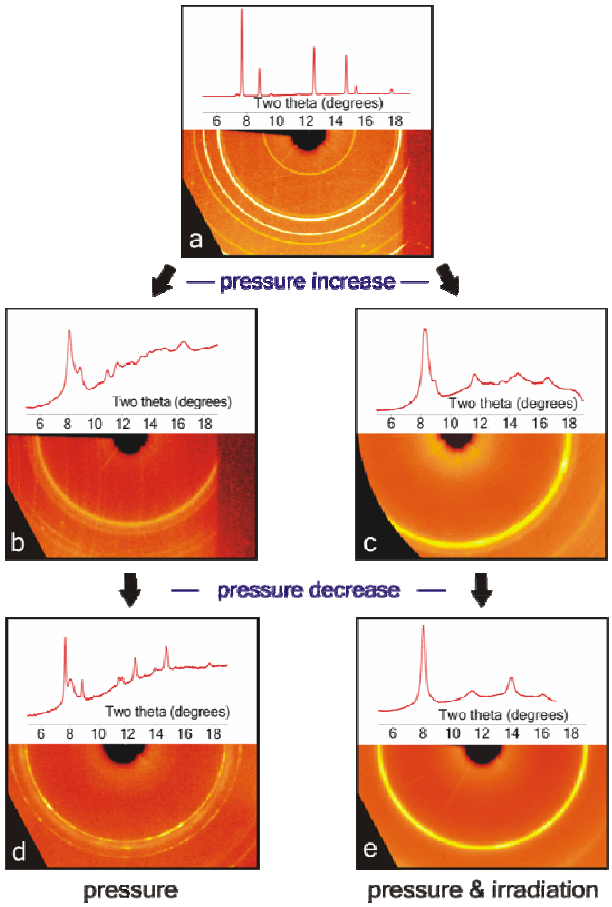

Figure 1: Synchrotron XRD images and patterns of $Gd_2Zr_2O_7$. (a) pyrochlore-structured starting material upon releasing pressure (b,d) without and (c,e) with irradiation [(c) 4 GeV xenon and (e) 7 GeV uranium ions of fluence 3×10^{12} cm^{-2}].

[1] M. Lang, F.X. Zhang, J. Zhang, J. Wang, B. Schuster, C. Trautmann, R. Neumann, U. Becker, and R.C. Ewing, Nature Materials 8 (2009) 793.

mklang@umich.edu

Influence of heavy-ion irradiation on the use of ruby as pressure calibrant

B. Schuster[1,2], R. Miletich[3], R. Neumann[1], C. Trautmann[1], and C. Weikusat[3]

[1]GSI, Darmstadt, Germany; [2]TU Darmstadt, Darmstadt, Germany; [3]Universität Heidelberg, Heidelberg, Germany

In recent years, samples pressurized in diamond anvil cells are being irradiated with energetic ion beams to investigate the response of solids to simultaneous exposure to ions and high pressure. The effects are numerous, e.g. inducing phase transitions far from their usual stability regime or creating and stabilizing phases that are normally not stable at ambient conditions, depending on the investigated material [1, 2]. A common method to calibrate the pressure in the DAC consists of adding a small ruby chip together with the actual sample into the pressure chamber [3]. The positions of the two luminescence lines R_1 and R_2 (694.28 nm and 692.85 nm) serve as pressure indicator [4]. However during the irradiation experiment, the ruby is exposed to the same radiation as the sample itself. Because the luminescence method is applied before and after irradiation to control the pressure inside the cell, the influence of ion radiation on the function of ruby as pressure calibrant had to be investigated.

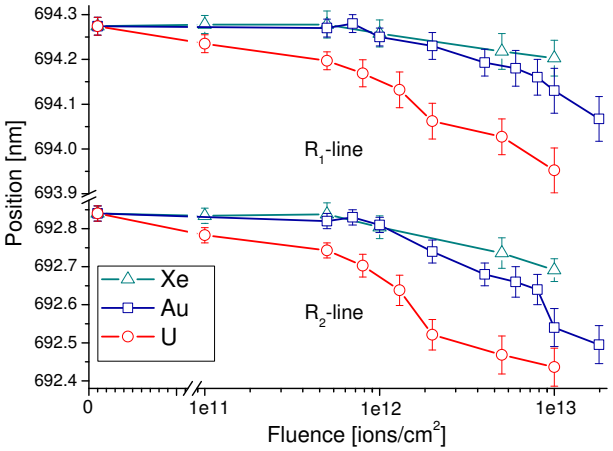

Figure 1: Position of the R_1 and R_2 lines versus fluence for Xe, Au, and U ions.

Several small ruby spheres (10-30 μm in diameter) were packed in between 10-μm thick aluminum foils and irradiated at the UNILAC using different ions (Xe, Au, and U) with a kinetic energy of 11.1 MeV/u. According to the SRIM code [5], the range of the ions is $\sim$60 μm in ruby and thus much larger than the size of the rubies. The stopping process of the ions is dominated by electronic excitation. The average electronic energy loss within the samples was (25$\pm$1.5) keV/nm for Xe, (37$\pm$1.9) keV/nm for Au, and (48$\pm$2.3) keV/nm for U ions. Irradiations of pressurized samples were performed at the SIS with Pb, Au, and Xe ions of an initial kinetic energy about 200 MeV/u so that the ion can reach the sample behind the first diamond ($\sim$2.5 mm) of the DAC. The irradiated rubies were analyzed by measuring the positions of the laser-excited fluorescence lines using a cooled CCD detector of a commercial Raman spectrometer (Horiba Jobin Yvon HR800) and a red He-Ne laser for excitation (exciting wavelength 632.8 nm).

The positions of both luminescence lines are plotted versus the fluence in Fig.1. For all tested ions, the luminescence lines shift to lower wavelength with increasing ion fluence, while the FWHM increases in a similar way. The shift is more pronounced for U than for lighter ions, probably due to the different electronic energy loss in the sample which is almost twice as high for U than for Xe ions.

The shift of the R_1 line, typically used for pressure calibration, is strongest in the case of 1×10^{13} U/cm^2, changing from (694.29$\pm$0.02) nm to (693.95$\pm$0.05) nm. Simultaneously its FWHM increases from (0.67$\pm$ 0.05) to (1.55$\pm$0.12) nm. According to the pressure calibration formula by Mao [4] such a shift of 0.34 nm corresponds to a pressure difference of almost 1 GPa from its actual value. Based on our results we suggest to adjust the calibration formula by including the irradiation effect by an additional term ε to:

$$P(GPa) = \frac{A}{B} \cdot \left[\left(\frac{\Delta\lambda + \lambda_0 + \varepsilon}{\lambda_0} \right)^B - 1 \right]$$

with A = 1904 and B = 7.665 [4]. $\varepsilon = D_\infty \left(1 - e^{-\sigma\Phi}\right)$ with Φ denoting fluence, D_∞ the saturation value of the R_1 shift which is 0.0069, and σ describing the damage cross section caused by one ion which is 2×10^{-12} cm^2 for U. Lighter ions show the same behaviour, but the saturation level could not be reached yet, making it difficult to propose actual values. Further experiments will be conducted.

In summary, the results show that heavy-ion irradiation causes a shift of the luminescence lines to lower wavelengths. For fluences up to 1×10^{12} ions/cm^2 (1×10^{11} for U) the effect is negligible, but for higher fluences one has to consider a pressure underestimate of approximately 1 GPa for 1×10^{13} uranium-ions/cm^2.

References

[1] B. Schuster, M. Lang, R. Klein, C. Trautmann, R. Neumann, and A. Benyagoub, Nucl. Instr. and Meth. B 267 (2009) 964

[2] M. Lang, F. Zhang, J. Zhang, J. Wang, B. Schuster, C. Trautmann, R. Neumann, U. Becker, and R.C. Ewing, Nature Materials 8 (2009) 793

[3] R.A. Forman, G.J. Piermarini, J.D. Barnett, and S. Block, Science 176 (1972) 248

[4] H.K. Mao, J. Xu, and P.M. Bell, Journal of Geophysical Research 91, (1986) 4673

[5] J.F. Ziegler and J.P. Biersack, http://www.srim.org (2008)

Heavy-ion irradiation at high pressure using the Paris-Edinburgh press

C. Weikusat[1], M. Burchard[1#], U.A. Glasmacher[1], S. Klotz[2], R. Miletich[1], C. Trautmann[3], R. Neumann[3]
[1]Institut für Geowissenschaften, Univ. Heidelberg, Germany, [2]Univ. P&M Curie, Paris, France, [3]GSI Materialforschung, Darmstadt, Germany

Up to now, diamond anvil cells (DAC) have been used for irradiation experiments with swift heavy ions and the simultaneous application of high pressures [1]. DACs allow spectroscopic measurements of the irradiated sample inside the cell, e.g. by Raman spectroscopy or x-ray diffraction. However, a drawback is given by their extremely small sample chamber available for sample volumes of less than 10^{-6} mm^3. Various measurement techniques and industrial applications would require larger volumes of irradiated material. Here, we report on first results of a successful test irradiation of a zircon sample ion-exposed inside a large-volume Paris-Edinburgh press (PE press) [2].

The PE press originally developed for neutron scattering, offers a defined radiation pathway as well as relatively high maximum pressure limits (up to 25 GPa). Compared with DAC, sample handling is relative easy, and the sample chamber is large, offering a volume up to several mm³. Pressure is applied by an oil pressure pump attached to the anvils. The large chamber volume provides higher experimental flexibility such as combining different materials of variable grain sizes (so-called mixing experiments), material with sandwich structures of several mm in size, and shear pressure experiments. To reduce ion-induced activation of the material within the central pressure cell, the design of the PE press was modified by thinning the cBN-anvils and using a plastic blend at the entrance part of the open channel. Via this path, the ion beam penetrates the steal material surrounding the irradiation chamber. Another precaution consists of using ultrapure silver as secondary pressure medium and capsule material. The sample chamber was directly drilled into the silver and has a thin hBN-plate on the bottom and a silver foil on top.

For easy and safe handling after irradiation, we developed a metal cave surrounding the PE press. To replace the expensive Cu-Be-alloy commonly used as gaskets material, different types of steal (mat. No. 1.7225, 1.1620 and 14305) were successfully tested.

The first test irradiation was performed with a mixture of zircon and rutile crystals, minerals with well-documented properties and high sensitivity for ion-induced damage that can easily be detected by Raman spectroscopy [3]. The zircon and rutile crystals of several mm in size were heated prior to ion exposure to remove any traces of previous radiation damage. Using the equipment available in cave A at the SIS, the PE-press cell with the samples pressurized to ~6 GPa was exposed to Xe ions of kinetic energy of 300 MeV/u. The applied fluence was 1.5×10^{12} ions/cm^2.

After the irradiation, the pressure was released, and the crystals were carefully extracted under an optical microscope. Raman spectra of the irradiated crystals and pristine zircon from the same batch were acquired under identical measurement parameters. Voigt functions were fitted to each band (Fig. 1).

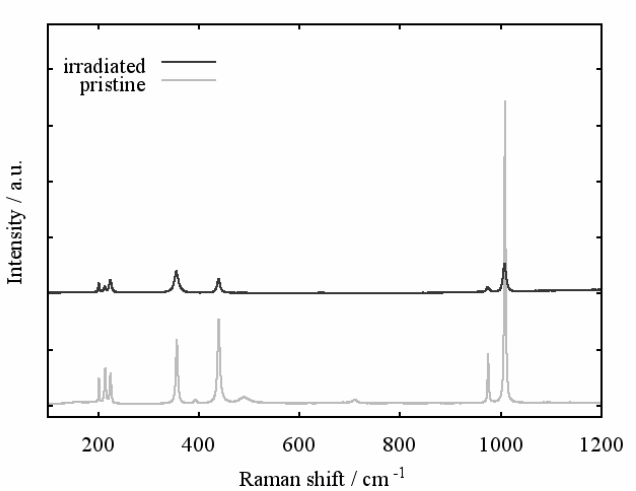

Figure 1. Raman spectra of zircon before and after irradiation under 6 GPa with 1.5×10^{12} Xe-ions/cm^2. The spectra were recorded outside the PE press.

Comparison of the Raman spectra reveals a significant decrease of band intensity after irradiation (Fig. 1). Fitting of each band shows an increase of the band width and a shift of the band centers to lower wavenumbers. Both effects are a clear indication of radiation damage in zircon [3].

In future experiments, we plan to heat the PE cell and vary the pressure and temperature in a systematic way. This will allow us to gain more insight in the specific properties of the zircon-reidite phase transition [4].

References

[1] U.A. Glasmacher, M. Lang, H. Keppler, F. Langenhorst, R. Neumann, D. Schardt, C. Trautmann, G.A. Wagner, Phys. Rev. Lett. **96** (2006) 195701.

[2] C. Weikusat, M. Burchard, U.A. Glasmacher, S. Klotz, R. Miletich, C. Trautmann, R. Neumann, GSI Scientific Report 2008 (2009) 345.

[3] M. Zhang, E.K.H. Salje, I. Farnan, A. Graeme-Barber, P. Daniel, R.C. Ewing, A.M. Clark, H. Leroux, J. Phys.: Condens. Matter, **12** (2000) 1915.

[4] M. Lang, F. Zhang, J. Lian, C. Trautmann, R. Neumann, R.C. Ewing, Earth and Planetary Science Letters **269** (2008) 291.

#michael.burchard@geow.uni-heidelberg.de

Ion tracks in apatite at high pressures. The effect of crystallographic track orientation on the elastic properties of fluorapatite under hydrostatic compression

P. Schouwink[1,#], R. Miletich[1], A. Ullrich[1], U.A. Glasmacher[1], C. Trautmann[2], R. Neumann[2], B. Kohn[3]

[1]Instut für Geowissenschaften, Univ. Heidelberg, Germany, [2]GSI, Darmstadt, Germany, [3]School of Earth Sci., Univ. Melbourne, Australia

Apatite comprises a group of minerals, usually referred to as fluorapatite, hydroxylapatite, and chlorapatite according to their endmember compositions Ca5(PO4)3X (X=F,OH,Cl). Apatite has been subject to numerous investigations due to the fact that it is produced and used in biological micro-environmental systems, and is the major inorganic component in (not only human) osseous tissues. The second prominent impact concerns fission-track dating in geosciences, which provides a modern geological dating tool and yields specific information on the low-temperature thermal history of rocks in various geological settings.

Static elasticity measurements at high pressures were performed on oriented fluorapatite single crystals, some of which contained oriented amorphous ion tracks produced with 2.2-GeV Au ions from the UNILAC. High-pressure experiments on irradiated and non-irradiated crystal sections were carried out in diamond-anvil high-pressure cells under hydrostatic conditions [1]. In-situ single-crystal diffraction was performed to determine the high-precision lattice parameters, simultaneously monitoring the widths of XRD Bragg peaks. High-pressure Raman spectra were analyzed with respect to the frequency shifts and widths of bands, which correspond to the Raman-active vibrational modes of the phosphate tetrahedra.

Swift heavy ion irradiation was found to induce anisotropic lattice expansion and tensile strain within the host lattice dependent on the orientation of the ion tracks with respect to the crystal axes. The relatively low Grüneisen parameter for the ν1b(Ag) mode, which has been assigned to originate from the amorphous volume fraction, and the $\gamma(\nu 1a)/\gamma(\nu 1b)$ ratio reveal compressive strain on the tracks consisting of amorphous material. The comparative compressibility for the host lattice evidences approximately equivalent bulk moduli, but significantly different pressure derivatives (the isothermal bulk moduli K_T = 88.4±0.7 GPa, $\partial K/\partial P$ = 6.3±0.3 for nonirradiated, K_T = 90.0±1.7 GPa, $\partial K/\partial P$ = 3.8±0.5 for irradiated samples). The axial compressibility moduli β-1 show significant differences, which correlate with the ion-track orientation (βa-1 = 240±5 GPa, βc-1 = 361±14 GPa, $\partial(\beta a\text{-}1)/\partial P$ = 11.3±1.2, $\partial(\beta c\text{-}1)/\partial$P = 11.6±3.4 for irradiation ⊥(100); 246±9 GPa, 364±57 GPa, 9.5±2.9, 14.7±14.1 for irradiation ⊥(001), and 230.7±3.6 GPa, 373.5±5.1 GPa, 19.2±1.4, 20.1±1.8 for non-irradiated samples).

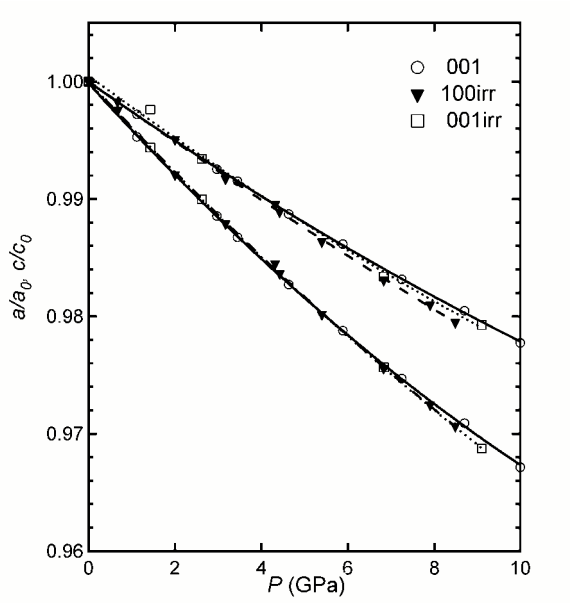

Figure 1: Static compression behaviour of crystallographic *a* and *c* axes of apatite single crystals irradiated parallel (001irr) and perpendicular (100irr) to the *c*-axis, in comparison with non-irradiated sample (001). (upper graph: c/c_o; lower graph: a/a_o)

Line widths of XRD Bragg peaks in irradiated apatites confirm the strain of the host lattice, which decreases with increasing pressure. By contrast, the bandwidths of Raman modes increase with pressure, and this is attributed to increasing strain gradients on the length scale of the short-range order. The investigations reveal considerable deviatoric stress on the [100]-oriented tracks due to the anisotropic elasticity, while the compression is uniform for the directions perpendicular to the tracks, which are aligned parallel to the *c*-axis. This difference might be considered to control the diffusion properties related to the annealing kinetics and its observed anisotropy, and hence to cause potential pressure effects on track-fading rates.

[1] P. Schouwink, R. Miletich, A. Ullrich, U.A. Glasmacher, C. Trautmann, R. Neumann, B.P. Kohn, *Ion tracks in apatite at high pressures. The effect of crystallographic track orientation on the elastic properties of fluorapatite under hydrostatic compression*, 2009 accepted for publication in Phys. Chem. Minerals, DOI 10.1007/s00269-009-0340-0

Pascal.Schouwink@min.uni-heidelberg.de

The hBN to wBN phase transition modified by heavy ion irradiation

R. Klein[1], P. Schouwink[2], R. Miletich[2], B. Schuster[1], C. Trautmann[1], and R. Neumann[1]
[1]GSI, Darmstadt, Germany; [2]University of Heidelberg, Germany

Boron nitride (BN) shows similarities to carbon, having a hexagonal (graphite-like) structure (hBN) and a cubic diamond type (cBN). Under ambient temperature conditions, hBN transforms irreversibly into wurtzitic BN (wBN) at pressures above 10.8 GPa [1]. We investigated the influence of ion irradiation on this displacive phase transition using *in situ* Raman spectroscopy and synchrotron X-ray diffractometry (XRD). To test the phase transition, powder samples (Sigma-Aldrich) as well as single crystals (fabricated in a high temperature / high pressure procedure [2]) were pressurized in a diamond anvil cell (DAC), using rhenium as gasket and a methanol-ethanol mixture as pressure transmitting medium. A ruby crystal served as pressure gauge to be read out via fluorescence spectroscopy. After each step of pressure increase, the sample was allowed to relax for 1 h before recording XRD data.

The exposure to heavy ions was performed at the UNILAC under vacuum and ambient temperature conditions using Au and Xe ions of 11.1 MeV/u specific energy and fluences between 5×10^{11} and 1×10^{13} ions/cm^2. Three irradiated single crystal samples and a pristine crystal were pressurized simultaneously in order to perform *Raman spectroscopy* employing a HR800 spectrometer (HORIBA) with a 17 mW He/Ne laser (λ = 632.8 nm). The Raman signal of the intra-layer E_{2g} vibration between the B and N atoms in hBN single crystals provides sufficiently high intensities to allow spectroscopic measurements of the sample in the DAC. The disappearance of the hexagonal phase is evidenced by the simultaneously vanishing E_{2g} band, with a band maximum at a wavenumber of ν = 1365 cm^{-1} (P = 0 GPa). We monitored the band intensity as a function of pressure (Fig. 1). For all samples, the vibrational E_{2g} mode diminishes by a few percent with increasing pressure up to 10.8 GPa, the slope becomes steeper for larger fluences. Above a critical value of about 11-12 GPa, the band intensity drops rapidly indicating a significant loss of the hexagonal phase. For the highest irradiation fluence (1×10^{13} Xe ions/cm^2), the band disappears entirely at 10.8 GPa, whereas for lower fluences this occurs gradually and at higher pressures. At 12 GPa, none of the samples shows traces of hBN.

X-ray diffraction studies were conducted on commercially available hBN powder samples. Pristine samples as well as specimens irradiated with Au ions (5×10^{11} and 1×10^{12} ions/cm^2) were investigated at the beamlines ID 27 of the ESRF (Grenoble, France), and ID 16 of the APS Argonne National Laboratory (Chicago, USA), applying pressures up to 25.0 GPa. A MAR345 IP detector was used for data collection. The X-ray beam was focused to 6×15 μm^2 at a fixed wavelength of λ = 0.37 Å (ESRF), and 0.41 Å (APS).

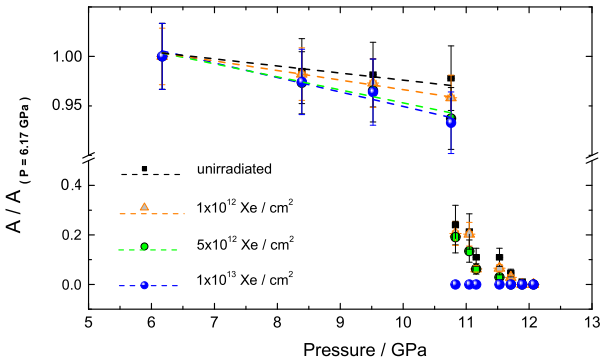

Figure 1: Intensity of E_{2g} Raman band of hBN (normalized to band intensity at 6.17 GPa) as a function of pressure. Depending on the fluence applied, the band disappears above a critical pressure.

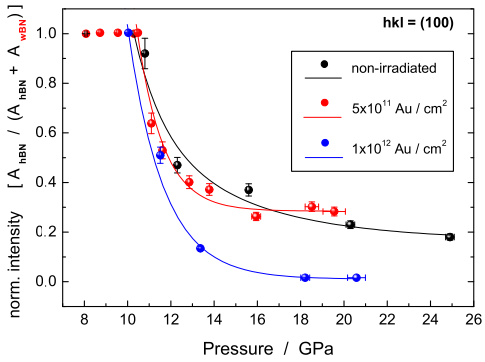

Figure 2: Normalized XRD intensities of (100) reflection of hBN compared to wBN as a function of pressure. Unity corresponds to pure hBN, zero indicates pure wBN.

As depicted in Fig. 2, only the hBN sample exposed to 1×10^{12} ions/cm^2 transformed entirely into wBN at 18.2 GPa.

Our Raman and XRD data clearly demonstrate that the irradiation of hBN with swift heavy ions prior to pressurization enhances the hBN to wBN phase transition. The transformation is more or less complete depending on the applied fluence. The effect is ascribed to damage creation inducing a buckling of the basal planes in hBN [3].

Acknowledgment. Provision of BN single crystals by T. Taniguchi is gratefully acknowledged.

References

[1] G. Kern *et al.*, Physical Review B 59 (1999) 8551.

[2] T. Taniguchi *et al.*, J. of Crystal Growth 303 (2007) 525.

[3] H. Wang *et al.*, Solid State Communications 149 (2009) 843.

Ultra High Vacuum - ERDA Investigation of NEG Coatings

M. Bender*[1], H. Kollmus[1], M. Wengenroth[1], and W. Assmann[2]
[1]GSI, Darmstadt, Germany; [2]Ludwig Maximilians University, Munich, Germany

In recent years, many large vacuum systems have been complemented by non-evaporable getter (NEG) coatings, including the GSI heavy ion synchrotron SIS 18. A detailed description of the production and operation of NEG thin films at GSI is given elsewhere [1]. Briefly, the getter coating consists of a metallic alloy, here TiZrV with roughly stoichiometric concentration. As a pure metallic surface is highly reactive with active gasses, the gettering process occurs by oxidation, nitration and carbonization of the metal by the dissociated residual gas components in the vacuum system. These reactions saturate increasingly the getter film and after a certain amount of pumped gas the NEG coating has to be reactivated by heating to about 200° C. This procedure is performed at the end of the UHV bake out and leads to a dissolution of the metal-gas-compounds, with the gas diffusing to deeper getter layers. Thus, the amount of pumped gas inside of the layer determines the overall (life time) capacity of the NEG film. While the stoichiometry and the activation behavior of NEG is usually investigated by XPS which is limited to the getter surface, we have investigated an activation and saturation cycle of the complete film thickness by means of elastic recoil detection analysis (ERDA) [2]. This technique allows element specific depth profiling of a sample of several hundred nm thickness. At GSI we are running a unique ERDA setup, operating at vacuum pressures in the 10^{-11} mbar regime. To our knowledge, it is the only UHV-ERDA setup worldwide and allows the detailed investigation of reactive samples such as NEG getters, since the gas load to the surface can be neglected at this pressure. The setup has been equipped with a heatable sample holder, that can heat samples up to 300° C with almost no influence on the vacuum. At higher temperatures the vacuum is slightly deteriorating.

With the described setup, we are able for the first time to present a detailed insight into the gas diffusion in the getter layer during an activation and saturation process. However, this was a pilot experiment to demonstrate the online monitoring qualitatively but not quantitatively. Two samples have been NEG coated at the GSI magnetron sputter facility [1], with a film thickness of about 600 nm. Both samples where first investigated as installed and showed the typical surface oxide peak of a saturated NEG, see fig. 1, top plot (black line; the surface is at energy 45 MeV and deeper layers are towards lower energies). Afterwards, the activation process was started with different temperatures, kept for different time durations. Selected states of the activation process are plotted in the figure, where the oxygen concentration is plotted in the upper and the carbon content in the lower system. Note that all plot data is normalized to equal TiZrV content. The decreasing oxide on the surface is already visible on the red line. At the green line the getter can already be regarded as activated. However, the temperature was further increased to 240° C and kept for up to 8 hours. It is clearly visible how the oxygen is diffusing. To intensify the diffusion we have increased the temperature to 350° C for 4 hours, see the magenta line. In the carbon plot one can observe a slight growing of the surface peak, pointing to a carbonization of the getter film, caused by the slight deterioration of the vacuum at 350° C.

Even the temperatures applied here are far beyond a regular activation process, we have shown how the complete getter layer is filled up by the pumped gas. The saturation process has also been monitored afterwards. During the injection of pure CO a new carbon and oxide peak is growing at the surface. Details can be found in [3].

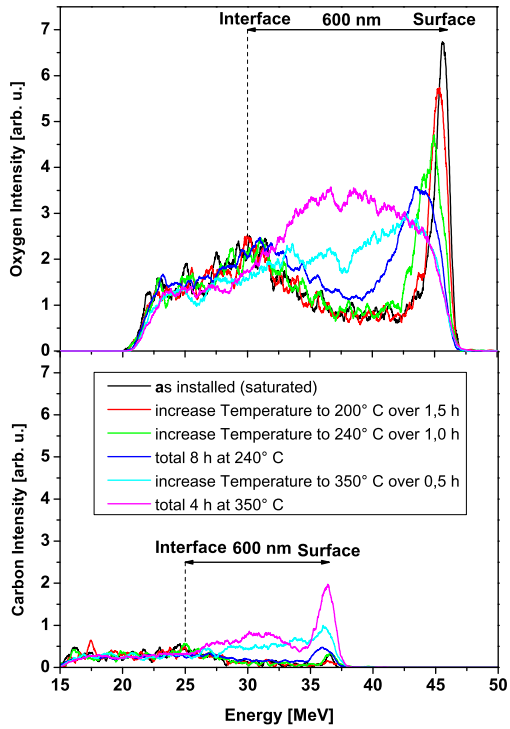

Figure 1: Oxygen and carbon concentration at different states of the performed activation cycle.

[2] M. C. Bellacioma, et al., Vacuum 82 (2008), p. 435
[2] H. D. Mieskes, et al., NIM **B** 146 (1998), p. 162
[3] M. Bender, et al., "UHV-ERDA Investigation of NEG Coatings", submitted to NIM **B**

*contact address: m.bender@gsi.de

In-situ Scanning Electron Microscopy at the UNILAC Accelerator

S. Amirthapandian* and W. Bolse#
Institut für Halbleiteroptik und Funktionelle Grenzflächen, Universität Stuttgart, Stuttgart, Germany
* on leave from: Material Physics Division, Indira Gandhi Centre for Atomic Research, Kalpakkam, India

Because of its technological potential, swift heavy ion (SHI) induced surface structuring has attracted growing interest during the last years. However, until now, very few in-situ analysis experiments during SHI irradiation of solids have been performed (STM [1], XRD [2]). Here we report about the development of an in-situ high resolution scanning electron microscope (HRSEM) at the new materials science beam-line at the UNILAC (M-branch). First results on ion-induced dewetting of a thin oxide film are presented [3].

Figure 1: Photograph of the in-situ HRSEM. The ion beam comes from the right and can either hit the target in the HRSEM analysis chamber or pass through the HRSEM for further experiments.

The instrument is a standard HRSEM (Zeiss, SUPRA 40). It is equipped with a GEMINI column, a FEG-source, an annular in-lens detector, an Everhart-Thornley scintillation detector, a 4-quadrant Si diode backscattered electron detector, and a large eucentric stage for precise positioning of the sample. Apart from that, an in-situ stage specially designed for our setup can be mounted on the eucentric stage, which provides additional tilt of 70° to -90° and continuous azimuthal rotation of the sample. Figure 1 shows a photograph of the experimental set-up, with the HRSEM in the centre and the incoming and outgoing beam-line sections at the right and left side, respectively. The incoming beam-line comprises beam shaping devices (apertures) and diagnostic devices (secondary-electron transmission monitor (SEETRAM), Faraday cup and luminescence target). The HRSEM is placed on a sand-filled box and is coupled to the beam- line through soft edge-welded bellows to suppress vibrations originating from surroundings and beam-line. The HRSEM was positioned such that its distance to accelerator components like magnets and high current power supplies is optimised with respect to electromagnetic noise. Because of these provisions, no significant degradation of the HRSEM resolution was observed. While all the pumps in the beam line were running, we could still image particles of sizes smaller than 5 nm.

* Work supported by BMBF contract No. 05KK7VS1
# w.bolse@ihfg.uni-stuttgart.de

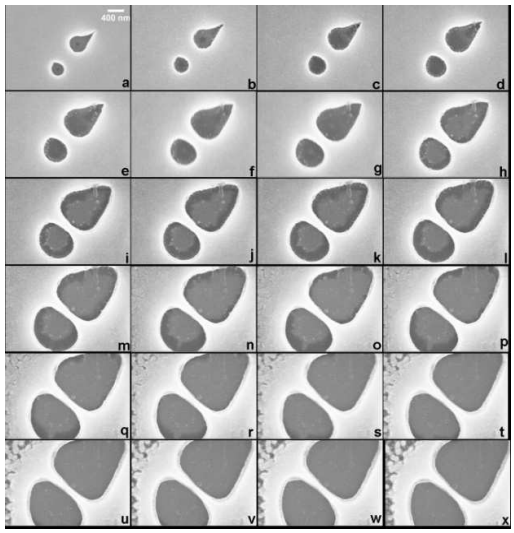

Figure 2: HRSEM images showing the growth of two dewetting holes in Fe_2O_3(50nm)/Si upon 3.6 MeV/u ^{197}Au ion irradiation. From (a) to (x) the irradiation fluence increases in steps of 5×10^{13} up to 11.5×10^{14} ions/cm^2.

For the first irradiation experiment, we selected a 50 nm thin Fe_2O_3 film on a Si-wafer. The sample was pre-irradiated with 195 MeV Au^+ ions (1×10^{14} ions/cm^2) and for this reason already exhibited holes of sub-µm sizes due to SHI induced dewetting [4]. It was mounted on the in-situ stage and exposed to 3.6 MeV/u ^{197}Au ions at normal incidence (-90^o tilt). The fluence ranged from 0.5×10^{14} ions/cm^2 to 11.5×10^{14} ions/cm^2 in steps of 0.5×10^{14} ions/cm^2. After each irradiation step, the beam was stopped and the stage was tilted back to the analysis position at 0^o. HRSEM images were recorded of one and the same spot throughout the whole experiment. Figure 2 shows the evolution of an initially almost circular and a highly asymmetric hole. During irradiation both holes grow in size, repel each other and deform. The observation of the evolution of individual nano- or micron-sized objects nicely demonstrates the unique potential of our setup for the investigation of SHI surface structuring.

[1]. A. Tripathi *et al.,* Rev. Sci. Instrum.72 (2001) 3884.
[2]. P.K. Kulriya *et al.,* Rev. Sci. Instrum.78 (2007) 113901.
[3]. S. Amirthapandian, F. Schuchart, W. Bolse, Rev. Sci. Instrum. 81 (2010) accepted for publication.
[4]. M.T. Moroff, diploma thesis, Stuttgart (2009)

In-situ Infrared Analysis of Ion Degraded Polyimide

T. Seidl[1,2,#], O. Baake[1], U.H. Hossain[1,2], A.O. Delgado[2,3], D. Severin[2], C. Trautmann[2], W. Ensinger[1]
[1]Technische Universität Darmstadt, Germany; [2]GSI, Darmstadt, Germany, [3]University of São Paulo, Brazil

Last year the new M-branch was installed and commissioned in the former Z1 area of the UNILAC experimental hall. Three new beamlines (M1, M2, M3) provide various in-situ analytical tools to study ion-induced effects and material modifications. Ion beams of up to 11.4 MeV/u are available.

In this project, we performed irradiation experiments in the multi-purpose chamber of the M3 beamline (Fig. 1) housing in-situ infrared and ultraviolet/visible-light transmission spectrometers as well as a residual gas analyzer. Samples can be cooled down to 8 K using a Gifford-McMahon refrigerator [1].

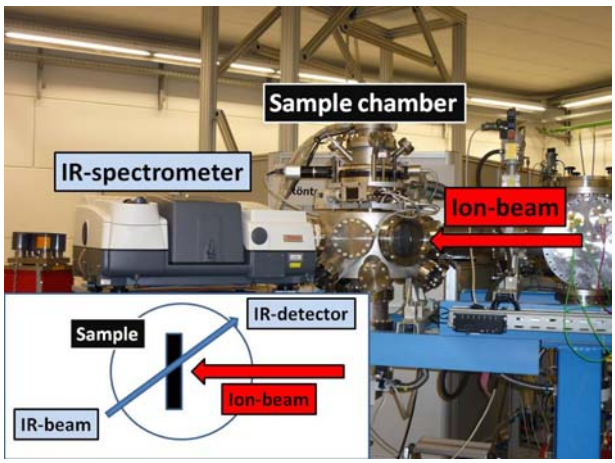

Figure 1: Photograph and scheme of multi-purpose chamber at M3 beamline with in-situ infrared spectroscopy.

The new instrumentation allows in-situ analysis and stepwise monitoring material changes after applying well-defined ion fluences. The spectroscopic measurements are performed during beam stops analysing the sample at the same spot at different fluences and thus avoiding problems because of varying film thickness or other sample inhomogeneities. Moreover, the analysis in vacuum avoids post-degradation of the polymer film due to reactions of long-living radicals with oxygen. In-situ analysis also allows recording relaxation processes occurring within minutes after stopping the beam.

Here, we report first results on ion-irradiated polymer foils analysed by in-situ infrared spectroscopy. As material we used 12-µm thick polypyromelitimide foils (Kapton HN, DuPont de Nemours). This high performance polymer finds wide applications as insulating material exposed to extreme conditions (e.g. spacecrafts, aircrafts, high dose and high temperature environment). The study is motivated by the need of lifetime estimations for Kapton as insulating material of the future superconducting FAIR magnets and better understanding details of the degradation mechanism. Compared with other polymers, Kapton exhibits high resistance against ionizing radiation.

#T.Seidl@gsi.de

However, when directly exposed to ion projectiles, the dielectric strength drops at rather low fluences [2].

The foils were irradiated with 5.6-MeV/u U ions up to a fluence of 10^{12} ions/cm^2. Degradation as a function of fluence was monitored during beam stops by recording infrared spectra in the wavenumber range 400-4000 cm^{-1}. As known from earlier ex-situ experiments, nearly all infrared bands decrease due to the degradation of the molecular structure [3]. In addition, some new bands appear in the range 2750-3000 cm^{-1} (Fig. 2). These bands are identified as saturated carbon-hydrogen bonds and/or carboxylic acids of different degradation fragments. They have not been observed, neither in spectra recorded ex situ [3] nor under thermal degradation or photochemistry alone, and seem to be a special feature of ion-beam induced processes. A special advantage of in-situ analysis is the observation of intensity changes of specific bands on a time scale of minutes: some bands decreasing (increasing) under irradiation, slightly increase (decrease) again during beam stop, indicating recovery of the initial polymer structure. Such short-term processes are difficult to observe by off-line analysis. Future investigations have to clarify if and which kinds of back reactions are responsible for this effect.

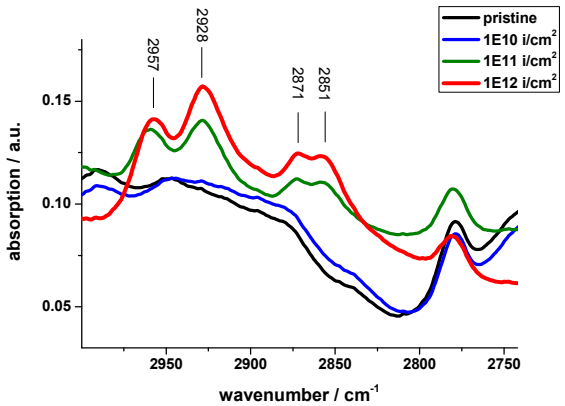

Figure 2: IR spectra of Kapton foils recorded in-situ at the new M3 beamline at the UNILAC. The irradiations were performed with U ions of 5.6 MeV/u.

[1] D. Severin, et al., *The M-Branch, a new UNILAC irradiation facility with in-situ analytical techniques for materials research*, GSI Scientific Report 2008 (2009) 362
[2] T. Seidl et al., *Dielectric Strength of Ion Irradiated Polyimide and Epoxy/Fiber Composites*, GSI Scientific Report 2008 (2009) 341
[3] Steckenreiter et. al., *Chemical Degradation of Polyimide and Polysulfone Films under the Irradiation with Swift Heavy Ions of Several Hundreds of MeV*, J. of Polym. Sci. Part A: Polymer Chemistry 37 (1999) 4318

PTFE degradation under heavy ion irradiation

A.O. Delgado[1,2#], M.A. Rizzutto[1], D. Severin[2], T. Seidl[2,3], C. Trautmann[2] and R. Neumann[2]
[1]University of São Paulo, Brazil; [2]GSI, Darmstadt, Germany; [3]Technische Universität Darmstadt, Germany.

Polytetrafluoroethylene (PTFE) shows an outstanding combination of chemical and physical properties such as excellent resistance to chemical reagents, thermal stability in a wide temperature range, high electric resistance, and low friction coefficient. However, PTFE is known to be extremely sensitive to high energy radiation undergoing scission of the main chain. As a result of the reduction of the molecular weight, the mechanical properties are deteriorated. In the nineties, it was found that PTFE cross-links under electron irradiation under specific conditions, in particular in oxygen free atmosphere and at temperatures just above the melting point (~ 340 °C). A recent study points out that this cross linking can be obtained even at room temperature irradiation using α-particles [1].

In the present work we studied the degradation of PTFE under heavy ion beam irradiation at room and cryo temperatures. PTFE films (25 and 50 µm thick, Enflo Canada Ltd.) were irradiated with different ions (C, Xe, and U) up to energies of 1.5 GeV and fluences of $1x10^{13}$ ions/cm^2 at the UNILAC. The M3-beam line of the new materials research M-Branch allows cryo-irradiations (T = 23-300 K) and online residual gas analysis of volatile degradation fragments. The irradiated PTFE foils were also analysed by offline FTIR spectroscopy.

Mass spectra recorded during room temperature ion irradiation show outgassing of several fragments (figure 1), with CF and CF_3 being the most dominant species. Almost no fragments are observed during the cryo-irradiation at 23 K. However, subsequent sample heating to room temperature leads to outgassing of the fragments starting above 150 K. This result indicates that at low irradiation temperatures small fragments are frozen in and accumulated in the sample.

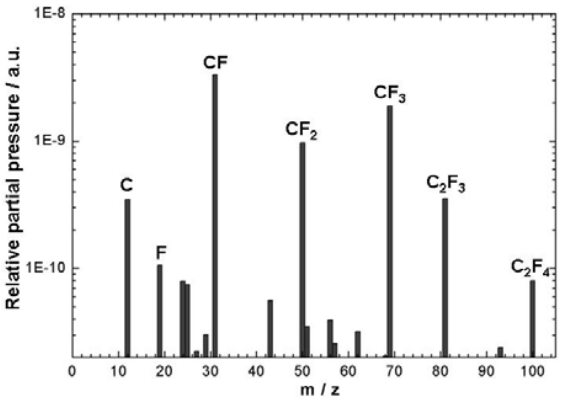

Figure 1: Mass spectra of PTFE outgassing during room temperature irradiation with 1.3 GeV U ions. Specific PTFE fragments are indicated.

*Work supported by CNPq, Brazil process No. 290010/2008-0.
#adelgado@if.usp.br

Offline FTIR analysis (figure 2) of the irradiated samples shows a decrease in the absorption intensity of the bands assigned to the CF_2 bonds, evidencing scission of the main polymer chain. The CF_2 degradation is accompanied by the formation of the CF_3 group indicated by two new bands, one at 738 cm^{-1} (terminal $-CF_3$ group) and another at 985 cm^{-1} ($-CF_3$ side group). Previous studies [2] have pointed out that temperatures around melting provide sufficient mobility to the free radicals in order to form CF_3 side groups. The present results give clear evidence that under heavy ion irradiation sample heating is not required. The ions obviously provide suitable conditions to produce radicals with sufficient high mobility to generate CF_3 groups.

In addition, we observe double bond formation and cross linked structures assigned to bands at 1671, 1717, 1730 and 1784 cm^{-1} (see figure 2). According to the following degradation route, the internal double bond formation (1717 and 1730 cm^{-1}) in irradiated PTFE is an indication of C–F bond scission. Normally, this scission is unlikely due to the higher stability of the C–F bonds, but the observed increase in the intensity of the respective absorption peaks reveals that this process plays a significant role in the degradation induced by swift heavy ions.

$$\sim CF_2 - CF_2 \sim \Rightarrow \sim \dot{C}F - \dot{C}F \sim + 2\dot{F}$$

$$\sim CF = CF \sim + 2\dot{F}$$

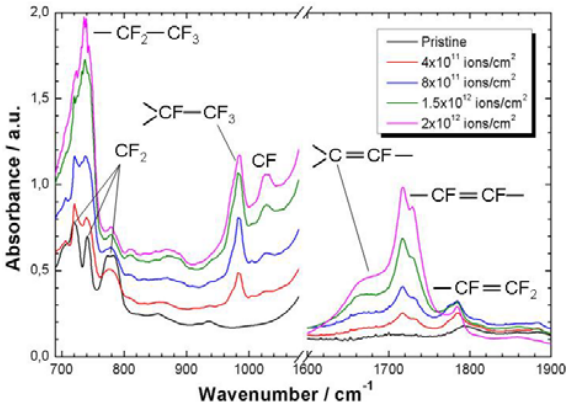

Figure 2: FTIR spectra of PTFE foils irradiated with 1.3 GeV U ions at room temperature. Some degraded and new-formed absorption bands are indicated.

References

[1] D.L. Pugmire, C.J. Wetteland, W.S. Duncan, R.E. Lakis, D.S. Schwartz, Polym. Degrad. Stab. 94 (2009) 1533.

[2] K. Lunkwitz, U. Lappan, U. Scheler, J. Fluor. Chem. 125 (2004) 863.

Heavy Ion Track-Etching of PEEK Membranes

V. Bayer[1], M. Ali[2], W. Ensinger[2], and R. Neumann[1]
[1]GSI, Darmstadt, Germany; [2]Technical University Darmstadt, Germany

Heavy ion tracks in polymer membranes can be transformed into micro- and nano-channels by means of wet-chemical etching. Up to now most commonly polycarbonate (PC), polyethylene therephthalate (PET) and polyimide (PI) membranes were employed for this purpose. For some applications such as proton conductive membranes for fuel cells, high resistance of the material against heat and solvents as well as good electric insulation are required. Among the polymeric materials, polyetheretherketone (PEEK) exhibits all the properties mentioned above. Furthermore, it has been demonstrated that the surface of PEEK can be chemically modified, using hydroxyl groups as a starting point [1]. Applying this kind of surface chemistry inside etched nanochannels would allow the introduction of additional functionality in the PEEK membrane.

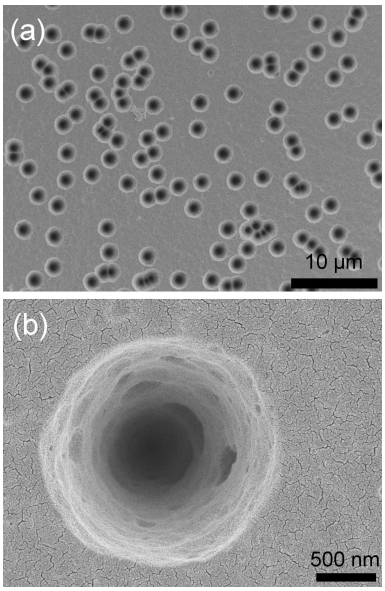

Figure 1: SEM images showing the top view of a PEEK membrane etched for 3 h at 85°C in 50% H_2SO_4 + 7% $KMnO_4$.

The possibility to etch heavy ion tracks in PEEK via wet chemistry has already been reported by C. Daubresse et al. [2]. However, to the best of our knowledge no systematic studies of the resulting channel geometry and size, and of the etch rates against different etching parameters have been made.
First etching experiments were performed with PEEK membranes of 50 μm thickness, which were irradiated with Pb ions with a fluence of 10^7 ions/cm^2. These membranes were immersed for variable time periods in an etching-bath containing 50% (v/v) H_2SO_4 and 7% (w/v) $KMnO_4$ at 75 to 85°C with continuous stirring. After etching, the membranes were washed carefully with deionized water and residues of manganese oxide were removed using diluted HCl.
Channel diameters were measured with high resolution scanning electron microscopy (SEM). The channels have a circular orifice and a relatively narrowly diameter distribution (Fig. 1a). From SEM images it can be deduced that the geometry along the channel axis is double conical. The cone angle becomes wider with reduced content of $KMnO_4$ (oxidizing agent), indicating a larger ratio of bulk- to track-etch rate.

The high-magnification image (Fig. 1b) shows the inside of a single channel. Here one can clearly see, that the surface is quite rough and contains large cavities. This phenomenon is also observable in channels in PET membranes and originates most probably from different etch rates in the crystalline and amorphous regions of a semicrystalline membrane.

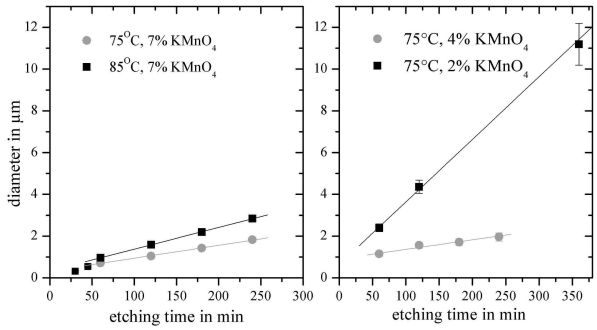

Figure 2: Channel diameter at membrane surface versus etching time for different temperatures and different concentrations of $KMnO_4$ in the etch bath.

The diameters plotted in Fig. 2 are measured from the channel orifice as seen in the top-view SEM images (Fig. 1), and were averaged over multiple channels. Obviously, the etch-curves show a linear behaviour for longer etching durations. The slope of the fit gives the bulk etch rate. Contrary to first expectations, reducing the percentaged content of oxidizing agent leads to higher bulk etch rates.

References

[1] O. Noiset, Y.-J. Schneider, J. Marchand-Brynaert, J. Polymer Science Part A: Polymer Chemistry, **35** (1997), 3779-3790

[2] C. Daubresse, E. Ferain, and R. Legras, Nulc. Instr. Meth. B, **122** (1997), 89-92

Controlling the Length of Conical Pores Etched in Ion-Tracked Poly(ethylene terephthalate) Membranes

H. Mukaibo and C. R. Martin[#]
University of Florida, FL, USA

Conically shaped pores were etched into 12-μm thick ion-tracked PET membranes [1,2] (track density 10^6 cm^{-2}). The irradiations of these films were performed at the UNILAC using heavy ions (e.g., Au or U) of 11.1 MeV/u. Etching was performed at 20 °C or at 30 °C, for various etch times. 5 M KOH in absolute methanol was used as the etch solution, and aqueous 1 M KCl and 1 M HCOOH solution was used as the stopping solution. Replicate of the pores was obtained by filling the pores with electrolessly deposited Au [3], and then chemically dissolving the PET template [2]. Representative field-emission scanning electron microscopy (FESEM) images of the gold cones prepared in this study are shown in Figure 1.

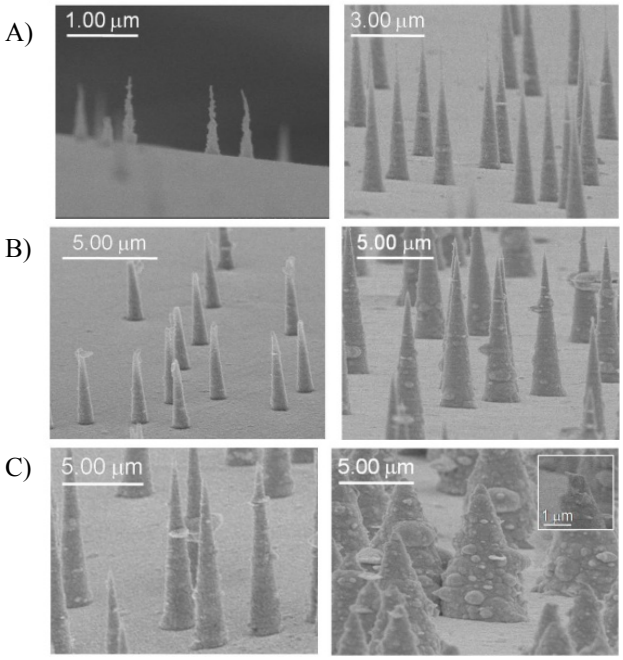

Figure 1: Representative FESEM images of gold cones obtained by replication of pores etched for A) 50 s, B) 175 s, C) 500 s. Left images: pores etched at 20 °C. Right images: pores etched at 30 °C.

The lengths of the cones are plotted against the etch time in Figure 2. At 20 °C, the length increases linearly with etch time. At 30 °C, the length initially increases but then decreases at longer etch times. This occurs because the etch rate is higher at the higher temperature [4] and as a result, the pores quickly (<150 s) break through the entire thickness of the membrane. Once the pores break through, the cone length becomes equivalent to membrane thickness. The decrease in length reflects the membrane thinning effect [2].

[#]crmartin@chem.ufl.edu

We have also found that membrane roughness increases with etch time and etch temperature. This causes the gold cones deposited in pores etched at long times and high temperatures to have very rough surfaces (Figure 1C).

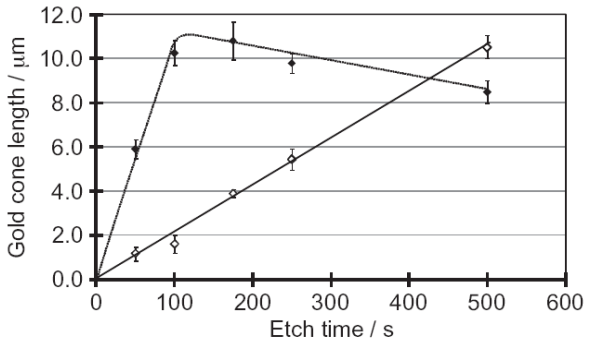

Figure 2: Plots of gold cone length versus etch time. Closed symbols (upper plot): pores etched at 30 °C. Open symbols (lower plot): pores etched at 20 °C. The line for the 20 °C plot is the linear regression best fit line. The line for the 30 °C plot was drawn to aid the eye. Error bars are associated with measurements from three identically etched membranes and ten cones for each membrane.

We also discovered an interesting etching phenomenon that results from the lamellar morphology of the PET membranes. Preferential penetration of the etch solution between the PET strata cause planar projections to form on the gold cones. These projections can be quite large for cones deposited in pores etched for long times at higher temperature [2].

An etching procedure was developed that allows for reproducible control of the length of conically shaped pores etched into PET membranes. These pores were used to prepare arrays of gold cones with length varying from 1 to 10 μm. We have found that membrane roughness increases with etch time and etch temperature. We also discovered that preferential penetration of the etch solution between the PET strata cause planar projections to form on the gold cones.

[1] P. Y. Apel, Y. E. Korchev, Z. Siwy, R. Spohr, M. Yoshida, *Nucl. Instrum. Methods Phys. Res., Sect. B* **2001**, *184*, 337-346.
[2] H. Mukaibo, L. P. Horne, D. Park and C. R. Martin, *Small* **2009**, *5*, 2474-2479.
[3] V. P. Menon, C. R. Martin, *Anal. Chem.* **1995**, *67*, 1920-1928.
[4] V. A. Oleinikov, Y. V. Tolmachyova, V. V. Berezkin, A. I. Vilensky, and B. V. McHedlishvili, *Radiat. Meas.* **1995**, *25*, 713–714.

Poly(vinylidene fluoride)-based ion-track membranes with asymmetrical pores

T. Yamaki[1,#], M. Asano[1], H. Koshikawa[1], Y. Maekawa[1], R. Neumann[2], C. Trautmann[2], K.-O. Voss[2]
[1]Japan Atomic Energy Agency (JAEA), Takasaki, Gunma 370-1292, Japan; [2]GSI, Darmstadt, Germany.

We have been working on ion-track membranes of poly(vinylidene fluoride) (PVDF) because they have attracted a renewed interest for their applications to fuel-cells [1]. There were two main conclusions: (i) The PVDF ion-track membranes can efficiently be prepared under milder etching conditions, i.e., without any oxidant additives in the alkaline etching solution [2]; and (ii) irradiation with ions of higher LET promotes chemical etching in both the track-core and -halo, thereby increasing the etching sensitivity and the resulting pore diameter [3]. In these previous studies, cylindrical pores were always developed because the energy deposition was almost uniform across the film. On the other hand, we found that an LET gradient along the ion path could lead to development of asymmetric pores [4].

Commercially available PVDF films of thickness 25 and 100 μm were irradiated at room temperature by 11.1 MeV/n ^{197}Au ions from the UNILAC. The fluence was fixed to 3×10^7 ions/cm^2. Subsequent track etching was performed in a 9 mol/dm^3 aqueous KOH solution at 80˚C in a teflon-coated vessel without stirring. After depositing a gold coating, the surface of the etched membranes was imaged by scanning electron microscopy (SEM).

Figure 1 illustrates the depth profile of the LET value calculated with the TRIM 1998 code. As can be seen, the LET rapidly decreases with beam energy loss and finally reaches zero at around 130 μm. According to the above concept, we irradiated a stack of two layers of PVDF in the configuration presented in Fig. 1. The first layer exposed to the incoming beam was 100 μm thick. The ^{197}Au ions were sufficiently energetic to pass through this film while they deposited their energy rather uniformly along the full path. In contrast, the thickness of the second layer was only 25 μm. The ions also passed through this film, however, the LET value was only 5.2 MeV/μm at the exit face compared with 19.6 MeV/μm at the entry face.

Figure 2 shows SEM images of the front and back surface of the second layer recorded after etching for 48 h. In agreement with our expectation, the entry face contained pore apertures with a diameter of 232±14 nm while, in contrast, the exit face had 50% smaller pore orifices with a diameter of 117±14 nm. Considering that in this film the LET continuously and very dramatically decreased along the track, it is reasonable to assume the formation of "conical" pores although the pore cross-section inside the membrane was not yet analyzed.

Compared with the widely employed asymmetric etching method involving chemical etching of only one side of the film [5], this new approach is based solely on the LET significantly varying in the thickness direction. One reason for our successful result is probably the very high sensitivity of the etching process assigned to the large difference between the track and bulk etch rate [2,3].

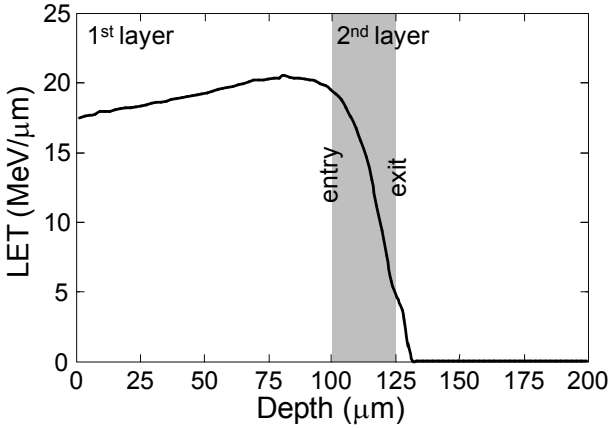

Figure 1: Depth profile of the LET for 11.1 MeV/n ^{197}Au ions in PVDF calculated by the TRIM 1998 code.

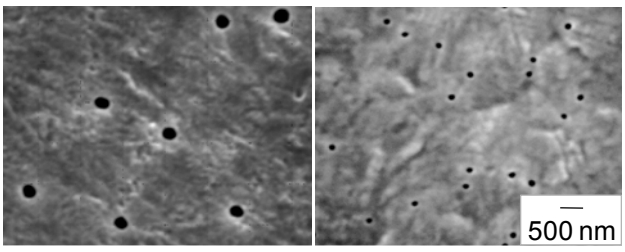

Figure 2: SEM micrographs of the front (left) and back (right) surface of the 25 μm-thick second layer of PVDF.

References

[1] T. Yamaki, Y. Kozone, A. Hiroki, M. Asano, H. Kubota, M. Yoshida, ECS Transactions 3 (2006) 103.
[2] T. Yamaki, R. Rohani, H. Koshikawa, S. Takahashi, S. Hasegawa, M. Asano, K.-O. Voss, R. Neumann, Y. Maekawa, Kobunshi Ronbunshu 65 (2008) 273.
[3] R. Rohani, T. Yamaki, H. Koshikawa, S. Takahashi, S. Hasegawa, M. Asano, Y. Maekawa, K.-O. Voss, C. Trautmann, R. Neumann, Nucl. Instr. Meth. B 267 (2009) 554.
[4] N. Nuryanthi, T. Yamaki, H. Koshikawa, M. Asano, K. Enomoto, S. Sawada, Y. Maekawa, K.-O. Voss, C. Trautmann, R. Neumann, Electrochemistry, in press.
[5] M.-C. Clochard, T.L. Wade, J.-E. Wegrowe, E. Balanzat, Nucl. Instr. Meth. B 265 (2007) 325.

yamaki.tetsuya@jaea.go.jp

Ion Beam Lithography for Cell Culture Substrates

M. Reinhardt[1#], M. Rauber[2,3], C. Trautmann[2], and S. Giselbrecht[1]
[1] Institute for Biological Interfaces, Karlsruhe Institute of Technology (KIT) Campus North; [2] GSI, Materials Research, Darmstadt; [3] Technische Universität Darmstadt, Germany

In the course of time more and more technologies and applications show the demand for micro- and nano structured devices. Beside the microelectronic industry with ever increasing integration densities, also life science disciplines request devices of smaller structures e.g. to be applied in cell biology, where microfluidic systems are used to address specific questions related to cell handling, manipulation, and analysis.

There exists a large variety of techniques used for patterning especially of polymeric materials on the micro- and nanoscale. To achieve structures of high aspect ratio, commonly applied methods are based on x-ray or ion beam lithography.

In this project, we demonstrate the creation of regular surface topographies in polycarbonate (PC) films using GeV heavy ions and chemical track etching. In a first step, the foils are exposed to the ion beam through a structured mask. The damaged material produced along the ion trajectories acts as positive resist that can be removed by chemical etching. This requires large fluences so that the irradiated material can be removed completely due to track overlapping, while the non-irradiated areas remain intact. Using a mask during ion irradiation allows the transfer of a pattern in the mask to the polymer film, producing topography structures of depth that corresponds to the range of the ions [1].

The aim of this project is to combine high-energy ion lithography and microthermoforming in order to create polymeric cell-culture substrates with a hierarchical architecture. Microthermoforming of 50-µm thick PC films allows e.g. the fabrication of microcavities of inner diameter ~ 300 µm and height up to 300 µm (Fig. 1).

Such chips, referred to as KITChip, are used in cell biology for 3-dimensional cell cultures and for studies of biochemical and biophysical effects on the behaviour and characteristics of cells.

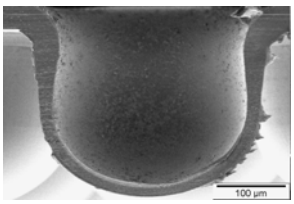

Figure 1: cross section of a thermoformed polycarbonate cavity (diameter: 300 µm, depth: 300 µm)

The here described approach is based on a process sequence corresponding to the SMART-technology (Substrate Modification and Replication by Thermoforming), which typically consists of three consecutive steps: (1) pre-modification (ion irradiation), (2) thermoforming, and (3) post-modification (chemical development) [2].

As starting material we used 50-µm thick PC films (OG461GL, supplied by LOFO) covered with a 30-µm thick Al-foil. The irradiation through a mask was performed at the UNILAC using U ions of 5.9 MeV/u energy (range in polymer film ~10 µm after passing the Al-foil) and a fluence of 10^{10} ions/cm^2. The mask consists of a ~25 µm thick gold absorber structure consisting of an array of 25×25 square-shaped apertures (40 µm × 40 µm).

For the microthermoforming process, the irradiated film was heated to 167°C and stretched into the mould by means of 20 bar nitrogen gas. Subsequently, the ion beam exposed areas of the formed film were removed by chemical etching in NaOH (20 min, ~ 65°C). This results in three-dimensional polymeric microcavities containing smaller surface substructures defined by the irradiation mask.

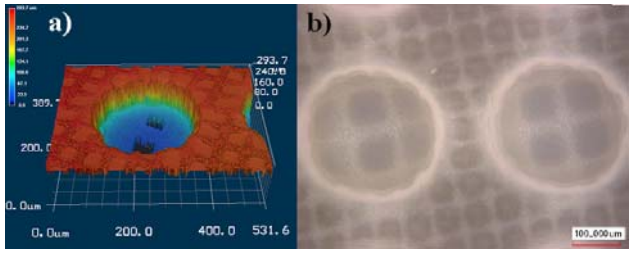

Figure 2: (a) 3-D image from profilometer scan of thermoformed cavity (diameter 300 µm, 200 µm depth) in PC film; (b) LSM image (top view) showing two cavities overlaid by micro aperture pattern (40 µm × 40 µm, depth ~10 µm) produced by ion irradiation through a structured mask and subsequent track etching.

Fig. 2 shows a height profile (a) and a laser scanning (LSM) image (b) of two structured substrates. The cavities have a depth of about 200 µm. The overlaid 10 µm deep square pattern that results from the ion beam irradiation and subsequent track etching is not only present in the cavities but on the entire surface.

Our first tests successfully demonstrate that thin-walled, thermoformed microcavities can be provided with micro topographies on the inner surface. This new SMART method still requires optimization of process parameters to avoid, e.g., holes in the thinnest part of the cavities generated during thermoforming when mechanically stretching the polymer film (Fig. 2a). Once different topographies can reliably be produced within our cavities, we will start to screen their effect on cell behaviour or differentiation.

[1] R. Spohr, *Ion Tracks and Microtechnology, Principles and Applications*. Braunschweig, Vieweg, 1990.
[2] S. Giselbrecht, T. Gietzelt, E. Gottwald, C. Trautmann, R. Truckenmüller, K.-F. Weibezahn, and A. Welle, *3D tissue culture substrates produced by microthermoforming of pre-processed polymer films,* Biomedical Microdevices 8, (2006) 191.

#martina.reinhardt@kit.edu

Track-Etched Nanopores in Polyimide Characterized by Small-Angle X-Ray Scattering

M. Engel[1#], B. Stühn[1], B. Kuttich[1] and C. Trautmann[2]
[1]Technische Universität Darmstadt, Germany; [2]GSI, Darmstadt, Germany

Chemical etching of ion tracks in polymers allows the fabrication of porous membranes with well-defined channel parameters (size, geometry, porosity, etc.). There exists much experience using polycarbonate (PC) and polyethylene terephthalate as matrix materials. Conical, biconical, and cylindrical pore shapes have been demonstrated by varying the etching conditions, e.g., composition, temperature, and pH-value of the etchant.

This project focuses on track-etched nanopores in polyimide (PI) membranes providing better temperature and chemical resistance than most other polymers. Based on previous recipes [1,2], we produced nearly cylindrical channels with diameters smaller than 100 nm. These nanopores were characterized using small-angle X-ray scattering (SAXS). In contrast to other methods (e.g., scanning electron microscopy or galvanic replication), this non-invasive technique has the advantage to yield quantitative information on the pore size and reveal small deviations from cylindrical geometry.

50-µm thick PI films (Kapton, from Dupont) were irradiated with Au and Xe ions of 11.1 MeV/nucleon energy. The fluence applied was between 1×10^{9} and 1×10^{10} ions/cm^2. Track etching of the irradiated films consisted of two steps, first immersion in hydrogen peroxide (H_2O_2) as sensitisation process and subsequent track etching in sodium hypochlorite (NaOCl). By selecting suitable temperatures of both solutions, pH value of NaOCl, and duration of the etching process, it is possible to control the pore geometry, i.e. cone angle and diameter. To achieve optimal cylindrical geometry, typical parameters are 90 °C and 2 h for sensitisation in H_2O_2 and 50 °C, pH = 9.9, and 15 to 45 min for the track etching in NaOCl. The resulting channels have diameters between 20 and 100 nm.

SAXS measurements were performed using a laboratory setup. The high electron density contrast allows short measurement times of about 30 min. The channels are two-dimensional, randomly distributed, but strictly collinear due to the parallel ion beam producing the tracks. Within the applied fluence regime, a scattering correlation between the pores can be neglected.

The parallel arrangement of the channels leads to a strongly anisotropic scattering pattern. Therefore, the use of a 2D-detector and the exact control of the sample orientation with respect to the X-ray beam are mandatory.

The measured intensity $I(\boldsymbol{q})$ is the absolute square of the scattered wave amplitude $A(\boldsymbol{q})$, which is the Fourier transform of the electron density distribution $\rho_e(\boldsymbol{r})$ that contains the information of the geometry of the channels as scattering objects:

$$I(\vec{q}) = |A(\vec{q})|^2 = \left|\int \rho_e(\vec{r}) \exp\{-i\vec{q}\vec{r}\} d\vec{r}\right|^2$$

where $q = 4\pi \sin(\theta)/\lambda$ denotes the scattering vector, 2θ is the scattering angle, and λ =1.54 Å is the wavelength of the X-rays. Figure 1 shows the scattered intensity as a function of q for different etched Kapton membranes.

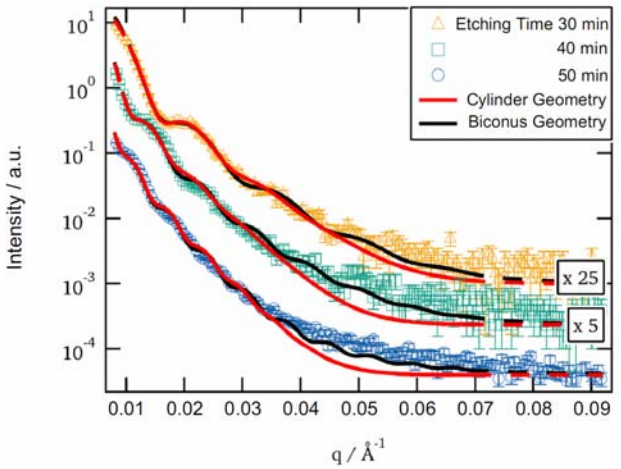

Figure 1: Scattering curves from three track-etched Kapton foils fitted by a model function based on cylindrical (red line) and biconical (black) pore geometry

The analysis of SAXS data requires an accurate model function including a specific geometry of the scattering object [3]. The solid lines in Fig. 1 assume cylindrical (red) and biconical (black) shape. With respect to the general slope and oscillations, the biconical model obviously provides a better fit. The fit parameters yield the following channel parameters:

etching (min)	small radius (nm)	large radius (nm)	opening angle (deg)
30	21.7(2)	29.7(4)	0.18(3)
40	34.0(2)	46.5(3)	0.29(1)
50	43.8(2)	58.6(1)	0.34(1)

[1] D. Dobrev, C. Trautmann und R. Neumann: "Novel two-step etching process for ion tracks in polyimide", GSI Scientific Report 2006, 2007.
[2] C. Trautmann, W. Brüchle, R. Spohr, J. Vetter, N. Angert, Pore geometry of etched ion tracks in polyimide, Nucl. Instr. and Meth. B 111 (1996) 70.
[3] M. Engel, B. Stühn, J.J. Schneider, M. Naumann: "Small-angle X-ray scattering (SAXS) of parallel, cylindrical well-defined nanopores: from random pore distribution to highly ordered samples", Appl. Phys. A 97 (2009) 99.

#Martin.Engel@merck.de

Guided transmission of Ne^{7+} ions through nanocapillaries in polymers: Scaling laws for higher projectile energies

N. Stolterfoht[1#], R. Hellhammer[1], Z. Juhász[2], B. Sulik[2], V. Bayer[3], C. Trautmann[3], E. Bodewits[4], A. J. de Nijs[4], H. M. Dang[4], and R. Hoekstra[4]

[1]Helmholtz-Zentrum Berlin für Materialien und Energie, Glienickerstr. 100, D-14109 Berlin, Germany
[2]Institute of Nuclear Research (ATOMKI), H-4001 Debrecen, Hungary
[3]GSI Helmholtz-Zentrum für Schwerionenforschung, Materialforschung, D-64291 Darmstadt, Germany
[4]KVI Atomic Physics, University of Groningen, 9747 AA Groningen, The Netherlands

In past few years, the guiding of highly charged ions through capillaries of mesoscopic dimensions has received great attention [1,2]. Various studies of the guiding phenomena have been performed with capillaries in highly insulating polyethylene terephthalate (PET) polymers [3]. For capillaries tilted with respect to the incident-beam direction, the ion guiding involves the deposition of positive charges at the inner wall of the capillaries in a self-organizing process. The charge deposition in the entrance region continues until the electric field becomes sufficiently large to deflect the ions in the directions of the capillary exit.

The fraction $f(\psi)$ of the guided ions at equilibrium can be quantized by the *guiding angle* ψ_c for which the normalized transmission fraction drops as $f(\psi_c) / f(0) = 1/e$. This definition of the guiding angle has been motivated by the observation that the tilt-angle dependence of the transmitted fraction can well be described by a Gaussian function. A similar definition has been introduced for the profile width σ_t, which describes the FWHM of the angular distribution of the ions transmitted through the capillaries. For the characteristic angles ψ_c and σ_t similar scaling laws have been established with respect to the charge-to-energy ratio q/E_p of the projectile [3].

In the present work, we study the guiding angle and profile width of the transmitted ions measured for the polymers PET and PC (polycarbonate) at KVI in Groningen (NL) [4]. The primary goal was the verification of the scaling laws for higher Ne^{7+} energies of up to 50 keV, corresponding to the projectile charge-to-energy ratio down to 0.14 kV^{-1}. The results are shown in Fig. 1.

The characteristic angles of both polymers PET and PC are compared with the previous scaling law, given by the relation

$$\psi_C = u\left(\frac{q}{E_p}\right)^{0.7} \quad \text{and} \quad \sigma_t = u_t\left(\frac{q}{E_p}\right)^{0.7} \qquad (1)$$

where u and u_t are adjustable parameters. Also, the semi empirical exponent 0.7 follows from the data fitting, however, within a very small variance range.

In Fig. 1 the results from Eq. (1) are given as solid lines, showing that the experimental data can well be scaled by the charge-to-energy ratio q/E_p. This conclusion is plausible since q/E_p is a well-known scaling parameter for ion trajectories in an electrostatic field. However, we note that the model calculations in Refs. [3,4] predict an exponent equal to unity. Hence, the empirical reproductions of the characteristic angles ψ_c and σ_t by means of the exponent 0.7 require further studies.

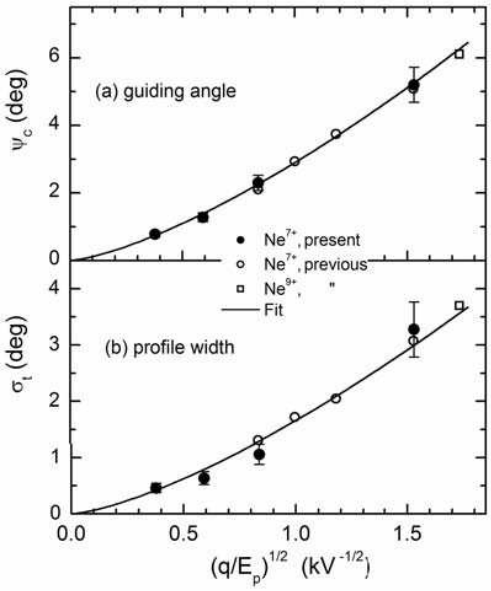

Figure 1: Scaling laws for the guiding angle ψ_c and the FWHM σ_t of the transmission profile, shown in (a) and (b), respectively. The angles are plotted as a function of the square root of the charge-to-energy ratio q/E_p. The present results are given as solid circles. The data, shown as open circles and squares, are taken from previous work [3]. The solid lines represent fit functions discussed in the text.

References

[1] N. Stolterfoht, J. H. Bremer, V. Hoffmann, R. Hellhammer, D. Fink, A. Petrov, and B. Sulik, Phys. Rev. Lett. **88**, 133201 (2002).

[2] K. Schiessl, W. Palfinger, K. Tökési, H. Nowotny, C. Lemell, and J. Burgdörfer, Phys. Rev. A **72**, 62902 (2005).

[3] N. Stolterfoht, R. Hellhammer, J. Bundesmann, and D. Fink, Phys. Rev. A **77**, 032905 (2008)

[4] N. Stolterfoht, R. Hellhammer, D. Fink, B. Sulik, Z. Juhász, V. Bayer, C. Trautmann E. Bodewits, H. M. Dang, and R. Hoekstra, Phys. Rev. A **79**, 042902 (2009) and references therein.

#nico@stolterfoht.com

Charge-Selective Transport of Protein Molecules through Solid-State Nanochannels

Q. H. Nguyen[1], M. Ali[1], W. Ensinger[1] and R. Neumann[2]
[1]Technische Universität Darmstadt, Germany; [2]GSI, Darmstadt, Germany.

In recent years, molecular transport through solid-state nanochannels mimicking selective transport properties of biological ion channels has attracted considerable attention. In both synthetic and biological channels, these properties strongly depend on size and surface charge. Especially, heavy ion track-etched nanochannels are widely used for selective transport and separation of molecules, including biomolecules. Up to now, surface charge manipulation of nanochannels, fabricated in polymer membranes, is mostly achieved by electroless gold plating and subsequent chemisorption of thiomolecules having variable charge polarity [1].

In this report, we describe a facile and straightforward approach for the manipulation of surface charge of nanochannels in polyethyleneterephthalate (PET) membranes via carbodiimide chemistry (Figure 1) [2]. At about neutral pH, carboxyl (-COO^-) groups which were generated during the track-etching process, import negative charge to the channel surface. After functionalization of these groups with ethylendiamine, the channel surface was positively charged due to protonation of terminal amino (-NH_3^+) groups. For the selective transport of charged biomolecules, the membranes with areal density of ~ 3 x 10^8 channels/cm^2 were used. The diameter (75 ± 4 nm) of cylindrical nanochannels was confirmed through FESEM images of gold nanowires deposited in these nanochannels. Charged protein molecules such as lysozyme and bovine serum albumin (BSA) were selected for mass-transport experiments. Briefly, the membrane was mounted between the two halves of a conductivity cell. The feed half-cell contains 10^{-4} M of a biomolecule in electrolyte solution, the permeate half-cell contains pure electrolyte solution. Both solutions were continuously stirred during the whole process. After a preset time, the biomolecule concentration in the permeate half-cell was determined by measuring the UV absorbance.

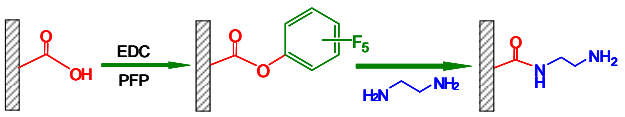

Figure 1: Reaction scheme of coupling chemistry

The amounts of BSA and lysozyme transported through the negatively charged channels versus time are plotted in Figure 2a. The diagram demonstrates that the flux of lysozyme was significantly higher than that of BSA. At pH 6.5, BSA (isoelectric point pI = 4.7) is negatively charged, while lysozyme (pI = 11.0) is positively charged. Therefore, the BSA molecules are rejected by the negatively charged nanochannel (-COO^-) while the lysozyme molecules can pass. The hydrodynamic radii of BSA and lysozyme are 3.8 nm and 1.8 nm, respectively. As a consequence, the lysozyme molecules can move more freely through the nanochannels, which support a higher flux. This implies that the selective transport of oppositely charged biomolecules across the membrane is governed both by their charge and size.

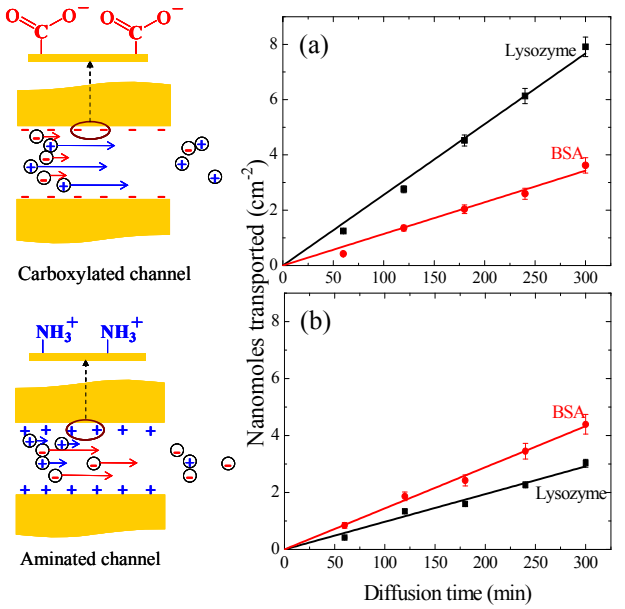

Figure2: Diffusion of BSA and lysozyme at pH 6.5 before (a) and after (b) modification with EDA

The flux of BSA and lysozyme through the positively charged aminated (-NH_3^+) nanochannels is presented in Figure 2b. The flux of BSA is higher than that of lysozyme, though the BSA molecules are larger than lysozyme. Here, positively charged lysozyme molecules are electrostatically repelled from the positively charged channels. Furthermore, the pronounced hydrophilic nature of BSA also facilitates its transport through the charged nanochannels. Therefore, in this case the electrostatic and hydrophobic/hydrophilic interactions between electrically charged biomolecules and the surface charge of nanochannels are more prominent than the size effects of these biomolecules.

In conclusion, the transport of charged biomolecules through these synthetic nanochannels mimics the charge-selective permeation of ions in biological membranes. We believe that this platform could also be used for the separation and discrimination of drug molecules by introducing selective functionalities inside the nanochannels.

References

[1] S. B. Lee and C. R. Martin, J. Am. Chem. Soc. (2002), 124, 11850
[2] M. Ali, V. Bayer, B. Schiedt, R. Neumann and W. Ensinger, Nanotechnology (2008), 19, 485711

Transport Properties of Single Solid-State Conical Nanochannels Functionalized with Polyprotic Acid Chains

M. Ali[1#], P. Ramirez[2], V. Bayer[3], R. Neumann[3] and W. Ensinger[1],
[1]Technische Universität Darmstadt, Germany; [2]Universidad Politécnica de Valencia, Spain; [3]GSI, Darmstadt, Germany.

Nanochannels, nanopipettes, and nanoelectrodes constitute a new generation of devices designed for single-molecule sensing and molecular separation.[1,2] Nanofluidic diodes based on asymmetric nanochannels with only one type of charge, and bipolar diodes and transistors, composed by regions of different charge juxtaposed in series, have been reported. Recently, we have demonstrated a nanofluidic diode with amphoteric chains (lysine or histidine) functionalized on the channel surface that shows a broad range of rectification properties. [3]

Here, we demonstrate that the single conical nanochannels functionalized with polyprotic acid chains show three levels of conductance that can be tuned externally (because of the *pH*-sensitive fixed charges). The selectivity and rectification properties are dictated by the nanometer-sized tip region and the intrinsic (geometric and electrostatic) asymmetries of the device permit the implemention of different functions on a single nanofluidic diode.

Single conical nanochannels were fabricated in heavy ion irradiated PET foils of 12 µm thickness by selective chemical etching of the damage trails caused by the ions along their trajectories,[4] resulting in the generation of carboxyl (-COO^-) groups on the channel surface. These groups were first converted into amine-reactive ester of pentafluorophenol (PFP) by reacting with an ethanolic solution containing *N*-(3-dimethylaminopropyl)-*N'*-ethylcarbodiimide (EDC) and PFP. Subsequently, the PFP ester groups were coupled with aminopropylphosphonic acid (APPA).

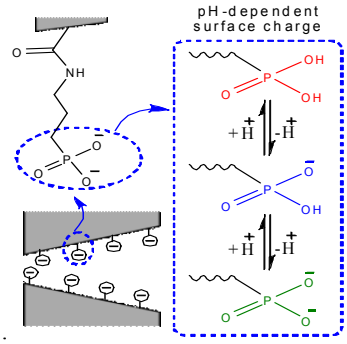

Figure 1: Schematic illustration of polyprotic acid groups inside the single conical nanochannel.

The single-nanochannel membrane modified with APPA was mounted between the two halves of the conductivity cell filled with the electrolyte solution, and the *pH* was adjusted by dilute HCl or KOH solutions. To measure the resulting ion current flowing through the nanochannel, a scanning triangle voltage from -2 to +2 V on the tip side was applied (the base side of the channel remained connected to the ground electrode). Figure 2 shows the current-voltage (*I-V*) curve in an electrolyte (0.1M KCl) solution for different *pH* values. At low *pH,* both ionisable hydroxyl groups of the terminated phosphonic acid (–PO_3H_2) are protonated which import neutral charge to the channel surface. The nanochannel is now non-selective to ions (anions and cations), leading to the loss of rectification. By increasing the *pH*, ionization starts and at *pH* 5 one of the hydroxyl groups is completely ionized and the mono-anion of the phosphate group (–HPO_3^-) is achieved (partly charged channel). At *pH* = 10, the double-charged anion –PO_3^{2-} is obtained (fully charged channel) as shown in Fig. 1. The net charge fixed to the channel wall is then negative, and the channel is now selective to cations. There is a high-conducting ("on") state for $V > 0$ and a low-conducting ("off") state for $V < 0$. Note that three levels of conductance at *pH* = 3, 5, and 10 can be identified, corresponding to the ionization equilibria of the two ionisable hydroxyl groups of polyprotic acid (Figure 1).

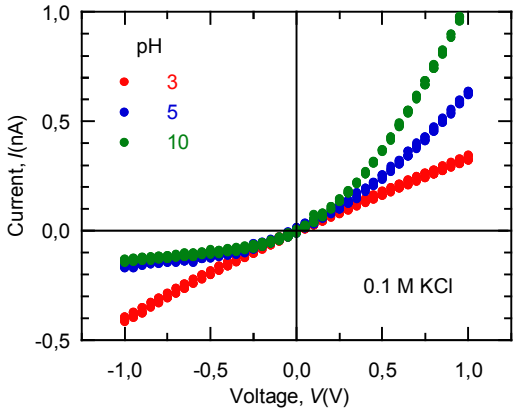

Figure 2: Current-voltage curves of a single conical channel functionalized with aminopropylphosphonic acid.

In conclusion, the polyprotic acid chains, functionalized on the conical nanochannel surface, give three well-defined conductance levels (0.37 nS at *pH* = 3, 1.06 nS at *pH* = 5, and 1.57 at *pH* = 10; all values measured at $V = 1$ V), that can be tuned by simply changing the *pH* of the external environment. The integration of a multi-level response on a unique nanofluidic diode could be useful for the construction of logic gates.

References

[1] M. Ali *et al., J. Am. Chem. Soc.* (2008), **130**, 16351
[2] E. N. Savariar *et al*., *Nat. Natechnol.* (2008), **3**, 112
[3] M. Ali *et al.*, *ACS Nano*, (2009), **3**, 603
[4] M. Ali *et al.*, *Nanotechnology* (2008) **19**, 485711

M.Ali@gsi.de

Field emission current limits of patches with cylindrical gold nanowires

A. Navitski[1], V. Sakharuk[1], F. Jordan[1], G. Müller[1,*], I. Alber[2], M.E. Toimil-Molares[2], C. Trautmann[2]
[1]Physics Department, University of Wuppertal; [2]GSI Helmholtzzentrum, Darmstadt, Germany

Based on the field emission (FE) results achieved with regular test arrays of gold [1] and platinum [2] nanowire (NW) patches, FE cathodes (Ø 5 mm) with a triangular patch array (Ø 150 µm, pitch 320 µm) of cylindrical Au-NW (10^7 cm^{-2}, Ø 200 nm, length 12 µm) were fabricated by means of a shadow mask during heavy ion irradiation of polycarbonate foils. The emitter distribution and local properties of such cathodes were measured with the field emission scanning microscope (FESM). Well-aligned FE from all patches was obtained at fields below 25 V/µm as shown in Fig. 1a which reveals typically 4-8 emitters per patch. This result confirms our strategy of emitter redundancy for improved FE homogeneity of NW cathodes.

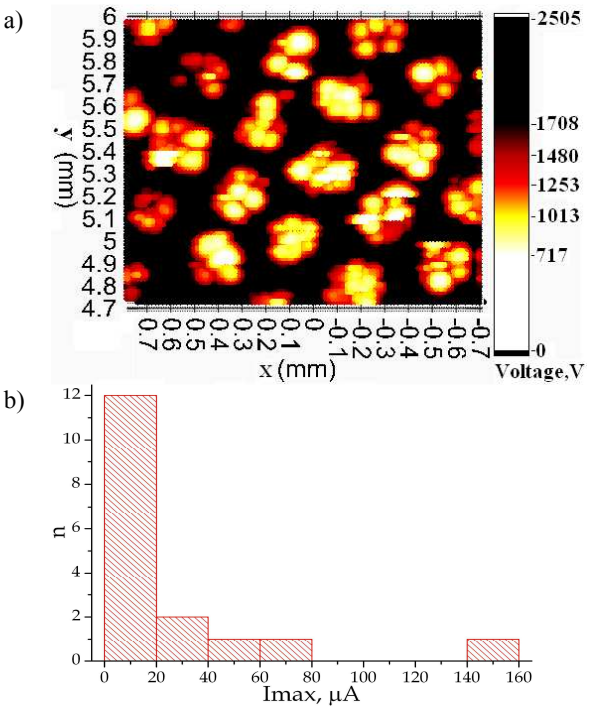

Figure 1: Regulated voltage map for 1 nA current (anode Ø 30 µm, gap 40 µm) of a structured Au-NW cathode (a) and histogram of maximum current of individual patches (anode Ø 100 µm) (b).

In contrast to the fairly reproducible electric onset field, strongly varying values were obtained for the maximum current I_{max} of selected patches (Fig. 1b). Most emitters were partially destructed already at a few µA, and the best patch provided a stable current of 140 µA at 45 V/µm. Stable currents of 100 µA per patch, i.e. current densities above 100 mA/cm^2 would make such structured Au-NW cathodes suitable for power devices.

* contact: gmueller@uni-wuppertal.de

In order to find possible reasons for the varying current limits of the Au-NW patches, we have started to look for correlations to the individual emitter morphology before and after current processing. Typical SEM images of the actual nanostructures are shown in Fig. 2. Obviously most cylindrical NW form random clusters (typ. about 10 NW) due to their given number density and length (Fig. 2a) which might by favourable for the current supply to the emitting tip. There are always much more NW clusters found in the patches than FE sites in the maps (Fig. 1a). It is remarkable that few solitary Au-NW are also present in the patches (Fig. 2b). Some broken ones reveal a ring-like contact area which causes limited mechanical and current stability. In case of reduced heat transfer to the substrate a significant uniform heating of cylindrical NW by FE currents results from electrothermal model calculations [2]. Therefore, the fabrication of cylindrical or conical NW with improved substrate contact is the main challenge for device applications of patch-structured Au-NW cathodes.

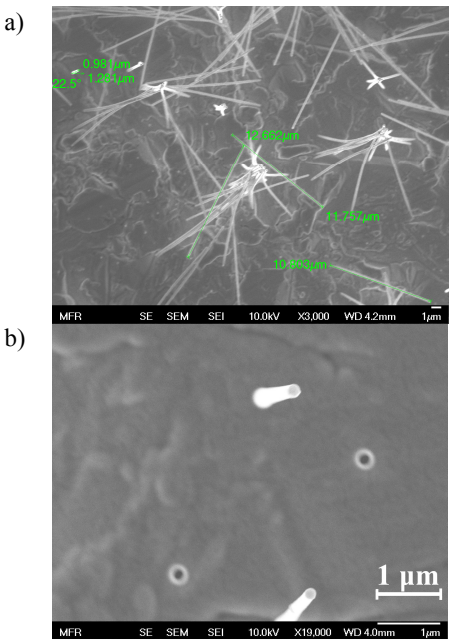

Figure 2: SEM images of clustered (a) and solitary Au-NW (b) found in the patches before current processing.

References

[1] A. Navitski, G. Müller, V. Sakharuk, T. Cornelius, C. Trautmann, S. Karim, Eur. Phys. J. Appl. Phys. 48, 30502 (2009).

[2] A. Navitski, V. Sakharuk, F. Jordan, G. Müller, S. Müller, M. Rauber, M.E. Toimil-Molares, C. Trautmann, Techn. Digest IVNC09, Hamamatsu, IEEE Cat. No. CFP09VAC-PRT, p. 137 (2009).

Preparation and Properties of Co-Doped ZnO Nanowires

Ionut Enculescu[1#], Monica Enculescu[1], Elena Matei[1], Nicoleta Preda[1], Marian Sima[1], Jean-Philippe Ansermet[2], Simon Granville[2], Maria Eugenia Toimil Molares[3], Reinhard Neumann[3]
[1]National Institute for Materials Physics, Bucharest, Romania, [2]Ecole Polytechnique Fédérale de Lausanne, Switzerland
[3]GSI, Darmstadt, Germany

Spintronics aims at developing a new generation of electronic materials for consumer products based on electron spin rather than on electron charge. Its main objective is the fabrication of new devices based on semiconductor materials with magnetic behavior (so called diluted magnetic semiconductors). These devices combine the manipulation of electrons as classically known in semiconductor devices with an additional degree of freedom namely the manipulation of spins. Doped zinc oxide is considered a major candidate for spintronics due to its ferromagnetic character and Curie-Weiss temperature above ambient [1-3]. Among all kind of nanostructures, nanowires are being used as building blocks in ultra miniaturized electronic and sensing devices [4]. Here, we describe the synthesis of Co doped ZnO nanowires by electrochemical deposition in nanoporous templates. For the electrodeposition of pure ZnO, we employed a 0.1 M $Zn(NO_3)_2$ electrolyte. Cobalt nitrate was added for electrodeposition of Co-doped ZnO nanowires. In both cases, addition of PVP (polyvinylpyrrolidone) to the electrolyte increased the template wettability and resulted thus in a larger pore filling efficiency in the case of polycarbonate membranes.

Figure 1a displays the polarization curves for the electrodeposition of undoped ZnO (dotted line) and Co-doped ZnO (solid line). The cathodic current for deposition of the Co-doped ZnO nanowire array starts increasing at a lower potential than its undoped ZnO counterpart.

The chronoamperometric curves in Fig. 1b also evidence differences between the deposition of pure ZnO and Co-doped ZnO nanowires at U = -800 mV at room temperature. In particular, it can be observed that the current employed for deposition of Co-doped ZnO nanowires is higher than the correspondent current for the growth of undoped ZnO nanowires at all stages of the deposition process. The higher nitrate concentration alone can not explain this increase in current, rather attributed by the authors to a catalytic effect of Co ions for the process of reduction of nitrate ions.

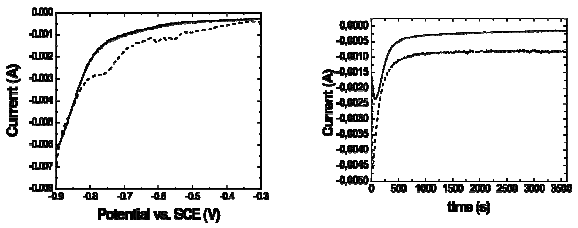

Figure 1: Electrochemical polarization (a) and chronoamprometric curves (b) for pure and doped ZnO deposition at U = -800 mV

Optical reflectance spectroscopy measurements provided the bandgap values for nanowire arrays synthesized at various deposition conditions. A band gap of 3.2 ± 0.1 and 3.1 ± 0.1 eV were measured for pure ZnO nanowires and Co doped ZnO nanowires, respectively. No systematic dependence of the bandgap value as a function of deposition potential was noticed. The scanning electron microscope image in Fig. 2 shows bundles of cylindrical cobalt doped ZnO nanowires obtained after dissolution of the polymer membrane. Energy dispersive X-ray analysis measurements revealed that the Co content in the nanowires deposited using the same electrolyte can be controlled by the electrochemical deposition potential.

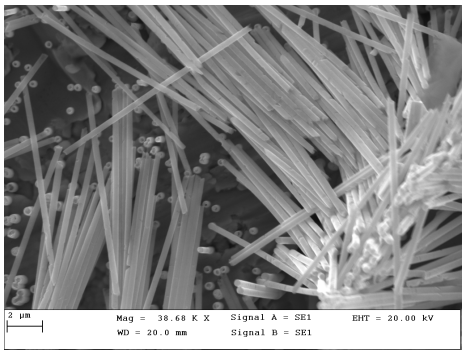

Figure 2: SEM image of bundles of cylindrical Co-doped ZnO nanowires

In addition, the magnetic behavior of doped ZnO nanowire arrays was characterized. For Co-doped nanowire arrays with Co concentrations lower than 5% showed paramagnetic behavior. For higher dopant concentration, the behavior became ferromagnetic up to room temperature.

A further goal will be the preparation of segmented nanowires with magnetic–nonmagnetic semiconductor junctions, which are expected to exhibit extremely interesting properties for spin injection experiments.

References

[1] T. Dietl, H. Ohno, F. Matsukura, J. Cibert, D. Ferrand; Science **287** (2000) 1019
[2] J. Cui, U. Gibson; Physical Review B **74** (2006) 045416
[3] B.D. Yuhas, D.O. Zitoun, P.J. Pauzauskie, R. He, P. Yang, Angew. Chem. Int. Ed. **45** (2006) 420
[4] Y. Huang, X. Duan, Q. Wie, Ch. Lieber, Directed Assembly of One-Dimensional Nanostructures into Functional Networks, Science **291** (2001) 630

#encu@infim.ro

Tuning the structure of nanowires through controlled segmenting

M. Rauber[1,2], S. Müller[2], R. Neumann[2], O. Picht[2], M. E. Toimil-Molares[2], and W. Ensinger[1]
[1]Technische Universität Darmstadt, Darmstadt, Germany; [2]GSI, Darmstadt, Germany

A common production method for nanowires is based on electrodeposition into cylindrical channels of a nanoporous template.[1] Since the nanostructures adopt the morphology given by the host material as they are created by reduction from an electrolyte solution, the deposition step can be considered as the most important factor that determines the structure.[2] Pt nanostructures are of particular interest because of their great potential for applications including catalysts, sensors, and electronic devices. While several shape-controlled Pt nanostructures have been reported, the synthesis of additional types is highly desirable.[3, 4]

Our approach to controlled nanostructuring gives rise to segmented all-Pt nanowires. As templates we used ion track-etched polycarbonate membranes. Pulse-reverse (PR) electrodeposition in combination with a suitably chosen electrolyte-template system influences the local electrolyte distribution inside the nanochannels. This method generates segments linked to nanowires by a novel growth mechanism. It allows the design of nanowires with a preset number of segments and interfaces. SEM images of segmented nanowires produced by PR deposition using constant anodic and cathodic pulse durations (t_a and t_c) reveal their characteristic structure (Figure 1). Sharp and striking interfaces can be identified. Shape and dimensions of the segments are homogeneous along most of the total wire length.

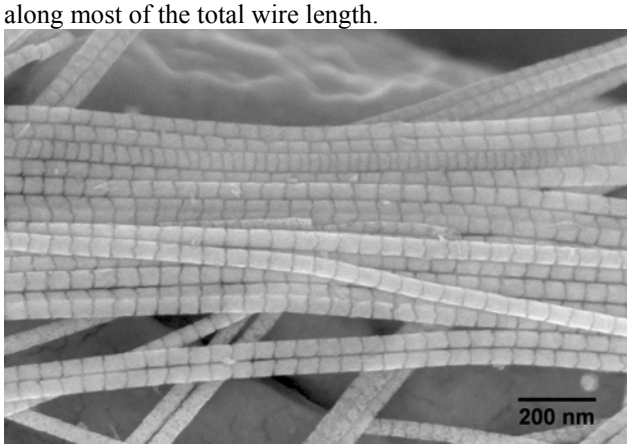

Figure 1: SEM image of segmented Pt nanowires produced by PR deposition.

The segment length can be adjusted as a function of t_c. By modulating the deposition pulse, it is also possible to obtain length- and sequence-controlled segmented nanowires for potential applications as encoded nanostructures with a large number of barcode patterns. For the implementation of binary information two distinguishable structure elements are required. Figure 2 shows a binary encoded nanowire consisting of two different types of segments. The longer segments (blue) stand for "1", while "0" is represented by shorter segments (red).

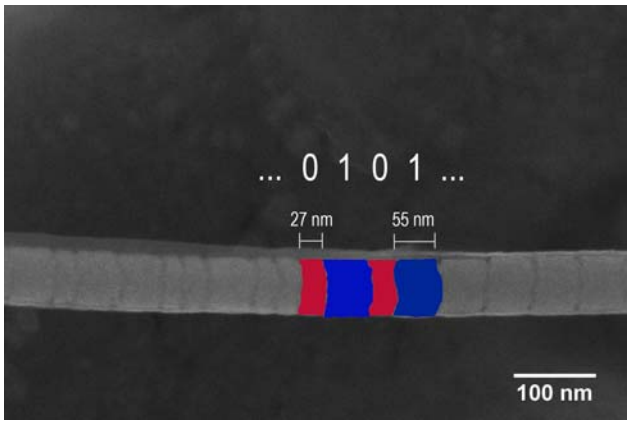

Figure 2: Binary encoded nanowire produced by modulating t_c to create two distinguishable structure elements.

TEM images provide additional insight into the substructure of segmented nanowires. The most interesting feature is that the segments are linked to each other only by a short section with reduced diameter in the center of the wire. Pronounced constrictions and void space are inevitable to create clear separation. It is apparent that the deviation from a continuously cylindrical shape given by the template can only be a result of a growth process that is essentially controlled by kinetics resulting in a configuration far from the equilibrium state.

Based on structural characterizations we may propose a growth mechanism. In contrast to the typical 3-D nucleation-coalescence growth mode reported for polycrystalline nanowires[2], in our case nucleation is observed only on a limited area at the front face of pre-existing segments. At the initial stage of segment growth, phase formation starts on a circular area at the center of each nanochannel as a cathodic pulse is applied. The localized formation of nuclei is directed by the Pt ion concentration and a direct consequence of the influence of electrokinetic effects on the local electrolyte distribution in small fluidic nanochannels, which provide an electrical double layer of significant thickness.

In this work we have demonstrated the production of segmented Pt nanowires by using a simple and highly effective PR electrodeposition method. Segmented single-metal nanowires may have great potential for various advanced technological applications because of the possibility to tune their properties by precisely controlling the structure.

References

[1] T. R. Kline et al., Inorg. Chem. 45 (2006) 7555.
[2] M. Tian et al., Nano Lett. 3 (2003) 919.
[3] Y. Song et al., J. Am. Chem. Soc. 126 (2003) 635.
[4] L. Soleymani, Nat. Nanotechnol. 4 (2009) 844.

Tuneable luminescence of dye doped nanorods*

M. Enculescu[1#], N. Preda[1], E. Matei[1], I. Enculescu[1], and C. Trautmann[2]
[1]NIMP, Magurele-Bucharest, Romania; [2]GSI, Darmstadt, Germany

Dye-doped single crystals such as potassium acid phthalate (KAP) and potassium dihydrogen phosphate (KDP) have been reported to present extremely interesting optical properties [1, 2]. It is expected that some problems related to the fabrication of dye-doped materials (polymers, glasses, etc) for lasing media can be overcome. An important step forward is represented by the synthesis of such interesting materials in an ultraminiaturized form. The template approach is a very efficient method for the controlled fabrication of nanosized objects with given geometrical properties (shape, diameter, length). Using electrochemical deposition this method is successfully applied for semiconducting and metallic nanowires [3, 4], whereas crystalline insulating nanorods can be grown by solution crystallization [5, 6]. This paper presents our study on luminescent properties of rhodamine 6G (Rh 6G) doped KAP and KDP nanorods grown by crystallization process from aqueous solution in track-etched polymer templates.

As templates we used polycarbonate (PC) foils irradiated at the UNILAC with swift heavy ions (Au, Pb, or U) of 11.1 MeV/nucleon specific energy. The fluence was in the range of 10^5-10^9 ions/cm^2. Chemical etching converts each ion track into a cylindrical pore. The number of the channels in the membrane corresponds to the applied ion fluence, while the diameter is controlled by the etching time. The track-etched membranes were placed on top of the saturated growth solution and left floating in ambient conditions for several days [6]. We obtained 100-nm diameter rods in 30-µm thick membranes and 5-µm diameter rods in 100-µm thick membranes.

Luminescence spectra were recorded using an Edinburgh Instruments FL920 spectrometer. The emission measurements were performed on PC membranes filled with dye-doped KAP and KDP nanorods. Figure 1 compares the spectra of nanorods (diameter 100 nm) and microrods (diameter 5 µm) under light excitation at 480 nm wavelength. For the 5-µm microrods, the emission band maximum is around 555 nm for Rh 6G doped KAP (full circles) and around 563 nm for Rh 6G doped KDP (full squares). The emission bands of 100-nm rods are red-shifted for both KAP and KDP at 581 nm for Rh 6G doped KAP (open circles) and at 602 nm for Rh 6G doped KDP (open squares).

This red shift for the smaller rod diameter is probably due to a higher dopant concentration, although the microrods and nanorods were grown from the same mother solution. This conclusion is based on the observation that the staining of the PC membranes becomes more intense with decreasing rod diameter. The difference between the emission maxima of micro and nanorods is larger for Rh 6G doped KDP (~ 15 nm) than for Rh 6G doped KAP (~ 2 nm).

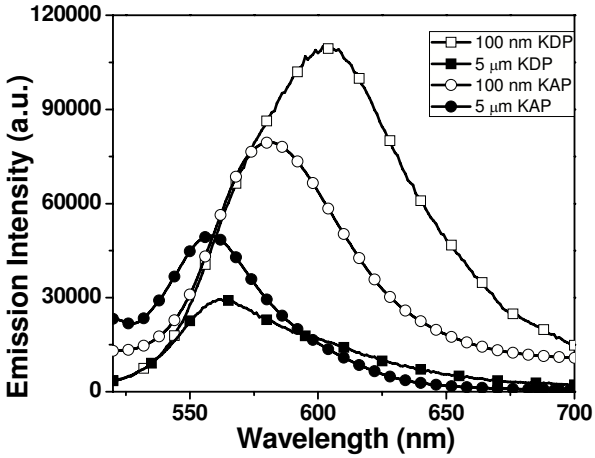

Figure 1: Emission spectra under light excitation at 480 nm of microrods (10^5 cm^{-2}) and nanorods (10^9 cm^{-2}): Rh 6G doped KAP rods of diameter 5 µm (full circles) and 100 nm (open circles), and Rh 6G doped KDP rods of diameter 5 µm (full squares) and 100 nm (open squares).

The template method was used for preparing insulating structures of Rh 6G doped nanorods of KAP and KDP in ion track templates. The emission wavelength can be controlled by adjusting the geometrical properties of the membranes. The PC membranes containing 100-nm diameter rods exhibit intense emission bands peaking at 581 nm (Rh 6G doped KAP) and 602 nm (Rh 6G doped KDP). Compared with micrometer rods, the emission of nanorods is red shifted for both filling materials due to an increased dye concentration inside the pores.

References

[1] M. Enculescu, Opt. Mater. 32, (2009) 281
[2] Yu. Velikhov, I. Pritula, I. Ganina, M. Kolybayeva, V. Puzikov, A.N. Levchenko, Cryst. Res. Technol. 42 (2007) 27
[3] T. Ohgai, I. Enculescu, C. Zet, L. Westerberg, K. Hjort, R. Spohr, R. Neumann, J. Appl. Electrochem. 36 (2006) 1157
[4] I. Enculescu, M. Sima, M. Enculescu, M. Enache, L. Ion, S. Antohe, R. Neumann, phys. stat. sol. (b) 244 (2007) 1607
[5] M. Enculescu, I. Enculescu, M. Sima, R. Neumann, C. Trautmann, J. Optoelectron. Adv. M. 9 (2007) 1561
[6] M. Enculescu, J. Optoelectr. Adv. M. 10 (2008) 1501

* Work supported by Romanian Ministry of Education and Research contract IDEI 344/2007
#mdatcu@infim.ro

TEM Measurements on $Bi_{1-x}Sb_x$ Nanowires*

S. Müller† [1], I. Alber[1], O. Picht[1], M. Rauber[1,3], W. Sigle[2], M. E. Toimil-Molares[1], and R. Neumann[1]

[1]GSI Helmholtz Centre for Heavy Ion Research, Darmstadt, Germany; [2]Max Planck Institute for Metals Research, Stuttgart, Germany; [3]TU Darmstadt, Germany

In 1993, Hicks and Dresselhaus published theoretical calculations of the electrical conductivity (σ), the Seebeck coefficient (S), and the thermal conductivity (κ) that predicted an enhanced thermoelectric figure of merit

$$ZT = \frac{\sigma S^2}{\kappa} T$$

for 2D quantum-well structures [1] and quantum wires [2], establishing a new direction in the search for more efficient thermoelectric materials. Promising low-dimensional materials being investigated for thermoelectric applications include bismuth and bismuth compounds. In particular, bulk bismuth telluride based compounds are widely used for room temperature thermoelectric applications, while bismuth antimony alloys exhibit high efficiencies at liquid nitrogen temperature [3]. The synthesis of bismuth compound nanowires with controlled size and crystallinity, and the systematic study of their thermoelectric properties will thus contribute to better understand the influence of mesoscopic and quantum size effects on the thermoelectric characteristics of nanostructured materials.

* Research supported by DFG Schwerpunktprogramm 1386

† Sven.Mueller@gsi.de

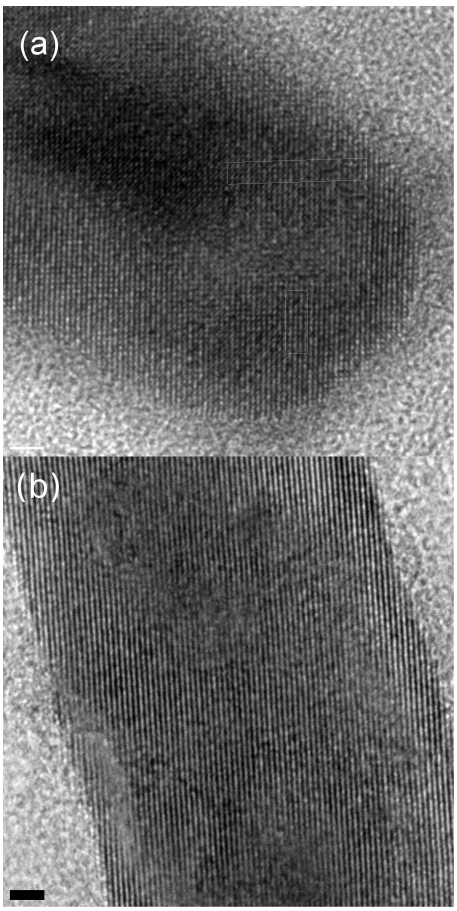

Figure 1: TEM images of $Bi_{1-x}Sb_x$ nanowires with a diameter of 20 nm and (a) $x = 0.18$, (b) $x = 0.26$. The scale bar is 2 nm.

c(Sb) in electrolyte	$1-x$	error	x	error
0.10	0.93	0.03	0.07	0.02
0.20	0.82	0.04	0.18	0.02
0.30	0.74	0.04	0.26	0.02
0.40	0.59	0.03	0.41	0.02

Table 1: Concentrations of Bi $1-x$ and Sb x in the nanowires compared to the concentration of Sb in the electrolyte.

We have successfully synthesized 20-nm diameter $Bi_{1-x}Sb_x$ nanowires with different composition by potentiostatic electrochemical deposition in ion track-etched membranes [4] applying the same voltage for all samples. Electrolytes with different relative concentration of Bi and Sb ions (c(Bi) and c(Sb), respectively) were employed. The concentration of Sb in the nanowires (x) was measured with a TEM-EDX system. The EDX spectra showed signals also from Pb and Al probably due to stray radiation and impurities introduced during the preparation for TEM. The values for $1-x$ and x are presented in Tab. 1, each representing the average of several measuring spots on nanowires fabricated with the same electrolyte. As a result, the concentration of Sb in the $Bi_{1-x}Sb_x$ nanowires can be controlled by the concentration of Sb ions in solution, in the case of potentiostatic deposition. HRTEM images revealed that all nanowires were polycrystalline, the average grain size increasing with increasing Sb concentration. This is in agreement with the fact that during deposition of nanowires with higher Sb concentrations, the current density was lower, i. e. the growth rate was slower.

References

[1] L. D. Hicks and M. S. Dresselhaus, PRB 47 (1993) 12727

[2] L. D. Hicks and M. S. Dresselhaus, PRB 47 (1993) 16631

[3] O. Rabin, Y.-M. Lin, M. S. Dresselhaus, APL 79 (2001) 81

[4] M. E. Toimil-Molares et al., Adv. Mater. 13 (2001) 6

Electrodeposition of Bismuth Telluride Nanowires in Ion Track-Etched Polymer Templates*

O. Picht[1,#], S. Müller[1], M. Rauber[2], S. Lauterbach[3], M.E. Toimil-Molares[1] and R. Neumann[1]
[1]GSI, Darmstadt, Germany; [2]Institute for Material Sciences, TU Darmstadt, Germany;
[3]Institute for Applied Geosciences, TU Darmstadt, Germany

For more than 50 years, materials based on bulk bismuth telluride have been in the scope of thermoelectric research. Even today, they represent the most common constituents for commercially available thermoelectric devices operating at room temperature (RT). As shown by theoretical investigations of Hicks and Dresselhaus [1], low-dimensional structures offer a promising route to further enhance the efficiency of thermoelectric devices. The reason for this conclusion lies in the altered physical properties of nanostructures and nanostructured materials, which makes it possible to separately adjust the different contributions to the figure of merit, namely the Seebeck coefficient, and the electrical as well as the thermal conductivity.

Experimental Setup

For electrodeposition of compound nanowires, 30-µm thick polymer templates were irradiated with energetic heavy ions such as Au, Pb, or U at the UNILAC linear accelerator of GSI. Subsequently, the latent ion tracks were transformed into nanopores by etching with 6M NaOH at 50°C. In the case of the bismuth telluride nanowires, we employed polycarbonate membranes with an average pore diameter as low as 30 nm. The deposition was performed in a thermostated three-electrode cell, with a saturated calomel reference electrode (SCE). The temperature was kept constant during deposition at either RT or 5°C. The electrolyte was based on 1 M nitric acid, 5 mM bismuth nitrate pentahydrate, and 7.5 mM Te powder [2]. The deposition potential was varied from -50 to -200 mV vs. SCE to control the transport of ion species towards the cathode, and thus influence the elemental composition and growth rate of the compound nanowires.

Results

The morphology of bismuth telluride nanowires was investigated by high resolution scanning electron microscopy (HRSEM). Applying high deposition potentials and RT leads to high growth rates, and thus to inhomogeneous and dendritic growth inside the nanopores. As a consequence the resulting wires display rough surfaces as illustrated in Fig. 1 (left). At lower deposition potentials and lower temperatures (6°C), homogeneous growth is obtained and the wires exhibit lower surface roughness (Fig. 1 (right)).

The composition of the nanowires has been examined by energy dispersive x-ray analysis (EDX). First results indicate that for the given electrolyte a potential of -75 mV vs. SCE is a suitable choice in order to obtain a bulk compound with a composition close to Bi_2Te_3. In addition, TEM measurements on nanowires with a diameter of 70 nm, grown at RT, indicate that dc electrodeposition with the given parameters leads to polycrystallinity.

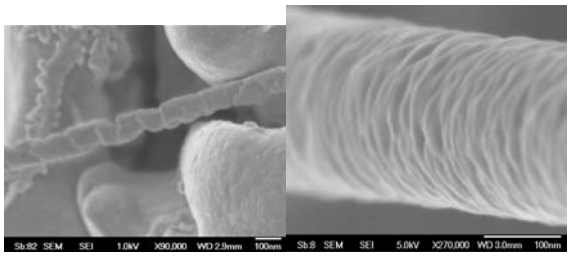

Figure 1: SEM micrographs of bismuth telluride wires. (left) Nanowire with rough surface and average diameter of 100 nm. The wire appears to consist of large segments with sizes of about 50 nm. Electrodeposition was performed with -150 mV vs. SCE at 6°C. (right) Smooth wire with average diameter of 220 nm. The deposition was carried out with -75 mV vs. SCE at 6°C.

Conclusion

Electrodeposition of compound nanowires is a complex procedure with several parameters that crucially influence the growth velocity and herewith, the morphology of the nanostructures. Both deposition behaviour and resulting wire morphology have been studied qualitatively. First EDX analysis of nanowire caps indicates a composition close to Bi_2Te_3. Further measurements will focus on a systematic investigation of the elemental composition and crystallinity as a function of the wire diameter and deposition parameters. In collaboration with the University of Applied Sciences in Wiesbaden/Rüsselsheim, single wires with submicron diameters will be characterised with regard to their thermoelectric properties by means of specially designed microchips [3,4].

References

[1] L.D. Hicks, M.S. Dresselhaus, Phys. Rev. B 47 (1993), 16631.
[2] P. Magri, C. Boulanger, J.M. Lecuire, J. Mater. Chem. 6 (1996), 773.
[3] F. Völklein, H. Reith, T.W. Cornelius, M. Rauber, R. Neumann, Nanotechnology 20 (2009), 325706
[4] F. Völklein, M. Schmitt, T.W. Cornelius, O.Picht, S. Müller, R. Neumann, Journal of Electronic Materials 38 (2009), 1109

* Work supported by DFG SPP 1165
# o.picht@gsi.de

Contrast enhancement for in-situ GFP microscopy at the microbeam

B. Merk*, B.E. Fischer, R. Neumann, F. Tobias, and K.-O. Voss
GSI, Darmstadt, Germany

In collaboration with GSI Biophysics, the microbeam, operated with ions from the UNILAC linear accelerator of GSI, is routinely employed for targeted irradiation of living cells in culture [1]. A custom-made fluorescence microscope is used both for beam targeting and for cell observation via fluorescent dyes that specifically highlight the biological agent of interest.
Green Fluorescent Protein (GFP) is often used to study dynamics of repair proteins shortly after broad-beam ion irradiation in a beamline microscope [2, 3]. A combination of the high-quality in-situ GFP microscopy, currently available at the X6 beamline microscope, with the accurate targeting of single ions performed at the X0 microbeam would greatly widen the possibilities of the microbeam for radiobiological studies. Here, we report on technical improvements of the in-situ GFP microscopy setup at the microbeam facility.

Contrast enhancement

GFP is excited by blue light of about 470 nm wavelength. Its fluorescence peaks at around 509 nm. Clearly, to achieve good contrast between areas of high GFP content and those of low content it is of utmost importance that green fluorescence from the target, traversed by the blue encitation light, originates exclusively from GFP. For this reason, we assessed the possible sources of errant green fluorescence. As expected, most of the stray fluorescent light originates from the 0.8 mm thick layer of cell culture medium. Additionally, a significant amount of green fluorescence stems from a printed circuit board (PCB) mounted in vacuum, carrying a number of high power white LEDs as well as a channeltron and a mechanical beam shutter. Replacing the white LEDs (that internally use wavelength-shifting fluorophores) with green LEDs and covering the PCB with black acrylic varnish almost entirely eliminates the green fluorescence. The cell culture medium, on the other hand, is a delicately adjusted combination of standard media plus a number of additives to achieve suitable conditions for culture growth and cell nourishment. Figure 1 presents the fluorescence of the two most commonly used media, Eagle's minimum essential medium (EMEM) and Dulbecco's modified Eagle's medium (DMEM). Both media are modified by specific additives that, among other ingredients, contain fetal calf serum, phenol red, and riboflavin. These three agents are found to be green fluorescent under blue excitation. A biologically conservative reduction of their concentration diminishes the original fluorescence background by 50%.

* b.merk@gsi.de

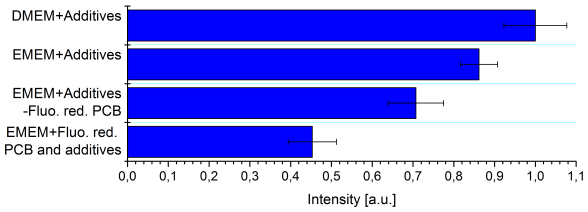

Figure 1: Overview of fluorescence background reduction

Control Software

To investigate the kinetics of fluorescent proteins after ion irradiation, it is necessary to record micrographs at defined points in time before and after the targeted ion traversal. For this purpose, the microbeam control software (written in C++ as a plugin to the ImagePro Plus software package) was extended to implement a flexible time-series of accurately concerted illumination and image recording. Figure 2 displays a panel of such a time series for GFP tagged NBS1 in two U2OS cells after targeted ion irradiation. NBS1 foci appear in the course of the first three minutes at the sites of single-ion traversals.

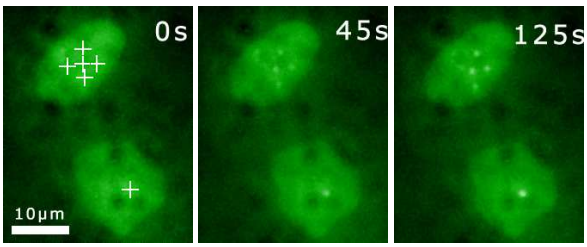

Figure 2: Left: Each center of the white crosses is irradiated with a single ion. Middle and right: After irradiation the recruitment of GFP tagged repair proteins is visible

Summary and Outlook

By reduction of the fluorescence background and thereby increase of the image contrast, in combination with the software extension, it is now possible to study dynamics and kinetics of GFP labeled proteins in-situ. Further improvement of image quality may be obtained with reduced thickness of the layer of cell medium.

References

[1] M. Heiss et al., Radiation Research 165 (2006) 23
[2] B. Jakob et al., PNAS 109 (2009) 3172-3177
[3] F. Tobias et al., Mutation Research (2009) (Article in press)

Depth Profile of Swift Heavy Ion–Induced Damage in HOPG

M. Tomut[1,2,#], M. Krause[1,3], C. Trautmann[1]
[1]GSI, Darmstadt, Germany, [2]NIMP, Bucharest, Romania, [3], TU Darmstadt, Germany

Graphite and carbon composites are materials of choice for various components for new-generation heavy-ion accelerators including collimators at LHC as well as targets and beam catchers at FAIR and FRIB. Ion-induced damage could ultimately be the limiting factor for the lifetime of these components. Depending on the beam, passing through or being stopped, the radiation damage mechanisms are different for each component. For example at the planned Super-FRS, the graphite production target works in transmission mode. Here, the primary beam loses energy mostly by inelastic collisions, while in the beam catchers the damage predominantly originates from elastic collision cascades (nuclear stopping). Information on radiation damage in graphite is mainly available from applications in nuclear fission power plants. The damage predominantly induced by neutrons is quantified in dpa (displacements per atom). For swift heavy ions, the dpa values are not relevant because they produce damage via electronic excitations and ionization, and the nature and quantity of the damage strongly depends on the material. The present work aims at assessing the damage in the nuclear and electronic stopping regimes by investigating layers of highly oriented pyrolytic graphite (HOPG) at different depths.

Samples of freshly cleaved HOPG (ZYA grade, NT-MDT) were irradiated at room temperature with 11.1 MeV/u ^{197}Au ions, at the UNILAC. The fluence was 5×10^{12} ions/cm^2, corresponding to almost complete coverage of the irradiated layer with ion tracks. The range (~100 µm) and energy loss were calculated using the SRIM 2008 code. The depth evolution of the damage of this ideal layered graphite structure was monitored by Raman spectroscopy. The depth information was obtained by stepwise removing 2-20 µm thick layers with an adhesive tape. This allowed us to follow the defect population density in the electronic and nuclear stopping regime.

Figure 1 shows a sequence of Raman spectra of irradiated HOPG at different cleaving steps. Ion-induced damage within graphitic planes is indicated by the presence of the defect peak (D) in addition to the graphitic peak (G) which corresponds to the normal Raman mode of single-crystalline graphite. The second-order 2D-peak is important when analysing bent graphitic planes which are also characteristic of irradiated graphite. The discussion of the second-order Raman spectra evolution will be presented in further publications.

To characterize the damage evolution, we calculated the ratio of the D- to G-peak area (A_D/A_G). This parameter is related to radiation induced effects such as crystallite size reduction, bond length and bond-angle disorder, in-plane vacancy clusters, and hybridization [1]. The evolution of A_D/A_G with depth is presented in Figure 2 along with the total and nuclear energy loss.

m.tomut@gsi.de

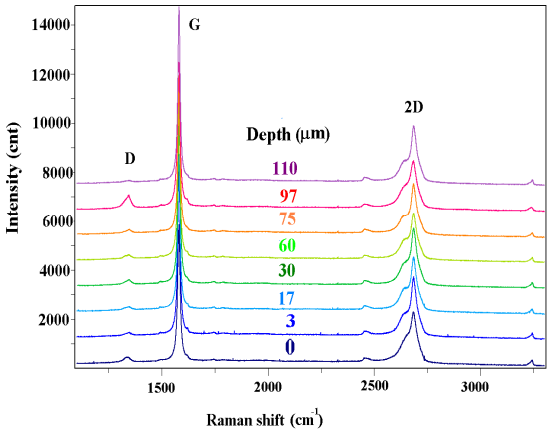

Figure 1: Raman spectra of HOPG irradiated with 5×10^{12} Au ions/cm^2 for different surfaces obtained by layer-by-layer cleaving.

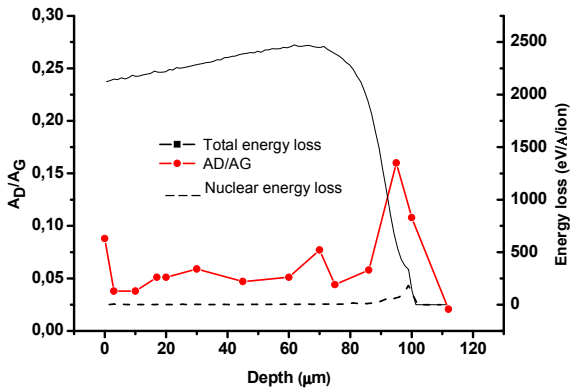

Figure 2: Depth profile of damage induced by 11.1 MeV/u Au ions and quantified by the area ratio of the D- and G-peak (A_D/A_G). Superimposed are the total energy loss (solid line) and nuclear energy loss (dashed line).

We notice that (A_D/A_G) as a function of depth increases at the original sample surface and within the last 10 µm before the ions come to rest. The damage mechanism in the region dominated by electronic stopping (up to 80 µm depth) seems to be less efficient than in the nuclear stopping regime (depth 90-100 µm). Similar experiments are planned for HOPG samples irradiated with higher ion fluences corresponding to strongly overlapping tracks, where profilometry measurements on isotropic graphite samples indicate a steep increase in beam-induced swelling [2].

[1] J. Ferrari *et al.*, Phys. Rev. B 61 (1999) 14095.
[2] M. Tomut *et al*., GSI Scientific Report (2007) 69.

DNA Damage after High-LET Exposure

M. Ensminger[1], S. Conrad[1], A. Beucher[1], G. Taucher-Scholz[2] and M. Löbrich[1]
[1]Darmstadt University of Technology, Germany; [2]GSI, Darmstadt, Germany

In the last few years carbon ions became an important tool in tumor therapy as they show a higher biological effectiveness compared to other kinds of radiation (e.g. X-rays). Although it has been known since years that particle induced DNA double strand breaks (DSBs) are more slowly repaired and that the fraction of residual breaks correlates with the cell killing capacity of high-LET radiation, the understanding of the molecular processes is still incomplete.

In this study we focus on the complexity of DSBs induced by heavy ions. Owing to the high ionisation density of high-LET particles, heavy ion irradiation induces DSBs that are generally more complex with additional lesions in very close proximity to the DSB. Recently we have reported that complex breaks require processing before repair, performed by the nuclease Artemis that is operating in a common repair pathway with the kinase ATM. Cells deficient in one of these factors are specifically defective in the repair of DSBs with slow repair kinetics and the level of unrepaired breaks seems to depend upon the complexity of the DSB ends. After α-particle irradiation a higher proportion of DSBs is repaired in an ATM and Artemis dependent manner than after X-irradiation. By contrast ATM and Artemis are dispensable for the repair of "clean" DSBs induced by the topoisomerase II inhibitor etoposide [1, 2].

To determine the amount of complex DSBs after heavy ions, we irradiated stationary wildtype (82-6 hTert) and Artemis deficient cells (CJ hTert) with ^{12}C (LET: 170keV/µm) ions using the UNILAC at the GSI. The repair of the DSBs was observed by PFGE analysis and compared to the repair after similar X-ray doses. The data demonstrate that DSBs induced by ^{12}C ions are more slowly repaired than breaks after X-irradiation. Furthermore, the level of unrepaired DSBs in Artemis defective cells compared to wildtype cells is higher after ^{12}C ions. While Artemis deficient cells exhibit only a very small repair defect after X-rays (≤10%), they show more than 30% unrepaired DSBs after ^{12}C ions (Fig.1A).

To confirm our results with another approach we established a γH2AX immunofluorescence assay for analysing DSB repair after high-LET irradiation. Here, human wildtype (HSF1) and Artemis defective (CJ179) cells were seeded on cover slips and irradiated with ^{12}C ions under a small angle to the beam. γH2AX foci along the ion tracks were analysed in G1 cells and compared to γH2AX foci numbers after X-irradiation. Similar to the results of the PFGE analysis we observed faster DSB repair kinetics after X-rays compared to ^{12}C ions. Moreover, the high repair defect in Artemis deficient cells was also detected with this approach (Fig.1B) therefore supporting our notion of a high proportion of complex DSBs after high-LET irradiation.

In the future, we aim to investigate the pathways involved in the repair of these Artemis-dependent DSBs after high-LET radiation. We suppose that at least in the G2 phase of the cell cycle homologous recombination may be the major pathway chosen to repair these complex breaks. Therefore, we plan to analyse DSB repair kinetics after heavy ions in G2 cells using the γH2AX foci assay.

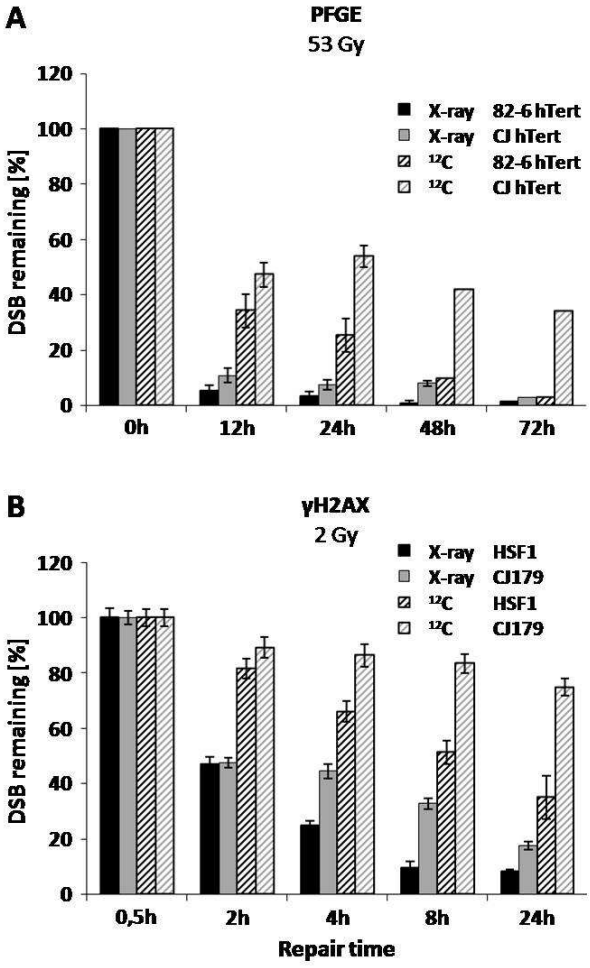

Fig.1: DSB repair in wildtype (82-6 hTert, HSF1) and Artemis deficient (CJ hTert, CJ179) cells after X-ray or ^{12}C ions measured by PFGE (A) or γH2AX immunofluorescence (B).

References

[1] E. Riballo, M. Kühne, N. Rief, A. Doherty, et al., Molecular Cell 16 (2004) 715-724
[2] A. Beucher, J. Birraux, L. Tchouandong, O. Barton et al., EMBO J. 28 (2009) 3413-3427

Establishing an approach to study histone modifications at DNA damage sites

F. Natale[1], M. Durante[1,2], M. C. Cardoso[2], and G. Taucher-Scholz[1,#]
[1]GSI, Darmstadt, Germany; [2]Technische Universität Darmstadt

Introduction

DNA double strand breaks (DSB) are hazardous lesions compromising genomic integrity. Thus, efficient DNA repair is crucial to prevent cells undergoing genomic instability and cancer. DNA DSBs are quickly recognized by damage sensors and the area surrounding the damage site is marked by phosphorylation of Ser139 on the H2AX histone variant (γH2AX). Such DSB specific histone modifications spread through megabases from the damage site, and seem to be excluded from heterochromatin[1]. Within the last years nuclear architecture and chromatin structure have gained importance in DNA repair, having the hypothesis that less compact chromatin regions are more accessible to DNA repair factors taken hold[2,3]. Thus, local decondensation of chromatin domains encompassing the DSB may play a crucial role in lesion processing. While it is well known that chromatin decondansation mechanisms involve several histone modifications, it is not clearly defined whether DNA damaging agents as ionizing radiations (IRs) and chemicals induce global changes in terms of histone modifications and, thus, chromatin structure. In addition, little is known about the modifications occuring on localised regions surrounding the DSB, and their effect on larger chromatin domains. Here we describe preliminary experiments to establish an approach allowing the analysis of histone modifications surrounding DSB sites induced by different types of IRs. In future work the correlation between radiation quality and chromatin decondensation processes should be addressed.

Experimental Setup

DNA DSBs and, consequently, γH2AX signals will be induced by irradiating cells with different types of IRs (X-rays, heavy ions). After fixation, lysis and chromatin shearing, immunoprecipitation (IP) is performed in order to pull down γH2AX-enriched chromatin fractions. Subsequent IP is performed probing such fractions with antibodies directed against different histone modifications in order to select specific modifications colocalising with γH2AX. Finally, the double-enriched fractions are analysed by polyacrylamide gel electrophoresis, followed by western blot and chemiluminescent detection.

Cell Line Characterization

To establish the experimental setup we first characterised the response to IRs of two suitable human tumour cell lines (HepG2 and U2OS) in terms of H2AX phosphorylation (Fig.1, upper panel) and γH2AX foci formation (Fig.1, lower graph). We found a lower basal level in U2OS cell line but a higher radiation-induced γH2AX in HepG2 cell line.

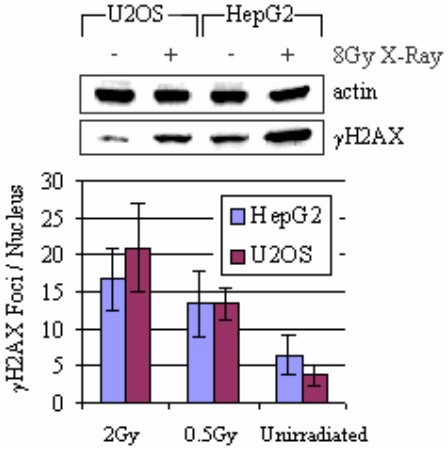

Figure 1: Induction of H2AX phosphorylation detected in Western blots (top) or as immunostained γH2AX foci upon X-Ray irradiation (bottom).

Immunoprecipitation

Next, we tested two different antibodies (Abs) directed against γH2AX for IP. A dose of 8Gy X-rays was delivered to cells in order to induce γH2AX. As shown in Figure 2, the monoclonal Ab, but not the polyclonal Ab was able to IP its target.

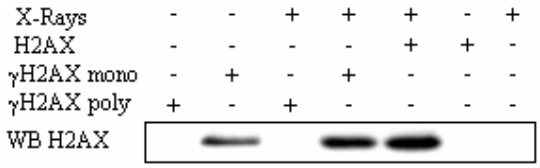

Figure 2: IP test of Abs (Upstate Biotechnologies) directed against γH2AX. γH2AX mono: mouse monoclonal Ab; γH2AX poly: rabbit polyclonal Ab. Lane 5: H2AX IP positive control (Ab from Bethyl Laboratories); Lane 6: no lysate control; Lane 7: no antibody control.

Conclusions and Perspectives

We demonstrate that the cell lines are suited for studying modifications at γH2AX sites since a clear radiation-induced signal is produced. In addition, the monoclonal antibody is able to specifically immunoprecipitate γH2AX upon irradiation and will be used in an approach, allowing the analysis of histone modifications associated to damaged sites.

References

[1] J. Kim *et al.*, JCB (2007)
[2] M. Falk *et al.*, Biochim Biophys Acta (2007)
[3] M. J. Kruhlak *et al.*, Cell Cycle (2006)

* Work supported by BMBF FZ n. 02S8355

#G.Taucher-Scholz@gsi.de

Recruitment of mRFP-XRCC1 to DNA damage in living cells

N. Averbeck[1], B. Jakob[1], A.L. Leifke[1], M. Durante[1,2], and G. Taucher-Scholz[1]
[1]GSI, Darmstadt, Germany; [2] TUD, Institut für Festkörperphysik, Darmstadt, Germany

The X-ray repair cross-complementing group 1 protein (XRCC1) is known to be involved in the efficient repair of DNA single-strand breaks caused by ionizing radiation and alkylating agents.

We described the fast recruitment of XRCC1-GFP to DNA strand breaks after heavy ion irradiation using beam line microscopy [1]. Now, we set out to investigate whether different XRCC1 recruitment kinetics could be observed during distinct cell cycle phases, since for the repair of DNA double strand breaks it is well known that cells utilize different repair mechanisms dependent on the cell cycle. In order to monitor the cell cycle phase we used a human cell-line that stably expresses a GFP-tagged G1/S cell cycle phase marker (from GE healthcare) that appears green in the microscope (Fig. 1 right). To further be able to monitor XRCC1 in these living cells we constructed a eukaryotic expression vector that expresses *N*-terminally mRFP-tagged human XRCC1. Thus, in cells that carry this vector mRFP-XRCC1 can be visualized by red fluorescence in the cell nucleus (Fig.1, left).

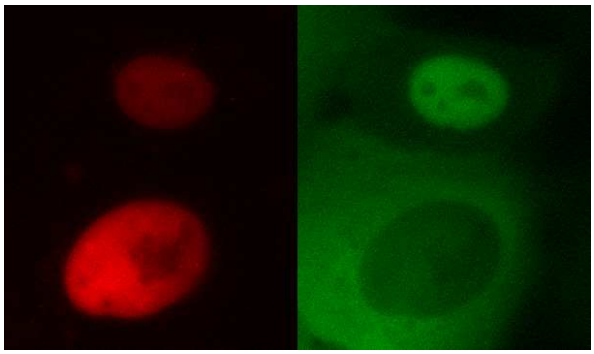

Figure 1: Two U2OS-G1/S cells expressing mRFP-XRCC1. Red: mRFP-XRCC1, green: GFP-G1/S cell cycle phase marker: cell at the top: G1 phase, cell at the bottom: G2 phase

In a next step we demonstrated the functionality of the expressed mRFP-XRCC1 construct by laser micro-irradiation (LMI). Upon laser irradiation mRFP-XRCC1 accumulates at the site of irradiation indicating an efficient binding of the chimerical protein at damaged DNA sites (Fig. 2, right). Analyzing the recruitment kinetics (Fig. 2, left) revealed similar kinetic constants compared to the established GFP-XRCC1 construct described in [1, 2]. This result further confirms the functional activity of mRFP-XRCC1.

Interestingly, a fraction of cells showed a transient binding behaviour of mRFP-XRCC1 to DNA lesions. Within this mRFP-XRCC1 population, however, this accounts only for a fraction of the accumulated mRFP-XRCC1 (Fig. 3). This might indicate two modes of XRCC1 binding to damaged DNA or the participation of XRCC1 in two distinct repair pathways that differ in the repair half-life. Whether or not the non-transient fraction of mRFP-XRCC1 is involved in the slow nucleotide excision repair (NER) of UV dependent photo-damage [3] and is therefore unique to laser micro-irradiation will be revealed in future investigations with charged particles.

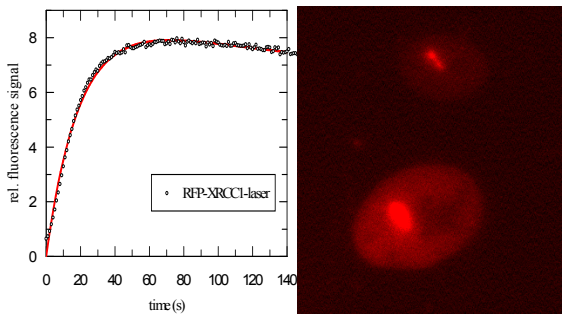

Figure 2: Recruitment kinetic of mRFP-XRCC1 to UV-laser induced DNA damage in the cells depicted in Fig. 1.

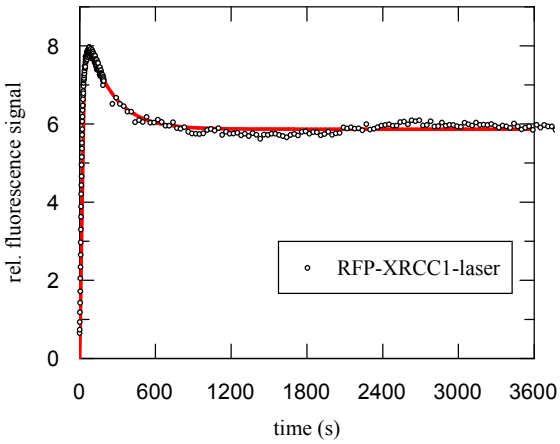

Figure 3: A portion of mRFP-XRCC1 recruited to DNA lesions shows transient lesion bindings after LMI.

Conclusion

We showed the functionality of the new mRFP-XRCC1 construct. The characteristics of the irradiation dependent fluorescence intensity behaviour point to two different modes of XRCC1 binding after LMI.

BMBF grant 03NUK001A

References

[1] F. Tobias et al. Mutation Research (2009) Nov 26. [Epub ahead of print]

[2] L. Lan et al. PNAS 101 (2004) 113738-43

[3] A. Nakagawa et al. J Invest Dermatol. 110 (1998) 143-8.

Repair of DNA Double-Strand Breaks in Mouse Tissues after Low dose irradiation

S. Grudzenski[1], A. Raths[1], D. Deckbar[1], C.E. Rübe[2] and M. Löbrich[1]
[1]Darmstadt University of Technology, Germany; GSI; [2]Department of Radiation Oncology, Saarland University

A lot is known about a cell's reaction to high doses of ionizing radiation (IR), but the impact of low doses (< 50 mGy) is not well understood. There is increasing evidence that different cellular responses may play a role after low dose IR and it becomes obvious that the results from high dose studies cannot be transferred directly to the low dose range. The most deleterious form of IR induced DNA damages is the double strand break (DSB), and its efficient repair is essential for the maintenance of the genomic integrity. The method of γH2AX or 53BP1 foci analysis provides the opportunity to detect a single DSB on the single cellular level and therefore allows to investigate DSB repair even after doses as low as a few mGy.

Previous DSB repair studies with confluent primary fibroblast using γH2AX foci analysis showed a decreased repair capacity with decreasing x-ray dose as well as a residual level of unrepaired DSBs [1].

To evaluate the significance of these findings we established the method of γH2AX and 53BP1 foci staining in mouse tissues after *in vivo* x-ray irradiation in collaboration with the group of C. Rübe (Figure 1) [2].

As previously described, the induction of DSBs after low dose irradiation is linear with dose and identical in all organs (Figure 2). Furthermore, we investigated the repair behaviour of DSBs after IR by counting 53BP1 foci in different organ tissues (brain, lung, heart, small intestine and kidney) 10 min, 5 h and 24 h after doses of 1 Gy, 100 mGy and 10m Gy (Figure 2). In line with the *in vitro* studies, we found a decreased repair capacity with decreasing dose as well as the existence of residual DSBs after extended repair times. These data confirm the physiological relevance of the previous *in vitro* studies and suggest that DSB repair may not be initiated below a certain level of induced DSBs. Further investigations aim to dissect whether other IR-inducing damages like base damages may trigger DSB repair which becomes especially apparent at the low dose level.

From *in vitro* studies, it is known that DSB repair differs in heterochromatic and euchromatic regions [3]. With the sensitive method of γH2AX foci staining we are not only able to quantify the DSBs but in combination with markers for different chromatin regions can investigate the localisation of the DSB. The establishment of these staining approaches now gives us the opportunity to investigate DSB repair after physiological doses in dependency of the genomic region to gain more mechanistic insight into the cellular response to low doses of IR.

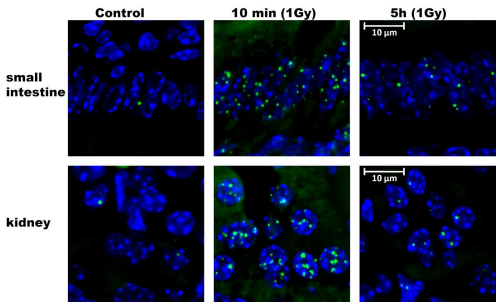

Figure 1: Immunofluorescence staining of 53BP1(bright foci) in unirradiated (control) nuclei of mouse small intestine and kidney, and 10 min or 5 hr after *in vivo* irradiation with 1 Gy.

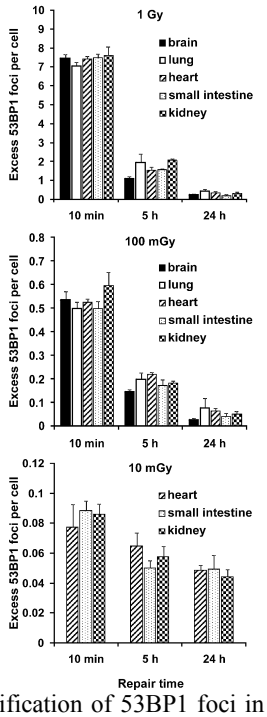

Figure 2: Quantification of 53BP1 foci in cells of mouse brain, lung, heart, small intestine and kidney 10 min, 5 h and 24 h after *in vivo* irradiation with 1 Gy, 100 mGy and 10 mGy.

References

[1] K. Rothkamm and M. Löbrich, *Proc Natl Acad Sci* 2003; 100, 5057-5062.
[2] C.E. Rübe, S. Grudzenski, et al., *Clin Cancer Res*. 2008; 14 (20) 6546-55.
[3] A.A. Goodarzi, A. T. Noon, et al., *Mol. Cell* 2008; 31, 167-177.

The telomere-associated proteins TRF1, TRF2 and TIN2 are recruited to UVA laser but not to ion-irradiated sites*

J. Splinter[1], B. Jakob[1], G. Becker[1], D. J. Chen[2], M. Durante[1,3], G. Taucher-Scholz[1]
[1]GSI, Darmstadt, Germany; [2]UT Southwestern Medical Center, Dallas, TX, USA; [3]TUD, Darmstadt, Germany

DNA is compacted into chromosomes in the nucleus of cells. The ends of these chromosomes (telomeres) are associated to proteins to form a dynamic cap that protects the DNA from being viewed as double-strand breaks (DSBs) and eliciting a DNA damage response. One of the proteins responsible for telomere capping is TRF2 (telomeric repeat binding factor 2). Recently this protein was also reported to function in homologous recombination repair of DSBs [1] and its recruitment to sites of laser microirradiation supporting an involvement in DNA repair was observed [2,3]. Here we demonstrate that 337nm-laser irradiation induces a fast recruitment of TRF2 and other telomere-associated proteins as TRF1[4] and TIN2 (TRF1-interacting nuclear protein 2), whereas densely ionizing charged particle irradiation give no indication of accumulation at sites of damaged DNA[4].

Results and Discussion

Recruitment of TRF2 was previously observed following UVA (390nm) [2] and 800nm-multiphoton laser microirradiation [3]. Here we show that a laser system with shorter wavelength (337nm) was also able to induce accumulation of TRF2 in human IBR3 fibroblasts (Fig. 1). The used cell line stably expresses a TRF2 protein tagged with a fluorescent marker (YFP) enabling real time monitoring of the TRF2 recruitment. However, following low energy xenon ion irradiation we did not find TRF2 signals at the sites of ion traversals (Fig. 1) visualized by immunostaining for the DSB marker γH2AX (red). This is in agreement to previous findings that high local doses following microprobe irradiation with 400 helium ions [3] were insufficient to induce a detectable TRF2 recruitment. Both findings indicate that TRF2 recruitment can not be solely related to high local DSB density as previously suggested by [2].

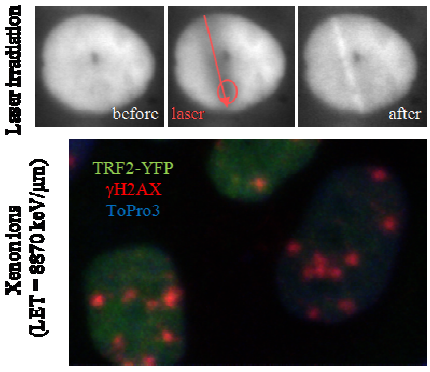

Figure 1: IBR3-TRF2-YFP cells were irradiated with a UVA laser or xenon ions as indicated. Cells fixed 1h after irradiation were stained for γH2AX. DNA: ToPro3.

Besides TRF2 other proteins as TRF1 and TIN2 are associated to telomeres and contribute to capping. To test whether these proteins show recruitment behaviour comparable to TRF2 we irradiated IBR3-TRF1-YFP and IBR3-TIN2-YFP cells with UVA laser (Fig. 2) or low energy xenon ions (Fig. 3). As observed for TRF2, both proteins are readily recruited to laser-irradiated sites, but not to sites of ion traversals despite the high density of DSBs induced (marked by γH2AX).

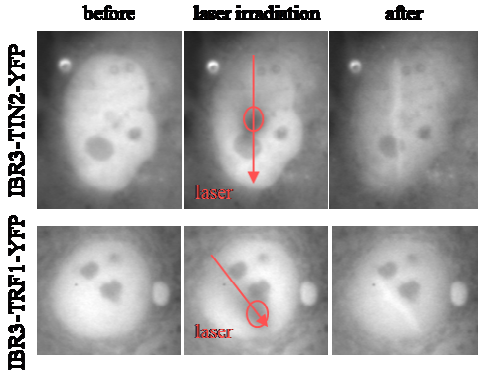

Figure 2: 337nm UVA laser-irradiated IBR3-TRF1-YFP and IBR3-TIN2-YFP cells.

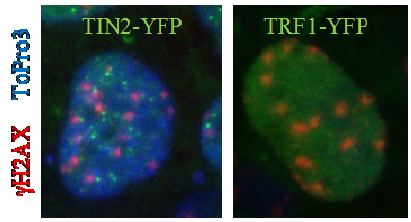

Figure 3: Xenon ion-irradiated IBR3-TIN2-YFP and IBR3-TRF1-YFP cells. Cells fixed 1h after irradiation were stained for γH2AX. DNA: ToPro3.

These data show that laser irradiation, in contrast to charged particles, induces DNA lesions that recruit telomere-associated proteins. Whether this recruitment is related to an active role in DNA repair as previously suggested [1,2] has to be addressed in further experiments.

References

[1] Z. Mao et al., Proc. Natl. Acad. Sci. USA 104 (2007) 13068.
[2] P. S. Bradshaw et al., Nat. Gen. 37 (2005) 193.
[3] E. S. Williams et al., Nat. Gen. 39 (2007) 696.
[4] J. Splinter et al. Mutagenesis (2010) Epub aop.

*This work was partly supported by BMBF contract [03NUK001A].

Requirement for PARP-1 in the recruitment of aprataxin to sites of DNA breaks

F. Tobias[1], O. Becherel[2], M. Lavin[2], G. Becker[1], M. Durante[1,3], G. Taucher-Scholz[1], and B. Jakob[1]
[1]GSI, Darmstadt, Germany, [2] Queensland Institute of Medical Research, Brisbane, Australia, [3] Technische Universität Darmstadt, Institut für Festkörperphysik, Darmstadt, Germany

Introduction

Poly-ADP ribose polymerase 1 (PARP-1) is a protein well described as a sensor for single strand DNA breaks (SSB) [1]. After its activation a localized poly(ADP-ribosyl)ation of proteins near the DNA breaks is initiated, which is necessary for efficient binding of other repair proteins like XRCC1. The aprataxin protein has interaction domains for both SSB-repair proteins such as PARP-1 and XRCC1 and double strand (DSB)-repair proteins like XRCC4 [2, 3]. This suggests a requirement for aprataxin in multiple repair pathways. Here the functional interaction of aprataxin and PARP-1 after heavy ion irradiation is analyzed using different imaging techniques [4].

Results

Aprataxin is not recruited to DNA damage sites in cell lacking PARP-1

First the dependency of aprataxin recruitment on PARP-1 was analyzed. In the course of this study it turned out that endogenous APTX is not present in PARP-1 deficient cells [2]. Therefore GFP-aprataxin was transiently transfected in PARP-1 deficient and wild type cells. Cells were irradiated with low energy heavy ions causing a very high and localized DNA lesion density along their trajectories. These damage sites were visualized with antibody staining against γH2AX (white arrows in figure 1). Aprataxin was recruited to the DNA damage sites in wild type cells but not in PARP-1 -/- cells. This result strongly suggests an essential role of PARP-1in the recruitment of aprataxin.

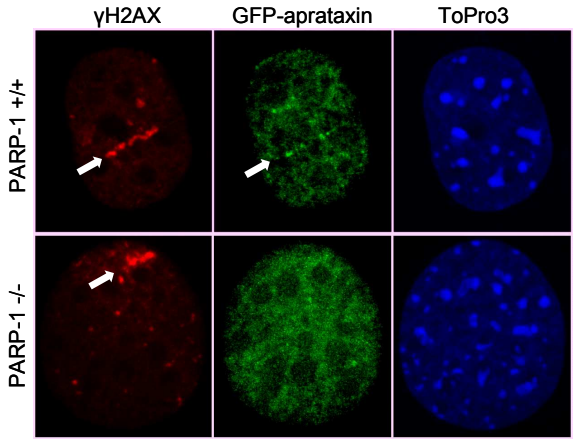

Figure 1: Recruitment of GFP labeled aprataxin in PARP +/+ and PARP -/- cells. Cells were irradiated with Xe ions (4.2 MeV/n; LET: 8815 keV/µm) in a streak pattern and fixed after 10 min. Streak pattern of DNA damage sites along the ion trajectories (white arrows) is shown with γH2AX staining. DNA is counterstained with ToPro3. [2]

Inhibition of PARP-1 activity causes delayed aprataxin accumulation

Next the dependency of aprataxin recruitment on PARP-1 activity was analyzed. Therefore HeLa cells stably expressing GFP-labelled aprataxin were used in combination with the PARP-1 inhibitor PJ-34. With the remote controlled beamline microscope real-time recruitment kinetics of aprataxin to DNA damage sites after low energy heavy ion irradiation were measured. The fluorescence signal of GFP-aprataxin was monitored over time in the irradiation induced foci and normalized to an intensity of 0 before irradiation and 1 for maximal fluorescence intensity. We found that with PARP-1 inhibition aprataxin is still recruited to DNA damage sites, but with delayed kinetics (figure 2). The signal was maximal after about 50 s in untreated cells compared to about 120 s in PARP-1 inhibited cells. This delay was confirmed using the PARP-1 inhibitor 3AB as an alternative [2].

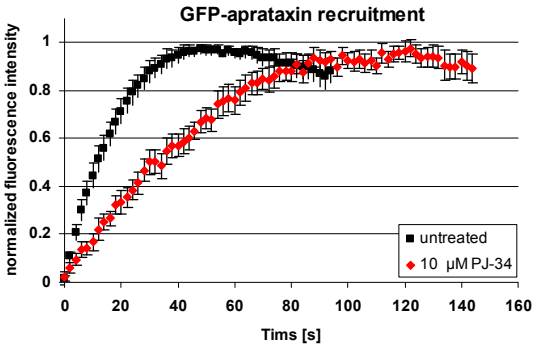

Figure 2: Recruitment kinetics of stably expressing GFP-aprataxin HeLa cells with and without inhibition of PARP-1 activity by 10µM PJ-34. Cells were irradiated with Sm ions (4.2 MeV/n; LET: 10290 keV/µm) at time point 0 second. GFP fluorescence intensities at the DNA damage sites were monitored over time. [2]

Conclusion

These data indicate that PARP-1 activity stimulates the recruitment of aprataxin, and demonstrate that PARP-1 protein is essential for aprataxin accumulation at damaged chromatin.

References

[1] K.W. Caldecott et al., Nature Rev Genetics, 2008.
[2] J. Harris et al., Human Molecular Genetics, 2009.
[3] P.M. Clements et al., DNA Repair, 2004.
[4] F. Tobias et al., Mutation Research, 2009.

Work supported by BMBF Grant 03NUK001A

Evaluation of a nuclear-wide γH2AX response after ion irradiation*

B. Meyer[1], KO. Voss[1], M. Herrlitz[1], B. Merk[1], M. Durante[1,2] and G. Taucher-Scholz[1]
[1]GSI, Darmstadt, Germany; [2]TUD, Darmstadt, Germany

Introduction

The phosphorylated form of the histone H2AX, called γH2AX, is a hallmark of damaged sites containing double-strand breaks, the most dangerous type of DNA damage. When visualized by fluorescent antibodies, ion irradiation leads to nuclear γH2AX signals detected either as foci or as streaks across the nucleus after perpendicular or low angle irradiation, respectively [1]. In addition, we found heavy ion irradiation to induce pan-nuclear γH2AX signals outside of the ion trajectory, evenly distributed over the whole nucleus and mostly weaker than the signal at the damage site (Fig. 1). Here, we describe this novel pan-nuclear response and present a newly established method to evaluate it.

Results

A simple method for the analysis of pan-nuclear signals is to determine the fraction of cells showing this response. While in unirradiated confluent human fibroblasts pan-nuclear γH2AX is visible in only 0-1% of cells, 80-86% are positive for this response after irradiation with chromium ions (6.5 MeV/u; $4 \cdot 10^6$p/cm^2). After irradiation with higher LET xenon ions (4.7 MeV/u; $3 \cdot 10^6$p/cm^2) even 99% show pan-nuclear γH2AX phosphorylation.

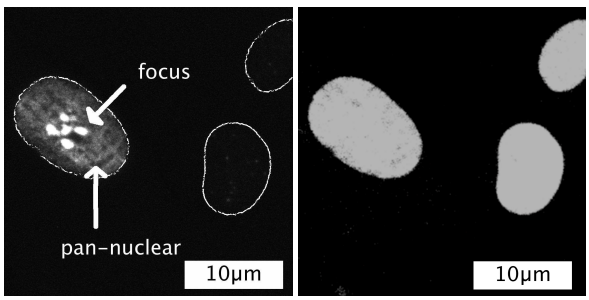

Figure 1: Pan-nuclear γH2AX signal (left) in human fibroblasts (AG1522) irradiated with 100 carbon ions (4.8 MeV/u). DNA counter staining (ToPro, right, thresholded). Nuclei showing only DNA staining (right) were not targeted for microbeam irradiation.

In order to evaluate the magnitude of the nuclear response when comparing cells responding as a function of dose or biochemical treatments we used the defined and aimed irradiation with the GSI heavy ion microprobe [2] to demonstrate the nuclear wide phosphorylation of γH2AX specifically in ion hit cells (Fig. 1). We established the quantitative evaluation of the γH2AX antibody fluorescence intensities within individual cell nuclei: In a confocal laser scanning micrograph of a cell, each voxel (or pixel when working in a 2D projection) that is DAPI/ToPro/PI positive (corresponding to the cell nucleus) is evaluated for its γH2AX fluorescence intensity. This intensity is – within appropriately controlled limits (no saturation, suitable excitation at constant power) - directly proportional to the level of H2AX phosphorylation. Figure 2 shows a γH2AX intensity histogram of cell nuclei with a pan-nuclear reaction (b) and that of unirradiated controls (a).

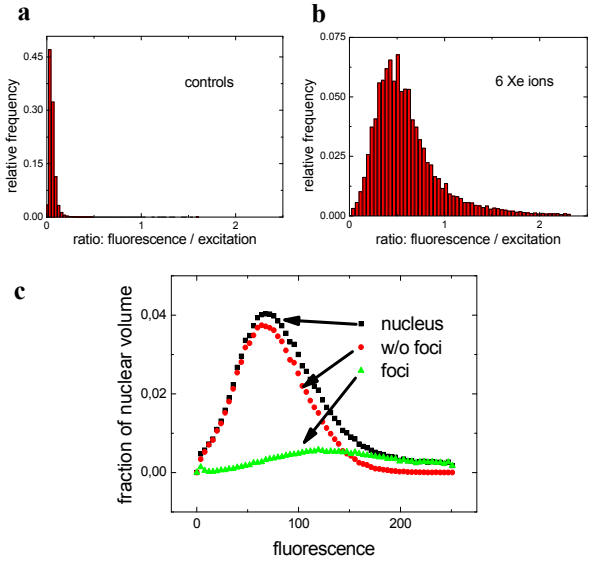

Figure 2: Histograms of a) γH2AX intensities in control and b) irradiated human fibroblasts (6 Xe ions/nucleus, 4.8MeV/u, microbeam). Fluorescence is normalized to the excitation intensities to compensate for small variations thereof. c) Pan-nuclear γH2AX signal as measured (black), with foci omitted (red), and difference (green; 10 Ni ions/nucleus, 4.8MeV/u, microbeam).

Both foci and pan-nuclear signals contribute to the histogram in Fig. 2b. Due to their high intensity and small volume, foci contribute within the higher-intensity tail of the histogram only. We verified this by manually excluding the foci in microscope images (Fig. 2c). Thus, the maximum of the fluorescence intensity histogram representing the most frequent intensity in the nucleus can safely be used as a measure for the pan-nuclear signal.

Conclusion

We established a method of evaluation for a novel pan-nuclear γH2AX response that will be used to further investigate fluence and LET dependence, as well as the kinases involved in the phosphorylation.

References

[1] Jakob B et al., Rad. Res. 2009 171:405-418
[2] Heiss M et al., Rad. Res. 2006 165:231-239

*This work was supported by BMBF Grant 03NUK001A

Analysis of aneuploidy in metaphase and interphase cells

R. Lee[1], V. Castiglia[2], M. Durante[1], P. Virsik[3] and S. Ritter[1,#]
[1] GSI, Darmstadt, Germany; [2] Università di Napoli Federico II, Italy; [3] University of Göttingen, Germany

Aneuploidy, i.e, changes in the copy number of chromosomes, has a profound impact on the health of the human population. The health consequences range from mental retardation to various neoplasms. A gain or loss of chromosomes can, for example, be induced by radiation. One of the assays for the detection of aneuploidy is the fluorescence *in situ* hybridization (FISH) technique. Screening by FISH can be performed not only on metaphase cells but also on interphase cells. The latter technique is faster and less expensive thereby allowing the analysis of large cell populations.

The aim of the present study was to compare the effectiveness of both FISH techniques for the detection of chromosome specific aneuploidy. As a target chromosome Y was chosen, because normal human male cells harbour only one copy simplifying the interpretation of the signals seen in interphase cells. Furthermore, information on aneuploidy of the Y chromosome in prostate cancer cell lines is needed, which are currently used in particle therapy related studies [1]. It has been shown that the chromosome Y is frequently lost in prostate cancer cells [2] and recent data suggest that this particular aneuploidy contributes to the carcinogenesis of the prostate [3].
For these reasons in first experiments peripheral blood lymphocytes obtained from a male volunteer and two prostate cancer cell lines derived either from a bone metastasis (PC3) or a brain metastasis (DU145) were used. Metaphase and interphase cells were harvested and dropped on glass slides. Samples were hybridized to whole chromosome DNA probes (MetaSystems, Germany) specific for chromosome Y following the protocol recommended by the manufacturer. After counterstaining with 4'-6-diamidino-2-phenylindole (DAPI), probe signals (fluorescein isothiocyanate, FITC) were evaluated under a fluorescence microscope. Images of the metaphases or interphase nuclei were captured with a CCD camera and analysed with the ISIS software (MetaSystems). Examples are shown in Fig. 1. In addition, selected samples were treated with multicolour FISH (mFISH) probes (MetaSystems) for a full karyotype analysis.

When signals were assessed in male lymphocytes at interphase, about 5 % cells were found to be Y chromosome negative (see Table 1). In contrast, in all metaphases analysed one Y chromosome was found suggesting that interphase FISH compared to metaphase analysis is less accurate producing a high false negative rate. In PC3 prostate cancer cells, loss of Y chromosome was found in all analyzed metaphases and this was confirmed by interphase analysis (Table 1). In DU145 cells all metaphases showed one positive signal (see Fig. 1 and Table 1). In addition, a full karyotype analysis by mFISH revealed that all DU145 metaphases carry a shortened Y chromosome translocated to an acentric part of chromosome 20 (see Fig. 2). These data suggest that both tumour cell lines, at least with respect to changes of the chromosome Y, are stable.

Altogether our study indicates that interphase FISH is less accurate than metaphase analyses with respect to aneuploidy detection. In particular, the fraction of aneuploid cells might be overestimated.

* Work supported by BMBF, Bonn, under contract 02S8497.
V.C. supported by summer student program at GSI in 2009.
s.ritter@gsi.de

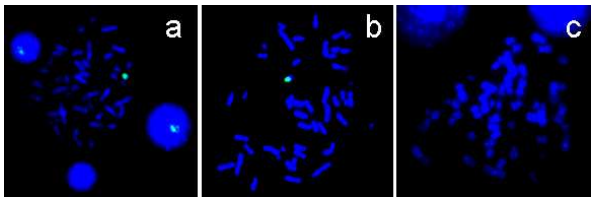

Figure 1: Staining of the Y chromosome (green) in metaphase and interphase cells (blue). (a) Lymphocytes: one metaphase and two interphases each with one Y chromosome signal and one interphase without a signal. (b) DU145 metaphase with a signal. (c) PC3 metaphase lacking a Y chromosome.

Table 1: Aneuploidy of chromosome Y in lymphocytes and prostate cancer cell lines measured in interphase and metaphases.

	Y chromosome	
Cell type	Positive	Negative
(a) Interphases		
Lymphocytes	2723	137
PC3	0	849
(b) Metaphases		
Lymphocytes	82	0
PC3	0	179
DU145	123	0

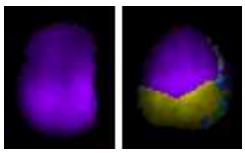

Figure 2: Analysis of the chromosome Y by the mFISH technique. Left: Normal chromosome Y (purple) in a lymphocyte metaphase. Right: Shortened chromosome Y translocated to a part of chromosome 20 (yellow) in a DU145 metaphase (right).

References

[1] P. Virsik, GSI scientific report 2009 (2010).
[2] J.J. Koenig, The Prostate 25 (1994) 281-291.
[3] S. Vijayakumar, Gene Chromo Cancer 44 (2005) 365-372.
[4] J. Bernardino, Cancer Genet Cytogenet 96 (1997) 123-128.

Complex and simple chromosomal exchanges induced by sparsely and densely ionizing radiation in vitro and in vivo*

C. Hartel[1], M. Durante[1], P. Hessel[1], R. Lee[1], S. Ritter[1] J. Debus[2] and A. Nikoghosyan[2]
[1]GSI, Darmstadt, Germany; [2]Radiology Clinics, University of Heidelberg, Heidelberg, Germany.

It is well-known that sparsely and densely ionizing radiations have a different relative biological effectiveness (RBE) for the induction of chromosomal aberrations. In addition, the different local dose distribution results in a different aberration spectrum. The most promising biomarker for densely ionizing radiation is the ratio C of complex (three or more breaks) to simple (two breaks) chromosomal exchanges [1].

The C-ratio induced in peripheral blood lymphocytes in vitro and in vivo by X-rays and C-ions was determined using the mFISH method. The cells were obtained from a healthy volunteer and irradiated in vitro or from prostate cancer patients undergoing radiotherapy with C-ion boost and IMRT (see [2] for details).

Figure 1 shows the number of simple and complex exchanges induced in lymphocytes by in vitro exposure to X-rays and C-ions with different energies. Based on these results the C-ratio was calculated. For X-ray irradiation, the C-ratio shows a clear dose-dependent increase from 0.06 ± 0.04 at 1 Gy to 0.54 ± 0.07 at 4 Gy. High-energy C-ions show values similar to X-rays, while spread-out Bragg peak (SOBP) C-ions induced a significantly higher C-ratio (0.71 ± 0.14 after 1 Gy and 0.62 ± 0.08 after 2 Gy).

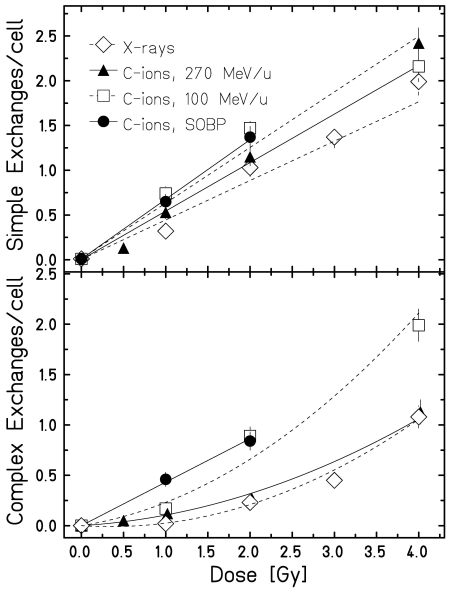

Figure 1: Simple and complex chromosomal exchanges induced in lymphocytes after in vitro exposure to X-rays and C-ions with energies of 270 MeV/u, 100 MeV/u and spread-out Bragg peak C-ions and detected by mFISH.

Figure 2 shows the yield of simple and complex exchanges found in lymphocytes from prostate cancer patients treated with C-ion boost followed by IMRT (C+IMRT) or with IMRT alone (IMRT and IMRT*, the latter group being treated with a larger target volume). The C-ratio, calculated from the data shown in Figure 2, was not significantly higher in the C+IMRT patients compared to the patients treated only with IMRT. This is in line with other studies, where no increased C-ratio was detected after external in vivo exposure in astronauts returning from long-term space flights, patients undergoing C-ion radiotherapy and mice exposed to Fe-ions [3,4]. In contrast, some studies investigating internal in vivo exposure to α-particle-emitters found a high fraction of complex aberrations [5].

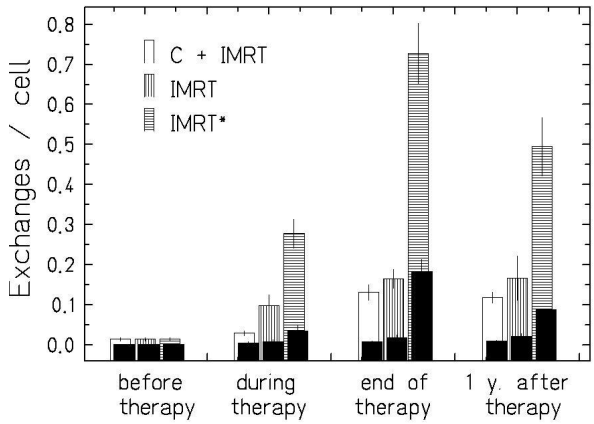

Figure 2: Simple exchanges (open bars) and complex exchanges (solid bars) found in lymphocytes from prostate cancer patients undergoing radiotherapy.

In conclusion, our data demonstrate that the C-ratio is elevated after high-LET in vitro irradiation, in agreement with previous in vitro studies. However, the usefulness of the C-ratio as a biomarker for densely ionizing radiation in vivo remains questionable. In the present study no elevated C-ratio was found in vivo in patients treated with C-ion boost compared to IMRT alone, as in most in vivo studies.

References

[1] C. Johannes et al. Radiat Res 161, (2004) p. 540–548.
[2] C. Hartel et al. Radiother Oncol (2010) *in press*.
[3] M. Durante et al. Cytogenet Genome Res 104 (2004) p. 240–244.
[4] N. Rithidech et al. Radiat Environ Biophys 46 (2007) p. 137–145.
[5] M.P. Hande, et al. Genes, Chromosomes & Cancer 44 (2005) p. 1–9.

* Work supported by Federal Ministry of Education and Research (BMBF, Bonn, Germany) under contract number 02S8203 and 02S8497.

First experiments on chromosome aberrations in mouse bone marrow cells irradiated in vivo

E. Nasonova [1,2], Ts. Chikhladze [2], M. Durante[1], R. Lee[1], and S. Ritter[1]
[1]GSI, Darmstadt, Germany; [2]JINR, Dubna, Russia

The analysis of chromosome aberrations in peripheral blood lymphocytes (PBL) of individuals exposed accidentally or occupationally to ionizing radiation is a frequently applied technique to assess the absorbed dose [1]. Based on the measured aberration yields risk estimates are derived, in particular for late effects such as carcinogenesis. PBL represent mature cells which are permanently committed to their fate. However, for a precise risk estimate, also the amount of damage produced in their ancestors, the haematopoietic stem cells, should be known. Radiation damage to haematopoietic stem cells might lead to a depressed immune system, a complete failure of haematopoiesis or the development of haematologic malignancies.

To contribute to this issue we recently compared several techniques for the isolation of haematopoietic stem cells from the bone marrow (BMC) of mice with respect to the yield and the quality of the obtained metaphase spreads. The protocols for BMC preparation differ significantly. However, because in the bone marrow the percentage of mitotic cells is small, their fraction is generally increased by the administration of a metaphase arresting agent (e.g. colcemid or colchicine). The direct method relies on the intra-peritoneal injection of colchicine or colcemid solution. After about 1 to 6 hours BMC are flushed from the femur and tibia. Immediately thereafter chromosome spreads are prepared [e.g. 2, 3]. Alternatively, BMC are harvested and cultured *in vitro* for 1-7 days. Then, metaphases are accumulated by mitotic inhibitors [e.g. 4, 5].

In our hands best results have been obtained with cultured preparations. However, to avoid that any cell selection occurs during *in vitro* cultivation, we reduced the time in culture to 2 hours. In brief, commonly used laboratory mouse strains CBA and C57BL/6 were used for the test. Male adults were sacrificed by cervical dislocation. Both femurs were dissected and BMBC were flushed out with culture medium (5 ml of RPMI 1640 supplemented by 20 % FCS and 0.1 mg/ml colcemid) using a syringe with a 23 g needle. Cells were collected into a conical tube and incubated 2 h at 37 °C in medium with colcemid. Following hypertonic treatment (0.075 M KCl, 15-20 min at 37 °C), cells were fixed with methanol:acetic acid (3:1). Subsequently, cells were washed twice with fresh fixative and dropped onto wet slides. As shown in figures 1 and 2 the modified protocol resulted in well spread metaphases that can be analysed following solid staining (Figure 1) or by applying advanced molecular cytogenetic staining techniques such as mFISH (Figure 2).

In future studies, this technique will be applied to measure the yield and the quality of chromosome aberrations induced in BMC by charged particles used in radiotherapy or encountered by astronauts during space missions.

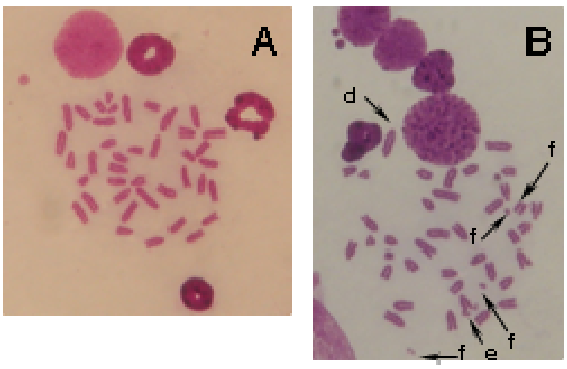

Figure 1: Giemsa-stained bone marrow metaphases of male mice (strain C57BL/6). Cells were cultured for 2 h *in vitro* before chromosome spreads were prepared: (A) a normal metaphase with 40 chromosomes, (B) damaged cell found 24 h after whole-body exposure to 1 Gy γ-rays. The observed aberrations (chromosome fragments (f), chromatid exchanges (e) and dicentric chromosome (d)) are indicated by arrows.

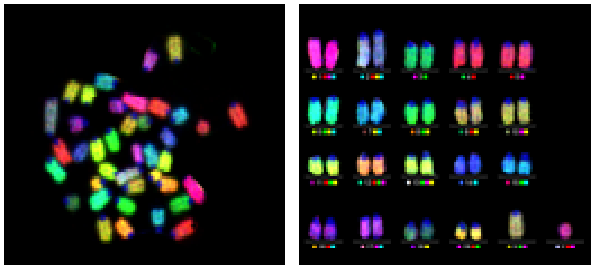

Figure 2: BMC of a male, unexposed mouse stained with the mFISH technique. Left: metaphase spread, right: corresponding karyotype. Hybridisation was performed with mouse mFISH probes (21XMouse, MetaSystems, Germany) according to the manufacturer's protocol. No rearrangements were found in 50 analyzed metaphases.

References

[1] IAEA. Tech. Rep. 405 (2001).
[2] Xiao Y. et al., Int.J.Radiat.Biol., 75: 1119-1128 (1999).
[3]. Peng Y. et al., Radiat.Res., 171: 474-483 (2009).
[4]. Lee J. et al., Anal. Biochem. 189, l-17 (1990).
[5] Rithideck et al., Rad.Env.Biophys. 46,137-145 (2007).

Investigation of Genomic Instability in Clonal Descendants after X-ray Irradiation

S. Zahnreich[1], M. Durante[1,3], C. Fournier[1], L. Melnikova[2], E. Nasonova[2], S. Ritter[1]
[1]GSI Helmholtzzentrum, Darmstadt, Germany, [2] JINR Dubna, Russia, [3]TU Darmstadt, Germany

Introduction

Exposure of normal human fibroblasts to ionizing radiation may cause a delayed instability of the genome in the descendants of the initially irradiated cells [1, 2]. This genomic instability appears as a *de novo* formation of structural chromosomal aberrations and is considered as a step towards malignant transformation and induced carcinogenesis [3]. The relevance of effects, related to genomic instability, observed in different experimental setups, cell strains and the dependence on radiation quality are still under debate [4]. In recent (or previous) experiments we have shown the occurrence of genomic instability in the progeny of mixed cell populations of fibroblasts initially irradiated with high doses of X-rays [2]. To circumvent a selective pressure and population dynamics on the yield and types of chromosomal aberrations in bulk cultures and to investigate the fate of single cells, colonies formed by single cells after irradiation with X-rays were isolated and analysed for cytogenetic changes in the present study.

Materials and Methods

Density inhibited monolayers of AG1522D fibroblasts were exposed to a single dose of 2 Gy or a fractionated daily dose of 8x2 Gy X-rays (250 kV, 16 mA). At 24 hours after irradiation the cells were seeded at a very low density to obtain colonies from single surviving cells. After isolation of the colonies, the populations were expanded. Structural chromosomal aberrations were scored regularly using solid Giemsa staining and the mFISH-technique, when cells were in close proximity to the end of their replicative life span. Transmissible chromosomal aberrations were termed "clonal" if they were present in at least two metaphases at the same time point of analysis.

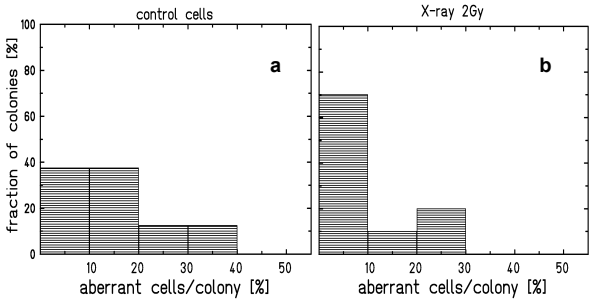

Figure1: Fractions of colonies from Giemsa analysis grouped in proportions of aberrant cells detected per colony scored in (a) 8 non-irradiated control colonies and (b) 10 colonies formed by cells initially irradiated with 2Gy X-rays.

* Work supported by BMBF (Bonn), grant 02S8497

Results and Conclusion

In single cell derived control populations a mean frequency of 14 ± 10 % (mean±SD) aberrant metaphases, were measured. As depicted in figure 1a, most colonies showed mild levels of instability with up to 20% aberrant metaphases while a few colonies had elevated levels up to 40% aberrant metaphases. After irradiation with 2 Gy X-rays, the mean level of aberrant metaphases was not elevated compared to control cells (11 ± 7%, SD). A high fraction of colonies (70%) showed levels below 10% aberrant cells (fig.1b). Irradiation of cells with a high dose of 8x2Gy X-rays, given in daily fractions, resulted in a similar response (mean 11% ± 8, SD, data not shown). The main types of structural chromosomal changes were dicentric chromosomes without acentric fragments as a result of telomeric fusions and chromosome and chromatid breaks. At the time point of analysis all populations were in close proximity to the end of their replicative life span, as assessed from counting population doublings. Preliminary results of mFISH analysis showed a dose dependent increase of radiation induced transmissible clonal aberrations (fig.2), but spontaneous, clonally expanding transmissible aberrations were also present in control as well as irradiated populations.

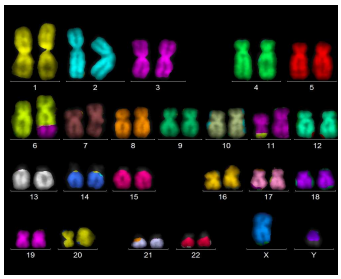

Figure2: mFISH stained karyotype of a single cell derived population initially irradiated with 2Gy X-rays showing the clonal translocation (6'-11) (11'-6) in 100% of the analyzed metaphases.

Conclusion

So far, in contrast to our previous results obtained for mixed populations [2], we could not detect any influence of X-ray exposure on genomic stability in the clonal descendants of irradiated cells. The frequency of chromosomal instability and the observed aberration types were not different comparing controls and the progeny of irradiated cells. Thus, in the absence of a selective pressure of the bulk population, the observed overall mild increase in the proportion of aberrant cells is related to *in-vitro* aging of the cells. In further experiments the effects of high LET exposure on genomic stability will be investigated in clonal descendants of irradiated cells.

References

[1] Kadhim M.A. *et al.*, Int. J. Radiat. Biol. 73, 1998, 143 -148
[2] Fournier C. *et al.*, Radiotherapy and Oncology 83, 2007, 277-282
[3] Hendry J.H., Radiotherapy and Oncology 59, 2001, 117-126
[4] Smith L.E. *et al.*, Health Phys 85, 2004, 23-29

Molecular RBE for thyroid cancer

D. Pignalosa[1], S. Ritter[2], and M. Durante[2,3]
[1]Federico II University, Naples, Italy; [2]GSI, Darmstadt, Germany; [3]TUD, Darmstadt, Germany.

Introduction

Cancer risk following exposure to energetic heavy ions is a major issue for space exploration and cancer ion beam therapy (1). However, no epidemiological data for exposure to heavy ions are available. Papillary thyroid carcinoma (PTC) is a known radiation-induced tumour. Several molecular studies have been performed to investigate genes involved in PTC occurrence. Rearrangements in human chromosome 10 and in particular intrachromosomal exchanges are recognized anomalies associated with PTC formation (2). Assuming that this type of aberrations is a biomarker of PTC risk, we aimed to estimate the relative biological effectiveness (RBE) of heavy ions using a molecular marker in vitro. We measured intrachanges in human thyroid follicular cells exposed to sparsely- or densely-ionizing radiation. The analysis of chromosomal aberrations was performed with the mBAND technique, which allows detection of both inter- and intra-chromosomal exchanges.

Materials and methods

We choose an immortalized thyroid cell line for the experiments. Cells were exposed to 2 Gy of X-rays and Fe-ions (1 GeV/n, LET = 150 keV/µm) at Brookhaven National Laboratory, and to 5.5 Gy of Ni-ions (6 MeV/n, LET = 3480 keV/µm) at the UNILAC. After irradiation, cells were trypsinized and re-seed in T75 culture flasks for the harvest procedure using the PCC (premature chromosome condensation) method. Chromosome preparations were hybridized using the mBAND kit for chromosome 10 and images were captured using an Olympus microscope equipped with UV lamp and appropriate filter sets. Processing and image analysis was performed with the ISIS software (MetaSystems). Chromosome analysis was performed with the ISIS software, and irradiated samples were normalized with data from the control. Aberrations were pooled in the following classes: simple exchanges, complex exchanges, fragments and intrachanges.

Results and discussions

More than 500 spreads were analyzed in irradiated and control samples. The highest frequency of aberrant cells (0.37±0.04) was observed in X-rays exposed samples. After Fe-ion and Ni-ion exposure the frequencies were 0.26±0.04 and 0.18±0.03, respectively. The target size in our experiments is smaller than the nucleus, because the DNA hybridized with mBAND for chromosome 10 accounts only for the 5% of the total genome. Considering the actual target size, at 2 Gy about 50% of the cells experience a direct Fe-ion traversal through chromosome 10, which may explain the lower aberration frequency compared to X-rays. For Ni-ions exposure the number of mean ion traversal is even lower. Concerning the spectrum of chromosomal aberrations, the low LET sample shows the highest frequency of simple interchange aberrations (0.29±0.04). Complex interchanges dominate after Fe-ion exposure, as expected for high-LET radiation. Intrachanges are always lower than interchanges, and differences among high- and low-LET radiation are not statistically significant (Fisher's exact test, $p > 0.14$). In Fig. 1 we reported the fraction of total aberrations. The intrachange class includes simple and complex intrachanges. Differences among different radiations are not statistically significant (as confirmed by Fisher´s exact test).

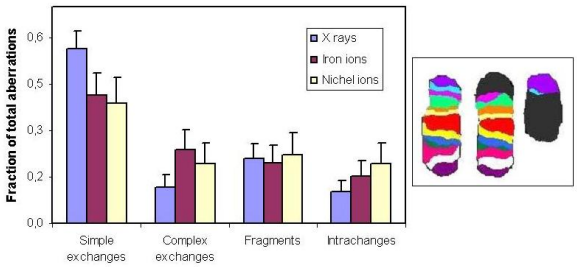

Figure 1: (Left) Fraction of total aberrations in HTori-3 cells exposed to low and high LET radiation. (Right) Normal chromosome 10 (a) and reciprocal translocation between chromosome 10 and an unstained chromosome (b,c)

Conclusions

We found no evidence that after heavy ion exposure the yield of inversions in chromosome 10 from human thyroid cells is statistically higher than after low LET exposure. Assuming that inversions in chromosome 10 represent a biomarker of PTC risk, we used this molecular endpoint to estimate the RBE of heavy ions. Based on the data presented here, we conclude that heavy ions are not necessarily more effective than X-rays in the induction of thyroid cancer through this mechanism.

References

[1] M. Durante and J.S. Loeffler. *Nat. Rev. Clin. Oncol.* 7, 35-43 (2010).

[2] A.Fusco, M.Grieco, M.Santoro, M.T.Berlingieri, S.Pilotti, M.A.Pierotti, P.G.Della and G.Vecchio. *Nature.* 328, 170-172 (1987).

The research was partly supported by Federal Ministry of Education and Research (BMBF) Bonn, Germany, under contract number 02S8497

The influence of nuclear geometry on the formation of chromosomal aberrations

D. Pignalosa[1], S. Ritter[2], and M. Durante[2,3]
[1]Federico II University, Naples, Italy; [2]GSI, Darmstadt, Germany; [3]TUD, Darmstadt, Germany.

Introduction

Interphase chromosomes are divided into discrete domains, with limited movement (1). Proximity of genes in the interphase nuclei is an important factor in determining chromosomal aberration yields and complexity. The topology effect should be evident for densely ionizing radiation, which produce DNA lesions localized along the linear tracks of the charged particles. For radiation protection, health risks derived from exposure to charged particles are related to the equivalent dose without any consideration of the geometry. We explored the role of nuclear topology in the formation of chromosome aberrations irradiating normal human fibroblasts with high-energy heavy ions from different directions. Cells with elliptical nuclei were grown in an aligned manner onto micrometer grooved culturing substrates to have a predetermined orientation with respect to the accelerated iron ions.

Materials and methods

Human fibroblasts were seeded in grooved substrates (2) and grown at 37°C for 1 week. Cell alignment and estimates of cell dimensions were obtained through Atomic Force Microscopy. Irradiation with Fe-ions (1 GeV/n), was performed in 3 different configurations: along the minor axis, the major axis or perpendicularly to the growth surface (b, c and d in Fig.1 respectively). Exposure was done in order to obtain isodose (1 Gy) or isofluence (1 particle per nucleus) samples.

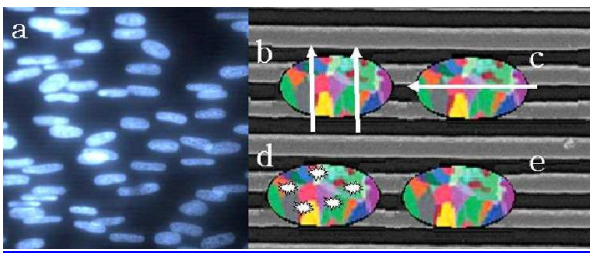

Fig. 1: (a) Cells in grooved substrates observed after Hoechst staining. (b-e) Diagrams representing irradiation set-up: through the minor (b) and long axis (c) and perpendicular to the growth surface (d). Unexposed cells (e).

After the exposure, cells were kept 24 h in an incubator and then reseeded in T75 culture flasks for chromosome harvest. At 24 h after reseeding chromosomes were prematurely condensation method (PCC). Chromosomes were stained with mFISH kit (Metasystems), and images were captured with a fluorescence microscope (Zeiss, Image Z1). Aberration analysis was performed with ISIS software.

Results and discussions

Fig. 2 shows the fraction of aberrant cells in the different configurations (see legend in Fig.1 for explanations). In the isodose condition, the short axis (b) presents approximately twice the fraction of aberrant cells than in the sample exposed through the long axis (c), and in (d) twice than in (b). This is a consequence of the statistics of particle traversal: according to Poisson statistics, approximately 37% of the cells in configuration (c) are not directly traversed by an iron ion at 1 Gy, while 0.5% only are non-hit in the configuration (d) at the same dose. In the isofluence condition, the values are approximately equal, with 20% of the fibroblasts carry visible chromosomal aberrations, independently on their geometrical configuration, and despite the difference in energy deposited in the whole nucleus.

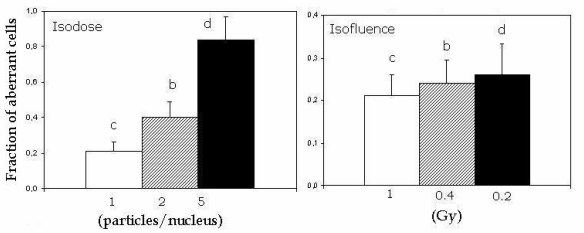

Figure 2: Fraction of aberrant cells in the isodose (left) and isofluence (right) conditions.

Conclusions

Analysis of chromosome aberrations shows that at the same radiation dose, the yield of chromosomal damage depends on the irradiation geometry and by cell nucleus architecture. The dose alone is not a good parameter to predict the genetic damage in human cells when different geometries and densely ionizing charged particles are involved. Under this condition, not only the dose but also the fluence should be taken in account.

References

[1] B. Jakob, J. Splinter, M. Durante, G. Taucher-Scholz, *Proc. Natl. Acad. Sci. USA* **106**, 3172-3177 (2009).

[2] F X.F. Walboomers, H.J. Croes, L.A. Ginsel, J.A. Jansen, *Biomaterials* **19**, 1861–1868 (1998).

The research was partly supported by Federal Ministry of Education and Research (BMBF) Bonn, Germany, under contract number 02S8497

Monte Carlo simulations of the time-course of aberrations and their distribution. Impact of LET and track structure*

J. Deperas-Standylo† [1,2], R. Lee[3], E. Nasonova[2,3], S. Ritter[3], E. Gudowska-Nowak[1], and M. Durante[3]

[1]Jagellonian University, Krakow, Poland; [2]JINR, Dubna, Russia; [3]GSI, Darmstadt, Germany

The biological effects of radiation generally originate from electronic collisions and ionizations in irradiated material. In the case of X-rays the energy is deposited uniformly within the cell nucleus and produces damage in a purely stochastic manner. In contrast, for particles the energy is deposited inhomogeneously along the trajectory of an ion penetrating the matter and the local dose decays with the square radial distance from the center of the track. This nonuniform energy distribution affects the yield and the distribution of aberrations among cells. In our recent studies [1] we presented a detailed analysis of the distribution of aberrations in human lymphocytes reaching mitosis at early or later times after low and high LET exposure. Aberration data were fit to stochastic distributions demonstrating that the observed delay is related to the number of particle traversals per cell nucleus [2]. To further examine how irradiated cells differ in their capability to divide, fluxes of aberrant and non-aberrant cells have been analyzed in the growing population with respect to an initial number of cells. To elucidate the relationship between the number of aberrations carried by a cell and the cell cycle progression delay, we have designed a Monte Carlo model (MC) which incorporates the number of particle hits per nucleus and simulates the progression of hit and non-hit cells through mitosis. The analysis of biological data and the results of numerical simulations clearly show the impact of the track structure on the formation of chromosome aberrations and their distribution among cells (see Fig.1, 2). The results reflect very well the influence of the aberration burden on cell cycle delay after exposure to charged particles and the dependence on the track structure (see Fig.2).

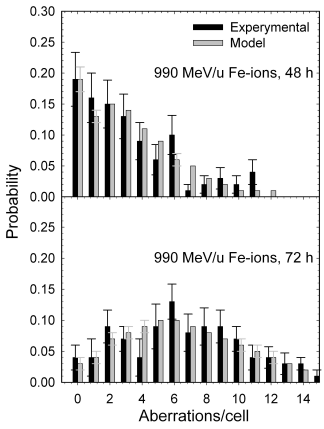

Figure 1: MC data compared to experimental data measured in human lymphocytes 48h and 72h after exposure to 2.3 Gy of 990MeV/u Fe-ions.

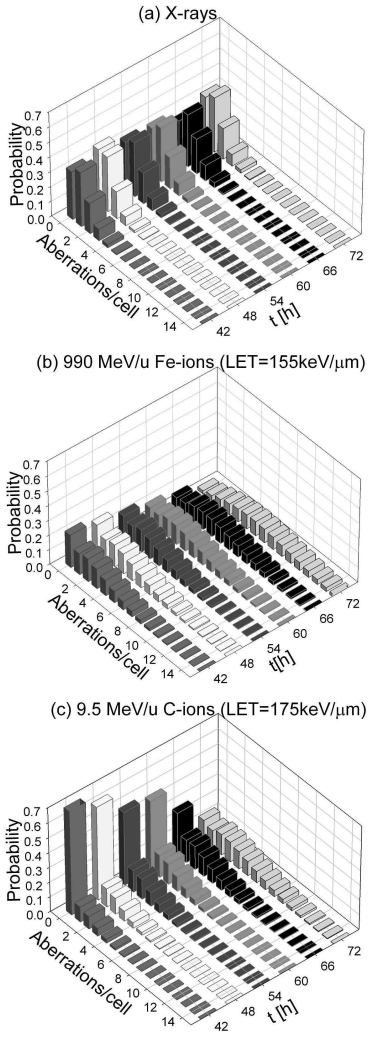

Figure 2: MC assay performed by 100 independent simulations for 100 cells (a) 2 Gy of X-rays, (b) 2.3 Gy of 990MeV/u Fe-ions and (c) 2 Gy of 9.5MeV/u C-ions.

*Project operated within the Foundation for Polish Science International Ph.D. Projects Programme co-financed by the European Regional Development Fund covering, under the agreement No. MPD/2009/6, the Jagiellonian University International Ph.D. Studies in Physics of Complex Systems. E.N. and R.L. were funded by the German Federal Ministry of Education and Research (BMBF), Bonn, under contract No. 02S8497

† joannadeperas@wp.pl

References

[1] J. Deperas-Standylo et al., Eur. Phys. J. D (submitted)

[2] E. Gudowska-Nowak et al., Int. J. Radiat. Biol. 81 (2005) 23.

Changes in the activity of ion-channels upon exposure to heavy ions

Bastian Roth[1], Marco Durante[1,2], Claudia Fournier[2], Markus Löbrich[1], Gerhard Thiel[1]
[1]TU Darmstadt, Germany; [2]GSI, Darmstadt, Germany;

Introduction

Ion channels are playing key roles in many physiological mechanisms ranging from the regulation of heart beat to the activity of neurons. A number of recent studies have also underscored the importance of various ion channels in the regulation of the cell cycle. To further study the role of ion irradiation on ion channels in the context of cell cycle control we performed measurements of channel activity in mammalian cells before and soon after irradiation. This was enabled by a portable patch-clamp device, which can be easily set up close to the radiation source. As a radiation source we used X-rays, low and high energy iron ions.

Materials and Methods

A549 cells were routinely cultured in alpha minimum essential medium (alpha MEM) containing 10% fetal calf serum (FCS). All cells were incubated in 5% $C0_2$/95% air at 37°C. A549 cells were irradiated at the SIS (GSI) with 2 and 7,5 Gy Fe-Ions (Energy: 1 GeV/u; LET: 170 keV/µm) and at the UNILAC (GSI) with 2 Gy Fe-Ions (Energy: 9,8 MeV/u; LET: 3050 keV/µm). All cells were irradiated at room temperature and were then patched immediately to study the kinetics of K^+ channel activation. Whole-cell recording was performed as described by [1]. In these experiments, A549 cells were stimulated at increased voltage pulses ranging from -40 mV to +80 mV in 20 mV voltage steps and duration of 800 ms from a holding voltage of -80 mV, during which time the current response was recorded.

Results and Conclusion

The data show that irradiation with 1 Gy of X-ray causes a cell specific increase in K^+ conductance (not shown). In the epithelial lung cancer cell line A549 irradiation resulted already within 30 min after treatment in a significant and lasting increase in the conductance of two K^+ channels, an outward rectifying K^+ channel and an instantaneous activating K^+ channel. As a consequence of the increased conductance of the instantaneous channel, cells hyperpolarized up to 10 mV. Preliminary experiments suggest that this hyperpolarization might stimulate cell division. This hypothesis is based on the fact that the same inhibitor, tetraethyl ammonium chloride (TEA), which blocks the irradiation sensitive K^+ channels, also reduces division of A549 cells. The same two K^+ channels which were activated by X-ray exposure were also augmented in response to heavy ion irradiation. The traces in Fig. 1a show the typical current response of a A549 cell under control conditions to a standard voltage protocol with test pulses between -40 mV and 80 mV. The total current response can be divided into two components, an instantaneous and a slow activating component; both kinetic components represent the activity of two distinct types of K^+ channels. Irradiation of the cells with 2 Gy or 7,5 Gy (Fig. 1c, d, e) from the SIS source results consistently in an increase in both currents.

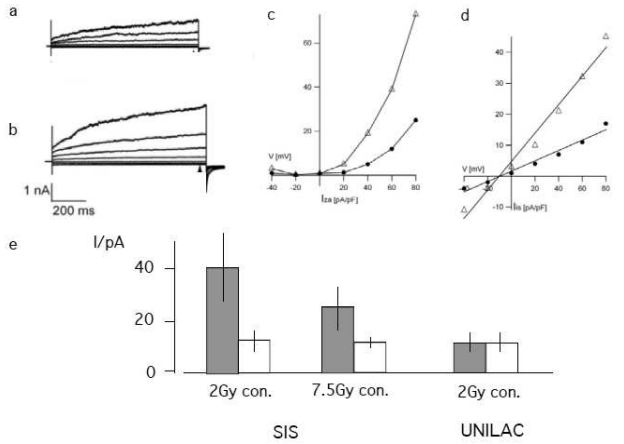

Figure 1: *Exemplary current-responses of A549 cells before (a) and after (b) irradiation with 2 Gy Fe-Ions at SIS. Currents were recorded in whole cell mode using the port-a-patch equipment. Mean current-response of time dependent K^+ current (c), and instantaneous K^+ current (d) before (solid symbols) and after (open symbols) irradiation with 2 Gy Fe-Ions. (e) Mean steady state currents (collected at the end of test pulse) for control cells (open bars) and cells exposed to 2 Gy or 7,5 Gy Fe-Ions at SIS or UNILAC.*

Similar experiments were also performed with the UNILAC as a radiation source. In this case, no stimulation of the channel activity was observed in contrast to high energy ions (Fig 1e). We speculate that the reason for the difference in response could be related to a reduced amount of reactive oxygen species accumulation after irradiation with the low-energy high-LET irradiation. This interpretation is supported by the fact that our data provide evidence for an intermediate role of radicals between radiation damage and channel activity (not shown). We found that the same increase in channel activity, which occurred after irradiation was also detectable in response to the addition of 1 mM hydrogen-peroxide to the incubation buffer of A549 cells (not shown).

References

[1] Fertig et. al., Biophyscial Journal 2002, 82

Clonal aberrations in hematopoietic stem and progenitor cells after irradiation with X-rays and high energetic carbon ions

D. Becker[1,3], L. Bauer[1,4], M. Durante[1], C. Fournier[1], S. Ritter[1], R. Marschalek[2], T. Tonn[3]
[1]GSI, Darmstadt, Germany; [2] Faculty of Pharmacology, Johann Wolfgang von Goethe University, Frankfurt, Germany; [3]Institute for Transfusion Medicine and Immunohaematology, Frankfurt, Germany; [4]University of Technology, Darmstadt, Germany

The increasing application of heavy ions in radiotherapy and the growing interest in protracted space travels are a strong motivation to expand the fundamental research in radiation biology. With respect to long term effects in different cell systems, in the majority of studies the occurrence of chromosomal aberrations is assessed, but only in lymphocytes. However, the investigation using hematopoietic stem and progenitor cells (HSPC) which are responsible for the permanent renewal of all blood cells, seem to be more appropriate. For this reason we are interested, if the irradiation of HSPC with X-rays or carbon ions has different effects on the occurrence of chromosomal aberrations and the clonal transmission to subsequent generations. As observed in lymphocytes, both radiation qualities induce distinct types of damage in affected cells [1]. Thus the complexity of DNA damages varies highly, whereas carbon ions should produce more complex chromosomal aberrations than X-rays.

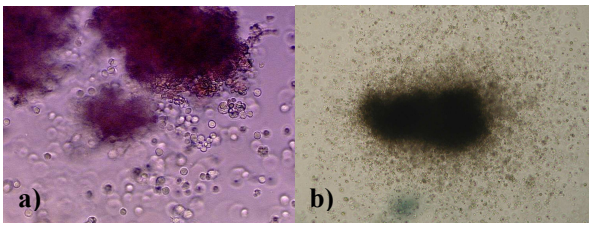

figure 1: morphology of colony forming cells (a) granulocyte-erythroid-monocyte-megakaryocyte progenitor cells (GEMM) (b) granulocyte-monocyte progenitor cells (GM).

HSPC were isolated from the peripheral blood of healthy donors as described elsewhere [2]. Briefly, low density mononuclear cells were enriched by Ficoll gradient. In a magnetic separation step the cells were stained with a CD34+ antibody, coupled with magnetic beads (QBEND/10, mouse IgG1, CD34 MicroBead Kit, Miltenyi Biotech). The labelled cells were positively enriched to purities of > 90 % using magnetic columns. The cells were irradiated with X-rays [16 mA, 250 kV] or with carbon ions [100 MeV/u, 29 keV/µm] at the SIS facility at GSI. To promote proliferation and differentiation of HSPC into colonies of different hematopoietic lineages (examples in figure 1), cells were cultured in semisolid methylcellulose supplemented with cytokines (Methocult GF H4434, StemCell Technologies, Vancouver), the so called colony-forming-unit-assay. At appropriate time points colonies were isolated after colcemid treatment and metaphase spreads were prepared according to standard techniques [3]. Selected samples were analyzed by 24-colour fluorescence in situ hybridisation (24XCyte mFISH kit, Metasystems, Altlussheim) to achieve a distinctive colour signature for each chromosome.

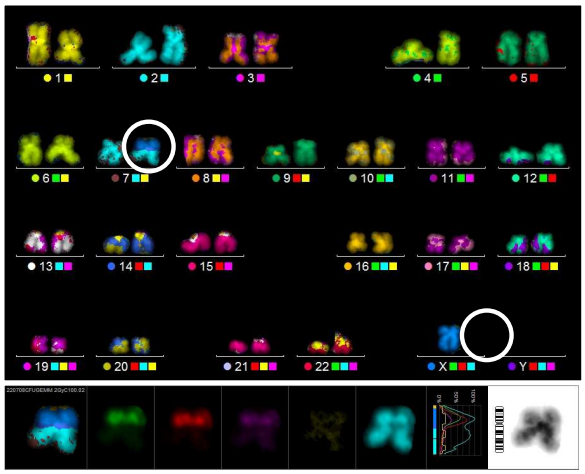

figure 2: mFISH analysis of a GEMM colony exposed to 2 Gy of carbon ions [29 keV/µm]. Clonal aberrations: 45 (del X', 7') + 7'-X in 43 metaphases analyzed.

In a first experiment, we analyzed colonies of different origin after irradiation with X-rays or carbon ions. In figure 2 the chromosomal pattern of an isolated GEMM colony shows a translocation between chromosomes 7 and X and loss of the respective fragments in all 43 analyzed metaphases. The yield of chromosomal damage was not different comparing HSPC after irradiation with X-rays and carbon ions. Both types of radiation predominantly induced reciprocal translocations, detected in 2/3 of all surviving colonies, whereas in 1/3 of the surviving colonies no aberrations were observed. Remarkably, in all these clones the chromosomal aberrations were transmitted clonally to the progeny of the irradiated cells.

Taken together, both radiation qualities induce a comparable pattern of chromosomal aberrations in the progeny of the irradiated cells. This observation will be confirmed in further experiments. In addition, in view of the high frequency of clonal aberrations in HSPC, the capacity and fidelity of the repair of radiation induced damage in HSPC will be compared to lymphocytes [supported by GSI, no. 178].

References

[1] Nasonova and Ritter (2004), Cytogenet Genome Res 104:216-220
[2] Becker et al (2009), Int J Radiat Biol, Vol. 85, No. 11:1051-1059
[3] IAEA (2001), Technical Reports, Series No. 405

Effects of heavy ionizing radiation on development and degeneration of Vertebrate photoreceptors and their protection by cytokines, as analysed in 3-dimensional cell culture models

Florian Frohns[1], Marco Durante[1,2], Claudia Fournier[2], Paul G. Layer[1]
[1] Technische Universität Darmstadt, Germany; [2] GSI, Darmstadt, Germany

Introduction

A major problem for the planning of long-term space flights are deleterious effects of heavy ion radiation (HIR) on the eye sight of astronauts (light flashes), eventually leading to loss of their photoreceptor cells [1]. Until now, the influence of ionizing radiation (IR) on the development and the survival of photoreceptors and other retinal cell types is only poorly understood. Therefore, mimicking formation of a 3D-retinal tissue, histotypic reaggregates (retinal spheroids) were used as an in vitro model for the investigation of retinal development after IR. In this ongoing work we intend to investigate the responsiveness of different retinal cell types to IR and also their capacity to form histotypical structures following IR treatment.

Materials and Methods

We investigated the effects of IR on the development of retinal spheroids raised from chick embryos, focussing on apoptosis of different cell types and the development of histotypic structures after IR.
Therefore retinae from six day old chick embryos were isolated and dissociated. Cell suspensions were cultivated on a rotation shaker to achieve sphere formation. Irradiation was performed after five days *in vitro*. After irradiation, the sphere development was documented by light microscopy for statistical analysis of sphere morphology. Differentiation of various cell types and the appearance of histotypical structures in spheres were examined by immunostaining of cryosections. Thereby, antibodies against photoreceptors (PR) as well as retinal glia cells (Müller glia) and a population of retinal interneurons were used. Analysis of the apoptosis rate in spheres was done by Chromatin staining with DAPI. Pyknotic nuclei of apoptotic cells were identified by their bright fluorescence due to their high chromatin condensation [2].

Results and Conclusion

Preliminary results of irradiation experiments showed a higher rate of cell mortality in spheres with increasing doses of IR, as it can be seen by analysis of whole-spheres and sphere cryosections.
Increasing doses of IR are accompanied with a darker appearance of the spheres, perceptible 24 hours after the treatment. This was quantified by measurements of the mean grey value of spheres (Fig 1 A). The darker appearance is due to a higher amount of pyknotic cell nuclei inside of the irradiated spheres (Fig. 1B, C). Although the identity of these pyknotic cells is still unknown, only a small number of PR progenitors belong to the population of these cells (Fig. 1). Accordingly, the differentiation of these cells is not affected, as it could be seen by immunostaining of markers expressed in mature PRs at 72 hours after irradiation (Fig.2).

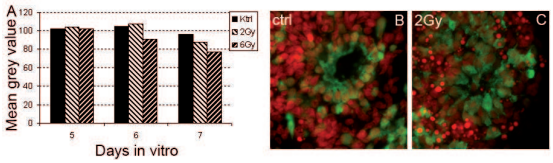

Figure 1: *Analysis of the influence of IR on retinal spheroid development. Measurements of the mean grey value of five day old spheres before and after irradiation with X-ray (90kV, 33,7 mA) show a darker appearance of spheres (A) due to a higher number of pyknotic nuclei with a bright red fluorescence in treated (C) than in control samples (B). Notice that only few PRs (green) belong to the pyknotic cell population.*

Despite of the high amount of pyknotic cells which are undergoing apoptosis due to irradiation, treated spheres show no obvious differences in their inner organization level. Even after the highest IR doses, histotypical structures like IPL-like areas could be observed. The latter ones still featured a complex wiring of processes from Müller glia (Fig. 2) and interneurons (not shown).

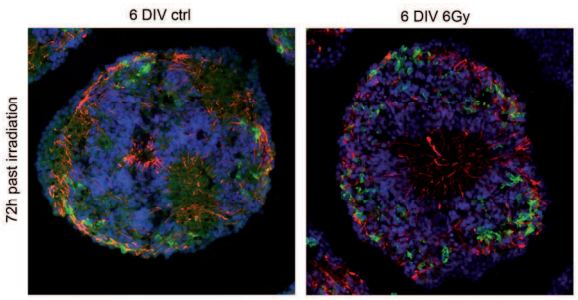

Figure 2: *Analysis of the influence of IR on PR differentiation and the Müller glia scaffold in retinal spheroids. Staining of nuclei (blue), PR rhodopsin (green) and Müller glia vimentin (red) show no differences in controls (A) and spheres treated with 6 Gy X-Ray (90kV, 33,7 mA) (B) 72 hours past irradiation.*

In further experiments we will analyse in more detail the identity of cells which are dying as a consequence of radiation exposure.

References

[1] W.G.Sannita et al., Vision Res, **46**, 2159-2165
[2] C. Dive et al., Biochim Biophys Acta, **1133**, 275-285.

Functional analysis of the angiogenic potential of A549 cells after carbon-ion and photon irradiation

F. Kamlah[1], A. Arenz[1], B. Bischoff[1], R. Engenhart-Cabillic[1], C. Fournier[2], J. Hänze[3], D. Hasan[3], J. Juricko[1], F. Rose[1], M. Scholz[2], U. Seay[3], and G. Taucher-Scholz[2]

[1]Dept. of Radiotherapy and Radiooncology, University of Marburg, Germany; [2]GSI, Darmstadt, Germany; [3]Department of Internal Medicine II/V, University of Gießen, Germany

Radiation therapy is an integral part of the multi disciplinary therapy of lung cancer. Genetic changes and the hypoxic tumor microenvironment favour therapy resistance of tumor cells. Clinical studies suggest that particle irradiation using carbon ions may improve the therapy response of solid tumors compared to photon radiation [1,2]. Occurrence of therapy resistance is related to the secretion of growth and angiogenic factors that stabilize the vasculature and induce tumor vascularization [3]. Here, we applied the matrigel plug assay to compare the effects of biologically equivalent irradiation doses of carbon ions (11.4 MeV/u) and photons (6 MV-X) on angiogenesis induced by A549 cells. For this purpose, carbon ion-, and photon-irradiated as well as untreated A549 cells were injected as a suspension with matrigel into nude mice, respectively. Ten days later, newly formed blood vessels in the matrigel plugs were analyzed by CD31 staining of endothelial cells. These *in vivo* experiments were maintained under pathogen-free conditions and handled in accordance with the European Communities recommendations for animal experiment-ation. We observed an increase in the vessel number in matrigel plugs of photon irradiated (6 Gy) cells when compared to the plugs of carbon ion irradiated (2 Gy) or control cells (Figure 1).

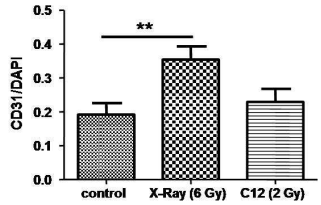

Figure 1. Matrigel plug assay: Irradiated cells were mixed with Matrigel and injected in nude mice subcutanouesly. 10 days after implantation, the plugs were analyzed by CD31 immunostaining. Data reflect the mean ± s.e.m. (n=5, * P<0.05, Mann-Withney-Test).

Realtime RT-PCR mRNA analysis of the differently treated A549 cells was performed in relation to porphobilinogen deaminase (PBGD) mRNA employed as a reference mRNA, that is constitutively expressed and not changed after irradiation. The effect of irradiation was confirmed by the induction of CDKN1A mRNA in A549 cells (4 h and 24 h) that is typically observed after both photon and carbon ion irradiation. Furthermore, we observed that the mRNA of the angiogenic stem cell factor (SCF) was upregulated twofold in A549 cells after photon irradiation but not after carbon ion irradiation or in control cells. Also, the protein level of SCF as measured by ELISA in the cell supernatent was upregulated (Figure 2 and 3). The expression levels of mRNAs are presented by the ΔΔCt values. ΔΔCt values=ΔCt control (unirradiated cells) - ΔCt of carbon ion or photon irradiated cells; ΔCt = Ct (mRNA of interest) – Ct (PBGD-mRNA). A difference of 1 corresponds approximately to a twofold increase of the mRNA.

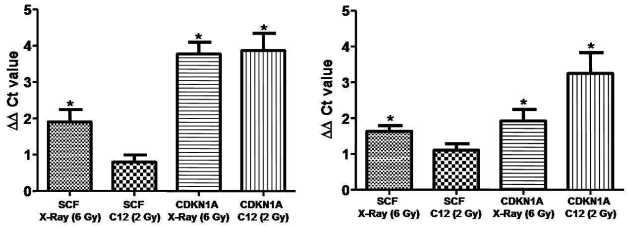

Figure 2. Realtime RT-PCR of SCF- and CDKN1A-mRNAs after carbon ion and photon irradiation (left [4 h]; right [24 h]). Data reflect the mean ± s.e.m. (n=3; *P<0.05, paired t-test).

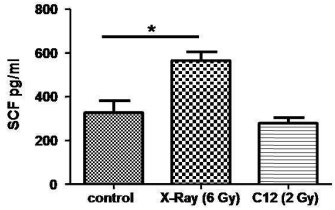

Figure 3. Quantitative measurement of SCF protein in the cell culture supernates of A549 cells (2% FCS) after irradiation. SCF is increased after photon irradiation, but not after C12 ion irradiation in A549 cell culture supernates. Data reflect the mean ± s.e.m. (n=3; *P<0.05, Mann-Withney-test).

In conclusion, our in vitro data demonstrate upregulation of the angiogenic factor SCF by photon but not by carbon ion irradiation this is accompanied by induction of angiogenesis as shown in the matrigel plug assay not observed with carbon ion irradiation.

In further experiments, the effects of irradiation on angiogenesis and on the expression of SCF will be characterized in a subcutaneous *in vivo* mouse tumor model. In addition, the angiogenic relevance of SCF employing a specific inhibitor of the SCF-receptor (C-Kit) will be tested.

References

[1] Schulz-Ertner, D. (2009) *Cancer J*, **15**, 306-311.
[2] Amirul Islam, M., Yanagi, T., Mizoe, J.E., Mizuno, H. and Tsujii, H. (2008) *Radiat Med*, **26**, 415-421.
[3] Dewhirst, M. W., Cao, Y., and Moeller, B. (2008) *Nat Rev Cancer* **8**, 425-437

Impact of the ectopic expression of telomerase on the radiosensitivity of human fibroblasts

T. Wetzel[1], P. Boukamp[2], M. Durante[1], C. Fournier[1], P. Hessel[1], W. Kraft-Weyrather[1], D. Krunic[2], J.Leykauf[2], S. Ritter[1]

[1]GSI, Darmstadt, Germany; [2]DKFZ, Heidelberg, Germany

Introduction:

Ectopic expression of telomerase can result in an immortal phenotype, suggesting a participation in the regulation of the activity of a variety of genes (cell growth, DNA repair, chromatin modification) in addition to its role in protecting chromosomal ends from degradation [1].

We set out to investigate the impact of the activity of telomerase on the radiosensitivity of human fibroblasts. Therefore, we used foreskin fibroblasts, wildtype (wt) and transfected with the catalytic subunit of human telomerase (hTERT). In a first step, we irradiated both cell strains with photons (x-ray) and performed a clonogenic survival assay. In addition, we assessed the length of the telomeres days after exposure. In a next step we want to investigate the long term genetic stability in the presence of telomerase.

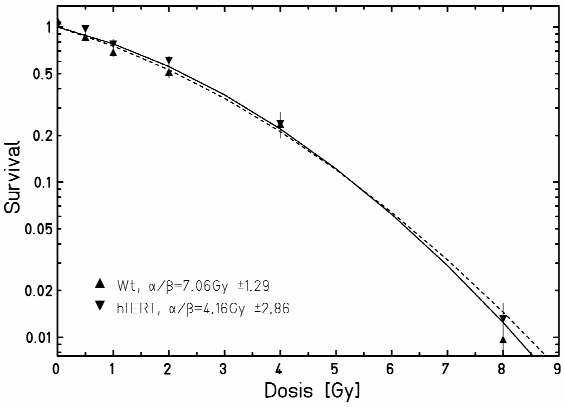

Figure 1: colony survival curve of VH7 Wt and –hTERT after irradiation with x-rays. Mean values of four experiments are shown.

Material and methods

Fibroblasts (VH7, wt and hTERT) were exposed to low and high doses (0,5 to 8 Gy) of x-rays. For comparison with previous experiments, we incubated the cells for one day after exposure before reseeding. To assess clonogenic survival, the cells were cultivated during 14 days, then they were stained and surviving colonies were counted. Four experiments for both wt and hTERT VH7 cells have been performed.

For the assessment of telomere length, fluorescence in situ hybridization, 3D image acquisition, deconvolution microscopy and image processing, as well as immunofluorescence staining for TRF2 protein were performed in 50 cells per sample as described elsewhere [2].

Results:

Comparing wt- and hTERT-transfected cells, no significant difference in the level of clonogenic survival can be seen in the measured dose range. The cell survival curves show the typical pattern for human fibroblasts after exposure to photons [3], characterized by a shoulder and an exponential decrease of the survival at higher doses. The parameters of clonogenic survival, α and β, are defined by the initial slope in the low dose range and by the increase of the slope at higher doses, respectively. A small ratio α/β is characteristic for relatively radioresistant cells. Respective ratios for wt and hTERT VH7 cells are similar (see fig. 1) and reveal a higher radiosensitivity as compared to other cell strains (data not shown). It is interesting to note that clonogenic survival is not influenced by telomerase. This is in agreement with published data for other cell strains [4].

Telomere length was investigated by measuring the telomere signal intensity (TSI) per nucleus that is proportional to the telomere length of a given cell. Telomerase is responsible for significantly elongated telomeres in VH7 hTERT cells compared to wt cells (not shown). X-rays induced slight telomere shortening in wt cells (figure 2A) and here the level of shortening correlated with the level of genomic instability (figure 2B, abnormal nuclei with micronuclei or chromatin bridges). This confirms previous results for a second cell strain. In VH7 hTERT cells we did neither detect obvious telomere shortening nor signs of genomic instability, arguing for hTERT overexpression to counteract the X-ray-damaging effect.

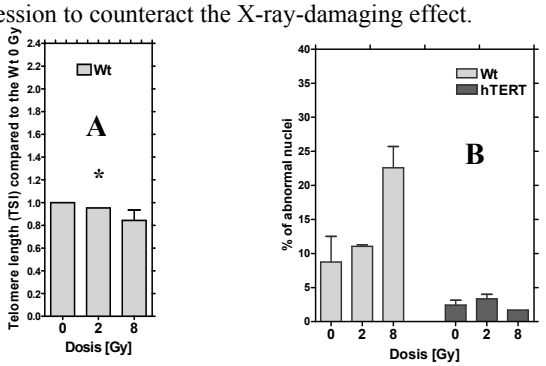

Figure 2: (A) Telomere length measurement in VH7 wt cells 72h after irradiation with x-rays. Mean values (± SEM; 4 samples) of two experiments are shown (* one exp.) (B) Percent of cells with signs of genomic instability (wt and hTERT).

References:

[1] Pirzio et al. (2004), Cytogenet Genome Res 104: 87-94
[2] Ermler et al. (2004), Eur. J.Cell Biol. 83: 681-690
[3] Fournier et al. (2001),Int. j. Radiat. Biol. 77/6: 713-722
[4] Kampinga et al. (2004), Int. J. Radiat. Biol. 80/5: 377-388

Influence of Particle Radiation on Cell Survival and Mitochondrial Function of Human Endothelial Cells

A. Helm[1,2], D. Pollet[2], M. Durante[1], D. Szypkowski[1], P. Hessel[1] and S. Ritter[1,#]
[1]GSI, Darmstadt, Germany; [2]Hochschule Darmstadt, Germany

Recent data indicate that there is an increased risk of cardiovascular disease among atomic bomb survivors and radiotherapy patients, typically developing with a long latency [1]. However, essentially no information is available on the potential cardiovascular risks (e.g. atherosclerosis, accelerated aging of blood vessels, cardiac arrhythmias) associated with space radiation, in particular heavy ions.

To address this issue, we have chosen human umbilical vein endothelial cells (HUVEC) as a model system. First we examined to what extent C-ions (9.8 MeV/u, LET: 170 keV/µm) or 250 kV X-rays affect the cell survival. Furthermore, the mitochondrial membrane potential ($\Delta\Psi_M$) was measured in long-term cultures. The $\Delta\Psi_M$ consists of a proton gradient used by the respiratory chain to generate the major amount of cellular energy. This endpoint was chosen because mitochondrial dysfunction and the resulting production of reactive oxygen species (ROS) are discussed as a main origin for cardiovascular diseases, in particular atherosclerosis [2]. To quantify the $\Delta\Psi_M$, cells were stained with the fluorescence dye JC-1 and analysed by flow cytometry. The monomeric form of JC-1 emits 528 nm (green) after excitation at 490 nm. Using protons of the $\Delta\Psi_M$ JC-1 dimerizes accompanied with a large shift in emission to 590 nm (red). Thus, cells containing mitochondria with intact $\Delta\Psi_M$ fluoresce predominantly red.

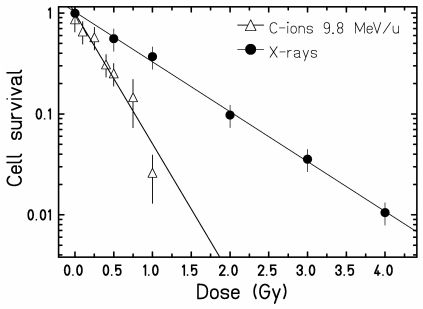

Fig. 1: Cell survival after exposure to C-ions or X-rays.

Measurement of the cell survival (colony forming assay) showed that C-ions are more effective than X-rays (Fig. 1) consistent with data reported for other cell types. To get information on mitochondrial function, the fraction of cells with prevalent red or green fluorescent mitochondria and the fraction of cells with both green and red fluorescent mitochondria were analysed up to 46 days post irradiation. Doses were chosen to assure long-term survival. As a positive control 2,4-dinitrophenol (DNP) was used because of its ability to uncouple the $\Delta\Psi_M$ as shown in Fig. 2.

After exposure to 0.75 and 1.5 Gy X-rays no differences in mitochondrial function between the irradiated samples and the negative control over the time were found (Fig. 3). Similarly, no differences were observed after exposure to 0.25 and 0.5 Gy C-ions (data not shown). In contrast, in several studies using tumour cells a degradation of $\Delta\Psi_M$ was induced by doses of about 10 Gy sparsely ionizing (e.g. [3]). As no effects could be found in the present study, the low doses used or the different cell type might be reasons. Further studies on $\Delta\Psi_M$ of HUVEC cells applying higher doses of both X-rays and heavy ions are in progress.

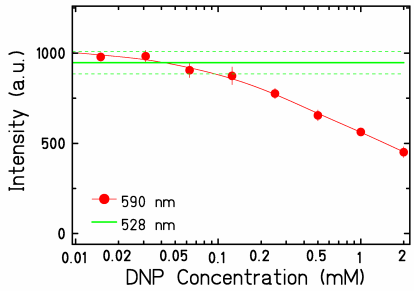

Fig. 2: Cellular response 10 minutes after treatment with DNP measured with a fluorescence reader. The monomeric fluorescence (528 nm) does not change as indicated by the mean value (solid line) and standard deviation (dotted line). With increasing DNP concentration the $\Delta\Psi_M$ collapses as seen in the decrease of the red fluorescence (590 nm).

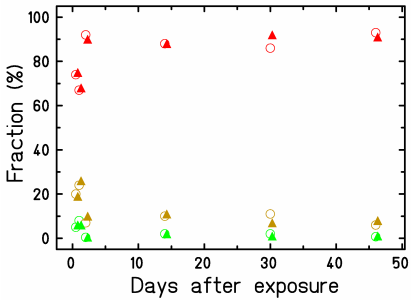

Fig. 3: Flow cytometric analysis of $\Delta\Psi_M$ after X-ray exposure (○: 0 Gy, ▲: 1.5 Gy). The fraction of cells with mainly red (red symbols), green (green symbols) or both fluorescent (yellow symbols) mitochondria are shown.

References

[1] Little et al., Radiat Res, 2008, 169(1), 99-109
[2] Di Lisa et al., Pharmacol Rep, 2009, 61, 123-130
[3] Wang et al., Clin Cancer Res, 2007, 13, 4891-4899
#s.ritter@gsi.de

Interplay of irradiation and age on the mitoproteome of human cell cultures

M. Frenzel[1], M. Durante[2], C. Fournier[2], S. Ritter[2] and N. A. Dencher[1]
[1]Technische Universität Darmstadt; [2]GSI, Darmstadt, Germany

Introduction:
According to the "free-radical theory of ageing" during ageing elevated levels of free radicals and reactive oxygen species (ROS) induce damages of lipids, proteins and nucleic acids in cells (1). Enhanced oxidative damage shortens lifespan (2). In mitochondria ~90% of the total cellular ROS is produced mostly by respiration. Respiratory chain dysfunction results in even higher ROS-levels (3). Therefore, mitochondria are the predominant source and the major target of ROS.
After exposure of human cell culture to X-rays or heavy ions the intracellular level of ROS is increasing rapidly within the first days after irradiation (4). Long-term studies analysing the ROS-level in the progeny of cells after X-ray exposure demonstrate that there is an age-dependent increase of ROS-level independent of irradiation (5). To reveal the effect of irradiation on mitochondria and their role in the ageing-process, several cell strains of different origin were irradiated (X-rays, carbon ions) and subcultured afterwards for ~230 days. Changes in the mitochondrial protein profile have been analysed.

Materials and Methods:
Confluent normal human dermal fibroblasts (NHDF), human foetal lung fibroblasts (WI38) and human dermal fibroblasts (AG1522D) were irradiated with X-rays (8 Gy) and AG1522D in a parallel experiment with carbon ions (100 MeV/u, Unilac). The cells were subcultured the first day after irradiation and thereafter every second week. At different time points mitochondria have been isolated, frozen in liquid nitrogen and stored at -80°C. Analysis of the mitochondrial proteome was performed using digitonin (8 g/g) for gentle solubilisation followed by two-dimensional blue-native/SDS gel electrophoresis (2D BN/SDS-PAGE). In the first dimension proteins, protein-complexes and -supercomplexes were separated in their native state according to their molecular mass using Coomassie Brilliant Blue G-250 dye (CBB). After denaturation the protein subunits are separated subsequently in the second dimension. Quantification of protein abundances occurred in the first as well as in the second dimension using colloidal CBB and fluorescent SYPRO Ruby dye, respectively.

Results and Conclusions:
Sample-analysis focused on two aims: (1) Age-related changes and (2) interplay of irradiation- and age-dependent changes on the mitochondrial proteome. The data discussed will be restricted to abundance changes of the ATP synthase, OxPhos supercomplexes ($I_1III_2IV_{0-3}$) and the heat shock protein (HSP)60.
(1) When comparing young and senescent non-irradiated cells, a decrease in the protein level of about 1.2 - 2-fold for the ATP synthase and about 2-fold for the OxPhos supercomplexes was observed. A lower level of OxPhos supercomplexes may cause a lower respiration rate. Due to its role as ATP generating enzyme, less ATP synthase may have an impact on the overall energy status of the cell. Therefore it is necessary to perform enzyme activity tests to verify the specific activities that could compensate the reduced amount of these enzymes. Similar results have been found in tissue (rat brain cortex), leading to the assumption of a general age-related mechanism (6).
The abundance of HSP60 transiently increased and thereafter decreased about 2-fold during senescence in non-irradiated cells (Fig. 1, blue). Besides its function as an important chaperone, mitochondrial HSP60 is a proapoptotic factor. A lower level of HSP60 may lead to an accumulation of misfolded and defect proteins in cells.

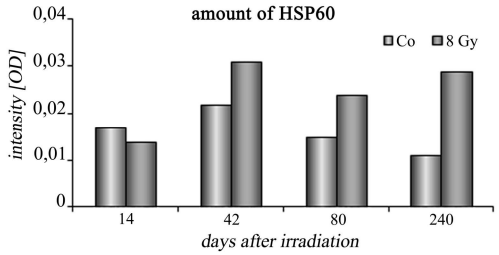

Fig. 1: Age-related (blue) and interplay of irradiation-(X-rays, 8 Gy) and age-dependent (red) changes in the abundance of HSP60 in NHDF cells.

(2) Irradiation-dependent changes of the mitochondrial proteome appeared delayed, e.g., as compared to damages in chromosomes. For the mitochondrial HSP60 app. 40-50 days after irradiation there was a 2-fold abundance increase, presumably due to its proapoptotic role. Afterwards the level remained quite constant until 230 days after irradiation (Fig. 1, red). In contrast to HSP60, no irradiation-related response was detected for the ATP synthase and the OxPhos supercomplexes in the first weeks after irradiation. Contrary to the observed age-related decline of the ATP synthase in non-irradiated cells, its protein-level remained constant after X-ray (8 Gy) irradiation until cells undergo senescence. After exposure to heavy ions, however, there was an age-related decrease comparable to controls, showing, that heavy ion irradiation is not affecting the ATP synthase abundance. For OxPhos supercomplexes in all progeny of irradiated cells (X-ray and heavy ions) the protein level was about 2-fold higher compared to controls in all cell cultures. No senescence-dependent decrease was observed.

References:
[1] D. Harman *et al.*, J. Geront, 1956, 298-300
[2] T. Eisenbach *et al.*, Nat. Cell. Biol., 2009, 1305-1314
[3] G. J. Kim *et al.*, Cancer Res., 2006, 10377-10383
[4] M. Colindres *et al.*, GSI-report 2007
[5] M. Frenzel *et al.*, GSI-report 2008
[6] M. Frenzel *et al.*, Exp. Geront., under revision, 2010

Therapeutical Radon exposure to the skin of patients*

S. Ktitareva, C. Fournier, G. Kraft, and W.K. Weyrather
GSI, Biophysics, Darmstadt, Germany

Clinical effects of radon

Radon is the oldest drug used by mankind. Ceremonial donations excavated at the hot radon springs in the Gastein valley, Austria, originate from the younger stone age. Today some 50 000 patients suffering from rheumatic deceases like ankylosing spondilytis are visiting the Radon therapy at Gastein, a few hundred thousands per year all over the world. Other radon therapies are located in Japan and at the uranium mining areas in Europe. Radon gas created in fission reactors is applied in Russia. A specific anti-inflamation effect is found lasting for a time period of 6-12 months that cannot be produced by sparsely ionizing radiation like beta or gamma emitters or direct x-ray exposure. These treatments work obviously via the action of the Alpha particles emitted by Radon and the daughter nuclei.

Radon application modes

In all cases, the patients are exposed to Radon either as pure gas or solved in water. Most popular with 20-30 000 patient per year is the exposure in the former gold mines at Bad Gastein. There the patients are exposed to the air having a radon concentration of 20-200 Bq/l at temperatures between 38-41°C for one hour.

Another radon gas exposure is the "Vapour Bath" (Dunstbad) at Bad Gastein[i] where the Radon gas collected at the hot water spring is transferred to small cabins that fit around the patients body and are heated to temperatures 31-40°C. The Radon leaves the patient cabin through the opening for the head so the patient is breathing an intense air/radon mixture of approx. 100 Bq/l depending on the radon production at the hot spring.

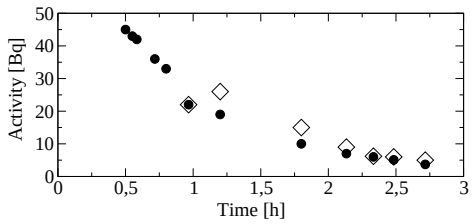

Figure 1: Alpha activity in arbitrary units measured at the skin of a patient at left • and right ◇ hand and at the forearm after radon exposure in a vapour bath.

Finally, Radon bathes of at least 400 litres are available in a standard procedure in many hotels which have a concentration of 1-3 kBq/l and at 37°C for 20 min[i]. Radon bathes are usually applied daily intermitting with one of the other applications during a treatment course of 6 days a week and at least two weeks [1].

Radon absorption

Although the very positive effects of radon are experienced by many patient over such a long time, the action mechanism is not know at all and topic of molecular biology research using other densely ionizing radiation [2]. But also the main pathway of radon uptake is still under discussion: the main target of the anti-inflammation effects is the backbone, but the location and the long duration cannot be directly or indirectly correlated to physical or biological parameters.

In order to obtain basic data we have accompanied the therapy applied to a patient by measuring the alpha activity at the skin[ii] starting immediately after the exposure until the counting rate became too low.

Measurements

All the three types of radon exposure were employed to measure the alpha activity at the skin of a patient (Fig. 1). Obviously after 2.5 hours the activity disappears in good agreement with the half-lives of the primary radon and the daughter nuclides. The measurements also yield that the pure vapour exposure is in average 5 times more effective than the mine exposure and again another three times more than the water bath. In addition it could be shown that only 1/3 of the surface activity could be removed by very stringent washing where the upper part of the skin was completely removed. This indicates that a significant fraction of the alpha emitting isotopes penetrates and can be metabolised. From the tumor therapy it is known that isotopes created in high charge states are very reactive and have a rapid turn over of a few hundred second only.

These measurements are presently analyzed in terms of radon diffusion in order to quantify the small fraction of reactive isotopes that can probably invade the body.

References

[1] H. Tempfer, W. Hofmann, A. Schober, H. Lettner and A.L. Dinu, "Deposition of radon progeny on skin surfaces and resulting radiation doses in radon therapy", J.Rad.Env.Biophys. (2010) in press.

[2] J. Klinger et al., "Investigation of effects related to inflammation in a human cell co-culture model after exposure to ionizing radiation", This annual report.

* work supported by the FOI Bad Gastein, Austria.

[i] we would like to thank the Hotel Bismark, Bad Hofgastein and the "Dunstbad" for their friendly help.

[ii] A CoMo 170 monitor of SEA, Germany.

Investigation of effects related to inflammation in a human cell co-culture model after exposure to ionizing radiation

Jonas Klinger[1], Marco Durante[1,2], Claudia Fournier[1], Gerhard Kraft[1], Sophie Richter[3], Susanne Ullrich[3]

[1]GSI, Darmstadt, Germany; [2]TU Darmstat, Germany; Hochschule Darmstadt, Germany

Introduction

The high efficiency of photons and radon in the treatment of chronic inflammatory diseases has been attributed to anti-inflammatory effects. High doses of ionizing radiation (IR) elicit pro-inflammatory reactions whereas for low doses anti-inflammatory effects have been reported. [1,2] However, the molecular mechanisms, especially the role of the pro- and anti-inflammatory cytokines e.g. TNF-α and TGF-β, are still unclear. Previously obtained results revealed only a slight reduction of the pro-inflammatory cytokines TNF-α and IL-1β in murine and human macrophages following exposure to X-rays., whereas no reduction was detected after irradiation with carbon ions. [3] Also, increased levels of TGF-β in the serum of patients suffering from ankylosing spondylitis have been observed after radon therapy [4]. The authors showed in an *in vitro* co-culture-model that the adhesion of primary lymphocytes to endothelial cells was reduced after irradiation with low doses of IR (0.5 Gy), in contrast to higher doses [5]. In our ongoing work we intend to investigate a potential anti-inflammatory effect in human lung cells of the epithelial and connective tissue, cultivated in co-culture after treatment with X-rays or charged particles of low energy.

Materials and Methods

Irradiation was performed using X-rays (250kV, 16mA) and carbon ions (LET 170keV/µm). For the measurement of cytokines in the cell culture supernatant, human lung fibroblasts, lymphocytes and human epithelial or endothelial cells were incubated for 24h after irradiation. ELISA assays were performed with *DuoSet Kits* from R&D Systems for human TGF-β and TNF-α.

An adhesion assay was performed using hybrid endothelial cells (EA.hy.926) in co-culture with lymphocytes or lymphocyte-like U-937 cells (tumor cell line). The EA.hy.926 cells were cultured to form a confluent monolayer. After irradiation they were stimulated with TNF-α (10ng/ml) and incubated for 24h. Subsequently the biotinylated lymphocytes were seeded onto the EA.hy.926 monolayer and incubated for 30min., afterwards the samples were washed, fixed, stained and adherent lymphocytes were counted using a fluorescent microscope.

Results and Conclusion

In first results obtained in the cell strains to be used in the co-culture model, we observed a significant increase in the amount of TGF-β produced by NHLF (data not shown), HUVEC and EA.hy.926 cells in response to photon and carbon ion exposure (**Fig.1**). We found that both radiation qualities induce the secretion of TGF-β in a dose dependent manner even at doses as low as 0.5 Gy. We could further show that the amount of TGF-β secreted by endothelial cells after irradiation with carbon ions is significantly higher compared to photons **(Fig.1)**. In contrast, the secreted amount of TNF-α remained for most cell strains unchanged after radiation exposure, except for a slight reduction of the amount secreted by stimulated macrophages and lymphocytes (data not shown).

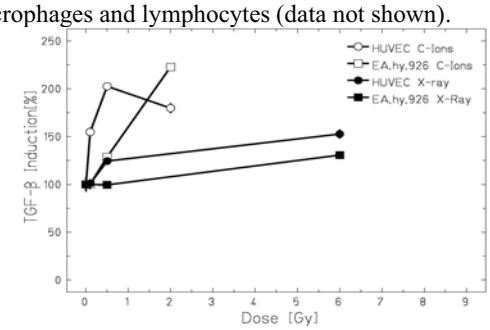

Figure 1: *Secretion of TGF-β secretion in endothelial cells (HUVEC, EA.hy.926) 24h after irradiation with X-ray (250kV, 16mA) or carbon ions (Energy: 9,8MeV/n; LET: 170keV/µm)*

Our results on the radiation induced changes in the adhesion of lymphocytes to endothelial cells confirm the results reported previously by Rödel et. al.[5]. Likewise we observe a significant decrease of adhesion after irradiation of endothelial cells with a low photon dose (0.5 Gy), but in a first experiment we did not detect a comparable effect after irradiation with carbon ions **(Fig.2)**. These results are not consistent with the observation of a higher secretion of TGF-β by endothelial cells after irradiation, as this should inhibit the adhesion of lymphocytes. Further experiments will be performed to clarify this.

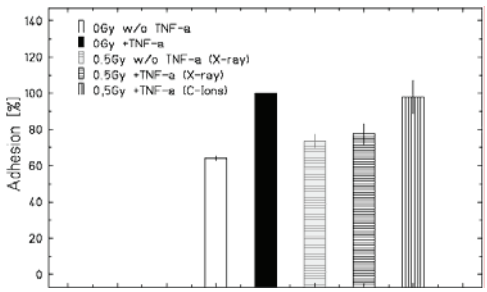

Figure 2: *Adhesion of lymphocytes to TNF-α (10ng/ml) stimulated endothelial cells 24h after irradiation with X-ray (250kV, 16mA) or carbon ions (Energy: 9,8MeV/n; LET: 170keV/µm)*

References

[1] Seegenschmiedt et.al., *Strahlenther. Onkol.* 180: 718-730 (2004).
[2] Piotrowski et. al., Neoplasma, 52/1: 56-62 (2005)
[3] Conrad et.al., J Radiat Res., 50/3:223-231(2009)
[4] Shehata et. al., Wien Klin Wochenschr (2006)
[5] Rödel et. al., Strahlenter Onkol., 180:194-200 (2004)

* Work supported by FOI BadGastein, Austria

Cellular response to heavy ions under hypoxic conditions

W. Tinganelli; M.Durante; C. von Neubeck; W. K.Weyrather
GSI, Darmstadt, Germany

Introduction

Hypoxia is a characteristics feature of locally advanced solid tumors resulting from an imbalance between oxygen supply and consumption. Tumor hypoxia is a therapeutic concern since it can produce cells much more radioresistent to the normal radiotherapy (Peter Vaupel et al 2009). To investigate the possibility to reduce this enhanced radioresistance by high LET radiation, experiments with carbon ions of different LETunder two different hypoxic states have been performed.

Material and methods

Cell line and culture condition

CHO-K1 (Chinese hamster ovary) cell line. Cells were grown in Ham's F12 medium supplemented with 10% fetal calf serum (FCS), and 1% Penicillin/Streptomycin and incubated in a humidified atmosphere at 37° and 5% CO_2.

Hypoxia exposure chamber

A special designed exposure chamber has been used, that allows irradiating cell cultures with x-rays or ions under defined oxygen conditions (Schicker 2008-2009). The chamber is made of polyetheretherketone (PEEK).

Cell samples

In order to support the growth in the hypoxia chamber the gas permeable foil bio-Folie25 was used (InVitro Systems & Services, Göttingen, Germany). The foil was attached with silicon grease on a polyvinyl chloride ring, thus providing a culture dish with a growth area of 4,5 cm^2. 24 hours prior to irradiation $5x10^4$ cells in 1.5 ml of culture medium were seeded into this dish and then the ring was closed with a second foil.
For the irradiation the cell sample ring was inserted into the hypoxia chamber. The chamber was closed and gased. After irradiation, the rings were removed from the chamber and the cells were trypsinized for the clonogenic survival assay. In all experiments analogously treated control curves were irradiated in air.

Results

OER after x-ray irradiation

Clonogenic survival of CHO-K1 cells after x-ray irradiation was measured under oxic conditions and two different hypoxic conditions: 95% N2; 5% CO2 and 94.5% N2; 5% CO2; 0.5% O2. Results are shown in fig.1. The OER under fully hypoxic conditions was 2.40 ± 0.15. Addition of 0.5% oxygen to the gas mixture reduced the OER to 1.41 ± 0.11

OER after carbon irradiation

Survival after carbon irradiation, fully hypoxic condition, has been measured at 2 positions in an extended Bragg-peak. Dose averaged LET of 100keV/µm and 130 keV/µm respectively. The results are shown in fig.2.

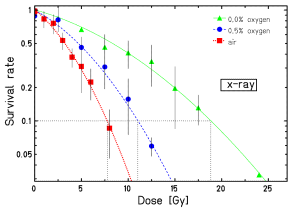

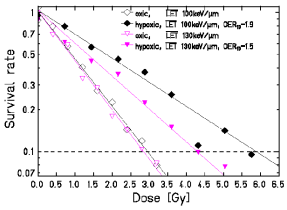

Figure(1) left. Survival of CHO-K1 cells after irradiation in air and under two different hypoxic states.
Figure(2)right. Survival of CHO-K1 cells after irradiation with carbon ions under oxic and fully hypoxic conditions.
The resulting RBE and OER values are shown in table 1.

LET [keV/μm]	OER	RBE10$_{oxic}$	RBE10$_{hypoxic}$
100	1.9	2.69	3.25
130	1.5	2.76	4.51

Table 1 RBE and OER after irradiation with carbon ions of two different dose averaged

Additional measurements have been performed at LET=100keV/µm comparing two different oxygenation states. The resulting OER 1.47 can probably be seen to be representative for the real tumor situation after carbon ion irradiation.
But it clearly has to be stated, that the results from carbon irradiation are only preliminary, as they have been produced in one beam-time only.

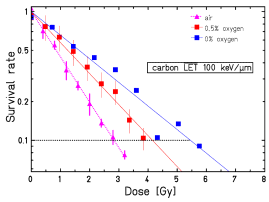

Figure(3) Survival of CHO-K1 cells with carbon ions with a dose averaged LET of 100keV/µm under oxic and two different hypoxic states.

References

(Schicker 2008-2009) C.Schicker, C. von Neubeck, U. Kopf, and W. Kraft-Weyrather. Patent: Ep 09 002 402.7, Zellkultur-Bestrahlungskammer, 2009.
(Schicker 2008-2009) C.Schicker, C. von Neubeck, U. Kopf, and W. Kraft-Weyrather. Patent: De 10 2008 010 918.5, Zellkultur-Bestrahlungskammer, 2008
(Peter Vaupel et al 2009) Peter Vaupel, Louis Harrison. Tumor Hypoxia: causative factors, Cmpensatory Mechanisms, and Cellular Rsponse. 12/09/2009

Clonogenic survival and apoptosis of prostate cancer cells irradiated with X-rays or carbon ions

P. Virsik[1,#], A. Gregus[1], P. Hessel[2], R. Lee[2] and S. Ritter[2]
[1]Dept. of Environm. Medicine, University of Göttingen, Germany, [1]GSI, Darmstadt, Germany

It is well known that in general, an increased oxidative stress is found in cancer cells (e.g. [1, 2]). Low and high LET radiations induce reactive oxidative species and thus increase the oxidative stress even more. Different cancer cells not only do repair the DNA damage differently, they also cope differently with oxidative stress. Increasing the oxidative stress before irradiation might possibly radiosensitize cancer cells. In order to better understand the different effects of C-ions on two different prostate cancer cell lines, characterized by different genetic profiles, we examined the effects of sodium selenite pre-treatment combined with irradiation on these cell lines. Cell inactivation and apoptosis were measured in radioresistant prostate cancer cells derived from a bone metastasis (PC-3) and from a brain metastasis (DU-145). Confluent cells were irradiated in G1-phase with 200 kV X-rays or with spread-out Bragg peak (SOBP) carbon ions (C-ions). Clonogenic survival was measured by standard colony assay. Sodium selenite was applied 6h before irradiation at concentrations non-toxic for humans (7.5 µM for PC-3, 7.5 or 20 µM for DU-145). Apoptosis was measured 24, 48 and 72 h after irradiation by morphological assay (fluorescent microscopy), TUNEL assay and caspase-3 activity assay (ELISA).

As can be seen in Fig. 1 and 2, the effects are quite different in the two studied cell lines. SOBP C-ions were more efficient in both cell lines with respect to cell survival (clonogenic assay). The RBE for 10 % survival of SOBP C-ions (without sodium selenite) is about 2 for PC-3 cells and 3.5 for DU-145 cells, confirming the superiority of C-ions in tumour therapy. In PC-3 cells, selenite at concentration of 7.5 µM shows the maximal radiosensitization (data not shown). In DU-145 cells, the maximal efficiency was observed at concentration of 20 µM, however for X-rays, only. No radiosensitization effect of selenite pre-treatment was observed for SOBP C-ions in this cell line. In PC-3 cells, where the selenite radiosensitization effect was present for X-rays and SOBP C-ions as well, survival curves indicate the presence of a resistant subpopulation. Apoptotic rates induced in the two cell lines after application of all treatment regimes are in agreement with these cell survival findings (data not shown), even the absence of any radiosensitization due to selenite pre-treatment for SOBP C-ions in DU-145 cells. The role of oxidative stress, repair of oxidative DNA damage and antioxidative capacity in the reaction of the studied cancer cells will be studied in further experiments. In addition, normal prostate epithelial cells PrEC will be examined as well.

* Work supported by BMBF, Bonn, under contract number 02S8497.

patricia.virsik@medizin.uni-goettingen.de

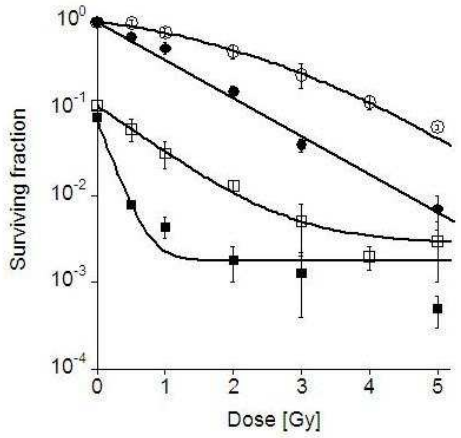

Fig.1. Clonogenic cell survival of PC-3 cells irradiated with graded doses of 200 kV X-rays (o) or SOBP C-ions (●) in comparison with sodium selenite pre-treated cells, X-rays plus selenite (□) and SOBP C-ions with selenite (■). Vertical bars represent standard deviations.

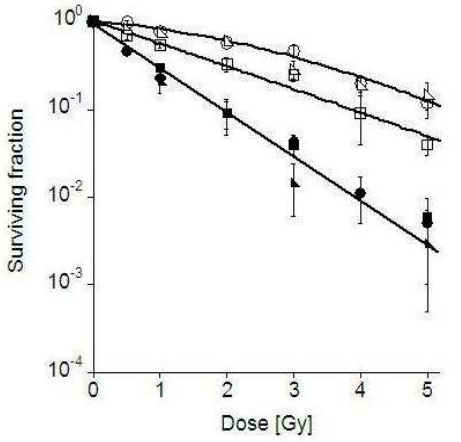

Fig.2. Clonogenic cell survival of DU-145 cells irradiated with graded doses of 200 kV X-rays (o) or SOBP C-ions (●) in comparison with sodium selenite pre-treated cells, X-rays plus 7.5µM selenite (Δ) or 20µM selenite (□) and SOBP C-ions with 7.5µM selenite (▲) or 20µM selenite (■).Vertical bars represent standard deviations.

References

[1] N.S. Brown and R. Bicknell, Breast Cancer Res 3 (2001) p. 323-327.
[2] J. Meesungnoen and J.P. Jay-Gerin, Radiation Res 171 (2009) p. 379-386.

Cytokine measurements in co-cultured rat cells

C. von Neubeck[1], W. K.-Weyrather[1], and M. Durante[1]
[1]GSI, Darmstadt, Germany.

Introduction

Inflammatory cytokines are secreted by damaged cells to induce in target cells reactions e.g. repair, death, enhanced proliferation or growth arrest. This report shows the results of cytokine measurements in co-cultured rat cells from prostate cancer, R-3327-AT-1 (RAT-1) and intestinal epithelium (IEC-6) after irradiation.

Material and methods

The both cell lines were irradiated in culture flasks with 6 Gy (RBE) of 250 kVp x-rays or 11.4 MeV/u carbon ions and cultivated in a 6-well plate/insert system (Greiner Bio-One GmbH, Germany). The porous insert membrane allows cell communication with soluble factors via the medium. At certain points during the experiment the cell culture supernatant was harvested for cytokine measurements and centrifuged at 4 °C for 3 min at 300 x *g*. In parallel, the total cell numbers in the well and in the insert were determined with a coulter counter. For analysis, the amount of measured cytokine in the cell culture supernatants has to be correlated to the cell numbers. This allows a conclusion about the secreted cytokine amount per cell and a comparison of different experiments.

ELISA assays (R&D Systems GmbH, Germany) were used to determine the amount of TGF-β, TNF-α and IL-2 in cell culture supernatants. The decision to analyze TGF-β, TNF-α and IL-2 was motivated by the results of the co-culture survival experiments [1] and the published effects in relevant literature of the cytokines on prostate and intestinal epithelium tissue.

Results

It was expected to find an inflammatory response after irradiation and that the involved molecules could be inflammatory cytokines. Based on the detected effect in the survival experiments [1] at least three factors could induce the effects whereas one factor is independent of irradiation and two were irradiation dependent. In survival assays the cells have almost no direct cell to cell contact so that the effect inducing substance should be a soluble factor which is mediated via the culture medium.

In the cell culture supernatants of all co-culture combinations no TNF-α or IL-2 could be measured. The possible source of TNF-α and IL-2 would have been the IEC-6 cells which are able to secret both cytokines which was shown with LPS-stimulation [2]. Obviously the co-culture conditions did not activate the same pathway as the LPS stimuli and did not induce TNF-α or IL-2 secretion.

Figure 1 shows the measured TGF-β amounts. It suggests huge differences between the experiments in which the measured TGF-β levels increased with time in all experiments. The adjustment of the TGF-β amount to 1 x 10^5 cells reveals that a more or less constant amount of TGF-β is produced by the cells. The detected differences were caused by the differing cell numbers seeded. Therefore, no differences between cells grown in Petri dishes or inserts and no differences between irradiated and unirradiated cells were detected. Furthermore, mono-culture or co-culture conditions had no influence on the TGF-β secretion.

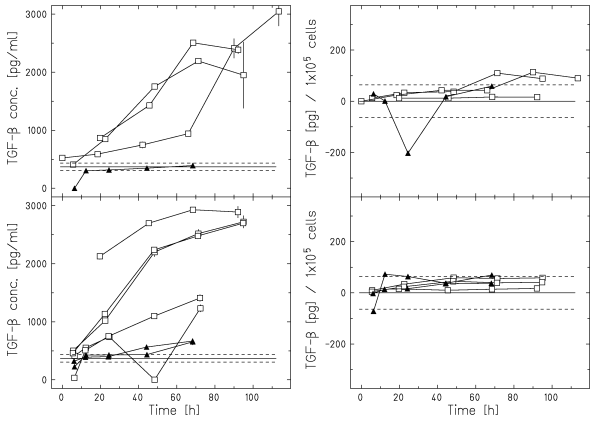

Figure 1: TGF-β measurements: left panels: total among of TGF-β in the sample adjusted for the serum level; right panels: TGF-β content normalized to 1 x 10^5 cells; on top: mono-culture of 6 Gy (RBE) irradiated RAT-1 cells; on bottom: co-culture of 6 Gy (RBE) irradiated RAT-1 cells and IEC-6 cells; 250 kVp x-ray experiments illustrated with open symbols and 11.4 MeV/u carbon ions with closed symbols; horizontal lines: TGF-β content of the culture medium.

Conclusion

To conclude neither TNF-α nor IL-2 were measured and the detected TGF-β amount did not alter due to the co-culture so that the observed effects in the survival experiments are probably not caused by one of the analyzed cytokines.

References

[1] C. von Neubeck et al. GSI scientific report 2008, p. 375.
[2] S.-Y. Lyu and W.-B. Park, *Archives of Pharmacal Research,* 2009*, 32*, 443-451

Putative relationship between the radiation induced accumulation of reactive oxygen species and programmed cell death

Till Dettmering[1,2], Marco Durante[1,2] and Claudia Fournier[1]
[1]GSI, Darmstadt, Germany; [2]TU Darmstadt, Germany

Introduction

Reactive oxygen species (ROS) are highly reactive by-products of cellular respiration, consisting mostly of superoxide anions (O_2.–) and hydrogen peroxide. They can damage cellular structures and are able to induce mutations, and both may result in premature cellular ageing or cell death [1]. Nevertheless, ROS are also important signaling molecules. During apoptosis, a form of programmed cell death, raised ROS levels mediate the release of cytochrome c, which is a crucial step for the progression of apoptosis [1]. In human fibroblasts, we observed a radiation-induced accumulation of intracellular ROS within the first week after irradiation [2]. We set out to investigate the relationship of this accumulation of ROS to other radiation induced effects, and as a first step we assessed whether apoptosis occurs in the same cells showing an enhanced level of ROS.

Methods

The occurrence of apoptosis was measured using the Annexin-V Apoptosis detection kit, which is based on the appearance of phosphatidyl serine-type membrane lipids during apoptosis. The accumulation of ROS was detected by the oxidation-related fluorescence intensification of Dihydroethidium (DHE). As a first step, we attempted to analyze apoptosis in fibroblasts using flow cytometry. However, since this method requires the sampled cells to be in suspension and the Annexin-V assay has been reported to be unreliable in enzymatically detached cells such as fibroblasts, we first used a non-adherently growing tumor cell line (U937) to test our hypothesis. U937 cells were irradiated with a dose of 10 Gy (X-ray) to reliably induce apoptosis and assayed after 24 hours using flow cytometry. Normal human fibroblasts (AG1522D) were assayed for the apoptotic phenotype by fluorescence microscopy.

Results and Conclusion

The unirradiated control cells (Fig. 1, left panel) show only a background of apoptotic cells (dashed circles); ROS (solid circles) are only accumulated by a small fraction of the cells (21%). However, a larger fraction of the irradiated cells (Fig. 1, right panel) is apoptotic and accumulates ROS (43%). Most importantly, apoptotic cells always show raised ROS levels, meaning that there is no detectable population of cells being apoptotic without an accumulation of ROS.

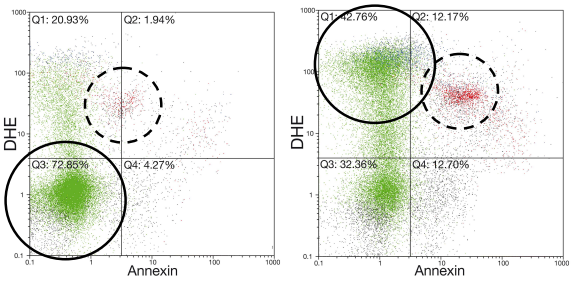

Fig. 1: Apoptosis (Annexin) and ROS (DHE) staining of U937 cells. Left: Unirradiated control cells show no accumulation of ROS and only a background of Annexin-positive cells. Right: 24 h after irradiation with 10 Gy of X-rays a pronounced accumulation of ROS is observable (solid circle), together with an increased number of apoptotic cells (dashed circle). Additionally, all apoptotic cells show raised levels of ROS.

The results obtained in U937 cells clearly indicate a simultaneous occurrence of radiation-induced apoptosis and accumulation of intracellular ROS, suggesting a correlation between both effects. Although ROS are related to the initiation of apoptosis, we do not know to date whether the measured apoptosis is a result of ROS accumulation or if ROS accumulate preferably in apoptotic cells. In any case, an imbalance between the intrinsic antioxidant defense and the amount of intracellular ROS has been discussed as a basis for the accumulation of ROS [3].

In fibroblasts (AG1522D), only low frequencies of apoptotic cells were detected, irrespective of the used dose or point in time after the measurement (not shown). Therefore, in fibroblasts the observed radiation-induced accumulation of ROS cannot be related to apoptosis and must be a result of other effects. According to the current knowledge on age dependent accumulation of ROS [4], we will further investigate the role of ROS accumulation in fibroblasts with respect to radiation induced premature senescence and genetic instability that has been observed previously [5].

References

[1] Orrenius et al. Annu Rev Pharmacol Toxicol 47: 143-183.
[2] Dettmering, T. (2009). GSI. TU Darmstadt. Diploma Thesis.
[3] Tulard, A., F. Hoffschir, et al. (2003). Free Radic Biol Med 35(1): 68-77.
[4] Passos, J. F. and T. von Zglinicki (2005). Exp Gerontol 40(6): 466-472
[5] Fournier, C. et al. (2007). Radiotherapy and Oncology 83: 277-282

Uncertainty of the relative biological effectiveness*

T. Friedrich[1], T. Elsässer[1], M. Durante[1,2], and M. Scholz[1]

[1]GSI, Darmstadt, Germany; [2]Institut für Festkörperphysik, Technische Universität Darmstadt, Darmstadt, Germany

Besides the inverted dose depth profile cancer therapy with carbon ions benefits from an enhanced relative biological effectiveness (RBE) compared to conventional photon radiation [1]. The RBE is defined as the ratio of a photon dose D_γ and a corresponding ion dose D_I yielding the same effect. Despite its simplicity this quantity depends on many factors such as tissue type, linear energy transfer (LET) and dose. In the zero-dose limit it can be expressed as $RBE_\alpha = \alpha_I/\alpha_\gamma$, where α_γ and α_I denote the initial slope of dose-effect relations. An analysis of its uncertainties is relevant for establishing precision goals for predictive models such as the LEM [2]. In the following we present properties of the uncertainty of RBE_α.

Experimental approach

We investigated standard deviations of α parameters for cell culture survival assays of different cell lines analyzed in several labs after both photon and ion irradiation. The accuracy limits occur both due to stochastic processes such as cell counting or cell killing and environmental factors such as nutrient supply and temperature leading to non-stochastic deviations. It turned out, that the standard deviations are in a comparable order of magnitude for all cases, and $\Delta\alpha \approx \Delta\alpha_\gamma \approx \Delta\alpha_I \approx 0.1\mathrm{Gy}^{-1}$ is a reasonable assumption. Applying conventional Gaussian error calculus leads under this assumption to

$$\Delta RBE_\alpha = \frac{\Delta\alpha}{\alpha_\gamma}\sqrt{1+RBE_\alpha^2} \quad .$$

Figure 1 demonstrates the validity for this simple error propagation model, which is applicable for sufficient large values of α_γ and α_I where the corresponding errors can be regarded as small.

Theoretic findings

For small values of α_γ the experimental determination of the RBE is not trivial, as RBE values will scatter over a large range and may take extraordinary high values. We attempted to understand this behaviour by considering the distribution function $P(RBE_\alpha)$ of RBE_α based on Gaussian distributed parameters α_γ and α_I with $\Delta\alpha \approx 0.1\,\mathrm{Gy}^{-1}$ as above. Using Monte Carlo simulation we were able to monitor the error propagation. By evaluating the ratio distribution of random variables [3] we also found an analytic expression for $P(RBE_\alpha)$. It turns out to be a long-tailed distribution, explaining the scatter of RBE values, c.f. Fig. 2. The median of RBE values serves as a better estimate for the true value than the arithmetic average. These findings quantify fluctuations of experimental RBE values and allow to estimate their uncertainty.

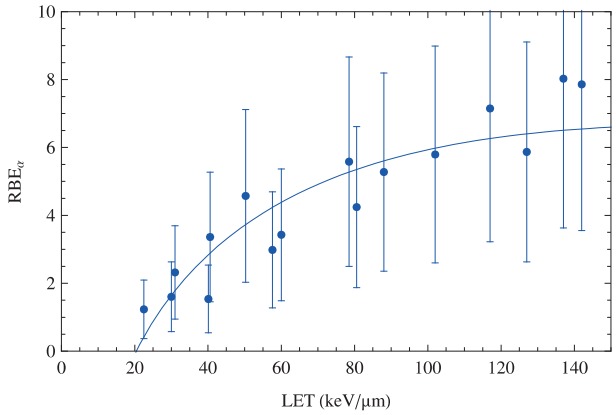

Figure 1: RBE_α vs LET for V79 cells irradiated with carbon ions. The solid line shows a non-linear fit to the data. The error bars were associated according to the simple experimentally motivated model presented in the text.

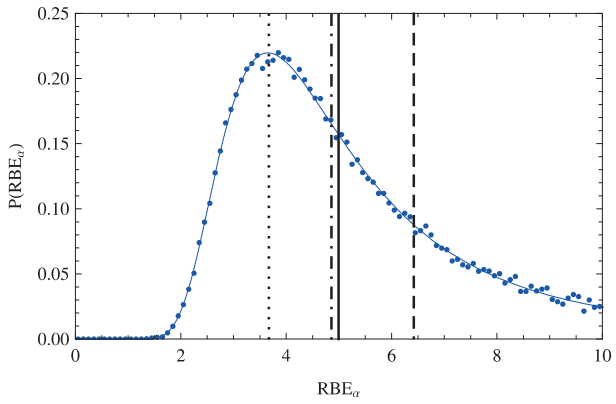

Figure 2: Distribution of RBE_α for $<\alpha_\gamma>= 0.2\,\mathrm{Gy}^{-1}$ and $<\alpha_I>= 1\,\mathrm{Gy}^{-1}$. Points: Monte Carlo simulation; solid curve: analytical treatment. The mean (dashed line) and most likely RBE_α (dotted line) of the distribution deviate by far from the design value (thick line). The median provides the best estimate (dashed-dotted line).

References

[1] E.J. Hall and A.J. Giaccia, "Radiobiology for the Radiologist", Lippincott Williams & Wilkins, Philadelphia (2006).

[2] M. Scholz et al., Radiat. Environ. Biophys. 36 (1997) 59.

[3] M.D. Springer, "The algebra of random variables", Wiley, New York (1979).

* Work supported by Siemens Healthcare.

An interface to calculate neutron RBE values using RBE tables based on the Local Effect Model*

G. Iancu[1], M. Durante[1], M. Krämer[1] and M. Scholz[1]
[1]GSI, Darmstadt, Germany

Introduction

The ALLEGRO European project aims to give a unified and consistent description as well as recommendations to be applied in estimating the risk of radiation therapy to the healthy tissue.

For a complete description of radiation field, neutrons and photons are also to be considered and their dose needs to be estimated. In the target region the dose contribution of these neutral particles remains rather low and gives only a very small correction to the dose delivered by charged particles. In the surrounding healthy tissue, where contributions from charged particles are very low, the relative contribution from the neutrons may become significant. The project thus aims at the estimation of the neutron contribution in the non-target regions.

Methods

TReatment planning for Particles (TRiP) [1,2] is the software successfully employed in the pilot project at GSI. At present, TRiP restricts its calculations to charged particles. To estimate the contribution of neutrons one needs to employ a Monte Carlo code. PHITS is the code of choice because of his very good results in calculating neutron spectra [3]. Besides the physical description, the increased biological effectiveness of neutrons needs to be taken into account.

The biological model used in TRiP[2] is the Local Effect Model [4,5]. Due to the fact that neutral radiation deposit dose through the interaction of secondary created charged particles with the target material, the estimation of biological effective dose for neutrons can be also performed based on the LEM, if the secondary charged particle spectra are known. These are to be calculated with PHITS.

To demonstrate the validity of this approach, an external interface has been developed which is able to read secondary charged particle produced by the TRiP program (describing the fragmentation of the primary beam) as well as from the PHITS program (describing the secondary recoil spectra from neutrons). This interface is based on the dose calculation algorithm reported in [6].

Results

The newly developed program is able to calculate physical and biological effective dose distributions for different input parameters and the corresponding linear-quadratic parameters.

The program has been validated by direct comparison to the TRiP calculations. Therefore the linear-quadratic parameters α and β where calculated as a function of depth in different monoenergetic Bragg-Peaks between 100 MeV/u and 300 MeV/u based on the charged particle spectra at the given depth as exported from the TRiP program. A very good agreement between between both approaches is found.

The program will be thus suitable for the application to the neutron secondary charged particle spectra. Thorough comparisons of the corresponding calculated biological effects will be performed for monoenergetic neutrons and broad neutron energy distributions, as they are typical for beams that were used for neutron therapy and for the neutrons produced in the fragmentation process of heavy ion beams.

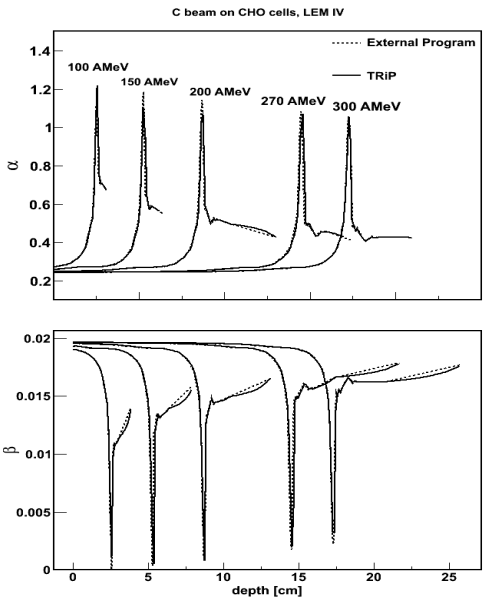

Figure 1 Comparison of the alpha and beta values between the external interface and TRiP

References

[1] M. Krämer, et al**,** *Phys. Med. Biol.*, **45** (11) :3299-3317 (2000)
[2] M. Krämer, M. Scholz, *Phys. Med. Biol.*, **45** (11) :3319-3330 (2000)
[3] H. Iwase, et all, *Rad. Prot. Dosim.*, **126** (1-4) :615-618 (2007)
[4] Th. Elsässer, M. Scholz, *Radiat. Res.*, **167** (3) :319-329 (2007)
[5] Th. Elsässer, M. Scholz, *Rad. Prot. Dosim.*, **122** (1-4) :475-477 (2006)
[6] M. Krämer, M. Scholz, *Phys. Med. Biol.*, **51** (8) :1959-1970 (2006)

* Work supported by EU, FP7-Fission-2008-3.2.1 Grant agreement 231965

Algorithms for Biological Dose Optimization in Ion Beam Radiotherapy

M. Horcicka[1], A. Buschbacher[1], A. Gemmel[2], M. Durante[1], and M. Krämer[1]
[1]GSI, Biophysics, Darmstadt, Germany; [2]Siemens AG, Particle Therapy, Erlangen, Germany

Introduction

From 1997 until 2008 about 440 cancer patients were successfully treated in the ion therapy project at GSI. The patient treatment planning was performed with the software TRiP [1, 2]. A crucial part of the treatment planning is the particle number optimization with the goal to achieve a target dose distribution as close as possible to the prescribed biological dose distribution. The optimization task can be mathematically expressed by the minimization of an objective function. In this report we examine modifications of the numerical methods, used to handle the optimization problem, which we discussed in [3] and [4].

Materials and Methods

The objective function is defined as follows:

$$X^2(\vec{N}) = \sum_{i \in Target} \frac{(D_{pre} - D^i_{bio}(\vec{N}))^2}{\Delta D^2_{pre}} + \sum_{i \in OAR} \frac{(D_{max} - D^i_{bio}(\vec{N}))^2}{\Delta D^2_{max}} \cdot \Theta(D^i_{bio}(\vec{N}) - D_{max}) \; .$$

$\vec{N}$: vector that contains the particle numbers
D_{pre} : prescribed dose within the target
D_{max} : maximum dose within OAR (Organ-At-Risk)
D^i_{bio} : actual biological dose at voxel i

Because $D^i_{bio}(\vec{N})$ is nonlinear in $\vec{N}$ the equation $\vec{N}_{opt} := \nabla X^2(\vec{N}) = \vec{0}$ can only be solved with iterative methods. We implemented the method of steepest descent (SD), conjugated gradients (CG) and the Levenberg-Marquardt minimization (LMM). These algorithms are described in [5]. For the CG-Method we tested the Fletcher-Reeves variant. The systems of linear equations which occur in the LMM are solved with the Cholesky-Method (LMM (Cholesky)) and a Krylow-Subspace-Method (LMM (Krylow)) [6]. The number of voxels and rasterspots are several ten-thousands which leads to long computation times.

Results and Discussion

The results of the numerical methods are illustrated in Fig.1 and Fig.2. Both LMM-Methods and the CG-Method show a good convergence behaviour in terms of iterations. On the other hand, the CG- and SD-Method minimize $X^2(\vec{N})$ fast concerning the time. Examinations showed that the coefficient matrices of the systems of linear equations have a sparse pattern. This can be exploited by the Krylow-Subspace-Methods. Hence, the LMM (Krylow) works much faster than the LMM (Cholesky). Because Krylow-Subspace-Methods are iterative solvers, they provide an approximated solution and this leads to smaller steps towards the minimum. The data were taken from the patient plan #135. Other patient plans show similar results.

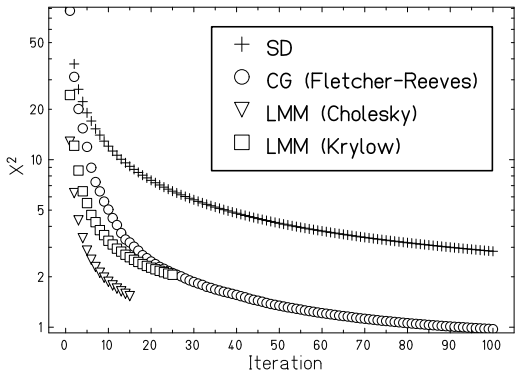

Figure 1: Convergence speed as a function of iterations.

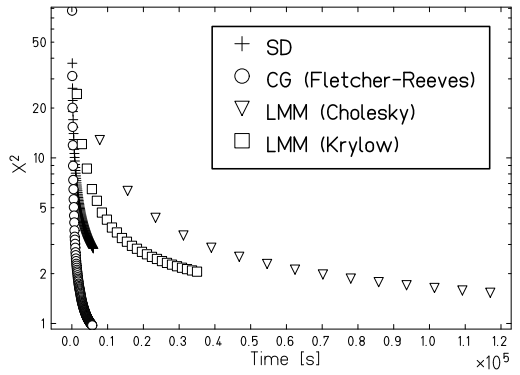

Figure 2: Convergence speed as a function of time.

Conclusion

The results show that the CG (Fletcher-Reeves) has better properties than the SD-Method used so far. Thus it is possible to optimize complete patient plans within an hour or less even on less powerful hardware.

References

[1] M. Krämer et al, Phys. Med. Biol., 45/11 (2000) 3299.
[2] M. Krämer et al, Phys. Med. Biol., 45/11 (2000) 3319.
[3] M. Horcicka et al, GSI Scientific Report 2007, 376.
[4] M. Horcicka et al, GSI Scientific Report 2008, 383.
[5] B. P. Flannery et al, *Numerical Recipes in C*, 2. Edition, 1992.
[6] A. Buschbacher, Dipl.-Thesis, GSI (2009).

An afterlife for treatment planning

M. Krämer[1], D. Schardt[1], and M. Durante[1]
[1]GSI, Darmstadt, Germany

For more than a decade, the TRiP software package served as the workhorse for patient treatment planning for the radiotherapy pilot project. With the end of the pilot project in 2008, the phase of direct clinical use also has come to an end. However, TRiP98 will enjoy a second life as a research prototype to support new developments in ion beam radiotherapy. It has more contributors and users than ever, including the current and upcoming dedicated radiotherapy facilities (HIT, Marburg, and potentially others).

Additional ion beam modalities

One of the future tasks is the extension of physical and radiobiological modelling to other modalities such as ^{1}H, ^{3}He, ^{7}Li, ^{16}O, which may have specific advantages. However, only realistic treatment planning studies will show the potential benefit of one ion modality over another. Prerequisites are validated base data sets, i.e. depth dose distributions, fragment spectra and intrinsic RBE tables. To this end TRiP98's internal transport code has been enhanced to deal with primary projectiles other than carbon. Semi-empirical cross section tables [1] cover the nuclear interaction, whereas [2] provides the energy loss information. In an initial test Bragg peak positions are verified against experimental data. Table 1 compares the predictions with measurements in Cave A [3]. In general agreement is within 0.5mm. With the chosen dE/dx code an ionization potential of 77eV is necessary to obtain consistency across all ion species and energies. It should be noted that at the level of sub-mm precision the mass defect of projectile nuclei other than carbon becomes significant. Accurate depth dose distributions need tuning of the nuclear reaction tables against absorption and fragmentation measurements. A preliminary result for a low energy ^{7}Li beam, with low contribution of nuclear reactions, is shown in Figure 1.

Miscellaneous developments

Optimization of dose distributions in complex configurations is an important aspect of treatment planning. Improved minimization algorithms [4] speed up this process by a factor ≈4 for the same result, leading to planning times of much less than an hour even for complex plans.

An ongoing effort is the inclusion of 4D treatment planning [5] into the code's mainstream, which we hope to complete in early 2010.

As the code system will have more users, for example in the framework of European projects (ULICE,Allegro), work is in progress to include import/export filters to facilitate data exchange with other planning systems (DICOM and others).

Proj.	E [MeV/u]	exp	calc
^{1}H	100	77.8	77.9
	125	115.4	115.5
	131.46	126.1	126.3
	150	158.9	159.1
	175	207.7	208
	200	261.6	261.8
	206.41	276.0	276.2
^{3}He	110	68.9	69.3
	140	105.6	105.9
	170	148.3	148.6
	190	179.8	180.1
	225	240.1	240.4
^{7}Li	100	60.6	60.6
	120	83.7	83.6
	160	138.6	138.5
	181	172.3	171.5
	200	203.7	203.6
	240	277.9	277.8

Table 1: Experimental and calculated peak positions [mm]

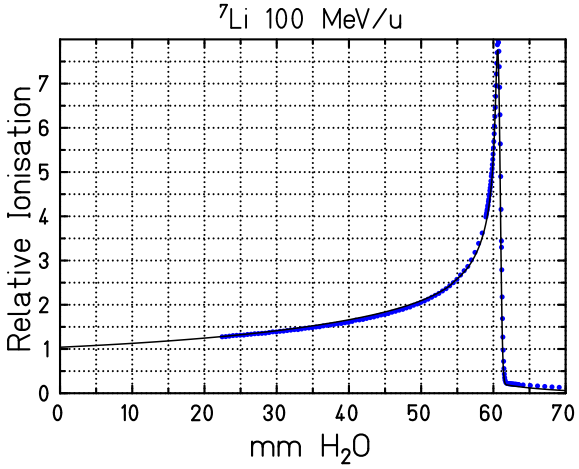

Figure 1: Depth dose distribution of ^{7}Li @ 100MeV/u. Symbols: measured, line: calculated.

References

[1] L. Sihver et al., Phys. Rev. C **47**, (1993) 1225

[2] M. H. Salomon, LBL Report **10446**, (1980)

[3] D. Schardt et al., GSI-Report 2008-1, p.373 and to be published

[4] M. Horcicka, this report

[5] D. Richter, this report

Calculation of microdosimetric spectra based on *TRAX* and its application for modelling *RBE* using the *MKM*.

M. Fernández[1,#,*], M. Scholz[1], T. Elsässer[1], M. Krämer[1] and M. Durante[1]
[1]GSI, Darmstadt, Germany;

Besides the absorbed dose, the *Relative Biological Effectiveness (RBE)* is the most important quantity in treatment planning with ion radiotherapy. The *RBE* depends on many different parameters, such as: the biological endpoint, the dose, the particle type and energy and the tissue under consideration. In consequence, the *RBE* will be different at any location in the treatment field. As the biological effect of the radiation should be homogenous in the target it is necessary to predict properly the *RBE* in each position. Due to the many factors on which the *RBE* depends, it arises the need of using biophysical modelling for its determination (since it is not feasible to experimentally measure the *RBE* for all possible parameter combinations). We will focus here on two models:

- the *Local Effect Model (LEM)* [1,2], which has been implemented in treatment planning in the GSI pilot project for ion beam tumor therapy, and
- the *Microdosimetric Kinetic Model (MKM)* from Hawkins [2] as implemented by Kase [6].

The objective of this work was to calculate the microdosimetric spectra, as required as input for the *MKM*, using the *TRAX* code [4] and to compare the corresponding biological effectiveness with the predictions of the *LEM*.

Implementation of the Microdosimetric Kinetic Model (MKM)

A survival curve defines the response of a tissue to a certain radiation and depends, among others, on the particle, its energy and the cell line under consideration. One of the main differences between both models is in the input dose distribution. For the *LEM* it is a radial dose distribution based on an analytical amorphous track structure description, while for the *MKM* we use a microdosimetric energy distribution.

Microdosimetry uses the energy deposition pattern at a microscopic level to relate the absorption of ionizing radiation in matter to the size and nature of the affected structures (cell and its components - site).

The *MKM* defines the survival as:

$$(\alpha_0 + \beta z_D^{*})D + \beta D^2 = \alpha^{*} D + \beta D^2 = -\ln S \quad (1)$$

where D is the absorbed dose, z_D is the dose mean specific energy by single energy deposition events in a domain, α_0 and β are parameters related with the number of lethal lesions. z_D^{*} is to be determined from eq. 2, where $\bar{l}$ and m are the mean chord length and the mass of the site, y is the mean lineal energy and $f_1(y)$ is its probability density and y_0 is the saturation parameter which depends on the size and biology of the cell.

$$z_D^{*} = \frac{\bar{l}}{m} \frac{y_0^2 \int (1 - e^{-y^2/y_0^2}) f_1(y)\, dy}{\int y\, f_1(y)\, dy} \quad (2)$$

The microdosimetric energy distributions have been calculated with *TRAX*. α_0, β and y_0 are empirical parameters. The *MKM* assumes that β depends only on the cell line and is independent on the *LET*. α_0 and y_0 are determined from the initial slope of the $\alpha^*(y_D)$ curve. The choice of these parameters is one of the main challenges as the model is very sensitive to them.

We have applied the *MKM* to determine the *RBE* values for carbon ions and proton in water for a wide range of energies and two different cell lines (*HSG* and *V79*). The results have been compared with experimental data, with *LEM* predictions and with *MKM* as implemented in [6].

Figure 1 shows the α^* vs. *LET* for carbon ions and for the *HSG* cell line. The experimental data were taken from [3] and [5]; *MKM* and the *modified LEM* curves from [6]. β is fixed to 0.0615 Gy^{-1}. For our *MKM*: α_0=0.057 Gy^{-1} and y_0=138.8 KeV/µm. The corresponding values reported by Kase [3] were α_0=0.13 Gy^{-1} and y_0=150 KeV/µm. All three approaches represent the experimental data; however, more comparisons are required to draw final conclusions about the possible systematic deviations between the approaches.

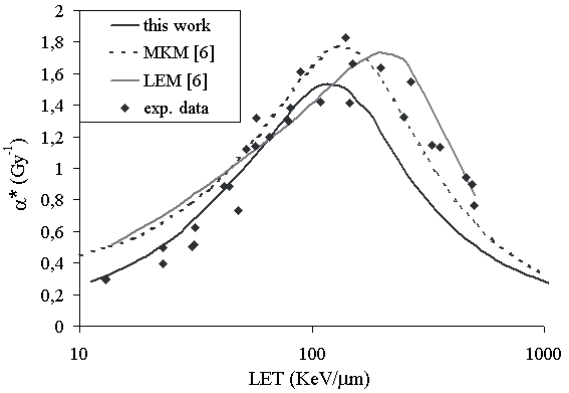

Fig. 1: Survival parameters for carbon (*HSG* cell line) calculated with the *MKM* implemented at GSI and compared with *Kase MKM*, our *LEM* and experimental data.

References

[1] M.Scholz and G.Kraft, Adv. Space Res. 18(1996), p. 5
[2] Elsässer and Scholz, Rad. Res. 2007
[2] R.B. Hawkins. Radiat. Res. 140 (1994), p. 366.
[3] Y. Kase et al. Radiat. Res. 166 (2006), p. 629.
[4] Krämer, this report.
[5] Furusawa et al. Rad. Res. 154-5 (2000), p. 485.
[6] Y. Kase et al. Phys. Med. Biol. 53 (2008), p. 37.

m.FernandezTomas@gsi.de
* granted from MEC (Spain): *Becas de Especialización en Organismos Internacionales*

Bragg curve measurements of ^{12}C and ^{56}Fe in aluminum

C. La Tessa[1], C. Schuy[1], D. Schardt[1], and M. Durante[1]
[1]GSI, Darmstadt, Germany

Several experiments for measuring depth-dose distribution of charged particles in water have been performed in the last decades because of their high relevance in ion therapy applications. Thus, the combination of energy and charge have been focused on feasible candidates for treatment of cancer with radiation. However, the request of Bragg curve measurements for higher energy and targets other than water has grown over the years. The need of a more extensive database find its roots in the increasing interest of space-related research, whose main goal is to assess and minimize the risk related to human exposure to space radiation. In fact, experimental investigations as well as theoretical approaches with Monte Carlo codes concerning the issue of radioprotection in space are both strongly related to a deep knowledge of the charged particles interaction with matter.

The experiment

An automatic system for Bragg curve measurements was developed and tested with 500 MeV/nucleon carbon and 1 GeV/nucleon iron beams, which are both relevant in space radiation environment. The target consisted of two aluminum wedges each mounted on a linear axis which could be controlled remotely. A variation of the wedges position was translated into a change of the target thickness. The choice of the target material was related to that fact that aluminum is commonly used for building space vessels. The energy loss by the beam in the target was measured with two ion chambers placed upstream and downstream of the system. A LabVIEW software, based on a program developed by P. Steidl, was implemented to control both the linear axes movement and the data acquisition. Tests prior to the experiment confirmed the accuracy of the software and its reliability. The experiment was performed in cave A at GSI in August 2009. The results are shown in Figures 1 and 2 for carbon and iron ions, respectively, and have been compared with predictions of PHITS Monte Carlo code [1].

The overall agreement between experimental and simulated data is very good, proving the accuracy of PHITS when reproducing the different physical processes involved in this case. The shape and height of the curves is very similar as well as the position of the peak. The largest discrepancy can be observed in the tail following the peak where PHITS is systematically lower than the measurements. This trend could be related to an inaccurate prediction of the fragments number and energy and therefore to the model for the calculation of the partial charge-changing cross section. A more detailed analysis of the results need to be conducted to investigate this discrepancy.

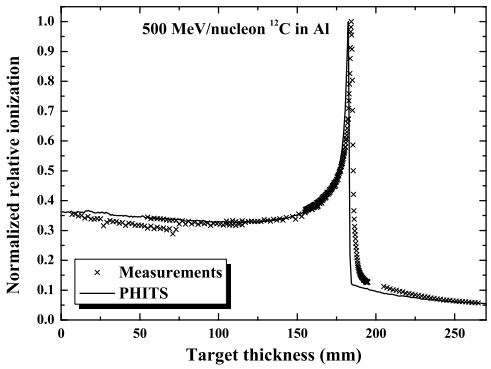

Figure 1: Measured and simulated Bragg curve of 500 MeV/nucleon carbon ions in aluminum.

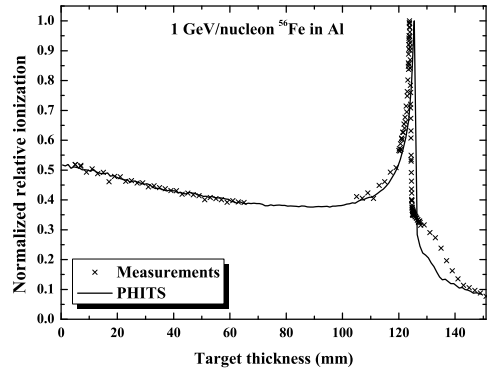

Figure 2: Measured and simulated Bragg curve of 1 GeV/nucleon iron ions in aluminum.

A non uniform behavior of the carbon measurements can be noticed in the plateau region where the data up 70 mm are off-set compared to the others. The shift is not physically relevant being the result of mechanical problems encountered at the beginning of the experiment. Improvements on the stability of the linear axis structure when moved remotely have solved the issue and increased the accuracy of the system. Implementations on both the mechanical structure and control software have been discussed and will be completed in view of further measurements.

References

[1] H Hiwase, K Niita and T. Nakamura, J. Nucl. Sci. Technol. 39 (2002), p. 1142.

Display functionality for TRiP*

S. Hild, M. Krämer, M. Durante, C. Bert
GSI, Darmstadt, Germany

Within the GSI ion beam therapy pilot project treatment plans were optimized and dose distributions were calculated by TRiP98 [1]. Segmentation of target volumes and evaluation of the calculated dose distribution, i.e. all steps involving data visualization and graphical user interfaces, were performed with VoxelPlan that is developed at DKFZ [2].

To allow assessment of treatment plans by TRiP and especially for development of user interaction possibilities for 4D treatment planning we started to develop a display functionality for TRiP.

Core functionality of treatment plan visualization is the display of computed tomography data, overlaid by the contours of the volumes of interest (VOI), and the dose distribution, either as iso-dose lines or by a transparent color-wash distribution. As indicated in figure 1 this core functionality was implemented conventionally by displaying axial, coronal, and sagittal planes of the 3D data. The panel on the lower right indicates the transfer function that determines window-level of the CT data as well as the rgbα-channels for the dose values.

Figure 1: The typical data representation of CT (gray-scale), dose (colorwash), and contours of the volumes of interest in the three main planes. The panel in the lower right determines the color representation of the data.

One of the main reasons that lead to the development of a display functionality is the need to display and evaluate 4D data. Based on the new 4D treatment planning functionality of TRiP [3] the display functions have full capability to display 4DCT, 4D contours, as well as 4D dose distributions. The user interacts with the 4D data by changing time phases similar and in addition to the change of slices in a 3D data set.

Especially for evaluation, e.g. of the internal target volume of a lung cancer case, the use of maximum intensity projections (MIP) is a valuable tool [4] and was thus implemented. For MIPs, multiple images are combined by showing the maximum intensity of all images per pixel. By choosing multiple motion phases of the 4DCT as contributing images e.g. a dense lung tumor will contribute to the maximum intensity and thus the full extent of the tumor will be displayed. Figure 2 shows an example MIP representation of a lung tumor in the sagittal direction.

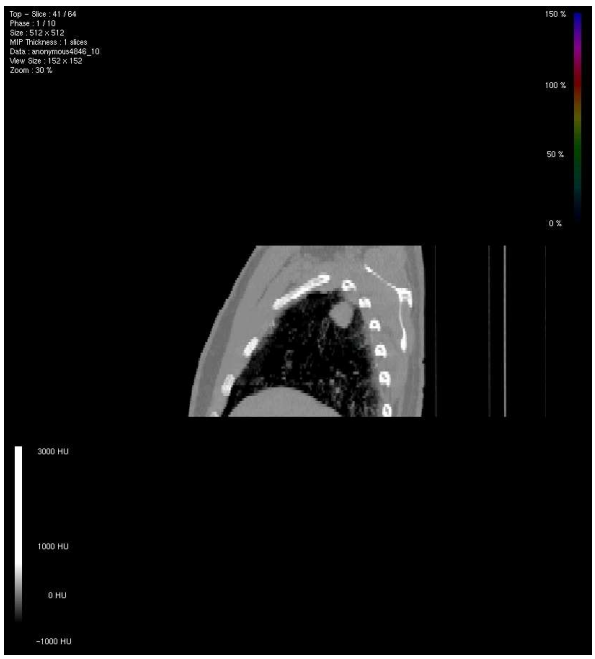

Figure 2: Example of a maximum intensity projection over multiple motion phases of a lung cancer case.

Future developments will focus on assessment of 4D treatment plans that requires implementation of other standards of 3D treatment plan visualization such as indication of the fields.

References

1. M. Krämer *et al.*, Phys. Med. Biol. 45 (2000) 3299
2. R. Bendl *et al.*, in *VIRTUOS - A program for VIRTUal radiOtherapy Simulation and verification*, edited by A. Hounsell Manchester, 1994), p. 226.
3. D. Richter et al, this annual report
4. E. Rietzel, A. K. Liu, G. T. Chen, and N. C. Choi, Int. J Radiat Oncol. Biol. Phys. 71 (2008) 1245

Dose calculations with TRAX

M. Krämer[1] and M. Durante[1]
[1]GSI, Darmstadt, Germany

The description of energy deposition at the lowest feasible level is a long term goal for radiological science, in particular in ion beam radiotherapy as well as in space radiation protection. For this purpose the MC code TRAX has been developed for many years [1, 2], which uses elementary interactions rather than condensed random walk.

Microdosimetric observables

The traditional microdosimetric approach uses observables such as the distribution of lineal energy deposition, y, and the specific energy deposition, z, to describe radiation quality with respect to damage in biological systems. A problem is, however, that there is no obvious link from purely physical observables to resulting biological effect. In recent developments, however, microdosimetric quantities have been used to predict biological damage with some success [3]. Hence there is a renewed interest in y- and z-distributions, which can be measured in gas at low pressure and readily simulated with elementary interaction codes. Figure 1 shows experimental results for the dose-weighted average of y, $y_D(b)$, as a function of distance, b, from the ion path in comparison with TRAX calculations. The strange shape of $y_D(b)$ as the counter moves out of the beam is clearly reproduced, as well as the almost constant contribution from δ-electrons at large distances. The higher energetic proton example shows significant discrepancies, which are not yet understood.

Macroscopic dose distributions

One is tempted to extend ab-initio calculations to describe macroscopic depth dose distributions of therapeutical relevance. A major problem, however, is the lack of accurate differential cross sections. To this end TRAX uses empirical cross sections [4], modified for high ion energies, and with empirical corrections to be in accordance with conventional energy loss tables [5]. With these ingredients and a lot of computing time it is indeed possible to reproduce one-dimensional projections of depth dose distributions. Figure 2 compares microscopic simulations with experimental results as well as with macroscopic calculations with the TRiP98 treatment planning system[5]. In general Bragg peak positions can be reproduced within less than 0.7 mm, and the dose values of both types of calculations are in good agreement. TRAX yields the width of the Bragg peaks in a natural way as a result of the emission of δ-electrons with a spectrum of kinetic energies. The deviations to the experimental results are due to nuclear interactions, not yet considered in TRAX, and deliberately switched off in the TRiP98 calculations.

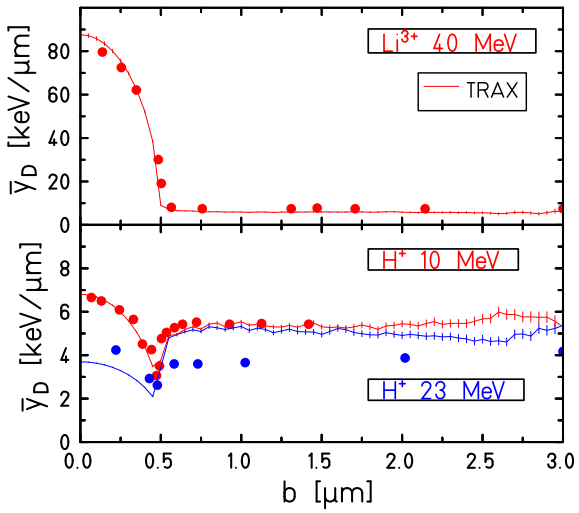

Figure 1: Measured [6] (site 1μm water equivalent) vs simulated y_D values as a function of distance from the ion path.

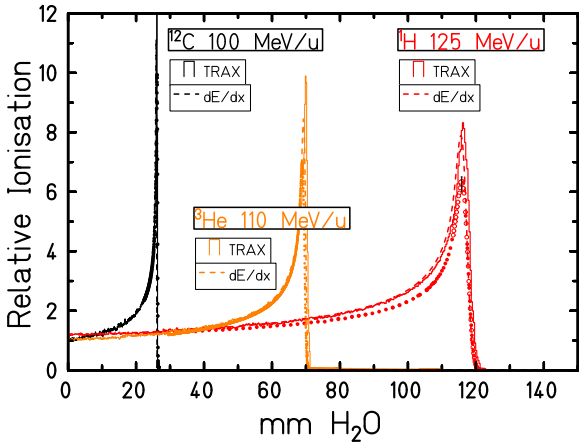

Figure 2: Depth dose distributions for various ions, symbols: experiment, solid lines: TRAX results, dashed lines: TRiP98 calculations without nuclear interactions.

References

[1] http://bio.gsi.de/DOCS/trax.html

[2] Krämer M., Kraft G. Rad. Env. Biophys., **33** (1994) 91-109

[3] M.Fernandez, this report

[4] M. E. Rudd et al., Rev. Mod. Phys., **64/2** (1992) 441

[5] M.Krämer, this report

[6] P.J. Kliauga, *Proc. 5th Symp. Microdosim. EUR 5452* (1976) 127-139

Dose profile in MATROSHKA for a standard cancer treatment with carbon

C. La Tessa[1], T. Berger[2], R. Kaderka[1], D. Schardt[1], G. Reitz[2], and M. Durante[1]
[1]GSI, Darmstadt, Germany; [2]DLR, Cologne, Germany

The ALLEGRO project is devoted to assess the long-term health risks related to a cancer treatment. The investigation concerns the most modern radiation treatments modalities, i.e. photons-IMRT, protons and carbon ions delivered with both passive modulations and active systems. One of the major hazard is well known to come from the dose delivered to the normal tissue surrounding the tumor. Moreover, light secondary particles, namely protons and neutrons, produced inside the patient can deposit a non negligible amount of energy far away from the treatment area: a small out-of-field dose, even though insignificant if compared to in-field dose, can cause a relevant damage if delivered to organs or tissues particularly sensitive to radiation. Therefore, one of the first tasks within ALLEGRO is to quantify the out-of-field dose absorbed after exposure to a standard cancer treatment with radiation. The measurements are going to be performed both with a water and with an anthropomorphic phantom and will provide magnitude and distribution of the dose absorbed outside the irradiated area. Moreover, a particular effort will be devoted for characterizing the neutron field produced from the interaction of the primary radiation with the target.

The irradiation of MATROSHKA

The first irradiation of an antrophomorphic phantom with carbon ions was achieved at GSI in August 2009. The experiment took place in the medical cave with full therapy conditions. The standard RANDO phantom MATROSHKA [1], of property of DLR, was irradiated with a total dose of 100 Gy delivered from one direction; the tumor area was placed in the center of the head and had a size of 5x5x2 cm^3. The phantom consisted of a head and a torso for a total of 30 slices up to 40 cm from the tumor area. Several slices were equipped with tubes containing thermoluminescence detectors TLD600(^{6}LiF:Mg,Ti) and TLD700(^{7}LiF:Mg,Ti). Two slices, at 25 and 40 cm from the tumor, contained holders for CR39 passive detectors and an active silicon detector (SSD—Silicon Scintillation Detector) [1]; moreover, a rod filled with TLDs was placed along the main axis of the phantom. A picture of MATROSHKA placed in the cave before exposure is shown in Figure 1 (left picture) together with a slice filled with TLDs (upper right corner) and the rings of the rod (lower right corner).

The analysis of the detectors provided a 3D dose profile inside the phantom. The results obtained from the TLDs inside the rod are shown in Figure 2. The absorbed dose decreases extremely fast with increasing distance from the tumor confirming the efficacy of carbon ions in sparing normal tissues during a treatment. Moreover, the out-of-field dose measured with TLD600 is systematically higher than with TLD700 starting at 10 cm away from the tumor center. Thus, the neutron dose contribution outside the treatment area is expected to be significant when not only the thermal component of the energy spectrum is considered.

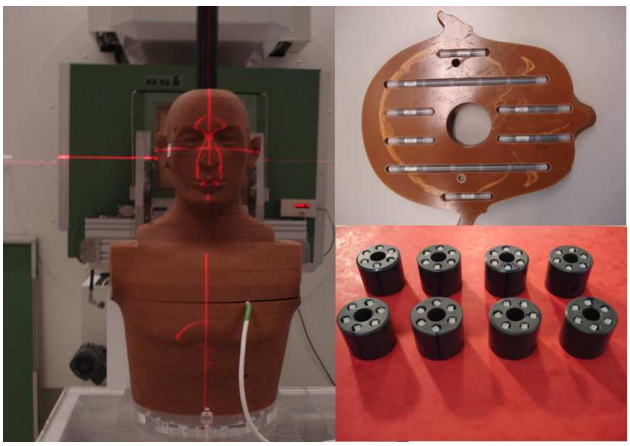

Figure 1: Setting of MATROSHKA in the medical cave before irradiation (left) with an example of a slice (upper right) and the rings of the rod (lower right) filled with TLDs.

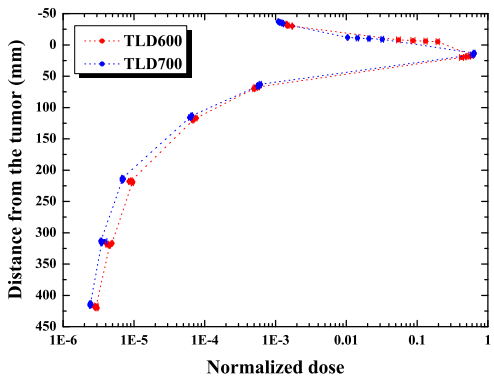

Figure 2: Dose distribution inside the rod; the values are normalized to the total dose delivered to the tumor.

References

[1] G. Reitz and T. Berger, Radiation Protection Dosimetry 120 (2006), p. 442.

Out-of-field dose measurements in radiotherapy for ALLEGRO

R. Kaderka*[1], C. LaTessa[1], D. Schardt[1], U. Ramm[2], J. Licher[2], and M. Durante[1]
[1]GSI, Darmstadt, Germany; [2]KGU, Frankfurt, Germany

Introduction

This report describes measurements of the out-of-field dose in a water phantom in radiotherapy irradiations for the ALLEGRO project. Details on the ALLEGRO project can be found in C. LaTessa's report in this publication [1].

Methods and preliminary results

These experiments compare the out-of-field dose delivered during different treatment techniques (photons, active and passive delivered protons and carbon ions) in standardized conditions. A water phantom is used as tissue-equivalent material and is irradiated with a rectangular field. The dose is measured in lateral direction in the plane of the field as shown in Fig. 1.
The composition of the out-of-field radiation changes with the treatment technique and thus also the biological effect. In photon therapy the out-of-field dose consists of photons and photoneutrons, whereas the main contributors to the out-of-field dose in ion therapy are nuclear fragments. Moreover not only the particle species but also the particle energy changes. Therefore it is essential to identify the particle and its energy contributing to the physical dose to determine the biological effect. To achieve this goal different detectors must be used.
The measurements in photon therapy are done with diamond detectors, ion chambers and bubble detectors. The diamond detector and ion chamber mainly measure the photon dose while the bubble detector is a passive detector specialized for neutron dosimetry.
The measurements of the photon contribution to the out-of-field dose in photon therapy are complete. However, only preliminary experiments have been performed with the bubble detectors. First they were exposed to an Am-Be source for calibration and for testing the stability of the detector response. The tests with the bubble detectors were successful so that the neutron measurements in photon therapy can soon be completed.
All irradiations were done at several institutes under patient conditions. The waterphantom was irradiated with a scanned carbon ion field at GSI. Photon irradiations were performed with a linac generating bremsstrahlung at the Klinikum Goethe Universitaet (KGU) in Frankfurt. The scanned proton irradation will be done at the Paul-Scherrer-Institut in Switzerland, also under patient conditions.
In the medical treatment room Cave M at GSI the waterphantom was irradiated with a 5×5 cm^2 field of 250 MeV/u ^{12}C ions. To measure the out-of-field dose a diamond detector was used.

* r.kaderka@gsi.de

The results of this measurement are compared to the out-of-field dose measured with a diamond detector during a photon irradation in Fig. 2. The dose is measured in the depth of maximum dose in the plane of the field and normalized to the isocentre.
The out-of-field dose of carbon is significantly lower than for photons. This difference is assumed to increase when neutrons are also considered; the dose coming from neutrons will be analyzed in future experiments. Future measurements will also give results from treatments with both active and passive proton beams.

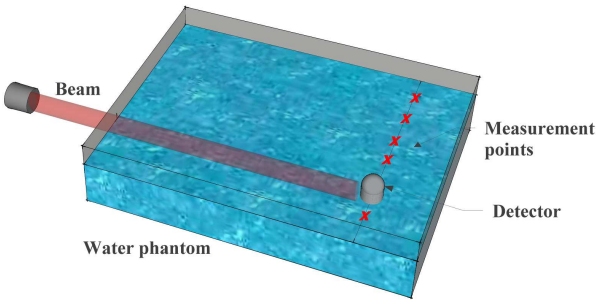

Figure 1: Principal setup of the water phantom measurements

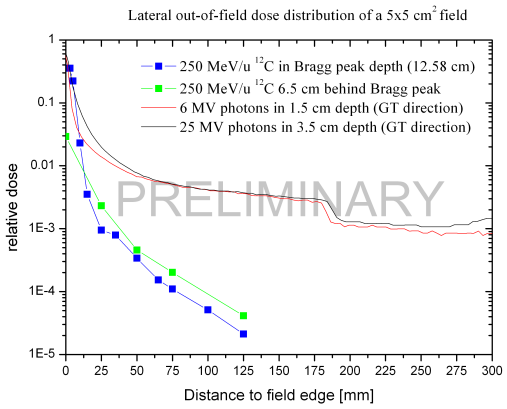

Figure 2: Comparison of the out-of-field dose of a 5×5 cm^2 field with a scanned carbon ion beam in Bragg peak depth and behind the Bragg peak, and a 6 and 25 MV photon beam in their respective maximum depth dose

References

[1] C. LaTessa et al., "MATROSHKA experiments for ALLEGRO", This publication

Fragmentation of 120 and 300 MeV/u ^{7}Li ions in a thick water target

G. Martino[1], R. Pleskaĉ[1], M. Durante[1,2], and D. Schardt[1]
[1]GSI, Darmstadt, Germany; [2]TU Darmstadt, Germany

The characteristics of the radiation field generated by ^{7}Li ion beams in water was investigated in Cave A. Such studies are needed to complement the present knowledge on the dose deposition of ions in tissue and to improve the physical models used for treatment planning. Fig.1 shows a sketch of the experimental setup. Primary particles and secondary light charged fragments escaping the water phantoms were identified with a ΔE-E telescope detector (Fig.2). The data were normalized to the number of incident ^{7}Li ions measured by a scintillator detector (SC) or by a parallel-plate ion chamber (IC).

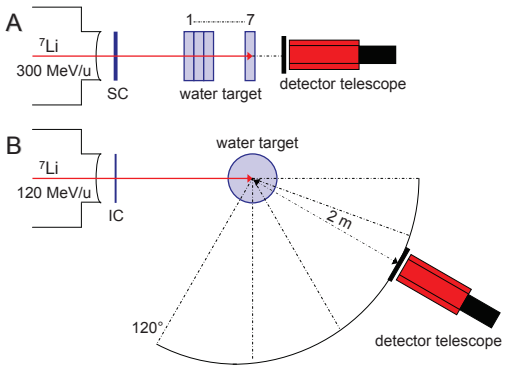

Figure 1: Experimental setup.

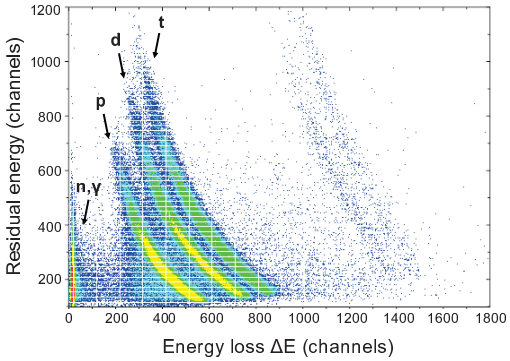

Figure 2: Correlation of energy loss ΔE and residual energy E measured with the telescope detector (θ=20°).

The attenuation of primary 300 MeV/u ^{7}Li ions passing through a water target of variable length was studied using setup A (Fig.1). The number of primary ions drops down exponentially by increasing the thickness of water (Fig3). The comparison with other heavier ion beams attenuations measured under similar condition at GSI [1] is shown.

Setup B was employed to evaluate the angular distribution of light fragments produced by a 120 MeV/u ^{7}Li beam stopped in a cylindrical water phantom of 15 cm diameter (the range of the primary beam in water is 8.25 cm). Angles in a wide range from 0° to 120° were investigated to complement recent experimental fragmentation studies [2] for 200 MeV/u ^{12}C ions showing that the angular distribution of protons is significantly broader than those of heavier fragments. Hydrogen fragments (p,d,t) (Fig.2) produced by ^{12}C and ^{7}Li exhibit a broad distribution, decreasing by several orders of magnitude from 0° to 120° (Fig.4). These data confirm the steep lateral dose fall-off which is an advantage of ion therapy [3].

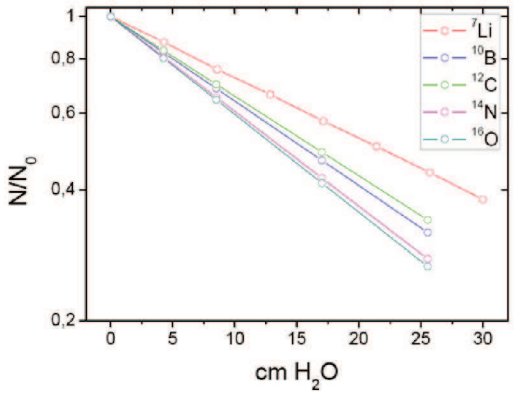

Figure 3: Attenuation of different ion beams as a function of the water thickness.

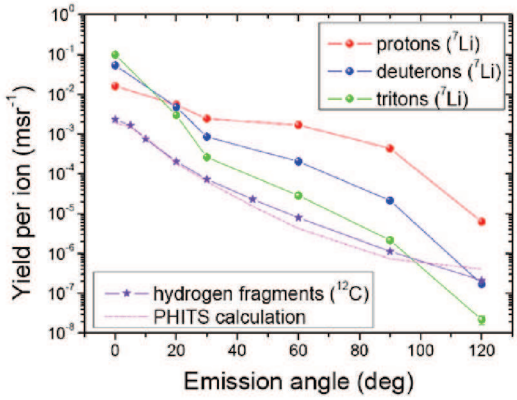

Figure 4: Angular distribution of light fragments produced by 120 MeV/u ^{7}Li and 200 MeV/u ^{12}C beams in water.

References

[1] I. Schall, D. Schardt et al., Nuclear Instruments and Methods in Physics Research Section B 117(3), 221-234 (1996).

[2] H. Iwase and D. Schardt, GSI Scientific Report 2008, p.387.

[3] G. Martino et al., GSI Scientific Report 2008, p.388.

Prediction of positron emitter distributions produced during ^{7}Li irradiation

M. Priegnitz[1], F. Fiedler[1], D. Kunath[1,2], K. Laube[1], K. Parodi[3], and W. Enghardt[1,2]
[1]FZ Dresden-Rossendorf, Germany; [2]OncoRay, TU Dresden, Germany; [3]Heidelberg Ion-Beam Therapy Center, Germany

Introduction

The clinical benefit of monitoring the applied dose in therapeutic carbon ion irradiation by means of in-beam PET has been proven at the experimental heavy ion treatment facility at GSI Helmholtzzentrum für Schwerionenforschung, Darmstadt. For future treatment of tumour patients the application of different ion species with atomic numbers between 1 (protons) and 8 (oxygen) is conceivable [1]. It is highly desirable to extend the in-beam PET method also to these ions, in order to have the ability of verifying the treatment. Therefore, the correct modeling of positron emitter production is necessary, which requires the knowledge of cross sections of all possible nuclear reactions occurring in the tissue during irradiation. For the majority of therapeutically interesting ions these cross sections are not available in the required energy range.

For the irradiation with ^{7}Li ions a novel approach for predicting the positron emitter distribution has been developed. The feasibility of this approach is investigated by comparing experimental data with the prediction of positron emitter distribution in polymethyl methacrylate (PMMA) and inhomogeneous targets.

Materials and Methods

Targets of water (W), graphite (Gr), polyethylene (PE) and PMMA have been irradiated with monoenergetic pencil-like beams of $^{7}Li^{3+}$ with therapeutically relevant energies (129 AMeV - 230 AMeV) at the experimental heavy ion treatment facility at GSI. Measurements of the irradiation induced β^{+}-activity has been performed by means of the in-beam PET scanner installed at the treatment site during the irradiation and further 30 min of decay afterwards [2].

By fitting the decay curves with a sum of exponentials, the amount of the most abundant positron emitters (^{11}C,^{15}O,^{10}C,^{13}N) at the end of the irradiation is obtained. Using this as input for the equations given in [3] the build-up of activity during irradiation can be calculated. Depth dependent thick target yields have been calculated as the ratio of the number of produced positron emitters to the number of incident particles for intervals of 10 AMeV energy loss along the beam path. A sufficiently precise prediction of the β^{+}-activity for a successful monitoring of the therapy is provided by consideration of interactions between impinging ions and C, O and H atoms of the tissue. Therefore, a yield database for the most abundant positron emitters mentioned above has been generated for water, PE and graphite as reference materials. It is supposed, that from a linear superposition of these yields a prediction of the positron emitter yield in any target of known stoichiometry is possible from this database (1).

$$Y_i(\vec{r}, \text{Target}) = a_1 Y_i(\vec{r}, \text{Gr}) + a_2 Y_i(\vec{r}, \text{W}) + a_3 Y_i(\vec{r}, \text{PE}) \quad (1)$$

where a_1, a_2, a_3 are coefficients depending on the target material and Y_i are the thick target yields in the energy interval i and depending on the spatial coordinate within the target $\vec{r}$.

Results

A comparison between experimentally obtained and predicted yields according to (1) is shown in Fig. 1 for a PMMA target and an inhomogeneous target composed of 4 cm graphite and 30 cm PE. Both targets have been irradiated with 162.3 AMeV ^{7}Li ions leading to a primary particle range of 12 cm. For the PMMA target the yields of ^{11}C and ^{15}O are presented, in the case of the inhomogeneous target only ^{11}C yields are given since the target does not contain any oxygen atoms which could disintegrate into ^{15}O. The relative mean errors between prediction and experiment are less than 15 %.

Summarizing the results of the performed experiments, the presented approach of predicting the positron emitter distribution for ^{7}Li irradiation provides promising results and will be further investigated for different materials and other ion beams.

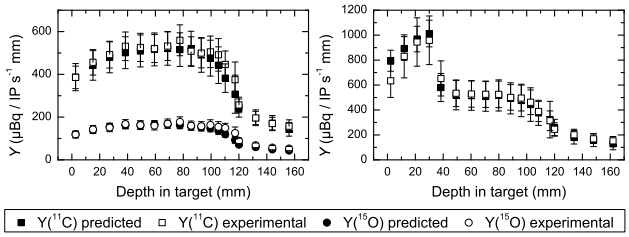

Figure 1: Comparison of predicted and experimentally obtained thick target yields of ^{11}C and ^{15}O in a PMMA target (left) and an inhomogeneous target (right) (4 cm graphite, 30 cm PE). The ^{7}Li beam enters the targets from the left with an entrance energy of 162.3 AMeV.

References

[1] J. Kempe, I. Gudowska and A. Brahme, Med. Phys. 34, pp 183-192, 2007

[2] M. Priegnitz, D. Möckel, K. Parodi *et al*, Phys. Med. Biol. 53, pp 4443-4453, 2008

[3] K. Parodi, W. Enghardt and T. Haberer, Phys. Med. Biol. 47, pp 21-36, 2002

Secondary Radiation During ^{7}Li Irradiation of a PMMA Phantom

T. Kormoll[1], F. Fiedler[2], A. Müller[2], and W. Enghardt[1,2]
[1]OncoRay, Dresden, Germany; [2]Forschungszentrum Dresden-Rossendorf, Dresden, Germany

Introduction

The recently initiated ENVISION* project inter alia aims at the development of in-beam dose verification systems based on promptly occurring secondary radiation during ion beam cancer irradiation. Especially a Compton camera system design will be studied. An important parameter for the optimization of such a system is the energy distribution and the fluence rate of the photon radiation field lateral to the irradiated volume. Additionally, the background due to the neutron component has to be scrutinized.

In preparation of further experiments and simulations the lateral radiation field of a phantom irradiated with carbon and lithium ions has been probed with two detector modules that were developed for photon detection within a narrow field of view.

Materials and Methods

A similar experiment was conducted using ^{12}C instead of ^{7}Li. The results can be found in [1].

All experiments were performed at the former medical cave M in slow extraction mode. One extraction cycle has a duration of 2 s. The pencil beam remained centered on the small face of the phantom. The irradiated phantom was a block of 9 cm × 9 cm × 40 cm consisting of polymethylmetacrylate (PMMA). Two scintillation detectors with an avalanche photodiode readout were placed alongside the phantom perpendicular to the beam at different depths. The modules are described in more detail in [2]. They are enclosed in a lead housing with a wall thickness of approximately 6 cm and provide a narrow field of view by the possibility to insert different collimator insets. LSO and lanthanum bromide crystals can be used.

Preamplifier signals are digitized on trigger and written to a hard disk for later analysis. The data acquisition allows for processing of finite sequences only. Such a sequence contains several events and can be analyzed for pulse heights and count rate. Count rate histograms have been calculated based on single sequences.

Results

The mean count rate and energy spectra recorded at different depths are shown for the lithium beam in figure 1. The distance of the detectors to the beam was 24.5 cm. The collimator aperture was 4 mm. The measurements were performed using LSO crystals. The beam energy was 230 *A*MeV which corresponds to a penetration depth of 21.8 cm. One spill contained approximately $9 \cdot 10^{8}$ particles.

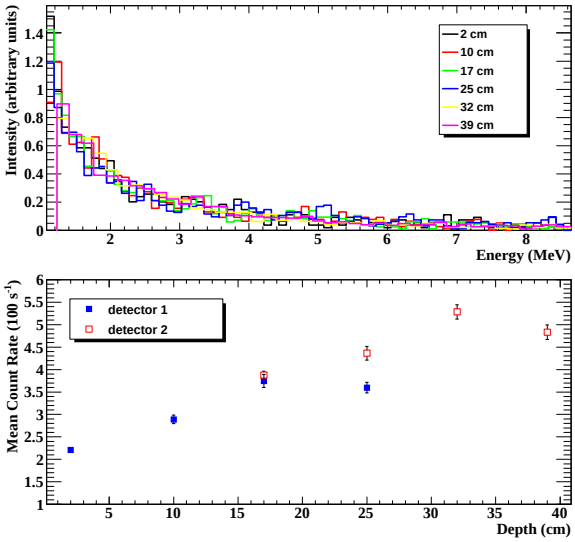

Figure 1: Normalized energy spectra (top) and the mean count rate (bottom) at different depths. The measured energy spectra show no dependence on the depth. The mean count rate increases with the depth. There is no significant change after the Bragg peak which is expected around 21.8 cm.

Conclusions

An increasing count rate is consistent with the neutron measurement in [3]. Thus, a possible explanation as well for the lack of structure in the count rate curve and the pulse height spectra is that because of the small aperture nearly all photons were absorbed while emerging neutrons were able to reach the sensitive volume essentially unaffected.

Further investigations are necessary and will be done in the framework of ENVISION.

References

[1] T. Kormoll, “In-vivo Dosimetrie harter Photonenstrahlen auf der Basis der Paarbildung”, Diploma thesis, TU Dresden, Dresden, Germany, 2009.

[2] T. Kormoll, D. Kunath and W. Enghardt, “3D In-vivo Dosimetry for Photon Radiotherapy Based on Pair Production”, IEEE NSS/MIC 2009 Conference Records, Orlando, Florida, October 2009, M06-5.

[3] E. Testa et al., “Monitoring the Bragg peak location of 73 MeV/u carbon ions by means of prompt γ-ray measurements”, Applied Physics Letters, 93, 2008.

*European NoVel Imaging Systems for ION therapy

Upgrade of the therapy control system for on-line dose compensation*

R. Lüchtenborg[1], N. Saito[1], N. Chaudhri[1], M. Durante[1], N. Kurz[1], E. Rietzel[1,2], and C. Bert[1]

[1]GSI, Biophysics, Darmstadt, Germany; [2]Siemens AG, Healthcare Sector, Workflow & Solutions, Particle Therapy, Erlangen, Germany

Introduction

Beam tracking is the potentially most conformal motion mitigation technique in scanned ion beam therapy. For translational motion, beam tracking has been shown to be feasible precisely [1]. If rotational or even deformable motion is present, dose deposition changes even if beam tracking is applied because beam tracking adapts the Bragg peak position only. Dose deposition to other regions, mainly the plateau region of the depth dose profile, might be subject to changes due to the changed beam path [2]. A dedicated method is needed for compensation of these dose changes.

Due to the variability in tumor motion and scanning progress these dose changes can only be compensated on-line, i.e. during treatment, based on measured target motion and scanning progress. The principle feasibility of on-line adaptation of individual voxel doses has been shown previously [3]. In this work the full implementation in an upgraded version of the therapy control system (TCS) is described and results of dedicated experiments are reported.

Materials and Methods

A method for on-line compensation of dose changes has been implemented in the TCS. For this purpose the beam tracking module has been extended to on-line calculate and accumulate dose changes of each individual voxel and adapt the applied particle numbers per voxel accordingly. These on-line calculations are based on the on-line measured target motion as well as data provided by an extension of the existing 4D treatment planning [2].

The implemented on-line dose compensation method requires both, enough computational power to properly perform the time-critical on-line calculations and sufficient on-line accessible memory to provide the dose compensation base data. To match both requirements the hardware of the TCS has been upgraded. A RIO4 processor board (CES, Switzerland) has been installed and the beam tracking software including the dose compensation upgrade has been ported to the new processor board.

Validation measurements have been performed. As only non-translational motion components cause dose changes rotational motion has been introduced by a dedicated rotational table. A water phantom with an array of four ionization chambers [4] has been used as detector system within the target volume. Three measurements have been done:

- REF: target was not rotated. Neither beam tracking nor dose compensation have been applied,
- POS: target was rotated by 14°. Beam tracking without dose compensation has been applied,
- FULL: target was rotated by 14°. Beam tracking with dose compensation has been applied.

Results

Calculation time per voxel depends on the treatment plan. However, for a test case the hardware upgrade resulted in a reduction from 860 µs to 30 µs.

Dose measurements from POS and FULL have been normalized to the REF results to directly assess the influence of rotation and the respective motion mitigation technique [5] (see Figure 1). The measurements show that the dose changes induced by the rotation can be substantially reduced when FULL is used.

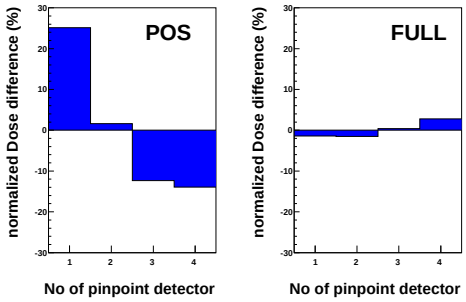

Figure 1: Dose measured by ionization chambers. Measurements are normalized to REF. While POS shows dose differences up to 25% they could be reduced to below 3% in case of FULL.

Conclusion

Validation measurements showed that the beam tracking TCS module was successfully extended by an on-line dose compensation functionality. The implemented software as well as the hardware upgrade ensure a sufficiently fast execution of the time-critical on-line calculations.

References

[1] C. Bert et al., *Med. Phys.* **34** (2007), pp. 4768–4771.

[2] C. Bert and E. Rietzel, *Rad. Onc.* **2** (2007).

[3] R. Lüchtenborg et al., *GSI Scientific Report* (2008), p. 396.

[4] C. Karger et al., *Med. Phys.* **26** (1999), pp. 2125-2132.

[5] R. Lüchtenborg, "On-line compensation of dose changes introduced by tumor motion during scanned particle therapy", Proc. WCMP 2009, Munich, 2009, pp. 449–452.

* Work supported by Siemens AG, Healthcare Sector, Workflow & Solutions, Particle Therapy, Erlangen, Germany

4D Treatment Planning Implementations for TRiP98

D. Richter[1], J. Trautmann[1], A. Schwarzkopf[1], M. Krämer[1], A. Gemmel[2], O. Jäkel[3], M. Durante[1], and C. Bert[1]

[1]GSI, Darmstadt, Germany; [2]Siemens Healthcare, Particle Therapy, Erlangen, Germany; [3]HIT, Heidelberg, Germany

Introduction

TRiP98 is a treatment planning program for heavy ion radiotherapy[1] with a scanned ion beam and was developed at GSI[2]. It has been successfully used in clinical routine from 1997-2008 for over 400 patients, predominantly with head and neck tumors[3]. The treatment of mobile tumors, such as lung tumors, with a scanned ion beam poses additional challenges, resulting into a higher complexity of the treatment planning process[4]. In order to meet these additional requirements, new implementations for 4D treatment planning in TRiP98 were necessary and were first carried out by Bert et al.[4] However a large part of the treatment planning was done using the 3D functionality of TRiP98 in a combination with external software. To overcome the drawbacks of this solution new efforts are being made to extend TRiP98 for true 4D treatment planning in a fully integrated and flexible way. The status of these implementations is presented.

4D implementations in TRiP98

The 4D functionality of TRiP98 has to encompass both, dose optimization and calulation. During the optimization step the particle numbers needed per raster spot are determined in order to achieve a given target dose. For 4D optimization the specific peculiarities of the applied motion mitigation techniques, such as gating, tracking or rescanning have to be considered[4]. 4D dose calculation in contrast to 3D dose calculation has to account for the movement of the target region during beam delivery. We have concentrated on 4D dose calculation as a first step, since this is an important prerequisite for 4D dose optimization.

4DCT and segmentation. Treatment planning for ion therapy is based on imaging information, comprising a 3D computed tomography and a segmentation of the CT dataset. For 4D treatment planning time resolved computed tomography (4DCT) and segmentation is needed, reflecting the anatomical changes during a typical time span, usually the breathing cycle of a patient[5]. The 4DCT provides a number (O(10)) of 3DCTs during the cycle, the so called 4DCT phases. In order to track anatomical changes in space and time, image registration is needed, providing transformation maps of voxel positions between different 4DCT phases. We implemented full 4DCT functionality by enhancing existing 3D structures in TRiP98. Since image registration itself is the result of an external software, different representations of the transformation maps of several registration programs can be read into TRiP98 and be applied to any 3D space point. 4D segmentation is obtained by applying the transformation maps to a segmentation dataset in one of the 4DCT phases. The integrated handling of 4DCTs, segmentation and image transformation efficiently replaces the previous sequential processing of the 3DCTs of each motion state.

Motion trajectory and scanner progress. In order to calculate the dose delivered to a certain anatomical position, the time structure of the beam delivery and its correlation to the movement of the irradiated region inside the patient have to be known. TRiP98 can read and handle several formats of external surrogate motion sensor trajectories, monitoring the patient motion. Additionally machine log files of the GSI scanner system were incorporated which represent the scanner progress. Establishing the time correlation between these two datasets, the motion phase in which a certain raster point has been irradiated is determined and is used as input to the 4D dose calculation functionality of TRiP98.

4D dose calculation. In contrast to 3D dose calculation 4D dose calculation takes into account the motion state of an anatomical position at the time of irradiation. For each anatomical position the dose contribution in each motion state is calculated and transformed to the reference 4DCT phase, using the transformation maps obtained by image registration. The total physical dose is calculated by summing up the individual contributions of each motion state. While the earlier implementation was relying on sequential calculation of dose contributions for each motion state in separate program calls and external summation which prevented the calculation of the relative biological effectiveness, the new dose calculation algorithm can handle all the steps internally. Hence, it is intrinsically capable of biological 4D dose calculation.

References

[1] G.Kraft, "Tumor Therapy with Heavy Charged Particles", Prog.Part.Nucl.Phys., **45** (2000) 473-544

[2] M. Krämer et al., "Treatment planning for heavy-ion radiotherapy: physical beam model and dose optimization", Phys.Med.Biol., **45** (2000) 3299-3317.

[3] O. Jäkel et al., "Treatment planning for heavy ion radiotherapy: clinical implementation and application", Phys. Med. Biol., **46** (2001) 1101-1116.

[4] C. Bert and E. Rietzel, "4D treatment planning for scanned ion beams", Semin. Radiat. Oncol., **4** (2007) 2-24.

[5] P. Keall, "4-dimensional computed tomography and treatment planning", Semin. Radiat. Oncol., **14** (2004) 81-90.

Quality Assurance test of the real-time beam tracking system *

N. Saito[1], C. Bert[1], N. Chaudhri[1], M. Durante[1], A. Gemmel[1,2], R. Lüchtenborg[1], G. Kraft[1] and E. Rietzel[2]

[1]GSI, Darmstadt, Germany; [2]Siemens AG, Particle Therapy, Erlangen, Germany

Introduction

For radiotherapy with external beams, quality assurance (QA) of beam delivery is mandatory. Dynamical irradiation which changes parameters of beam delivery devices during the irradiation has to be assessed with a great caution. At GSI a dynamic beam delivery system, so called beam tracking system [1] was developed and integrated into the GSI therapy system [2] to irradiate moving tumours with ion beams. The beam tracking system can control ion beams laterally with the scanning magnets of the rasterscan system [2] and longitudinally with a range shifter depending on the real-time information of target motion and scanning points based on a pre-calculated beam displacements from time-resolved treatment planning (4DTP) [3]. A method of beam tracking QA was investigated and experimentally tested by measuring dose delivered with beam tracking for a patient treatment plan.

Materials and Methods

Analogue to a quality assurance method of the GSI scanned ion beam therapy for static tumours [2], beam tracking can be assessed by comparing measured dose with nominal dose at 24 pin-point ionization chambers (IC) arranged three dimensionally in a water phantom. A 4DTP for a lung cancer patient [3] was chosen as a test case of the beam tracking QA method. A reference irradiation sequence of 7389 scanning spots and a list of beam displacements (dx:0~5 mm, dy:-10~0 mm, dz:-8~19 mm) for 10 motion phases (amplitude binning) were stored in the beam tracking system. To perform beam tracking, a cyclic motion signal from a motion phantom was used. The motion signal was recorded to calculate nominal dose for the performed motion sequence. Three different scenarios, 3D-, 2D- and no-beam tracking, were performed with carbon ion beams to observe the impact of beam tracking failure on the dose comparisons with the assumption of perfect 3D-beam tracking for nominal dose calculation for all three cases.

Results

Obtained dose values at the 24 ICs in the water phantom are plotted in the figure 1 for the measured (light gray) and nominal (dark gray) 3D tracking cases. The dose values agree well between the measured and nominal values, and results in a mean difference (measured - nominal) of 1.2 % of the prescribed dose (1 Gy) with a standard deviation of 2.8 % of the prescribed dose. This implies the performed 3D beam tracking was successfully working as expected for this scenario. The second scenario simulates an imperfect beam tracking with lateral only 2D beam tracking by deactivating the range shifter. In comparison to calculated perfect 3D tracking, the measured dose of the 2D beam tracking resulted in a slightly larger deviation of 4.7 % with the mean difference of 2.4% which is still acceptable as dose difference on the measurement positions for this particular case, but the larger deviation indicates the imperfect beam tracking. The last scenario is an extreme case as a total failure of the beam tracking. The measured dose with no-beam tracking disagrees with the calculated dose of a perfect 3D beam tracking case (figure 2), and it resulted in the large mean difference of 7.8% with an unacceptable standard deviation of 17.5%.

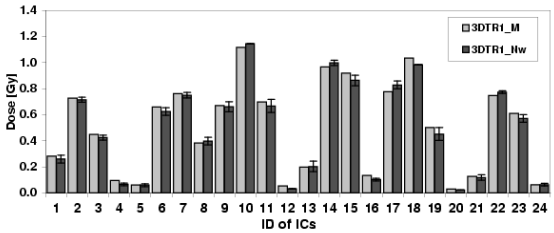

Figure 1: Comparison of measured (light gray) and nominal (dark gray) dose at 24 IC positions for the 3D tracking case.

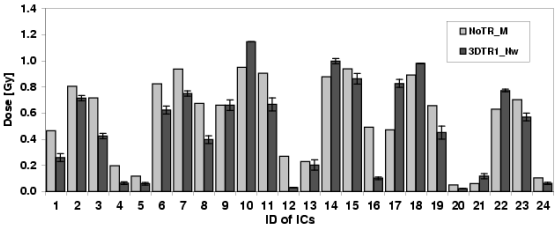

Figure 2: Comparison of measured (light gray) and nominal (dark gray) dose for a case of total failure. The nominal dose was calculated assuming perfect 3D beam tracking.

Conclusion

The QA method for the GSI beam tracking system worked successfully to distinguish beam tracking qualities, normal 3D-, imperfect 2D- and total failure of beam tracking.

References

[1] N. Saito et al., Phys. Med. Biol. 54 (2009) 4849
[2] G. Kraft, Nucl. Instr. and Meth. A 454 (2000) 1
[3] C. Bert and E. Rietzel, Radiat. Oncol. 2 (2007) 24

* Work supported by Siemens AG, Particle Therapy

Optimisation of an ion optical range adaptation method for beam tracking of moving tumours with scanned ion beams*

A. Constantinescu[1,2], N. Saito[1], N. Chaudhri[1], M. Durante[1,2], and C. Bert[1]
[1]GSI, Darmstadt, Germany; [2]Technische Universität Darmstadt, Germany

Introduction

An ion optical solution for beam tracking of moving tumours with scanned ion beams is currently being investigated at GSI [1, 2]. Thereby the longitudinal compensation is achieved by using the deflection magnets of the therapy beam line to direct the particle beam to different positions on a static energy degrader with variable thickness, which is installed upstream of the scanning magnets. Thus the range of the Bragg-peak can in principle be adjusted within $\sim 1\,\mathrm{ms}$ as no mechanical device is required. The initial feasibility of this method was studied both in simulations as well as in experiments [1, 3]. In order to optimise the method, systematic studies have to be carried out. Simulations results concerning the wedge shape and its material will be presented here.

Material and Methods

The presented simulations were carried out for the GSI therapy beam line by using the ion beam transport code MOCADI [4]. The beams were deflected in the horizontal x-direction, thus to the thinner (negative x values) or thicker (positive x values) part of the ramp degrader, with a maximum of $\pm 30\,\mathrm{mm}$ (taking the middle thickness of the material as reference). Beam widths in the lateral directions (x, y) as well as the resulting particles ranges were studied for the obtained beam spots at isocenter.
In order to compare the impact of the ramp degrader design on the outcome, three different slopes were used with a thickness change per lateral shift of 0.35, 0.47 and $0.58\,\mathrm{mmH_2O/mm}$ ($\mathrm{mmH_2O}$: water equivalent thickness).
For the material studies, plastic (C_9H_{10}, density $\rho = 1.032\,\mathrm{g/cm^3}$), graphite ($\rho = 2.23\,\mathrm{g/cm^3}$) and aluminium ($\rho = 2.69\,\mathrm{g/cm^3}$) degraders were implemented in the simulations. The comparison was carried out by keeping the thickness in water equivalent length constant so that the particles had the same energy after passing the different degrader materials at the same x-position.

Results

As an example for the comparison of the three different slopes, the lateral beam spot distributions for a graphite degrader are plotted in fig.1. As expected for the studied cases, the beam spot always looks best for the most shallow slope, independent of the traversed material thickness. The widths of the range distribution in full width half maximum (FWHM) resulted in 1.1, 1.3 and 1.6 $\mathrm{mmH_2O}$ for the slope of 0.35, 0.47 and 0.58 $\mathrm{mmH_2O/mm}$, respectively. Hence the range width is dependent on the amount of slope, whereas the most shallow slope yields the smallest value.

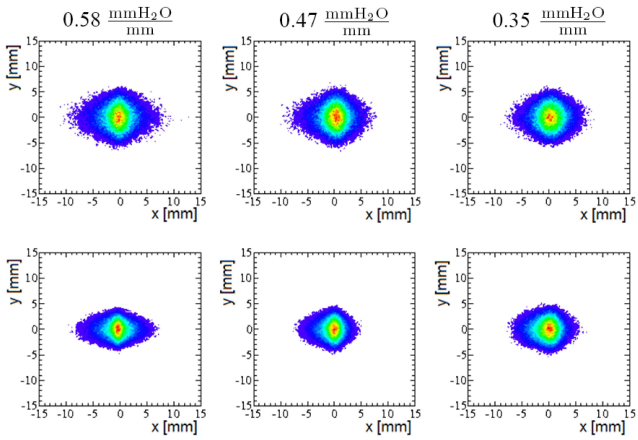

Figure 1: Beam spots at the isocenter for ions passing the degrader material at x-position +15 mm (upper panels) and -15 mm (lower panels) for different slopes of the ramp degrader (shown above).

Studying the different materials, the obtained lateral beam widths at isocenter yielded similar results for graphite and plastic, while the widths for aluminium were always slightly wider due to bigger angular scattering (e.g. the FWHM of y was on average 11 % higher for aluminium compared to graphite and 14 % bigger than for plastic).

Conclusion

Different materials and shapes of a ramp degrader have been systematically studied in order to optimise the ion-optical solution for range adaptation for beam tracking of moving tumours with scanned ion beams. Further optimisation is currently in progress.

References

[1] N.Chaudhri et al., GSI Sci. Rep. 2007 (2008) 382
[2] R.Pleskac et al., GSI Sci. Rep. 2007 (2008) 383
[3] N.Chaudhri, PhD Thesis, Universität Heidelberg, in progress
[4] T.Schwab, PhD Thesis, Universität Giessen, GSI Report 1991

* Work is in part supported by Siemens AG, Particle Therapy

On the difference of 3D and 4D in-beam PET for a periodically moving target

K. Laube[1], C. Bert[2], N. Chaudhri[2], F. Fiedler[1], K. Parodi[3], E. Rietzel[4], N. Saito[2], and W. Enghardt[1,5]
[1]FZD, Dresden; [2]GSI, Darmstadt; [3]HIT, Heidelberg; [4]Siemens Healthcare, Erlangen; [5]OncoRay, TU Dresden

Introduction

From 1997 to 2008 the treatment of more than 400 patients with ^{12}C ions at the experimental heavy ion treatment facility at GSI has been successfully monitored *in vivo* and *in situ* by means of 3D in-beam PET. The promising clinical results of the ion therapy for static tumor entities encourages to apply it to more frequent ones like lung cancer. Due to the sensitivity of the ion range to density changes along the beam path and the complex active beam delivery for these intrafractional moving tumors it is desirable to have excellent quality assurance techniques like a time-resolved (4D) in-beam PET dose monitoring.

Materials and Methods

For the experiments a homogeneous $(80\times50\times30)\,\mathrm{mm}^3$ PMMA target was centered in the field of view of the double-head PET scanner BASTEI at the former medical treatment site at GSI [1]. The phantom performed a one-dimensional sinusoidal motion with a period of about 3.5 s and a maximum elongation of 10 mm to the left and right in beam's eye view. A monoenergetic pencil beam of ^{12}C ions was rescanned parallel to the motion direction over a horizontal line of a length of 44 mm. According to the actual target elongation the beam direction was instantaneously adapted by the lateral tracking system [2]. A second irradiation was done with the same irradiation plan but static phantom as reference. The measurements of the ion beam induced β^+-activity in the target were performed during the irradiation which lasted about 85 s and for additional 5 min with ongoing target motion (or static target for the reference). The decay events of both, the moving and static target measurement were backprojected by the 3D algorithm under consideration of the detector efficiency and an attenuation correction. For the 4D backprojection of the moving target experiment the listmode data were sorted by amplitude of the recorded and locally sine-fitted target position into 9 motion phases. For each of them a 3D backprojection was calculated with a corresponding attenuation correction and the 9 results were coregistered onto the average location.

Results

The resulting β^+-activity distributions containing about 8×10^6 events and the profiles along the motion and beam scanning direction at the depth of the Bragg peak are shown in figure 1. The 4D backprojection looks similar to the static reference with the steep lateral activity fall-off. The maximum difference along the profile between the 4D backprojection and the 3D backprojection of the static target is only about 4 % and is located outside the high activity region in the target. An obvious difference can be found for the 3D evaluation. Because of the unconsidered target motion the activity is smeared beyond the lateral phantom margins while the high activity region in the center of the target is limited to a narrower range. This results in a difference to the static reference along the profile within the target of up to 17 %. The changes of the shape of the lateral field extension compared to the static reference can be described by the width of the 80 % - 20 % lateral fall-off region. It almost doubles from 7.6 mm for the reference to 14.2 mm for the uncorrected evaluation and stays approximately constant with 8.3 mm for the time-resolved in-beam PET measurement.

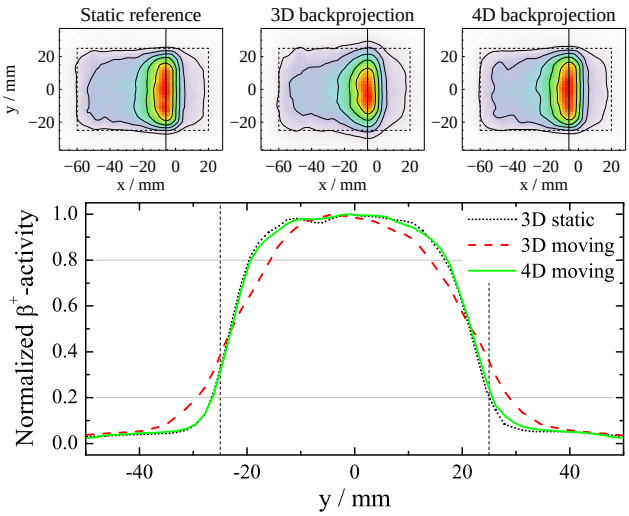

Figure 1: Top: color coding of the top view of the activity distributions in the target (dashed) for the static reference (left) as well as 3D (middle) and 4D (right) backprojection of the moving phantom with the incident beam coming from the left. Bottom: normalized profiles along the vertical solid lines (top) at the Bragg peak depth of 54 mm in the targets.

Conclusion

A 4D activity reconstruction is necessary for in-beam PET of complex moving target irradiation since even for a simple one-dimensional motion with only a small amplitude the real dose distribution could not be identified. Further investigations on in-beam PET measurements of more complex targets and motion patterns are necessarily required.

References

[1] W. Enghardt *et al.*, Nucl. Instr. Meth. A 525, 2004, pp. 284–8
[2] C. Bert *et al.*, Med. Phys. 34, 2007, pp. 4768–71

Motion tracking using MV-fluoroscopy*

P. Steidl[1], J. Bürkelbach[2], D. Richter[1], D. Müssig[1], G. Sroka-Perez[2], Th. Haberer[3], M. Durante[1], and Ch. Bert[1]

[1]GSI, Darmstadt, Germany; [2]Heidelberg University Hospital, Heidelberg, Germany; [3]HIT, Heidelberg, Germany

For radiotherapy of organs influenced by respiratory motion using a scanned particle beam [1] rescanning [2], gating [3], and beam tracking [4] have been proposed. For gating and especially for beam tracking a high tumor conformity of the applied dose distribution can be achieved. One requirement to reach this goal is precise motion monitoring during treatment delivery and investigation of tumor motion before treatment to allow a suitable treatment planning.

To date, most of the patients with tumors in moving organs (e.g. lung, liver and pancreas) are treated with MV-photon irradiation. Precise information of the tumor motion during treatment delivery can be determined by orthogonal kV x-ray fluoroscopy with the drawback of administering additional radiation dose to the patient. As an alternative with less spatial information but without additional dose MV-fluoroscopy can be used by detecting the irradiation exiting the patient during normal treatment [5].

To prepare data acquisition for patients an initial phantom study was performed. Using the SIEMENS ARTISTE photon accelerator at the Kopfklinik Heidelberg MV-fluorocsopic images of a sliding table were taken. This sliding table is able to move sinusoidally with an amplitude of 1.5–2.5 cm and a period of 2–5 s. A few little screws were used as fiducial markers. The phantom was irradiated by a $20 \times 20\,\mathrm{cm}^2$ field of 6 MV photons and the transmitting irradiation was detected with the ARTISTE's flat panel detector (EPID - s. fig. 2). Amplitude and period were varied.

For data analysis software has been developed which extracts the frames from the fluoroscopy data and tracks within a predefined region of interest the marker in each frame. Figure 3 shows as an example four frames of a fluoroscopic image sequence. One can see that the code is able to track the marker (darker circle) which is true for all measured data. An example of an extracted trajectory is shown in figure 1.

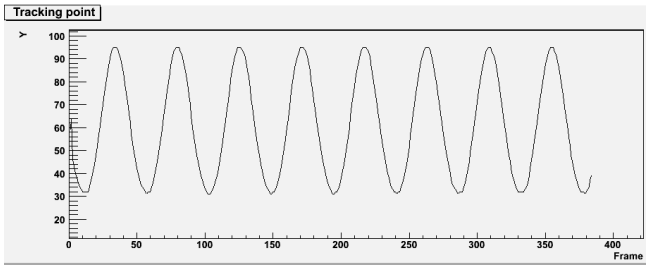

Figure 1: Example of an extracted trajectory. The pixel-shift in y is plotted against the frame number.

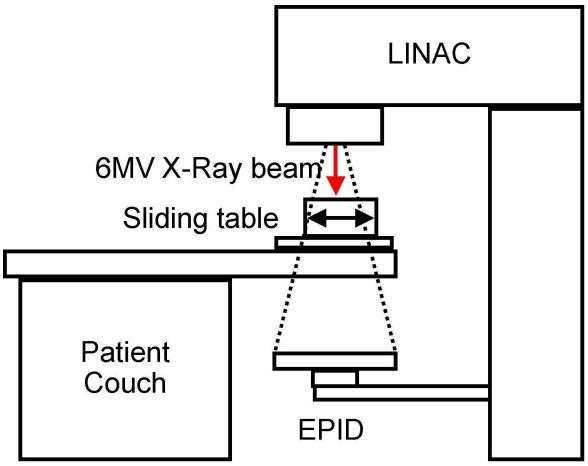

Figure 2: Scetch of the setup.

References

[1] T. Haberer, W. Becher, and D. Schardt (1993), Nucl. Instrum. Meth. A 330, p. 296

[2] M. H. Phillips, E. Pedroni, H. Blattmann, T. Boehringer, A. Coray, and S. Scheib (1992), Phys Med Biol 37, p. 223

[3] S. Minohara, T. Kanai, M. Endo, K. Noda, and M. Kanazawa (2000), Int J Radiat Oncol 47, p. 1097

[4] C. Bert, N. Saito, A. Schmidt, N. Chaudhri, D. Schardt, and E. Rietzel (2007), Med Phys 34:12, p. 4768

[5] J. Wilbert, J. Jurgen Meyer, K. Baier, M. Guckenberger, Ch. Herrmann, R. Hess, Ch. Janka, L. Ma, T. Mersebach, A. Richter, M. Roth, K. Schilling, and M. Flentje (2008), Med Phys 35:9, p. 3911

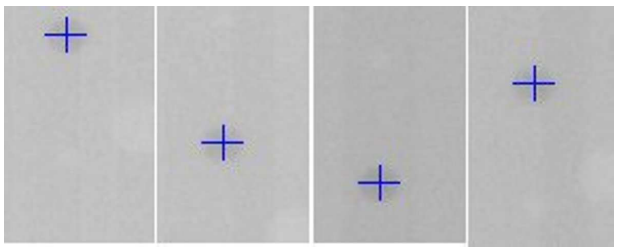

Figure 3: Example of regions of interest extracted from four frames of a fluoroscopy sequence. The cross marks the found tracking point which matches the marker position.

*Supported by the German Research Foundation (DFG), Clinical Research Unit 214

Intensity controlled mechanical scanning for heavy ion experiments

C. Schuy[1], M. Durante[1], and D. Schardt[1]
[1]GSI, Darmstadt, Germany

The planned SIS100 synchrotron of the future FAIR facility makes high demands on the experimental setup of the proposed BIOMAT cave [1] due to the high energies it will provide. To satisfy these demands with regard to a scanning system, a new mechanical target scanning system was developed and tested.

Concept

In contrast to the magnet raster scanning system, where the beam is actively moved to the next raster point when the planned number of particles is detected [2], the target scanner moves the target to the appropriate position using fast, position controlled, linear motors [3] and a special target holder.

Operation method

Digital inputs of the step motor drivers are wired to the NXT-output (Next Point), which is sent if a raster point's planned number of particles is reached, of SAMS [4]. The drivers are programmed in a way that, that each time they detect a NXT signal the target is moved one step in the horizontal direction. After a planned number of signals occurred, the drivers trigger a line break and a new line is irradiated.

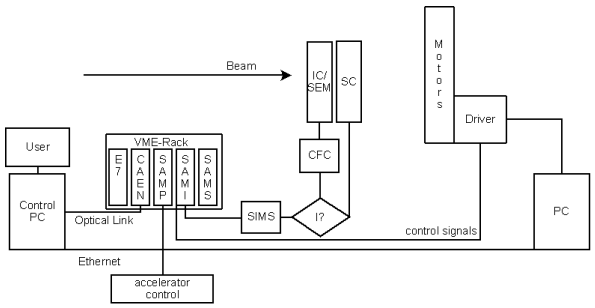

Figure 1: Schematic diagram of the target scanning system.

On-line experiments with ^{12}C beams

A performance test of the target scanning system and a comparison with the magnetic scanning system, used in GSI, was realized during a beam time in August 2009 in cave M.

Homogeneity test

A 44x44 mm^2 area was scanned using different step sizes and compared to the established raster scanner. The homogeneity in the region of interest is on a comparable level regardless of the scanning technique used and above 95%.

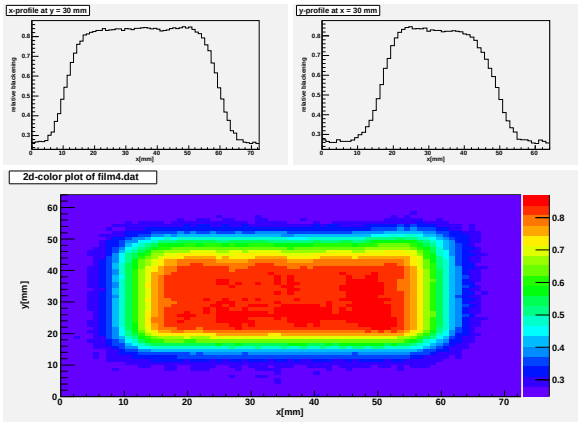

Figure 2: 2d-color plot of target scanning using 2 mm step size.

Speed test

To test the number of NXT signals per spill the target scanning system can handle, a plan with 2 mm step size was irradiated using different beam intensities. The experiments showed that the target scanning system can handle approximately 25 NXT per spill which is about one order of magnitude less than the magnetic scanner can handle.

References

[1] BIOMAT Project Group, "High-Energy Irradiation Facility for Biophysics and Materials Research.", www.gsi.de/fair/experiments/biomat/TP_BIOMAT_final.pdf, 2005

[2] P. Steidl, "A new control system for the high-energy raster-scan facility at GSI and precision measurements of Bragg ionisation function." Diploma Thesis, 2008

[3] Nami Saito et al., "Speed and accuracy of a beam tracking system for treatment of moving targets with scanned ion beams.", Phys. Med. Biol., PMB/31095/PAP/225077, 2009

[4] Jan Hoffmann, "Steuerungs- und Auslesemodul - technische Spezifikation GSI", 2008

Fast adaptation of ion beam range for beam tracking: beam characterization*

N. Chaudhri[1], N. Saito[1], C. Bert[1], B. Franczak[1], P. Steidl[1], E. Rietzel[2], and D. Schardt[1]
[1]GSI, Darmstadt, Germany; [2]Siemens AG, Erlangen, Germany

Introduction

An ion-optical based fast adaptation of ion beam range for the treatment of moving targets with beam tracking was investigated. The method employs a deflection of the ion beam on a small single wedge-degrader positioned between two bending magnets for range adaptation [1, 2]. A prototype system was implemented at the therapy beam line at GSI and beam parameters of energy-adapted beams were characterized.

Material and Methods

The prototype system for the fast adaptation of ion beam range utilizes the bending magnets of the therapy beam line. Two types of wedge-degraders (size: $62\times62\,mm^2$) for the beam energy adaptation were considered, i.e. ramp-degraders and stair like step-degraders. The degraders were made of PMMA (density=$\sim$1.165 mg/cm^3) and each of the two was constructed with two different designs (ramp slopes: R_3=0.33 and R_5=0.53; three steps S_3 and eight steps S_{pyr}; maximum thickness: 34 mm PMMA). The degraders were mounted at a suitable beam waist between the bending magnets using high vacuum capable and electronically controllable positioners.

To minimize energy broadening of the beam through the ramp-degrader and also the beam transmission, the ion-optical settings of the beam line were modified. In particular, a very small beam focus on the degrader was aimed. This was performed with the beam line analysis and design program MIRKO [3]. For The optimized settings energy degradation and transport of adapted beam were simulated using MOCADI [4].

Experiments were performed for carbon ion beams with an initial energy of E_i $\sim$200 MeV/u. During the experiments, the modification of magnets' settings, i.e. beam deflection and alignment of the adapted beam was controlled with MIRKO. The beam energy adaptation calculated in simulations for E_i were used in experiments. Multi-wire position grids within the beam line and at isocenter were employed for measuring beam lateral profiles. Depth dose profiles at the range of the adapted beam were acquired by measuring Bragg peak with a range telescope.

The measured lateral and depth profiles (in the Bragg peak region) of the adapted beam were quantified for size by fitting the measured data with a Gaussian distribution. The results are denoted as full width at half maximum (FWHM).

* We thank for the support provided by Siemen AG, Healthcare Sector, Particle Therapy, Germany

Results

Beam deflections of up to $\pm$24 mm on wedge-degraders were performed. The beam focus was stable on each beam-deflection and the mean spot size at the degrader position was $\sim$4 mm FWHM.

At isocenter, the beam spot size was 5–11 mm FWHM. The beam distribution with the step-degrader was of Gaussian shape whereas with the ramp-degrader the distribution was of widened bottoms in comparison to Gaussian shape.

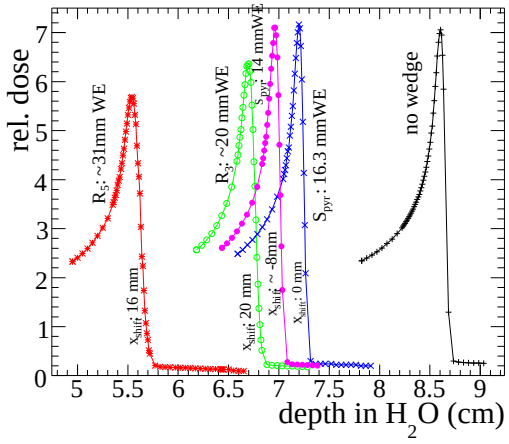

Figure 1: The adapated beam range in water corresponds to the position of the deflected beam on the degrader.

With the employed degraders range adaptation of up to $\pm$15 mm WE was achieved. The computed mean range FWHM using ramp-degraders was $\sim$1.8 mm WE and $\sim$1.3 mm WE for R_5 and R_3, respectively. The difference between measured and nominal range was $\leq$0.3 mm WE. Figure 1 shows the measured Bragg peaks at isocenter for different deflected positions (x_{shift}) on various degraders. The step-degraders showed Bragg peak characteristics comparable to measurements without a degrader while ramp-degraders produced Bragg peaks with broader width and lower height.

The results show the feasibility of the method for range adaptation in beam tracking for moving targets. Further investigations to optimize this method are in progress.

References

[1] N. Chaudhri et al., GSI Report 2007:p.382(2008)
[2] R. Pleskac et al., GSI Report 2007:p.383(2008)
[3] B. Franczak B., Europhysics Conference: v.215(1984)
[4] T. Schwab, PhD Thesis, Universität Giessen(1991)

Dosimetric Studies for Rescanning in scanned particle therapy*

D. Müssig[1], M. Durante[1], and C. Bert[1]
[1]GSI, Biophysics, Darmstadt, Germany

Introduction

Treatment of moving targets can result in local over and under dosage due to interference effects of the beam application and the motion of the target, so called interplay. Rescanning is one option to mitigate effects of tumor motion in scanned particle therapy [1, 2]. Rescanning is based on statistical methods that show that the dosimetric effect of interplay will average and lead to a homogeneous coverage of the clinical target volume if a sufficiently high number of rescans and margins that cover for the motion extent are used. [3].

Beam application in the rescan-mode sets new demands on deflecting magnets, energy variation, and dosimetry because ideally the treatment time is conserved when re-irradiating each point by the number of rescans with proportionally reduced irradiation time and dose per run. Therefore we performed dosimetric studies with the rescan implementation at the carbon therapy cave of GSI to investigate if the dose can be delivered as prescribed.

Material & Methods

A target area of 100 x 100 mm^2 was planned to be irradiated homogeneously (treatment plan parameters: single energy 200.28 MeV/u, 3 x 3 mm^2 raster point grid, 6.7 mm lateral beam full width at half maximum, scan path: horizontal lines, $5 \cdot 10^5$ particles per beam position) with different number of rescans (5-19x, two independent measurements per rescan). We used several detectors to determine the dose among them an array of 24 ionization chambers [4] within the target region and a Farmer chamber [5] in the entrance channel. The detectors were arranged without overlap in beam's eye view as indicated in figure 1.

To isolate the dosimetric impact of rescanning all experiments were performed without target motion. In addition, we normalized the dose readings from rescan irradiations by the outcome of a conventional irradiation as formerly used for patient treatments to exclude e.g. calibration uncertainties of the ionization chambers.

Results

Figure 2 shows the results for the Farmer chamber and the average values for the ionization chamber array. Deviations from the conventional delivery mode are smaller than 2%. No linear correlation of the dosimetric outcome with the number of rescans (Pearson's r-test, $p < 0.01$) was observed.

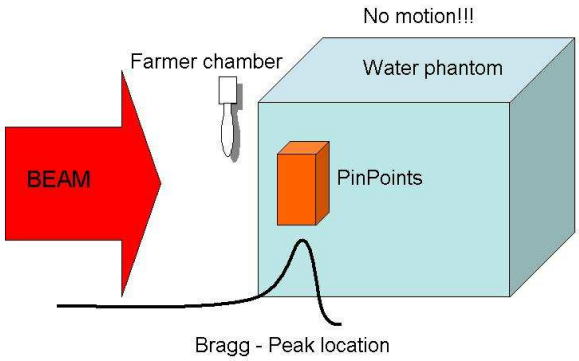

Figure 1: Schematic of the experimental setup.

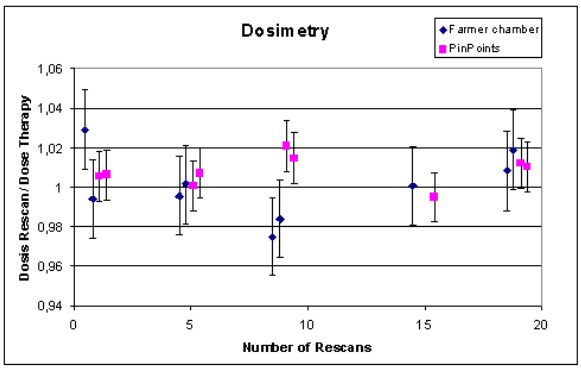

Figure 2: The dose in the rescan mode showed no linear correlation with the number of rescans. The values are distributed around the rescan numbers for visualization purposes.

Conclusion

Initial tests showed that the application of a treatment plan in rescan mode causes no deviations with respect to the delivered dose. Further investigations with intensity modulated plans of patient treatments will follow.

References

[1] Bert et al., *Phys. Med. Biol.* **53** (2008), 2253 -2265
[2] Phillips et al., *Phys. Med. Biol.* **37** (1992) 223-243
[3] Bortfeld et al., *Phys. Med. Biol.* **47** (2002) 2203-2220
[4] Karger et al., *Med. Phys*. **26** (1999), 2125-2132
[5] Farmer Ionisation Chamber 30001, PTW Freiburg

* This work is in part supported by Siemens AG, Particle Therapy and the EU-FP7 project ULICE (Union of Light Ion Centres in Europe)

The Status of the FIRST Project

R. Pleskac[1], C. Agodi[2], O. Angerer[3], T. Aumann[1], G. Battistoni[4], S. Bianchin[1], T.T. Böhlen[14], K. Boretzky[1], A. Boudard[8], G.A.P. Cirrone[2], M. Combet[8], G. Cuttone[2], M. DeNapoli[2], J.-E. Ducret[8], M. Durante[1], F. Haas[11], M. Heil[1], E. Iarocci1[2], A. Kelic-Heil[1], M. Labalme[9], P. Legou[8], S. Leray[8], A. Mairani[4], F.P. Marchetto[13], V. Monaco[13], M.C. Morone[5], A. Mostacci[7], P. Nieminen[3], V. Patera[12], G. Raciti[2], E. Rapisarda[2], C. Ray[10], M.V. Ricciardi[1], F.P. Romano[2], R. Sacchi[13], P. Sala[4], M.-D. Salsac[8], G. Santin[3], A. Sarti[12], D. Schardt[1], C. Scheidenberger[1], A. Sciubba[12], C. Sfienti[2], H. Simon[1], E. Spiriti[6], and M. Winkler[1]

[1]GSI Helmholtzzentrum für Schwerionenforschug GmbH, Darmstadt, Germany; [2]INFN - Laboratori Nazionali del Sud, Catania, Italy; [3]ESA - European Space Research & Technology Centre (ESTEC), Noordwijk, Netherlands; [4]INFN – Sezione di Milano, Milano, Italy; [5]INFN – Sezione di Roma Tor Vergata, Rome, Italy; [6]INFN – Sezione di Roma Tre, Rome, Italy; [7]Università degli Studi di Roma "La Sapienza", Roma, Italy; [8]DSM/IRFU/SPhN CEA Saclay, Gif sur Yvette, France; [9]Laboratoire de Physique Corpusculaire de Caen, Caen, France; [10]Institut de Physique Nucleaire de Lyon, Villeurbanne, France; [11]Institut Pluridisciplinaire Hubert Curien, Strasbourg, France; [12]INFN - Laboratori Nazionali di Frascati, Frascati (Rome), Italy; [13]INFN – Sezione di Torino, Torino, Italy; [14]CERN – European Organization for Nuclear Research, Geneve, Switzerland

The study of fragmentation processes is relevant in different fields of physics concerning both basic research as well as applications. We plan to fill the lack of experimental data and propose to perform extensive measurements on projectile fragmentation of ^{12}C and ^{16}O beams at intermediate energies (200-1000 MeV/u) on several thin targets (C, Si and Au). The GSI accelerator facility in combination with an extended version of the ALADiN and the LAND detector set-up offers the unique opportunity to perform high-accuracy measurements by studying projectile fragmentation products in coincidence. Different reaction mechanisms can be better understood via the analysis of the total and double differential cross sections as a function of the energy and the opening angle relative to the beam. The data set we plan to obtain is highly relevant for the benchmarking of different Monte Carlo codes. The future treatment planning systems for hadrontherapy are supposed to be fully Monte Carlo based codes.

The proposed experimental setup considers many different detectors or components working in a harmony: the target chamber in front of the magnet, the ALADiN magnet and the TP-MUSIC IV, the ALADiN ToF Wall and the LAND behind the magnet. All detectors operating either in the vacuum or in a gas (apart the LAND) have to be applied to extract full information on the detected particles on the event-by-event basis. The primary beam delivered from the SIS-18 accelerator is hitting a start scintillator and then analyzed by the beam gaseous monitor and with a certain probability doing a reaction in a thin solid target. Behind the target the primary beam particles or very forward (heavier) reaction products are registered first in the silicon vertex detector, analyzed in the ALADiN magnetic field and at the end detected by one of detectors described above. Compared to that lightest reaction products emitted under big opening angles have not to be necessarily registered in the silicon vertex detector, but with in the highest probability in a mall or big Si-CsI hodoscope or in a calorimeter covering even larger angles. The main aim is to extend the angular acceptance of the proposed setup mainly for protons.

The FIRST project [1,2] (Fragmentation of Ions Relevant for Space and Therapy) is an international collaboration between 14 institutes and universities from Germany, Italy, France, Netherlands and Switzerland.

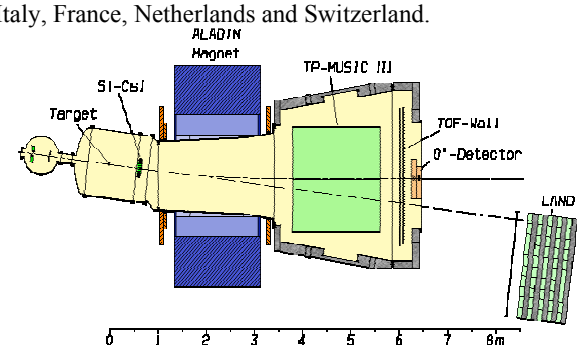

Figure 1: The ALADiN experimental setup together with the LAND.

The collaboration was formed at GSI in December 2008 and in February 2009 a proposal for the FIRST experiments was already presented in front of the G-PAC and approved. Preparative works are planned for 2009 and 2010 in cave B and main experiments during 2011 in cave C. The former ALADiN detector setup has to be completely restarted after many years of inactivity and therefore a basic check up of its certain parts, especially the TP-MUSIC IV chamber or the ALADiN ToF wall is mandatory.

References

[1] FIST Collaboration, "Extensive Study of Nuclear Reactions of Interest for Medical and Space Applications", Project Proposal, January 2009

[2] R.Pleskac et al., "FIRST Project", XLVIII International Winter Meeting on Nuclear Physics, Bormio, Italy, January 2010

Status of the ESA projects at GSI

M. Durante[1, 2], D. Schardt[1], S. Metzger[3] and O. Angerer[4]
[1]GSI, Darmstadt, Germany, [2]Techinical University of Darmstadt, Germany, [3]Fraunhofer Institute, Euskirchen, Germany, [4]ESA-ESTEC, Nordwijk, The Netherlands

Introduction

GSI is currently running different projects sponsored by the European Space Agency (ESA) on the effects of space radiations in humans and on microelectronics. The programs started in 2008 [1] and continued in 2009 with several experiments run by external user with the support of the GSI Biophysics group. The Annex building that was used in the past for the particle therapy program run at GSI is now been converted in an ESA laboratory for external users performing experiments in space radiation biology, physics, and electronics.

Space radiobiology

The radiobiology study launched in 2008 following the recommendations of the IBER study group [2] has selected 13 research proposals which started to perform experiments at GSI on different systems. Beams of C and Fe-ions were provided at energies between 11 and 1000 MeV/n. A total of 30 shifts were used by external users, with 110 samples exposed at UNILAC, and 295 at SIS. Figs. 1 and 2 show two examples of experiments within the IBER project.

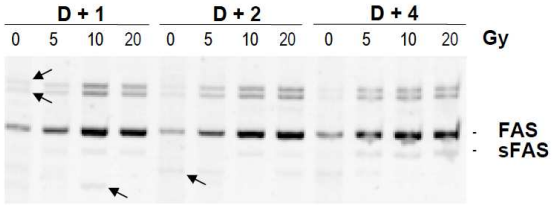

Figure 1: First example of alternative splicing in human genes following exposure to heavy ions. Electrophoresis of RT-PCR amplification products of the FAS transcripts. SK-N-BE cells were irradiated with iron ions (1 GeV/n) at the indicated doses and harvested at the indicated times. FAS and sFAS indicate the products of amplification of membrane associated and soluble FAS receptor, respectively. Arrows indicate the presence of amplification products of unexpected sizes, i.e. alternative splicing of this gene, which is in the apoptosis pathway. Photo kindly provided by Dr. Charles Lambert (University of Liege, Belgium), experiment AO-IBER-18 (CORALS).

New experiments within the IBER program are already scheduled in Spring 2010 using N and Ni-ions at energies between 400 and 1000 MeV/n.

Radiation damage to microelectronics

Effects of relativistic heavy ions on microelectronics components have been measured within the project led by the Fraunhofer Institute for Technological Trend

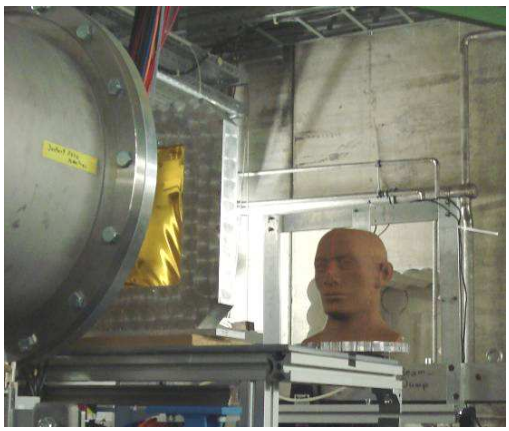

Figure 2: Irradiation of the MATROSHKA phantom in Cave A at the SIS accelerator. MATROSHKA is filled with several active and passive detectors and has been used in the past on the International Space Station to measure organ doses in low-Earth orbit. Photo kindly provided by Dr. Thomas Berger (DLR, Germany), experiment AO-IBER-12 (MATROSHKA).

Analysis using the GSI accelerator (Fig. 3). First experiments measured the cross-section for the induction of single-event upsets (SEU) in an ESA standard-microelectronic chip using Au ions at 1 GeV/n. The measurements of the cross sections were consistent with the results obtained using low-energy ions at similar LET. Experiments with uranium ions at 1 GeV/n are scheduled in 2010.

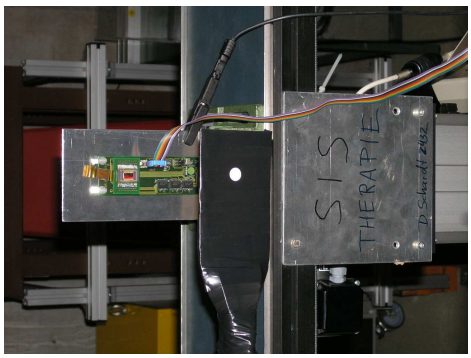

Figure 3: Irradiation of the ESA SEU monitor at the SIS accelerator. A scintillator is placed in from of the motherboard for fluence measurements. Photo by Fraunhofer Institute.

References

[1] M. Durante *et al. GSI Rep.* (2008) 404
[2] M. Durante *et al.*, *Adv. Space Res*. **39** (2007) 1082-1086

WoS publications to the programme 'Physics of hadrons and nuclei' (incl. the FAIR project) published in 2009

Compiled by K. Große, BuD

001 Abraamyan, K. U.; Friesen, A. V.; Kozhin, M. A.; Nikitin, S. A.; Reznikov, S. G.; Baznat, M. I.; Gudima, K. K.; Lebedev, S. A.*; Nazarenko, M. A.; Ososkov, G. A.; Sissakian, A. N.; Sorin, A. S.; Toneev, V. D.: **Resonance structure in the gamma gamma invariant mass spectrum in pC and dC interactions.** *Physical review C, Nuclear physics / Phys. Rev. C* **80**(3), 2009: 034001. DOI:10.1103/physrevc.80.034001

002 Abriola, D.; Bostan, M.; Erturk, S.; Fadil, M.; Galan, M.; Juutinen, S.; Kibedi, T.; Kondev, F.; Luca, A.; Negret, A.; Nica, N.; Pfeiffer, B.*; Singh, B.; Sonzogni, A.; Janos, T.; Tuli, J.; Venkova, T.; Zuber, K.: **Nuclear Data Sheets for A=84.** *Nuclear Data Sheets / Nucl. Data Sheets* **110**(11), 2009: 2815–+. DOI:10.1016/j.nds.2009.10.002

003 Adamian, G. G.*; Antonenko, N. V.*; Scheid, W.: **Production of new superheavy nuclei in complete fusion reaction.** *Acta physica Polonica B, Particle physics and field theory, nuclear physics, theory of relativity / Acta Phys. Pol. B* **40**(3), 2009: 737–740. URL OPEN ACCESS.

004 Adamova, D.; Agakichiev, G.*; Antonczyk, D.; Appelshäuser, H.*; Belaga, V.; Bielcikova, J.; Braun-Munzinger, P.*; Busch, O.; Cherlin, A.; Damjanovic, S.; Dietel, T.; Dietrich, L.; Drees, A.; Dubitzky, W.; Esumi, S. I.; Filimonov, K.; Fomenko, K.; Fraenkel, Z.; Garabatos, C.*; Glässel, P.; Holeczek, J.; Kalisky, M.; Kniege, S.; Kushpil, V.; Maas, A.*; Marin, A.*; Milosevic, J.; Milov, A.; Miskowiec, D.*; Panebrattsev, Y.; Petchenova, O.; Petracek, V.; Pfeiffer, A.; Ploskon, M.*; Rak, J.; Ravinovich, I.; Rehak, P.; Sako, H.*; Schmitz, W.; Schuchmann, S.; Sedykh, S.*; Shimansky, S.; Stachel, J.; Sumbera, M.; Tilsner, H.; Tserruya, I.; Wessels, J. P.; Wienold, T.; Wurm, J. P.; Xie, W.; Yurevich, S.; Yurevich, V.: **Modification of jet-like correlations in Pb-Au collisions at 158A GeV/c.** *Physics letters B / Phys. Lett. B* **678**(3), 2009: 259–263. DOI:10.1016/j.physletb.2009.05.048

005 Agakichiev, G.; Agodi, C.; Alvarez-Pol, H.; Atkin, E.; Badura, E.*; Balanda, A.; Bassi, A.; Bassini, R.; Bellia, G.; Belver, D.; Belyaev, A. V.; Benovic, M.; Bertini, D.*; Bielcik, J.*; Böhmer, M.; Boiano, C.; Bokemeyer, H.*; Bartolotti, A.; Boyard, J. L.; Brambilla, S.; Braun-Munzinger, P.*; Cabanelas, P.; Castro, E.; Chepurnov, V.; Chernenko, S.; Christ, T.; Coniglione, R.; Cosentino, L.; Dahlinger, M.*; Daues, H. W.*; Destefanis, M.; Diaz, J.; Dohrmann, F.; Dressler, R.; Duran, I.; Dybczak, A.; Eberl, T.; Enghardt, W.; Fabbietti, L.; Fateev, O. V.; Fernandez, C.; Finocchiaro, P.; Friese, J.; Fröhlich, I.; Fuentes, B.; Galatyuk, T.*; Garabatos, C.*; Garzon, J. A.; Genolini, B.; Gernhäuser, R.; Gilardi, C.; Gilg, H.; Golubeva, M.; Gonzalez-Diaz, D.*; Grosse, E.; Guber, F.; Hehner, J.*; Heidel, K.; Heinz, T.*; Hennino, T.; Hlavac, S.; Hoffmann, J.*; Holzmann, R.*; Homolka, J.; Hutsch, J.; Ierusalimov, A. P.; Iori, I.; Ivashkin, A.; Jaskula, M.; Jourdain, J. C.; Jurkovic, M.; Kämpfer, B.; Kajetanowicz, M.; Kanaki, K.; Karavicheva, T.; Kastenmüller, A.; Kidon, L.; Kienle, P.; Kirschner, D.; Koenig, I.*; Koenig, W.*; Körner, H. J.; Kolb, B. W.*; Kopf, U.*; Korcyl, K.; Kotte, R.; Kozuch, A.; Krizek, F.; Krücken, R.; Kühn, W.; Kugler, A.; Kulessa, R.; Kurepin, A.; Kurtukian-Nieto, T.; Lang, S.*; Lange, J. S.; Lapidus, K.; Lehnert, J.; Leinberger, U.*; Lichtblau, C.; Lins, E.; Lippmann, C.; Lorenz, M.; Magestro, D.*; Maier, L.; Maier-Komor, P.; Maiolino, C.; Malarz, A.; Marek, T.; Markert, J.; Metag, V.; Michalska, B.; Michel, J.; Migneco, E.; Mishra, D.; Moriniere, E.; Mousa, J.; Münch, M.*; Müntz, C.*; Naumann, L.; Nekhaev, A.; Niebur, W.*; Novotny, J.; Novotny, R.; Ott, W.*; Otwinowski, J.; Pachmayer, Y. C.; Palka, M.*; Parpottas, Y.; Pechenov, V.; Pechenova, O.; Cavalcanti, T. P.; Petri, M.; Piattelli, P.; Pietraszko, J.*; Pleskac, R.; Ploskon, M.; Pospisil, V.; Pouthas, J.; Prokopowicz, W.; Przygoda, W.; Ramstein, B.; Reshetin, A.; Ritman, J.; Roche, G.; Rodriguez-Prieto, G.; Rosenkranz, K.; Rosier, P.; Roy-Stephan, M.; Rustamov, A.*; Sabin-Fernandez, J.; Sadovsky, A.; Sailer, B.; Salabura, P.; Salz, C.; Sanchez, M.; Sapienza, P.; Schäfer, D.; Schicker, R. M.*; Schmah, A.*; Schön, H.*; Schön, W.*; Schroeder, C.*; Schroeder, S.; Schwab, E.*; Senger, P.*; Shileev, K.; Simon, R. S.*; Skoda, M.; Smolyankin, V.; Smykov, L.; Sobiella, M.; Sobolev, Y. G.; Spataro, S.; Spruck, B.; Stelzer, H.*; Ströbele, H.; Stroth, J.*; Sturm, C.; Sudol, M.; Suk, M.; Szczybura, M.; Taranenko, A.; Tarantola, A.; Teilab, K.; Tiflov, V.; Tikhonov, A.; Tlusty, P.; Toia, A.; Traxler, M.*; Trebacz, R.; Troyan, A. Y.; Tsertos, H.; Turzo, I.; Ulrich, A.; Vassiliev, D.; Vazquez, A.; Volkov, Y.; Wagner, V.; Wallner, C.; Walus, W.; Wang, Y.; Weber, M.*; Wieser, J.; Winkler, S.; Wisniowski, M.; Wojcik, T.; Wüstenfeld, J.; Yurevich, S.*; Zanevsky, Y. V.; Zeitelhack, K.; Zentek, A.; Zhou, P.; Zovinec, D.*; Zumbruch, P.*; HADES Collaboration: **The high-acceptance dielectron spectrometer HADES.** *The European physical*

journal A, Hadrons and nuclei / Eur. Phys. J. A **41**(2), 2009: 243–277. DOI:10.1140/epja/i2009-10807-5

006 Agakishiev, G.; Agodi, C.; Balanda, A.; Bellia, G.; Belver, D.; Belyaev, A.; Bielcik, J.*; Blanco, A.; Bortolotti, A.; Boyard, J. L.; Braun-Munzinger, P.*; Cabanelas, P.; Chernenko, S.; Christ, T.; Coniglione, R.; Destefanis, M.; Diaz, J.; Dohrmann, F.; Duran, I.; Dybczak, A.; Eberl, T.; Fabbietti, L.; Fateev, O.; Ferreira-Marques, R.; Finocchiaro, P.; Fonte, P.; Friese, J.; Fröhlich, I.; Galatyuk, T.*; Garzon, J. A.; Gernhäuser, R.; Gil, A.; Gilardi, C.; Golubeva, M.; Gonzalez-Diaz, D.*; Grosse, E.; Guber, F.; Heilmann, M.; Heinz, T.*; Hennino, T.; Holzmann, R.*; Ierusalimov, A.; Iori, I.; Ivashkin, A.; Jurkovic, M.; Kämpfer, B.; Kanaki, K.; Karavicheva, T.; Kirschner, D.; Koenig, I.*; Koenig, W.*; Kolb, B. W.*; Kotte, R.; Kozuch, A.; Krasa, A.; Krizek, F.; Krücken, R.; Kühn, W.; Kugler, A.; Kurepin, A.; Lamas-Valverde, J.; Lang, S.*; Lange, J. S.; Lapidus, K.; Lopes, L.; Lorenz, M.; Maier, L.; Maiolino, C.; Mangiarotti, A.; Marin, J.; Markert, J.; Metag, V.; Michalska, B.; Michel, J.; Moriniere, E.; Mousa, J.; Münch, M.*; Müntz, C.; Naumann, L.; Novotny, R.; Otwinowski, J.; Pachmayer, Y. C.; Palka, M.*; Parpottas, Y.; Pechenov, V.; Pechenova, O.; Cavalcanti, T. P.; Piattelli, P.; Pietraszko, J.*; Pospisil, V.; Przygoda, W.; Ramstein, B.; Reshetin, A.; Roy-Stephan, M.; Rustamov, A.*; Sadovsky, A.; Sailer, B.; Salabura, P.; Sapienza, P.; Schmah, A.; Schroeder, C.*; Schwab, E.*; Simon, R. S.*; Sobolev, Y. G.; Spataro, S.; Spruck, B.; Ströbele, H.*; Stroth, J.*; Sturm, C.; Sudol, M.*; Tarantola, A.; Teilab, K.; Tlusty, P.; Traxler, M.*; Trebacz, R.; Tsertos, H.; Wagner, V.; Weber, M.; Wisniowski, M.; Wojcik, T.; Wüstenfeld, J.; Yurevich, S.; Zanevsky, Y.; Zhou, P.; Zumbruch, P.*; HADES Collaboration: **Measurement of charged pions in ^{12}C+^{12}C collisions at 1 A GeV and 2 A GeV with HADES.** *The European physical journal A, Hadrons and nuclei / Eur. Phys. J. A* **40**(1), 2009: 45–59. DOI:10.1140/epja/i2008-10746-7

007 Agakishiev, G.; Balanda, A.; Bannier, B.; Bassini, R.; Belver, D.; Belyaev, A. V.; Blanco, A.; Böhmer, M.; Boyard, J. L.; Braun-Munzinger, P.*; Cabanelas, P.; Castro, E.; Chernenko, S.; Christ, T.; Destefanis, M.; Diaz, J.; Dohrmann, F.; Dybczak, A.; Eberl, T.; Fabbietti, L.; Fateev, O. V.; Finocchiaro, P.; Fonte, P.; Friese, J.; Fröhlich, I.; Galatyuk, T.*; Garzon, J. A.; Gernhäuser, R.; Gil, A.; Gilardi, C.; Golubeva, M.; Gonzalez-Diaz, D.*; Guber, F.; Heilmann, M.; Heinz, T.*; Hennino, T.; Holzmann, R.*; Ierusalimov, A.; Iori, I.; Ivashkin, A.; Jurkovic, M.; Kämpfer, B.; Kanaki, K.; Karavicheva, T.; Kirschner, D.; Koenig, I.*; Koenig, W.*; Kolb, B. W.*; Kotte, R.; Krizek, F.; Krücken, R.; Kühn, W.; Kugler, A.; Kurepin, A.; Lang, S.*; Lange, J. S.*; Lapidus, K.; Liu, T.; Lopes, L.; Lorenz, M.; Maier, L.; Mangiarotti, A.; Markert, J.; Metag, V.; Michalska, B.; Michel, J.; Mishra, D.; Moriniere, E.; Mousa, J.; Müntz, C.; Naumann, L.; Otwinowski, J.; Pachmayer, Y. C.; Palka, M.*; Parpottas, Y.; Pechenov, V.; Pechenova, O.; Cavalcanti, T. P.; Pietraszko, J.*; Przygoda, W.; Ramstein, B.; Reshetin, A.; Roy-Stephan, M.; Rustamov, A.*; Sadovsky, A.; Sailer, B.; Salabura, P.; Schmah, A.; Schwab, E.*; Sobolev, Y. G.; Spataro, S.; Spruck, B.; Ströbele, H.*; Stroth, J.*; Sturm, C.; Sudol, M.; Tarantola, A.; Teilab, K.; Tlusty, P.; Traxler, M.*; Trebacz, R.; Tsertos, H.; Wagner, V.; Weber, M.; Wisniowski, M.; Wojcik, T.; Wüstenfeld, J.*; Yurevich, S.; Zanevsky, Y. V.; Zhou, P.; Zumbruch, P.*; HADES Collaboration: **ϕ decay: A relevant source for K^- production at energies available at the GSI Schwerionen-Synchrotron (SIS)?.** *Physical review C, Nuclear physics / Phys. Rev. C* **80**(2), 2009: 025209. DOI:10.1103/physrevc.80.025209

008 Agakishiev, G.; Balanda, A.; Bassini, R.; Belver, D.; Belyaev, A. V.; Blanco, A.; Böhmer, M.; Boyard, J. L.; Braun-Munzinger, P.*; Cabanelas, P.; Castro, E.; Chernenko, S.; Christ, T.; Destefanis, M.; Diaz, J.; Dohrmann, F.; Dybczak, A.; Eberl, T.; Fabbietti, L.; Fateev, O. V.; Finocchiaro, P.; Fonte, P.; Friese, J.; Fröhlich, I.; Galatyuk, T.; Garzon, J. A.; Gernhäuser, R.; Gil, A.; Gilardi, C.; Golubeva, M.; Gonzalez-Diaz, D.*; Guber, F.; Hennino, T.; Holzmann, R.*; Iori, I.; Ivashkin, A.; Jurkovic, M.; Kämpfer, B.; Kanaki, K.; Karavicheva, T.; Kirschner, D.; Koenig, I.*; Koenig, W.*; Kolb, B. W.*; Kotte, R.; Krizek, F.; Krücken, R.; Kühn, W.; Kugler, A.; Kurepin, A.; Lang, S.*; Lange, J. S.; Lapidus, K.; Liu, T.; Lopes, L.; Lorenz, M.; Maier, L.; Mangiarotti, A.; Markert, J.; Metag, V.; Michalska, B.; Michel, J.; Mishra, D.; Moriniere, E.; Mousa, J.; Müntz, C.; Naumann, L.; Otwinowski, J.; Pachmayer, Y. C.; Palka, M.*; Parpottas, Y.; Pechenov, V.; Pechenova, O.; Pietraszko, J.*; Przygoda, W.; Ramstein, B.; Reshetin, A.; Roy-Stephan, M.; Rustamov, A.*; Sadovsky, A.; Sailer, B.; Salabura, P.; Schmah, A.; Sobolev, Y. G.; Spataro, S.; Spruck, B.; Ströbele, H.; Stroth, J.*; Sturm, C.; Sudol, M.; Tarantola, A.; Teilab, K.; Tlusty, P.; Traxler, M.*; Trebacz, R.; Tsertos, H.; Wagner, V.; Weber, M.; Wisniowski, M.; Wojcik, T.; Wüstenfeld, J.* Yurevich, S.; Zanevsky, Y. V.; Zhou, P.; Zumbruch, P.*; HADES Collaboration: **Deep Subthreshold Xi(-) Production in Ar plus KCl Reactions at 1.76A GeV.** *Physical review letters / Phys. Rev. Lett.* **103**(13), 2009: 132301. DOI:10.1103/physrevlett.103.132301

009 Aksyutina, Y.*; Johansson, H. T.*; Aumann, T.*; Boretzky, K.*; Borge, M. J. G.; Chatillon, A.; Chulkov, L. V.*; Cortina-Gil, D.*; Pramanik, U. D.; Emling, H.*; Forssen, C.; Fynbo, H. O. U.; Geissel, H.*; Ickert, G.*; Jonson, B.; Kulessa, R.; Langer, C.*; Lantz, M.; LeBleis, T.*; Lindahl, A. O.; Mahata, K.*; Meister, M.; Münzenberg, G.*; Nilsson, T.; Nyman, G.; Palit, R.; Paschalis, S.; Prokopowicz, W.*; Reifarth, R.*; Richter, A.; Riisager, K.; Schrieder, G.; Simon, H.*; Sümmerer, K.*; Tengblad, O.; Weick, H.*; Zhukov, M. V.: **Properties of the ^{7}He ground state from ^{8}He neutron knockout.** *Physics letters B / Phys. Lett. B* **679**(3), 2009: 191–196. DOI:10.1016/j.physletb.2009.07.044

010 Al-Dahan, N.; Podolyak, Z.; Regan, P. H.; Gorska, M.*; Grawe, H.;* Maier, K. H.; Gerl, J.*; Pietri, S. B.; Wollersheim, H. J.*; Alkhomashi, N.; Deo, A. Y.; Bacelar, A. M. D.; Farrelly, G.; Steer, S. J.; Bruce, A. M.; Boutachkov, P.*; Domingo-Pardo, C.; Algora, A.; Benlliure, J.; Bracco, A.; Calore, E.; Casarejos, E.; Cullen, I. J.; Detistov, P.; Dombradi, Z.; Doncel, M.; Farinon, F.*; Gelletly, W.; Geissel, H.*; Goel, N.*; Grebosz, J.; Hoischen, R.*; Kojouharov, I.*; Kurz, N.*; Lalkovski, S.; Leoni, S.; Molina, F.; Montanari, D.; Morales, A. I.; Musumarra, A.; Napoli, D. R.; Nicolini, R.; Nociforo, C.*; Prochazka, A.*; Prokopowicz, W.*; Rubio, B.; Rudolph, D.*; Schaffner, H.*; Strmen, P.; Szarka, I.; Swan, T.; Thomas, J. S.; Valiente-Dobon, J. J.; Verma, S.; Walker, P. M.; Weick, H.*: **Nuclear structure "southeast" of ^{208}Pb: Isomeric states in ^{208}Hg and ^{209}Tl.** *Physical review C, Nuclear physics / Phys. Rev. C* **80**(6), 2009: 061302. DOI:10.1103/physrevc.80.061302

011 Al-Dahan, N.; Podolyak, Z.; Regan, P. H.; Steer, S. J.; Bacelar, A. M. D.; Alkhomashi, N.; Gorska, M.*; Gerl, J.*; Wollersheim, H. J.*; Pietri, S. B.*; Grawe, H.*; Deo, A. Y.; Farrelly, C.; Boutachkov, P.*; Domingo-Pardo, C.*; Algora, A.; Benlliure, J.; Bracco, A.; Bruce, A. M.; Calore, E.; Casarejos, E.; Cullen, I. J.; Detistov, P.; Dombradi, Z.; Doncel, M.; Farinon, F.; Geissel, H.*; Gelletly, W.; Goel, N.*; Grebosz, J.; Hoischen, R.; Kojouharov, I.*; Kurz, N.*; Lalkovski, S.; Leoni, S.; Molina, F.; Montanari, D.; Morales, A. I.; Musumarra, A.*; Napoli, D. R.; Nicolini, R.; Nociforo, C.*; Prochazka, A.*; Prokopowicz, W.*; Rubio, B.; Rudolph, D.*; Schaffner, H.*; Strmen, P.; Szarka, I.; Swan, T.; Valiente-Dobon, J. J.; Verma, S.; Walker, P. M.; Weick, H.*: **Isomeric states in ^{208}Hg and ^{209}Tl populated in fragmentation of ^{238}U.** *Acta physica Polonica B, Particle physics and field theory, nuclear physics, theory of relativity / Acta Phys. Pol. B* **40**(3), 2009: 871–874. URL OPEN ACCESS.

012 Alekseev, M.; Alexakhin, V. Y.; Alexandrov, Y.; Alexeev, G. D.; Amoroso, A.; Austregesilo, A.; Badelek, B.; Balestra, F.; Ball, J.; Barth, J.; Baum, G.; Bedfer, Y.; Bernhard, J.; Bertini, R.; Bettinelli, M.; Birsa, R.; Bisplinghoff, J.; Bordalo, P.; Bradamante, F.; Bravar, A.; Bressan, A.; Brona, G.; Burtin, E.; Bussa, M. P.; Chapiro, A.; Chiosso, M.; Chung, S. U.; Cicuttin, A.; Colantoni, M.; Crespo, M. L.; Dalla Torre, S.; Dafni, T.; Das, S.; Dasgupta, S. S.; Denisov, O. Y.; Dhara, L.; Diaz, V.; Dinkelbach, A. M.; Donskov, S. V.; Doshita, N.; Duic, V.; Dunnweber, W.; Efremov, A.; Eversheim, P. D.; Eyrich, W.; Faessler, M.; Ferrero, A.; Finger, M.; Finger, M.; Fischer, H.; Franco, C.; Friedrich, J. M.; Garfagnini, R.; Gautheron, F.; Gavrichtchouk, O. P.; Gazda, R.; Gerassimov, S.; Geyer, R.; Giorgi, M.; Gobbo, B.; Goertz, S.; Grabmuller, S.; Grajek, O. A.; Grasso, A.; Grube, B.; Gushterski, R.; Guskov, A.; Haas, F.; von Harrach, D.; Hasegawa, T.; Heckmann, J.; Heinsius, F. H.; Hermann, M.; Hermann, R.; Herrmann, F.; Hess, C.; Hinterberger, F.; Horikawa, N.; Hoppner, C.; d'Hose, N.; Ilgner, C.; Ishimoto, S.; Ivanov, O.; Ivanshin, Y.; Iven, B.; Iwata, T.; Jahn, R.; Jasinski, P.; Jegou, G.; Joosten, R.; Kabuss, E.; Kang, D.; Ketzer, B.; Khaustov, G. V.; Khokhlov, Y. A.; Kisselev, Y.; Klein, F.; Klimaszewski, K.; Koblitz, S.; Koivuniemi, J. H.; Kolosov, V. N.; Komissarov, E. V.; Kondo, K.; Konigsmann, K.; Konopka, R.; Konorov, I.; Konstantinov, V. F.; Korzenev, A.; Kotzinian, A. M.; Kouznetsov, O.; Kowalik, K.; Kramer, M.; Kral, A.; Kroumchtein, Z. V.; Kuhn, R.; Kunne, F.; Kurek, K.; Le Goff, J. M.; Lednev, A. A.; Lehmann, A.; Levorato, S.; Lichtenstadt, J.; Liska, T.; Maggiora, A.; Maggiora, M.; Magnon, A.; Mallot, G. K.; Mann, A.; Marchand, C.; Marroncle, J.; Martin, A.; Marzec, J.; Massmann, F.; Matsuda, T.; Maximov, A. N.; Meyer, W.; Michigami, T.; Mikhailov, Y. V.; Moinester, M. A.; Mutter, A.; Nagaytsev, A.; Nagel, T.; Nassalski, J.; Negrini, S.; Nerling, F.; Neubert, S.; Neyret, D.; Nikolaenko, V. I.; Olshevsky, A. G.; Ostrick, M.; Padee, A.; Panknin, R.; Panzieri, D.; Parsamyan, B.; Paul, S.; Pawlukiewicz-Kaminska, B.; Perevalova, E.; Pesaro, G.; Peshekhonov, D. V.; Piragino, G.; Platchkov, S.; Pochodzalla, J.; Polak, J.; Polyakov, V. A.; Pontecorvo, G.; Pretz, J.; Quintans, C.; Rajotte, J. F.; Ramos, S.; Rapatsky, V.; Reicherz, G.; Reggiani, D.; Richter, A.; Robinet, F.; Rocco, E.; Rondio, E.; Ryabchikov, D. I.; Samoylenko, V. D.; Sandacz, A.; Santos, H.; Sapozhnikov, M. G.; Sarkar, S.; Sbrizzai, G.; Schiavon, P.; Schill, C.; Schmitt, L.*; Schroder, W.; Shevchenko, O. Y.; Siebert, H. W.; Silva, L.; Sinha, L.; Sissakian, A. N.; Slunecka, M.; Smirnov, G. I.; Sosio, S.; Sozzi, F.; Srnka, A.; Stolarski, M.; Sulc, M.; Sulej, R.; Takekawa, S.; Tessaro, S.; Tessarotto, F.; Teufel, A.; Tkatchev, L. G.; Venugopal, G.; Virius, M.; Vlassov, N. V.; Vossen, A.; Weitzel, Q.; Windmolders, R.; Wislicki, W.; Wollny, H.; Zaremba, K.; Zemlyanichkina, E.; Ziembicki, M.; Zhao, J.; Zhuravlev, N.; Zvyagin, A.: **Measurement of the longitudinal spin transfer to Λ and $\bar{\Lambda}$ hyperons in polarised muon DIS.** *The European physical journal: C, Particles and fields / Eur. Phys. J. C* **64**(2), 2009: 171–179. DOI:10.1140/epjc/s10052-009-1143-7

013 Alekseev, M.; Alexakhin, V. Y.; Alexandrov, Y.; Alexeev, G. D.; Amoroso, A.; Austregesilo, A.; Badelek, B.; Balestra, F.; Ball, J.; Barth, J.; Baum, G.; Bedfer, Y.; Bernhard, J.; Bertini, R.; Bettinelli, M.; Birsa, R.; Bisplinghoff, J.; Bordalo, P.; Bradamante, F.; Bravar, A.; Bressan, A.; Brona, G.; Burtin, E.; Bussa, M. P.; Chapiro, A.; Chiosso, M.; Chung, S. U.; Cicuttin, A.; Colantoni, M.; Crespo, M. L.; Torre, S. D.; Dafni, T.; Das, S.; Dasgupta, S. S.; Denisov, O. Y.; Dhara, L.; Diaz, V.; Dinkelbach, A. M.; Donskov, S. V.; Doshita, N.; Duic, V.; Dunnweber, W.; Efremov, A.; El Alaoui, A.; Eversheim, P. D.; Eyrich, W.; Faessler, M.; Ferrero, A.; Finger, M.; Finger, M.; Fischer, H.; Franco, C.; Friedrich, J. M.; Garfagnini, R.; Gautheron, F.; Gavrichtchouk, O. P.; Gazda, R.; Gerassimov, S.; Geyer, R.; Giorgi, M.; Gobbo, B.; Goertz, S.; Grabmuller, S.; Grajek, O. A.; Grasso, A.; Grube, B.; Gushterski, R.; Guskov, A.; Haas, F.; Hagemann, R.; von Harrach, D.; Hasegawa, T.; Heckmann, J.; Heinsius, F. H.; Hermann,

R.; Herrmann, F.; Heß, C.; Hinterberger, F.; Horikawa, N.; Hoppner, C.; d'Hose, N.; Ilgner, C.; Ishimoto, S.; Ivanov, O.; Ivanshin, Y.; Iwata, T.; Jahn, R.; Jasinski, P.; Jegou, G.; Joosten, R.; Kabuss, E.; Kafer, W.; Kang, D.; Ketzer, B.; Khaustov, G. V.; Khokhlov, Y. A.; Kiefer, J.; Kisselev, Y.; Klein, F.; Klimaszewski, K.; Koblitz, S.; Koivuniemi, J. H.; Kolosov, V. N.; Komissarov, E. V.; Kondo, K.; Konigsmann, K.; Konopka, R.; Konorov, I.; Konstantinov, V. F.; Korzenev, A.; Kotzinian, A. M.; Kouznetsov, O.; Kowalik, K.; Krämer, M.; Kral, A.; Kroumchtein, Z. V.; Kuhn, R.; Kunne, F.; Kurek, K.; Le Goff, J. M.; Lednev, A. A.; Lehmann, A.; Levorato, S.; Lichtenstadt, J.; Liska, T.; Maggiora, A.; Maggiora, M.; Magnon, A.; Mallot, G. K.; Mann, A.; Marchand, C.; Marroncle, J.; Martin, A.; Marzec, J.; Massmann, F.; Matsuda, T.; Maximov, A. N.; Meyer, W.; Michigami, T.; Mikhailov, Y. V.; Moinester, M. A.; Mutter, A.; Nagaytsev, A.; Nagel, T.; Nassalski, J.; Negrini, S.; Nerling, F.; Neubert, S.; Neyret, D.; Nikolaenko, V. I.; Olshevsky, A. G.; Ostrick, M.; Padee, A.; Panknin, R.; Panzieri, D.; Parsamyan, B.; Paul, S.; Pawlukiewicz-Kaminska, B.; Perevalova, E.; Pesaro, G.; Peshekhonov, D. V.; Piragino, G.; Platchkov, S.; Pochodzalla, J.; Polak, J.; Polyakov, V. A.; Pontecorvo, G.; Pretz, J.; Quintans, C.; Rajotte, J. F.; Ramos, S.; Rapatsky, V.; Reicherz, G.; Reggiani, D.; Richter, A.; Robinet, F.; Rocco, E.; Rondio, E.; Ryabchikov, D. I.; Samoylenko, V. D.; Sandacz, A.; Santos, H.; Sapozhnikov, M. G.; Sarkar, S.; Savin, I. A.; Sbrizzai, G.; Schiavon, P.; Schill, C.; Schmitt, L.*; Schroder, W.; Shevchenko, O. Y.; Siebert, H. W.; Silva, L.; Sinha, L.; Sissakian, A. N.; Slunecka, M.; Smirnov, G. I.; Sosio, S.; Sozzi, F.; Srnka, A.; Stolarski, M.; Sulc, M.; Sulej, R.; Takekawa, S.; Tessaro, S.; Tessarotto, F.; Teufel, A.; Tkatchev, L. G.; Venugopal, G.; Virius, M.; Viassov, N. V.; Vossen, A.; Weitzel, Q.; Wenzl, K.; Windmolders, R.; Wislicki, W.; Wollny, H.; Zaremba, K.; Zavertyaev, M.; Zemlyanichkina, E.; Ziembicki, M.; Zhao, J.; Zhuravlev, N.; Zvyagin, A.; COMPASS Collaboration: **Flavour separation of helicity distributions from deep inelastic muon-deuteron scattering.** *Physics letters B / Phys. Lett. B* **680**(3), 2009: 217–224. DOI:10.1016/j.physletb.2009.08.065

014 Alekseev, M.; Alexakhin, V. Y.; Alexandrov, Y.; Alexeev, G. D.; Amoroso, A.; Austregisilio, A.; Badelek, B.; Balestra, F.; Ball, J.; Barth, J.; Baum, G.; Bedfer, Y.; Bernhard, J.; Bertini, R.; Bettinelli, M.; Birsa, R.; Bisplinghoff, J.; Bordalo, P.; Bradamante, F.; Bravar, A.; Bressan, A.; Brona, G.; Burtin, E.; Bussa, M. P.; Chapiro, A.; Chiosso, M.; Chung, S. U.; Cicuttin, A.; Colantoni, M.; Crespo, M. L.; Dalla Torre, S.; Dafni, T.*; Das, S.; Dasgupta, S. S.; Denisov, O. Y.; Dhara, L.; Diaz, V.; Dinkelbach, A. M.; Donskov, S. V.; Doshita, N.; Duic, V.; Dunnweber, W.; Efremov, A.; El Alaoui, A.; Eversheim, P. D.; Eyrich, W.; Faessler, M.; Ferrero, A.; Finger, M.; Finger, M.; Fischer, H.; Franco, C.; Friedrich, J. M.; Garfagnini, R.; Gautheron, F.; Gavrichtchouk, O. P.; Gazda, R.; Gerassimov, S.; Geyer, R.; Giorgi, M.; Gobbo, B.; Goertz, S.; Grabmüller, S.; Grajek, O. A.; Grasso, A.; Grube, B.; Gushterski, R.; Guskov, A.; Haas, F.; Hagemann, R.; von Harrach, D.; Hasegawa, T.; Heckmann, J.; Heinsius, F. H.; Hermann, R.; Herrmann, F.; Hess, C.; Hinterberger, F.; von Hodenberg, M.; Horikawa, N.; Höppner, C.; d'Hose, N.; Ilgner, C.; Ishimoto, S.; Ivanov, O.; Ivanshin, Y.; Iwata, T.; Jahn, R.; Jasinski, P.; Jegou, G.; Joosten, R.; Kabuss, E.; Käfer, W.; Kang, D.; Ketzer, B.; Khaustov, G. V.; Khokhlov, Y. A.; Kiefer, J.; Kisselev, Y.; Klein, F.; Klimaszewski, K.; Koblitz, S.; Koivuniemi, J. H.; Kolosov, V. N.; Komissarov, E. V.; Kondo, K.; Konigsmann, K.; Konorov, I.; Konstantinov, V. F.; Korzenev, A.; Kotzinian, A. M.; Kouznetsov, O.; Kowalik, K.; Krämer, M.; Kral, A.; Kroumchtein, Z. V.; Kuhn, R.; Kunne, F.; Kurek, K.; Le Goff, J. M.; Lednev, A. A.; Lehmann, A.; Levorato, S.; Lichtenstadt, J.; Liska, T.; Maggiora, A.; Maggiora, M.; Magnon, A.; Mallot, G. K.; Mann, A.; Marchand, C.; Marroncle, J.; Martin, A.; Marzec, J.; Massmann, F.; Matsuda, T.; Maximov, A. N.; Meyer, W.; Michigami, T.; Mikhailov, Y. V.; Moinester, M. A.; Mutter, A.; Nagaytsev, A.; Nagel, T.; Nassalski, J.; Negrini, S.; Nerling, F.; Neubert, S.; Neyret, D.; Nikolaenko, V. I.; Olshevsky, A. G.; Ostrick, M.; Padee, A.; Panknin, R.; Panebianco, S.; Panzieri, D.; Parsamyan, B.; Paul, S.; Pawlukiewicz-Kaminska, B.; Perevalova, E.; Pesaro, G.; Peshekhonov, D. V.; Piragino, G.; Platchkov, S.; Pochodzalla, J.; Polak, J.; Polyakov, V. A.; Pontecorvo, G.; Pretz, J.; Quintans, C.; Rajotte, J.-F.; Ramos, S.; Rapatsky, V.; Reicherz, G.; Reggiani, D.; Richter, A.; Robinet, F.; Rocco, E.; Rondio, E.; Ryabchikov, D. I.; Samoylenko, V. D.; Sandacz, A.; Santos, H.; Sapozhnikov, M. G.; Sarkar, S.; Savin, I. A.; Sbrizza, G.; Schiavon, P.; Schill, C.; Schmitt, L.*; Schröder, W.; Shevchenko, O. Y.; Siebert, H.-W.; Silva, L.; Sinha, L.; Sissakian, A. N.; Slunecka, M.; Smirnov, G. I.; Sosio, S.; Sozzi, F.; Srnka, A.; Stolarski, M.; Sulc, M.; Sulej, R.; Takekawa, S.; Tessaro, S.; Tessarotto, F.; Teulfel, A.; Tkatchev, L. G.; Venugopal, G.; Virius, M.; Vlassov, N. V.; Vossen, A.; Weitzel, Q.; Wenzl, K.; Windmolders, R.; Wislicki, W.; Wollny, H.; Zaremba, K.; Zavertyaev, M.; Zemlyanichkina, E.; Ziembicki, M.; Zhao, J.; Zhuravlev, N.; Zvyagin, A.: **Gluon polarisation in the nucleon and longitudinal double spin asymmetries from open charm muoproduction.** *Physics letters B / Phys. Lett. B* **676**(1-3), 2009: 31–38. DOI:10.1016/j.physletb.2009.04.059

015 Algora, A.; Jordan, D.; Estevez, E.; Tain, J. L.; Rubio, B.; Agramunt, J.; Perez-Cerdan, A. B.; Molina, F.; Caballero, L.; Nacher, E.; Bernabeu, J.; Gadea, A.; Krasznahorkay, A.; Hunyadi, M. D.; Gulyas, J.; Vitez, A.; Csatlos, M.; Csige, L.; Aysto, J.; Penttila, H.; Moore, I. D.; Eronen, T.; Jokinen, A.*GAST; Nieminen, A.; Hakala, J.; Karvonen, P.; Kankainen, A.; Saastamoinen, A.; Rissanen, J.; Kessler, T.; Weber, C.*; Ronkainen, J.; Rahaman, S.*; Elomaa, V.; Hager, U.; Rinta-Antila, S.; Sonoda, T.; Burkard, K.*; Hüller/Huller, W.*; Doring, J.; Gierlik, M.; Kirchner, R.*; Mukha, I.; Plettner, C.; Roeckl, E.* EMAIL; Cano-Ott, D.; Batist, L.*GAST; Valiente, J. J.; Gelletly,

W.; Yoshida, T.; Nichols, A. L.; Sonzogni, A.; Perajarvi, K.: **Practical applications of the total absorption technique.** *Revista mexicana de fisica* **55**(2), 2009: 6–12. Also part of: PNI

016 Algora, A.; Jordan, D.; Estevez, E.; Tain, J. L.; Rubio, B.; Agramunt, J.; Perez-Cerdan, A. B.; Molina, F.; Caballero, L.; Nacher, E.; Bernabeu, J.; Gadea, A.; Krasznahorkay, A.; Hunyadi, M. D.; Gulyas, J.; Vitez, A.; Csatlos, M.; Csige, L.; Aysto, J.; Penttila, H.; Moore, I. D.; Eronen, T.; Jokinen, A.; Nieminen, A.; Hakala, J.; Karvonen, P.; Kankainen, A.; Saastamoinen, A.; Rissanen, J.; Kessler, T.; Weber, C.; Ronkainen, J.; Rahaman, S.; Elomaa, V.; Hager, U.; Rinta-Antila, S.; Sonoda, T.; Burkard, K.; Huller, W.; Doring, J.; Gierlik, M.; Kirchner, R.; Mukha, I.; Plettner, C.; Roeckl, E.; Cano-Ott, D.; Batist, L.; Valiente, J. J.; Gelletly, W.; Yoshida, T.; Nichols, A. L.; Sonzogni, A.; Perajarvi, K.: **Practical applications of the total absorption technique.** *Revista mexicana de fisica / Rev. Mex. Fis.* **55**(2), 2009: 6–12.

017 Alkhomashi, N.; Regan, P. H.; Podolyak, Z.; Pietri, S.; Garnsworthy, A. B.; Steer, S. J.; Benlliure, J.; Caserejos, E.; Casten, R. F.; Gerl, J.*; Wollersheim, H. J.*; Grebosz, J.; Farrelly, G.; Gorska, M.*; Kojouharov, I.*; Schaffner, H.*; Algora, A.; Benzoni, G.; Blazhev, A.; Boutachkov, P.; Bruce, A. M.; Bacelar, A. M. D.; Cullen, I. J.; Caceres, L.*; Doornenbal, P.*; Estevez, M. E.; Fujita, Y.; Gelletly, W.; Hoischen, R.*; Kumar, R.; Kurz, N.*; Lalkovski, S.; Liu, Z.; Mihai, C.; Molina, F.; Morales, A. I.; Mucher, D.; Prokopowicz, W.*; Rubio, B.; Shi, Y.; Tamii, A.; Tashenov, S.*; Valiente-Dobon, J. J.; Walker, P. M.; Woods, P. J.; Xu, F. R.: **$\beta-$-delayed spectroscopy of neutron-rich tantalum nuclei: Shape evolution in neutron-rich tungsten isotopes.** *Physical review C, Nuclear physics / Phys. Rev. C* **80**(6), 2009: 064308. DOI:10.1103/physrevc.80.064308

018 Alkhomashi, N.; Regan, P. H.; Podoyak, Z.; Pietri, S. B.; Garnsworthy, A. B.; Steer, S. J.; Benlliure, J.; Caserejos, E.; Gorska, M.*; Gerl, J.*; Wollersheim, H. J.*; Grebosz, J.*; Kurz, N.*; Kojouharov, I.*; Schaffner, H.*; Alcora, A.; Benzoni, G.; Blazhev, A.*; Boutachkov, P.; Bruce, A. M.; Caceres, L.; Doornenbal, P.*; Bacelar, A. M. D.; Cullen, I. J.; Estevez, M. E.; Farrelly, G.; Fujita, Y.; Gelletly, W.; Hoischen, R.; Kumar, R.; Lalkovski, S.; Liu, Z.; Mihai, C.; Molina, F.; Mucher, D.; Rubio, B.; Tamii, A.; Tashenov, S.*; Valiente-Dobon, J. J.; Walker, P. M.; Woods, P. J.: **β^--delayed and isomer spectroscopy of neutron-rich Ta and W isotopes.** *Acta physica Polonica B, Particle physics and field theory, nuclear physics, theory of relativity / Acta Phys. Pol. B* **40**(3), 2009: 875–878. URL OPEN ACCESS.

019 Alt, C.; Anticic, T.; Baatar, B.; Barna, D.; Bartke, J.; Betev, L.; Bialkowska, H.; Blume, C.; Boimska, B.; Botje, M.; Bracinik, J.; Bramm, R.; Bunccic, P.; Cerny, V.; Christakoglou, P.; Chvala, O.; Cramer, J. G.; Csato, P.; Dinkelaker, P.; Eckardt, V.; Flierl, D.; Fodor, Z.; Foka, P.*; Friese, V.*; Gal, J.; Gazdzicki, M.; Genchev, V.; Georgopoulos, G.; Gladysz, E.; Grebieszkow, K.; Hegyi, S.; Höhne, C.*; Kadija, K.; Karev, A.; Kliemant, A.; Kniege, S.; Kolesnikov, V. I.; Kornas, E.; Korus, R.; Kowalski, M.; Kraus, I.*; Kreps, M.; Kresan, D.; van Leeuwen, M.; Levai, P.; Litov, L.; Lungwitz, B.; Makariev, M.; Malakhov, A. I.; Mateev, A.; Melkumov, G. L.; Mischke, A.; Mitrovski, A.; Molnar, J.; Mrowczynski, S.; Nicolic, V.; Palla, G.; Panagiotou, A. D.; Panayotov, D.; Petridis, A.; Pikna, M.; Prindle, D.; Pühlhofer, F.; Renfordt, R.; Roland, C.; Roland, G.; Rybczynski, M.; Rybicki, A.; Sandoval, A.*; Schmitz, N.; Schuster, T.; Seyboth, P.; Sikler, F.; Sitar, B.; Skrzypczak, E.; Stefanek, G.; Stock, R.; Ströbele, H.; Susa, T.; Szentpetery, I.; Sziklai, J.; Szymanski, P.; Trubnikov, V.; Varga, D.; Vassiliou, M.; Veres, G. I.; Vesztergombi, G.; Vranic, D.*; Wetzler, A.; Wlodarczyk, Z.; Yoo, I. K.; NA49 Collaboration: **Energy dependence of particle ratio fluctuations in central Pb plus Pb collisions from $\sqrt{S_{NN}}$=6.3 to 17.3 GeV.** *Physical review C, Nuclear physics / Phys. Rev. C* **79**(4), 2009: 044910. DOI:10.1103/physrevc.79.044910

020 Alvarez-Pol, H.; Benlliure, J.; Casarejos, E.; Audouin, L.; Cortina-Gil, D.; Enqvist, T.*; Fernandez, B.; Junghans, A. R.; Jurado, B.; Napolitani, P.*; Pereira, J.; Rejmund, F.; Schmidt, K.-H.*; Yordanov, O.*: **Production cross-sections of neutron-rich Pb and Bi isotopes in the fragmentation of ^{238}U.** *The European physical journal A, Hadrons and nuclei* **42**(3), 2009: 485–488. DOI:10.1140/epja/i2009-10856-8

021 Alvarez-Pol, H.; Benlliure, J.; Casarejos, E.; Audouin, L.; Cortina-Gil, D.; Enqvist, T.*; Fernandez, B.; Junghans, A. R.; Jurado, B.; Napolitani, P.; Pereira, J.; Rejmund, F.; Schmidt, K.-H.*; Yordanov, O.*: **Production cross-sections of neutron-rich Pb and Bi isotopes in the fragmentation of ^{238}U.** *The European physical journal A, Hadrons and nuclei / Eur. Phys. J. A* **42**(3), 2009: 485–488. DOI:10.1140/epja/i2009-10856-8

022 Andreyev, A. N.; Antalic, S.; Ackermann, D.*; Bianco, L.; Franchoo, S.; Heinz, S.*; Heßberger, F. P.*; Hofmann, S.*; Huyse, M.; Kojouharov, I.*; Kindler, B.*; Lommel, B.*; Mann, R.*; Nishio, K.; Page, R. D.; Ressler, J. J.; Sapple, P.; Streicher, B.; Saro, S.; Sulignano, B.*; Thomson, J.; Van Duppen, P.; Venhart, M.: **α decay of ^{194}At.** *Physical review C, Nuclear physics / Phys. Rev. C* **79**(6), 2009: 064320. DOI:10.1103/physrevc.79.064320

023 Andreyev, A. N.; Antalic, S.; Ackermann, D.*; Cocolios, T. E.; Comas, V. F.*; Elseviers, J.; Franchoo, S.; Heinz, S.*; Heredia, J. A.*; Heßberger, F. P.*; Hofmann, S.* Huyse, M.; Khuyagbaatar, J.; Kojouharov, I.*; Kindler, B.*; Lommel, B.*; Mann, R.*; Page, R. D.; Rinta-Antila, S.; Sapple, P. J.; Saro, S.; Van Duppen, P.; Venhart, M.; Watkins, H. V.: **Decay of the 9/2$^-$ isomer in ^{181}Tl and mass determination of low-lying states in ^{181}Tl, ^{177}Au,**

and ^{173}Ir. *Physical review C, Nuclear physics / Phys. Rev. C* **80**(2), 2009: 024302. DOI:10.1103/physrevc.80.024302

024 Andreyev, A. N.; Antalic, S.; Ackermann, D.*; Cocolios, T. E.; Comas, V. F.*; Elseviers, J.; Franchoo, S.; Heinz, S.*; Heredia, J. A.*; Heßberger, F. P.*; Hofmann, S.*; Huyse, M.; Khuyagbaatar, J.*; Kojouharov, I.*; Kindler, B.*; Lommel, B.*; Mann, R.*; Page, R. D.; Rinta-Antilla, S.; Sapple, P. J.; Saro, S.*GAST; Van Duppen, P.; Venhart, M.; Watkins, H. V.: α **decay of ^{180,181}Pb.** *Physical review C, Nuclear physics* **80**(5), 2009: 054322. DOI:10.1103/physrevc.80.054322

025 Andreyev, A. N.; Antalic, S.; Ackermann, D.*; Cocolios, T. E.; Comas, V. F.*; Elseviers, J.; Franchoo, S.; Heinz, S.*; Heredia, J. A.*; Heßberger, F. P.*; Hofmann, S.*; Huyse, M.; Khuyagbaatar, J.*; Kojouharov, I.*; Kindler, B.*; Lommel, B.*; Mann, R.*; Page, R. D.; Rinta-Antilla, S.; Sapple, P. J.; Saro, S.; Van Duppen, P.; Venhart, M.; Watkins, H. V.: α **decay of ^{180,181}Pb.** *Physical review C, Nuclear physics / Phys. Rev. C* **80**(5), 2009: 054322. DOI:10.1103/physrevc.80.054322

026 Andreyev, A. N.; Antalic, S.; Ackermann, D.*; Cocolios, T. E.; Comas, V. F.; Elseviers, J.; Franchoo, S.; Heinz, S.*; Heredia, J. A.*; Heßberger, F. P.*; Hofmann, S.*; Huyse, M.; Khuyagbaatar, J.*; Kojouharov, I.*; Kindler, B.*; Lommel, B.*; Mann, R.*; Page, R. D.; Rinta-Antila, S.; Sapple, P. J.; Saro, S.; Van Duppen, P.; Venhart, M.; Watkins, H. V.: **Identification and decay of the 0.48 ms 13/2$^+$ isomer in ^{181}Hg.** *Physical review C, Nuclear physics / Phys. Rev. C* **80**(4), 2009: 044334. DOI:10.1103/physrevc.80.044334

027 Andronic, A.*; Beutler, F.; Braun-Munzinger, P.*; Redlich, K.; Stachel, J.*: **Statistical hadronization of heavy flavor quarks in elementary collisions: Successes and failures.** *Physics letters B / Phys. Lett. B* **678**(4), 2009: 350–354. DOI:10.1016/j.physletb.2009.06.051

028 Andronic, A.*; Beutler, F.; Braun-Munzinger, P.*; Redlich, K.; Stachel, J.*: **Thermal description of hadron production in e$^+$e$^-$ collisions revisited.** *Physics letters B / Phys. Lett. B* **675**(3-4), 2009: 312–318. DOI:10.1016/j.physletb.2009.04.024

029 Andronic, A.*; Braun-Munzinger, P.*; Stachel, J.: **Thermal hadron production in relativistic nuclear collisions.** *Acta physica Polonica B, Particle physics and field theory, nuclear physics, theory of relativity / Acta Phys. Pol. B* **40**(4), 2009: 1005–1012. URL OPEN ACCESS.

030 Andronic, A.*; Braun-Munzinger, P.*; Stachel, J.: **Thermal hadron production in relativistic nuclear collisions: The hadron mass spectrum, the horn, and the QCD phase transition.** *Physics letters B / Phys. Lett. B* **673**(2), 2009: 142–145. DOI:10.1016/j.physletb.2009.02.014

031 Andronic, A.*; Braun-Munzinger, P.*; Stachel, J.: **[Erratum] Thermal hadron production in relativistic nuclear collisions: The hadron mass spectrum, the horn, and the QCD phase transition (vol 673, pg 142, 2009).** *Physics letters B / Phys. Lett. B* **678**(5), 2009: 516–516. DOI:10.1016/j.physletb.2009.06.021

032 Andronic, A.*; Garabatos, C.*; Gonzalez-Diaz, D.*; Kalweit, A.*; Uhlig, F.*: **A comprehensive study of rate capability in Multi-Wire Proportional Chambers.** *Journal of Instrumentation / J. Instrum.* **4**, 2009: P10014. DOI:10.1088/1748-0221/4/10/p10014 OPEN ACCESS.

033 Antalic, S.; Heßberger, F. P.*; Hofmann, S.*; Ackermann, D.*; Heinz, S.*; Kindler, B.*; Kojouharov, I.*; Leino, M.; Lommel, B.*; Mann, R.*; Nishio, K.; Saro, S.; Sulignano, B.*; Venhart, M.: **Study of K-isomers in odd-mass nuclei at SHIP.** *Acta physica Polonica B, Particle physics and field theory, nuclear physics, theory of relativity / Acta Phys. Pol. B* **40**(3), 2009: 763–766. URL OPEN ACCESS.

034 Anticic, T.; Baatar, B.; Barna, D.; Bartke, J.; Beck, H.; Betev, L.; Bialkowska, H.; Blume, C.; Boimska, B.; Book, J.; Botje, M.; Bracinik, J.; Buncic, P.; Cerny, V.; Christakoglou, P.; Chung, P.; Chvala, O.; Cramer, J. G.; Csato, P.; Dinkelaker, P.; Eckardt, V.; Fodor, Z.; Foka, P.*; Friese, V.*; Gal, J.; Gazdzicki, M.; Genchev, V.; Grebieszkow, K.; Hegyi, S.; Höhne, C.*; Kadija, K.; Karev, A.; Kresan, D.; Kolesnikov, V. I.; Kowalski, M.; Kraus, I.*; Kreps, M.; Laszlo, A.; Lacey, R.; van Leeuwen, M.; Levai, P.; Litov, L.; Lungwitz, B.; Makariev, M.; Malakhov, A. I.; Mateev, M.; Melkumov, G. L.; Meurer, C.; Mischke, A.; Mitrovski, M.; Molnar, J.; Mrowczynski, S.; Nicolic, V.; Palla, G.; Panagiotou, A. D.; Panayotov, D.; Petridis, A.; Peryt, W.; Pikna, M.; Pluta, J.; Prindle, D.; Pühlhofer, F.; Renfordt, R.; Roland, C.; Roland, G.; Rybczynski, M.; Rybicki, A.; Sandoval, A.*; Schmitz, N.; Schuster, T.; Seyboth, P.; Sikler, F.; Sitar, B.; Skrzypczak, E.; Slodkowski, M.; Stefanek, G.; Stock, R.; Strabel, C.; Ströbele, H.; Susa, T.; Szentpetery, I.; Sziklai, J.; Szuba, M.; Szymanski, P.; Utvic, M.; Varga, D.; Vassiliou, M.; Veres, G. I.; Vesztergombi, G.; Vranic, D.*; Wlodarczyk, Z.; Wojtaszek, A.; Yoo, I. K.; NA49 Collaboration: **System-size dependence of Λ and Ξ production in nucleus-nucleus collisions at 40A and 158A GeV measured at the CERN Super Proton Synchrotron.** *Physical review C, Nuclear physics / Phys. Rev. C* **80**(3), 2009: 034906. DOI:10.1103/physrevc.80.034906

035 Anticic, T.; Baatar, B.; Barna, D.; Bartke, J.; Betev, L.; Bialkowska, H.; Blume, C.; Boimska, B.; Botje, M.; Bracinik, J.; Buncic, P.; Cerny, V.; Christakoglou, P.; Chung, P.; Chvala, O.; Cramer, J. G.; Csato, P.; Dinkelaker, P.; Eckardt, V.; Fodor, Z.; Foka, P.*; Friese, V.*; Gal, J.; Gadzicki, M.; Genchev, V.; Gladysz, E.; Grebieszkow, K.; Hegyi, S.; Höhne, C.*; Kadija, K.; Karev, A.; Kikola, D.; Kolesnikov, V. I.; Kornas, E.; Korus, R.; Kowalski, M.;

Kreps, M.; Laszlo, A.; Lacey, R.; van Leeuwen, M.; Levai, P.; Litov, L.; Lungwitz, B.; Makariev, M.; Malakhov, A. I.; Mateev, M.; Melkumov, G. L.; Mischke, A.; Mitrovski, M.; Molnar, J.; Mrowczynski, S.; Nicolic, V.; Palla, G.; Panagiotou, A. D.; Panayotov, D.; Petridis, A.; Peryt, W.; Pikna, M.; Pluta, J.; Prindle, D.; Puhlhofer, F.; Renfordt, R.; Roland, C.; Roland, G.; Rybczynski, M.; Rybicki, A.; Sandoval, A.*; Schmitz, N.; Schuster, T.; Seyboth, P.; Sikler, F.; Sitar, B.; Skrzypczak, E.; Slodkowski, M.; Stefanek, G.; Stock, R.; Strabel, C.; Ströbele, H.; Susa, T.; Szentpetery, I.; Sziklai, J.; Szuba, M.; Szymanski, P.; Trubnikov, V.; Utvic, M.; Varga, D.; Vassiliou, M.; Veres, G. I.; Vesztergombi, G.; Vranic, D.*; Wlodarczyk, Z.; Wojtaszek, A.; Yoo, I. K.; NA49 Collaboration*: **Energy dependence of transverse momentum fluctuations in Pb plus Pb collisions at the CERN Super Proton Synchrotron (SPS) at 20A to 158A GeV.** *Physical review C, Nuclear physics / Phys. Rev. C* **79**(4), 2009: 044904. DOI:10.1103/physrevc.79.044904

036 Averbeck, R.*: **Charm and bottom production at RHIC.** *Progress in particle and nuclear physics* **62**(2), 2009: 318–322. DOI:10.1016/j.ppnp.2008.12.016

037 Bacelar, A. M. D.; Bruce, A. M.; Podolyak, Z.; Lalkovski, S.; Pietri, S.; Al-Dahan, N.; Gorska, M.*; Algora, A.; Alkhomashi, N.; Benlliure, J.; Boutachkov, P.*; Bracco, A.; Calore, E.; Casarejos, E.; Cullen, I. J.; Deo, A. Y.; Detistov, P.; Dombradi, Z.; Domingo-Pardo, C.*; Doncel, M.; Farinon, F.; Farrelly, G. F.; Geissel, H.*; Gelletly, W.; Gerl, J.*; Goel, N.*; Grebosz, J.*; Hoischen, R.*; Kojouharov, I.*; Kurz, N.*; Leoni, S.; Molina, F.; Morales, A. I.; Montanari, D.; Musumarra, A.; Nicolini, R.; Napoli, D. R.; Nociforo, C.*; Prochazka, A.*; Prokopowicz, W.*; Regan, P. H.; Rubio, B.; Rudolph, D.; Verma, S.; Steer, S. J.; Strmen, P.; Swan, T. P. D.; Szarka, I.; Valiente-Dobon, J. J.; Walker, P. M.; Weick, H.*; Wollersheim, H. J.*: **Angular momentum population in fragmentation reactions.** *Acta physica Polonica B, Particle physics and field theory, nuclear physics, theory of relativity / Acta Phys. Pol. B* **40**(3), 2009: 889–892. URL OPEN ACCESS.

038 Bäcker, A.; Dietz, B.; Friedrich, T.*; Miski-Oglu, M.; Richter, A.; Schäfer, F.; Tomsovic, S.: **Friedel oscillations in microwave billiards.** *Physical Review E / Phys. Rev. E* **80**(6), Part 2, 2009: 066210. DOI:10.1103/physreve.80.066210

039 Barbieri, C.*; Hjorth-Jensen, M.: **Quasiparticle and quasihole states of nuclei around ^{56}Ni.** *Physical review C, Nuclear physics / Phys. Rev. C* **79**(6), 2009: 064313. DOI:10.1103/physrevc.79.064313

040 Bazavov, A.; Bhattacharya, T.; Cheng, M.; Christ, N. H.; Detar, C.; Ejiri, S.; Gottlieb, S.; Gupta, R.; Heller, U. M.; Huebner, K.; Jung, C.; Karsch, F.; Laermann, E.; Levkova, L.; Miao, C.; Mawhinney, R. D.; Petreczky, P.; Schmidt, C.; Soltz, R. A.; Soeldner, W.*; Sugar, R.; Toussaint, D.; Vranas, P.: **Equation of state and QCD transition at finite temperature.** *Physical Review D / Phys. Rev. D* **80**(1), 2009: 014504. DOI:10.1103/physrevd.80.014504

041 Bednarczyk, P.; Grebosz, J.; Maj, A.; Kmiecik, M.; Meczyrnski, W.; Styczen, J.; Wollersheim, H.-J.*; Gerl, J.*; Gorska, M.*; Reiter, P.; Bracco, A.; Camera, F.: **Gamma-ray angular distribution in Coulomv excitation experiments at intermediate energies as a signature of electromagnetic and nuclear forces in peripheral collisions.** *Acta physica Polonica B, Particle physics and field theory, nuclear physics, theory of relativity / Acta Phys. Pol. B* **40**(3), 2009: 853–858. URL OPEN ACCESS.

042 Belver, D.; Blanco, A.; Cabanelas, P.; Carolino, N.; Castro, E.; Diaz, J.; Fonte, P.; Garzon, J. A.; Gonzalez-Diaz, D.*; Gil, A.; Koenig, W.*; Lopes, L.; Mangiarotti, A.; Oliveira, O.; Pereira, A.; Silva, C.; Sousa, C. C.; Zapata, M.: **The HADES RPC inner TOF wall.** *Nuclear instruments & methods in physics research, Section A, Accelerators, spectrometers, detectors and associated equipment / Nucl. Instrum. Methods Phys. Res. Sect. A-Accel. Spectrom. Dect. Assoc. Equip.* **602**(3), 2009: 687–690. DOI:10.1016/j.nima.2008.12.090

043 Belver, D.; Cabanelas, P.; Castro, E.; Diaz, J.; Garzon, J. A.; Gil, A.; Gonzalez-Diaz, D.*; Koenig, W.*; Traxler, M.*; Zapata, M.: **Performances of the Front-End Electronics for the HADES RPC TOF wall on a ^{12}C beam.** *Nuclear instruments & methods in physics research, Section A, Accelerators, spectrometers, detectors and associated equipment / Nucl. Instrum. Methods Phys. Res. Sect. A-Accel. Spectrom. Dect. Assoc. Equip.* **602**(3), 2009: 788–791. DOI:10.1016/j.nima.2008.12.135

044 Benabderrahmane, M. L.; Herrmann, N.; Wisniewski, K.; Kecskemeti, J.; Andronic, A.*; Barret, V.; Basrak, Z.; Bastid, N.; Buehler, P.; Cargnelli, M.; Caplar, R.; Cordier, E.; Deppner, I.; Crochet, P.; Dupieux, P.; Dzelalija, M.; Fabbietti, L.; Fodor, Z.; Gasik, P.; Gasparic, I.; Grishkin, Y.; Hartmann, O. N.; Hildenbrand, K. D.*; Hong, B.; Kang, T. I.; Kienle, P.; Kirejczyk, M.; Kim, Y. J.*; Kis, M.; Koczon, P.*; Korolija, M.; Kotte, R.; Lebedev, A.; Leifels, Y.*; Lopez, X.; Manko, V.; Marton, J.; Mangiarotti, A.; Merschmeyer, M.; Matulewicz, T.; Petrovici, M.; Piasecki, K.; Rami, F.; Reischl, A.; Reisdorf, W.*; Rogowska, M.; Ryu, M. S.; Schmidt, P.; Schüttauf, A.*; Seres, Z.; Sikora, B.; Sim, K. S.; Simion, V.; Siwek-Wilczynska, K.; Smolyankin, V.; Suzuki, K.; Tyminski, Z.*; Widmann, E.; Xiao, Z. G.*; Yamazaki, T.; Yushmanov, I.; Zhang, X. Y.; Zhilin, A.; Zmeskal, J.; Bratkovskaya, E.*; Cassing, W.: **Measurement of the In-Medium K^0 Inclusive Cross Section in π^--Induced Reactions at 1.15 GeV/c.** *Physical review letters / Phys. Rev. Lett.* **102**(18), 2009: 182501. DOI:10.1103/physrevlett.102.182501

045 Bender, M.; Kollmus, H.*; Reich-Sprenger, H.*;

Toulemonde, M.; Assmann, W.: **An inelastic thermal spike model to calculate ion induced desorption yields.** *Nuclear instruments & methods in physics research, Section B, Beam interactions with materials and atoms / Nucl. Instrum. Methods Phys. Res. Sect. B-Beam Interact. Mater. Atoms* **267**(6), 2009: 885–890. DOI:10.1016/j.nimb.2009.02.039

046 Betz, B.*; Gyulassy, M.; Noronha, J.; Torrieri, G.: **Anomalous conical di-jet correlations in pQCD vs AdS/CFT.** *Physics letters B / Phys. Lett. B* **675**(3-4), 2009: 340–346. DOI:10.1016/j.physletb.2009.04.026

047 Bhang, H.; Ajimura, S.; Aoki, K.; Banu, A.; Fukuda, T.; Hashimoto, O.; Hwang, J. I.; Kameoka, S.; Kang, B. H.; Kim, E.; Kim, J. H.; Kim, M.; Maruta, T.; Miura, Y.; Miyake, Y.; Nagae, T.; Nakamura, M.; Nakamura, S. N.; Noumi, H.; Okada, S.; Okayasu, Y.; Outa, H.; Park, H.; Saha, P. K.; Sato, Y.; Sekimoto, M.; Shin, S.; Takahashi, T.; Tamura, H.; Tanida, K.; Toyata, A.; Tsukada, K.; Watanabe, T.; Yim, H. J.: **Mechnism of the nonmesonic weka decay of Lambda hypernuclei and the three-body process.** *Modern Physics Letters A / Mod. Phys. Lett. A* **24**(11-13), 2009: 1023–1026. URL

048 Bianchin, S.*; Achenbach, P.; Ajimura, S.; Borodina, O.*; Fukuda, T.; Hoffmann, J.*; Kavatsyuk, M.; Koch, K.*; Koike, T.; Kurz, N.*; Maas, F.*; Minami, S.*; Mizoi, Y.; Nagae, T.; Nakajima, D.*; Okamura, A.; Ott, W.*; Özel, B.*; Pochodzalla, J.; Rappold, C.*; Saito, T. R.*; Sakaguchi, A.; Sako, M.; Sekimoto, M.; Sugimura, H.; Takahashi, T.; Tamura, H.; Tanida, K.; Trautmann, W.*: **The HYPHI project: hypernuclear spectroscopy with stable heavy ion beams and rare isotope beams at GSI and FAIR.** *International journal of modern physics E, Nuclear physics / Int. J. Mod. Phys. E-Nucl. Phys.* **18**(10), 2009: 2187–2191. DOI:10.1142/s0218301309014536

049 Bianchin, S.*; Achenbach, P.; Ajimura, S.; Borodina, O.*; Fukuda, T.; Hoffmann, J.*; Kavatsyuk, M.; Koch, K.*; Koike, T.; Kurz, N.*; Maas, F.*; Minami, S.*; Mizoi, Y.; Nagae, T.; Nakajima, D.*; Okamura, A.; Ott, W.*; Özel, B.*; Pochodzalla, J.; Rappold, C.*; Saito, T. R.*; Sakaguchi, A.; Sako, M.; Sekimoto, M.; Sugimura, H.; Takahashi, T.; Tamura, H.; Tanida, K.; Trautmann, W.*: **The HYPHI project: hypernuclear spectroscopy with stable heavy ion beams and rare isotope beams at GSI and FAIR.** *International journal of modern physics E, Nuclear physics* **18**(10), 2009: 2187–2191. DOI:10.1142/s0218301309014536

050 Blanco, A.; Cabanelas, P.; Belver, D.; Castro, E.; Diaz, J.; Fonte, P.; Gil, A.; Garzon, J. A.; Gonzalez-Diaz, D.*; Heinz, T.*; Koenig, W.*; Lopes, L.; Muentz, C.; Palka, M.*; Pietraszko, J.*; Rustamov, A.*; Schwab, E.*; Sobolev, Y.; Tarantola, A.; Teilab, K.; Traxler, M.; Trebacz, R.; Wuestenfeld, J.; Yurevich, S.*: **In-beam measurements of the HADES-TOF RPC wall.** *Nuclear instruments & methods in physics research, Section A, Accelerators, spectrometers, detectors and associated equipment / Nucl. Instrum. Methods Phys. Res. Sect. A-Accel. Spectrom. Dect. Assoc. Equip.* **602**(3), 2009: 691–695. DOI:10.1016/j.nima.2008.12.091

051 Bockstiegel, C.; Steinhauser, S.; Clerc, H. G.; Grewe, A.; Heinz, A.; De Jong, M.; Muller, J.; Voss, B.; Junghans, A. R.; Kelic, A.; Schmidt, K. H.: **Global view on fission channels.** *International journal of modern physics E, Nuclear physics / Int. J. Mod. Phys. E-Nucl. Phys.* **18**(4), 2009: 873–878, Sp. Iss. SI. URL

052 Boine-Frankenheim, O.*; Kornilov, V.*: **Transverse Schottky noise spectrum for bunches with space charge.** *Physical Review Special Topics - Accelerators and Beams / Phys. Rev. Spec. Top.-Accel. Beams* **12**(11), 2009: 114201. DOI:10.1103/physrevstab.12.114201 OPEN ACCESS.

053 Boine-Frankenheim, O.*; Kornilov, V.*: **Transverse Schottky noise spectrum for bunches with space charge.** *Physical Review Special Topics - Accelerators and Beams* **12**(11), 2009: 114201. DOI:10.1103/physrevstab.12.114201 OPEN ACCESS.

054 Bonnet, E.; Borderie, B.; Le Neindre, N.; Rivet, M. F.; Bougault, R.; Chbihi, A.; Dayras, R.; Frankland, J. D.; Galichet, E.; Gagnon-Moisan, F.; Guinet, D.; Lautesse, P.; Lukasik, J.; Mercier, D.; Parlog, M.; Rosato, E.; Roy, R.; Sfienti, C.*; Vigilante, M.; Wieleczko, J. P.; Zwieglinski, B.: **Fragment properties of fragmenting heavy nuclei produced in central and semi-peripheral collisions.** *Nuclear physics A, Nuclear and hadronic physics / Nucl. Phys. A* **816**, 2009: 1–18. DOI:10.1016/j.nuclphysa.2008.11.005

055 Borowska, L.; Terenetsky, K.; Verbitsky, V.; Fritzsche, S.*: **Analytical potential for the elastic scattering of light halo nuclei below and close to the Coulomb barrier.** *Physical review C, Nuclear physics / Phys. Rev. C* **79**(4), 2009: 044605. DOI:10.1103/physrevc.79.044605 Also part of: PNI

056 Borschevsky, A.; Pershina, V.*; Eliav, E.; Kaldor, U.: **Electron affinity of element 114, with comparison to Sn and Pb.** *Chemical Physics Letters / Chem. Phys. Lett.* **480**(1-3), 2009: 49–51. DOI:10.1016/j.cplett.2009.08.059

057 Bousonville, M.*; Rausch, J.: **Universal picosecond timing system for the Facility for Antiproton and Ion Research.** *Physical Review Special Topics - Accelerators and Beams / Phys. Rev. Spec. Top.-Accel. Beams* **12**(4), 2009: 042801. DOI:10.1103/physrevstab.12.042801 OPEN ACCESS.

058 Braun-Munzinger, P.*; Wambach, J.*: **Colloquium: Phase diagram of strongly interacting matter.** *Reviews of Modern Physics/Supplement / Rev. Mod. Phys.* **81**(3), 2009: 1031–1050. DOI:10.1103/revmodphys.81.1031

059 Cabanelas, P.; Morales, M.; Garzon, J. A.; Gil, A.; Gonzalez-Diaz, D.*; Blanco, A.; Belver, D.; Casarejos, E.; Fonte, P.; Koenig, W.*; Lopes, L.; Palka, M.*; Pietraszko, J.*; Traxler, M.*; Weber, M.: **Performances of 4-gap timing RPCs for relativistic ions in the range Z=1-6.** */ J. Instrum.* **4**, 2009: P11007. DOI:10.1088/1748-0221/4/11/p11007 OPEN ACCESS.

060 Caceres, L.*; Gorska, M.*; Jungclaus, A.; Pfützner, M.; Grawe, H.*; Nowacki, F.; Sieja, K.*; Pietri, S.; Rudolph, D.; Podolyak, Z.; Regan, P. H.; Werner-Malento, E.; Detistov, P.; Lalkovski, S.; Modamio, V.; Walker, J.; Andgren, K.; Bednarczyk, P.*; Benlliure, J.; Benzoni, G.; Bruce, A. M.; Casarejos, E.; Cederwall, B.; Crespi, F. C. L.; Doornenbal, P.*; Geissel, H.*; Gerl, J.*; Grebosz, J.*; Hadinia, B.; Hellström, M.; Hoischen, R.*; Ilie, G.; Khaplanov, A.; Kmiecik, M.; Kojouharov, I.*; Kumar, R.; Kurz, N.*; Maj, A.; Mandal, S.; Montes, F.*; Martinez-Pinedo, G.*; Myalski, S.; Prokopowicz, W.*; Schaffner, H.*; Simpson, G. S.; Steer, S. J.; Tashenov, S.*; Wieland, O.; Wollersheim, H. J.*: **Spherical proton-neutron structure of isomeric states in ^{128}Cd.** *Physical review C, Nuclear physics / Phys. Rev. C* **79**(1), 2009: 011301. DOI:10.1103/physrevc.79.011301

061 Christiansen, P.; Dobrin, A.; Gros, P.; Gustafsson, H. A.; Ivanov, M.*; Kowalski, M.; Oskarsson, A.; Österman, L.; Stenlund, E.: **The influence of detector effects on TPC performance.** *Nuclear instruments & methods in physics research, Section A, Accelerators, spectrometers, detectors and associated equipment / Nucl. Instrum. Methods Phys. Res. Sect. A-Accel. Spectrom. Dect. Assoc. Equip.* **609**(2-3), 2009: 149–155. DOI:10.1016/j.nima.2009.08.052

062 Cotrufo, A.; Plotnikov, A.*; Yershova, O.*; Anghinolfi, M.; Piombo, D.: **A hydrophone prototype for ultra high energy neutrino acoustic detection.** *Nuclear instruments & methods in physics research, Section A, Accelerators, spectrometers, detectors and associated equipment / Nucl. Instrum. Methods Phys. Res. Sect. A-Accel. Spectrom. Dect. Assoc. Equip.* **604**(1-2), 2009: S219–S221. DOI:10.1016/j.nima.2009.03.231

063 Dönigus, B.*: **Heavy flavour capabilities of the ALICE transition radiation detector.** *Progress in particle and nuclear physics* **62**(2), 2009: 323–324. DOI:10.1016/j.ppnp.2008.12.014

064 Dietz, B.; Friedrich, T.*; Harney, H. L.; Miski-Oglu, M.; Richter, A.; Schäfer, F.; Verbaarschot, J.; Weidenmüller, H. A.: **Induced Violation of Time-Reversal Invariance in the Regime of Weakly Overlapping Resonances.** *Physical review letters / Phys. Rev. Lett.* **103**(6), 2009: 064101. DOI:10.1103/physrevlett.103.064101

065 Dietz, B.; Friedrich, T.*; Miski-Oglu, M.; Richter, A.; Schäfer, F.; Seligmann, T. H.: **Nonperiodic echoes from quantum mushroom-billiard hats.** *Physical Review E / Phys. Rev. E* **80**(3), Part 2, 2009: 036212. DOI:10.1103/physreve.80.036212

066 Doan, Q. T.; Curien, D.; Stezowski, O.; Dudek, J.; Mazurek, K.; Gozdz, A.; Piot, J.; Duchene, G.; Gall, B.; Molique, H.; Richet, M.; Medina, P.; Guinet, D.; Redon, N.; Schmitt, C.; Jones, P.; Peura, P.; Ketelhut, S.; Nyman, M.; Jakobsson, U.; Greenlees, P. T.; Julin, R.; Juutinen, S.; Rahkila, P.; Maj, A.; Zuber, K.; Bednarczyk, P.; Schunck, N.; Dobaczewski, J.; Astier, A.; Deloncle, I.; Verney, D.; De Angelis, G.; Gerl, J.*: **Search for fingerprints ot tetrahedral symmetry in ^{156}Gd.** *Acta physica Polonica B, Particle physics and field theory, nuclear physics, theory of relativity / Acta Phys. Pol. B* **40**(3), 2009: 725–730. URL OPEN ACCESS.

067 Domingo-Pardo, C.; Goel, N.; Engert, T.*; Gerl, J.; Isaka, M.; Kojouharov, I.; Schaffner, H.: **A Position Sensitive γ-Ray Scintillator Detector With Enhanced Spatial Resolution, Linearity, and Field of View.** *IEEE Transactions on Medical Imaging* **28**(12), 2009: 2007–2014. DOI:10.1109/tmi.2009.2027436

068 Doornenbal, P.; Scheit, H.; Aoi, N.; Takeuchi, S.; Li, K.; Takeshita, E.; Wang, H.; Baba, H.; Deguchi, S.; Fukuda, N.; Geissel, H.*; Gernhäuser, R.; Gibelin, J.; Hachiuma, I.; Hara, Y.; Hinke, C.; Inabe, N.; Itahashi, K.; Itoh, S.; Kameda, D.; Kanno, S.; Kawada, Y.; Kobayashi, N.; Kondo, Y.; Krücken, R.; Kubo, T.; Kuboki, T.; Kusaka, K.; Lantz, M.; Michimasa, S.; Motobayashi, T.; Nakamura, T.; Nakao, T.; Namihira, K.; Nishimura, S.; Ohnishi, T.; Ohtake, M.; Orr, N. A.; Otsu, H.; Ozeki, K.; Satou, Y.; Shimoura, S.; Sumikama, T.; Takechi, M.; Takeda, H.; Tanaka, K. N.; Tanaka, K.; Togano, Y.; Winkler, M.*; Yanagisawa, Y.; Yoneda, K.; Yoshida, A.; Yoshida, K.; Sakurai, H.: **Spectroscopy of ^{32}Ne and the Island of Inversion.** *Physical review letters / Phys. Rev. Lett.* **103**(3), 2009: 032501. DOI:10.1103/physrevlett.103.032501

069 Dragojevic, I.; Gregorich, K. E.; Düllmann, C. E.*; Dvorak, J.; Ellison, P. A.; Gates, J. M.; Nelson, S. L.; Stavsetra, L.; Nitsche, H.: **New isotope ^{263}Hs.** *Physical review C, Nuclear physics / Phys. Rev. C* **79**(1), 2009: 011602. DOI:10.1103/physrevc.79.011602

070 Düllmann, C. E.*; Gregorich, K. E.; Pang, G. K.; Dragojevic, I.; Eichler, R.; Folden, C. M.; Garcia, M. A.; Gates, J. M.; Hoffman, D. C.; Nelson, S. L.; Sudowe, R.; Nitsche, H.: **Gas chemical investigation of hafnium and zirconium complexes with hexafluoroacetylacetone using preseparated short-lived radioisotopes.** *Radiochimica acta / Radiochim. Acta* **97**(8), 2009: 403–418. DOI:10.1524/ract.2009.1630 OPEN ACCESS.

071 Dvorak, J.; Brüchle, W.*; Düllmann, C. E.*; Dvorakova, Z.; Eberhardt, K.; Eichler, R.; Jäger, E.*; Nagame, Y.; Qin, Z.*; Schädel, M.*; Schausten, B.*; Schimpf, E.*; Schuber, R.; Semchenkov, A.*; Thörle, P.; Türler, A.; Wegrzecki, M.; Yakushev, A.: **Cross section limits for the**

^{248}**Cm(**^{25}**Mg, 4n-5n)**^{268,269}**Hs reactions.** *Physical review C, Nuclear physics / Phys. Rev. C* **79**(3), 2009: 037602. DOI:10.1103/physrevc.79.037602

072 Dzhioev, A. A.; Vdovin, A. I.; Ponomarev, V. Y.; Wambach, J.*: **Charge-exchange transitions in hot nuclei.** *Physics of atomic nuclei / Phys. Atom. Nuclei* **72**(8), 2009: 1320–1331. DOI:10.1134/s1063778809080079

073 Elomaa, V. V.; Vorobjev, G. K.*; Kankainen, A.; Batist, L.; Eliseev, S.*; Eronen, T.; Hakala, J.; Jokinen, A.; Moore, I. D.; Novikov, Y. N.*; Penttila, H.; Popov, A.; Rahaman, S.; Rissanen, J.; Saastamoinen, A.; Schatz, H.*; Seliverstov, D. M.; Weber, C.; Äystö, J.: **Quenching of the SnSbTe Cycle in the rp Process.** *Physical review letters / Phys. Rev. Lett.* **102**(25), 2009: 252501. DOI:10.1103/physrevlett.102.252501 Also part of: PNI

074 Esbensen, H.; Reifarth, R.*: **Coulomb dissociation of C-15 and radiative neutron capture on** ^{14}**C (vol 80, 024608, 2009).** *Physical review C, Nuclear physics / Phys. Rev. C* **80**(5), 2009: 059904. DOI:10.1103/physrevc.80.059904

075 Esbensen, H.; Reifarth, R.*: **[Erratum]Coulomb dissociation of** ^{15}**C and radiative neutron capture on** ^{14}**C (vol 80, 024608, 2009).** *Physical review C, Nuclear physics* **80**(5), 2009: 059904. DOI:10.1103/physrevc.80.059904

076 Eshraqi, M.; Franchetti, G.*; Lombardi, A. M.: **Emittance control in rf cavities and solenoids.** *Physical Review Special Topics - Accelerators and Beams / Phys. Rev. Spec. Top.-Accel. Beams* **12**(2), 2009: 024201. DOI:10.1103/physrevstab.12.024201 OPEN ACCESS.

077 Eto, M.; Nakano, E.*; Nitta, M.: **Effective world-sheet theory of color magnetic flux tubes in dense QCD.** *Physical Review D / Phys. Rev. D* **80**(12), 2009: 125011. DOI:10.1103/physrevd.80.125011

078 Eto, M.; Nakano, E.*; Nitta, M.: **Non-Abelian global vortices.** *Nuclear Physics B / Nucl. Phys. B* **821**(1-2), 2009: 129–150. DOI:10.1016/j.nuclphysb.2009.06.013

079 Farrelly, G. F.; Podolyak, Z.; Steer, S. J.; Pietri, S.; Xu, F. R.; Werner-Malento, E.*; Shizuma, T.; Regan, P. H.; Rudolph, D.; Garnsworthy, A. B.; Hoischen, R.; Gorska, M.*; Gerl, J.*; Wollersheim, H. J.*; Kurtukian-Nieto, T.; Benzoni, G.; Becker, F.*; Bednarczyk, P.*; Caceres, L.*; Doornenbal, P.*; Geissel, H.*; Grebosz, J.*; Kelic, A.*; Kojouharov, I.*; Kurz, N.*; Montes, F.*; Prokopowicz, W.*; Saito, T.*; Schaffner, H.*; Tashenov, S.*; Heinz, A.; Pfüzner, M.; Jungclaus, A.; Balabanski, D. L.; Brandau, C.; Bruce, A. M.; Catford, W. N.; Cullen, I. J.; Dombradi, Z.; Estevez, E.; Gelletly, W.; Ilie, G.; Jolie, J.; Jones, G. A.; Kmiecik, M.; Kondev, F. G.; Krucken, R.; Lalkovski, S.; Liu, H. L.; Liu, Z.; Maj, A.; Myalski, S.; Schwerrel, S.; Walker, P. M.; Wieland, O.: **Revision of the K-isomer in** ^{190}**W-190(116).** *Acta physica Polonica B, Particle physics and field theory, nuclear physics, theory of relativity / Acta Phys. Pol. B* **40**(3), 2009: 885–888. URL OPEN ACCESS.

080 Fischer, C. S.*: **Deconfinement Phase Transition and the Quark Condensate.** *Physical review letters / Phys. Rev. Lett.* **103**(5), 2009: 052003. DOI:10.1103/physrevlett.103.052003

081 Fischer, C. S.*; Maas, A.; Pawlowski, J. M.: **On the infrared behavior of Landau gauge Yang-Mills theory.** *Annals of Physics / Ann. Phys.* **324**(11), 2009: 2408–2437. DOI:10.1016/j.aop.2009.07.009

082 Fischer, C. S.*; Mueller, J. A.: **Chiral and deconfinement transition from Dyson-Schwinger equations.** *Physical Review D / Phys. Rev. D* **80**(7), 2009: 074029. DOI:10.1103/physrevd.80.074029

083 Fischer, C. S.*; Nickel, D.; Williams, R.: **On Gribov's supercriticality picture of quark confinement.** *The European physical journal: C, Particles and fields / Eur. Phys. J. C* **60**(1), 2009: 47–61. DOI:10.1140/epjc/s10052-008-0821-1

084 Fischer, C. S.*; Pawlowski, J. M.*: **Uniqueness of infrared asymptotics in Landau gauge Yang-Mills theory. II..** *Physical Review D / Phys. Rev. D* **80**(2), 2009: 025023. DOI:10.1103/physrevd.80.025023

085 Fischer, C. S.*; Williams, R.: **Probing the Gluon Self-Interaction in Light Mesons.** *Physical review letters / Phys. Rev. Lett.* **103**(12), 2009: 122001. DOI:10.1103/physrevlett.103.122001

086 Fischer, D.; Schulz, M.; Schneider, K.*; Ciappina, M. F.; Kirchner, T.; Kelkar, A.; Hagman, S.; Grieser, M.; Kuhnel, K. U.; Moshammer, R.; Ullrich, J.: **Systematic analysis of double-ionization dynamics based on four-body Dalitz plots.** *Physical review A, Atomic, molecular, and optical physics / Phys. Rev. A* **80**(6), 2009: 062703. DOI:10.1103/physreva.80.062703

087 Fischer, E.; Khodzhibagiyan, H.; Kovalenko, A.; Schnizer, P.: **Fast Ramped Superferric Prototypes and Conclusions for the Final Design of the SIS 100 Main Magnets.** *IEEE transactions on applied superconductivity / IEEE Trans. Appl. Supercond.* **19**(3), Part 2, 2009: 1087–1091. DOI:10.1109/tasc.2009.2019013

088 Fischer, E.; Schnizer, P.; Kurnyshov, R.; Schnizer, B.; Shcherbakov, P.: **Numerical Analysis of the Operation Parameters of Fast Cycling Superconducting Magnets.** *IEEE transactions on applied superconductivity / IEEE Trans. Appl. Supercond.* **19**(3), Part 2, 2009: 1266–1269. DOI:10.1109/tasc.2009.2018746

089 Flanagan, K. T.; Vingerhoets, P.; Avgoulea, M.; Billowes, J.; Bissell, M. L.; Blaum, K*; Cheal, B.; De Rydt, M.; Fedosseev, V. N.; Forest, D. H.; Geppert,

C.; Köster, U.; Kowalska, M.; Krämer, J.; Kratz, K. L.; Krieger, A.; Mane, E.; Marsh, B. A.; Materna, T.; Mathieu, L.; Molkanov, P. L.; Neugart, R.; Neyens, G.; Nörtershäuser W.*; Seliverstov, M. D.; Serot, O.; Schug, M.; Sjoedin, M. A.; Stone, J. R.; Stone, N. J.; Stroke, H. H.; Tungate, G.; Yordanov, D. T.; Volkov, Y. M.: **Nuclear Spins and Magnetic Moments of ^{71,72,73}Cu: Inversion of $\pi 2p_{3/2}$ and $\pi 1f_{5/2}$ Levels in ^{75}Cu.** *Physical review letters / Phys. Rev. Lett.* **103**(14), 2009: 142501. DOI:10.1103/physrevlett.103.142501 Also part of: PNI

090 Floch, E.; Walter, F.; Stafiniak, A.; Marzouki, F.; Schroeder, C.; Leibrock, H.; Fischer, E.; Moritz, G.: **Quench Measurement on SIS100 Dipole Model.** *IEEE transactions on applied superconductivity / IEEE Trans. Appl. Supercond.* **19**(3), Part 2, 2009: 2450–2453. DOI:10.1109/tasc.2009.2019061

091 Fröhlich, I.; Agakishiev, G.; Agodi, C.; Balanda, A.; Bellia, G.; Belver, D.; Belyaev, A.; Blanco, A.; Bohmer, M.; Boyard, J. L.; Braun-Munzinger, P.*; Cabanelas, P.; Castro, E.; Chernenko, S.; Christ, T.; Destefanis, M.; Diaz, J.; Dohrmann, F.; Dybczak, A.; Eberl, T.; Fabbietti, L.; Fateev, O.; Finocchiaro, P.; Fonte, P.; Friese, J.; Galatyuk, T.; Garzon, J. A.; Gernhäuser, R.; Gil, A.; Gilardi, C.; Golubeva, M.; Gonzalez-Diaz, D.; Grosse, E.; Guber, F.; Heilmann, M.; Hennino, T.; Holzmann, R.*; Ierusalimov, A.; Iori, I.; Ivashkin, A.; Jurkovic, M.; Kampfer, B.; Kanaki, K.; Karavicheva, T.; Kirschner, D.; Koenig, I.; Koenig, W.; Kolb, B. W.; Kotte, R.; Kozuch, A.; Krasan, A.; Krizek, F.; Krucken, R.; Kuhn, W.; Kugler, A.; Kurepin, A.; Lamas-Valverde, J.; Lang, S.; Lange, J. S.; Lapidus, K.; Lopes, L.; Maier, L.; Mangiarotti, A.; Marin, J.; Markert, J.; Metag, V.; Michalska, B.; Michel, J.; Mishra, D.; Moriniere, E.; Mousa, J.; Müntz, C.; Naumann, L.; Novotny, R.; Otwinowski, J.; Pachmayer, Y. C.; Palka, M.; Parpottas, Y.; Pechenov, V.; Pechenova, O.; Cavalcanti, T. P.; Pietraszko, J.; Przygoda, W.; Ramstein, B.; Reshetin, A.; Roy-Stephan, M.; Rustamov, A.; Sadovsky, A.; Sailer, B.; Salabura, P.; Schmah, A.; Simon, R.; Sobolev, Y. G.; Spataro, S.; Spruck, B.; Ströbele, H.; Stroth, J.; Sturm, C.; Sudol, M.; Tarantola, A.; Teilab, K.; Tlusty, P.; Traxler, M.; Trebacz, R.; Tsertos, H.; Veretenkin, I.; Wagner, V.; Wen, H.; Wisniowski, M.; Wojcik, T.; Wüstenfeld, J.; Yurevich, S.; Zanevsky, Y.; Zhou, P.; Zumbruch, P.: **Meson and dielectron production with HADES.** *International Journal of Modern Physics A: Particles and Fields, Gravitation and Cosmology / Int. J. Mod. Phys. A* **24**(2-3), 2009: 317–326.

092 Franchetti, G.*; Hofmann, I.*; Fischer, W.; Zimmermann, F.: **Incoherent effect of space charge and electron cloud.** *Physical Review Special Topics - Accelerators and Beams / Phys. Rev. Spec. Top.-Accel. Beams* **12**(12), 2009: 124401. DOI:10.1103/physrevstab.12.124401 OPEN ACCESS.

093 Galatyuk, T.; HADES Collaboration: **Dielecton measurements in NN interactions at a beam energy of 1.25 GeV with HADES.** *International Journal of Modern Physics A: Particles and Fields, Gravitation and Cosmology / Int. J. Mod. Phys. A* **24**(2-3), 2009: 599–602.

094 Garnsworthy, A. B.; Regan, P. H.; Pietri, S.; Sun, Y.; Xu, F. R.; Rudolph, D.; Gorska, M.*; Caceres, L.; Podolyak, Z.; Steer, S. J.; Hoischen, R.*; Heinz, A.; Becker, F.*; Bednarczyk, P.*; Doornenbal, P.*; Geissel, H.*; Gerl, J.*; Grawe, H.; Grebosz, J.*; Kelic, A.*; Kojouharov, I.*; Kurz, N.*; Montes, F.*; Prokopwicz, W.*; Saito, T.*; Schaffner, H.*; Tachenov, S.*; Werner-Malento, E.; Wollersheim, H. J.*; Benzoni, G.; Blank, B.; Brandau, C.*; Bruce, A. M.; Camera, F.; Catford, W. N.*; Cullen, I. J.; Dombradi, Z.; Estevez, E.; Gelletly, W.; Ilie, G.; Jolie, J.; Jones, G. A.; Jungclaus, A.; Kmiecik, M.; Kondev, F. G.; Kurtukian-Nieto, T.; Lalkovski, S.; Liu, Z.; Maj, A.; Myalski, S.; Pfützner, M.; Schwertel, S.; Shizuma, T.; Simons, A. J.; Walker, P. M.; Wieland, O.: **Isomeric states in neutron-deficient A $\sim$ to 80-90 nuclei populated in the fragmentation of ^{107}Ag.** *Physical review C, Nuclear physics / Phys. Rev. C* **80**(6), 2009: 064303. DOI:10.1103/physrevc.80.064303

095 Gerl, J.*: **Nuclear spectroscopy studies at GSI from RISING to HISPEC/DESPEC.** *Acta physica Polonica B, Particle physics and field theory, nuclear physics, theory of relativity / Acta Phys. Pol. B* **40**(3), 2009: 767–778. URL OPEN ACCESS.

096 Gil, A.; Belver, D.; Cabanelas, P.; Castro, E.; Diaz, J.; Garzon, J. A.; Gonzalez-Diaz, D.; Koenig, W.; Stankova, V.; Traxler, M.: **Distributed Low-Voltage System for the Front End of the HADES Timing RPC Wall.** *IEEE transactions on nuclear science / IEEE Trans. Nucl. Sci.* **56**(2), 2009: 382–387. DOI:10.1109/tns.2009.2014845

097 Goecke, T.; Fischer, C. S.*; Williams, R.: **Finite-volume effects and dynamical chiral symmetry breaking in QED$_3$.** *Physical review: B, Condensed matter and materials physics / Phys. Rev. B* **79**(6), 2009: 064513. DOI:10.1103/physrevb.79.064513

098 Golovkov, M. S.; Grigorenko, L. V.*; Ter-Akopian, G. M.; Fomichev, A. S.; Oganessian, Y. T.; Gorshkov, V. A.; Krupko, S. A.; Rodin, A. M.; Sidorchuk, S. I.; Slepneva, R. S.; Stepantsov, S. V.; Wolski, R.; Pang, D. Y.; Chudoba, V.; Korsheninnikov, A. A.; Kuzmin, E. A.; Nikolskii, E. Y.; Novatskii, B. G.; Stepanov, D. N.; Roussel-Chomaz, P.; Mittig, W.; Ninane, A.; Hanappe, F.; Stuttge, L.; Yukhimchuk, A. A.; Perevozchikov, V. V.; Vinogradov, Y. I.; Grishechkin, S. K.; Zlatoustovskiy, S. V.: **The ^{8}He and ^{10}He spectra studied in the (t, p) reaction.** *Physics letters B / Phys. Lett. B* **672**(1), 2009: 22–29. DOI:10.1016/j.physletb.2008.12.052

099 Gonzalez-Diaz, D.*; Morales, M.; Ferreira, L. F.; Garzon, J. A.; Gonzalez-Castano, D.; Pecharroman, C.: **The role of the Resistive Plate response function in bring-**

ing an RPC to a stationary situation. *Nuclear instruments & methods in physics research, Section A, Accelerators, spectrometers, detectors and associated equipment / Nucl. Instrum. Methods Phys. Res. Sect. A-Accel. Spectrom. Dect. Assoc. Equip.* **602**(3), 2009: 713–718. DOI:10.1016/j.nima.2008.12.097

100 Gonzalez, P.; de Guevara, P. L.; Torres, E. L.; Marin, A.*; Serradilla, E.; ALICE Collaboration: **Simulation study of $\chi_c \rightarrow J/I + \gamma$ detection with $J/I \rightarrow e^+e^-$ in pp collisions in the ALICE experiment at LHC.** *The European physical journal: C, Particles and fields / Eur. Phys. J. C* **61**(4), 2009: 899–903. DOI:10.1140/epjc/s10052-009-0895-4

101 Gorska, M.*; Caceres, L.*; Grawe, H.*; Pfuetzner, M.; Jungclaus, A.; Pietri, S.; Werner-Malento, E.; Podolyak, Z.; Regan, P. H.; Rudolph, D.; Detistov, R.; Lalkovski, S.; Modamio, V.; Walker, J.; Beck, T.*; Bednarczyk, P.*; Doornenbal, P.*; Geissel, H.*; Gerl, J.*; Grebosz, J.*; Hoischen, R.*; Kojouharov, I.*; Kurz, N.*; Prokopowicz, W.*; Schaffner, H.*; Weick, H.*; Wollersheim, H.-J.*; Andgren, K.; Benlliure, J.; Benzoni, G.; Bruce, A. M.; Casarejos, E.; Cederwall, B.; Crespi, F. C. L.; Hadinia, B.; Hellström, M.; Ilie, G.; Khaplanov, A.; Kmiecik, M.; Kumar, R.; Maj, A.; Mandal, S.; Montes, F.*; Myalski, S.; Simpson, G. S.; Steer, S. J.; Tashenov, S.*; Wieland, O.; Dombradi, Z.; Reiter, R.; Sohler, D.: **Evolution of the N=82 shell gap below ^{132}Sn inferred from core excited states in ^{131}In.** *Physics letters B / Phys. Lett. B* **672**(4-5), 2009: 313–316. DOI:10.1016/j.physletb.2009.01.027

102 Gorska, M.; Grawe, H.; Caceres, L.; Algora, A.; Bohmer, M.; Boutachkov, P.; Eppinger, K.; Faestermann, T.GAST; Fujita, Y.; Gadea, A.; Garnsworthy, A.; Gelletly, W.; Gerl, J.; Gernhauser, R.; Hinke, C.; Jungclaus, A.; Kojouharov, I.; Krucken, R.; Maier, L.GAST; Molina, P.; Pfutzner, M.; Pietri, S.; Podolyak, Z.; Regan, P. H.; Rubio, B.; Rudolph, D.; Wollersheim, H. J.; RISING Collaboration: **Nuclear structure addressed at GSI/RISING.** *International journal of modern physics E, Nuclear physics / Int. J. Mod. Phys. E-Nucl. Phys.* **18**(4), 2009: 759–766, Sp. Iss. SI.

103 Grahn, T.; Petts, A.; Scheck, M.; Butler, P. A.; Dewald, A.; Hornillos, M. B. G.; Greenlees, P. T.; Görgen, A.; Helariutta, K.; Jolie, J.; Jones, P.; Julin, R.; Juutinen, S.; Ketelhut, S.; Krücken, R.; Kröll, T.; Leino, M.; Ljungvall, J.; Maierbeck, P.; Melon, B.; Nyman, M.; Page, R. D.; Pissulla, T.; Rahkila, P.; Saren, J.; Scholey, C.; Semchenkov, A.*; Sorri, J.; Uusitalo, J.; Wadsworth, R.; Zieliska, M.: **Evolution of collectivity in ^{180}Hg and ^{182}Hg.** *Physical review C, Nuclear physics / Phys. Rev. C* **80**(1), 2009: 014324. DOI:10.1103/physrevc.80.014324

104 Grigorenko, L. V.*; Wiser, T. D.; Mercurio, K.; Charity, R. J.; Shane, R.; Sobotka, L. G.; Elson, J. M.; Wuosmaa, A. H.; Banu, A.; McCleskey, M.; Trache, L.; Tribble, R. E.; Zhukov, M. V.: **Three-body decay of ^{6}Be.** *Physical review C, Nuclear physics / Phys. Rev. C* **80**(3), 2009: 034602. DOI:10.1103/physrevc.80.034602

105 Grigorenko, L. V.*; Wiser, T. D.; Miernik, K.; Charity, R. J.; Pfützner, M.; Banu, A.; Bingham, C. R.; Cwiok, M.; Darby, I. G.; Dominik, W.; Elson, J. M.; Ginter, T.; Grzywacz, R.; Janas, Z.; Karny, M.; Korgul, A.; Liddick, S. N.; Mercurio, K.; Rajabali, M.; Rykaczewski, K.; Shane, R.; Sobotka, L. G.; Stolz, A.; Trache, L.; Tribble, R. E.; Wuosmaa, A. H.; Zhukov, M. V.: **Complete correlation studies of two-proton decays: ^{6}Be and ^{45}Fe.** *Physics letters B / Phys. Lett. B* **677**(1-2), 2009: 30–35. DOI:10.1016/j.physletb.2009.04.085

106 Groening, L.*; Barth, W.*; Bayer, W.*; Clemente, G.*; Dahl, L.*; Forck, P.*; Gerhard, P.*; Hofmann, I.*; Kaiser, M. S.*; Maier, M.*; Mickat, S.;* Milosic, T.*; Jeon, D.; Uriot, D.: **Experimental Evidence of the 90^o Stop Band in the GSI UNILAC.** *Physical review letters / Phys. Rev. Lett.* **102**(23), 2009: 234801. DOI:10.1103/physrevlett.102.234801

107 Groening, L.*; Hofmann, I.*; Barth, W.*; Bayer, W.*; Clemente, G.*; Dahl, L.*; Forck, P.*; Gerhard, P.*; Kaiser, M. S.*; Maier, M.*; Mickat, S.*; Milosic, T.*; Yaramyshev, S.*; Uriot, D.: **Experimental Evidence of Space Charge Driven Emittance Coupling in High Intensity Linear Accelerators.** *Physical review letters* **103**(22), 2009: 224801. DOI:10.1103/physrevlett.103.224801

108 Groening, L.*; Hofmann, I.*; Barth, W.*; Bayer, W.; Clemente, G.*; Dahl, L.*; Forck, P.*; Gerhard, P.*; Kaiser, M. S.*; Maier, M.*; Mickat, S.*; Milosic, T.*; Yaramyshev, S.*; Uriot, D.: **Experimental Evidence of Space Charge Driven Emittance Coupling in High Intensity Linear Accelerators.** *Physical review letters / Phys. Rev. Lett.* **103**(22), 2009: 224801. DOI:10.1103/physrevlett.103.224801

109 Gupta, R. K.; Niyti, ; Manhas, M.; Hofmann, S.; Greiner, W.: **Role of static deformation and compact orientation of target nucleus in measured fusion, fusion-fission and capture cross-sections of ^{244}Pu+ ^{48}Ca reaction.** *International journal of modern physics E, Nuclear physics / Int. J. Mod. Phys. E-Nucl. Phys.* **18**(3), 2009: 601–619. URL

110 Höhne, C.*: **SPS energy scan results and physics prospects at FAIR.** *Nuclear physics A, Nuclear and hadronic physics / Nucl. Phys. A* **830**, 2009: 369C–376C. DOI:10.1016/j.nuclphysa.2009.10.032

111 Höhne, C.*: **SPS energy scan results and physics prospects at FAIR.** *Nuclear physics A, Nuclear and hadronic physics* **830**, 2009: 369C–376C. DOI:10.1016/j.nuclphysa.2009.10.032

112 Hashimoto, T.; Ishiyama, H.; Watanabe, Y. X.; Hi-

rayama, Y.; Imai, N.; Miyatake, H.; Jeong, S. C.; Tanaka, M. H.; Yoshikawa, N.; Nomura, T.; Mitsuoka, S.; Nishio, K.; Sato, T. K.; Osa, A.; Ichikawa, S.; Matsuda, M.; Ikezoe, H.; Das, S. K.; Mizoi, Y.; Fukuda, T.; Sato, A.; Shimoda, T.; Otsuki, K.*; Kajino, T.: **A new measurement of the astrophysical ^{8}Li(d, t)^{7}Li reaction.** *Physics letters B / Phys. Lett. B* **674**(4-5), 2009: 276–280. DOI:10.1016/j.physletb.2009.03.031

113 Hedlund, E.; Malyshev, O. B.; Westerberg, L.; Krasnov, A.; Semenov, A. S.; Leandersson, M.; Zajec, B.; Kollmus, H.*; Bellachioma, M. C.*; Bender, M.*; Krämer, A.*; Reich-Sprenger, H.*: **Heavy-ion induced desorption of a TiZrV coated vacuum chamber bombarded with 5 MeV/u Ar8+ beam at grazing incidence.** *Journal of Vacuum Science and Technology A / J. Vac. Sci. Technol. A* **27**(1), 2009: 139–144. DOI:10.1116/1.3032914

114 Hedlund, E.; Westerberg, L.; Malyshev, O. B.; Edqvist, E.; Leandersson, M.; Kollmus, H.*; Bellachioma, M. C.*; Bender, M.; Krämer, A.*; Reich-Sprenger, H.*; Zajec, B.; Krasnov, A.: **Ar ion induced desorption yields at the energies 5-17.7 MeV/u.** *Nuclear instruments & methods in physics research, Section A, Accelerators, spectrometers, detectors and associated equipment / Nucl. Instrum. Methods Phys. Res. Sect. A-Accel. Spectrom. Dect. Assoc. Equip.* **599**(1), 2009: 1–8. DOI:10.1016/j.nima.2008.09.052

115 Heil, M.*; Juseviciute, A.; Käppeler, F.; Gallino, R.; Pignatari, M.; Uberseder, E.: **Neutron Capture Cross Sections for the Weak s Process.** *Publications of the Astronomical Society of Australia / Publ. Astron. Soc. Aust.* **26**(3), 2009: 243–249. DOI:10.1071/as08064

116 Hempel, M.; Pagliara, G.*; Schaffner-Bielich, J.*: **Conditions for phase equilibrium in supernovae, protoneutron, and neutron stars.** *Physical Review D / Phys. Rev. D* **80**(12), 2009: 125014. DOI:10.1103/physrevd.80.125014

117 Herzberg, R. D.; Moon, S.; Eeckhaudt, S.; Greenlees, P. T.; Butler, P. A.; Page, T.; Afanasjev, A. V.; Amzal, N.; Bastin, J. E.; Becker, F.; Bender, M.; Bruyneel, B.; Cocks, J. F. C.; Darby, I. G.; Dorvaux, O.; Eskola, K.; Gerl, J.*; Grahn, T.; Gray-Jones, C.; Hammond, N. J.; Hauschild, K.; Heenen, P. H.; Helariutta, K.; Herzberg, A.; Heßberger, F.*; Houry, M.; Hurstel, A.; Humphreys, R. D.; Jones, G. D.; Jones, P. M.; Julin, R.; Juutinen, S.; Kankaanpää, H.; Kettunen, H.; Khoo, T. L.; Korten, W.; Kuusiniemi, P.; LeCoz, Y.; Leino, M.; Leppanen, A. P.; Lister, C. J.; Lucas, R.; Muikku, M.; Nieminen, P.; Nyman, M.; Page, R. D.; Page, T.; Pakarinen, J.; Pritchard, A.; Rahkila, P.; Reiter, P.; Sandzelius, M.; Saren, J.; Schlegel, C.*; Scholey, C.; Theisen, C.; Trzaska, W. H.; Uusitalo, J.; Wiens, A.; Wollersheim, H. J.*: **Structure of rotational bands in ^{253}No.** *The European physical journal A, Hadrons and nuclei / Eur. Phys. J. A* **42**(3), 2009: 333–337. DOI:10.1140/epja/i2009-10855-9

118 Herzberg, R.-D.; Moon, S.; Eeckhaudt, S.; Greenlees, P. T.; Butler, P. A.; Page, T.; Afanasjev, A. V.; Amzal, N.; Bastin, J. E.; Becker, F.; Bender, M.*; Bruyneel, B.; Cocks, J. F. C.; Darby, I. G.; Dorvaux, O.; Eskola, K.; Gerl, J.*; Grahn, T.; Gray-Jones, C.; Hammond, N. J.; Hauschild, K.; Heenen, P. H.; Helariutta, K.; Herzberg, A.; Heßberger, F.*; Houry, M.; Hurstel, A.; Humphreys, R. D.; Jones, G. D.; Jones, P. M.; Julin, R.; Juutinen, S.; Kankaanpää, H.; Kettunen, H.; Khoo, T. L.; Korten, W.; Kuusiniemi, P.; LeCoz, Y.; Leino, M.; Leppänen, A. P.; Lister, C. J.; Lucas, R.; Muikku, M.; Nieminen, P.; Nyman, M.; Page, R. D.; Page, T.; Pakarinen, J.; Pritchard, A.; Rahkila, P.; Reiter, P.; Sandzelius, M.; Saren, J.; Schlegel, C.*; Scholey, C.; Theisen, C.; Trzaska, W. H.; Uusitalo, J.; Wiens, A.; Wollersheim, H. J.*: **Structure of rotational bands in ^{253}No.** *The European physical journal A, Hadrons and nuclei* **42**(3), 2009: 333–337. DOI:10.1140/epja/i2009-10855-9

119 Heßberger, F. P.*; Hofmann, S.*; Streicher, B.*; Sulignano, B.*; Antalic, S.; Ackermann, D.*; Heinz, S.*; Kindler, B.; Kojouharov, I.*; Kuusiniemi, P.; Leino, M.; Lommel, B.*; Mann, R.*; Popeko, A. G.; Saro, S.; Uusitalo, J.; Yeremin, A. V.: **Decay properties of neutron-deficient isotopes of elements from Z=101 to Z=108.** *The European physical journal A, Hadrons and nuclei / Eur. Phys. J. A* **41**(2), 2009: 145–153. DOI:10.1140/epja/i2009-10826-2

120 Heuser, J. M.*; CBM Collaboration*: **The Compressed Baryonic Matter Experiment at FAIR: Progress with feasibility studies and detector developments.** *Nuclear physics A, Nuclear and hadronic physics / Nucl. Phys. A* **830**, 2009: 563C–566C. DOI:10.1016/j.nuclphysa.2009.09.048

121 Heuser, J. M.*; CBM Collaboration: **The Compressed Baryonic Matter Experiment at FAIR: Progress with feasibility studies and detector developments.** *Nuclear physics A, Nuclear and hadronic physics* **830**, 2009: 563C–566C. DOI:10.1016/j.nuclphysa.2009.09.048

122 Hudan, S.; McIntosh, A. B.; Black, J.; Mercier, D.; Metelko, C. J.; Yanez, R.; de Souza, R. T.; Chbihi, A.; Famiano, M.; Fregeau, M. O.; Gauthier, J.; Moisan, J.; Roy, R.; Bianchin, S.*; Schwarz, C.*; Trautmann, W.*; Botvina, A. S.: **Charge correlations and isotopic distributions of projectile fragmentation events in ^{124}Xe + ^{112}Sn at EA=50 MeV.** *Physical review C, Nuclear physics / Phys. Rev. C* **80**(6), 2009: 064611. DOI:10.1103/physrevc.80.064611

123 Ivanov, Y. B.*; Russkikh, V. N.*: **On freeze-out problem in relativistic hydrodynamics.** *Physics of atomic nuclei / Phys. Atom. Nuclei* **72**(7), 2009: 1238–1244. DOI:10.1134/s1063778809070187

124 Ivanov, Y. B.*; Voskresensky, D. N.*: **Nonlocal form of quantum off-shell kinetic equation.** *Physics of atomic nuclei / Phys. Atom. Nuclei* **72**(7), 2009: 1168–1179. DOI:10.1134/s1063778809070096

125 Jachimowicz, P.; Kowal, M.; Rozmej, P.; Skalski, J.; Sobiczewski, A.: **Non-axial octupole deformation of a heavy nucleus.** *International journal of modern physics E, Nuclear physics / Int. J. Mod. Phys. E-Nucl. Phys.* **18**(4), 2009: 1088–1093, Sp. Iss. SI. URL

126 Jeon, D.; Groening, L.*; Franchetti, G.*: **Fourth order resonance of a high intensity linear accelerator.** *Physical Review Special Topics - Accelerators and Beams / Phys. Rev. Spec. Top.-Accel. Beams* **12**(5), 2009: 054204. DOI:10.1103/physrevstab.12.054204 OPEN ACCESS.

127 Käppeler, F.; Bisterzo, S.; Gallino, R.; Heil, M.*; Pignatari, M.; Reifarth, R.*; Straniero, O.; Walter, S.; Winckler, N.*; Wisshak, K.: **Time-Scales of the s Process: from Minutes to Ages.** *Publications of the Astronomical Society of Australia / Publ. Astron. Soc. Aust.* **26**(3), 2009: 209–216. DOI:10.1071/as08052

128 Kalantar-Nayestanaki, N.; Moeini, H.; Mahjour-Shafiei, M.; Aksouh, F.; Beckert, K.; Beller, P.; Boretzky, K.; Chatillon, A.; Corsi, A.; Egelhof, P.; Emling, H.; Ickert, G.; Ilieva, S.; Kozhuharov, C.; Le Bleis, T.; Le Xuang, X. C.; Litvinov, Y.; Mahata, K.; Meier, J. P.; Nolden, F.; Popp, U.; Simon, H.; Steck, M.; Stöhlker, T.; Weick, H.; Zalite, A.; Kiselev, O.; Jourdan, J.; Kiselev, D.; Werthmuller, D.; Paschalis, S.; EXL Collaboration: **First feasibility study for EXL with prototype detectors at the ESR and detector simulations.** *International journal of modern physics E, Nuclear physics / Int. J. Mod. Phys. E-Nucl. Phys.* **18**(2), 2009: 524–530. URL

129 Kanungo, R.; Nociforo, C.*; Prochazka, A.*; Aumann, T.*; Boutin, D.; Cortina-Gil, D.; Davids, B.; Diakaki, M.; Farinon, F.*; Geissel, H.*; Gernhäuser, R.; Gerl, J.*; Janik, R.; Jonson, B.; Kindler, B.*; Knöbel, R.*; Krücken, R.; Lantz, M.; Lenske, H.; Litvinov, Y.*; Lommel, B.*; Mahata, K.*; Maierbeck, P.; Musumarra, A.; Nilsson, T.; Otsuka, T.; Perro, C.; Scheidenberger, C.*; Sitar, B.; Strmen, P.; Sun, B.*; Szarka, I.; Tanihata, I.; Utsuno, Y.; Weick, H.*; Winkler, M.*: **One-Neutron Removal Measurement Reveals ^{24}O as a New Doubly Magic Nucleus.** *Physical review letters / Phys. Rev. Lett.* **102**(15), 2009: 152501. DOI:10.1103/physrevlett.102.152501

130 Kasamatsu, Y.; Toyoshima, A.; Asai, M.; Tsukada, K.; Li, Z. J.; Ishii, Y.; Toume, H.; Sato, T. K.; Kikuchi, T.; Nishinaka, I.; Nagame, Y.; Haba, H.; Kikunaga, H.; Kudou, Y.; Oura, Y.; Akiyama, K.; Sato, W.; Ooe, K.; Fujisawa, H.; Shinohara, A.; Goto, S.; Hasegawa, T.; Kudo, H.; Nanri, T.; Araki, M.; Kinoshita, N.; Yokoyama, A.; Fan, F. L.; Qin, Z.; Dullmann, C. E.*; Schädel, M.*; Kratz, J. V.: **Anionic Fluoro Complex of Element 105, Db.** *Chemistry Letters* **38**(11), 2009: 1084–1085. DOI:10.1246/cl.2009.1084

131 Kasamatsu, Y.; Toyoshima, A.; Asai, M.; Tsukada, K.; Li, Z. J.; Ishii, Y.; Toume, H.; Sato, T. K.; Kikuchi, T.; Nishinaka, I.; Nagame, Y.; Haba, H.; Kikunaga, H.; Kudou, Y.; Oura, Y.; Akiyama, K.; Sato, W.; Ooe, K.; Fujisawa, H.; Shinohara, A.; Goto, S.; Hasegawa, T.; Kudo, H.; Nanri, T.; Araki, M.; Kinoshita, N.; Yokoyama, A.; Fan, F. L.; Qin, Z.; Düllmann, C. E.*; Schädel, M.*; Kratz, J. V.: **Anionic Fluoro Complex of Element 105, Db.** *Chemistry Letters / Chem. Lett.* **38**(11), 2009: 1084–1085. DOI:10.1246/cl.2009.1084

132 Ketelhut, S.; Greenlees, P. T.; Ackermann, D.*; Antalic, S.; Clement, E.; Darby, I. G.; Dorvaux, O.; Drouart, A.; Eeckhaudt, S.; Gall, B. J. P.; Görgen, A.; Grahn, T.; Gray-Jones, C.; Hauschild, K.; Herzberg, R. D.; Heßberger, F. P.*; Jakobsson, U.; Jones, G. D.; Jones, P.; Julin, R.; Juutinen, S.; Khoo, T. L.; Korten, W.; Leino, M.; Leppänen, A. P.; Ljungvall, J.; Moon, S.; Nyman, M.; Obertelli, A.; Pakarinen, J.; Parr, E.; Papadakis, P.; Peura, P.; Piot, J.; Pritchard, A.; Rahkila, P.; Rostron, D.; Ruotsalainen, P.; Sandzelius, M.; Saren, J.; Scholey, C.; Sorri, J.; Steer, A.; Sulignano, B.; Theisen, C.; Uusitalo, J.; Venhart, M.; Zielinska, M.; Bender, M.; Heenen, P. H.: **gamma-Ray Spectroscopy at the Limits: First Observation of Rotational Bands in ^{255}Lr.** *Physical review letters / Phys. Rev. Lett.* **102**(21), 2009: 212501. DOI:10.1103/physrevlett.102.212501

133 Kim, M.; Ajimura, S.; Aoki, K.; Banu, A.*; Bhang, H.; Fukuda, T.; Hashimoto, O.; Hwang, J. I.; Kameoka, S.; Kang, B. H.; Kim, E.; Kim, J. H.; Maruta, T.; Miura, Y.; Miyake, Y.; Nagae, T.; Nakamura, M.; Nakamura, S. N.; Noumi, H.; Okada, S.; Okayasu, Y.; Outa, H.; Park, H.; Saha, P. K.; Sato, Y.; Sekimoto, M.; Takahashi, T.; Tamura, H.; Tanida, K.; Toyoda, A.; Tshoo, K.; Tsukada, K.; Watanabe, T.; Yim, H. J.: **Three-Body Nonmesonic Weak Decay of the $^{12}_{\Lambda}$C Hypernucleus.** *Physical review letters / Phys. Rev. Lett.* **103**(18), 2009: 182502. DOI:10.1103/physrevlett.103.182502

134 Klimkiewicz, A.; Paar, N.; Adrich, P.*; Fallot, M.*; Boretzky, K.*; Aumann, T.*; Cortina-Gil, D.; Pramanik, U. D.; Elze, T. W.; Emling, H.*; Geissel, H.*; Hellström, M.*; Jones, K. L.*; Kratz, J. V.; Kulessa, R.; Nociforo, C.*; Palit, R.; Simon, H.*; Surowka, G.; Sümmerer, K.*; Vretenar, D.; Walus, W.: **Collective diploe excitations in neutron-rich nuclei from ^{132}Snmass region, the nuclear symmetry energy and neutron skins.** *Acta physica Polonica B, Particle physics and field theory, nuclear physics, theory of relativity / Acta Phys. Pol. B* **40**(3), 2009: 589–592. URL OPEN ACCESS.

135 Knoll, J.*: **Continuous decoupling and freeze-out.** *Acta physica Polonica B, Particle physics and field theory, nuclear physics, theory of relativity / Acta Phys. Pol. B* **40**(4), 2009: 1037–1043. URL OPEN ACCESS.

136 Knoll, J.*: **Continuous decoupling of dynamically**

expanding systems. *Nuclear physics A, Nuclear and hadronic physics / Nucl. Phys. A* **821**, 2009: 235–250. DOI:10.1016/j.nuclphysa.2009.01.079

137 Koch, B.; Bleicher, M.; Stöcker, H.*: **Exclusion of black hole disaster scenarios at the LHC.** *Physics letters B / Phys. Lett. B* **672**(1), 2009: 71–76. DOI:10.1016/j.physletb.2009.01.003

138 Koide, T.; Nakano, E.*; Kodama, T.: **Shear Viscosity Coefficient and Relaxation Time of Causal Dissipative Hydrodynamics in QCD.** *Physical review letters / Phys. Rev. Lett.* **103**(5), 2009: 052301. DOI:10.1103/physrevlett.103.052301

139 Kollmus, H.*; Krämer, A.*; Bender, M.*; Bellachioma, M. C.*; Reich-Sprenger, H.*; Mahner, E.; Hedlun, E.; Westerberg, L.; Malyshev, O. B.; Leandersson, M.; Edqvist, E.: **Energy scaling of the ion-induced desorption yield for perpendicular collisions of Ar and U with stainless steel in the energy range of 5 and 100 MeV/u.** *Journal of Vacuum Science and Technology A / J. Vac. Sci. Technol. A* **27**(2), 2009: 245–247. DOI:10.1116/1.3065979

140 Korpa, C. L.; Lutz, M. F. M.*; Riek, F.*: **Covariant and self-consistent vertex corrections for pions and isobars in nuclear matter.** *Physical review C, Nuclear physics / Phys. Rev. C* **80**(2), 2009: 024901. DOI:10.1103/physrevc.80.024901

141 Kozlova, E.; Strasik, I.; Fertman, A.; Mustafin, E.; Radon, T.; Hinca, R.; Pavlovic, M.; Fehrenbacher, G.; Geissel, H.; Golubev, A.; Iwase, H.; Schardt, D.: **Benchmark Test of the FLUKA Monte Carlo Code for Residual Production with 500 and 950 MeV/u Uranium Beams on Copper and Stainless Steel Targets.** *Nuclear Technology / Nucl. Technol.* **168**(3), 2009: 747–751, Sp. Iss. SI. URL

142 Kraft-Bermuth, S.*; Andrianov, V. A.*; Bleile, A.*; Echler, A.+; Egelhof, P.*; Kiseleva, A.*; Kiselev, O.*; Meier, H. J.*; Meier, J. P.*; Shrivastava, A.*; Weber, M.*; Golser, R.; Kutschera, W.; Priller, A.; Steier, P.; Vockenhuber, C.: **Calorimetric low temperature detectors for low-energetic heavy ions and their application in accelerator mass spectrometry.** *Review of scientific instruments / Rev. Sci. Instrum.* **80**(10), 2009: 103304. DOI:10.1063/1.3213622

143 Kumar, R.*; Molina, F. G.; Pietri, S.; Casarejos, E.; Algora, A.; Benlliure, J.; Doornenbal, P.*; Gerl, J.*; Gorska, M.*; Kojouharov, I.*; Podolyak, Z.; Prokopowicz, W.*; Regan, P. H.; Rubio, B.; Schaffner, H.*; Tashenov, S.*; Wollersheim, H. J.*: **Testing of a DSSSD detector for the stopped RISING project.** *Nuclear instruments & methods in physics research, Section A, Accelerators, spectrometers, detectors and associated equipment / Nucl. Instrum. Methods Phys. Res. Sect. A-Accel. Spectrom. Dect. Assoc. Equip.* **598**(3), 2009: 754–758. DOI:10.1016/j.nima.2008.08.155

144 Kurtukian-Nieto, T.; Benlliure, J.; Schmidt, K.-H.*; Audouin, L.; Becker, F.*; Blank, B.; Borzov, I. N.*; Casarejos, E.; Fernandez-Ordonez, M.; Giovinazzo, J.; Henzlova, D.*; Jurado, B.; Langanke, K.*; Martinez-Pinedo, G.*; Pereira, J.; Rejmund, F.; Yordanov, O.*: **Recent progress in measuring β half-lives of nuclei approaching the r-process waiting point A=195.** *Nuclear physics A, Nuclear and hadronic physics / Nucl. Phys. A* **827**(1-4), 2009: 587C–589C. DOI:10.1016/j.nuclphysa.2009.05.129

145 Le Fèvre, A.*; Aichelin, J.; Hartnack, C.; Lukasik, J.*; Müller, W. F. J.*; Orth, H.*; Schwarz, C.*; Sfienti, C.*; Trautmann, W.*; Turzo, K.*; Zwieglinski, B.; Chbihi, A.; Frankland, J. D.; Wieleczko, J. P.; Vigilante, M.; ALADIN INDRA GSI Collaboration: **Bimodality: A general feature of heavy ion reactions.** *Physical review C, Nuclear physics / Phys. Rev. C* **80**(4), 2009: 044615. DOI:10.1103/physrevc.80.044615

146 Leupold, S.; Lutz, M. F. M.*: **Hadronic three-body decays of light vector mesons.** *The European physical journal A, Hadrons and nuclei / Eur. Phys. J. A* **39**(2), 2009: 205–212. DOI:10.1140/epja/i2008-10707-2

147 Leupold, S.; Lutz, M. F. M.*; Wagner, M.: **Chiral partners and their electromagnetic radiation (Ingredients for a systematic in-medium calculation).** *Progress in particle and nuclear physics* **62**(2), 2009: 543–548. DOI:10.1016/j.ppnp.2008.12.042

148 Levai, P.; Skokov, V. V.*T: **Strange and charm quark-pair production in a strong non-Abelian field.** *Journal of physics G, Nuclear and particle physics / J. Phys. G-Nucl. Part. Phys.* **36**(6), 2009: 064068. DOI:10.1088/0954-3899/36/6/064068

149 Limphirat, A.; Kobdaj, C.; Bleicher, M.; Yan, Y. P.; Stöcker, H.*: **Strange and non-strange particle production in antiproton-nucleus collisions in the UrQMD model.** *Journal of physics G, Nuclear and particle physics / J. Phys. G-Nucl. Part. Phys.* **36**(6), 2009: 064049. DOI:10.1088/0954-3899/36/6/064049

150 Li, Q. F.; Bleicher, M.; Stöcker, H.*: **A new solution to the BTB time-related puzzle.** *Acta physica Polonica B, Particle physics and field theory, nuclear physics, theory of relativity / Acta Phys. Pol. B* **40**(4), 2009: 1217–1223. URL OPEN ACCESS.

151 Li, Q. F.; Steinheimer, J.; Petersen, H.; Bleicher, M.; Stöcker, H.*: **Effects of a phase transition on HBT correlations in an integrated Boltzmann + hydrodynamics approach.** *Physics letters B / Phys. Lett. B* **674**(2), 2009: 111–116. DOI:10.1016/j.physletb.2009.03.012

152 Litvinova, E.*; Feldmeier, H.*; Dobaczewski, J.; Flambaum, V.: **Nuclear structure of lowest ^{229}Th states and time-dependent fundamental constants.** *Physical review C, Nuclear physics / Phys. Rev. C* **79**(6), 2009: 064303. DOI:10.1103/physrevc.79.064303

153 Litvinova, E.*; Loens, H. P.*; Langanke, K.*; Martinez-Pinedo, G.*; Rauscher, T.; Ring, P.; Thielemann, F. K.; Tselyaev, V.: **Low-lying dipole response in the relativistic quasiparticle time blocking approximation and its influence on neutron capture cross sections.** *Nuclear physics A, Nuclear and hadronic physics / Nucl. Phys. A* **823**, 2009: 26–37. DOI:10.1016/j.nuclphysa.2009.03.009

154 Litvinova, E.*; Ring, P.; Tselyaev, V.; Langanke, K.*: **Relativistic quasiparticle time blocking approximation. II. Pygmy dipole resonance in neutron-rich nuclei.** *Physical review C, Nuclear physics / Phys. Rev. C* **79**(5), 2009: 054312. DOI:10.1103/physrevc.79.054312

155 Litvinov, Y. A.: **Mass and lifetime measurements at the present ESR facility.** *International journal of modern physics E, Nuclear physics / Int. J. Mod. Phys. E-Nucl. Phys.* **18**(2), 2009: 323–334. URL

156 Madurga, M.; Borge, M. J. G.; Alcorta, M.; Fraile, L. M.; Fynbo, H. O. U.; Jonson, B.; Kirsebom, O.; Martinez-Pinedo, G.*; Nilsson, T.; Nyman, G.; Perea, A.; Poves, A.; Riisager, K.; Tengblad, O.; Tengborn, E.; Van der Walle, J.: **Evidence of a new state in ^{11}Be observed in the ^{11}Li β-decay.** *Physics letters B / Phys. Lett. B* **677**(5), 2009: 255–259. DOI:10.1016/j.physletb.2009.05.050

157 Mahata, K.*; Johansson, H. T.*; Paschalis, S.; Simon, H.*; Aumann, T.*: **Position reconstruction in large-area scintillating fibre detectors.** *Nuclear instruments & methods in physics research, Section A, Accelerators, spectrometers, detectors and associated equipment / Nucl. Instrum. Methods Phys. Res. Sect. A-Accel. Spectrom. Dect. Assoc. Equip.* **608**(2), 2009: 331–335. DOI:10.1016/j.nima.2009.07.012

158 Maierbeck, P.; Gernhäuser, R.; Krücken, R.; Kroll, T.; Alvarez-Pol, H.; Aksouh, F.*; Aumann, T.*; Behr, K.*; Benjamim, E. A.; Benlliure, J.; Bildstein, V.; Böhmer, M.; Boretzky, K.*; Borge, M. J. G.; Brünle, A.*; Bürger, A.; Caamano, M.; Casarejos, E.; Chatillon, A.*; Chulkov, L. V.*; Cortina-Gil, D.; Enders, J.; Eppinger, K.; Faestermann, T.; Friese, J.; Fabbietti, L.; Gascon, M.; Geissel, H.*; Gerl, J.*; Gorska, M.*; Hansen, P. G.; Jonson, B.; Kanungo, R.*; Kiselev, O.*; Kojouharov, I.*; Klimkiewicz, A.*; Kurtukian, T.; Kurz, N.*; Larsson, K.*; Le Bleis, T.*; Mahata, K.*; Maier, L.; Nilsson, T.; Nociforo, C.*; Nyman, G.; Pascual-Izarra, C.; Perea, A.; Perez, D.; Prochazka, A.*; Rodriguez-Tajes, C.; Rossi, D.; Schaffner, H.*; Schrieder, G.*; Schwertel, S.; Simon, H.*; Sitar, B.; Stanoiu, M.*; Sümmerer, K.*; Tengblad, O.; Weick, H.*; Winkler, S.; Brown, B. A.; Otsuka, T.; Tostevin, J.; Rae, W. D. M.: **Structure of ^{55}Ti from relativistic one-neutron knockout.** *Physics letters B / Phys. Lett. B* **675**(1), 2009: 22–27. DOI:10.1016/j.physletb.2009.03.049

159 Marganiec, J.; Dillmann, I.; Pardo, C. D.*; Käppeler, F.: **Neutron capture cross sections of ^{184}W and ^{186}W.** *Physical review C, Nuclear physics / Phys. Rev. C* **80**(2), 2009: 025804. DOI:10.1103/physrevc.80.025804

160 Marganiec, J.; Dillmann, I.; Pardo, C. D.; Käppeler, F.; Reifarth, R.*; Gallino, R.; Pignatari, M.; Grabmayr, P.: **Neutron capture cross sections of ^{74}Ge, ^{76}Ge, and ^{75}As at 25 keV.** *Physical review C, Nuclear physics / Phys. Rev. C* **79**(6), 2009: 065802. DOI:10.1103/physrevc.79.065802

161 Marginean, N.; Bucurescu, D.; Ur, C. A.; Mihai, C.; Corradi, L.; Farnea, E.; Filipescu, D.; Fioretto, E.; Ghita, D.; Guiot, B.; Gorska, M.*; Ionescu-Bujor, M.; Iordachescu, A.; Jelavic-Malenica, D.; Lenzi, S. M.; Mason, P.; Marginean, R.; Mengoni, D.; Montagnoli, G.; Napoli, D. R.; Pascu, S.; Pollarolo, G.; Recchia, F.; Stefanini, A. M.; Silvestri, R.; Sava, T.; Scarlassara, F.; Szilner, S.; Zamfir, N. V.: **Evolution of deformation in the neutron-rich krypton isotopes: The ^{96}Kr nucleus.** *Physical review C, Nuclear physics / Phys. Rev. C* **80**(2), 2009: 021301. DOI:10.1103/physrevc.80.021301

162 Marin, A.*; ALICE Collaboration: **Exploring the LHC medium with direct photons.** *The European physical journal: C, Particles and fields / Eur. Phys. J. C* **61**(4), 2009: 735–740. DOI:10.1140/epjc/s10052-009-0926-1

163 Mengoni, D.; Valiente-Dobon, J. J.; Gadea, A.; Farnea, E.; Lenzi, S. M.; Lunardi, S.; Dewald, A.; Pissulla, T.; Szilner, S.; Stefanini, A. M.; Broda, R.; Recchia, F.; Algora, A.; Angus, L.; Aydin, S.; Bazzacco, D.; Benzoni, G.; Bizzeti, P. G.; Bizzeti-Sona, A. M.; Boutachkov, P.*; Corradi, L.; Crespi, F.; de Angelis, G.; Fioretto, E.; Görgen, A.; Gorska, M.*; Gottardo, A.; Grodner, E.; Howard, A.; Krolas, W.; Leoni, S.; Mason, P.; Menegazzo, R.; Montanari, D.; Montagnoli, G.; Napoli, D. R.; Obertelli, A.; Pawlat, T.; Rubio, B.; Sahin, E.; Scarlassara, F.; Smith, J. F.; Steppenbeck, D.; Ur, C. A.; Wady, P. T.; Wrzesinski, J.: **Lifetime measurements of excited states in neutron-rich nuclei around ^{48}Ca.** *Acta physica Polonica B, Particle physics and field theory, nuclear physics, theory of relativity / Acta Phys. Pol. B* **40**(3), 2009: 485–488. URL OPEN ACCESS.

164 Minaev, S.; Ratzinger, U.; Podlech, H.; Busch, M.; Barth, W.*: **Superconducting, energy variable heavy ion linac with constant β, multicell cavities of CH-type.** *Physical Review Special Topics - Accelerators and Beams / Phys. Rev. Spec. Top.-Accel. Beams* **12**(12), 2009: 120101. DOI:10.1103/physrevstab.12.120101 OPEN ACCESS.

165 Miskowice, D.*: **UNICOR experiment independent HBT analysis.** *Acta physica Polonica B, Particle physics and field theory, nuclear physics, theory of relativity / Acta*

Phys. Pol. B **40**(4), 2009: 1243–1248. URL OPEN ACCESS.

166 Mohr, P.; Bisterzo, S.; Gallino, R.; Kappeler, F.; Kneissl, U.; Winckler, N.*: **Properties of the 5^- state at 839 keV in ^{176}Lu and the s-process branching at A=176.** *Physical review C, Nuclear physics / Phys. Rev. C* **79**(4), 2009: 045804. DOI:10.1103/physrevc.79.045804

167 Morales, A. I.; Benlliure, J.; Regan, P. H.; Podolyak, Z.; Gorska, M.*; Alkhomashi, N.; Pietri, S.; Kumar, R*.; Casarejos, E.; Agramunt, J.; Algora, A.; Alvarez-Pol, H.; Benzoni, G.; Blazhev, A.; Boutachkov, P.*; Bruce, A. M.; Caceres, L. S.*; Cullen, I. J.; Bacelar, A. M. D.; Doornenbal, P.*; Dragosavac, D.; Estevez, M. E.; Farrelly, G.; Fujita, Y.; Garnsworthy, A. B.; Gelletly, W.; Gerl, J.*; Grebosz, J.*; Hoischen, R.; Kojouharov, I.*; Kurz, N.*; Lalkovski, S.; Liu, Z.; Perez-Loureiro, D.; Prokopowicz, W.*; Mihai, C.; Molina, F.; Mücher, D.; Rubio, B.; Schapffner, H.; Steer, S. J.; Tamii, A.; Tashenov, S.*; Dobon, J. J. V.; Verma, S.; Walker, P. M.; Wollersheim, H. J.*; Woods, P. J.: **β-delayed γ-ray spectroscopy of heavy neutron rich nuclei south of Lead.** *Acta physica Polonica B, Particle physics and field theory, nuclear physics, theory of relativity / Acta Phys. Pol. B* **40**(3), 2009: 867–870. URL OPEN ACCESS.

168 Mosconi, M.; Heil, M.*; Käppeler, F.; Plag, R.*; Mengoni, A.; Nolte, R.: **Monoenergetic Neutrons for Stellar Applications.** *Publications of the Astronomical Society of Australia / Publ. Astron. Soc. Aust.* **26**(3), 2009: 232–236. DOI:10.1071/as08044

169 Mueller, H.; Floch, E.; Moritz, G.; Shim, S. Y.: **Design Study for the SIS 300 Main Quadrupoles.** *IEEE transactions on applied superconductivity / IEEE Trans. Appl. Supercond.* **19**(3), Part 2, 2009: 1146–1149. DOI:10.1109/tasc.2009.2019293

170 Mukha, I.; Timofeyuk, N. K.; Sümmerer, K.*; Acosta, L.; Alvarez, M. A. G.; Casarejos, E.; Chatillon, A.; Cortina-Gil, D.; Espino, J. M.; Fomichev, A.; Garcia-Ramos, J. E.; Geissel, H.*; Gomez-Camacho, J.; Grigorenko, L.*; Hofmann, J.*; Kiselev, O.*; Korshenininkov, A.; Kurz, N.*; Litvinov, Y.*; Martel, I.; Nociforo, C.*; Ott, W.; Pfützner, M.; Rodriguez-Tajes, C.; Roeckl, E.*; Stanoiu, M.*; Weick, H.*; Woods, P. J.: **Observation of narrow states in nuclei beyond the proton drip line: ^{15}Fe and ^{16}Ne.** *Physical review C, Nuclear physics / Phys. Rev. C* **79**(6), 2009: 061301. DOI:10.1103/physrevc.79.061301

171 Muller, J. A.; Fischer, C. S.*: **Studying pion effects on the chiral phase transition.** *Progress in particle and nuclear physics* **62**(2), 2009: 549–550. DOI:10.1016/j.ppnp.2008.12.034

172 Mustafin, E.*; Seidl, T.*; Plotnikov, A.*; Strasik, I.*; Pavlovic, M.; Miglierini, M.; Stancek, S.; Fertman, A.; Lancok, A.: **Ion irradiation studies of construction materials for high-power accelerators.** *Radiation Effects and Defects in Solids / Radiat. Eff. Defects Solids* **164**(7-8), 2009: 460–469. DOI:10.1080/10420150902949894 Also part of: PNI

173 Mutterer, M.; Trzaska, W. H.; Kopatch, Y. N.; Sillanpää, M.; von Kalben, J.; Khlebnikov, S. V.; Schrieder, G.*; Tyurin, G. P.: **Particle identification with time-of-flight and pulse-shape discrimination in neutron-transmutation-doped silicon detectors.** *Nuclear instruments & methods in physics research, Section A, Accelerators, spectrometers, detectors and associated equipment / Nucl. Instrum. Methods Phys. Res. Sect. A-Accel. Spectrom. Dect. Assoc. Equip.* **608**(2), 2009: 275–286. DOI:10.1016/j.nima.2009.06.060

174 Myalski, S.; Maj, A.; Podolyak, Z.; Becker, F.*; Bednarczyk, P.*; Benzoni, G.; Blank, B.; Brandau, C.; Bruce, A. M.; Caceres, L.*; Camera, F.; Catford, W. N.; Cullen, I. J.; Dombradi, Z.; Doornenbal, P.*; Estevez, E.; Garnsworthy, A. B.; Geissel, H.*; Gelletly, W.; Gerl, J.*; Gorska, M.*; Grawe, H.; Grebosz, J.*; Heinz, A.; Hoischen, R.; Ilie, G.; Jones, G. A.; Jungclaus, A.; Kelic, A.*; Kmiecik, M.; Kojouharov, I.*; Kondev, F. G.; Kurtukian-Nieto, T.; Kurz, N.*; Lalkovski, S.; Liu, Z.; Montes, F.*; Pfützner, M.; Pietri, S.; Prokopowicz, W.*; Regan, P. H.; Rudolph, D.; Saito, T.*; Schaffner, H.*; Schwertel, S.; Shizuma, T.*; Simon, A. J.; Steer, S. J.; Tashenov, S.*; Walker, P. M.; Werner-Malento, E.; Wieland, O.; Wollersheim, H. J.*: **Isomeric ratios for nuclei with Z= 62-67 and A=142-152 produced in the relativistic fragmentation pf ^{208}Pb.** *Acta physica Polonica B, Particle physics and field theory, nuclear physics, theory of relativity / Acta Phys. Pol. B* **40**(3), 2009: 879–883. URL OPEN ACCESS.

175 Nakajima, D.*; Özel-Tashenov, B.*; Bianchin, S.*; Borodina, O.*; Bozkurt, V.*; Göküzüm, B.*; Kavatsyuk, M.; Minami, S.*; Rappold, C.*; Saito, T. R.*; Achenbach, P.; Ajimura, S.; Ayerbe, C.; Fukuda, T.; Hayashi, Y.; Hiraiwa, T.; Hoffmann, J.*; Koch, K.*; Kurz, N.*; Lepyoshkina, O.; Maas, F.*; Mizoi, Y.; Mochizuki, T.; Moritsu, M.; Nagae, T.; Nungesser, L.; Okamura, A.; Ott, W.*; Pochodzalla, J.; Sakaguchi, A.; Sako, M.; Schmidt, C. J.*; Sugimura, H.; Tanida, K.; Träger, M.*; Trautmann, W.*; Voltz, S.*: **Scintillating fiber detectors for the HypHI project at GSI.** *Nuclear instruments & methods in physics research, Section A, Accelerators, spectrometers, detectors and associated equipment / Nucl. Instrum. Methods Phys. Res. Sect. A-Accel. Spectrom. Dect. Assoc. Equip.* **608**(2), 2009: 287–290. DOI:10.1016/j.nima.2009.06.068

176 Nasirov, A. K.; Giardina, G.; Mandaglio, G.; Manganaro, M.; Hanappe, F.; Heinz, S.*; Hofmann, S.*; Muminov, A. I.; Scheid, W.: **Quasifission and fusion-fission in reactions with massive nuclei: Comparison of reactions leading to the Z=120 element.** *Physical review C, Nuclear physics / Phys. Rev. C* **79**(2), 2009: 024606.

DOI:10.1103/physrevc.79.024606

177 Neff, T.*; Feldmeier, H.*: **Microscopic Description of Few-Body Systems in the Fermionic Molecular Dynamics Approach.** *Few-Body Systems / Few-Body Syst.* **45**(2-4), 2009: 145–147. DOI:10.1007/s00601-009-0030-y

178 Nolden, F.: **Beams at storage rings from proton to uranium.** *International journal of modern physics E, Nuclear physics / Int. J. Mod. Phys. E-Nucl. Phys.* **18**(2), 2009: 474–483.

179 Pagliara, G.*; Hempel, M.; Schaffner-Bielich, J.*: **New Possible Quark-Hadron Mixed Phase in Protoneutron Stars.** *Physical review letters / Phys. Rev. Lett.* **103**(17), 2009: 171102. DOI:10.1103/physrevlett.103.171102

180 Pancin, J.; Chaminade, T.; Drouart, A.; Fernandez, B.; Kebbiri, M.; Naqvi, F.*; Riallot, M.: **Secondary electrons detectors for beam tracking: micromegas and wire chamber.** */ J. Instrum.* **4**, 2009: P12012. DOI:10.1088/1748-0221/4/12/p12012 OPEN ACCESS.

181 Parkhomenko, A.; Hofmann, S.; Sobiczewski, A.: **Structure effects on the decay of superheavy nuclei.** *International journal of modern physics E, Nuclear physics / Int. J. Mod. Phys. E-Nucl. Phys.* **18**(4), 2009: 1071–1078, Sp. Iss. SI. URL

182 Perez-Loureiro, D.; Alvarez-Pola, H.; Benlliure, J.; Blank, B.; Casarejos, E.; Dragosavac, D.; Föhr, V.*; Gascon, M.; Gawlikowicz, W.; Heinz, A.; Helariutta, K.; Kelic, A.*; Lukic, S.*; Montes, F.*; Plenkowski, L.; Schmidt, K.-H.*; Staniou, M.*; Subotic, K.; Sümmerer, K.*; Taieb, J.; Trzcinska, A.: **Production of medium-mass neutron rich nuclei from fragmentation of fission residues around Sn.** *Acta physica Polonica B, Particle physics and field theory, nuclear physics, theory of relativity / Acta Phys. Pol. B* **40**(3), 2009: 863–866. URL OPEN ACCESS.

183 Perkowski, J.; Andrzejewski, J.; Srebrny, J.; Bruce, A. M.; Droste, C.; Grodner, E.; Kisielinski, M.; Korman, A.; Kowalczyk, M.; Kownacki, J.; Krol, A.; Marganiec, J.*; Mierzejewski, J.; Morek, T.; Sobczak, K.; Trzaska, W. H.; Zielinska, M.: **Absolute E3 and M2 transition probabilities for the electromagnetic decay of the $I^{\pi} = K^{\pi}=8^{-}$ isomeric state in ^{132}Ce.** *The European physical journal A, Hadrons and nuclei / Eur. Phys. J. A* **42**(3), 2009: 379–382. DOI:10.1140/epja/i2009-10820-8

184 Perkowski, J.; Andrzejewski, J.; Srebrny, J.; Bruce, A. M.; Droste, C.; Grodner, E.; Kisielinski, M.; Korman, A.; Kowalczyk, M.; Kownacki, J.; Krol, A.; Marganiec, J.; Mierzejewski, J.+; Morek, T.; Sobczak, K.; Trzaska, W. H.; Zielinska, M.: **Absolute E3 and M2 transition probabilities for the electromagnetic decay of the $I^{\pi} = K^{\pi}=8^{-}$ isomeric state in ^{132}Ce.** *The European physical journal A, Hadrons and nuclei* **42**(3), 2009: 379–382. DOI:10.1140/epja/i2009-10820-8

185 Pershina, V.*; Anton, J.*; Jacob, T.: **Electronic structures and properties of MAu and MOH, where M = Tl and element 113.** *Chemical Physics Letters / Chem. Phys. Lett.* **480**(4-6), 2009: 157–160. DOI:10.1016/j.cplett.2009.08.069

186 Pershina, V.*; Anton, J.; Jacob, T.: **Theoretical predictions of adsorption behavior of elements 112 and 114 and their homologs Hg and Pb.** *The Journal of Chemical Physics / J. Chem. Phys.* **131**(8), 2009: 084713. DOI:10.1063/1.3212449

187 Pershina, V.*; Borschevsky, A.; Eliav, E.; Kaldor, U.: **[Publisher note] Adsorption of inert gases including element 118 on noble metal and inert surfaces from ab initio Dirac-Coulomb atomic calculations(vol 129, 144106, 2008).** *The Journal of Chemical Physics / J. Chem. Phys.* **130**(19), 2009: 199902. DOI:10.1063/1.3152123

188 Petersen, H.; Steinheimer, J.; Bleicher, M.; Stöcker, H.*: **The $< m(T) >$ excitation function: freeze-out and equation of state dependence.** *Journal of physics G, Nuclear and particle physics / J. Phys. G-Nucl. Part. Phys.* **36**(5), 2009: 055104. DOI:10.1088/0954-3899/36/5/055104

189 Pezer, R.; Gasenzer, T.*; Buljan, H.: **Single-particle density matrix for a time-dependent strongly interacting one-dimensional Bose gas.** *Physical review A, Atomic, molecular, and optical physics / Phys. Rev. A* **80**(5), 2009: 053616. DOI:10.1103/physreva.80.053616

190 Pezer, R.; Gasenzer, T.*; Buljan, H.: **Single-particle density matrix for a time-dependent strongly interacting one-dimensional Bose gas.** *Physical review A, Atomic, molecular, and optical physics* **80**(5), 2009: 053616. DOI:10.1103/physreva.80.053616

191 Podolyak, Z.; Farrelly, G. F.; Regan, P. H.; Garnsworthy, A. B.; Steer, S. J.; Gorska, M.*; Benlliure, J.; Casarejos, E.; Pietri, S.; Gerl, J.*; Wollersheim, H. J.*; Kumar, R.; Molina, F.; Algora, A.; Alkhomashi, N.; Benzoni, G.; Blazhev, A.; Boutachkov, P.*; Bruce, A. M.; Caceres, L.*; Cullen, I. J.; Bacelar, A. M. D.; Doornenbal, P.*; Estevez, M. E.; Fujita, Y.; Gelletly, W.; Geissel, H.*; Grawe, H.*; Grebosz, J.*; Hoischen, R.*; Kojouharov, I.*; Lalkovski, S.; Liu, Z.; Maier, K. H.; Mihai, C.; Mücher, D.; Rubio, B.; Schaffner, H.*; Tamii, A.; Tashenov, S.*; Valiente-Dobon, J. J.; Walker, P. M.; Woods, P. J.: **Proton-hole excitation in the closed shell nucleus ^{205}Au.** *Physics letters B / Phys. Lett. B* **672**(2), 2009: 116–119. DOI:10.1016/j.physletb.2009.01.007

192 Podolyak, Z.; Steer, S. J.; Pietri, S.; Gorska, M.*; Regan, P. H.; Rudolph, D.; Garnsworthy, A. B.; Hoischen, R.; Gerl, J.*; Wollersheim, H. J.*; Grawe, H.*; Maier, K. H.;

Becker, F.*; Bednarczyk, P.*; Caceres, L.*; Doornenbal, P.*; Geissel, H.*; Grebosz, J.*; Kelic, A.*; Kojouharov, I.*; Kurz, N.*; Montes, F.*; Prokopowicz, W.*; Saito, T.*; Schaffner, H.*; Tashenov, S.*; Heinz, A.; Kurtukian-Nieto, T.; Benzoni, G.; Pfutzner, M.; Jungclaus, A.; Balabanski, D. L.; Brandau, C.; Brown, B. A.; Bruce, A. M.; Catford, W. N.; Cullen, I. J.; Dombradi, Z.; Estevez, M. E.; Gelletly, W.; Ilie, G.; Jolie, J.; Jones, G. A.; Kmiecik, M.; Kondev, F. G.; Krucken, R.; Lalkovski, S.; Liu, Z.; Maj, A.; Myalski, S.; Schwertel, S.; Shizuma, T.; Walker, P. M.; Werner-Malento, E.; Wieland, O.: **Structure of neutron-rich nuclei around the N=126 closed shell; the yrast structure of ^{205}Au$_{126}$ up to spin-parity I$^{\pi}$ =.** *The European physical journal A, Hadrons and nuclei / Eur. Phys. J. A* **42**(3), 2009: 489–493. DOI:10.1140/epja/i2009-10794-5

193 Podolyak, Z.; Steer, S. J.; Pietri, S.; Xu, F. R.; Liu, H. L.; Regan, P. H.; Rudolph, D.; Garnsworthy, A. B.; Hoischen, R.*; Gorska, M.*; Gerl, J.*; Wollersheim, H. J.*; Kurtukian-Nieto, T.; Benzoni, G.; Shizuma, T.; Becker, F.*; Bednarczyk, P.*; Caceres, L.*; Doornenbal, P.*; Geissel, H.*; Grebosz, J.*; Kelic, A.*; Kojouharov, I.*; Kurz, N.*; Montes, F.*; Prokopowicz, W.*; Saito, T.*; Schaffner, H.*; Tashenov, S.*; Heinz, A.; Pfützner, M.; Jungclaus, A.; Balabanski, D. L.; Brandau, C.*; Bruce, A. M.; Catford, W. N.; Cullen, I. J.; Dombradi, Z.; Estevez, E.; Gelletly, W.; Ilie, G.; Jolie, J.; Jones, G. A.; Kmiecik, M.; Kondev, F. G.; Krücken, R.; Lalkovski, S.; Liu, Z.; Maj, A.; Myalski, S.; Schwertel, S.; Walker, P. M.; Werner-Malento, E.*; Wieland, O.: **Weakly deformed oblate structures in $^{198}_{76}$Os$_{122}$.** *Physical review C, Nuclear physics / Phys. Rev. C* **79**(3), 2009: 031305. DOI:10.1103/physrevc.79.031305

194 Pomorski, M.; Ciobanu, M.*; Mer, C.; Rebisz-Pomorska, M.; Tromson, D.; Bergonzo, R.: **Position-sensitive radiation detectors made of single crystal CVD diamond.** *Physica Status Solidi A / Phys. Status Solidi A-Appl. Mat.* **206**(9), 2009: 2109–2114, Sp. Iss. SI. DOI:10.1002/pssa.200982229

195 Recchia, F.; Bazzacco, D.; Farnea, E.; Gadea, A.; Venturelli, R.; Beck, T.*; Bednarczyk, P.; Buerger, A.; Dewald, A.; Dimmock, M.; Duchene, G.; Eberth, J.; Faul, T.; Gerl, J.*; Gernhaeuser, R.; Hauschild, K.; Holler, A.; Jones, P.; Korten, W.; Kroll, T.; Krücken, R.; Kurz, N.*; Ljungvall, J.; Lunardi, S.; Maierbeck, P.; Mengoni, D.; Nyberg, J.; Nelson, L.; Pascovici, G.; Reiter, P.; Schaffner, H.*; Schlarb, M.; Steinhardt, T.; Thelen, O.; Ur, C. A.; Dobon, J. J. V.; Weisshaar, D.: **Position resolution of the prototype AGATA triple-cluster detector from an in-beam experiment.** *Nuclear instruments & methods in physics research, Section A, Accelerators, spectrometers, detectors and associated equipment / Nucl. Instrum. Methods Phys. Res. Sect. A-Accel. Spectrom. Dect. Assoc. Equip.* **604**(3), 2009: 555–562. DOI:10.1016/j.nima.2009.02.042

196 Redlich, K.; Andronic, A.*; Beutler, F.; Braun-Munzinger, P.*; Stachel, J.: **Canonical statistical model and hadron production in e^{+}e^{-} annihilations.** *Journal of physics G, Nuclear and particle physics / J. Phys. G-Nucl. Part. Phys.* **36**(6), 2009: 064021. DOI:10.1088/0954-3899/36/6/064021

197 Reifarth, R.*; Chau, L. P.; Heil, M.*; Käppeler, F.; Meusel, O.; Plag, R.*; Ratzinger, U.*; Schempp, A.; Volk, K.: **Opportunities for Nuclear Astrophysics at FRANZ.** *Publications of the Astronomical Society of Australia / Publ. Astron. Soc. Aust.* **26**(3), 2009: 255–258. DOI:10.1071/as08061URL:

198 Reifarth, R.'*; Heil, M.*; Käppeler, F.; Plag, R.*: **PINO-a tool for simulating neutron spectra resulting from the ^{7}Li (p,n) reaction.** *Nuclear instruments & methods in physics research, Section A, Accelerators, spectrometers, detectors and associated equipment / Nucl. Instrum. Methods Phys. Res. Sect. A-Accel. Spectrom. Dect. Assoc. Equip.* **608**(1), 2009: 139–143. DOI:10.1016/j.nima.2009.06.046

199 Riek, F.*; Lutz, M. F. M.*; Korpa, C. L.: **Photoabsorption off nuclei with self-consistent vertex corrections.** *Physical review C, Nuclear physics / Phys. Rev. C* **80**(2), 2009: 024902. DOI:10.1103/physrevc.80.024902

200 Ring, P.; Litvinova, E. V.*: **Particle-vibrational coupling in covariant density-functional theory.** *Physics of atomic nuclei / Phys. Atom. Nuclei* **72**(8), 2009: 1285–1304. DOI:10.1134/s1063778809080055

201 Rollet, S.; Agosteo, S.; Fehrenbacher, G.*; Hranitzky, C.; Radon, T.*; Wind, M.: **Intercomparison of radiation protection devices in a high-energy stray neutron field, Part I: Monte Carlo simulations.** *Radiation Measurements / Radiat. Meas.* **44**(7-8), 2009: 649–659. DOI:10.1016/j.radmeas.2009.03.029

202 Rollet, S.; Agosteo, S.; Fehrenbacher, G.*; Hranitzky, C.; Radon, T.*; Wind, M.: **Intercomparison of radiation protection devices in a high-energy stray neutron field, Part I: Monte Carlo simulations.** *Radiation Measurements* **44**(7-8), 2009: 649–659. DOI:10.1016/j.radmeas.2009.03.029

203 Rupp, G.; Petrich, D.; Käppeler, F.; Kaltenbaek, J.; Leugers, B.; Reifarth, R.*: **High pressure gas spheres for neutron and photon experiments.** *Nuclear instruments & methods in physics research, Section A, Accelerators, spectrometers, detectors and associated equipment / Nucl. Instrum. Methods Phys. Res. Sect. A-Accel. Spectrom. Dect. Assoc. Equip.* **608**(1), 2009: 152–156. DOI:10.1016/j.nima.2009.06.098

204 Rzaca-Urban, T.; Sieja, K.*; Urban, W.; Nowacki, F.; Durell, J. L.; Smith, A. G.; Ahmad, I.: **(h$_{11/2}$,g$_{7/2}$)$_{9-}$ neutron excitation in ^{92,94,96}Sr.** *Physical review C, Nuclear physics / Phys. Rev. C* **79**(2), 2009: 024319.

DOI:10.1103/physrevc.79.024319

205 Sanchez, R.*; Zakova, M.; Andjelkovic, Z.; Bushaw, B. A.; Dasgupta, K.; Ewald, G.*; Geppert, C.*; Kluge, H.-J.*; Kramer, J.; Nothhelfer, M.; Tiedemann, D.; Winters, D. F. A.*; Nörtershäuser, W.: **Absolute frequency measurements on the 2S -¿ 3S transition of lithium-6,7.** *New Journal of Physics / New J. Phys.* **11**, 2009: 073016. DOI:10.1088/1367-2630/11/7/073016 OPEN ACCESS.

206 Schepers, G.*; Bettoni, D.; Branford, D.; Britting, A.; Carassiti, V.; Cecchi, A.; Dodokhof, V. K.; Duren, M.; Ehrenfried, M.; Eyrich, W.; Föhl, K.; Glazier, D.; Hoek, M.; Hohler, R.*; Kaiser, R.*; Lehmann, A.; Lehmann, D.*; Lu, S.; Marton, J.; Merle, O.; Peters, K.*; Pizzolotto, C.; Rosner, G.; Schmidt, R.; Schmitt, L.*; Schönmeier, R.; Schwarz, C.*; Seitz, B.; Sfienti, C.*; Suzuki, K.; Teufel, A.; Vodopianov, A. S.; Watts, D.: **RICH for PANDA.** *Nuclear instruments & methods in physics research, Section A, Accelerators, spectrometers, detectors and associated equipment / Nucl. Instrum. Methods Phys. Res. Sect. A-Accel. Spectrom. Dect. Assoc. Equip.* **598**(1), 2009: 143–146. DOI:10.1016/j.nima.2008.08.079

207 Schmidt, K. H.: **About the inconsistency between Bohr-Wheelers transition-state method and Kramers rate in nuclear fission.** *International journal of modern physics E, Nuclear physics / Int. J. Mod. Phys. E-Nucl. Phys.* **18**(4), 2009: 850–860, Sp. Iss. SI. URL

208 Schmidt, K.; Santini, E.; Vogel, S.; Sturm, C.; Bleicher, M.; Stöcker, H.*: **Production and evolution path of dileptons at energies accessible to the HADES detector.** *Physical review C, Nuclear physics / Phys. Rev. C* **79**(6), 2009: 064908. DOI:10.1103/physrevc.79.064908

209 Schmitt, C.*; Kelic, A.*; Schmidt, K.-H.*; Heinz, A.*; Jurado, B.*; Nadtochy, P. N.*: **Fragmentation of radioactive beams for tailoring fission transients.** *International journal of modern physics E, Nuclear physics / Int. J. Mod. Phys. E-Nucl. Phys.* **18**(10), 2009: 2150–2154. DOI:10.1142/s0218301309014469

210 Schmitt, C.*; Kelic, A.*; Schmidt, K.-H.*; Heinz, A.*; Jurado, B.*; Nadtochy, P. N.*: **Fragmentation of radioactive beams for tailoring fission transients.** *International journal of modern physics E, Nuclear physics* **18**(10), 2009: 2150–2154. DOI:10.1142/s0218301309014469

211 Schnizer, P.*; Schnizer, B.; Akishin, P.; Fischer, E.: **Theory and application of plane elliptic multipoles for static magnetic fields.** *Nuclear instruments & methods in physics research, Section A, Accelerators, spectrometers, detectors and associated equipment / Nucl. Instrum. Methods Phys. Res. Sect. A-Accel. Spectrom. Dect. Assoc. Equip.* **607**(3), 2009: 505–516. DOI:10.1016/j.nima.2009.06.007

212 Schnizer, P.; Schnizer, B.; Akishin, P.; Fischer, E.: **Plane elliptic or toroidal multipole expansions for static fields Applications within the gap of straight and curved accelerator magnets.** *COMPEL / Compel-Int. J. Comp. Math. Electr. Electron. Eng.* **28**(4), 2009: 1044–1058. DOI:10.1108/03321640910959099

213 Schüttauf, A.*; Ciobanu, M.*; Hildenbrand, K. D.*; Kis, M.; Deppner, I.; Herrmann, N.*; Kim, Y. J.*; Kang, T. I.*; Koczon, P.*; Lopez, X.*; Leifels, Y.*; Petrovici, M.; Piasecki, K.; Reuschl, A.; Reisdorf, W.*; Ryu, M. S.*; Simion, V.*; Zernezki, N.; Zhang, X.: **Multi-strip MRPCs for FOPI.** *Nuclear instruments & methods in physics research, Section A, Accelerators, spectrometers, detectors and associated equipment / Nucl. Instrum. Methods Phys. Res. Sect. A-Accel. Spectrom. Dect. Assoc. Equip.* **602**(3), 2009: 679–681. DOI:10.1016/j.nima.2008.12.088

214 Schulz, M.; Ciappina, M. F.; Kirchner, T.; Fischer, D.*; Moshammer, R.; Ullrich, J.: **Role of elastic projectile-electron scattering in double ionization of helium by fast proton impact.** *Physical review A, Atomic, molecular, and optical physics / Phys. Rev. A* **79**(4), Part A, 2009: 042708. DOI:10.1103/physreva.79.042708

215 Schwarz, C.*: **Development of the PANDA barrel DIRC.** */ J. Instrum.* **4**, 2009: P12016. DOI:10.1088/1748-0221/4/12/p12016 OPEN ACCESS.

216 Schwarz, C.*: **The front end electronics of the PANDA barrel DIRC.** */ J. Instrum.* **4**, 2009: P12002. DOI:10.1088/1748-0221/4/12/p12002 OPEN ACCESS.

217 Schwiening, J.*; BABAR-DIRC Collaboration*: **Construction and performance of the BABAR-DIRC.** *Journal of Instrumentation / J. Instrum.* **4**, 2009: P10004. DOI:10.1088/1748-0221/4/10/p10004 OPEN ACCESS.

218 Senger, P.*: **Probing dense baryonic matter.** *Progress in particle and nuclear physics* **62**(2), 2009: 375–380. DOI:10.1016/j.ppnp.2008.12.007

219 Senger, P.*; Galatyuk, T.*; Kiseleva, A.*; Kresan, D.*; Lebedev, A.; Lebedev, S.*; Lymanets, A.: **The compressed baryonic matter experiment at FAIR.** *Journal of physics G, Nuclear and particle physics / J. Phys. G-Nucl. Part. Phys.* **36**(6), 2009: 064037. DOI:10.1088/0954-3899/36/6/064037

220 Sfienti, C.*; Adrich, P.*; Aumann, T.*; Bacri, C. O.; Barczyk, T.; Bassini, R.; Bianchin, S.*; Boiano, C.; Botvina, A. S.*; Boudard, A.; Brzychczyk, J.; Chbihi, A.; Cibor, J.; Czech, B.; De Napoli, M.; Ducret, J. E.; Emling, H.*; Frankland, J. D.; Hellstöom, M.*; Henzlova, D.*; Imme, G.; Iori, I.; Johansson, H.*; Kezzar, K.*; Lafriakh, A.; Le Fèvre, A.*; Le Gentil, E.; Leifels, Y.*; Lühning, J.*; Lukasik, J.*; Lynch, W. G.; Lynen, U.*; Majka, Z.; Mocko, M.; Müller, W. F. J.*; Mykulyak, A.; Orth, H.*; Otte, A. N.*; Palit, R.; Pawlowski, P.; Pullia, A.; Raciti, G.*GAST; Rapisarda, E.*GAST; Sann, H.; Schwarz,

C.*; Simon, H.*; Sümmerer, K.*; Trautmann, W.*; Tsang, M. B.; Verde, G.; Volant, C.; Wallace, M.; Weick, H.*; Wiechula, J.*; Wieloch, A.; Zwieglinski, B.: **Isotopic Dependence of the Nuclear Caloric Curve.** *Physical review letters / Phys. Rev. Lett.* **102**(15), 2009: 152701. DOI:10.1103/physrevlett.102.152701

221 Shrivastava, A.; Caamano, M.; Rejmund, M.; Navin, A.; Rejmund, F.; Schmidt, K.-H.*; Lemasson, A.; Schmitt, C.; Gaudefroy, L.; Sieja, K.*; Audouin, L.; Bacri, C. O.; Barreau, G.; Benlliure, J.; Casarejos, E.; Derkx, X.; Fernandez-Dominguez, B.; Golabek, C.; Jurado, B.; Roger, T.; Taieb, J.: **Prompt γ-ray spectroscopy of isotopically identified fission fragments.** *Physical review C, Nuclear physics / Phys. Rev. C* **80**(5), 2009: 051305. DOI:10.1103/physrevc.80.051305

222 Shrivastava, A.; Caamano, M.; Rejmund, M.; Navin, A.; Rejmund, F.; Schmidt, K.-H.*; Lemasson, A.; Schmitt, C.; Gaudefroy, L.; Sieja, K.; Audouin, L.; Bacri, C. O.; Barreau, G.; Benlliure, J.; Casarejos, E.; Derkx, X.; Fernandez-Dominguez, B.; Golabek, C.; Jurado, B.; Roger, T.; Taieb, J.: **Prompt γ-ray spectroscopy of isotopically identified fission fragments.** *Physical review C, Nuclear physics* **80**(5), 2009: 051305. DOI:10.1103/physrevc.80.051305

223 Sieja, K.*; Martinez-Pinedo, G.*; Coquard, L.; Pietralla, N.: **Description of proton-neutron mixed-symmetry states near ^{132}Sn within a realistic large scale shell model.** *Physical review C, Nuclear physics / Phys. Rev. C* **80**(5), 2009: 054311. DOI:10.1103/physrevc.80.054311

224 Sieja, K.*; Martinez-Pinedo, G.*; Coquard, L.; Pietralla, N.: **Description of proton-neutron mixed-symmetry states near ^{132}Sn within a realistic large scale shell model.** *Physical review C, Nuclear physics* **80**(5), 2009: 054311. DOI:10.1103/physrevc.80.054311

225 Sieja, K.*; Nowacki, F.; Langanke, K.; Martinez-Pinedo, G.*: **Shell model description of zirconium isotopes.** *Physical review C, Nuclear physics / Phys. Rev. C* **79**(6), 2009: 064310. DOI:10.1103/physrevc.79.064310

226 Simon, H.; ELISe Collaboration: **Technical realization of the ELISe experiment at FAIR.** *International journal of modern physics E, Nuclear physics / Int. J. Mod. Phys. E-Nucl. Phys.* **18**(2), 2009: 367–372. URL

227 Skokov, V. V.*; Illarionov, A. Y.; Toneev, V. D.*: **Estimate of magnetic field strength in heavy-ion collisions.** *International Journal of Modern Physics A: Particles and Fields, Gravitation and Cosmology / Int. J. Mod. Phys. A* **24**(31), 2009: 5925–5932. DOI:10.1142/s0217751x09047570

228 Skokov, V. V.*; Voskresensky, D. N.*: **Hydrodynamical description of a hadron-quark first-order phase transition.** *JETP Letters / Jetp Lett.* **90**(4), 2009: 223–227. DOI:10.1134/s0021364009160012

229 Skokov, V. V.*; Voskresensky, D. N.*: **Hydrodynamical description of first-order phase transitions: Analytical treatment and numerical modeling.** *Nuclear physics A, Nuclear and hadronic physics / Nucl. Phys. A* **828**(3-4), 2009: 401–438. DOI:10.1016/j.nuclphysa.2009.07.012

230 Sorokin, M. V.; Papaleo, R. M.; Schwartz, K.*: **Elastic atomic displacements and color center creation in LiF crystals irradiated with 3-, 9-and 12-MeV Au ions.** *Applied Physics A: Materials Science and Processing / Appl. Phys. A-Mater. Sci. Process.* **97**(1), 2009: 143–146. DOI:10.1007/s00339-009-5296-x

231 Soyeur, M.; Lutz, M. F. M.: **Dynamics of strong and radiative decays of $\mathbf{D_s}$ mesons.** *International Journal of Modern Physics A: Particles and Fields, Gravitation and Cosmology / Int. J. Mod. Phys. A* **24**(2-3), 2009: 417–421.

232 Stafiniak, A.; Floch, E.; Schroeder, C.; Marzouki, F.; Walter, F.: **The GSI Cryogenic Prototype Test Facility-First Experience Gained on 2-Phase-Flow Superconducting Prototype Magnets of the FAIR Project.** *IEEE transactions on applied superconductivity / IEEE Trans. Appl. Supercond.* **19**(3), Part 2, 2009: 1150–1153. DOI:10.1109/tasc.2009.2017871

233 Stafiniak, A.; Kosobudzki, G.: **Sources of Error in AC Losses Measurement Using V-I Method.** *IEEE transactions on applied superconductivity / IEEE Trans. Appl. Supercond.* **19**(3), Part 3, 2009: 3110–3114. DOI:10.1109/tasc.2009.2017725

234 Steck, M.; Dimopoulou, C.; Dolinskii, A.; Gorda, O.; Gostishchev, V.; Knie, K.; Litvinov, S.; Nolden, F.; Peschke, C. E; Obradors-Campos, D.: **Status of the design of the FAIR storage rings.** *International journal of modern physics E, Nuclear physics / Int. J. Mod. Phys. E-Nucl. Phys.* **18**(2), 2009: 411–419. URL

235 Steer, S. J.; Podolyak, Z. S.; Pietri, S.; Gorska, M.; Farrelly, G. F.; Regan, P. H.; Rudolph, D.; Garnsworthy, A. B.; Hoischen, R.; Gerl, J.; Wollersheim, H. J.; Grawe, H.; Maier, K. H.; Becker, F.; Bednarczyk, P.; Caceres, L.; Doornenbal, P.; Geissel, H.; Grebosz, J.; Kelic, A.; Kojouharov, I.; Kurz, N.; Montes, F.; Prokopowicz, W.; Saito, T.; Schaffner, H.; Tashenov, S.; Heinz, A.; Kurtukian-Nieto, T.; Benzoni, G.; Pfutzner, M.; Jungclaus, A.; Balabanski, D. L.; Brandau, C.; Brown, A.; Bruce, A. M.; Catford, W. N.; Cullen, I. J.; Dombradi, Z. S.; Estevez, M. E.; Gelletly, W.; Ilie, G.; Jolie, J.; Jones, G. A.; Kmiecik, M.; Kondev, F. G.; Krucken, R.; Lalkovski, S.; Liu, Z.; Maj, A.; Myalski, S.; Schwertel, S.; Shizuma, T.; Walker, P. M.; Werner-Malento, E.; Wieland, O.: **Isomeric decay studies in neutron-rich N approximate to 126 nuclei.** *International journal of modern physics E, Nuclear physics / Int.*

J. Mod. Phys. E-Nucl. Phys. **18**(4), 2009: 1002–1007, Sp. Iss. SI. URL Also part of: PNI

236 Steinheimer, J.; Augustin, I.*; Andronic, A.*; Saito, T.*; Senger, P.*; Stoecker, H.*: **Strangeness at the International Facility for Antiproton and Ion Research.** *Journal of physics G, Nuclear and particle physics / J. Phys. G-Nucl. Part. Phys.* **36**(6), 2009: 064036. DOI:10.1088/0954-3899/36/6/064036

237 Steinheimer, J.; Mitrovski, M.; Schuster, T.; Petersen, H.; Bleicher, M.; Stöcker, H.*: **Strangeness fluctuations and MEMO production at FAIR.** *Physics letters B / Phys. Lett. B* **676**(1-3), 2009: 126–131. DOI:10.1016/j.physletb.2009.04.062

238 Steinheimer, J.; Petersen, H.; Burau, G.; Bleicher, M.; Stoecker, H.*: **Strangeness Production and Local Thermalization in an Integrated Boltzmann + Hydrodynamics Approach.** *Acta physica Polonica B, Particle physics and field theory, nuclear physics, theory of relativity / Acta Phys. Pol. B* **40**(4), 2009: 999–1004. URL OPEN ACCESS.

239 Steinheimer, J.; Stoecker, H.*; Augustin, I.*; Andronic, A.*; Saito, T.*; Senger, P.*: **Strangeness at the international Facility for Antiproton and Ion Research.** *Progress in particle and nuclear physics* **62**(2), 2009: 313–317. DOI:10.1016/j.ppnp.2008.12.037

240 Steppke, A.; Geithner, R.; Hechler, S.; Nawrodt, R.; Neubert, R.; Vodel, W.; Schwickert, M.; Reeg, H.; Seidel, P.: **Application of LTS-SQUIDs in Nuclear Measurement Techniques.** *IEEE transactions on applied superconductivity / IEEE Trans. Appl. Supercond.* **19**(3), Part 1, 2009: 768–771. DOI:10.1109/tasc.2009.2019542

241 Stoecker, H.*; Augustin, I.*; Steinheimer, J.; Andronic, A.*; Saito, T.*; Senger, P.*: **Highlights of strangeness physics at FAIR.** *Nuclear physics A, Nuclear and hadronic physics / Nucl. Phys. A* **827**(1-4), 2009: 624C–629C. DOI:10.1016/j.nuclphysa.2009.05.137

242 Stokic, B.*; Friman, B.*; Redlich, K.: **Kurtosis and compressibility near the chiral phase transition.** *Physics letters B / Phys. Lett. B* **673**(3), 2009: 192–196. DOI:10.1016/j.physletb.2009.02.018

243 Strasik, I.; Kozlova, E.; Mustafin, E.; Hofmann, I.; Smolyakov, A.; Sobolevsky, N.; Latysheva, L.; Pavlovic, M.: **Simulation of the residual activity induced by high-energy heavy ions.** *Nuclear Technology / Nucl. Technol.* **168**(3), 2009: 643–647, Sp. Iss. SI. URL

244 Strasik, I.; Kozlova, E.; Mustafin, E.; Hofmann, I.; Smolyakov, A.; Sobolevsky, N.; Latysheva, L.; Pavlovic, M.: **Simulation of the residual activity induced by high-energy heavy ions.** *Nuclear Technology* **168**(3), 2009: 643–647, Sp. Iss. SI.

245 Strasik, I.*; Pavlovic, M.: **Improvements to the SRIM simulations.** *Radiation Effects and Defects in Solids / Radiat. Eff. Defects Solids* **164**(7-8), 2009: 470–476. DOI:10.1080/10420150902949910

246 Struckmeier, J.: **Extended Hamilton Lagrange formalism and its application to Feynmans path inetrgral for relativistic quantum physics.** *International journal of modern physics E, Nuclear physics / Int. J. Mod. Phys. E-Nucl. Phys.* **18**(1), 2009: 79–108. URL

247 Sudol, M.* Agakishiev, G.; Agodi, C.; Balanda, A.; Bellia, G.; Belver, D.; Belyaev, A.; Bielcik, J.*; Blanco, A.; Bortolotti, A.; Boyard, J. L.; Braun-Munzinger, P.*; Cabanelas, P.; Chernenko, S.; Christ, T.; Coniglione, R.; Destefanis, M.; Diaz, J.; Dohrmann, F.; Duran, I.; Dybczak, A.; Eberl, T.; Fabbietti, L.; Fateev, O.; Ferreira-Marques, R.; Finocchiaro, P.; Fonte, P.; Friese, J.; Fröhlich, I.; Galatyuk, T.*; Garzon, J. A.; Gernhäuser, R.; Gil, A.; Gilardi, C.; Golubeva, M.; Gonzalez-Diaz, D.*; Grosse, E.; Guber, F.; Heilmann, M.; Heinz, T.*; Hennino, T.; Holzmann, R.*; Ierusalimov, A.; Iori, I.; Ivashkin, A.; Jurkovic, M.; Kämpfer, B.; Kanaki, K.; Karavicheva, T.; Kirschner, D.; Koenig, I.*; Koenig, W.*; Kolb, B. W.*; Kotte, R.; Kozuch, A.; Krasa, A.; Krizek, F.; Krücken, R.; Kühn, W.; Kugler, A.; Kurepin, A.; Lamas-Valverde, J.; Lang, S.*; Lange, J. S.; Lapidus, K.; Lopes, L.; Lorenz, M.; Maier, L.; Maiolino, C.; Mangiarotti, A.; Marin, J.; Markert, J.; Metag, V.; Michalska, B.; Michel, J.; Moriniere, E.; Mousa, J.; Münch, M.*; Müntz, C.; Naumann, L.; Novotny, R.; Otwinowski, J.; Pachmayer, Y. C.; Palka, M.*; Parpottas, Y.; Pechenov, V.; Pechenova, O.; Cavalcanti, T. P.; Piattelli, P.; Pietraszko, J.*; Pospisil, V.; Przygoda, W.; Ramstein, B.; Reshetin, A.*GAST; Roy-Stephan, M.; Rustamov, A.*; Sadovsky, A.; Sailer, B.; Salabura, P.; Sapienza, P.; Schmah, A.; Schroeder, C.*; Schwab, E.*; Simon, R.*; Sobolev, Y. G.; Spataro, S.; Spruck, B.; Ströbele, H.; Stroth, J.*; Sturm, C.; Tarantola, A.; Teilab, K.; Tlusty, P.; Traxler, M.*; Trebacz, R.; Tsertos, H.; Wagner, V.; Weber, M.; Wisniowski, M.; Wojcik, T.; Wüstenfeld, J.; Yurevich, S.*; Zanevsky, Y.; Zhou, P.; Zumbruch, P.*: **Measurement of low-mass e^+e^- pair production in 1 and 2 A GeV C-C collision with HADES.** *The European physical journal: C, Particles and fields / Eur. Phys. J. C* **62**(1), 2009: 81–84. DOI:10.1140/epjc/s10052-009-1006-2

248 Sugita, K.; Fischer, E.; Khodzhibagiyan, H.; Muller, H.; Macavei, J.; Moritz, G.: **Design Study of the Multipole Corrector Magnet for SIS 100.** *IEEE transactions on applied superconductivity / IEEE Trans. Appl. Supercond.* **19**(3), Part 2, 2009: 1154–1157. DOI:10.1109/tasc.2009.2017707

249 Sun, B. H.; Geissel, H.; Hausmann, M.; Kozhuharov, C.; Knobel, R.; Litvinov, Y. A.; Meng, J.; Patyk, Z.; Radon, T.; Scheidenberger, C.: **Identification of Time-of-Flight spectra for Isochronous Mass Measurements.** *Chinese*

Physics C / Chin. Phys. C **33**, 2009: 161–163. Also part of: PNI

250 Sun, B.; Knobel, R.; Litvinov, Y. A.; Nakajima, S.; Geissel, H.; Meng, J.; Beckert, K.; Bosch, F.; Boutin, D.; Brandau, C.; Chen, L.; Cullen, I. J.; Dimopoulou, C.; Fabian, B.; Hausmann, M.; Klepper, O.; Kozhuharov, C.; Kurcewicz, J.; Litvinov, S. A.; Mazzocco, M.; Montes, F.; Münzenberg, G.; Musumarra, A.; Nociforo, C.; Nolden, F.; Ohtsubo, T.; Ozawa, A.; Patyk, Z.; Plass, W. R.; Scheidenberger, C.; Steck, M.; Suzuki, T.; Walker, P. M.; Weick, H.; Winckler, N.; Winkler, M.; Yamaguchi, T.: **Large-scale mass measurements of short-lived nuclides with the isochrononous mass spectrometry at GSI.** *International journal of modern physics E, Nuclear physics / Int. J. Mod. Phys. E-Nucl. Phys.* **18**(2), 2009: 346–351. URL

251 Suzuki, K.; Berger, M.; Bühler, P.; Fabbietti, L.; Hartmann, O.; Herrmann, N.; Kienle, P.; Kis, M.; Leifels, Y.*; Marton, J.; Münzer, R.; Schafhauser, M.; Widmann, E.; Yamazaki, T.; Zmeskal, J.; FOPI Collaboration*: **Search for the Kaonic Nuclear State, K(-)pp, in the exclusive pp -¿ p Lambda K+ channel.** *Nuclear physics A, Nuclear and hadronic physics / Nucl. Phys. A* **827**(1-4), 2009: 312C–314C. DOI:10.1016/j.nuclphysa.2009.05.063

252 Tahir, N. A.*; Schmidt, R.; Brugger, M.; Assmann, R.; Shutov, A.; Lomonosov, I. V.; Fortov, V. E.; Piriz, A. R.; Deutsch, C.; Hoffmann, D. H. H.: **Interaction of Super Proton Synchrotron beam with solid copper target: Simulations of future experiments at HiRadMat facility at CERN.** *Nuclear instruments & methods in physics research, Section A, Accelerators, spectrometers, detectors and associated equipment / Nucl. Instrum. Methods Phys. Res. Sect. A-Accel. Spectrom. Dect. Assoc. Equip.* **606**(1-2), 2009: 186–192. DOI:10.1016/j.nima.2009.03.086

253 Taieb, J.; Belier, G.; Chatillon, A.; Granier, T.; Kelic, A.; Ricciardi, V.; Schmidt, K. H.; Voss, B.; Coste-Delclaux, M.; Diop, C.; Jouanne, C.; Schmitt, C.; Aiche, M.; Czajkowski, S.; Jurado, B.; Audouin, L.; Peyre, J.; Rosier, P.; Tassan-Got, L.; Bertoumieux, E.; Dore, D.; Dupont, E.; Letourneau, A.; Panebianco, S.: **ELISe: a new facility for unprecedented experimental nuclear fission studies.** *International journal of modern physics E, Nuclear physics / Int. J. Mod. Phys. E-Nucl. Phys.* **18**(4), 2009: 767–772, Sp. Iss. SI. URL

254 Taylor, M. J.; Bentley, M. A.; Rudolph, D.; Fahlander, C.; Golubev, P.; Hoischen, R.; Reiter, P.; Gerl, J.*; Gorska, M.*: **A new simulation package to model detector systems with fragmentation reactions and ion separators: Application to the LYCCA-0 system.** *Nuclear instruments & methods in physics research, Section A, Accelerators, spectrometers, detectors and associated equipment / Nucl. Instrum. Methods Phys. Res. Sect. A-Accel. Spectrom. Dect. Assoc. Equip.* **606**(3), 2009: 589–597. DOI:10.1016/j.nima.2009.05.003

255 Thiamova, G.*; Rowe, D. J.: **Large boson number IBM calculations and their relationship to the Bohr model.** *The European physical journal A, Hadrons and nuclei / Eur. Phys. J. A* **41**(2), 2009: 189–195. DOI:10.1140/epja/i2009-10810-x

256 Trautmann, W.*; Adrich, P.*; Aumann, T.*; Bacri, C. O.; Barczyk, T.; Bassini, R.; Bianchin, S.*; Boiano, C.; Botvina, A. S.*; Boudard, A.; Brzychczyk, J.; Chbihi, A.; Cibor, J.; Czech, B.; De Napoli, M.; Ducret, J. E.; Emling, H.*; Frankland, J. D.; Hellström, M.*; Henzlova, D.*; Imme, G.; Iori, I.; Johansson, H.*; Kezzar, K.*; Lafriakh, A.; Le Fèvre, A.*; Le Gentil, E.; Leifels, Y.*; Lühning, J.*; Lukasik, J.*; Lynch, W. G.; Lynen, U.*; Majka, Z.; Mocko, M.; Müller, W. F. J.*; Mykulyak, A.*; Orth, H.*; Otte, A. N.*; Palit, R.*; Pawlowski, P.; Pullia, A.; Raciti, G.; Rapisarda, E.; Sann, H.*; Schwarz, C.*; Sfienti, C.*; Simon, H.*; Sümmerer, K.*; Tsang, M. B.; Verde, G.; Volant, C.; Wallace, M.; Weick, H.*; Wiechula, J.*; Wieloch, A.; Zwieglinski, B.: **Isotopic dependence of the caloric curve.** *Progress in particle and nuclear physics* **62**(2), 2009: 407–412. DOI:10.1016/j.ppnp.2008.12.006

257 Trautmann, W.*; Chartier, M.; Leifels, Y.*; Lemmon, R. C.; Li, Q.; Lukasik, J.; Pagano, A.; Pawlowski, P.; Russotto, P.; Wu, P.: **Differential neutron-proton squeeze-out.** *Progress in particle and nuclear physics* **62**(2), 2009: 425–426. DOI:10.1016/j.ppnp.2008.12.012

258 Tselyaev, V.; Speth, J.; Krewald, S.; Litvinova, E.*; Kamerdzhiev, S.; Lyutorovich, N.; Avdeenkov, A.; Grümmer, F.: **Description of the giant monopole resonance in the even-A $^{112-124}$Sn isotopes within a microscopic model including quasiparticle-phonon coupling.** *Physical review C, Nuclear physics / Phys. Rev. C* **79**(3), 2009: 034309. DOI:10.1103/physrevc.79.034309

259 Tsukada, K.; Haba, H.; Asai, M.; Toyoshima, A.; Akiyama, K.; Kasamatsu, Y.; Nishinaka, I.; Ichikawa, S.; Yasuda, K.; Miyamoto, Y.; Hashimoto, K.; Nagame, Y.; Goto, S.; Kudo, H.; Sato, W.; Shinohara, A.; Oura, Y.; Sueki, K.; Kikunaga, H.; Kinoshita, N.; Yokoyama, A.; Schädel, M.*; Brüchle, W.*; Kratz, J. V.: **Adsorption of Db and its homologues Nb and Ta, and the pseudo-homologue Pa on anion-exchange resin in HF solution.** *Radiochimica acta / Radiochim. Acta* **97**(2), 2009: 83–89. DOI:10.1524/ract.2009.1577 OPEN ACCESS.

260 Tsukada, K.; Haba, H.; Asai, M.; Toyoshima, A.; Akiyama, K.; Kasamatsu, Y.; Nishinaka, I.; Ichikawa, S.; Yasuda, K.; Miyamoto, Y.; Hashimoto, K.; Nagame, Y.; Goto, S.; Kudo, H.; Sato, W.; Shinohara, A.; Oura, Y.; Sueki, K.; Kikunaga, H.; Kinoshita, N.; Yokoyama, A.; Schädel, M.*; Brüchle, W.*; Kratz, J. V.: **Adsorption of Db and its homologues Nb and Ta, and the pseudo-homologue Pa on anion-exchange resin in HF solution.** *Radiochimica acta* **97**(2), 2009: 83–89. DOI:10.1524/ract.2009.1577 OPEN ACCESS.

261 Uberseder, E.; Reifarth, R.*; Schumann, D.; Dillmann, I.; Pardo, C. D.; Gorres, J.; Heil, M.*; Käppeler, F.; Marganiec, J.; Neuhausen, J.; Pignatari, M.; Voss, F.; Walter, S.; Wiescher, M.: **Measurement of the ^{60}F(n,γ)^{61}Fe Cross Section at Stellar Temperatures.** *Physical review letters / Phys. Rev. Lett.* **102**(15), 2009: 151101. DOI:10.1103/physrevlett.102.151101

262 Urban, W.; Sieja, K.*; Simpson, G. S.; Faust, H.; Rzaca-Urban, T.; Zlomaniec, A.; Lukasiewicz, M.; Smith, A. G.; Durell, J. L.; Smith, J. F.; Varley, B. J.; Nowacki, F.; Ahmad, I.: **New isomers and medium-spin structure of the ^{95}Y nucleus.** *Physical review C, Nuclear physics / Phys. Rev. C* **79**(4), 2009: 044304. DOI:10.1103/physrevc.79.044304 Also part of: PNI

263 Valiente-Dobon, J. J.; Mengoni, D.; Gadea, A.; Farnea, E.; Lenzi, S. M.; Lunardi, S.; Dewald, A.; Pissulla, T.; Szilner, S.; Broda, R.; Recchia, F.; Algora, A.; Angus, L.; Bazzacco, D.; Benzoni, G.; Bizzeti, P. G.; Bizzeti-Sona, A. M.; Boutachkov, P.*; Corradi, L.; Crespi, F.; de Angelis, G.; Fioretto, E.; Görgen, A.; Gorska, M.*; Gottardo, A.; Grodner, E.; Guiot, B.; Howard, A.; Krolas, W.; Leoni, S.; Mason, P.; Menegazzo, R.; Montanari, D.; Montagnoli, G.; Napoli, D. R.; Obertelli, A.; Pawlat, T.; Rubio, B.; Sahin, E.; Scarlassara, F.; Silvestri, R.; Stefanini, A. M.; Smith, J. F.; Steppenbeck, D.; Ur, C. A.; Wady, P. T.; Wrzesinski, J.; Maglione, E.; Hamamoto, I.: **Lifetime Measurements of the Neutron-Rich N=30 Isotones ^{50}Ca and ^{51}Sc: Orbital Dependence of Effective Charges in the fp Shell.** *Physical review letters / Phys. Rev. Lett.* **102**(24), 2009: 242502. DOI:10.1103/physrevlett.102.242502

264 Van de Walle, J.; Aksouh, F.; Behrens, T.; Bildstein, V.; Blazhev, A.; Cederkäll, J.; Clement, E.; Cocolios, T. E.; Davinson, T.; Delahaye, P.; Eberth, J.; Ekström, A.; Fedorov, D. V.; Fedosseev, V. N.; Fraile, L. M.; Franchoo, S.; Gernhauser, R.; Georgiev, G.; Habs, D.; Heyde, K.; Huber, G.; Huyse, M.; Ibrahim, F.; Ivanov, O.; Iwanicki, J.; Jolie, J.; Kester, O.*; Köster, U.; Kröll, T.; Krücken, R.; Lauer, M.; Lisetskiy, A. F.*; Lutter, R.; Marsh, B. A.; Mayet, P.; Niedermaier, O.; Pantea, M.; Raabe, R.; Reiter, P.; Sawicka, M.; Scheit, H.; Schrieder, G.; Schwalm, D.; Seliverstov, M. D.; Sieber, T.; Sletten, G.; Smirnova, N.; Stanoiu, M.*; Stefanescu, I.; Thomas, J.-C.; Valiente-Dobon, J. J.; Van Duppen, P.; Verney, D.; Voulot, D.; Warr, N.; Weisshaar, D.; Wenander, F.; Wolf, B. H.; Zielinska, M.: **Low-energy Coulomb excitation of neutron-rich zinc isotopes.** *Physical review C, Nuclear physics / Phys. Rev. C* **79**(1), 2009: 014309. DOI:10.1103/physrevc.79.014309

265 Wadsworth, R.; Singh, B. S. N.; Steer, A. N.; Jenkins, D. C.; Bentley, M. A.; Brock, T.; Davies, P.; Glover, R.; Pattabiraman, N. S.; Scholey, C.; Grahn, T.; Greenlees, P. T.; Jones, P.; Jakobsson, U.; Julin, R.; Juutinen, S.; Ketelhut, S.; Leino, M.; Nyman, M.; Perua, P.; Pakarinen, J.; Rahkila, P.; Ruotslainen, P.; Sorri, J.; Uusitalo, J.; Lister, C. J.; Butler, P. A.; Dimmock, M.; Joss, D. T.; Thomson, J.; Rinta-Antila, S.; Cederwall, B.; Hadinia, B.; Sandzelius, M.; Atac, A.; Betterman, L.; Blazhev, A.; Braun, N.; Finke, F.; Geibel, K.; Ilie, G.; Iwasaki, H.; Jolie, J.; Reiter, P.; Scholl, C.; Warr, N.; Boutachkov, P.*; Caceres, L.*; Domingo, C.*; Engert, T.*; Farinon, F.*; Gerl, J.*; Goel, N.*; Gorska, M.*; Grawe, H.*; Kurz, N.*; Kojuharov, I.*; Pietri, S.*; Nociforo, C.*; Prochazka, A.*; Wollersheim, H.-J.*; Eppinger, K.; Faestermann, T.; Hinke, C.; Hoischen, R.; Krücken, R.; Gottardo, A.; Liu, Z.; Woods, P.; Grebosz, J.; Merchant, E.; Nyberg, J.; Soderstrom, P. A.; Podolyak, Z.; Regan, P.; Steer, S.; Pfutzner, M.; Rudolph, D.: **The northwest frontier: spectroscopy of N $\sim$ Z nuclei below masss 100.** *Acta physica Polonica B, Particle physics and field theory, nuclear physics, theory of relativity / Acta Phys. Pol. B* **40**(3), 2009: 611–620. URL OPEN ACCESS.

266 Weissbach, F.*; Hencken, K.; Kiselev, D.; Trautmann, D.: **Improved radiative corrections to e,e'p experiments: Explicit treatment of kinematical corrections in multiphoton bremsstrahlung.** *Physical review C, Nuclear physics / Phys. Rev. C* **80**(2), 2009: 024602. DOI:10.1103/physrevc.80.024602

267 Weissbach, F.*; Hencken, K.; Trautmann, D.; Sick, I.: **Improved radiative corrections and proton charge form factor from the Rosenbluth separation technique.** *Physical review C, Nuclear physics / Phys. Rev. C* **80**(6), 2009: 064605. DOI:10.1103/physrevc.80.064605

268 Wiechula, J.*; ALICE TPC Collaboration: **Commissioning and Calibration of the ALICE TPC.** *Nuclear physics A, Nuclear and hadronic physics / Nucl. Phys. A* **830**, 2009: 531C–534C. DOI:10.1016/j.nuclphysa.2009.10.046

269 Wiegel, B.; Agosteo, S.; Bedogni, R.; Caresana, M.; Esposito, A.; Fehrenbacher, G.*; Ferrarini, M.; Hohmann, E.; Hranitzky, C.; Kasper, A.; Khurana, S.; Mares, V.; Reginatto, M.; Rollet, S.; Ruhm, W.; Schardt, D.*; Silari, M.; Simmer, G.; Weitzenegger, E.: **Intercomparison of radiation protection devices in a high-energy stray neutron field, Part II: Bonner sphere spectrometry.** *Radiation Measurements / Radiat. Meas.* **44**(7-8), 2009: 660–672. DOI:10.1016/j.radmeas.2009.03.026

270 Wiegel, B.; Agosteo, S.; Bedogni, R.; Caresana, M.; Esposito, A.; Fehrenbacher, G.*; Ferrarini, M.; Hohmann, E.; Hranitzky, C.; Kasper, A.; Khurana, S.; Mares, V.; Reginatto, M.; Rollet, S.; Rühm, W.; Schardt, D.*; Silari, M.; Simmer, G.; Weitzenegger, E.: **Intercomparison of radiation protection devices in a high-energy stray neutron field, Part II: Bonner sphere spectrometry.** *Radiation Measurements* **44**(7-8), 2009: 660–672. DOI:10.1016/j.radmeas.2009.03.026

271 Wieland, O.; Bracco, A.; Camera, F.; Benzoni, G.; Blasi, N.; Brambilla, S.; Crespi, F. C. L.; Leoni, S.; Mil-

lion, B.; Nicolini, R.; Maj, A.; Bednarczyk, P.*; Grebosz, J.; Kmiecik, M.; Meczynski, W.; Styczen, J.; Aumann, T.*; Banu, A.*; Beck, T.*; Becker, F.*; Caceres, L.; Doornenbal, P.*; Emling, H.*; Gerl, J.*; Geissel, H.*; Gorska, M.*; Kavatsyuk, O.*; Kavatsyuk, M.*; Kojouharov, I.*; Kurz, N.*; Lozeva, R.*; Saito, N.*; Saito, T.*; Schaffner, H.*; Wollersheim, H. J.; Jolie, J.; Reiter, P.; Warr, N.; deAngelis, G.; Gadea, A.; Napoli, D.; Lenzi, S.; Lunardi, S.; Balabanski, D.; LoBianco, G.; Petrache, C.; Saltarelli, A.; Castoldi, M.; Zucchiatti, A.; Walker, J.; Burger, A.: **Search for the Pygmy Dipole Resonance in ^{68}Ni at 600 MeV/nucleon.** *Physical review letters / Phys. Rev. Lett.* **102**(9), 2009: 092502. DOI:10.1103/physrevlett.102.092502

272 Winckler, N.*; Geissel, H.*; Litvinov, Y. A.*; Beckert, K.*; Bosch, F.*; Boutin, D.*; Brandau, C.*; Chen, L.; Dimopoulou, C.*; Essel, H. G.*; Fabian, B.; Faestermann, T.; Fragner, A.; Haettner, E.; Hess, S.*; Kienle, P.; Knobel, R.*; Kozhuharov, C.*; Litvinov, S. A.*; Mazzocco, M.*; Montes, F.; Münzenberg, G.*; Nociforo, C.*; Nolden, F.*; Patyk, Z.; Plass, W. R.*; Prochazka, A.*; Reda, R.*; Reuschl, R.*; Scheidenberger, C.*; Steck, M.*; Stöhlker, T.*; Torilov, S. Y.; Trassinelli, M.; Sun, B.*; Weick, H.*; Winkler, M.*: **Orbital electron capture decay of hydrogen- and helium-like ^{142}Pm ions.** *Physics letters B / Phys. Lett. B* **679**(1), 2009: 36–40. DOI:10.1016/j.physletb.2009.07.019 Also part of: PNI

273 Winger, J. A.; Ilyushkin, S. V.; Rykaczewski, K. P.; Gross, C. J.; Batchelder, J. C.; Goodin, C.; Grzywacz, R.; Hamilton, J. H.; Korgul, A.; Krolas, W.; Liddick, S. N.; Mazzocchi, C.; Padgett, S.; Piechaczek, A.; Rajabali, M. M.; Shapira, D.; Zganjar, E. F.; Borzov, I. N.*: **Large β-Delayed Neutron Emission Probabilities in the ^{78}Ni Region.** *Physical review letters / Phys. Rev. Lett.* **102**(14), 2009: 142502. DOI:10.1103/physrevlett.102.142502

274 Winters, D. F. A.; Stöhlker, T.: **Atomic physics at storage rins: recent results from ESR and future perspectives at FAIR.** *International journal of modern physics E, Nuclear physics / Int. J. Mod. Phys. E-Nucl. Phys.* **18**(2), 2009: 359–366. URL Also part of: PNI

275 Zabrodin, E. E.; Arsene, I. C.; Bleibel, J.; Bleicher, M.; Bravina, L. V.; Burau, G.; Faessler, A.; Fuchs, C.; Nilsson, M. S.; Tywoniuk, K.; Stöcker, H.*: **EOS at FAIR energies and the role of resonances.** *Journal of physics G, Nuclear and particle physics / J. Phys. G-Nucl. Part. Phys.* **36**(6), 2009: 064065. DOI:10.1088/0954-3899/36/6/064065

276 Zapp, K. C.*; Stachel, J.; Wiedemann, U. A.: **LPM-Effect in Monte Carlo Models of Radiative Energy Loss.** *Nuclear physics A, Nuclear and hadronic physics / Nucl. Phys. A* **830**, 2009: 171C–174C. DOI:10.1016/j.nuclphysa.2009.10.091

277 Zapp, K. C.*; Stachel, J.; Wiedemann, U. A.: **LPM-Effect in Monte Carlo Models of Radiative Energy Loss.** *Nuclear physics A, Nuclear and hadronic physics* **830**, 2009: 171C–174C. DOI:10.1016/j.nuclphysa.2009.10.091

278 Zapp, K.*; Stachel, J.; Wiedemann, U. A.: **Local Monte Carlo Implementation of the Non-Abelian Landau-Pomeranchuk-Migdal Effect.** *Physical review letters / Phys. Rev. Lett.* **103**(15), 2009: 152302. DOI:10.1103/physrevlett.103.152302

279 Zinner, N. T.; Molmer, K.; Özen, C.*; Dean, D. J.; Langanke, K.*: **Shell-model Monte Carlo simulations of the BCS-BEC crossover in few-fermion systems.** *Physical review A, Atomic, molecular, and optical physics / Phys. Rev. A* **80**(1), 2009: 013613. DOI:10.1103/physreva.80.013613

Other publications to the programme 'Physics of hadrons and nuclei' (incl. the FAIR project) published in 2009

Compiled by K. Große, I. Kraus, V. R. W. Schaa et al.

001 Al-Turany, M.; Uhlig, F.: **FairRoot Framework.** In: *PoS(ACAT08)048*,

002 Al-Turany, M.; Uhlig, F.: **GPU's for event reconstruction in the FairRoot Framework.** In: *Journal of Physics: Conference Series*,

003 Andrianov, A.; K. Beckert, A. Bleile, Ch. Chatterjee, A. Echler, P. Egelhof, A. Gumberidze, S. Ilieva, O. Kiselev, C. Kilbourne, H.-J. Kluge, S. Kraft-Bermuth, D. Mc Cammon, J. P. Meier, R. Reuschl, T. Stöhlker, M. Trassinelli: **Precise Lamb Shift Measurements in Hydrogen-Like Heavy Ions - Status and Perspectives.** In: B. Cabrera, A. Miller, B. Young: *Proc. of the 13th Int. Workshop on Low Temperature Detectors, LTD13, AIP Conf. Proc. 1185*, 99p.

004 Böhme, C.; Dietrich, J.; Kamerdzhiev, V.; P. Forck, P.*; Giacomini, T.*; Liakin, D.: **Beam Test of the FAIR IPM Prototype in COSY.** In: *9th European Workshop on Beam Diagnostics and Instrumentation for Particle Accelerators, 25-27 May, 2009, Basel, Switzerland*, TUPB12p.

005 Bär, R.*; Krause, U.*; Schaa, V. R. W.*; Schiebel, W.*; Thieme,M.*: **Development of a New Control System for the FAIR Accelerator Complex at GSI.** In: *12th International Conference on Accelerator and Large Experimental Physics Control Systems, October 12-16, 2009, Kobe, Japan*, TUP107p.

006 Barth, W.; Dahl, L. A.*; Eickhoff, H.*; Groening, L.*: **A New High Energy UNILAC as a High Current Heavy Ion Injector for the FAIR-Synchrotrons.** In: *23rd Particle Accelerator Conference, 4-8 May 2009, Vancouver, BC, Canada*, FR5REP059p.

007 Beck, D.* H.*; Brand, H.*; Hahn, H.*; Herfurth, F.*; Koszudowski, S.*; Marx, G.; Schweikhard, L.; Ziegler, E.: **A Pulse-Pattern Generator Using LabVIEW FPGA.** In: *12th International Conference on Accelerator and Large Experimental Physics Control Systems, October 12-16, 2009, Kobe, Japan*, TUP058p.

008 Bellachioma, M. C.*; Kollmus, H.*; Krämer, A.*; Kurdal, J.*; Reich-Sprenger, H.*; Bender, M.: **Thin Film Coating for the Upgrade of the Ion Synchrotron SIS18 at GSI.** In: *23rd Particle Accelerator Conference, 4-8 May 2009, Vancouver, BC, Canada*, MO6RFP014p.

009 Berdermann, E.: **Advanced Diamond Particle Detectors.** In: *Nuclear Physics News* **19***(2)*, DOI:10.1080/10506890902740218

010 Berdermann, E.; Ciobanu, M.: **CVD-Diamond Detectors for Experiments with Hadrons, Nuclei, and Atoms.** In: Sussmann, R. S. (Ed.): *CVD Diamond for Electronic Devices and Sensors;*, Wiley,

011 Berdermann, E.; Ciobanu, M.; Herrmann, N.; Hildenbrand, K. D.; Kis, M.; Koenig, W.; Pomorski, M.; Rebisz-Pomorska, M.; Schüttauf, A.: **Diamond Start Detectors.** In: *Proceedings of the IEEE NSS-MIC, Orlando, 2009, Conference Record*, IEEE,

012 Berdermann, E.; Pomorski, M.; de Boer, W.; Ciobanu, M.; Dunst, S.; Grah, C.; Kis, M.; Koenig, W.; Lange, W.; Lohmann, W.; L ovrincic, R.; Moritz, P.; Morse, J.; Mueller, S.; Pucci, A.; Schreck, M.; Rahman, S.; Träger, M.: **Diamond detectors for hadron physics research.** In: *Proceedings of the 20th European Conference on Diamond, Diamond-Like Materials, Carbon Nanotubes, and Nitrides (DIAMOND 2009)*, Amsterdam: Elsevier, DOI:10.1016/j.diamond.2009.11.019

013 Blaum, K.; Block, M.: **Precision Penning trap mass measurements on exotic ions: Status and perspectives.** In: *Hyp. Int. 194*, 65p.

014 Boine-Frankenheim, O.*; Chorniy, O.*: **RF Barrier Compression with Space Charge for the FAIR Synchrotrons.** In: *23rd Particle Accelerator Conference, 4-8 May 2009, Vancouver, BC, Canada*, TH5PFP021p.

015 Boine-Frankenheim, O.*; Kornilov, V.*; Paret, S.*: **Transverse Schottky Noise with Space Charge.** In: *23rd Particle Accelerator Conference, 4-8 May 2009, Vancouver, BC, Canada*, TU3PBC03p.

016 Bousonville, M.*; Rausch, J.: **Reference Signal Generation With Direct Digital Synthesis for FAIR.** In: *11th International Conference on Heavy Ion Accelerator Technology, 08-12 June 2009, Venezia, Italy*, A1STp.

017 Bousonville, M.; Rausch, J.: **Velocity of Signal Delay Changes in Fibre Optic Cables.** In: *9th European Workshop on Beam Diagnostics and Instrumentation for Par-*

ticle Accelerators, 25-27 May, 2009, Basel, Switzerland, TUPB35p.

018 Brandau, C. et al.: **Isotope shifts in dielectronic recombination: From stable to in-flight-produced nuclei.** In: *Journal of Physics: Conf. Series 194*, 012023p.

019 Brodhage, R. B.; Minaev, S.; Podlech, H.; Ratzinger, U.; Tiede, R.; G. Clemente, G.*; Groening, L.*: **Prototype Construction of a Coupled CH-DTL Proton Linac for FAIR.** In: *23rd Particle Accelerator Conference, 4-8 May 2009, Vancouver, BC, Canada*, FR5REP060p.

020 Bussmann, M. H.; Schramm, U.; Birkl, G.; Walther, T.; Dimopoulou, C.*; Kozhuharov, C.*; Kühl, T.*; Nörtershäuser, W.*; Steck, F.*; Stöhlker, T.*; Winters, D. F. A.*; Geppert, C.; Wen, W. Q. X.; Zhang, D.; Novotny, C.: **Laser Cooling at ESR, CSR and FAIR.** In: *Workshop on Beam Cooling and Related Topics, 31 August-4 September 2009, Lanzhou, China*, MOA1MCIO01p.

021 Ciobanu, M.; Herrmann, N.; Hildenbrand, K. D.; Kis,M.; Schüttauf, A.: **PADI-2,-3 and -4: The second iteration of the Fast Preamplifier - Discriminator ASIC for Time-of-Flight Measurements at CBM.** In: *IEEE NSS-MIC, Orlando, 2009, Conference Record*, IEEE,

022 Clemente, G.*; Barth, W.*; Groening, L.*; Orzhekhovskaya, A.*; Yaramyshev, S.*; Kolomiets, A.; Minaev, S.; Ratzinger, U.;: **End To End Simulations of the GSI Linear Accelerator Facility.** In: *10th International Computational Accelerator Physics Conference, Aug 31 - Sep 4, 2009, San Francisco, CA, USA*, TH4IOPK02p.

023 Dahl, L.*: **The GSI UNILAC Upgrade Program to Meet FAIR Requirements.** In: *11th International Conference on Heavy Ion Accelerator Technology, 08-12 June 2009, Venezia, Italy*, FR1Tp.

024 Dimopoulou, C.*; Dolinskyy, A.*; Heine, R. G.*; Katayama, T.*; Laier, U.*; Nolden, F.*; Schreiber, G.*; Steck, F.*: **The Versatile NESR Storage Ring with Powerful Electron Cooling.** In: *Workshop on Beam Cooling and Related Topics, 31 August-4 September 2009, Lanzhou, China*, THM2MCIO02p.

025 Dolinskyy, A.*; Dimopoulou, C.*; Gorda, O. E.*; Litvinov, S. A.*; Nolden, F.*; Peschke, C.*; Steck, M.*: **Stability Boundary of Ion Beams in the FAIR Storage Rings.** In: *23rd Particle Accelerator Conference, 4-8 May 2009, Vancouver, BC, Canada*, TH6PFP078p.

026 Egelhof, P.; Kraft-Bermuth, S.: **Future Perspectives for the Application of Low Temperature Detectors in Heavy Ion Physics.** In: B. Cabrera, A. Miller, B. Young: *Proc. of the 13th Int. Workshop on Low Temperature Detectors, LTD13, AIP Conf. Proc. 1185*, 761p.

027 Ejiri, S.; Karsch, F.; Laermann, E.; Miao, C.; Mukherjee, S.; Petreczky, P.; Schmidt, C.; Soeldner, W.; Unger, W.: **On the magnetic equation of state in (2+1)-flavor QCD.** In: *Physical Review D* **80**, DOI:10.1103/PhysRevD.80.094505

028 E. Mustafin, E.*; Floch, E.*; Plotnikov, A.*; Schubert, E.*; Seidl, T.*; Strasik, I.*; Latysheva, L.; Smolyakov, A.: **Irradiation of Superconducting Magnet Components for FAIR.** In: *11th International Conference on Heavy Ion Accelerator Technology, 08-12 June 2009, Venezia, Italy*, A4Tp.

029 F. Becker, F.*; Andre, C.*; Forck, P.*; Haseitl, R.*; Hug, A.*; Walasek-Höhne, B.*; Bieniosek, F.; Ni, P. A.; Hoffmann, D. H. H.: **Beam Induced Fluoresence Monitor and Imaging Spectrography of Different Working Gases.** In: *9th European Workshop on Beam Diagnostics and Instrumentation for Particle Accelerators, 25-27 May, 2009, Basel, Switzerland*, TUPB02p.

030 Fehrenbacher, G.: **Strahlenschutzplanung für Teilchentherapieanlagen.** In: *Leben mit Strahlung- von den Grundlagen zur Praxis, 41. Jahrestagung Fachverband für Strahlenschutz*, 300p.

031 Fischer, E. S.*; Bleile, A.*; Floch, E.*; Macavei, J.*; Mierau, A.*; Schnizer, P.*; Schroeder, C.*; Stafiniak, A.*; Walter, F.*; Gaertner, W.; Sikler, G.: **Fast Ramped Superferric Prototype Magnets of the FAIR Project – First Test Results and Design Update.** In: *23rd Particle Accelerator Conference, 4-8 May 2009, Vancouver, BC, Canada*, MO6PFP065p.

032 Fischer, E. S.*; Mierau, A.*; Schnizer, P.*; Akishin, P. G.; Kurnyshov, R. V.; Schnizer, B.; P.A. Shcherbakov, P. A.: **Measured and Calculated Field Properties of the SIS 100 Magnets Described Using Elliptic and Toroidal Multipoles.** In: *23rd Particle Accelerator Conference, 4-8 May 2009, Vancouver, BC, Canada*, TH5PFP057p.

033 Franchetti, G.*; Bayer, W. B.*; Becker, F.*; Chorniy, O.*; Forck, P.*; Giacomini, T.*; Hofmann, I.*; Kirk, M. M.*; Mohite, T. S.*; Omet, C.*; Parfenova, A. S.*; Schütt, P.*: **High Intensity Benchmarking Studies in the SIS18 Synchrotron.** In: *23rd Particle Accelerator Conference, 4-8 May 2009, Vancouver, BC, Canada*, TH5PFP022p.

034 Franchetti, G.*; Hofmann, I.*; Sorge, S.*; V.V. Kapin, V. V.: **High Intensity Nonlinear Dynamics in SIS100.** In: *23rd Particle Accelerator Conference, 4-8 May 2009, Vancouver, BC, Canada*, TH5PFP023p.

035 Groening, L.*; Barth, W.*; Bayer, W. B.*; Clemente, G.*; Dahl, L. A.*; Forck, P.*; Gerhard, P.*; Hofmann, I.*; Kaiser, M.*; Maier, M. T.*; Mickat, S.*; Milosic, T.*; Riehl, G. A.*; Vormann, H.*; Yaramyshev, S.*; Jeon, D.; Tiede, R.; Uriot, D.: **Linac Code Benchmarking with High Intensity Experiments at the UNILAC.** In: *23rd Particle Accelerator Conference, 4-8 May 2009, Vancouver, BC, Canada*, TU3PBI02p.

036 Groening, L.*; Barth, W.*; Bayer, W. B.*; Clemente, G.*; Dahl, L. A.*; Forck, P.*; Gerhard, P.*; Hofmann, I.*; Kaiser, M.*; Maier, M. T.*; Mickat, S.*; Milosic, T.*; Riehl, G. A.*; Vormann, H.*; Yaramyshev, S.*; Jeon, D.; Uriot, D.; Tiede; R.: **Comparison of Different Simulation Codes with UNILAC Measurements for High Beam Currents.** In: *10th International Computational Accelerator Physics Conference, Aug 31 - Sep 4, 2009, San Francisco, CA, USA,* TU1IOPK02p.

037 Gütlich, E.*; Forck, P.*; Walasek-Höhne, B.*; Ensinger, W.: **High Current Ion Beam Investigations on Inorganic Scintillation Screens.** In: *9th European Workshop on Beam Diagnostics and Instrumentation for Particle Accelerators, 25-27 May, 2009, Basel, Switzerland,* TUPB04p.

038 Haenichen, L.; Müller, W. F. O.; Weiland, T.; Al-Khateeb, A. M.*; Boine-Frankenheim, O.*: **Comparison of Analytical and Numerical Results for Broadband Coupling Impedance.** In: *23rd Particle Accelerator Conference, 4-8 May 2009, Vancouver, BC, Canada,* TH5PFP091p.

039 Haseitl, R.*; Andre, C.*; Becker, F.*; Forck, P.*: **ProfileView - A Data Acquisition System for Beam Induced Fluorescence Monitors.** In: *9th European Workshop on Beam Diagnostics and Instrumentation for Particle Accelerators, 25-27 May, 2009, Basel, Switzerland,* MOPD42p.

040 Herfurth, F.; Barth, W.; Clemente, G.; Dahl, L. A.*; Gerhard, P.*; Kaiser, M.*; Kluge, H. J.*; Koszudowski, S.*; Kozhuharov, C.*; Quint, W.*; Sokolov, A.*; Stöhlker, T.*; Vorobjev, G.*; Kester, O. K.; Pfister, j., Ratzinger, u., Sauer, A. c, Schempp, A: **The HITRAP Decelerator Linac at GSI.** In: *23rd Particle Accelerator Conference, 4-8 May 2009, Vancouver, BC, Canada,* WE4PBC05p.

041 Hoffmann, T.*; Höppner, K.*; Kowina, P.*; Lang, K.*; Schwickert, M.*; J. Bobnar, J.; Janza, G.; Sah, S.; Sekoranja, M.; Verstovcek, I.: **A New DAQ Installation for the SIS18 Beam Position Monitoring System at GSI.** In: *12th International Conference on Accelerator and Large Experimental Physics Control Systems, October 12-16, 2009, Kobe, Japan,* THP047p.

042 Hoffmann, T.*; Schwickert, M.*; G. Jania, G.: **FESA at FAIR - The Front-End Software Architecture.** In: *23rd Particle Accelerator Conference, 4-8 May 2009, Vancouver, BC, Canada,* FR5REP009p.

043 Hofmann, I.*; Orzhekhovskaya, A.*; Yaramyshev, S.*; Alber, I.; Harres, K.; Roth, M.: **Laser Accelerated Ions and their Potential for Therapy Accelerators.** In: *11th International Conference on Heavy Ion Accelerator Technology, 08-12 June 2009, Venezia, Italy,* FR6Tp.

044 Hülsmann, P.*; Balss, R.*; Klingbeil, H.*; Laier, U.*: **Bunch Compression for FAIR.** In: *23rd Particle Accelerator Conference, 4-8 May 2009, Vancouver, BC, Canada,* TU5PFP023p.

045 Jeon, D.; Franchetti, G.*; Groening, L.*: **A Fourth Order Resonance of a High Intensity Linac.** In: *23rd Particle Accelerator Conference, 4-8 May 2009, Vancouver, BC, Canada,* FR5REP078p.

046 Katayama, T.*; Dolinskyy, A.*; Franzke, B.*; Litvinov, S. A.*; Nolden, F.*; Steck, F.*; Möhl, D.; L. Thorndahl, L.: **Numerical Design Study of Stochastic Stacking of 3 GeV Anti-Proton Beam in the RESR for the FAIR Project.** In: *Workshop on Beam Cooling and Related Topics, 31 August-4 September 2009, Lanzhou, China,* MOA2MCIO02p.

047 Kelic, A.; Stoecker, H.: **FAIR - Cosmic Matter in the Lab.** In: *AIP Conference Proceedings 1175,* Heidelberg: Springer, DOI:

048 Kester, O.; Barth, W.*. Dahl, L.*; Gerhard, P.*; Herfurth, F.*; Kaiser, M.*; Kluge, H.-J.*; Koszudowski, S.*; Kozhuharov, C.*; Clemente, G.*; Maero, G.*; Quint, W.*; Sokolov, A.*; Stöhlker, T.*; Vinzenz, W.*; Vorobjev, G.*; Winters, D.*; Pfister, J.; Ratzinger, U.; Sauer, A.; Schempp, A.: **Status of Construction and Commissioning of the GSI HITRAP Decelerator.** In: *11th International Conference on Heavy Ion Accelerator Technology, 08-12 June 2009, Venezia, Italy,* FR2Tp.

049 Kikuchi, T.; Dietrich, J.; Maier, R.; Prasuhn, D.; Stockhorst, H.; T. Katayama, T.*: **Simulation Study of Simultaneous Use of Stochastic Cooling and Electron Cooling with Internal Target at COSY and HESR.** In: *Workshop on Beam Cooling and Related Topics, 31 August-4 September 2009, Lanzhou, China,* THPMCP005p.

050 Klimkiewicz, A. et al: **Pygmy Dipole Strength in Exotic Nuclei and the Equation of State.** In: *Nuclear structure ad dynamics '09: Proceedings of the International Conference, AIP Conf. Proc., August 26, 2009, Vol. 1165,* 181-184p. DOI:10.1063/1.3232065

051 Kobayakawa, H.; Boine-Frankenheim, O.: **Synchrotrons and Storage Rings.** In: Stock, R: *Encyclopedia of applied high energy and particle physics,* 561p.

052 Kojouharova, J.; Lago, S.; Wollersheim, H.-J.; Kojouharov, I.; Gerl, J.: **Study of operational characteristics of pixelated germanium detector.** In: *Proceedings of the 11th Congress on Theoretical and applied mechanics, Sept. 2-5, Borovetz, Bulgaria,*

053 Kornilov, V.*; Boine-Frankenheim, O.*: **Simulation Studies and Code Validation For The Head-Tail Instability With Space Charge.** In: *10th International Computational Accelerator Physics Conference, Aug 31 - Sep 4, 2009, San Francisco, CA, USA,* TU2IOPK02p.

054 Kowina, P.*; Forck, P.*; Kaufmann, W.*; Moritz, P.*; Wolfheimer, F.; Weiland, T.: **FEM Simulations - A Powerful Tool for BPM Design.** In: *9th European Workshop on Beam Diagnostics and Instrumentation for Particle Accelerators, 25-27 May, 2009, Basel, Switzerland,* MOOC03p.

055 Laier, U.*; Hülsmann, P.*; Ningel, K.-P.*; Schreiber, G.*: **Design of an MA Based RF System for the Collector Ring at FAIR.** In: *23rd Particle Accelerator Conference, 4-8 May 2009, Vancouver, BC, Canada,* TU5PFP024p.

056 Lens, D.; Hülsmann, P.*; Klingbeil, H.*: **Beam Loading Effects on the RF Control Loops of a Double-Harmonic Cavity System for FAIR.** In: *23rd Particle Accelerator Conference, 4-8 May 2009, Vancouver, BC, Canada,* WE5PFP100p.

057 Litvinov, S. A.*; Dolinskyy, A.*; Gorda, O. E.*; Nolden, F.*; Steck, M.*: **An Alternative Ion-Optical Mode of the Recuperated Experimental Storage Ring (RESR).** In: *23rd Particle Accelerator Conference, 4-8 May 2009, Vancouver, BC, Canada,* FR5REP118p.

058 Lommel, B.; Kindler, B.: **Targets for Particle Accelerators.** In: Stock, R: *Encyclopedia of Applied High Energy and Particle Physics,*

059 Lommel, B.; Kindler, B.: **Targets for Particle Accelerators.** In: Stock, R: *Encyclopedia of applied high energy and particle physics,* 619p.

060 Malzacher, P.; Manafov, A.: **PROOF on Demand.** In: *Journal of Physics: Conference Series,*

061 Mehler, M.*; Klingbeil, H.*; Kumm, U.* Laier, U.*; Ningel, K.-P.*: **The Damping of Longitudinal Quadrupole Oscillations at GSI.** In: *23rd Particle Accelerator Conference, 4-8 May 2009, Vancouver, BC, Canada,* WE5PFP079p.

062 Milosic, T.*; Forck, P.*; Liakin, D.: **Longitudinal Emittance Measurement Using Particle Detectors.** In: *9th European Workshop on Beam Diagnostics and Instrumentation for Particle Accelerators, 25-27 May, 2009, Basel, Switzerland,* TUPD18p.

063 Müller, R.*; Fitzek, J.; Ondreka, D.*: **Evaluation of the LHC Software Architecture for Data Supply and Setting Management within the FAIR Control System.** In: *12th International Conference on Accelerator and Large Experimental Physics Control Systems, October 12-16, 2009, Kobe, Japan,* THP012p.

064 Nociforo, C et al.: **Shell Closure N=16 in 24O.** In: *AIP Conf. Proc. 1165,* 90p.

065 Nolden, F.*;: **Numerical Analysis of Low-Intensity Schottky Spectra Recorded as Time Series.** In: *Workshop on Beam Cooling and Related Topics, 31 August-4 September 2009, Lanzhou, China,* THPMCP001p.

066 Nolden, F.*; Hettrich, R.*; Jandewerth, U.*; Peschke, C.*; Petri, P.*; Steck, F.*: **Prototype Pick-up Tank for CR Stochastic Cooling at FAIR.** In: *Workshop on Beam Cooling and Related Topics, 31 August-4 September 2009, Lanzhou, China,* MOA1MCIO03p.

067 Nürnberg, F.; Logan, B. G.; Alber, I.; Harres, K.; Roth, M.; Schollmeier, M.; Barth, W.*; Eickhoff, H.*; Hofmann, I.*; A. Friedman, A.; Grote, D. P.: **Capture and Control of Laser-Accelerated Proton Beams: Experiment and Simulation.** In: *23rd Particle Accelerator Conference, 4-8 May 2009, Vancouver, BC, Canada,* FR5RFP007p.

068 Parfenova, A. S.*; Franchetti, G.*: **Linear and Nonlinear Beam Optics Studies in the SIS18.** In: *23rd Particle Accelerator Conference, 4-8 May 2009, Vancouver, BC, Canada,* TH6PFP053p.

069 Peschke, C.; Jandewerth, U.; Nolden, F.; Petri, P.; Steck, F.: **Prototype Pick-up Module for CR Stochastic Cooling at FAIR.** In: *Workshop on Beam Cooling and Related Topics, 31 August-4 September 2009, Lanzhou, China,* THPMCP003p.

070 Peters, A.; Feldmeier, E.; Steiner, R.; Eickhoff, H.*; Knapp, T.*; Welsch, C. P.*; Schömers, C.: **Magnetic Field Control in Synchrotrons.** In: *23rd Particle Accelerator Conference, 4-8 May 2009, Vancouver, BC, Canada,* MO6PFP017p.

071 Plotnikov, A.*; Floch, E.*; Mustafin, E.*; Schubert, E.*; Seidl, T.*; Strasik, I.*; Smolyakov, A.: **Preparation of the Irradiation Test and Cave HHD of GSI Darmstadt.** In: *11th International Conference on Heavy Ion Accelerator Technology, 08-12 June 2009, Venezia, Italy,* A3Tp.

072 Pyka, N.*; Blell, U.*; Mühle, C.*; Saa Hernandez, A.*; Spiller, J. P.*; Stadlmann, J.*: **SIS100/300 Extraction System Design Beam Dynamics and Technological Challenges.** In: *23rd Particle Accelerator Conference, 4-8 May 2009, Vancouver, BC, Canada,* TU6RFP034p.

073 Rauch, U.*; Forck, P.*; Hülsmann, P.*; Kowina, P.*; Moritz, P.*: **Baseband Tune Measurements at GSI SIS-18 using Direct Digitized BPM Signals.** In: *9th European Workshop on Beam Diagnostics and Instrumentation for Particle Accelerators, 25-27 May, 2009, Basel, Switzerland,* TUPD16p.

074 Roy, B.J.: **In beam test of a DIRC Cherenkov radiator with SiPM.** In: *Proceedings of the Int. Symp. on Nucl. Phys., Vol.54,* 668p.

075 Roy, B.J.: **SiPM as photon counter for Cherenkov detector.** In: *Proceedings of the Int. Symp. on Nucl. Phys., Vol.54,* 666p.

076 Schädel, M.*; Türler, A.: **Ein Platz für Schwergewichte.** In: *Physik Journal* **8***(6)*, 35–40p.

077 Schmitt, L.: **The PANDA Detector at FAIR.** In: *Proceedings of the 18th Particles and Nuclei International Conference*,

078 Schwarz, C.: **The PANDA detector at FAIR.** In: *Hyperfine Interact. 194*, 107p.

079 Schwickert, M.*; Forck, P.*; Kowina, P.*; Giacomini, T.*; Reeg, H.*; Schlörit, A.*: **Beam Diagnostic Developments for FAIR.** In: *9th European Workshop on Beam Diagnostics and Instrumentation for Particle Accelerators, 25-27 May, 2009, Basel, Switzerland*, WEOA04p.

080 Serrano, J.; Alvarez, P.; Cattin, M.; Cota, E. G.; Lewis, J. H.; Oliveira Fernandes Moreira, P. M.; Wlostowski, T.; Bär, R.*; Fleck, T.*; Kreider, M.*; Prados, C.*; Rauch, S.*; J. Dedi, J.; Gaderer, G.; Loschmidt, P.: **The White Rabbit Project.** In: *12th International Conference on Accelerator and Large Experimental Physics Control Systems, October 12-16, 2009, Kobe, Japan*, TUC004p.

081 Sikler, G.; Gaertner, W.; Wessner, A.; Fischer, E. S.*; Floch, E.*; Krämer, D.*; Macavei, J.*; Schnizer, P.*; Schröder, C.*; Walter, F.*: **Fabrication of a Prototype of a Fast Cycling Superferric Dipole-Magnet.** In: *23rd Particle Accelerator Conference, 4-8 May 2009, Vancouver, BC, Canada*, MO6PFP043p.

082 Smirnov, A. V.; Ahmanova, E. V.; Bykovsky, V.; Kobets, A. G.; Meshkov, I. N.; Pivin, R.; Rudakov, A. Y.; Sidorin, A. O.; Yakovenko, S.; Dietrich, J.; Katayama, T.*.; Krestnikov, D. A.: **Application of Cooling Methods to NICA Project.** In: *Workshop on Beam Cooling and Related Topics, 31 August-4 September 2009, Lanzhou, China*, MOM2MCIO02p.

083 Smirnov, A. V.; Meshkov, I. N.; Pivin, R.; Sidorin, A. O.; Dimopoulou, C.*; Schreiber, G.*; Steck, F.*; Krestnikov, D. A.: **Particle Accumulation with a Barrier Bucket RF System.** In: *Workshop on Beam Cooling and Related Topics, 31 August-4 September 2009, Lanzhou, China*, TUM2MCIO02p.

084 Spiller, P. J.*; Bozyk, L. H. J.*; Puppel, P.*; Stadlmann, J.*: **Synchrotron Operation with Intermediate Charge State Heavy Ion Beams.** In: *23rd Particle Accelerator Conference, 4-8 May 2009, Vancouver, BC, Canada*, TU6PFP063p.

085 Steck, F.*;: **Status of the FAIR Project.** In: *Workshop on Beam Cooling and Related Topics, 31 August-4 September 2009, Lanzhou, China*, THM1MCIO01p.

086 Steck, M.*; Bär, R.*; Blell, U.*; Dimopoulou, C.*; Dolinskyy, A.*; Forck, P.*; Franzke, B.*; Gorda, O. E.*; Gostishchev, V.*; Jandewerth, U.*; Katayama, T.*; Klingbeil, H.*; Knie, K.*; Krämer, A.*; Laier, U.*; Leibrock, H.*; Litvinov, S. A.*; Mühle, C.*; Nolden, F.*; Peschke, C.*; Petri, P.*; Ramakers, H.*; Schurig, I.*; Schwickert, M.*; Welker, H.; Möhl, D.; Thorndahl, L.: **Advanced Design of the FAIR Storage Ring Complex.** In: *23rd Particle Accelerator Conference, 4-8 May 2009, Vancouver, BC, Canada*, FR1GRI03p.

087 Stockhorst, H.; Maier, R.; Prasuhn, D.; Stassen, R.; Katayama, T.*; Thorndahl, L.: **Compensation of Mean Energy Loss due to an Internal Target by Application of a Barrier Bucket and Stochastic Momentum Cooling at COSY.** In: *Workshop on Beam Cooling and Related Topics, 31 August-4 September 2009, Lanzhou, China*, TUM2MCIO01p.

088 Strasik, I.*; Mustafin, E.*; Floch, E.*; Seidl, T.*; Plotnikov, A.*; Schubert, E.*; Smolyakov, A.*: **Depth-Profiling of the Residual Activity Induced by High-energy Uranium Ions in Thin Stainless Steel Target.** In: *11th International Conference on Heavy Ion Accelerator Technology, 08-12 June 2009, Venezia, Italy*, A5TTp.

089 Tahir, N. A.*; Fortov, V. E.; Lomonosov, I.; Shutov, A.; Hoffmann, D. H. H.; R. Piriz, R.; R. Schmidt, R.: **Interaction of the Large Hadron Collider 7 TeV/c Proton Beam with a Solid Copper Target.** In: *23rd Particle Accelerator Conference, 4-8 May 2009, Vancouver, BC, Canada*, FR5REP036p.

090 Tahir, T. A.*; Deutsch, C.; Fortov, V. E.; Lomonosov, I.; Shutov, A.; Hoffmann, D. H. H.; Piriz, R.: **Studies of High Energy Density Matter Using Intense Ion Beams at FAIR at Darmstadt: The HEDgeHOB Collaboration.** In: *23rd Particle Accelerator Conference, 4-8 May 2009, Vancouver, BC, Canada*, TU6PFP038p.

091 Thieme, M.*; Panschow, W.*; Rauch, S.*; Zweig, M.*: **Single Board Computer for Device Control in the FAIR Accelerator Control System.** In: *12th International Conference on Accelerator and Large Experimental Physics Control Systems, October 12-16, 2009, Kobe, Japan*, TUP060p.

092 Vodel, W.; Geithner, R.; Neubert, R.; Seidel, P.; Peters, A.; M. Schwickert, M.*: **An LTS SQUID-Based High Precision Measurement Tool for Nuclear Physics.** In: *23rd Particle Accelerator Conference, 4-8 May 2009, Vancouver, BC, Canada*, TH5RFP046p.

093 Vossberg, M.; Mueller, N.; Schempp, A.; W. Barth, W.*; Dahl, L. A.*: **The New GSI HLI-RFQ for CW-Operation.** In: *23rd Particle Accelerator Conference, 4-8 May 2009, Vancouver, BC, Canada*, FR5REP064p.

094 Yaramyshev, S.*; Barth, W.*; Maier, M.*; Orzhekhovskaya, A.*; Schlitt, B.*; Vormann, H.*, R. Cee, R.; Peters, A.: **Upgrade of the HIT Injector LINAC-Frontend.** In: *11th International Conference on Heavy Ion Accelerator Technology, 08-12 June 2009, Venezia, Italy,*

TH9p.

095 Yin, X.*; Fu, S.; Peng, J.: **Space-Charge Driven Emittance Coupling in CSNS Linac.** In: *23rd Particle Accelerator Conference, 4-8 May 2009, Vancouver, BC, Canada*, TH5PFP024p.

WoS publications to the programme 'Large-scale facilities for research with photons, neutrons and ions' published in 2009

Compiled by K. Große, BuD

001 Adonin, A.*; Turtikov, V.; Ulrich, A.; Jacoby, J.; Hoffmann, D. H. H.*; Wieser, J.: **Intense heavy ion beams as a pumping source for short wavelength lasers.** *Laser and particle beams / Laser Part. Beams* **27**(3), 2009: 379–391. DOI:10.1017/s0263034609000494

002 Algora, A.; Jordan, D.; Estevez, E.; Tain, J. L.; Rubio, B.; Agramunt, J.; Perez-Cerdan, A. B.; Molina, F.; Caballero, L.; Nacher, E.; Bernabeu, J.; Gadea, A.; Krasznahorkay, A.; Hunyadi, M. D.; Gulyas, J.; Vitez, A.; Csatlos, M.; Csige, L.; Aysto, J.; Penttila, H.; Moore, I. D.; Eronen, T.; Jokinen, A.*GAST; Nieminen, A.; Hakala, J.; Karvonen, P.; Kankainen, A.; Saastamoinen, A.; Rissanen, J.; Kessler, T.; Weber, C.*; Ronkainen, J.; Rahaman, S.*; Elomaa, V.; Hager, U.; Rinta-Antila, S.; Sonoda, T.; Burkard, K.*; Hüller/Huller, W.*; Doring, J.; Gierlik, M.; Kirchner, R.*; Mukha, I.; Plettner, C.; Roeckl, E.* EMAIL; Cano-Ott, D.; Batist, L.*GAST; Valiente, J. J.; Gelletly, W.; Yoshida, T.; Nichols, A. L.; Sonzogni, A.; Perajarvi, K.: **Practical applications of the total absorption technique.** *Revista mexicana de fisica* **55**(2), 2009: 6–12. Also part of: HANU

003 Ali, M.; Mafe, S.; Ramirez, P.; Neumann, R.*; Ensinger, W.: **Logic Gates Using Nanofluidic Diodes Based on Conical Nanopores Functionalized with Polyprotic Acid Chains.** *Langmuir / Langmuir* **25**(20), 2009: 11993–11997. DOI:10.1021/la902792f

004 Ali, M.; Ramirez, P.; Mafe, S.; Neumann, R.*; Ensinger, W.: **A pH-Tunable Nanofluidic Diode with a Broad Range of Rectifying Properties.** *ACS Nano / ACS Nano* **3**(3), 2009: 603–608. DOI:10.1021/nn900039f

005 Amaro, P.; Santos, J. P.; Parente, F.; Surzhykov, A.*; Indelicato, P.: **Resonance effects on the two-photon emission from hydrogenic ions.** *Physical review A, Atomic, molecular, and optical physics / Phys. Rev. A* **79**(6), 2009: 062504. DOI:10.1103/physreva.79.062504

006 Apel, P. Y.; Blonskaya, I. V.; Cornelius, T. W.*; Neumann, R.*; Spohr, R.*; Schwartz, K.*; Skuratov, V. A.; Trautmann, C.*: **Influence of temperature during irradiation on the structure of latent track in polycarbonate.** *Radiation Measurements / Radiat. Meas.* **44**(9-10), 2009: 759–762, Sp. Iss. SI. DOI:10.1016/j.radmeas.2009.09.008

007 Artemyev, A. N.*; Shabaev, V. M.; Stöhlker, T.*; Surzhykov, A. S.*: **Negative-continuum dielectronic recombination into excited states of highly charged ions.** *Physical review A, Atomic, molecular, and optical physics / Phys. Rev. A* **79**(3), 2009: 032713. DOI:10.1103/physreva.79.032713

008 Banas, D.; Pajek, M.; Stöhlker, T.*; Beyer, H. F.*; Bohm, S.; Bosch, F.*; Brandau, C.*; Czarnota, M.; Chatterjee, S.*; Dousse, J. C.; Fritzsche, S.*; Gumberidze, A.*; Hagmann, S.*; Kozhuharov, C.*; Kumar, A.*; Liesen, D.*; Mokler, P. H.*; Muller, A.; Reuschl, R.*; Schmidt, E. W.; Sierpowski, D.; Spillmann, U.*; Surzhykov, A.*; Szlachetko, J.; Tashenov, S.*; Trotsenko, S.*; Verma, P.*; Warczak, A.: **The enhancement effect in K-shell radiative recombination of U^{92+} ions with cooling electrons.** *European Physical Journal, Special Topics / Eur. Phys. J.-Spec. Top.* **169**, 2009: 15–18. DOI:10.1140/epjst/e2009-00966-y

009 Barness, D.; Sinvani, M.; Shaulov, A.; Trautmann, C.*; Tamegai, T.; Yeshurun, Y.: **Magnetic flux oscillations in partially irradiated $Bi_2Sr_2CaCu_2O_{8+\delta}$ crystals.** *Journal of Applied Physics / J. Appl. Phys.* **105**(7), 2009: 07E310. DOI:10.1063/1.3068647

010 Basko, M. M.*; Maruhn, J.; Tauschwitz, An.: **An efficient cell-centered diffusion scheme for quadrilateral grids.** *Journal of Computational Physics / J. Comput. Phys.* **228**(6), 2009: 2175–2193. DOI:10.1016/j.jcp.2008.11.031

011 Baur, G.; Beigman, I. L.; Shevelko, V. P.; Tolstikhina, I. Y.; Stöhlker, T.*: **Ionization of highly charged relativistic ions by neutral atoms and ions.** *Physical review A, Atomic, molecular, and optical physics / Phys. Rev. A* **80**(1), 2009: 012713. DOI:10.1103/physreva.80.012713

012 Beck, D.*; Blaum, K.*; Bollen, G.; Delahaye, P.; George, S.*; Guenaut, C.; Herfurth, F.*; Herlert, A.; Lunney, D.; Schweikhard, L.; Yazidjian, C.: **Electric and magnetic field optimization procedure for Penning trap mass spectrometers.** *Nuclear instruments & methods in physics research, Section A, Accelerators, spectrometers, detectors and associated equipment / Nucl. Instrum. Methods Phys. Res. Sect. A-Accel. Spectrom. Dect. Assoc. Equip.* **598**(2), 2009: 635–641. DOI:10.1016/j.nima.2008.09.019

013 Bedrane, Z.; Inal, M. K.; Fritzsche, S.*: **Effect of directional energetic electrons on the density diagnostic of hot plasmas.** *Journal of physics B, Atomic, molecular and optical physics / J. Phys. B-At. Mol. Opt. Phys.* **42**(5), 2009: 055701. DOI:10.1088/0953-4075/42/5/055701

014 Beyer, H. F.*; Attia, D.; Banas, D.; Le Bigot, E. O.; Bosch, F.*; Dousse, J. C.; Förster, E.; Gumberidze, A.*; Hagmann, S.*; Hess, S.*; Hoszowska, J.; Indelicato, P.; Jagodzinski, P.; Kozhuharov, C.*; Krings, T.; Liesen, D.*; Ma, X.; Manil, B.; Mohos, I.; Pajek, M.; Protic, D.; Reuschl, R.*; Rzadkiewicz, J.; Simionovici, A.; Spillmann, U.*; Stachura, Z.; Stöhlker, T.*; Trassinelli, M.; Trotsenko, S.*; Warczak, A.; Wehrhan, O.; Ziegler, E.: **Crystal optics for hard-X-ray spectroscopy of highly charged ions.** *Spectro chimica acta, Part B, Atomic Spectroscopy / Spectroc. Acta Pt. B-Atom. Spectr.* **64**(8), 2009: 736–743, Sp. Iss. SI. DOI:10.1016/j.sab.2009.05.019

015 Bieron, J.; Gaigalas, G.; Gaidamauskas, E.; Fritzsche, S.*; Indelicato, P.; Jonsson, P.: **Multiconfiguration Dirac-Hartree-Fock calculations of the electric dipole moment of radium induced by the nuclear Schiff moment.** *Physical review A, Atomic, molecular, and optical physics / Phys. Rev. A* **80**(1), 2009: 012513. DOI:10.1103/physreva.80.012513

016 Blaum, K.; Kracke, H.; Kreim, S.; Mooser, A.; Mrozik, C.; Quint, W.*; Rodegheri, C. C.; Schabinger, B.; Sturm, S.; Ulmer, S.; Wagner, A.; Walz, J.; Werth, G.: **g-factor experiments on simple systems in Penning traps.** *Journal of physics B, Atomic, molecular and optical physics / J. Phys. B-At. Mol. Opt. Phys.* **42**(15), 2009: 154021. DOI:10.1088/0953-4075/42/15/154021

017 Bodewits, E.; Dang, H. M.; de Nijs, A. J.; Winters, D. F. A.*; Hoekstra, R.: **Atomic electron energy spectra of slow He^{2+} ions impinging on metallic surfaces.** *Nuclear instruments & methods in physics research, Section B, Beam interactions with materials and atoms / Nucl. Instrum. Methods Phys. Res. Sect. B-Beam Interact. Mater. Atoms* **267**(4), 2009: 594–597. DOI:10.1016/j.nimb.2008.11.043

018 Borowska, L.; Terenetsky, K.; Verbitsky, V.; Fritzsche, S.*: **Analytical potential for the elastic scattering of light halo nuclei below and close to the Coulomb barrier.** *Physical review C, Nuclear physics / Phys. Rev. C* **79**(4), 2009: 044605. DOI:10.1103/physrevc.79.044605 Also part of: HANU

019 Breitenfeldt, M.; Audi, G.; Beck, D.*; Blaum, K.; George, S.; Herfurth, F.*; Herlert, A.; Kellerbauer, A.; Kluge, H.-J.*; Kowalska, M.; Lunney, D.; Naimi, S.; Neidherr, D.; Schatz, H.; Schwarz, S.; Schweikhard, L.: **Penning trap mass measurements of $^{99-109}$Cd with the ISOLTRAP mass spectrometer, and implications for the rp process.** *Physical review C, Nuclear physics / Phys. Rev. C* **80**(3), 2009: 035805. DOI:10.1103/physrevc.80.035805

020 Chantler, C. T.; Laming, J. M.; Silver, J. D.; Dietrich, D. D.; Mokler, P. H.*; Finch, E. C.; Rosner, S. D.: **Hydrogenic Lamb shift in Ge^{31+} and the fine-structure Lamb shift.** *Physical review A, Atomic, molecular, and optical physics / Phys. Rev. A* **80**(2), 2009: 022508. DOI:10.1103/physreva.80.022508

021 Chen, L.*; Litvinov, Y. A.*; Plaß, W. R.*; Beckert, K.*; Beller, P.*; Bosch, F.*; Boutin, D.; Caceres, L.*; Cakirli, R. B.; Carroll, J. J.; Casten, R. F.; Chakrawarthy, R. S.; Cullen, D. M.; Cullen, I. J.; Franzke, B.*; Geissel, H.*; Gerl, J.*; Gorska, M.*; Jones, G. A.; Kishada, A.; Knöbel, R.*; Kozhuharov, C.*; Litvinov, S. A.*; Liu, Z.; Mandal, S.*; Montes, F.*; Münzenberg, G.*; Nolden, F.*; Ohtsubo, T.; Patyk, Z.; Podolyak, Z.; Propri, R.; Rigby, S.; Saito, N.*; Saito, T.*; Scheidenberger, C.*; Shindo, M.; Steck, M.*; Ugorowski, P.; Walker, P. M.; Williams, S.; Weick, H.*; Winkler, M.*; Wollersheim, H.-J.*; Yamaguchi, T.: **Schottky Mass Measurement of the ^{208}Hg Isotope: Implication for the Proton-Neutron Interaction Strength around Doubly Magic ^{208}Pb.** *Physical review letters / Phys. Rev. Lett.* **102**(12), 2009: 122503. DOI:10.1103/physrevlett.102.122503

022 Crespillo, M. L.; Otto, M.; Munoz-Martin, A.; Olivares, J.; Agullo-Lopez, F.; Seibt, M.; Toulemonde, M.; Trautmann, C.*: **Optimization of nanopores obtained by chemical etching on swift-ion irradiated lithium niobate.** *Nuclear instruments & methods in physics research, Section B, Beam interactions with materials and atoms / Nucl. Instrum. Methods Phys. Res. Sect. B-Beam Interact. Mater. Atoms* **267**(6), 2009: 1035–1038. DOI:10.1016/j.nimb.2009.02.028

023 Cubaynes, D.; Guilbaud, S.; Wuilleumier, F. J.; Meyer, M.; Heinecke, E.; Riek, K.; Zimmermann, P.; Yalcinkaya, M.; Fritzsche, S.*; Strakhova, S. I.; Grum-Grzhimailo, A. N.: **Photoionization from the 2p subshell of the laser-excited aligned $Na2p^6 3p\ ^2P_{3/2}$ state.** *Physical review A, Atomic, molecular, and optical physics / Phys. Rev. A* **80**(2), 2009: 023410. DOI:10.1103/physreva.80.023410

024 Duan, J. L.; Cornelius, T. W.*; Liu, J.; Karim, S.; Yao, H. J.; Picht, O.*; Rauber, M.*; Müller, S.*; Neumann, R.*: **Surface Plasmon Resonances of Cu Nanowire Arrays.** *Journal of Physical Chemistry C / J. Phys. Chem. C* **113**(31), 2009: 13583–13587. DOI:10.1021/jp902894r

025 Duan, J.; Liu, J.; Cornelius, T. W.*; Yao, H.; Mo, D.; Chen, Y.; Zhang, L.; Sun, Y.; Hou, M.; Trautmann, C.*; Neumann, R.*: **Magnetic and optical properties of cobalt nanowires fabricated in polycarbonate ion-track templates.** *Nuclear instruments & methods in physics research, Section B, Beam interactions with materials and atoms / Nucl. Instrum. Methods Phys. Res. Sect. B-Beam Interact. Mater. Atoms* **267**(16), 2009: 2567–2570, Sp. Iss. SI. DOI:10.1016/j.nimb.2009.05.015

026 Duan, J.; Liu, J.; Cornelius, T. W.*; Yao, H.; Mo, D.; Chen, Y.; Zhang, L.; Sun, Y.; Hou, M.; Trautmann, C.*; Neumann, R.*: **Magnetic and optical properties of cobalt nanowires fabricated in polycarbonate ion-track templates.** *Nuclear instruments & methods in physics research, Section B, Beam interactions with materials and atoms* **267**(16), 2009: 2567–2570, Sp. Iss. SI. DOI:10.1016/j.nimb.2009.05.015

027 Eichhorn, C.; Fritzsche, S.*; Löhle, S.; Knapp, A.; Auweter-Kurtz, M.: **Time-resolved fluorescence spectroscopy of two-photon laser-excited 8p, 9p, 5f, and 6f levels in neutral xenon.** *Physical Review E / Phys. Rev. E* **80**(2), Part 2, 2009: 026401. DOI:10.1103/physreve.80.026401

028 Eitel, G.; Block, M.*; Czasch, A.; Dworschak, M.; George, S.; Jagutzki, O.; Ketelaer, J.; Ketter, J.; Nagy, S.*; Rodriguez, D.; Smorra, C.; Blaum, K.: **Position-sensitive ion detection in precision Penning trap mass spectrometry.** *Nuclear instruments & methods in physics research, Section A, Accelerators, spectrometers, detectors and associated equipment / Nucl. Instrum. Methods Phys. Res. Sect. A-Accel. Spectrom. Dect. Assoc. Equip.* **606**(3), 2009: 475–483. DOI:10.1016/j.nima.2009.04.046

029 Ekström, A.; Cederkäll, J.; DiJulio, D. D.; Fahlander, C.; Hjorth-Jensen, M.; Blazhev, A.*; Bruyneel, B.; Butler, P. A.; Davinson, T.; Eberth, J.; Fransen, C.; Geibel, K.; Hess, H.; Ivanov, O.; Iwanicki, J.; Kester, O.*; Kownacki, J.; Köster, U.; Marsh, B. A.; Reiter, P.; Scheck, M.; Siebeck, B.; Siem, S.; Stefanescu, I.; Toft, H. K.; Tveten, G. M.; Van de Walle, J.; Voulot, D.; Warr, N.; Weisshaar, D.; Wenander, F.; Wrzosek, K.; Zielinska, M.: **Electric quadrupole moments of the 2^1_+ states in $^{100,102,104}Cd$.** *Physical review C, Nuclear physics / Phys. Rev. C* **80**(5), 2009: 054302. DOI:10.1103/physrevc.80.054302

030 Ekström, A.; Cederkäll, J.; DiJulio, D. D.; Fahlander, C.; Hjorth-Jensen, M.; Blazhev, A.; Bruyneel, B.; Butler, P. A.; Davinson, T.; Eberth, J.; Fransen, C.; Geibel, K.; Hess, H.; Ivanov, O.; Iwanicki, J.; Kester, O.*; Kownacki, J.; Köster, U.; Marsh, B. A.; Reiter, P.; Scheck, M.; Siebeck, B.; Siem, S.; Stefanescu, I.; Toft, H. K.; Tveten, G. M.; Van de Walle, J.; Voulot, D.; Warr, N.; Weisshaar, D.; Wenander, F.; Wrzosek, K.; Zielinska, M.: **Electric quadrupole moments of the 2^+_1 states in ^{100}Cd-100, ^{102}Cd-102,Cd-104.** *Physical review C, Nuclear physics* **80**(5), 2009: 054302. DOI:10.1103/physrevc.80.054302

031 Elomaa, V. V.; Vorobjev, G. K.*; Kankainen, A.; Batist, L.; Eliseev, S.*; Eronen, T.; Hakala, J.; Jokinen, A.; Moore, I. D.; Novikov, Y. N.*; Penttila, H.; Popov, A.; Rahaman, S.; Rissanen, J.; Saastamoinen, A.; Schatz, H.*; Seliverstov, D. M.; Weber, C.; Äystö, J.: **Quenching of the SnSbTe Cycle in the rp Process.** *Physical review letters / Phys. Rev. Lett.* **102**(25), 2009: 252501. DOI:10.1103/physrevlett.102.252501 Also part of: HANU

032 Engel, M.; Stuhn, B.; Schneider, J. J.; Cornelius, T.*; Naumann, M.: **Small-angle X-ray scattering (SAXS) off parallel, cylindrical, well-defined nanopores: from random pore distribution to highly ordered samples.** *Applied Physics A: Materials Science and Processing / Appl. Phys. A-Mater. Sci. Process.* **97**(1), 2009: 99–108. DOI:10.1007/s00339-009-5346-4

033 Faestermann, T.; Bosch, F.*; Hertenberger, R.; Maier, L.; Krücken, R.; Rugel, G.: **Could the GSI decay rate oscillations be observed in a standard electron capture decay experiment?.** *Physics letters B / Phys. Lett. B* **672**(3), 2009: 227–229. DOI:10.1016/j.physletb.2009.01.031

034 Filinov, V. S.; Bonitz, M.; Ivanov, Y. B.*; Skokov, V. V.*; Levashov, P. R.; Fortov, V. E.: **Equation of State of Strongly Coupled Quark-Gluon Plasma - Path Integral Monte Carlo Results.** *Contributions to Plasma Physics / Contrib. Plasma Phys.* **49**(7-8), 2009: 536–543, Sp. Iss. SI. DOI:10.1002/ctpp.200910053

035 Flanagan, K. T.; Vingerhoets, P.; Avgoulea, M.; Billowes, J.; Bissell, M. L.; Blaum, K*; Cheal, B.; De Rydt, M.; Fedosseev, V. N.; Forest, D. H.; Geppert, C.; Köster, U.; Kowalska, M.; Krämer, J.; Kratz, K. L.; Krieger, A.; Mane, E.; Marsh, B. A.; Materna, T.; Mathieu, L.; Molkanov, P. L.; Neugart, R.; Neyens, G.; Nörtershäuser W.*; Seliverstov, M. D.; Serot, O.; Schug, M.; Sjoedin, M. A.; Stone, J. R.; Stone, N. J.; Stroke, H. H.; Tungate, G.; Yordanov, D. T.; Volkov, Y. M.: **Nuclear Spins and Magnetic Moments of ^{71,72,73}Cu: Inversion of $\pi 2p_{3/2}$ and $\pi 1f_{5/2}$ Levels in ^{75}Cu.** *Physical review letters / Phys. Rev. Lett.* **103**(14), 2009: 142501. DOI:10.1103/physrevlett.103.142501 Also part of: HANU

036 Fritzsche, S.*: **Maple procedures for the coupling of angular momenta. An up-date of the RACAH module.** *Computer Physics Communications / Comput. Phys. Commun.* **180**(10), 2009: 2021–2023. DOI:10.1016/j.cpc.2009.06.018

037 Fritzsche, S.*; Grum-Grzhimailo, A. N.; Gryzlova, E. V.; Kabachnik, N. M.: **Sequential two-photon double ionization of Kr atoms.** *Journal of physics B, Atomic, molecular and optical physics / J. Phys. B-At. Mol. Opt. Phys.* **42**(14), 2009: 145602. DOI:10.1088/0953-4075/42/14/145602

038 Fritzsche, S.*; Kabachnik, N. M.*; Surzhykov, A.*; Stöhlker, T.*: **Breit interaction effects on the Kα angular distribution following the dielectronic recombination of high-Z ions.** *Nuclear instruments & methods in physics research, Section B, Beam interactions with materials and atoms / Nucl. Instrum. Methods Phys. Res. Sect. B-Beam Interact. Mater. Atoms* **267**(2), 2009: 257–259. DOI:10.1016/j.nimb.2008.10.016

039 Fritzsche, S.*; Surzhykov, A.*; Stöhlker, T.*: **Dominance of the Breit Interaction in the X-Ray Emission of Highly Charged Ions Following Dielectronic Recombination.** *Physical review letters / Phys. Rev. Lett.* **103**(11), 2009: 113001. DOI:10.1103/physrevlett.103.113001

040 Gonta, D.; Fritzsche, S.*: **Control of entanglement and two-qubit quantum gates with atoms crossing a detuned optical cavity.** *Journal of physics B, Atomic, molecular and optical physics / J. Phys. B-At. Mol. Opt. Phys.* **42**(14), 2009: 145508. DOI:10.1088/0953-4075/42/14/145508

041 Gonta, D.; Radtke, T.; Fritzsche, S.*: **Generation of two-dimensional cluster states by using high-finesse bimodal cavities.** *Physical review A, Atomic, molecular, and optical physics / Phys. Rev. A* **79**(6), 2009: 062319. DOI:10.1103/physreva.79.062319

042 Grinenko, A.; Gericke, D. O.; Varentsov, D.*: **Ramp wave loading experiments driven by heavy ion beams: A feasibility study.** *Laser and particle beams / Laser Part. Beams* **27**(4), 2009: 595–600. DOI:10.1017/s0263034609990310

043 Gumberidze, A.; Stöhlker, T.*; Beyer, H. F.*; Bosch, F.*; Bräuning-Demian, A.*; Hagmann, S.*; Kozhuharov, C.*; Kühl, T.*; Mann, R.*; Indelicato, P.; Quint, W.*; Schuch, R.; Warczak, A.: **X-ray spectroscopy of highly-charged heavy ions at FAIR.** *Nuclear instruments & methods in physics research, Section B, Beam interactions with materials and atoms / Nucl. Instrum. Methods Phys. Res. Sect. B-Beam Interact. Mater. Atoms* **267**(2), 2009: 248–250. DOI:10.1016/j.nimb.2008.10.079

044 Herfurth, F.: **Precise nuclear physics measurements with ion traps.** *International journal of modern physics E, Nuclear physics / Int. J. Mod. Phys. E-Nucl. Phys.* **18**(2), 2009: 392–404.

045 Hoffmann, D. H. H.; Blazevic, A.; Tahir, N. A.; Udrea, S.; Varentsov, D.; Zhao, Y.: **High energy density physics with intense particle and laser beams.** *International journal of modern physics E, Nuclear physics / Int. J. Mod. Phys. E-Nucl. Phys.* **18**(2), 2009: 381–391. URL

046 Hoffmann, D. H. H.; Fortov, V. E.; Kuster, M.; Mintsev, V.; Sharkov, B. Y.; Tahir, N. A.*; Udrea, S.; Varentsov, D.; Weyrich, K.*: **High energy density physics generated by intense heavy ion beams.** *Astrophysics and Space Science / Astrophys. Space Sci.* **322**(1-4), 2009: 167–177. DOI:10.1007/s10509-009-0001-2

047 Kaiser, C.; Weiss, G.; Cornelius, T. W.*; Toimil-Molares, M. E.*; Neumann, R.*: **Low temperature magnetoresistance measurements on bismuth nanowire arrays.** *Journal of physics Condensed matter / J. Phys.-Condes. Matter* **21**(20), 2009: 205301. DOI:10.1088/0953-8984/21/20/205301

048 Ketelaer, J.; Blaum, K.; Block, M.*; Eberhardt, K.; Eibach, M.; Ferrer, R.; George, S.; Herfurth, F.*; Ketter, J.; Nagy, S.; Repp, J.; Schweikhard, L.; Smorra, C.; Sturm, S.; Ulmer, S.: **Recent developments in ion detection techniques for Penning trap mass spectrometry at TRIGA-TRAP.** *The European physical journal A, Hadrons and nuclei / Eur. Phys. J. A* **42**(3), 2009: 311–317. DOI:10.1140/epja/i2008-10711-6

049 Koresheva, E. R.; Aleksandrova, I. V.; Koshelev, E. L.; Nikitenko, A. I.; Timasheva, T. P.; Tolokonnikov, S. M.; Belolipetskiy, A. A.; Kapralov, V. G.; Sergeev, V. T.; Blazevic, A.*; Weyrich, K.*; Varentsov, D.*; Tahir, N. A.*; Udrea, S.; Hoffmann, D. H. H.: **A study on fabrication, manipulation and survival of cryogenic targets required for the experiments at the Facility for Antiproton and Ion Research: FAIR.** *Laser and particle beams / Laser Part. Beams* **27**(2), 2009: 255–272. DOI:10.1017/s0263034609000342

050 Kowalska, M.; Naimi, S.; Agramunt, J.; Algora, A.; Audi, G.; Beck, D.*; Blank, B.; Blaum, K.; Böhm, C.; Breitenfeldt, M.; Estevez, E.; Fraile, L. M.; George, S.; Herfurth, F.*; Herlert, A.; Kellerbauer, A.; Lunney, D.; Minaya-Ramirez, E.; Neidherr, D.; Olaizola, B.; Riisager, K.; Rosenbusch, M.; Rubio, B.; Schwarz, S.; Schweikhard, L.; Warring, U.: **Preparing a journey to the east of ^{208}Pb with ISOLTRAP: Isobaric purification at A=209 and new masses for $^{211-213}$Fr and ^{211}Ra.** *The European physical journal A, Hadrons and nuclei / Eur. Phys. J. A* **42**(3), 2009: 351–359. DOI:10.1140/epja/i2009-10835-1

051 Kozlova, E.; Strasik, I.; Fertman, A.; Mustafin, E.; Radon, T.; Hinca, R.; Pavlovic, M.; Fehrenbacher, G.; Geissel, H.*; Golubev, A.; Iwase, H.; Schardt, D.: **Benchmark test of the fluka Monte Carlo code for residual production with 500 and 950 MeV/u Uranium beams on Copper and stainless steel targets.** *Nuclear Technology* **168**(3), 2009: 747–751, Sp. Iss. SI.

052 Kramer, J.; Blaum, K.*; De Rydt, M.; Flanagan, K. T.; Geppert, C.*; Kowalska, M.; Lievens, P.; Neugart, R.; Neyens, G.; Nörtershäuser, W.*; Stroke, H. H.; Vingerhoets, P.; Yordanov, D. T.: **Nuclear ground-state spin and magnetic moment of ^{21}Mg.** *Physics letters B / Phys. Lett. B* **678**(5), 2009: 465–469. DOI:10.1016/j.physletb.2009.06.063

053 Kühnel, M.; Petridis, N.; Winters, D. F. A.*; Popp, U.*; Dörner, R.; Stöhlker, T.*; Grisenti, R. E.*: **Low-Z internal target from a cryogenically cooled liquid microjet source.** *Nuclear instruments & methods in physics research, Section A, Accelerators, spectrometers, detectors and associated equipment / Nucl. Instrum. Methods Phys. Res. Sect. A-Accel. Spectrom. Dect. Assoc. Equip.* **602**(2), 2009: 311–314. DOI:10.1016/j.nima.2008.12.212

054 Kumar, A.*; Trotsenko, S.*; Volotka, A. V.; Banas, D.; Beyer, H. F.*; Bräuning, H.*; Gumberidze, A.*; Hag-

mann, S.*; Hess, S.*; Kozhuharov, C.*; Reuschl, R.*; Spillmann, U.*; Trassinelli, M.*; Weber, G.*; Stöhlker, T.*: **Spectral shape of the 2E1 decay from 2s state in He-like tin.** *European Physical Journal, Special Topics / Eur. Phys. J.-Spec. Top.* **169**, 2009: 19–22. DOI:10.1140/epjst/e2009-00967-x

055 Kurka, M.; Rudenko, A.; Foucar, L.; Kühnel, K. U.; Jiang, Y. H.; Ergler, T.; Havermeier, T.; Smolarski, M.; Schössler, S.; Cole, K.; Schöffler, M.; Dörner, R.; Gensch, M.; Düsterer, S.; Treusch, R.; Fritzsche, S.*; Grum-Grzhimailo, A. N.; Gryzlova, E. V.; Kabachnik, N. M.; Schröter, C. D.; Moshammer, R.; Ullrich, J.: **Two-photon double ionization of Ne by free-electron laser radiation: a kinematically complete experiment.** *Journal of physics B, Atomic, molecular and optical physics / J. Phys. B-At. Mol. Opt. Phys.* **42**(14), 2009: 141002. DOI:10.1088/0953-4075/42/14/141002

056 Kwiatkowski, A. A.; Barquest, B. R.; Bollen, G.; Campbell, C. M.; Lincoln, D. L.; Morrissey, D. J.; Pang, G. K.; Prinke, A. M.; Savory, J.; Schwarz, S.; Folden, C. M.; Melconian, D.; Sjue, S. K. L.; Block, M.*: **Precision test of the isobaric multiplet mass equation for the A=32, T=2 quintet.** *Physical review C, Nuclear physics / Phys. Rev. C* **80**(5), 2009: 051302. DOI:10.1103/physrevc.80.051302

057 Kwiatkowski, A. A.; Barquest, B. R.; Bollen, G.; Campbell, C. M.; Lincoln, D. L.; Morrissey, D. J.; Pang, G. K.; Prinke, A. M.; Savory, J.; Schwarz, S.; Folden, C. M.; Melconian, D.; Sjue, S. K. L.; Block, M.*: **Precision test of the isobaric multiplet mass equation for the A=32, T=2 quintet.** *Physical review C, Nuclear physics* **80**(5), 2009: 051302. DOI:10.1103/physrevc.80.051302

058 Lang, M.; Lian, J.; Zhang, J. M.; Zhang, F. X.; Weber, W. J.; Trautmann, C.*; Ewing, R. C.: **Single-ion tracks in $Gd_2Zr_{2-x}Ti_xO_7$ pyrochlores irradiated with swift heavy ions.** *Physical review: B, Condensed matter and materials physics / Phys. Rev. B* **79**(22), 2009: 224105. DOI:10.1103/physrevb.79.224105

059 Lang, M.; Zhang, F. X.; Ewing, R. C.; Lian, J.; Trautmann, C.; Wang, Z. W.: **Structural modifications of $Gd_2Zr_{2-x}TixO_7$ pyrochlore induced by swift heavy ions: Disordering and amorphization.** *Journal of Materials Research / J. Mater. Res.* **24**(4), 2009: 1322–1334. DOI:10.1557/jmr.2009.0151

060 Lang, M.; Zhang, F. X.; Lian, J.; Trautmann, C.; Neumann, R.; Ewing, R. C.: **Combined high pressure and heavy-ion irradiation: a novel approach.** *Journal of Synchrotron Radiation / J. Synchrot. Radiat.* **16**, Part 6, 2009: 773–777. DOI:10.1107/s0909049509034384

061 Lang, M.; Zhang, F. X.; Zhang, J. M.; Wang, J. W.; Schuster, B.*; Trautmann, C.*; Neumann, R.*; Becker, U.; Ewing, R. C.: **Nanoscale manipulation of the properties of solids at high pressure with relativistic heavy ions.** *Nature Materials / Nat. Mater.* **8**(10), 2009: 793–797. DOI:10.1038/nmat2528

062 Lineva, N.*; Kozhuharov, C.*; Hagmann, S.*; Krämer, M.*; Kraft, G.*: **Low-energy electrons emitted in collisions of heavy ions with solid state targets.** *Nuclear instruments & methods in physics research, Section B, Beam interactions with materials and atoms / Nucl. Instrum. Methods Phys. Res. Sect. B-Beam Interact. Mater. Atoms* **267**(6), 2009: 891–895. DOI:10.1016/j.nimb.2009.02.038 Also part of: Cancer

063 Mahgoub, M.; Krücken, R.; Faestermann, T.; Bergmaier, A.; Bucurescu, D.; Hertenberger, R.; Kröll, T.; Wirth, H.-F.; Lisetskiy, A. F.*: **Role of cross-shell excitations in the reaction ^{54}Fe ($\vec{d}$, p)^{55}Fe.** *The European physical journal A, Hadrons and nuclei / Eur. Phys. J. A* **40**(1), 2009: 35–43. DOI:10.1140/epja/i2008-10727-x

064 Maiorova, A. V.; Pavlova, O. I.; Shabaev, V. M.; Kozhuharov, C.*; Plunien, G.; Stöhlker, T.*: **Parity nonconservation in the radiative recombination of electrons with heavy hydrogen-like ions.** *Journal of physics B, Atomic, molecular and optical physics / J. Phys. B-At. Mol. Opt. Phys.* **42**(20), 2009: 205002. DOI:10.1088/0953-4075/42/20/205002

065 Maiorova, A. V.; Surzhykov, A.*; Tashenov, S.; Shabaev, V. M.; Fritzsche, S.*; Plunien, G.; Stöhlker, T.*: **Polarization studies on the two-step radiative recombination of highly charged, heavy ions.** *Journal of physics B, Atomic, molecular and optical physics / J. Phys. B-At. Mol. Opt. Phys.* **42**(12), 2009: 125003. DOI:10.1088/0953-4075/42/12/125003

066 Maloy, S. A.; Trautmann, C.*; Was, G. S.: **Preface; Proceedings of the Symposium on Particle Beam Induced Radiation Effects in Materials Preface.** *Journal of Nuclear Materials / J. Nucl. Mater.* **389**(2), 2009: VII–VII. DOI:10.1016/j.jnucmat.2009.02.020

067 Manika, I.; Maniks, J.; Toulemonde, M.; Schwartz, K.*: **Dislocation mobility study of heavy ion induced track damage in LiF crystals.** *Nuclear instruments & methods in physics research, Section B, Beam interactions with materials and atoms / Nucl. Instrum. Methods Phys. Res. Sect. B-Beam Interact. Mater. Atoms* **267**(6), 2009: 949–952. DOI:10.1016/j.nimb.2009.02.019

068 Matveev, V. I.; Ryabchenko, S. V.; Matrasulov, D. U.; Rakhimov, K. Y.; Fritzsche, S.*; Stöhlker, T.*: **Electron loss of fast heavy projectiles in collision with neutral targets.** *Physical review A, Atomic, molecular, and optical physics / Phys. Rev. A* **79**(4), Part A, 2009: 042710. DOI:10.1103/physreva.79.042710

069 Moore, J. D.; Cohen, L. F.; Yeshurun, Y.; Caplin, A. D.; Morrison, K.; Yates, K. A.; McGilvery, C. M.;

Perkins, J. M.; McComb, D. W.; Trautmann, C.*; Ren, Z. A.; Yang, J.*; Lu, W.; Dong, X. L.; Zhao, Z. X.: **The effect of columnar defects on the pinning properties of $NdFeAsO_{0.85}$ conglomerate particles.** *Superconductor Science and Technology* **22**(12), 2009: 125023. DOI:10.1088/0953-2048/22/12/125023

070 Moore, J. D.; Cohen, L. F.; Yeshurun, Y.; Caplin, A. D.; Morrison, K.; Yates, K. A.; McGilvery, C. M.; Perkins, J. M.; McComb, D. W.; Trautmann, C.*; Ren, Z. A.; Yang, J.; Lu, W.; Dong, X. L.; Zhao, Z. X.: **The effect of columnar defects on the pinning properties of $NdFeAsO_{0.85}$ conglomerate particles.** *Superconductor Science and Technology / Supercond. Sci. Technol.* **22**(12), 2009: 125023. DOI:10.1088/0953-2048/22/12/125023

071 Mustafin, E.*; Seidl, T.*; Plotnikov, A.*; Strasik, I.*; Pavlovic, M.; Miglierini, M.; Stancek, S.; Fertman, A.; Lancok, A.: **Ion irradiation studies of construction materials for high-power accelerators.** *Radiation Effects and Defects in Solids / Radiat. Eff. Defects Solids* **164**(7-8), 2009: 460–469. DOI:10.1080/10420150902949894 Also part of: HANU:Accelerator

072 Nörtershäuser, W.*; Tiedemann, D.; Zakova, M.; Andjelkovic, Z.; Blaum, K.; Bissell, M. L.; Cazan, R.; Drake, G. W. F.; Geppert, C.*; Kowalska, M.; Kramer, J.; Krieger, A.; Neugart, R.; Sanchez, R.*; Schmidt-Kaler, F.; Yan, Z. C.; Yordanov, D. T.; Zimmermann, C.: **Nuclear Charge Radii of ^{7,9,10}Be and the One-Neutron Halo Nucleus ^{11}Be.** *Physical review letters / Phys. Rev. Lett.* **102**(6), 2009: 062503. DOI:10.1103/physrevlett.102.062503

073 Najjari, B.; Voitkiv, A. B.; Artemyev, A.*; Surzhykov, A.*: **Simultaneous electron capture and bound-free pair production in relativistic collisions of heavy nuclei with atoms.** *Physical review A, Atomic, molecular, and optical physics / Phys. Rev. A* **80**(1), 2009: 012701. DOI:10.1103/physreva.80.012701

074 Naumova, N.; Schlegel, T.*; Tikhonchuk, V. T.; Labaune, C.; Sokolov, I. V.; Mourou, G.: **Hole Boring in a DT Pellet and Fast-Ion Ignition with Ultraintense Laser Pulses.** *Physical review letters / Phys. Rev. Lett.* **102**(2), 2009: 025002. DOI:10.1103/physrevlett.102.025002

075 Naumova, N.; Schlegel, T.*; Tikhonchuk, V. T.; Labaune, C.; Sokolov, I. V.; Mourou, G.: **Ponderomotive ion acceleration in dense plasmas at super-high laser intensities.** *The European physical journal: D, Atomic, molecular and optical physics / Eur. Phys. J. D* **55**(2), 2009: 393–398. DOI:10.1140/epjd/e2009-00250-2

076 Navitski, A.; Müller, G.; Sakharuk, V.; Cornelius, T. W.*; Trautmann, C.*; Karim, S.: **Efficient field emission from structured gold nanowire cathodes.** *European Physical Journal Applied Physics / Eur. Phys. J.-Appl. Phys* **48**(3), 2009: 30502. DOI:10.1051/epjap/2009167

077 Navitski, A.; Müller, G.; Sakharuk, V.; Cornelius, T. W.*; Trautmann, C.*; Karim, S.: **Efficient field emission from structured gold nanowire cathodes.** *European Physical Journal Applied Physics* **48**(3), 2009: 30502. DOI:10.1051/epjap/2009167

078 Neidherr, D.; Audi, G.; Beck, D.*; Blaum, K.; Böhm, C.; Breitenfeldt, M.; Cakirli, R. B.; Casten, R. F.; George, S.; Herfurth, F.*; Herlert, A.; Kellerbauer, A.; Kowalska, M.; Lunney, D.; Minaya-Ramirez, E.; Naimi, S.; Noah, E.; Penescu, L.; Rosenbusch, M.; Schwarz, S.; Schweikhard, L.; Stora, T.: **Discovery of ^{229}Rn and the Structure of the Heaviest Rn and Ra Isotopes from Penning-Trap Mass Measurements.** *Physical review letters / Phys. Rev. Lett.* **102**(11), 2009: 112501. DOI:10.1103/physrevlett.102.112501

079 Neidherr, D.; Cakirli, R. B.; Audi, G.; Beck, D.*; Blaum, K.; Böhm, C.; Breitenfeldt, M.; Casten, R. F.; George, S.; Herfurth, F.*; Herlert, A.; Kellerbauer, A.; Kowalska, M.; Lunney, D.; Minaya-Ramirez, E.; Naimi, S.; Rosenbusch, M.; Schwarz, S.; Schweikhard, L.: **High-precision Penning-trap mass measurements of heavy xenon isotopes for nuclear structure studies.** *Physical review C, Nuclear physics / Phys. Rev. C* **80**(4), 2009: 044323. DOI:10.1103/physrevc.80.044323

080 Nix, A.-K.; Gehrke, H.-G.; Krauser, J.; Trautmann, C.*; Weidinger, A.; Hofsäss, H.: **Track-etched nanopores in spin-coated polycarbonate films applied as sputtering mask.** *Nuclear instruments & methods in physics research, Section B, Beam interactions with materials and atoms / Nucl. Instrum. Methods Phys. Res. Sect. B-Beam Interact. Mater. Atoms* **267**(6), 2009: 1032–1034. DOI:10.1016/j.nimb.2009.02.029

081 Novotny, C.; Bernhardt, B.; Bing, D.; Ewald, G.*; Geppert, C.; Gwinner, G.; Huber, G.; Karpuk, S.; Kluge, H. J.; Kühl, T.; Nörtershäuser, W.; Reinhardt, S.; Saathoff, G.; Schwalm, D.; Stöhlker, T.; Wolf, A.: **Towards a precision test of time dilation at high velocity.** *Canadian Journal of Physics / Can. J. Phys.* **87**(7), 2009: 749–756. DOI:10.1139/p08-149

082 Novotny, C.; Huber, G.; Karpuk, S.; Reinhardt, S.; Bing, D.; Schwalm, D.; Wolf, A.*; Bernhardt, B.; Hänsch, T. W.; Holzwarth, R.; Saathoff, G.; Udem, T.; Nörtershäuser, W.*; Ewald, G.*; Geppert, C.*; Kühl, T.*; Stöhlker, T.*; Gwinner, G.: **Sub-Doppler laser spectroscopy on relativistic beams and tests of Lorentz invariance.** *Physical review A, Atomic, molecular, and optical physics / Phys. Rev. A* **80**(2), 2009: 022107. DOI:10.1103/physreva.80.022107

083 Nürnberg, F.; Schollmeier, M.*; Brambrink, E.; Blazevic, A.*; Carroll, D. C.; Flippo, K.; Gautier, D. C.; Geissel, M.; Harres, K.; Hegelich, B. M.; Lundh, O.; Markey, K.; McKenna, P.; Neely, D.; Schreiber, J.; Roth, M.: **Radiochromic film imaging spectroscopy of laser-**

accelerated proton beams. *Review of scientific instruments / Rev. Sci. Instrum.* **80**(3), 2009: 033301. DOI:10.1063/1.3086424

084 Olivares, J.; Crespillo, M. L.; Caballero-Calero, O.; Ynsa, M. D.; Garcia-Cabanes, A.; Toulemonde, M.; Trautmann, C.*; Agullo-Lopez, F.: **Thick optical waveguides in lithium niobate induced by swift heavy ions ($\sim$ to 10 MeV/amu) at ultralow fluences.** *Optics Express / Opt. Express* **17**(26), 2009: 24175–24182. URL OPEN ACCESS.

085 Orban, I.; Altun, Z.; Källberg, A.; Simonsson, A.; Andler, G.; Paal, A.; Blom, M.; Lofgren, P.; Trotsenko, S.*; Bohm, S.; Schuch, R.: **Experimental dielectronic recombination rate coefficients for Na-like S VI and Na-like Ar VIII.** *Astronomy & astrophysics / Astron. Astrophys.* **498**(3), 2009: 909–914. DOI:10.1051/0004-6361/200911799

086 Piriz, A. R.; Cela, J. J. L.; Tahir, N. A.*: **Linear analysis of incompressible Rayleigh-Taylor instability in solids.** *Physical Review E / Phys. Rev. E* **80**(4), Part 2, 2009: 046305. DOI:10.1103/physreve.80.046305

087 Piriz, A. R.; Cela, J. J. L.; Tahir, N. A.*: **Rayleigh-Taylor instability in elastic-plastic solids.** *Journal of Applied Physics / J. Appl. Phys.* **105**(11), 2009: 116101. DOI:10.1063/1.3139267

088 Piriz, A. R.; Cela, J. J. L.; Tahir, N. A.*: **Richtmyer-Meshkov instability as a tool for evaluating material strength under extreme conditions.** *Nuclear instruments & methods in physics research, Section A, Accelerators, spectrometers, detectors and associated equipment / Nucl. Instrum. Methods Phys. Res. Sect. A-Accel. Spectrom. Dect. Assoc. Equip.* **606**(1-2), 2009: 139–141. DOI:10.1016/j.nima.2009.03.094

089 Piriz, S. A.; Piriz, A. R.; Tahir, N. A.*: **Rayleigh-Taylor instability in ion beam driven ablation fronts.** *Physics of plasmas / Phys. Plasmas* **16**(8), 2009: 082706. DOI:10.1063/1.3212592

090 Popok, V. N.; Jensen, J.; Vuckovic, S.; Mackova, A.; Trautmann, C.*: **Formation of surface nanostructures on rutile (TiO_2): comparative study of low-energy cluster ion and high-energy monoatomic ion impact.** *Journal of Physics D: Applied Physics / J. Phys. D-Appl. Phys.* **42**(20), 2009: 205303. DOI:10.1088/0022-3727/42/20/205303

091 Rajasekaran, P. R.; Wolff, J.; Zhou, C.; Kinsel, M.; Trautmann, C.*; Aouadi, S.; Kohli, P.: **Two dimensional anisotropic etching in tracked glass.** *Journal of Materials Chemistry / J. Mater. Chem.* **19**(43), 2009: 8142–8149. DOI:10.1039/b913151e OPEN ACCESS.

092 Rohani, R.; Yamaki, T.; Koshikawa, H.; Takahashi, S.; Hasegawa, S.; Asano, M.; Maekawa, Y.; Voss, K. O.*; Trautmann, C.*; Neumann, R.*: **Enhancement of etch rate for preparation of nano-sized ion-track membranes of poly(vinylidene fluoride): Effect of pretreatment and high-LET beam irradiation.** *Nuclear instruments & methods in physics research, Section B, Beam interactions with materials and atoms / Nucl. Instrum. Methods Phys. Res. Sect. B-Beam Interact. Mater. Atoms* **267**(3), 2009: 554–557. DOI:10.1016/j.nimb.2008.12.005

093 Roth, M.; Alber, I.; Bagnoud, V.*; Brown, C. R. D.; Clarke, R.; Daido, H.; Fernandez, J.; Flippo, K.; Gaillard, S.; Gauthier, C.; Geissel, M.; Glenzer, S.; Gregori, G.; Günther, M.; Harres, K.; Heathcote, R.; Kritcher, A.; Kugland, N.; LePape, S.; Li, B.; Makita, M.; Mithen, J.; Niemann, C.; Nürnberg, F.; Offermann, D.; Otten, A.; Pelka, A.; Riley, D.; Schaumann, G.; Schollmeier, M.*; Schütrumpf, J.; Tampo, M.; Tauschwitz, A.*; Tauschwitz, An.: **Proton acceleration experiments and warm dense matter research using high power lasers.** *Plasma Physics and Controlled Fusion* **51**(12), 2009: 124039. DOI:10.1088/0741-3335/51/12/124039

094 Roth, M.; Alber, I.; Bagnoud, V.*; Brown, C. R. D.; Clarke, R.; Daido, H.; Fernandez, J.; Flippo, K.; Gaillard, S.; Gauthier, C.; Geissel, M.; Glenzer, S.; Gregori, G.; Günther, M.; Harres, K.; Heathcote, R.; Kritcher, A.; Kugland, N.; LePape, S.; Li, B.; Makita, M.; Mithen, J.; Niemann, C.; Nürnberg, F.; Offermann, D.; Otten, A.; Pelka, A.; Riley, D.; Schaumann, G.; Schollmeier, M.*; Schütrumpf, J.; Tampo, M.; Tauschwitz, A.; Tauschwitz, An.*: **Proton acceleration experiments and warm dense matter research using high power lasers.** *Plasma Physics and Controlled Fusion / Plasma Phys. Control. Fusion* **51**(12), 2009: 124039. DOI:10.1088/0741-3335/51/12/124039

095 Saha, J. K.; Mukherjee, T. K.; Fritzsche, S.*; Mukherjee, P. K.: **The effect of a 2s vacancy on two-electron-one-photon lines: Relativistic approach.** *Physics Letters A / Phys. Lett. A* **373**(2), 2009: 252–255. DOI:10.1016/j.physleta.2008.11.012

096 Sanchez, R.; Zakova, M.; Geppert, C.; Kramer, J.; Krieger, A.; Tiedemann, D.; Nörtershäuser, W.: **Frequency-comb-based measurements of lithium and beryllium isotopes for nuclear structure studies.** *Canadian Journal of Physics / Can. J. Phys.* **87**(7), 2009: 825–834. DOI:10.1139/p09-026

097 Schlegel, T.*; Naumova, N.; Tikhonchuk, V. T.; Labaune, C.; Sokolov, I. V.; Mourou, G.: **Relativistic laser piston model: Ponderomotive ion acceleration in dense plasmas using ultraintense laser pulses.** *Physics of plasmas / Phys. Plasmas* **16**(8), 2009: 083103. DOI:10.1063/1.3196845

098 Schuster, B.*; Lang, M.; Klein, R.*; Trautmann, C.*; Neumann, R.*; Benyagoub, A.: **Structural phase transi-**

tion in ZrO2 induced by swift heavy ion irradiation at high-pressure. *Nuclear instruments & methods in physics research, Section B, Beam interactions with materials and atoms / Nucl. Instrum. Methods Phys. Res. Sect. B-Beam Interact. Mater. Atoms* **267**(6), 2009: 964–968. DOI:10.1016/j.nimb.2009.02.046

099 Schwarz, S.; Block, M.*; Bollen, G.; Campbell, C. M.; Facina, M.; Ferrer, R.; Folden, C. M.; Kwiatkowski, A. A.; Morrissey, D. J.; Pang, G. K.; Prinke, A. M.; Ringle, R. J.; Savory, J.; Schury, P. H.: **Precision Penning trap mass measurements of rare isotopes produced by projectile fragmentation.** *The European physical journal A, Hadrons and nuclei / Eur. Phys. J. A* **42**(3), 2009: 323–326. DOI:10.1140/epja/i2009-10808-4

100 Schwarz, S.; Block, M.*; Bollen, G.; Campbell, C. M.; Facina, M.; Ferrer, R.; Folden, C. M.; Kwiatkowski, A. A.; Morrissey, D. J.; Pang, G. K.; Prinke, A. M.; Ringle, R. J.; Savory, J.; Schury, P. H.: **Precision Penning trap mass measurements of rare isotopes produced by projectile fragmentation.** *The European physical journal A, Hadrons and nuclei* **42**(3), 2009: 323–326. DOI:10.1140/epja/i2009-10808-4

101 Sengül, M. Y.; Güclü, M. C.; Fritzsche, S.*: **Bound-free electron-positron pair production in relativistic heavy-ion collisions.** *Physical review A, Atomic, molecular, and optical physics / Phys. Rev. A* **80**(4), 2009: 042711. DOI:10.1103/physreva.80.042711

102 Sertova, N.; Balanzat, E.; Toulemonde, M.; Trautmann, C.*: **Investigation of initial stage of chemical etching of ion tracks in polycarbonate.** *Nuclear instruments & methods in physics research, Section B, Beam interactions with materials and atoms / Nucl. Instrum. Methods Phys. Res. Sect. B-Beam Interact. Mater. Atoms* **267**(6), 2009: 1039–1044. DOI:10.1016/j.nimb.2009.02.045

103 Sil, A. N.; Anton, J.; Fritzsche, S.*; Mukherjee, P. K.; Fricke, B.: **Spectra of heliumlike carbon, aluminium and argon under strongly coupled plasma.** *The European physical journal: D, Atomic, molecular and optical physics / Eur. Phys. J. D* **55**(3), 2009: 645–652. DOI:10.1140/epjd/e2009-00258-6

104 Sil, A. N.; Anton, J.; Fritzsche, S.*; Mukherjee, P. K.; Fricke, B.: **Spectra of heliumlike carbon, aluminium and argon under strongly coupled plasma.** *The European physical journal: D, Atomic, molecular and optical physics* **55**(3), 2009: 645–652. DOI:10.1140/epjd/e2009-00258-6

105 Smorra, C.; Blaum, K.; Eberhardt, K.; Eibach, M.; Ketelaer, J.; Ketter, J.; Knuth, K.; Nagy, S.*: **A carbon-cluster laser ion source for TRIGA-TRAP.** *Journal of physics B, Atomic, molecular and optical physics / J. Phys. B-At. Mol. Opt. Phys.* **42**(15), 2009: 154028. DOI:10.1088/0953-4075/42/15/154028

106 Stöhlker, T.*; Banas, D.; Bräuning, H.*; Fritzsche, S.*; Geyer, S.*; Gumberidze, A.; Hagmann, S.*; Hess, S.*; Kozhuharov, C.*; Kumar, A.*; Martin, R.*; O'Rourke, B. E.*; Reuschl, R.*; Spillmann, U.*; Surzhykov, A.*; Tashenov, S.*; Trotsenko, S.*; Weber, G.*; Winters, D. F. A.*: **Polarization and angular correlation studies of X-rays emitted in relativistic ion-atom collisions.** *European Physical Journal, Special Topics / Eur. Phys. J.-Spec. Top.* **169**, 2009: 5–14. DOI:10.1140/epjst/e2009-00965-0

107 Steer, S. J.; Podolyak, Z. S.; Pietri, S.; Gorska, M.; Farrelly, G. F.; Regan, P. H.; Rudolph, D.; Garnsworthy, A. B.; Hoischen, R.; Gerl, J.; Wollersheim, H. J.; Grawe, H.; Maier, K. H.; Becker, F.; Bednarczyk, P.; Caceres, L.; Doornenbal, P.; Geissel, H.; Grebosz, J.; Kelic, A.; Kojouharov, I.; Kurz, N.; Montes, F.; Prokopowicz, W.; Saito, T.; Schaffner, H.; Tashenov, S.; Heinz, A.; Kurtukian-Nieto, T.; Benzoni, G.; Pfutzner, M.; Jungclaus, A.; Balabanski, D. L.; Brandau, C.; Brown, A.; Bruce, A. M.; Catford, W. N.; Cullen, I. J.; Dombradi, Z. S.; Estevez, M. E.; Gelletly, W.; Ilie, G.; Jolie, J.; Jones, G. A.; Kmiecik, M.; Kondev, F. G.; Krucken, R.; Lalkovski, S.; Liu, Z.; Maj, A.; Myalski, S.; Schwertel, S.; Shizuma, T.; Walker, P. M.; Werner-Malento, E.; Wieland, O.: **Isomeric decay studies in neutron-rich N approximate to 126 nuclei.** *International journal of modern physics E, Nuclear physics / Int. J. Mod. Phys. E-Nucl. Phys.* **18**(4), 2009: 1002–1007, Sp. Iss. SI. URL Also part of: HANU

108 Stolterfoht, N.; Hellhammer, R.; Juhasz, Z.; Sulik, B.; Bayer, V.*; Trautmann, C.*; Bodewits, E.; de Nijs, A. J.; Dang, H. M.; Hoekstra, R.: **Guided transmission of Ne^{7+} ions through nanocapillaries in insulating polymers: Scaling laws for projectile energies up to 50 keV.** *Physical review A, Atomic, molecular, and optical physics / Phys. Rev. A* **79**(4), Part A, 2009: 042902. DOI:10.1103/physreva.79.042902

109 Sun, B. H.; Geissel, H.; Hausmann, M.; Kozhuharov, C.; Knobel, R.; Litvinov, Y. A.; Meng, J.; Patyk, Z.; Radon, T.; Scheidenberger, C.: **Identification of Time-of-Flight spectra for Isochronous Mass Measurements.** *Chinese Physics C / Chin. Phys. C* **33**, 2009: 161–163. Also part of: HANU

110 Surzhykov, A.; Radtke, T.; Indelicato, P.; Fritzsche, S.*: **Photon polarization in the two-photon decay of heavy hydrogen-like ions.** *European Physical Journal, Special Topics / Eur. Phys. J.-Spec. Top.* **169**, 2009: 29–34. DOI:10.1140/epjst/e2009-00969-8

111 Surzhykov, A.*; Santos, J. P.; Amaro, P.; Indelicato, P.: **Negative-continuum effects on the two-photon decay rates of hydrogenlike ions.** *Physical review A, Atomic, molecular, and optical physics / Phys. Rev. A* **80**(5), 2009: 052511. DOI:10.1103/physreva.80.052511

112 Surzhykov, A.*; Santos, J. P.; Amaro, P.; Indelicato, P.: **Negative-continuum effects on the two-photon decay rates of hydrogenlike ions.** *Physical review A, Atomic, molecular, and optical physics* **80**(5), 2009: 052511. DOI:10.1103/physreva.80.052511

113 Surzhykov, A.*; Stöhlker, T.*; Fritzsche, S.*: **Fine-structure effects on the polarization of Kα_1 radiation from heavy, highly-charged ions.** *Nuclear instruments & methods in physics research, Section B, Beam interactions with materials and atoms / Nucl. Instrum. Methods Phys. Res. Sect. B-Beam Interact. Mater. Atoms* **267**(2), 2009: 251–253. DOI:10.1016/j.nimb.2008.10.014

114 Tahir, N. A.*; Lomonosov, I. V.; Shutov, A.; Fortov, V. E.; Geissel, M.; Piriz, A. R.; Deutsch, C.; Hoffmann, D. H. H.: **Review of high energy density physics: The HEDgeHOB Collaboration.** *Nuclear instruments & methods in physics research, Section A, Accelerators, spectrometers, detectors and associated equipment / Nucl. Instrum. Methods Phys. Res. Sect. A-Accel. Spectrom. Dect. Assoc. Equip.* **606**(1-2), 2009: 128–133. DOI:10.1016/j.nima.2009.03.095

115 Tahir, N. A.*; Matveichev, A.; Kim, V.; Ostrik, A.; Shutov, A.*GAST; Sultanov, V.; Lomonosov, I. V.; Piriz, A. R.*GAST; Hoffmann, D. H. H.: **Three-dimensional simulations of a solid graphite target for high intensity fast extracted uranium beams for the Super-FRS.** *Laser and particle beams / Laser Part. Beams* **27**(1), 2009: 9–17. DOI:10.1017/s0263034609000020

116 Tahir, N. A.*; Piriz, A. R.; Wouchuk, G.; Shutov, A.; Lomonosov, I. V.; Deutsch, C.; Hoffmann, D. H. H.; Fortov, V. E.: **High Energy Density physics and Laboratory Planetary Science using intense heavy ion beams at FAIR facility at Darmstadt: the HEDgeHOB collaboration.** *Astrophysics and Space Science / Astrophys. Space Sci.* **322**(1-4), 2009: 179–188. DOI:10.1007/s10509-008-9962-9

117 Tahir, N. A.*; Piriz, A. R.; Wouchuk, G.; Shutov, A.; Lomonosov, I. V.; Fortov, V. E.; Deutsch, C.; Hoffmann, D. H. H.: **Laboratory planetary science studies using intense heavy ion beams at FAIR: The HEDgeHOB collaboration.** *Nuclear instruments & methods in physics research, Section A, Accelerators, spectrometers, detectors and associated equipment / Nucl. Instrum. Methods Phys. Res. Sect. A-Accel. Spectrom. Dect. Assoc. Equip.* **606**(1-2), 2009: 177–185. DOI:10.1016/j.nima.2009.03.087

118 Tahir, N. A.*; Schmidt, R.; Brugger, M.; Assmann, R.; Shutov, A.; Lomonosov, I. V.; Gryaznov, V.; Piriz, A. R.; Udrea, S.; Hoffmann, D. H. H.; Fortov, V. E.; Deutsch, C.: **Generation of warm dense matter and strongly coupled plasmas using the High Radiation on Materials facility at the CERN Super Proton Synchrotron.** *Physics of plasmas / Phys. Plasmas* **16**(8), 2009: 082703. DOI:10.1063/1.3204137

119 Tahir, N. A.*; Schmidt, R.; Brugger, M.; Shutov, A.; Lomonosov, I. V.; Piriz, A. R.; Hoffmann, D. H. H.: **Simulations of full impact of the Large Hadron Collider beam with a solid graphite target.** *Laser and particle beams / Laser Part. Beams* **27**(3), 2009: 475–483. DOI:10.1017/s0263034609990206

120 Tahir, N. A.*; Schmidt, R.; Shutov, A.; Lomonosov, I. V.; Piriz, A. R.; Hoffmann, D. H. H.; Deutsch, C.; Fortov, V. E.: **Large Hadron Collider at CERN: Beams generating high-energy-density matter.** *Physical Review E / Phys. Rev. E* **79**(4), Part 2, 2009: 046410. DOI:10.1103/physreve.79.046410

121 Tahir, N. A.; Spiller, P.; Shutov, A.; Lomonosov, I. V.; Piriz, A. R.; Redmer, R.; Hoffmann, D. H. H.; Fortov, V. E.; Deutsch, C.; Bock, R. M.: **Proposed High Energy Density Physics Research Using Intense Particle Beams at FAIR: The HEDgeHOB Collaboration.** *IEEE transactions on plasma science / IEEE Trans. Plasma Sci.* **37**(7), Part 2, 2009: 1267–1275. DOI:10.1109/tps.2009.2022012

122 Tauschwitz, An.*; Efremov, V.; Maruhn, J. A.; Rosmej, F. B.; Tauschwitz, A.*: **Quasi-static heating of stack targets with intense ion beams for equation of state measurements.** *Nuclear instruments & methods in physics research, Section B, Beam interactions with materials and atoms / Nucl. Instrum. Methods Phys. Res. Sect. B-Beam Interact. Mater. Atoms* **267**(14), 2009: 2449–2452. DOI:10.1016/j.nimb.2009.04.011

123 Tauschwitz, An.; Novikov, V. G.; Tauschwitz, A.*; Rosmej, F. B.; Abdallah, J.; Onkels, E.*; Jacoby, J.; Maruhn, J. A.: **Intense ion beams as a tool for opacity measurements in warm dense matter.** *Applied physics B, Lasers and optics / Appl. Phys. B-Lasers Opt.* **95**(1), 2009: 13–16. DOI:10.1007/s00340-009-3444-9

124 Trassinelli, M.*; Kumar, A.*; Beyer, H. F.*; Indelicato, P.; Märtin, R.*; Reuschl, R.*; Kozhedub, Y. S.; Brandau, C.*; Bräuning, H.*; Geyer, S.*; Gumberidze, A.*; Hess, S.*; Jagodzinski, P.; Kozhuharov, C.*; Liesen, D.*; Spillmann, U.*; Trotsenko, S.*; Weber, G.*; Winters, D. F. A.*; Stöhlker, T.*: **Observation of the 2p(3/2) -¿ 2s(1/2) intra-shell transition in He-like uranium.** *Europhysics letters / EPL* **87**(6), 2009: 63001. DOI:10.1209/0295-5075/87/63001

125 Ubieto-Diaz, M.; Rodriguez, D.; Lukic, S.; Nagy, S.*; Stahl, S.; Blaum, K.: **A broad-band FT-ICR Penning trap system for KATRIN.** *International Journal of Mass Spectrometry / Int. J. Mass Spectrom.* **288**(1-3), 2009: 1–5. DOI:10.1016/j.ijms.2009.07.003

126 Ubieto-Diaz, M.; Rodriguez, D.; Lukic, S.; Nagy, S.*; Stahl, S.; Blaum, K.: **A broad-band FT-ICR Penning trap system for KATRIN.** *International Journal of Mass Spectrometry* **288**(1-3), 2009: 1–5. DOI:10.1016/j.ijms.2009.07.003

127 Ulmer, S.*; Kracke, H.; Blaum, K.; Kreim, S.; Mooser, A.; Quint, W.; Rodegheri, C. C.; Walz, J.: **The quality factor of a superconducting rf resonator in a magnetic field.** *Review of scientific instruments / Rev. Sci. Instrum.* **80**(12), 2009: 123302. DOI:10.1063/1.3271537

128 Urban, W.; Sieja, K.*; Simpson, G. S.; Faust, H.; Rzaca-Urban, T.; Zlomaniec, A.; Lukasiewicz, M.; Smith, A. G.; Durell, J. L.; Smith, J. F.; Varley, B. J.; Nowacki, F.; Ahmad, I.: **New isomers and medium-spin structure of the ^{95}Y nucleus.** *Physical review C, Nuclear physics / Phys. Rev. C* **79**(4), 2009: 044304. DOI:10.1103/physrevc.79.044304 Also part of: HANU

129 Völklein, F.; Schmitt, M.; Cornelius, T. W.*; Picht, O.*; Müller, S.*; Neumann, R.*: **Microchip for the Measurement of Seebeck Coefficients of Single Nanowires.** *Journal of Electronic Materials / J. Electron. Mater.* **38**(7), 2009: 1109–1115. DOI:10.1007/s11664-009-0714-6

130 Vogel, M.; Quint, W.*: **Laser spectroscopy by a radiofrequency measurement on a single ion in a Penning trap.** *New Journal of Physics / New J. Phys.* **11**, 2009: 013024. DOI:10.1088/1367-2630/11/1/013024 OPEN ACCESS.

131 Vogel, M.; Quint, W.*: **Trap-assisted precision spectroscopy of highly charged ions.** *Journal of physics B, Atomic, molecular and optical physics / J. Phys. B-At. Mol. Opt. Phys.* **42**(15), 2009: 154016. DOI:10.1088/0953-4075/42/15/154016

132 Volklein, F.; Reith, H.; Cornelius, T. W.*; Rauber, M.*; Neumann, R.*: **The experimental investigation of thermal conductivity and the Wiedemann-Franz law for single metallic nanowires.** *Nanotechnology / Nanotechnology* **20**(32), 2009: 325706. DOI:10.1088/0957-4484/20/32/325706

133 Wan, J. J.; Dong, C. Z.; Ding, X. B.; Ma, X. W.; Rzadkiewicz, J.*; Stöhlker, T.*; Fritzsche, S.*: **Radiative electron capture and subsequent radiative decay in collisions of $^{89+}$U ions with N_2.** *Physical review A, Atomic, molecular, and optical physics / Phys. Rev. A* **79**(2), 2009: 022707. DOI:10.1103/physreva.79.022707

134 Winckler, N.*; Geissel, H.*; Litvinov, Y. A.*; Beckert, K.*; Bosch, F.*; Boutin, D.*; Brandau, C.*; Chen, L.; Dimopoulou, C.*; Essel, H. G.*; Fabian, B.; Faestermann, T.; Fragner, A.; Haettner, E.; Hess, S.*; Kienle, P.; Knobel, R.*; Kozhuharov, C.*; Litvinov, S. A.*; Mazzocco, M.*; Montes, F.; Münzenberg, G.*; Nociforo, C.*; Nolden, F.*; Patyk, Z.; Plass, W. R.*; Prochazka, A.*; Reda, R.*; Reuschl, R.*; Scheidenberger, C.*; Steck, M.*; Stöhlker, T.*; Torilov, S. Y.; Trassinelli, M.; Sun, B.*; Weick, H.*; Winkler, M.*: **Orbital electron capture decay of hydrogen- and helium-like ^{142}Pm ions.** *Physics letters B / Phys. Lett. B* **679**(1), 2009: 36–40. DOI:10.1016/j.physletb.2009.07.019 Also part of: HANU

135 Winters, D. F. A.; Stöhlker, T.: **Atomic physics at storage rins: recent results from ESR and future perspectives at FAIR.** *International journal of modern physics E, Nuclear physics / Int. J. Mod. Phys. E-Nucl. Phys.* **18**(2), 2009: 359–366. URL Also part of: HANU

136 Yameen, B.; Ali, M.; Neumann, R.*; Ensinger, W.; Knoll, W.; Azzaroni, O.: **Ionic Transport Through Single Solid-State Nanopores Controlled with Thermally Nanoactuated Macromolecular Gates.** *Small / Small* **5**(11), 2009: 1287–1291. DOI:10.1002/smll.200801318

137 Yameen, B.; Ali, M.; Neumann, R.*; Ensinger, W.; Knoll, W.; Azzaroni, O.: **Synthetic Proton-Gated Ion Channels via Single Solid-State Nanochannels Modified with Responsive Polymer Brushes.** *Nano letters / Nano Lett.* **9**(7), 2009: 2788–2793. DOI:10.1021/nl901403u

138 Yameen, B.; Ali, M.; Neumann, R.; Ensinger, W.; Knoll, W.; Azzaroni, O.: **Single Conical Nanopores Displaying pH-Tunable Rectifying Characteristics. Manipulating Ionic Transport With Zwitterionic Polymer Brushes.** *Journal of the American Chemical Society / J. Am. Chem. Soc.* **131**(6), 2009: 2070–+. DOI:10.1021/ja8086104

139 Yan, Z. C.; Nörtershäuser, W.; Drake, G. W. F.: **High Precision Atomic Theory for Li and Be^+: QED Shifts and Isotope Shifts (vol 100, 243002, 2008).** *Physical review letters / Phys. Rev. Lett.* **102**(24), 2009: 249903. DOI:10.1103/physrevlett.102.249903

140 Zhang, J. M.; Lang, M.; Lian, J.; Liu, J.; Trautmann, C.*; Della-Negra, S.; Toulemonde, M.; Ewing, R. C.: **Liquid-like phase formation in $Gd_2Zr_2O_7$ by extremely ionizing irradiation.** *Journal of Applied Physics / J. Appl. Phys.* **105**(11), 2009: 113510. DOI:10.1063/1.3124370

Other publications to the programme 'Large-scale facilities for research with photons, neutrons and ions' published in 2009

Compiled by K. Kreidi, Beauftragte für Forschung

001 Bagnoud, V.; Zimmer, D.; Ecker, B.; Kuehl, T.: **A technique for measuring B-integral in chirped-pulse amplifiers.** In: *IEE Proceedings CLEO/QELS,*

002 Dahl, L.A.; Barth, W.; Gerhard, P.; Herfurth, F.;Kaiser, M.; Kester, O.; Kluge, H.-J., Koszudowski, S.; Kozhuharov, C.; Maero, G.; Quint, W.; Sokolov, A.; Stöhlker, T.; Vinzenz, W.; Vorobjev, G.; Winters, D.F.A.;Hofmann, B.; Pfister, J.;Ratzinger, U.;Sauer, A.C.;Schempp, A.: **The HITRAP Decelerator Project at GSI - Status and Commissioning Report.** In: *LINAC08 Conference Proceedings*, 100-102p.

003 Guilbaud, O.; Ros, D.; Kazamias, S.; Zielbauer, B.; Habib, J.; Pittman, M.; Cassou, K.; Ple, F.; Farinet, M.; Klisnick, A.; de Dortan, F.; Lacombe, S.; Porcel, E.; Le Sech, C.; du Penhoat, M.-A.; Touati, A.; Marsi, M.; Fajardo, M.; Zeitoun, P.; Joyeux, D.: **LASERIX : premier bilan du fonctionnement de l'installation.** In: *EDP sciences*, DOI:10.1051/uvx/2009010

004 Guilbaud, O.; Ros, D.; Kazamias, S.; Zielbauer, B.; Habib, J.; Pittman, M.; Farinet, M.; Zimmer, D.; Yu, T.; Klisnick, A.; de Dortan, F.; Lacombe, S. ; Porcel, E. ; Le Sech, C. ; du Penhoat, M.-A. ; Touati, A. ; Marsi, M.; Joyeux, D.: **Recent progress on the LASERIX facility.** In: *Proceedings of the SPIE 7451,*

005 Habib, J.; Klisnick, A.; Guilbaud, O.; Joyeux, D.; Zielbauer, B.; Kazamias, S.; Pittman, M.; Ros, D.; de Dortan, F.: **Coherence temporelle et largeur spectrale des lasers XUV transitoires pompes en incidence rasante.** In: *EDP sciences*, DOI:10.1051/uvx/2009025

006 Harasimowicz, J.; Welsch, C.P.: **Beam Instrumentation for the Future Ultra low Energy Storage Ring at FLAIR.** In: *Hyperfine Interact.***194** *(1-3)*, 177p. DOI:10.1007/s10751-009-0047-0

007 Hess, S., Bräuning, H., Spillmann, U., Brandau, C., Geyer, S., Hagmann, S., Hegewald, M., Kozhuharov, C., Krings, T., Kumar, A., Märtin, R., Protic, D., O'Rourke, B.E., Reuschl, R., Trassinelli, M., Trotsenko, S., Weber, G., Winters, D.F.A., Stöhlker, T: **Polariza-tion studies of radiative electron capture into highly-charged uranium ions.** In: *Journal of Physics: Conference Series* **163***(1)*,

008 Kühl, T., Aurand, B., Bagnoud, V.; Ecker, B., Eisenbarth, U.,Fils, J., Hochhaus, D., Javorkova, D., Neumayer, P., Zielbauer, B., Zimmer, D., Habib, J., Kazamias, S., Klisnick, A., Ros, D., Seres, J., Spielmann, C.,Ursescu, D.: **X-ray laser developments at PHELIX.** In: *Proceedings of the SPIE 7451,*

009 Kühl, T.; Bagnoud, V.; Bruske, C.; Borneis, S.; Ecker, B.; Eisenbarth, U.; Fils, J.; Goette, S.; Hahn, T.; Hoch-haus, D.; Javorkova, D.; Knobloch, F.; Kreutz, M.; Kunzer, S.; Merz-Mantwill, T.; Onkels, E.; Reemts, D.; Tauschwitz, A.; Witte, K.; Zielbauer, B.; Zimmer, D.: **Versatile High-Energy and Short-Pulse Operation of PHELIX.** In: *Springer Proceedings in Physics 130,*

010 Liehn, S.; Le Sech, C.; Porcel, E.; Zielbauer, B.; Habib, J.; Kazamias, S.; XGuilbaud, O.; Pittman, M.; Ros, D.; Hervé du Penhoat, M.-A.; Touati, A.; Remita, H.; Lacombe, S.: **Biological effects induced by low energy x-rays: effects of nanoparticles.** In: *Proceedings of the. SPIE 7451*, 74510p.

011 Minaya Ramirez, E.; Audi, G.; Beck, D.; Blaum, K.; Böhm, C.; Borgmann, C.; Breitenfeldt, M.; Chamel, N.; George, S.; Goriely, S.; Herfurth, F.; Herlert, A.;Kellerbauer, A.; Kowalska, M.; Lunney, D.; Naimi, S.; Neidherr, D.; Pearson, J.M.; Rosenbusch, M.; Schwarz, S.; Schweikhard, L.: **Neutron drip-line topography.** In: *AIP Conference Proceedings 1165,*

012 Neumann, R.: **Materials Research with Energetic Heavy Ions at GSI.** In: *Springer Proceedings in Physics 127,*

013 O'Rourke, B.E., Geyer, S., Silze, A., Sokolov, A., Vorobjev, G., Winters, D.F.A., Kester, O., Stöhlker, T.: **The SPARC EBIT at GSI: Commissioning and Future Plans at the HITRAP Beamline.** In: *Journal of Physics: Conference Series, 163(1), 2009,*

014 Papash, A.; Welsch, C.P.: **On the Possibility of Realizing Shortest Bunches in Low-energy Storage Rings.** In: *Particle Physics and Nuclei Letters* **6** *(3)*, DOI:10.1134/S1547477109030054

015 Pfister, J.; Nörenberg, R.; Ratzinger, U.; Barth, W.; Dahl, L.; Forck, P.; Herfurth, F.; Kester, O.; Stöhlker, T.: **Commissioning of the HITRAP Decelerator using a Single-shot Pepper Pot Emittance Meter.** In: *LINAC08*

Conference Proceedings, 564p.

016 Putignano, M; Kühnel, K.-U.; Schröter, C.-D.; Welsch, C.P.: **A fast, low perturbation ionization beam profile monitor based on a gas-jet curtain for the ultra low energy storage ring.** In: *Hyperfine Interact.* **194** *(1-3)*, 189p. DOI:10.1007/s10751-009-0049-y

017 Reuschl, R., Banas, D., Beyer, H.F., Gumberidze, A., Hess, S., Indelicato, P., Liesen, D., Protic, D., Spillmann, U., Stöhlker, T., Trassinelli, M., Trotsenko, S. Weber, G.: **Experimental Developments for the Lamb Shift Investigation in Heavy Ions:.** In: *Third IUPAP international Conference on Women in Physics. AIP Conference Proceedings 1119*,

018 Rodegheri, C.C.; Blaum, K.; Kracke, H.; Kreim, S.; Mooser, A.; Mrozik, C.; Quint, W.; Ulmer, S.; Walz, J.: **Developments for the direct determination of the g-factor of a single proton in a Penning trap.** In: *Hyperfine Interactions* **194**, 93p.

019 Ros, D. ; Guilbaud, O. ; Kazamias, S.; Pittman, M. ; Lagron, J.-C. ; Zielbauer, B.; Habib, J.; Chambaret, J.-P.; Mourou, G.; Cassou, K. ; Cros, B.; Maynard, G.; Zeitoun, Ph. ; Sebban, S. ; Gautier, J.; Klisnick, A.; de Rossi, S.; Jacquemot, S.; Audebert, P.; Rus, B.; Zim-mer, D.; Kühl, T.: **Perspectives of XUV sources deve-lopment on LASERIX facility, ILE, and ELI.** In:

020 Schabinger, B.; Sturm, S.; Blaum, K.; Quint, W.; Wagner, A.; Werth, G.: **Creation of highly-charged calcium ions for the g-factor determination of the bound electron.** In: *14th International Conference on the Physics of Highly-Charged Ions (HCI 2008) J. Phys. Conf. Ser.***163**, 012108p. DOI:10.1088/1742-6596/163/1/012108

021 Schmid, P.; Kühnel, K.-U.; Papash, A.; Welsch, C.P.: **Preliminary Design of an Extraction Scheme for the USR.** In: *Hyperfine Interact.* **194***(1-3)*, 183p. DOI:10.1007/s10751-009-0048-z

022 Seres, J.; Bagnoud, V.; Hochhaus, D.; Ecker, B.; Zimmer, D.; Spielmann, C.; Kuehl, T.: **High harmonics for seeding.** In: *IEE Proceedings CLEO/QELS 2009*,

023 Seres, J.; Hochhaus, D.; Ecker, B.; Zimmer, D.; Kuehl, T.; Spielmann, C.: **High-order Harmonic Source for X-ray Laser Seeding driven by Two-color Laser Field.** In: *CLEO/IQEC, OSA Technical Digest, 14-19 June*, DOI:10.1109/CLEOE-EQEC.2009.5196330

024 Seres, J.; Hochhaus, D.; Ecker, B.; Zimmer, D.; Spielmann, C.; Kuehl, T.: **Two-Color Driven High-Order Harmonic Source for X-Ray Laser Seeding.** In: *CLEO/IQEC, OSA Technical Digest*,

025 Surzhykov, A., Fritzsche, S., Kabachnik, N.M., Stöhlker, T.: **Theoretical progress in studying the characteristic x-ray emission from heavy few-electron ions.** In: *Journal of Physics: Conference Series* **80**, 012710p. DOI:10.1088/1742-6596/163/1/012008

026 Trautmann, C.: **Micro- and Nanoengineering with Ion Tracks.** In: *Ion Beams in Nanoscience and Technology*,

027 Weber, G., Omet, C., DuBois, R.D., de Lucio, O., Stöhlker, T., Brandau, C., Gumberidze, A., Hagmann, S., Hess, S., Kozhuharov, C., Reuschl, R., Spiller, P., Spillmann, U., Steck, M., Thomason, M., Trotsenko, S.: **Beam lifetimes and ionization cross sections of U^{28}.** In: *Physical Review Special Topics - Accelerators and Beams* **12***(8)*, 084201p. DOI:10.1103/PhysRevSTAB.12.084201

028 Welsch, C.P.; Harasimowicz, J.; Kühnel, K.-U.; Papash, A.; Putignano, M.; Schmid, P.; Ullrich, J.: **Present status of the USR Project.** In: *Hyperfine Interact.* **194***(1-3)*, 137p. DOI:10.1007/s10751-009-0041-6

029 Zhang, S., Suske, J., Fischer, D., Kuehnel, K.U., Hagmann, S., Voitkiv, A., Najjaril, B., Krauss, A., Moshammer, R., Ullrich, J. Ma, X.: **Electron angular distributions in He single ionization impact by H_2^+ ions at 1 MeV.** In: *Journal of Physics: Conference Series* **163**, 012041p. DOI:10.1088/1742-6596/163/1/012041

030 Zielbauer, B.; Guilbaud, O.; Habib, J.; Kazamias, S.; Pittman, M.; Zimmer, D.; Kühl, T.; Ros, D.; Liehn, S.; Le Sech, C.; Porcel, E.; Herve du Penhoat, M.A.; Touati, A.; Lacombe, S.: **10 Hz Mo X-Ray Laser operation at LASERIX: First application experiment in radiobiology.** In: *Proceedings of the Ultrafast Optics Conference*,

031 Zimmer, D.; Bagnoud, V.; Ecker, B.; Eisenbarth, U.; Habib, J.; Hochhaus, D.; Javorkova, D.; Kazamias, S.; Kuehl, T.; Ros, D.; Ursescu, D.; Zielbauer, B.: **An Improved Double-Pulse Non-Normal Incidence Pump-ing Geometry for Transient Collisionally Excited Soft X-Ray Lasers.** In: *Springer Proceedings in Physics 130*,

032 Zimmer, D.; Bagnoud, V.; Ecker, B.; Hochhaus, D.; Kuehl, T.; Ros, D.; Zielbauer, B.; Aurand, B.: **Low pumping energy threshold for a Ni-like Sm x-ray laser pumped in the double-pulse non-normal incidence pumping geometry.** In: *Proceedings of the Ultrafast Optics Conference*,

033 Zimmer, D.; Zielbauer, B.; Guilbaud, O. ; Habib, J. ; Kazamias, S.; Pittman, M.; Ros, D.; Bagnoud, V.; Ecker, B.; Hochhaus, D.; Kuehl, T.: **Characterization of a 10Hz double-pulse non-normal incidence pumped transient collisional Ni-like molybdenum soft x-ray laser for applications.** In: *Proceedings of the SPIE 7451, 2009*,

WoS Publications to the programme 'Health' in the field 'Cancer research' published in 2009

Compiled by K. Große, BuD

001 An, H. X.; You, A.; Juricko, J.; Fokas, E.; Hanze, J.; Rose, F.; Fournier, C.; Taucher-Scholz, G.; Engenhart-Cabillic, R.: **Gene expression profiling of lung cancer cells irradiated by carbon and X-rays.** *Strahlentherapie und Onkologie : Journal of Radiation Oncology, Biology, Physics / Strahlenther. Onkol.* **185**, 2009: 47–47.

002 Becker, D.*; Elsässer, T.*; Tonn, T.*; Seifried, E.; Durante, M.*; Ritter, S.*; Fournier, C.*: **Response of human hematopoietic stem and progenitor cells to energetic carbon ions.** *International journal of radiation biology / Int. J. Radiat. Biol.* **85**(11), 2009: 1051–1059. DOI:10.3109/09553000903232850

003 Bert, C.*; Gemmel, A.*; Saito, N.*; Rietzel, E.*: **Gated Irradiation With Scanned Particle Beams.** *International journal of radiation oncology, biology, physics / Int. J. Radiat. Oncol. Biol. Phys.* **73**(4), 2009: 1270–1275. DOI:10.1016/j.ijrobp.2008.11.014

004 Bettega, D.; Calzolari, P.; Hessel, P.*; Stucchi, C. G.; Weyrather, W. K.*: **Neoplastic Transformation Induced by Carbon Ions.** *International journal of radiation oncology, biology, physics / Int. J. Radiat. Oncol. Biol. Phys.* **73**(3), 2009: 861–868. DOI:10.1016/j.ijrobp.2008.07.067

005 Combs, S. E.; Bohl, J.; Elsässer, T.*; Weber, K. J.; Schulz-Ertner, D.; Debus, J.; Weyrather, W. K.*: **Radiobiological evaluation and correlation with the local effect model (LEM) of carbon ion radiation therapy and temozolomide in glioblastoma cell lines.** *International journal of radiation biology / Int. J. Radiat. Biol.* **85**(2), 2009: 126–137. DOI:10.1080/09553000802641151

006 Conrad, S.; Ritter, S.*; Fournier, C.*; Nixdorff, K.: **Differential Effects of Irradiation with Carbon Ions and X-Rays on Macrophage Function.** *Journal of Radiation Research / J. Radiat. Res.* **50**(3), 2009: 223–231. DOI:10.1269/jrr.08115 OPEN ACCESS.

007 Domingo-Pardo, C.; Goel, N.; Engert, T.; Gerl, J.; Isaka, M.; Kojouharov, I.; Schaffner, H.: **A Position Sensitive γ-Ray Scintillator Detector With Enhanced Spatial Resolution, Linearity, and Field of View.** *IEEE Transactions on Medical Imaging / IEEE Trans. Med. Imaging* **28**(12), 2009: 2007–2014. DOI:10.1109/tmi.2009.2027436

008 Durante, M.*: **Applications of Particle Microbeams in Space Radiation Research.** *Journal of Radiation Research / J. Radiat. Res.* **50**, 2009: A55–A58. DOI:10.1269/jrr.09007s OPEN ACCESS.

009 Elsässer, T.*; Gemmel, A.*; Scholz, M.*; Schardt, D.*; Krämer, M.*: **The relevance of very low energy ions for heavy-ion therapy.** *Physics in medicine and biology / Phys. Med. Biol.* **54**(7), 2009: N101–N106. DOI:10.1088/0031-9155/54/7/n03

010 Fischer, B. E.*; Voss, K.-O.*; Du, G.*: **Targeted irradiation of biological cells using an ion microprobe - Why a small beam spot is not sufficient for success.** *Nuclear instruments & methods in physics research, Section B, Beam interactions with materials and atoms / Nucl. Instrum. Methods Phys. Res. Sect. B-Beam Interact. Mater. Atoms* **267**(12-13), 2009: 2122–2124. DOI:10.1016/j.nimb.2009.03.068

011 Fokas, E.; Kraft, G.*; An, H. X.; Engenhart-Cabillic, R.: **Ion beam radiobiology and cancer: Time to update ourselves.** *Biochimica et Biophysica Acta: Reviews on Cancer / Biochim. Biophys. Acta-Rev. Cancer* **1796**(2), 2009: 216–229. DOI:10.1016/j.bbcan.2009.07.005

012 Fournier, C.*; Barberet, P.*; Pouthier, T.*; Ritter, S.*; Fischer, B.*; Voss, K. O.*; Funayama, T.; Hamada, N.; Kobayashi, Y.; Taucher-Scholz, G.*: **No Evidence for DNA and Early Cytogenetic Damage in Bystander Cells after Heavy-Ion Microirradiation at Two Facilities.** *Radiation research / Radiat. Res.* **171**(5), 2009: 530–540. DOI:URL:http://www.bioone.org//pdf/10.1667/RR1457.1

013 Gudowska-Nowak, E.; Psonka-Antonczyk, K.; Weron, K.; Elsässer, T.*; Taucher-Scholz, G.*: **Distribution of DNA fragment sizes after irradiation with ions.** *Chinese Journal of Organic Chemistry / Eur. Phys. J. E* **30**(3), 2009: 317–324. DOI:10.1140/epje/i2009-10522-7

014 Gudowska-Nowak, E.; Psonka-Antonczyk, K.; Weron, K.; Elsässer, T.*; Taucher-Scholz, G.*: **Distribution of DNA fragment sizes after irradiation with ions.** *Chinese Journal of Organic Chemistry* **30**(3), 2009: 317–324. DOI:10.1140/epje/i2009-10522-7

015 Harris, J. L.; Jakob, B.*; Taucher-Scholz, G.*; Dianov, G. L.; Becherel, O. J.; Lavin, M. F.: **Aprataxin,**

poly-ADP ribose polymerase 1 (PARP-1) and apurinic endonuclease 1 (APE1) function together to protect the genome against oxidative damage. *Human molecular genetics / Hum. Mol. Genet.* **18**(21), 2009: 4102–4117. DOI:10.1093/hmg/ddp359 OPEN ACCESS.

016 Jakob, B.*; Splinter, J.*; Durante, M.*; Taucher-Schoiz, G.*: **Live cell microscopy analysis of radiation-induced DNA double-strand break motion.** *Proceedings of the National Academy of Sciences of the United States of America / Proc. Natl. Acad. Sci. U. S. A.* **106**(9), 2009: 3172–3177. DOI:10.1073/pnas.0810987106 OPEN ACCESS.

017 Jakob, B.*; Splinter, J.*; Taucher-Scholz, G.*: **Positional Stability of Damaged Chromatin Domains along Radiation Tracks in Mammalian Cells.** *Radiation research / Radiat. Res.* **171**(4), 2009: 405–418. DOI:URL:http://www.bioone.org//pdf/10.1667/RR1520.1

018 Kamlah, F.; Hanze, J.; Arenz, A.; Hasan, D.; Juricko, J.; Taucher-Scholz, G.; Fournier, C.; Scholz, M.; Engenhart-Cabilic, R.; Rose, F.: **Angiogenic Factor gene expression in human Lung adenocarcinoma (A(549)) Cells after Carbon ion (C-(12))- and Photon irradiation.** *Strahlentherapie und Onkologie : Journal of Radiation Oncology, Biology, Physics / Strahlenther. Onkol.* **185**, 2009: 151–151.

019 Krämer, M.*: **Swift ions in radiotherapy - Treatment planning with TRiP98.** *Nuclear instruments & methods in physics research, Section B, Beam interactions with materials and atoms / Nucl. Instrum. Methods Phys. Res. Sect. B-Beam Interact. Mater. Atoms* **267**(6), 2009: 989–992. DOI:10.1016/j.nimb.2009.02.015

020 Kraft, G.*; Kraft, S. D.: **Research needed for improving heavy-ion therapy.** *New Journal of Physics / New J. Phys.* **11**, 2009: 025001. DOI:10.1088/1367-2630/11/2/025001 OPEN ACCESS.

021 Lineva, N.*; Kozhuharov, C.*; Hagmann, S.*; Krämer, M.*; Kraft, G.*: **Low-energy electrons emitted in collisions of heavy ions with solid state targets.** *Nuclear instruments & methods in physics research, Section B, Beam interactions with materials and atoms / Nucl. Instrum. Methods Phys. Res. Sect. B-Beam Interact. Mater. Atoms* **267**(6), 2009: 891–895. DOI:10.1016/j.nimb.2009.02.038 Also part of: PNI

022 Maalouf, M.; Alphonse, G.; Colliaux, A.; Beuve, M.; Trajkovic-Bodennec, S.; Battiston-Montagne, P.; Testard, I.; Chapet, O.; Bajard, M.; Taucher-Scholz, G.*; Fournier, C.*; Rodriguez-Lafrasse, C.: **Different Mechanisms of Cell Death in Radiosensitive and Radioresistant P53 Mutated Head and Neck Squamous Cell Carcinoma Cell Lines Exposed to Carbon Ions and X-Rays.** *International journal of radiation oncology, biology, physics / Int. J. Radiat. Oncol. Biol. Phys.* **74**(1), 2009: 200–209. DOI:10.1016/j.ijrobp.2009.01.012

023 Ochab-Marcinek, A.; Gudowska-Nowak, E.*; Nasonova, E.*; Ritter, S.*: **Modeling radiation-induced cell cycle delays.** *Radiation and Environmental Biophysics / Radiat. Environ. Biophys.* **48**(4), 2009: 361–370. DOI:10.1007/s00411-009-0239-7

024 Palmowski, M.; Peschke, P.; Huppert, J.; Hauff, P.; Reinhardt, M.; Maurer, M.; Karger, C. P.; Scholz, M.*; Semmler, W.; Huber, P. E.; Kiessling, F. M.: **Molecular Ultrasound Imaging of Early Vascular Response in Prostate Tumors Irradiated with Carbon Ions.** *Neoplasia : An International Journal for Oncology Research / Neoplasia* **11**(9), 2009: 856–863. URL OPEN ACCESS.

025 Parodi, K.; Saito, N.*; Chaudhri, N.*; Richter, C.; Durante, M.*; Enghardt, W.; Rietzel, E.*; Bert, C.*: **4D in-beam positron emission tomography for verification of motion-compensated ion beam therapy.** *Medical physics / Med. Phys.* **36**(9), 2009: 4230–4243. DOI:10.1118/1.3196236

026 Peschke, P.; Karger, C. P.; Scholz, M.; Elsässer, T.; Debus, J.; Huber, P.: **Response of experimental prostate tumors to single doses of photons and carbon ions.** *Strahlentherapie und Onkologie : Journal of Radiation Oncology, Biology, Physics / Strahlenther. Onkol.* **185**, 2009: 43–43.

027 Psonka-Antonczyk, K.*; Elsässer, T.*; Gudowska-Nowak, E.; Taucher-Scholz, G.*: **Distribution of Double-Strand Breaks Induced by Ionizing Radiation at the Level of Single DNA Molecules Examined by Atomic Force Microscopy.** *Radiation research / Radiat. Res.* **172**(3), 2009: 288–295. DOI:10.1667/rr1772.1

028 Saito, N.*; Bert, C.*; Chaudhri, N.*; Gemmel, A.*; Schardt, D.*; Durante, M.*; Rietzel, E.*: **Speed and accuracy of a beam tracking system for treatment of moving targets with scanned ion beams.** *Physics in medicine and biology / Phys. Med. Biol.* **54**(16), 2009: 4849–4862. DOI:10.1088/0031-9155/54/16/001

029 Uzavva, A.; Ando, K.; Koike, S.; Furusawa, Y.; Matsumoto, Y.; Takai, N.; Hirayama, R.; Watanabe, M.; Scholz, M.*; Elsässer, T.*; Peschke, P.: **Comparison of Biological Effectiveness of Carbon-Ion Beams in Japan and Germany.** *International journal of radiation oncology, biology, physics / Int. J. Radiat. Oncol. Biol. Phys.* **73**(5), 2009: 1545–1551. DOI:10.1016/j.ijrobp.2008.12.021

030 Voss, U.; Holzmann, R.*; Tuin, I.; Hobson, J. A.: **Lucid Dreaming: A State of Consciousness with Features of Both Waking and Non-Lucid Dreaming.** *Sleep / Sleep* **32**(9), 2009: 1191–1200.

031 Weber, U.; Kraft, G.: **Comparison of Carbon Ions Versus Protons.** *The Cancer Journal / Cancer J.* **15**(4), 2009: 325–332.

032 Wirkner, U.; Rittmuller, C.; Trinh, S.; Scholz, M.; Abdollahi, A.; Huber, P.: **Heavy ion 12-C radiation: Effect on primary human cell cultures studied by whole transcriptome analysis.** *Strahlentherapie und Onkologie : Journal of Radiation Oncology, Biology, Physics / Strahlenther. Onkol.* **185**, 2009: 148–148.

International and national Collaborations of GSI

Compiled by K. Kreidi, C. Kausch, I. Kraus

The AIC Collaboration

Spokesperson: R. Krücken

Boehler, P. [1], Bosch, F. [5], Cargnelli, J. [1], Fabbietti, L. [4], Franzke, B. [5], Fuhrmann, H. [1], Hayano, R.S. [8], Hirtl, A. [1], Kozhuharov, C. [5], Krücken, R. [4], Lenske, H. [3], Litvinov, Y. [5], Marton, J. [1], Nolden, F. [5], Ring, P. [4], Shatunov, Y.M. [7], Skrinsky, A. N. [7], Vostrikov, V. [7], Widmann, E. [2], Wycech, S. [6], Yamaguchi, T. [9], Zmeskal, J. [1]

1 Stefan Meyer Institute Vienna (Austria)
2 University of Vienna (Austria)
3 Justus-Liebig Universität Giessen (Germany)
4 Technische Universität München (Germany)
5 GSI Helmholtzzentrum für Schwerionenforschung GmbH, Darmstadt (Germany)
6 Soltan Institute for Nuclear Studies, IPJ, Warsaw (Poland)
7 BINP Novosibirsk (Russia)
8 University of Tokyo (Japan)
9 Saitama University (Japan)

Aladin 2000

Spokesperson: Trautmann, W.

Adrich, P. [1], Aumann, T. [1], Bacri, C.O. [2], Barczyk, T. [3], Bassini, R. [4], Bianchin, S. [1], Boiano, C. [4], Botvina, A.S. [1], Boudard, A. [5], Brzychczyk, J. [3], Chbihi, A. [6], Cibor, J. [7], Czech, B. [7], De Napoli, M. [8], Ducret, J.-E. [5], Emling, H. [1], Frankland, J.D. [6], Hellström, M. [1], Henzlova, D. [1], Immè, G. [8], Iori, I. [4], Johansson, H. [1], Kezzar, K. [1], Lafriakh, A. [5], Le Fèvre, A. [1], Le Gentil, E. [5], Leifels, Y. [1], Lühning, J. [1], Lukasik, J. [1], Lynch, W.G. [9], Lynen, U. [1], Majka, Z. [3], Mocko, M. [9], Müller, W.F.J. [1], Mykulyak, A. [1], Orth, H. [1], Otte, A.N. [1], Palit, R. [1], Pawlowski, P. [7], Pullia, A. [4], Raciti, G. [8], Rapisarda, E. [8], Sann, H. [1], Schwarz, C. [1], Sfienti, C. [1], Simon, H. [1], Sümmerer, H. [1], Trautmann, W. [1], Tsang, M.B. [9], Verde, G. [9], Volant, C. [5], Wallace, M. [9], Weick, H. [1], Wiechula, J. [1], Wieloch, A. [3], Zwieglínski, B. [10]

1 GSI Helmholtzzentrum für Schwerionenforschung GmbH, Darmstadt Germany
2 Institut de Physique Nucléaire, IN2P3 et Université, Orsay France
3 Institute of Physics, Jagiellonian University, Krakow Poland
4 Istituto di Scienze Fisiche, Università and INFN, Milano Italy
5 DAPNIA/SPhN, CEA/Saclay, Gif-sur-Yvette France
6 GANIL, CEA et IN2P3-CNRS, Caen France
7 IFJ-PAN, Krakow Poland
8 Dipartimento di Fisica dell'Università and INFN-LNS, Catania Italy
9 Department of Physics and NSCL, MSU, East Lansing, MI 48824 USA
10 A. Soltan Institute for Nuclear Studies, Warsaw Poland

ALICE

Spokesperson: Schukraft, J.

The ALICE Collaboration, A Large Ion Collider Experiment at CERN LHC
http://aliceinfo.cern.ch/Collaboration/General/Members/index.html

ALICE TPC

Spokesperson: Braun-Munzinger, P.

The ALICE TPC Collaboration, The Time Projection Chamber of the ALICE experiment at LHC
http://www-alice.gsi.de/trd/

ALICE TRD

Spokesperson: Stachel, J.

The ALICE TRD Collaboration, The Transition Radiation Detector of the ALICE experiment at LHC

http://www-alice.gsi.de/tpc/

BES-III

Spokesperson: Wang, Y.F.

Ablikim, M [1], Achasov, M.N. [5], An, L. [9], An, Q. [31], An, Z.H. [1], Bai, J.Z. [1], Ban, Y. [18], Berger, N. [1], Bian, J.M. [1], Boyko, I., Bytev, V. [13], Briere, R.A. [3], Cai, X. [1], Cao, G.F. [1], Cao, X.X. [1], Chang, J.F. [1], Chelkov, G. [13], Chen, C.H. [1], Chen, G. [1], Chen, H.S. [1], Chen, L.P. [1], Chen, M.L. [1], Chen, P. [1], Chen, S.J. [16], Chen, Y.B. [1], Chu, Y.P. [1], Cronin-Hennessy, D. [30], Dai, H.L. [1], Dai, J.P. [1], Dedovich, D. [13], Deng, Z.Y. [1], Denysenko, I. [13], Destefanis, M. [32], Ding, Y. [14], Dong, L.Y. [1], Dong, M.Y. [1], Du, S.X. [36], Duan, M.Y. [21], Fang, J. [1], Feng, C.Q. [31], Fu, C.D. [1], Fu, J.L. [16], Gao, Y. [27], Geng, C. [31], Gong, W.X. [1], Götzen, K [7], Greco, M. [32], Grishin, S. [13], Gu, Y.T. [9], Guo, A.Q. [17], Guo, L.B. [15], Guo, Y.P. [17], Han, S.Q. [15], Harris, F.A. [29], He, K.L. [1], He, M. [1], He, Z.Y. [17], Heng, Y.K. [1], Hou, Z.L. [1], Hu, H.M. [1], Hu, J.F. [6], Hu, T. [1], Hu, X.W. [16], Huang, B. [1], Huang, G.M. [11], Huang, J.S. [10], Huang, X.T. [20], Huang, Y.P. [1], Ji, C.S. [31], Ji, H.B. [1], Ji, Q. [1], Ji, X.B. [1], Ji, X.L. [1], Jia, L.K. [1], Jiang, L.L. [1], Jiang, X.S. [1], Jiao, J.B. [20], Jin, D.P. [1], Jin, S. [1], Komamiya, S. [26], Kuehn, W., Lange, S. [28], Leung, J.K.C. [25], Li, Cheng [31], Li, Cui [31], Li, D.M. [36], Li, F. [1], Li, G. [1], Li, J. [1], Li, J.C. [1], Li, Lei [1], Li, Lu [1], Li, Q.J. [1], Li, W.D. [1], Li, W.G. [1], Li, X.L. [20], Li, X.N. [1], Li, X.Q. [17], Li, X.R. [1], Li, Y.X. [36], Li, Z.B. [23], Liang, H. [31], Liang, T.R. [17], Liang, Y.F. [22], Liang, Y.L. [28], Liao, X.T. [1], Liu, B.J. [24], Liu, C.L. [3], Liu, C.Y. [1], Liu, F. [1], Liu, F. [11], Liu, F.H. [21], Liu, G.C. [1], Liu, H. [1], Liu, H.B. [6], Liu, H.M. [1], Liu, H.W. [1], Liu, J. [1], Liu, J.P. [34], Liu, K. [18], Liu, K.Y. [14], Liu, Q. [29], Liu, S.B. [31], Liu, X.C. [1], Liu, X.H. [1], Liu, Y. [1], Liu, Y.B. [17], Liu, Y.F. [17], Liu, Y.W. [31], Liu, Z.A. [1], Lu, G.R. [10], Lu, J.G. [1], Lu, Q.W. [21], Lu, X.R. [6], Lu, Y.P. [1], Luo, C.L. [15], Luo, M.X. [35], Luo, T. [1], Luo, X.L. [1], Ma, C.L. [6], Ma, F.C. [14], Ma, H.L. [1], Ma, Q.M. [1], Ma, X. [1], Ma, X.Y. [1], Maggiora, M. [32], Mao, Y.J. [18], Mao, Z.P. [1], Min, J. [1], Mo, X.H. [1], Muchnoi, M.Y. [5], Nefedov, Y. [13], Ning, F.P. [21], Olsen, S.L. [19], Ouyang, Q. [1], Pelizaeus, M. [2], Peters, K. [7], Ping, J.L. [15], Ping, R.G. [1], Poling, R. [30], Pun, C.S.J. [25], Qi, M. [16], Qian, S. [1], Qiao, C.F. [6], Qiu, J.F. [1], Rong, G. [1], Ruan, X.D. [9], Sarantsev, A. [13], Shao, M. [31], Shen, C.P. [29], Shen, X.Y. [1], Sheng, H.Y. [1], Sonoda, S. [26], Spataro, S. [32], Spruck, B. [28], Sun, D.H. [1], Sun, G.X. [1], Sun, J.F. [10], Sun, S.S. [1], Sun, X.D. [1], Sun, Y.J. [31], Sun, Y.Z. [1], Sun, Z.J. [1], Sun, Z.T. [31], Tang, C.J. [22], Tang, X. [1], Tian, H.L. [1], Toth, D. [30], Varner, G.S. [29], Wan, X. [1], Wang, B.Q. [18], Wang, J.K. [1], Wang, K. [1], Wang, L.L. [4], Wang, L.S. [1], Wang, P. [1], Wang, P.L. [1], Wang, Q. [1], Wang, S.G. [18], Wang, X.D. [21], Wang, X.D. [31], Wang, X.L. [31], Wang, Y.F. [1], Wang, Y.Q. [20], Wang, Z. [1], Wang, Z.G. [1], Wang, Z.Y. [1], Wei, D.H. [8], Wen, S.P. [1], Wiedner, U. [2], Wu, L.H. [1], Wu, N. [1], Wu, Y.M. [1], Wu, Z. [1], Xiao, Z.J. [15], Xie, Y.G. [1], Xu, G.F. [1], Xu, G.M. [18], Xu, H. [1], Xu, M. [9], Xu, M. [31], Xu, X.P. [11], Xu, Y. [17], Xu, Z.Z. [31], Xue, Z. [31], Yan, L. [31], Yan, W.B. [31], Yan, Y.H. [12], Yang, H.X. [1], Yang, M. [1], Yang, P. [17], Yang, S.M. [1], Yang, Y.Y. [8], Ye, M. [1], Ye, M.H. [4], Yu, B.X. [1], Yu, C.X. [17], Yu, L. [11], Yuan, C.Z. [1], Yuan, Y. [1], Zeng, Y. [12], Zhang, B.X. [1], Zhang, B.Y. [1], Zhang, C.C. [1], Zhang, D.H. [1], Zhang, H.H. [23], Zhang, H.Y. [1], Zhang, J.W. [1], Zhang, J.Y. [1], Zhang, J.Z. [1], Zhang, L. [16], Zhang, S.H. [1], Zhang, X.Y. [20], Zhang, Y. [1], Zhang, Y.H. [1], Zhang, Z.P. [31], Zhao, C. [31], Zhao, H.S. [1], Zhao, J. [31], Zhao, J.W. [1], Zhao, L. [1], Zhao, L. [31], Zhao, M.G. [17], Zhao, Q. [1], Zhao, S.J. [36], Zhao, T.C. [33], Zhao, X.H. [16], Zhao, Y.B. [1], Zhao, Z.G. [31], Zhemchugov, A. [13], Zheng, B. [1], Zheng, J.P. [1], Zheng, Y.H. [6], Zheng, Z.P. [1], Zhong, B. [15], Zhong, J. [2], Zhou, L. [1], Zhou, Z.L. [1], Zhu, C. [1], Zhu, K. [1], Zhu, K.J. [1], Zhu, Q.M. [1], Zhu, X.W. [1], Zhu, Y.S. [1], Zhu, Z.A. [1], Zhuang, J. [1], Zou, B.S. [1], Zou, J.H. [1], Zuo, J.X. [1], Zweber, P. [30]

1 Institute of High Energy Physics, Beijing China
2 Bochum Ruhr-University, Bochum Germany
3 Carnegie Mellon University, Pittsburgh USA
4 China Center of Advanced Science and Technology, Beijing China
5 G.I. Budker Institute of Nuclear Physics SB RAS (BINP), Novosibirsk Russia
6 Graduate University of Chinese Academy of Sciences, Beijing China
7 GSI Helmholtzzentrum für Schwerionenforschung GmbH, Darmstadt Germany
8 Guangxi Normal University, Guilin China
9 Guangxi University, Naning China
10 Henan Normal University, Xinxiang China
11 Huazhong Normal University, Wuhan China
12 Hunan University, Changsha China
13 Joint Institute for Nuclear Research, Dubna Russia
14 Liaoning University, Shenyang China
15 Nanjing Normal University, Nanjing China
16 Nanjing University, Nanjing China
17 Nankai University, Tianjin China
18 Peking University, Beijing China
19 Seoul National University, Seoul Korea
20 Shandong University, Jinan China
21 Shanxi University, Taiyuan China
22 Sichuan University, Chengdu China
23 Sun Yat-Sen University, Guangzhou China
24 The Chinese University of Hong Kong, Shatin Hong Kong
25 The University of Hong Kong, Pokfulam Hong Kong
26 The University of Tokyo, Tokyo Japan
27 Tsinghua University, Beijing China
28 Justus-Liebig-Universität Gießen, Gießen Germany
29 University of Hawaii, Honolulu USA
30 University of Minnesota, Minneapolis USA
31 University of Science and Technology of China, Hefei China
32 University of Turin and INFN, Turin Italy
33 University of Washington, Seattle USA

34 Wuhan University, Wuhan China
35 Zhejiang University, Hangzhou China
36 Zhengzhou University, Zhengzhou China

BioMat

Spokesperson: Durante, M.

AMS-Project [8], Bettega, D. [11], Cirio, R. [5], Durante, M. [12], Kraft, G. [12], Krasavin, E. [6], Mewaldt, R. [1], Miller, J. [7], Narici, L. [13], Okayasu, R. [9], O'Sullivan, D. [4], Picozza, P. [13], Reitz, G. [3], Ritter, S. [12], Schardt, D. [12], Scholz, M. [12], Schuhmacher, H. [10], Sihver, L. [2], Valtonen, E. [14]

1 CALTECH, Space Radiation Laboratory (USA)
2 Chalmers Univ. of Technology, Nuclear Science and Engineering (SWEDEN)
3 DLR Köln (GERMANY)
4 Dublin Institute for Advanced Studies (IRELAND)
5 INFN Torino (ITALY)
6 JINR Dubna (RUSSIA)
7 LBL Berkeley (USA)
8 Massachusetts Institute of Technology (USA)
9 NIRS Chiba (JAPAN)
10 PTB Braunschweíg (GERMANY)
11 University of Milano (ITALY)
12 GSI-Darmstadt (GERMANY)
13 Univ. of Rome (ITALY)
14 Univ. of Turku (FINNLAND)

CARAT

Spokesperson: Berdermann, E.

Berdermann, E. [1], Bergonzo, P. [11], Connell, S. H. [19], de Boer, W. [10], Golser, R. [8], Graafsma, H. [9], Liechtenstein, V. [16], Lohmann, W. [3], Morse, J. [13], Nebel, C. [15], Nesladek, M. [12], O'Shea, V. [7], Petrovici, M. [6], Pucci, A. [5], Pullia, A. [14], Schreck, M. [4], Sellin, P. [17], Stolz, A. [18], Verona-Rinati, G. [2]

1 GSI Helmholtzzentrum für Schwerionenforschung GmbH, Darmstadt, Germany
2 INFN Sezione di Roma 2, Italy
3 DESY-Zeuthen, Germany
4 University of Augsburg, Germany
5 University of Heidelberg, Germany
6 IFIN-HH Bucharest, Romania
7 University of Glasgow, UK
8 VERA Laboratory Vienna, Austria
9 Hasylab, Hamburg, Germany
10 KIT Karlsruhe, Germany
11 CEA/LIST Saclay, France
12 Limburgs University Centre, Belgium
13 ESRF Grenoble, France
14 Università e Sezione INFN di Milano, Italy
15 Fraunhofer Institut für Angewandte Festkörperforschung, Germany
16 Kurchatov Institute, Moscow, Russia
17 University of Surrey, UK
18 MSU East-Lansing, USA
19 University of the Witwatersrand, Johannesburg, South Afrika

CBM

Spokesperson: Senger, P.
http://www.iop.org/EJ/article/0954-3899/35/10/109803/g8_10_109803.pdf?request-id=ecddcbd5-641a-4e52-9b84-a41f9b059a12

Department of Physics, Aligarh Muslim University India
Department of Physics and Technology, University of Bergen Norway
Institute of Physics India
National Institute for Physics and Nuclear Engineering (NIPNE) Romania
Atomic and Nuclear Physics Department, University of Bucharest Romania
Eötvös University Hungary
KFKI Research Institute for Particle and Nuclear Physics (KFKI-RMKI) Hungary
Department of Physics, Panjab University India
Laboratório de Instrumentacao e Física Experimental de Partículas (LIP) Portugal
Gesellschaft für Schwerionenforschung (GSI) Germany
Institut für Strahlenphysik, Forschungszentrum Dresden-Rossendorf (FZD) Germany
Veksler and Baldin Laboratory of High Energies, Joint Institute for Nuclear Research (JINR-VBLHE): Russia
Laboratory of Particle Physics, Joint Institute for Nuclear Research (JINR-LPP) Russia
Laboratory of Information Technologies Joint Institute for Nuclear Research (JINR-LIT): Russia
Institut für Kernphysik, Universität Frankfurt Germany
Petersburg Nuclear Physics Institute (PNPI) Russia
Department of Modern Physics, University of Science & Technology of China (USTC) China
Kirchhoff-Institut für Physik, Universität Heidelberg (KIP) Germany
Physikalisches Institut, Universität Heidelberg Germany

Zentrales Institut für Technische Informatik, Universität Heidelberg Germany
Physics Department, University of Rajasthan India
Department of Physics, University of Jammu India
Institute of Nuclear Physics And Its Application, University of Silesia Poland
Department of Physics and Meteorology, Indian Institute of Technology India
High Energy Physics Division, Saha Institute of Nuclear Physics India
Department of Physics and Department of Electronic Science, University of Calcutta India
Variable Energy Cyclotron Centre (VECC) India
"AGH University of Science
and Technology Poland"
Marian Smoluchowski Institute of Physics, Jagiellonian University Poland
Department of Nuclear Physics, National Taras Shevchenko University of Kyiv Ukraine
Institute for Nuclear Research (INR) Russia
Alikhanov Institute for Theoretical and Experimental Physics (ITEP) Russia
Lomonosov Moscow State University (SINP-MSU) Russia
Kurchatov Institute Russia
Moscow Engineering Physics Institute (MEPhI) Russia
Institut für Kernphysik, Westfälische Wilhelms Universität Münster Germany
University of Cyprus Cyprus
Obninsk State Technical University for Nuclear Power Engineering Russia
Czech Technical University (CTU) Czech Republic
Institute for High Energy Physics (IHEP) Russia
Pusan National University (PNU) Korea
"Nuclear Physics Institute, Academy of Sciences of the Czech
Republic Czech Republic"
Department of Physics, Korea University Korea
University of Split Croatia
Department of Physics, University of Kashmir India
V.G. Khlopin Radium Institute (KRI) Russia
St. Petersburg State Polytechnic University (SPbSPU) Russia
"(IPHC), IN2P3-CNRS and
Univesit´e Louis Pasteur Strasbourg France"
Department of Physics, Banaras Hindu University India
Institute of Experimental Physics, Warsaw University Poland
Institute of Particle Physics, Hua-zhong Normal University China
Rudjer Boskovic Institute Croatia

Charms

Spokesperson: A.Kelic-Heil

Armbruster, P. [1], Audouin, L. [3], Bacquias A. [6], Benlluire, J. [2], Bernas, M. [3], Botvina, A. [15], Boudard, A. [4], Casarejos, E. [2], Danielewicz, P. [11], Ducret, J.-E. [4], Enqvist, T. [18], Foehr, V. [1], Heinz, A. [13], Helariutta, K. [17], Henzl, V. [12], Henzlova, D. [12], Ignatyuk, A. [14], Junghans, A. [9], Jurado, B. [6], Karpov, A. [16], Kelic-Heil, A. [1], Kurtukian, T. [6], Leray, S. [4], Lukic, S. [10], Lunev, V. [14], Nadtchoky, P. [14], Napolitani, P. [7], Pereira, J. [11], Pleskac, E. [1], Rejmund, F. [7], Ricciardi, M.V. [1], Schmidt, K.-H. [1], Schmitt, C. [5], Stephan, C. [3], Taieb, L. [8], Tassan-Got, L. [3], Yordanov, O. [19]

1 GSI - Helmholtzzentrum für Schwerionenforschung mbH, Darmstadt, Germany
2 University of Santiago de Compostela, Spain
3 Institute de Physique Nuclaire, Orsay, France
4 CEA Saclay,DAPNIA/SPhN, Bruyere le Chatel, France
5 IPNL, Universite Lyon, Lyon, France
6 CENBG, Bordeaus-Gradignan, France
7 GANIL, Caen, France
8 CEA Saclay, DEN/DM2S/SERMA/LENR, Bruyere le Chatel, France
9 Forschungszentrum Rossendorf, Rossendorf, Germany
10 Forschungszentrum Karlsruhe, Karlsruhe,, Germany
11 NSCL, Michigan State University, East Lansing, USA
12 LANL, Los Alamos, New Mexico, USA
13 Yale University, Yale, USA
14 IPPE, Obninsk, Russia
15 INR RAS Moscow, Russia
16 Joint Institut of Nuclear Research (JINR), Dubna, Russia
17 University of Helsinki, Helsinki, Finland
18 CUPP Project, Pysalmi, Finland
19 Sofia University, Sofia, Bulgaria

DESPEC

Spokesperson: B. Rubio

Aeystö, Juha [24], Algora, Alejandro [1], Angulo, Carmen [12], Back, Tobjorn [10], Batist, Leonid [16], Bhattacharya, Chandana [32], Blank, Bertram [3], Cata-Danil, Gheorghe [17], Doncel, Maria [28], Engert, Tobias [5], Erduran, Nizamettin [8], Faestermann, Thomas [19], Gerl, Jürgen [5], Górska, Magdalena [5], Harissopulos, Sotirios [14], Huyse, Mark [11], Iordachescu, Alexandru [15], Jan, Saren [9], Johnson, Arne [29], Jokinen, Ari [24], Jolie, Jan [21], Jungclaus, Andrea [4], Kettunen, Heikki [24], Kratz, Karl-

Ludwig [26], Leino, Matti [24], Maj, Adam [7], Negret, Alexandru [15], Nociforo, Chiara [5], Nyberg, Johan [31], Page, R. D. [25], Penttillae, Heikki [24], Pfützner, Marek [33], Plaß, Wolfgang [23], Regan, Patrick [30], Reiter, Peter [21], Rinto-Antila, Sami [20], Rubio, Berta [6], Rudolph, Dirk [13], Sagrado Garcia, Inmaculada [28], Sarkar, Maitreyee [18], Scheidenberger, Christoph [5], Scholey, Catherine [24], Simpson, John [2], Spohr, Klaus [27], Uusitalo, Juha [24], Walker, Philip [30], Woods, Phil [22], Zamfir, Victor [15]

1 ATOMKI Debrecen, Hungary
2 CCLRC Daresbury, United Kingdom
3 CENBG Bordeaux, France
4 CSIC Madrid, Spain
5 GSI - Helmholtzzentrum für Schwerionenforschung mbH, Darmstadt, Germany
6 IFIC Valencia, Spain
7 IFJ PAN Krakow, Poland
8 Istanbul University, Turkey
9 JYFL, Finland
10 KTH Stockholm, Sweden
11 KU Leuven, Belgium
12 Louvain-la-Neuve, Belgium
13 Lund University, Sweden
14 NCSR Athens, Greece
15 NIPNE Bucharest, Romania
16 PNPI Gatchina, Russia
17 Politechnical University of Bucharest, Romania
18 Saha Inst. Kolkata, India
19 TU Munich, Germany
20 Univ. Liverpool, United Kingdom
21 University of Cologne, Germany
22 University of Edinburgh, United Kingdom
23 University of Giessen, Germany
24 University of Jyväskylä, Finland
25 University of Liverpool, United Kingdom
26 University of Mainz, Germany
27 University of Paisley, United Kingdom
28 University of Salamanca, Spain
29 University of Stockholm, Sweden
30 University of Surrey, United Kingdom
31 Uppsala University, Sweden
32 VECC Kolkata, India
33 Warsaw University, Poland

E114 - Chemistry

Spokesperson: A. Yakushev

Ackermann, D. [1], Düllmann, C.E. [1], Eberhardt, K. [3], Even, J. [3], Gates, J. [2], Gorshkov, A, [2], Graeger, R. [2], Heßberger, F.P. [1], Hild, D. [3], Hübner, A. [1], Jäger, E. [1], K. Nishio [8], Khuyagbaatar, J. [1], Kindler, B. [1], Kratz, J.V. [3], Krier, J. [1], Lahiri, S. [6], Lommel, B. [1], Nayak, D. [6], Omtvedt, J.P. [5], Pershina, V. [1], Runke, J. [3], Samadani, F. [5], Schädel, M. [1], Schausten, B. [1], Schimpf, E. [1], Steiner, J. [1], Thörle-Pospiech, P. [3], Türler, A. [2], Türler, A. [4], Türler, A. [7], Wiehl, N. [3], Yakushev, A. [2]

1 GSI - Helmholtzzentrum für Schwerionenforschung mbH, Darmstadt, Germany
2 Institut für Radiochemie, Technische Universität München, Garching, Germany
3 Institut für Kernchemie, Johannes-Gutenberg Universität, Mainz, Germany
4 Labor für Radio- und Umweltchemie, PSI, Villigen, Switzerland
5 University of Oslo, Oslo, Norway
6 SAHA Institute Of Nuclear Physics, Kolkata, India
7 Univ. Bern, Bern, Switzerland
8 JAEA, Tokai-mura, Ibaraki, Japan

E114 – Physics

Spokesperson: C.E.Düllmann

Ackermann, D. [1], Andersson, L.-L. [10], Block, M. [1], Brüchle, W. [1], Düllmann, C.E. [1], Dvorak, J. [6, 13], Eberhardt, K. [3], Ellison, P. [6, 13], Essel, H. [1], Even, J. [3], Gates, J. [2], Gorshkov, A, [2], Graeger, R. [2], Gregorich, K.E. [6], Hartmann, W. [1], Herzberg, R.-D. [10], Heßberger, F.P. [1], Hild, D. [3], Hübner, A. [1], Jäger, E. [1], Khuyagbaatar, J. [1], Kindler, B. [1], Kratz, J.V. [3], Krier, J. [1], Kurz, N. [1], Lahiri, S. [12], Liebe, D. [3], Lommel, B. [1], Maiti, M. [12], Nitsche, H. [6, 13], Omtvedt, J.P. [7], Parr, E. [10], Pershina, V. [1], Rudolph, D. [9], Runke, J. [3], Schädel, M. [1], Schausten, B. [1], Schimpf, E. [1], Semchenkov, A. [8], Steiner, J. [1], Thörle-Pospiech, P. [3], Türler, A. [2, 4, 14], Uusitalo, J. [5], Wegrzecki, M. [15], Wiehl, N. [3], Yakushev, A. [2], Zhin, Q. [11]

1 GSI - Helmholtzzentrum für Schwerionenforschung mbH, Darmstadt,-Germany
2 Institut für Radiochemie, Technische Universität München, Garching,-Germany
3 Institut für Kernchemie, Johannes-Gutenberg Universität, Mainz,-Germany
4 Labor für Radio- und Umweltchemie, PSI, Villigen,-Switzerland
5 University of Jyväskylä, Jyväskylä,-Finland
6 Nuclear Science Division, LBNL, Berkeley,-USA
7 University of Oslo, Oslo,-Norway
8 Nuclear Science Division, LBNL, Berkeley,-Norway
9 University of Lund, Lund,-Sweden
10 University of Liverpool, Liverpool,-United Kingdom
11 Institute of Modern Physics, Lanzhou,-China
12 SAHA Institute Of Nuclear Physics, Kolkata,-Indien
13 University of California, Berkeley,-USA

14 Univ. Bern, Bern,-Switzerland 15 ITE, Warsaw,-Poland

ELISe

Spokesperson: Simon, H.

Adachi, Tatsuya [18], Aïche, Mourad [5], Al-Khalili, Jim [34], Alvarez Rodriguez, Raquel [8], Amaro Soriano, Jose Enrique [11], Antonov, Anton N. [14], Artukh, Anatoly [17], Audouin, Laurent [15], Aumann, Thomas [12], Avdeichikov, Vladimir [19], Barreau, Gérard [5], Barton, Charles [35], Belier, Gilbert [3], Berthoumieux, Eric [4], Bertulani, Carlos [24], Boretzky, Konstanze [12], Borge, Maria José [8], Caballero, Juan Antonio [33], Catford, Wilton [34], Chartier, Marielle [30], Chatillon, Audrey [3], Chulkov, Leonid [23], Cullen, David [32], Czajkowski, Serge [5], Danilin, Boris [23], Distler, Michael O. [31], Dolinskii, Alexei [12], Doré, Diane [4], Dupont, Emmeric [4], Egelhof, Peter [12], Emling, Hans [12], Enders, Joachim [25], Ershov, Sergey N. [17], Fernandez Ramirez, Cesar [8], Fomichev, Andrey [17], Fraile Prieto, Luis Mario [26], Franzke, Bernhard [12], Fujiwara, Mamoru [20], Gaidarov, Mitko K. [14], Garrido, Eduardo [8], Geissel, Hans [12], Golovkov, Mikhail [17], Gorshkov, Alexandr Vladimirovich [17], Granier, Thierry [3], Grigorenko, Leonid [17], Grishkin, Yuji [13], Harakeh, Muhsin [18], Heinz, Andreas [36], Hencken, Kai [27], Ivanov, Martin V. [14], Jenkins, David [35], Johansson, Håkan [6], Johnson, Ron [34], Jonson, Björn [6], Jourdan, Juerg [27], Junghans, Arnd [9], Jurado, Beatriz [5], Kadrev, Dimitre N. [14], Kalantar-Nayestanaki, Nasser [18], Kamerdzhiev, Sergey Pavlovich [16], Karataglidis, Steven [21], Kato, Seigo [37], Kelic-Heil, Aleksandra [12], Kester, Oliver [12], Khan, Elias [15], Klygin, Sergey [17], Koop, Ivan A. [1], Korsheninnikov, Alexei [23], Krupko, Sergey [17], Krusche, Bernd [27], Kurz, Nikolaus [12], Kuzmin, Eugenii [23], Lallena Rojo, Antonio M. [11], Lemmon, Roy [2], Lenske, Horst [29], Letourneau, Alain [4], Lisin, Valery P. [13], Litvinov, Yuri [12], Litvinova, Elena V. [12], Logatchov, Pavel V. [1], Lopez Herraiz, Joaquin [26], Merkel, Harald [31], Meshkov, Igor Nikolaevitch [17], Moya de Guera, Elvira [26], Müller, Ulrich [31], Münzenberg, Gottfried [12], Mushkarenkov, Alexander Nikolaevich [13], Nedorezov, Vladimir [13], Nilsson, Thomas [6], Nolden, Fritz [12], Nyman, Goran [6], Otboev, Aleksej V. [1], Panebianco, Stefano [4], Parkhomchuk, Vasily V. [1], Pietralla, Norbert [25], Polonski, Andrey Leonidovich [13], Rauscher, Thommy [27], Rejmund, Fanny [10], Richter, Achim [25], Ridikas, Danas [4], Rodin, Alexander [17], Rodriguez Vignote, Javier [12], Rohe, Daniela [27], Rudnev, Nikolay V. [13], Sarriguren, Pedro [8], Schmidt, Karl-Heinz [12], Schmitt, Christelle [10], Schrieder, Gerhard [25], Seleznev, I.A. [17], Sereda, Yuri [17], Shatilov, Dmitry N. [1], Shatunov, Yury M. [1], Shiyankov, Sergej V. [1], Sidorchuk, Sergey [17], Simon, Haik [12], Skrinsky, Alexandr N. [1], Steck, Markus [12], Stepantsov, Sergey [17], Stevenson, Paul [34], Suda, Toshimi [22], Syresin, E.M. [17], Taieb, Julien [3], Tassan-Got, Laurent [15], Ter-Akopian, Gurgen [17], Teterev, Yuri [17], Trautmann, Dirk [27], Turinge, Andrey Arisovich [13], Udias-Moinelo, Jose [7], Volkov, Vasiliy A. [23], Vorontsov, Andrey N. [17], Weick, Helmut [12], Woertche, Heinrich [18], Zhukov, Mikhail [6], Zilges, Andreas [28]

1 BINP Novosibirsk, Russia
2 CCLRC Daresbury, United Kingdom
3 CEA Bruyeres-le-Chatel, France
4 CEA Saclay/ IRFU, France
5 CENBG, France
6 Chalmers University of Technology, Sweden
7 Complutense University of Madrid, Spain
8 CSIC Madrid, Spain
9 FZ Rossendorf, Germany
10 GANIL, Caen, France
11 Granada University, Spain
12 GSI - Helmholtzzentrum für Schwerionenforschung mbH, Darmstadt, Germany
13 INR RAS Moscow, Russia
14 INRNE BAS Sofia, Bulgaria
15 IPN Orsay, France
16 IPPE Obninsk, Russia
17 JINR Dubna, Russia
18 KVI Groningen, The Netherlands
19 Lund University, Sweden
20 RCNP Osaka, Japan
21 Rhodes University Grahamstown, South Africa
22 RIKEN, Japan
23 RRC Kurchatov Institute Moscow, Russia
24 Texas A&M University - Commerce, USA
25 TU Darmstadt, Germany
26 Universidad Complutense de Madrid, Spain
27 University of Basel, Switzerland
28 University of Cologne, Germany
29 University of Giessen, Germany
30 University of Liverpool, United Kingdom
31 University of Mainz, Germany
32 University of Manchester, United Kingdom
33 University of Sevilla, Spain
34 University of Surrey, United Kingdom
35 University of York, United Kingdom
36 Yale University, USA
37 Yamagata University, Japan

EXL

Spokesperson: Chartier, M.

Algora, Alejandro [1], Al-Khalili, Jim [38], Alkhasov, Georgij [20], Alvarez Rodriguez, Raquel [7], Artukh, Anatoly [14], Aumann, Thomas [9], Avdeichikov, Vladimir [17], Beaumel, Didier [13], Bhattacharya, Sudeb [23], Blumenfeld, Yorick [13], Böhmer, Michael [28], Boretzky, Konstanze [9], Bortignon, Pierfrancesco [11], Bracco, Angela [36], Catford, Wilton [38], Chartier,

Marielle [34], Chulkov, Leonid [22], Coleman-Smith, Patrick [4], Colo, Gianluca [11], Creswell, John [34], Csatlos, Margit [1], Datta Pramanik, Ushasi [23], Davinson, Tom [31], Dolinskii, Alexei [9], Dörner, Reinhard [32], Egelhof, Peter [9], Ekström, Curt [25], Emling, Hans [9], Enders, Joachim [27], Eränen, Simo [24], Eremin, Vladimir [12], Faestermann, Thomas [28], Feldmeier, Hans [9], Fernandez Dominguez, Beatriz [34], Fernandez Ramirez, Cesar [7], Fomichev, Andrey [14], Fraile Prieto, Luis Mario [29], Franczak, Bernhard [9], Freer, Martin [3], Fujita, Yoshitaka [19], Gacsi, Zoltan [1], Garrido, Eduardo [7], Geissel, Hans [9], Gerl, Jürgen [9], Gernhäuser, Roman [28], Golovkov, Mikhail [14], Golovtsov, Victor [20], Golubev, Pavel [17], Grisenti, Robert [32], Grzonka, Dieter [8], Gulyas, Janos [1], Gusev, Yuri [20], Harakeh, Muhsin [16], Heil, Michael [9], Hencken, Kai [30], Hunyadi, Matyas [1], Ilieva, Stoyanka [9], Isaksson, Lennart [17], Jakobsson, Bo [17], Johnson, Eon [38], Jonson, Björn [5], Kailas, S. [2], Kalantar-Nayestanaki, Nasser [16], Kalliopuska, Juha [24], Kanungo, Rituparna [26], Khan, Elias [13], Khanzadeev, Alexei [20], Khusainov, Abdurachman [20], Kienle, Paul [28], Kisselev, Oleg [21], Klygin, Sergey [14], Kononenko, Genadiy [14], Korsheninnikov, Alexei [22], Kozhuharov, Christophor [9], Krasznahorkay, Attila [1], Kratz, Jens Volker [35], Krings, Thomas [8], Kroell, Thorsten [27], Krücken, Reiner [28], Krupko, Sergey [14], Krusche, Bernd [30], Lazarus, Ian [4], Le, Xuan Chung [9], Lemmon, Roy [4], Lepine-Szily, Alinka [37], Leske, Jörg [27], Letts, Simon [4], Litvinov, Yuri [9], Lopez Herraiz, Joaquin [29], Mahjour-Shafiei, Masoud [39], Maier, Ludwig [28], Martinez-Perez, Cristina [7], Moeini, Hussein [16], Möller, Oliver [27], Moreno, Oscar [7], Moya de Guera, Elvira [29], Murin, Yurij [15], Mutterer, Manfred [9], Neff, Thomas [9], Nilsson, Thomas [5], Nociforo, Chiara [9], Nolden, Fritz [9], Nyman, Goran [5], Ogloblin, Aleksey [22], Peschke, Claudius [9], Peyre, Jean [13], Pietralla, Norbert [27], Plaß, Wolfgang [33], Popescu, L.A. [16], Popp, Ulrich [9], Pouthas, Joel [13], Prokofiev, Alexander [25], Protic, Davor [8], Pucknell, Vic [4], Pusttovoit, A. [20], Rathmann, Frank [8], Rauscher, Thommy [30], Reich-Sprenger, Hartmut [9], Reifarth, Rene [9], Rigollet, Catherine [16], Rodin, Alexander [14], Rodriguez Vignote, Javier [9], Rossi, Dominic [9], Sarriguren, Pedro [7], Savran, Deniz [27], Scarpaci, Jean-Antoine [13], Scheidenberger, Christoph [9], Schrieder, Gerhard [27], Seliverstov, Dmitri [20], Sereda, Yuri [14], Shevchik, E. [14], Shrivastava, Aradhana [2], Sidorchuk, Sergey [14], Simon, Haik [9], Skaza, Flore [13], Steck, Markus [9], Stevenson, Paul [38], Stoehlker, Thomas [9], Streicher, Brano [9], Stroth, Joachim [32], Sümmerer, Klaus [9], Sun, Zhiyu [10], Suzuki, Ken [28], Teterev, Yuri [14], Thielemann, Friedel [30], Thornhill, Jim [34], Thungstrom, Goran [18], Tuboltsev, Yuri [12], Typel, Stefan [9], Udias-Moinelo, Jose [6], Verbitskaya, Elena [12], Von Schmid, Mirko [35], Vorontsov, Andrey N. [14], Weick, Helmut [9], Westerberg, Lars [25], Winkler, Martin [9], Woertche, Heinrich [16], Woods, Phil [31], Xiao, Guoqing [10], Zalite, Andrej [20], Zerguerras, Thomas [13]

1 ATOMKI Debrecen, Hungary
2 BARC Mumbai, India
3 Birmingham University, United Kingdom
4 CCLRC Daresbury, United Kingdom
5 Chalmers University of Technology, Sweden
6 Complutense University of Madrid, Spain
7 CSIC Madrid, Spain
8 FZ Jülich, Germany
9 GSI - Helmholtzzentrum für Schwerionenforschung mbH, Darmstadt, Germany
10 IMP Lanzhou, China
11 INFN Milan, Italy
12 Ioffe PTI St.Petersburg, Russia
13 IPN Orsay, France
14 JINR Dubna, Russia
15 Khlopin Radium Institute St. Petersburg, Russia
16 KVI Groningen, The Netherlands
17 Lund University, Sweden
18 Mid Sweden University, Sweden
19 Osaka University, Japan
20 PNPI Gatchina, Russia
21 PSI Villigen, Switzerland
22 RRC Kurchatov Institute Moscow, Russia
23 SINP Kolkata, India
24 Technical Research Center of Finland, Finland
25 The Svedberg Laboratory, Sweden
26 TRIUMF, Canada
27 TU Darmstadt, Germany
28 TU Munich, Germany
29 Universidad Complutense de Madrid, Spain
30 University of Basel, Switzerland
31 University of Edinburgh, United Kingdom
32 University of Frankfurt, Germany
33 University of Giessen, Germany
34 University of Liverpool, United Kingdom
35 University of Mainz, Germany
36 University of Milan, Italy
37 University of Sao Paulo, Brasilia
38 University of Surrey, United Kingdom
39 University of Tehran, Iran

The FLAIR Collaboration

Spokesperson: E. Widmann

Andler, G. [39], Bagge, L. [39], Balashov, V.V. [37], Barna, D. [18], Bassalleck, B. [50], Beier, T. [8], Beyer, H. [8], Blaum, K. [15], Bloch, I. [15], Block, M. [8], Borneis, S. [8], Bosch, F. [8], Boucard, S. [7], Bräuning-Demian, A. [8], Bühler, P. [1], Bureyeva, L.A. [34], Burgdörfer, J. [2], Cargnelli, M. [1], Charlton, M. [43], Corradini, M. [23], Cozhuharov, C. [7], Danared, H. [39], Dax, A. [25], Djekic, S. [15], Dörner, R. [11], Eikema, K.S.E. [40], Engström. M. [39], Franzke, B. [7], Fujiwara, M. C. [3], Gabrielse, G. [46], George, S. [15], Gillitzer, A. [13], Gotta, D. [13], Grzonka, D. [13], Hagmann, S. [7], Hayano, R.S. [25], Herfurth, F. [7], Hessels, E. A. [4], Hogervorst, W. [40], Holzscheiter, M.H. [50], Hori, M. [25], Horváth, B. [17], Horvath, D. [18], Indelicato, P. [7], Ishikawa, T. [25], Jastrzebski, [29], Juhasz, B. [1,17], Källberg, A. [39], Kanai, Y. [24], Karshenboim, S. G. [31], Kellerbauer, A. [7], Kienle, P. [1],

Kilian, K. [13], Kingsberry, P. [50], Kluge, H.-J. [7], Knudsen, H. [5], Kobets, A. [36], Komaki, K.-I. [26], Korotaev, Yu. [36], Kostelecky, Alan [47], Kühl, T. [7], Kuroda, N. [24], Labzowsky, L.N. [32], Le Bigot, É.-O. [7], Leali, M [23], Lemell, C. [2], Liesen, D. [7], Liljeby, L. [39], Lindroth, E. [38], Lodi Rizzini, E. [23], Löfgren, P. [39], Maggiore, C. [48], Mann, R. [7], Marton, H. [1], McCollough, R. [44], Meshkov, I. [36], Minaev, S. [35], Mohri, A. [24], Mokler, P. [7], Møller, S. P. [6], Müller, A. [12], Myers, E.G. [45], Nagata, Y. [24], Nefiodov, A.V. [33], Nolden, F. [7], Noordam, C. [41], Nörtershäuser, W. [15], Oelert, W. [13], Orth, H. [7], Paál, A. [39], Pachucki, K. [30], Plunien, G. [9], Quint, W. [7], Ratzinger, U. [10], Ray, A. [20], Rensfelt, K.-G. [39], Ritman, J. [13], Saenz, A. [16], Saito, H. [24], Schempp, A. [10], Schuch, R. [38], Schuessler, Hans A. [49], Segal, D.M. [42], Seleznev, I. [36], Shabaev, V.M. [32], Shibata, M. [24], Sidorin, A. [36], Simonsson, A. [39], Skeppstedt, Ö. [39], Smirnov, A. [36], Soff, G. [9], Stahl, S. [15], Steck, M. [7], Stöhlker, T. [7], Syresin, E. [36], Takacs, E. [19], Takács, E. [17], Takési, K. [17], Testera, G. [22], Thompson, R.C. [42], Tino, G. M. [21], Tomaselli, M. [7], Torii, H.A. [26], Trubnikov, G. [36], Trzcinska, A. [29], Ubachs, W. [40], Uggerhoj, U.I. [5], Venturelli, L. [23], Verdu, J. [15], Vogel, M. [15], Wada, M. [24], Walz, J. [15], Weber, C. [15], Werth, G. [15], Widmann, E. [1], Wolf, A. [14], Wycech, S. [28], Yakovenko, S. [36], Yamazaki, Y. [27], Yoshida, S. [2], Zmeskal, H. [1], Zurlo, N. [23]

1 Stefan Meyer Institut für subatomare Physik, Österreichische Akademie der Wissenschaften, Wien (Austria)
2 Institute for Theoretical Physics, Vienna University of Technology (Austria)
3 TRIUMF National Laboratory, Vancouver (Canada)
4 Department of Physics and Astronomy, York University, Toronto (Canada)
5 Department of Physics and Astronomy, Aarhus University (Denmark)
6 Institute for Storage Ring Facilities, Aarhus University (Denmark)
7 École Normale Supérieure et Université P. et M. Curie, Laboratoire Kastler-Brossel, Paris (France)
8 GSI Darmstadt (Germany)
9 Institut für theoretische Physik, Technische Universität Dresden (Germany)
10 Institut für Angewandte Physik, Universität Frankfurt (Germany)
11 Institut für Kernphysik, Universität Frankfurt (Germany)
12 Institut für Kernphysik, Universität Giessen ()
13 Forschungszentrum Jülich GmbH, FZJ (Germany)
14 Max-Planck Institut für Kernphysik, Heidelberg (Germany)
15 Johannes-Gutenberg-Universität Mainz, Institut für Physik (Germany)
16 Institut für Physik, Humboldt-Universität zu Berlin (Germany)
17 Institute of Nuclear Research of the Hungarian Academy of Sciences (ATOMKI), Debrecen (Hungary)
18 KFKI Research Inst. for Particle and Nuclear Physics, Budapest (Hungary)
19 Department of Experimental Physics, University of Debrecen (Hungary)
20 Variable Energy Cyclotron Center, Kolkata (India)
21 Dipartimento di Fisica, Laboratorio LENS, INFN, Universita' degli Studi di Firenze (Italy)
22 Istituto Nazionale di Fisica Nucleare, INFN Genova (Italy)
23 Dipartimento di Chimica e Fisica per l'Ingegneria e per i Materiali-Universita' di Brescia & INFN-Gruppo Collegato di Brescia (Italy)"
24 RIKEN, Wako, Atomic Physics Laboratory (Japan)
25 University of Tokyo, Department of Physics (Japan)
26 University of Tokyo, Institute of Physics (Japan)
27 Institute of Physics, University of Tokyo, and Atomic Physics Laboratory, RIKEN, Wako (Japan)
28 Soltan Institute for Nuclear Studies, IPJ, Warsaw (Poland)
29 Warsaw University, Heavy Ion Laboratory (Poland)
30 Warsaw University, Institute of Theoretical Physics (Poland)
31 D.I. Mendeleev Institute for Metrology (VNIIM), St. Petersburg (Russia)
32 Department of Physics, St. Petersburg State University (Russia)
33 St. Petersburg Nuclear Physics Institute (Russia)
34 Institute of Spectroscopy of the RAS, Troitsk (Russia)
35 Institute for Experimental and Theoretical Physics, Moskva (Russia)
36 JINR Dubna (Russia)
37 Institute of Nuclear Physics, Moscow State University (Russia)
38 Stockholm Universitet, Department of Atomic Physics (Sweden)
39 Manne Siegbahn Laboratory (MSL), Stockholm (Sweden)
40 Laser Centre Vrije Universiteit, LCVU, Amsterdam, Department of Physics and Astronomy (The Netherlands)
41 FOM Institute for Atomic and Molecular Physics, Amsterdam (The Netherlands)
42 Imperial College, London, Dept. of Physics, Blackett Lab. (United Kingdom)
43 University of Wales Swansea, Department of Physics (United Kingdom)
44 Queen's University, Belfast (United Kingdom)
45 Florida State University, Tallahassee, Department of Physics (USA)

46 Department of Physics, Harvard University, Cambridge, Massachusetts (USA)
47 Indiana University, Bloomington, Indiana (USA)
48 Pbar Labs, LLC Santa Fe, New Mexiko (USA)
49 Department of Physics, Texas A&M University, College Station, Texas (USA)
50 University of New Mexico, Albuquerque (USA)

FOPI

Spokesperson: Herrmann, N.

Basrak, Z. [1], Bastid, N. [2], Fabbietti, L. [3], Fodor, Z. [4], Herrmann, N. [5], Hong, B. [6], Kotte, R. [7], Matulewicz, T. [8], Petrovici, M. [9], Rami, F. [10], Wiedmann, E. [11], Yushmanov, I. [12], Zhilin, A. [13]

1 Institute for Theoretical and Experimental Physics, ITEP, Moscow, Russia
2 Warsaw University,Institut of Experimental Physics, Nuclear Physics Division, Poland
3 RBI Zagreb,, Kroatia
4 Korea University, Seoul, Department of Physics, Korea
5 NIPNE National Institute for Physics and Nuclear Engineering, NIPNE, Bucharest, Romania
6 Institut de Recherches Subatomiques, IRes, Strasbourg, France
7 Stefan-Meyer-Institut für subatomare Physik, Austria
8 Forschungszentrum Dresden-Rossendorf, Institut für Kern- und Hadronenphysik, Germany
9 Technische Universität München, Physik-Department E12, Germany
10 Laboratoire de Physique Corpusculaire, LPC, Clermont-Ferrand, France
11 Russian Resarch Center "Kurchatov Instiute", Moscow, Russia
12 Ruprecht-Karls-Universität Heidelberg, I. Physikalisches Institut, Germany
13 KFKI Research Instiute for Particle and Nuclear Physics, Budapest, Hungary

HADES

Spokesperson: Salabura, P.

Agakishiev, G. [8], Alves, R. [2], Balanda, A. [3], Bassini, R. [9], Bellia, G. [1], Belver, D. [16], Belyaev, A.V. [6], Blanco, A. [2], Böhmer, M. [12], Boiano, C. [9], Boyard, J. L. [14], Braun-Munzinger, P. [4], Cabanelas, P. [16], Capela, C. [2], Carolino, N. [2], Castro, E. [16], Cavinato, M. [9], Chernenko, S. [6], Christ, T. [12], Destefanis, M. [8], Díaz, J. [17], Dohrmann, F. [5], Dybczak, A. [3], Eberl, T. [12], Enghardt, W. [5], Fateev, O.V. [6], Ferreira-Marques, R. [2], Finocchiaro, P. [1], Fonte, P. [2], Friese, J. [12], Fröhlich, I. [7], Galatyuk, T. [4], Garzón, J. A. [16], Gernhäuser, R. [12], Gil, A. [17], Gilardi, C. [8], Golubeva, M. [10], González-Díaz, D. [4], Grosse, E. [5], Guber, F. [10], Heidel, K. [5], Heilmann, M. [7], Heinz, T. [4], Hennino, T. [14], Holzmann, R. [4], Hutsch, J. [5], Ierusalimov, A.P. [6], Iori, I. [9], Ivashkin, A. [10], Jurkovic, M. [12], Kajetanowicz, M. [3], Kämpfer, B. [5], Karavicheva, T. [10], Kirschner, D. [8], Koenig, I. [4], Koenig, W. [4], Kolb, B. W. [4], Kotte, R. [5], Kozuch, A. [3], Krizek, F. [15], Krücken, R. [12], Kugler, A. [15], Kühn, W. [8], Kurepin, A. [10], Lang, S. [4], Lange, J. S. [8], Lapidus, K. [10], Lopes, L. [2], Lorenz, M. [7], Maier, L. [12], Mangiarotti, A. [2], Markert, J. [7], Metag, V. [8], Michalska, B. [3], Michel, J. [7], Morinière, E. [14], Mousa, J. [13], Müntz, C. [7], Naumann, L. [5], Neves, C. [2], Novotny, R. [8], Otwinowski, J. [3], Pachmayer, Y. C. [7], Palka, M. [4], Parpottas, Y. [13], Pechenov, V. [8], Pechenova, O. [8], Pereira, A. [2], Pérez Cavalcanti, T. [8], Pietraszko, J. [4], Przygoda, W. [3], Rabin, N. [11], Ramstein, B. [14], Razin, S.V. [6], Reshetin, A. [10], Riboldi, S. [9], Rosier, P. [14], Rustamov, A. [4], Sadovsky, A. [10], Sailer, B. [12], Salabura, P. [3], Schmah, A. [4], Schwab, E. [4], Silva, J. [2], Smolyankin, V. [11], Sobiella, M. [5], Sobolev, Yu.G. [15], Solovieva, T. [10], Sousa, C. [2], Spataro, S. [8], Spruck, B. [8], Ströbele, H. [7], Stroth, J. [7], Sturm, C. [7], Sudol, M. [4], Tarantola, A. [7], Teilab, K. [7], Tiflov, V. [10], Tlusty, P. [15], Traxler, M. [4], Trebacz, R. [3], Troyan, A.Yu. [6], Tsertos, H. [13], Usenko, E. [10], Veretenkin, I. [10], Vieira, M. [2], Visotski, S. [11], Wagner, V. [15], Weber, M. [12], Wisniowski, M. [3], Wüstenfeld, J. [5], Yurevich, S. [4], Zanevsky, Y.V. [6], Zhou, P. [5], Zumbruch, P. [4]

1 Istituto Nazionale di Fisica Nucleare - Laboratori Nazionali del Sud, Catania (Italy)
2 LIP-Laboratório de Instrumentação e Física Experimental de Partículas, Coimbra (Portugal)
3 Smoluchowski Institute of Physics, Jagiellonian University of Cracow, Cracow (Poland)
4 GSI Helmholtzzentrum für Schwerionenforschung GmbH, Darmstadt (Germany)
5 Institut für Strahlenphysik, Forschungszentrum Dresden-Rossendorf, Dresden (Germany)
6 Joint Institute of Nuclear Research, Dubna (Russia)
7 Institut für Kernphysik, Goethe-Universität, Frankfurt (Germany)
8 II.Physikalisches Institut, Justus Liebig Universität Giessen, Giessen (Germany)
9 Istituto Nazionale di Fisica Nucleare, Sezione di Milano, Milano (Italy)
10 Institute for Nuclear Research, Russian Academy of Science, Moscow (Russia)
11 Institute of Theoretical and Experimental Physics, Moscow (Russia)
12 Physik Department E12, Technische Universität München, Garching (Germany)

13 Department of Physics, University of Cyprus, Nicosia (Cyprus)
14 Institut de Physique Nucléaire (UMR 8608), CNRS/IN2P3 - Université Paris Sud, Orsay Cedex (France)
15 Nuclear Physics Institute, Academy of Sciences of Czech Republic, Rez (Czech Republic)
16 Departamento de Física de Partículas, Univ. de Santiago de Compostela, Santiago de Compostela (Spain)
17 Instituto de Física Corpuscular, Universidad de Valencia-CSIC, Valencia (Spain)

The HEDgeHOB Collaboration

Spokesperson: D.H.H. Hoffmann

Adamyan, V.M. [28], Audebert, P. [17], Baimetov, F. [1], Batani, D. [42], Cowan, T. [43], Davidson, R.C. [30], Faenov, A.Ya. [26], Fernandez, J. [21], Fortov, V. [8], Gauthier, J.-C. [40], Gericke, D.O. [45], Glenzer, S. [19], Habs, D. [23], Hoffmann, D.H.H. [7,33], Jacoby, J. [13], Jungwirth, K. [29], Kalal, M. [3], Kim, Ch. J. [15], Kong, H.J. [14], Koresheva, E. [20], Li, R. [9], Logan, G. [18], Maron, Y. [44], Maynard, G. [22], Mehlhorn, T. [32], Meyer-ter-Vehn, J. [24], Mintsev, V. [12], Ogawa, M. [35], Piriz, A.R. [36], Redmer, R. [39], Rosmej, F. B. [41], Sauerbrey, R. [6], Schlanges, M. [4], Schmidt, R. [5], Sharkov, B. [10], Smirnov, V.P. [27], Son, E. [25], Suk, H. [16], Tkachenko, .M. [37], Ulrich, A. [34], Vatulin, V. [11], Zepf, M. [31], Zhernokletov, M. [2], Zwicknagel, G. [38]

1 Al-Farabi Kazakh National University (KNU). Almaty (Kazakhstan)
2 All-Russian Institute of Experimental Physics (VNIIEF), Sarov (Russia)
3 Czech Technical University (CTU), Prague (Czech Republic)
4 Ernst Moritz Arndt Universität Greifswald (Germany)
5 European Organization for Nuclear Research (CERN) (Switzerland)
6 Friedrich-Schiller-Universität Jena (Germany)
7 GSI, Plasmaphysik (Germany)
8 Institute for High Energy Densities of RAS (IHED), Moscow (Russia)
9 Institute for Optics and Fine Mechanics CAS (IOFM), Shanghai (China)
10 Institute for Theoretical and Experimental Physics (ITEP), Moscow (Russia)
11 Institute for Theoretical and Mathematical Physics (ITMP), Sarov (Russia)
12 Institute of Problems of Chemical Physics RAS (IPCP), Chernogolovka (Russia)
13 Johann-Wolfgangn-Goethe Universität, Frankfurt (Germany)
14 Korea Advanced Institute of Science and Technology (KAIST), Daejeon (S. Korea)
15 Korea Atomic Energy Research Institute (KAERI), Daejeon (S. Korea)
16 Korea Electrotechnology Research Institute (KERI), Changwon (S. Korea)
17 Laboratorie pour lUtilisation des Lasers Intenses (LULI), Palaiseau (France)
18 Lawrence Berkeley National Laboratory (LBNL), Berkeley (USA)
19 Lawrence Livermore National Laboratory (LLNL), Livermore (USA)
20 Lebedev Physical Institute RAS (LPI), Moscow (Russia)
21 Los Alamos National Laboratory (LANL), Los Alamos (USA)
22 LPGP, CNRS-UMR8578, Universite Paris XI (LPGP), Paris (France)
23 Ludwig-Maximilians-Universität München (Germany)
24 Max-Planck-Institut für Quantenoptik, Garching (Germany)
25 Moscow Institute of Physics and Technology (MIPT), Moscow (Russia)
26 Multi-charged Ion Spectra Data Center (MISDC) of VNIIFTRI, Mendeleevo (Russia)
27 NFI, Russian Research Center “Kurchatov Institute” (NFI), Moscow (Russia)
28 Odessa National University (ONU), Odessa (Ukraine)
29 PALS Research Center, IP (PALS), Prague (Czech. Republik)
30 Princeton University (PU), Princeton (USA)
31 Queens University of Belfast (QUB) (UK)
32 Sandia National Laboratories (SNL), Albuquerque (USA)
33 Technische Universität Darmstadt (Germany)
34 Technische Universität München (Germany)
35 Tokyo Institute of Technology (TIT), Tokyo (Japan)
36 Universidad de Castilla La Mancha (UCLM), Ciudad Real (Spain)
37 Universidad Politecnica de Valencia (UPV), Valencia (Spain)
38 Universität Erlangen (Germany)
39 Universität Rostock (Germany)
40 Universite de Bordeaux (UB), Talence (France)
41 Universite de Provence (UP), Marseille (France)
42 University of Milano (UM) (Italy)
43 University of Nevada (UNR), Reno (USA)
44 Weizmann Institute of Sciences (WIS), Rehovot (Israel)
45 Centre for Fusion, Space and Astrophysics, University of Warwick, Coventry (UK)

HISPEC

Spokesperson: Zs. Podolyak

Ackermann, Dieter [8], Aeystö, Juha [43], Algora, Alejandro [2], Al-Khalili, Jim [53], Angulo, Carmen [21], Atac, Ayse [1], Back, Tobjorn [18], Balabanski, Dimiter [13], Batist, Leonid [27], Baur, Gerhard [7], Bednarczyk, Piotre [8], Benlliure, Jose [50], Bentley, Mike [54], Bhattacharya, Chandana [56], Borge, Maria José [6], Borzov, Ivan [14], Boston, Andrew [45], Bucurescu, Dorel [24], Cata-Danil, Gheorghe [28], Cederwall, Bo [18], Chapman, Robert [48], Crespo, Raquel [44], Cullen, David [46], Dewald, Alfred [38], Dombradi, Zsolt [2], Doncel, Maria [49], Dracoulis, George [3], Dudek, Jerzy [15], Engert, Tobias [8], Erduran, Nizamettin [16], Espino, Jose [51], Fahlander, Claes [22], Feldmeier, Hans [8], Fujita, Yoshitaka [26], Gerl, Jürgen [8], Gloeckle, Walter [30], Gomez, Joaquin [51], Górska, Magdalena [8], Grebosz, Jerzy [11], Greenlees, Paul [43], Harissopulos, Sotirios [23], Hass, Michael [33], Hencken, Kai [35], Huyse, Mark [19], Jan, Saren [17], Jenkins, David [54], Johnson, Arne [52], Jolie, Jan [38], Julin, Rauno [43], Jungclaus, Andrea [6], Korten, Wolfram [5], Kownacki, Jan [57], Krasznahorkay, Attila [2], Kreiner, Andres [32], Labiche, Marc [4], Leino, Matti [43], Lemmon, Roy [4], Lenske, Horst [41], Mach, Henryk [55], Maj, Adam [11], Mandal, Samit [39], Martel, Ismael [42], Meczinski, Witold [11], Muralithar, Sivaramakrishnan [25], Negret, Alexandru [24], Neyens, Gerda [19], Nociforo, Chiara [8], Nolan, Paul [45], Novikov, Yuri [27], Novikov, Yuri [27], Nyberg, Johan [55], Paul, Eddie [45], Petrick, Martin [41], Petrovici, Alexandrina [24], Podolyak, Zsolt [53], Redondo, Daniel Galaviz [44], Regan, Patrick [53], Reiter, Peter [38], Rinto-Antila, Sami [34], Rubio, Berta [10], Rudolph, Dirk [22], Sagrado Garcia, Inmaculada [49], Saito, Nami [8], Saito, Takehiko [8], Sarkar, Maitreyee [31], Scheidenberger, Christoph [8], Scheit, Heiko [29], Simpson, John [4], Smith, Andrew [46], Sohler, D. [2], Speidel, Karl-Heinz [37], Spohr, Klaus [48], Styczen, Jan [11], Suresh Kumar, Suresh [12], Tengblad, Olof [6], Vaagen, Jan [36], Van Duppen, Piet [19], Varley, Brian [46], Vitturi, A. [47], Von Oertzen, Wolfram [9], Wadsworth, Bob [54], Walker, Philip [53], Woertche, Heinrich [20], Woods, Phil [40], Zamfir, Victor [24]

1 Ankara University, Turkey
2 ATOMKI Debrecen, Hungary
3 Australian National University, Australia
4 CCLRC Daresbury, United Kingdom
5 CEA Saclay, France
6 CSIC Madrid, Spain
7 FZ Jülich, Germany
8 GSI - Helmholtzzentrum für Schwerionenforschung mbH, Darmstadt, Germany
9 HMI Berlin, Germany
10 IFIC Valencia, Spain
11 IFJ PAN Krakow, Poland
12 Indian Insitute of technology Roorkee, India
13 INRNE BAS Sofia, Bulgaria
14 IPPE Obninsk, Russia
15 IreS Strasbourg, France
16 Istanbul University, Turkey
17 JYFL, Finland
18 KTH Stockholm, Sweden
19 KU Leuven, Belgium
20 KVI Groningen, The Netherlands
21 Louvain-la-Neuve, Belgium
22 Lund University, Sweden
23 NCSR Athens, Greece
24 NIPNE Bucharest, Romania
25 NSC New Delhi, India
26 Osaka University, Japan
27 PNPI Gatchina, Russia
28 Politechnical University of Bucharest, Romania
29 RIKEN, Japan
30 Ruhr-University of Bochum, Germany
31 Saha Inst. Kolkata, India
32 TANDAR, Argentina
33 The Weizmann Institute of Science Rehovot, Israel
34 Univ. Liverpool, United Kingdom
35 University of Basel, Switzerland
36 University of Bergen, Norway
37 University of Bonn, Germany
38 University of Cologne, Germany
39 University of Delhi, India
40 University of Edinburgh, United Kingdom
41 University of Giessen, Germany
42 University of Huelva, Spain
43 University of Jyväskylä, Finland
44 University of Lisboa, Portugal
45 University of Liverpool, United Kingdom
46 University of Manchester, United Kingdom
47 University of Padova, Italy
48 University of Paisley, United Kingdom
49 University of Salamanca, Spain
50 University of Santiago de Compostela, Spain
51 University of Sevilla, Spain
52 University of Stockholm, Sweden
53 University of Surrey, United Kingdom
54 University of York, United Kingdom
55 Uppsala University, Sweden
56 VECC Kolkata, India
57 Warsaw University, Poland

The HITRAP Collaboration

Blaum, K. [7], Burgdörfer, J. [4], Fischer, A. [3], Grandin, J.-P. [6], Gross, J. [3], Hoekstra, R. [9], Jungmann, K. [9], Lindroth, E [5], Madzunkuv, S. [5], Morgenstern, R. [9], Schuch, R. [5], Simon, A [8], Thompson, R. [10], Ullrich, J. [7], Warczak, A. [8], Werth, G. [1], Wilschut, H. A. [9], Wolf, A. [7], Zschornak, G. [2]

1 Johannes-Gutenberg-Universität Mainz (Germany)
2 TU Dresden (Germany)
3 Hochschule Darmstadt (Germany)
4 TU Wien, Institute for Theoretical Physics (Austria)
5 Stockholm Universitet, Department of Atomic Physics (Sweden)
6 GANIL, Caen, Recoil Ion Momentum Spectroscopy (France)
7 Max-Planck Institut für Kernphysik, Heidelberg (Germany)
8 Jagellonian University Krakow, Institute of Physics, IFUJ (Poland)
9 Kernfysich Versneller Instituut, KVI, Rijksuniversiteit Groningen, Ion-Surface Interaction, (The Netherlands)
10 Imperial College, London (United Kingdom)

hotQCD

Bazazov, A. [1], Bhattacharya, T. [2], Cheng, M. [3], Christ, N.H. [4], DeTar, C. [5], Ejiri, S. [8], Gottlieb, S. [6], Gupta, R. [2], Heller, U.M. [7], Huebner, K. [8], Jung, C. [8], Karsch, F. [8,9], Laermann, E. [9], Lvkova, L. [5], Miao, C. [8], Mavhinney, R.D. [4], Petreczky, P. [8,1], Schmidt, C. [9], Soltz, R.A. [3], Soeldner, W. [11], Sugar, R. [12], Toussaint, D. [1], Vranas, P. [3]

1 Physics Department, University of Arizona, Tucson, Arizona 85721, USA, USA
2 Theoretical Division, Los Alamos National Laboratory, Los Alamos, New Mexico 87545, USA, USA
3 Physics Division, Lawrence Livermore National Laboratory, Livermore California 94550, USA, USA
4 Physics Department, Columbia University, New York, New York 10027, USA, USA
5 Physics Department, University of Utah, Salt Lake City, Utah 84112, USA, USA
6 Physics Department, Indiana University, Bloomington, Indiana 47405, USA, USA
7 American Physical Society, One Research Road, Ridge, New York 11961, USA, USA
8 Physics Department, Brookhaven National Laboratory, Upton, New York 11973, USA, USA
9 Fakultät für Physik, Universität Bielefeld, D-33615 Bielefeld, Germany, Germany
10 RIKEN-BNL Research Center, Brookhaven National Laboratory, Upton, New York 11973, USA, USA
11 ExtreMe Matter Institute EMMI, GSI Helmholtzzentrum für Schwerionenforschung, Planckstr. 1, D-64291 Darmstadt, Germany, Germany
12 Physics Department, University of California, Santa Barbara, California 93106, USA, USA

The ILIMA Collaboration

Spokesperson: P. Walker

Audi, G. [4], Badura, E. [7], Blaum, K. [5], Bosch, F. [7], Boutin, D. [7], Bürvenich, T.J. [6], Chen, L. [7], Cullen, D. [18], Di, Z. [9], Dickel, T. [9], Dolinskii, A. [7], Egelhof, P. [7], Faestermann, T. [8], Festermann T. [8], Franczak, B. [7], Franzke, B. [7], Geissel, H. [7], Gusev, Y. [16], Hausmann, M. [20], Herfurth, F. [7], Hoffmann, J. [7], Janas, Z. [15], Kienle, P. [8], Kluge, H.-J. [7], Knöbel, R. [9], Kozhuharov, C. [7], Kratz, K.-L. [5], Krücken, R. [8], Kurz, N. [7], Lalazissis, G. [10], Litvinov, S. [7], Litvinov, Y. [7], Lunney, D. [4], Madland, D.G. [19], Maier, L. [8], Mao, R. [2], Matos, M. [20], Montes Contretas, F.A. [7], Münzenberg, G. [7], Nesmiyan, I. [7], Nickel, F. [7], Nolden, F. [7], Novikov, Y. [16], Novikov, Y. [16], Ohtsubo, T. [11], Ott, W. [7], Ozawa, A. [12], Patyk, Z. [14], Petrick, M. [9], Pfeiffer, B. [5], Pfützner, M. [15], Plaß, W. [9], Podolyak, Z. [17], Quint, W. [7], Ring, P. [8], Schatz, H. [20], Scheidenberger, C. [7], Seliverstov, D. [16], Simon, H. [7], Steck, M. [7], Sümmerer, K. [7], Sun, B. [7], Sun, Z. [2], Takahashi, K. [1], Typel, S. [7], Vorobjev, G. [16], Vretenar, D. [3], Walker, P. [17], Weick, H. [7], Winkler, M. [7], Xiao, G. [2], Yamaguchi, T. [13], Zhong, L. [17]

1 Universite Libre de Bruxelles (Belgium)
2 Institute of Modern Physics, IMP, Lanzhou (China)
3 University of Zagreb (Croatia)
4 Centre de Spectrométrie Nucléaire et de Spectrométrie de Masse (CSNSM), Orsay (France)
5 Johannes-Gutenberg-Universität Mainz (Germany)
6 Goethe-Universität, Frankfurt (Germany)
7 GSI Helmholtzzentrum für Schwerionenforschung GmbH, Darmstadt (Germany)
8 Technische Universität München (Germany)
9 Universität Giessen (Germany)
10 Aristotle University of Thessaloniki (Greece)
11 Niigata University (Japan)
12 RIKEN (Japan)
13 Saitama University (Japan)
14 Soltan Institute for Nuclear Studies, IPJ, Warsaw (Poland)
15 Warsaw University (Poland)
16 Petersburg Nuclear Physics Institute (PNPI) Gatchina (Russia)
17 University of Surrey (United Kingdom)
18 University of Manchester (United Kingdom)
19 Los Alamos National Laboratory (USA)
20 NSCL Michigan State University (USA)

The ISOLTRAP Collaboration

Spokesperson: K. Blaum

Audi, G. [1], Beck, D [2], Blaum, K. [3], Böhm, C. [4], Bollen, G. [8], Borgmann, C. [3], Breitenfeldt, M. [5], Fink, D. [4], George, S. [3], Herfurth, F. [2], Herlert, A. [7], Kellerbauer, A. [3], Kluge, H.-J. [2], Kluge, H.-J. [3], Kowalska, M. [7], Kreim, S. [3], Lunney, D. [1], Minaya-Ramirez, E. [1], Naimi, S. [1], Neidherr, D. [4], Rosenbusch, M. [5], Schwarz, S. [8], Schweikhard, L. [5], Warring, U. [3], Zuber, K. [6]

1 Centre de Spectrométrie Nucléaire et de Spectrométrie de Masse (CSNSM), Orsay (France)
2 GSI Helmholtzzentrum für Schwerionenforschung GmbH, Darmstadt (Germany)
3 Max-Planck Institut für Kernphysik, Heidelberg (Germany)
4 Institute of Physics, Johannes Gutenberg Universität Mainz (Germany)
5 University of Greifswald, Institute of Physics, Greifswald (Germany)
6 TU Dresden, Institute of Nuclear and Particle Physics (Germany)
7 CERN, Geneva (Switzerland)
8 NSCL at Michigan State University, East Lansing, Michigan (USA)

JointGEM

Spokesperson: Zmeskal, H.; Voss, B.

http://www.oeaw.ac.at/smi/jointgem

Annand, J.[8] ; Bencivenni, B.[3]; Bragadireanu, M.[7]; Chattopadhyay, S.[9]; Garcia, F.[6]; Ketzer, B.[5]; Nikulin, V.[10]; Ranieri, A.[2]; Voss, B. [4], Zmeskal, H. [1]

1 Österreichische Akademie der Wissenschaften - SMI Vienna
2 Istituto Nazionale di Fisica Nucleare - Sezione di Bari
3 Istituto Nazionale di Fisica Nucleare - Laboratori Nazionali di Frascati
4 GSI Helmholtzzentrum für Schwerionenforschung GmbH, Darmstadt
5 Technische Universität München
6 Helsingin yliopisto
7 Institutul National de Cercetare
8 University of Glasgow
9 Variable Energy Cyclotron Center
10 Petersburg Nuclear Physics Institute, Gatchina

The LASPEC Collaboration

Spokesperson: Blaum, K.; Nörtershäuser, W.

Äystö, J. [2], Billowes, J. [10], Blaum, K. [16], Bushaw, B.A. [14], Campbell, P. [10], Crespo López-Urrutia, J.R. [8], Dax, A. [15], Flanagan3, K. [3], Geppert, C. [4,5], Habs, D. [7], Huber, G. [6], Huyse, M. [1], Jokinen, A. [2], Kessler, T. [2], Koudriavtsev, I. [1], Krämer, J. [5], Krieger, A. [5], Kühl, T. [4], Le Blanc, F. [3], Lunney, D. [3], Moore, I. [2], Neyens, G. [1], Nörtershäuser, W. [4,5], Perajarvi, K. [2], Rodriguez, D. [11], Sanchez, R. [4,5], Scheidenberger, C. [4], Schneider, D. [13], Seliverstov, M. [12], Sewtz, M. [7], Szerypo, J. [7], Thirolf, P.G. [7], Ullrich, J. [8], Van Duppen, P. [1], Wendt, K. [6], Zimmermann, C. [9]

1 Instituut voor Kern- en Stralingsfysica, Katholieke Universiteit Leuven, Heverlee (Belgium)
2 Department of Physics, University of Jyväskylä, F-Jyväskylä (Finland)
3 Centre de Spectrométrie Nucléaire et de Spectrométrie de Masse, Orsay Campus (France)
4 GSI Helmholtzzentrum für Schwerionenforschung GmbH, Darmstadt (Germany)
5 Institut für Kernchemie, Johannes Gutenberg-Universität Mainz (Germany)
6 Institut für Physik, Johannes Gutenberg-Universität Mainz (Germany)
7 Department of Physics, Ludwig-Maximilians University München, Garching (Germany)
8 Max-Planck-Institut für Kernphysik, Heidelberg (Germany)
9 Insitute of Physics, Eberhard-Karls University, Tübingen (Germany)
10 Departement of Physics and Astronomy, University of Manchester (Great Britain)
11 University of Granada, Granada (Spain)
12 CERN, PH-Dept. / ISOLDE, Geneva (Switzerland)
13 Lawrence Livermore National Laboratory, Livermore (USA)
14 Pacific Northwest National Lab, PNNL, Richland (USA)

15 Department of Physics, University of Tokyo (Japan)
16 Physikalisches Institut, Ruprecht-Karls-Universität Heidelberg (Germany)

The MATS Collaboration

Spokesperson: Blaum, K.

Audi, G. [4], Äystö, J. [3], Bachelet, C. [19], Beck, D. [8], Bender, M. [19], Blaum, K. [7], Bloch, I. [9], Block, M. [8], Blomley, L. [2], Bollen, G. [19], Breitenfeld, M. [5], Crespo López-Urrutia, J.R. [7], Das, P. [14], Dickel, T. [10], Dickel, Timo [13], Dworschak, M. [8], Eberhardt, K. [9], Eliseev, S. [15], Ferrer, R. [9], Geissel, H. [8], George, S. [9], Geppert, C. [8], Guénaut, C. [19], Gusev, Y. [15], Habs, D. [11], Habs, Dietrich [12], Heenen, P.-H. [1], Heinz, S. [8], Helert, A. [5], Herfurth, F. [8], Jokinen, A. [3], Kellerbauer, A. [7], Kester, O. [8], Ketelaer, J. [9], Kolhinen, V. [11], Kreim, S. [9], Litvinov, Y.A. [8], Lunney, D. [4], Martel, I. [16], Marx, G. [5], Matos, M. [19], Moore, I. [3], Nagy, S. [9], Neidherr, D. [9], Nörtershäuser, W. [9], Novokov, Y.N. [15], Petrick, M. [10], Plaß, W.R. [10], Popov, A. [15], Quint, W. [8], Ray, A. [14], Reinhard, P.-G. [6], Rodriguez, D. [17], Schabinger, B. [9], Scheidenberger, C. [8], Schneider, D. [20], Schramm, Ullrich [12], Schuch, R. [18], Schwarz, S. [19], Schweikhard, L. [5], Seliverstof, M. [15], Seliverstov, D. [15], Sewtz, M. [11], Solders, A. [18], Stahl, S. [9], Suhonen, M. [18], Szerypo, J. [11], Thirolf, P.G. [11], Ullrich, J. [7], Vorobjev, G. [15], Weber, C. [3], Winkler, M. [8], Yazidjian, C. [8], Ziegler, F. [5]

1 Universite Libre de Bruxelles (Belgium)
2 TRIUMF National Laboratory Vancouver (Canada)
3 Department of Physics, P.O. Box 35, FIN-40014 University of Jyväskylä (Finland)
4 IN2P3-CNRS Orsay (France)
5 Ernst Morit Arndt Universität Greifswald, Institut für Physik (Germany)
6 Friedrich-Alexander Universität Erlangen, Institut für Physik II (Germany)
7 Max-Planck Institut für Kernphysik, Heidelberg (Germany)
8 GSI Darmstadt (Germany)
9 Institut für Physik, Institut für Kernchemie, Universität Mainz (Germany)
10 II. Institut für Physik, Justus-Liebig Universität Gießen (Germany)
11 Institut für Physik, Ludwig-Maximilians Universität München (Germany)
12 Ludwig-Maximilians-Universität München (Germany)
13 Justus-Liebig-Universität (Germany)
14 Variable Energy Cyclotron Center, Kolkata (India)
15 St. Petersburg Nuclear Physics Institute, St. Petersburg State University (Russia)
16 Departamento de Física aplicada, Universidad de Huelva (Spain)
17 University of Granada (Spain)
18 Stockholm University (Sweden)
19 Michigan State University, East Lansing (USA)
20 Lawrence Livermore National Laboratory (USA)

MC-PAD

Spokesperson: Joram, C.

http://mc-pad.web.cern.ch/mc-pad/

1 AGH University of Science and Technology, Poland
2 GSI Darmstadt, Germany
3 Deutsches Elektronen-Synchrotron, Germany
4 Jozef Stefan Institute, Slovenia
5 Laboratori Nazionali di Frascati, Italy
6 The National Institute for Nuclear Physics and High Energy Physics, Netherlands
7 Paul Scherrer Institut, Switzerland
8 University of Hamburg, Germany
9 Institute of Nuclear Physics, Polish Academy of Sciences, Poland
10 National Institute of Material Physics, Romania
11 Photonis SAS Holding, France
12 Micron Semiconductor LTD., United Kingdom
13 Evatronix SA, Poland

NA49

Spokesperson: Seyboth P.

Anticic, T. [22], Baatar, B. [8], Barna, D [4], Bartke, J. [6], Beck, H. [9], Betev, L. [10], Bialkowska, H. [19], Blume, C. [9], Bogusz, M. [21], Boimska, B. [19], Book, J. [9], Botje, M. [1], Bracinik, J. [3], Bunvcic, P. [10], Cerny, V. [3], Cetner, T. [21], Christakoglou, P. [1], Chung, P. [18], Chvala, O. [14], Cramer, J.G. [18], Eckhardt, V. [13], Fischer, H.G. [10], Fodor, Z. [4], Foka, P. [7], Friese, V. [7], Gazdicki, M. [11], Grebieszkow, K. [21], Hoehne, C. [7], Kadija, K. [22], Karev, A. [10], Kolesnikov, V.I. [8], Kowalski, M. [6], Kresan, D. [7], Kreps, M. [3], Laszlo, A. [4], Lacey, R. [18], Leeuwen, M.van [1], Mackowiak, M. [21], Makariev, M. [17], Malakov,

A.I. [8], Mateev, M. [21], Melkumov, G.L. [8], Mitrovski, M. [9], Mrowczynski, S. [11], Nicolic, V. [22], Palla, G. [4], Panagiotou, A.D. [2], Peryt, W. [21], Pikna, M. [3], Pluta, J. [21], Prindle, D. [15], Puehlhofer, F. [12], Renfordt, R. [9], Roland, C. [5], Roland, G. [5], Rybczynski, M. [11], Rybicki, A. [6], Sandoval, A. [7], Schmitz, N. [13], Schuster, T. [9], Seyboth, P. [13], Sikler, F. [4], Sitar, B. [3], Skrzypczak, E. [20], Slodkowski, M. [21], Stefanek, G. [11], Stock, R. [9], Stroebele, H. [9], Susa, T. [22], Szuba, M. [21], Utvic, M. [9], Varga, D. [3], Vassiliou, M. [2], Veres, G.I. [4], Versztergombi, G. [4], Vranic, D. [7], Wenig, S. [10], Wlodarczyk, Z. [11], Wojtaszek-Szwarc, A. [11]

1 NIKHEF, Amsterdam (Netherlands)
2 Department of Physics, University of Athens, Athens (Greece)
3 Eotvos Lorant University, Budapest (Hungary)
4 KFKI Research Institute for Particle and Nuclear Physics, Budapest (Hungary)
5 MIT, Cambridge (USA)
6 H. Niewodniczanski Institute of Nuclear Physics, Polish Academy of Sciences, Cracow (Poland)
7 Gesellschaft für Schwerionenforschung (GSI), Darmstadt (Germany)
8 Joint Institute for Nuclear Research, Dubna (Russia)
9 Fachbereich Physik der Universitaet, Frankfurt (Germany)
10 CERN, Geneva (Switzerland)
11 Institute of Physics, Jan Kochanowski University, Kielce (Poland)
12 Fachbereich Physik der Universitaet, Marburg (Germany)
13 Max-Planck-Institut fuer Physik, Munich (Germany)
14 Inst. of Particle and Nuclear Physics, Charles Univ., Prague (Czech Republic)
15 Nuclear Physics Laboratory, University of Washington, Seattle, WA (USA)
16 Atomic Physics Department, Sofia Univ. St. Kliment Ohridski, Sofia (Bulgaria)
17 Institute for Nuclear Research and Nuclear Energy, BAS, Sofia (Bulgaria)
18 Department of Chemistry, Stony Brook Univ. (SUNYSB), Stony Brook (USA)
19 Institute for Nuclear Studies, Warsaw (Poland)
20 Institute for Experimental Physics, University of Warsaw, Warsaw (Poland)
21 Faculty of Physics, Warsaw University of Technology, Warsaw (Poland)
22 Rudjer Boskovic Institute, Zagreb (Croatia)

PANDA

Spokesperson: Wiedner, U.

Abazov, V.M. [14], Achenbach, P. [28], Agnello, M. [44], Alberto, D. [42], Alexeev, G. [14], Al-Turany, M. [13], Amoroso, A. [42], Anselmino, M. [42], Arefiev, A. [14], Astakhov, V.I. [14], Augustin, I. [13], Babei, M. [23], Bäck, T. [39], Balanutsa, V. [30], Baldin, E. [35], Barabanov, M.Yu. [14], Bardan, W. [11], Bargholtz, C. [40], Batyunya, B.V. [14], Beck, R. [4], Becker, J. [3], Belikov, N. [38], Belostotski, S. [41], Bersani, A. [20], Bertini, R. [43], Bettoni, D. [18], Bialkowski, E. [10], Bianconi, A. [5], Biegun, A. [23], Birsa, R. [45], Boca, G. [37], Borsuk, S. [50], Botta, E. [42], Boukharov, A. [31], Bradamante, F. [45], Bragadireanu, M. [6], Braghieri, A. [37], Brandys, P. [12], Branford, D. [15], Bressan, A. [45], Bressani, T. [42], Brinkmann, K.-T. [4], Budzanowski, A. [10], Bühler, P. [52], Büscher, M. [24], Bussa, M.P. [42], Busso, L. [42], Calén, H. [48], Calvo, D. [43], Caprini, M. [6], Carassiti, V. [18], Cecchi, A. [18], Cederwall, B. [39], Chernetsky, V. [30], Chlopik, A. [50], Clarkson, T. [22], Clement, H. [46], Coli, S. [43], Costanza, S. [37], Czech, B. [10], Czyzewski, T. [12], Czyzycki, W. [12], Dalpiaz, P. [18], Davidenko, A. [38], Davydov, Yu.I. [14], De Mori, F. [42], De Napoli, M. [7], De Remigis, P. [43], Demekhin, A. [30], Denig, A. [28], Deppe, H. [13], Derevschikov, A. [38], Díaz, J. [49], Distler, M. [28], Dmowski, K. [51], Dobbs, S. [17], Dodokhov, V. Kh. [14], Dolgolenko, A. [30], Domagala, M. [12], Dormenev, V. [29], Dosdall, R. [24], Drexler, P. [21], Dulach, B. [19], Düren, M. [21], Dzhygadlo, R. [24], Efremov, A.A. [14], Ekstrom, C. [47], Erni, W. [1], Euan, C. [22], Eyrich, W. [16], Fedorets, P. [30], Fedorov, A. [29], Fedunov, A.G. [14], Feldbauer, F. [3], Feliciello, A. [43], Ferrero, L. [42], Feshchenko, A.A. [14], Filippli, A. [43], Filo, G. [12], Fioravanti, E. [18], Fissum, K. [27], Fiutowski, T. [9], Flemming, H. [13], Foehl, K. [21], Fontana, A. [37], Friedel, P. [3], Fritsch, M. [28], Gagyi-Palffy, Z. [21], Galoyan, A.S. [14], Garzia, I. [18], Gavrilov, G. [41], Genova, P. [37], Gerasimov, A. [30], Gerén, L. [40], Gerl, J. [13], Giacoppo, F. [7], Gianotti, P. [19], Gil, D. [11], Gillitzer, A. [24], Giraudo, G. [43], Glazenborg-Kluttig, A. [23], Glazier,D. [15], Goldenbaum, F. [24], Goncharenko, Y. [38], Goryachev, V. [30], Götzen, K. [13], Grape, S. [48], Grasso, A. [42], Greco, M. [42], Grigoryan, S. [14], Grishin, V. [38], Gruber, A. [52], Guaraldo, G. [19], Guliyev, E. [23], Guzik, Z. [50], Hansen, K. [27], Hawranek, P. [11], Hayrapetyan, A. [21], Heinsius, F. H. [3], Held, T. [3], Heng, Y. [2], Hennino, T. [36], Hill, G. [22], Hinterberger, F. [4], Hoek, M. [22], Hohler, R. [13], Höistad, B. [48], Höppner, C. [32], Iazzi, F. [44], Idzik, N. [9], Imre, M. [36], Ireland, D. [22], Isaksson, L. [27], Izotov, A. [41], Jaekel, R. [4], Jha, V. [24], Johansson, T. [48], Jothi, V.S. [23], Kachanov, V. [38], Kaiser, R. [22], Kamys, B. [11], Kaplan, D. [8], Karmokov, A. [14], Kavatsyuk, M. [23], Kazmierczak, P. [11], Keri, T. [22], Keshelashvili, I. [1], Ketzer, B. [32], Khoukaz, A. [33], Kienle, P. [52], Kisiel, J. [25], Kisselev, A. [41], Kistryn, St. [11], Kliczewski, S. [10], Kliemt, R. [4], Koch, H. [3], Konorov, I. [32], Konstantinov, D. [38], Kopec, J. [50], Kopf, B. [3], Korcyl, K. [11], Kormilitsin, V. [38], Korzeniewski, R. [51], Korzihik, M. [29], Koshurnikov, E.K. [14], Kotov, K. [35], Kotulla, M. [21], Kozela, A. [10], Kozlowski, T. [50], Kravchenko, P. [41], Kravtsov, V. [38], Krawczyk, M. [12], Krusche, B. [1], Krzemien, W. [11], Kudaev, V.Ch. [14], Kuehn, W. [21], Kugathasan, T. [42], Kulessa, P. [10], Kunne, R. [36], Kupsc, A. [48], Lange, S. [21], Lavezzi, L. [37], Le Galliard, C. [36], Le Normand, J.-P. [36], Lehmann, A. [16], Lehmann, D. [13], Lehmann, I. [22], Lehrach, A. [24], Lemmens, P. [23],

Lewandowski, B. [13], Leyhe, M. [3], Li, S. [26], Li, Z. [26], Lisowski, E. [12], Liu, H. [2], Liu, M. [21], Liu, Z. [2], Livingston, K. [22], Lobanov, V.I. [14], Lobanov, Yu.Yu. [14], Loehner, H. [23], Lucherini, V. [19], Lühning, J. [13], Lumsden, P. [22], Lundin, M. [27], M. [3], Maas, F. [13], MacGregor, D. [22], Macri, M. [20], Maggiora, M. [42], Magiera, A. [11], Maier, R. [24], Makarov, A.F. [14], Malgorzata, K. [10], Malinina, L.V. [14], Malyshev, O. [31], Malyshev, V.L. [14], Manaenkov, S. [41], Mann, A. [32], Marcello, S. [42], Marchand, D. [36], Marciniewski, P. [48], Marinelli, M. [20], Marishev, I. [31], Maroni, A. [36], Martin, A. [45], Marton, J. [52], Matulenko, Y. [38], Mazza, G. [43], McKinnon, B. [22], Melnik, Y. [38], Melnychuk, D. [50], Mertens, M. [24], Meschanin, A. [38], Messchendorp, J. [23], Metag, V. [21], Metreveli, Z. [17], Miklukho,O. [41], Minaev, N. [38], Mindur, B. [9], Mishra, D. [13], Missevitch, O. [29], Mochalov, V. [38], Montagna, P. [37], Mora Espi, M.C. [28], Morozov, D. [38], Morra, O. [43], Moskal, P. [11], Motzko, C. [3], Murray, M. [22], Mustafaev, G.A. [14], Nanova, M. [21], Naryshkin, D. [41], Negrini, M. [18], Neubert, S. [32], Nogach, L. [38], Novotny, R. [21], Nurushev, S. [38], Ohm, H. [24], Olshevskiy, A.G. [14], Ong, S. [36], Orth, H. [13], Ortiz, A. [49], Pace, E. [19], Pantea, D. [6], Parodi, R.F. [20], Pasyuk, M.A. [14], Paul, S. [32], Peleganchuk, S. [35], Pelizäus, Pychy, J. [3], Perevalova, E.A. [14], Peters, K. [13], Pietraszek, J. [12], Piskun, A.A. [14], Plominski, M. [50], Pocheptsov, T.A. [14], Pochodzalla, J. [28], Poelman, T. [23], Pontecorvo, G. [14], Pouthas, J. [36], Prasuhn, D. [24], Protopopescu, D. [22], Przemyslawm, D. [51], Przyborowski, D. [9], Pysz, K. [10], Ramstein, B. [36], Randriamalala, T. [24], Rapisarda, E. [7], Rausmann, T. [33], Ritman, J. [24], Rivetti, A. [43], Rodionov, V.K. [14], Rogov, Yu.N. [14], Rosier, P. [36], Rosner, G. [22], Roth, B. [3], Rotondi, A. [37], Rudy, Z. [11], Ryazantsev, A. [38], Saito, T. [13], Salabura, P. [11], Salmin, R.A. [14], Samartsev, A.G. [14], Sanchez Lorente, A. [28], Sanchez, S. [28], Sapozhnikov, M.G, Shabratova, G.S. [14], Savrie, M. [18], Schadmand, S. [24], Schäfer, W. [10], Schepers, G. [13], Schmidt, C. [4], Schmidt, C.J. [13], Schmitt, L. [13], Schönmeier, P. [21], Schröder, B. [27], Schröder, T. [3], Schulze, J. [3], Schwarz, C. [13], Seitz, B. [22], Semenov, A. [31], Semenov, P. [38], Serbanut, G.C. [42], Seth, K. [17], Sfienti, C. [7], Shen, X. [2], Siudak, R. [10], Skachkov, N.B. [14], Skachkova, A.N. [14], Slowinski, B. [51], Smit, H. [23], Smyrski, J. [11], Soloviev, L. [38], Sosio, S. [42], Spataro, S. [21], Stancari, G. [18], Steinacher, M. [1], Steinke, M. [3], Stenzel, H. [21], Stockmanns, T. [24], Strackbein, C. [21], Strokovsky, E.A. [14], Sudol, M. [36], Suleimanov, M.K. [14], Sun, Z. [26], Swientek, K. [9], Szczurek, A. [10], Szewinski, J. [50], Szymanska, K. [44], Tann, B. [17], Täschner, A. [33], Tegnér, P.-E. [40], Teshev, R.Sh. [14], Teufel, A. [16], Theneau, C. [36], Thiel, M. [21], Thoma, U. [4], Thomé, E. [48], Tikhonov, Y. [35], Tokmenin, V.V. [14], Tomaradze, A. [17], Tomasi-Gustafsson, E. [36], Tosello, F. [43], Traczyk, K. [50], Tudorache, A. [6], Tudorache, V. [6], Uzhinsky, V. [14], Uzunian, A. [38], van de Wiele, J. [36], van der Weele, J.C. [23], Varma, R. [34], Vasiliev, A. [38], Veretennikov, D. [41], Vikhrov, V. [41], Vodopyanov, A. [14], Voss, B. [13], Wang, O. [2], Watts, D. [15], Weitzel, Q. [32], Wendel, C. [4], Wessels, J. [33], Wheadon, R. [43], Widmann, E. [52], Wieczorek, P. [13], Wiedner, U. [3], Wilms, A. [13], Winnebeck, A. [4], Wintz, P. [24], Wojnar, L. [12], Woods, P. [15], Wronska, A. [11], Würschig, T. [4], Xu, H. [26], Xu., H. [2], Yakutin, A. [38], Yang, G. [22], Yang, S. [21], Zaporozhets, S.A. [14], Zaunick, H.-G. [4], Zerguerras, T. [36], Zhdanov, A. [41], Zhong, J. [3], Zhuravlev, N.I. [14], Zlomanczuk, J. [48], Zmeskal, J. [52], Zorin, A.G. [14], Zwieglinski, B. [50]

1 Universität Basel Switzerland
2 Institute of High Energy Physics, Chinese Academy of Sciences, Beijing China
3 Universität Bochum, I. Institut für Experimentalphysik Germany
4 Universität Bonn, Helmholtz-Institut für Strahlen- und Kernphysik Germany
5 Università di Brescia Italy
6 Institutul National de C & D pentru Fizica si Inginerie Nucleara "Horia Hulubei",Bukarest-Magurele Romania
7 Dipartimento di Fisica e Astronomia dell'Università di Catania and INFN, Sezione di Catania Italy
8 IIT Chicago USA
9 AGH University of Science and Technology, Crakow Poland
10 IFJ, Institute of Nuclear Physics PAN, Cracow Poland
11 Instytut Fizyki, Uniwersytet Jagiellonski, Cracow Poland
12 Uniwersytet Cracow Poland
13 GSI Helmholtzzentrum für Schwerionenforschung GmbH, Darmstadt Germany
14 Veksler-Baldin Laboratory of High Energies (VBLHE), Joint Institute for Nuclear Research, Dubna Russia
15 University of Edinburgh United Kingdom
16 Friedrich Alexander Universität Erlangen-Nürnberg Germany
17 Northwestern University, Evanston USA
18 Università di Ferrara and INFN, Sezione di Ferrara Italy
19 INFN-Laboratori Nazionali di Frascati Italy
20 INFN, Sezione di Genova Italy
21 Justus Liebig-Universität Gießen, II. Physikalisches Institut Germany
22 University of Glasgow United Kingdom
23 Kernfysisch Versneller Instituut, University of Groningen Netherlands
24 Forschungszentrum Jülich, Institut für Kernphysik, Jülich Germany
25 University of Silesia, Katowice Poland
26 Chinese Academy of Science, Institute of Modern Physics, Lanzhou China
27 Lunds Universitet, Department of Physics, Lund Sweden
28 Johannes Gutenberg-Universität, Institut für Kernphysik, Mainz Germany
29 Research Institute for Nuclear Problems, Belarus State University, Minsk Belarus
30 Institute for Theoretical and Experimental Physics, Moscow Russia
31 Moscow Power Engineering Institute, Moscow Russia
32 Technische Universität München Germany

33 Westfälische Wilhelms-Universität Münster Germany
34 IIT Bombay, Department of Physics, Mumbai India
35 Budker Institute of Nuclear Physics, Novosibirsk Russia
36 Institut de Physique Nucléaire, Orsay France
37 Dipartimento di Fisica Nucleare e Teorica, Università di Pavia, INFN, Sezione di Pavia Italy
38 Institute for High Energy Physics, Protvino Russia

PRESPEC

Spokesperson: Algora, A.

Algora, A. [30], Applebe, D.E. [24], Atanasova, L. [5], Balabanski, D.L. [12], Banu, A. [1], Bassini, R. [13], Beck, T. [1], Becker, F. [1], Bedanarczyk, P. [1], Belier, G. [7], Benlliure, J. [6], Bentley, M.A. [21], Benzini, G. [13], Blasi, N. [13], Blazhev, A. [2], Boiano, C. [13], Bonnes, U. [32], Bracco, A. [13], Brambilla, S. [13], Bruce, A.M. [27], Brünle, A. [1], Bürger, A. [22], Butler, P.A. [25], Caceres, L. [1], Camera, F. [13], Caserejos, E. [6], Catford, W.N. [4], Chamoli, S.K. [11], Clark, R.M. [20], Cortina Gil, D. [6], Cullen, D.M. [19], Curien, D. [31], Damyanova, G. [5], Daugas, J.M. [7], Davidson, T. [26], Detistov, P. [5], Devin, J. [31], Doornenbal, P. [1], Faestermann, T. [28], Fahlander, C. [23], Fayz, K. [24], Freeman, S.J. [19], Gelletly, W. [4], Georgiev, G. [18], Gerl, J. [1], Glanishki, K. [12], Goldring, G. [11], Gorska, M. [1], Grawe, H. [1], Grebosz, J. [14], Griffiths, R. [24], Grzywacz, R. [1], Hass, M. [11], Hellström, M. [23], Herzberg, R.D. [25], Hoffmann, J. [1], Hübel, H. [22], Ilie, G. [2], Ionescu-Bujor, M. [16], Iordachescu, A. [16], Joilie, J. [2], Jungclaus, A. [17], Kindler, B. [1], Kmiecik, M. [14], Kojouharov, I. [1], Korgul, A. [15], Krücken, R. [28], Kulessa, R. [33], Kurtukian Nieto, T. [6], Kurz, N. [1], Lach, M. [14], Lazarus, I. [24], Leoni, S. [13], Leske, J. [22], Liu, Z. [4], Lo Bianco, G. [12], Lommel, B. [1], Mach, H. [29], Maj, A. [14], Mallion, S. [3], Mammond, G. [21], Matea, I. [9], Mazurek, K. [14], Meczyndki, W. [14], Meot,V. [7], Million, B. [13], Münch, M. [1], Münzenberg, G. [1], Mutterer, M. [32], Nara Singh, B.S. [11], Neyens, G. [3], Nolan, P. [25], Orlandi, R. [19], Page, R.D. [25], Petrache, C. [12], Pfützner, M. [15], Podolyal, Zs. [4], Pucknell, V.F.E. [24], Regan, P.H. [4], Regev, I. [11], Reiter, P. [2], Richard, A. [2], Roig, O. [7], Rubio, B. [30], Rudolph, D. [23], Saltarelli, A. [12], Scherillo, A. [2], Schwengner, R. [10], Seddon, D. [25], Simpson, G. [8], Simpson, J. [25], Smith, A.G. [19], Speidel, K.-H. [22], Striepling, T. [2], Styczen, J. [14], Tsekhanivich, I.S. [8], Turzo, K. [3], Vaintraub, S. [11], Van Duppen, P. [3], Vermeulen, N. [3], von Kalben, J. [32], Wadsworth, R. [21], Walker, P.M. [4], Warr, N. [2], Wieland, O. [13], Williams, S. [4], Woods, P. [26], Zamfir, V. [16]

1 GSI - Helmholtzzentrum für Schwerionenforschung mbH, Darmstadt, Germany
2 Institut für Kernphysik, Universität zu Köln, Köln, Germany
3 K.U. Leuven, Belgium
4 University of Surrey; Guildford, United Kingdom
5 University of Sofia, Sofia, Bulgaria
6 Universidad de Santiago de Compostela, Santiago de Compostela, Spain
7 CEA, Bruyere le Chatel, France
8 ILL, Grenoble, France
9 CENBG, Bordeaux, France
10 IKHP, Rossendorf, Germany
11 Weizmann Institute of Science, Rehovot, Israel
12 University of Camerino, Italy
13 University of Milano, Milano, Italy
14 IFJPAN Krakow, Krakow, Poland
15 Warsaw University, Warsaw, Poland
16 NIPNE Bucharest, Romania
17 Universidad Autonomia de Madrid, Madrid, Spain
18 ISOLDE-CERN, Geneva, Switzerland
19 Manchester University, Manchester, United Kingdom
20 Lawrence Berkeley National Laboratory (LNBL), Berkeley, USA
21 University of York, Heslington, United Kingdom
22 Universität Bonn, Bonn, Germany
23 University of Lund, Lund, Sweden
24 CLCR Daresbury, Daresbury, United Kingdom
25 University of Liverpool, Liverpool, United Kingdom
26 University of Edinburgh, Edinburg, United Kingdom
27 University of Brighton, Brighton, United Kingdom
28 TU München, München, Germany
29 Uppsala University, Uppsala, Sweden
30 IFIC Valencia, Valencia, Spain
31 IRES Strasbourg, Strasbourg, France
32 TU Darmstadt, Darmstadt, Germany
33 Jagiellonian University, Cracow, Poland

R3B

Spokesperson: T. Aumann

Aksouh, Farouk [9], Aksyutina, Yuliya [15], Algora, Alejandro [4], Al-Khalili, Jim [60], Alkhasov, Georgij [35], Alvarez Pol, Hector [58], Aumann, Thomas [18], Avdeichikov, Vladimir [31], Barton, Charles [61], Bemmerer, Daniel [16], Benlliure, Jose [58], Bertulani, Carlos [41], Bhattacharya, Chandana [64], Bhattacharya, Sudeb [39], Böhmer, Michael [46], Boilley, David [17], Boretzky, Konstanze [18], Borge, Maria Jose [12], Botvina, Alexander [22], Boudard, Alain [9], Caesar, Christoph [55], Calvino, Francisco [62], Casarejos, Enrique [58], Catford, Wilton [60], Cederkäll, Joakim [31], Cederwall, Bo [30], Chapman, Robert [57], Chartier, Marielle [54], Chatillon, Audrey [8], Chen, Ruofu [21], Cherciu, Madalinllie [24], Chulkov, Leonid [38], Coleman-Smith, Patrick [7], Cortina, Dolores [58], Crespo, Raquel [53], Csatlos, Margit [4], Cullen, David [56], Czech, Bronislaw [20], Danilin, Boris

[38], Datta Pramanik, Ushasi [39], Davinson, Tom [50], Di Julio, Douglas [31], Ducret, Jean-Eric [14], Duran, Ignacio [58], Egelhof, Peter [18], Elvers, Michael [49], Emling, Hans [18], Enders, Joachim [45], Eränen, Simo [40], Eremin, Vladimir [25], Ershov, Sergey N. [29], Ershova, Olga [51], Espana, Sanuel [47], Faestermann, Thomas [46], Fedorov, Dmitri [1], Feldmeier, Hans [18], Fernandez Dominguez, Beatriz [54], Fissum, Kevin [31], Fomichev, Andrey [29], Forssén, Christian [10], Fraile Prieto, Luis Mario [47], Freeman, Sean [56], Freer, Martin [6], Friese, Jürgen [46], Fynbo, Hans [1], Gacsi; Zoltan [4], Galaviz Redondo, Daniel [12], Garrido, Eduardo [12], Gastineau, Bernard [13], Geissel, Hans [18], Gelletly, William [60], Genolini, B. [26], Gerl, Jürgen [18], Gernhäuser, Roman [46], Golovkov, Mikhail [29], Golubev, Pavel [31], Gorshkov, Alexandr Vladimirovich [29], Górska, Magdalena [18], Grigorenko, Leonid [29], Grosse, Eckart [16], Gulyas, Janos [4], Haiduc, Maria [32], Hasegan, Dumitu [24], Heil, Michael [18], Heinz, Andreas [65], Hoffmann, Jan [18], Hunyadi, Matyas [4], Ignatyuk, Anatoly V. [27], Ilie, Cherciu Madalin [24], Isaksson, Lennart [31], Jakobsson, Bo [31], Jensen, Aksel [1], Johansson, Hakan [10], Johnson, Ron [60], Jonson, Björn [10], Junghans, Arnd [16], Kailas, S. [5], Kalliopuska, Juha [40], Kanungo, Rituparna [44], Kelic-Heil, Aleksandra [18], Kern, Linda [45], Kezzar, Khalid [9], Khanzadeev, Alexei [35], Kisselev, Oleg [36], Klimkiewicz, Adam [18], Kmiecik, Maria [20], Kojouharov, Ivan [18], Korsheninnikov, Alexei [38], Krasznahorkay, Attila [4], Kratz, Jens Volker [55], Kroell, Thorsten [45], Krücken; Reiner [46], Krupko, Sergey [29], Kulessa, Reinhard [28], Kurz, Nikolaus [18], Kuzmin, Eugenii [38], Labiche, Marc [7], Langanke, Karl-Heinz [18], Langer, Christoph [51], Lapoux, Valerie [9], Larsson, Kristian [18], Lazarus, Ian [7], Le Bleis, Tudi [18], Legou, Philippe [14], Leifels, Yvonne [18], Lemmon, Roy [7], Lenske, Horst [52], Lepine-Szily, Alinka [59], Leray, Sylvie [14], Letts, Simon [7], Li, Songlin [21], Liang, Xiaoying [57], Lukasik, Jerzy [20], Mahata, Kripa [5], Maj, Adam [20], Marganiec; Justyna [18], Meister, Mikael [10], Mittig, Wolfgang [17], Müntz, Christian [51], Mutterer, Manfred [18], Nakamura, Takashi [43], Neff, Thomas [18], Nilsson, Thomas [10], Nociforo, Chiara [18], Nolan, Paul [54], Nolen, Jerry [3], Nyman, Goran [10], Obradors, Diego [18], Ogloblin, Aleksey [38], Oi, Makito [60], Pachalis, Stefanos [54], Palit, Rudrajyoti [42], Panin, Valerie [18], Pawlowski, Piotr [20], Pietralla, Norbert [45], Pietri, Stephane [60], Plag, Ralf [51], Podolyak, Zsolt [60], Pollacco, Emanuel [9], Potlog, Mihai [24], Prasad, Rajeshawi [2], Pucknell, Vic [7], Redondo, Daniel Galaviz [53], Regan, Patrick [60], Reifarth, Rene [18], Reiter, Peter [49], Rejmund, Fanny [17], Ricciardi, Maria Valentina [18], Richter, Achim [45], Riisager, Karsten [1], Rodin, Alexander [29], Rossi, Dominic [18], Roussel-Chomaz, Patricia [17], Rubio, Berta [19], Saito, Takehiko [18], Salsac, Marie-Delphine [9], Savajols, Herve [17], Savran, Deniz [45], Scheit, Heiko [37], Schmidt, Karl-Heinz [18], Schmitt, Christelle [17], Schrieder, Gerhard [45], Sharma, Manoj Kumar [2], Sherrill, Bradley [33], Shrivastava, Aradhana [5], Shulgina, Natalia [38], Sidorchuk, Sergey [29], Simenel, Cedric [9], Simon, Haik [18], Simpson, John [7], Singh, B.P. [2], Singh, Pushpendra Pal [2], Sonnabend, Kerstin [45], Spohr, Klaus [57], Stanoiu, Mihai [18], Stevenson, Paul [60], Streicher, Brano [18], Stroth, Joachim [51], Sümmerer, Klaus [18], Tain, Jose L. [19], Tanihata, Isao [34], Tashenov, Stanislav [30], Tengblad, Olof [12], Thompson, Ian [60], Tostevin, Jeffrey A. [60], Trautmann, Wolfgang [18], Tuboltsev, Yuri [25], Turrion, Manuela [12], Typel, Stefan [18], Udias-Moinelo, Jose [11], Vaagen, Jan [48], Verbitskaya, Elena [25], Veselsky, Martin [23], Wagner, Andreas [16], Walus, Wladyslaw [28], Wamers, Felix [18], Weick, Helmut [18], Westerberg, Lars [63], Wimmer, Christine [51], Winkler, Martin [18], Woods, Phil [50], Xu, Hushan [21], Yakorev, Dmitry [16], Zegers, Remco [33], Zhang, Yu-Hu [21], Zhukov, Mikhail [10], Zieblinski, Miroslaw [28], Zilges, Andreas [49]

1 Aarhus University, Denmark
2 Aligarh Muslim University, India
3 ANL Argonne, USA
4 ATOMKI Debrecen, Hungary
5 BARC Mumbai, India
6 Birmingham University, United Kingdom
7 CCLRC Daresbury, United Kingdom
8 CEA Bruyeres-le-Chatel, France
9 CEA Saclay, France
10 Chalmers University of Technology, Sweden
11 Complutense University of Madrid, Spain
12 CSIC Madrid, Spain
13 DAPNIA CEA Saclay, France
14 DAPNIA/SPhN, CEA Saclay, France
15 EMMI-GSI Darmstadt, Germany
16 FZ Rossendorf, Germany
17 GANIL, France
18 GSI - Helmholtzzentrum für Schwerionenforschung mbH, Darmstadt, Germany
19 IFIC Valencia, Spain
20 IFJ PAN Krakow, Poland
21 IMP Lanzhou, China
22 INR RAS Moscow, Russia
23 Institute of Physics SAS Bratislava, Slovakia
24 Institute of Space Sciences, Romania
25 Ioffe PTI St. Petersburg, Russia
26 IPN Orsay, France
27 IPPE Obninsk, Russia
28 Jagellonian University Krakow, Poland
29 JINR Dubna, Russia
30 KTH Stockholm, Sweden
31 Lund University, Sweden
32 NIPNE Bucharest, Romania
33 NSCL/MSU, USA
34 Osaka University, Japan
35 PNPI Gatchina, Russia
36 PSI Villigen, Switzerland
37 RIKEN, Japan
38 RRC Kurchatov Institute Moscow, Russia
39 SINP Kolkata, India
40 Technical Research Center of Finland, Finland
41 Texas A&M University - Commerce, USA
42 TIFR Mumbai, India
43 Tokyo Institute of Technology, Japan
44 TRIUMF, Canada
45 TU Darmstadt, Germany
46 TU Munich, Germany
47 Universidad Complutense de Madrid, Spain
48 University of Bergen, Norway
49 University of Cologne, Germany

50 University of Edinburgh, United Kingdom
51 University of Frankfurt, Germany
52 University of Giessen, Germany
53 University of Lisboa, Portugal
54 University of Liverpool, United Kingdom
55 University of Mainz, Germany
56 University of Manchester, United Kingdom
57 University of Paisley, United Kingdom
58 University of Santiago de Compostela, Spain
59 University of Sao Paulo, Brasilia
60 University of Surrey, Guildford, United Kingdom
61 University of York, United Kingdom
62 UPC Barcelona, Spain
63 Uppsala University, Sweden
64 VECC, India
65 Yale University, USA

RD42

Spokesperson: H. Kagan, P. Weilhammer

http://graybook.cern.ch/programmes/experiments/r_d/RD42.html

1 Ohio State University, USA
2 CERN, Switzerland
3 GSI Darmstadt, Germany
4 Fachhochschule Wiener Neustadt, Austria
5 University of Toronto, Canada
6 cea - Centre d'Etudes de Saclay, France
7 Institut Pluridisciplinaire Hubert Curien (IPHC), France
8 Univ. Bonn, Physikalisches Institut, Germany
9 Universität Karlsruhe, Germany
10 Università & INFN, Catania, Italy
11 Università & INFN, Firenze, Italy
12 Università & INFN, Torino, Italy
13 NIKHEF, Netherlands
14 ITEP Institute for Theoretical and Experimental Physics (ITEP), Russia
15 Moscow Physical Engineering Institute (MePhI), Russia
16 A.F. Ioffe Physical Technical Inst., Russia
17 Jozef Stefan Institute, Slovenia
18 University of New Mexico, USA
19 Fermi National Accelerator Laboratory (Fermilab), USA
20 University of Colorado, Department of Physics, USA
21 University of California, Los Angeles (UCLA), USA
22 Rutgers, State University of New Jersey, Department of Physics and Astronomy, USA

RD51

Spokesperson: Ropelewski, L., Titov, M.

http://rd51-public.web.cern.ch/RD51-Public/Organization/RD51MemberListAlphabetic.pdf
http://rd51-public.web.cern.ch/RD51-Public/Organization/RD51MemberListByInstitute.pdf

RISING

Spokesperson: Rudolph, Dirk

Algora, A. [30], Applebe, D.E. [24], Atanasova, L. [5], Balabanski, D.L. [12], Banu, A. [1], Bassini, R. [13], Beck, T. [1], Becker, F. [1], Bedanarczyk, P. [1], Belier, G. [7], Benlliure, J. [6], Bentley, M.A. [21], Benzini, G. [13], Blasi, N. [13], Blazhev, A. [2], Boiano, C. [13], Bonnes, U. [32], Bracco, A. [13], Brambilla, S. [13], Bruce, A.M. [27], Brünle, A. [1], Bürger, A. [22], Butler, P.A. [25], Caceres, L. [1], Camera, F. [13], Caserejos, E. [6], Catford, W.N. [4], Chamoli, S.K. [11], Clark, R.M. [20], Cortina Gil, D. [6], Cullen, D.M. [19], Curien, D. [31], Damyanova, G. [5], Daugas, J.M. [7], Davidson, T. [26], Detistov, P. [5], Devin, J. [31], Doornenbal, P. [1], Faestermann, T. [28], Fahlander, C. [23], Fayz, K. [24], Freeman, S.J. [19], Gelletly, W. [4], Georgiev, G. [18], Gerl, J. [1], Glanishki, K. [12], Goldring, G. [11], Gorska, M. [1], Grawe, H. [1], Grebosz, J. [14], Griffiths, R. [24], Grzywacz, R. [1], Hass, M. [11], Hellström, M. [23], Herzberg, R.D. [25], Hoffmann, J. [1], Hübel, H. [22], Ilie, G. [2], Ionescu-Bujor, M. [16], Iordachescu, A. [16], Joilie, J. [2], Jungclaus, A. [17], Kindler, B. [1], Kmiecik, M. [14], Kojouharov, I. [1], Korgul, A. [15], Krücken, R. [28], Kulessa, R. [33], Kurtukian Nieto, T. [6], Kurz, N. [1], Lach, M. [14], Lazarus, I. [24], Leoni, S. [13], Leske, J. [22], Liu, Z. [4], Lo Bianco, G. [12], Lommel, B. [1], Mach, H. [29], Maj, A. [14], Mallion, S. [3], Mammond, G. [21], Matea, I. [9], Mazurek, K. [14], Meczyndki, W. [14], Meot,V. [7], Million, B. [13], Münch, M. [1], Münzenberg, G. [1], Mutterer, M. [32], Nara Singh, B.S. [11], Neyens, G. [3], Nolan, P. [25], Orlandi, R. [19], Page, R.D. [25], Petrache, C. [12], Pfützner, M. [15], Podolyal, Zs. [4], Pucknell, V.F.E. [24], Regan, P.H. [4], Regev, I. [11], Reiter, P. [2], Richard, A. [2], Roig, O. [7], Rubio, B. [30], Rudolph, D. [23], Saltarelli, A. [12], Scherillo, A. [2], Schwengner, R. [10], Seddon, D. [25], Simpson, G. [8], Simpson, J. [25], Smith, A.G. [19], Speidel, K.-H. [22], Striepling, T. [2], Styczen, J. [14],

Tsekhanivich, I.S. [8], Turzo, K. [3], Vaintraub, S. [11], Van Duppen, P. [3], Vermeulen, N. [3], von Kalben, J. [32], Wadsworth, R. [21], Walker, P.M. [4], Warr, N. [2], Wieland, O. [13], Williams, S. [4], Woods, P. [26], Zamfir, V. [16]

1 GSI - Helmholtzzentrum für Schwerionenforschung mbH, Darmstadt, Germany
2 Institut für Kernphysik, Universität zu Köln, Köln, Germany
3 K.U. Leuven, Belgium
4 University of Surrey; Guildford, United Kingdom
5 University of Sofia, Sofia, Bulgaria
6 Universidad de Santiago de Compostela, Santiago de Compostela, Spain
7 CEA, Bruyere le Chatel, France
8 ILL, Grenoble, France
9 CENBG, Bordeaux, France
10 IKHP, Rossendorf, Germany
11 Weizmann Institute of Science, Rehovot, Israel
12 University of Camerino, Italy
13 University of Milano, Milano, Italy
14 IFJPAN Krakow, Krakow, Poland
15 Warsaw University, Warsaw, Poland
16 NIPNE Bucharest, Romania
17 Universidad Autonomia de Madrid, Madrid, Spain
18 ISOLDE-CERN, Geneva, Switzerland
19 Manchester University, Manchester, United Kingdom
20 Lawrence Berkeley National Laboratory (LNBL), Berkeley, USA
21 University of York, Heslington, United Kingdom
22 Universität Bonn, Bonn, Germany
23 University of Lund, Lund, Sweden
24 CLCR Daresbury, Daresbury, United Kingdom
25 University of Liverpool, Liverpool, United Kingdom
26 University of Edinburgh, Edinburg, United Kingdom
27 University of Brighton, Brighton, United Kingdom
28 TU München, München, Germany
29 Uppsala University, Uppsala, Sweden
30 IFIC Valencia, Valencia, Spain
31 IRES Strasbourg, Strasbourg, France
32 TU Darmstadt, Darmstadt, Germany
33 Jagiellonian University, Cracow, Poland

SHIP

Spokesperson: S.Hofmann

Ackermann, D. [1], Andreyev, A.N. [11], Antalic, S. [3], Bianco, L. [4], Block, M [1], Burkhard, H.G. [1], Cocolios, Th. [6], Comas, V. [1], Craig-Jones, C. [4], Cullen, D. [7], Darby, I. [4], Eberhardt, K. [12], Eremin, A.V. [2], Franchoo, S. [8], Gan, Z. [10], Hartmann, W. [1], Heinz, S. [1], Henderson, R.A. [13], Heredia, J. [1], Herzberg, R.-D. [4], Heßberger, F.P. [1], Hofmann, S. [1], Huebner, A. [1], Huyse, M. [6], Kenneally, J.M. [13], Ketelhut,S. [5], Khuyagbaatar, J. [1], Kindler, B. [1], Kojouharov, I. [1], Kratz, J.V. [12], Leino, M. [5], Lommel, B. [1], Mann, R. [1], Maurer, J. [1], Moody, K.J. [13], Nelson, S.L. [13], Nishio, K. [9], Page, R.D. [4], Papadakis, P. [4], Popeko, A.G. [2], Rinta-Anttila, S. [4], Rostron, D. [4], Runke, J. [12], Sapple, P. [4], Saro, S. [3], Shaughnessy, D.A. [13], Steiner, J. [1], Stoyer, M.A. [13], Thomson, J. [4], Thörle-Pospiech, P. [12], Trautmann, N. [12], Uusitalo, J. [5], Van Duppen, P. [6], Watkins, H. [4], Wilk, P.A. [13]

1 GSI - Helmholtzzentrum für Schwerionenforschung mbH, Darmstadt, Germany
2 Joint Institute for Nuclear Research (JINR), Dubna, Russia
3 Comenius University, Bratislava, Slovakia
4 University of Liverpool, Liverpool, United Kingdom
5 University of Jyväskylä, Jyväskylä, Finland
6 University of Leuven, Leuven, Belgium
7 University of Manchester, Manchester, United Kingdom
8 Institut de Physique Nucléaire d'Orsay, Orsay, France
9 Japan Atomic Energy Agency (JAEA), Tokai, Japan
10 Institute of Modern Physics, Lanzhou, China
11 University of Paisley, Paisly, United Kingdom
12 Institut für Kernchemie, Johannes - Gutenberg Universität Mainz, Mainz, Germany
13 University of California,Lawrence Livermore National Laboratory Livermore, USA

SHIPTRAP

Spokesperson: M.Block

Ackermann, D. [1], Blaum,K. [2], Block, M. [1], Burkhard, H.G. [1], Droese, Ch. [3], Dworschak,M. [1], Eberhardt, K. [5], Eibach, M. [2], Eliseev, S. [2], Gibinski, A. [5], Haettner, E. [4], Herfurth, F. [1], Heßberger, F.P. [1], Hofmann, S. [1], Ketelaer, J. [2], Khuyagbaatar, J. [1], Mann, R. [1], Marx, G. [3], Maurer, J. [1], Nagy, S. [2], Nesterenko, D. [6], Novikov, Yu. [6], Plass, W. [4], Popeko, A.G. [7], Ramirez Minaya, E. [10], Rodriguez, D. [8], Rudolph, D. [12], Scheidenberger, Ch. [1], Schweikhard, L. [3], Thirolf, P. [9], Walther, T. [11], Weber, C.H. [9]

1 GSI - Helmholtzzentrum für Schwerionenforschung mbH, Darmstadt, Germany
2 Max-Planck-Institut für Kernphysik, Hedelberg, Germany
3 Ernst-Moritz-Arndt-Universität, Institut für Physik, Greifswald, Germany
4 II. Phys. Institut, Justus-Liebig-Universität, Gießen, Germany
5 Johannes-Gutenberg Universität, Mainz, Germany
6 St. Petersburg Nuclear Physics Institute, Gatchina, St. Petersburg, Russia
7 Joint Institute for Nuclear Research (JINR), Dubna D91, Russia
8 Universuty of Granada, Granada, Spain
9 Fakultät für Physik, Ludwig-Maximilians-Universität München, Garching, Germany
10 Helmholtz - Institut Mainz, Mainz, Germany
11 Technische Universität Darmstadt, Darmstadt, Germany
12 University of Lund, Lund, Sweden

The SPARC Collaboration

Spokesperson: Schuch, R.

Afaneh, F. [56], Ali, R. [56], Ali, S. [80], Amaro, P. [66], Andler, G. [80], Andreev, O,Y. [68], Anton, J. [32], Artemyev, A. [68], Attia, D. [20], Aumayr, F. [2], Backe, H. [34], Bagge, L. [81], Balashov, V. [70], Bans, D. [60], Barros, A. [87], Baur, G. [35], Beck, D. [37], Becker, F. [37], Becker-de-Mos, B. [37], Beier, T. [37], Beyer, H. [37], Birkl, G. [38], Blanco, F. [76], Blaum, K. [29], Block, M. [37], Böhm, S. [80], Bosch, Fritz [37], Brandau, C. [37], Bräuning, H. [37], Bräuning-Demian, A. [37], Briggs, J. [39], Ciortea, C. [67], Cisneros, C. [57], Costa, A. [66], Costa, M. [66], Currell, F. [87], Danared, H. [81], Dangendorf, V. [40], Dauvergne, D. [21], Dias, A. [66], Dilling, J. [4], Dimopoulou, C. [37], Ding, D. [7], Djekic, S. [34], Dong, C. [8], Dörner, R. [41], Dousse, J.-C. [84], Drukarev, E. [69], DuBois, R. [90], Dumitriu, D.-E. [67], Egelhof, P. [37], Egoavil, R. [59], Eichler, J. [42], Engström, M. [81], Enss, C. [91], Enulescu, A. [67], Fainstein, P.D. [1], Ferro, F. [80], Fischer, D. [29], Fleischmann, A. [30], Fluerasu, D. [67], Fogle, M. [92], Förster, E. [44], Fricke, B. [32], Fritzsche, S. [37], Gao, K. [9], Garcia, G. [77], Gaul, E. [93], Glans, P. [82], Goidenko, I. [68], Gotta, D. [35], Guerra, M. [66], Gulyas, L. [49], Gumberidze, A. [37], Gwinner, G. [5], Habs, D. [45], Hagmann, S. [41], Hahn, T. [37], Hanafy, H. [19], Hanif, M. [58], Healy, E. [22], Hedendahl, D. [83], Hencken, K. [85], Herfurth, F. [37], Herlert, A. [36], Hobein, M. [80], Hoekstra, R. [86], Horbatsch, M. [6], Huber, G. [34], Huerga, C. [78], Hutton, R. [10], Igor, G. [68], Indelicato, P. [23], Jakubassa-Amundsen, D. [45], Jentschura, U. [39], Kadhane, U. [50], Kamber, E. [94], Karpuk, S. [34], Keitel, C.-H. [29], Kester, O. [37], Kirchner, T. [6], Kluge, H.-J. [37], Kozhuharov, C. [37], Krings, T. [35], Kühl, T. [37], Kumar, A. [37], Labzowsky, L.N. [68], Lamour, E. [22], Lanzano, G. [54], Le Bigot, E.O. [23], Lemell, C. [3], Lestinsky, M. [29], Liesen, D. [37], Liljebi, L. [81], Limao-Vieira, P. [66], Lindgren, I. [83], Lindroth, E. [80], Lisitsa, V. [71], Ma, X. [10], Macek, J. [92], Madsen, L.B. [18], Madzunkov, S. [80], Manchikanti, K. [50], Manil, B. [24], Mann, R. [37], Manson, S. [95], Marinkovic, B. [75], Marques, J.P. [66], Märtin, R. [37], Martin, S. [21], Marx, G.H. [36], Mathur, D. [50], Matrasulov, D. [103], Mitra, D. [51], Mohamed, T. [19], Mokler, P. [37], Moneta, M. [61], Morgenstern, R. [86], Moshammer, R. [29], Mukherjee, M. [37], Müller, A. [26], Nefoidov, A. [69], Nörtershäuser, W. [34], Nörtershäuser, W. [37], Novotny, C. [34], Pachuki, K. [63], Paiva, A. [66], Pal'Chikov, V. [72], Parente, F. [66], Pisk, K. [16], Plunien, G. [46], Potvliege, R. [88], Prigent, C. [22], Protic, D. [35], Quint, W. [37], Radu, A.-T. [67], Rahaman, S. [37], Rathmann, F. [35], Reinhardt, S. [29], Renner, O. [17], Reuschl, R. [37], Richard, P. [96], Robin, A. [86], Rothard, H. [24], Rozet, J.-P. [22], Rzadkiewicz, J. [62], Saathoff, G. [29], Saenz, A. [43], Salomonson, S. [83], Samek, S. [64], Sanchez, R. [37], Santos, J.P. [66], Savin, D.W. [97], Scheid, W. [27], Schenk, G. [28], Schenkel, T. [98], Schippers, S. [26], Schlath"olter, T. [86], Schmidt-Böcking, H. [41], Schneider, D. [99], Schramm, U. [45], Schuch, R. [80], Schuetzhold, R. [46], Schulz, M. [90], Schweikhard, L. [36], Segal, D. [89], Sepp, W.-D. [33], Shabaev, V. [68], Shaw, M. [79], Shevelko [73], Shinpaugh, J. [100], Silver, E. [101], Simionovici, A. [25], Simon, A. [64], Simon, H. [37], Simonsson, A. [81], Skeppstedt, Ö. [81], Solders, A. [80], Spillmann, U. [37], Stachura, Z. [65], Stahl, S. [34], Stiebing, K. [41], Stöhlker, T. [37], Sulik, B. [49], Suri, B. [52], Suric, T. [16], Surzhykov, A. [29], Surzhykov, A. [37], Szlachetko, J. [84], Tanis, J. [94], Tashenov, S. [37], Thompson, R. [89], Timmermanns, R. [86], Tokesi, K. [49], Tomaselli, M. [37], Trassinelli, M. [22], Trautmann, D. [85], Tribedi, L. [50], Trotsenko, S. [37], Ullrich, J. [29], Ursescu, D. [37], Varentsov, V. [74], Verma, P. [53], Vernhet, D. [22], Vikor, G. [80], Vogel, M. [34], Voitkiv, A. [29], Volotka, A. [46], Walters, J. [87], Wang, J. [12], Warczak, A. [64], Weber, C. [37], Weber, G. [37], Weidemüller, M. [31], Welsch, C. [29], Whelan, C. [102], Wie, B. [10], Williart, A. [79], Winters, D. [37], Wolf, A. [29], Ximeng, C. [13], Yamazaki, Y. [55], Yerokhin, V. [68], Zeng, X. [14], Zhang, F.-S. [10], Zhu, L. [15], Zhu, X. [10], Zilges, A. [38], Zou, Y. [11], Zouros, T. [48], Zouros, T.J.M. [48], Zschornack, G. [46], Zwicknagel, G. [47]

1 Centro Atomico Bariloche (Argentinia)
2 TU Wien, Inst. f. Allgemeine Physik (Austria)
3 TU Wien, Inst. f. Theoretische Physik (Austria)
4 TRIUMF National Laboratory Vancouver (Canada)
5 University of Manitoba (Canada)
6 York University (Canada)
7 Inst.Atomic and Molecular Phys., Jilin University (China)
8 Physics Department, Northwest Normal University (China)
9 Wuhan Institute of Physics and Mathematics (China)
10 Institute of Modern Physics Institute, Fudan University (China)

11 Applied Ion Beam Physics Laboratoy, Fudan University (China)
12 Institute of Applied Physics and Computational Mathematics (China)
13 Lanzhou University (China)
14 China Institute os Atomic Energy (China)
15 University of Science and Technology of China (China)
16 Ruder Boskovic Institute, Zagreb (Croatia)
17 Institute of Physics, Czech Academy of Sciences (Czech. Republic)
18 Department of Physics and Astronomy, University of Aarhus (Denmark)
19 Physics Dep., Beni-Suef Faculty of Science, Cairo University (Egypt)
20 Laboratoire Kastler-Brossel Paris (UPMC/ENS) (France)
21 Institut de Physique Nucléaire de Lyon (France)
22 Institut des NanoSciences de Paris (France)
23 Lab. Kastler Brossel, ENS, UPMC (France)
24 Center of Research on Ions Materials and Photonics (CIMAP), Caen (France)
25 Ecole Normale Superieure - Lyon (France)
26 Institut für Atom- und Molekülphysik, Universität Giessen (Germany)
27 Institut für Theoretische Physik der Universität Giessen (Germany)
28 Institut für Theoretische Physik, TU-Clausthal (Germany)
29 Max-Planck-Institut für Kernphysik Heidelberg (Germany)
30 Kirchhoff-Institut für Physik, Universität Heidelberg (Germany)
31 Physikalisches Institut der Universität Heidelberg (Germany)
32 Theoretische Physik, Universität Kassel (Germany)
33 Institut für Physik, Universität Kassel (Germany)
34 Johannes Gutenberg Universität Mainz (Germany)
35 IKP Forschungszentrum Juelich (Germany)
36 Institut für Physik, Ernst-Moritz-Arndt-Universität Greifswald (Germany)
37 GSI Helmholtzzentrum für Schwerionenforschung GmbH, Darmstadt (Germany)
38 Institut für Angewandte Physik, TU Darmstadt (Germany)
39 Universität of Freiburg (Germany)
40 Physikalisch-technische Bundesanstalt, Braunschweig (Germany)
41 Institut für Kernphysik, Universität Frankfurt (Germany)
42 Hahn-Meitner-Institut Berlin (Germany)
43 Humboldt-Universität zu Berlin (Germany)
44 Institut für Optik, Universität Jena (Germany)
45 Ludwig-Maximilians-Universität München (Germany)
46 Institut fuer Theoretische Physik, TU Dresden (Germany)
47 Theoretische Physik, Universität Erlangen (Germany)
48 Atom. and Mol. Divis. Dept. of Physics, University of Crete (Greece)
49 Inst. of Nuclear Research (MTA ATOMKI), Debrecen (Hungary)
50 Tata Institute of Fundamental Research (India)
51 Saha Institute of Nuclear Physics (India)
52 Bhabha Atomic Research Centre (India)
53 Vaish College, Rohtak, India (presently Atomic physics GSI) (India)
54 Inst. Naz. Fisica Nucleare, Dip. di Fisica, Catania (Italy)
55 University of Tokyo & RIKEN (Japan)
56 The Hashemite University, Physics Department (Jordan)
57 CCF Universidad Nacional Autónoma de México (Mexico)
58 B Z university multan, Pakistan (Pakistan)
59 Instituto Peruano de Energia Nuclear (Peru)
60 Swietokrzyska Academy, Institute of Physics (Poland)
61 Instytut Fizyki, Uniwersytet £ódzki (Poland)
62 Soltan Institute for Nuclear Studies, IPJ, Warsaw (Poland)
63 Institute of Theoretical Physics, Warsaw University (Poland)
64 Jagiellonian University Institute of Physics, Cracow (Poland)
65 Institute of Nuclear Physics of Polish Academy of Sciences (Poland)
66 Universidade de Lisboa (Portugal)
67 National Institute for Physics and Nuclear Engineering (Romania)
68 St. Petersburg State University, Institute of Physics (Russia)
69 Petersburg Nuclear Physics Institute (Russia)
70 Moscow State University (Russia)
71 RRC "Kurchatov Institute" (Russia)
72 Institute of Metrology for Time and Space at VNIIFTRI (Russia)
73 Viatcheslav; Lebedev Physical Institute (Russia)
74 V.G.Khlopin Radium Institute, St.Petersburg (Russia)
75 Institute of Physics, Belgrade (Serbia and Montenegro)
76 Univ Complutense Madrid, Atomic and Molecular Physics Dept (Spain)
77 Consejo Superior de Investigaciones Científicas (CSIC), Madrid (Spain)
78 Hospital Universitario La Paz (Spain)
79 UNED- Universidad a Distancia (Spain)
80 Stockholm University (Sweden)
81 Manne Siegbahn Laboratory (Sweden)
82 Mid-Sweden University (Sweden)
83 Department of Physiscs at Göteborg University (Sweden)
84 Physics Department of the University of Fribourg (Switzerland)

85 Institut für Physik, Universität Basel (Switzerland)
86 KVI Atomic Physics, RijksUniversiteit Groningen (The Netherlands)
87 Queen's University Belfast (United Kingdom)
88 Department of Physics, The University of Durham (United Kingdom)
89 Imperial College London (United Kingdom)
90 University of Missouri-Rolla (USA)
91 Brown University, Physics Department (USA)
92 Oak Ridge National Laboratory (USA)
93 Univeristy of Texas at Austin (USA)
94 Western Michigan University (USA)
95 Georgia State University (USA)
96 Kansas State University (USA)
97 Columbia Astrophysics Laboratory, Columbia University (USA)
98 E. O. Lawrence Berkeley National Laboratory (USA)
99 Lawrence Livermore National Laboratory (USA)
100 East Carolina University (USA)
101 Harvard-Smithsonian Center for Astrophysics (USA)
102 Old Dominion university, Norfolk, Virginia (USA)
103 Heat Physics Department of the Uzbek Academy of Sciences (Uzbekistan)

SPECTRAP

Albrecht, S. [3], Andjelkovic, Z. [1,2], Bharadia, S. [5], Birkl, G. [3], Cazan, R. [1], Church, D. [6], Coto, R.L. [4], Geppert, C. [1,2], Hannen, V. [4], Jöhren, R. [4], Nörtershäuser, W. [1,2], Quint, W. [2], Segal, D. [5], Thompson, R. [5], Vogel, M. [5], Weinheimer, C. [4], Winters, D. [2]

1 Institut für Kernchemie, Johannes Gutenberg-Universität Mainz, Germany
2 GSI Helmholtzzentrum für Schwerionenforschung GmbH, Germany
3 Fachbereich Physik, Technische Universität Darmstadt, Germany
4 Institut für Kernphysik, Westfälische Wilhelms-Universität Münster, Germany
5 Department of Physics, Imperial College London,, United Kongdom
6 Department of Physics, Texas A&M University, USA

Super-FRS

Spokesperson: Hans Geissel

Ackermann, Dieter [6], Aumann, Thomas [6], Äystö, Juha [10], Behr, Karl-Heinz [6], Beniliure, Jose [18], Berz, Martin [13], Brandau, Carsten [6], Brünle, Adolf [6], Chakrabarti, Alok [20], Dendooven, Peter [12], Fehrenbacher, Georg [6], Floch, Eric [6], Geissel, Hans [6], Gerl, Jürgen [6], Gleim, Martin [6], Gorska, Magda [6], Hüller, Wilfried [6], Iwase, Hiroshi [11], Janik, Rudolf [4], Jokinen, Ari [10], Kalimov, Alexander [15], Kauschke, Marion [6], Kelic, Alexandra [6], Kindler, Birgit [6], Kozlova, Ekaterina [6], Kubo, Toshiyuki [16], Kurz, Nikolaus [6], Leibrock, Hanno [6], Lettry, Jacques [3], Litvinov, Yuri [6], Lommel, Bettina [6], Mahrun, Joachim A. [17], Manikonda, Shashikant [1], Marbs, Andreas [7], Mondal, Manos [20], Moritz, Gebhard [6], Morrissey, David [14], Mühle, Carsten [6], Münzenberg, Gottfried [6], Nociforo, Chiara [6], Nolen, Jerry A. [1], Plass, Wolfgang [8], Podolyak, Zsolt [19], Pschorn, Ina [6], Radon, Torsten [6], Ramakers, Heinz [6], Richter, Herta [3], Saren, Jan [10], Savard, Guy [1], Scheidenberger, Christoph [6], Shatunov, Yuri [2], Sherrill, Brad M. [14], Simon, Haik [6], Sitar, Brano [4], Stieglitz, Robert [5], Stoppel, Leonid [5], Strmen, Peter [4], Sümmerer, Klaus [6], Tahir, Naeem A. [6], Tauschwitz, Anna [17], Tomut, Marilena [6], Vobly, Pavel [2], Weick, Helmut [6], Wilfinger, Roman [3], Winfield, John [6], Winkler, Martin [6], Xiang, Yu [6], Yavor, Mikhail [9], Zeller, Albert F. [14]

1 ANL, USA
2 BINP, Novosibirsk, Russia
3 CERN, Switzerland
4 Comenius University Bratislava, Slovakia
5 FZK Karlsruhe, Germany
6 GSI - Helmholtzzentrum für Schwerionenforschung mbH, Darmstadt, Germany
7 Mainz, FH Mainz, Germany
8 II. Phys. Inst., University Giessen, Germany
9 Inst. of Analyt. Phys., RAS, St. Petersburg, Russia
10 University of Jyväskylä, Finland
11 KEK, Tsukuba, Japan
12 KVI Groningen, Netherlands
13 MSU, USA
14 NSCL, MSU, USA
15 Polytech. University St. Petersburg, Russia
16 RIKEN, Japan
17 Theor. Phys., University Frankfurt, Germany
18 Uni St. Diago de Compostella, Spain
19 University of Surrey, UK
20 VECC Kolkata, India

TASCA

Spokesperson: M. Schädel

Ackermann, D. [1], Andersson, L.-L.: [9], Block, M. [1], Brüchle, W. [1], Düllmann, C.E. [1], Dvorak, J. [6], Dvorak, J. [12], Eberhardt, K. [3], Ellison, P. [6], Ellison, P. [12], Essel, H. [1], Even, J. [3], Forsberg, U. [8], Gates, J. [2], Gobulev,P. [8], Gorshkov, A. [2], Graeger, R. [2], Gregorich, K.E. [6], Herzberg, R.-D. [9], Heßberger, F.P. [1], Jäger, E. [1], Khuyagbaatar, J. [1], Kindler, B. [1], Kratz, J.V. [3], Krier, J. [1], Kurz, N. [1], Lahiri, S. [11], Liebe, D. [3], Lommel, B. [1], Maiti, M. [11], Nayak, D. [11], Niewisch, L. [5], Omtvedt, J.P. [7], Parr, E. [9], Rudolph, D. [8], Runke, J. [3], Samadani, F. [7], Schädel, M. [1], Schausten, B. [1], Schimpf, E. [1], Semchenkov, A. [7], Thörle-Pospiech, P. [3], Türler, A. [2], Türler, A. [4], Türler, A. [13], Uusitalo, J. [5], Wiehl, N. [3], Yakushev, A. [2], Zhin, Q. [10]

1 GSI - Helmholtzzentrum für Schwerionenforschung mbH, Darmstadt, Germany
2 Institut für Radiochemie, Technische Universität München, Garching, Germany
3 Institut für Kernchemie, Johannes-Gutenberg Universität, Mainz, Germany
4 Labor für Radio- und Umweltchemie, PSI, Villigen, Switzerland
5 University of Jyväskylä, Jyväskylä, Finland
6 Nuclear Science Division, LBNL, Berkeley, USA
7 University of Oslo, Oslo, Norway
8 University of Lund, Lund, Sweden
9 University of Liverpool, Liverpool, United Kingdom
10 Institute of Modern Physics, Lanzhou, China
11 SAHA Institute Of Nuclear Physics, Kolkata, India
12 University of California, Berkeley, USA
13 Univ. Bern, Bern, Switzerland

TASIPec

Spokesperson: D. Rudolph

Ackermann, D. [1], Andersson, L.-L. [6], Düllmann, C.E. [1], Eberhardt, K. [2], Even, J. [2], Forsberg, U. [5], Gellanki, J. [5], Gerl, J. [1], Gobulev,P. [5], Herzberg, R.-D. [6], Heßberger, F.P. [1], Hoischen, R. [1], Jäger, E. [1], Khuyagbaatar, J. [1], Kojouharov, I. [1], Kratz, J.V. [2], Krier, J. [1], Kurz, N. [1], Merchan, E. [1,5,7], Parr, E. [6], Prokopowicz, W. [1], Rudolph, D. [5], Schädel, M. [1], Schaffner, H. [1], Schausten, B. [1], Schimpf, E. [1], Semchenkov, A. [4], Thörle-Pospiech, P. [2], Türler, A. [2,3,8], Wollersheim, H.-J. [1], Yakushev, A. [2]

1 GSI - Helmholtzzentrum für Schwerionenforschung mbH, Darmstadt, Germany
2 Institut für Radiochemie, Technische Universität München, Garching, Germany
3 Institut für Kernchemie, Johannes-Gutenberg Universität, Mainz, Germany
4 Labor für Radio- und Umweltchemie, PSI, Villigen, Switzerland
5 University of Oslo, Oslo, Norway
6 University of Lund, Lund, Sweden
7 University of Liverpool, Liverpool, United Kingdom
8 Universidad Nacional de Colombia, Bogota, Colombia
9 Univ. Bern, Bern, Switzerland

The TRIGASPEC Collaboration

Spokesperson: Blaum, K.; Nörtershäuser, W.

Beck, D. [1], Beyer, H. [2,3], Blaum, K. [2,3], Block, T.M. [1], Düllmann, C. [4], Eberhardt, K. [4], Eibach, M. [3,4], Eitel, G. [5], Ferrer, R. [6], George, S. [6], Geppert, C. [4], Hammen, M. [4], Herfurth, F. [1], Ketelaer, J. [7], Ketter, J. [2,3], Kluge, H.-J. [1], Knuth, K. [7], Krämer, J. [4], Kratz, J.V. [4], Krieger, A. [4], Lunney, D. [8], Nagy, S. [1,2], Neidherr, D. [9], Neugart, R. [4], Nörtershäuser, W. [1,4], Repp, J. [2,3], Sanchez, R. [1,4], Sieber, B. [4], Smorra, C. [3,4], Trautmann, N. [4], Weber, C. [10]

1 GSI Helmholtzzentrum für Schwerionenforschung GmbH, Darmstadt (Germany)
2 Max-Planck-Institut für Kernphysik, Heidelberg (Germany)
3 Physikalisches Institut, Ruprecht-Karls-Universität Heidelberg, Heidelberg (Germany)
4 Institut für Kernchemie, Johannes Gutenberg-Universität Mainz, (Germany)
5 Aerodynamisches Institut, RWTH Aachen, University (Germany)
6 National Superconducting Cyclotron Laboratory, Michigan State University (USA)
7 Institut für Physik, Johannes Gutenberg-Universität Mainz (Germany)
8 Centre de Spectrométrie Nucléaire et de Spectrométrie de Masse, Orsay Campus (France)
9 CERN, PH-Dept. / ISOLDE, Geneva (Switzerland)

10 Ludwig-Maximilians-Universität München, Gar- ching (Germany)

The WDM Collaboration

Spokesperson: F.B. Rosmej

Abdallah Jr, J. [17], Adonin, A. [3], Aleksandrova, I. V. [14], Basko, M. [12], Beigman, I. [13], Chtcherbakov, V. I. [14], Demura, A. [10], Faenov, A. Y. [11], Fertmann, A. [12], Golubev, A. A. [12], Gromov, A. I. [14], Hoffmann, D. H. H. [7], Jacoby, J. [3], Kapralov, V.G. [15], Kizivetter, D. V. [15], Koresheva, E. R. [14], Koshelev, E. L. [14], Kostriukov, A. Y. [15], Kuteev, B. V. [15], Kühl, Th. [7] ; Lee, R. W. [18], Lisitsa, V. S. [10], Maruhn, J. [4], Merkuliev, Y. A. [14], Nagai, K. [8], Nikitenko, A. I. [14], Nishimura, H. [8], Norimatsu, T. [8], Osipov, I. E. [14], Pikuz, T. A. [11], Redmer, R. [6], Riley, D. [16], Rosmej, F. B. [1], Schlegel, T. [7], Sergeev, V. Y. [15], Sharkov, B. [12], Stamm, R. [1], Tauschwitz, Anna [4], Tauschwitz, A. [7], Timasheva, T. P. [14], Tolokonnikov, S. M. [14], Tolstikhina, I.Y. [13], Turtikov, V. [12], Ullrich, J. [5], Vainshtein, L. A. [13], Wahl, H. [7], Weyrich, K. [7], Yamazaki, Y. [9], Zeitoun, P. [2]

1 Universite de Provence, PIIM-DGP, Marseille (France)
2 LOA-ENSTA, Palaiseau (France)
3 Johann Wolfgang Goethe Universität, Institut für AP, Frankfurt (Germany)
4 Johann Wolfgang Goethe Universität, Institut für TP, Frankfurt (Germany)
5 Max-Planck Institut für Kernphysik, Heidelberg (Germany)
6 University of Rostock, Institute of Physics, Rostock (Germany)
7 GSI-Darmstadt, Plasmaphysik (Germany)
8 Institute of Laser Engineering, Osaka (Japan)
9 The Institute of Physical and Chemical Research RIKEN, Saitama (Japan)
10 Kurchatov Institute, Moscow (Russia)
11 MISDC VNIFFTRI, Mendeleevo (Russia)
12 ITEP, Moscow (Russia)
13 Lebedev Physical Institute, Laboratory of Optics, Moscow (Russia)
14 Lebedev Physical Institute,Thermonuclear Target Laboratory, Moscow (Russia)
15 State Polytechnic University of St. Petersburg, Plasma Physics Laboratory, St. Petersburg (Russia)
16 Queens University, Belfast (United Kingdom)
17 LANL, Los Alamos (USA)
18 LLNL, Livermore (USA)

EU projects at GSI

Compiled by EU-Büro

FAIR Design Study 'DIRAC secondary-Beams'/FP6 (515873)
<http://www.gsi.de/fair/EU-Design-Study/index.html>
Coordinator: GSI, Darmstadt (Germany)
Project coordinator: F. Weißbach
Steering committee: F. Weißbach (GSI), H. Stöcker (GSI), P. Gianotti (Frascati), R. Krücken (München), R. Maier (FZJ), B. Franzke (GSI), D. Krämer (GSI)
Contact at GSI: F. Weißbach,
Projekt endete am 31. Jan. 2009

FAIR Construction 'DIRAC-PHASE 1'/FP6 (515876)
<http://www.gsi.de/fair/EU-Construction/index.html>
Coordinator: GSI, Darmstadt (Germany)
Project coordinator: I. Lemm
Steering committee: H. Stöcker (GSI), H. Eickhoff (GSI), J.-E. Ducret (CEA), H. Ströbele (U-Frankfurt/M.)
Contact at GSI: I. Lemm

EURISOL-Design Study/FP6 (515768)
<http://www.eurisol.org>
Coordinator: INFN-LNL (Italy)
Project coordinator: Y. Blumenfeld (IPN-Orsay)
Project coordinator at GSI: K.-H. Schmidt
Contact at GSI: A. Kelic
Projekt endete am: 31. July. 2009

EUROTRANS/FP6 (516520)
<http://www.fzd.de/DB/Cms?pOid=20823>
Coordinator: FZK, Karlsruhe (Germany)
Project coordinator: J. U. Knebel (NUCLEAR)
Project coordinator at GSI: K.-H. Schmidt
Contact at GSI: A. Kelic

FAIR-PP/FP7 (211382)
<http://www.gsi.de/fair/FAIR-Preparatory-Phase/index_e.html>
Coordinator: GSI, Darmstadt (Germany)
Project Coordinator: F. Weißbach
Contact at GSI: F. Weißbach

NuPNET/FP7 (202914)
<http://www.nupnet-eu.org/>
Coordinator: CNRS (France)
Project Coordinator: S. Galès
Project Coordinator at GSI: I. Reinhard
Contact at GSI: I. Reinhard

HiPER/FP7 (211737)
<http://www.hiper-laser.org/>
Coordinator: STFC (UK)
Project Coordinator: M. Dunne
Project Coordinator at GSI: K. Witte
Contact at GSI: T. Stöhlker

Laserlab Europe cont./FP7 (212025)
<http://www.laserlab-europe.net>
Coordinator: Forschungsverb. Berlin (Germany)
Project coordinator: W. Sandner (Berlin)
Project coordinator at GSI: T. Kühl
Contact at GSI: T. Kühl

SLHC-PP/FP7 (212114)
< http://info-slhc-pp.web.cern.ch/info-SLHC-PP/GB.htm>
Coordinator: CERN, Geneva (Switzerland)
Project coordinator: L.Evans
Project coordinator at GSI: G. Fehrenbacher
Contact at GSI: G. Fehrenbacher

SPIRAL2-PP/FP7 (212692)
<http://www.spiral2pp.eu/>
Coordinator: GANIL, Caen (France)
Project Coordinator: Lewitowicz
Project Coordinator at GSI: J. Gerl
Contact at GSI: J. Gerl

MC-PAD/FP7 (214560)
<http://mc-pad.web.cern.ch/>
Coordinator: CERN, Geneva (Switzerland)
Project Coordinator: C. Joram
Project Coordinator at GSI: C. Schmidt
Contact at GSI: C. Schmidt

MC DITANET/FP7 (215080)
<http://www.kip.uni-heidelberg.de/DITANET/>
Coordinator: KPI Heidelberg (Germany)
Project Coordinator: C. Welsch
Project Coordinator at GSI: P. Forck
Contact at GSI: P. Forck

MC Partner/FP7 (215840)
<http://partner.web.cern.ch/partner/>
Coordinator: CERN, Geneva (Switzerland)
Project Coordinator: M. Dosanjh
Project Coordinator at GSI: W. Kraft-Weyrather
Contact at GSI: W. Kraft-Weyrather

EGEE III/FP7 (222667)
<http://www.eu-egee.org/>
Coordinator: CERN, Geneva (Switzerland)
Project Coordinator: B. Jones
Project Coordinator at GSI: P. Malzacher
Contact at GSI: P. Malzacher

HADRONPHYSICS 2/FP7 (227431)
<http://www.hadronphysics2.eu/>
Coordinator: INFN Frascati (Italy)
Project coordinator: C. Guaraldo (LNF-INFN)
Project coordinator at GSI: F. Weißbach
Contact at GSI: F. Weißbach

EuCARD/FP7 (227579)
<http://www.eu-egee.org/>
Coordinator: CERN, Geneva (Switzerland)
Project Coordinator: J.-P. Koutchouk
Project Coordinator at GSI: J. Stadlmann
Contact at GSI: J. Stadlmann

Laserlab Europe II/FP7 (228334)
<http://www.laserlab-europe.net>
Coordinator: Forschungsverb. Berlin (Germany)
Project coordinator: W. Sandner (Berlin)
Project coordinator at GSI: T. Kühl
Contact at GSI: T. Kühl

ULICE/FP7 (228436)
<http://ulice.web.cern.ch/ULICE>
Coordinator:CNAO (Italy)
Project Coordinator: Roberto Orecchia
Project Coordinator at GSI: W. Kraft-Weyrather
Contact at GSI: W. Kraft-Weyrather

MC ILP-ULTRA/FP7 (230777)
Coordinator: CNRS (France)
Project Coordinator: Tikhonchuk
Project Coordinator at GSI: T. Schlegel
Contact at GSI: T. Schlegel

ALLEGRO/FP7 (231965)
<www.allegroproject.eu/>
Coordinator: Università Pavia (Italy)
Project coordinator: A. Ottolenghi
Project coordinator at GSI: M. Durante
Contact at GSI: M. Durante, C. Kausch,

GSI Projektträger / KKS

D. Müller / I. Reinhard

Projektträger des Bundesministeriums für Bildung und Forschung (BMBF)

GSI is the managing institution for the BMBF project funding (so called "Verbundforschung") in the field of "Hadron- and Nuclear Physics". These public funds are foreseen to support research groups at universities in Germany to strengthen their ability to participate in experiments and projects performed at scientific institutions like GSI and CERN which are funded to a significant level from federal resources.

BMBF project funding: 232 running projects with a total budget of 88,5 Mio. € (16,1 Mio. € in 2009).

GSI F&E contracts ("Forschungs- und Entwicklungsvereinbarungen")

Since 1969 GSI has special research and development contracts with German universities to strengthen the collaboration between these universities and GSI. Mainly resources for personnel are provided to enhance the participation of PhD students and young Post-Docs within GSI projects.

GSI F&E Contracts: 99 running projects with a total budget of 13,1 Mio. € (4,2 Mio. € in 2009).

Helmholtz Association "Initiative and Networking Fund (IVF)"

This fund is one of the Helmholtz Association's key instruments in achieving its strategic goals in Research and Innovation. It consists mainly of "Helmholtz Virtual Institutes" (Networks between GSI and University groups) and a programm to promote Young Researchers.

GSI-HGF-IVF: 7 running projects with a total budget of 8,3 Mio. € (1,5 Mio. € in 2009).

EU Framework Programm 6, EURONS

GSI is the managing institution for the European Integrated Infrastructure Initiative (I3) in nuclear structure physics (EURONS). It consists of 45 institutions in 21 countries. The EURONS project ended in December 2008. In 2009 the final report was submitted to and accepted by the EC.

EURONS: 27 projects with a total budget of 14,0 Mio. € (3,6 Mio. € in 2008).

Workshops, meetings, seminars and talks at the GSI in 2009

Compiled by K. Große

S. Carignano, Torino: **Heavy-quark bound states in a deconfined quark-gluon plasma.** Theorie-Seminar, 07.01.2009.

Marcel Toulemonde, Univ. Caen: **Material modifications and sputtering by swift heavy ions: Role of the Electron-phonon coupling.** Physik dichter Plasmen mit Schwerionen- und Laserstrahlen, 13.01.2009.

Stephan Paul/TU München: **Origin and Structure of the Universe: Science at the Cluster of Excellence in Munich.** GSI Kolloquium, 13.01.2009.

Valentin Batteiger, MPQ Garching: **Precision spectroscopy on single Magnesium ions in the weak binding limit.** Atomphysik-Seminar, 14.01.2009.

Clotilde Boulanger, Nicolas Stein, Institut Jean Lamour, Dpt Chimie et Physique des Solides et des Surfaces, CNRS - Nancy Universit - Universit Paul Verlaine, Metz, France: **Electrodeposition of thermoelectric compounds: Application to nanowires.** Seminar der Materialforschung, 20.01.2009.

Sven Löchner: **Untersuchung von Strahlungseffekten in anwendungsspezifischen integrierten Schaltungen (ASIC).** IT/EE-Palaver, 20.01.2009.

Ingo Peter, GSI: **Superbeschleuniger in Genf und in Darmstadt - LHC und FAIR, warum wir beide brauchen.** Wissenschaft für Alle, 21.01.2009.

Sebastian Heß, GSI: **Compton polarimetry of K- and L-REC radiation into highly charged uranium with a novel 2D Si(Li) X-ray Polarimeter.** Atomphysik-Seminar, 21.01.2009.

J. V. Kratz/Universität Mainz: **Chemical properties of the superheavy elements.** GSI Kolloquium, 27.01.2009.

Robert Lovrincic, Kirchhoff-Institut für Physik, Universität Heidelberg: **Dynamic conductivity of chromium thin films on diamond from infrared spectra.** Seminar der Materialforschung, 27.01.2009.

Adam Krol University of Lodz, Poland: **Triaxiality as an important factor in the K quantum number violation, on the example of K-isomer decay in 132Ce.** NuSTAR Seminar, 28.01.2009.

Marcel Toulemonde, CIRIL Caen, France: **Surface material modifications by slow and high charge ions: Role of the electron-phonon coupling.** Atomphysik-Seminar, 28.01.2009.

Waturu Horiuchi, Niigata: **Correlations and excitations of light nuclei.** Theorie-Seminar, 28.01.2009.

30th International Workshop on Physics of High Energy Density in Matter. 31.01-05.02.2009.

Hans Pfeiffenberger, AWI Bremerhaven: **AG Forschungsdaten der Allianz deutscher Wissenschaftsorganisationen - auf dem Weg zu einer Policy im Umgang mit Forschungsdaten.** IT/EE-Palaver, 03.02.2009.

Isao Tanihata/Osaka: **At the limit of existance.** GSI Kolloquium, 03.02.2009.

Harald Friedrich, TU München: **Scattering, quantum reflection, and near threshold quantization.** Theorie-Seminar, 04.02.2009.

Monika Zakova, Johannes Gutenberg-Universität Mainz: **Nuclear Charge Radii Measurements of 7,10,11Be with Laser Spectroscopy.** Atomphysik-Seminar, 04.02.2009.

Sophie Heinz, GSI: **Study of di-nuclear systems at SHIP.** NuSTAR Seminar, 04.02.2009.

Norito Ishikawa, Advanced Science Research Center, Japan Atomic Energy Agency (JAEA), Tokai-mura, Ibaraki, Japan: **Ion track formation in oxide ceramics irradiated with high energy.** Seminar der Materialforschung, 05.02.2009.

Larry McLerran, BNL: **Quarkyonic Matter and the Large Number of Colors Limit of QCD.** Sonderseminar, 09.02.2009.

Geiger Mode APDs for Frontier Detector Systems. 09.-10.02.2009.

Georg Schreyer, Norbert Willnecker, Keithley Instruments: **Einfach, schnell und zuverlässing Messen und Testen.** IT/EE-Palaver, 10.02.2009.

M.-C. Clochard and J.-E. Wegrowe, Laboratoire des Solides Irradis (LSI), Ecole Polytechnique, Palaiseau, France: **Functionalized nanoporous track-etched membranes: fabrication and applications - A brief overview of the applications for charge, spin and heat transport.** Seminar der Materialforschung, 10.02.2009.

Markus Oberthaler/Heidelberg: **Wave mechanics observed with a lens.** GSI Kolloquium, 10.02.2009.

Matthias Clausen and Jan Hatje / DESY: **CSS - Control System Studio - A New Operator Toolkit.** Sonderseminar, 11.02.2009.

Matthias Clausen and Jan Hatje / DESY: **Hands-On Session: CSS - Control System Studio - A New Operator Toolkit.** Sonderseminar, 11.02.2009.

Juliane Ginsel, GSI: **Effektives Nukleon-Kern-Potential**

aus mikroskopischen Vielteilchenrechnungen. Theorie-Seminar, 12.02.2009.

Shaukat Khan, TU Dortmund: **Future Plans for DELTA in Dortmund.** Beschleuniger-Palaver, 12.02.2009.

Volker Lindenstruth: **Green IT Würfel.** IT/EE-Palaver, 17.02.2009.

Gerhard Schwehm, European Space Astronomy Centre: **ESAs Rosetta-Mission - Die lange Reise zum Kometen Churyumov-Gerasimenko.** Wissenschaft für Alle, 25.02.2009.

XXVIII. PANDA Collaboration Meeting. 02.-06.03.2009.

Xin-Nian Wang (LBNL): **QCD and Heavy-Ion Collisions.** Sonderseminar, 03.03.2009.

Symposium on the Physics of Dense Baryonic Matter. 09.-10.03.2009.

13th CBM Collaboration Meeting. 10.-13.03.2009.

Vladimir Filinov, JIHT, RAS: **Path Integral Monte Carlo Simulations of Strongly Coupled Quantum Coulomb Systems and Quark-Gluon Plasma.** Sonderseminar, 11.03.2009.

Lars Lietzau, Merck KGaA: **Flüssigkristalle - Schnelle Moleküle für bewegte Bilder.** Wissenschaft für Alle, 18.03.2009.

Giuliano Franchetti, GSI - FAIR-AT: **Experimental studies of the high intensity driven emittance growth and beam loss in SIS18.** Beschleuniger-Palaver, 19.03.2009.

Achim Schwenk, TRIUMF: **Neutron-Rich Nuclei and Nuclear Matter from Chiral Interactions.** EMMI-Seminar, 23.03.2009.

Achim Schwenk: **Neutron-Rich Nuclei and Nuclear Matter From Chiral Interactions.** Sonderseminar, 23.03.2009.

Harald Deppe, Holger Flemming: **Entwicklung eines 4 Kanal TDC ASIC für die Flugzeitmessung bei CBM.** IT/EE-Palaver, 24.03.2009.

NUSTAR Annual Meeting. 25.-27.03.2009.

B. Manuel Hegelich, Los Alamos National Laboratory, Los Alamos, USA, und Ludwig-Maximilian Univ. München:: **Laser-driven particle beams: Prospects for GeV ions and coherent keV X-ray sources.** Physik dichter Plasmen mit Schwerionen- und Laserstrahlen, 31.03.2009.

Tobias Fischer, Univ. Basel: **Core collapse supernova simulations in spherical symmetry: state of the art of present models.** Theorie-Seminar, 01.04.2009.

C. Konrad Gelbke/MSU: **Michigan State Universitys plans for a Facility for Rare Isotope Beams.** GSI Kolloquium, 14.04.2009.

Gert Aarts, Swansea University: **Simulations at Finite Chemical Potential and the Sign Problem.** EMMI-Seminar, 20.04.2009.

Wilfried Nörtershäuser, Johannes Gutenberg-Universität Mainz: **Wie Laser uns helfen die Welt zu verstehen.** Wissenschaft für Alle, 22.04.2009.

Bertrand Delamotte, LPTMC Paris: **Momentum dependence of correlation functions: calculations and results obtained for systems at or out-of-equilibrium.** EMMI-Seminar, 27.04.2009.

R3B Collaboration Meeting - NuSTAR. 27.04-30.05.2009.

Mathias Münch: **SNMP als Werkzeug für System- und Netzwerküberwachung.** IT/EE-Palaver, 28.04.2009.

X.Q. Yan, MPI für Quantenoptik, Garching: **GeV mono-energetic proton beam generation in laser foil-plasma interactions.** Physik dichter Plasmen mit Schwerionen- und Laserstrahlen, 28.04.2009.

Carsten Müller, MPI-K Heidelberg: **Energetic electron-ion recollisions in intense laser fields.** Atomphysik-Seminar, 29.04.2009.

U. Blell, FAIR-Synchrotrons/GSI: **Schnell gepulste Magnete für FAIR.** Beschleuniger-Palaver, 30.04.2009.

Klaus Jungmann/KVI: **The Atomic Nucleus - A Precision Laboratory.** GSI Kolloquium, 05.05.2009.

N. Medvedev, Universität Kaiserslautern: **Excitation and relaxation of electronic subsystem at fs- timescales.** Physik dichter Plasmen mit Schwerionen- und Laserstrahlen, 05.05.2009.

EXL-ELISe Joint Collaboration Meeting on Technical Issues - NuSTAR. 05.05.2009.

Andrey Volotka, TU Dresden: **Hyperfine structure and g factor in heavy ions: Towards a test of QED in strong fields.** Atomphysik-Seminar, 06.05.2009.

Maitreyee Saha Sarkar, Saha Institute of Nuclear Physics: **Nuclear structure around 132Sn core: probable new features in semi-magic Sn isotopes.** NuSTAR Seminar, 06.05.2009.

Marco Pignatari: **Neutron capture nucleosynthesis in the explosive He-burning shell in massive stars.** Theorie-Seminar, 07.05.2009.

Stefan Haller: **Digitale Zertifikate.** IT/EE-Palaver, 12.05.2009.

Lothar Schmidt, Inst. für Kernphysik, Univ. Frankfurt: **Young-type interference in collisions between Helium and molecular Hydrogen ions.** Atomphysik-Seminar, 13.05.2009.

Wilfried Nörtershäuser, Uni Mainz: **The nuclear charge radius of Be-11 and recent achievements in high-resolution laser spectroscopy at GSI.** NuSTAR Seminar, 13.05.2009.

M. M. Basko, J. Maruhn, Anna Tauschwitz, V. G. Novikov,

GSI, Darmstadt (ITEP, Moscow); University of Frankfurt; KIAM, Moscow: **Two-dimensional hydrodynamics with heat conduction and radiation transport.** Physik dichter Plasmen mit Schwerionen- und Laserstrahlen, 19.05.2009.

Marco Durante: **The Program for Biophysics Research at the Future FAIR Facility.** Sonderseminar, 19.05.2009.

Peter Wieczorek: **Entwicklung eines ladungsempfindlichen Vorverstärkers zur Auslese von Lawinenfotodioden.** IT/EE-Palaver, 19.05.2009.

Franz von Feilitzsch/TU München: **Low energy neutrino astronomy.** GSI Kolloquium, 19.05.2009.

Zbigniew Majka:: **Status of FAIR.** Sonderseminar, 19.05.2009.

Joachim Enders, Technische Universität Darmstadt: **Quanten mit höchster Energie - Der Mensch unter Dauerbeschuss.** Wissenschaft für Alle, 20.05.2009.

Pawel Danielewicz, MSU: **Symmetry Energy in the Nuclear Surface.** Theorie-Seminar, 20.05.2009.

Shinya Wanajo, TU München: **Nucleosynthesis in the neutrino-driven outflows of core-collapse supernovae.** NuSTAR Seminar, 20.05.2009.

CHARM 2009 - Third International Workshop on Charm Physics. 20.-22.05.2009.

Gabriel Schaumann, Detector and Target Laboratory, TU Darmstadt: **Micro-Target Fabrication: The Challenge posed by High Repetition Rate Systems.** Physik dichter Plasmen mit Schwerionen- und Laserstrahlen, 26.05.2009.

Peter Zumbruch: **EPICS: Experimental Physics and Industrial Control System.** IT/EE-Palaver, 26.05.2009.

Andrey Surzhykov, University of Heidelberg and GSI, Darmstadt: **Electron-electron and electron-photon interactions in the presence of strong electromagnetic fields.** Atomphysik-Seminar, 27.05.2009.

Carsten Brandau, GSI: **Applications of dielectronic recombination in nuclear physics.** NuSTAR Seminar, 27.05.2009.

A. R. Piriz, Universidad de Castilla-La Mancha, Spain: **Sonderseminar: Rayleigh - Taylor Instability in solids.** Physik dichter Plasmen mit Schwerionen- und Laserstrahlen, 28.05.2009.

ENC/EIC Workshop. 28.-30.05.2009.

Peter Winter University of Illinois at Urbana-Champaign, U.S.A.: **In a muon's lifetime: From Fermi's constant to calibrating the sun.** Sonderseminar, 02.06.2009.

Theodor Schlegel, GSI: **Ponderomotive Ion Acceleration and Fast Ion Ignition with Ultraintense Laser Pulses.** Physik dichter Plasmen mit Schwerionen- und Laserstrahlen, 02.06.2009.

Felix Riek/Texas A u. M: **Medium Effects in Rho-Meson Photoproduction at JLAB.** Theorie-Seminar, 03.06.2009.

D.O. Gericke, Centre for Fusion, Space and Astrophysics, Department of Physics, University of Warwick: **Theory and Simulations of Warm Dense Matter - Application to X-Ray Thomson Scattering.** Physik dichter Plasmen mit Schwerionen- und Laserstrahlen, 09.06.2009.

Dam Thanh Son, Institute for Nuclear Theory, University of Washington, Seattle: **Viscosity, quark gluon plasma, and string theory.** EMMI-Seminar, 09.06.2009.

Helmut Dosch, DESY: **Grand Challenges for Megafacilities.** GSI Kolloquium, 09.06.2009.

Chiara Nociforo, GSI: **N =14,16 shell closure in O isotopes.** NuSTAR Seminar, 10.06.2009.

XXIX. PANDA Collaboration Meeting. 15.-19.06.2009.

Andre Hirschberg, Cristie Data Products: **DeDuplizierung als Heilmittel gegen Datenexplosionen.** IT/EE-Palaver, 16.06.2009.

Lyn Evans/CERN: **The Large Hadron Collider, commissioning and re-commissioning.** GSI Kolloquium, 16.06.2009.

Paul Neumayer, Extreme Matter Institute (EMMI), Lawrence Livermore National Laboratory, Livermore, CA, USA: **Charakterisierung dichter Plasmen mit Röntgen-Thomsonstreuung.** Physik dichter Plasmen mit Schwerionen- und Laserstrahlen, 16.06.2009.

Ekaterina Kozlova, GSI: **Shielding design for the target area of the Super-FRS.** NuSTAR Seminar, 17.06.2009.

Katharina Kubicek, MPI-K Heidelberg: **Determination of x-ray transition energies in highly charged ions without reference lines at the Heidelberg EBIT.** Atomphysik-Seminar, 17.06.2009.

Devesh K. Avasthi, Inter University Accelerator Centre, New Delhi; India: **Engineering and synthesis of nanostructures by ion beams.** Seminar der Materialforschung, 18.06.2009.

Ina Mildner: **CERN - FERN!.** Frauen führen Frauen, 18.06.2009.

Erik Brambrink, LULI, Ecole Polytechnique, Palaiseau, France: **Exploring the inner earth core boundary: The characterization of iron under high pressure and temperature.** Physik dichter Plasmen mit Schwerionen- und Laserstrahlen, 23.06.2009.

F. Thielemann/Universität Basel: **Astrophysics and Nuclear Physics: How, where and via which aspects does Nuclear Physics enter the Understanding of Astrophysical Objects.** GSI Kolloquium, 23.06.2009.

Birgit Schabinger, Univ. Mainz: **Towards a g-factor determination of the electron bound in highly charged,**

medium-heavy ions. Atomphysik-Seminar, 24.06.2009.

Ilka Petermann, GSI: **R-process nucleosynthesis calculations with complete nuclear physics input.** NuSTAR Seminar, 24.06.2009.

Sebastian Hess, GSI: **Die Farbe des Universums.** Wissenschaft für Alle, 24.06.2009.

Ingo Hofmann, GSI: **Laser Acceleration of Protons and Ions - Perspectives as New Accelerator Concept.** Beschleuniger-Palaver, 30.06.2009.

Jano Gebelein, KIP Heidelberg: **An approach to system-wide fault tolerance for FPGAs.** IT/EE-Palaver, 30.06.2009.

Jens DIlling, TRIUMF: **Penning trap experiments on the most exotic nuclei on Earth.** NuSTAR Seminar, 30.06.2009.

Kai Zuber/TU-Dresden: **Auf der Suche nach dem doppelten Betazerfall.** GSI Kolloquium, 30.06.2009.

O. Renner, Institute of Physics, Academy of Sciences CR, Prague, Czech Republic: **Advanced X - ray Spectroscopy of Hot Dense Plasmas: Laser - Produced Plasma - Wall Interaction.** Physik dichter Plasmen mit Schwerionen- und Laserstrahlen, 30.06.2009.

Krzysztof Pachucki, Univ. Wasaw: **Fine, hyperfine, and nuclear structure effects in small atomic and molecular systems.** Atomphysik-Seminar, 01.07.2009.

Uwe Greife, Colorado School of Mines: **Proton capture measurements with radioactive ion beams.** NuSTAR Seminar, 01.07.2009.

Gianluca Gregori, Rutherford Appleton Laboratory (UK): **Equation of state of giant planets with high power lasers.** Physik dichter Plasmen mit Schwerionen- und Laserstrahlen, 07.07.2009.

Dmitry A. Glazov, z.Zt. TU Dresden: **g Factor of Highly Charged Ions. Screened QED Corrections.** Atomphysik-Seminar, 08.07.2009.

L. Groening: **Results of the HIPPI-Experiments campaign at the UNILAC.** Beschleuniger-Palaver, 10.07.2009.

Dmitry Varentsov, GSI: **PRIOR - Proton Microscope for FAIR.** Physik dichter Plasmen mit Schwerionen- und Laserstrahlen, 14.07.2009.

Thomas R. Rodriguez, GSI: **Nuclear structure studies with beyond mean field methods.** Theorie-Seminar, 15.07.2009.

Thomas Walther, TU Darmstadt: **Entangled Photons and more ....** Atomphysik-Seminar, 15.07.2009.

Petr Navratil, LLNL: **Ab initio many-body calculations of light ion reactions.** Theorie-Seminar, 22.07.2009.

EMMI Workshop - Quark-Gluon Plasma meets Cold Atoms Episode II. 03.-08.08.2009.

EMMI Workshop on Virtual Bremsstrahlung and HADES. 12.08.2009.

Marcus Bäumer (Vortragender) und Dipl.-Chem. Arne Wittstock, Institut für Angewandte und Physikalische Chemie, Universität Bremen: **Heterogeneous Catalyst Engineering: Illusion or Reality?** Seminar der Materialforschung, 18.08.2009.

Heinrich Hora, Universität von New South Wales, Sydney, Australien: **Lasergetriebene Kernfusion von Wasserstoff-Bor: Neuer Zugang zu sauberer Kernenergie.** Physik dichter Plasmen mit Schwerionen- und Laserstrahlen, 18.08.2009.

High Energy Proton Microscopy HEPM-2009. 24.-25.08.2009.

Linear and nonlinear dynamics in the CERN SPS (as a test for the LHC). Beschleuniger-Palaver, 27.08.2009.

Shoji Nagamiya, Director of J-PARC Center: **J-PARC Project and Its Science.** GSI Kolloquium, 31.08.2009.

EMMI Workshop - Quarks, Hadrons and the Phase Diagram of QCD. 31.08-03.09.2009.

5th SPARC Collaboration Symposium. 01.-04.09.2009.

Atsushi Umeya, RIKEN: **Lambda-Sigma coupling effect in neutron-rich p-shell hypernuclei in a shell-model calculation.** NuSTAR Seminar, 07.09.2009.

XXX. PANDA Collaboration Meeting. 07.09-09.11.2009.

Yoichi Ikeda, RIKEN: **Energy dependence of K N interaction and strange dibaryon resonance.** Theorie-Seminar, 09.09.2009.

M. Voskresenskaya, GSI: **Neutrino scattering on nuclei - Interacting nucleon gas - Equation of state of nuclear matter.** Theorie-Seminar, 15.09.2009.

Kei-Ichi Kondo, Uni Tokyo, Chiba: **Recent progress in dual superconductor picture for quark confinement.** Theorie-Seminar, 16.09.2009.

Walter Schön: **Das lustre Filesystem bei GSI.** IT/EE-Palaver, 22.09.2009.

David Ondreka, GSI: **Die Zukunft der Datenversorgung für GSI und FAIR.** Beschleuniger-Palaver, 24.09.2009.

Heiko Scheit: **32Ne and the Island of Inversion: first in-beam gamma-ray spectroscopy study at the Radioactive Ion Beam Factory.** NuSTAR Seminar, 24.09.2009.

Tadafumi Kishimoto: **Study of 48Ca double beta decay and CANDLES.** NuSTAR Seminar, 24.09.2009.

Marcus Pattloch, DFN Berlin: **DFN-PKI: Leistungen, Erfahrungen und Perspektiven.** IT/EE-Palaver, 29.09.2009.

Isfried Petzenhauser, GSI: **Grundlegende Untersuchungen zur Stoßleistungstechnik des Magnetischen Horns am FAIR p-bar Target.** Beschleuniger-Palaver, 01.10.2009.

14th CBM collaboration meeting. 05.-09.10.2009.

Kenji Morita, GSI: **QCD sum rule approach to heavy quarkonia at finite temperature.** Theorie-Seminar, 07.10.2009.

RISING Symposium. 07.10.2009.

Frank Nürnberg, TU Darmstadt: **Warp Simulations for Capture and Control of Laser-Accelerated Proton Beams.** Physik dichter Plasmen mit Schwerionen- und Laserstrahlen, 13.10.2009.

Tetsuya Yamaki, Japan Atomic Energy Agency (JAEA): **Formation and Chemical Etching of Heavy Ion Tracks in Fluoropolymer Films.** Seminar der Materialforschung, 13.10.2009.

Anastasiya Bondarevskaya, St. Petersburg State University: **Highly charged ion beam polarization and its application to the search for the parity nonconservation effects in ions.** Atomphysik-Seminar, 14.10.2009.

TASCA 09 - 8th Workshop on Recoil Separator for Superheavy Element Chemistry. 14.10.2009.

H.-J. Kunze, Ruhr-University: **X-ray lasing in capillary discharges based on charge exchange between ions.** Physik dichter Plasmen mit Schwerionen- und Laserstrahlen, 20.10.2009.

B.K. Panigrahi, Indira Gandhi Centre for Atomic Research, Kalpakkam, India: **Use of ion accelerators and computer simulation towards development of radiation resistant materials.** Seminar der Materialforschung, 22.10.2009.

Burkhard Schillinger, TU München: **Neutron Imaging - a tool complementary to X-rays.** Physik dichter Plasmen mit Schwerionen- und Laserstrahlen, 27.10.2009.

Horst Göringer: **gStore und lustre - Experimentdatenspeicherung bei GSI.** IT/EE-Palaver, 27.10.2009.

Sebastian Raeder, Inst. für Physik, Univ. Mainz: **Isotope selective trace-analysis of actinides for radioprotection using Resonance Ionisation Mass Spectrometry.** Atomphysik-Seminar, 28.10.2009.

Javier Menendez, Universidad Autonoma de Madrid: **Nuclear Structure for Neutroniless Double-Beta Decay.** EMMI-Seminar, 02.11.2009.

CBM-China Meeting. 02.-04.11.2009.

Zuzanna Siwy, Department of Physics and Astronomy, University of California, Irvine, USA: **Ion Transport through Nanopores: From Living Cells to Ionic Diodes and Transistors.** Seminar der Materialforschung, 03.11.2009.

Claudia Veronika Meister, TU Darmstadt: **On the search for new methods of short-time earthquake prediction.** Physik dichter Plasmen mit Schwerionen- und Laserstrahlen, 03.11.2009.

Fritz Nolden, GSI: **A new resonant Schottky pick-up for the ESR.** Atomphysik-Seminar, 04.11.2009.

Ivo Seitenzahl / MPI Astrophysik Garching: **Effect of Auger and internal conversion electrons on late-time supernova light curves.** Theorie-Seminar, 04.11.2009.

Ivo Seitenzahl, MPI Astrophysik Garching: **Effect of Auger and internal conversion electrons on late-time supernova light curves.** Theorie-Seminar, 04.11.2009.

Su-Ming Weng, TU Darmstadt und Institute of Physics, Chinese Academy of Sciences, Beijing, China: **High - Power Laser Plasma Interaction by Fokker - Planck Simulations.** Physik dichter Plasmen mit Schwerionen- und Laserstrahlen, 10.11.2009.

Torbjörn Rander, TU Berlin: **Nano-scale imaging using X-ray holography.** Seminar der Materialforschung, 10.11.2009.

Jochen Walz, Universität Mainz: **Precision Experiments with Antiprotons and Antihydrogen to Investigate Fundamental Physics.** Atomphysik-Seminar, 11.11.2009.

Takuya Furuta / LPC Caen: **Applications of Antisymmetrized Molecular Dynamics.** Theorie-Seminar, 11.11.2009.

A. Popp, Max-Planck-Institute for Quantum Optics, Garching: **Soft-X-Ray Undulator-Radiation from Laser-Wakefield-Accelerated Electrons.** Physik dichter Plasmen mit Schwerionen- und Laserstrahlen, 17.11.2009.

Ruediger Berlich, FZ Karlsruhe: **Distributed Parametric Optimization using the Geneva Library.** IT/EE-Palaver, 17.11.2009.

Alban Kellerbauer, MPI Heidelberg: **Cold Antiprotons for Antimatter Gravity Studies.** Atomphysik-Seminar, 18.11.2009.

Frank Nürnberg, GSI: **Warp Simulations for Capture and Control of Laser-Accelerated Proton Beams.** Beschleuniger-Palaver, 19.11.2009.

Thomas Halfmann, Institute of Applied Physics, TU Darmstadt: **Storage of Light in Atomic Coherences.** Atomphysik-Seminar, 21.11.2009.

EMMI Workshop FAIR Lattice QCD Days at GSI. 23.-24.11.2009.

Beatrice Schuster, GSIand& TU Darmstadt: **Materials at extreme conditions: Combining high pressure and heavy-ion irradiation.** Physik dichter Plasmen mit Schwerionen- und Laserstrahlen, 24.11.2009.

Alexander Rothkopf, Tokyo University: **Proper Heavy Quark**

Potential from Lattice QCD. EMMI-Seminar, 25.11.2009.

R.D. DuBois, Missouri University of Science and Technology: **Using Antimatter to Study Matter: Positron-Atom Inelastic Interactions and Kinematics.** Atomphysik-Seminar, 25.11.2009.

V.B. Shutov, JINR, Dubna: **Electron string ion sources applied for formation of highly charged ion beams.** Atomphysik-Seminar, 26.11.2009.

Ulrich Schramm, FZ Dresden-Rossendorf: **Scaling of proton energies in ultra-short pulse laser plasma acceleration - and future projects at FZ Dresden-Rossendorf.** Physik dichter Plasmen mit Schwerionen- und Laserstrahlen, 01.12.2009.

Sarah Porteboeuf, Universite de Nantes: **Study of hard processes with the EPOS event generator at LHC energies.** EMMI-Seminar, 02.12.2009.

V.B. Shutov, JINR, Dubna: **Electron string ion sources applied for formation of highly charged ion beams.** Atomphysik-Seminar, 02.12.2009.

Radek Pleskac: **Fragmentation of 7Li beams in water.** Biophysics Seminar, 03.12.2009.

XXXI. PANDA Collaboration Meeting. 07.-10.12.2009.

Martin Droba, Goethe Universität Frankfurt: **Non-Neutral Plasma and High Intensity Beam Physics.** Physik dichter Plasmen mit Schwerionen- und Laserstrahlen, 08.12.2009.

Alexey Sokolov, GSI: **Charge Breeding in SPARC EBIT.** Atomphysik-Seminar, 09.12.2009.

CARAT 09 - Workshop on Advanced Diamond Detectors. 13.-15.12.2009.

Greg Chubarian, Texas, Cyclotron Institute: **Production of rare isotope beams at the TAMU Cyclotron Institute (T-REX project).** NuSTAR Seminar, 15.12.2009.

Festseminar anlässlich des 60. Geburtstages von Theodor Schlegel. Physik dichter Plasmen mit Schwerionen- und Laserstrahlen, 15.12.2009.

Alexander E. Volkov, Kurchatov Institute: **Kinetics of the electronic subsystem of ion irradiated dielectrics during the early stage of track formation.** Seminar der Materialforschung, 16.12.2009.

Dmitry Kamanin and Yuri Pyatkov, Dubna: **Recent results on clustering in cold nuclei.** NuSTAR Seminar, 16.12.2009.

K. Vantournhout/Gent: **Nuclear Pasta with a touch of quantum / Towards fully antisymmetrised dynamics for bulk fermion systems.** Theorie-Seminar, 16.12.2009.

Pierre-Michel Hillenbrand, Univ. Gießen: **Double ionization of highly charged Sn ions by electron impact.** Atomphysik-Seminar, 16.12.2009.

Andreas Heinz, Yale: **Evolution of nuclear shell-structure along N=126 and N=152.** NuSTAR Seminar, 18.12.2009.

Conference contributions and Talks

Compiled by K. Kreidi, C. Kausch, I. Kraus
GSI, Darmstadt, Germany

Ackermann, Dieter
Superheavy Elements - Investigating the Properties of Exotic High-Z Nuclear Matter
International Symposium on Nuclear Physics
Mumbai, India, 8.12.-12.12.2009

Ackermann, Dieter
Superheavy Element Synthesis and Nuclear Structure
Nuclear Structure and Dynamics 2009
Dubrovnik, Croatia, 4.5.-8.5.2009

Ackermann, Dieter
Lessons Learned from SHIP (and TASCA) Detectors and Related Issues
Super Separator Spectrometer (S3) Workshop
GANIL, Caen, France, 16.6.-17.6.2009

Aksyutina, Yuliya
Studies of light unbound nuclear systems beyond the dripline
NUSTAR Seminar, GSI
Darmstadt, Germany, 21.11.2009

Al-Turany, M.
GPU's for event reconstruction in the FairRoot Framework
CHEP 2009
Prag, März 2009

Al-Turany, M.
FairRoot Framwork
Model 2009
Tagbilaran, Bohol, Philippines, Mai 2009

Andjelkovic, Z.
Ion capture and non-destructive detection in the SPECTRAP experiment
Frühjahrstagung der DPG Atome, Moleküle, Quantenoptik und Plasmen
Hamburg (Germany), 2.–6. März 2009

Andronic, A
Hadron production at chemical equilibrium
Workshop on Nuclear Matter Physics at SIS100
Darmstadt (Germany), 27.Apr.09

Andronic, A.
Heavy quark(onium) at LHC: the statistical hadronization case
SQM'09
Buzios (Brazil), 27.09-02.10.2009

Andronic, A.
The horn, the hadron mass spectrum and the QCD phase diagram
NN2009
Beijing (China), 16-21 August 2009

Andronic, A.
Statistical hadronization of charm: energy dependence and in-medium effects
Heavy Quarkonia Production in Heavy-Ion Collisions
Trento (Italy), 25-29. Mai 2009

Arcones, A.
Influence of light nuclei on neutrino-driven supernova outflows
CompStar 2009
Coimbra (Portugal), 11.02.2009

Arcones, A.
Neutrino-driven supernova outflows and nucleosynthesis
Seminar, Department of Physics
Basel (Switzerland), 26.02.2009

Arcones, A.
Nucleosynthesis studies in neutrino-driven winds: influence of the nuclear physics input
432. Heraeus-Seminar: Nucleosynthesis – making the elements of the universe
Bad Honnef (Germany), 05.06.2009

Arcones, A.
Nucleosynthesis studies in neutrino-driven winds: influence of the nuclear physics input
Nuclear Physics in Astrophysics IV
Frascati (Italy), 08.06.2009

Arcones, A.
Electron fraction based on NSE and beta-equilibrium; Nucleonsynthesis in neutrino-driven winds
Workshop "Microphysics in Computational Relativistic Astrophysics
Kopenhagen (Denmark), 28.08.2009

Artikova, S.
Beam Halo Studies with the QUASAR Group.
University of Maryland
Maryland (USA), 13.November 2009.

Aumann, Thomas
Reactions with neutron-proton asymmetric nuclei R3B
Second International Conference on Nuclear Fragmentation NUFRA2009
Kemer Antalya, Turkey, 27.9.-4.10.2009

Aumann, Thomas
Reactions with high-energy radioactive beams for astrophysics

5th European Summer School on Experimental Nuckear Astrophysics
Santa Tecla, Catania Italy, 20.9. - 27.9. 2009

Aumann, Thomas
The dipole response of neutron-rich nuclei investigated with LAND@GSI
Collective Motion in Nuclei under Extreme Conditions (COMEX 3)
Mackinac Island, USA, 2.6.-5.6.2009

Aumann, Thomas
Quasifree Scatterimg with radioactive beams
Nuclear Structure and Dynamics 2009
Dubrovnik, Croatia, 4.5.-8.5.2009

Aumann, Thomas
Struktur und Dynamik von exotischen Kernen weit weg vom Stabilitätstal
Arbeitstreffen Kernphysik
Schleching, Germany, 26.2. - 5.3.2010

Averbeck, R.
The charm and beauty of RHIC
Kolloquium zur "Struktur und Dynamik der elementaren Materie
Frankfurt, 08.01.09

Averbeck, R.
PHENIX perspectives for the RHIC energy scan
Workshop on "The Physics of Dense Baryonic Matter“
GSI, 10.03.09

Averbeck, R.
Urknall im Labor - Was Kern-Kern Kollisionen ueber die Materie des fruehen Universums verraten
Physikalisches Kolloquium
Darmstadt, 08.05.09

Bender, M.
Experimental and Theoretical Studies on Heavy ion Induced Desorption
Seminar at CERN VSC-group
Geneva (Switzerland), 28.September 2009.

Berdermann, E.
Single-crystal CVD-diamond detectors
Workshop Detectors for Super-FRS
GSI Darmstadt, 11. February 2009

Berdermann, E.
Early Diamond-on-Iridium (DoI) samples
1st CARAT Workshop
GSI, 13. - 15.12. 2009

Berdermann, E. (invited)
Diamond detectors for hadron physics research
20th Europ. Conf. on Diamond, Diamond-Like Materials, Carbon Nanotubes, and Nitrides (DIAMOND 2009)
Athens (Greece), 6. -10.10.2009

Bert, C.
Motion management in radiation therapy
DPG Frühjahrstagung
München, 9.-13.3.2009

Bert, C.
Moving targets II:Implications for (scanned) heavy ion beam therapy
IBIBAM
Köln, 6.-10.7.2009

Bert, C.
Current developments of beam tracking with scanned ion beams
Real-Time Motion Adaptive Radiation Therapy Workshop
Lübeck, 14/ September 2009

Bert, C.
Influence of target motion on (scanned) particle beam irradiation
PTCOG 48
Heidelberg, 29/ September 2009

Block, Michael
First Direct Mass Measurements of 252-254No with SHIPTRAP
International Symposium on Exotic Nuclei, EXON-2009
Sochi, Russia, 28.9.-2.10.2009

Block, Michael
First Penning Trap Mass Spectrometry of Transuranium Isotopes
APPLICATION OF LASERS AND STORAGE DEVICES IN ATOMIC NUCLEI RESEARCH 2009
Posen, Polen, 22.5.-25.5.2009

Block, Michael
Perspectives for Penning Trap Mass Measurements of Super Heavy Elements
Workshop on Atomic Physics with Rare Atoms
Ann Arbor, USA, 1.6.-3.6.2009

Block, Michael
First Direct Mass Measurements of 252-254No with SHIPTRAP
Radioacvitve Nuclear Beams (RNB) 2009
Grand Rapids, USA, 26.5.-30.5.2009

Block, Michael
First Direct Mass Measurements of Nobelium Isotopes
DPG-Frühjahrstagung 2009, 1. Hauptvortrag im FV Massenspektrometrie
Hamburg, Germany, 2.3.-6.3.2009

Block, Michael
High-Precision Mass Measurements of Neutron-rich Fe and Co Isotopes at LEBIT
Workshop on Nuclear structure of the neutron-rich region around Z=28 towards and beyond N=50
Leuven, Belgium, 9.3.-11.3.2009

Boretzky, Konstanze
Dipole strength in neutron-rich Ni and Sn isotopes

The first EURISOL UG topical meeting – The formation and structure r-process nuclei, between N=50 and 82 (including 78Ni and 132Sn areas)
Boutachkov, Plamen
Development of detectors for slowed down beams at GSI
Low Current, Low Energy Beam Diagnostics
Hirschegg, Austria, 24.11.2009

Boutachkov, Plamen
The hunt for missing isomers
Seminarreihe
TU Darmstadt, Germany, 19.11.2009

Boutachkov, Plamen
Development of detectors for slowed down beams at GSI
DPG Frühjahrstagung
Bochum, Germany, 16.03.2009

Bräuning, H.
Polarization Measurements of Radiative Electron Capture in Highly Charged Ions.
DAE-BRNS Symposium on Atomic, Molecular and Optical Physics, IUAC
New Dehli (India), 10.Februar 2009

Braun-Munzinger, P.

Resultate von RHIC und Pl ¨ane fu ¨r

Quarkmateriestudien mit ALICE am LHC
Kolloquium, Uni Giessen
Giessen (Germany), 02.Feb.09

Braun-Munzinger, P.
Hadron production in ultra-relativistic nuclear collisions and the QCD phase boundary
Symposium on dense baryonic matter, GSI
Darmstadt (Germany), 09.Mrz.09

Braun-Munzinger, P.
Heavy quarks, quarkonia, and the quark-gluon plasma
QM2009, student program
Knoxville (USA), 29.Mrz.09

Braun-Munzinger, P.
Hadron production in ultra-relativistic nuclear collisions and the QCD phase boundary
symposium on quantum field theories in extreme environments
Paris (France), April 23-25, 2009

Braun-Munzinger, P.
Relativistic nuclear collisions, 6 lectures
doctoral training program on "Strongly correlated Quantum Systems", ECT*
Trento (Italy), April 27 -29, 2009

Braun-Munzinger, P.

Lessons from RHIC and Discovery Potential at LHC
2ndCracow-Warsaw workshop on LHC physics
Warsaw (Poland), 18.Mai.09

Braun-Munzinger, P.
Statistical hadronization, charmonia, and the QCD phase boundary
ECT* workshop on charmonia in the QGP
Trento (Italy), May 25-29, 2009

Braun-Munzinger, P.
Hadron production in ultra-relativistic nuclear collisions and the QCD phase boundary
CPOD09 symposium
Brookhaven (USA), 01.Jun.09

Braun-Munzinger, P.
Relativistic Nuclear Collisions
FIAS colloquium
Frankfurt (Germany), 18.Jun.09

Braun-Munzinger, P.
Quarkonia and the Quark-Gluon Plasma
EMMI and XXVI Max Born workshop
Wroclaw (Poland), 01.Jul.09

Braun-Munzinger, P.
The ALICE experiment at LHC, status and plans, plenary talk
LP09 conference
Hamburg (Germany), 01.Aug.09

Braun-Munzinger, P.
ALICE@LHC, detector status and physics plans
RNC seminar, LBNL
Berkeley (USA), 22.Sep.09

Braun-Munzinger, P.
Charmonium, a special bound state, a probe for deconfinement in ultra- relativistic nuclear collisions
colloquium, nuclear science division, LBNL
Berkeley (USA), 23.Sep.09

Braun-Munzinger, P.
On local equilibration in ultra-relativistic nuclear collisions, panel dis- cussion
SQM2009
Buzios (Brazil), 28.Sep.09

Braun-Munzinger, P.
Physics of ultra-relativistic nuclear collisions
Minerva-Gentner Sympo- sium 2009: experiment confronts string theory
Berlin (Germany), 13.Okt.09

Braun-Munzinger, P.
Reise zum Urknall
Saturday Morning Physics
Darmstadt (Germany), 01.Dez.09

C.P.Welsch
The USR at FLAIR.

FLAIR Meeting at MSL
Stockholm (Sweden), 5.Februar 2009

Castillo, J.
Experimental investigations of relativistic hydrodinamics and the ideal fluid scenario at RHIC
Relativistische Schwerionenphysik Seminar
Darmstadt (Germany), 15.Jan.09

Castillo, J.
Shear viscosity/entropy ratio in Cold Atoms
Relativistische Schwerionenphysik Seminar
Darmstadt (Germany), 29.Jan.09

Castillo, J.
Multiplicity fluctuations and forward-backward correlations in proton-proton collisions at LHC energies
ECT* Doctoral Training Programme
Trento (Italy), 28.Mai.09

Cazan, R.
Towards sympathetic cooling of trapped ions with laser-cooled Mg+ ions for mass spectrometry and laser spectroscopy
VIII International Workshop: APPLICATION OF LASERS AND STORAGE DEVICES IN ATOMIC NUCLEI RESEARCH - Recent Achievements and Future Prospects
Poznan (Poland), 22.-25. Juni 2009

Ciobanu, M.
First results from PADI-2
13th CBM Collaboration Meeting
GSI, 10.-13. March 2009

Ciobanu, M.
Regarding the DC biasing of MAPD detectors
CBM ToF Palaver
GSI, 4. May 2009

Ciobanu, M.
Regarding the matching of PADI-1 to strip RPCs
CBM ToF Palaver
GSI, 25. May 2009

Ciobanu, M.
RPC-FEE Status Report
14th CBM Collaboration Meeting
Split (Croatia), 6.-9. October 2009

Domingo-Pardo, Cesar
Nuclear Astrophysics at CERN n_TOF
Workshop on Nuclear Astrophysics Opportunities at the Underground Laboratory in Canfranc
Barcelona, Spain, 18.-20.1.2009

Domingo-Pardo, Cesar
Simulations for AGATA at GSI
HISPEC/DESPEC Meeting
GSI, Darmstadt, Germany, 23.-24.3.2009

Domingo-Pardo, Cesar
Nuclear Astrophysics at CERN n_TOF and at FAIR DESPEC
Annual NUSTAR Meeting
GSI, Darmstadt, Germany, 23.-27.3.2009

Domingo-Pardo, Cesar
MC Simulations for the campaign of AGATA at GSI
VIIIth AGATA Week
Köln,Germany, 30.3.2009-3.4.2009

Domingo-Pardo, Cesar
s-process nucleosynthesis in massive stars: new (n,gamma) measurements on 60Fe, 62Ni and 64Ni
Nuclear Physics in Astrophysics IV
Frascati, Italy, 8.-12.6.2009

Domingo-Pardo, Cesar
Simulations for the campaign of AGATA at GSI
Workshop on AGATA at GSI
GSI, Darmstadt, 15.-16.7.2009

Domingo-Pardo, Cesar
Applying gamma-imaging techniques in nuclear physics experiments
Seminar for the Visit of the Saudi Arabian Delegation
GSI, Darmstadt, 16.09.2009

Domingo-Pardo, Cesar
Monte Carlo Simulations for the PreSPEC campaign of AGATA at GSI
HISPEC/DESPEC Meeting
Darmstadt, Germany, 5.-6.10.2009

Domingo-Pardo, Cesar
Neutron Capture Measurements for Nuclear Astrophysics at CERN n_TOF
Invited Seminar
Laboratori Nazionali di Legnaro, Legnaro, Italy,

Domingo-Pardo, Cesar
A Novel 3D Scanner for gamma-tracking detectors
Detector systems networking workshop
TU Darmstadt, Germany, 24.11.2009

Domingo-Pardo, Cesar
Nuclear Astrophysics at FAIR (Invited)
VIII Latin American Symposium on Nuclear Physics and Applications
Santiago, Chile, 14.-19.12.2009

Düllmann, Christoph Emanuel
Decay properties of 'chemical isotopes' of light even-Z transactinides
7th Workshop on the Chemistry and Physics of the Heaviest Elements
Mainz, Germany, 11.10.-13.10.2009

Düllmann, Christoph Emanuel
Studies of the reaction 244Pu(48Ca,3-4n)188,289_114 at TASCA
7th Workshop on the Chemistry and Physics of the Heaviest Elements
Mainz, Germany, 11.10.-13.10.2009

Düllmann, Christoph Emanuel
Physikalische Vorseparation - Eine neue Technik für spannende Chemieexperimente mit schwersten Elementen
GDCH - Wissenschaftsforum Chemie 2009,
Frankfurt a. Main, 30.8.-2.9.2009

Düllmann, Christoph Emanuel
Chemistry behind a separator: lessons from BGS and TASCA for S3
Super Separator Spectrometer (S3) Workshop
GANIL, Caen, France, 16.6.-17.6.2009

Düllmann, Christoph Emanuel
GSI Nuclear Chemistry Studies of Superheavies
International Symposium - Periodic Table of D.I. Mendeleev -The New Superheavy Elements
Dubna, Russia, 20.1.-21.1.2009

Durante, M.
Space radiation biology
General seminar of the Fraunhofer Institue, Euskirchen
Euskirchen (Germany), 4/ März 2009

Durante, M.
Heavy ions in therapy and space
General seminar of CEA, Saclay
Saclay (France), March 20, 2009.

Durante, M.
Heavy ion radiobiology in therapy and space
Colloquia of DKFZ
Heidelberg (Germany), April 8, 2009.

Durante, M.
Radiation Biophysics at GSI
Meeting of the Korean Phyisical Sciety
Seoul (Korea), April 23, 2009.

Durante, M.
Havy ion therapy
GSI-KACS Symposium
Ryadh (Saudi Arabia), May 2, 2009.

Durante, M.
Radiation Protection in Space
General Seminar at FIAS
Frankfurt (Germany), May 28, 2009.

Durante, M.
View for particle tehrapy in the future
Summary talk at the ENLIGHT meeting
Valencia (Spain), June 19, 2009.

Durante, M.
Radiation biology on the Moon
ESA Exploration Meeting
Nordwijk (The Netherlands), June 26, 2009.

Durante, M.
Space radiation protection
RADAM meeting
Frankfurt (Germany), July 3, 2009.

Durante, M.
Heavy ion induuced chromosomal aberartions
10th ICEM Symposium
Florence (Italy), August 24, 2009.

Durante, M.
Heavy ion biophysics
34th ERRS Meeting
Prague (Czech Republic), August 28, 2009.

Durante, M.
Heavy ions in therapy
World Congress on Medcial Physics
Munich (Germany), September 11, 2009.

Durante, M.
Heavy ions from tehrapy to space
38th PTCOG, Heidelberg
Heidelberg (Germany), October 2, 2009.

Durante, M.
Heavy ion induced chromosomal aberartion
Microdosimetry Symposium
Verona (Italy), October 28, 2009

Durante, M.
Heavy ion biophysics
FANTOM Summer School
Emmen (the Netherklands), November 2, 2009.

Durante, M.
Mathematical models in radiation biophysics
Meeting of the TPS collaboration
Turin (Italy), November 6, 2009.

Dworsckak, Michael
First direct Penning trap mass measurements on transuranium elements with SHIPTRAP
Tours Symposium on Nuclear Physics and Astrophysics VII
Kobe, Japan, 15.-21.11.2009

Dworsckak, Michael
First direct Penning trap mass measurements on transuranium elements with SHIPTRAP
Institute of Modern Physics, Chinese Academy of Sciences
Lanzhou, China,, 23.11.2009

Dworsckak, Michael
First direct Penning trap mass measurements on transuranium elements with SHIPTRAP
Seminar Institute of Theoretical Physics, Chinese Academy of Sciences
Peking, China,, 26.11.2009

Egelhof, Peter
The EXL Target Recoil Detector – Overview on Status and Perspectives
EXL/ELISe Joint Collaboration Meeting on Technical Issues
GSI, Darmstadt, 4.5.-6.5.2009

Egelhof, Peter

Future Perspectives for the Application of Low Temperature Detectors in Heavy Ion Physics
13th Int. Workshop on Low Temperature Detectors, LTD13
Stanford, USA, 20.7.-24.7.2009

Egelhof, Peter
Exotic Nuclei Studied in Direct Reactions at Low Momentum Transfer – Recent Results and Future Perspectives at FAIR
6th Int. Workshop on Direct Reactions with Exotic Beams, DREB 2009
Tallahasseee, USA, 16.12.-19.12.2009

Eibach, M.
Penning trap mass measurements and laser spectroscopy on neutron-rich fission products extracted from the research reactor TRIGA-Mainz
Frühjahrstagung der DPG Atome, Moleküle, Quantenoptik und Plasmen
Hamburg (Germany), 2.–6. März 2009

Elsässer, T.
Modellierung der biologischen Wirkung von Ionenstrahlen
Seminar Partikeltherapie
Marburg (Germany), 1/ März 2009

Elsässer, T.
Dosimetry and RBE of pulsed particle beams
440th Heraeus Seminar
Fraueninsel (Germany), 16/ September 2009

Elsässer, T.
Status of LEM and future perspective
ENLIGHT Meeting
Valencia (Spain), 18/ Juni 2009

Elsässer, T.
Modelling biological effects of heavy ions: from therapy to space
VI. Conf. On Rad. Damaage
Frankfurt (Germany), 2/ Juli 2009

Elsässer, T.
Biological Treatment Planning
PTCOG48 Educ. Workshop
Heidelberg (Germany), 29/ September 2009

Fehrenbacher, G.
Radiation safety planning for particle therapy facilties
41. Jahrestagung Fachverband für Strahlenschutz
Alpbach, Tirol, Österreich, 21.-25.September2009

Feldmeier, H.
Shells, Clusters and Halos – Concepts to solve the nuclear many-body problem
Seminar, Niigata University
Niigata (Japan), 14.05.2009

Feldmeier, H.
UCOM – The unitary correlation operator method
Seminar, University of Tokyo
Tokio (Japan), 11.06.2009

Feldmeier, H.
Shells, Clusters and Halos
Seminar, TNP RIKEN
Wako (Japan), 08.06.2009

Feldmeier, H.
UCOM – The unitary correlation operator method
YITP International Workshop on Developments of nuclear structure models from the viewpoint of nuclear force
Tokio (Japan), 22.05.2009

Feldmeier, H.
Exotic Structures in Light Nuclei
EXON 2009 International Symposium on Exotic Nuclei
Sochi (Russia), 28.09.2009

Fils, J.
Scientific opportunities and technological issues of the Extreme Light Infrastructure
Light at Extreme Intensities 2009
Brazov (Romania), 16. - 21. Oktober 2009

Friedrich, T.
Uncertainties in RBE for Carbon Ions
PTCOG 48
Heidelberg (Germany), 3/ Oktober 2009

Friman, B.
Fluctuations near the chiral critical endpoint
EMMI Workshop on Quarks, Hadrons and the Phase Diagram of QCD
St. Goar (Germany), 31.08.2009

Fritzsche, S.
Direct and sequential multi-photon processes (2 Lectures)
International Summer School on FEL and Synchrotron Radiation
Pühajärve (Estland), Mai 2009

Fritzsche, S.
How well do we understand the electronic structure and properties of medium and heavy elements?
VIII International Workshop on Applications of Lasers and Storage Devices in Atomic Nuclei Research
Poznan (Poland), 24.Juni 2009

Fritzsche, S.
A Computer-Algebraic Approach to the Simulation of Multi-Qubit Systems.
International Conference on Mathematical Modeling and Computational Physics
Dubna, Russia, 08.Juli 2009

Fuchs, R.
Wissenschaftlicher Gerätebau - Die Zentrale Technik als Partner der Wissenschaft
Abschiedskolloqium für Herrn Dr. Rainer Barfuß at GKSS
Geesthacht (Germany), 19. März 2009

Geissel, Hans
New Experiments with Stored Exotic Nuclei at the FRS-ESR Facility
Nuclear Structure and Dynamics 2009
Dubrovnik, Croatia, 4-8. 5. 2009

Geissel, Hans
NUSTAR Experiments
Graduierten Kolleg, Justus-Liebig University Giessen
Giessen,, 16.04.2009

Geissel, Hans
Present and Future Experiments with Stored Exotic Nuclei
International Symposium on Exotic Nuclei, EXON-2009
Sochi, Russia, 28.9-2.10.2008

Geissel, Hans
Experiments with Exotic Nuclei at GSI
RIKEN Seminar
Tokyo, Japan, 26.11.2009

Geissel, Hans
Experiments with stored exotic nuclei at GSI and FAIR
Tours Symposium on Nuclear Physics and Astrophysics VII
Kobe, Japan, 17-20.11.2009

Geissel, Hans
Present and future experiments with exotic nuclei
Seminar, University Warsaw
Warsaw, Poland, 16.12.2009

Geppert, Ch.
Frequenzkammgestützte Laserspektroskopie kurzlebiger Isotope zur Kernladungsradiusbestimmung des Halokerns 11Be.
DPG Spring Meeting 2009
Hamburg (Germany), 04.März2009

Geppert, Ch.
Frequenzkammgestütze Laserspektroskopie kurzlebiger Isotope zur Kernladungsradienbestimmung des Halokerns 11Be (Hauptvortrag)
Frühjahrstagung der DPG Atome, Moleküle, Quantenoptik und Plasmen
Hamburg (Germany), 2.–6. März 2009

Gerl, Jürgen
In-Beam and Decay Spectroscopy at GSI and FAIR
CAP Conference
Moncton, Canada, 08.06.2009

Gerl, Jürgen
From RISING to HISPEC/DESPEC
Frontiers in Gamma Ray Spectroscopy
Mumbai, India, 2.-4.3.2009

Gerl, Jürgen
PRESPEC
NUSTAR Annual Meeting
GSI, Darmstadt, Germany, 23.-27.3.2009

Gerl, Jürgen
NUSTAR Detector set-ups
Detector systems networking workshop
TU Darmstadt, Germany, 24.11.2009

Gerl, Jürgen
PRESPEC Fast Beam Campaign
PRESPEC Physics Workshop
GSI, Darmstadt, Germany, 23.06.2009

Gerl, Jürgen
gamma spectroscopy, instrumentation development and associated applications
Seminarreihe
LBNL Berkeley, USA, 8.2009

Gerl, Jürgen
The Physics of Exotis Nuclei
Seminarreihe
Univ. Bogota, Colombia, 2.2009

Gonzalez-Diaz, D
Design and Optimization of the CBM Time of Flight Wall
IEEE Nuclear Science Symposium and Medical Imaging conference
Orladndo, Florida, October 25-31, 2009

Göringer, H.
gStore und lustre: Experimentdatenspeicherung bei GSI
ITEE-Palaver
GSI Darmstadt, 27. Oktober 2009

Gorska, M.
Recent Results from RISING.
IAP Belgian Research Initiative on eXotic nuclei (BRIX), Annual Workshop
Leuven (Belgium), 15. Juni 2009.

Gorska, M.
Shell structure deduced from isomer and beta decay data on exotic nuclei.
ECT - European Centre for Theoretical Studies in Nuclear Physics and Related Areas, Shell Confrontation and Convergence in Nuclear Theory
Trient (Italy), 27. Juli-31. Juli 2009.

Gorska, M.
Gamma-ray spectroscopy of exotic nuclei at GSI.
10th International Conference on Nucleus-Nucleus Collissions (NN2009)
Beijing, China, 16. August-21. August 2009.

Gorska, M.
Sn-100 and recent spectroscopy on exotic nuclei.
Tours symposium on Nuclear Physics and Astrpophysics VII
Kobe, Japan, 16.-20. November 2009.

Gorska, M.
Structure of heavy Cd and in isotopes up to N = 82.
The first EURISOL Users Group Topical Meeting, Laboratori Nazionali del Sud - INFN
Catania, Italy, 9.-11. Dezember 2009.

Götte, S.:
The PHELIX Control System (PCS).
Internal Seminar on Laser Technology, Helmholtz Institut Jena
Jena (Germany), 6. November 2009.

Götte, S.:
LabVIEW for Big Physics: The PHELIX Control System.
National Instruments, BIG PHYSICS Round Table 2
Paris (France), Februar 2009

Götzen, K.
Physics at BES-III
Seminar on Strong Interactions
München (Germany), 23. 11. 2009

Götzen, K.
Physics at BES-III
Graduiertenkolleg und EMG Seminar
Mainz (Germany), 18. 11. 2009

Götzen, K.
The PANDA Experiment at FAIR
Troia09, 2nd International Conference on Hadron Physics
Cannakkale (Turkey), 10.-14. Sep. 2009

Götzen, K.
Recent results on hadron spectroscopy from BES
7th International Workshop on e+ e- Collisions from phi to psi
Beijing (China), 13.-16. Okt. 2009

Grisenti, R.
Cryogenically cooled liquid droplet beams: basic properties and applications in plasma and condensed matter physics.
Arizona State University
Tampe, (Arizona), 26. März 2009.

Grisenti, R.
Size characterization and laser-driven explosion of nanometer- to micrometer-sized liquid helium droplets.
Laser Plasma Accelerator Workshop - LPAW 2009
Kardamili (Greece), 22.-26. Juni 2009.

Hagmann, S.
Multi-Electron Continua and -Cusps in Strongly Perturbing Ion-Atom Collisions.
ISIAC 2009, Old Dominion Univ.
Norfolk, Virginia (USA), 18.Juli 2009

Harasimowicz, J.
Diagnostics for the USR, low current BPMs.
Workshop on Low Energy, Low Intensity Beams
Hirschberg (Germany), 25. November 2009

Harasimowicz, J.
Beam Instrumentation for the USR.
INFN-LNF
Rome (Italy), 27.Oktober 2009

Hartel, Carola
"mFISH analysis of cytogenetic damage in lymphocytes of prostate cancer patients treated with IMRT and Carbon ions.
Heavy ions in therapy and space
Koeln (Germany), 6.-10.7.2009

Heil, Michael
Selected recent experimental nuclear astrophysics results at GSI and future perspectives
Nuclear Structure and Dynamics 2009
Dubrovnik, Croatia, 4.5.-8.5.2009

Heil, Michael
Coulomb Dissociation experiments at GSI for Nuclear Astrophysics
Nuclear Physics in Astrophysics IV
Frascati, Italy, 8.6.-12.6.2009

Heinz, Sophie
Di-nuclear system studies at Coulomb barrier energies
International Conference on Nuclear Structure and Related Topics (NSRT)
Dubna, Russia, 30.6.-4.7.2009

Heinz, Sophie
Recent experiments at SHIP
Bogoliubov Laboratory of Theoretical Physics
Dubna, Russia, 26.06.2009

Heinz, Sophie
Study of di-nuclear systems and cluster evaporation at SHIP
Justus-Liebig Universität Gießen
Gießen, Germany, 06.11.2009

Herfurth, F.
The HITRAP decelerator linac at GSI.
Particle Accelerator Conference PAC'09
Vancouver (Canada), 06.Mai 2009

Herfurth, F.
HITRAP – Heavy, Highly-Charged Ions and Antiprotons at Rest
XXXI Mazurian Lakes Conference on Physics
Piaski (Poland), 31.August 2009

Herfurth, F.
Direct mass measurements in the trans-fermium region with the Penning trap mass spectrometer SHIPTRAP.
XXXI Mazurian Lakes Conference on Physics
Piaski (Poland), 3.September 2009

Hofmann, Sigurd

Superheavy Elements by Cold Fusion
International Symposium - Periodic Table of D.I. Mendeleev - The New Superheavy Elements
JINR, Dubna, Russia, 20.-21.1.2009

Hofmann, Sigurd
Study of Superheavy Elements at the GSI SHIP
American Chemical Society, 237th National Meeting
Salt Lake City, UT, USA, 22.3.-26.3.2009

Hofmann, Sigurd
Superheavy Elements
KSA-FAIR future collaboration KACST
Riyadh, Saudi Arabia, 1.-5.5.2009

Hofmann, Sigurd
Experiments on Superheavy Elements
16th Nuclear Physics Workshop 'Maria and Pierre Curie'
Kazimierz Dolny, Poland, 23.9.-25.9.2009

Hofmann, Sigurd
Studies of SHE at SHIP
International Symposium on Exotic Nuclei, EXON-2009
Sochi, Russia, 28.9.-2.10.2009

Hofmann, Sigurd
Study of SHE at SHIP
Tours Symposium on Nuclear Physics and Astrophysics VII
Kobe, Japan, 15.-21.11.2009

Hofmann, Sigurd
On the Discovery of Superheavy Elements
Carlsbad Section of the American Nuclear Society WIPP
Carlsbad, NM, USA, 16.03.2009

Hofmann, Sigurd
On the Discovery of the Heaviest Elements
T2-Seminar, LANL
Los Alamos, NM, USA, 18.03.2009

Holzmann, R.
Dilepton production at SIS energies studied with HADES
10th International Conference on Nucleus-Nucleus Collisions NN2009
Beijing (China), August 16-21, 2009

Huhn, C.
Linux Desktop Management with old school NFS-root boot
HEPiX Fall 2009 meeting
Lawrence Berkeley National Laboratory 1, Cyclotron Road, Berkeley, CA, 94720 USA, 29-Oct-2009 16:30 (America/Los_Angeles)

Ilieva, Stoyanka Kirilova
Nuclear Matter Density Distributions of 12Be, 14Be and 8B Nuclei from Elastic Proton Scattering
Annual NuSTAR Meeting 2009
GSI, Darmstadt,

Jakob, B.
Live cell imaging at the beamline
Microbeam Workshop
Bordeaux (Frankreich), 25 - 27 März 2009

Jakob, B.
Positional Stability of Multiple Radiation Induced DNA Double-Strand Breaks Supports „Contact First-Hypothesis“ of Chromosomal Exchanges
ISCA
St. Goar, 11 - 12 Juli 2009

Jakob, B.
Spatiotemporal Dynamics of Double-Strand Break Repair and Genetic Effects of Charged Particles
GBS
Essen, 30 September - 2 Oktober 2009

Junginger, T.
RF characterization of superconducting samples.
Gentner Day, CERN
Geneva (Switzerland), 18. November 2009

Junginger, T.
Electromagnetic Simulations for the Magnetic Shielding of the SPL.
3rd SPL Collaboration Meeting at CERN
Geneva (Switzerland), 11.Oktober 2009

Junginger, T.
RF characterization of superconducting samples.
SRF Workshop
Berlin (Germany), 17.-25.September 2009

Junginger:, T.
Calculating Cavity Fields by Analytical and Numerical Approaches.
Joint Universities Accelerator School
Archamps (France), 24.Februar 2009

Kalweit, A.
Particle Identification with the ALICE Time Projection Chamber
DPG Frühjahrstagung 2009
Bochum (Germany), 20.Mrz.09

Kalweit, A.
dE/dx measurements in large volume TPCs
11th International Conference on Advanced Technology and Particle Physics
Como (Italy), 07.Okt.09

Kalweit, A.
Proton-Proton Physik mit ALICE
Arbeitstreffen deutscher Kernphysiker
Schleching (Austria), 26.Feb.09

Kalweit, A.
Calibration and cosmic ray data analysis of the ALICE Time Projection Chamber
Marie Curie training workshop on Particle Detectors (MC-PAD)
Cracow (Poland), 16.Sep.09

Karsch, F.
QCD thermodynamics – 30 years of heated debates
Workshop on Quantum Field Theory in Extreme Environments
Paris (France), 25.04.2009

Karsch, F.
Exploring the Properties of QCD at Non-Zero Temperature and Density
NIC-Beirat
Zeuthen (Germany), 17.06.2009

Karsch, F.
Magnetic Equation of State of (2+1)-flavor QCD
EMMI Workshop on Quarks, Hadrons and the Phase Diagram of QCD
St. Goar (Germany), 01.09.2009

Karsch, F.
The QCD Phase Diagram from Lattice Regularized QCD
DNP/JPS meeting
Hawaii (USA), 15.10.2009

Kisel, I.
Tracking on GPUs (CBM and ALICE)
IRTG School
Bergen (Norway), February 09-13, 2009

Kisel, I.
Development of Online Event Selection in CBM
DPG-09
Bochum (Germany), March 16-20, 2009

Kisel, I.
First Level Event Selection Package of the CBM Experiment
Computing in High Energy Physics CHEP09
Prague (Czech), 26.Mrz.09

Kisel, I.
Online Event Selection in the CBM Experiment
Real-Time Conference RT09
Beijing (China), May 10-15, 2009

Kisel, I.
Event Reconstruction in STS
CBM at SIS100
Dubna (Russia), May 19-22, 2009

Kisel, I.
Online Event Selection in Heavy Ion Experiments
Mathematical Modeling and Computational Physics MMCP'2009
Dubna (Russia), July 7-11, 2009

Kisel, I.
CBM Fast Tracking
CBM FLES Kick-off Meeting
GSI (Germany), 02.Okt.09

Kisel, I.
Online Event Selection
CBM-China Meeting
Beijing (China), November 2-4, 2009

Kisel, I.
Online Event Selection in CBM
HIC for FAIR
Darmstadt (Germany), 24.Nov.09

Kisel, I.
Online Event Reconstruction in HEP Experiments
FIAS Colloquium
Frankfurt (Germany), 03.Dez.09

Kluge, H.-J.
Atomic physics techniques for studying nuclear ground state properties, fundamental interactions and symmetries: Status and perspectives.
Int. Workshop on Application of Lasers and Storage Devices in Atomic Nuclei Research
Poznan (Poland), 22.-25. Juni 2009

Kluge, H.-J.
High-Accuracy Mass Spectrometry for Fundamental Studies.
18th Int. Mass Spectrometry Conference 2009
Bremen (Germany), 30. August - 04. September 2009

Kluge, H.-J.
Precision experiments at lowest energies for fundamental tests and constants.
434. WE-Heraeus-Seminar
Bad Honnef (Germany), 15. - 17. Juni 2009

Koenig, Ilse
The HADES Oracle database and its interfaces for experimentalists.
Computing in High Energy and Nuclear Physics
Prague, Czech Republic, März, 2009

Koenig, W
High Rate MIPs Diamond Detectors with a Time Resolution σ < 50 ps ?
1st CARAT WORKSHOP
Darmstadt (Germany)Dec. 13-15, 2009,

Koenig,W
Diamonds as fast timing detectors for MIPS: The HADES proton-beam monitor/start detector
Frühjahrstagung DPG Hadronen und Kerne + Nuclear Physics Board EuNPC
Bochum (Germany), March 16-20, 2009

Kojouharov, Ivan
Encapsulated Germanium Detector with Electromechanical Cooling
11th European Symposium on Semiconductor Detectors
Wildbad Kreuth, Germany, 7.-11.6.2009

Kojouharov, Ivan
Surface characterisation of Germanium detectors
11th European Symposium on Semiconductor Detectors
Wildbad Kreuth, Germany, 7.-11.6.2009

Kojouharov, Ivan
Germanium Detectors for Hypernuclear Physics
SPHERE kick-off event
Univ. Mainz, Germany, 3.-5.7.2009

Kraft, Gerhard
"Ion beam therapy"
Heraeus-Schule
Bad Honnef (Germany), 14/ Februar 2009

Kraft, Gerhard
"Ionenstrahl Therapie
Deutsche Fachschaften Chemie, Jahrestagung
Marburg (Germany), 22/ Mai 2009

Kraft, Gerhard
"Particle imaging in biology"
Prior Workshop GSI
Darmstadt (Germany), 25/ August 2009

Kraft, Gerhard
"Schwerionen Tumortherapie"
Physikalisch-Technische Bundesanstalt, Kolloquium
Braunschweig (Germany), 3/ September 2009

Kraft, Gerhard
"What is new in particle radiobiology?"
PTCOG, Invited talk
Heidelberg (Germany), 1/ Oktober 2009

Kraft, Gerhard
"Entwicklung der Schwerionentherapie in Darmstadt"
Jahresversammlung Zentralverband deutscher Apotheker
Darmstadt (Germany), 5/ Oktober 2009

Kraft, Gerhard
"Metrological issues of heavy ion therapy"
Physikalisch-Technische Bundesanstalt
Braunschweig (Germany), 24/ Oktober 2009

Kraft, Gerhard
"Tumor Therapie mit schweren Ionen"
RKA Innovations Forum
Frankfurt (Germany), 2/ November 2009

Kraft-Weyrather, Wilma
Radiobiology for Hadrontherapy
ENLIGHT Meeting
Valencia (Spain), 18/ Juni 2009

Kraft-Weyrather, Wilma
Biological Quality Assurance
PTCOG
Heidelberg (Germany), 1/ September 2009

Krämer, J.
Collinear Laser Spectroscopy on Neutron-rich Fission Products at the Research Reactor TRIGA Mainz
VIII International Workshop: APPLICATION OF LASERS AND STORAGE DEVICES IN ATOMIC NUCLEI RESEARCH - Recent Achievements and Future Prospects
Poznan (Poland), 22.-25. Juni 2009

Kraemer, M.
Ion Beam Transport Calculations and Treatment Plans in Particle Therapy
RADAM 2009
Frankfurt (Germany), Juli 2009

Kraemer, M.
Ion Beam Transport Calculations and Treatment Plans in Particle Therapy
FIAS Seminar
Frankfurt (Germany), 11/ November 2009

Kraemer, M.
On TRAX & TRiP
Danish Workshop for Proton and Heavy-Ion Dosimetry
Aarhus (Denmark), November 2009

Krieger, A.
High voltage calibration at ISOLDE/CERN using collinear spectroscopy
VIII International Workshop: APPLICATION OF LASERS AND STORAGE DEVICES IN ATOMIC NUCLEI RESEARCH - Recent Achievements and Future Prospects
Poznan (Poland), 22.-25. Juni 2009

Krieger, A.
Hochspannungskalibration durch kollineare Laserspektroskopie an ISOLDE/CERN
Frühjahrstagung der DPG Hadronen und Kerne
Bochum (Germany), 16.-20. März 2009

Kühl, T.
X-Ray Laser developments at PHELIX
SPIE Conference Optics + Photonics
San Diego, 2. - 6. August 2009.

Kühl, T.
Application of Lasers and Storage Devices in Atomic Nuclei Research.
VIII International Workshop
Poznan, 22.-25. Juni 2009

Langanke, K.
The Facility for Antiproton and Ion Research
Akademischer Verein
Darmstadt (Germany), 23.01.2009

Langanke, K.
5 Lectures on Nuclear Astrophysics
Engelbrecht School
Stellenbosch (South Africa), 25.01.2009

Langanke, K.
Summary talk
Nuclear Astrophysics Meeting in honor of Claus Rolfs
Capri (Italy), 16.05.2009

Langanke, K.
The FAIR Change for Nuclear Astrophysics

Bethe Lecture
Bonn (Germany), 25.06.2009

Langanke, K.
Nuclear Aspects of Supernovae
10th International Conference on Nucleus-Nucleus Collisions
Beijing (China), 20.08.2009

Langanke, K.
2 Lectures on Nuclear Astrophysics
Summerschool, Unversity of Beijing
Beijing (China), 23.08.2009

Langanke, K.
Weak Interaction Rates for Supernova Simulations
University of Copenhagen
Kopenhagen (Denmark), 28.08.2009

Langanke, K.
FAIR from a few-body perspective
Few-Body Conference
Bonn (Germany), 02.09.2009

Langanke, K.
3 Lectures on Nuclear Astrophysics
UK Graduate School
Leicester (Great Br itain), 09.12.2009

Langanke, K.
Neutrino-Nucleus Reactions
Erice School on Neutrinos in Cosmology, in Astro-, Particle- and Nuclear Physics
Erice (Italy), 21.09.2009

Langanke, K.
FAIR – a new era in Nuclear Astrophysics
5th European Summer School on Experimental Nuclear Astrophysics
Santa Tecla (Italy), 23.09.2009

Langanke, K.
Physics in Darmstadt
Accelerator School
Darmstadt (Germany), 28.09.2009

Langanke, K.
Neutrino-Nucleus Reactions for Supernovae
Neutrino Conference
Heidelberg (Germany), 09.11.2009

Langanke, K.
FAIR – a new era for Nuclear Physics
Annual Meeting of the Spanish Physics Society
El Escorial (Spain), 26.11.2009

Langanke, K.
Highlights in Nuclear Astrophysics
Lecture for Graduate Students, Tokyo Institute of Technology
Tokio (Japan), 02.12.2009

Lee, Ryonfa
High LET induced chromosome aberrations detected by mFISH
9th International Symposium on Chromosome aberrations
Sankt Goar (Germany), 11.-12.7.2009

Lee, Ryonfa
mFISH study of aberrations in lymphocytes of prostate cancer patients treated with IMRT and C-ions: an update
37th Annual Meeting of the European Radiation Research Society
Prague (Czech Republic), 26.-29.8.2009

Leifels, Y.
Baryonic matter – what do we know about it?
European Nuclear Physics Conference
Bochum (Germany), 16.-20.März 2009

Leifels, Y.
Constraining the depth of the KN-potential in dense nuclear matter
Workshop on Simulations of low and intermediate Heavy-ion Collisions
Trento (Italy), 15.-20.Mai 2009

Leifels, Y.
Investigation of hadronic matter properties with heavy-ion collisions
Nuclear Physics School
Otranto(Italy), 5.-10.Juni 2009

Leifels, Y.
Isospin dependent observables in FOPI
Workshop on „How to constrain the high density symmetry energy“
Zagreb (Kroatia), 15.-18. Oktober

Litvinov, Yuri
Mass and lifetime measurements of stored exotic nuclei
Advanced Sem. WS09/10 "Physics with stored and cooled ions", Max-Planck Inst. für Kernphysik
Heidelberg, Germany, 18.11.2009

Litvinov, Yuri
Nuclear Physics with Stored Exotic Nuclei. I - Decay Studies of Highly Charged Ions
Institute of Modern Physics, Chinese Academy of Sciences
Lanzhou, China,, 14.10.2009

Litvinov, Yuri
Nuclear Physics with Stored Exotic Nuclei. I - Direct Mass Measurements"
Institute of Modern Physics, Chinese Academy of Sciences
Lanzhou, China,, 12.10.2009

Litvinov, Yuri
Beta-Decay of Highly-Charged Ions
International Symposium on Exotic Nuclei, EXON-2009
Sochi, Russia, 28.9.-2.10.2009

Litvinov, Yuri

Non-exponential Two-Body Beta Decay of Stored Hydrogen-Like Ions
Joint Theory and High-Energy-Physics Seminar, ONOI
Gatchina, Russia, 24.9.2009

Litvinov, Yuri
Direct Mass Measurements in Storage Rings
31st Mazurian Lakes Conference on Physics "Nuclear Physics and the Road to FAIR"
Piaski, Poland, 30.8.-6.9.2009

Litvinov, Yuri
Beta-Decay of Highly-Charged Ions
10th International Conference on Nucleus-Nucleus Collisions NN2009
Beijing, China, 16.8-21.8.2009

Litvinov, Yuri
Non-Exponential Decay in Electron Capture of Heavy Ions
Gordon Research Conference 2009 (Nuclear Physics), Bryant University
Smithfield, USA,, 12.6.-17.6.2009

Litvinov, Yuri
Non-Exponential Decay in Electron Capture of Heavy Ions
Gordon Research Conference 2009 (Nuclear Physics),Colby Sawyer College,
New London, USA, 21.-6.-26.6.2009

Litvinov, Yuri
Orbital Electron-Capture Rates from Few-Electron Ions
International Workshop on Atomic Effects in Nuclear Excitations and Decay, ECT
Trient, Italy, 15.-19.6.2009

Litvinov, Yuri
Non-Exponential Decay in Electron Capture of Heavy Ions
April Meeting of the American Physical Society
Denver, USA, 2.-5.5.2009

Litvinov, Yuri
Experimental Status of the GSI Oscillations
Graduiertentag Basel-Graz-Tübingen on "Hadronen im Vakuum, in Kernen und Sternen"
Tübingen, Germany, 24.04.2009

Litvinov, Yuri
Non-Exponential Decay in Electron Capture of Heavy Ions
1st European Nuclear Physics Conference, Ruhr-Universität Bochum
Bochum, Germany, 16.3.-20.3.2009

Litvinov, Yuri
Lebensdauermessungen an hochgeladenen Ionen
Colloquium Justus-Liebig Universität Giessen
Giessen, Germany, 09.03.2009

Litvinova, E.
Relativistic many-body description of low-energy nuclear dynamics
International Conference "Nuclear Structure and Related Topics"
Dubna (Russia), 30.06.2009

Litvinova, E.
Microscopic studies of low-lying dipole strength in neutron-rich nuclei and its role in r-process nucleosynthesis
432. Heraeus-Seminar: Nucleosynthesis – making the elements of the universe
Bad Honnef (Germany), 05.06.2009

Litvinova, E.
Relativistic many-body description of low-energy nuclear excitations
Annual NuSTAR meeting 2009
Darmstadt (Germany), 26.03.2009

Löher, B.
Photon/Neutron Discrimination with Digital Pulse Shape Analysis.
DPG Spring Meeting, Bochum
Bochum (Germany), 16. März 2009

Lutz, M.
Hadronic and electromagnetic decays of charmed molecules
447. Heraeus-Seminar: Charmed Exotics
Bad Honnef (Germany), 11.08.2009

Malzacher, P.
The Alice Tier-2 at GSI
International Symposium on Grid Computing
Taipei, 21. April 2009

Malzacher, P.
Geant4 the Physics Simulation Package, an Overview
China Institute of Atomic Energy, Peking, 13. Mai 2009

Malzacher, P.
How to Use Geant4?
China Institute of Atomic Energy, Peking, 14. Mai 2009

Malzacher, P.
The FAIR SSC Workpackage
EGEE'09
Barcelona, 23. September 2009

Malzacher, P.
FAIR, The Facility for Antiproton and Ion Research
EGEE'09
Barcelona, 21. September 2009

Manafov, A.
Status report: "PROOF on Demand"
ALICE Offlineweek
CERN, März 2009

Manafov, A.
Status report: "PROOF on Demand"
ALICE Offlineweek
CERN, Juni 2009

Manafov, A.
Status report: "PROOF on Demand"
ALICE Offlineweek
CERN, Oktober 2009

Manafov, A.
PROOF on Demand
CHEP 2009
Prag, März 2009

Manafov, A.
PROOF on Demand
DPG Frühjahrstagung
Bochum, März 2009

Marin, A.
Perspectives for the measurement of the chi_c radiative decay in the ALICE experiment at the LHC
DPG spring meeting
Bochum (Germany), 16-20. Mar 2009

Marin, A.
Perspectives for the measurement of the chi_c radiative decay in the ALICE experiment at the LHC (poster)
QM2009
Jaipur (India), 30. Mar - 04. Apr 2009

Marin, A.
The quest for the Quark Gluon Plasma with ALICE at the LHC
Fysikermotet 2009
Roros (Norway), 12-14. August 2009

Märtin, R.
X-ray Crystal Spectroscopy of Highly Charged Ions.
Seminar Atom- und Molekülphysik, Goethe-Universität
Frankfurt am Main (Germany), 1. Juni 2009

Martinez-Pinedo, G.
Nuclear Physics aspects of explosive nucleosynthesis
432. WE-Heraeus-Seminar: Nucleosynthesis - making the Elements in the Universe
Bad Honnef (Germany), 03.06.2009

Martinez-Pinedo, G.
Nucleosíntesis explosiva en Supernovas
XXXII Bienal de Física
Ciudad Realn (Spain), 08.09.2009

Martinez-Pinedo, G.
Neutrinos and Explosive Nucleosynthesis
Erice School on Neutrinos in Cosmology, in Astro-, Particle- and Nuclear Physics
Erice (Italy), 21.09.2009

Martinez-Pinedo, G.
Supernova Evolution and Explosive Nucleosynthesis
5th European Summer School on Experimental Nuclear Astrophysics
Santa Tecla (Italy), 25.09.2009

Martinez-Pinedo, G.
Spin-Isospin Excitations in Nuclear Astrophysics
ECT* Workshop on Strong, Weak and Electromagnetic Interactions to probe Spin-Isospin Excitations
Trento (Italy), 30.09.2009

Martinez-Pinedo, G.
The European Spallation as a Source of neutrinos for nuclear astrophysics applications
Workshop on Neutrino, Neutron, Nuclear, Medical and Muon Physics at ESS
Lund (Sweden), 03.12.2009

Martinez-Pinedo, G.
The role of nuclear physics in r-process nucleosynthesis
The first EURISOL UG topical meeting - The formation and structure of r-process nuclei, between N=50 and 82 (including 78Ni and 132Sn areas)
Catania (Italy), 10.12.2009

Martinez-Pinedo, G.
Stellar nucleosynthesis and supernova explosions
Großes Physikalische Kolloquium, Köln Universität
Köln (Germany), 15.12.2009

Marx, G.
Status der MATS Facility
Frühjahrstagung der DPG Atome, Moleküle, Quantenoptik und Plasmen
Hamburg (Germany), 2.-6. März 2009

Meyer, B.
Effects of Histone Acetyl Transferase Tip60 Recruitment to Complex DNA Lesions (Poster, Travel Award)
women in radiation sciences - a century after marie curie
München, Mai 2009

Meyer, B.
Modification of Chromatin in Connection with the Induction and Repair of Ion-induced DNA Lesions (Vortrag, Travel Award)
Heavy Ion in Therapy and Space
Köln, 06 - 10 Juli 2009

Miskowiec, D.
Viscosity and HBT
WPCF 2009
Geneva (Switzerland), 15.Okt.09

Neff, T.
Clusters and Halos studied in Fermionic Molecular Dynamics
EENEN09: First EMMI-EFES Workshop
Darmstadt (Germany), 10.02.2009

Neff, T.
Clustering and halos in nuclei
Workshop "Special Symmetries and Ab Initio Methods for Light Nuclei"
Baton Rouge (USA), 20.02.2009

Neff, T.
Nuclear Interactions, Correlations and Many-Body Methods
XL. Arbeitstreffen Kernphysik
Schleching (Germany), 26.02.2009

Neff, T.
Microscopic study of Neon isotopes including the two-proton halo 17Ne
DPG-Frühjahrstagung/European Nuclear Physics Conference
Bochum (Germany), 19.03.2009

Neff, T.
Shells, Clusters and Halos
IOP Nuclear Physics Conference
Birmingham (Great Britain), 06.04.2009

Neff, T.
Clusters and halos in light nuclei
NSD07 Nuclear Structure and Dynamics
Dubrovnik (Croatia), 07.05.2009

Neff, T.
The Unitary Correlation Operator Method
12th International Conference on Nuclear Reaction Mechanisms
Varenna (Italy), 18.06.2009

Neff, T.
Clusters and halos: a challenge for nuclear structure
Gordon Research Conference Nuclear Chemistry
New London (USA), 22.06.2009

Neff, T.
Microscopic description of alpha-clustering in 12C and other light nuclei
6th Workshop on aspect of alpha correlations and alpha condensation in nuclear systems
Rostock (Germany), 06.08.2009

Neff, T.
Cluster structures within fermionic molecular dynamics
19th Internation IUPAP Conference on Few-Body Problems in Physics
Bonn (Germany), 04.09.2009

Neff, T.
Collective Cluster Modes in Light Nuclei
5th Workshop on Shape-Phase Transitions and Critical Point Phenomena in Nuclei
Istanbul (Turkey), 18.09.2009

Neff, T.
Structure of light nuclei studied in Fermionic Molecular Dynamics
University of Surrey Nuclear Physics Seminar
Guildford (Great Britain), 10.11.2009

Neff, T.
Structure of light nuclei studied in Fermionic Molecular Dynamics
Uni Basel Seminar aus Astro-, Kern- und Teilchenphysik
Basel (Switzerland), 19.11.2009

Neumann R.
Atomic physics and lasers.
Workshop KSA-FAIR future collaboration
Riyadh (Saudi-Arabia), 2.-4. Mai 2009

Neumann, R.
Materials science with ion beams.
Workshop KSA-FAIR future collaboration
Riyadh (Saudi-Arabia), 2.-4. Mai 2009

Neumann, R.
Herstellung und Funktionalisierung von Nanokanälen für die biochemische Analytik.
Nanotechnologieforum Hessen
Hanau (Germany), 26.November 2009

Neumann, R.
Ionic transport through and biosensing with single conical nanochannels.
11th Pacific Polymer Conference
Cairns (Australia), 10.Dezember 2009

Neumann, R.
Materials research with energetic heavy ions at GSI
Osaka Prefecture University
Osaka (Japan), 18.Februar.2009

Neumann, R.
Materials research with energetic heavy ions at GSI
Advanced Science Research Center, Japan Atomic Energy Agency (JAEA)
Tokai-mura (Japan), 25. Februar 2009

Neumann, R.
Materials research with energetic heavy ions at GSI
Australian National University
Canberra (Australia), 03. Dezember 2009

Nociforo, Chiara
Shell Closure N=16 in 24O
Nuclear Structure and Dynamics
Dubrovnik, Croatia, 4.5.-8.5.2009

Nociforo, Chiara
Shell and halo structure of n-rich light nuclei
Tours 2009
Kobe, Japan, 16.11.-20.11.2009

Nociforo, Chiara
High-resolution momentum measurement reveals 24O as doubly magic nucleus
Direct Reaction with Exotic Beams
Tallahassee, Florida, USA, 16.12.-19.12.2009

Nörtershäuser, W.

Lasers used in radioactive beam experiments (4 Lectures).
Euroschool on Exotic Beams
Leuven, September 2009

Nörtershäuser, W.
Nuclear Charge Radii of Light Halo Nuclei.
XXXI Mazurian Lakes Conference on Physics: Nuclear Physics and the Road to FAIR
Piaski (Polen), 02.September 2009

Nörtershäuser, W.
Precision laser spectroscopy of light exotic isotopes.
Institutsseminar des Physikalischen Instituts Tübingen
Tübingen (Germany), 24.Juli 2009

Nörtershäuser, W.
Laser spectroscopy of halo nulei.
VIII International Workshop: APPLICATION OF LASERS AND STORAGE DEVICES IN ATOMIC NUCLEI RESEARCH - Recent Achievements and Future Prospects
Poznan (Poland), 22.-25. Juni 2009

Nörtershäuser, W.
Bericht zur ISOLDE.
Jahrestagung des Kommitees für Hadronen und Kerne.
Bad Honnef, 11.Dezember 2009

Nörtershäuser, W.
Laser spectroscopy on relativistic lithium beams for a test of Lorentz invariance.
VIII International Workshop: APPLICATION OF LASERS AND STORAGE DEVICES IN ATOMIC NUCLEI RESEARCH - Recent Achievements and Future Prospects
Poznan (Poland), 22.-25. Juni 2009

Nörtershäuser, W.
The nuclear charge radius of Be-11 and recent achievements in high-resolution laser spectroscopy at GSI.
Bothe Kolloquium
MPIK Heidelberg, 10.Juni 2009

Nörtershäuser, W.
Nuclear Charge Radii of 7, 9, 10Be and the One-Neutron Halo Nucleus 11Be
8th International Conference on Radio Active Nuclear Beams (RNB8)
Grand Rapids, Michigan (USA), 26.-30. Mai 2009

Nörtershäuser, W.
Atomkern mit Heiligenschein - Laserspektroskopische Bestimmung des Kernladungsradius von Be-11
Atomphysik Seminar Universität Gießen
Gießen (Germany), 7.Mai 2009

Nothhelfer, M.
On the long and winding road towards HFS-Spectroscopy of Li-like 209Bi80+
VIII International Workshop: APPLICATION OF LASERS AND STORAGE DEVICES IN ATOMIC NUCLEI RESEARCH - Recent Achievements and Future Prospects
Poznan (Poland), 22.-25. Juni 2009

Novotny, Ch.
Test of Time Dilatation in SRT at the GSI Storage Ring
Klausurtagung des Forschungszentrums Elementarkräfte und Mathematische Grundlagen (EMG)
Mainz (Germany), 21.-22. Oktober 2009

Novotny, Ch.
Doppler-freie Spektroskopie an schnellen Lithium-Ionen am Experimentier-Speicherring der GSI (Fachvortrag)
Frühjahrstagung der DPG Atome, Moleküle, Quantenoptik und Plasmen
Hamburg (Germany), 2.–6. März 2009

Oliver Boine-Frankenheim
Schottky spectrum in intense ion beams
Particle Accelerator Conference
Vancouver, CA, 4-8 Mai 2009

Pershina, Valeria
Theoretical Predictions of the Experimental Behavior of the Heaviest Elements
7th Workshop on the Chemistry and Physics of the Heaviest Elements
Mainz, Germany, 11.10.-13.10.2009

Pershina, Valeria
Electronic Structure and Gase-Phase Behavior of the Heaviest Elements
International Symposium on Exotic Nuclei, EXON-2009
Sochi, Russia, 28.9.-2.10.2009

Pershina, Valeria
Fully Relativistic 4c-DTF Study of Adsorption of the Heaviest Elements and their Homologs on Gold surface
DFT09
Lyon, France, 31.8.-4.9.2009

Pershina, Valeria
Theoretical Predictions of Chemical Properties and Experimental Behavior of the Heaviest Elements
International Symposium - Periodic Table of D.I. Mendeleev -The New Superheavy Elements
Dubna, Russia, 20.1.-21.1.2009

Petermann, I.
R-process nucleosynthesis calculations with complete nuclear physics input
DPG-Frühjahrstagung/European Nuclear Physics Conference
Bochum (Germany), 18.03.2009

Petermann, I.

R-process nucleosynthesis calculations with complete nuclear physics input
Nuclear Physics in Astrophysics IV
Frascati (Italy), 08.06.2009

Peters, K.
Experimental Review on Open Charm Spectroscopy
Workshop, OpenCharm@PANDA
Mainz (Germany), 19. Nov. 2009

Peters, K.
Hadron Physics at FAIR
sFAIR Meeting
Örebro (Schweden), 16. Nov. 2009

Peters, K.
Status of BES3
Sommerschule
Bosen (Germany), 2. Sep. 2009

Peters, K.
Antiprotonic production of exotic hadrons: a survey
447. Heraeus Seminar "QCD Exotics"
Bad Honnef (Germany), 12. Aug. 2009

Peters, K.
The Future of Hadron Physics at European Facilities
APS: Topical Group on Hadron Physics
Denver (USA), 1. Mai 2009

Peters, K.
PANDA at FAIR
India FAIR Meeting
Hyderabad (Indien), 18. Apr. 2009

Peters, K.
Status of FAIR
INFN Seminar
Ferrara (Italy), 25. März 2009

Peters, K.
The BES3 Experiment
KVI Seminar
Groningen (Netherlands), 24. Feb. 2009

Pfeiffer, Bernd
Wir sind alle Sternenstaub - Die Entstehung der Elemente
5th Russbach Workshop on Nuclear Astrophysics
Russbach am Pass Gschütt, Austria, 2.3.-6.3.2009

Pfeiffer, Bernd
The Atomic Mass Evaluation
5th Russbach Workshop on Nuclear Astrophysics
Russbach am Pass Gschütt, Austria, 2.3.-6.3.2009

Pfeiffer, Bernd
The Atomic Mass Evaluation - An Example of Nuclear Physics Data for Fundamental Physics and Application
Nuclear Data Week at Brookhaven Nuclear Data Center
Upton, NY, USA, 4.11.-6.11.2009

Pfister, J.
Commissioning of the HITRAP Decelerator using a Single-shot Pepper Pot Emittance Meter: A Status Report.
73. Jahrestagung und DPG Frühjahrstagung der Sektion AMOP
Hamburg (Germany), 03.März 2009

Pfister, J.
HITRAP low energy diagnostics and emittance measurement.
DITANET Workshop on "Low Current, low Energy Beam Diagnostics"
Hirschberg (Germany), 24.November 2009

Picht, O.
Synthesis and Properties of Nanowires fabricated by Ion Track Technology
Laboratoire dÈlectrochimie des Matériaux (LEM), Université Paul Verlaine
Metz (France, 6. November 2009

Pietraszko, J.
Strangeness Production at SIS measured with HADES
10th International Conference on Nucleus-Nucleus Collisions NN2009
Beijing (China), August 16-21, 2009

Pietri, Stephane
Recent results in gamma spectroscopy at GSI
RNB8
, 27.05.2009

Plaß, Wolfgang
Novel Developments for Multiple-Reflection Time-of-Flight Mass Spectrometry
18th International Mass Spectrometry Conference
Bremen, Germany, 30.08.-04.09.2009

Plaß, Wolfgang
Multiple-Reflection Time-of-Flight Mass Spectrometry of Exotic Nuclei
57th ASMS Conference on Mass Spectrometry
Philadelphia, USA, 31.05.-04.06.2009

Plaß, Wolfgang
MCP Detectors for Picosecond Timing
Workshop on Fast Cherenkov Detectors
Gießen, Germany, 11.05.-13.05.2009

Putignano, M.
A Novel Gas Curtain Beam Profile Monitor.
Workshop on Low Energy, Low Intensity Beams
Hirschberg (Germany), 25. November 2009

Quint, W.
HITRAP - a facility for experiments on heavy highly charged ions and antiprotons.
FLAIR Collaboration Meeting MSI
Stockholm (Sweden), 2. Februar 2009

Quint, W.
Bound electron g-factor measurements at HITRAP.

Helmholtz-Begutachtung at BESSY
Berlin (Germany), 23. April 2009

Quint, W.
Tests of quantum electrodynamics at HITRAP.
Heraeus Seminar
Bad Honnef (Germany), 17. Juni 2009

Reifarth, Rene
Nuclear data for physics and astrophysics at FAIR and FRANZ
n_TOF winter school
Florence, Italy, 27.03.2009

Reifarth, Rene
The s-process – overview and selected recent developments
Nuclear Physics in Astrophysics IV
Frascati, Italy, 8.6.-12.6.2009

Reifarth, Rene
Nuclear astrophysics using n-TOF facilities with a view to a possible future program at the ESS
Neutrino, Neutron, Nuclear, Medical and Muon Physics at ESS
Lund, Sweden, 2.12.-4.12.2009

Reifarth, Rene
Experiments close to stability contributing to our understanding of the r-process
The first EURISOL UG topical meeting – The formation and structure r-process nuclei, between N=50 and 82 (including 78Ni and 132Sn areas)
Reifarth, Rene
Direct and indirect measurements for nuclear astrophysics at FRANZ and GSI
Universität Wien – VERA Seminar
Vienne, Austria, 15.01.2009

Reifarth, Rene
(p,g) Experimente am Experimentellen Speichering der GSI
IKF Seminar, Goethe Universität Frankfurt
Frankfurt a. M., Germany, 09.07.2009

Reifarth, Rene
(p,g) experiments at the Experimental Storage Ring at GSI
LANSCE Seminar, LANL
Los Alamos, USA, 21.09.2009

Reifarth, Rene
Von Sternenexplosionen und der Synthese der Elemente
Physikalischer Verein
Frankfurt a.M., Germany, 14.11.2009

Reisdorf, W.
Some problems extracting the EOS from HI data
Workshop on Simulations of low and intermediate Heavy-ion Collisions
Trento (Italy), 15.-20.Mai 2009

Reisdorf, W.
Systematics of heavy ion collisions at SIS
Seminar
MSU East-Lansing (USA), 15. Dezember

Ricciardi, Maria Valentina
Results obtained with ABLA07
International Topical Meeting on Nuclear Research Applications and Utilization of Accelerators (AccApp09); Stellite Meeting on Nuclear Spallation Reactions
Vienna, Austria, 4.5-8.5.2009

Ricciardi, Maria Valentina
The Role of Nuclear-Structure Effects in the Study of the Properties of Hot Nuclear Matter
2nd Conference on Nuclear Fragmentation (NUFRA2009)
Kemer Antalya, Turkey, 27.9.-4.10.2009

Ricciardi, Maria Valentina
Even-odd effect in the yields of nuclear-reaction products
Seminar at CENBG
Bordeaux, France, 09.11.2009

Ritter, Silvia
Heavy ion induced chromosome aberrations: new insights achieved by new technologies
9th International Symposium on Chromosome aberrations
Sankt Goar (Germany), 11.-12.7.2009

Rosmej, O.
Nanostructure irradiated by nanosecond and picosecond PHELIX-laser pulses
EMMI-workshop on Plasma Physics with Intence Ion and Laser Beams
Moscow (Russia), 14.-15. May 2009

Rosmej, O.
X-Ray spectroscopy as a powerful tool in experiments with laser and heavy ion beams
Plasma Physics Seminar UNI-Frankfurt
Frankfurt (Russia), 28. May 2009

Roy, B.
The PANDA experiment at FAIR
Univ. of South Carolina
Columbia-SC (USA), Nov. 2009

Rustamov, A.
Inclusive meson production at 3.5 GeV pp collisions with the HADES spectrometer
XIII International Conference on Hadron Spectroscopy
Tallahassee, Florida, USA, Nov. 29-Dec. 4, 2009

Sanchez, R.
Frequency-Comb based laser spectroscopy of Halo Nuclei: The nuclear charge radius of Beryllium-11.
Nuclear Structure and Dynamics Conference
Dubrovnik (Croatia), 08.Mai.2009

Sanchez, R.

High-Precision Laser Spectroscopy on the 2S-3S Transition of Lithium-7 and Lithium-6.
VIII International Workshop: Application of Lasers and Storage Devices in Atomic Nuclear Research
Poznan (Poland), 22.Juni 2009

Sánchez, R.
High-Precision Laser Spectroscopy on the 2S - 3S Transition of 7Li and 6Li
VIII International Workshop: APPLICATION OF LASERS AND STORAGE DEVICES IN ATOMIC NUCLEI RESEARCH - Recent Achievements and Future Prospects
Poznan (Poland), 22.-25. Juni 2009

Schädel, Matthias
Superheavy Elements Research at TASCA
Asian-Pacific Symposium on Radiochemistry 2009 (APSORC-09)
Napa, USA, 29.11.-4.12.2009

Schädel, Matthias
TASCA - A New Tool un the Quest for Superheavy Element Studies
7th Workshop on the Chemistry and Physics of the Heaviest Elements
Mainz, Germany, 11.10.-13.10.2009

Schädel, Matthias
Transfer and Fusion Aspects of the Synthesis of Heavy ans Superheavy Nuclides
American Chemical Society, 237th National Meeting
Salt Lake City, USA, 22.3.-26.3.2009

Schädel, Matthias
The TransActinide Separator and Chemical Apparatus at GSI - Status and Perspectives
Lawrence Livermore National Laboratory
Livermore, USA, 08.12.2009

Schädel, Matthias
Institut Für Kernchemie, Johannes-Gutenberg Universität Mainz
Mainz, Germany, 20.07.2009

Schädel, Matthias
Superheavy Element Research at GSI
RIKEN Nishina Center for Accelerator Based Science and CNS, Univ. of Tokyo
Wako-shi, Japan, 02.03.2009

Schädel, Matthias
Superheavy Element Research at GSI
JAEA Advanced Science Research Center,
Tokai, Japan, 25.02.2009

Schardt, D.
Zielgenaue 3D-Bestrahlung von Tumoren mit hochenergetischen Ionen
Institutskolloquium Fraunhofer Gesellschaft
Euskirchen (Germany), 11 March 2009

Schardt, D.
Phosphenes in Carbon Ion Tumor Therapy
Symposium Heavy Ions in Therapy and Space
Köln (Germany), 6-10 July 2009

Schardt, D.
Physical characterization of carbon ion therapy beams: precision Bragg curve measurements and fragmentation studies
NUFRA 2009 Second Int. Conf. on Nuclear Fragmentation
Kemer (Antalya/Turky), 27 Sept – 4 Oct 2009

Schardt, D.
Physical characterization of light-ion beams at the GSI therapy unit
Workshop on Nuclear Models for use in Hadrontherapy
Jülich (Germany), 8-9 Oct 2009

Schardt, D.
Tumor therapy with carbon ions at GSI Darmstadt
Working Session on Hadrontherapy
Sevilla (Spain), Centro de Acceleradores, 14 Dec 2009

Scheidenberger, Christoph
NUSTAR experiments at GSI and FAIR
KVI/GSI collaboration meeting
Groningen, Netherlands, 16.04.2009

Scheidenberger, Christoph
Nuclear physics experiments at GSI
Colloquium Phys. Inst. Xi'An Universität
Xi'An, China,)9. 7. 2009

Scheidenberger, Christoph
NUSTAR experiments at GSI and FAIR
Colloquium Inst. for Mod. Phys. Lanzhou
Lanzhou, China,, 07.07.2009

Scheidenberger, Christoph
Nucleosynthesis studied in the laboratory - recent results from GSI
WE - Heraeus-Seminar 'Nukleosynthesis making the Elements in the Universe'
Bad Honnef, Germany, 4.-6.6.2009

Scheidenberger, Christoph
Scientific collaboration in nuclear physics
Topical Conference: 'Belgium and Germany: Partners in innovation and education'
Brussels, Belgium, 14.-15. 10. 2010

Scheidenberger, Christoph
NUSTAR present and future experimental programme
NUSTAR-09, 2nd NUSTAR Collaboration Meeting 2009
Dubna, Russia, 6.-10.10.2010

Scheidenberger, Christoph
The Physics programme at Giessen University
66th NuPECC Meeting
Egelsbach, Germany, 10.-11.10.2010

Schmidt, C. J.

GSI Part of: MC-PAD Network: Partners, objectives, organisation and work plan; MC-Pad Training Projects
MC-PAD Kick-off meeting
CERN (Switzerland), 14.January 2009

Schmidt, C. J.
Status of the n-XYTER and CBM-XYTER development line
Workshop Detectors for Super-FRS
GSI, 11. February 2009

Schmidt, C. J.
Activities on n-XYTER FEBs, testing, engineering run
13th CBM Collaboration Meeting
GSI, 10.-13. March 2009

Schmidt, C. J.
XYTER Family Planning, FEE for Tracking Detector Applications
13th CBM Collaboration Meeting
GSI, Regarding the DC biasing of MAPD detectors

Schmidt, C. J.
CBM-MUCH Front-End and Readout Electronics, Suggestions for India´s Involvement in Electronics for CBM
Meeting Indian Participation in FAIR
Hyderabad (India), 18.Apr.09

Schmidt, C. J.
GSI Detector Laboratory, Environment, Technologies, Engagements and Research
Work meeting at KACST
Riyadh (Saudi Arabien),

Schmidt, C. J.
Technical challenges of the CBM and MVD Silicon Tracking Systems 2009
3rd work meeting of CBM-MPD STS Consortium
Sortavala (Russia), 1. - 4. June 2009

Schmidt, C. J.
n-XYTER Front-End Boards
3rd work meeting of CBM-MPD STS Consortium
Sortavala (Russia), 1. - 4. June 2009

Schmidt, C. J.
n-XYTER Engineering Run Preparations
14th CBM Collaboration Meeting
Split (Croatia), 6.-9- October 2009

Schmidt, C. J.
Front end electronics summary talk
14th CBM Collaboration Meeting
Split (Croatia), 6.-9. October 2009

Schmidt, C. J.
CBM Front End Electronics and Data Acquisition - an Exhibit on Activities
HIC for FAIR Detector Workshop
Darmstadt, 24.Nov.09

Schmidt, C. J.
CBM Front End Electronics and Data Acquisition
CBM-China Workshop
Beijing (China), Nov.09

Schmidt, C. J.
n-XYTER, a self triggered, sparcifying readout ASIC for high rates and high signal densities, chip architecture and testing results
n-XYTER Engineering Run Submission Readiness Review Meeting
Heidelberg, 21. December 2009

Schmidt, C. J.
CBM Front End Electronics and Data Acquisition - an Exhibit on Activities
5th India-CBM Collaboration Meeting
Banaras (India), 28.-29. December 2009

Schmidt, C. J. (invited)
CASCADE with NRSE, Fast Intensity Modulation Techniques used in Quasielastic Neutron Scattering, a MIEZE Realization
Int. Conf. on Neutron Scattering (ICNS 2009)
Knoxville (USA), 3.-7. May 2009

Schmitt, L.
The FAIR Project - Overview of Facility and Experiments
G-APD Workshop, GSI
Darmstadt (Germany), 9. Feb. 2009

Schmitt, L.
Antimatter at FAIR
KSA-FAIR Workshop, KACST
Riyadh (Saudi-Arabia), 3. Mai 2009

Schmitt, L.
The Straw Tube Tracker of the PANDA Experiment
IEEE Nuclear Science Symposium
Orlando (USA), 27. Okt. 2009

Schmitt, L.
Hard Exclusive Processes in PANDA
Workshop on Hard Exclusive Processes
München (Germany), 11. Nov. 2009

Schmitt, L.
The PANDA Experiment
Open Charm Physics At PANDA
Mainz (Germany), 19. Nov. 2009

Schmitt, L.
The PANDA Experiment
HIC for FAIR Detector Systems Networking Workshop
Darmstadt (Germany), 24. Nov. 2009

Scholz, M.
Modellierung der biologischen Wirkung von Ionenstrahlen: Grundlagen und mögliche Anwendungen in der Bor-Neutronen-Einfangtherapie

Seminar Kernchemie
Mainz (Germany), 20/ April 2009

Scholz, M.
Biological Treatment Planning - Challenges Resulting from Spot Scanning
Erice Workshop Hadrontherapy
Erice (Italy), 27/ April 2009

Scholz, M.
Biological Plan Optimization for Carbon Ion Therapy
ESTRO Teaching Course Proton and Ion Therapy
Villigen (Germany), 11/ Mai 2009

Scholz, M.
Treatment Planning for Ion Beam Therapy: Comparison of the HIMAC and GSI approach
ENLIGHT Meeting
Valencia (Spain), 18/ Juni 2009

Scholz, M.
Biophysical Modelling in Treatment Planning for Carbon Ion Therapy
IBA S.A .Internal Seminar
Louvain-la-Neuve (Belgium), 29/ Juni 2009

Scholz, M.
Treatment Planning for Ion Beam Therapy: Comparison of the HIMAC and GSI approach
IBIBAM 2009
Köln (Germany), 6/ Juli 2009

Scholz, M.
Uncertainties in Treatment Planning for Ion Beam Therapy: Experimental and Modelling Aspects
World Congress Medical Physics
München (Germany), 9/ September 2009

Scholz, M.
Biological Aspects of Carbon Ion Therapy
PTCOG48 Educ. Workshop
Heidelberg (Germany), 29/ September 2009

Schuh, M.
Higher order modes in the SPL, transverse and longitudinal effects.
3rd SPL Collaboration Meeting at CERN
Geneva (Switzerland), 11.Oktober 2009

Schuh, M.
Studies for the SPL at CERN.
SPL Workshop at CERN
Geneva (Switzerland), 25./26.Juni 2009

Schuh, M.
Higher Order Modes in the Superconducting Cavities of the SPL.
Gentner Day, CERN
Geneva (Switzerland), 18.November 2009.

Schwarz, C.
The PANDA Barrel DIRC
FEDAQ09 Meeting
Bodenmais (Germany), Apr. 2009

Schwarz, C.
The PANDA Barrel DIRC
Workshop On Fast Cherenkov Detectors: Photon Detection, DIRC Design And DAQ
Gießen (Germany), Mai 2009

Schwarz, C.
The PANDA Barrel DIRC Frontend electronics & DAQ
Workshop On Fast Cherenkov Detectors: Photon Detection, DIRC Design And DAQ
Gießen (Germany), Mai 2010

Schwarz, C.
The PANDA Barrel DIRC Reconstruction methods
Workshop On Fast Cherenkov Detectors: Photon Detection, DIRC Design And DAQ
Gießen (Germany), Mai 2011

Schwarz, K.
ALICE T2-Zentrum bei GSI
DPG Frühjahrstagung
Bochum, März 2009

Schwarz, K.
Interaktive Datenanalyse mit stationären und dynamisch erzeugten PROOF –Clustern
DPG Frühjahrstagung
Bochum, März 2009

Schwarz, K.
<nop>PandaGrid – a Tool for Physics
DPG Frühjahrstagung
Bochum, März 2009

Schwarz, K.
Availability of ALICE grid resources in Germany
ALICE Offline Week
CERN, Oktober 2009

Schwarz, K.
Status GSIAF
ALICE Offline Week
CERN, Juni 2009

Schwarz, K.
Computing for FAIR
Model 2009
Tagbilaran, Bohol, Philippines, Mai 2009

Schwarz, K.
Introduction to Grid Computing and Applications
Model 2009
Tagbilaran, Bohol, Philippines, Mai 2009

Schwarz, K.
ALICE Tier2 at GSI
CHEP 2009
Prag, März 2009

Schwarz, K.
Computing in High Energy and Nuclear Physics
China Institute of Atomic Energy, Mai 2009

Schwarz, K.
<nop>AliRoot/FAIRRoot tutorial
China Institute of Atomic Energy, Mai 2009

Schwiening, J.
The Barrel DIRC Detector for the PANDA Experiment at FAIR
IEEE Nuclear Science Symposium
Orlando (USA), 25.-31. Okt. 2009

Schwiening, J.
Construction and Performance of the BaBar DIRC
Workshop On Fast Cherenkov Detectors: Photon Detection, DIRC Design And DAQ
Gießen (Germany), Mai 2012

Senger, P.
Exploring neutron star matter in the laboratory- The CBM Experiment at FAIR/SIS300; SIS 300 Pre-consortium Meeting

IHEP
Protvino (Russia), March 19-20, 2009

Senger, P.
The Compressed Baryonic Matter experiment at the Facility for Antiproton and Ion Research
Bhabba Atomic Research Center
Mumbai (India), April 16, 2009

Senger, P.
The Facility for Antiproton and Ion Research Status and Perspectives
Meeting on Indian participation in FAIR
ECIL
Hyderabad (India), April 18, 2009

Senger, P.
Exploring dense nuclear matter with heavy-ion collisions
Workshop KSA-FAIR future collaboration
King Abdul Aziz City for
Science and Technology
(KACST)
Riyadh (Saudi Arabia), May 2-4, 2009

Senger, P.
Charm measurements with the Compressed Baryonic Matter experiment at FAIR
Quarkonium Production in Heavy-Ion Collisions
ECT*
Trento (Italy), May 25-29, 2009

Senger, P.
The Compressed Baryonic Matter experiment at FAIR
- 3rd Work Meeting of the CBM-MPD STS Consortium
Sortavala, Karelia (Russia), June 1 - 4, 2009

Senger, P.
CBM at FAIR: capabilities for charm and dilepton studies CPOD 2009
Brookhaven National Lab
Upton, NY (USA), June 8-12, 2009

Senger, P.
Strangeness production in heavy-ion collisions
Hyp-X @J-PARC
Kyoto University
Tokai (Japan), Sept. 12 – 18, 2009

Senger, P.
Nuclear Matter Physics NICA
NICA Roundtable Workshop IV: Physics at NICA
JINR
Dubna (Russia), Sept. 9-12, 2009

Senger, P.
Exploring the properties of strongly interacting matter at high baryon densities NuPECC LRP2010 Scoping Workshop
FIAS
Frankfurt am Main (Germany), Oct. 12-13, 2009

Senger, P.
The Compressed Baryonic Matter experiment
at the Facility for Antiproton and
Ion Research Heavy Ion Meeting
Hanyang University
Seoul (Korea), Oct. 31, 2009

Senger, P.
The Compressed Baryonic Matter experiment at FAIR China- CBM Meeting
Tsinghua University
Beijing (China), Nov. 2 – 4, 2009

Senger, P.
The Facility for Antiproton and Ion Research
and the Compressed Baryonic Matter Experiment
VIII Latin American Symposium on Nuclear Physics and Applications
Universidad de Chile
Santiago (Chile), Dec. 15-19, 2009

Sieja, K.
New island of inversion around N=40
XVI Colloque GANIL
Giens (France), 09.09.2009

Sieja, K.
Shell evolution towards and beyond 78Ni
Workshop on Confrontation and convergence in nuclear theory
Trento (Italy), 29.07.2009

Sieja, K.
Shell-model studies of N=40-50 region
Workshop on Nuclear structure of the neutron-rich region around Z=28 towards and beyond N=50
Leuven (Belgium), 10.03.2009

Sieja, K.
Recent shell model studies of nuclei from Ni56 to Sn132

Seminar, Centre d'Etudes Nuclèaires de Bordeaux Gradignan
Bordeaux (France), 12.06.2009

Sieja, K.
Recent shell model studies of nuclei from Ni56 to Sn132
Seminar, Institut Pluridisciplinaire Hubert Curien
Strasbourg (France), 17.03.2009

Simon, Haik
Nuclear Structure at the limits of existence
10th International Conference on Nucleus-Nucleus Collisions (NN2009)
Beijing, China, 16.8.-21.8.2009

Söldner, W.
QCD in the Early Universe
Winter School
Schladming (Austria), 03.03.2009

Söldner, W.
Lattice QCD and Supercomputing
Sonderkolloquium Gittereichtheorie
Mainz (Germany), 25.03.2009

Söldner, W.
Lattice QCD at finite T and finite mu_B
RNM meeting
Darmstadt (Germany), 02.12.2009

Sommer, B.
Das SPECTRAP-Experiment und erste Tests mit einer Offline-Ionenquelle
Frühjahrstagung der DPG Atome, Moleküle, Quantenoptik und Plasmen
Hamburg (Germany), 2.–6. März 2009

Splinter, J.
DNA double-strand break dynamics on charged particle tracks in the context of chromatin density (Vortrag/Travel award)
GBS
Essen, 30 September - 2 Oktober 2009

Stöcker, H.
Scientific goals, technical lay-out and status of preparations of the international FAIR project
CERN Science Policy Committee
Genf (Switzerland), 16.03.2009

Stöcker, H.
Cosmic Matter in the FAIR Laboratory
DPG-Frühjahrstagung/European Nuclear Physics Conference
Bochum (Germany), 17.03.2009

Stöcker, H.
Physics at FAIR – Prospects for novel fission studies
4th International Workshop on Nuclear Fission and Fission-Product Spectroscopy, Institut Laue-Langevin
Cadarache (France), 16.05.2009

Stöcker, H.
Signatures of Mini Black Holes at the LHC
Heidelberg (Germany), 25.07.2009

Stöcker, H.
Physics at FAIR
NN2009
Beijing (China), 18.08.2009

Stöcker, H.
Extra Dimensions and Mini BlackHoles
GSI
Darmstadt (Germany), 04.09.2009

Stöcker, H.
Panel discussion on physics opportunities in the next decade in view of strangeness abd heavy flavor in matter
SQM2009
Buzios (Brasil), 28.09.2009

Stöcker, H.
The FAIR Modularized Start Version
NuPECC Meeting
Darmstadt (Germany), 11.10.2009

Stöcker, H.
Physics Highlights at GSI and the Future FAIR-facility
Physikalisches Kolloquium
Dresden (Germany), 27.10.2009

Stöhlker, Th.
Atomic Physics at GSI and FAIR.
Heraeus-Seminar "Atomic Theory for Fundamental Interactions and Simple Systems in Strong Fields"
Bad Honnef (Germany), 19.Januar.2009

Stöhlker, Th.
Physics at EBITS and Advanced Research Light Sources.
3rd workshop on Physics at EBITS and Advanced Research Light Sources (PEARL)
Dublin (Ireland), 09.Mai 2009

Stöhlker, Th.
Atomic Physics in Strong Fields: Precision Experiments with Stored and Cooled Highly Charged Ions.
EGAS 2009
Gdansk (Poland), 11.Juli 2009

Stöhlker, Th.
Polarization and Angular Correlation of X-Ray Emitted in Relativistic Ion-Atom Collisions.
ISIAC 2009, Old Dominion Univ.
Norfolk, Virginia (USA), 18.Juli 2009

Stöhlker, Th.
Relativistic Atomic Physics with FAIR
Int. Graduate School, Universität Basel (Physik)
Basel (Switzerland), 19.Januar 2009

Stöhlker, Th.
GSI and FAIR, an Overview

High-Energy Proton Microscopy Workshop, GSI
Darmstadt (Germany), 25. August 2009

Stöhlker, Th.
Overview of the Plasma and Atomic Physics Activities at GSI
EMMI workshop on plasma physics with intense laser and heavy ion beams
Moskau (Russia), 14. Mai 2009

Stöhlker, Th.
Current Status of the SPARC Collaboration
Lissabon (Portugal), 1. September 2009

Stöhlker, Th.
Die Physik starker Felder auf dem Teststand
Pizza Night, Universität Heidelberg
Heidelberg (Germany), 26. Januar 2009

Stöhlker, Th.
Die faszinierende Welt starker Felder: Experimente mit hochgeladenen Ionen
Kolloquium Universität Jena
Jena (Germany), 16. November 2009

Stöhlker, Th.
Atomic Physics at FAIR
Atomphysik-Seminar, Uni. Giessen
Giessen (Germany), 17. Dezember 2009

Stöhlker, Th.
Towards PNC Experiments in High-Z He-like Ions
Semiar, HI-Jena
Jena (Germany), Dezember 2009

Stroth, Joachim
The physics program of CBM
Symposium on The Physics of Dense Baryonic Matter
Darmstadt, März, 2009

Stroth, Joachim
Dense nuclear matter: an experimentalists view
Nuclear Matter Physics at SIS100
Darmstadt, April, 2009

Stroth, Joachim
The Origin of Mass: Hadron physics experiments at GSI (excerpt)
KSA – FAIR Workshop, KACST
Riyadh, Saudi Arabien, Mai, 2009

Stroth, Joachim
Pixel detectors for high-resolution vertex reconstruction in CBM
KSA – FAIR Workshop, KACST
Riyadh, Saudi Arabien, Mai, 2009

Stroth, Joachim
The physics of compressed nuclear matter at SIS and FAIR
The 10th International Conference on Nucleus-Nucleus Collisions
Beijing, China, August 16-21, 2009

Stroth, Joachim
The physics of compressed nuclear matter at SIS and FAIR
Mazurian Lakes Conference on Physics
Piaski, Polen, September, 2009

Stroth, Joachim
The HADES physics program: status and future
Jahrestagung des Komitees Hadronen und Kerne
Bad Honnef, Dezember, 2009

Surzhykov, A.
Two-photon emission from few-electron heavy ions: Angle-and polarization-resolved studies.
The 5th SPARC symposium and collaboration meeting
Lisbon (Portugal), September 2009

Surzhykov, A.
Angle and polarization resolved analysis of relativistic ion-atom collisions: A probe for strong-filed phenomena.
International Symposium on (e,2e), Double Photoionization and Related Topics & the 15th International Symposium on Polarization and Correlation in Electronic and Atomic Collisions
Lexington (USA), 30. Juli - 1 August 2009.

Surzhykov, A.
DIRAC: Computer-algebra tool for studying the structure and dynamics of highly-charged, heavy ions.
The International Conference on Mathematical Modeling and Computational Physics
Dubna (Russia), 7.-11. Juli 2009.

Surzhykov, A.
Relativistic quantum dynamics in extremely strong electromagnetic fields.
Spring meeting of German Physical Society
Hamburg (Germany), 2.-6. März 2009.

Surzhykov, A.
Polarization and correlation phenomena in relativistic atomic collisions.
426th WE-Heraeus-Seminar
Bad Honnef (Germany), 18.-21. Januar 2009

Taucher-Scholz, G.
Clustered DNA damage: Spatiotemporal dynamics and cellular effects
Women in radiation sciences - a century after Marie Curie
München, 18. - 20. Mai 2009

Taucher-Scholz, G.
Heavy ion-induced damage visualization: from plasmid DNA to living cells
RADAM
Frankfurt, FIAS, 1-4 Juli 2009

Taucher-Scholz, G.
Damage response to heavy ion-induced double-strand breaks
Heavy Ion in Therapy and Space

Köln, 06. - 10. Juli 2009

Taucher-Scholz, G.
Wechselwirkung verschiedener Reparaturwege bei der Prozessierung von DNA Strahlenschäden
Kompetenzverbund für Strahlenforschung KVSF
Essen, 30 September 2009

Taucher-Scholz, G.
Proton and Heavy Ion Radiotherapy
55th Annual RRS Meeting
Savannah (USA), 4. - 7. Oktober 2009

Taucher-Scholz, G.
Overview of radiobiology at GSI
Microbeam Workshop
Bordeaux (Frankreich), 25 - 27 März 2009

Tauschwitz, A.
Radiative Properties of Warm Dense Matter - The Programm of the WDM-Collaboration at FAIR.
International Conference on Inertial Fusion Sciences & Applications 2009
San Francisco (USA), 6.-11. September 2009

Tiedemann, D.
Bestimmung der Kernladungsradien von 7, 10Be und dem Neutronen-Halokern 11Be
Frühjahrstagung der DPG Hadronen und Kerne
Bochum (Germany), 16.-20. März 2009

Tobias, F.
Travel award
NASA space radiation summer school.
New York (USA), 27 Mai – 19 Juni 2009

Tobias, F.
Binding dynamics of repair proteins at DNA damage sites after charged particle irradiation (Poster/Travel Award)
GBS
Essen, 30 September - 2 Oktober 2009

Tomut, M.
Stability of Swift Heavy Ion-Irradiated Carbon Materials
Stripper and Target Technology for High Power Heavy Ion Beams Workshop, Facility for Rare Isotope Beams (FRIB) at MSU
Michigan (USA), 6.-8. Dezember 2009

Trautmann, C.
Nanotechnology using MeV-GeV heavy ions
Seminar at the Australian National University
Canberra (Australia), 19. März 2009

Trautmann, C.
How heavy ions modify solids. Basic aspects and Application in micro and nanoscience
Kolloquium at the University of Jena
Jena (Germany), 29. Juni 2009

Trautmann, C.
Material modifications of SiO2 irradiated with heavy ions of MeV-GeV energy
Workshop on Nanostructures in Silica (NaiS '09)
Saariselkä (Finland), 7. September 2009

Trautmann, C.
Research at GSI with MeV-GeV Ion Beams
Forschungsklausur, University of Darmstadt
Michelstadt (Germany), 30. Oktober 2009

Trautmann, W.
Neutron-Proton Elliptic Flow in Au + Au
XLVII International Winter Meeting on Nuclear Physics
Bormio (Italy), 26.-30. Jan. 2009

Trautmann, W.
Flow at 100 and 400 A MeV
Workshop on Simulations of Low and Intermediate Energy Heavy Ion Reactions
Trento (Italy), 11.-15. Mai 2009

Trautmann, W.
The symmetry energy in nuclear reactions
The 10th International Conference on Nucleus-Nucleus collisions
Beijing (China), 16.-21. Aug. 2009

Trautmann, W.
The symmetry energy in nuclear reactions
The International Workshop on Nuclear Dynamics in Heavy-Ion Reactions and the Symmetry Energy (IWND2009)
Shanghai (China), 23.-25. Aug. 2009

Trautmann, W.
Limiting temperatures in multifragmentation
Second International Conference on Nuclear Fragmentation (NUFRA2009) - From Basic Research to Applications
Antalya (Turkey), 27. Sep. - 4. Okt. 2009

Trautmann, W.
Isotopic Flows in Au+Au at 400 A MeV
ESF Exploratory Workshop on How to Constrain the High Density Symmetry Energy - HiDeSymEne
Zagreb (Croatia), 16.-18. Okt. 2009

Trautmann, W.
Closing Remarks
International Workshop on Multifragmentation and Related Topics (IWM2009)
Catania (Italy), 4.-7. Nov. 2009

Typel, S.
Indirect methods and halo nuclei
Doppel-Graduiertentag, International Graduate School Basel-Graz-Tübingen
Basel (Switzerland), 19.02.2009

Typel, S.
Indirect methods for nuclear astrophysics
6th Workshop on Nuclear Astrophysics
Rußbach (Austria), 03.03.2009

Typel, S.
Equation of state for astrophysical applications
6th Workshop on Nuclear Astrophysics
Rußbach (Austria), 06.03.2009

Typel, S.
A Supernovae equation of state with light and heavy clusters
DPG-Frühjahrstagung/European Nuclear Physics Conference
Bochum (Germany), 19.03.2009

Typel, S.
A Supernovae equation of state with light and heavy clusters
432. Heraeus-Seminar: Nucleosynthesis – making the elements of the universe
Bad Honnef (Germany), 05.06.2009

Typel, S.
Nuclear matter equation of state with light clusters
6th Workshop on aspect of alpha correlations and alpha condensation in nuclear systems
Rostock (Germany), 06.08.2009

Typel, S.
A Supernovae equation of state with light and heavy clusters
NUFRA 2009, International Conference on Nuclear Fragmentation
Kemer (Turkey), 30.09.2009

Typel, S.
Clusters in nuclear matter
HIC4FAIR workshop on dense QCD phases in heavy-ion collisions and supernovae
Prerow (Germany), 12.10.2009

Varentsov, D.
Status of High Energy Density Research at GSI
Moscow Workshop on the Non-ideal Plasma Physics (NPP-2009), Presidium RAS, Moscow, Russia, 30.11 - 1.12.2009,
Moscow (Russia), 30. November - 1. Dezember 2009

Vogel, M.
"Blind spectroscopy" - Precision laser spectroscopy without optical detection
VIII International Workshop: APPLICATION OF LASERS AND STORAGE DEVICES IN ATOMIC NUCLEI RESEARCH - Recent Achievements and Future Prospects
Poznan (Poland), 22.-25. Juni 2009

Voskresenskaya, M.
Neutrino scattering on nuclei and interacting nucleon gas and equation of state of nuclear matter
HIC4FAIR workshop on dense QCD phases in heavy-ion collisions and supernovae
Prerow (Germany), 12.10.2009

Voss, B.
Non-standard dosimetry based on Diamond
11th ICATPP Conference on Astroparticle, Particle, Space Physics, Detectors and Medical Physics Applications
Como, Italy, 5.-9. October 2009

Voss, B.
Status of the GEM-TPC Prototype
28th PANDA collaboration meeting
Darmstadt (Germany), 2.-6. March 2009

Voss, B.
The PANDA GEM-Trackers
28th PANDA collaboration meeting
Darmstadt (Germany), 2.-6. March 2009

Voss, B.
The FOPI/CB-ELSA GEM-TPC, a precursor prototype for the PANDA TPC
DPG spring meeting
Bochum (Germany), 15.-20. March 2009

Voss, B.
Planar GEM-Trackers
PANDA Mecanical workshop
Darmstadt (Germany), 2.-3. April 2009

Voss, B.
The Planar-GEM Tracker system for PANDA
FP7 JointGEM Kickoff Meeting
Munich (Germany), 6. April 2009

Voss, B.
The status of the FOPI/ELSA GEM-TPC
FP7 JointGEM Kickoff Meeting
Munich (Germany), 6. April 2009

Voss, B.
The FOPI GEM-TPC
FOPI collaboration meeting
Darmstadt (Germany), 20. April 2009

Voss, B.
Planar GEM-Trackers for PANDA
PANDA FE & DAQ workshop
Bodenmais (Germany), 23. April 2009

Voss, B.
Requirements on a DCS system for GEM-based detectors
29th PANDA collaboration meeting
Torino (Italy), 15.-19. June 2009

Voss, B.
Update on the status of the PANDA GEM-TPC prototype
29th PANDA collaboration meeting
Torino (Italy), 15.-19. June 2009

Voss, B.
Short Status Summary on the FOPI/CB-ELSA GEM-TPC
GEM-TPC Face-2-face meeting
Darmstadt (Germany), 29. July 2009

Voss, B.

Short Status Summary on the PANDA (-prototype) GEM-TPC
30th PANDA collaboration meeting
FZJ Jülich (Germany), 7.-11. September 2009

Voss, B.
Design studies on the PANDA GEM-TPC
30th PANDA collaboration meeting
FZJ Jülich (Germany), 7.-11. September 2009

Voss, B.
Update on the Planar-GEM Trackers
31th PANDA collaboration meeting
Darmstadt (Germany), 7.-11. Decemver 2009

Voss, B.
Brief Status Summary on the FOPI/CB-ELSA GEM-TPC
31th PANDA collaboration meeting
Darmstadt (Germany), 7.-11. Decemver 2009

Voss, K.-O.
Die Schwerionenmikrosonde der GSI - Gezielte Bestrahlung von lebenden Zellen
6. Nanotechnologieforum Hessen
Hanau (Germany), 26.November 2009

Wambach, J.
The Phase Diagram of Strongly Interacting Matter
Kolloquium
Graz (Austria), 14.01.2009

Wambach, J.
Summary talk
Conference CSQCD II
Beijing (China), 24.05.2009

Wambach, J.
Phases of strongly interacting matter: the 2+1 PQM model
EMMI workshop and XXVI Max Born Symposium
Wroclaw (Poland), 07.09.2009

Weber, D.
Transformation of nuclear potentials from partial wave representation into operator representation
DPG-Frühjahrstagung/European Nuclear Physics Conference
Bochum (Germany), 16.03.2009

Weber, G.
Angular distribution and linear polarization of Ly-a1 radiation in H-like uranium.
SPARC Collaboration Meeting 2009 at University of Lisbon
Lisbon (Portugal), 4.September 2009

Weber, G.
Linear Polarization and Angular Distribution of Lya1 Radiation in H-like Uranium.
EAS-Tagung 2009
Riezlern (Austria), 9.Februar 2009

Weick, Helmut
Recent Results from Experiments with Stored Exotic Nuclei
NUSTAR in Russia meeting
Dubna, Russia, 5.10.-10.10.2009

Weick, Helmut
Calculations for the HRS and presentation of the MR-TOF separator
high resolution mass separator for SPIRAL II
Bordeaux, France, 12.11.-13.11.2009

Weick, Helmut
In-Ring Spectrometer
EXL/ELISe meeting on technical issues
GSI, Germany, 04.05.-06.05.2009

Weick, Helmut

KVI/GSI collaboration meeting
Groningen, Netherlands, 16.04.-17.04.2009

Weick, Helmut
Four Rings for NUSTAR
Annual NUSTAR meeting
GSI, Germany, 23.03.-27.03.2009

Weick, Helmut
An Overview on Fragment Separators at Relativistic Energies
Seminar
CERN, France, 23.04.2009

Weick, Helmut
Determination of proton radii and neutron skin thickness of p-sd shell nuclei by charge change reactions
FRS-User meeting
GSI, Germany, 29.10.2009

Weick, Helmut
Access to proton and neutron radial distributions using delta-resonance excitation
FRS-User meeting
GSI, Germany, 29.10.2009

Weick, Helmut
Status report
ILIMA meeting
GSI, Germany, 24.03.2009

Welsch, C.P.
FLAIR - A Facility for Low-energy Antiproton and Ion Research.
Workshop on Low Energy, Low Intensity Beams
Hirschberg (Germany), 25. November 2009

Welsch, C.P.
Accelerator Physics for Antimatter Research & Instrumentation.
SAC meeting, Cockcroft Institute
Warrington (UK), 2. November 2009

Welsch, C.P.
Beam Instrumentation for CLIC.

CLIC meeting at CERN
Geneva (Switzerland), 20.August 2009

Welsch, C.P.
Teilchenbeschleuniger - Unersetzbare Werkzeuge für die Forschung.
DPG School
Bad Honneff (Germany), 6. Juli 2009

Welsch, C.P.
Definition of Particle Beams.
DITANET School on Beam Instrumentation
ondon, 31. März 2009

Wilms, A.
APD development for the PANDA EMC
DPG Frühjahrstagung 2009
Bochum (Germany), 16.-20. März 2009

Wilms, A.
Rectangularly Shaped LAAPDs for PANDA
IEEE Nuclear Science Symposium
Orlando (USA), 25.-31. Okt. 2009

Wilms, A.
APD development for PANDA & Co.
HIC for FAIR Detector Systems Networking Workshop
Darmstadt (Germany), 24. Nov. 2009

Winkler, Martin
Status of Super-FRS
Annual NUSTAR Meeting
GSI, Darmstadt, 25.3.-27.3.2009

Winkler, Martin
From FRS to Super-FRS
Artic Fidipro-EFES
Saariselkä, Finland, 20.4.-24.4.2009

Winters, D.
Precision tests of quantum electrodynamics in the strong and critical-field regime.
WE Heraeus-Seminar "Precision Experiments at Lowest Energies for Fundamental Tests and Constants"
Bad Honnef (Germany), 16. Juni 2009

Winters, D.
News from the ESR storage ring
5th SPARC Collaboration Symposium. Caparica campus, New university of Lisbon
Lisbon (Portugal), 3. September 2009

Zakova, M.
Nuclear charge radius determination of the halo nucleus Be-11.
Klausurtagung des Forschungszentrums Elementarkräfte und Mathematische Grundlagen (EMG)
Mainz (Germany), 21.-22. Oktober 2009

Zakova, M.
High-resolution collinear laser spectroscopy as a tool for precise high-voltage determination
Frühjahrstagung der DPG Atome, Moleküle, Quantenoptik und Plasmen
Hamburg (Germany), 2.–6. März 2009

Zielbauer,B.
10 Hz Mo X-Ray Laser operation at LASERIX - First application experiment in radiobiology.
Ultrafast Optics / High Field Short Wavelength - UFO VII / HFSW XIII
Arcachon (France), 31.August – 4.September 2009

Zoric, M.
Analysis of neutron/proton elliptic flow in Au+Au collisions
Workshop on "How to constrain the high density symmetry energy"
Zagreb (Kroatia), 15.-18. Oktober

Zynovyev, M.
Optimizing I/O Performance for ESD Analysis
ALICE Offline Week
CERN, Geneve, 28. Oktober 2009

Committee and Referee activities

Compiled by K. Kreidi, C. Kausch, I. Kraus
GSI, Darmstadt, Germany

Ackermann, D.
GANIL Forward Look FORUM, Commitee member
EURISOL User Executive Committee, Commitee member
Scientific Council GANIL, Council member
Wissenschaftlicher Ausschuss der GSI, Ausschussmitglied
Physical Review C, Referee
Physical Review Letters, Referee
Journal of Physics G, Referee
Physics Letters B, Referee

Al-Turany, M.
Journal of Physics : Conference Series, Referee
Jordan Journal of Physics, Referee

Averbeck, R.
Publikation in Phys. Lett. B, Gutachten/report

Bagnoud, V.
ILE technical committe for Apollon-10P, Mitglied/Member

Berdermann, E.
Publikation in Diamond and Related Materials, referee
HadronPhysics2 Collaboration Committee, spokesperson WP15 CARAT-Advanced Diamond Detectors
CBM Technical Board, member, START detector

Bert, C
Medical Physics, Gutachten
Physics in Medicine and Biology, Gutachten
Int. J. Radiat. Oncol. Biol. Phys., Gutachten
Sensors, Gutachten
Swiss National Science Foundation, Gutachten

Braun-Munzinger, P.
Science Policy Committee, CERN, member
Humboldt Professorship Selection Committee, member

D. Schardt
ENVISION (EU-Project) Steering Committee, Member
Phys. Med. Biol., Reviewer
Nucl. Instrum. Meth. B, Reviewer
Radiation and Environmental Biophysics, Reviewer

Durante, M.
Radiation and Environmental Biophysics (Berlin), Associate Editor
European Journal of Medical Physics (Heidelberg), Associate Editor
Radiobiology and Radioecology (Moscow),, Associate Editor
Radiat. Meas., Referee
Journal of Radiation Research (Tokyo), Associate Editor
Radiat. Res., Referee
Nucl. Instr. and Meth., Referee
Radiation and Environmental Biophysics, Referee
Int. J. Radiat. Biol., Referee
J. Radiat. Res., Referee
Adv. Space Res., Referee
Br.J. Radiol., Referee
Medical Physics, Referee
J. Cell Physiol., Referee
Physica Medica, Referee
Committee Space Research (COSPAR), Member
Board of reviewers of the European Space Agency (ESA), Member of the
ESA Life Sciences Advisory Group (LSAG), Member
ESA Topical Team (TT) on Space Radiation Research., Chairman
GANIL, Caen (France),, Member of the Program Advisory Committee (PAC)
KVI accelerator, Groningen (The Netherlands)., Member of the Program Advisory Committee (PAC)
NASA Summer School, Brookhaven (USA)., Member of the Board of Professors
European Science Foundation (ESF), Member of the Council of Reviewers

Egelhof, P.
Int. Conf. on Nuclear Physics at Storage Rings, STORIAdvisory Comittee,

Feldmeier, H.
EENEN09, First EMMI-EFES Workshop on Neutron Rich Nuclei, GSI, Organisator
Physical Review C, Gutachter
Physical Review Letters, Gutachter
Journal of Physics G, Gutachter
Nuclear Physics A, Gutachter

European Physical Journal A, Gutachter

Fournier, C.
AIFIRA micro- and nanobeam facility, CENBG, Bordeaux, France, member of the user panel

Friman, B.
Scientific Board of ECT*, Chairman

Nuclear Physics A, Associate Editor

Fritzsche, S.
Atomic Data Nuclear Data Tables, Gutachten/report

Computer Physics Communication, Special Editor

Hyperfine Interactions, Gutachten/report

Physical Review A, Gutachten/report

Physical Review Letters, Gutachten/report

Quantum Information Processes, Gutachten/report

Fuchs, R.
HGF Arbeitskreises "Wissenschaftlicher Gerätebau", Vorsitzender/Chair

Garabatos, J.
STAR review committee, member

Gerl, J.
Humboldt Stiftung, Gutachter

QNRF, Gutachter

AGATA Steering Committee, Member

AGATA Steering Committee, Member

PRESPEC Steering Committee, Member

RISING Steering Committee, Member

EXOGAM Steering Committee, Member

PARIS Steering Committee, Member

HISPEC/DESPEC Management Board, Member

NUSRAR Board of Representatives, Scientific secretary

Publikation in Nucl. Instr. Meth. A, Gutachten/report

Publikation in Phys. Rev. C, Gutachten/report

Publikation in Physics Letters B, Gutachten/report

Gonzalez-Diaz, D.
Resistive Plate Chamber workshop 2010, Advisory committee

Hagmann, S.
manuscripts submitted to Phys. Rev. Lett., 3 Gutachten/reports

manuscripts submitted to Phys. Rev. A, 2 Gutachten/reports

Heinz, S.
EPJ A, Refereee

J. Phys. G, Refereee

Herfurth, F.
Publikation in Nucl. Instr. Meth. A, Gutachten/report

Publikation in Int. J. Mass Spectrometry, Gutachten/report

Publikation in J. Phys. B, Gutachten/report

Publikation in Eur. Phys. J. A, Gutachten/report

Heßberger, F.P.
NuPPEC Longrange Plan 2010, Member WP3, Superheavy Elements

Hofmann, S.
PAC Dubna, PAC member

Jakob, B.
Eur Phys. J. -D, Gutachten

Trends in Cell Biology, Gutachten

Int. J. Rad. Biol., Gutachten

Karsch, F.
School “Phases of Strongly Interaction Matter”, Paris, 9.-13. März 2009, Koorganisator

Kluge, H.-J.
Committee of the PTB Braunschweig for the Helmholtz Prize, Mitglied/Member

Advisory Board for Danish CERN Physics, Mitglied/Member

Publikation Hyperfine Interactions, Gutachten/report

Kolb, B.W.
IEEE Transactions on Nuclear Science, Gutachten/report

Kühl, Th.
International Advisory Committee of PALS, Mitglied/Member

Access Board of Laserlab Europe, Mitglied/Member

International Committee on Ultra-High Intensity Lasers (ICUIL), Mitglied/Member

Langanke, K.
Gutachterausschuss, BMBF, Mitglied

Program Advisory Committee, GANIL, Mitglied

Scientific Advisory Committee, RIKEN, Mitglied

Scientific Advisory Committee, FRIB, Mitglied

Advisory Committee, JINA, Mitglied

Program Advisory Committee, RIKEN, Mitglied

Scientific Council, EMMI, Mitglied

Scientific Council, HIC for FAIR, Mitglied

Nuclear Physics A, Supervisory Editor

Leifels, Y.
Publikation in Phys. Lett. B, Gutachten/report

Lutz, M.
Berufungskommission, W2 Theorie-Professur, Universität Giessen, Mitglied
PANDA, Theory Advisory Group (TAG), Mitglied
Physical Review C, Gutachter
Physical Review D, Gutachter
Nuclear Physics A, Gutachter
European Physical Journal A, Gutachter
Journal of Physics G, Gutachter

Martinez-Pinedo, G.
Nuclear Physics A, Gutachter
European Physical Journal A, Gutachter
Physical Review C, Gutachter
Monthly Notices Royal Astronomical Society, Gutachter
Physica Scripta, Gutachter
Physics Letters B, Gutachter
Physical Review Letters, Gutachter
Journal of Cosmology and Astroparticle Physics, Gutachter
Start program of the Austrian FWF, Gutachter
Michigan State University, Gutachter
Outstanding Junior Investigator Program of the US DOE, Gutachter
Agencia Nacional de Promoción Científica y Tecnológica (Argentina), Gutachter
Agència de Gestió d'Ajuts Universitaris i de Recerca (Catalonia), Gutachter

Masciocchi, S.
EMMI fellowship committee, member
Berufungsverfahren "Experimentelle Kernphysik (W2 EMMI)" an der Goethe-Universität, member

Mathias Münch
DLR IK-M, Gutachter IT-Überprüfungen

Neff, T.
European Physical Journal A, Gutachter
Journal of Physics G, Gutachter
Nuclear Physics A, Gutachter
Physical Review C, Gutachter
Physics Letters B, Gutachter
Progress of Theoretical Physics, Gutachter

Nörtershäuser, W.
DFG-Antrag, Gutachten/report
Publikation in Nucl. Instr. Meth. Phys. Res., Gutachten/report
Publikation in J. Phys. B, Gutachten/report
Publikation in Hyperfine Interactions, Gutachten/report
Koordinationsausschuss des Forschungszentrums EMG (Elementarkräfte und Mathematische Grundlagen), Mitglied/member

O. Boine-Frankenheim
Publikation in Phys. Rev. ST Accel. Beams, Gutachten/report

Pfeiffer, B.
Nuclear Data Sheets, Refereee

Pietraszko, J.
Publikation in Nucl. Instr. Meth. A, Gutachten/report
Publikation in Acta Physica Polonica B, Gutachten/report

Quint, W.
Publikation bei J. Phys. B, 2 Gutachten/report
Publikation bei Eur. Phys. J. A., Gutachten/report
Bewerbung an Graduiertenprogramm (USA), 5 Gutachten/report
Diplomarbeit Uni Heidelberg, Zweitgutachten/second report
Doktorarbeit Uni Heidelberg, 2 Erstgutachten/ first report
Bewerbung auf eine PostDocstelle Uni Heidelberg, Gutachten/report
Doktoranden-Bewerbung bei GSI Graduiertenprogramm, Gutachten/report

Ritter, S
Mutat. Res., Gutachten
Int. J. Radiat. Biol., Gutachten
Diplomarbeit, Hochschule Darmstadt, Gutachten
Programme Committee, ISCA 2009, Rheinfels, Germany, Organisation
Local Organizing Committee, ISCA 2009, Rheinfels, Germany, Organisation
Committee for Young Scientist Awards, IBIBAM 2009, Gutachten
Organizing Committee, 9th Microbeam Workshop, Organisation

Schmidt, C. J.
MC-PAD Supervisory Board, member, scientist in charge at GSI for
CBM Technical Board, member

Scholz, M.
Radiation Research, Gutachten
Z. Med. Physik, Gutachten
ICRU, Committee Member

Schwarz,Kilian
Journal of Physics : Conference Series, Refereee
Future Generation Computer Systems, Referee

Schwiening, J.
IEEE Transactions on Nuclear Science, Gutachten/report

Journal of Instrumentation (JINST), Gutachten/report

Söldner, W.
Physical Review D, Gutachter

Stöcker, H.
GSI Wissenschaftliches Direktorium, Vorsitzender

Präsidium der Helmholtz-Gemeinschaft Deutscher Forschungszentren, Vize-Präsident

Helmholtz-Gemeinschaft Deutscher Forschungszentren Forschungsbereich "Struktur der Materie", Koordinator

Vorstand des Frankfurt Institute for Advanced Studies (FIAS), Goethe Universität Frankfurt, Mitglied

Leitung der Frankfurt International Graduate School of Sciences (FIGSS), Goethe Universität Frankfurt, Direktor

Alexander-von-Humboldt-Stiftung, Gutachter

Deutscher Akademischer Austauschdienst (DAAD), Gutachter

Polytechnische Gesellschaft Frankfurt am Main, Mitglied

Acatec (Deutsche Akademie der Technikwissenschaften), Mitglied

ad hoc OECD Global Science Forum Working Group on Nuclear Physics (Commission C 12), Mitglied

Working Group 9 on International Cooperation in Nuclear Physics (ICNP) of the International Union of Pure and Applied Physics (IUPAP), Mitglied

Board of the FAIR-Russia Research Center, Institute for theoretical and experimental physics, Moscow, Russia, Mitglied

Council of the Foundation of the Beilstein Institute, Frankfurt, Mitglied des Stiftungsrates

Advisory Board of the H. & E. Kleber Foundation, Mitglied des Beirats

Advisory Board of the Alfons und Gertrud Kassel Foundation, Mitglied des Beirats

Advisory Board of the Margarete und Herbert Puschmann Foundation, Mitglied des Beirats

Nuclear Physics Board of the European Physical Society, Mitglied

Institute of Physics (London) – Journal of Physics G, Senior Advisory Board Member

International Journal of Modern Physics E – Nuclear Physics, Editor

Modern Physics Letters A – Particles and Fields; Gravitation; Cosmology; Nuclear Physics, Editor

NuPECC, Mitglied

Stöhlker, Th
Publications in Phys. Rev. Letters, Gutachten/report

Publications in Phys. Rev. A, Gutachten/report

Engineering and Physical Sciences Research Council, UK, Gutachten/report

Doktorarbeit Uni Heidelberg, 3 Zweitgutachten

Diplomarbeit Uni Heidelberg, 1 Zweitgutachten

Doktorarbeit Uni Frankfurt, 4 Erstgutachten

Diplomarbeit Uni Frankfurt, 2 Erstgutachten

Helmholtz Graduate School HIRe, Gutachter/Application committee

FLAIR Steering Committee, Deputy Spokesperson

SPARC collaboration board, Contact person

GANIL Scientific Council, Mitglied/Member

Lanzhou, International Advisory Committee, Mitglied/Member

Direktorium des Helmholtz-Insitutes Jena, Mitglied/Member, Vorsitz

International Advisory Committee for the EBIS/T symposium, Mitglied/Member

International Advisory Committee, HCI2010, Mitglied/Member

HGF Programm PNI, Topic speaker (Topic Ions)

Publications in Journal of Physics B, Gutachten/report

Stroth, Joachim
Scientific Council of EMMI, Mitglied/Member

Scientific Council of HIC for FAIR, Mitglied/Member

Scientific Advisory Commitee of ELBE at FZD, Vorsitzenden/Chair

Advisory Board of the Centre of Experimental Nuclear Astrophysics and Nuclear Physics, Mitglied/Member

Eropean Physics Journal A, Gutachten/report

HADES Executive Board, Mitglied/Member

CBM Management Board, Mitglied/Member

Taucher-Scholz, G.
KVSF Kompetenzverbund Strahlenforschung, Vorstand

Radiaton Research, Gutachten

J. of Radiation Res. (Japan), Gutachten

Mutagenesis, Gutachten

Nucleic Acid Research, Gutachten

Trautmann, C.
Journal Beam Interactions with Materials and Atoms, Nuclear Instruments and Methods in Physics Research, Section B, Elsevier, Mitherausgeberin/Editor

Program Committee of the 17th International Conference on Ion Beam Modification of Materials (IBMM), Member

Panel on Committee of Visitors (COV) for the Materials Sciences and Engineering Division in the DOE Office of Basic Energy Sciences, Member

MRS-Symposium on “Materials for Nuclear Applications and Extreme Environments”, San Francisco 2010, Co-Chair/stellvertretender Vorsitz

Working group of Nuclear Physics European Collaboration Committee (NuPECC) to prepare new long range plan (LRP2010), Member

GANIL prospective core group, Member

Program Advisory Board on FAIR-related irradiation experiments (F-PAC), Member

Internal Scientific Advisory Board of GSI (Wissenschaftlicher Ausschuß), Member

Typel, S.

Nuclear Physics A, Gutachter

European Physical Journal A, Gutachter

Physical Review C, Gutachter

Voss, B.

PANDA Technical Board, Member, Endcap GEM

Publication in Medical Physics, Referee

Wambach, J.

European Physical Journal A, Associate Editor

Physical Review Letters, Associate Editor

Kommittee Hadronen und Kerne, Mitglied

NuPECC, Mitglied

NIC Direktorium, Mitglied

NIC Wissenschaftlicher Rat, Mitglied

EMMI scientific council, Mitglied

HIC4FAIR, Programmbereichsleiter

Welsch, C.P.

DITANET Steering Committee and Supervisory Board, Vorsitzenden/Chair

FLAIR Steering Committee, Mitglied/member

70 Helmholtz research groups in "Structure of matter", Sprecher/spokesperson

Selection Committee for the acceptance of outstanding students to the

Studienstiftung des Deutschen Volkes, Mitglied/member

Advisory Committee of the Joint Universities Accelerator School, Mitglied/member

European Commission in Accelerator Sciences, Wissenschaftlicher Beirat/scientific Advisor

Physics department Safety Committee meetings (Liverpool), Vorsitzender/Chair

Cockcroft Institute Education Committee, Mitglied/member

Cockcroft Institute Management Committee, Mitglied/member

Environment Committee, physics department (Liverpool), Mitglied/member

Will, C.

HFG Arbeitskreis "Frauen in Forschungszentren", Vorsitzende/Chair

Wilms, A.

Journal of Instrumentation (JINST), Gutachten/report

Teaching activities of GSI staff

Compiled by K. Kreidi, C. Kausch, I. Kraus
GSI, Darmstadt, Germany

Ackermann, Dieter (28.6.-4.7.2009): **Superheavy Elements and the Limits of Nuclear Stabilit.** UEE 2009 European Summer University 'The Secret of the Atomic Nucleus', Straßburg, France, Vorlesung

Appelshäuser, H.; M. Bleicher, C. Blume, R. Dörner, C. Greiner, W. Greiner, J. Stroth, J. Maruhn, H. Ströbele, K. Peters, D. Rischke, H. Schmidt-Böcking, S. Schramm, R. Stock, H. Stöcker (SS 2009): **Kolloquium zur Struktur der elementaren Materie und zur Astrophysik.** Uni Frankfurt, Kolloquium

Aumann, Thomas (SS09): **Experimentelle Methoden zur Untersuchung exotischer Kerne.** Johannes-Gutenberg Universität Mainz,

Averbeck, N. (WS2008/2009): **Biophysik von Zellen und Zellverbänden.** TU Darmstadt, Vorlesung/lecture

Averbeck, R (SS09): **Kern- und Teilchenphysik.** Tu Darmstadt, Übungen/Vorlesungsvertretung

Bert, C., Krämer M. et al. (SS 2009): **Grundlagen der Strahlentherapie mit Protonen und schweren Ionen.** U Heidelberg, Vorlesung

Bert, C., Krämer M. et al. (SS 2009): **Kurs und Praktikum Strahlenphysik und Strahlenschutz.** U Heidelberg, Kurs und Praktikum

Bert, C., Krämer M. et al. (WS2008/2009): **Kurs und Praktikum Strahlenphysik und Strahlenschutz.** U Heidelberg, Kurs und Praktikum

Bert, C., Krämer M. et al. (WS2009/2010): **Kurs und Praktikum Strahlenphysik und Strahlenschutz.** U Heidelberg, Kurs und Praktikum

Bert, C., Krämer M. et al. (SS 09 und WS 09/10): **Seminar zur Therapie mit Protonen und Ionenstrahlen.** U Heidelberg, Seminar

Bleicher, M.; C. Blume, D. Rischke, H. Appelshäuser, J. Schaffner-Bielich, J. Stroth, S. Schramm, H. Stöcker, R. Stock, H. Ströbele (WS 2008/2009): **Relativistic Nuclear Matter, gemeinsam mit der GSI und TU in Darmstadt und der Universität Heidelberg.** Uni Frankfurt, Seminar

Bleicher, M.; C. Blume, D. Rischke, H. Appelshäuser, J. Schaffner-Bielich, J. Stroth, S. Schramm, R. Stock, H. Stöcker, H. Ströbele (SS 2009): **Relativistic Nuclear Matter, gemeinsam mit der GSI und TU in Darmstadt und der Universität Heidelberg.** Uni Frankfurt, Seminar

Bleicher, M.; C. Blume, R. Dörner, C. Greiner, W. Greiner, J. Jacoby, J. Maruhn, H. Appelshäuser, K. Klaus Peters, J. Stroth, U. Ratzinger, D. Rischke, S. Schramm, H. Schmidt-Böcking, R. Stock, H. Stöcker, H. Ströbele (SS 2009): **Interuniversitäres Schwerionenseminar gemeinsam mit der GSI in Darmstadt.** Uni Frankfurt, Seminar

Bleicher, M.; C. Blume, R. Dörner, C. Greiner, W. Greiner, J. Jacoby, J. Maruhn, H. Appelshäuser, K. Peters, J. Stroth, U. Ratzinger, D. Rischke, J. Schaffner-Bielich, S. Schramm, H. Schmidt-Böcking, R. Stock, H. Stöcker, H. Ströbele (WS 2008/2009): **Interuniversitäres Schwerionenseminar gemeinsam mit der GSI in Darmstadt.** Uni Frankfurt, Seminar

Bleicher, M.; C. Blume, R. Dörner, C. Greiner, W. Greiner, J. Maruhn, H. Appelshäuser, K. Peters, J. Stroth, D. Rischke, J. Schaffner-Bielich, S. Schramm, H. Schmidt-Böcking, H. Stöcker, H. Ströbele, R. Stock (WS 2008/2009): **Kolloquium zur Struktur der elementaren Materie und zur Astrophysik.** Uni Frankfurt, Kolloquium

Bock, R.; Rosmej, O.; Stöhlker, Th., Hoffmann, D.H.H.;Mulser, P.; Roth, M.; Jacoby, J.; Maruhn, J.A.; Kühl, Th. (WS 2009/2010): **Seminar der GSI, der TU Darmstadt und der Universitäten Frankfurt und Mainz zur Physik dichter Plasmen mit Schwerionen- und Laserstrahlen.** Universität Mainz, TU Darmstadt, Universität Frankfurt, Seminar

Boine-Frankenheim (SS09): **Beschleunigerphysik.** TU Darmstadt, Vorlesung/lecture

Boine-Frankenheim (SS09): **Ausgewählte Themen der Beschleunigerpysik und Technik.** TU Darmstadt, Seminar

Bräuning, H. (SS 2009): **Höhere experimentelle Atomphysik.** Inst. für Atom- und Molekülphysik, Univ. Giessen, Vorlesung/lecture

Bräuning, H. (WS 2009/2010): **Angewandte Atomphysik.** Inst. für Atom- und Molekülphysik, Univ. Giessen, Vorlesung/lecture

Bräuning, H. (WS09/10): **Atomphysik Seminar.** Universität Giessen, Seminar

Braun-Munzinger, P. (SS09): **Structure of Hadrons and Nuclei.** TU Darmstadt, Vorlesung/lecture

Braun-Munzinger, P. (WS09): **From QGP to cold quantum gases.** TU Darmstadt, Seminar

Braun-Munzinger, P.; B. Friman, J. Wambach, H. Oeschler, M. Buballa (WS 2009/2010): **Relativistische Schwerionenphysik.** TU Darmstadt, Seminar

Deiss, B.; H. Stöcker (WS 2008/2009): **Struktur und Dynamik extragalaktischer Systeme (WP).** Uni Frankfurt, Vorlesung

Düllmann, Christoph E. (WS08/09): **Chemie und Kernchemie der schwersten Elemente.** Johannes-Gutenberg Universität Mainz, Vorlesung

Düllmann, Christoph E. (SS09): **Chemie und Kernchemie der schwersten Elemente.** Johannes-Gutenberg Universität Mainz, Vorlesung

Düllmann, Christoph E. (WS09/10): **Chemie und Kernchemie der schwersten Elemente.** Johannes-Gutenberg Universität Mainz, Vorlesung

Düllmann, Christoph E. (Februar 2009): **Einführung zur GSI.** GSI - Für Fortbildungszentrum für Techn. Und Umwelt, Karlsruher Inst. für Technologie, Univ. des Landes Baden-Württemberg, Vorlesung

Düllmann, Christoph E. (Februar 2009): **Einführung in die Thematik der Superschweren Elemente.** GSI - Für Fortbildungszentrum für Techn. Und Umwelt, Karlsruher Inst. für Technologie, Univ. des Landes Baden-Württemberg, Vorlesung

Düllmann, Christoph E. (21.9.2009): **Einführung zur GSI.** Fortbildungszentrum für Techn. Und Umwelt, Karlsruher Inst. für Technologie, Univ. des Landes Baden-Württemberg, Vorlesung

Düllmann, Christoph E. (21.9.2009): **Einführung in die Thematik der Superschweren Elemente.** Fortbildungszentrum für Techn. Und Umwelt, Karlsruher Inst. für Technologie, Univ. des Landes Baden-Württemberg, Vorlesung

Durante, M. (SS 2009): **Radiation Biophysics.** TU Darmstadt, Vorlesung/lecture

Durante, M. (SS 2009): **Radiation Biophysics.** TU Darmstadt, Vorlesung/lecture

Egelhof, Peter (SS09): **Grundlagen und Anwendungen kalorimetrischer Tieftemperaturdetektoren.** Johannes-Gutenberg Universität Mainz, Seminar

Egelhof, Peter (SS09): **Kernphysikalische Aspekte der Astrophysik.** Johannes-Gutenberg Universität Mainz, Vorlesung

Egelhof, Peter (SS09): **Übungen zur Vorlesung: Kernphysikalische Aspekte der Astrophysik.** Johannes-Gutenberg Universität Mainz, Übungen

Feldmeier, F. (SS 2009): **Modern Aspects of Nuclear Structure.** Yukawa Institute of Theoretical Physics, Kyoto, Vorlesung

Feldmeier, H. (WS 2009/2010): **Theoretische Kernphysik.** TU Darmstadt, Vorlesung

Feldmeier, H. (WS 2009/2010): **Theoretische Kernphysik.** TU Darmstadt, Übung

Feldmeier, H.; B. Friman, J. Wambach, K. Langanke, M. Lutz (WS 2009/2010): **Theorie-Seminar zu Kern- und Schwerionenphysik.** TU Darmstadt, Seminar

Feldmeier, H.; B. Friman, J. Wambach, K. Langanke, M. Lutz (WS 2009/2010): **Theorieseminar GSI.** TU Darmstadt, Seminar

Feldmeier, H.; Friman, B.; Wambach, J.; Langanke, K.; Lutz, M. (SS 2009): **Theorieseminar GSI.** TU Darmstadt, Seminar

Feldmeier, H.; Friman, B.; Wambach, J.; Langanke, K.; Lutz, M. (SS 2009): **Theorie-Seminar zu Kern- und Schwerionenphysik.** TU Darmstadt, Seminar

Feldmeier, H.; K. Langanke, R. Roth, J. Wambach (WS 2009/2010): **Forschungspraktika: Theoretische Kern- und Vielteilchenphysik.** TU Darmstadt, Praktikum

Feldmeier, H.; K. Langanke, R. Roth, J. Wambach, G. Martinez-Pinedo (WS 2009/2010): **Forschungspraktika: Nukleare Astrophysik und Kernstrukturtheorie.** TU Darmstadt, Praktikum

Feldmeier, H.; Langanke, K.; Roth, R.; Wambach, J. (SS 2009): **Forschungspraktika: Theoretische Kern- und Vielteilchenphysik.** TU Darmstadt, Praktikum

Feldmeier, H.; Langanke, K.; Roth, R.; Wambach, J.; Martinez-Pinedo,G. (SS 2009): **Forschungspraktika: Nukleare Astrophysik und Kernstrukturtheorie.** TU Darmstadt, Praktikum

Fournier, C. (SS 2009): **Angewandte Strahlenbiologie.** Hochschule Darmstadt, Vorlesung

Friman, B. (WS 2009/2010): **Elementarteilchenphysik.** TU Darmstadt, Vorlesung

Friman, B.; M. Lutz, J. Wambach (WS 2009/2010): **Forschungspraktika: Theoretische Hadronen- und Schwerionenphysik.** TU Darmstadt, Praktikum

Fritzsche, S. (SS 2009): **Quantum Information Theory. An Introduction.** Universität Oulu Fi-90014 Oulu, Finland, Vorlesung/lecture

Fritzsche, S. (13.11.2009): **Coherence transfer in the excitation and decay of atoms.** Kumpula Computational Chemistry and Physics(KCCP), Helsinki University A.I. Virtasen aukio, Kolloquium/colloquium

Geppert, Ch. (19.01.2009): **The BeTINa-Experiment at CERN-ISOLDE.** Universität Münster (Physik), Institut für Kernchemie, Kolloquium/colloquium

Gorska, M. (21.1.-1.2.2009): **Nuclear Structure.** XIV Theoretical Nuclear Physics School, Itaipava, Brasil, Vorlesung

Götzen, K. (Sep. 2009): **Hadron Physics with Antiprotons.** GSI Darmstadt, Vorlesung / lecture

Greiner, C.; M. Bleicher, J. Maruhn, H. Stöcker, D. Rischke, S. Schramm (SS 2009): **Seminar on the Theory of Elementary Matter.** Uni Frankfurt, Seminar

Greiner, C.; D. Rischke, H. Stöcker, S. Schramm (SS 2009): **Chiral Models in Nuclear and Particle Physics.** Uni Frankfurt, Seminar

Greiner, C.; J. Maruhn, M. Bleicher, D. Rischke, H. Stöcker, J. Schaffner-Bielich, S. Schramm (WS 2008/2009): **Seminar on the Theory of Elementary Matter (WP).** Uni Frankfurt, Seminar

Greiner, W.; C. von der Malsburg, M. Meyer-Hermann, R. Berger, I. Mishustin, J.Triesch, W. Singer, H. Stöcker, A. Solv'yov (SS 2009): **Interdisciplinary FIAS Colloquium.** FIAS, Kolloquium

Grisenti, R. (WS 09/10): **Atomphysik II.** Goethe Universität Frankfurt am Main, Vorlesung / lecture.

Herfurth, F. (SS 09): **Laserspektroskopie und Massenspektrometrie an gespeicherten Teilchen.** Universität Mainz (Physik), Vorlesung/lecture

Herfurth, F. (01.07.2009): **Highly Charged Ions at Rest - The HITRAP Project.** MPI-K, Heidelberg (Physik), Kolloquium/colloquium

Hoehne, C. (WS 2008/09): **Übungen und Ergänzungen zur Vl Kernphysik 1.** Inst. f. Kernphysik, Univ. Frankfurt, Übung + Ergänzung / Exercise + supplement

Hoehne, C. (SS 2009): **Übungen zur Einführung in die Kern- und Elementarteilchenphysik.** Inst. f. Kernphysik, Univ. Frankfurt, Übung + Ergänzung / Exercise + supplement

Hoehne, C. (WS 2009/10): **Übungen und Ergänzungen zur Vl Kernphysik 1.** Inst. f. Kernphysik, Univ. Frankfurt, Übung + Ergänzung / Exercise + supplement

Hoffmann, D.; N. Pietralla, R. Roth, J. Wambach (WS 2009/2010): **Schwerionenphysik.** TU Darmstadt, Seminar

Jakob, B. (WS2008/2009): **Biophysik von Zellen und Zellverbänden.** TU Darmstadt, Vorlesung/lecture

Karsch, F. (WS 2009/2010): **Gitterfeldtheorien.** Uni Bielefeld, Vorlesung

Karsch, F. (WS 2009/2010): **Quantum Fields and Strongly Interacting Matter.** Uni Bielefeld, Seminar

Karsch, F. (WS 2009/2010): **Aktuelle Fragen der Elementarteilchenphysik.** Uni Bielefeld, Seminar

Kluge, H.-J. (04.06.2009): **Neue Entwicklungen und Anwendungen hochgenauer Massenspektrometrie.** Universität Greifswald, Kolloquium/colloquium

Kraft-Weyrather, W. (WS2009/2010): **Master Course Medical Physics "Special RadiotherapyTechniques".** Uniklinik Mannheim, Master Course

Kraemer, M. (SS 2009): **Praktikum und Vorlesung Linearbeschleuniger.** Uni Heidelberg, Vorlesung/Praktikum

Kraemer, M. (SS 2009): **Seminar zur Therapie mit Protonen und Ionenstrahlen.** Uni Heidelberg, Seminar

Kraemer, M. (WS 2009/2010): **Praktikum und Vorlesung Linearbeschleuniger.** Uni Heidelberg, Vorlesung/Praktikum

Kraemer, M. (WS 2009/2010): **Seminar zur Therapie mit Protonen und Ionenstrahlen.** Uni Heidelberg, Seminar

Kühl, Th. (SS 2009): **Seminar zum F-Praktikum.** Johannes Gutenberg Universität Mainz (Physik), Seminar

Kühl, Th., Nörtershäuser, W. (WS 2008/2009): **Physik des Lasers.** Johannes Gutenberg Universität Mainz (Physik), Vorlesung/lecture

Langanke, K.; Wambach, J. (SS 2009): **Nukleare Astrophysik II.** TU Darmstadt, Vorlesung

Leifels, Y. (WS09/10): **PEP 5 (Kern-, Teilchen- und Festkörperphysik).** Universität Heidelberg, Übungen

Liesen, D. (SS 2009): **Oberseminar über Atomphysik.** Universität Heidelberg, Vorlesung/lecture

Liesen, D. (WS 2009/2010): **Oberseminar über Atomphysik.** Universität Heidelberg, Vorlesung/lecture

Litvinov, Yuri (SS09): **Laserspektroskopie, Fallen und ihre Anwendungen.** Universität Heidelberg, Germany, Vorlesung

Litvinov, Yuri (03.08-25.09): **Nuclear Astrophysics at the ESR.** International Summer Student Program, GSI, Darmstadt, Germany, Vorlesung

Litvinov, Yuri (23.08-27.08): **Mass measurements.** 5th International Summer School on Subatomic Physics "Some New facet of Nuclear Physics", Peking University, Beijing, China, Vorlesung

Litvinov, Yuri (WS09): **Physics with Stored and Cooled Particles.** Universität Heidelberg, Germany, Vorlesung

Lutz, M. (SS 2009): **Einführung in Quantenfeldtheorien.** TU Darmstadt, Vorlesung

Lutz, M. (SS 2009): **Einführung in Quantenfeldtheorien.** TU Darmstadt, Übung

Malzacher, P. (WS 2008/2009): **Introduction to C/C++.** Universität Franfurt, Vorlesung+Übung

Malzacher, P. (WS 2008/2009): **Software Design and Construction.** Universität Franfurt, Vorlesung+Übung

Malzacher, P. (WS 2009/2010): **Introduction to C/C++.** Universität Franfurt, Vorlesung+Übung

Malzacher, P. (WS 2009/2010): **Software Design and Construction.** Universität Franfurt, Vorlesung+Übung

Märtin, R. (Juni 2009): **Übungen zur experimentelle Physik IV (Atom- und Molekülphysik).** Universität Heidelberg, Tutorium

Martinez-Pinedo, G. (WS 2009/2010): **Einführung in theoretische Astrophysik.** TU Darmstadt, Vorlesung

Neumann, R. (SS09): **Materialforschung und Nanotechnologie mit energiereicher Strahlung I.** Universität Heidelberg, Vorlesung/lecture

Nörtershäuser, W. (07.05.2009): **Atomkern mit Heiligenschein - Laserspektroskopische Bestimmung des Kernladungsradius von Be-11.** Universität Gießen, Seminar/seminar

Nörtershäuser, W. (10.06.2009): **The nuclear charge radius of Be-11 and recent achievements in high-resolution laser spectroscopy at GSI.** MPIK Heidelberg (Physik), Bothe Kolloquium

Nörtershäuser, W. (24.07.2009): **Precision laser spectroscopy of light exotic isotopes.** Physikalisches Institut Universität Tübingen (Physik), Seminar/seminar

Nörtershäuser, W., Herfurth, F. (SS 2009): **Laserspektroskopie und Massenspektrometrie an gespeicherten Teilchen.** Johannes Gutenberg Universität Mainz (Physik), Vorlesung/lecture

Peters, K. (WS08/09): **Interuniversitäres Schwerionenseminar gemeinsam mit der GSI Darmstadt.** Johann Wolfgang Goethe Universität Frankfurt, Seminar / seminar

Peters, K. (WS08/09): **Kolloquium zur Struktur der elementaren Materie und zur Astrophysik.** Johann Wolfgang Goethe Universität Frankfurt, Seminar / seminar

Peters, K. (WS08/09): **Resonanzphysik der Hadronen.** Johann Wolfgang Goethe Universität Frankfurt, Vorlesung / lecture

Peters, K. (SS09): **Interuniversitäres Schwerionenseminar gemeinsam mit der GSI Darmstadt.** Johann Wolfgang Goethe Universität Frankfurt, Seminar / seminar

Peters, K. (SS09): **Kolloquium zur Struktur der elementaren Materie und zur Astrophysik.** Johann Wolfgang Goethe Universität Frankfurt, Seminar / seminar

Peters, K. (SS09): **Physik der Teilchendetektoren.** Johann Wolfgang Goethe Universität Frankfurt, Vorlesung / lecture

Peters, K. (WS09/10): **Interuniversitäres Schwerionenseminar gemeinsam mit der GSI Darmstadt.** Johann Wolfgang Goethe Universität Frankfurt, Seminar / seminar

Peters, K. (WS09/10): **Kolloquium zur Struktur der elementaren Materie und zur Astrophysik.** Johann Wolfgang Goethe Universität Frankfurt, Seminar / seminar

Peters, K. (WS09/10): **Resonanzphysik der Hadronen.** Johann Wolfgang Goethe Universität Frankfurt, Vorlesung / lecture

Peters, K. (Aug. 2009): **Hadron Physics with Antiprotons.** GSI Darmstadt, Vorlesung / lecture

Quint, W. (WS 2008/2009): **Quantenelektrodynamik.** Universität Heidelberg (Physik), Vorlesung/lecture

Quint, W. (SS 2009): **Advanced Seminar on AMO Physics.** KIP, Universität Heidelberg, Vorlesung/lecture

Reifarth, Renee (SS09): **Einführung in die Astronomie II.** Goethe Universität Frankfurt, Vorlesung

Reifarth, Renee (WS09/10): **Einführung in die Astronomie I.** Goethe Universität Frankfurt, Vorlesung

Reifarth, Renee (SS09): **Astrophysikalisches Praktikum.** Goethe Universität Frankfurt, Praktikum

Rischke, D.; C. Greiner, J. Schaffner-Bielich, H. Stöcker, S. Schramm (WS 2008/2009): **Chiral Models in Nuclear and Particle Physics (WP).** Uni Frankfurt, Seminar

Rischke, D.; M. Bleicher, H. Stöcker, C. Greiner (SS 2009): **Fluid dynamics for heavy ion collisions.** Uni Frankfurt, Seminar

Rischke, D.; M. Bleicher, H. Stöcker, C. Greiner (WS 2008/2009): **Fluid dynamics for heavy ion collisions (WP).** Uni Frankfurt, Seminar

Rosmej, O. (WS 2009/2010): **Röntgenstrahlung im Universum und Labor.** IAP, Goethe-Universität Frankfurt am Main, Vorlesung/lecture

Roth, R.; Feldmeier, H.; Langanke, K.; Martinez-Pinedo, G.; Neff, T. (SS 2009): **Kernstruktur und nukleare Astrophysik.** TU Darmstadt, Seminar

Schädel, Matthias (39983): **Chemitry and Physics of Superheavy Elements - Fascination and Challanges**

of Science Beyond the Actinides. Summer Scholl on Actinide Science & Applications, ITU Karlsruhe, Vorlesung

Scheidenberger, Christoph (WS08/09): **Experimentelle nukleare Astrophysik.** Justus-Liebig Universität Gießen, Germany, Vorlesung + Übungen

Scheidenberger, Christoph (WS08/09): **Physikalische Ziele des internationalen FAIR Projektes.** Justus-Liebig Universität Gießen, Germany, Seminar

Scheidenberger, Christoph (WS08/09): **Anleitung zu wissenschaftlichen Arbeiten.** Justus-Liebig Universität Gießen, Germany, Seminar

Scheidenberger, Christoph (WS08/09): **Mitarbeiterseminar.** Justus-Liebig Universität Gießen, Germany, Seminar

Scheidenberger, Christoph (SS09): **Physik mit schweren Ionen.** Justus-Liebig Universität Gießen, Germany, Vorlesung

Scheidenberger, Christoph (SS09): **Experimentelle Kern- und Elementarteilchenphysik.** Justus-Liebig Universität Gießen, Germany, Seminar

Scheidenberger, Christoph (SS09): **Anleitung zu wissenschaftlichen Arbeiten.** Justus-Liebig Universität Gießen, Germany, Seminar

Scheidenberger, Christoph (SS09): **Mitarbeiterseminar.** Justus-Liebig Universität Gießen, Germany, Seminar

Schwarz, C. (WS08/09): **Fortgeschrittenenpraktikum der Kernphysik.** Johann Wolfgang Goethe Universität Frankfurt, Praktikum/practical course

Schwarz, C. (SS09): **Fortgeschrittenenpraktikum der Kernphysik.** Johann Wolfgang Goethe Universität Frankfurt, Praktikum/practical course

Schwarz, C. (WS09/10): **Fortgeschrittenenpraktikum der Kernphysik.** Johann Wolfgang Goethe Universität Frankfurt, Praktikum/practical course

Stöcker, H. (SS 2009): **Einführung in die Physik 2 für Studierende der Biologie und des Lehramts L3 Physik, E-Learning Begleitveranstaltung zur Vorlesung.** Uni Frankfurt, E-Learning

Stöcker, H. (WS 2008/2009): **E-Learning Begleitveranstaltung zur Vorlesung "Einführung in die Physik I für Studierende des Lehramts L3-Physik, der Chemie und anderer Naturwissenschaften".** Uni Frankfurt, E-Learning

Stöcker, H. (WS 2008/2009): **E-Learning Begleitveranstaltung zur Vorlesung "Physik für Mediziner".** Goethe Universität Frankfurt, E-Learning

Stöcker, H. (WS 2008/2009): **E-Learning Begleitveranstaltung zur Vorlesung "Einführung in die Physik I für Studierende der Biologie und des Lehramts L3 Physik".** Uni Frankfurt, E-Learning

Stöcker, H. (SS 2009): **Einführung in die Physik 2 für Studierende des Lehramts L3-Physik, der Chemie und anderer Naturwissenschaften,E-Learning Begleitveranstaltung zur Vorlesung.** Uni Frankfurt, E-Learning

Stöcker, H. (SS 2009): **Experimentalphysik 2, E-Learning Begleitveranstaltung zur Vorlesung.** Uni Frankfurt, E-Learning

Stöcker, H. (SS 2009): **Einführung in die Physik für Studierende der Pharmazie, E-Learning Begleitveranstaltung zur Vorlesung.** Uni Frankfurt, E-Learning

Stöcker, H. (WS 2008/2009): **E-Learning Begleitveranstaltung zur Vorlesung "Einführung in die Physik für Studierende der Pharmazie".** Uni Frankfurt, E-Learning

Stöcker, H. (WS 2008/2009): **E-Learning Begleitveranstaltung zur Vorlesung "Experimentalphysik 1".** Uni Frankfurt, E-Learning

Stöcker, H.; R. Berger, A. Solv'yov, W. Greiner, C. von der Malsburg, W. Singer, M. Meyer-Hermann, I. Mishustin, J. Jochen Triesch (SS 2009): **FIGSS Seminar.** FIAS, Seminar

Stöcker, H.; R. Berger, A. Solv'yov, W. Greiner, C. von der Malsburg, W. Singer, M. Meyer-Hermann, I. Mishustin, J. Triesch (WS 2008/2009): **FIGSS Seminar.** Uni Frankfurt, Seminar

Stöhlker, Th. (19.02.2009): **Relativistic Atomic Physics with FAIR.** Int. Graduate School, Universität Basel (Physik), Seminar/seminar

Stöhlker, Th. (): **.** ,

Stöhlker, Th. (17.12.2009): **FAIR Atomic Physics.** Strahlenzentrum der Universität Giessen (Atomphysik), Seminar

Stöhlker, Th. (SS 2009): **Oberseminar über Atomphysik.** Universität Heidelberg, Vorlesung/lecture

Stöhlker, Th. (WS 2009/2010): **Oberseminar über Atomphysik.** Universität Heidelberg, Vorlesung/lecture

Stöhlker, Th. (19.01.2009): **Atomic Physics at GSI and FAIR.** Atomic Theory for Fundamental Interactions and Simple Systems in Strong Fields, Seminar

Stöhlker, Th., Surzhykov, A. (SS 2009): **Experiments in modern atomic physics and their theoretical foundations.** Ruprecht Karls Universität Heidelberg (Physik), Vorlesung/lecture.

Stroth, Joachim (SS09): **Enführung in die Struktur der Materie 4, Teilchen und Kerne.** Goethe-Universität, Vorlesung/lecture

Stroth, Joachim (WS09/10): **Subatomare Physik 1: Kernphysik.** Goethe-Universität, Vorlesung/lecture

Surzhykov, A. (WS 2008/2009): **Advances in theoretical atomic physics.** Ruprecht Karls Universität Heidelberg (Physik), Vorlesung/lecture.

Toimil-Molares, M.E. (WS 2009/2010): **Nanostructures: Synthesis, properties and applications.** Universität Heidelberg (Physik), Vorlesung/lecture.

Trautmann, C. (WS 2009): **Materialmodifizierung und Nanotechnologie mit energiereichen Schwerionen.** Fachhochschule Wiesbaden, Vorlesung/lecture

Trautmann, W. (WS08/09): **Kernphysik für Studierende des Lehramtes an Haupt- und Realschulen.** Johann Wolfgang Goethe Universität Frankfurt, Vorlesung / lecture

Trautmann, W. (SS09): **Moderne Physik.** Johann Wolfgang Goethe Universität Frankfurt, Vorlesung / lecture

Trautmann, W. (WS09/10): **Kernphysik für Studierende des Lehramtes an Haupt- und Realschulen.** Johann Wolfgang Goethe Universität Frankfurt, Vorlesung / lecture

Wambach, J. (WS 2009/2010): **Allgemeine Relativitätstheorie.** TU Darmstadt, Vorlesung

Wambach, J. (WS 2009/2010): **Allgemeine Relativitätstheorie.** TU Darmstadt, Übung

Wambach, J. (WS 2009/2010): **Mitarbeiterseminar.** TU Darmstadt, Seminar

Wambch, J.; Friman, B.; Buballa, M.; Lutz, M. (SS 2009): **Forschungspraktika: Theoretische Hadronen- und Schwerionenphysik.** TU Darmstadt, Praktikum

Welsch, C.P. (SS 2009): **PHYS246 - Accelerators and Radioisotopes in Medicine.** Universität Liverpool (Physik), Vorlesung/lecture

Welsch, C.P. (SS 2009): **PHYS370 - Advanced Electromagnetism.** Universität Liverpool (Physik), Tutorium/tutorial

Welsch, C.P. (SS 2009): **Introduction to the Physics and Technology of Particle Accelerators.** Universität Heidelberg (Physik), Vorlesung (Blockseminar)/lecture (compact course)

Welsch, C.P. (WS 2009/2010): **Introduction to the Physics and Technology of Particle Accelerators.** Universität Heidelberg (Physik), Vorlesung (Blockseminar)/lecture (compact course)

Welsch, C.P. (WS 2009/2010): **Journal Club "Applied Physics" with a focus on Accelerator Sciences.** Universität Heidelberg (Physik), Seminar/seminar

Welsch, C.P. (WS 2009/2010): **PHYS481 - Accelerator Physics.** Universität Liverpool (Physik), Vorlesung + Übung/lecture + Excercise

Welsch, C.P. (WS 2009/2010): **PHYS259 - Second Year Practical Laboratories.** Universität Liverpool (Physik), Proaktikum/practical course

Welsch, C.P. (WS 2009/2010): **Journal Club "Applied Physics" with a focus on Accelerator Sciences.** Universität Heidelberg (Physik), Seminar/seminar

Welsch, C.P. (30.3. - 3.4.2009): **DITANET School on Beam Diagnostics.** Universität London (Physik), Seminar/seminar

Welsch, C.P. (6.-10.7.2009): **DPG School on Accelerator and High Energy Physics.** Bad Honnef (Physik), Seminar/seminar

Winters, D. (SS 2009): **Moleküle: Wasserstoff-Molekül Ion H2+ und Wasserstoff-Molekül H2, Physik IV - Atomphysik (Prof. Dubbers).** Kirchhoff-Institut für Physik, Universität Heidelberg (Physik), Vorlesung/lecture

Winters, D. (SS 2009): **Das Weizsäcker Tröpfchen Modell (Teil I), Instabile Kerne --> Zerfall (Teil II), Physik IV - Atomphysik (Prof. Dubbers).** Kirchhoff-Institut für Physik (KIP), Universität Heidelberg (Physik), Vorlesung/lecture

Winters, D. (WS 2009/2010): **Helium atom, HFS and g-factor, Advanced Atomic, Molecular and Optical Physics.** Universität Heidelberg (Physik), Vorlesung/lecture

Winters, D. (WS 2009/2010): **He atom, HCI, storage rings, EBIT, Advanced Atomic, Molecular and Optical Physics.** Universität Heidelberg (Physik), Vorlesung/lecture

Winters, D. (WS 2009/2010): **Problem class: : experimental atomic physics, Advanced Atomic, Molecular and Optical Physics.** Universität Heidelberg (Physik), Vorlesung/lecture

Winters, D. (WS 2009/2010): **Penning and Paul Traps, Mass spectrometry, Advanced Atomic, Molecular and Optical Physics.** Universität Heidelberg (Physik), Vorlesung/lecture

PhD, Master, Bachelor, Habilitation and Diploma theses in 2009

Compiled by Große, BuD

Aksyutina, Yuliya: **[GSI Diss 2009-13] Light Unbound Nuclear Systems beyond the Dripline [14.08.2009].** Dissertation: Univ. Frankfurt/M. HANU.

Ali, M.: **Nanopores with modified surfaces for sensor application.** Dissertation: TU Darmstadt. PNI.

Bailhache, Raphaelle: **Calibration of the ALICE Transition Radiation Detector and a Study of Z0 and Heavy Quark Production in pp Collisions at the LHC.** Dissertation: Darmstadt. HANU.

Bousonville, Michael: **[GSI Diss 2009-08] Optische Übertragung phasensynchroner Taktsignale unter Verwendung des Wellenlängen-Multiplex-Verfahrens [27.04.2009].** Dissertation: TU Darmstadt. HANU:ACC.

Buschbacher, Alwin: **[GSI Dipl 2009-11] Nichtlineare Optimierung der Teilchenfluenz für die biologisch effektive Dosis in der Schwerionentherapie: Effiziente numerische Lösung auftretender Gleichungssysteme [22.09.2009].** Diplom: Hochschule Darmstadt. HANU.

Bussmann, Michael: **[GSI Diss 2009-05] Laser-Cooled Ion Beams and strongly coupled plasmas for precision experiments [17.03.2008].** Dissertation: Univ. München. PNI.

Cayzak, W.: **Entwicklung eines CVD-Diamantspektrometers zur Messung der Ladungs-zustände von Schwerionen in lasererzeugten Plasmen.** Master: TU Darmstadt. PNI.

Doron, B.: **FluxInstablities in Partially Irradiated Bi2SR2CaCu2O8+d.** Dissertation: Bar-Ilan University. PNI.

Droese, Christian: **[GSI Dipl 2009-09] Minimierung des systematischen Fehlers und Hochpräzisionsmassenmessung an neutronenarmen Rn- und Ra-Isotopen mit SHIPTRAP [21.11.2009].** Dissertation: Univ. Greifswald. HANU.

Dworschak, Michael Gerhard: **[GSI Diss 2009-15] First direct mass measurements on nobelium and lawrencium with the Penning trap mass spectrometer SHIPTRAP [08.12.2009].** Dissertation: . PNI.

Ecker, Boris: **[GSI Dipl 2009-08] Aufbau eines kompakten Röntgenlasers [31.05.2009].** Diplom: Univ. Mainz. PNI.

Egberts, J.: **Investigations in transverse beam profile measurements with high dynamic range.** Diplom: Universität Heidelberg. PNI.

Eibach, Martin: **[GSI Dipl 2009-06] Characterization of a carbon aerosol generator in a helium gas-jet for the extraction of fission products from the research reactor TRIGA Mainz.** Diplom: Univ. Mainz. PNI.

Engel, M.: **Ion track templates for two-component polymer systems.** Dissertation: TU Darmstadt. PNI.

Galatyuk, Tatyana: **[GSI Diss 2009-12] Di-electron spectroscopy in HADES and CBM: from p + p and n + p collisions at GSI to Au + Au collisions at FAIR [17.07.2009].** Dissertation: Univ. Frankfurt/M. HANU.

Gemmel, Alexander: **[GSI Diss 2009-09] Berechnung der RBW-gewichteten Dosis und biologische Dosimetrie für bewegte Zielvolumina in der Tumortherapie mit gescannten Kohlenstoffionen [20.05.2009].** Dissertation: TU Darmstadt. Cancer.

Guntoro, Andre: **Algorithm, Application Mapping, Design and Realization of the Time-Frequency Representation ith Flexible Kernels based on their Lifting Scheme.** Dissertation: Darmstadt. HANU:ACC.

Hochhaus, Daniel: **[GSI Dipl 2009-05] Erzeugung hoher Harmonischer zum Seeden eines Röntgenlasers [31.05.2009].** Diplom: Univ. Mainz. PNI.

How, W.: **On the state of Knowledge in High Energy and Accelerator Physics at High School Level.** Bachelor: Universität Liverpoo. PNI.

Huzel, D.: **Fabrication of Au Nanowires based on Ion Track-Etched Polymer and Mica Templates.** Diplom: Universität Heidelberg. PNI.

Ilieva, Stoyanka: **[GSI Diss 2009-02] Investigation of the nuclear matter density distributions of the exotic ^{12}Be, ^{14}Be and ^{8}B nuclei by elastic proton scattering in inverse kinematics [26.01.2009].** Dissertation: Univ. Mainz. PNI.

Jordan, F.: **Herstellung und mikroskopische Untersuchungen von strukturierten Gold-Nanodrähten für Feldemissionskathoden.** Bachelor: Bergische Universität Wuppertal. PNI.

Khuyagbaatar, Jadambaa: **Nuclear Structure Investigation of the Neutron deficient isotopes of Th, Cm, Cf and Fm.** Dissertation: St. Petersburg. HANU.

Knobloch-Maas, R.: **Messungen des Energieverlusts von Ionenstrahlen in lasererzeugten Plasmen.** Dissertation: TU Darmstadt. PNI.

Koszudowski, Stephan: **[GSI Diss 2009-07] Developments for the HITRAP Cooler Trap and mass measurements around A=96 at SHIPTRAP [08.07.2009].** Dissertation: Univ. Heidelberg. PNI.

Kraus, D.: **XUV Spektroskopie an lasererzeugten Hohlraumplasmen.** Master: TU Darmstadt. PNI.

Kreim, Susanne Waltraud: **[GSI Diss 2010-02] Direct Observation of a Single Proton in a Penning Trap [25.08.2009].** PNI: Univ. Mainz. HANU.

Krieger, Andreas: **[GSI Dipl 2009-02] Aufbau eines jodstabilisierten Farbstofflasers zur kollinearen Spektroskopie und sein Einsatz zur Hochspannungsmessung an ISOLDE [13.11.2008].** Diplom: Univ. Mainz. PNI.

Kühnel, M.: **Entwicklung einer kryogenen Cluster- und Tröpfchenquelle als internes Target am Experimentierspeicherring ESR.** Diplom: Goethe-Universität Frankfurt. PNI.

Kuttich, B.: **Herstellung und Charakterisierung zylindrischer Nanoporen in Polyimid.** Bachelor: TU Darmstadt. PNI.

Lago, Samuel: **[GSI Dipl 2009-01] Untersuchung von elektrischen Feldverteilungen und Ladungsträgersammlung in ortsempfindlichen Germanium Detektoren [27.1.2009].** Diplom: Hochschule Darmstadt. HANU.

Le Bleis, Tudi: **Experimental Study of Collective Electric Dipole Mode in Neutron-Rich Nickel Nuclei.** Dissertation: Strasbourg (France). HANU.

Lovrincic, R.: **Über die Bestimmung der dynamischen Leitfähigkeit dünner Metallfilme auf der (100)-Diamantoberfläche mittels Infrarot-Spektroskopie.** Dissertation: Kirchhoff Institut Universität Heidelberg. PNI.

Märtin, Renate: **[GSI Dipl 2009-03] Entwicklung eines Kristallspektrometers zur Untersuchung von Innerschalenübergängen in hochgeladenen Ionen [24.03.2009].** Diplom: Univ. Frankfurt/M. PNI.

Merk, B.: **Integrierung eines LED-Belichtungssystems und weitere Verbesserungen der Lebendzellbeobachtung am Fluoreszenzmikroskop der Schwerionen-Mikrosonde der GSI.** Diplom: Universität Heidelberg. PNI.

Neubeck, Cläre von: **[GSI Diss 2009-14] Radiobiological experiments for carbon ion prostate cancer therapy: interplay of normal and tumor cells in co-culture and measurement of the oxygen enhancement ratio [28.09.2009].** Dissertation: TU Darmstadt. Cancer.

Omet, Mathieu: **[GSI Bachelor 2009-01] Entwicklung, Aufbau und Test eines Hochfrequenz-Amplitudendetektors für den Recycled Experimental Storage Ring RESR bei der Facility for Antiproton and Ion Research FAIR [5.1.2009].** Bachelor: TU Damrstadt. HANU.

Repp, Julia: **[GSI Dipl 2009-07] Setup of a non-destructive ion detection system and magnetic field investigations for precision mass measurements at TRIGA-TRAP [30.04.2009].** Diplom: Univ. Mainz. PNI.

Reuschl, Regina: **[GSI Diss. 2009-04] Untersuchungen zur Lamb-Verschiebung in schweren Ein- und Zwei-Elektronen-Systemen [29.01.2009].** Dissertation: Univ. Frankfurt/M. PNI.

Schnohr, C.: **Ion-induced radiation damage in semiconductors.** Dissertation: Universität Canberra. PNI.

Schömers, C.: **Untersuchungen zur Magnetfeld-Regelung an normalleitenden Synchrotronen.** Diplom: Universität Heidelberg. PNI.

Sommer, Anna Bettina: **[GSI Dipl 2009-10] Design, Aufbau und Test eines Niederenergie-Strahltransportes für das SPECTRSP-Experiment [03.12.2009].** Diplom: Univ. Gießen. HANU.

Spillmann, Uwe: **[GSI Diss 2009-03] Charakterisierung und erster experimenteller Einsatz von ortsauflösenden, energiedispersiven Germanium-Detektoren zur Präzisionsspektroskopie an schweren Ionen [16.02.2009].** Dissertation: Univ. Frankfurt/M. PNI.

Stork, H.: **Ortsaufgelöste NMR an schwerionenbestrahlten Kristallen.** Dissertation: TU Darmstadt. PNI.

Tiedemann, Dirk: **[GSI Diss 2009-10] Nuclear charge radius determination of ^{7,10}Be and the one-neutron halo nucleus ^{11}Be [05.06.2009].** Dissertation: Univ. Mainz. PNI.

Trotsenko, Sergiy: **[GSI Diss 2009-11] Experimental Studies of Exotic Transitions in High-Z Few-Electron Ions [24.06.2009].** Dissertation: Univ. Frankfurt/M. PNI.

Wiechula, Jens: **[GSI Diss 2010-01] Commissioning and Calibration of the ALICE-TPC [21.04.2009].** Dissertation: Univ. Frankfurt/M. HANU.

Winckler, Nicolas: **Nuclear orbital electron capture of stored highly-ionized ^{140}Pr and ^{142}Pm ions.** Dissertation: Giessen. HANU.

Wladimir Engelhardt: **Anwendung von DMU an großen Baugruppen in CATIA V5.** Bachelor: TU Darmstadt. HANU.

Beamtime balance of the year 2009						
Expnr.	**Spokesperson**	**Affiliation**	**Short title**	**Area**	**Ion**	**Shifts main (parasitic)**
B, S000, U000	Barth, Spiller, Scheeler	GSI	Commissioning, machine experiments	UNILAC, SIS	1H, 12C, 181Ta, 40Ar, 129Xe, 197Au, 238U	**169(51)**
E000	Grisenti	Univ. Frankfurt	New ESR gas-target	ESR	238U	**15**
E028	Egelhof	GSI	Detector test	Z7	48Ca	**0(4)**
E048, E055	Walker, Litvinov	Univ. Surrey, GSI	Schottky mass spectroscopy	ESR	197Au	**22**
E062	Heil	GSI	p - induced reaction rates	ESR	96Ru	**39**
E067	Karpuk	Univ. Mainz	Test of time dilatation	ESR	7Li	**11**
E074	Warczak	Univ. Krakau	Double electron capture	ESR	40Ar	**7**
E075	Herfurth	GSI	Commssioning HITRAP	HITRAP	58Ni, 136Xe	**38**
E093	Thorn	GSI	Polarisation of Lyman radiation	ESR	238U	**16**
E096	Brandau	TU München	Dielectronic recombination	ESR	238U	**22**
FORS	Forster	Ingenieurbüro Ingolstadt	Radiation protection	HTB	12C	**2**
FRS00	Nociforo	GSI	Detector tests	FRS	56Fe, 96Ru, 238U	**0(26)**
S272	Tanihata	RCNP Osaka	Matter density distribution	FRS	40Ar	**0(18)**
S304	Ducret	CEA Saclay	Exclusive spallation measurements	HTC, HTD	136Xe, 197Au	**18**
S306	Datta Pramanik	SI Kolkata	1/2 orbitals in neutron-rich nuclei	HTC	40Ar	**22**
S319	Saito	GSI	Hypernuclear spectroscopy	HTC	6Li	**34**
S320	Bieniosek	LBNL Berkeley	WDM	HHT	238U	**0(3)**
S321	Ulrich	TU München	HI -pumped excimer lasers	HHT	238U	**0(6)**
S331	Mintsev	ICPC Chernogolovka	High-energy-density matter	HHT	238U	**0(17)**

S337	Gadea	LNL Legnaro	Structure of 132In	FRS	238U	**9**
S338	Herrmann	Univ. Heidelberg	Strangeness in heavy-ion collisions	HTB	58Ni, 96Ru	**106**
S349	Fabbietti	TU München	Kaonic nuclear cluster	HTB	1H	**52(12)**
S350	Benzoni	INFN Milano	Moving along Z=82	FRS	238U	**15**
S351	Yamazaki	RIKEN	Coherent resonant excitation	HTA	238U	**12**
S356	Franchetti	GSI	High-current-beam physics	HHD	40Ar	**11**
S357	Ducret	CEA Saclay	Detector test	HTC	197Au	**2**
S358	Khanzadeev	PNPI St.Petersburg	Nuclear spatial structure	FRS	1H	**0(2)**
S361	Bruce	Univ. Brighton	Shape evolution	FRS	238U	**9**
S366	Heuser	GSI	Detector tests for CBM	HTD	1H	**0(12)**
S367	Tauschwitz	GSI	Opacity measurements	HHT	197Au, 238U	**0(13)**
S386	Schwarz	GSI	DIRCs for the PANDA - detector	HTD	1H	**0(12)**
S392	Kurcewicz	GSI	New isotopes from Hf to Np	FRS	238U	**17**
S394	Lemmon	CCLRC Daresbury	Constraining the symmetry energy	HTD	238U	**0(9)**
SBIO	Schardt	GSI	Biology expewriments at SIS	HTA, HTM	12C, 56Fe	**16**
SESA	Schardt	GSI	Irradiation exp.for ESA at SIS	HTA, HTM	12C, 56Fe	**10**
SMAT	Schuster, Trautmann	GSI	Materials research at SIS	HTA	238U	**8(12)**
STHE	Enghardt, Schardt	TU Dresden, GSI	Experiments on therapy	HTA, HTM	1H, 7Li, 12C	**6(16)**
U165	Werner	Univ. Bielefeld	Multifragmentation of molecules	UX4	238U	**4**
U182	Kratz	Univ. Mainz	Chemical properties of elements 106 and 108	UX8	40Ar	**13**
U211	Heinz	GSI	Even - even nucleus 260Sg	UY7	58Ni	**0(11)**
U218	Doornenbal	GSI	Coulomb excitation	UX7	48Ca	**3**

U225	Heßberger	GSI	Nuclear structure investigations	UY7	48Ca, 54Cr	**35(37)**
U226	Roth	TU Darmstadt	Energy loss and charge distribution	UZ6	34S, 40Ar, 48Ca	**0(37)**
U232	Nishio	JAEA Tokai	Production of 268Hs	UY7	34S	**57**
U236	Jungclaus	Univ. Madrid	Magnetic moments and lifetimes	UX7	122Sn, 124Sn	**26**
U238	Block	GSI	Mass measurements at SHIPTRAP	UY7	48Ca	**22(31)**
U239	Düllmann	GSI	Towards element 117	UX8	48Ca, 58Ni	**112(5)**
U243	Yakushev	TU München	Chemical characterisation of element 114	UX8	48Ca	**106**
U249	Berdermann	GSI	Test of diamond detectors	HTA	6Li	**0(12)**
U251	Heinz	GSI	Carbon custer evaporation	UY7	48Ca	**0(30)**
UBIO	Scholz	GSI	Biology experiments at UNILAC	UX6	12C, 56Fe, 58Ni, 96Ru, 136Xe, 238U	**21(45)**
UESA	Scholz	GSI	Irradiation exp.for ESA at UNILAC	UX6	12C, 56Fe	**2**
UMAT	Severin, Trautmann, Voss	GSI	Materials research at UNILAC	UX0, UM - branch	12C, 54Cr, 129Xe,197Au, 238U	**100(70)**

18.12.2009, D.Liesen

The Helmholtz Institutes in Mainz and Jena

Frank Maas[1,2,4] and Thomas Stöhlker[1,3,5]

[1]GSI, Darmstadt, Germany; [2]Johannes Gutenberg University, Mainz, Germany; [3]Ruprecht Karls University, Heidelberg, Germany; [4]Helmholtz-Institut Mainz, 55099 Mainz, Germany; [5]Helmholtz-Institut Jena, 07743 Jena, Germany

The Helmholtz Institutes

The direct and close scientific collaboration of a Helmholtz center and an university is at the base of the concept for the new Helmholtz Institutes. The idea of creating a branch of the Helmholtz center on the university campus fosters this collaboration by its proximity and sustainability. The University and the Helmholtz center join forces based on a cooperation agreement.

End of 2008 the german parliament has provided extra funds for the foundation of three Helmholtz Institutes, to be created in the federal states of Rhineland-Palatinate, Thuringia and the Saarland. In December 2008 there has been a call for ideas on the creation of Helmholtz Institutes which has been followed in January 2009 by letters of interest. Deadline for proposals was end of March 2009, followed by a review with an international committee end of April 2009. The first two Helmholtz Institutes in Mainz, Rhineland-Palatinate, and Jena, Thuringia, have been founded in June, 2009. The Helmholtz Institute in Saarbrücken, Saarland has followed soon after.

On June 5, the senate of the Helmholtz association has recommended the foundation of the Helmholtz Institute Mainz and the Helmholtz Institute Jena, followed soon after by the signature of a memorandum of understanding for the foundation of both Helmholtz institutes. The Helmholtz Institute Mainz (HIM) and the Helmholtz Institute Jena (HIJ) have started their operation on July 1, 2009.

The Helmholtz Institute Mainz

The institute is based on the internationally recognized role of researchers in the field of nuclear and particle physics from Johannes Gutenberg University Mainz and GSI and on the unique research infrastructure and opportunities being offered by GSI in Darmstadt and its upcoming international FAIR facility. The research direction of HIM makes visible contributions to the present research program of GSI and the FAIR program. The existence of a powerful technical and scientific infrastructure on the Mainz campus is essential for the new institute which builds on these assets concentrating on new projects and experiments at GSI/FAIR. The institute with its chief scientists, junior scientists and scientific staff integrates into the academic system of the University and its Faculties of Physics and Chemistry. Building on its scientific strongholds and close relations to GSI/FAIR in the fields of hadron structure, antiprotonic systems and super-heavy element synthesis, the new institute is a major contributor to the profile and the success of the unique international FAIR enterprise and at the same time shapes and sharpens the profile of excellence of Johannes Gutenberg University Mainz.

The Helmholtz-Institute Mainz on Structure, Symmetry and Stability of Matter and Antimatter focuses these relations with respect to the present research program at GSI and the future FAIR facility and will sustainably strengthen this research with high visibility. HIM is embedded in a highly productive research infrastructure on the campus of the Johannes Gutenberg University Mainz with the pulsed research reactor TRIGA and the 1.5 GeV electron accelerator MAMI. The existing expertise in the fields of atomic, nuclear, hadron, and accelerator physics at Mainz University and at GSI are unique and will yield new and leading contributions to the program at GSI and FAIR.

The precise quantitative understanding of the effects of strong interaction in atomic, nuclear, and particle physics is the general research goal of HIM. Due to exciting new developments both in theory and experiment, this seems to be attainable in many cases. The research program will concentrate on the following main lines:

- Investigation of the fundamental questions of space-time, spin and flavor structure of proton and antiproton and their interaction, yielding finally a tomography of hadrons.
- Investigation of the limits of the symmetries of the standard model in many systems as a search for exciting new physics beyond the standard model complementary to the high energy frontier at LHC: anti- hydrogen, gravitation, exotic mesons, glue balls, CPT- and CP-violating variables, dark matter, neutrino interaction, hypernuclei and charm in nuclei.
- Investigation of the limits of stability in nuclei: exploring the chemistry and physics of superheavy elements including the production and detection of new superheavy elements.
- Research for and design and construction of highest luminosity particle accelerators and their detector integration which represent the ground for the experimental work proposed here.

In order to address these topics, a research program concentrated on contributions to the PANDA project at the HESR, to the antiprotonic atomic physics program at FLAIR, to an 8 MV electron cooler at the HESR and the prototyping for a CW low-energy linear accelerator for the production of superheavy elements with participation at GSI/FAIR is foreseen as well as a long range activity, namely a feasibility study for an electron-nucleon collider for a possible future upgrade of FAIR.

HIM will be a condensation nucleus in an international context. There are important structural elements of the proposed Helmholtz Institute in Mainz which will serve this purpose: an international guest scientists program including the organization of workshops and conferences, and the establishment of young investigator groups. Structured PhD-education of young researchers will be ensured by the common GSI-University Mainz research school MainS, which is integrated in the existing Helmholtz Graduate School HGS-HIRE.

The scientific program of HIM together with its structural aspects has been evaluated to be excellent in all aspects by the international evaluation committee. The core activity of HIM is aligned with and will strengthen the strategy of the Helmholtz programs Physics of Hadrons and Nuclei and Physics with Photons, Neutrons and Ions along the mission of the Helmholtz Association. The Helmholtz Institute is funded to 90% by the BMBF via the Helmholtz association and to 10% by the state Rhineland-Palatinate and will reach a steady state annual budget of 5,5 Mio Euro in 2011. This will be complemented by about 4,9 Mio Euro from Mainz University in the form of infrastructure. The State Rhineland-Palatinate has announced the funding for a building to host the HIM on the Mainz University campus.

The Helmholtz Insitute Jena

An intriguing field of research has opened up in combining particle accelerator and laser technology. Striking examples are the free-electron laser and precision laser spectroscopy on cooled highly charged ions confined in storage rings and traps. Ultrahigh-power lasers now create a situation, in which intense laser light can interact with accelerated particles and actively control their acceleration. This way technologies and applications of particle accelerators and high-power lasers have become increasingly entangled.

The new Helmholtz Institute Jena (HIJ) includes, as partners, the two Helmholtz research centres active in this field, the Deutsches Elektronen Synchrotron DESY and the GSI Helmholtzzentrum für Schwerionenforschung, as well as the Friedrich Schiller-University (FSU) at Jena. It will focus on new and unique scientific and technological applications enabled by combining the expertise of these internationally renowned institutions in the fields of advanced particle acceleration, lasers, and x-ray science and technology. The proposed institute will also play a key role in making efficient use of the unique experimental infrastructures: the large-scale heavy-ion facilities at GSI and at the future international FAIR facility, the free electron laser FLASH at DESY and the future european XFEL as well as the world class laser installations POLARIS at FSU and PHELIX at GSI. In the future, a collaboration with the Forschungszentrum Dresden-Rossendorf FZD with their dedicated electron accelerator and laser sources is anticipated.

The efforts for approaching the challenging goals of the institute are divided into the following five areas:

- Improving the performance of petawatt laser systems: The focus of the project is high-energy high-repetition rate laser technology. Deliverables of the project are the proof of principle for a high-repetition-rate petawatt-class laser at FAIR, with the experimental demonstration of the key technological issues at the POLARIS and PHELIX facilities and a major upgrade of the existing facilities in terms of pulse contrast and polarization control .

- Merging advanced solid-state laser technology with FEL sources: The long-term goal of this research area is the development of high-repetition-rate phase-stabilized few-cycle lasers for seeding free-electron lasers, for two-color pump probe experiments and eventually for the generation of intense attosecond hard x-ray pulses at the European XFEL.

- Laser particle acceleration: Laser particle acceleration is an exciting new approach providing ultra-short and brilliant particle pulses for a number of novel applications. This re-search area will benefit from GSI's competence in conditioning ions via monochromatization and bunch rotation, their expertise at PHELIX as well as FZD's and DESY's expertise in the handling and diagnosing of sub-ps-scale high-charge electron bunches.

- X-ray science, including high-resolution x-ray spectroscopy, polarimetry and laser-based x-ray generation: GSI, DESY and FSU are key centres of competence in x-ray spectrometry and instrumentation. The new institute will use the combination of this world-leading expertise for the development of novel spectrometers and polarimeters with unprecedented levels of resolution needed for, e.g., detecting QED effects in strong laser and Coloumb fields. It will also develop novel x-ray sources, e.g. for seeding FELs or for diagnostics of WDM.

- QED and relativistic ionization: The extremely high field strengths provided by heavy ions and/or petawatt lasers provide access to strong-field phenomena like relativistic many-particle ionization or even strong-field QED. It enables unprecedented studies of fundamental physics complementary to collider experiments. The vision of this project is to establish high-power lasers as a new tool for fundamental physics.

This research program follows the institute‘s mission of excellence in fundamental and applied research, which is also confirmed by the evaluation of the HIJ, initiated by the HGF, and it should bring clear strategic benefit to GSI (with FAIR) and DESY (with XFEL) as well as to the Friedrich Schiller-University.

The ExtreMe Matter Institute EMMI

P. Braun-Munzinger[1,2,3] and C. Ewerz[1,4]

[1]ExtreMe Matter Institute EMMI, GSI, Darmstadt, Germany; [2]GSI, Darmstadt, Germany; [3]TU Darmstadt, Germany; [4]University of Heidelberg, Germany

In November 2007 the senate of the Helmholtz foundation decided to fund the Helmholtz Alliance 'Cosmic Matter in the Laboratory' in the framework of the Helmholtz Alliance program. This program offers financial resources in order to create opportunities to investigate new topics and to innovatively advance research topics of current interest. The alliances aim to strategically enhance the profiles of the participating Helmholtz Centres and to transfer successful developments into one of the Helmholtz Association's research programs. The research performed within the Helmholtz Alliances is collaborative and brings universities, Helmholtz Centres and other non-university research institutions together. In the case of the alliance 'Cosmic Matter in the Laboratory' the funding contribution from the Helmholtz Association amounts to 18.745 Mio. Euro for six years.

A key step in the strategic positioning of the Helmholtz Alliance 'Cosmic matter in the Laboratory' is to establish a new, world-leading institute for research on matter at the extremes of density and temperature: the ExtreMe Matter Institute EMMI hosted by GSI. It has been founded when the alliance started in April 2008.

The scientific aim of the ExtreMe Matter Institute is to perform forefront research in the area of matter under extreme conditions. This comprises in particular four key areas of the research field 'Structure of Matter' of the Helmholtz Association:

- quark-gluon plasma and the phase structure of strongly interacting matter
- neutron matter
- electromagnetic plasmas of high energy density
- cold quantum gases and extreme states in atomic physics.

The relevant science themes range from the quark-gluon plasma as it existed shortly after the Big Bang to ultracold quantum gases created in laboratory experiments, and from hot and highly compressed classical bulk plasmas to the astrophysically relevant dense medium of nucleons and neutrons that governs the properties of the evolution of supernovae and neutron stars. It hence comprises the study of the coldest, of the hottest, and of the densest known forms of matter in the Universe. The key idea is to conduct this research in an interdisciplinary framework, based upon common underlying concepts for the theoretical and phenomenological understanding of the physical phenomena in the four areas.

Under the lead management of the GSI Helmholtz Centre for Heavy Ion Research the Alliance links 13 German and international research centers and universities as partner institutions:

- GSI Helmholtzzentrum für Schwerionenforschung, Darmstadt, Germany
- Forschungszentrum Jülich, Germany
- Ruprecht-Karls-Universität Heidelberg, Germany
- Johann Wolfgang Goethe Universität Frankfurt, Germany
- FIAS Frankfurt Institute for Advanced Studies, Germany
- Technische Universität Darmstadt, Germany
- Universität Münster, Germany
- Université VI, Paris, France
- Max-Planck-Institut für Kernphysik, Heidelberg, Germany
- Lawrence Berkeley National Laboratory, Berkeley, USA
- Joint Institute for Nuclear Astrophysics (JINA), USA
- RIKEN, Saitama, Japan
- University of Tokyo, Japan.

In addition, the Alliance benefits from the expertise of internationally renowned scientist who are closely linked to it as Associated Partners for the four research fields. Currently, the Alliance has 30 Associated Partners, among them two Nobel laureates. In 2009 a *Memorandum of Understanding for common projects* between the Joint Institute for High Temperatures RAS (JIHT) in Moskow, GSI and EMMI has been signed in order to strengthen the international collaboration. It is planned to establish a similar collaboration with the newly founded Helmholtz-Institut Jena. Also in order to foster the international networking, the instrument of an EMMI Visiting Professor has been established which allows to invite renowned experts to EMMI for extended periods in order to collaborate with EMMI members on concrete projects.

The central steering body of EMMI and of the Alliance is the Scientific Council, consisting of the EMMI Director, of one representative from each partner institution, and of two representatives of the Associated Partners. In December 2009 Prof. Johannes Wessels (University of Münster) has been elected as the new chairman of the Scientific Council. He follows Prof. James Symons (LBNL) in this office. The management of EMMI consists of the Scientific Director Prof. Peter Braun-Munzinger, the EMMI Administrator Dr. Heidrun Bojahr, the Scientific Coordinator Prof. Carlo Ewerz, and further administrative and IT support personnel. In 2009 the EMMI Program Advisory Committee consisting of eight external experts (two from each of the main research areas of EMMI) has been established. It advises EMMI on questions of the general scientific orientation and on the selection of workshop and program proposals.

As a central part of the EMMI activities four EMMI Fel-

low Groups – one for each of the main research areas – are established at GSI with tenure-track positions for the group leaders (EMMI Fellows) and further non-tenured positions. In 2009, two EMMI Fellows – Dr. Alexandre Gumberidze (atomic physics) and Dr. Paul Neumayer (plasma physics) – already started to build up their groups.

The partner institutions have committed themselves to creating 14 further new professorships (tenure-track and tenure) in the framework of the Alliance. While two of these positions (at MPI für Kernphysik and Univ. Münster) had been filled already in 2008, four other positions have been filled in 2009 at TU Darmstadt, Univ. of Heidelberg, FIAS and LBNL. Further positions are expected to be filled in 2010.

On the GSI site a new building with an attractive design is being constructed. Its main user will be the ExtreMe Matter Institute. The building will offer office space for about 200 scientists, a lecture hall and four seminar rooms. It will hence provide a unique infrastructure for the activities of EMMI, in particular for workshops and programs.

An important activity of the ExtreMe Matter Institute EMMI is to organize and to host such workshops and research programs on topical and interdisciplinary subjects in the area of matter under extreme conditions. Eight EMMI workshops took place in 2009, several of them were devoted particularly to the discussion of interdisciplinary aspects. The workshops lasted between one and five days, the number of participants varied between 30 and 70.

EMMI is strongly committed to fostering the education and training of young researchers through a postdoctoral research program and structured training of graduate students. EMMI collaborates closely with the nearby graduate schools like the Helmholtz Graduate School for Heavy-Ion Research (HGS-HIRe) and the Heidelberg Graduate School of Fundamental Physics (HGSFP) in order to ensure an optimal training for all doctoral students within EMMI.

In 2009 the research within EMMI resulted in a large number of publications. Among the highlights are the following:

- First proton-proton collisions were created and observed at the Large Hadron Collider LHC at CERN. EMMI scientists are members of the ALICE experiment and have contributed to the first publication of results obtained at the LHC.
- In reactions with radioactive beams at GSI (at the LAND-R3B setup) extremely neutron-rich nuclei beyond the neutron dripline could be studied, in particular ^{9}He and ^{10}He. The kinematically complete measurement of the decay of these unbound systems allows one to investigate two- and three-body correlations in such extremely neutron-rich systems.
- In a collaboration of atomic and nuclear physics the isotopic shift in the dielectric recombination of Li-like Nd^{57+} was shown for the first time. With that a new method has been established to determine the charge radii of exotic nuclei which is relevant for future experiments with short-lived isotopes.
- A collaboration of atomic and plasma physics concentrated on common experiments at the ESR and at the high power laser PHELIX at GSI. One focus is the creation of new light sources via intense laser pulses. It was possible to establish a new technique for the creation of a XUV laser. This will be of high interest for future experiments in the laser spectroscopy of highly charged ions.
- In an international collaboration a new view on the phase diagram of QCD was proposed. In this proposal there is a triple point instead of a critical endpoint. The corresponding experimental consequences will be tested at the RHIC collider at BNL (USA) and with the CBM experiment at FAIR.
- New interdisciplinary collaboration efforts have been established between the research on cold quantum gases and on the quark-gluon plasma. This subject was in particular the focus of several EMMI workshops. Interestingly, a better understanding of these apparently very different physical systems can be gained using common concepts and methods. An example is the use of string theory methods to describe these systems and their behavior.

Statutory organs and scientific advisory committees of GSI (2009)

Compiled by K.-D. Groß

Supervisory Board/Aufsichtsrat:

Dr. B. Vierkorn-Rudolph [chair],
Bundesministerium für Bildung und Forschung, Bonn/Berlin (Germany),
as representative of the Federal Republic of Germany

Ministerialrat Dr. R. Koepke,
Bundesministerium für Bildung und Forschung, Bonn/Berlin (Germany),
as representative of the Federal Republic of Germany

Ministerialdirigent Dr. R. Bernhardt,
Hessisches Ministerium für Wissenschaft und Kunst, Wiesbaden (Germany),
as representative of the State Hessen in Germany

Prof. Dr. R. Klanner,
Universität Hamburg/DESY (Germay),
as representatives of the Scientific Council of the GSI

Scientific Directorate/Wissenschaftliches Direktorium WD:

Prof. Dr. H. Stöcker, C. Neumann,
Dr. H. Eickhoff, Prof. Dr. K.-H. Langanke, B. Schönfelder,

Divisions/Direktionsbereiche:

Accelerator: H. Eickhoff
Administration: C. Neumann
Human Resources and Legal Service: A. Lambert
Finances and Controlling: J. Heilmann
FAIR TD: D. Krämer
Research: K. Langanke
Scientific and Technical Infrastructure: B. Schönfelder

Research Departments/Forschungsabteilungen:

ALICE: P. Braun-Munzinger
Atomic Physics: T. Stöhlker
Biophysics: M. Durante
CBM: P. Senger
FOPI: Y. Leifels
FRS: H. Geissel
HADES: J. Stroth
Hadron Physics I: K. Peters
Hadron Physics II: F. Maas
Materials Research: R. Neumann
Nuclear Reactions and Astrophysics: T. Aumann
Nuclear Structure Physics: C. Scheidenberger
Plasma Physics and PHELIX: T. Stöhlker
Superheavy Element/Nuclear Chemitry: F.-P. Hessberger/M. Schädel
Theory: Lattice QCD: F. Karsch

Theory: Nuclear Structure and Astrophysics: H. Feldmeier
Theory: Transport and Simulation: H. Stöcker
Theory: QCD and Hadron Physics: J. Wambach

Scientific Council/Wissenschaftlicher Rat WR:
<http://www.gsi.de/informationen/users/EAC/wr/>

R. Klanner [chair], Universität Hamburg (Germany); D. von Harrach [vice chair], Johannes-Gutenberg-Universität Mainz (Germany); R. Hayano, University of Tokyo, (Japan); K.-H. Kampert, Bergische Universitt Wupeprtal (Germany); C. Leemann, Thomas Jefferson National Accelerator Facility, Newport News (USA); B. Mueller, Duke University, Durham, North Carolina (USA); S. Myers, CERN AB, Geneva (Switzerland); T. Roser, BNL, Upton (USA); A. Shotter, TRIUMF, Vancouver (Canada); M. Soyeur, DSM/DAPNIA/SPhN, Gif-sur-Yvette (France); R. Sauerbrey, Forschungszentrum Rossendorf, Dresden (Germany); D. Vernhet, Université Paris (France); M. C. Wiescher, University of Notre Dame, Notre Dame, Indiana (USA).
Secretary: K.-D. Groß

Scientific Committee/Wissenschaftlicher Ausschuss WA:
<http://www-w2k.gsi.de/wa/scientific_committee.htm>

H. Simon [chair]; Y. Leifels [vice chair]; D. Ackermann; E. Badura; J. Heuser; B. Lommel; M. Lutz; P. Malzacher; M. Mnch; M. Reich-Sprenger; S. Richter; M. Scholz; L. Schmitt; G. Schreiber; M. Steck; C. Trautmann; G. Walter; H. Weick; A. Bruning-Demian (guest); H. Kreiser (guest).

Scientific Advisory Committees to GSI

GSI General Programme Advisory Committee G-PAC:
<http://www.gsi.de/informationen/users/EAC/ea/>

J. Aichelin, SUBATECH, Nantes (France); W. Catford, University of Surrey, Guildford (UK); P. Giubellino, INFN Turin, Torino (Italy); R. Hoekstra, KVI Groningen, Groningen (The Netherlands); R. Krücken, Technische Universität München, Physik-Department (Germany); M. Lewitowicz, GANIL, Caen (France); T. Peitzmann, Utrecht University (The Netherlands); N. Pietralla, Technische Universität Darmstadt, Darmstadt (Germany); H. Schatz, Michigan State University, East Lansing (USA); M. Wada, RIKEN, Saitama (Japan); M. Weidemüller, Universität Freiburg (Germany); E. Widmann, Stefan-Meyer-Institut für subatomare Physik, Österreichische Akademie der Wissenschaften, Vienna (Austria).
Secretary: A. Tauschwitz

GSI Phelix and Plasmaphysics Program Advisory Committee (PPAC):
<http://www.gsi.de/informationen/users/EAC/ppac/>

M. H. R. Hutchinson [Chair], Rutherford Appleton Lab (United Kingdom); S. Jacquemot, LULI, Ecole Polytechnique, Palaiseau (France); G. Logan, LBL Berkeley (USA); T. A. Mehlhorn, Sandia National Laboratories, Albuquerque (USA); R. Sauerbrey, Forschungszentrum Rossendorf, Dresden (Germany); B. Sharkov, Inst. of Theoretical and Experimental Physics Moscow (Russia).
Secretary: K. Füssel

GSI Biophysics & Radio-Biology Program Advisory Committee (Bio-PAC):
<http://www.gsi.de/informationen/users/EAC/bio-pac/>

G. Iliakis [Chair], Institut für Medizinische Strahlenbiologie Universitätsklinikum Essen (Germany); F. A. Cucinotto, NASA Johson Space Center, Houston TX (USA); R. Engenhardt-Cabillic, Klinik für Strahlentherapie Philipps-Universität Marburg Klinikum (Germany); B. Michael, Gray Lab (Cancer Research Trust), Mount-Vernon-Hospital, Northwood (United Kingdom); R. Okayasu, National Institute of Radiological Sciences, Chiba-shi (Japan); E. Pedroni, Paul Scherrer Institut, Villigen (Switzerland).
Secretary: K. Füssel

GSI Materials Research Program Advisory Committee (Mat-PAC):

<http://www.gsi.de/informationen/users/EAC/mat-pac/>

P. Apel, JINR Dubna (Russia); S. Bouffard, CEA-CNRS-ENSICAEN Caen (France); K. Hjort, University of Uppsala (Sweden); W. Wesch, Friedrich Schiller Universittät Jena (Germany).
Secretary: A. Tauschwitz

Program Advisory Committee for FAIR-Related Beam Time Proposals (F-PAC):

J. Stadlmann (Chair), GSI; Z. Maika, FAIR; L. Schmitt, GSI; W. Mller, GSI; C. Trautmann, GSI.
Secretary: A. Tauschwitz

GSI Users' Group Executive Committee (UEC):

<http://www.gsi.de/forschung/usersgroup/index.html>

P. Regan (UK)[Chair-elect]; N. Bastid (France); W. Cassing (Germany); D. Cortina (Spain); D. Dauvergne (France); W. Ensinger (Germany); T. Faestermann (Germany); J. Jacoby (Germany); A. Jungclaus (Spain); J. Kratz (Germany); T. Khl (Germany); M. Lbrich (Germany); T. Matulewicz (Poland); A. Mller (Germany); M. Pfutzner (Poland); P. Salabura (Poland); B. Schuster (Germany) A. Trler (Germany).

Scientific Coordination:

Dr. K. D. Groß

Facts and Figures

Compiled by J. Heilmann, C. Kausch

Gesellschafter/Shareholders since 1969, December 17th

Federal Republic of Germany	90% of budget (and of share capital)
State of Hesse/Land Hessen	10% of budget (and of share capital)

Accelerators

FAIR	Facility for Antiprotons and Ion Research		pre- construction R&D
UNILAC	UNIversal Linear ACcelerator	13 MeV/u for U	in operation since 1976
SIS	Schwer-Ionen-Synchrotron	50–1000 MeV/u for U	in operation since 1989
ESR	Experimental Storage Ring	3–400 MeV/u for U	in operation since 1990

Users of the accelerator complex

In 2009, GSI provided access to about 25 experimental areas to more than 1550 scientific users.

GSI Funding in Mio. Euro

research area Structure of Matter	71.5	
research area Health	3.8	
Helmholtz Institutes (Mainz and Jena)	4.2	
FAIR	10.5	
joint initiative for innovation and research (IVF)	2.6	
special funding from the German economic stimulus package	2.9	
third party funding and special support	8.2	
total budget		**103.7 Mio. Euro**

Personnel 2009 in person years

research area Structure of Matter	387	
FAIR-activities (Structure of Matter)	142	
research area Health	28	
management and management support	79	
scientific and technical infrastructure	201	
personnel involved in projects funded by nat./internat. funding agencies	122	
total personnel		**959 person years**

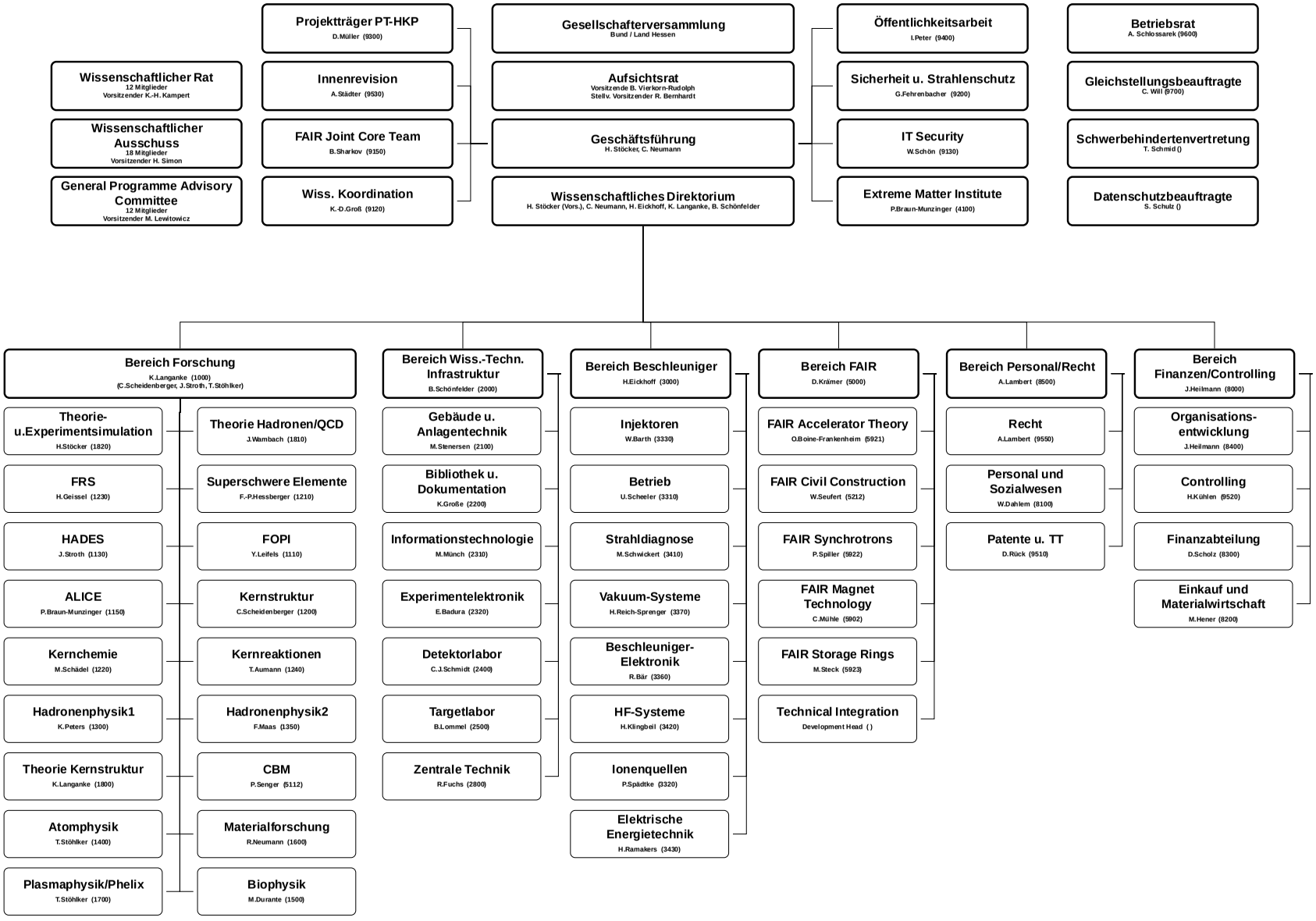

Stand Dezember 2009

List of Authors